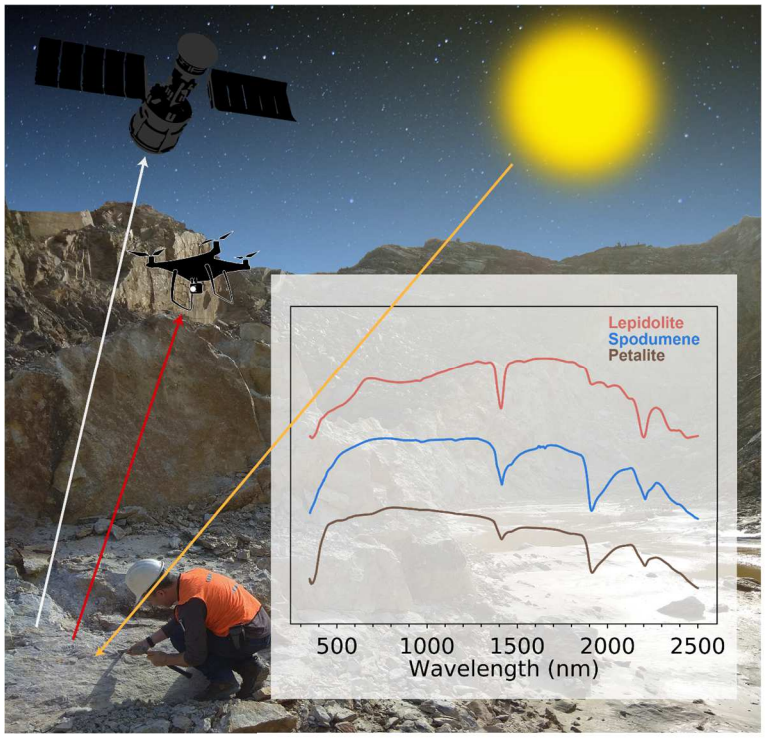

Remote sensing applied to lithium mineralizations: insights for lithium exploration

Joana Maria Cardoso Fernandes

Doutoramento em Geociências

Departamento de Geociências, Ambiente e Ordenamento do Território

2021

Orientador

Alexandre Martins Campos de Lima, Professor Associado Faculdade de Ciências da Universidade do Porto

Coorientador

Ana Cláudia Moreira Teodoro, Professora Associada com Agregação Faculdade de Ciências da Universidade do Porto

Maria Encarnación Roda-Robles, Professora Titular do Departamento de Geologia da Universidade do País Basco

Joana Maria Cardoso Fernandes has been financially supported within the compass of a Ph.D. Thesis, ref. SFRH/BD/136108/2018, by Portuguese national funds from the Ministério da Ciência, Tecnologia e Ensino Superior (MCTES) through FCT– Fundação para a Ciência e a Tecnologia, I.P., and co-financed by the European Social Fund (ESF) through POCH – Programa Operacional Capital Humano – and NORTE 2020 regional program.

The work conducted in this thesis was also supported by Portuguese National Funds through the FCT projects UIDB/04683/2020 and UIDP/04683/2020 - ICT (Institute of Earth Sciences), and the European projects ERA-MIN/0001/2017 – LIGHTS and 869274 — GREENPEG — H2020-SC5-2018-2019-2020.

Agradecimentos

Esta tese representa o culminar de uma longa jornada de trabalho que não seria possível sem a contribuição, ajuda, e paciência de várias pessoas que caminharam a meu lado, ao longo destes três últimos anos. A todos quero expressar a minha imensa gratidão!

Quero desde já começar por agradecer profundamente aos meus orientadores, o Prof. Alexandre Lima, a Prof. Ana Cláudia Teodoro, e a Prof. Encarnación Roda-Robles, que foram incansáveis na supervisão científica de todos os trabalhos, no apoio a nível académico e também por todos os conselhos dados que me ajudaram a chegar a este exato momento. Quero agradecer pela confiança depositada em mim e por me terem providenciado várias oportunidades, aqui e no estrangeiro, de desenvolvimento científico, académico e até mesmo pessoal. Ao Prof. Alexandre, quero agradecer em especial a disponibilização de todos os meios necessários à concretização deste trabalho, a ajuda em todas as saídas de campo, e toda a preocupação com o desenrolar da minha carreira profissional. À Prof. Ana Cláudia, obrigada por todo o acompanhamento, por me contagiar com a sua energia inovadora e vanguardista, incentivando-me abraçar novos desafios, e por partilhar comigo todos os ensinamentos provenientes da sua experiência. À Prof. Encarnación agradeço pelo acompanhamento e preocupação, muitas vezes à distância, e por todos os ensinamentos teóricos e práticos que contribuíram para eu fosse (ainda mais) organizada e tivesse (ainda mais) rigor científico. Ao longo desta jornada, mais de que orientadores científicos tornaram-se amigos e mentores, sendo verdadeiros exemplos a seguir não só como investigadores, professores, mas também como colegas e pais/mães de família.

Para além de toda a orientação, gostaria também de agradecer pela disponibilidade e ajuda de vários outros docentes e investigadores.

À Prof. Maria do Anjos queria agradecer por todas as horas passadas comigo ao microscópio, por todos os ensinamentos e acompanhamento feito no âmbito das interpretações petrográficas e litogeoquímicas, e pelo apoio nas saídas de campo. É sempre um prazer aprender com quem fala apaixonadamente sobre aquilo com que trabalha.

À Dr. Mônica Perrotta agradeço por toda a sua contribuição ao nível da espetroscopia de refletância e deteção remota, e pela paciência na revisão cuidadosa de todas as interpretações espetrais. Obrigada por partilhar comigo o “bichinho” e o gosto de tentar decifrar a mineralogia espetral.

Ao Prof. Nelson Pires com quem aprendi a programar em *Python*, queria agradecer por toda ajuda com a otimização de *scripts* e partilha de dados. As bases de programação que me transmitiu, através de exemplos simples mas adequados, foram o pilar e fio condutor de toda esta tese não só no desenvolvimento de algoritmos de deteção remota, mas na análise dos espetros de refletância e no tratamento dos diversos dados geoquímicos.

Queria também deixar um agradecimento a todos os colegas e parceiros do projeto LIGHTS, com os quais tive o prazer de colaborar e aprender, muitas vezes à distância, e cuja contribuição permitiu enriquecer diversos trabalhos realizados no âmbito desta tese.

Expresso também a minha gratidão pela forma como fui gentilmente acolhida no Departamento de Geologia da Universidade do País Basco, nomeadamente pelo Prof. Alfonso Pesquera e Prof. Pedro Gil-Crespo, e pela disponibilidade das técnicas de preparação de amostras e análises químicas. Deixo também um agradecimento especial ao Jon Errandonea e à Idoia Garate, com os quais foi um verdadeiro prazer colaborar no âmbito do projeto GREENPEG, quer em saídas de campo quer nas várias discussões frutíferas que tivemos ao longo do tempo, presencialmente ou à distância.

Aos colegas do espaço geologia, Cátia Dias, Ricardo Ribeiro, Jessica Lima, Filipa Dias, Filipe Gonçalves, Julia Tucker e Rui Frutuoso, sempre com paciência para me ouvir, prontos para trocar ideias e disponíveis para ajudar quer no campo quer na preparação de amostras, obrigada pois a vossa ajuda foi imprescindível. Quero também agradecer os meus restantes colegas de doutoramento nomeadamente ao Ubaldo Gemusse, à Sara Leal, e à Ana Marta Gonçalves, obrigada por partilharem um pouco vosso percurso e experiência comigo. Expresso também o meu agradecimento aos estudantes de mestrado que tive o prazer de acompanhar de perto, João Silva, Douglas Santos, Cátia Rodrigues, Ariane Pinto, e que também contribuíram para a realização deste trabalho.

Quero agradecer à Felmica, Minerais Industriais, S. A. (MOTA CERAMIC SOLUTIONS®), em particular ao Dr. Paulo Moutela e Dr. Hélder Albuquerque, pela disponibilidade e permissão para recolha de amostras e pela partilha de dados.

De igual forma, quero deixar um agradecimento ao Laboratório Nacional de Energia e Geologia (LNEG; Laboratório de S. M. Infesta), e em particular ao Dr. Augusto Filipe, pela célere colaboração no envio e partilha de dados.

Deixo também um agradecimento aos técnicos do Departamento de Geociências, Ambiente e Ordenamento do Território, nomeadamente à Dra. Cândida Neto e à D. Irene Costa, pela ajuda com as análises geoquímicas e preparação de amostras.

Por fim, mas não menos importante, agradeço do fundo do coração todo o apoio incondicional dado pelos meus amigos e pela minha família. Obrigada pela vossa compreensão e motivação nos momentos mais difíceis e pelo vosso entusiasmo na celebração de todas as novas conquistas.

Um agradecimento especial ao meu irmão, pela paciência e ajuda à distância com a programação em *Matlab* ou na digitalização dos meus apontamentos.

Aos meus pais e aos pais do António, agradeço por todo suporte e por me terem permitido focar nesta jornada, ajudando-me e aliviando-me o peso das tarefas domésticas. Quero deixar um agradecimento especial à minha mãe Manuela, que mais do que minha mãe é também a minha melhor amiga: obrigada por tudo!

Ao António, que me ajudou de mil e uma formas ao longo deste percurso, quer na revisão de inglês, na elaboração de figuras, formatação das tabelas, mas acima de tudo que me ouviu vezes sem conta, me limpou as lágrimas e fez de tudo para cuidar de mim quando eu não tinha tempo para o fazer, obrigada! Foste a minha rocha e porto de abrigo. Esta tese não existiria sem ti…

Resumo

É impossível ignorar a crescente importância e procura de lítio (Li) para diversas aplicações industriais de entre as quais se destaca a produção de baterias recarregáveis de iões de Li, maioritariamente para o fabrico de veículos elétricos e outras tecnologias de baixo carbono. De momento, o Li é considerado crítico para a União Europeia, sendo que os maiores depósitos de Li europeus são em pegmatitos. Em paralelo, atingir uma prospeção mineral sustentável é, hoje em dia, uma grande preocupação. Sendo assim, são necessários métodos de prospeção menos intrusivos e mais "amigos" do ambiente para a identificação de novos depósitos de Li.

O objetivo desta tese é desenvolver métodos de prospeção inovadores – algoritmos de deteção remota – capazes de identificar pegmatitos de Li sem contacto direto com a superfície. De forma a validar e aperfeiçoar os métodos desenvolvidos, vários estudos petrográficos, geoquímicos e espetrais complementares foram desenvolvidos para caracterizar: (i) as assinaturas específicas da mineralização em Li, (ii) as paragéneses minerais associadas, e (iii) os estilos de alteração. Paralelamente, outros métodos capazes de identificar pegmatitos escondidos em profundidade foram aplicados para complementar a abordagem feita com recurso à deteção remota.

A área de estudo deste trabalho é o campo aplitopegmatítico de Fregeneda (Salamanca, Espanha)-Almendra (Vila Nova de Foz Côa, Portugal), onde estão mapeados diferentes tipos de filões mineralizados em Li.

Diferentes estratégias podem ser utilizadas para detetar remotamente mineralizações de Li usando dados de satélite, sendo que as principais dificuldades identificadas em aplicações passadas foram: (i) falta de um processo automático para a identificação de pegmatitos de Li; (ii) encontrar o balanço certo entre resolução espacial e espetral; (iii) presença de vegetação ou outro tipo de coberturas que possam mascarar a assinatura dos pegmatitos de Li; e (iv) inexistência de conhecimento detalhado da paragénese de alteração específica e estilo de alteração hidrotermal associados. No âmbito deste trabalho, foram propostos novos avanços metodológicos bem como automatização de algoritmos *machine learning* já propostos na literatura para discriminar com sucesso ocorrências de pegmatitos de Li e outras áreas-alvo para a prospeção de Li. Mais ainda, foram compiladas duas grandes bases de dados abertas através da recolha de espetros de reflectância e de espetros LIBS (*laser-induced breakdown spectroscopy*) de minerais e rochas ricas em Li, que estão disponíveis para qualquer utilizador e que servirão de base para o desenvolvimento de outras novas aplicações. A interpretação

de espetros de refletância representativos permitiu obter um conhecimento aprofundado sobre o comportamento espetral dos minerais de Li: enquanto a lepidolite pode ser identificada através das suas feições de absorção diagnósticas, a espodumena e petalite não apresentam nenhuma feição diagnóstica, sendo os seus espetros dominados pela presença de argilas. Para além disso, os resultados demonstram a capacidade de os sensores hiperespetrais em discriminar os pegmatitos de Li das restantes litologias da área de estudo, abrindo assim novas possibilidades para a descoberta de pegmatitos a nível mundial. O reprocessamento de dados históricos de sedimentos de corrente foi eficaz na identificação de novos pegmatitos mineralizados em Li. Além disso, avaliou-se a adequabilidade de diferentes abordagens metodológicas tendo em conta as distintas fases de prospeção, o que pode ser útil para outros trabalhos semelhantes. Estudos geoquímicos compreensivos mostraram que a intrusão de pegmatitos na região de Fregeneda-Almendra provocou reações exomórficas que formaram halos metassomáticos, enriquecidos em elementos como o Li, Cs e Rb, que podem atingir distâncias de 4 a 5 vezes a espessura dos filões. Tais halos podem ser usados na identificação de pegmatitos em profundidade através do uso de ferramentas portáteis, por exemplo, mas outros métodos de prospeção inovadores poderão ser desenvolvidos no futuro. Por fim, foram usadas ferramentas de prospectividade mineral, nomeadamente algoritmos *machine learning*, para integrar dados de deteção remota, geoquímicos e geológicos, e produzir mapas com alvos de prospeção, capazes de identificar áreas com maior potencial para mineralização em Li com possibilidade de investigação futura.

Em última análise, este trabalho apresenta metodologias novas e aperfeiçoadas, assim como novos conhecimentos para a prospeção de Li que têm grande impacto no estado da arte e que podem levar a uma prospeção mineral mais sustentável e eficiente.

Palavras-chave: Lítio, Deteção Remota, Prospeção mineral, Geoquímica, Pegmatito, M*achine learning*, Bibliotecas espetrais, Espetroscopia de refletância, LIBS, Dados hiperespetrais, Sedimentos de corrente, Halos metassomáticos, Preditividade mineral

Abstract

It is impossible to ignore the growing importance and demand of lithium (Li) for several industrial applications among which the production of rechargeable Li-ion batteries stands outs, mainly for the construction of electric vehicles and other low-carbon technologies. Currently, Li is considered critical for the European Union, being the major European Li-deposits hosted in pegmatites. Moreover, achieving sustainable mineral exploration is of big concern. Therefore, less intrusive, environmentally-friendly exploration methods are needed to identify new Li-deposits.

The objective of this thesis was to develop innovative exploration methods – remote sensing algorithms – capable of identifying Li-pegmatites at distance. To validate and improve the developed methods several complementary petrographic, geochemical, and spectral studies were employed to characterize: (i) the specific signatures of the Li-mineralization, (ii) associated mineral assemblages, and (iii) alteration footprints. In parallel, other methods capable of identifying hidden, buried pegmatites were employed to complement the remote sensing approach. The study area of this work was the Fregeneda (Salamanca, Spain)-Almendra (Vila Nova de Foz Côa, Portugal) aplite-pegmatite field where distinct types of Li-bearing dykes are mapped.

Different strategies can be employed to remotely detect Li-mineralizations using satellite data, but the main difficulties identified in past applications were: (i) lack of an automated process for Li-pegmatite identification; (ii) finding the right balance between spatial and spectral resolution; (iii) vegetation or other coverages that can mask the signature of Li-pegmatites; and (iv) lack of detailed knowledge on the specific alteration paragenesis and style of the related hydrothermal alteration. In the scope of this work, new methodological advances and automatization of machine learning algorithms were proposed to successfully discriminate Li-pegmatite occurrences and other target areas for Li-exploration. Also, two large and openly available datasets were composed through the collection of reflectance and laser-induced breakdown spectroscopy (LIBS) spectra of Li-minerals and rocks that are available to any user and that will serve as a starting point for the development of other new applications. The interpretation of key reference spectra provided insightful knowledge on the spectral behavior of Li-minerals: lepidolite can be discriminated through its diagnostic absorption features, while spodumene and petalite do not have any diagnostic feature, with their spectral behavior dominated by the presence of clays. Moreover, the results demonstrate the potential to use hyperspectral sensors to discriminate Li-pegmatites from the remaining lithologies in the case

study area, opening new possibilities for Li-pegmatite discoveries around the world. The reprocessing of historical stream sediment datasets was effective in the identification of new Li-mineralized pegmatites. Additionally, the applicability of distinct methodological approaches was evaluated concerning different exploration stages, which can be of help for other similar studies. A comprehensive geochemical study demonstrated that pegmatite intrusion in the Fregenda-Almendra area led to exomorphic reactions forming metasomatized halos, enriched in elements such as Li, Cs, and Rb, that can reach up to 4 to 5 times the thickness of the dykes. These haloes can be used to identify buried pegmatites through the use of portable tools, for example, but other innovative exploration methods could be developed in the future. Finally, mineral prospectivity mapping tools, namely machine learning algorithms, were employed to integrate remote sensing, geochemical and geological data to produce target exploration maps and identify the areas with higher potential for Li-mineralization that are worthy of future investigation.

Ultimately, this work provides new and improved methods as well as new insights for Li-exploration, that have a high impact on the state of the art and can lead to more sustainable and efficient mineral exploration.

Keywords: Lithium, Remote sensing, Mineral exploration, Geochemistry, Pegmatite, Machine learning algorithms, Spectral libraries, Reflectance spectroscopy, LIBS, Hyperspectral data, Stream sediments, Metasomatic haloes, Mineral Prospectivity Mapping

Table of contents

Agradecimentos 3

Resumo 7

Abstract 9

Abbreviations 13

Introduction 19

Background 19

Objectives 20

Thesis structure and outline 21

Case study: The Fregeneda-Almendra area 23

References 36

Chapter I: State of the art 47

I.1. Constraints and potentials of remote sensing data/techniques applied to Lithium (Li)-pegmatites 47

I.2. Detecting Lithium (Li) Mineralizations from Space: Current Research and Future Perspectives 52

Chapter II: Development of new remote sensing algorithms 87

II.1. Semi-Automatization of Support Vector Machines to Map Lithium (Li) Bearing Pegmatites 89

Chapter III: Spectral libraries for Li-exploration 123

III.1. Building the spectral libraries 125

III.1.1. Tools for Remote Exploration: A Lithium (Li) Dedicated Spectral Library of the Fregeneda–Almendra Aplite–Pegmatite Field 125

III.1.2. Analyses of Li-Rich Minerals Using Handheld LIBS Tool 141

III.2. Interpretation of the reflectance spectra of Lithium (Li) minerals and pegmatites: a case study for mineralogical and lithological identification in the Fregeneda-Almendra area ... 162

Chapter IV: Geochemical exploration techniques as a complementary tool 211

IV.1. Stream sediment analysis for Lithium (Li) exploration in the Douro region (Portugal): a comparative study of the spatial interpolation and catchment basin approaches 215

IV.2. Metasomatic effect of granitic aplite-pegmatite dykes in psammopelitic metasediments; mass-transfer quantification from whole-rock lithogeochemistry at La Fregeneda–Almendra (Central Iberian Zone) 252

Chapter V: Data integration and prospectivity mapping 297

V.1. Lithium Potential Mapping Using Artificial Neural Networks: A Case Study from Central Portugal 299

Discussion 335

Conclusions 345

References 347

Appendices 421

Abbreviations

The following abbreviations were used:

Actlabs	Activation Laboratories Ltd.
ANN	Artificial Neural Network
ASTER	Advanced Spaceborne Thermal Emission and Reflection Radiometer
AUC	area under the curve
avgnn	average nearest neighbor
BRGM	Bureau de Recherches Géologiques et Minières
C-A	concentration area
CEM	constrained energy minimization
CIA	Chemical Index of Alteration
CIZ	Central Iberian Zone
CNN	convolutional neural network
CPRM	Geological Survey of Brazil
crs	continuum removed spectra
CSIRO	Commonwealth Scientific and Industrial Research Organization
CSV	comma-separated values
CV	cross-validation
CXG	Complexo Xisto–Grauváquico (Schist–graywacke complex)
DBNs	deep belief networks
DEM	digital elevation model
DL	deep learning
DTs	decision trees
E	East

EDA	exploratory data analysis
EOS	Earth Observing System
EPMA	electron probe microanalysis
ESA	European Space Agency
ESE	East-southeast
ESF	European Social Fund
ETM+	Enhanced Thematic Mapper Plus
EU	European Union
FA	Fregeneda-Almendra
FAF	Fregenedra-Almendra pegmatitic field
FCR–LAC	Figueira de Castelo Rodrigo–Lumbrales Anatectic Complex
FIS	fuzzy inference system
FWHM	full-width at half maximum
GIS	Geographic Information System
GTMZ	Galicia-Trás-os-Montes Zone
HFSE	High-Field Strength Elements
HREE	Heavy Rare Earth Elements
HSI	hyperspectral imaging data
ICP-MS	Inductively Coupled Plasma - Mass Spectrometer
ICP-OES	inductively coupled plasma - optical emission spectrometry
ICT	Institute of Earth Sciences
ICV	Index of Compositional Variability
IDW	inverse distance weighting
IOCG	iron oxide-copper-gold

IQR	interquartile range
ISE	Ion Selective Electrode
JM	Jeffries–Matusita
k-NN	k-Nearest Neighbor
Lab	laboratory
LCS	land cover signature classification
LCT	Lithium-Cesium-Tantalum
Li	lithium
LIBS	laser-induced breakdown spectroscopy
LIGHTS	Lightweight Integrated Ground and Airborne Hyperspectral Topological Solution
LNEG	National Laboratory of Energy and Geology
LREE	Light Rare Earth Elements
LSU	linear spectral unmixing
LULC	land-use/land-cover
MEPL	Mêda–Escalhão–Penedono–Lumbrales
MF	matched filtering
MLAs	machine learning algorithms
MNF	minimum noise fraction
MPM	Mineral prospectivity mapping
MSAM	Modified Spectral Angle Mapper
MSI	Multispectral Instrument
MSS	Multispectral Scanner System
MTMF	mixture-tuned matched filtering
N	North

NASA	National Aeronautics and Space Administration
NBR	Normalized Burn Ratio
N-CIZ	North-Central Iberian Zone
NE	Northeast
NEdL	noise equivalent radiance
NIBAS	Neoproterozoic Iberian Average Shale
NIR	Near Infra-Red
NNW	North-northwest
NW	Northwest
OA	overall accuracy
OLI	Operational Land Imager
ORDaR	OTELo Research Data Repository
OSD	Ollo de Sapo Domain
OSM	Open Street Map
PA	producer's accuracy
PAAS	Post Archean Australian Shale
Pb	lead
PC	Principal Component
PCA	principal component analysis
PNG	portable network graphics
PPI	pixel purity index
PRISMA	Prototype Research Instruments and Space Mission technology Advancement
pts	points
RBF	radial basis function

REE	rare-earth element
RF	random forest
RGB	red, green, blue
ROC	receiver operating characteristic
ROI	region of interest
S	South
SAEs	stacked auto-encoders
SAM	spectral angle mapper
S-CIZ	Southern Central Iberian Zone
SE	Southeast
SEM	scanning electron microscopy
SEM-EDS	Scanning Electron Microscopy with Energy Dispersive Spectroscopy
SFM	Serviço de Fomento Mineiro
SGC	Schist-Graywacke Complex
SGD	Schist-Greywacke Domain
SNAP	Sentinel Application Platform
SNV	standard normal variate
SOM	self-organizing maps
SSE	South-southeast
SSW	South-southwest
SVM	support vector machine
SW	Southwest
SWIR	shortwave infrared
TD	transformed divergence

TE	thermoelectrically
TIR	thermal infrared
TIRS	Thermal Infrared Sensor
TM	Thematic Mapper
UA	user's accuracy
UCC	Upper Continental Crust
USGS	United States Geological Survey
UTF	unicode transformation format
VHMS	volcanic-hosted massive sulfide
VMS	volcanogenic massive sulfide
VNIR	visible and near-infrared
W	West
WGS	World Geodetic System
WNW	West-northwest
XRD	X-ray diffraction
XRF	X-Ray Fluorescence
Zn	zinc

Introduction

Background

In the past decade, green technologies represent an important sector of the economy capable of tackling the current environmental issues (Christmann *et al.*, 2015). Thus, in recent years there has been an increasing demand for critical raw materials, that are key to this green energy transition and global decarbonization, therefore having great economic and strategic relevance (Blengini *et al.*, 2020). One of these strategic raw materials is lithium (Li) that, when incorporated in compounds such as Li Hydroxide (LiOH), is used in the production of rechargeable Li-ion batteries mainly used in high-tech consumer electronics (like smartphones) and electric vehicles.

According to Kesler *et al.* (2012), the major European Li-deposits are hosted in pegmatites, being Europe a net-importer of Li (Grosjean *et al.*, 2012; Arrobas *et al.*, 2017). That is why this commodity is now considered critical for the European Union, not only for its economic importance but also for possible risk of supply (European Commission: DG Internal Market Industry Entrepreneurship and SMEs, 2020). The pursuit for more environment-friendly means of transportation and the changing motorization industry is already creating big pressure to meet market demands on a global scale (Gourcerol *et al.*, 2019). The perspective of intensive Li exploitation in the near future makes the identification of new Li deposits fundamental, with mining and exploration companies trying to achieve fast but accurate results in targeting potentially economic areas.

On the other hand, social acceptance of mineral exploration is nowadays a big concern in Europe and worldwide. Achieving sustainable mineral exploration is a major goal and less intrusive sensing techniques are being developed to replace, as far as possible, high-impact activities such as drilling (Kesselring *et al.*, 2020; Ruiz-Coupeau *et al.*, 2020). Additionally, due to a lack of knowledge about what is mineral exploration and the frequent confusion between exploration and mining activities, populations and the local power fear for the security of their homes, animals, and crops. Therefore, it is crucial to introduce innovative, more conscious, environmental-friendly exploration techniques especially during the early stages of exploration campaigns where the sustainability factors can decide the success of a project (Kesselring *et al.*, 2020).

Remote sensing is one of the alternative tools since it represents one of the less intrusive exploration methods, especially when the sensors are satellite-born. Remote sensing

techniques have been used in mineral exploration for more than four decades now (Sabins, 1999), and new applications of remote sensors to geological problems are emerging (Van der Werff & Van der Meer, 2016; Abrams & Yamaguchi, 2019). One of the main advantages is the existence of freely available images capable of covering large areas of interest. However, most of these techniques can only detect surface pegmatite-hosted deposits. Thus, it is necessary to complement the remote sensing approach with other methods capable of identifying hidden, buried pegmatites. In the past, the importance of geochemical campaigns was already established, allowing the discovery of non-outcropping pegmatites such as the Dibs pegmatite (Bird River Greenstone Belt, Manitoba, Canada) in 1996 and 1997 (Galeschuk & Vanstone, 2007; Martins *et al.*, 2017). Moreover, with the advent of portable semi-quantitative analytical equipment, there is a new undisclosed potential for *in situ* geochemical exploration without the need for (so many) sample collection and extraction.

Objectives

The main objective of this thesis was to use new tools and develop new methodologies capable of identifying Li-deposits through remote sensing data/techniques. In the end, Li-target exploration maps were produced through the integration of the spectral data, acquired by satellite sensors, with the pre-existing and the new geological field data.

Moreover, the research conducted in the scope of this thesis aimed to fill different gaps, namely: (i) the inexistence of Sentinel-2 applications in geology; (ii) the inexistence of a reference reflectance spectrum for petalite; and (iii) the lack of an automated, low-impact, environmentally friendly toolset for Li-pegmatite exploration.

The specific objectives of this thesis included:

- Use remote and lab techniques to identify the specific combinations of signatures characteristic of the Li-mineralization;
- Validation of the remote sensing data acquired through *in situ* spectroscopic calibration and simultaneous acquisition of samples;
- Petrographic and geochemical characterization of the alteration footprints related to Li-bearing pegmatites and the associated mineral assemblages;
- Construction of a spectral library for Li-minerals and associated alteration minerals;
- Geochemical, spectral and geological data processing, integration, and interpretation for production of Li-target explorations maps.

By fulfilling each of the aforementioned objectives, the present work provides new insights for Li exploration that can be of great interest and significance for exploration and mining companies, allowing to decrease the impacts of the early stages of mining and increase the efficiency and sustainability of mineral exploration. Moreover, the knowledge and tools established in the ambit of this thesis can contribute to a better social acceptance of mineral exploration, by focusing on less intrusive exploration techniques.

Thesis structure and outline

This thesis is structured into four main parts. The first part relates to the present section where an introduction to the theme and study area are made. The objectives of the research are also stated.

The second part corresponds to the core of the thesis and is divided into five chapters according to their subject and the specific objectives. Each chapter is then composed of one or more scientific (review or research) articles (published, submitted, or to be submitted to international peer-reviewed journals) and by a separate general introduction, outlining their motivation and their relationship to other published (or not) research conducted in the scope of this thesis. Chapter I is composed of two articles dedicated to reviewing the state of the art of remote sensing applications to Li exploration. Chapter II concerns the development of new remote sensing algorithms for Li pegmatite exploration, with one research article focusing on the field of machine learning algorithms. Chapter III presents three articles dedicated to the construction of spectral libraries for Li exploration and interpretation of key reflectance spectra and consequent implications for exploration. Chapter IV concerns the use of distinct geochemical exploration methods in two separate research articles. The first related to the treatment of historical stream sediment datasets, and the second dedicated to the study and characterization of the metasomatic alteration haloes formed as a result of pegmatite emplacement in the metasedimentary host rocks. Finally, Chapter V sums up the previous findings in a research article that integrates geochemical, spectral, and geological data for the production of Li potential maps. There is a possible overlap of content namely in the background and geological setting between the chapters in Part II and the introduction made in Part I. Also, the bibliography is presented at the end of each section (corresponding to the respective articles) as well as at the end of the thesis (in Part III).

The third part of the thesis corresponds to the general discussion of the research findings and conclusions, where open questions and future research directions are highlighted. As mentioned before, the references are also given by chapter in this part.

Lastly, the fourth part corresponds to all materials presented as appendices that can be the original publications of journal articles, conference proceedings and abstracts (among others), and supplementary geochemical, petrographic, or spectral data collected in the scope of this thesis and relevant to the content of the main core of the research and discussion of the results. Another advisory note is that all publications are organized according to the logical continuity of the work and not the timeline of their publication. For further clarification, Table 1 presents the logical order of published journal articles and indexed conference proceedings.

Table 1. Logical order of the main publications (journal articles/conference proceedings) in which this thesis is based.

Order	Authors (Year)	Title	Journal/Conference
1 (Chapter I)	Cardoso-Fernandes *et al.* (2019a)	Constraints and potentials of remote sensing data/techniques applied to lithium (Li) pegmatites	The Canadian Mineralogist
2 (Chapter I)	Cardoso-Fernandes *et al.* (2020d)	Detecting Lithium (Li) Mineralizations from Space: Current Research and Future Perspectives	Applied Sciences
3 (Appendix I.2.)	Santos *et al.* (2019)	Remote sensing techniques to detect areas with potential for lithium exploration in Minas Gerais, Brazil	SPIE Remote Sensing 2019
4 (Appendix I.2.)	Cardoso-Fernandes *et al.* (2020c)	Multi-scale approach using remote sensing techniques for lithium pegmatite exploration: first results	IGARSS 2020
5 (Appendix I.2.)	Cardoso-Fernandes *et al.* (2019b)	Evaluating the performance of support vector machines (SVMs) and random forest (RF) in Li pegmatite mapping: Preliminary results	SPIE Remote Sensing 2019
6 (Appendix I.2.)	Cardoso-Fernandes *et al.* (2020f)	Lithium (Li) pegmatite mapping using Artificial Neural Networks (ANNs): preliminary results	IGARSS 2020
7 (Chapter II)	Cardoso-Fernandes *et al.* (2020e)	Semi-Automatization of Support Vector Machines to Map Lithium (Li) Bearing Pegmatites	Remote Sensing
8 (Chapter III)	Cardoso-Fernandes *et al.* (2021a)	Tools for Remote Exploration: A Lithium (Li) Dedicated Spectral Library of the Fregeneda–Almendra Aplite–Pegmatite Field	Data
9 (Chapter III)	Fabre *et al.* (2021)	Analyses of Li-Rich Minerals Using Handheld LIBS Tool	Data

10 (Appendix I.2.)	Cardoso-Fernandes *et al.* (2020b)	Reflectance spectroscopy to validate remote sensing data/algorithms for satellite-based lithium (Li) exploration (Central East Portugal)	SPIE Remote Sensing 2020
11 (Appendix I.2.)	Cardoso-Fernandes *et al.* (2020a)	Characterization of lithium (Li) minerals from the Fregeneda-Almendra region through laboratory spectral measurements: a comparative study	SPIE Remote Sensing 2020
12 (Chapter III)	Cardoso-Fernandes *et al.* (2021b)	Interpretation of the reflectance spectra of Lithium (Li) minerals and pegmatites: a case study for mineralogical and lithological identification in the Fregeneda-Almendra area	Remote Sensing
13 (Chapter IV)	Cardoso-Fernandes *et al.* (Submitted)	Stream sediment analysis for Lithium (Li) exploration in the Douro region (Portugal): a comparative study of the spatial interpolation and catchment basin approaches	Journal of Geochemical Exploration
14 (Chapter IV)	Errandonea-Martin *et al.* (To be submitted)	Metasomatic effect of granitic aplite-pegmatite dykes in psammopelitic metasediments; mass-transfer quantification from whole-rock lithogeochemistry at La Fregeneda–Almendra (Central Iberian Zone)	Ore Geology Reviews
15 (Chapter V)	Köhler *et al.* (2021)	Lithium Potential Mapping Using Artificial Neural Networks: A Case Study from Central Portugal	Minerals

Case study: The Fregeneda-Almendra area

The study area of this work is the Fregeneda (Salamanca, Spain)-Almendra (Vila Nova de Foz Côa, Portugal) aplite-pegmatite field (Figure 1). This area is divided into two sectors: the eastern (Spanish) side and the western (Portuguese) one – Figure 2. The aplite-pegmatite field is delimitated at the north by the Douro River, at east by the Vilariça's fault valley and the border between Portugal and Spain is materialized by the Douro and Águeda rivers (Figure 2 and Figure 3).

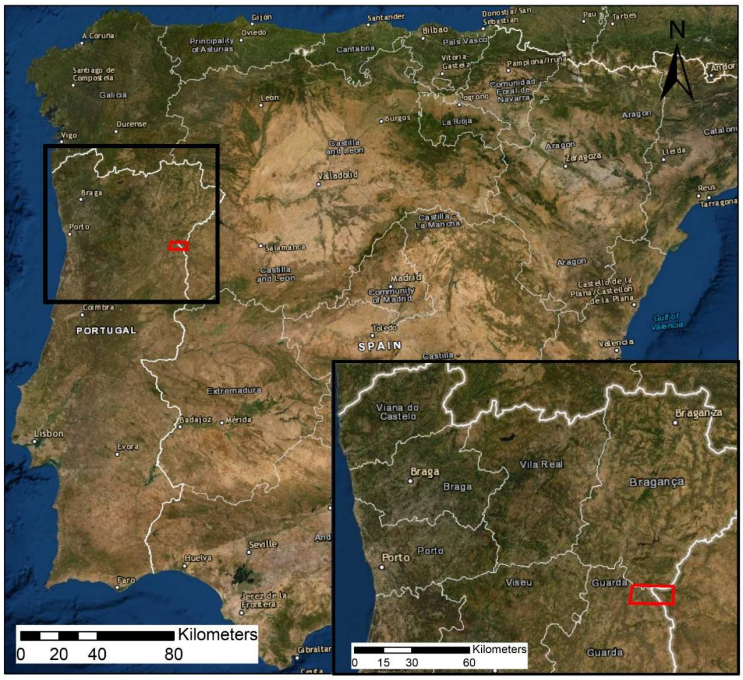

Figure 1. Location of the study area in the Iberian Peninsula.

The Fregeneda-Almendra pegmatite field is part of an NNW-SSE striking belt (with around 500 km in length and 150 km in width), where Li-mineralization occurs in aplite-pegmatite dykes and leucogranitic cupolas (Roda-Robles *et al.*, 2016; Roda-Robles *et al.*, 2018). More specifically, the study area is located within the Central Iberian Zone (CIZ) (Julivert *et al.*, 1974), one of the biggest and most complete fragments of the European Variscan Belt which occupies a central portion of the Iberian Massif (Pérez-Estaún *et al.*, 2004). The CIZ is composed of Neoproterozoic to Early Paleozoic metasedimentary sequences, intruded by several Variscan granitoids (Dias *et al.*, 2000; Martínez Catalán *et al.*, 2004; Roda-Robles *et al.*, 2018).

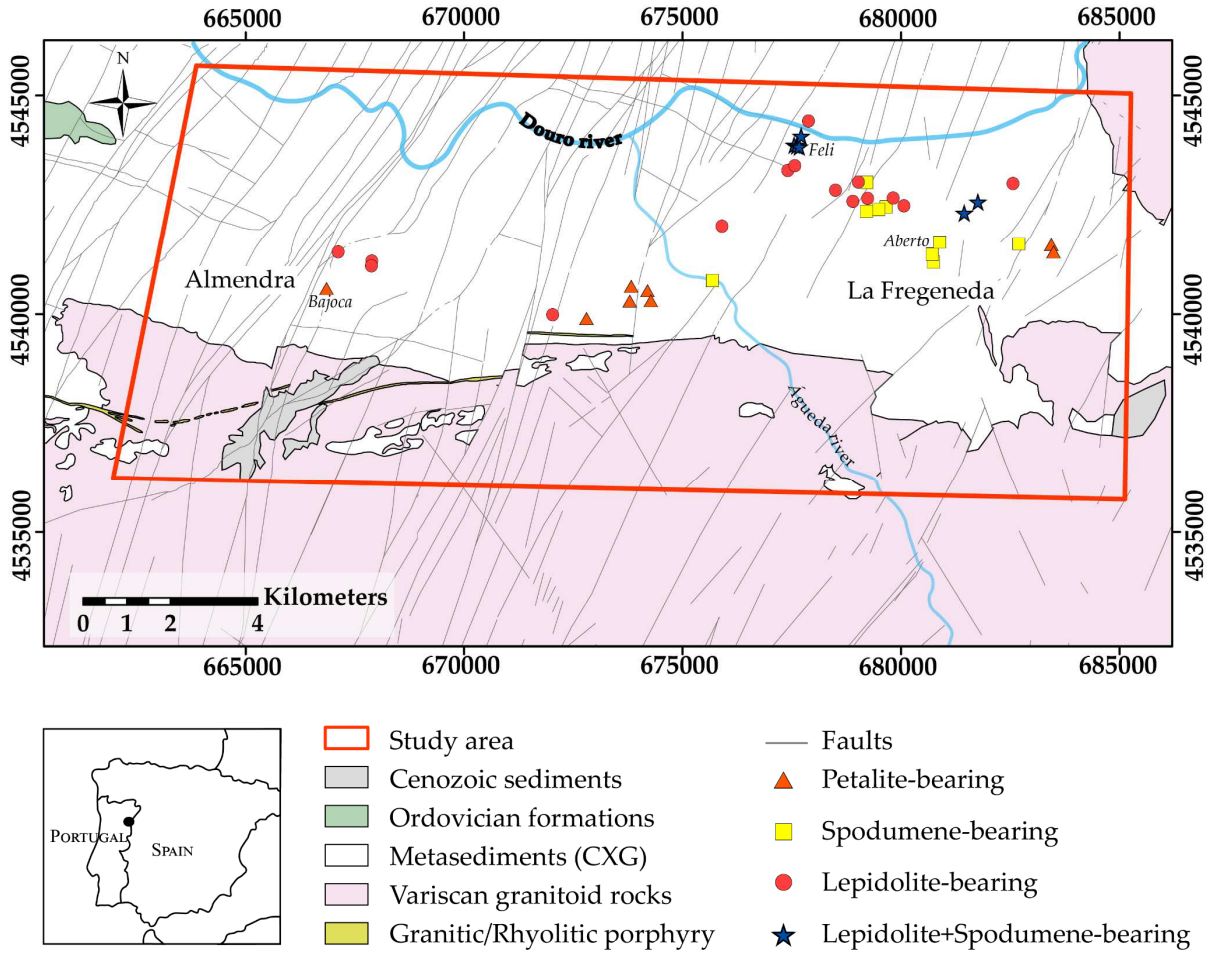

Figure 2. Simplified geological map of the Fregeneda-Almendra area, highlighting the different Li-bearing aplite-pegmatite dykes adapted from Silva and Ribeiro (1991, 1994); Vieira (2010) in Cardoso-Fernandes *et al.* (2020e). The open-pit mines of Bajoca, Feli, and Alberto, currently exploiting Li-pegmatites, are also marked. The map projection is Universal Transverse Mercator zone 29N from the WGS84 datum.

In the Fregeneda-Almendra area there is a narrow E-W strip of Upper Proterozoic to the Lower Cambrian metasedimentary rocks (Díez Balda *et al.*, 1990; Rodríguez Alonso *et al.*, 2004), limited to the north by the Lower Ordovician quartzites from the Poiares' syncline and to the south by the Figueira de Castelo Rodrigo–Lumbrales Anatectic Complex (FCR–LAC; Figure 2) (Pereira *et al.*, 2017). This pre-Ordovician metasedimentary belt corresponds to a monotonous pelitic-sandy flysch series denominated as Complexo Xisto-Grauváquico (CXG) (Costa, 1950; Teixeira, 1955; Rodríguez Alonso *et al.*, 2004). The series resulted from the accumulation of a thick sediment column (8000 m to 11000 m), under tectonic instability, in a foreland basin created by the CIZ's compartmentation in fault-delimited blocks, during the Cadomian orogeny (San José *et al.*, 1990; Rodríguez Alonso *et al.*, 2004).

All Li-rich pegmatite dykes are emplaced in the Douro Group, a stratigraphic succession, characterized by interlayered phyllites and metagreywackes with turbiditic features (Sousa,

1982; Sousa, 1983, 1984) that can be correlated with other pre-Ordovician metasediments of the CIZ, corresponding to flyschoid deposits of the northern continental margin of Gondwana (Valladares *et al.*, 2002; Gutiérrez-Alonso *et al.*, 2003; Rodríguez Alonso *et al.*, 2004; Villaseca *et al.*, 2014). The Douro Group is divided into six sequential stratigraphic formations that are, from the base to the top: Bateiras, Ervedosa, Rio Pinhão, Pinhão, Desejosa, and S. Domingos, with the basal formations presenting a distal turbiditic character, whilst the top formations present a proximal turbiditic character (Sousa, 1982; Sousa, 1983).

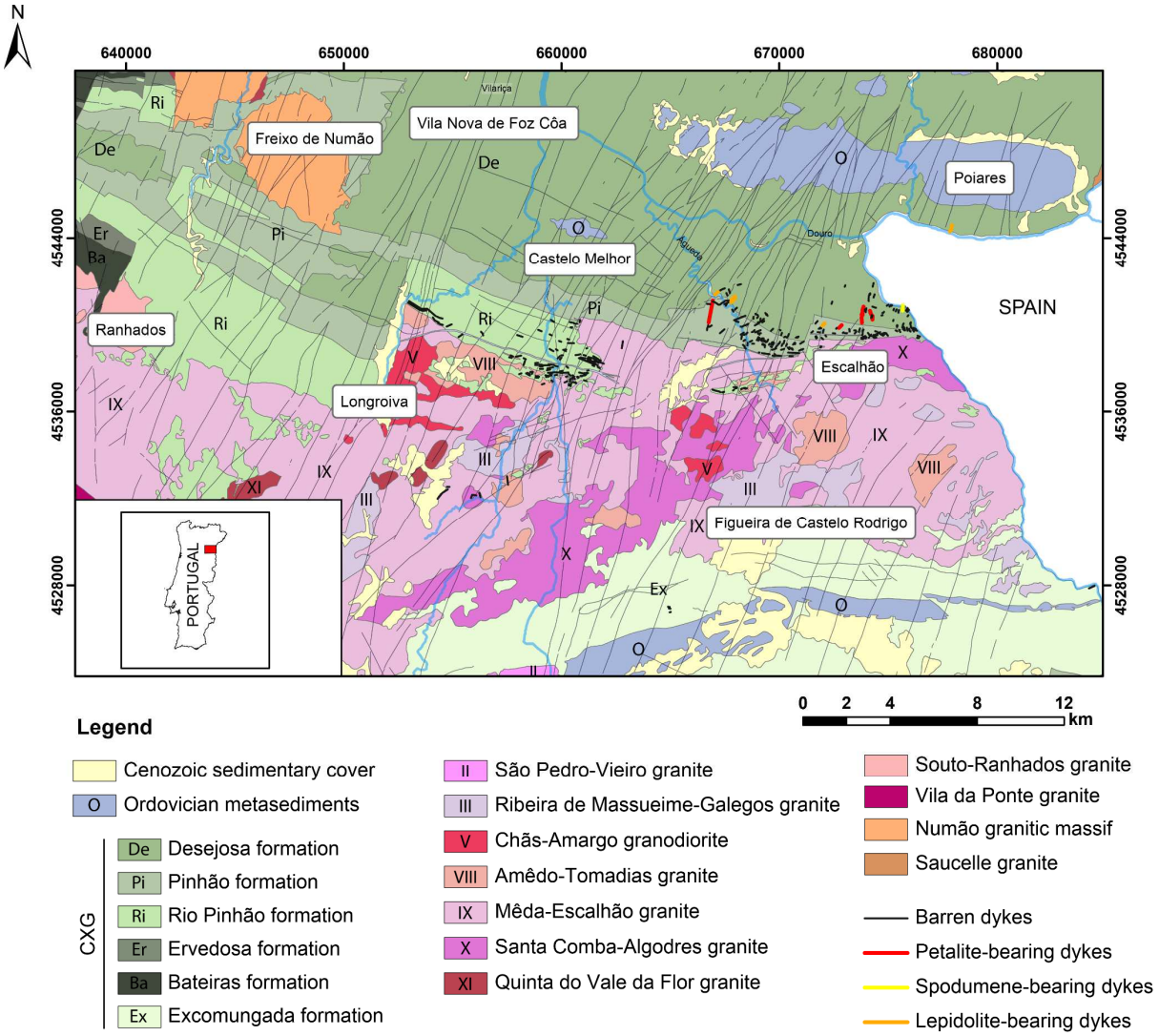

Figure 3. Detailed, regional geological map of the Douro region, adapted from Carvalhosa (1960); Ribeiro and Silva (2000); Silva et al. (1990a); Silva et al. (1990b) and unpublished geological data at the scale of 1:25,000. Roman numerals are from Ribeiro and Silva (2000). Location and classification of the Portuguese aplite-pegmatite dykes from Vieira (2010).

In the Fregeneda-Almendra pegmatite field, only tree formations can be mapped (Figure 3): Rio Pinhão, and Pinhão, with fewer cartographic expression, and the Desejosa formation, the

most representative within this group (Silva *et al.*, 1990a; 1990b; Silva & Ribeiro, 1991, 1994). The formation of Rio Pinhão is characterized by dark-grey metagraywackes and metaquartzograywackes, with fine intercalations of dark stripped phyllites (Sousa, 1982; Sousa, 1983; Silva & Ribeiro, 1991). The phyllites often have a calc-silicate nature, with cordierite, andalusite, and garnet porphyroblasts easily identified. Outcrops of the Rio Pinhão formation can also occur in spots, within the granites of the FCR–LAC, where migmatites can also be observed (Silva *et al.*, 1990a; 1990b; Silva & Ribeiro, 1991, 1994; Gaspar, 1997). The transition to the overlaying Pinhão formation is marked by the disappearance of metagraywackes and the prevalence of chloritic phyllites instead (Silva & Ribeiro, 1991, 1994).

The Pinhão formation corresponds to a finely stratified green sequence, composed of alternating chloritic phyllites and metaquartzograywackes, with magnetite and pyrite often found within the phyllites (Sousa, 1982; Sousa, 1983; Silva & Ribeiro, 1991, 1994). Andalusite-bearing spotted schists are typical of this formation as a result of metamorphism, which obliterated the original green color (Silva & Ribeiro, 1994). The Pinhão formation occurs in an E-W elongated strip rejected by two NNE-SSW trending strike-slip faults, one in the Bajoca mine zone (Silva *et al.*, 1990a; 1990b). The passage to the lower Rio Pinhão formation is marked by the presence of the metagreywacke benches, while the transition to the upper Desejosa formation is gradual and manifested by a greyish striped sequence (Silva & Ribeiro, 1991).

Finally, the Desejosa formation corresponds to a monotonous layered sequence, characterized by dark striped phyllites finely intercalated with whitish psammites (Sousa, 1982; Sousa, 1983; Silva & Ribeiro, 1991). Locally, frequent intercalations with calc-silicate rocks occur, especially calc-silicate metagreywackes are observed as well as metric benches of intraformational metaconglomerates to the top (Sousa, 1982; Sousa, 1983, 1984; Silva & Ribeiro, 1991, 1994; Gaspar, 1997). At northeast, the Desejosa formation is overlayed by the Lower Ordovician quartzites from the Poiares' syncline and contacts with the alternating Ordovician quartzites and phyllites from the Castelo Melhor's syncline (Silva *et al.*, 1990a; Silva *et al.*, 1990b; Silva & Ribeiro, 1991, 1994). The transition to the Ordovician formations can be gradual or abrupt, but most of the time the passage is gradual, without substantial unconformity (Silva & Ribeiro, 1991, 1994).

Regarding the Ordovician metasediments of the region, they are divided into two different ages: the Tremadocian S. Gabriel and Quinta da Ventosa formations, and the Arenigian Quartzitic formation (outcropping in the Poiares' syncline; Figure 3). The Quartzitic formation is composed, from base to the top, of light-gray compact impure quartzites (sometimes

ferruginous), dark to dark-grey phyllites and quartzophyllites, and alternating quartzites and phyllites with a variable layering thickness (Silva & Ribeiro, 1991, 1994). Locally, there are also several Cenozoic sedimentary deposits including fluvial and slope deposits, alluvions, and fault-related arkoses (Silva & Ribeiro, 1991, 1994) – Figure 2.

In what concerns the structure and deformation of the case study area, a polyphasic Variscan deformation is evident, accompanied by an overprint of different metamorphic events (Silva & Ribeiro, 1994; Silva, 2013). Three deformation phases – D_1, D_2 and D_3 – defined by Noronha *et al.* (1979) are recognized in the CIZ. The D_1 phase produced crustal thickening between 365-340 Ma (Dallmeyer *et al.*, 1997) and created open folds mainly NW-SE trending and with a sub-vertical axial plane in the CIZ's central part, from which two sectors with vergent folds diverge: one sector with folds vergent to SW and other to NE (Ribeiro *et al.*, 1979; Ribeiro, 1990; Ribeiro *et al.*, 1990). The second phase (D_2) is considered a non-coaxial deformation, associated with tangential shear zones responsible for the transport and emplacement of the tectonic nappes of the allochthonous complex in the NW of Iberia (e.g. Ribeiro *et al.*, 2006; Rodrigues, *et al.*, 2011). In the CIZ, D_2 corresponds to an extensional event that took place between 340 and 320 Ma and lead to the formation of NNE-SSW normal faults, sub-perpendicular to the D_1 folds (Pereira 1987; Ribeiro *et al.*, 1990; Martínez Catalán *et al.*, 2014; Gutiérrez-Alonso *et al.*, 2018). During the third deformation phase (D_3), between 320 and 305 to 295 Ma (Silva, 2013; Valle Aguado *et al.*, 2017), large open sub-vertical folds WNW-ESE trending, coaxial with the D_1 folds, developed with associated sub-vertical cleavage of crenulation (Ribeiro *et al.*, 1979; Díez Balda *et al.*, 1990; Pereira *et al.*, 1993). Simultaneously, this phase was responsible for the conjugation of ductile sub-vertical sinistral and dextral shearing zones with a distensive component, respectively, WNW-ESE to NW-SE trending, and NNW-SSE trending (Ribeiro, 1974, Ribeiro *et al.*, 1979; Iglésias & Ribeiro, 1981a; Iglésias & Ribeiro, 1981b). The reactivation of fragile-ductile sub-vertical shear zones was concurrent with the emplacement of crustal melts (Silva, 2013; Valle Aguado *et al.*, 2017; Ferreira *et al.*, 2019). Late-Variscan tectonics resulted in NE–SW to NNE–SSW strike-slip faults that cut the previous structures (Silva & Ribeiro, 1991, 1994; Rodríguez Fernández et al., 2000)

Associated with the crustal thickening that occurred between D_1 and D_2 deformation phases, the metasediments suffered a continuous prograde regional Barrovian-type metamorphism, generally of low-grade in the greenschist facies (Martínez *et al.*, 1990; Dias da Silva *et al.*, 2017). The higher-grade zones were observed within the antiforms and metamorphic domes (Vieira, 2010; Silva, 2013). During the pre-D_3 migmatization of the crust that produced the granitic melts during the episode of crustal extension, there was another metamorphic event,

of the Buchan-type (Silva, 2013). The isograde from the first metamorphic event were superposed by younger ones, related to a syn- to post-D_3 metamorphic retrogradation (Silva, 2013). Additionally, the coetaneous installation of various granitic bodies produced contact metamorphism responsible for the late and post-D_3 (over)growth of biotite, andalusite, cordierite, and chloritoid (López-Plaza *et al.*, 1982; Silva & Ribeiro, 1991; Martín-Izard *et al.*, 1992; Silva & Ribeiro, 1994; Silva, 2013; Dias da Silva *et al.*, 2017). In the Almendra region, the regional metamorphism in the greenschist facies did not overcome the chlorite zone, even though it reached the biotite zone in the Fregeneda region (López-Plaza *et al.*, 1982; Martín-Izard *et al.*, 1992; Silva & Ribeiro, 1994). In the vicinities of the FCR–LAC, the sin- to late-D3 thermal peak reached the sillimanite zone, with the metamorphic grade increasing progressively to the south, in the direction of the FCR-LAC (Silva & Ribeiro, 1991, 1994). The metamorphic isograde have a W-E trend, parallel to the granites (Silva & Ribeiro, 1991, 1994) – Figure 4.

In the surrounding region of the Fregeneda-Almendra aplite-pegmatite field, the most important granitic occurrences are (Figures 2-4): (i) at the south, the granites from the FCR–LAC, previously named as Mêda–Penedono–Lumbrales granitic complex by Bea *et al.* (1987) *in* Vieira (2010); (ii) the Saucelle granite at northeast; (iii) the non-outcropping granite of Feli, detected by drilling holes between the Riba D'Alva mine (Portugal) and Feli mine (Spain) (Carnicero, 1981; Vieira, 2010); and (iv) the non-outcropping Bajoca granite also intersected by drill cores (Ribeiro, 2001). All these granitoids have intruded the metasedimentary sequences of the CXG.

In the case of the FCR–LAC, most of the granitic facies correspond to syn-Variscan (concomitant D3), S-type, two-mica granites ranging from fine- to coarse-grained (Silva & Ribeiro, 1991, 1994; Pereira *et al.*, 2017; Ferreira *et al.*, 2019; Ferreira *et al.*, 2020). These facies correlate with the S_1 suite of highly peraluminous, Ca-poor, two-mica syn-D_3 leucogranites, defined by Villaseca (2011) and Roda-Robles *et al.* (2018). There is also a fine-to-medium-grained, biotitic granodiorite (Silva & Ribeiro, 1991, 1994; Ribeiro, 2001; Ferreira *et al.*, 2019), as well as late-D3 two-mica granites with smaller cartographic expression (Silva & Ribeiro, 1991, 1994). U-Pb zircon data show that most facies are clearly syn-D_3, with ages in the range 318.7±4.8–313 Ma (Pereira *et al.*, 2018; Ferreira *et al.*, 2019) while the late-D3 facies were dated by U-Pb as 300.0±2.2 Ma old (Ferreira *et al.*, 2019). The FCR-LAC exhumation was assisted by first-order shear zones (Pereira *et al.*, 2017; Ferreira *et al.*, 2019).

The Saucelle granite is composed of undeformed late- to post-D3 two-micas (muscovite >> biotite), medium-to-coarse-grained leucogranite (Silva & Ribeiro, 1994; Rodríguez Fernández

et al., 2000). It is installed in the Vila Real-Carviçais antiform and intruded the Desejosa formation (Silva & Ribeiro, 1994) and correlates with the S_2 suite of Villaseca (2011) and Roda-Robles *et al.* (2018), of P-rich, Ca-poor, highly peraluminous late-D_3 granites. The non-outcropping Feli granite is characterized as a leucocratic, fine-to-medium-grained with muscovite >> biotite granite, dated as 305.0 ± 3.3 Ma old (Ar/Ar in micas) that is cross-cut by a Li-mica+spodumene pegmatite dyke (Vieira, 2010). Little is known about the Bajoca granite besides that is leucocratic, fined grained with biotite and muscovite. Currently, petrographic and geochemical assays are being conducted.

In the Fregeneda-Almendra area, 11 different types of veins have been recognized (Figure 4) considering their mineralogy, morphology, and internal structure (Roda, 1993; Roda-Robles *et al.*, 1999; Vieira, 2010): T1 – Simple intragranitic pegmatite dykes; T2 – Quartz dykes with andalusite; T3 – Aplite-pegmatite dykes and apophysis; T4 – Simple, concordant pegmatite dykes; T5 – Potassium feldspar-bearing aplite-pegmatite dykes; T6 – Simple, discordant aplite-pegmatite dykes; T7 – Petalite-bearing aplite-pegmatite dykes; T8 – Spodumene-bearing aplite-pegmatite dykes; T9 – Li-mica and spodumene-bearing aplite-pegmatite dykes; T10 – Li-mica-rich aplite-pegmatite dykes; T11 – Quartz veins with cassiterite (Figure 4). All these types can be grouped into three categories: (i) sterile, emplaced within (intragranitic, type 1) or near (concordant bodies, types 2, 3, and 4) the granites of the FCR–LAC; (ii) intermediate, discordant bodies (types 5 and 6); (iii) evolved, discordant dykes with a N10º–50ºE strike, enriched in Li-, F- and/or Sn (types 7, 8, 9, 10, and 11) (Roda, 1993; Roda-Robles *et al.*, 1999; Vieira, 2010; Vieira *et al.*, 2011).

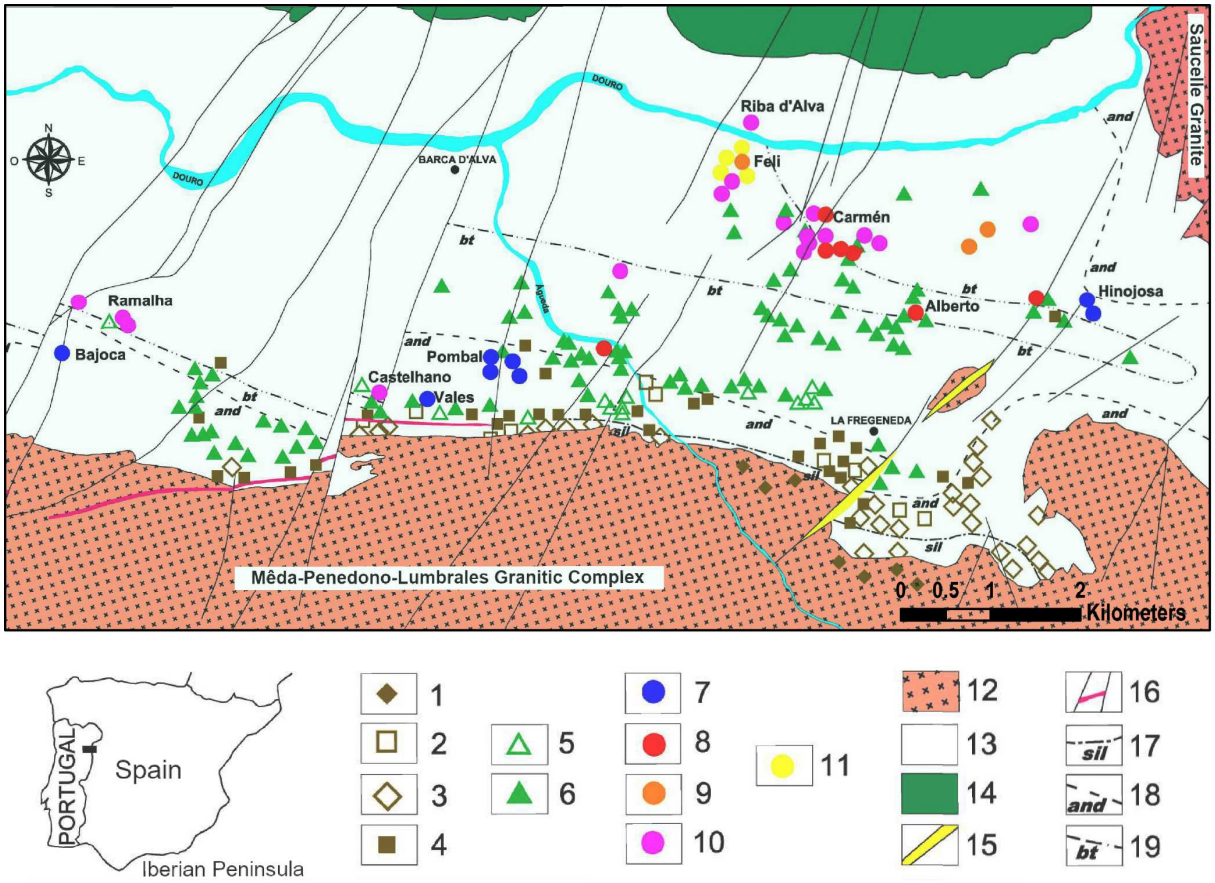

Figure 4. Vein distribution within Fregeneda-Almendra aplite-pegmatite field and simplified geological. Adapted from Vieira (2010). Dyke types: (1) intragranitic - T1; (2) quartz with andaluzite - T2; (3) apophysis - T3; (4) simple discordant -T4; (5) with potassium feldspar - T5; (6) simple discordant - T6; (7) with petalite - T7; (8) with spodumene - T8; (9) with Li-mica and spodumene - T9; (10) with Li-mica - T10; (11) quartz with cassiterite - T11. (12) Syn- to late-D3 granites; (13) metasediments (CXG); (14) Ordovician formations; (15) quartz dykes; (16) granitic/rhyolitic porphyry and faults. Isograds: (17) sillimanite; (18) andaluzite; (19) biotite.

The intermediate and evolved dykes are emplaced in the CXG metasediments, showing a zoned distribution pattern from barren to evolved dykes and an increasing fractionation degree northwards as the distance to the granites of the FCR–LAC increases (Vieira, 2010; Vieira *et al.*, 2011). Moreover, barren dykes occur in the higher-grade metamorphic zones, petalite-bearing aplite-pegmatites only occur in the andalusite-sillimanite; and spodumene-bearing dykes are emplaced in the biotite and/or chlorite zones (Vieira, 2010; Vieira *et al.*, 2011) – Figure 4. The evolved dykes are enriched in Li, F, Sn, Rb, Nb>Ta, B, and P, with types 7 to 10 fitting into the LCT family, Rare Element-Li subclass from the Complex type of the Černý and Ercit (2005) classification (Vieira, 2010).

According to Roda (1993), Roda-Robles *et al.* (1999), and Vieira (2010) the Li-bearing dykes can be described as the following:

T7 – Petalite-bearing aplite-pegmatite dykes

The petalite-bearing dykes (T7) have N-S to N30ºE general trend and sub-vertical dip, and a thickness from 1 to 30 m. Mineralogically, they are mainly composed of petalite, quartz, albite, and potassium feldspar. Minor phases include muscovite and cassiterite. Montebrasite, columbite-tantalite oxides, and eucryptite occur as accessory phases. Although they are heterogeneous bodies, with zones with a higher enrichment in petalite, no internal zoning was described. They are more abundant in the Portuguese side of the pegmatite field, outcropping in the Pinhão and Desejosa formations, further away from the FCR–LAC granites when compared to T1-T6 dykes. Tourmalinization is visible in the contact with the host rocks. The best example is the dyke from the Bajoca mine (Almendra). The referred dyke outcrops as a two-meter thick dyke and its thickness increases with the depth, reaching up to 30 m (Figure 5).

(a) **(b)**

Figure 5. (a) Petalite-bearing dyke (T7) reaching 30 m in thickness, exploited in the Bajoca open-pit mine (May 2019). (b) Aggregate of petalite crystals, in the Bajoca stockpile.

T8 – Spodumene-bearing aplite-pegmatite dykes

The spodumene-bearing dykes (T8) are very similar to the petalite ones in terms of mineralogy, dimension, and attitude. The main difference is the dominant phase – spodumene – and its association with primary petalite in some dykes (in the Alberto mine, La Fregeneda, Spain; Figure 6). Other than spodumene and petalite, the dyke mineralogy includes potassium feldspar, albite, and quartz as major phases. Muscovite can occur as a minor phase, and montebrasite, Fe-Mn phosphates, and cassiterite as accessory minerals. In the contact with

the host rocks, tourmalinization is also observed. T8 dykes are more abundant in the eastern side of the Fregeneda-Almendra pegmatite field (between La Fregeneda and Hijinosa del Duero) and the main body outcrops in the Alberto mine. On the western (Portuguese) side, only one dyke has been discovered in the location of Vau (near the Águeda river).

(a) **(b)**

Figure 6. (a) Spodumene-bearing dyke (T8) with about 2.6 m of thickness, exploited in the Alberto open-pit mine (November 2019). (b) Spodumene crystal (more than 10 cm long) from the Alberto stockpile.

T9 – Li-mica and spodumene-bearing aplite-pegmatite dykes

Type 9 is the least common type with only three known occurrences in the Spanish side of the field. These dykes present quartz, feldspars, dominant Li-bearing muscovite (and lepidolite in minor amounts), and spodumene as the main phases. Muscovite, cassiterite, and montebrasite occur in a smaller percentage. Accessory phases include apatite, columbite-tantalite oxides, Fe-Mn phosphates, and eucryptite. Despite not showing an internal concentric zoning, T9 dykes often present an internal banded structure with quartz- and lepidolite-rich zones alternating with zones richer in potassium feldspar and albite (Figure 7). The spodumene occurs as prismatic crystals associated with Li-mica and potassium feldspar, defining a comb-like structure normal to the contacts with the host rocks. They outcrop even further away from the granites when compared with the previously described dykes and show tourmalinization in the contact. They are also sub-vertical and discordant with the host rocks – N-S to N30ºE trend. The best exemplar of T9 dykes is the dyke from the Feli mine (La Fregeneda, Spain).

(a) **(b)**

Figure 7. (a) Contact of the main Li-mica+spodumene-bearing dyke (T9) with the host rocks in the Feli open-pit mine. Internal banded structure parallel to the contact wall. (b) Another example of the internal banded structure in the Feli mine, showing not only compositional but also textural heterogeneity.

T10 – Li-mica-rich aplite-pegmatite dykes

Like the previous type, these dykes outcrop in the areas farthest from the granites. They are sub-vertical and aligned according to an N10º to N40ºE direction, discordant from the host rocks which show tourmalinization in the contact zone. Their thickness is usually less than 3 meters (Figure 8). Mineralogically, the dominant phases are quartz, feldspar, and Li-mica (Li-muscovite and lepidolite). Muscovite, cassiterite, montebrasite, and Nb-Ta oxides can occur in smaller percentages. Although it is not common, T10 dykes can present a layered structure parallel to the contacts, similar to the one observed in T9.

Figure 8. Li-mica-rich dyke (T10) within the Bajoca mining concession.

It is also noteworthy that intermediate dykes (T6) outcropping further away from the FCR–LAC contact, show montebrasite as a common accessory phase. Structural and geochemical similarities between type 6 dykes (simple discordant) and types 7 (petalite) and 8 (spodumene) took Vieira (2010) to suspect that some of the type 6 dykes could hold complex non-outcropping mineralizations.

Over the years, different hypotheses were proposed to explain dyke emplacement in the Fregeneda-Almendra pegmatite field. López-Plaza *et al.* (1982) considered that for the Fregeneda area the emplacement of the sterile dykes was conditioned by a D_3 shear zone. In what concerns the mineralized aplite-pegmatite dykes, Martín-Izard *et al.* (1992) proposed that the dykes near Feli were controlled by a shear zone related to the uplift of a non-outcropping granitic dome; Viegas (1983) and López-Plaza *et al.* (1982) consider that the dykes were emplaced in N10º-N25ºE tension fractures. These tension fractures are related to the tension relief that caused the late-Variscan strike-slip faults (Viegas, 1983). López-Plaza *et al.* (1982) describe the fractures as cross joints aligned perpendicularly to the axis of the folds. The same authors also refer that some of the NNE-SSW dykes present a curvature that may indicate that the shear zone which controlled the emplacement of the sterile dykes was still active. Vieira

(2010) concluded that aplite-pegmatite dykes were the result of several (magmatic syn-, late- and post-D3) differentiation processes and are controlled by the regional structures: the sterile dykes are emplaced in D_3 structures and the mineralized dykes are installed in late-Variscan NNE-SSW and NE-SW strike-slip faults. Silva (2013) proposed for the eastern side of the field that some of the strike-slip faults are posterior to the dyke emplacement and cooling and that some dykes were installed before D_3.

Roda-Robles *et al.* (2018) compiled a series of mineralogical, textural, and compositional data related to different Li-mineralizations as well as the granitic rocks of the CIZ. The authors concluded that the Li-rich bodies (including the Fregeneda-Almendra aplite-pegmatites) are related to the granites S_1 and S_2 of the classification proposed by Villaseca *et al.* (2014), where S_1 represents two-mica peraluminous leucogranites while S_2 corresponds to a P-rich highly peraluminous granite suite. However, the possible petrogenetic linkage between the aplite-pegmatites and the outcropping granites of the region is not yet completely understood (Vieira *et al.*, 2011).

References

Abrams, M., & Yamaguchi, Y. (2019). Twenty Years of ASTER Contributions to Lithologic Mapping and Mineral Exploration. *Remote Sensing, 11*(11), 1394.

Arrobas, D. L. P., Hund, K. L., Mccormick, M. S., Ningthoujam, J., & Drexhage, J. R. (2017). *The Growing Role of Minerals and Metals for a Low Carbon Future*. Washington, DC, USA: The World Bank.

Bea, F., Fershtater, G. & Corretgé, L. G. (1992). The geochemistry of phosphorus in granite rocks and effect of aluminium. *Lithos*, 29: 43–56. In: Vieira, R. (2010). Aplitopegmatitos com Elementos Raros da Região entre Almendra (V. N. de Foz-Côa) e Barca d'Alva (Figueira de Castelo Rodrigo). Campo Aplitopegmatítico da Fregeneda-Almendra. *phD Thesis*. Universidade do Porto, Portugal, p. 276.

Blengini, G. A., Latunussa, C. E. L., Eynard, U., Torres de Matos C., Wittmer, D., Georgitzikis, K., Pavel, C., Carrara, S., Mancini, L., Unguru, M., Blagoeva, D., Mathieux, F. & Pennington D. (2020). Study on the EU's list of Critical Raw Materials Final Report. *European Commission.* https://doi.org/10.2873/11619

Cardoso-Fernandes, J., Lima, A., Roda-Robles, E., & Teodoro, A. C. (2019a). Constraints and potentials of remote sensing data/techniques applied to lithium (Li)-pegmatites. *The Canadian Mineralogist, 57*(5), 723-725. doi: 10.3749/canmin.AB00004.

Cardoso-Fernandes, J., Silva, J., Dias, F., Lima, A., Teodoro, A. C., Barrès, O., Cauzid, J., Perrotta, M., Roda-Robles, E., & Ribeiro, M. A. (2021a). Tools for Remote Exploration: A Lithium (Li) Dedicated Spectral Library of the Fregeneda–Almendra Aplite–Pegmatite Field. *Data, 6*(3), 33. doi: 10.3390/data6030033.

Cardoso-Fernandes, J., Silva, J., Lima, A., Teodoro, A. C., Perrotta, M., Cauzid, J., & Roda-Robles, E. (2020a). *Characterization of lithium (Li) minerals from the Fregeneda-Almendra region through laboratory spectral measurements: a comparative study.* Paper presented at the SPIE Remote Sensing, Earth Resources and Environmental Remote Sensing/GIS Applications XI, doi: https://doi.org/10.1117/12.2573941.

Cardoso-Fernandes, J., Silva, J., Lima, A., Teodoro, A. C., Perrotta, M., Cauzid, J., Roda-Robles, E., & Ribeiro, M. A. (2020b). *Reflectance spectroscopy to validate remote sensing data/algorithms for satellite-based lithium (Li) exploration (Central East Portugal).* Paper presented at the SPIE Remote Sensing, Earth Resources and Environmental Remote Sensing/GIS Applications XI, doi: https://doi.org/10.1117/12.2573929.

Cardoso-Fernandes, J., Silva, J., Perrotta, M. M., Lima, A., Teodoro, A. C., Ribeiro, M. A., Dias, F., Barrès, O., Cauzid, J., & Roda-Robles, E. (2021b). Interpretation of the Reflectance Spectra of Lithium (Li) Minerals and Pegmatites: A Case Study for Mineralogical and Lithological Identification in the Fregeneda–Almendra Area. *Remote Sensing, 13*(18), 3688. doi: 10.3390/rs13183688.

Cardoso-Fernandes, J., Teodoro, A. C., Lima, A., & Roda Robles, E. (2020f, 26 Sept.-2 Oct. 2020). *Lithium (Li) pegmatite mapping using Artificial Neural Networks (ANNs): preliminary results.* Paper presented at the IGARSS 2020 - 2020 IEEE International Geoscience and Remote Sensing Symposium, Waikoloa, HI, USA, 557-560. doi: 10.1109/IGARSS39084.2020.9323852.

Cardoso-Fernandes, J., Teodoro, A. C., Lima, A., & Roda-Robles, E. (2019b, 9–12 September 2019). *Evaluating the performance of support vector machines (SVMs) and random forest (RF) in Li-pegmatite mapping: preliminary results.* Paper presented at the SPIE Remote Sensing, Strasbourg, France, doi: 10.1117/12.2532577.

Cardoso-Fernandes, J., Teodoro, A. C., Lima, A., & Roda-Robles, E. (2020e). Semi-Automatization of Support Vector Machines to Map Lithium (Li) Bearing Pegmatites. *Remote Sensing, 12*(14), 2319. doi: 10.3390/rs12142319.

Cardoso-Fernandes, J., Teodoro, A. C., Lima, A., Mielke, C., Körting, F., Roda-Robles, E., & Cauzid, J. (2020c, 26 Sept.-2 Oct. 2020). *Multi-scale approach using remote sensing techniques for lithium pegmatite exploration: first results.* Paper presented at the IGARSS 2020 - 2020 IEEE International Geoscience and Remote Sensing Symposium, Waikoloa, HI, USA, 5226-5229. doi: 10.1109/IGARSS39084.2020.9323705.

Cardoso-Fernandes, J., Teodoro, A. C., Lima, A., Perrotta, M., & Roda-Robles, E. (2020d). Detecting Lithium (Li) Mineralizations from Space: Current Research and Future Perspectives. *Applied Sciences, 10*(5), 1785. doi: 10.3390/app10051785.

Carnicero, M. A. (1981). Granitoides del Centro Oeste de la Provincia de Salamanca. Clasificación y correlación. *Cuad. Lab. Xeol. Laxe,* 2: 45–49. In: Vieira, R. (2010). Aplitopegmatitos com Elementos Raros da Região entre Almendra (V. N. de Foz-Côa) e Barca d'Alva (Figueira de Castelo Rodrigo). Campo Aplitopegmatítico da Fregeneda-Almendra. *phD Thesis*. Universidade do Porto, Portugal, p. 276.

Carvalhosa, A. (1960). Carta Geológica de Portugal na escala 1/50.000 – folha 15-D – Figueira de Castelo Rodrigo. Serviços Geológicos de Portugal, Lisboa, Portugal.

Černý, P., & Ercit, T. S. (2005). Classification of granitic pegmatites revisited. *Can. Mineral., 43*, 2005–2026.

Christmann, P., Gloaguen, E., Labbé, J.-F., Melleton, J., & Piantone, P. (2015). Chapter 1 - Global Lithium Resources and Sustainability Issues. In A. Chagnes & J. Światowska (Eds.), *Lithium Process Chemistry* (pp. 1-40). Amsterdam: Elsevier.

Costa, J. C. S. d. (1950). *Notícia sobre uma carta geológica do Buçaco, de Nery Delgado*. Lisboa, Portugal: Serviços Geológicos de Portugal,

Dallmeyer, R. D., Catalán, J. R. M., Arenas, R., Gil Ibarguchi, J. I., Gutiérrez, Alonso, G., Farias, P., Bastida, F., & Aller, J. (1997). Diachronous Variscan tectonothermal activity in the NW Iberian Massif: Evidence from 40Ar/39Ar dating of regional fabrics. *Tectonophysics, 277*(4), 307-337. doi: https://doi.org/10.1016/S0040-1951(97)00035-8.

Dias da Silva, Í., Gómez-Barreiro, J., Martínez Catalán, J. R., Ayarza, P., Pohl, J., & Martínez, E. (2017). Structural and microstructural analysis of the Retortillo Syncline (Variscan belt, Central Iberia). Implications for the Central Iberian Orocline. *Tectonophysics, 717*, 99-115. doi: https://doi.org/10.1016/j.tecto.2017.07.015.

Dias, G., Noronha, F., & Ferreira, N. (2000). Variscan Plutonism in the Central Iberian Zone, Northern Portugal. In *Eurogranites 2000, Field Meeting, Guide Book* (pp. 1-15).

Díez Balda, M. A., Vegas, R., & Lodeiro, G. (1990). Central Iberian Zone: structure. In R. D. Dallmeyer & E. Martinez Garcia (Eds.), *Pre-Mesozoic geology of the Iberian Peninsula* (pp. 172–188). Berlim: Springer Verlag.

European Commission: DG Internal Market Industry Entrepreneurship and SMEs. (2020). *Critical Raw Materials Resilience: Charting a Path towards greater Security and Sustainability* (COM(2020) 474 final). Brussels. Retrieved from: https://eur-lex.europa.eu/legal-content/EN/ALL/?uri=COM:2020:474:FIN

Fabre, C., Ourti, N. E., Mercadier, J., Cardoso-Fernandes, J., Dias, F., Perrotta, M., Koerting, F., Lima, A., Kaestner, F., Koellner, N., Linnen, R., Benn, D., Martins, T., & Cauzid, J. (2021). Analyses of Li-Rich Minerals Using Handheld LIBS Tool. *Data, 6*(6), 68. doi: 10.3390/data6060068.

Ferreira, J. A., Bento dos Santos, T., Pereira, I., & Mata, J. (2019). Tectonically assisted exhumation and cooling of Variscan granites in an anatectic complex of the Central Iberian Zone, Portugal: constraints from LA-ICP-MS zircon and apatite U–Pb ages. *International Journal of Earth Sciences, 108*(7), 2153-2175. doi: 10.1007/s00531-019-01755-1.

Ferreira, J. A., Mata, J., Bento dos Santos, T., & Pereira, I. (2020). The role of melting on the geochemical evolution and isotopic variability of an anatectic complex in the Iberian Variscides. *Lithos, 378-379*, 105769. doi: https://doi.org/10.1016/j.lithos.2020.105769.

Galeschuk, C. R., & Vanstone, P. J. (2007). Exploration techniques for rare-element pegmatite in the Bird River greenstone belt, southeastern Manitoba. In B. Milkereit (Ed.), *Proceedings of Exploration 07: Fifth Decennial International Conference on Mineral Exploration* (pp. 823–839).

Gaspar, L. (1997). *Contribuição para o estudo das mineralizações de volfrâmio (W), estanho (Sn) e lítio (Li) do sector Barca de Alva – Escalhão.* (Master thesis), Faculdade de Ciências da Universidade de Lisboa, Portugal, 267.

Gourcerol, B., Gloaguen, E., Melleton, J., Tuduri, J., & Galiegue, X. (2019). Re-assessing the European lithium resource potential – A review of hard-rock resources and metallogeny. *Ore Geology Reviews, 109*, 494-519. doi: https://doi.org/10.1016/j.oregeorev.2019.04.015.

Grosjean, C., Miranda, P. H., Perrin, M., & Poggi, P. (2012). Assessment of world lithium resources and consequences of their geographic distribution on the expected development of the electric vehicle industry. *Renewable and Sustainable Energy Reviews, 16*(3), 1735-1744. doi: https://doi.org/10.1016/j.rser.2011.11.023.

Gutiérrez-Alonso, G., Fernández-Suárez, J., Jeffries, T. E., Jenner, G. A., Tubrett, M. N., Cox, R., & Jackson, S. E. (2003). Terrane accretion and dispersal in the northern Gondwana margin. An Early Paleozoic analogue of a long-lived active margin. *Tectonophysics, 365*(1), 221-232. doi: https://doi.org/10.1016/S0040-1951(03)00023-4.

Gutiérrez-Alonso, G., Fernández-Suárez, J., López-Carmona, A., & Gärtner, A. (2018). Exhuming a cold case: The early granodiorites of the northwest Iberian Variscan belt—A Visean magmatic flare-up? *Lithosphere, 10*(2), 194-216. doi: 10.1130/l706.1.

Iglésias, M. & Ribeiro, A. (1981a). Zones de cisaillement ductile dans l'arc Ibéro-Armoricain. *Comun. Serv. Geol. Portugal*, 67 (1): 85–88.

Iglésias, M., & Ribeiro, A., (1981b). Position stratigraphique de la formation Ollo de Sapo dans la region de Zamora (Espagne) – Miranda do Douro (Portugal). *Comun. Serv. Geol. Portugal*, 67 (1): 141–146.

Julivert, M., Fontboté, J., Ribeiro, A., & Conde, L. (1974). Memória explicativa del Mapa Tectónico de la Península Ibérica y Baleares. Esc.: 1/ 1000000. In*st. Geol. Min. España,* Madrid. 133 pp.

Kesselring, M., Wagner, F., Kirsch, M., Ajjabou, L., & Gloaguen, R. (2020). Development of Sustainable Test Sites for Mineral Exploration and Knowledge Spillover for Industry. *Sustainability, 12*(5), 2016. doi: 10.3390/su12052016.

Köhler, M., Hanelli, D., Schaefer, S., Barth, A., Knobloch, A., Hielscher, P., Cardoso-Fernandes, J., Lima, A., & Teodoro, A. C. (2021). Lithium Potential Mapping Using Artificial Neural Networks: A Case Study from Central Portugal*. Minerals, 11*(10), 1046. doi: 10.3390/min11101046.

López-Plaza, M., Carnicero, A., & Gonzalo, J. C. (1982). Estudio geológico del campo filoniano de La Fregeneda (Salamanca). *STUDIA GEOLOGICA SALMANTICENSIA, XVII*, 89-98.

Martínez Catalán, J. R., Martínez Poyatos, D., Bea, F., & (Coords.). (2004). Zona Centroibérica: Introducción. In J. A. Vera (Ed.), *Geología de España* (pp. 68-69). Madrid: Sociedad Geológica de España/ Instituto Geológico y Minero de España (SGE-IGME).

Martínez Catalán, J. R., Rubio Pascual, F. J., Montes, A. D., Fernández, R. D., Barreiro, J. G., Dias Da Silva, Í., Clavijo, E. G., Ayarza, P., Alcock, J. E., Schulmann, K., Martínez Catalán, J. R., Lardeaux, J. M., Janoušek, V., & Oggiano, G. (2014). The late Variscan HT/LP metamorphic event in NW and Central Iberia: relationships to crustal thickening, extension, orocline development and crustal evolution. In *The Variscan Orogeny: Extent, Timescale and the Formation of the European Crust* (Vol. 405, pp. 0): Geological Society of London.

Martínez, F. J., Corretgé, L. G. & Suárez, O. (1990). The Central Iberian Zone (autochthonous sequences): distribution, characteristics and evolution of metamorphism. In: R. D. Dallmeyer & E. Martínez García (Eds), Pre-Mesozoic Geology of Iberia. Springer-Verlag. Berlim. p. 207–211.

Martín-Izard, A., Reguilón, R., & Palero, F. (1992). Las mineralizaciones litiníferas del oeste de Salamanca y Zamora. *Estudios Geológicos, 48*, 19-30.

Martins, T., Linnen, R. L., Fedikow, M. A. F., & Singh, J. (2017). Whole-rock and mineral geochemistry as exploration tools for rare-element pegmatite in Manitoba: examples from the Cat Lake–Winnipeg River and Wekusko Lake pegmatite fields (parts of NTS 52L6, 63J13). In *Report of Activities 2017* (pp. 42–51). Manitoba Growth, Enterprise and Trade, Manitoba Geological Survey.

Noronha, F., Ramos, J. M. F., Rebelo, J. A., Ribeiro, A., & Ribeiro, M. L. (1979). Essai de corrélation des phases de déformation hercynienne dans le Nord-Ouest Péninsulaire. *Bol. Soc. Geol. Portugal, 21*(2-3), 227-237.

Pereira, E. (1987). Estudo geológico estrutural da região de Celorico de Bastos e sua interpretação geodinâmica. *PhD thesis.* Fac. Ciências Univ. de Lisboa. 274 p. In: Dias, R., Ribeiro, A., Coke, C., Pereira, E., Rodrigues, J., Castro, P., Moreira, N., Rebelo, J. (2013). Evolução estrutural dos sectores setentrionais do Autóctone da Zona Centro-Ibérica. In: Dias, R., Araújo, A., terrinha, P., Kullberg, J.C. (Eds).

Geologia de Portugal. Volume I – Geologia Pré-mesozóica de Portugal, Escolar Editora. pp. 73-147.

Pereira, E., Ribeiro, A. & Meireles, C. (1993). Cisalhamentos Hercínicos e controlo das mineralizações de Sn-W, Au e U na Zona Centro Ibérica, em Portugal. *Cuaderno Lab. Xeolóxico de Laxe*. Coruña. Vol. 18, pp.89-119.

Pereira, I., Dias, R., Bento dos Santos, T., & Mata, J. (2017). Exhumation of a migmatite complex along a transpressive shear zone: inferences from the Variscan Juzbado–Penalva do Castelo Shear Zone (Central Iberian Zone). *Journal of the Geological Society, 174*(6), 1004. doi: 10.1144/jgs2016-159.

Pereira, M. F., Díez Fernández, R., Gama, C., Hofmann, M., Gärtner, A., & Linnemann, U. (2018). S-type granite generation and emplacement during a regional switch from extensional to contractional deformation (Central Iberian Zone, Iberian autochthonous domain, Variscan Orogeny). *International Journal of Earth Sciences, 107*(1), 251-267. doi: 10.1007/s00531-017-1488-3.

Pérez-Estaún, A., Bea, F., Bastida, F., Marcos, A., Martínez Catalán, J. R., Martínez Poyatos, D., Arenas, R., Díaz García, F., Azor, A., Simancas, J. F., & González Lodeiro, F. (2004). La cordillera varisca europea: el Macizo Ibérico. In J. A. Vera (Ed.), *Geología de España* (pp. 21-25). Madrid: Sociedad Geológica de España/ Instituto Geológico y Minero de España (SGE-IGME).

Ribeiro, A. (1974). Contribution à l'étude tectonique de Trás-os-Montes oriental. *Mem. Serv. Geol. Portugal, Lisboa*, 24 (Nova Série). 168 p.

Ribeiro, A. (1990). Part IV – Central-Iberian Zone. Introduction. In: Dallmeyer, R. D. & Martinez Garcia, E. (Eds.) *Pre-Mesozoic Geology of Iberia*, Springer-Verlag, Berlin, Heidelberg, pp. 143-144.

Ribeiro, A., Antunes, M., Ferreira, M., Rocha, R., Soares, A., Zbyszewski, G., Almeida, F., Carvalho, D. & Monteiro, J. (1979). Introduction à la Géologie Générale du Portugal. *Serv. Geol. Portugal*, Lisboa.114 p.

Ribeiro, A., Pereira, E. & Dias, R. (1990). Structure in the Northwest of the Iberian Peninsula. In: Dallmeyer, R.D. & Martinez Garcia, E. (Eds.): *Pre-Mesozoic Geology of Iberia*, Springer-Verlag, Berlin, Heidelberg, pp. 220-236.

Ribeiro, A., Pereira, E., & Rodrigues, J. (2006). Tectónica. In: Pereira, E. (Coord.), Carta Geológica de Portugal na escala 1:200000 – Notícia explicativa da Folha 2, Lisboa, *Serv. Geol. Portugal*, 69-76.

Ribeiro, M. L. (2001). *Notícia explicativa da carta geológica simplificada do Parque Arqueológico do Vale do Côa*. Vila Nova de Foz Côa, Portugal: Parque Arqueológico do Vale do Côa, 71.

Ribeiro, M.L., Silva, A.F. (2000). Carta Geológica Simplificada do Parque Arqueológico do Vale do Côa. Instituto Geológico e Mineiro and Parque Arqueológico do Vale do Côa, Vila Nova de Foz Côa, Portugal.

Roda, E. (1993). *Distribución, Caracteristicas y Petrogenesis de las Pegmatitas de La Fregeneda (Salamanca).* (PhD thesis), Facultad de Ciencia y Tecnología de la Universidad del País Vasco (UPV/EHU), Bilbao, Spain, 199.

Roda-Robles, E., Pesquera, A., Gil-Crespo, P. P., Vieira, R., Lima, A., Garate-Olave, I., Martins, T., & Torres-Ruiz, J. (2016). Geology and mineralogy of Li mineralization in the Central Iberian Zone (Spain and Portugal). *Mineralogical Magazine, 80*(1), 103-126. doi: 10.1180/minmag.2016.080.049.

Roda-Robles, E., Pesquera, A., Velasco, F., & Fontan, F. (1999). The granitic pegmatites of the Fregeneda area (Salamanca, Spain): characteristics and petrogenesis. *Mineral. Mag., 63*(4), 535–558.

Roda-Robles, E., Villaseca, C., Pesquera, A., Gil-Crespo, P. P., Vieira, R., Lima, A., & Garate-Olave, I. (2018). Petrogenetic relationships between Variscan granitoids and Li-(F-P)-rich aplite-pegmatites in the Central Iberian Zone: Geological and geochemical constraints and implications for other regions from the European Variscides. *Ore Geology Reviews, 95*, 408-430. doi: https://doi.org/10.1016/j.oregeorev.2018.02.027.

Rodrigues, J., Pereira, E., & Ribeiro, A. (2011). Complexo de Mantos Parautóctones do NE de Portugal: Estrutura interna e Tectonoestratigrafia. In: Dias, R., Araújo, A., terrinha, P., Kullberg, J.C. (Eds). *Geologia de Portugal. Volume I – Geologia Pré-mesozóica de Portugal*, Escolar Editora. pp. 269-325.

Rodríguez Alonso, M. D., Díez Balda, M. A., Perejón, A., Pieren, A., Liñán, E., López Díaz, F., Moreno, F., Gámez Vintaned, J. A., Gónzalez Lodeiro, F., Martínez Poyatos, D., & Vegas, R. (2004). Domínio del Complejo Esquisto-Grauváquico: Estratigrafía. La secuencia litoestratigráfica del Neoproterozóico-Cámbrico Inferior. In J. A. Vera (Ed.),

Geología de España (pp. 78-81). Madrid: Geol. España/Inst. Geol. Min. España (SGE-IGME).

Rodríguez Fernández, L. R., Díez Montes, A., Escuder, J. & Carrasco, R. (2000). Hoja geológica número 448 (Vilvestre). Mapa Geológico de España a Escala 1:50.000 (2ª serie). Madrid: Instituto Geológico y Minero de España (IGME). Retrieved from http://info.igme.es/cartografiadigital/geologica/Magna50Hoja.aspx?intranet=false&id=448B

Ruiz-Coupeau, S., Jürgens, B., Keßelring, M., & Herrero-Solana, V. (2020). Sustainability in Mineral Exploration—Exploring Less Invasive Technologies via Patent Analysis. *Sustainability, 12*(22), 9761. doi: 10.3390/su12229761.

Sabins, F. F. (1999). Remote sensing for mineral exploration. *Ore Geology Reviews, 14*(3), 157-183. doi: https://doi.org/10.1016/S0169-1368(99)00007-4.

San José, M. A., Pieren, A. P., Garcia-Hidalgo, J. F., Vilas, L., Herranz, P., Pelaez, J. R., & Perejon, A. (1990). Central Iberian Zone. Autochthonous sequences: Ante-Ordovician stratigraphy. In R. D. Dallmeyer & E. Martinez Garcia (Eds.), *Pre-Mesozoic Geology of Iberia* (pp. 147- 159). Berlin, Heidelberg: Springer-Verlag.

Santos, D., Teodoro, A., Lima, A., & Cardoso-Fernandes, J. (2019, 9–12 September 2019). *Remote sensing techniques to detect areas with potential for lithium exploration in Minas Gerais, Brazil.* Paper presented at the SPIE Remote Sensing, Strasbourg, France, doi: https://doi.org/10.1117/12.2532744.

Silva, A. F. d., & Ribeiro, M. L. (1991). *Notícia Explicativa da folha 15-A Vila Nova de Foz Côa*. Lisboa, Portugal: Serviços Geológicos de Portugal, 52.

Silva, A. F. d., & Ribeiro, M. L. (1994). *Notícia Explicativa da folha 15-B Freixo de Espada à Cinta*. Lisboa, Portugal: Instituto Geológico e Mineiro, 48.

Silva, A. F., Santos, A. J., Ribeiro, A., & Ribeiro, M. L. (1990b). *Carta Geológica de Portugal na escala 1/50.000 – folha 15-A – Vila Nova de Foz Côa*. Lisboa, Portugal: Serviços Geológicos de Portugal, 1 map.

Silva, A. F., Santos, A. J., Ribeiro, A., Cabral, J., & Ribeiro, M. L. (1990a). *Carta Geológica de Portugal na escala 1/50.000 – folha 15-B – Freixo de Espada à Cinta*. Lisboa, Portugal: Serviços Geológicos de Portugal, 1 map.

Silva, I. (2013). *Geología de las zonas Centro Ibérica y Galicia – Trás-Os-Montes en la parte oriental del Complejo de Morais.* (phD thesis), Universidad de Salamanca, Spain, Portugal/España, 445.

Sousa, M. B. (1982). *Litostratigrafia e estrutura do "Complexo Xisto-Grauváquico Ante-Ordovícico" – Grupo do Douro (Nordeste de Portugal).* (PhD thesis), Centro de Geociências da Universidade de Coimbra, Coimbra, Portugal, 222.

Sousa, M. B. (1983). Considerações paleogeográficas e ensaio de correlação das formações do Grupo do Douro (CXG) com as formações ante-Ordovícicas da Zona Centro-Ibérica. *Memórias e Notícias, Publicações do Museu e Laboratório Mineralógico e Geológico da Universidade de Coimbra, 65*, 65-98.

Sousa, M. B. (1984). Considerações sobre a estratigrafia do Complexo Xisto-Grauváquico (CXG) e sua relação com o Paleozóico Inferior. *Cuadernos de Geología Ibérica, 9*, 9-36.

Teixeira, C. (1955). *Notas sobre geologia de Portugal o complexo xisto-grauváquico ante-ordoviciano*. Lisboa, Portugal: Empresa Literaria Fluminense Lda., 48.

Valladares, M. I., Ugidos, J. M., Barba, P., & Colmenero, J. R. (2002). Contrasting geochemical features of the Central Iberian Zone shales (Iberian Massif, Spain): implications for the evolution of Neoproterozoic–Lower Cambrian sediments and their sources in other peri-Gondwanan areas. *Tectonophysics, 352*(1), 121-132. doi: https://doi.org/10.1016/S0040-1951(02)00192-0.

Valle Aguado, B., Azevedo, M. R., Nolan, J., Medina, J., Costa, M. M., Corfu, F., & Martínez Catalán, J. R. (2017). Granite emplacement at the termination of a major Variscan transcurrent shear zone: The late collisional Viseu batholith. *Journal of Structural Geology, 98*, 15-37. doi: https://doi.org/10.1016/j.jsg.2017.04.002.

Van der Werff, H., & Van der Meer, F. (2016). Sentinel-2A MSI and Landsat 8 OLI Provide Data Continuity for Geological Remote Sensing. *Remote Sensing, 8*(11), 883. doi: 10.3390/rs8110883.

Viegas, L. (1983). *Recursos minerais de volfrâmio e estanho na região de Freixo-Escalhão*. Relatório interno do Serviço de Fomento Mineiro. Porto, 45. (Unpublished).

Vieira, R. (2010). *Aplitopegmatitos com elementos raros da região entre Almendra (V.N. de Foz Côa) e Barca d'Alva (Figueira de Castelo Rodrigo). Campo aplitopegmatítico da*

Fregeneda- Almendra. (PhD thesis), Faculdade de Ciências da Universidade do Porto, Porto, Portugal, XXVI, 273.

Vieira, R., Roda-Robles, E. n., Pesquera, A., & Lima, A. (2011). Chemical variation and significance of micas from the Fregeneda-Almendra pegmatitic field (Central-Iberian Zone, Spain and Portugal). *American Mineralogist, 96*(4), 637-645. doi: 10.2138/am.2011.3584.

Villaseca, C. (2011). *On the origin of granite types in the Central Iberian Zone: contribution from integrated U-Pb and Hf isotope studies of zircon.* Paper presented at the VIII Congresso Ibérico de Geoquímica, Castelo Branco, Portugal, 271–276.

Villaseca, C., Merino, E., Oyarzun, R., Orejana, D., Pérez-Soba, C., & Chicharro, E. (2014). Contrasting chemical and isotopic signatures from Neoproterozoic metasedimentary rocks in the Central Iberian Zone (Spain) of pre-Variscan Europe: Implications for terrane analysis and Early Ordovician magmatic belts. *Precambrian Research, 245*, 131-145. doi: https://doi.org/10.1016/j.precamres.2014.02.006.

Chapter I: State of the art

This chapter aims at providing the reader with background information about the use of remote sensing in Li-exploration. In a first stage, the works and achievements made concerning remote sensing data and techniques applied to Li-pegmatite exploration in the Fregeneda-Almendra area were discussed (Cardoso-Fernandes *et al.*, 2019). Also, the constraints observed in previous works were identified and research directions were proposed to overcome them. From this review of the state of the art resulted a peer-reviewed journal article (section I.1.). Subsequently, the research was expanded to a comprehensive bibliographic search concerning all past application studies of remote sensing data and techniques to any kind of Li-deposit (hard rock or brine). This resulted in a published review article where each approach was critically evaluated through the identification of their weaknesses and strengths (Cardoso-Fernandes *et al.*, 2020). In the end, several suggestions to overcome the difficulties highlighted were proposed and new research perspectives were presented (section I.2.). Based on this work, an encyclopedia entrance was created concerning the detecting of Li mineralizations from space (Cardoso-Fernandes, 2020; Appendix I.3.).

References

Cardoso-Fernandes, J., Lima, A., Roda-Robles, E., & Teodoro, A. C. (2019). Constraints and potentials of remote sensing data/techniques applied to lithium (Li)-pegmatites. *The Canadian Mineralogist, 57*(5), 723-725. doi: 10.3749/canmin.AB00004.

Cardoso-Fernandes, J., Teodoro, A. C., Lima, A., Perrotta, M., & Roda-Robles, E. (2020). Detecting Lithium (Li) Mineralizations from Space: Current Research and Future Perspectives. *Applied Sciences, 10*(5), 1785. doi: 10.3390/app10051785.

Cardoso-Fernandes, J. (2020). "Detecting Lithium (Li) Mineralizations from Space". In *Scholarly Community Encyclopedia*. https://encyclopedia.pub/785.

I.1. CONSTRAINTS AND POTENTIALS OF REMOTE SENSING DATA/TECHNIQUES APPLIED TO LITHIUM (Li)-PEGMATITES

Joana Cardoso-Fernandes, Alexandre Lima, Encarnación Roda-Robles, Ana Cláudia Teodoro

The Canadian Mineralogist, 2019, **57 (5)**, 723–725.

Keywords: lithium, pegmatite, remote sensing, exploration, Fregeneda-Almendra, Portugal, Spain.

Introduction

Lithium (Li) is a mineral commodity increasingly sought after mainly because it is essential to the production of rechargeable Li-ion batteries mainly used in high-tech consumer electronics (like smartphones) and in the green-power industry. This increasing demand of Li is mainly driven by the electric car industry, in the pursuit for more environment-friendly means of transportation, and it will result in an intensive Li exploitation in the near future. Consequently, there is great pressure for mining and exploration companies to achieve fast but accurate results in targeting potentially economic areas. New and untraditional Li exploration methods are needed in order to meet the market expectations. One of these exploration methods could be remote sensing, which has shown good results in targeting gold and copper deposits for example. Remote sensing is the science which obtains, processes and interprets data that records the interaction between matter and electromagnetic energy at distance (Sabins 1997). Recently, the first steps towards its application in Li exploration were made.

In Europe the most important Li-bearing deposits are the ones hosted in pegmatites (Kesler et al. 2012), and one of the main areas of interest in Europe is the Iberian Peninsula where several aplite-pegmatite fields were already recognized. The Fregeneda-Almendra aplite-pegmatite field is one of these cases and was selected as the study area since the sparse vegetation allows the application of remote sensing techniques.

The Fregeneda-Almendra aplite-pegmatite field

The Fregeneda-Almendra (FA) aplite-pegmatite field lies within the Central Iberian Zone, which occupies the central portion of the Iberian Massif. In the FA field different types of pegmatite veins were defined according to their mineralogy, morphology and internal structure (Roda-Robles 1993, RodaRobles et al. 1999, Vieira 2010). These dikes intruded the pre-Ordovician metasediments of the schistmetagraywacke complex (Carrington da Costa 1950) and are located north of the syn-Variscan Mêda-Penedono-Lumbrales granitic complex. They show a zonal distribution from barren aplite-pegmatites to bodies enriched in Li, F, Sn, Rb, Nb. Ta, B, P and Be, with increasing fractionation degree as the distance to the granitic complex becomes greater. Within the evolved pegmatites, five types of dikes have been characterized: petalite-

rich, spodumene-rich, lepidolite-spodumene-rich, lepidolite-rich and cassiterite-rich pegmatites.

Recently, in the FA area, some remote sensing algorithms such as RGB (red, green, blue) combinations, band ratios, principal component analysis (PCA) and image classification (using the Maximum Likelihood algorithm) were applied to identify Li-pegmatites (Cardoso-Fernandes et al. 2018, Cardoso-Fernandes et al. 2019).

Remote sensing and Li-pegmatites

In Li exploration, the previous works show that there are two main approaches to the application of the image processing methods: (i) the recognition of hydrothermally altered zones associated with the mineralized zones; (ii) the direct identification of Li-bearing minerals. These approaches were made using different types of multispectral products: Landsat 5 TM, Landsat 8 OLI, ASTER and Sentinel-2. In what concerns the first approach, the application of classic techniques with the known band combinations showed some contradictory results. On one hand, RGB combinations are capable of identifying some hydrothermal alteration near the Li-bearing pegmatites while the band ratio technique failed to identify minerals associated with hydrothermal alteration (like iron oxides and clays) near the open-pit mines where their presence was described. Also, the application of PCA, on only certain bands where the target minerals present characteristic absorption or reflectance features, allowed to identify the presence of iron minerals in some mines while only the ASTER sensor allowed to identify hydroxyl-bearing minerals like clays (Cardoso-Fernandes et al. 2019). All the existing RGB band combinations used in this approach were defined for other deposit types and therefore are not the most adequate to Li-exploration due to the different nature of the deposits and their associated mineralogy and alteration style. Detailed studies on the type of alteration associated with the Li-bearing pegmatites could help to develop new band combinations more robust to Li-exploration.

Regarding the second approach, different self-proposed RGB combinations were capable of discriminating Li-bearing pegmatites with good exposition from the host rocks for all sensors excepting the Sentinel-2 (Cardoso-Fernandes et al. 2019). The impossibility to discriminate the Li-pegmatites with Sentinel-2 images reflects the importance of thermal bands, which Sentinel-2 does not have available. Besides, other methods showed good results in highlighting Li-mineralizations, namely several band ratios and the application of PCA in certain subsets of bands. Finally, a first attempt to supervised image classification was made

by Cardoso-Fernandes et al. (2018). In this study, a conventional classification algorithm Maximum Likelihood was employed and it positively identified the three open pit mines as Li-bearing areas. Nonetheless, this classification also produced several false positives and some confusion between the metasedimentary rocks and the granites.

Overall, we can identify the main difficulties/ challenges in the application of remote sensing to Li-pegmatite exploration as being: (i) the vegetation coverage that even when sparse can mask out other spectral signals; (ii) the relation between the aplite-pegmatite dikes dimensions and the image pixel size which results in a small exposition; (iii) the spectral resolution of sensors due to the importance of the thermal infrared region in Li-mineral identification and due to the fact that a higher number of bands increases the capability of mineral discrimination; (iv) the spectral similarity of some classes mainly between the Li-bearing pegmatites and urbanized areas or agricultural fields.

Considering all this, even though some of the applied methodologies allowed a good discrimination of the Li-pegmatites, it is clear that more robust remote sensing techniques need to be applied and detailed spectral, petrographic and geochemical studies must be conducted in order to: (i) discriminate the areas with similar spectral behavior; (ii) identify the characteristics of hydrothermal alteration associated with the Li-bearing pegmatites and its spectral features.

To overcome the identified difficulties, several strategies are now being considered. The pixel size problem can be resolved by diminishing the pixel using very high-resolution images, namely WorldView3. Also drone flights will allow to validate the results obtained with the satellite images. On the other hand, the construction of a spectral library of the different minerals and rocks will be the key to fully discriminate the spectral signatures obtained in the satellite products and also to validate the techniques applied. Lastly, to improve the image classification results, unconventional techniques such as machine learning algorithms are being used.

Acknowledgments

The authors would like to thank the financial support provided by FCT– Fundação para a Ciência e a Tecnologia with the ERA-MIN/0001/2017 – LIGHTS project and to FEDER through the operation POCI-01-0145-FEDER-007690 funded by the Programa Operacional Competitividade e Internacionalização – COMPETE2020 and by National Funds through FCT – Fundação para a Ciência e a Tecnologia within ICT, R&D Unit (reference UID/

GEO/04683/2013). Joana Cardoso-Fernandes is financially supported by FCT within the compass of a Ph.D. Thesis, ref. SFRH/BD/136108/2018.

References

CARDOSO-FERNANDES, J., LIMA, A., & TEODORO, A.C. (2018). Potential of Sentinel-2 data in the detection of lithium (Li)-bearing pegmatites: a study case. Proceedings Volume 10790, SPIE Remote Sensing, SPIE, 15 pp.

CARDOSO-FERNANDES, J., TEODORO, A.C., & LIMA, A. (2019). Remote sensing data in lithium (Li) exploration: A new approach for the detection of Li-bearing pegmatites. International Journal of Applied Earth Observation and Geoinformation 76, 10–25.

CARRINGTON DA COSTA, J. (1950). Notícia sobre uma carta geológica do Buçaco, de Nery Delgado. Comunicações dos Serviços Geológicos de Portugal, Lisboa, 28 pp. (in Portuguese).

KESLER, S.E., GRUBER, P.W., MEDINA, P.A., KEOLEIAN, G.A., EVERSON, M.P., & WALLINGTON, T.J. (2012). Global lithium resources: Relative importance of pegmatite, brine and other deposits. Ore Geology Reviews 48, 55–69.

RODA-ROBLES, E. (1993). Distribución, Caracteristicas y Petrogenesis de las Pegmatitas de La Fregeneda (Salamanca). Ph.D. Thesis, Department of Mineralogy & Petrology – UPV, Bilbao, Spain, 199 pp. (in Spanish).

RODA-ROBLES, E., PESQUERA, A., VELASCO, F., & FONTAN, F. (1999). The granitic pegmatites of the Fregeneda area (Salamanca, Spain). characteristics and petrogenesis. Mineralogical Magazine 63, 535–558.

SABINS, F.F. (1997). Remote Sensing—Principles and Interpretation. 3rd Edition, W.H. Freeman, New York City, New York.

VIEIRA, R. (2010). Aplitopegmatitos com Elementos Raros da Região entre Almendra (V. N. de Foz-Côa) e Barca d'Alva (Figueira de Castelo Rodrigo). Campo Aplitopegmatíıtico da Fregeneda-Almendra. Ph.D. Thesis. Universidade do Porto, Porto, Portugal, 276 pp. (in Portuguese).

I.2. Detecting Lithium (Li) Mineralizations from Space: Current Research and Future Perspectives

Joana Cardoso-Fernandes, Ana C. Teodoro, Alexandre Lima, Mônica Perrotta and Encarnación Roda-Robles

Applied Sciences, 2020, **10(5)**, 1785.

Abstract: Optical and thermal remote sensing data have been an important tool in geological exploration for certain deposit types. However, the present economic and technological advances demand the adaptation of the remote sensing data and image processing techniques to the exploration of other raw materials like lithium (Li). A bibliometric analysis, using a systematic review approach, was made to understand the recent interest in the application of remote sensing methods in Li exploration. A review of the application studies and developments in this field was also made. Throughout the paper, the addressed topics include: (i) achievements made in Li exploration using remote sensing methods; (ii) the main weaknesses of the approaches; (iii) how to overcome these difficulties; and (iv) the expected research perspectives. We expect that the number of studies concerning this topic will increase in the near future and that remote sensing will become an integrated and fundamental tool in Li exploration.

Keywords: satellite data; image processing algorithms; pegmatite; brine; lithological mapping; mineral alteration mapping; geobotanical mapping

1. Introduction

Optical and thermal remote sensing data, namely satellite-acquired images, have been an important tool in geological exploration allowing to target exploration areas for more than four decades. The major contribution that remote sensing offers to mineral exploration was reviewed in several works dedicated to this topic [1–5]: it provides information in a fairly quick, inexpensive, and non-intrusive way, which favors mining and exploration companies especially in inaccessible remote areas. However, Rajesh [3], in an overview of the use of remote sensing and Geographic Information Systems (GIS) in mineral exploration, points out the difficulty of

directly pinpointing mineralizations using only remote sensing data, highlighting the importance of the integration with other types of geological data.

Sabins [6], in one of the first reviews about the types of data and image processing methods for mineral exploration, describes two main approaches to target mineral deposits: (i) structural and lithological mapping; and (ii) hydrothermal alteration mapping. Later, Rajesh [3] proposed three approaches: (i) lithological mapping; (ii) structural mapping; and (iii) alteration mapping. These approaches have been applied since the 1970s to identify very distinct types of mineral deposits. The more common applications include porphyry copper [7–17] and gold [18–28] deposits. Other applications may include: iron ore deposits [19,29–32], volcanogenic massive sulfide ore (VMS) deposits [33–35], several skarn-hosted deposits [36–39], chromite deposits [40–43], uranium deposits [39,44], rare earth elements (REE) exploration [36,45], brine and evaporite deposits [46,47], porphyry molybdenum deposits [48,49], zinc-lead (Zn-Pb) deposits [50], diamond [51] and bauxite exploration [52].

Regarding the types of data used, multispectral products, namely Landsat and Advanced Spaceborne Thermal Emission and Reflection Radiometer (ASTER) sensor imagery, played an important part in geological remote sensing [4,5,53]. Abrams and Yamaguchi [54] reviewed ASTER's contributions to mineral exploration and lithological mapping. The success of the ASTER sensor in geological exploration was mainly due to a higher spectral resolution in the short-wave infrared (SWIR) and thermal infrared (TIR), specially designed for geological applications, which improved its lithological and mineral mapping capabilities, particularly in the identification of alteration minerals [4,53–55]. The importance of TIR (including ASTER's TIR subsystem) in the discrimination of minerals and rocks was revised by Ninomiya and Fu [55]. These authors highlight several studies in which the TIR region was fundamental for mineral discrimination, namely where silicate minerals occur, and reviewed the spectral indices proposed for lithological mapping using ASTER-TIR data. Nonetheless, the advent of hyperspectral remote sensing allowed the direct identification and quantification of specific minerals which represented a key contribution to mineral exploration [3,53]. Cudahy [4] in a review on mineral mapping projects for exploration led by Commonwealth Scientific and Industrial Research Organization (CSIRO) in Australia, pointed out that hyperspectral remote sensing can be less popular among exploration companies because of limited spatial coverage, the relatively high-cost of quality datasets, and the inherent complexity of hyperspectral data.

Despite the successful application of different types of remote sensing data to distinct mineral deposits, the current growing economic and technological advances, which rely on other

mineral commodities, highlights the need to use and adapt remote sensing data and image processing techniques on new deposit types. Nowadays, green technologies, like electric vehicles, represent an important sector of the economy [56] and lithium (Li) has become a critical metal to the green-power industry [57,58]. However, Li exploration with the resource of remote sensing data and techniques represents an emergent field, with several difficulties and unknown possibilities. Taking this into account, this review aims at (i) providing information about what can be accomplished in Li exploration using remote sensing methods; (ii) identifying the main difficulties associated with this kind of deposits; and (iii) providing insights on how to overcome these difficulties as well as future research perspectives. This paper presents the first summary of the developments made in the field of remote sensing applied to Li exploration and we consider it to be timely and appropriate due to the high global demand of this metal to the production of Li-ion batteries [58]. Additionally, this review can help to promote new applications and to solve new exploration problems.

2. Li Exploration Using Remote Sensing

This section aims at summarizing past and current applications of remote sensing data and image processing techniques to Li exploration at first, and then highlights the main weaknesses associated with each methodology already proposed.

2.1. Advancements in Satellite-Based Remote Sensing

Despite the latest interest in this topic, the first application of remote sensing to Li mineralizations started in 1982. Lefevre [59] conducted a multitemporal study (from 1975 to 1976) using Landsat Multispectral Scanner System (MSS) images to detect geobotanical anomalies caused by dispersal halos of metals, such as lithium, tungsten, and arsenic, associated with the Collete granite and the Beauvoir domes. To extract the spectral signature of the circular anomaly, band ratios 7/5 and 7/6 (band 5: 0.6 to 0.7µm; band 6: 0.7 to 0.8 µm; band 7: 0.8 to 1.1 µm) were applied to the images. Comparing the spectral anomalies of the vegetation with the soil geochemical maps, the author concluded that there was a clear correspondence between spectral and geochemical anomalies. However, such spectral anomalies could be related to the presence of the other metals in the vegetation's leaves and not necessarily due to the presence of Li.

Over a decade ago, Perrotta et al. [60] used ASTER images for a trial mapping of Li-bearing pegmatites in the Vale do Jequitinhonha region, Brazil. The authors used visible, near-infrared (VNIR), and SWIR data to evaluate the spectral signatures of gem- and Li pegmatites, and related alteration minerals. For that, the target spectra were determined through the estimation of the pixel purity index (PPI) either directly in the atmospherically-corrected images or after applying a minimum noise fraction (MNF) transformation of the data. PPI was estimated since the mean spectra of each sample group, where the pixel samples were identified in ASTER images, failed as reference spectra. The obtained reference spectra were used to classify the ASTER image using the spectral angle mapper (SAM) and the mixture-tuned matched filtering (MTMF), having the last supervised method outperform the first since SAM was also sensible to roads, agricultural fields, or areas around the main drainage lines.

Mendes et al. [61] applied a similar methodology in the identification of Li minerals' spectral signatures in view of future identification of unknown ore deposits in the Vale do Jequitinhonha region, Brazil. To achieve that goal, reference spectra of Li-bearing minerals, as well as associated alteration minerals and soils, were collected in the laboratory. However, only the open-pit mines delimited in image data were used as training areas after the spectra obtained in the laboratory failed to serve as a reference for the classification process. Similar to before, an MNF transformation was applied to the ASTER VNIR and SWIR bands in order to segregate the noise. Statistical analysis was applied to the MNF to determine the reference pixels with the highest PPI, from which tree reference signatures were selected. Afterward, two supervised classification methods were employed, SAM and MTMF, only where the location of metasediment outcrops, while the other lithologies where masked. Although both methods were able to correctly identify the spectral features of pegmatite intrusions, the SAM classifier also mapped other features, like roads or agricultural fields, while MTMF only identified a small number of pixels to have similar spectral behavior to the reference spectra. The solution proposed by Mendes et al. [61] was to produce a final target potential map through the Boolean intersection of the results obtained from the application of MTMF and SAM techniques.

Another remote sensing approach to Li pegmatite exploration was made recently in the Fregeneda-Almendra (Salamanca, Spain–Vila Nova de Foz Côa, Portugal) pegmatite field. Cardoso-Fernandes et al. [62], in a preliminary stage, presented the potential of the Sentinel-2 Multispectral Instrument (MSI) in Li mapping. The study attempted to identify Li pegmatites mainly based on the recognition of the associated alteration halos. To achieve that goal, several methods applied to other deposit types were adapted to the Sentinel-2 images, including RGB (red, green, blue) combinations, band ratios and principal component analysis

(PCA). These methodologies allowed to predict the occurrence of iron oxides and clay minerals, and to discriminate between non-altered and hydrothermally-altered zones. The authors also tried to directly identify Li pegmatites based on their spectral behavior. Using the reference spectra of spodumene (a Li-bearing mineral), the band ratio 3/8 was proposed to discriminate the presence of Li-bearing minerals. Another approach was to use a supervised image classification to map Li-bearing pegmatites. The classification was performed on the resultant bands from the application of PCA, using the land cover signature classification (LCS) and the maximum likelihood (ML) algorithms simultaneously. The reference spectral curves used to classify the image were the ones collected in training sites identified in the Sentinel-2 images. The training areas included open-pit mines exploiting Li minerals. Although the algorithm employed allowed to correctly identify the Li pegmatites in exploitation, it also generated some false positives and misclassified some metasedimentary areas. The authors [62] also highlighted the need and importance of the acquisition of mineral spectra to improve the classification output. Considering the results given in this work, Cardoso-Fernandes et al. [63] presented two new different approaches: (i) identification of hydrothermal alteration minerals associated with the Li-bearing pegmatites; and (ii) direct identification of Li minerals. These methods were applied in different types of multispectral cloud-free products, namely, Landsat-5 Thematic Mapper (TM), Landsat-8 Operational Land Imager (OLI) and Thermal Infrared Sensor (TIRS), ASTER, and Sentinel-2 MSI. The alteration mapping results differ from one image processing method to another [63]: while RGB combinations highlighted hydrothermally-altered areas near the Li-bearing pegmatites, the common band ratios applied were unsuccessful in the identification of iron oxides and clay minerals in the open-pit mines where they were described [64]. Additionally, Selective PCA, i.e., PCA applied in a subset of bands chosen based on characteristic absorption or reflectance features of the target minerals, only identified the occurrence of iron minerals in some of the open pits. The ASTER sensor was the one that showed better performance since hydroxyl-bearing minerals like clays were solely identified in the ASTER image [63], reflecting the higher mapping capabilities of ASTER due to its better spectral resolution. On the other hand, some spectral confusion with areas affected by wildfires and with agricultural fields hindered the results. In what concerns the approach to directly identify Li minerals, Cardoso-Fernandes et al. [63] proposed new algorithms capable of identifying the Li pegmatites with better exposition (i.e., outcropping area) (see Appendix A). In the case of RGB combinations (ASTER 5-1-14 and 2-1-13; Landsat-8 7-3-11 and 2-1-11; Landsat-5 7-2-6 and 2-1-6), it was possible to discriminate the Li-bearing pegmatites from the host rocks (metapelites) [63]. However, this discrimination could not be achieved using Sentinel-2 images due to the lack of TIR bands and the importance of this

region of the electromagnetic spectrum in silicate minerals [55,65] like the Li-bearing silicates (spodumene and petalite) that occur in the Fregeneda-Almendra area. The proposed band ratios (ASTER 7/6 and 1/3, Landsat-8 3/5, Landsat-5 2/4, Sentinel-2 3/8) and selective PCA based on subsets of two and four bands were also able to highlight the Li pegmatites, isolating the related spectral inputs, although the authors recommend the use of the two-band subset for PCA since it reduces unnecessary noise [63]. Despite the success in Li pegmatite discrimination, all methods manifested spectral confusion with urbanized areas and agricultural fields. These spectral confusions are consistent with the ones reported by other authors in different regions of the world [60,61], pointing to the need to spectrally separate the classes.

In follow-up work, Santos et al. [66] applied the algorithms proposed by Cardoso-Fernandes et al. [63] to evaluate their performance in drawing potential exploration areas in other Li pegmatites occurrences, namely in the pegmatite fields of Araçuaí and São João Del Rei in Brazil. The methods (RGB combinations, band ratios, and selective PCA) and the algorithms employed (see Appendix A) showed variable performances in the two pegmatite fields. Additionally, Li pegmatite identification was more accurate in the São João Del Rei region than in Araçuaí, having the vegetation coverage in the second area negatively influenced the results according to the authors [66]. It is worth mentioning the ability of RGB combinations to discriminate Li pegmatites from both host rocks and associated tailings and mine dumps, with the exception of the Landsat-5 images [66]. Additionally, in the São João Del Rei area, the most successful band ratios were the ones proposed based on the reference spectrum of lepidolite (a Li-bearing mica): Landsat-5 3/7, Landsat-8 4/7 and Sentinel-2 4/7 [63]. Regarding the ratios proposed for spodumene, only ASTER 1/3 was able to highlight Li mineralized areas. In the Araçuaí area, the spodumene based ratios were the most accurate in Li pegmatite identification. In what concerns selective PCA, the two-band subset produced better results in the São João Del Rei pegmatite field while the four-band subset worked better in Araçuaí [66]. Overall, selective PCA presented the most accurate results while band rationing was the least efficient method in Li pegmatite identification [66]. On the other hand, no limitations were found in the use of Sentinel-2 images, unlike that reported in other works [63]. This may suggest that the ability to discriminate Li pegmatites using Sentinel-2 images might rely on the composition of the host rocks. Nevertheless, the results obtained were very significant, contributing to the state of the art of this field, since not only did it confirm the methodology proposed by Cardoso-Fernandes et al. [63] but also showed its ability to detect other pegmatite occurrences with Li potential besides the known target areas. Currently, field validation is in progress to check if Li mineralization is in fact present in the potential areas identified.

Moreover, in the Alto Ligonha province (Mozambique), Gemusse et al. [67] used ASTER and Landsat-8 images to map hydrothermal alteration minerals associated with Li-bearing pegmatites, since several pegmatites in the region present a thick kaolinitic weathering crust. The two satellite products were used to produce land cover classification maps with the SAM supervised algorithm. Although the ASTER image classification obtained a higher overall accuracy, both products allowed to identify the spectral signatures of hydrothermal clay alteration (kaolin occurrences) associated with pegmatites [67]. This identification was also supported by published spectral libraries. Additionally, field samples of Li minerals, such as lepidolite and spodumene, were collected and analyzed using an ASD HandHeld2 spectroradiometer [67]. However, the spectroradiometer only covers the VNIR region of the spectra, so it was not possible to discriminate the two Li minerals in these wavelengths. Nonetheless, the classification results, using the target signatures collected in the satellite products, were able to identify two potential areas for future pegmatite exploration [67]. The authors also concluded that ASTER and Landsat-8 provide complementary information on mineral composition. Still in the Alto Ligonha region, different satellite products (namely ASTER, Landsat-8, and Sentinel-2) and different remote sensing algorithms were compared to target Li pegmatites [68]. The algorithms include three supervised classification methods—minimum distance, SAM, and ML—and one unsupervised algorithm: k-means clustering. The land cover classifications maps were compared as well as the performance accuracy of each classifier. Contrary to expected, the minimum distance attained the best accuracy while ML showed the worst performance [68] but no explanation to the fact is given. Perhaps these results reflect the quality of the training data. Despite the disparity between the results obtained with the different classifiers, Gemusse et al. [68] stated that the classification maps show clay minerals, such as kaolinite and montmorillonite, resultant from pegmatite alteration. These maps were validated through field investigations, geological maps and previous works and reports [68]. The authors also noted that the satellite product that achieves the best accuracy for the SAM and minimum distance algorithm was the Sentinel-2. More work is necessary, since the results may indicate a positive contribution from the increased spatial resolution of the sensor.

In a work focused on the application of image classification in Li pegmatite exploration, Cardoso-Fernandes et al. [69] compared the performance between two machine learning algorithms (MLAs), support vector machine (SVM) and random forest (RF), in the Fregeneda-Almendra area, using Sentinel-2A images. For details on model selection and parametrization, the original publication should be consulted [69]. This work represents the first application of MLAs in Li pegmatite mapping. Both algorithms (SVM and RF) correctly mapped the

occurrence of Li pegmatites in the open-pit mines [69]. Although SVM achieved a higher overall accuracy (98.54%), the RF model (built using class balancing strategies; overall accuracy of 97.70%) was able to correctly classify a larger number of mapped Li-bearing pegmatites [69]. Additionally, some of the areas classified by SVM and RF as Li pegmatites correspond with the regions of interest delimited in previous studies [63] or to barren mapped pegmatites. Despite the potential shown by this type of approach, these techniques still produced several false positives resultant from the spectral similarity of Li pegmatites with other lithologies, namely metasedimentary rocks [69]. This may indicate that more high spatial resolution images are needed. Moreover, other difficulties were encountered (see Section 2.2), mainly associated with the high number of classes defined in the image, having the authors [69] concluded that both SVM and RF were overfitting at a class level, despite this kind of algorithms being less prone to overfit than other machine learning techniques [70–73]. This illustrates that this kind of approach can be optimized. All the developments mentioned so far concerned the application of remote sensing the hard-rock Li deposits. However, new applications in other Li deposits are emerging. One example is the “Space enabled exploration and monitoring of Cornwall Lithium resources” research project dedicated to Li brine exploration [74]. The project aims at targeting underground geothermal Li brines through the integration of several multispectral and SAR products to produce geological, active faulting, and vegetation maps [74]. The geological mapping will be achieved in two stages: (i) the first consists on geological mapping using Landsat-8 and Sentinel-2 images with subsequent integration of geophysical data; and (ii) the second will focus on mineral alteration mapping using multispectral (ASTER and Worldview-3) and airborne hyperspectral data (HyMAp) [74]. On its turn, SAR data, namely Sentinel-1 scenes, will be used to map in detail fault systems that may structurally control Li brines. Another approach will consist of the detection of vegetation with possible Li anomalies [74].

Another deposit type that may have big potential for remote sensing applications are metasediment-hosted Li deposits like the Valdeflores (Cáceres, Spain) case where the mineralization occurs in Li-bearing micas [75,76]. This deposit would have been formed by a pervasive metasomatism that resulted in a target area of approximately 250 × 500 m [75] which means that the spatial resolution of the sensors would no longer be a problem as in pegmatite deposits. Additionally, the metasomatic formation of white mica in other mineral deposits is usually accompanied by wavelength changes of the 2200 nm absorption feature that can be used to target mineralizations using hyperspectral sensors [4]. A similar approach could be applied to detect Li micas in metasedimentary rocks.

2.1.1. Brief Overview

To understand the recent interest in the application of remote sensing methods in Li exploration and to provide an overall picture of the state of the research, we searched the number of publications in the Scopus bibliographic database using specific keywords (“Remot * sens *” AND “Lithium” AND “Mineral *”; “Satellite” AND “Lithium” AND “Mineral *”; “Remot * sens *” AND “Lithium”).

After search refinement, title and abstract screening and eligibility check, a total of nine publications from the initial 261 were included in the analysis (representing 3.4% of the total). Despite this number being considered low for bibliographic analysis [77], it highlights the existent gap in the literature in Li exploration using remote sensing data/techniques. All documents were analyzed by type, country, and citations. The co-occurrence of keywords was also analyzed considering their frequency. The VOSviewer software was employed for network visualization of the data through clustered density maps. Table 1 presents a summary of information on the nine publications included in the analysis.

Table 1. SCOPUS search results concerning publications related to Li exploration using remote sensing data and techniques.

Authors (Year)	Title	Citations
Cardoso-Fernandes et al. (2019)	Constraints and potentials of remote sensing data/techniques applied to lithium (Li) pegmatites	-
Cardoso-Fernandes et al. (2019)	Remote sensing data in lithium (Li) exploration: A new approach for the detection of Li-bearing pegmatites	6
Santos et al. (2019)	Remote sensing techniques to detect areas with potential for lithium exploration in Minas Gerais, Brazil	-
Cardoso-Fernandes et al. (2019)	Evaluating the performance of support vector machines (SVMs) and random forest (RF) in Li pegmatite mapping: Preliminary results	-
Rossi et al. (2018)	An earth observation framework for the lithium exploration	-
Cardoso-Fernandes et al. (2018)	Potential of Sentinel-2 data in the detection of lithium (Li)-bearing pegmatites: A study case	4
Gemusse et al. (2018)	Pegmatite spectral behavior considering ASTER and Landsat 8 OLI data in Naipa and Muiane mines (Alto Ligonha, Mozambique)	1
Dai et al. (2017)	Geological mapping and ore-prospecting study using remote sensing technology in Jiajika area of Western Sichuan Province	1
Lefevre (1982)	Remote sensing of geobotanical anomalies in mineral exploration: a Landsat 1 processing methodology Echassieres, Allier, France	-

The average publication year is 2014, with eight documents (88.9%) published after 2016, which reflects the recent interest in this field. Almost all documents were published in English (7; 77.8%), with the exception of one document published in Chinese (11.1%) and another one in French (11.1%) (Figure 1a). When analyzing the type of document, five publications (55.6%) correspond to conference papers while the remaining four documents (44.4%) correspond to journal articles (Figure 1b). The publications received a total of 12 citations, with an average of 1.3 citations per document since there are four documents (44.4%) with at least one citation (Table 1).

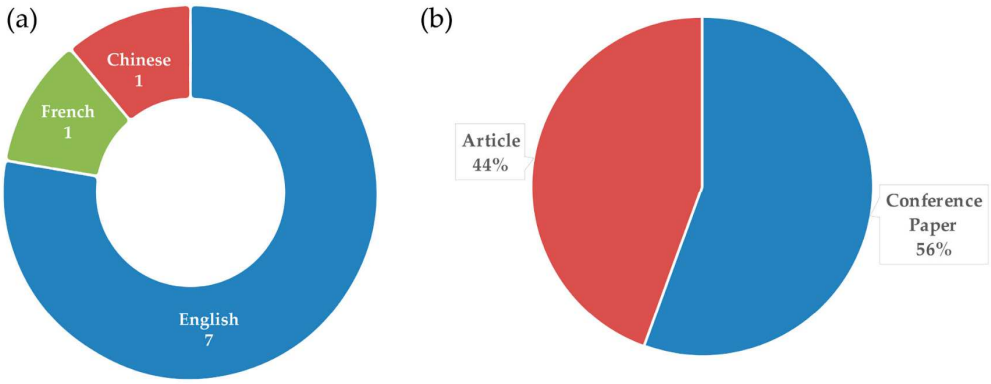

Figure 1. (a) Donut chart showing the distribution of the documents' language. (b) Pie chart with the distribution of the documents' type.

The co-occurrence of author and index keywords was also analyzed (Figure 2), being "remote sensing", "lithium", and "granite" the most frequent keywords occurring eight, seven, and four times, respectively.

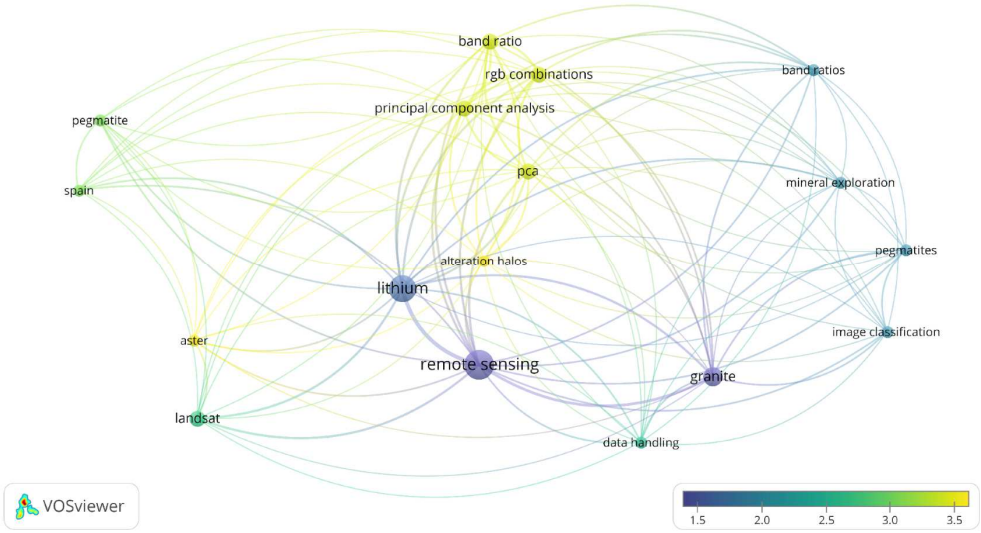

Figure 2. Co-occurrence of author and index keywords. Each circle represents a different keyword, being the size proportional to the respective number of occurrences. The color represents the average citation associated with each keyword, while the lines represent the link strength between different keywords. The minimum number of occurrences of a keyword considered was two, with 17 keywords having met the criteria.

Regarding the geographic distribution of the publications, most of the studies were conducted by researchers with European affiliations (Figure 3a): Portugal ranked first with six publications (66.7% of the total), followed by Spain with two studies (22.2% of the total), and by France and the United Kingdom with one document each (representing 11.1% of the total). On the other hand, as can be seen in Figure 3, the study area considered in each work not always corresponds to the affiliation country of the authors. Despite most studies areas being located in Europe, other applications were made in the American, African, and Asian continents (Figure 3b).

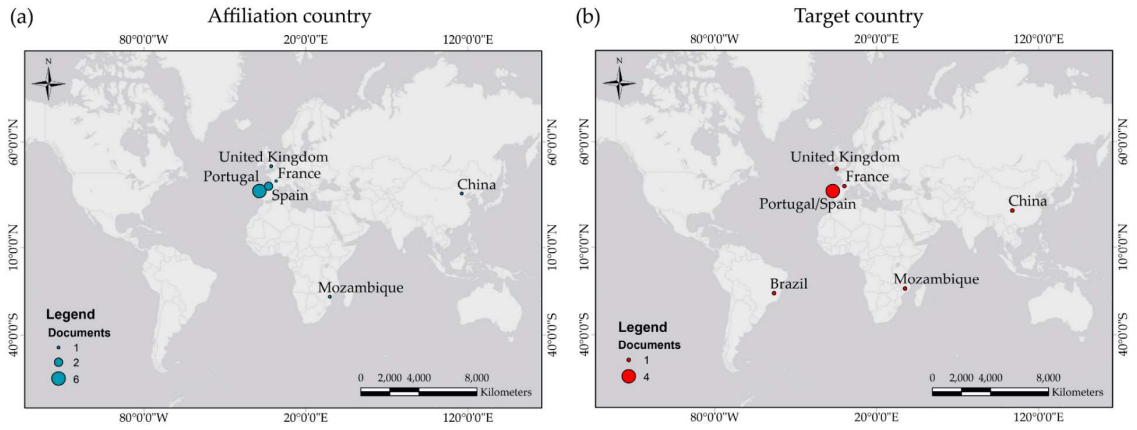

Figure 3. (a) Geographic distribution of the retrieved publications taking into account the affiliation country. (b) Geographic distribution of the analyzed publications considering the study area of the work. In some cases, the study area encompasses more than one country (Portugal/Spain).

2.2. Main Challenges

The difficulties encountered in the previously mentioned applications are mainly related to the inherent characteristics of Li deposits, especially in the case of Li pegmatites which are characterized by low areas of exposition due to their dimensions (pegmatites are relatively narrow bodies).

Mendes et al. [61] reported difficulties in the direct application of the spectral signatures of Li-bearing minerals obtained in the laboratory to identify similar targets in the ASTER images. The authors [61] attributed this challenge to: (i) the low spatial resolution of the images when compared to the target area; (ii) spectral noise resultant from mixture of the materials presented in a pixel; and (iii) the low spectral resolution of the ASTER sensor when compared to the laboratory spectroradiometer.

Cardoso-Fernandes et al. [63] highlighted that the main problem associated with the identification by the hydrothermal alteration approach is that the applied RGB combinations, band ratios, and the subsets used for selective PCA correspond to algorithms proposed for the identification of other deposit types with distinct alteration styles and mineral assemblages. Thus, in order to optimize alteration mapping associated with Li pegmatites is fundamental to characterize the associated alteration minerals and possible alteration halos in the host rocks. The knowledge on the alteration halos would allow directing the image processing methods to specific minerals and it could help to discriminate between barren and Li-mineralized pegmatites. Furthermore, the possible recognition of the associated alteration halos from satellite sensors would also allow increasing the target exposition area, allowing to overcome the pegmatite thickness problem.

Based on the works conducted in the Fregeneda-Almendra area, Cardoso-Fernandes et al. [78] made a preliminary attempt to identify the main constraints in Li pegmatite exploration using satellite remote sensing as being: (i) the vegetation coverage that masks the target spectral signatures; (ii) the small pegmatite size when compared to pixel size (the exposition problem); (iii) the small number of bands and/or the lack of thermal bands in some satellite sensors (the spectral resolution problem); and (iv) the spectral resemblance between the Li pegmatites and urbanized areas or agricultural fields. These challenges are in line with the difficulties identified in other pegmatite locations [60,61,66].

In what concerns the vegetation coverage, Cudahy [4] stated, for other applications, that even when green vegetation is sparse, dry vegetation can negatively influence the spectral signature of each image pixel. At least in the Fregeneda-Almendra region, dry vegetation is more abundant than green vegetation. However, no attempts to minimize its influence were made (only green vegetation was masked). On the other hand, Cudahy [4] adverted that unmixing the spectral signatures of both green and dry vegetation is preferred than masking them. For that, Rodger and Cudahy [79] developed an unmixing method for hyperspectral sensors in which a vegetation corrected continuum depth is obtained. Despite multispectral products such as ASTER not being the most adequate to measure the spectral features of dry vegetation, it is still possible to obtain an approximate dry vegetation index [4].

Nonetheless, the compromise between spatial and spectral resolution is, in our opinion, the principal challenge in Li pegmatite exploration. This is best exemplified in the work that attempted to classify Sentinel-2 images using MLAs [69]. Although Sentinel-2 represents the free multispectral product with better spatial resolution and, therefore, the one with the best capability to overcome the pegmatite exposition problem, several misclassification errors

resulted from the absence of bands in the TIR region. These misclassifications include the spectral mixing between Li pegmatites and the metasedimentary host rocks [69]. Additionally, the relatively high number of classes, identified in the image for the classification process, contributed to a higher data complexity that may have hindered the obtained results. The reduction of the number of classes, through masking of classes with no interest in Li exploration, will certainly help to optimize the algorithm performance, as recognized by the authors [69].

Another critical challenge to Li exploration based on satellite data is that in spite of the many diagnostic spectral features of Li minerals, to the best of our knowledge, it was not possible to identify so far, a unique spectral feature solely caused by the presence of Li in the structure of minerals.

Taking all this into account, it is our opinion that there are yet several developments to be made in the field of remote sensing applied to Li-mineralizations, and new algorithms and methodologies to be developed in space and Earth sciences. More insights on other remote sensing data products are given in Chapter 3.

3. Future Perspectives

A discussion on the available data products and image classification algorithms is made in the attempt to solve some of the problems identified (Section 2.2). The special requirements of Li exploration are taken into account. New types of approaches and applications to other Li deposits are addressed.

3.1. Data Products Used for the Research

Past applications (Section 2.1) included products such as ASTER, Landsat-5, Landsat-8, and Sentinel-2 images. For the purpose of this review, we will only consider the more recent products since our goal is to help in choosing the best product for future studies.

The ASTER is an imaging instrument onboard of Terra satellite, the flagship satellite of NASA's Earth Observing System (EOS), launched in December 1999 [80]. It resulted from a collaboration between NASA and Japan's Ministry of Economy Trade and Industry—METI [80]. ASTER captures medium-high spectral resolution data in 14 bands whose spatial resolution varies with wavelength: 15 m in the VNIR, 30 m in the SWIR, and 90 m in the TIR [81]. ASTER also provides a stereo viewing capability for digital elevation model creation [80,81]. The temporal resolution is 16 days. Due to sensor failure, SWIR data acquired since April of 2008

is not available [82]. Nonetheless, as mentioned before, ASTER's specific characteristics greatly contributed to mineral exploration, especially in alteration mapping associated with gold and porphyry copper deposits [53,54]. A review of the different "on-demand" ASTER products can be found in the work of Pour and Hashim [83].

The Landsat program represents the world's longest continuously acquired collection of space-based moderate-resolution multispectral land remote sensing data [84]. It is the result of a joint effort of the United States Geological Survey (USGS) and the National Aeronautics and Space Administration (NASA). Until now, Landsat counts with seven successful and one failed mission [84]. The last mission corresponds to Landsat-8, which was launched in 2013. Landsat-9 is planned to be launched in December 2020 [84]. Landsat-8 carries two different instruments: (i) the Operational Land Imager (OLI); and (ii) the Thermal Infrared Sensor (TIRS). Each image product contains nine spectral bands with a spatial resolution of 30 m for bands 1–7 and 9, and 15 m for band 8 (panchromatic); and two thermal bands (10 and 11) are collected at 100 m, but resampled for 30 m [85]. Each band consists of a 16-bit grayscale image. The scene size is 170 km × 185 km [85]. The temporal resolution is 16 days. Key publications in geological remote sensing (at least until the time of publication) from both the Landsat and the ASTER eras can be found in van der Meer et al. [53].

The Sentinel-2 mission includes the recent twin satellites Sentinel-2A and Sentinel-2B launched in the frame of the European Union's Copernicus Program [86]. Since the satellites are out of phase with each other, the temporal resolution is five days at the equator [87]. Both satellites acquire information in 13 spectral bands in the VNIR-SWIR regions: four bands at 10 m spatial resolution, six bands at 20 m, and three bands at 60 m [87]. The orbital swath width is 290 km. A comparison between Landsat-8, Sentinel-2 and ASTER bands is established in Table 2 and in Figure 2.

Table 2. Characteristics of sensors with potential for remote sensing of Li deposits [81,85,88,89].

Sensor Name		Spectral Region (μm)			Nr. of Bands	Spatial Resolution (m)		
		VNIR	SWIR	TIR		VNIR	SWIR	TIR
Landsat-8 OLI/TIRS		0.43–0.88	1.57–2.29	10.60–12.51	11	30	30	100
ASTER		0.52–0.86	1.60–2.43	8.13–10.95	14	15	30	90
Sentinel-2 MSI	A	0.42–0.94	1.52–2.38	-	12	10	20	-
	B	0.42–0.94	1.52–2.37					
WorldView-3		0.40–1.04	1.20–2.37	-	16	1.24	3.70	-

Van der Meer et al. [53] refer to the importance of the Sentinel-2 mission to ensure data continuity, especially after the failure of ASTER's SWIR module. However, the application of Sentinel-2 images for geological studies is scarce when compared to the previously mentioned satellite sensors, especially when it comes to geological exploration. The first articles in the literature regarding this satellite address their potential to alteration and iron/gossan mapping, while others highlight the correspondence between ASTER, Landsat 8, and Sentinel-2 VNIR and SWIR bands [90–93]. More recent studies highlight the possible contribution and suitability of Sentinel-2 images for geological mapping [94,95] and for geological fault detection [96]. Ge et al. [97] applied different MLAs, Artificial Neural Network (ANN), k-Nearest Neighbor (k-NN), RF and SVM, to Sentinel-2 images in order to perform lithological classification in an ophiolite complex in Inner Mongolia, China. Hu et al. [98] compared the use of Sentinel-2, ASTER, and Hyperion in hydrothermally-altered mineral mapping associated with porphyry copper deposits. Cardoso-Fernandes et al. [62] and Cardoso-Fernandes et al. [63] already showed some potentialities and limitations of the use of Sentinel-2 in Li pegmatite identification. Overall, some of these works show that, on the contrary of what it was thought, Sentinel-2 might not be able to replace ASTER in the acquisition of data for geological applications, due to the lack of a TIR sensor. Until now there is no free or commercial product capable of responding to the necessities of geological mapping and exploration, so other solutions need to be explored. The potential of the combined use of multi- and hyperspectral satellite data in mineral exploration was already discussed by Mielke et al. [93].

In what concerns the compromise between spatial and spectral resolution, the answer may rely on commercial satellites such as WorldView-3. Launched in 2014 by DigitalGlobe, World-View-3 is a high-resolution multispectral sensor that measures reflected radiance in eight VNIR bands (at 1.24 m spatial resolution) and eight SWIR bands (at 3.70 m resolution) although SWIR data is resampled to a 7.5 m pixel size for commercial distribution [99] (Table 2; Figure 4). WorldView-3 also has a panchromatic band with 0.31 m of spatial resolution [99]. The swath width is 13.1 km. Despite lacking a TIR sensor, WorldView-3 has good potential for mineral mapping since its bandpasses are very similar to the ASTER VNIR-SWIR ones [4,54]. Additionally, such high resolution can help to tackle the vegetation problems due to the sensors' ability to map between trees [4].

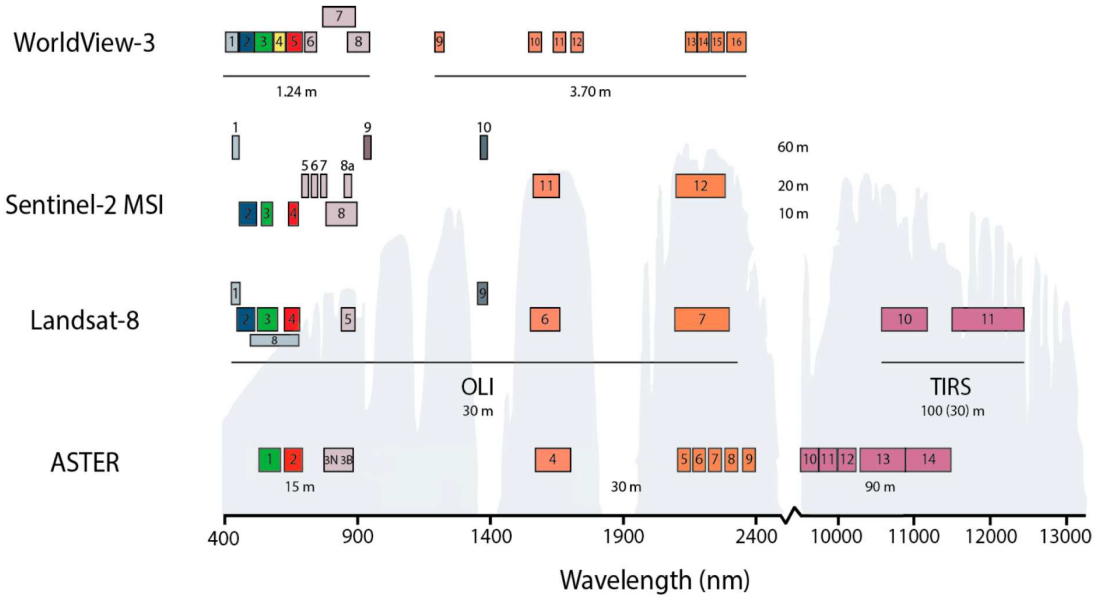

Figure 4. Comparison between ASTER, Landsat 8, Sentinel-2, and WorldView-3 bands. Adapted from USGS Landsat Program [100]. ASTER [81]: 1 green; 2 red; 3N/3B—NIR nadir-looking/NIR backward-looking; 4–9 SWIR; 10–14 TIR. Landsat-8 [89]: 1 coastal aerosol; 2 blue; 3 green; 4 red; 5 NIR; 6 SWIR 1; 7 SWIR 2; 8 Panchromatic; 9 cirrus; 10 TIRS 1; 11 TIRS 2. Sentinel-2 [88]: 1 coastal aerosol; 2 blue; 3 green; 4 red; 5, 6, 7, and 9 vegetation red edge; 8 NIR; 10 cirrus; 11 and 12 SWIR. WorldView-3 [99]: 1 coastal; 2 blue; 3 green; 4 yellow; 5 red; 6 red edge; 7 NIR 1; 8 NIR 2; 9–16 SWIR.

To overcome the remaining inherent difficulties of Li exploration, other types of remote sensing platforms should be considered. Nowadays, drone-borne hyperspectral sensors are a reality. In fact, such an approach is being used to quickly identifying target areas for Li exploration within the “Lightweight Integrated Ground and Airborne Hyperspectral Topological Solution” (LIGHTS) project [101]. However, this kind of data has one big limitation due to the high associated cost of mounting the equipment in the drone, of around 200,000 USD. Nonetheless, it is our opinion this kind of approach will be highly sought after in the future, once the drone and hyperspectral camera prices go down.

3.2. Image Processing Algorithms

In the past, several authors have reviewed the different techniques and image processing algorithms that can be applied to geological remote sensing in general [102,103] or in mineral exploration [5,6]. Some even group the image processing methods into functional categorization schemes. Sabins [104] defined three categories: (i) image restoration; (ii) image enhancement; and (iii) information extraction. Later, in 2016, Asadzadeh and Souza Filho [103]

proposed a new scheme in which the techniques are divided into knowledge-based and data-driven approaches.

Common image processing algorithms employed in mineral exploration are: (i) RGB combinations [105,106]; (ii) band ratios [6,105]; (iii) PCA [28,107]; (iv) MNF [21,105,106]; (v) matched filtering (MF) [24,105]; (vi) linear spectral unmixing (LSU) [11,51]; (vii) constrained energy minimization (CEM) [17,21]; (viii) least square fitting method [105]; (ix) independent component analysis [50]. and supervised algorithms such as (x) SAM [8,108], and (xi) MTNF [8,15]. Methods such as MNF, PPI, and SAM have already been applied to pegmatite detection in Southern Namibia using airborne hyperspectral data (HyMap) [109]. For the same region, Oshigami et al. [110] proposed a new classification method named continuum-removal MSAM that combined the Modified Spectral Angle Mapper (MSAM) and continuum-removal methods. Using HyMap images, the authors produced mineral index maps to target common pegmatite minerals such as lepidolite and other white micas. In the Cornwall region, United Kingdom, Ellis and Scott [111] used lepidolite as a pathfinder for topaz-bearing granites in an environmental monitoring study. For that, HyMap airborne images were used and methods like MNF, PPI, and MTMF were employed.

Recently, great attention has been given to non-parametric classifiers such as machine and deep learning algorithms. These techniques have been applied in land-use/land-cover (LULC) problems with great success, outperforming classical algorithms [112–115]. In 2014, Yu et al. [116] conducted a meta-analysis and synthesis of satellite-based land-cover mapping studies, concluding that, from all classification methods (used more than 10 times out of the 1651 analyzed studies), MLAs, namely ensemble classifiers, ANN and SVM, are the methods that achieved a performance better than the average accounted in the 1651 experiments.

Although the number of applications is smaller when compared to the LULC studies, similar results have been obtained in lithological mapping and mineral exploration [40,117–121]. Yu et al. [117], in 2012, developed an automated approach to lithological mapping in Northwestern India where different SVMs with the radial basis function (RBF) kernel were trained using ASTER, ASTER-derived digital elevation model (DEM), and aeromagnetic data. The tested number of input features ranged from 14 to 33, having the classification accuracy increased with the increasing number of layers. When compared with a classical classifier, SVM clearly outperformed ML, achieving a much higher accuracy [117]. Cracknell et al. [118] applied RF and self-organizing maps (SOM) to map lithology and volcanic-hosted massive sulfide (VHMS) alteration in Tasmania. The input data included airborne geophysical, soil geochemical and Landsat-7 Enhanced Thematic Mapper Plus (ETM+) spectral data. The approach provided

new geological detail and allowed to identify areas of interest for geological and VHMS alteration mapping. According to the authors [118], the combination of supervised and unsupervised MLAs delivered a robust mean to analyze and map complex, challenging terrains. In 2016, Parakh et al. [119] compared the performance between RF and SVM in lithological mapping in India using Landsat-8, ASTER, and DEM data. Additionally, band-depth images from the analysis of laboratory spectra were used as input for the fuzzy inference system (FIS) to further discriminate between amphibolite and mica-schist. Overall, the performance of RF and SVM was similar although RF provided a higher accuracy for the minor class [119]. Bahrambeygi and Moeinzadeh [120] compared SVM and ANN in hyperspectral mapping of ophiolite terrains in Iran using Hyperion images, the ANN having achieved higher accuracy. Latifovic et al. [121], in 2018, assessed the performance of convolutional neural networks (CNN) in lithological mapping in Northwestern Canada. Different data layers were used to train the network including Landsat TM/ETM+ scenes, aerial photos, and high-resolution DEM data. The performance of CNN was evaluated in two sampling scenarios: the first uses samples collected over the area to be mapped, while the second scenario corresponds to an independent test area. Secondly, the performance of CNN was confronted with the one attained using the more widely used RF algorithm [121]. In the first scenario, both algorithms showed similar results with an average accuracy of around 76%. However, in the independent test sets, CNN outperformed RF by 4%.

Most of these works show that the classification accuracy is improved when additional data is added to the satellite-acquired one. This follows the line of thought of Rajesh [3] that remote sensing data by itself may not be sufficient to identify new mineral deposits. Therefore, it would be important to try to integrate satellite data with other types of data in Li exploration. This type of logic could also be applied to techniques employed, that is, several classifiers could be combined to form a better predictor (using ensemble methods like AdaBoost or bagging). Such an approach can help to overcome the weaknesses of single classifiers [122].

In the past recent years, several reviews have been published on either the use of a specific MLA or on the comparison of a set of machine and/or deep learning algorithms. Mountrakis et al. [72] presented various applications of SVM in remote sensing as well as several algorithmic advances and SVM variants developed. Belgiu and Drăguţ [70] reviewed the use of RF as a classifier in remote sensing. The authors also highlight developments made and new applications in the field of remote sensing, besides pointing out future directions. Maxwell et al. [123] reviewed MLAs from an applied perspective, focusing on SVM, decision trees (DTs), boosted DTs, RF, ANNs, and k-NN, the choice of proper algorithms, their implementation,

training data requirements (class balancing problems for example), parameter tuning, computational costs, and availability of MLAs in remote sensing software packages. Li et al. [124] survey and compare the performances achieved by typical deep learning (DL) methods, such as model CNNs, stacked auto-encoders (SAEs), and deep belief networks (DBNs). The authors also presented a systematic review of developments made in pixel-wise and scene wise approaches using DL methods.

Despite the great performance achieved by MLAs in the field of computer vision and image processing [122,124], some difficulties are expected in what concerns their application to Li exploration. The first and most obvious obstacle is the in-depth knowledge about the MLAs and DL required for any geoscientist/geologist to conduct such an approach. The second is related to the nature of the classification problem since mineral exploration in general, and Li exploration in particular, inherently differ from classical applications, such as LULC problems. Finally, the amount of training associated with each algorithm and the need to parameterize the algorithms are another major obstacle. This parametrization can be more difficult in some MLAs like SVM but, overall, past studies show that the parameters tend to be case sensitive and therefore fundamental [112,123]. New developments on how to transfer learning from one case study to another are needed and they will definitely increase the importance and usage of MLAs and DL in mineral exploration. On the other hand, there are still a great number of potentialities to explore in Li exploration that are constantly increasing with the new models and algorithms being proposed. These include adaptations of the original algorithms (e.g., oblique RF classification [125] or transductive SVM [126]) and the use of non-traditional optimization algorithms, such as genetic algorithms and particle swarm optimization, with MLAs [127]. The application of MLAs in sub-pixel classification (e.g., [128]) could also help to decrease the impact of mixed pixels in medium spatial resolution images.

4. Summary and Conclusions

Despite the early attempt to target Li mineralizations with the launch of the Landsat missions, there is an unequivocal exponential growth on the publication numbers in the last decades. Nonetheless, since it still is an emergent field, the studies are limited to a small number of research groups, mainly based in Europe. However, considering the market demand for this raw material, we expect that many other studies will flourish in the near future all around the globe.

In general, past application studies relied on four distinct approaches: (i) geobotanical mapping; (ii) lithological mapping; (iii) mineral alteration mapping; and (iv) Li minerals/Li pegmatite discrimination. Different types of satellite products with distinct characteristics were employed as well as diverse image processing algorithms ranging from simple logical or mathematical operations (band ratios) to more evolved and complex algorithms like MLAs.

Overall, the objectives and the research questions addressed in this review were successfully accomplished/answered:

1. What can be accomplished in Li exploration using remote sensing methods? The reviewed publications show that it is possible to identify the spectral features of pegmatite intrusions and to discriminate the Li-bearing pegmatites from the host rocks (despite the misclassification errors in the lithological mapping approach). Depending on the type of host rock, this discrimination may not be possible without using TIR data. The proposed approach to directly identify Li minerals/Li pegmatites was confirmed in other areas of the globe. To some extent, the alteration mapping approach works to target Li pegmatites, although it is more promising in highly weathered areas such as in the Alto Ligonha region (Mozambique).

2. What are the main difficulties? Both the alteration mapping and Li pegmatite mapping results differ regarding the area or the image processing method applied, which points to the lack of an automated proceeding to target Li-mineralizations. Other noted difficulties are related to the spectral confusion with urbanized areas and agricultural fields or spectral noise resultant from mixing at the pixel level. From our knowledge, these problems are inherently caused by low spectral and spatial resolution, respectively. The vegetation coverage is another difficulty since it masks the Li minerals/Li pegmatites spectral signatures. In specific areas of the world, there may be problems in the hydrothermal alteration approach since the Li pegmatites may present distinct alteration styles and mineral assemblages not detected by the common techniques.

3. How to overcome these difficulties? Currently, there is no existing or expected satellite product capable of responding to all the necessities of Li exploration. Despite lacking thermal bands, WorldView-3 is probably the closest product available capable of dealing with the spatial and spectral resolution compromise. Additionally, WorldView-3 high spatial resolution can help to tackle the vegetation difficulties. Another solution to dampen the effects of vegetation is the spectral unmixing of both green and dry vegetation. To optimize the alteration mapping approach, a detailed geological characterization of the associated alteration minerals and possible alteration halos in the host rocks can lead to the development of specific, more efficient algorithms. Other types of remote sensing data, namely drone-borne

hyperspectral sensors, may constitute a more efficient Li exploration tool in the future. For now, such an approach is not feasible due to the high associated costs.

4. What are the future research perspectives? We believe that there are several developments to be made in the field of remote sensing applied to Li mineralizations in the future. The constant increase and development of MLAs, in specific, offers unlimited possibilities to be explored. Less common techniques, such as the adaptation of the original MLAs or the combination of several classifiers into one single predictor, can help to achieve a better performance in Li exploration. The integration of remote sensing data with geological information (mineral prospectivity) will increase the ability to target new deposits. The development and improvement of the geobotanical approach may enable Li exploration using remote sensing in highly vegetated areas, which for now is unthinkable. The generalization of the mentioned approaches to other Li deposit types (e.g., brines) will also contribute to establishing remote sensing as a fundamental tool in Li exploration.

Author Contributions

All the authors designed and schematized the manuscript; J.C.-F. wrote the original draft; A.C.T., A.L., M.P., and E.R.-R. revised and edited the paper. All authors have read and agreed to the published version of the manuscript.

Funding

The authors would like to thank the financial support provided by FCT—Fundação para a Ciência e a Tecnologia with the ERA-MIN/0001/2017—LIGHTS project, FEDER through operation POCI-01-0145-FEDER-007690 funded by the Programa Operacional Competitividade e Internacionalização—COMPETE2020 and by National Funds through FCT within the ICT, R and D Unit (reference UIDB/04683/2020). The University of the Basque Country (UPV/EHU) contributed economically with grant GIU18/084. Joana Cardoso-Fernandes is financially supported within the compass of a Ph.D. Thesis, ref. SFRH/BD/136108/2018, by national funds from MCTES through FCT, and co-financed by the European Social Fund (ESF) through POCH—Programa Operacional Capital Humano.

Conflicts of Interest

The authors declare no conflict of interest.

Appendix A. Spectral Indices

Appendix A.1. RGB Combinations

In 2019, Cardoso-Fernandes et al. [63] proposed different RGB combinations to target Li-bearing pegmatites using atmospherically corrected, surface reflectance ASTER, Landsat-5, Landsat-8, and Sentinel-2 products (Table A1).

Table A1. Proposed RGB combinations for Li pegmatite detection [63].

Sensor	RGB Combination
ASTER	5-1-14
	2-1-13
Landsat-5 TM	7-2-6
	2-1-6
Landsat-8 OLI/TIRS	7-3-11
	2-1-11
Sentinel-2 MSI	3-2-12

Appendix A.2. Band Ratios

Band ratios were also proposed to identify Li pegmatites [62,63]. These ratios were based on spectral absorption features of Li minerals, such as spodumene and lepidolite (Table A2).

Table A2. Band ratios proposed to identify Li pegmatites [62,63].

Sensor	Band Ratio
ASTER	7/6
	1/3
Landsat-5 TM	2/4
	3/7
Landsat-8 OLI/TIRS	3/5
	4/7
Sentinel-2 MSI	3/8
	4/12

Appendix A.3. PCA

Cardoso-Fernandes et al. [63] also selected two- and four-band subsets for the application of selective PCA to isolate target spectral signatures of Li pegmatites (Table A3). Input data were the ASTER, Landsat-5, Landsat-8, and Sentinel-2 raw bands.

Table A3. Band subsets for selective PCA in Li pegmatite identification.

Sensor	Band Subset
ASTER	1, 3
	1, 3, 11, 14
Landsat-5 TM	2, 4
	1, 2, 4, 6
Landsat-8 OLI/TIRS	3, 5
	2, 3, 5, 11
Sentinel-2 MSI	3, 8
	2, 3, 8, 11

References

1. El-Baz, F. Remote sensing and mapping of Earth resources. *Terra Nova* **1990**, *2*, 446–454.
2. Meer, V.D. Bakker validated surface mineralogy from high-spectral resolution remote sensing: A review and a novel approach applied to gold exploration using AVIRIS data. *Terra Nova* **1998**, *10*, 112–119.
3. Rajesh, H.M. Application of remote sensing and GIS in mineral resource mapping—An overview. *J. Mineral. Petrol. Sci.* **2004**, *99*, 83–103.
4. Cudahy, T. Mineral mapping for exploration: An Australian journey of evolving spectral sensing technologies and industry collaboration. *Geosciences* **2016**, *6*, 52.
5. Rajan Girija, R.; Mayappan, S. Mapping of mineral resources and lithological units: A review of remote sensing techniques. *Int. J. Image Data Fusion* **2019**, *10*, 79–106.
6. Sabins, F.F. Remote sensing for mineral exploration. *Ore Geol. Rev.* **1999**, *14*, 157–183.
7. Abbaszadeh, M.; Hezarkhani, A. Enhancement of hydrothermal alteration zones using the spectral feature fitting method in Rabor area, Kerman, Iran. *Arab. J. Geosci.* **2011**, *6*, 1957–1964.

8. Bishop, C.A.; Liu, J.G.; Mason, P.J. Hyperspectral remote sensing for mineral exploration in Pulang, Yunnan Province, China. *Int. J. Remote Sens.* **2011**, *32*, 2409–2426.

9. Di Tommaso, I.; Rubinstein, N. Hydrothermal alteration mapping using ASTER data in the Infiernillo porphyry deposit, Argentina. *Ore Geol. Rev.* **2007**, *32*, 275–290.

10. Farahbakhsh, E.; Shirmard, H.; Bahroudi, A.; Eslamkish, T. Fusing ASTER and QuickBird-2 Satellite Data for detailed investigation of porphyry copper deposits using PCA.; Case study of Naysian Deposit, Iran. *J. Indian Soc. of Remote Sens.* **2016**, *44*, 525–537.

11. Hosseinjani, M.; Tangestani, M.H. Mapping alteration minerals using sub-pixel unmixing of ASTER data in the Sarduiyeh area, SE Kerman, Iran. *Int. J. Digit. Earth* **2011**, *4*, 487–504.

12. Hosseinjani Zadeh, M.; Honarmand, M. A remote sensing-based discrimination of high- and low-potential mineralization for porphyry copper deposits; a case study from Dehaj–Sarduiyeh copper belt, SE Iran. *Eur. J. Remote Sens.* **2017**, *50*, 332–342.

13. Hosseinjani Zadeh, M.; Tangestani, M.H.; Roldan, F.V.; Yusta, I. Sub-pixel mineral mapping of a porphyry copper belt using EO-1 Hyperion data. *Adv. Space Res.* **2014**, *53*, 440–451.

14. Pour, A.B.; Hashim, M. Identification of hydrothermal alteration minerals for exploring of porphyry copper deposit using ASTER data, SE Iran. *J. Asian Earth Sci.* **2011**, *42*, 1309–1323.

15. Pour, A.B.; Hashim, M. Hydrothermal alteration mapping from Landsat-8 data, Sar Cheshmeh copper mining district, south-eastern Islamic Republic of Iran. *J. Taibah Univ. Sci.* **2015**, *9*, 155–166.

16. Safari, M.; Maghsoudi, A.; Pour, A.B. Application of Landsat-8 and ASTER satellite remote sensing data for porphyry copper exploration: A case study from Shahr-e-Babak, Kerman, south of Iran. *Geocarto Int.* **2017**, *33*, 1186–1201.

17. Zhang, N.; Zhou, K. Identification of hydrothermal alteration zones of the Baogutu porphyry copper deposits in northwest China using ASTER data. *J. Appl. Remote Sens.* **2017**, *11*.

18. Amer, R.; Kusky, T.; El Mezayen, A. Remote sensing detection of gold related alteration zones in Um Rus area, Central Eastern Desert of Egypt. *Adv. Space Res.* **2012**, *49*, 121–134.

19. Ciampalini, A.; Garfagnoli, F.; Antonielli, B.; Moretti, S.; Righini, G. Remote sensing techniques using Landsat ETM+ applied to the detection of iron ore deposits in Western Africa. *Arab. J. Geosci.* **2012**, *6*, 4529–4546.

20. El-Magd, I.A.; Mohy, H.; Basta, F. Application of remote sensing for gold exploration in the Fawakhir area, Central Eastern Desert of Egypt. *Arab. J. Geosci.* **2014**, *8*, 3523–3536.

21. Gabr, S.; Ghulam, A.; Kusky, T. Detecting areas of high-potential gold mineralization using ASTER data. *Ore Geol. Rev.* **2010**, *38*, 59–69.

22. Gabr, S.S.; Hassan, S.M.; Sadek, M.F. Prospecting for new gold-bearing alteration zones at El-Hoteib area, South Eastern Desert, Egypt, using remote sensing data analysis. *Ore Geol. Rev.* **2015**, *71*, 1–13.

23. Hassan, S.M.; Ramadan, T.M. Mapping of the late Neoproterozoic Basement rocks and detection of the gold-bearing alteration zones at Abu Marawat-Semna area, Eastern Desert, Egypt using remote sensing data. *Arab. J. Geosci.* **2014**, *8*, 4641–4656.

24. Liu, L.; Zhou, J.; Han, L.; Xu, X. Mineral mapping and ore prospecting using Landsat TM and Hyperion data, Wushitala, Xinjiang, northwestern China. *Ore Geol. Rev.* **2017**, *81*, 280–295.

25. Moradi, M.; Basiri, S.; Kananian, A.; Kabiri, K. Fuzzy logic modeling for hydrothermal gold mineralization mapping using geochemical, geological, ASTER imageries and other geo-data, a case study in Central Alborz, Iran. *Earth Sci. Inform.* **2014**, *8*, 197–205.

26. Zhang, X.; Pazner, M.; Duke, N. Lithologic and mineral information extraction for gold exploration using ASTER data in the south Chocolate Mountains (California). *ISPRS J. Photogramm. Remote Sens.* **2007**, *62*, 271–282.

27. Zoheir, B.A. Controls on lode gold mineralization, Romite deposit, South Eastern Desert, Egypt. *Geosci. Front.* **2012**, *3*, 571–585.

28. Crósta, A.P.; Souza Filho, C.R.; Azevedo, F.; Brodie, C. Targeting key alteration minerals in epithermal deposits in Patagonia, Argentina, using ASTER imagery and principal component analysis. *Int. J. Remote Sens.* **2003**, *24*, 4233–4240.

29. Bersi, M.; Saibi, H.; Chabou, M.C. Aerogravity and remote sensing observations of an iron deposit in Gara Djebilet, southwestern Algeria. *J. Afr. Earth Sci.* **2016**, *116*, 134–150.

30. Ducart, D.F.; Silva, A.M.; Toledo, C.L.B.; Assis, L.M.D. Mapping iron oxides with Landsat-8/OLI and EO-1/Hyperion imagery from the Serra Norte iron deposits in the Carajás Mineral Province, Brazil. *Braz. J. Geol.* **2016**, *46*, 331–349.

31. Duuring, P.; Hagemann, S.G.; Novikova, Y.; Cudahy, T.; Laukamp, C. Targeting iron ore in banded iron formations using aster data: Weld range greenstone belt, yilgarn craton, western australia. *Econ. Geol.* **2012**, *107*, 585–597.

32. Rajendran, S.; Thirunavukkarasu, A.; Balamurugan, G.; Shankar, K. Discrimination of iron ore deposits of granulite terrain of Southern Peninsular India using ASTER data. *J. Asian Earth Sci.* **2011**, *41*, 99–106.

33. Berger, B.R.; King, T.V.V.; Morath, L.C.; Philli, J.D. Utility of high-altitude infrared spectral data in mineral exploration: Application to Northern Patagonia Mountains, Arizona. *Econ. Geol.* **2003**, *98*, 1003–1018.

34. Van Der Meer, F.; Vazquez-Torres, M.; Van Dijk, P.M. Spectral characterization of ophiolite lithologies in the Troodos Ophiolite complex of Cyprus and its potential in prospecting for massive sulphide deposits. *Int. J. Remote Sens.* **2010**, *18*, 1245–1257.

35. Wang, G.; Du, W.; Carranza, E.J.M. Remote sensing and GIS prospectivity mapping for magmatic-hydrothermal base- and precious-metal deposits in the Honghai district, China. *J. Afr. Earth Sci.* **2017**, *128*, 97–115.

36. Rowan, L.C.; Mars, J.C. Lithologic mapping in the Mountain Pass, California area using Advanced Spaceborne Thermal Emission and Reflection Radiometer (ASTER) data. *Remote Sens. Environ.* **2003**, *84*, 350–366.

37. Mazhari, N.; Malekzadeh Shafaroudi, A.; Ghaderi, M. Detecting and mapping different types of iron mineralization in Sangan mining region, NE Iran, using satellite image and airborne geophysical data. *Geosci. J.* **2017**, *21*, 137–148.

38. Xu, Y.; Chen, J.; Meng, P. Detection of alteration zones using hyperspectral remote sensing data from Dapingliang skarn copper deposit and its surrounding area, Shanshan County, Xinjiang Uygur autonomous region, China. *J. Vis. Commun. Image Represent.* **2019**, *58*, 67–78.

39. Salles, R.D.R.; Souza Filho, C.R.; Cudahy, T.; Vicente, L.E.; Monteiro, L.V.S. Hyperspectral remote sensing applied to uranium exploration: A case study at the Mary

Kathleen metamorphic-hydrothermal U-REE deposit, NW, Queensland, Australia. *J. Geochem. Explor.* **2017**, *179*, 36–50.

40. Othman, A.; Gloaguen, R. Improving Lithological Mapping by SVM classification of spectral and morphological features: The Discovery of a new chromite body in the mawat ophiolite complex (Kurdistan, NE Iraq). *Remote Sens.* **2014**, *6*, 6867–6896.
41. Eslami, A.; Ghaderi, M.; Rajendran, S.; Pour, A.B.; Hashim, M. Integration of ASTER and landsat TM remote sensing data for chromite prospecting and lithological mapping in Neyriz ophiolite zone, south Iran. *Resour. Geol.* **2015**, *65*, 375–388.
42. Pournamdari, M.; Hashim, M. Detection of chromite bearing mineralized zones in Abdasht ophiolite complex using ASTER and ETM+ remote sensing data. *Arab. J. Geosci.* **2013**, *7*, 1973–1983.
43. Rajendran, S.; al-Khirbash, S.; Pracejus, B.; Nasir, S.; Al-Abri, A.H.; Kusky, T.M.; Ghulam, A. ASTER detection of chromite bearing mineralized zones in Semail Ophiolite Massifs of the northern Oman Mountains: Exploration strategy. *Ore Geol. Rev.* **2012**, *44*, 121–135.
44. Gemail, K.; Abd-El Rahman, N.M.; Ghiath, B.M.; Aziz, R.N. Integration of ASTER and airborne geophysical data for mineral exploration and environmental mapping: A case study, Gabal Dara, North Eastern Desert, Egypt. *Environ. Earth Sci.* **2016**, *75*.
45. Zimmermann, R.; Brandmeier, M.; Andreani, L.; Mhopjeni, K.; Gloaguen, R. Remote sensing exploration of Nb-Ta-LREE-Enriched carbonatite (Epembe/Namibia). *Remote Sens.* **2016**, *8*, 620.
46. Sabins, F.F.; Miller, R.M. Resource assessment—Salar Uyuni and vicinity. In Proceedings of the Tenth Thematic Conference on Geologic Remote Sensing (Ann Arbor, MI, Environmental Research Institute of Michigan), San Antonio, TX, USA, 9–12 May 1994; pp. 9–12.
47. Öztan, N.S.; Süzen, M.L. Mapping evaporate minerals by ASTER. *Int. J. Remote Sens.* **2011**, *32*, 1651–1673.
48. Bedini, E. Mineral mapping in the Kap Simpson complex, central East Greenland, using HyMap and ASTER remote sensing data. *Adv. Space Res.* **2011**, *47*, 60–73.
49. Liu, L.; Zhou, J.; Yin, F.; Feng, M.; Zhang, B. The reconnaissance of mineral resources through aster data-based image processing, interpreting and ground inspection in the Jiafushaersu area, West Junggar, China. *J. Earth Sci.* **2014**, *25*, 397–406.

50. Beiranvand Pour, A.; Park, T.-Y.; Park, Y.; Hong, J.; Zoheir, B.; Pradhan, B.; Ayoobi, I.; Hashim, M. Application of multi-sensor satellite data for exploration of Zn–Pb Sulfide mineralization in the franklinian basin, north greenland. *Remote Sens.* **2018**, *10*, 1186.

51. Kruse, F.A.; Boardman, J.W. Characterization and mapping of kimberlites and related diatremes using hyperspectral remote sensing. In Proceedings of the 2000 IEEE Aerospace Conference. Proceedings (Cat. No.00TH8484), Big Sky, MT, USA, 25 March 2000; Volume 3, pp. 299–304.

52. Mujabar, P.S.; Dajkumar, S. Mapping of bauxite mineral deposits in the northern region of Saudi Arabia by using advanced spaceborne thermal emission and reflection radiometer satellite data. *Geo Spat. Inf. Sci.* **2018**, *22*, 35–44.

53. Van der Meer, F.D.; van der Werff, H.M.A.; van Ruitenbeek, F.J.A.; Hecker, C.A.; Bakker, W.H.; Noomen, M.F.; van der Meijde, M.; Carranza, E.J.M.; Smeth, J.B.D.; Woldai, T. Multi- and hyperspectral geologic remote sensing: A review. *Int. J. Appl. Earth Obs. Geoinf.* **2012**, *14*, 112–128.

54. Abrams, M.; Yamaguchi, Y. Twenty years of ASTER contributions to lithologic mapping and mineral exploration. *Remote Sens.* **2019**, *11*, 1394.

55. Ninomiya, Y.; Fu, B. Thermal infrared multispectral remote sensing of lithology and mineralogy based on spectral properties of materials. *Ore Geol. Rev.* **2019**, *108*, 54–72.

56. Christmann, P.; Gloaguen, E.; Labbé, J.-F.; Melleton, J.; Piantone, P. Chapter 1—Global lithium resources and sustainability issues. In *Lithium Process Chemistry*; Chagnes, A., Światowska, J., Eds.; Elsevier: Amsterdam, The Netherlands, 2015; pp. 1–40.

57. Grosjean, C.; Miranda, P.H.; Perrin, M.; Poggi, P. Assessment of world lithium resources and consequences of their geographic distribution on the expected development of the electric vehicle industry. *Renew. Sustain. Energy Rev.* **2012**, *16*, 1735–1744.

58. Arrobas, D.L.P.; Hund, K.L.; Mccormick, M.S.; Ningthoujam, J.; Drexhage, J.R. *The Growing Role of Minerals and Metals for a Low Carbon Future*; The World Bank: Washington, DC, USA, 2017.

59. Lefevre, M.J. Teledetection d'anomalies geobotaniques appliquee a la recherche miniere par la methode de traitement d'images, Echassieres (Allier). *Bull. Société Géologique Fr.* **1982**, 127–130.

60. Perrotta, M.M.; Souza Filho, C.R.; Leite, C.A.S. Mapeamento espectral de intrusões pegmatíticas relacionadas a mineralizações de lítio, gemas e minerais industriais na região do vale do Jequitinhonha (MG) a partir de imagens ASTER. In Proceedings of the Anais do XII Simpósio Brasileiro de Sensoriamento Remoto, Goiânia, Brasil, 16–21 April 2005; pp. 1855–1862.

61. Mendes, D.; Perrotta, M.M.; Costa, M.A.C.; Paes, V.J.C. Mapeamento espectral para identificação de assinaturas espectrais de minerais de lítio em imagens ASTER (NE/MG). In Proceedings of the Anais do XVIII Simpósio Brasileiro de Sensoriamento Remoto, Santos-SP, Brasil, 28–29 May 2017; pp. 5273–5280.

62. Cardoso-Fernandes, J.; Teodoro, A.C.; Lima, A. Potential of Sentinel-2 data in the detection of lithium (Li)-bearing pegmatites: A study case. In Proceedings of the SPIE, SPIE Remote Sensing, Berlin, Germany, 10–13 September 2018; Michel, U., Schulz, K., Eds.; SPIE: Bellingham, WA, USA, 2018; p. 15.

63. Cardoso-Fernandes, J.; Teodoro, A.C.; Lima, A. Remote sensing data in lithium (Li) exploration: A new approach for the detection of Li-bearing pegmatites. *Int. J. Appl. Earth Obs. Geoinf.* **2019**, *76*, 10–25.

64. De Almeida, C.M.P. Estudo Do Filão Aplitopegmatítico Da Mina Da Bajoca, Almendra: Contribuição Científico-Tecnológica. MsC Thesis, Faculdade de Ciências da Universidade do Porto, Porto, Portugal, 2003.

65. Spatz, D.M. Remote sensing characteristics of the sediment- and volcanic-hosted precious metal systems: Imagery selection for exploration and development. *Int. J. Remote Sens.* **1997**, *18*, 1413–1438.

66. Santos, D.; Teodoro, A.; Lima, A.; Cardoso-Fernandes, J. Remote sensing techniques to detect areas with potential for lithium exploration in Minas Gerais, Brazil. In Proceedings of the SPIE, SPIE Remote Sensing, Strasbourg, France, 9–12 September 2019; Schulz, K., Michel, U., Nikolakopoulos, K.G., Eds.; SPIE: Bellingham, WA, USA, 2019.

67. Gemusse, U.; Lima, A.; Teodoro, A. Pegmatite spectral behavior considering ASTER and Landsat 8 OLI data in Naipa and Muiane mines (Alto Ligonha, Mozambique). In Proceedings of the SPIE, SPIE Remote Sensing, Berlin, Germany, 10–13 September 2018; Michel, U., Schulz, K., Eds.; SPIE: Bellingham, WA, USA, 2018.

68. Gemusse, U.; Lima, A.; Teodoro, A. Comparing different techniques of satellite imagery classification to mineral mapping pegmatite of Muiane and Naipa: Mozambique. In

Proceedings of the SPIE, SPIE Remote Sensing, Strasbourg, France, 9–12 September 2019; Schulz, K., Michel, U., Nikolakopoulos, K.G., Eds.; SPIE: Bellingham, WA, USA, 2019.

69. Cardoso-Fernandes, J.; Teodoro, A.C.; Lima, A.; Roda-Robles, E. Evaluating the performance of support vector machines (SVMs) and random forest (RF) in Li-pegmatite mapping: Preliminary results. In Proceedings of the SPIE, SPIE Remote Sensing, Strasbourg, France, 9–12 September 2019; Schulz, K., Michel, U., Nikolakopoulos, K.G., Eds.; SPIE: Bellingham, WA, USA, 2019.
70. Belgiu, M.; Drăguţ, L. Random forest in remote sensing: A review of applications and future directions. *ISPRS J. Photogramm. Remote Sens.* **2016**, *114*, 24–31.
71. Breiman, L. Random forests. *Mach. Learn.* **2001**, *45*, 5–32.
72. Mountrakis, G.; Im, J.; Ogole, C. Support vector machines in remote sensing: A review. *ISPRS J. Photogramm. Remote Sens.* **2011**, *66*, 247–259.
73. Vapnik, V.N. *The Nature of Statistical Learning Theory*; Springer: New York, NY, USA, 1995.
74. Rossi, C.; Spittle, S.; Bayaraa, M.; Pandey, A.; Henry, N. An earth observation framework for the lithium exploration. In Proceedings of the IGARSS 2018—2018 IEEE International Geoscience and Remote Sensing Symposium, Valencia, Spain, 22–27 July 2018; pp. 1616–1619.
75. Pesquera, A.; Torres-Ruiz, J.; Gil-Crespo, P.P.; Velilla, N. Chemistry and genetic implications of tourmaline and Li-F-Cs micas from the Valdeflores area (Caceres, Spain). *Am. Mineral.* **1999**, *84*, 55–69.
76. Torres-Ruiz, J.; Pesquera, A.; Gil, P.P.; Casas, J. Tourmalinites and Sn-Li mineralization in the Valdeflores area (Cáceres, Spain). *Mineral. Petrol.* **1996**, *56*, 209–223.
77. Tavares, P.A.; Beltrão, N.; Guimarães, U.S.; Teodoro, A.; Gonçalves, P. Urban ecosystem services quantification through remote sensing approach: A systematic review. *Environments* **2019**, *6*, 51.
78. Cardoso-Fernandes, J.; Lima, A.; Roda-Robles, E.; Teodoro, A.C. Constraints and potentials of remote sensing data/techniques applied to lithium (Li)-pegmatites. *Can. Mineral.* **2019**, *57*, 723–725.

79. Rodger, A.; Cudahy, T. Vegetation corrected continuum depths at 2.20µm: An approach for hyperspectral sensors. *Remote Sens. Environ.* **2009**, *113*, 2243–2257.

80. Jet Propulsion Laboratory (JPL). ASTER: Advanced Spaceborne Thermal Emission and Reflection Radiometer. Available online: **https://asterweb.jpl.nasa.gov/index.asp** (accessed on 16 January 2020).

81. Jet Propulsion Laboratory (JPL). ASTER: Instrument Characteristics. Available online: **https://asterweb.jpl.nasa.gov/characteristics.asp** (accessed on 16 January 2020).

82. Jet Propulsion Laboratory (JPL). ASTER User Advisory. Available online: **https://asterweb.jpl.nasa.gov/swir-alert.asp** (accessed on 16 January 2020).

83. Pour, A.B.; Hashim, M. The application of ASTER remote sensing data to porphyry copper and epithermal gold deposits. *Ore Geol. Rev.* **2012**, *44*, 1–9.

84. United States Geological Survey (USGS). Landsat Satellite Missions. Available online: **https://www.usgs.gov/land-resources/nli/landsat/landsat-satellite-missions** (accessed on 16 January 2020).

85. United States Geological Survey (USGS). Landsat 8. Available online: **https://www.usgs.gov/land-resources/nli/landsat/landsat-8** (accessed on 16 January 2020).

86. European Space Agency (ESA). Observing the Earth: Copernicus. Available online: **http://www.esa.int/Our_Activities/Observing_the_Earth/Copernicus/Overview4** (accessed on 7 March 2018).

87. European Space Agency (ESA). Missions: Sentinel-2. Overview. Available online: **https://sentinel.esa.int/web/sentinel/missions/sentinel-2/overview** (accessed on 16 January 2020).

88. European Space Agency (ESA). Radiometric Resolutions. Available online: **https://earth.esa.int/web/sentinel/user-guides/sentinel-2-msi/resolutions/radiometric** (accessed on 16 January 2020).

89. United States Geological Survey (USGS). Landsat 8 Band Designations. Available online: **https://www.usgs.gov/media/images/landsat-8-band-designations** (accessed on 16 January 2020).

90. Van der Meer, F.D.; van der Werff, H.M.A.; van Ruitenbeek, F.J.A. Potential of ESA's Sentinel-2 for geological applications. *Remote Sens. Environ.* **2014**, *148*, 124–133.

91. Van der Werff, H.; Van der Meer, F. Sentinel-2 for mapping iron absorption feature parameters. *Remote Sens.* **2015**, *7*, 12635–12653.

92. Van der Werff, H.; Van der Meer, F. Sentinel-2A MSI and Landsat 8 OLI provide data continuity for geological remote sensing. *Remote Sens.* **2016**, *8*, 883.

93. Mielke, C.; Bösche, N.; Rogass, C.; Segl, K.; Gauert, C.; Kaufmann, H. Potential applications of the Sentinel-2 multispectral sensor and the Enmap hyperspectral sensor in mineral exploration. *EARSeL eProceedings* **2014**, *13*, 93–102.

94. Fal, S.; Maanan, M.; Baidder, L.; Rhinane, H. The contribution of sentinel-2 satellite images for geological mapping in the south of tafilalet Basin (Eastern Anti-Atlas, Morocco). *Int. Arch. Photogramm. Remote Sens. Spat. Inf. Sci.* **2019**, 75–82.

95. Al-Nahmi, F.; Saddiqi, O.; Hilali, A.; Rhinane, H.; Baidder, L.; El arabi, H.; Khanbari, K. Application of remote sensing in geological mapping, case study Al Maghrabah Area—Hajjah Region, Yemen. *ISPRS Ann. Photogramm. Remote Sens. Spat. Inf. Sci.* **2017**, 63–71.

96. Elhag, M.; Alshamsi, D. Integration of remote sensing and geographic information systems for geological fault detection on the island of Crete, Greece. *Geosci. Instrum. Methods Data Syst.* **2019**, *8*, 45–54.

97. Ge, W.; Cheng, Q.; Tang, Y.; Jing, L.; Gao, C. Lithological classification using sentinel-2A data in the shibanjing ophiolite complex in Inner Mongolia, China. *Remote Sens.* **2018**, *10*, 638.

98. Hu, B.; Xu, Y.; Wan, B.; Wu, X.; Yi, G. Hydrothermally altered mineral mapping using synthetic application of Sentinel-2A MSI, ASTER and Hyperion data in the Duolong area, Tibetan Plateau, China. *Ore Geol. Rev.* **2018**, *101*, 384–397.

99. DigitalGlobe Inc. Data Sheet for WorldView 3. Available online: **http://content.satimagingcorp.com.s3.amazonaws.com/media/pdf/WorldView-3-PDF-Download.pdf** (accessed on 16 January 2020).

100. USGS Landsat Program. Comparison of #Landsat 7, 8, #Sentinel 2, #ASTER & #MODIS Bands. View Band Designations for All #Landsat Sensors. Available

online: **https://twitter.com/usgslandsat/status/837696716417687553** (accessed on 22 December 2017).

101. Lightweight Integrated Ground and Airborne Hyperspectral Topological Solution. Available online: **http://lights.univ-lorraine.fr/** (accessed on 29 January 2020).

102. Cloutis, E.A. Review article hyperspectral geological remote sensing: Evaluation of analytical techniques. *Int. J. Remote Sens.* **1996**, *17*, 2215–2242.

103. Asadzadeh, S.; Souza Filho, C.R. A review on spectral processing methods for geological remote sensing. *Int. J. Appl. Earth Obs. Geoinf.* **2016**, *47*, 69–90.

104. Sabins, F.F. *Remote Sensing Principles and Interpretation*, 3rd ed.; W. H. Freeman: New York, NY, USA, 1997; p. 494.

105. Mia, B.; Fujimitsu, Y. Mapping hydrothermal altered mineral deposits using Landsat 7 ETM+ image in and around Kuju volcano, Kyushu, Japan. *J. Earth Syst. Sci.* **2012**, *121*, 1049–1057.

106. Ali, A.; Pour, A. Lithological mapping and hydrothermal alteration using Landsat 8 data: A case study in ariab mining district, red sea hills, Sudan. *Int. J. Basic Appl. Sci.* **2014**, *3*.

107. Loughlin, W.P. Component analysis for alteration mapping. *Photogram. Eng. Rem. Sens.* **1991**, *57*, 1163–1169.

108. Rowan, L.C.; Mars, J.C.; Simpson, C.J. Lithologic mapping of the Mordor, NT, Australia ultramafic complex by using the Advanced Spaceborne Thermal Emission and Reflection Radiometer (ASTER). *Remote Sens. Environ.* **2005**, *99*, 105–126.

109. Momose, A.; Miyatake, S.; Arvelyna, Y.; Nguno, A.; Mhopjeni, K.; Sibeso, M.; Muyongo, A.; Muvangua, E. Mapping pegmatite using HyMap data in southern Namibia. In Proceedings of the 2011 IEEE International Geoscience and Remote Sensing Symposium, Vancouver, BC, Canada, 24–29 July 2011; pp. 2216–2217.

110. Oshigami, S.; Yamaguchi, Y.; Uezato, T.; Momose, A.; Arvelyna, Y.; Kawakami, Y.; Yajima, T.; Miyatake, S.; Nguno, A. Mineralogical mapping of southern Namibia by application of continuum-removal MSAM method to the HyMap data. *Int. J. Remote Sens.* **2013**, *34*, 5282–5295.

111. Ellis, R.J.; Scott, P.W. Evaluation of hyperspectral remote sensing as a means of environmental monitoring in the St. Austell China clay (kaolin) region, Cornwall, UK. *Remote Sens. Environ.* **2004**, *93*, 118–130.

112. Noi, P.T.; Kappas, M. Comparison of random forest, k-Nearest neighbor, and support vector machine classifiers for land cover classification using Sentinel-2 imagery. *Sensors* **2017**, *18*, 18.

113. Tavares, P.A.; Beltrão, N.E.S.; Guimarães, U.S.; Teodoro, A.C. Integration of Sentinel-1 and Sentinel-2 for Classification and LULC Mapping in the Urban Area of Belém, Eastern Brazilian Amazon. *Sensors* **2019**, *19*, 1140.

114. Pal, M.; Mather, P.M. Support vector machines for classification in remote sensing. *Int. J. Remote Sens.* **2005**, *26*, 1007–1011.

115. Oommen, T.; Misra, D.; Twarakavi, N.K.C.; Prakash, A.; Sahoo, B.; Bandopadhyay, S. An objective analysis of support vector machine based classification for remote sensing. *Math. Geosci.* **2008**, *40*, 409–424.

116. Yu, L.; Liang, L.; Wang, J.; Zhao, Y.; Cheng, Q.; Hu, L.; Liu, S.; Yu, L.; Wang, X.; Zhu, P.; et al. Meta-discoveries from a synthesis of satellite-based land-cover mapping research. *Int. J. Remote Sens.* **2014**, *35*, 4573–4588.

117. Yu, L.; Porwal, A.; Holden, E.-J.; Dentith, M.C. Towards automatic lithological classification from remote sensing data using support vector machines. *Comput. Geosci.* **2012**, *45*, 229–239.

118. Cracknell, M.J.; Reading, A.M.; McNeill, A.W. Mapping geology and volcanic-hosted massive sulfide alteration in the Hellyer–Mt Charter region, Tasmania, using Random Forests™ and Self-Organising Maps. *Aust. J. Earth Sci.* **2014**, *61*, 287–304.

119. Parakh, K.; Thakur, S.; Chudasama, B.; Tirodkar, S.; Porwal, A.; Bhattacharya, A. Machine learning and spectral techniques for lithological classification. In Proceedings of the SPIE Asia-Pacific Remote Sensing, New Delhi, India, 4–7 April 2016.

120. Bahrambeygi, B.; Moeinzadeh, H. Comparison of support vector machine and neutral network classification method in hyperspectral mapping of ophiolite mélanges–A case study of east of Iran. *Egypt. J. Remote Sens. Space Sci.* **2017**, *20*, 1–10.

121. Latifovic, R.; Pouliot, D.; Campbell, J. Assessment of convolution neural networks for surficial geology mapping in the South Rae Geological Region, Northwest Territories, Canada. *Remote Sens.* **2018**, *10*, 307.

122. Géron, A. *Hands-On Machine Learning with Scikit-Learn and TensorFlow: Concepts, Tools, and Techniques to Build Intelligent Systems*; O'Reilly Media Inc.: Sebastopol, CA, USA, 2017; p. 568.

123. Maxwell, A.E.; Warner, T.A.; Fang, F. Implementation of machine-learning classification in remote sensing: An applied review. *Int. J. Remote Sens.* **2018**, *39*, 2784–2817.

124. Li, Y.; Zhang, H.; Xue, X.; Jiang, Y.; Shen, Q. Deep learning for remote sensing image classification: A survey. *Wiley Interdiscip. Rev. Data Min. Knowl. Discov.* **2018**, *8*, e1264.

125. Menze, B.H.; Kelm, B.M.; Splitthoff, D.N.; Koethe, U.; Hamprecht, F.A. On oblique random forests. In *Machine Learning and Knowledge Discovery in Databases*; Springer: Berlin/Heidelberg, Germany, 2011; pp. 453–469.

126. Bruzzone, L.; Chi, M.; Marconcini, M. A novel transductive SVM for semisupervised classification of remote-sensing images. *IEEE Trans. Geosci. Remote Sens.* **2006**, *44*, 3363–3373.

127. Sarmah, D.K. A survey on the latest development of machine learning in genetic algorithm and particle swarm optimization. In *Optimization in Machine Learning and Applications*; Kulkarni, A.J., Satapathy, S.C., Eds.; Springer: Singapore, 2020; pp. 91–112.

128. Kumar, A.; Ghosh, S.K.; Dadhwal, V.K. Full fuzzy land cover mapping using remote sensing data based on fuzzy c-means and density estimation. *Can. J. Remote Sens.* **2007**, *33*, 81–87.

Chapter II: Development of new remote sensing algorithms

Most of the existing processing methods employed in the literature allow discriminating between hydrothermally altered and unaltered rocks (Pour & Hashim, 2015; Abrams & Yamaguchi, 2019; Ge *et al.*, 2020). In this chapter, the new methodological advances and achievements made in the scope of this work to directly identify Li-pegmatites are presented. At the same time, traditional techniques such as red, green, and blue (RGB) combinations, band ratios, and principal component analysis (PCA) were validated in other areas of the globe (Santos *et al.*, 2019; 2021; Gemusse *et al.*, 2021). For the Fregeneda-Almendra area, and in the ambit of the "Lightweight Integrated Ground and Airborne Hyperspectral Topological Solution" (LIGHTS) project (http://lights.univ-lorraine.fr/), the integration of different types of remote sensing data into distinct exploration stages were discussed (Cardoso-Fernandes *et al.*, 2020a). The results of these additional contributions resulted in two peer-reviewed conference proceedings that can be found in Appendix I.2 and two abstracts presented in national meetings (Appendix I.3).

Building on the previously employed classical techniques (Cardoso-Fernandes *et al.*, 2019a), distinct non-parametric, machine learning algorithms (MLAs) were tested and optimized. These techniques (MLAs) have gained great importance and become popular not only in remote sensing applications, but also in the geological area, due to their ability to outperform traditional parametric classifiers (Oommen *et al.*, 2008; Yu *et al.*, 2012; Cracknell *et al.*, 2014; Geranian *et al.*, 2016; Noi & Kappas, 2017). In preliminary attempts, the performance of the Support Vector Machine (SVM) and Random Forest (RF) algorithms in the Fregeneda-Almendra case study area was evaluated (Cardoso-Fernandes *et al.*, 2019b). Next, Artificial Neural Networks (ANNs) were also considered for Li-pegmatite identification (Cardoso-Fernandes *et al.*, 2020b). These results, published in two peer-reviewed conference proceedings, are shown in Appendix I.2. However, several overfitting problems were observed considering all three MLAs. Consequently, this approach needed to be improved to overcome the overfitting of the algorithms and reduce the number of false positives, to obtain more plausible, robust, and realistic target exploration maps. The new proposed methodological advances and semi-automatization of the classification process resulted in a peer-reviewed journal article (Section II.1). The source code developed during this study (in a Python environment) was published as Supplementary Material and can be found in Appendix I.4.

References

Abrams, M., & Yamaguchi, Y. (2019). Twenty Years of ASTER Contributions to Lithologic Mapping and Mineral Exploration. *Remote Sensing, 11*(11), 1394.

Cardoso-Fernandes, J., Teodoro, A. C., & Lima, A. (2019a). Remote sensing data in lithium (Li) exploration: A new approach for the detection of Li-bearing pegmatites. *International Journal of Applied Earth Observation and Geoinformation, 76*, 10-25. doi: https://doi.org/10.1016/j.jag.2018.11.001.

Cardoso-Fernandes, J., Teodoro, A. C., Lima, A., & Roda Robles, E. (2020b, 26 Sept.-2 Oct. 2020). *Lithium (Li) pegmatite mapping using Artificial Neural Networks (ANNs): preliminary results.* Paper presented at the IGARSS 2020 - 2020 IEEE International Geoscience and Remote Sensing Symposium, Waikoloa, HI, USA, 557-560. doi: 10.1109/IGARSS39084.2020.9323852.

Cardoso-Fernandes, J., Teodoro, A. C., Lima, A., & Roda-Robles, E. (2019b, 9–12 September 2019). *Evaluating the performance of support vector machines (SVMs) and random forest (RF) in Li-pegmatite mapping: preliminary results.* Paper presented at the SPIE Remote Sensing, Strasbourg, France, doi: 10.1117/12.2532577.

Cardoso-Fernandes, J., Teodoro, A. C., Lima, A., Mielke, C., Körting, F., Roda-Robles, E., & Cauzid, J. (2020a, 26 Sept.-2 Oct. 2020). *Multi-scale approach using remote sensing techniques for lithium pegmatite exploration: first results.* Paper presented at the IGARSS 2020 - 2020 IEEE International Geoscience and Remote Sensing Symposium, Waikoloa, HI, USA, 5226-5229. doi: 10.1109/IGARSS39084.2020.9323705.

Cracknell, M. J., Reading, A. M., & McNeill, A. W. (2014). Mapping geology and volcanic-hosted massive sulfide alteration in the Hellyer–Mt Charter region, Tasmania, using Random Forests™ and Self-Organising Maps. *Australian Journal of Earth Sciences, 61*(2), 287-304. doi: 10.1080/08120099.2014.858081.

Ge, W., Cheng, Q., Jing, L., Wang, F., Zhao, M., & Ding, H. (2020). Assessment of the Capability of Sentinel-2 Imagery for Iron-Bearing Minerals Mapping: A Case Study in the Cuprite Area, Nevada. *Remote Sensing, 12*(18), 3028. doi: 10.3390/rs12183028.

Gemusse, U., Cardoso-Fernandes, J., Santos, D., Teodoro, A., Lima, A. (2021). *Prospeção dos Pegmatitos de Muiane e Naipa (Moçambique) a partir de técnicas de Deteção Remota, usando imagens do sensor ASTER*. Abstract presented at *Jornadas do ICT*, *Porto*, 2021.

Geranian, H., Tabatabaei, S. H., Asadi, H. H., & Carranza, E. J. M. (2016). Application of Discriminant Analysis and Support Vector Machine in Mapping Gold Potential Areas for Further Drilling in the Sari-Gunay Gold Deposit, NW Iran. *Natural Resources Research, 25*(2), 145-159. doi: 10.1007/s11053-015-9271-2.

Noi, P. T., & Kappas, M. (2017). Comparison of Random Forest, k-Nearest Neighbor, and Support Vector Machine Classifiers for Land Cover Classification Using Sentinel-2 Imagery. *Sensors (Basel), 18*(1). doi: 10.3390/s18010018.

Oommen, T., Misra, D., Twarakavi, N. K. C., Prakash, A., Sahoo, B., & Bandopadhyay, S. (2008). An Objective Analysis of Support Vector Machine Based Classification for Remote Sensing. *Mathematical Geosciences, 40*(4), 409-424. doi: 10.1007/s11004-008-9156-6.

Pour, A. B., & Hashim, M. (2015). Hydrothermal alteration mapping from Landsat-8 data, Sar Cheshmeh copper mining district, south-eastern Islamic Republic of Iran. *Journal of Taibah University for Science, 9*(2), 155-166. doi: 10.1016/j.jtusci.2014.11.008.

Santos, D., Teodoro, A., Lima, A., & Cardoso-Fernandes, J. (2019, 9–12 September 2019). *Remote sensing techniques to detect areas with potential for lithium exploration in Minas Gerais, Brazil.* Paper presented at the SPIE Remote Sensing, Strasbourg, France, doi: https://doi.org/10.1117/12.2532744.

Santos, D., Teodoro, A., Lima, A., Cardoso-Fernandes, J. (2021). *Aplicação de Métodos para Identificação de Novos Depósitos de Pegmatitos LCT e NYF: GREENPEG um Projeto Europeu*. Abstract presented at *Jornadas do ICT*, *Porto*, 2021.

Yu, L., Porwal, A., Holden, E.-J., & Dentith, M. C. (2012). Towards automatic lithological classification from remote sensing data using support vector machines. *Computers & Geosciences, 45*, 229-239. doi: https://doi.org/10.1016/j.cageo.2011.11.019.

II.1. Semi-Automatization of Support Vector Machines to Map Lithium (Li) Bearing Pegmatites

Joana Cardoso-Fernandes, Ana C. Teodoro, Alexandre Lima and Encarnación Roda-Robles

Remote Sensing, 2020, 12(14), 2319

Abstract: Machine learning (ML) algorithms have shown great performance in geological remote sensing applications. The study area of this work was the Fregeneda–Almendra

region (Spain–Portugal) where the support vector machine (SVM) was employed. Lithium (Li)-pegmatite exploration using satellite data presents some challenges since pegmatites are, by nature, small, narrow bodies. Consequently, the following objectives were defined: (i) train several SVM's on Sentinel-2 images with different parameters to find the optimal model; (ii) assess the impact of imbalanced data; (iii) develop a successful methodological approach to delineate target areas for Li-exploration. Parameter optimization and model evaluation was accomplished by a two-staged grid-search with cross-validation. Several new methodological advances were proposed, including a region of interest (ROI)-based splitting strategy to create the training and test subsets, a semi-automatization of the classification process, and the application of a more innovative and adequate metric score to choose the best model. The proposed methodology obtained good results, identifying known Li-pegmatite occurrences as well as other target areas for Li-exploration. Also, the results showed that the class imbalance had a negative impact on the SVM performance since known Li-pegmatite occurrences were not identified. The potentials and limitations of the methodology proposed are highlighted and its applicability to other case studies is discussed.

Keywords: machine learning, remote sensing, lithological mapping, supervised classification, Sentinel-2, mineral exploration, Lithium, pegmatite

1. Introduction

Recently, there has been an increasing demand for lithium (Li) as a mineral commodity driven by the electric car industry, in which Li is one of the batteries' main components. This increasing demand will result in an intensive Li exploitation soon, and untraditional Li-exploration methods that allow exploration companies to quickly delineate potentially economic areas are to meet the market expectations. With that goal in mind, some authors have attempted to identify Li-bearing pegmatites with different remote sensing data (ASTER, Landsat-5, Landsat-8, and Sentinel-2) and different image processing techniques [1–6]. Cardoso-Fernandes, et al. [7] recently reviewed the approaches and developments made to Li-exploration using remote sensing data and image processing techniques, pointing out their weaknesses and strengths.

The study area of this work is the Fregeneda–Almendra (Salamanca, Spain—Vila Nova de Foz Côa, Portugal) region, where different Li-bearing pegmatites were mapped using ASTER, Landsat-5, Landsat-8, and Sentinel-2 data, and several image processing

algorithms, such as RGB combinations, band ratios, and principal component analysis (PCA) were employed [1,2]. Although these techniques allowed to vector known Li-pegmatites and other potential areas, spectral confusion with urbanized areas or agricultural fields was noticeable. Therefore, a more powerful technique capable of vectoring Li-pegmatites with more confidence is needed, to make the use of remote sensing data in Li-exploration more significant for exploration companies.

During the last decades, there has also been a growing application of machine learning (ML) in the field of geology, either in satellite-based geological mapping [8–12] or in mineral prospectivity mapping [13–16]. Their growing popularity is due to their ability to outperform classical classification algorithms (e.g., [8,16]). While the use of ML to map Li-pegmatites may seem promising, two main problems can be identified beforehand: (i) pegmatites are relatively small bodies and (ii) generally have low exposition. This means that in an image classification approach, Li-pegmatites correspond to a scarce class with few training samples, and some ML algorithms are sensitive to training data size and class imbalance. Furthermore, the objectives of geological exploration are different from the objectives of Land Use/Land Cover (LULC) classification. In a LULC classification problem, all classes bear the same importance and both false positives and false negatives need to be avoided. In a geological exploration, and in this case, the Li-bearing pegmatite class is the target class. Consequently, misclassifications affecting other classes are less important. Besides, false positives (i.e., over-estimating the Li-pegmatite class) may not constitute a problem while false negatives (i.e., not identifying pixels that correspond in fact to Li-pegmatites on the ground) are serious and should be avoided.

Taking this into account, the choice of correct ML algorithms is paramount to successfully map and identify Li-pegmatites. That is why in a preliminary study in the Fregeneda–Almendra region, ML algorithms like support vector machines (SVM's) and random forest (RF) were employed to classify Sentinel-2 images [5]. According to several authors, these algorithms, when compared with classical and other ML techniques, are less sensitive to the training size [17,18] and more capable of dealing with imbalanced datasets [19]. The preliminary results obtained in this study area [5] were unsatisfactory. Both algorithms presented overfitting problems, achieving perfect to almost perfect accuracy scores at a class level, but then failing to correctly map some classes in the whole image [5]. Moreover, the discrimination between Li-pegmatites and the host-rocks was very low which ultimately resulted in a large number of Li-pegmatite false positives [5].

Moreover, algorithm parameterization is still a major difficulty in the sense that most of the time ML algorithms cannot achieve good performance without optimization [18,19]. Therefore, we believe that the previous results can be improved through better algorithm parameterization and improvement of training data. For this improved approach, SVM's were chosen due to their challenging optimization when compared with RF. Several models were optimized and tested, including kernelized and non-kernelized SVM. The objectives of this study were then to (i) train several SVM's on Sentinel-2 images with different parameters to find the optimal model; (ii) assess the impact of imbalanced data through the comparison of different class-balancing strategies; and (iii) improve the previously employed methodology and delineate target areas for Li-exploration. This work also aimed to answer distinct research questions, namely: (i) how to overcome the overfitting challenges; (ii) which factors most influence the SVM performance; (iii) can the SVM classification process be automatized; (iv) what are the main challenges and benefits of using SVM in Li-pegmatite mapping; and (v) can the methodology be extrapolated to other study areas. Ultimately, this research intends to fill the literature gap by contributing to the state of the art regarding the use of ML in Li-pegmatite mapping, by clarifying how SVM can be helpful in Li-pegmatite exploration.

The Fregeneda–Almendra Pegmatite Field

The Fregeneda–Almendra (FA) pegmatite field lies within the Central Iberian Zone of the Iberian Massif, spreading from Portugal (Almendra) to Spain (La Fregeneda). The border is materialized by the Águeda river, and the pegmatite field is delimitated to the north by the Douro river and to the east by the Vilariça's fault. The study area of this work comprises most of the FA field where different types of pegmatite dykes were defined (Figure 1) taking into account their mineralogy, morphology, and internal structure [20–22]. These bodies intruded on the metasedimentary rocks of the Schist-Graywacke Complex (SGC) [23,24]. To the south the syn-Variscan Mêda-Penedono-Lumbrales granitic complex outcrops. Within the more evolved aplite–pegmatites, there are four dyke-types containing Li-bearing minerals: petalite-rich, spodumene-rich, lepidolite–spodumene-rich, and lepidolite-rich. All the Li-pegmatites are discordant from the host-rock main foliation and are emplaced in the same fracture set, striking from N-S to N30 °E. The petalite-rich dykes can reach a maximum thickness of 5 m to 30 m [22,25]. The spodumene-rich dykes are very similar to the petalite ones in terms of mineralogy, attitude, and dimension, with a thickness ranging from 4 m to 15 m [22,25]. Both dyke-types present no internal zonation. The lepidolite–spodumene-rich

dykes present a common internal layering and thickness usually less than 15 m [22,25]. The thinner dykes are the lepidolite-rich, with a thickness lesser than 3 m and occasionally with internal banded structure (where lepidolite-rich layers alternate with albite-rich ones) [22,25].

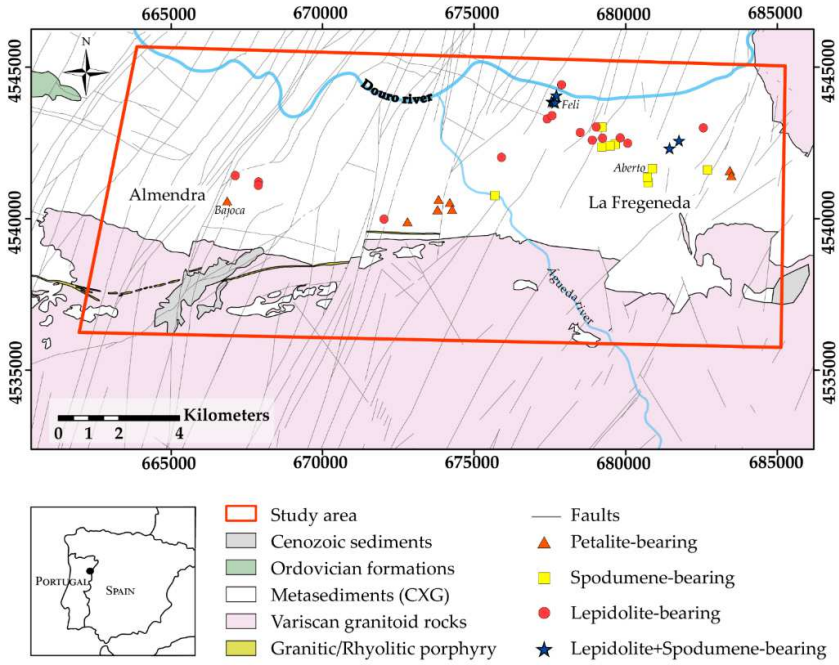

Figure 1. Location and geological map of the study area where the different aplite–pegmatite dykes outcrop (adapted from [22,26,27]). Open-pit mines of Bajoca, Feli and Alberto are also highlighted. The map projection is Universal Transverse Mercator zone 29 N from the WGS84 datum.

In the FA area, there are three locations were these Li-dykes are being exploited in open-pit mines (Figure 1). This type of excavation favors the application of remote sensing data/techniques, because it increases pegmatite exposition at the surface. Moreover, each open-pit mine exploits a different pegmatite dyke-type. The Bajoca mine, located near Almendra in the Portuguese side of the field, exploits a petalite-rich dyke with up to 30 m of thickness [22]. The Alberto mine, near La Fregeneda in Spain, exploits several spodumene-rich dykes with varying thicknesses. Despite spodumene being the predominant Li-bearing phase, primary petalite can also be found in these dykes [22]. Finally, in the Feli mine, located near the Douro river on the Spanish side of the pegmatite field, a lepidolite–spodumene-rich dike is exploited.

Currently, other complementary studies are being developed in the FA area to help target Li-mineralizations. Stream sediment analysis of more than 3000 samples is being employed on the Portuguese side to identify areas with Li-potential. Spectral studies are being conducted using a laboratory spectroradiometer to build a spectral database of Li-bearing minerals.

Moreover, as stated by Cardoso-Fernandes, et al. [7], the knowledge on the alteration halos associated with Li-pegmatites could favor alteration mapping techniques, thus increasing the size of the target areas and possibly allowing to vector near-surface hidden dykes. For that, more than 70 host-rocks samples are being characterized through geochemical studies. Overall, the expected results will help to improve Li-pegmatite remote mapping capabilities. The ability to recognize Li-pegmatites remotely is of great interest to the exploration/mining industry. Firstly, it would allow to decrease the time and costs of field campaigns. Secondly, the social acceptance of mineral exploration is becoming a major concern in Europe. Consequently, less intrusive exploration methods such as remote sensing are increasingly becoming an integral part of the companies' exploration strategies.

2. Support Vector Machines (SVM's)

Support vector machines (SVM's) are a non-parametric classification technique based on statistical learning theory [28], and therefore no assumption on the distribution of the data is made. The SVM technique tries to find an optimal hyperplane that separates the dataset into a defined number of classes. This optimal hyperplane is the decision boundary that maximizes the distance of the margin between the class bounding hyperplanes (also called supporting hyperplanes). The bounding hyperplanes are parallel to the optimal hyperplane and are defined by the training samples that are closest to the boundary–the support vectors (Figure 2).

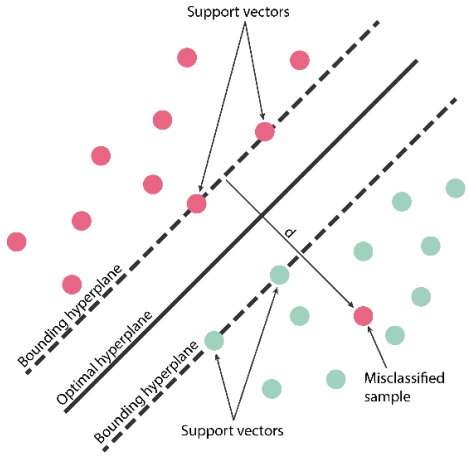

Figure 2. The support vector machines (SVM) method: the optimal hyperplane separates the two classes and is parallel to the bounding hyperplanes on which the support vectors lie. The distance between these two bounding hyperplanes is called the margin, and the distance *d* between the bounding hyperplane and the outlier (misclassified sample) indicates that there are slack variables (modified from [8]).

SVM is by nature a binary classifier, but it can be extended for multiclass classification, using the 'one-against-all' or 'one-against-one' strategies [8,17]. In the 'one-against-all' strategy, k SVM models are built (where k is equal to the number of classes), each of them separating one class from the remaining. In the 'one-against-one' approach, k(k-1)/2 SVM classifiers are built and trained for all possible two-class combinations out of k classes [29]. In other words, a sample is classified as one of two classes for each model and the output class label is decided by the majority votes.

Since the SVM is inherently a linear classifier, it assumes that the multispectral feature data are linearly separable in the input space [17]. However, in practice, the data can be noisy and different classes may not be entirely separable due to class overlap [8,17]. This limitation can be overcome using techniques like the soft margin method [30] and the kernel trick that map the data into a higher dimension known as feature space and add additional variables called slack variables to accommodate outliers. This projection is done under the assumption that a linear boundary may exist in that higher-dimensional feature space [18]. In what concerns the soft-margin technique, the training samples are allowed to fall on the opposite side of the decision boundary (the optimal hyperplane) and the limit of the violation of the bounding hyperplanes is set by the slack variables. To each sample classified on the wrong side of the boundary, there is a penalty associated, in this case, it is the cost hyperparameter C [30]. A smaller C value will result in a larger margin that will allow for more violations, but this may lead to an inappropriate (large) number of support vectors [8,18]. Oppositely, a higher C value means a narrower margin that will limit violations. This can result in a more complex decision boundary and may cause the model to lose its generalization capability and even overfit the data [8,18]. In remote sensing, an overfitting model can explain very well the variance of the training data, while having a low capability to generalize to the whole image. Consequently, a classical sign that a model is overfitting the data is when the performance on the training set is notably better than in the testing/validation dataset [31]. In the kernel trick case, some of the more popular kernel functions(K) are, for two input vectors x_i e x_j:

$$\text{Linear: } K(x_i,x_j) = \gamma x_i x_j; \quad (1)$$

$$\text{Polynomial of degree d: } K(x_i,x_j) = (\gamma x_i x_j + r)^d,\ \gamma > 0; \quad (2)$$

$$\text{Radial basis function (RBF): } K(x_i,x_j) = \exp\{-\gamma||x_i - x_j||^2,\ \gamma > 0; \quad (3)$$

$$\text{Sigmoid: } K(x_i,x_j) = \tanh(\gamma x_i x_j + r),\ \gamma > 0; \quad (4)$$

where the γ (gamma parameter) serves as an inner product coefficient in the polynomial function (Equation (2)) and in the hyperbolic tangent function of the sigmoid kernel (Equation (4)), while controlling the kernel width in RBF (Equation (3)) [13,31]. In the specific case of the RBF kernel (Equation (3)), the γ parameter defines the range of influence of each training sample. A higher γ decreases the range of influence of sample which results in a more irregular decision boundary, while a smaller γ increases the range of influence of each sample, leading to a smoother boundary [31]. The parameter *d* corresponds to the degree of the polynomial function (Equation (2)). The parameter *r* is used for both the polynomial (Equation (2)) and sigmoid (Equation (4)) kernels, and controls in Equation (2) how much the model is influenced by high-degree polynomials versus low-degree polynomials [31].

3. Data and Methodology

3.1. Dataset

As mentioned before, pegmatite exposition can be very small when compared with the spatial resolution of several free satellite products [7,32]. Despite the fact that lack of thermal band can limit the applicability of Sentinel-2 images in Li-pegmatite identification [2], its medium to high spatial resolution (10–60 m) may be crucial in a classification exercise where the target class presents the lowest exposition. Therefore, a Sentinel-2B satellite product, acquired on 07/09/2019 (tile number T29TPF), was used. The product's processing level is 2A and its projection is Universal Transverse Mercator zone 29 N, WGS84 datum.

The Sentinel-2 mission includes a constellation of two twin satellites placed in the same sun-synchronous orbit, phased at 180° to each other: Sentinel-2A and Sentinel-2B [33]. On-board, the Multispectral Instrument (MSI) acquires information in 13 spectral bands from the visible-near infrared (VNIR) to the short-wave infrared (SWIR), but only the bands in bold in Table 1 were used in the image classification approach. These bands are the most adequate for geological purposes since minerals and rocks have important absorption features in the correspondent wavelengths. Additionally, the remaining Sentinel-2 bands have specific applications, such as detecting coastal aerosols (band 1), vegetation (bands 5, 6 and 7), water vapor (band 9), and clouds (band 10).

Table 1. Sentinel-2B Band's Characteristics [34].

Band Number	Central Wavelength (nm)	Bandwidth (nm)	Spatial Resolution (m)
1	442.3	21	60
2	492.1	66	10
3	559.0	36	10
4	665.0	31	10
5	703.8	16	20
6	739.1	15	20
7	779.7	20	20
8	833.0	106	10
8A	864.0	22	20
9	943.2	21	60
10	1376.9	30	60
11	1610.4	94	20
12	2185.7	185	20

Since it is a Level 2A product, the bands were already provided in surface reflectance [35]. Basic pre-processing operations such as resampling all bands to a 10-m spatial resolution, as well as spectral and geographic sub-setting were performed using the Sentinel Application Platform (SNAP) software [36].

3.1.1. Sampling and Training Areas Definition

The training areas were defined based on (i) areas directly identified by visual inspection of the Sentinel-2 images, namely of a natural color composite (RGB combination 4-3-2) and the calculation of the Normalized Burn Ratio (NBR) index; (ii) extremely high-resolution images provided by Google Earth [37], Esri World Imagery [38] and by drone flights made over a known outcropping Li-pegmatite (0.025 m resolution); (iii) the Portuguese Geological Map at 1:50,000 [26,27]; and (iv) field reconnaissance.

The definition of training areas corresponded to an iterative process: for each set of training samples, class separability measurements (see Section 3.1.2) and spectral analysis were made until satisfactory results were obtained in order to select the best training areas and therefore proceed with the classification process. To improve the classification results and class separability, the number of user-defined classes was diminished when compared to previous attempts [5]. Urbanized and vegetated areas as well as the water bodies were masked out from the image, using the information provided by the Portuguese and Spanish LULC Maps (COS 2015; COS 2018; SIOSE 2014) and the Scene Classification maps

provided in the Sentinel-2 Level 2A products [35]. In addition, some lithological units were deliberately left out from the classification due to small exposition (Ordovician Formations; Figure 1) or to great spatial correlation with other classes (Cenozoic sediments; Figure 1). The selected training areas contain 3053 pixels distributed by 5 classes and 33 regions of interest (ROIs) as presented in Table 2.

Table 2. Distribution of Training Pixels by Classes and regions of interest (ROIs).

Class name	Total Pixel Number	Training Pixels	Testing Pixels	ROI Number
Agricultural fields	1230	894	336	8
Burned areas	205	80	125	2
Granite	1231	987	244	9
Li-bearing pegmatite	43	17	26	5
Metasediments	344	166	178	9

Since different classes occupy different areas on the ground, sample acquisition was not even between classes. The major problem was in the identification of samples from the Li-bearing pegmatite class because of their small exposition. Although the training areas included samples not only from the outcropping dykes, but also from ore stockpiles, the resulting dataset was still very imbalanced as can be seen in Table 2. The spectral responses of the classes for the training pixel samples were computed directly from the Sentinel-2B image—Figure 3.

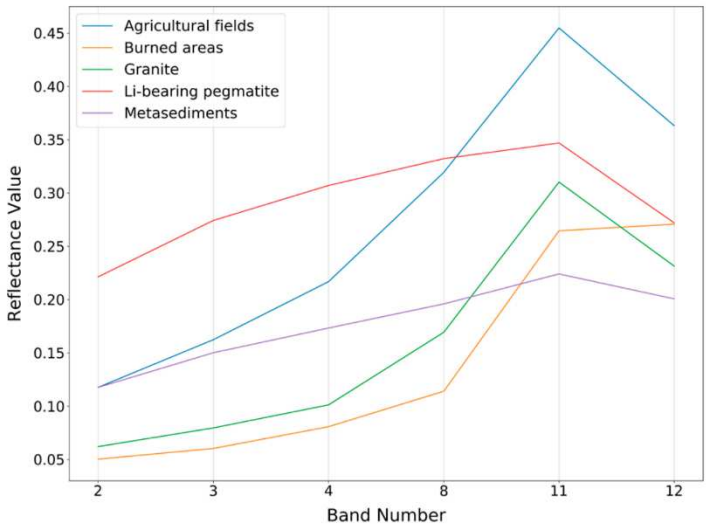

Figure 3. Mean spectral signatures based on the training pixels selected for each class.

3.1.2. Class Separability

As referred before, the evaluation of the spectral separability between pairs of training classes is an important step of the training areas refinement process. Therefore, a quantitative measurement of class separation was made using the Jeffries–Matusita (JM) distance and transformed divergence (TD) matrix. These spectral distances were computed using PCI's Geomatica 2018 software [39] and the values obtained are presented in Table 3. Both distances present values between 0 and 2, where 0 means a complete overlap between the signatures of two classes, and 2 indicates a complete separation between classes [40]. In general, values higher than 1.9 indicate a very good class separability, values between 1.7 and 1.9 correspond to a good class separability, while values below 1.7 indicate that the classes are difficult to separate. These measurements can give an insight into the classification accuracy: a higher-class separability should indicate a better classification result.

Table 3. Jeffries–Matusita (JM) (Blue) and transformed divergence (TD) (Orange) Separability Measures for Each Pair of Classes.

	Li-Bearing Pegmatite	**Metasediments**	**Granite**	**Burned Areas**	**Agricultural Fields**
Li-Bearing Pegmatite		2.000	2.000	2.000	2.000
Metasediments	1.977		2.000	2.000	2.000
Granite	2.000	1.998		2.000	1.994
Burned Areas	2.000	2.000	2.000		2.000
Agricultural Fields	1.998	1.994	1.865	2.000	

Table 3 shows that all classes have a good separability, with exception of the pair Granite–Agricultural fields which is the one with minimum separability. Using the JM distance, the average separability obtained was 1.983, the minimum separability obtained was 1.865, while the maximum separability achieved was 2.000. Similarly, minimum and maximum separability obtained with the TD matrix were between 1.994 and 2.000, with an average separability of 1.999.

3.2. Parameter Tuning, Cross-Validation, and Model Evaluation

To achieve high accuracy, optimization of the parameters and kernel functions is required, because they are site-sensitive [18,19]. Parameter tuning and model evaluation was

achieved using the open-source library scikit-learn [41] (version 0.20.1) for Python programming language.

Initially, all training samples were shuffled and randomly divided into training and test sets (25% for testing and 75% for training) using a stratified iterator to ensure that both sets contained samples from Li-bearing pegmatites. However, after a considerable number of trials, all the models presented the same signs of overfitting with almost perfect training scores and very high-test scores. In a classical overfitting example, the test score should be very low in comparison to the training score. However, when analyzing the results, it was possible to conclude that the training and test subsets were not independent. This means that the variance of the training and test data were very similar. Consequently, SVM not only learned very well the patterns of the training data, but also from the test subset. Only when applying the models to the whole image (i.e., when introducing new, independent data), the performance score would drop drastically as typical in overfitting models. Thus, a different strategy had to be employed to ensure that the training and testing data were independent. Considering that all samples from the same ROI would have similar spectral behavior, instead of randomly splitting the individual samples, a procedure to randomly split the ROIs into training and test subsets was adopted (Figure 4). Additional information, as well as the source code employed in this procedure, is available in Section 1 of the Supplementary Materials.

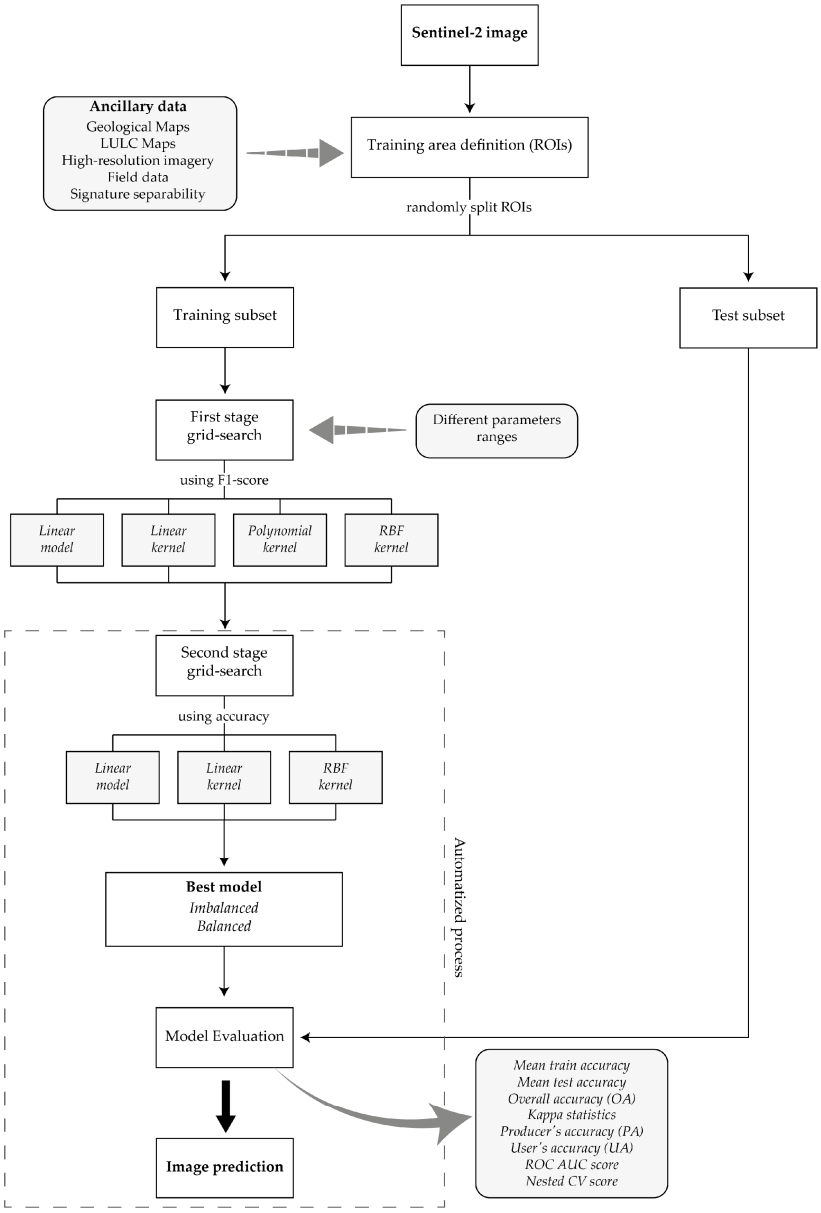

Figure 4. Flowchart of the image classification process.

The choice of the best kernel (among linear, polynomial and RBF) and of best parameters was accomplished by a two-staged grid-search with cross-validation (CV). Besides the kernelized SVM models, the Linear model (that assumes the data is linearly separable without using any kernel function [31]) was also evaluated (Figure 4). While scikit-learn's kernelized SVM classifier uses a 'one-against-one' multiclass strategy, the Linear model employs "one-vs-the-rest" [42].

The first stage grid-search represents a coarser grid-search: the Linear model (non-kernelized SVM) and all the different kernels were tested separately, using several ranges for

the parameters, which either increased in a logarithmic or exponential fashion (see for example [19,43]). Each parameter range was cross-validated using a stratified 5-fold CV. This means that the original training set was split into five groups (maintaining the original proportion of samples per class), and in each fold, one group was retained in turn to use as a validation set, while the model was trained in the remaining 4/5 of the data. After the 5 folds were completed, the score obtained in each fold was averaged, obtaining the mean test score for every parameter input or combination. The best parameter(s) were the ones that obtained a higher mean CV test score. In this step, to optimize the discrimination between the target class (Li-bearing pegmatite) and the host rocks (Metasediments) the employed metric score was the F1-score of these two classes. The F1-score is the harmonic mean of precision and recall, where precision measures the accuracy of positive predictions and recall measures how many positive samples are correctly detected by the classifier [31].

The first stage grid-search is mainly based on the knowledge of the operator since different ranges will return very distinct optimal parameter(s). The sensitivity of SVM to the setting of the parameter range was already described by other authors [44]. Therefore, the results of each range should be interpreted carefully and an increase or decrease of the search space may be necessary to improve the grid-search outputs. When choosing the best range, several criteria must be considered besides the CV test score, namely the values of the returned parameter(s). This means that when the obtained scores are similar, the operator should opt for the one with a smaller C and/or gamma, for example, to avoid choosing a rigid model that may overfit the data [31].

To try to balance the dataset, three different approaches were applied: (i) use a built-in class-weight parameter; (ii) downsampling; and (iii) upsampling. In the first case, a weight is attributed to each class during the training phase to account for class imbalance: this weight can be user-defined, or it can be set automatically to the inversely proportional to class frequency (the so-called “balanced” mode). In this work, we decided to use the “balanced” option. In what concerns the downsampling process, the classes with more observations are randomly sampled without replacement, to obtain several samples equal to the size of the smallest class. On the other hand, upsampling is the process that for each observation of the largest class, randomly selects from the other classes with replacement. For more information on the first stage grid-search, see Section 2 of the Supplementary Materials.

In the second stage grid-search, a stratified 5-fold CV was again implemented, but this time with linear increments around the best parameter values returned in the first step. Whenever possible, the incremental steps employed were the same used by Oommen, et al. [43]. In

this second stage, the polynomial kernel was not included, since the best degree obtained in the first stage was always equal to one, and the first-degree polynomial corresponds to the linear kernel when the parameter r equals to zero (Equations (1) and (2)). The downsampling and upsampling strategies were also excluded from the second stage, because the introduction of a random sampling process (that did not consider the ROIs) leads to overtraining problems. Consequently, in the second stage grid-search, only three models were trained for both the imbalanced and balanced data using the class-weight parameter. The choice of the best model was automatized (see Section 3 of the Supplementary Materials) and in the end, two models, one built on the imbalanced data and one using the class-weight option, were applied to the whole image (Figure 4). This means that on the contrary of what happened in the first stage (where each model was trained separately), in the second stage the three models were confronted in the same grid-search and the best model was automatically return. Only the best model returned were subjected to the "Model evaluation" step of Figure 4.

In what concerns the model evaluation, the metric score employed to choose the best model in the second stage was the accuracy. Besides the mean train accuracy and mean test accuracy obtained in the CV, the overall accuracy and the Kappa statistics were also computed. To evaluate the classification at the class level, the producer's and user's accuracy were calculated. Knowing the true and predicted classes of the test data, the confusion matrix gives insight for each class on how many samples were correctly classified, how many were misclassified, and on which class the samples were incorrectly classified. The matrix diagonal represents the samples that were correctly classified in the respective class and the OA is calculated by dividing the sum of the correctly classified instances by the total number of pixels [45]. The producer's accuracy (PA) is obtained by dividing the number of correct pixels in a given class by the total number of pixels of that class in the test set, and indicates the probability of a training sample being correctly classified [46]. On the other hand, the user's accuracy (UA) can be computed by dividing the number of correct pixels in a determined class by the total number of pixels that were classified in that class. It indicates the reliability of the map and gives the probability that a pixel classified as of belonging to a certain class actually belongs to that class on the ground [45,46]. The Kappa statistic corresponds to a measure of agreement between the classifier output and reference data [47]. To access the influence of the correct choice of model in the Li-pegmatite class, receiver operating characteristic (ROC) curves were computed for all the models tested during the second stage grid-search. The ROC curve plots the true positive rate (or for recall)

against the false positive rate (fraction of negative samples misclassified as positive) [31]. The area under the curve (AUC) score was calculated to compare the different classifiers.

The ability of each model to generalize to unknown data was evaluated by applying a nested CV. This procedure allows multiple splits of CV instead of just one (the training-validation split), thus reducing the risk of biasing model evaluations by using different portions of the data for parameter selection and model evaluation. In practice, the procedure corresponds to a CV of the first CV: the inner loop is for parameter tuning and model selection, the outer loop is dedicated to evaluating the model's performance. In this work, the outer loop consisted of a 3-fold CV. The source code employed in this procedure is available in Section 3 of the Supplementary Materials.

4. Results

The automatized process allowed to choose the best model for both the imbalanced and balanced datasets. Data balancing had an impact on SVM performance since the best model found was the Linear model (non-kernelized SVM) for the imbalanced data and the RBF kernel for the dataset balanced using the class weight option.

The results from the second stage grid-search with CV and from the model evaluation step are presented in Table 4. In general, both models reached a similar performance, although the Linear-SVM obtained a higher train score. The RBF-SVM was the model that achieved a higher test score during the CV process, but the Linear-SVM attained a better OA and Kappa hat statistics. The models' generalization capability (nested CV score) was also very similar.

Based on the metrics, especially on the attained OA and Kappa hat, the Linear-SVM appears to be the best model. Plotting the ROC curves for each model tested in the second stage grid-search and computing the respective AUC score allowed to assess the models' performance exclusively on the Li-pegmatite class (Figure 5). The results show that the use of class balancing strategies improved the performance on the Li-pegmatite class for the Linear model and for the Linear kernel. In the balanced dataset, the best model found through the automatized process, the RBF kernel, was the one that achieved a higher AUC. However, in the case of imbalanced data, the RBF kernel was still the one with the highest AUC, despite the Linear model being chosen as the best model with the automatized process. This happened because the automatized process selects the best model based on the performance in all classes while the AUC score only accounts for the Li-pegmatite class.

Table 4. Classification Performance Summary for the Two Models Built.

Model	Imbalanced	Balanced
	Linear Model	**RBF Kernel**
Parameter(s)	C = 32	C = 0.2 γ= 4.4
Mean train score (CV)	0.980643	0.941802
Mean test score (CV)	0.917444	0.93750
Overall accuracy (OA)	0.852585	0.832783
Kappa hat	0.801678	0.777337
Nested CV score	0.906241	0.906229

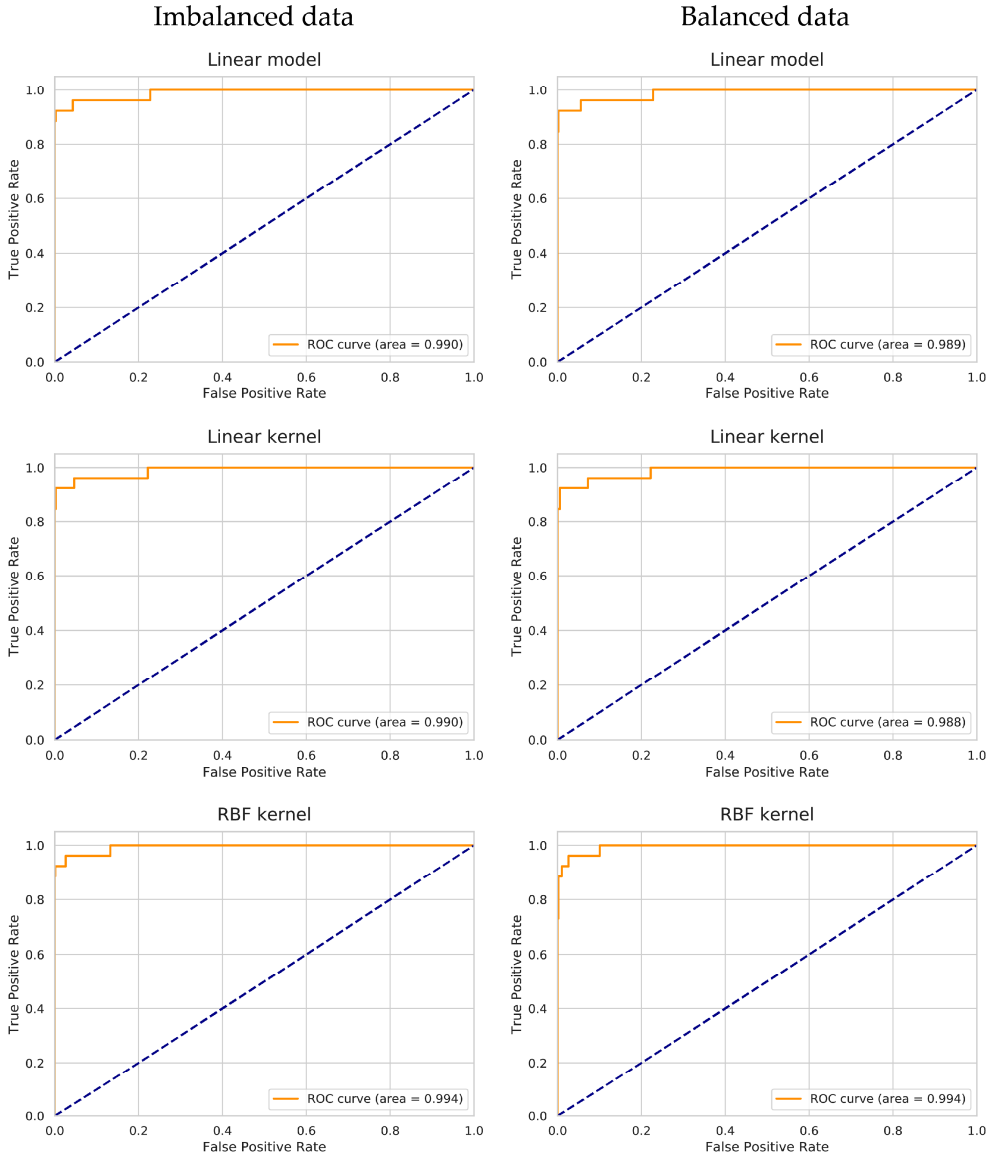

Figure 5. Receiver operating characteristic (ROC) curves and area under the curve (AUC) scores for each of the models tested in the second stage grid-search for both the imbalanced and balanced data.

To analyze and compare in detail the accuracy performance on each class the confusion matrices were computed for the Linear-SVM (Figure A1) and the RBF-SVM (Figure 6). The UA and PA were computed considering the respective confusion matrix and are presented in Table 5.

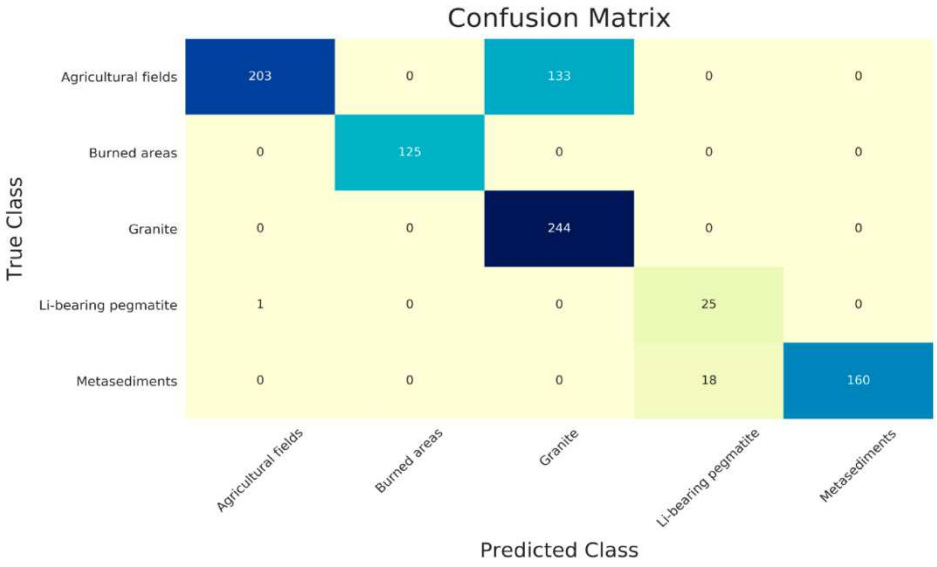

Figure 6. Confusion matrix for the RBF-SVM model built on the balanced dataset.

Table 5. User's and producer's accuracy (UA and PA) for Both the Linear-SVM and Radial Basis Function (RBF)-SVM Models. Values in percentage (%).

Class	Imbalanced		Balanced	
	PA	UA	PA	UA
Agricultural fields	64.58	93.53	61.01	99.51
Burned areas	100.00	100.00	100.00	100.00
Granite	98.77	66.94	100.00	65.07
Li-bearing pegmatite	88.46	100.00	96.15	59.52
Metasediments	94.94	100.00	90.45	100.00

As can be observed, in both models, the greater misclassification errors happened between the Agricultural fields and Granite classes. Regarding the Li-bearing pegmatite class, the Linear-SVM model was the one that maximized the discrimination between the mineralized dykes and the host rocks, but this was done at a cost—a higher number of false negatives. Conversely, the RBF-SVM model minimized the misclassification of true samples from the Li-bearing pegmatite class at the cost of a higher confusion with the metasedimentary host-rocks. These results are in line with the interpretations with the final classification maps obtained for Linear-SVM (Figure 7) and for RBF-SVM (Figure 8).

The comparison between the two classification maps indicated that the overall performance of each class changed from one model to the other. For example, the RBF-SVM model was able to correctly classify all the areas affected by wildfires while the Linear-SVM model misclassified some of these areas as Metasediments. On the other hand, the Linear-SVM model was the one that better identified the Agricultural Fields, whereas the RBF-model only showed good performance in the classification of the Agricultural Fields located over a granitic basement. Both models showed problems in the classification of the Metasediments that were often classified as Granites.

In what concerns the target class, Li-bearing pegmatite, the Linear-SVM was able to minimize the occurrence of false positives. Therefore, the pixels classified as belonging to the Li-class were limited, almost exclusively, to small areas inside the known open-pit mines. On the other hand, the RBF-SVM was able to identify other possible target areas beyond the known occurrences. As this is the final goal of mineral exploration, the results obtained with RBF-SVM are preferred even though some areas where Metasediments outcrop were classified as Li-bearing pegmatite (top left corner and top center of the classified image—Figure 8). These results are contradictory to the quantitative model analysis achieved with the OA and Kappa statistics. That is why it is fundamental to evaluate the models using distinct statistical methods. Moreover, the results obtained with each model were qualitatively analyzed and evaluated.

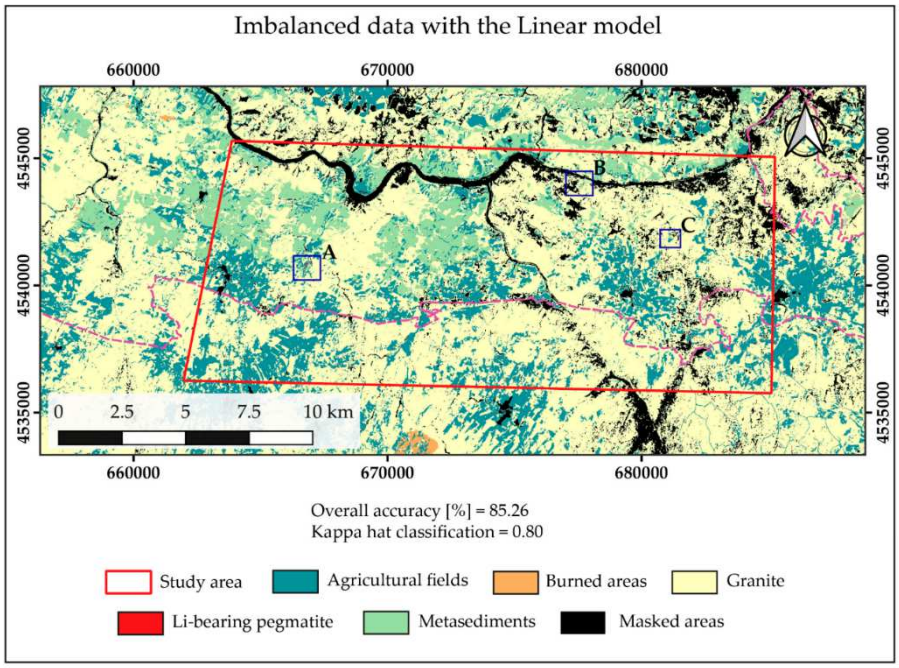

Figure 7. Final classification map based on the Linear-SVM model built with imbalanced data. Three open-pit mines exploiting Li-minerals are identified: A—Bajoca, B—Feli, and C—Alberto. The dashed purple line represents the simplified contact between the Metasediments and the Granite. Zoom images of the open-pit mines can be found in Figure 9.

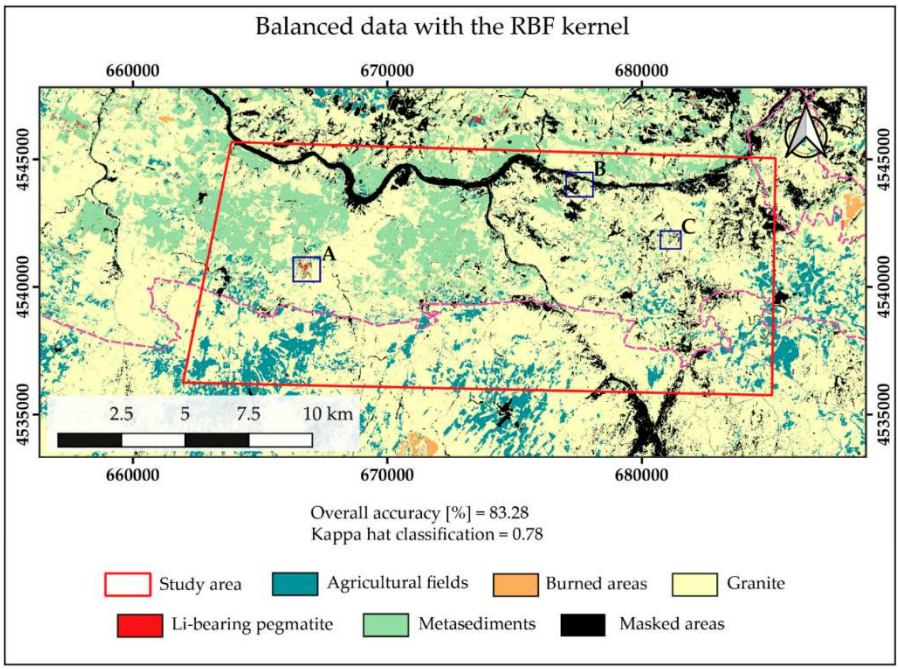

Figure 8. Final classification map based on the RBF-SVM model built with the balanced data. A—Bajoca mine, B—Feli mine, and C—Alberto mine. Dashed purple line: simplified contact between the Metasediments and the Granite. Zoom images of the open-pit mines can be found in Figure 9.

The performance of the models was evaluated in their capacity to correctly identify known target areas. As mentioned before, in the Fregenda–Almendra area there are three open-pit mines currently exploiting Li-bearing pegmatites: the Bajoca mine on the Portuguese side, and the Feli and Alberto mines in Spain. From the 43 Li-pegmatite samples defined for training and evaluation, 42 of those samples belonged to the Bajoca mine (outcropping pegmatite and ore stockpile). The remaining sample was collected from one outcropping pegmatite in the Alberto mine. The classification results obtained for these three target areas using both algorithms are presented in Figure 9.

The results obtained for the Feli mine were similar using the two algorithms, identifying the presence of Li-bearing pegmatite in the open-pit and next to the two waste piles (to the left of the open-pit). However, in the case of the Bajoca and Alberto mines, the Linear-SVM classified a much smaller area as being Li-bearing pegmatite when compared to the RBF model. Oppositely, the RBF-SVM identifies some false positives like in the dirt road that leads to the Bajoca mine (Figure 9). Regarding the other classes, both models overestimated the occurrence of Granite where in fact metasedimentary rocks occur. Moreover, the Linear-SVM misclassified some pixels inside the open-pits as being Agricultural Fields. This misclassification was less frequent with the RBF model.

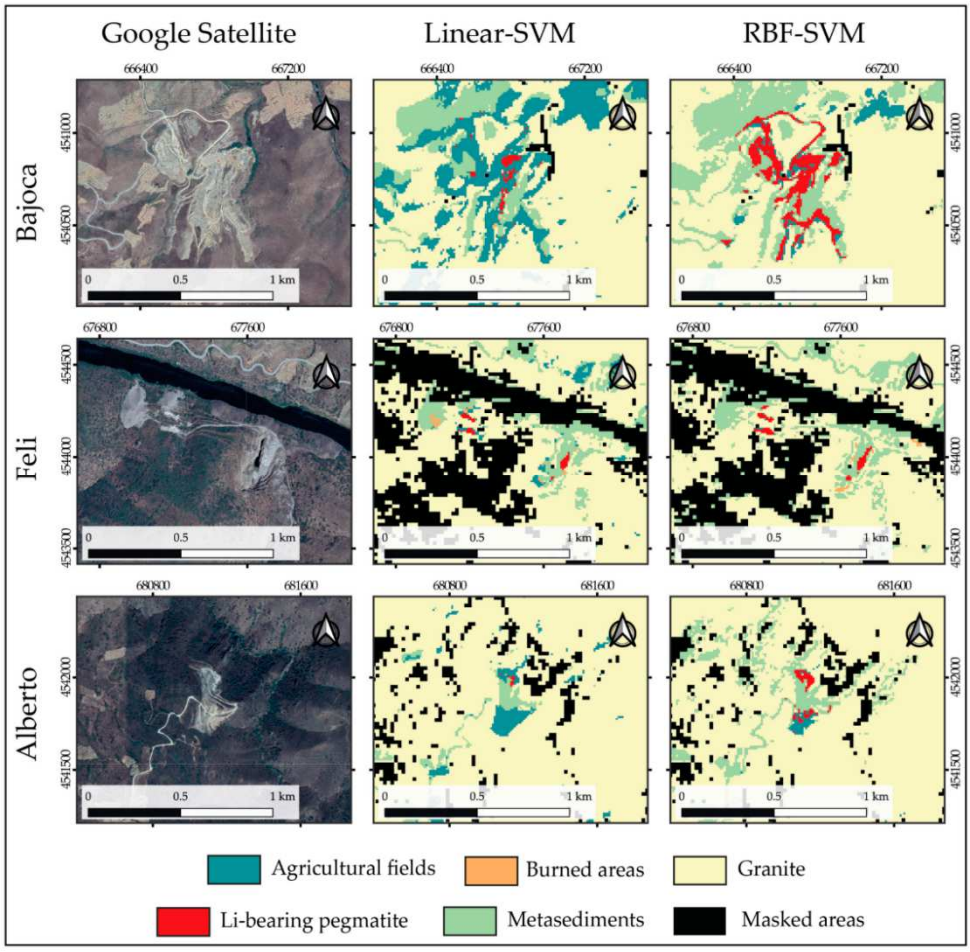

Figure 9. Evaluation of the models' performance in the known open-pit mines exploiting Li-bearing pegmatite.

On the contrary to what happens in the Bajoca mine, the ore stockpiles, where the extracted Li-pegmatite from the Feli and Alberto mines are stored, are not located near the open-pits. Therefore, these two known stockpiles were also used to verify the models' performance in the classification of the Li-bearing pegmatite class (Figure 10). Field campaigns allowed to verify that Li-minerals are present in these stockpiles (Figure 10b). In the case of the Feli stockpile, both models were able to identify the occurrence of Li-bearing pegmatite. Inversely, on the Alberto stockpile, only the RBF-SVM correctly identified most of the areas where Li-pegmatite is present. In what concerns the remaining classes, besides the areas misclassified as Granite, the Linear-SVM was the model that correctly identified most of the Agricultural Fields.

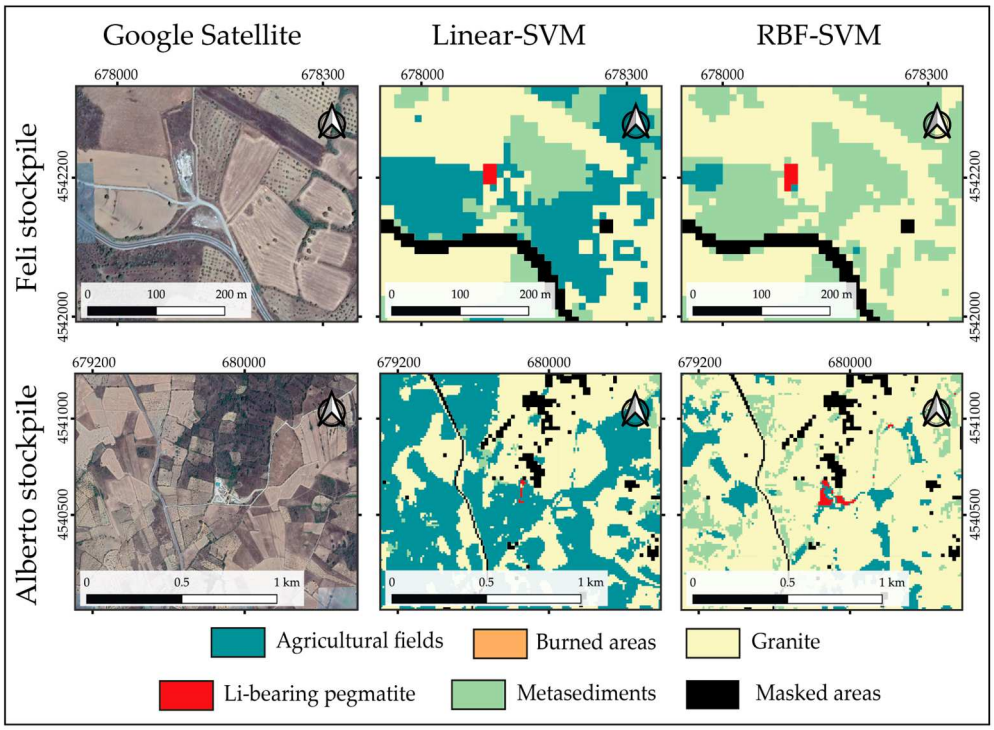

(**a**)

(**b**)

Figure 10. Evaluation of the models' performance in known ore stockpiles containing Li-bearing minerals (a). (b) Field photograph of a spodumene crystal (a Li-bearing mineral) from the Alberto stockpile.

A previous attempt to use ML algorithms in Li-bearing pegmatite identification showed that the model parameterization and optimization were not enough to avoid overfitting, which ultimately led to a large number of Li-pegmatite false positives [5]. In this study, several methodological improvements were made. Besides reducing the area to be classified and the number of classes through masking of undesired classes, a new strategy to split the training data into training and test subsets was proposed. This new strategy resulted in a higher

independency between the two subsets, since sample location was taken into consideration in the split. Inevitably, the random sampling process introduced when using the downsampling and upsampling strategies made the developed ROI-based splitting strategy infeasible. This led to overfitting problems and, therefore, these strategies were excluded from the classification. The proper definition of the range of the tested parameters was crucial to optimize the models during the first stage grid-search, and several literature-based ranges were tested. While several authors have also employed grid-search techniques to determine the best parameter(s) [8,18,19,43,48], this step is not always employed, with some authors achieving parameterization through the trial and error method [14]. Other authors have opted to not optimize the models and used the default parameters or other specific sets of parameters [9,10,12,49]. The observation of the first stage results allowed to select the right parameters, but also to exclude the polynomial kernel, reinforcing the importance of the intervention of the operator at the beginning of the classification process.

The second stage grid-search automatically returned two different models respectively for the imbalanced and balanced datasets, which is the first indication that class imbalance may affect the obtained results. The Linear-SVM trained on the imbalance data and the RBF-SVM trained using the class-weight option showed, at turn, better performance depending on the class. Both models achieved a better ability to discriminate the target class (Li-pegmatite) from the host rocks, thus reducing the number of false positives when compared to the SVM model trained in the previous work of Cardoso-Fernandes, et al. [5]. This corroborates that the methodological adjustments made in the current study helped to improve the SVM performance.

Nonetheless, the results obtained with each model for the Li-bearing pegmatite class were very distinct. The Linear-SVM presented the best discrimination between Li-pegmatite and Metasediments, while missing to correctly classify pixels with known Li-pegmatite exposition. Oppositely, the RBF-SVM avoided the occurrence of Li-pegmatite false negatives while classifying Metasediments and dirt roads as areas with Li-potential. Increasing the discrimination between Metasediments and Li-pegmatites may only be achieved with a better spatial resolution data. In the Fregeneda–Almendra pegmatite field, dyke thickness can range between 4 m and 15 m in the case of the spodumene-bearing dykes, and between 5 m and 30 m in the petalite-bearing ones [25]. Even in the largest dyke that outcrops in the Bajoca mine, metasedimentary enclaves can be found in the middle of the pegmatite, which contributes to pixel mixing, since the Sentinel-2 bands used in this work have between 10 m to 20 m of spatial resolution. In addition, the slightly different mineral paragenesis of the Feli

mine (with lepidolite), when compared with Alberto or Bajoca, may have influenced the performance of Linear-SVM.

The interpretations of the final classification maps (Figure 7 and Figure 8) are supported by the computed statistical metrics and respective confusion matrices (Figure A1 and Figure 6). When looking at the performance metrics at a class level, Linear-SVM reached a better performance on the test set (Figure A1), which may indicate more overtraining and fewer ability to generalize to unknown data, when compared with RBF-SVM. When dealing with imbalanced datasets, special attention should be given when interpreting the results obtained with global metrics such as OA and Kappa hat, since the influence that minor classes such as Li-pegmatite have on the final output can be masked by the majority class(es) [44,50]. That is why it is important to qualitatively assess the performance of the models. Zoom images concerning known Li-pegmatite expositions (Figure 9 and Figure 10) support the previous interpretations that the RBF-SVM performs better in Li-pegmatite identification, when compared with the Linear-SVM. Moreover, the results obtained highlight that the developed methodology can identify Li-pegmatite occurrences beyond those that were used as training instances.

In what concerns the remaining lithological classes, both models overestimated the occurrence of Granite in areas where Metasediments occur. This can be mainly explained by the spectral confusion with the Agricultural fields class, especially in the case of the RBF-model. The phenomenon is not only corroborated by the computed confusion matrices, but also by the signature separability measures (see Section 3.1.2.). The overestimation of the Granite class can also be linked to the difficulty to correctly classify the metasedimentary rocks since (i) they outcrop in less extent when compared with the granites, (ii) are often covered by vegetation or (iii) serve for olive/almond tree plantations. This happens because granites are not so easily weathered as the metasediments, and regolith tends to form over the latter. Taking this into account, a regolith–geology mapping approach like the one employed by De Boissieu, et al. [9] could help improve the results.

On the other hand, considering that in geological exploration false negatives should be avoided, the RBF-SVM built using a class balancing strategy is therefore the preferred model to define areas with Li-potential. In satellite image classification, the RBF is often the preferred kernel, commonly showing good performance [12,19,43,49]. Melgani and Bruzzone [51] concluded that the RBF-kernel achieved higher OA than the Linear-model in hyperspectral image classification. Geranian, et al. [16] have compared the performance attained with different kernels in mineral prospectivity mapping and concluded the RBF

achieved the best results. However, in a similar study, Zuo and Carranza [13] found the sigmoid kernel to be the optimal function.

Contrary to the expected and opposed to previous studies [5], the results also show that the class imbalance had a higher impact on the SVM performance (Figure 5, Figure 7, Figure 8, Figure 9 and Figure 10). This is of particular interest and importance, since Maxwell, et al. [18] stated that, for SVM, balancing the data had a negligible effect on UA and PA of the rare classes of the Indian pine dataset, Indiana (USA). Noi and Kappas [19] also concluded that SVM was less impacted by sample size and class imbalance than other ML algorithms. However, despite its robustness to data imbalance, the SVM algorithm works by minimizing the overall error (that is inherently biased toward the majority class) which can lead to the underprediction of the less-abundant class [18,50]. In this work, the Li-class was underpredicted using the imbalanced dataset when compared to the balanced one. Ultimately, class imbalance affected the ability to predict the Li-pegmatite class not only in possibly target areas, but also where Li-pegmatite occurrences are known.

Overall, the methodological developments made in this study represent a major contribution not only to the state of the art of Li-pegmatite satellite-based exploration, but also to the application of ML algorithms to remote sensing lithological mapping. The step-by-step optimization made in this study is proof that ML algorithms, particularly SVM, are not easy and ready to apply (at least to some specific applications such as mineral exploration). The major difficulty in Li-pegmatite exploration using remote sensing data is their relatively small size and exposition. This means that, in an image classification problem, the target class is by nature a small, underrepresented class. Therefore, the adaptations proposed to achieve the optimal parameters proved to be fundamental to successfully deal with class imbalance. Detailed insights on algorithm parameterization were given, so that the methodology can be replicated in other case studies. Algorithm optimization was reached at several levels, namely: (i) data splitting for training and testing; (ii) strategy do deal with data imbalance; (iii) type of SVM model and kernel function; (iv) associated hyperparameter(es); and (v) metric score employed in the CV process. When using a grid-search with CV to find the best parameters, commonly used metrics are the OA and Kappa statistics [8,18,19]. As part of the algorithm optimization, a more innovative strategy was employed in the first stage grid-search where the parameters were chosen based on the F1-score of just two classes: the Li-pegmatite and the Metasediments. Moreover, the semi-automatization of the SVM classification process allowed to simplify the choice of the best model among several

options. In this case, the results obtained with the RBF-SVM allowed to delineate target areas for Li-exploration.

However, the developed methodology still has some shortcomings. The main limitation is that some smaller pegmatite occurrences and other potential areas for Li-exploration were missed while trying to increase the discrimination between the Li-pegmatite class and the Metasediments. This can be related or accentuated by the low ratio between pegmatite size and the satellite image spatial resolution. This issue was vastly explained in previous studies [7,32]. Another major concern in ML and deep learning (DL) remote sensing applications is the ability to transfer learning between case studies [52]. Unfortunately, there is no current solution for this problem, but in this study, we wanted to ensure that the improved methodology and SVM optimization could be applied to other datasets and study areas. To achieve this goal, the first stage grid-search was optimized to discriminate the target area from the host-rocks. Thus, when applying to another area, the operator should adapt the source code available in Section 2 of Supplementary Materials, to create a personalized metric score concerning the Li-bearing pegmatite and the existing host-rocks. In this metric score, a beta coefficient can be added to the F1-score, thus creating an F-beta score that allows the operator to adjust the relative importance of precision and recall, according to characteristics of the study area.

6. Conclusions

In this study, untraditional approaches were developed and employed to improve SVM performance in Li-pegmatite mapping. Several kernelized and non-kernelized SVM's models with different parameter ranges were trained to find the optimal model. Overall, the objectives of this work were accomplished, and the research questions proposed were addressed with the new methodological advances proposed:

1. To overcome and avoid overfitting, a new splitting strategy based on the regions of interest (ROIs) was developed and applied with success to create the training and test subsets.
2. The choice of an adequate metric score proved to be essential not only in the parameter optimization but also in the model evaluation step. To maximize the discrimination between the target (Li-pegmatites) and the host rocks, a customized metric score was created for the first stage grid-search with CV.

3. A semi-automatized process allowed to choose the best model among several options. However, a blind automatization of the SVM classification is not yet possible, since the intervention of the operator is fundamental at the beginning of the model training and parameterization.
4. The methodological adjustments proposed in this study improved the previously obtained results with SVM for the same study area, by reducing model overfitting and improving the discrimination between Li-pegmatites and their host-rock. The best model found with the semi-automatized process was the one built with the RBF kernel and using the class-weight option to account for imbalanced data.
5. Contrary to the results obtained by other authors, this study shows that the class imbalance had a negative impact on the SVM performance, and the adaptations made to account for the imbalanced nature of the data were crucial for successfully delineating Li-pegmatite occurrences.
6. On the other hand, the qualitative assessment of the SVM models' performance highlighted the success and potential of the methodology in the identification of known Li-pegmatite occurrences beyond those used for training. Other target areas for Li-exploration were also delineated using the RBF-SVM model.
7. The main limitation found was that some smaller pegmatite occurrences and other potential areas for Li-exploration were missed while trying to optimize class separability and reduce overfitting. Therefore, the right balance between increasing the separability of Li-pegmatite/host-rocks and minimizing false negatives needs to be found. This can be achieved with higher resolution satellite images. Different ML algorithms can also be compared.
8. Furthermore, the methodological optimization made in this study already provides tools to personalize and help generalize its application to other locations. This approach could also be modified to map remotely other types of pegmatites containing important mineral commodities like rare elements and gemstones.

Despite the encountered limitations, these results still represent a major contribution to the state of art regarding the use of ML in Li-pegmatite mapping. Moreover, the newly developed methodological approach can be very helpful for the exploration/mining industry, since the ability to remotely map mineralized pegmatites can reduce the costs of exploration campaigns while increasing the social acceptance of mineral exploration through the use of more conscientious environmental practices.

Supplementary Materials

The source code developed in this study is available online at http://www.mdpi. com/2072-4292/12/14/2319/s1, Section 1: Splitting the data into training and test subsets; Section 2: First stage grid-search; Section 3: Second stage grid-search, model evaluation and image prediction.

Author Contributions

All the authors conceived and designed the experiments; J.C.-F. performed the experiments and conducted the research; all the authors analyzed the data; J.C.-F. wrote the paper; A.C.T., A.L., and E.R.-R. revised the paper. All authors have read and agreed to the published version of the manuscript.

Funding

The authors would like to thank the financial support provided by FCT—Fundação para a Ciência e a Tecnologia, I.P., with the ERA-MIN/0001/2017—LIGHTS project. The work was also supported by National Funds through the FCT project UIDB/04683/2020—ICT (Institute of Earth Sciences). Joana Cardoso-Fernandes is financially supported within the compass of a Ph.D. Thesis, ref. SFRH/BD/136108/2018, by national funds from MCTES through FCT, and co-financed by the European Social Fund (ESF) through POCH—Programa Operacional Capital Humano. The Spanish Ministerio de Ciencia, Innovacion y Universidades (Project RTI2018-094097-B-100, with ERDF funds) and the University of the Basque Country (UPV/EHU) (grant GIU18/084) also contributed economically.

Acknowledgments

The authors would like to thank N. Pires (University of Porto) for helping with Python coding.

Conflicts of Interest

The authors declare no conflict of interest. The funders had no role in the design of the study; in the collection, analyses, or interpretation of data; in the writing of the manuscript, or in the decision to publish the results.

Appendix A

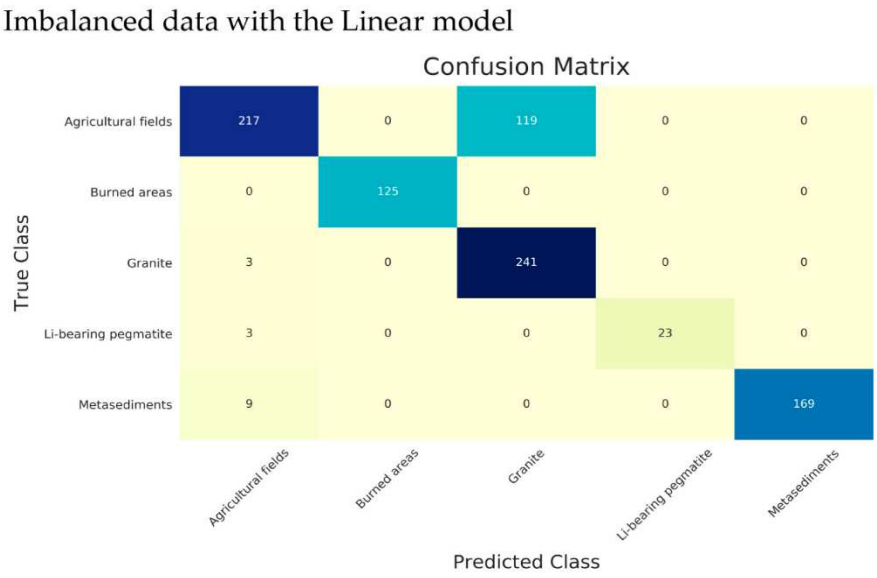

Figure A1. Confusion matrix for the Linear-SVM model built on the imbalanced dataset.

References

1. Cardoso-Fernandes, J.; Teodoro, A.C.; Lima, A. Potential of Sentinel-2 data in the detection of lithium (Li)-bearing pegmatites: A study case. In Proceedings of the SPIE Remote Sensing, Berlin, Germany, 10–13 September 2018; p. 15.

2. Cardoso-Fernandes, J.; Teodoro, A.C.; Lima, A. Remote sensing data in lithium (Li) exploration: A new approach for the detection of Li-bearing pegmatites. *Int. J. Appl. Earth Obs. Geoinf.* 2019, *76*, 10–25.

3. Perrotta, M.M.; Souza Filho, C.R.; Leite, C.A.S. Mapeamento espectral de intrusões pegmatíticas relacionadas a mineralizações de lítio, gemas e minerais industriais na região do vale do Jequitinhonha (MG) a partir de imagens ASTER. In Proceedings of the Anais do XII Simpósio Brasileiro de Sensoriamento Remoto, Goiânia, Brazil, 16–21 April 2005; pp. 1855–1862.

4. Mendes, D.; Perrotta, M.M.; Costa, M.A.C.; Paes, V.J.C. Mapeamento espectral para identificação de assinaturas espectrais de minerais de lítio em imagens ASTER (NE/MG). In Proceedings of the Anais do XVIII Simpósio Brasileiro de Sensoriamento Remoto, Santos-SP, Brazil, 28–29 May 2017; pp. 5273–5280.

5. Cardoso-Fernandes, J.; Teodoro, A.C.; Lima, A.; Roda-Robles, E. Evaluating the performance of support vector machines (SVMs) and random forest (RF) in Li-pegmatite mapping: Preliminary results. In Proceedings of the SPIE Remote Sensing, Strasbourg, France, 9–12 September 2019.

6. Santos, D.; Teodoro, A.; Lima, A.; Cardoso-Fernandes, J. Remote sensing techniques to detect areas with potential for lithium exploration in Minas Gerais, Brazil. In Proceedings of the SPIE Remote Sensing, Strasbourg, France, 9–12 September 2019.

7. Cardoso-Fernandes, J.; Teodoro, A.C.; Lima, A.; Perrotta, M.; Roda-Robles, E. Detecting Lithium (Li) Mineralizations from Space: Current Research and Future Perspectives. *Appl. Sci.* 2020, *10*, 1785.

8. Yu, L.; Porwal, A.; Holden, E.-J.; Dentith, M.C. Towards automatic lithological classification from remote sensing data using support vector machines. *Comput. Geosci.* 2012, *45*, 229–239.

9. De Boissieu, F.; Sevin, B.; Cudahy, T.; Mangeas, M.; Chevrel, S.; Ong, C.; Rodger, A.; Maurizot, P.; Laukamp, C.; Lau, I.; et al. Regolith-geology mapping with support vector machine: A case study over weathered Ni-bearing peridotites, New Caledonia. *Int. J. Appl. Earth Obs. Geoinf.* 2018, *64*, 377–385.

10. Othman, A.A.; Gloaguen, R. Improving Lithological Mapping by SVM Classification of Spectral and Morphological Features: The Discovery of a New Chromite Body in the Mawat Ophiolite Complex (Kurdistan, NE Iraq). *Remote Sens.* 2014, *6*, 6867–6896.

11. Latifovic, R.; Pouliot, D.; Campbell, J. Assessment of Convolution Neural Networks for Surficial Geology Mapping in the South Rae Geological Region, Northwest Territories, Canada. *Remote Sens.* 2018, *10*, 307.

12. Gasmi, A.; Gomez, C.; Zouari, H.; Masse, A.; Ducrot, D. PCA and SVM as geo-computational methods for geological mapping in the southern of Tunisia, using ASTER remote sensing data set. *Arab. J. Geosci.* 2016, *9*, 753.

13. Zuo, R.; Carranza, E.J.M. Support vector machine: A tool for mapping mineral prospectivity. *Comput. Geosci.* 2011, *37*, 1967–1975.

14. Abedi, M.; Norouzi, G.-H.; Bahroudi, A. Support vector machine for multi-classification of mineral prospectivity areas. *Comput. Geosci.* 2012, *46*, 272–283.

15. Rodriguez-Galiano, V.; Sanchez-Castillo, M.; Chica-Olmo, M.; Chica-Rivas, M. Machine learning predictive models for mineral prospectivity: An evaluation of neural networks, random forest, regression trees and support vector machines. *Ore Geol. Rev.* 2015, *71*, 804–818.

16. Geranian, H.; Tabatabaei, S.H.; Asadi, H.H.; Carranza, E.J.M. Application of Discriminant Analysis and Support Vector Machine in Mapping Gold Potential Areas for Further Drilling in the Sari-Gunay Gold Deposit, NW Iran. *Nat. Resour. Res.* 2016, *25*, 145–159.

17. Mountrakis, G.; Im, J.; Ogole, C. Support vector machines in remote sensing: A review. *ISPRS J. Photogramm. Remote Sens.* 2011, *66*, 247–259.

18. Maxwell, A.E.; Warner, T.A.; Fang, F. Implementation of machine-learning classification in remote sensing: An applied review. *Int. J. Remote Sens.* 2018, *39*, 2784–2817.

19. Noi, P.T.; Kappas, M. Comparison of Random Forest, k-Nearest Neighbor, and Support Vector Machine Classifiers for Land Cover Classification Using Sentinel-2 Imagery. *Sensors* 2017, *18*, 18.

20. Roda, E. Distribución, Caracteristicas y Petrogenesis de las Pegmatitas de La Fregeneda (Salamanca). Ph.D. Thesis, UPV/EHU, Bilbao, Spain, 1993.

21. Roda-Robles, E.; Pesquera, A.; Velasco, F.; Fontan, F. The granitic pegmatites of the Fregeneda area (Salamanca, Spain): Characteristics and petrogenesis. *Miner. Mag.* 1999, *63*, 535–558.

22. Vieira, R. Aplitopegmatitos com elementos raros da região entre Almendra (V.N. de Foz Côa) e Barca d'Alva (Figueira de Castelo Rodrigo). Campo aplitopegmatítico da Fregeneda- Almendra. Ph.D. Thesis, Faculdade de Ciências da Universidade do Porto, Porto, Portugal, 2010.

23. Costa, J.C.S.D. *Notícia sobre uma carta geológica do Buçaco, de Nery Delgado*; Serviços Geológicos de Portugal: Lisboa, Portugal, 1950.

24. Teixeira, C. *Notas sobre geologia de Portugal o complexo xisto-grauváquico ante-ordoviciano*; Empresa Literaria Fluminense Lda.: Lisboa, Portugal, 1955; p. 48.

25. Roda-Robles, E.; Vieira, R.; Pesquera, A.; Lima, A. Chemical variations and significance of phosphates from the Fregeneda-Almendra pegmatite field, Central Iberian Zone (Spain and Portugal). *Miner. Pet.* 2010, *100*, 23–34.

26. Silva, A.F.d.; Rebelo, J.A.; Ribeiro, M.L. *Notícia Explicativa da folha 11-C Torre de Moncorvo*; Serviços Geológicos de Portugal: Lisboa, Portugal, 1989; p. 65.

27. Silva, A.F.d.; Ribeiro, M.L. *Notícia Explicativa da folha 15-A Vila Nova de Foz Côa*; Serviços Geológicos de Portugal: Lisboa, Portugal, 1991; p. 52.

28. Vapnik, V.N. *The Nature of Statistical Learning Theory*; Springer: New York, NY, USA, 1995.

29. Knerr, S.; Personnaz, L.; Dreyfus, G. Single-layer learning revisited: A stepwise procedure for building and training a neural network. In *Neurocomputing*; Soulié, F.F., Hérault, J., Eds.; Springer: Berlin/Heidelberg, Germany, 1990; pp. 41–50.

30. Cortes, C.; Vapnik, V. Support-vector networks. *Mach. Learn.* 1995, *20*, 273–297.

31. Géron, A. *Hands-On Machine Learning with Scikit-Learn and TensorFlow: Concepts, Tools, and Techniques to Build Intelligent Systems*; O'Reilly Media, Inc.: Sebastopol, CA, USA, 2017; p. 568.

32. Cardoso-Fernandes, J.; Lima, A.; Roda-Robles, E.; Teodoro, A.C. Constraints and potentials of remote sensing data/techniques applied to lithium (Li)-pegmatites. *Can. Miner.* 2019, *57*, 723–725.

33. Missions: Sentinel-2. Available online: https://sentinel.esa.int/web/sentinel/missions/sentinel-2 (accessed on 20 April 2020).

34. MultiSpectral Instrument (MSI) Overview. Available online: https://sentinel.esa.int/web/sentinel/technical-guides/sentinel-2-msi/msi-instrument (accessed on 20 April 2020).

35. Sentinel-2 MSI: Products and Algorithms. Available online: https://sentinel.esa.int/web/sentinel/technical-guides/sentinel-2-msi/products-algorithms (accessed on 20 April 2020).

36. SNAP. Available online: https://step.esa.int/main/toolboxes/snap/ (accessed on 20 April 2020).

37. Google Earth Pro. Available online: https://www.google.com/intl/en_uk/earth/desktop/ (accessed on 3 August 2018).

38. Esri World Imagery. Available online: https://www.arcgis.com/home/item.html?id=10df2279f9684e4a9f6a7f08febac2a9 (accessed on 9 May 2019).

39. Geomatica 2018. Available online: https://www.pcigeomatics.com/ (accessed on 12 July 2019).

40. Geomatica Help. Available online: http://www.pcigeomatics.com/geomatica-help/ (accessed on 23 April 2019).

41. Pedregosa, F.; Varoquaux, G.; Gramfort, A.; Michel, V.; Thirion, B.; Grisel, O.; Blondel, M.; Prettenhofer, P.; Weiss, R.; Dubourg, V.; et al. Scikit-learn: Machine Learning in Python. *J. Mach. Learn. Res.* 2012, *12*, 2825–2830.

42. 1.4. Support Vector Machines—Scikit-Learn 0.20.4 Documentation. Available online: https://scikit-learn.org/0.20/modules/svm.html#svm-classification (accessed on 24 April 2020).

43. Oommen, T.; Misra, D.; Twarakavi, N.K.C.; Prakash, A.; Sahoo, B.; Bandopadhyay, S. An Objective Analysis of Support Vector Machine Based Classification for Remote Sensing. *Math. Geosci.* 2008, *40*, 409–424.

44. Müller, A.C.; Guido, S. Chapter 5. Model Evaluation and Improvement. In *Introduction to Machine Learning with Python: A Guide for Data Scientists*; Schanafelt, D., Ed.; O'Reilly Media, Inc.: Sebastopol, CA, USA, 2016; pp. 251–303.

45. Story, M.; Congalton, R. Accuracy assessment: A user's perspective. *Photogramm. Eng. Remote Sens.* 1986, *52*, 397–399.

46. Congalton, R.G. A review of assessing the accuracy of classifications of remotely sensed data. *Remote Sens. Environ.* 1991, *37*, 35–46.

47. Cohen, J. A Coefficient of Agreement for Nominal Scales. *Educ. Psychol. Meas.* 1960, *20*, 37–46.

48. Cracknell, M.J.; Reading, A.M.; McNeill, A.W. Mapping geology and volcanic-hosted massive sulfide alteration in the Hellyer–Mt Charter region, Tasmania, using Random Forests™ and Self-Organising Maps. *Aust. J. Earth Sci.* 2014, *61*, 287–304.

49. Pal, M.; Mather, P.M. Support vector machines for classification in remote sensing. *Int. J. Remote Sens.* 2005, *26*, 1007–1011.

50. He, H.; Garcia, E.A. Learning from Imbalanced Data. *IEEE Trans. Knowl. Data Eng.* 2009, *21*, 1263–1284.

51. Melgani, F.; Bruzzone, L. Classification of hyperspectral remote sensing images with support vector machines. *IEEE Trans. Geosci. Remote Sens.* 2004, *42*, 1778–1790.

52. Li, Y.; Zhang, H.; Xue, X.; Jiang, Y.; Shen, Q. Deep learning for remote sensing image classification: A survey. *Wiley Interdiscip. Rev. Data Min. Knowl. Discov.* 2018, *8*, e1264.

Chapter III: Spectral libraries for Li-exploration

The availability of reference spectral data is paramount for technical and spectroscopic support during exploration campaigns. For example, in remote sensing, reflectance spectra provide a calibration source of the remotely sensed data and allow validating the atmospheric corrections made to satellite-acquired images. Moreover, the knowledge on the position of diagnostic absorption features can help to better direct the image processing methods employed.

This chapter aims at describing the collection process of the spectral data and the construction of two distinct spectral libraries (section III.1.). The first concerns reflectance spectra of distinct Li-bearing minerals and different lithologies outcropping in the case study area obtained using a spectroradiometer (Cardoso-Fernandes *et al.*, 2021c). The second library is composed of Laser-induced breakdown spectroscopy (LIBS) spectra of Li-bearing minerals and rocks not only from the Fregeneda-Almendra area but from other localities in the world (Fabre *et al.*, 2021). Both spectral libraries were built in the ambit of the LIGHTS project, resulting from the collaboration of the different partners, and are freely available for download in open-source repositories, Zenodo and ORDaR, respectively.

Additionally, the second section of this chapter is dedicated to the interpretation of representative reflectance spectra to understand how Li-bearing minerals and rocks can be discriminated using multi- and hyperspectral data. In a preliminary stage, reflectance spectroscopic studies were used to validate the results obtained in a previous supervised classification attempt through the Support Vector Machine (SVM) and Random Forest (RF) algorithms (Cardoso-Fernandes *et al.*, 2020b; Cardoso-Fernandes *et al.*, 2019). Also, a comparative study concerning Li-bearing minerals from the case study area was conducted based on selected samples (Cardoso-Fernandes *et al.*, 2020a). These works resulted in two peer-reviewed conference proceedings available in Appendix I.2. Other smaller contributions in national journals or meetings can be found in Appendix I.3 (Cardoso-Fernandes *et al.*, 2021b; Silva *et al.*, 2020; Silva *et al.*, 2021). After a field campaign conducted in July 2020, that allowed enlarging the existing spectral library, a multidisciplinary approach, encompassing optical microscopy, X-ray diffraction (XRD), Scanning Electron Microscopy with Energy Dispersive Spectroscopy (SEM-EDS), and Li quantification through Inductively Coupled Plasma - Optical Emission Spectrometry (ICP-OES), allowed characterizing the mineral assemblage resultant from the alteration of Li-bearing minerals and rock samples. These results were confronted with the respective reflectance spectra to provide valuable insights for remote exploration of Li-pegmatites worldwide. This research resulted in an international

conference abstract (Cardoso-Fernandes *et al.*, 2021a) and a peer-reviewed journal article (section III.2.; Cardoso-Fernandes *et al.*, 2021d).

References

Cardoso-Fernandes, J., Dias, F., Lima, A., Anjos Ribeiro, M., Perrotta, M., Roda-Robles, E., & Teodoro, A. C. (2021a, 19–30 Apr). *Petalite alteration products from the Bajoca pegmatite (Central Portugal): a multiapproach for lithium exploration.* Paper presented at the EGU General Assembly 2021, online, doi: 10.5194/egusphere-egu21-2364.

Cardoso-Fernandes, J., Lima, A., Teodoro, A., Silva, J. (2021b). *Reflectance spectroscopy of minerals and rocks: a case study for lithological classification*. Abstract presented at *Jornadas do ICT*, *Porto*, 2021.

Cardoso-Fernandes, J., Silva, J., Dias, F., Lima, A., Teodoro, A. C., Barrès, O., Cauzid, J., Perrotta, M., Roda-Robles, E., & Ribeiro, M. A. (2021c). Tools for Remote Exploration: A Lithium (Li) Dedicated Spectral Library of the Fregeneda–Almendra Aplite–Pegmatite Field. *Data, 6*(3), 33. doi: 10.3390/data6030033.

Cardoso-Fernandes, J., Silva, J., Lima, A., Teodoro, A. C., Perrotta, M., Cauzid, J., & Roda-Robles, E. (2020a). *Characterization of lithium (Li) minerals from the Fregeneda-Almendra region through laboratory spectral measurements: a comparative study.* Paper presented at the SPIE Remote Sensing, Earth Resources and Environmental Remote Sensing/GIS Applications XI, doi: https://doi.org/10.1117/12.2573941.

Cardoso-Fernandes, J., Silva, J., Lima, A., Teodoro, A. C., Perrotta, M., Cauzid, J., Roda-Robles, E., & Ribeiro, M. A. (2020b). *Reflectance spectroscopy to validate remote sensing data/algorithms for satellite-based lithium (Li) exploration (Central East Portugal).* Paper presented at the SPIE Remote Sensing, Earth Resources and Environmental Remote Sensing/GIS Applications XI, doi: https://doi.org/10.1117/12.2573929.

Cardoso-Fernandes, J., Silva, J., Perrotta, M. M., Lima, A., Teodoro, A. C., Ribeiro, M. A., Dias, F., Barrès, O., Cauzid, J., & Roda-Robles, E. (2021d). Interpretation of the Reflectance Spectra of Lithium (Li) Minerals and Pegmatites: A Case Study for Mineralogical and Lithological Identification in the Fregeneda–Almendra Area. *Remote Sensing, 13*(18), 3688. doi: 10.3390/rs13183688.

Cardoso-Fernandes, J., Teodoro, A. C., Lima, A., & Roda-Robles, E. (2019, 9–12 September 2019). *Evaluating the performance of support vector machines (SVMs) and random forest (RF) in Li-pegmatite mapping: preliminary results.* Paper presented at the SPIE Remote Sensing, Strasbourg, France, doi: 10.1117/12.2532577.

Fabre, C., Ourti, N. E., Mercadier, J., Cardoso-Fernandes, J., Dias, F., Perrotta, M., Koerting, F., Lima, A., Kaestner, F., Koellner, N., Linnen, R., Benn, D., Martins, T., & Cauzid, J. (2021). Analyses of Li-Rich Minerals Using Handheld LIBS Tool. *Data, 6*(6), 68. doi: 10.3390/data6060068.

Silva, J., Cardoso-Fernandes, J., Teodoro, A., Lima, A. (2020). "As Assinaturas Espectrais dos Minerais de Lítio do Campo Aplito-Pegmatítico de Fregeneda-Almendra". *GeoCore* 5, 22-23.

Silva, J., Teodoro, A., Lima, A., Cardoso-Fernandes, J., Cauzid, Jean (2021). *Espectroscopia de Reflectância no Campo Aplito-Pegmatítico de Fregeneda-Almendra: Estudo das Assinaturas Espectrais dos Minerais de Lítio*. Abstract presented at *Jornadas do ICT*, *Porto*, 2021.

III.1. Building the spectral libraries

III.1.1. Tools for Remote Exploration: A Lithium (Li) Dedicated Spectral Library of the Fregeneda–Almendra Aplite–Pegmatite Field

Joana Cardoso-Fernandes, João Silva, Filipa Dias, Alexandre Lima, Ana C. Teodoro, Odile Barrès, Jean Cauzid, Mônica Perrotta, Encarnación Roda-Robles, Maria Anjos Ribeiro

Data, 2021, **6 (3)**, 33.

Abstract: The existence of diagnostic features in the visible and infrared regions makes it possible to use reflectance spectra not only to identify mineral assemblages but also for calibration and classification of satellite images, considering lithological and/or mineral mapping. For this purpose, a consistent spectral library with the target spectra of minerals and rocks is needed. Currently, there is big market pressure for raw materials including lithium (Li) that has driven new satellite image applications for Li exploration. However, there are no reference spectra for petalite (a Li mineral) in large, open spectral datasets. In this work, a spectral library was built exclusively dedicated to Li minerals and Li pegmatite exploration through satellite remote sensing. The database includes field and laboratory spectra collected

in the Fregeneda–Almendra region (Spain–Portugal) from (i) distinct Li minerals (spodumene, petalite, lepidolite); (ii) several Li pegmatites and other outcropping lithologies to allow satellite-based lithological mapping; (iii) areas previously misclassified as Li pegmatites using machine learning algorithms to allow comparisons between these regions and the target areas. Ancillary data include (i) sample location and coordinates, (ii) sample conditions, (iii) sample color, (iv) type of face measured, (v) equipment used, and for the laboratory spectra, (vi) sample photographs, (vii) continuum removed spectra files, and (viii) statistics on the main absorption features automatically extracted. The potential future uses of this spectral library are reinforced by its major advantages: (i) data is provided in a universal file format; (ii) it allows users to compare field and laboratory spectra; (iii) a large number of complementary data allow the comparison of shape, asymmetry, and depth of the absorption features of the distinct Li minerals.

Dataset: http://doi.org/10.5281/zenodo.4575375.

Dataset License: CC-BY.

Keywords: reflectance spectroscopy, spectrometer, geological exploration, remote sensing, pegmatite, lithium.

1. Summary

The use of reflectance spectroscopy to identify minerals through diagnostic absorption features in the visible and infrared regions has been described by several authors in recent decades [1–4]. Due to these diagnostic features, the acquired mineral spectra can be employed in several knowledge-based satellite image classification approaches to delineate target areas for mineral occurrences [5,6]. Moreover, field spectra allows ground-checking of the remotely sensed data (e.g., [7–9]) and validation of the atmospheric corrections made to satellite images.

The recent growing economic importance of lithium (Li), mainly due to its application in batteries for electric cars, has triggered several attempts to use satellite images to target the occurrence of Li minerals and Li pegmatites [10–14]. Reference spectra for some of the most

important Li minerals, such as spodumene and lepidolite, can be found in the United States Geological Survey (USGS) [15] and ECOSTRESS [16] spectral libraries. Nonetheless, there are no reference spectra for petalite in these open domain spectral libraries. The Geological Survey of Brazil (CPRM) has been trying to address this issue by compiling a spectral database with a Li minerals' dedicated section, but so far the petalite diagnostic features have not been identified [17].

To fill in this gap and to complement the development of image classification algorithms for Li exploration, a spectral database was built in this work based on samples collected in the Fregeneda–Almendra aplite–pegmatite field (Figure 1). In this region, spodumene, petalite, and lepidolite minerals occur in evolved pegmatites [18,19] that intruded metasedimentary rocks belonging to the "Complexo Xisto–Grauváquico" (CXG) [20].

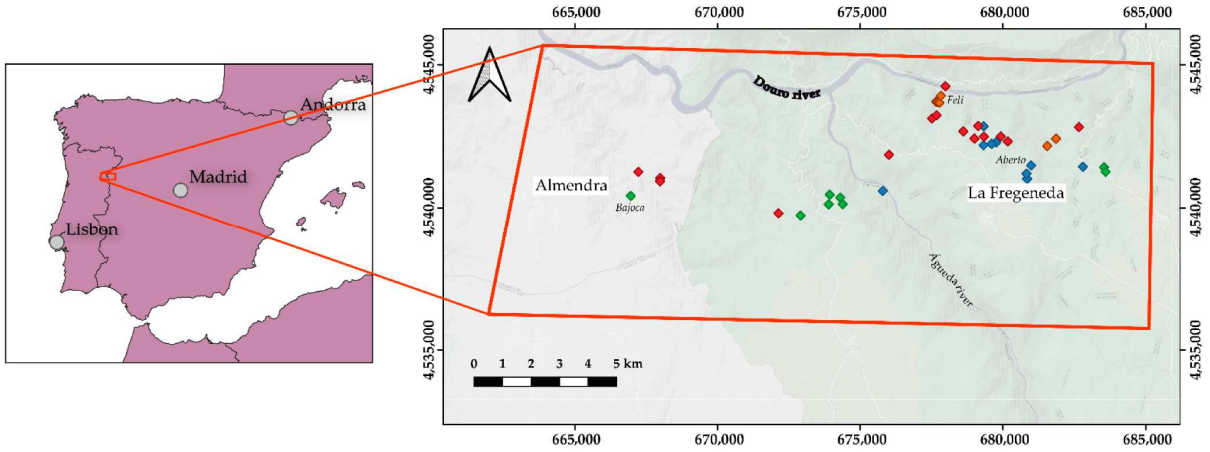

Figure 1. Location of the Fregeneda–Almendra pegmatite field in the Iberian Peninsula. Diamonds represent pegmatites containing Li minerals: green–petalite; blue–spodumene; red–lepidolite; orange–spodumene + lepidolite [18,19]. The map projection is Universal Transverse Mercator zone 29N from the WGS84 datum.

The spectral library is composed of field and laboratory spectra not only of Li minerals (spodumene, petalite, lepidolite) but also from the main outcropping lithologies of the Fregeneda–Almendra area (granitoid rocks, CXG metasediments, Li pegmatite). These rock spectra were mainly acquired in areas of good exposition so they could be used as training areas for satellite-based lithological mapping. Additionally, to allow further investigation on the ability to discriminate Li minerals and Li pegmatites from other lithologies, the spectra from areas misclassified as Li pegmatites using machine learning algorithms [13] are also provided. The comparison of the aforementioned data can allow users to evaluate the degree of spectral similarity between the target minerals/rocks and the remaining within-scene elements.

Complementary data such as (i) the sample location and coordinates (when available), (ii) degree of alteration of the sample, (iii) sample color, (iv) type of face measured, and (v) equipment used, are provided for each spectrum. Spectra acquisition and curation are described thoroughly. For the laboratory spectra, also available are (i) sample photographs, (ii) respective continuum removed spectra files, and (iii) details on the main absorption features automatically extracted.

This spectral database was established in the ambit of the “Lightweight Integrated Ground and Airborne Hyperspectral Topological Solution” (LIGHTS) project, whose goal is to develop a tool that combines remote sensing data acquired at different scales with geological and geochemical data to rapidly identify target areas for Li exploration [21,22]. However, such a database could be useful for other ongoing research projects, namely: (i) the fiber laser plasma spectroscopy system for real-time element analysis (FLaPsys) project, which aims at developing an advanced spectroscopy system capable of real-time element identification and quantification mainly applied to Li mineralizations [23], and in which laser-induced breakdown spectroscopy (LIBS) will be correlated with the visible and infrared data acquired; (ii) new exploration tools for a European pegmatite green-tech resources (GREENPEG) project which aims at improving responsible exploration in Europe for pegmatites through the development of integrated, multi-method exploration toolsets that include satellite image processing and airborne and ground-based geophysics and geochemical approaches [24]. Part of this spectral database was already the basis for some publications [25,26], but more works are expected in the future since there is great potential in this dataset whose main advantages include: (i) that the data are provided in a universal text file format that is not dependent on software; (ii) the ability to compare field and laboratory spectra for 52 coincident spots; (iii) finally, the details and statistics of the extracted features provided allow the user to compare the shape, asymmetry, and depth of the absorption features of the distinct Li minerals, including petalite.

2. Data Description

The spectral database is divided into two subsets; the first concerning the spectra collected in the laboratory and the second corresponding to the spectra acquired in the field. The spectra were organized into categories within each subset according to their application purpose (Table 1). To allow a rapid and easy identification of the spectra, the spectrum naming was made considering logical codes embedded in the spectrum title (Table 1). Consequently, information such as the location of the sample and analyzed lithology/mineralogy can be

readily extracted based just on the spectrum name. Besides the codes of Table 1, each spectrum has its associated measurement number.

Table 1. String, numerical, and alphanumerical codes used for spectrum naming and identification.

	Code	Observation
Purpose of the sample	L	Li mineral database
	TA	Training areas
	SC	Spectral confusion (represents false positive areas)
Lithology	G	Granitoid rock
	LP	Li pegmatite
	M	Metasedimentary rock
Mineralogy	Lep	Lepidolite
	Pet	Petalite
	Spd	Spodumene
Location	AL	Almendra
	ALB	Alberto open pit mine
	BJ	Bajoca open pit mine
	FE	Feli open pit mine
	FG	Fregeneda
	HD	Hinojosa de Duero
	999	3-digit numbers represent the GPS point number
Multiple samples	A1 to An	Code given to distinct hand samples collected at the same location (where n = number of samples)
Equipment used	sr	SR-6500 (Spectral Evolution, Inc., Haverhill, MA, USA)
	asd	FieldSpec 4 (ASD, Inc., untsville, AL, USA)
Other	f	Spectra collected in the field under real conditions

All spectra are provided in a universal UTF-8 text file format that can be read in any proprietary or open-source software, representing measurements made in the visible and near-infrared (VNIR) and shortwave infrared (SWIR) regions. From a total of 340 spectra collected in the laboratory, 84 represent Li minerals, 196 correspond to the outcropping lithologies of the Fregeneda–Almendra area that can be used as training areas for satellite image classification, and 60 spectra were collected from samples in Li pegmatite false-positive areas identified in previous satellite image classification attempts [13]. Additionally, 75 field spectra are presented in the spectral database (35 measurements of Li minerals and 40 measurements of distinct Li pegmatites). As mentioned in Table 1, two spectrometers were used for spectral measurements. For the data acquired with the SR-6500 equipment, the UTF-8 text files are

composed of a 28 line-header containing information about the equipment and acquisition settings and two columns, the first with the wavelength (in nanometers or nm) and the second with the measured reflectance (in percentage). In the case of the spectra acquired with the ASD FieldSpec 4, there are just two columns, one with the wavelength (in nm) and the other with absolute reflectance values. For each subset (field and laboratory spectra) there is a *.xlsx table containing important ancillary data:

- Spectrum name
- Acquisition equipment
- Sample type
- Sample conditions
- Sample face type
- Sample color
- Location
- Coordinates (Universal Transverse Mercator zone 29N from the WGS84 datum).

The coordinates are only available for samples collected *in situ* and, therefore, samples collected in ore stockpiles (for example) do not have this kind of information registered. For the spectra acquired in the laboratory, additional information is also provided, namely: (i) sample photographs with the analyzed spots highlighted, (ii) a UTF-8 text file with the respective continuum removed spectra (with absolute reflectance values); (iii) PNG files showing for each spectrum the main absorption features and a CSV file summarizing the main statistics of each feature (Section 3.2).

3. Methods

3.1. Spectra Acquisition

Two field campaigns were carried out in February and July of 2020 to collect the data to build the spectral library. At the time of the first campaign, there was no portable spectrometer available in the University of Porto to collect spectra *in situ*, therefore representative samples from 25 locations were taken to the GeoRessources laboratory (University of Lorraine). The spectral measurements were performed with the SR-6500 equipment. Due to difficulties in accessing pegmatites containing spodumene on the field, samples from an existing Li mineral collection at the University of Porto were also analyzed. In the second field survey, favorable weather conditions (absence of clouds) allowed collection of spectra from several Li

pegmatites and the different Li minerals in 35 locations dispersed along the Fregeneda–Almendra pegmatite field. In this case, the ASD FieldSpec 4 spectrometer was used. Samples were retrieved in 28 of these 35 locations to collect further spectra under a controlled environment at the University of Porto, using the same equipment. Either in the field or the laboratory, the two spectrometers were calibrated using a Spectralon (Labsphere) plate with a maximum reflectance higher than 95% for the 250–2500 nm region, and higher than 99% for 400–1500 nm interval. In the field, the calibration was repeated every time the solar lighting conditions changed (about each 30′). Regarding the acquisition settings, to improve the signal-to-noise ratio, each of the spectra acquired in the laboratory represented the average of 40 scans. To expedite spectra acquisition in the field, this value was lowered to 30 scans. However, when using the ASD FieldSpec 4 equipment, five spectra were acquired in each analyzed spot. These five spectra were averaged afterward (Section 3.2) and only the final spectrum was provided in the spectral library. The characteristics of each spectrometer are compared in Table 2. The major differences are observed in terms of the spectral resolution with the SR-6500 outperforming the ASD FieldSpec 4.

Table 2. Comparison of the main characteristics of the employed spectrometers [27,28].

	Spectral Evolution SR-6500	**ASD FieldSpec 4**
	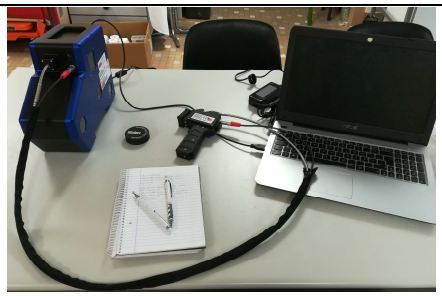	
Spectral Range	350–2500 nm	350–2500 nm
Spectral Resolution	Ultra-High Resolution • 1.5 nm @ 700 nm • 3.0 nm @ 1500 nm • 3.8 nm @ 2100 nm	Standard resolution • 3 nm @ 700 nm • 10 nm @ 1400 nm • 10 nm @ 2100 nm
Spectral sampling (bandwidth)	1 nm increments	• 1.4 nm @ 350–1000 nm • 1.1 nm @ 1001–2500 nm
Wavelength reproducibility	0.1 nm	0.1 nm
Wavelength accuracy	0.5 nm	0.5 nm
Channels	2151	2151
Detectors	• 1024 element TE-cooled silicon photodiode array detector (VNIR) • 512 element TE-cooled InGaAs photodiode array detector (SWIR 1) • 512 element TE-cooled extended InGaAs photodiode array detector (SWIR 2)	VNIR detector: 512 element silicon array SWIR 1 detector: Graded Index InGaAs Photodiode, Two-Stage TE Cooled SWIR 2 detector: Graded Index InGaAs Photodiode, Two-Stage TE Cooled
Noise Equivalent Radiance (NEdL)	• 0.8×10^{-9} W/cm^2/nm/sr @ 400 nm • 0.3×10^{-9} W/cm^2/nm/sr @ 1500 nm • 5.8×10^{-9} W/cm^2/nm/sr @ 2100 nm	• 1.0×10^{-9} W/cm^2/nm/sr @ 700 nm • 1.2×10^{-9} W/cm^2/nm/sr @ 1400 nm • 1.9×10^{-9} W/cm^2/nm/sr @ 2100 nm
Weight	4.99 kg (11 pounds)	5.44 kg (12 lbs)
Contact probe	Internal light source: • Halogen bulb: 4.25 V, 1.06 A Spot size: • 10 mm	Internal light source: • Halogen bulb: 12–18 V, 6.5 W Spot size: • 10 mm
Field pistol grip	—	Natural lighting Spot size as a function of distance to the sample

3.2. Spectra Curation and Treatment

The spectra acquired with ASD FieldSpec 4 were post-processed using the ASD ViewSpec Pro™ software [29]. The first step included averaging each of the five spectra collected for

each spot. To the averaged spectrum, a splice correction was applied to remove the offset between detectors that is caused by differences in their sensibility [29] (Figure 2). Finally, the final spectra were exported to UTF-8 text files. In the case of the spectra collected using the SR-6500, a simple conversion from SED to the UTF-8 text file was necessary. The SpectraGryph software [30] was used to analyze each spectrum individually to exclude the ones with measurement errors or with noticeable noise caused by the presence of vegetation, for example.

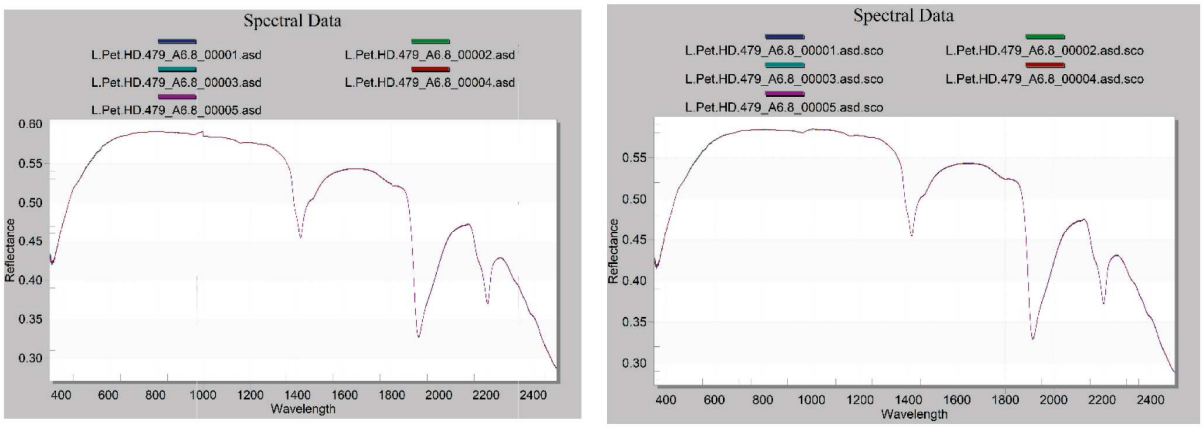

(a) (b)

Figure 2. Splice correction process: (a) before and (b) after applying the correction. The VNIR and SWIR2 ranges are adjusted using the endpoints (~1000 to 1800 nm) and shape of the curve of the SWIR1 range since this detector is more stable to temperature changes [29].

To allow a more detailed analysis of each spectrum, a hull quotient procedure was applied to remove the continuum and normalize the spectra (Figure 3). This was accomplished in a Python environment using the *pysptools* library [31] based on the technique proposed by Clark and Roush [2]. First, a convex hull was fitted to the spectrum (Figure 3a) connecting the hull points (corresponding to local maxima) [32]. Afterwards, the convex hull (continuum) was removed through a hull-quotient process and the measured reflectance values were divided by the convex hull [2,33,34]. The continuum removal process is of great importance because it not only allows the comparison of the data obtained with different spectrometers but also allows the enhancement and correct determination of the absorption features [32–34]. The *pysptools* library was used to automatically extract the main absorption features (Figure 3b–d) and to calculate their associated statistics according to the work of Kokaly [35]. To avoid the extraction of non-significant features, a baseline value of 0.93 was employed: all features below the baseline were kept and the ones above it were rejected [31] (Figure 3). For each spectrum, a CSV file was automatically created summarizing the statistics of each absorption

feature. Table 3 shows a list of the extracted statistics and the respective abbreviation used in the CSV files. The Supplementary Materials provided shows the adaptation of the *pysptools* functions to batch process this particular spectral library.

Table 3. List of the statistics automatically extracted for each spectrum and respective abbreviations used in the resultant CSV file.

Abbreviation	Extracted Statistics
id	feature number
area	area
cstart_wvl	continuum start wavelength
cstop_wvl	continuum stop wavelength
cslope	continuum slope
abs_wvl	center wavelength
abs_depth	absorption depth
FWHM_delta	full-width at half maximum

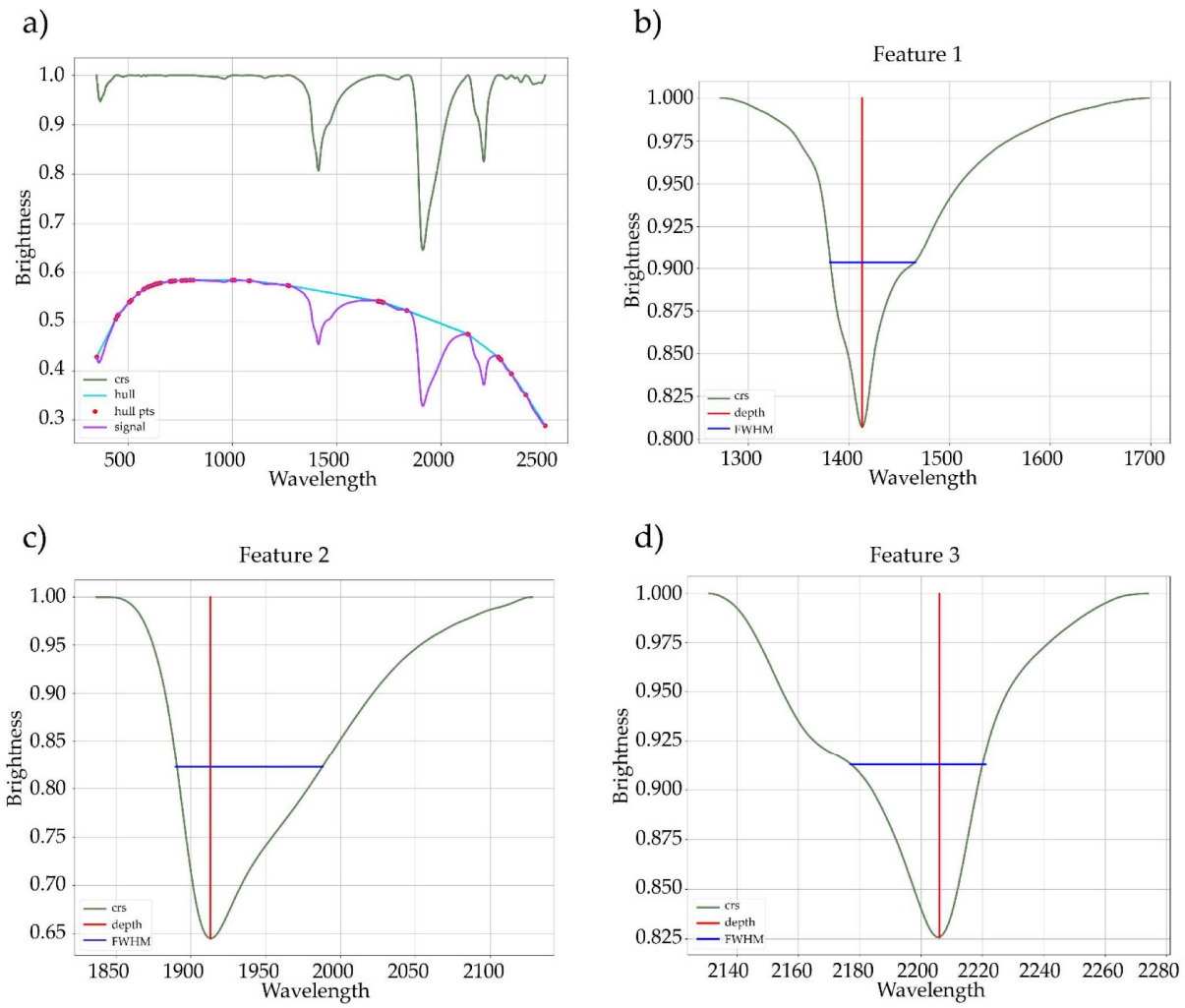

Figure 3. (a) Convex hull fitting to the original signal and the respective continuum removed spectrum (crs); (b–d) automatic extraction of the main absorption features using the *pysptools* library [31]. pts–points; FWHM–full width at half maximum.

4. User Notes

This spectral database has the advantage of presenting field and laboratory spectra for 52 analyzed spots, allowing comparisons and evaluation of the influence of the acquisition conditions on the final spectra. Additionally, field spectra are expected to better match the spectral signatures acquired by airborne sensors. However, as can be seen in Figure 4, field spectra present additional sharp bands around 1400 and 1800 nm caused by atmospheric water that should be removed before additional processing.

A final note on the usage of the automatically extracted features that are available for all spectra acquired in the laboratory. As aforementioned, a baseline value was set to determine which absorption features to extract. Therefore, setting a different baseline may produce different results and change the features' statistics. Additionally, different results can be obtained if the features are extracted considering the whole spectrum or spectra subset matching a given region of interest [34]. According to the user's objectives, one of the two methods may be more appropriate.

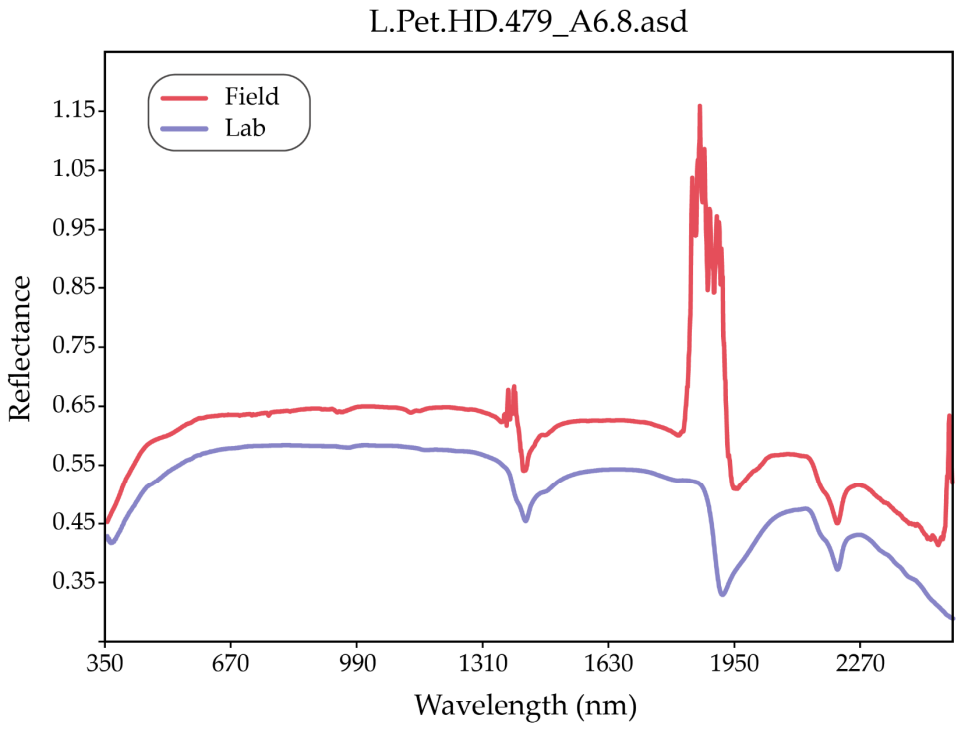

Figure 4. Comparison of laboratory and field spectra obtained for the same petalite sample. Notice the spikes in the field spectrum caused by the presence of water in the atmosphere.

Supplementary Materials

The source code adapted in this study to remove the continuum and automatically extract the main absorption features is available online at https://www.mdpi.com/2306-5729/6/3/33/s1.

Author Contributions

Conceptualization, J.C.-F., A.L., and A.C.T.; methodology, J.C.-F., A.L., and A.C.T.; software, J.C.-F.; formal analysis J.C.-F., J.S., M.P., and M.A.R.; investigation, J.C.-F., J.S., F.D., A.L., A.C.T., M.P., and M.A.R.; resources A.L., E.R.-R., O.B., and J.C.; data curation, J.C.-F., J.S., and F.D.; writing—original draft preparation, J.C.-F.; writing—review and editing, all remaining authors; visualization, J.C.-F., J.S., and F.D.; supervision, A.L., A.C.T., M.A.R., M.P., E.R.-R., and O.B.; project administration, J.C., A.L., and A.C.T.; funding acquisition, J.C. and A.L. All authors have read and agreed to the published version of the manuscript.

Funding

The authors are grateful for the financial support provided by FCT– Fundação para a Ciência e a Tecnologia, I.P., through the ERA-MIN/0001/2017–LIGHTS project and also the 869274–GREENPEG–H2020-SC5-2018-2019-2020 project. The work was also supported by National Funds through the FCT project UIDB/04683/2020–ICT (Institute of Earth Sciences). Joana Cardoso-Fernandes and Filipa Dias are financially supported within the compass of their respective Ph.D. theses, ref. SFRH/BD/136108/2018 and ref. 2020.05534.BD, by national funds from MCTES through FCT, and cofinanced by the European Social Fund (ESF) through POCH—Programa Operacional Capital Humano—and NORTE 2020 regional program. The Spanish Ministerio de Ciencia, Innovacion y Universidades (Project RTI2018-094097-B-100, with ERDF funds) and the University of the Basque Country (UPV/EHU) (grant GIU18/084) also contributed economically. The French National Research Agency (ANR–10–LABX 21–LABEX RESSOURCES 21) partly supported Master Student personal grant and the 776804–NEXT– H2020-SC5-2017 project participated to equipment purchase.

Data Availability Statement

The data presented in this study are publicly archived in the Zenodo platform: https://zenodo.org/record/4575375#.YFAgGNwRVPY (accessed on 16 March 2021).

Conflicts of Interest

The authors declare no conflict of interest.

Abbreviations

The following abbreviations are used in this manuscript:

CPRM	Geological Survey of Brazil
crs	continuum removed spectra
CSV	comma-separated values
CXG	Complexo Xisto–Grauváquico (Schist–graywacke complex)
FWHM	full-width at half maximum
Lab	laboratory
LIBS	laser-induced breakdown spectroscopy
Li	lithium
NEdL	noise equivalent radiance
PNG	portable network graphics
pts	points
SWIR	shortwave infrared
TE	thermoelectrically
USGS	United States Geological Survey
UTF	unicode transformation format
VNIR	visible and near-infrared
WGS	World Geodetic System

References

1. Hunt, G.R.; Salisbury, J.W. Visible and near-infrared spectra of minerals and rocks: I Silicate minerals. *Modern Geol.* **1970**, *1*, 283–300.
2. Clark, R.N.; Roush, T.L. Reflectance spectroscopy: Quantitative analysis techniques for remote sensing applications. *J. Geophys. Res. Space Phys.* **1984**, *89*, 6329–6340.
3. Clark, R.N.; King, T.V.V.; Klejwa, M.; Swayze, G.A.; Vergo, N. High spectral resolution reflectance spectroscopy of minerals. *J. Geophys. Res. Space Phys.* **1990**, *95*, 12653–12680.
4. Pontual, S.; Merry, N.J.; Gamson, P. Spectral interpretation field manual. In *GMEX Spectral Analysis Guides for Mineral Exploration*, 3rd ed.; AusSpec International Ltd.: Queenstown, New Zealand, 2008; Volume 1.
5. Asadzadeh, S.; Filho, C.R.D.S. A review on spectral processing methods for geological remote sensing. *Int. J. Appl. Earth Obs. Geoinf.* **2016**, *47*, 69–90.
6. Naleto, J.L.C.; Perrotta, M.M.; da Costa, F.G.; Filho, C.R.D.S. Point and imaging spectroscopy investigations on the Pedra Branca orogenic gold deposit, Troia Massif, Northeast Brazil: Implications for mineral exploration in amphibolite metamorphic-grade terrains. *Ore Geol. Rev.* **2019**, *107*, 283–309.
7. Pour, A.B.; Hashim, M. Hydrothermal alteration mapping from Landsat-8 data, Sar Cheshmeh copper mining district, south-eastern Islamic Republic of Iran. *J. Taibah Univ. Sci.* **2015**, *9*, 155–166.
8. Teodoro, A.C.; Veloso-Gomes, F. Quantification of the Total Suspended Matter Concentration around the Sea Breaking Zone from In Situ Measurements and Terra/Aster Data. *Mar. Georesour. Geotechnol.* **2007**, *25*, 67–80.
9. Rivard, B.; Zhang, J.; Feng, J.; Sanchez-Azofeifa, A.G. Remote predictive lithologic mapping in the Abitibi Greenstone Belt, Canada, using airborne hyperspectral imagery. *Can. J. Remote Sens.* **2009**, *35*, 95.
10. Cardoso-Fernandes, J.; Teodoro, A.C.; Lima, A.; Perrotta, M.; Roda-Robles, E. Detecting Lithium (Li) Mineralizations from Space: Current Research and Future Perspectives. *Appl. Sci.* **2020**, *10*, 1785.

11. Cardoso-Fernandes, J.; Teodoro, A.C.; Lima, A. Remote sensing data in lithium (Li) exploration: A new approach for the detection of Li-bearing pegmatites. *Int. J. Appl. Earth Obs. Geoinf.* **2019**, *76*, 10–25.

12. Cardoso-Fernandes, J.; Lima, A.; Roda-Robles, E.; Teodoro, A.C. Constraints and potentials of remote sensing data/techniques applied to lithium (Li)-pegmatites. *Can. Mineral.* **2019**, *57*, 723–725.

13. Cardoso-Fernandes, J.; Teodoro, A.C.M.; Lima, A.; Roda-Robles, E. Evaluating the performance of support vector machines (SVMs) and random forest (RF) in Li-pegmatite mapping: Preliminary results. In *Earth Resources and Environmental Remote Sensing/GIS Applications X*; SPIE: Bellingham, DC, USA, 2019; Volume 11156, p. 111560Q.

14. Cardoso-Fernandes, J.; Teodoro, A.C.; Lima, A.; Roda-Robles, E. Semi-Automatization of Support Vector Machines to Map Lithium (Li) Bearing Pegmatites. *Remote Sens.* **2020**, *12*, 2319.

15. Kokaly, R.F.; Clark, R.N.; Swayze, G.A.; Livo, K.E.; Hoefen, T.M.; Pearson, N.C.; Wise, R.A.; Benzel, W.M.; Lowers, H.A.; Driscoll, R.L.; et al. *USGS Spectral Library Version 7, 1035*; USGS: Reston, VA, USA, 2017; p. 68.

16. Meerdink, S.K.; Hook, S.J.; Roberts, D.A.; Abbott, E.A. The ECOSTRESS spectral library version 1.0. *Remote Sens. Environ.* **2019**, *230*, 111196.

17. Costa, M.A.C.; Perrotta, M.M.; Melo, T.G.; Turra, B. Estudos Espectrais. In *Avaliação do Potencial do Lítio no Brasil: Área do Médio Rio Jequitinhonha, Nordeste de Minas Gerais: Texto Explicativo e Mapas*; Paes, V.J.C., Santos, L.D., Tedeschi, M.F., Betiollo, L.M., Eds.; CPRM: Belo Horizonte, Brazil, 2016; p. 276.

18. Roda, E.; Fontan, F.; Pesquera, A.; Velasco, F. The phosphate mineral association of the granitic pegmatites of the Fregeneda area (Salamanca, Spain). *Mineral. Mag.* **1996**, *60*, 767–778.

19. Vieira, R. Aplitopegmatitos com Elementos Raros da Região Entre Almendra (V.N. de Foz Côa) e Barca d'Alva (Figueira de Castelo Rodrigo). Campo Aplitopegmatítico da Fregeneda-Almendra. Ph.D. Thesis, Faculdade de Ciências da Universidade do Porto, Porto, Portugal, 2010.

20. Costa, J.C.S. *Notícia Sobre uma Carta Geológica do Buçaco, de Nery Delgado*; Serviços Geológicos de Portugal: Lisboa, Portugal, 1950.

21. LIGHTS (Lightweight Integrated Ground and Airborne Hyperspectral Topological Solution). Available online: **http://lights.univ-lorraine.fr/** (accessed on 9 November 2020).

22. Cardoso-Fernandes, J.; Teodoro, A.C.; Lima, A.; Mielke, C.; Korting, F.; Roda-Robles, E.; Cauzid, J. Multi-Scale Approach using Remote Sensing Techniques for Lithium Pegmatite Exploration: First Results. *IGARSS* **2020**, 5226–5229.

23. PROJECTS: FLAPSYS. Available online: **https://www.inesctec.pt/pt/projetos/flapsys** (accessed on 9 November 2020).

24. GREENPEG. Available online: **https://www.greenpeg.eu/** (accessed on 9 November 2020).

25. Cardoso-Fernandes, J.; Silva, J.; Lima, A.; Teodoro, A.C.; Perrotta, M.; Cauzid, J.; Roda-Robles, E. Characterization of lithium (Li) minerals from the Fregeneda–Almendra region through laboratory spectral measurements: A comparative study. In *Earth Resources and Environmental Remote Sensing/GIS Applications XI*; SPIE: Bellingham, DC, USA, 2020; Volume 11534, p. 115340N.

26. Cardoso-Fernandes, J.; Silva, J.; Lima, A.; Teodoro, A.C.; Perrotta, M.; Cauzid, J.; Roda-Robles, E.; Ribeiro, M.D.A. Reflectance spectroscopy to validate remote sensing data/algorithms for satellite-based lithium (Li) exploration (Central East Portugal). In *Earth Resources and Environmental Remote Sensing/GIS Applications XI*; SPIE: Bellingham, DC, USA, 2020; Volume 11534, p. 115340M.

27. Full Range Photodiode Array UV-VIS-NIR-SWIR. Available online: **https://spectralevolution.com/products/hardware/compact-lab-spectroradiometers/** (accessed on 5 November 2020).

28. ASD FieldSpec 4 Standard-Res Spectroradiometer. Available online: **https://www.malvernpanalytical.com/en/products/product-range/asd-range/fieldspec-range/fieldspec-4-standard-res-spectroradiometer#specs** (accessed on 5 November 2020).

29. ASD Inc. ViewSpec Pro™ User Manual. ASD Document 600555 Rev. A. Boulder, 2008. Available

online: http://geoinfo.amu.edu.pl/geoinf/m/spektr/viewspecpro.pdf (accessed on 4 November 2020).

30. Menges, F. Spectragryph Optical Spectroscopy Software, Version 1.2.14. Available online: http://www.effemm2.de/spectragryph/ (accessed on 22 July 2020).
31. Therien, C. Welcome to the PySptools Documentation. Available online: https://pysptools.sourceforge.io/ (accessed on 22 July 2020).
32. Van Der Meer, F. Spectral curve shape matching with a continuum removed CCSM algorithm. *Int. J. Remote Sens.* **2000**, *21*, 3179–3185.
33. Carrino, T.A.; Crósta, A.P.; Toledo, C.L.B.; Silva, A.M. Hyperspectral remote sensing applied to mineral exploration in southern Peru: A multiple data integration approach in the Chapi Chiara gold prospect. *Int. J. Appl. Earth Obs. Geoinf.* **2018**, *64*, 287–300.
34. Continuum Removal. Available online: https://www.l3harrisgeospatial.com/docs/ContinuumRemoval.html (accessed on 6 November 2020).
35. Kokaly, R.F. PRISM: Processing Routines in IDL for Spectroscopic Measurements (Installation Manual and User's Guide, Version 1.0); 2011-1155; Reston, VA, 2011. Available online: https://pubs.usgs.gov/of/2011/1155/pdf/ofr2011-1155-17oct2011.pdf (accessed on 6 November 2020).

III.1.2. Analyses of Li-Rich Minerals Using Handheld LIBS Tool

Cécile Fabre, Nour Eddine Ourti, Julien Mercadier, Joana Cardoso-Fernandes, Filipa Dias, Mônica Perrotta, Friederike Koerting, Alexandre Lima, Friederike Kaestner, Nicole Koellner, Robert Linnen, David Benn, Tania Martins and Jean Cauzid

Data, 2021, **6 (6)**, 68.

Abstract: Lithium (Li) is one of the latest metals to be added to the list of critical materials in Europe and, thus, lithium exploration in Europe has become a necessity to guarantee its mid- to long-term stable supply. Laser-induced breakdown spectroscopy (LIBS) is a powerful analysis technique that allows for simultaneous multi-elemental analysis with an excellent coverage of light elements (Z < 13). This data paper provides more than 4000 LIBS spectra obtained using a handheld LIBS tool on approximately 140 Li-content materials (minerals,

powder pellets, and rocks) and their Li concentrations. The high resolution of the spectrometers combined with the low detection limits for light elements make the LIBS technique a powerful option to detect Li and trace elements of first interest, such as Be, Cs, F, and Rb. The LIBS spectra dataset combined with the Li content dataset can be used to obtain quantitative estimation of Li in Li-rich matrices. This paper can be utilized as technical and spectroscopic support for Li detection in the field using a portable LIBS instrument.

Dataset: https://doi.org/10.24396/ORDAR-65.

Dataset License: CC-BY

Keywords: lithium, LIBS, handheld tool, exploration, Li-mineral.

1. Summary

Since the emergence of laser-induced breakdown spectroscopy (LIBS) [1,2], it has been utilized in numerous geological studies. This is due to the large range of potentially detected elements, which makes it a promising technique for the future. For a better overview, one can read the numerous papers and reviews on the applications of LIBS for geological purposes [3–18]. One may recall that the Perseverance rover on Mars, similar to the previous Curiosity rover, uses the LIBS technique (with the ChemCam and SuperCam instruments, respectively). Since 2012, the ChemCam tool has provided several thousand LIBS analyses on Martian soils and rocks for the geological interpretation of the Gale crater [19–23]. The SuperCam instrument, which arrived on Mars in February 2021, has already obtained remote LIBS–Raman–VNIR analyses of calibration targets and Martian rocks and soils [24–26].

More recently, portable LIBS tools have been widely used for the analysis of rocks, minerals, economic elements, and light elements [18,27–34]. Although quantitative data are mainly obtained from metal studies [30,35], for more complex materials such as geological mineral mixtures or rocks, standards and calibrations need to be designed to obtain consistent data when using the LIBS technique and, thus, the handheld LIBS tools [6,17,36–43]. The LIGHTS (Lightweight Integrated Ground and airborne Hyperspectral Topological Solutions) project aims at facilitating the exploration of new lithium (Li) resources, which mainly consist of

pegmatites (http://lights.univ-lorraine.fr accessed on 1 May 2021). One of the richest regions in Europe is in Northern Portugal and North-Western Spain. These outcrops were specially selected to test the simultaneous acquisition of hyperspectral imaging data (HSI) and *in situ* analyses using handheld tools (LIBS, VNIR, SWIR). The project is dedicated to recognizing the most favorable targets from remotely sensed data and immediately following these up with ground measurements. In fact, by avoiding lab interpretation after the remote sensing work and the ground-truthing, the duration of exploration processes could be considerably shortened. This would require near real-time data processing based on chemometrics and artificial intelligence [44,45]. One previous data paper reported the acquisition of VNIR and SWIR spectra in the field from outcrops and various reference minerals [46] within the same project. As the LIBS handheld tool provides fast identification of trace elements, i.e., Li (Figure 1); here we aimed to establish the calibration curve of Li content in different matrices. These univariate calibrations can be used in LIBS applications [42,47–52].

(**a**) (**b**)

Figure 1. (a) Full portable LIBS operating on a pegmatite outcrop; some of the detected elements and the LIBS spectra can be seen on the screen; (**b**) transfer of the data from the Z300 to the laptop using the Profile Builder interface.

2. Data Description

The database mainly includes laboratory LIBS spectra obtained from homogeneous Li-bearing minerals such as spodumene (LiAlSi2O6), petalite (LiAlSi4O10), amblygonite or montebrasite ($LiAl(PO_4)(F,OH)$), lepidolite ($K_2(Li,Al)_{5-6}(Si_{6-7}Al_{2-1}O_{20})(OH,F)_4$), zinnwaldite ($KLiFeAl(AlSi_3)O_{10}(OH,F)_2$), and altered Li minerals [53]. Various LIBS analyses were also

directly performed on Li-rich pegmatites at fresh outcrops in the field in Portugal by our Portuguese colleagues [46,54,55]. LIBS analyses were additionally performed on different powder pellets (obtained from the FAME project) and glasses made up of crushed powders from homogenized minerals. These samples (pellets and glasses) were specially tested to check the potential matrix effect that occurs during plasma formation and its emission.

In this study, 134 samples were analyzed using the handheld LIBS tool, covering the main minerals investigated during the LIGHTS project. In order to help the users of our dataset, the Li concentrations of minerals, calculated using bulk analysis such as ICP-OES, are available on the LIBS_database_file.csv with other important information, such as (i) the name of sample/spectra; (ii) sample matrix: mineral/rock, pressed pellet, synthetic glass; (iii) mineralogy if known; (iv) main trace elements detected by LIBS; (v) number of point analysis (mean number of available spectra) by sample; (vi) Li concentration (%). A first description of the samples is reported in the Table 1.

Table 1. Description of the samples with their providers, their geological origin if known, and matrix. More information is available in the LIBS_database_file (.csv) (see data reference).

Partners	Samples	Minerals
Université de Lorraine, France	Rocks, minerals, glasses, pellets	Lepidolite, spodumene, Kunzite, petalite, hindenite
University of Western Ontario and MGS, Canada	Rocks, thin sections, glass	Lepidolite, spodumene, petalite
Geological Service of Brazil, Brazil	Rocks	Spodumene, amblygonite
GFZ, Germany	Powders	Li-rich pegmatite

According to the rock mineralogy, the number of LIBS spectra acquired in each area (higher than 45) is sufficient to provide consistent data that reveal the mean composition of the rock. The relationship between the granulometry of the rock and the LIBS analyses is detailed in [17,56]. Thus, all the LIBS spectra presented in this data paper are representative of each composition. The relative standard deviations that were obtained from the different samples, and particularly for the lithium emission peaks, were between 7% for the powder pellets and 15% for the minerals. Previous studies have already reported the potential of handheld LIBS for lithium applications [18,32,57].

2.1. Format of the LIBS Spectra Files

Concerning data acquisition, the spectra can be directly displayed on the portable tool just after the analyses and the mean spectra are provided on the Profile Builder (internal software). These LIBS data (spectra) can be exported from the device to the user's computer by opening the communication between the LIBS and the computer (USB connection or Wi-Fi). Different options are possible such as raw LIBS spectra, mean raw spectra, or all individual and/or mean spectra calibrated in wavelength. Here, two different kinds of spectra, obtained after cleaning the laser shots to avoid any dust contamination, are available in this dataset (as downloaded from the LIBS tool):

(i) Firstly, 4362 LIBS files correspond to the raw LIBS spectra with no processing treatment; thus, each spectra value corresponds to a point (corresponding to several laser shots) on the samples. These spectra values are not calibrated in wavelengths; thus, the identification of the elements is difficult due to potential shifts in nm as a result of the detectors. The raw spectra correspond to the LIBS spectra obtained at each point, are recorded in csv format, and they correspond to three columns: the first for pixels, the second for the wavelengths, and the last for the intensity (arbitrary intensity, counts on the detector), with the column titles being "pixel", "wavelength", and "intensity". For the raw data, the initial format was built as IDmineral_yearmonthday_hour_PM_Spectrumnumber_PixelData.csv. These spectra can be downloaded from seven separate folders with explicit names that correspond to the providers and/or matrices (i.e., Univ. Lorraine, Canada, Brazil, GFZ, thin sections, powders, etc.). The open access website of ORDaR (OTELo Research Data Repository) is https://doi.org/10.24396/ORDAR-65.

(ii) Secondly, 369 average LIBS spectra values calculated for each area are available. It should be highlighted that these LIBS spectra were directly recorded from the handheld LIBS tool and the spectra were calibrated in wavelength in order to facilitate element identification (as the element peaks are very narrow) by adding artificial pixels. The LIBS mean spectra values also correspond to .csv files. These calibrated spectra are the mean spectra obtained at several points, and they correspond to two columns: the first for wavelengths and the second for the intensity (arbitrary intensity, counts on the detector), with the column titles being "wavelength" and "intensity". The initial format was built as IDmineral_yearmonthday_hour_AM_AverageSpectrum.csv; for the spectra associated with the analysis number, IDmineral_yearmonthday_hour_PM_Spectrumnumber.csv

was used. In this study, the AverageSpectrum.csv was always kept for the major part of the spectra, and the beginning of the filename corresponds to the mineral ID. A typical name of these spectra is "IDMineral_20190417_041453_PM_AverageSpectrum" with the ID mineral at the beginning, the YearMonthDay_hourminutesecond time of the acquisition, and the notification of the AverageSpectrum. These spectra can be downloaded from the LIBS LIBS_spectra_DATAPAPER.zip.

2.2. Mineral Samples

The sample collection is composed of 128 minerals (spodumene ($LiAlSi_2O_6$), petalite ($LiAlSi_4O_{10}$), amblygonite ($LiAl(PO_4)(F,OH)$), lepidolite ($K_2(Li,Al)_{5-6}(Si_{6-7}Al_{2-1}O_{20})(OH,F)_4$), zinnwaldite ($KLiFeAl(AlSi_3)O_{10}(OH,F)_2$)), and rock samples: 51 samples correspond to outcrop minerals/rocks from the Fregenda–Almendra pegmatite field, 30 minerals correspond to reference minerals from official suppliers, personal collections, or partners (MGS, Univ. Ontario, Suffel Collection, GeoRessources), and 41 LIBS spectra located on 24 different thick sections (provided by Univ. Ontario) correspond to individual minerals analyzed using LIBS. Nine rock samples were provided by Monica Perrotta from the Brazilian Geological Survey.

2.3. Thin Rock Sections

The analyzed thin rock sections (1 cm × 2 cm × 0.5 mm) correspond to muscovite samples where LA-ICP-MS analyses (individual points) on different micas were already performed, and the LIBS analysis was performed to compare the two techniques (not presented in this paper). In these minerals, the main elements detected using LIBS were obviously Al, Si, Mg, K, Na, Fe, Ca, and Li, but numerous trace elements were also detected such as Cs, Rb, Ta, Be, and Sr [58].

2.4. Powder Pellets

One portion of the samples corresponds to powder pellets with low Li content. One portion of the powders was provided by the FAME project (from the lepidolite pegmatite of Gonçalo in Portugal (GLi and TPR samples)), and the other portion of the pellets was from Bajoca outcrop rocks (the location can be found on the Bajoca_sample_location.csv file). These powders are less enriched in lithium than the Li-mineral samples. The particulate size of the powders used for the pellets was approximately 150+/−10 µm. The powders were poured into steel molds

with a diameter of 26 mm and a thickness of 2 mm to be finally compacted under 6.5 ton cm^{-2} for 1 min, since a pressure below 3 ton cm^{-2} can disturb the LIBS intensities [31,59].

2.5. Best Conditions for LIBS Analysis

Solid samples are more suitable for LIBS, and marked asperities on the sample surface can lead to a loss of ablation and problems with the plasma emission. However, for classical LIBS element detection, the signal is usually sufficient for identification even if the sample is not strictly flat (for the scale of the window 3 mm × 4 mm). For quantitative applications, a strict flatness is required, which can be compensated for by normalization if the matrix is the same [36,40,42]. If bulk estimation is the aim of the study, samples must be homogeneous at the laser beam scale (or on the area analyzed by several laser shots). The granulometry of the rock is the most critical point to be investigated before any geochemical interpretation, especially for analyses performed on micrometric areas (μLIBS, μXRF, Raman, VNIR, etc.). Multiplying the number of analyses on the rock is required in order to obtain the bulk composition [17,39,56]. Crushed and homogenized samples can be investigated by making pressed pellets. LIBS analysis is slightly destructive with an ablated layer of several to dozens of micrometers per laser shot depending on the smoothness of the material. As a series of laser shots is usually emitted, the sample thickness should be a minimum of 40 micrometers (corresponding to common thin rock sections). Finely grained samples may be homogeneous enough and provide good data but there is no way of knowing if there is a hidden feature below the sample surface, shallow enough to contribute to the signal. As such, confidence in results from such samples is not at the level it would be for homogenized ones.

3. Methods

3.1. Laser-Induced Breakdown Spectroscopy Technique

More information can be obtained through various specific papers as regards the spectroscopic aspects of the LIBS technique and its application in geology and more recently on Martian soil and rock ChemCam analyses [2,3,17,23,29,34,60]. The portable LIBS tool has a very safe design and avoids any laser operating in the air, allowing the geologists to perform analyses safely in the field. A pre-ablation shot at very low intensity is always emitted and if low or no plasma emission is detected, the device automatically stops. These devices now rely on Li batteries, which may require transportation authorization when traveling by road, boat, or

plane. The batteries are usually below the threshold for road transportation. They should, however, be declared for boat or plane trips. The normal regulation, based on risk mitigation, is to avoid transporting Li batteries in the hold and to keep them with the traveler. A maximum number of batteries per traveler may be imposed by the transport company.

3.2. LIBS Spectra Acquisition (Z300 Instrument)

All LIBS spectra acquisitions were obtained using one unique handheld instrument (Z300 SciAps © instruments). Depending on the samples and the size of the minerals, the number of mean spectra values acquired can be from 3 to 5 different analyzed zones corresponding to 9 and 15 points, respectively. Thus, the most relevant information regarding acquisition is available in the LIBS_Database_file.csv file.

3.2.1. Laser Parameters and Ablation

When using the portable Z300 LIBS instrument, the parameters of the laser cannot be modified. For Z300 analyses, the characteristics for all the spectra were 5–6 mJ/pulse, 10 Hz repetition rate for the analysis and for the cleaning shot, and a 1064 nm pulsed NdYAG laser source. The use of laser ablation allows one to “clean” the first micrometers of the surface to avoid any dust contamination. Here, we used cleaning mode firing and made only one laser cleaning shot that was not recorded.

3.2.2. Wavelength Range of the Detectors

LIBS analysis does not require a prerequisite of the detected elements, and their detection only depends on the wavelength. Here, Z300 provides an extended spectrometer range from 190 to 950 nm, allowing for the detection of the major and trace elements present in the rocks such as F, N, O, Br, Cl, Rb, Cs, and S.

3.2.3. Number of Measurements

The Z300 tool provides an image of the sample through a camera to optimize the correct location of the sampled points. As repeating the measurement can improve the error bars, a 2D raster of 15 points can be used to obtain a kind of bulk content. Therefore, the laser is fired

in discreet increments in two dimensions (X-Y) with a number of points/locations depending on the samples.

- For Li minerals, which were reported as reference minerals and analyzed in GeoRessources laboratory of Université de Lorraine, the LIBS rasters were centered along a three points by five points rectangle with four laser shots at each point (with one laser cleaning shot to avoid any dust contamination). This grid was duplicated for each sample and 30 LIBS spectra were obtained to mimic a bulk composition. Then, the mean average LIBS spectra values were recorded and they corresponded to the database reported here (258 mean spectra). To ensure that we were on a non-altered mineral, the selected zones were based on the selection of the most color-homogenized zone observed on the entire sample (larger than 3 mm square). This protocol was also followed for the bulk analysis.

- For powder pellets, which were realized at GeoRessources and analyzed there, the grid was three points by three points with five laser shots at each point (one cleaning laser shot). Five different random locations were studied and 45 LIBS spectra were recorded. For this data paper, each LIBS reference spectrum on each pellet corresponds to the mean LIBS of 45 spectra (Figure 2).

Figure 2. (a) Schematic representation of the analytical protocol for the LIBS analysis on powder pellets, with the five different random zones, nine points for each; (b) images of powder pellets with random areas of analysis; the nine craters can be seen as a square, and the crater size is around 100 µm due to the smoothness of the material.

3.2.4. Atmosphere and Time Gating Measurement

All of the LIBS analyses were performed under ambient air added to a constant argon purge (13 mPsi), yielding enhancement in signal particularly for emissions in the deep UV (190 to 300 nm). Here, concerning the temporal conditions of the plasma analysis, the delay time was fixed as follows: the beginning of the acquisition of the LIBS emission was 400 ns and the acquisition time window was fixed to 1 ms. Then, in case of molecular recombination during the plasma emission (such as CaF or AlO), the large bands could be detected [31,61]. For the LIBS acquisition parameters, no file can be downloaded directly, but the information is available on the panel control of the Profile Builder interface.

3.3. LIBS Spectra Analysis

The reading and the interpretation of the LIBS spectra can be done using the Profile Builder for the recognition of the detected element emission lines. It is possible to explore the spectra and to normalize the spectra to the total area if necessary (in the case of a change in the ablated volume, point by point), and it is possible to obtain the net intensity under the peaks to provide a calibration curve directly using the Profile Builder software after defining standards. All the detected and non-detected elements can be downloaded in a .csv format if necessary. Various different software programs can be used to treat the spectra or to establish calibration curves [36,43]. In the following for example, we use SpectraGryph (http://spectroscopy.ninja accessed on 1 May 2021).

3.3.1. Detected Elements

The major elements detected by the handheld LIBS tool for all the minerals mainly corresponded to Al, Si, O, Mg, Ca, Li, Na, K, and Fe (Figure 3). Minor and trace elements depending on the mineral origins, such as Be, Sr, Ba, Cs, Sn, Cs, Ta, W, etc., were also identified in numerous LIBS spectra provided in this database. The main trace elements detected in these Li-rich materials are reported in the LIBS_database_file.csv. The reference emission lines can also be obtained online from various websites and, for example, from the NIST LIBS database (https://physics.nist.gov/PhysRefData/ASD/LIBS/libsform.html accessed on 1 May 2021).

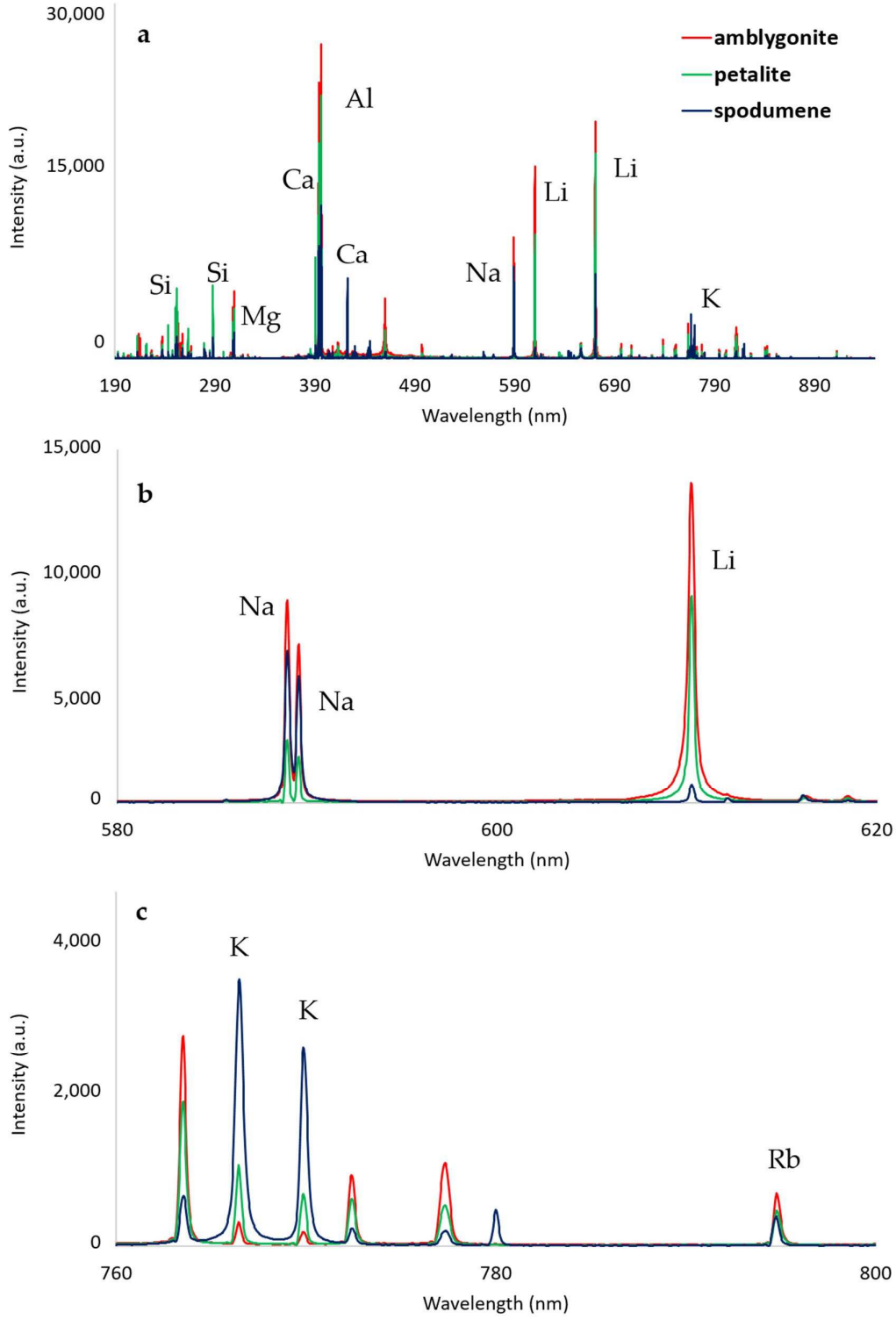

Figure 3. LIBS spectra obtained from different Li-rich minerals: amblygonite (4371-ambly-PF-M-0031-A2_2_20191), petalite (4183-peta-LB-R-0013-A_3_2019112), and spodumene (Boa-RS-Spo-M_20190417_043329_PM). (a) Spectra in the entire wavelength range; (b) zoomed image of the Na doublet and Li emission lines; (c) zoomed image of the K and Rb emissions lines from the VNIR. The major element emission lines are shown on the spectra; the LIBS spectra are not normalized.

3.3.2. Spectra Treatment

For the LIBS spectra treatment, a qualitative comparison between different samples can be performed by looking at the peak areas under the selected emission with an individual baseline. The relative standard deviations obtained for the Li emission lines were approximately 18% for the Li minerals and 13% for the pellets. These values can be linked to the heterogeneity of the rocks, to their granulometry regarding the beam size of the laser (approximately 50 µm), and to a possible change in the ablated volume point by point. Ratios between different emission lines can also be proposed for comparison. A careful selection of the emission spectra for such a treatment is necessary to avoid any overlapping of other emission lines or saturation of the detector. The use of the mean value obtained from various spectra is preferred in order to provide a bulk vision of the elements detected in the minerals. When bulk analysis is available or if the concentration of the element in the sample can be obtained, a calibration curve can be established to obtain the contents of unknown samples, associating each analyzed area with its element content [43]. Normalization of the LIBS spectra (for example, normalization to the entire spectra or using the standard normal variate (SNV) method) can also be performed if the matrices are very different from each other in terms of chemistry or hardness [17,40]. Multivariate techniques can also be applied to the LIBS spectra to classify the samples or to obtain calibration curves of the different elements [62–64].

4. User Notes

Further notes on the usage of the dataset that will help other researchers to quickly get their hands on the dataset and work with it.

Author Contributions

Conceptualization, C.F. and J.C.; methodology, C.F., N.E.O., and J.C.; validation, C.F. and N.E.O.; formal analysis, N.E.O., J.C.-F., and C.F.; investigation, C.F.; resources, A.L., M.P., F.Kaestner, N.K., F.Koerting., J.C.-F., R.L., T.M., D.B., and J.M.; data curation, C.F. and N.E.O.; writing—original draft preparation, C.F.; writing—review and editing, C.F., N.E.O., F.Koerting)., and J.C.-F.; visualization, C.F.; supervision, C.F. and J.C.; project administration, J.C.; funding acquisition, J.C. All authors have read and agreed to the published version of the manuscript. Please turn to the CRediT taxonomy for the term explanation. Authorship must be

limited to those who have contributed substantially to the work reported. All authors have read and agreed to the published version of the manuscript.

Funding

This research was funded by the ERA-MIN/0001/2017–LIGHTS project. The work was also supported by Portuguese National Funds through the FCT– Fundação para a Ciência e a Tecnologia, I.P., project UIDB/04683/2020-ICT (Institute of Earth Sciences). Joana Cardoso-Fernandes and Filipa Dias are financially supported within the compass of their respective Ph.D. Theses, ref. SFRH/BD/136108/2018 and ref. 2020.05534.BD, by national funds from MCTES through FCT, and co-financed by the European Social Fund (ESF) through POCH–Programa Operacional Capital Humano–and NORTE 2020 regional program.

Institutional Review Board Statement

Not applicable.

Informed Consent Statement

Not applicable.

Data Availability Statement

All of the files mentioned on this study can be found in open access at the following address: https://doi.org/10.24396/ORDAR-65.

Acknowledgments

We acknowledge Robert Linnen for his synthetized glasses and also Tania Martin and Marc Binnen for their mineral investigation. We thank the Suffel Collection, department of Ontario, for providing some of the Li-rich minerals. We acknowledge SciAps Company for technical support. Pierre-Yves Arnould is acknowledged for his technical support for ORDaR (OTELo Research Data Repository) website.

Conflicts of Interest

The authors declare no conflict of interest. The funders had no role in the design of the study; in the collection, analyses, or interpretation of data; in the writing of the manuscript, or in the decision to publish the results.

References

1. Radziemski, L.J. From LASER to LIBS, the path of technology development. *Spectrochim. Acta Part B At. Spectrosc.* **2002**, *57*, 1109– 1113, doi:10.1016/s0584-8547(02)00052-6.
2. Cremers, D.A.; Radziemski, L.J. History and fundamentals of LIBS. In *Laser Induced Breakdown Spectroscopy: Fundamentals and Applications*; Cambridge University Press: Cambridge, UK, 2006; pp. 9–16.
3. Harmon, R.S.; De Lucia, F.C.; McManus, C.E.; McMillan, N.J.; Jenkins, T.F.; Walsh, M.E.; Miziolek, A. Laser-induced breakdown spectroscopy—An emerging chemical sensor technology for real-time field-portable, geochemical, mineralogical, and environmental applications. *Appl. Geochem.* **2006**, *21*, 730–747, doi:10.1016/j.apgeochem.2006.02.003.
4. Alvey, D.C.; Morton, K.; Harmon, R.S.; Gottfried, J.L.; Remus, J.J.; Collins, L.M.; Wise, M.A. Laser-induced breakdown spectroscopy-based geochemical fingerprinting for the rapid analysis and discrimination of minerals: The example of garnet. *Appl. Opt.* **2010**, *49*, C168–C180, doi:10.1364/ao.49.00c168.
5. Rossi, M.; Dell'Aglio, M.; De Giacomo, A.; Gaudiuso, R.; Senesi, G.S.; de Pascale, O.; Capitelli, F.; Nestola, F.; Ghiara, M.R. Multimethodological investigation of kunzite, hiddenite, alexandrite, elbaite and topaz, based on laser-induced breakdown spectroscopy and conventional analytical techniques for supporting mineralogical characterization. *Phys. Chem. Miner.* **2013**, *41*, 127– 140, doi:10.1007/s00269-013-0631-3.
6. Díaz, D.; Hahn, D.W.; Molina, A. Quantification of gold and silver in minerals by laser-induced breakdown spectroscopy. *Spectrochim. Acta Part B At. Spectrosc.* **2017**, *136*, 106–115, doi:10.1016/j.sab.2017.08.008.
7. Castello, M.; Constantin, M.; Laflamme, M. Measurements of Gold in Ores by LIBS.; Quebec City, 23 August 2017. Available online: https://numerique.banq.qc.ca/patrimoine/details/52327/3081324 (accessed on 21 June 2021)

8. Harhira, A.; Bouchard, P.; Rifai, K.; Haddad, J.E.; Sabsabi, M.; Blouin, A.; Laflamme, M. Advanced La-ser-Induced Breakdown Spectroscopy (LIBS) Sensor for Gold Mining. 2017. Available online: https://nrc-publications.canada.ca/eng/view/ft/?id=e302005a-66d5-4a1e-921d-d2cdb0ba0e77 (accessed on 1 April 2021)

9. McMillan, N.J.; Curry, J.; Dutrow, B.L.; Henry, D.J. Identification of the Host Lithology of Tourmaline Using Laser-Induced Breakdown Spectroscopy for Application in Sediment Provenance and Mineral Exploration. *Can. Miner.* **2018**, *56*, 393–410, doi:10.3749/canmin.1800004.

10. Rifai, K.; Doucet, F.; Özcan, L.; Vidal, F. LIBS core imaging at kHz speed: Paving the way for real-time geochemical applications. *Spectrochim. Acta Part B At. Spectrosc.* **2018**, *150*, 43–48, doi:10.1016/j.sab.2018.10.007.

11. Fabre, C.; Devismes, D.; Moncayo, S.; Pelascini, F.; Trichard, F.; Lecomte, A.; Bousquet, B.; Cauzid, J.; Motto-Ros, V. Elemental imaging by laser-induced breakdown spectroscopy for the geological characterization of minerals. *J. Anal. At. Spectrom.* **2018**, *33*, 1345–1353, doi:10.1039/c8ja00048d.

12. Jolivet, L.; Leprince, M.; Moncayo, S.; Sorbier, L.; Lienemann, C.-P.; Motto-Ros, V. Review of the recent advances and applications of LIBS-based imaging. *Spectrochim. Acta Part B At. Spectrosc.* **2019**, *151*, 41–53, doi:10.1016/j.sab.2018.11.008.

13. Bi, Y.; Yan, M.; Dong, X.; Li, Z.; Zhang, Y.; Li, Y. Recognition of 25 natural geological samples using a modified correlation analysis method and laser-induced breakdown spectroscopic data. *Optics* **2018**, *158*, 1058–1062, doi:10.1016/j.ijleo.2017.12.167.

14. McManus, C.E.; Dowe, J.; McMillan, N.J. Quantagenetics® analysis of laser-induced breakdown spectroscopic data: Rapid and accurate authentication of materials. *Spectrochim. Acta Part B At. Spectrosc.* **2018**, *145*, 79–85, doi:10.1016/j.sab.2018.04.010.

15. Busser, B.; Moncayo, S.; Coll, J.-L.; Sancey, L.; Motto-Ros, V. Elemental imaging using laser-induced breakdown spectroscopy: A new and promising approach for biological and medical applications. *Coord. Chem. Rev.* **2018**, *358*, 70–79, doi:10.1016/j.ccr.2017.12.006.

16. Akhmetzhanov, T.F.; Labutin, T.A.; Zaytsev, S.M.; Drozdova, A.N.; Popov, A.M. Determination of the Mn/Fe Ratio in Ferromanganese Nodules Using Calibration-Free Laser-Induced Breakdown Spectroscopy. *Opt. Spectrosc.* **2019**, *126*, 316–320, doi:10.1134/s0030400x19040027.

17. Fabre, C. Advances in Laser-Induced Breakdown Spectroscopy analysis for geology: A critical review. *Spectrochim. Acta Part B At. Spectrosc.* **2020**, *166*, 105799, doi:10.1016/j.sab.2020.105799.

18. Lawley, C.J.; Somers, A.M.; Kjarsgaard, B.A. Rapid geochemical imaging of rocks and minerals with handheld laser induced breakdown spectroscopy (LIBS). *J. Geochem. Explor.* **2021**, *222*, 106694, doi:10.1016/j.gexplo.2020.106694.

19. Vasavada, A.R.; Grotzinger, J.P.; Arvidson, R.E.; Calef, F.J.; Crisp, J.; Gupta, S.; A Hurowitz, J.; Mangold, N.; Maurice, S.; E Schmidt, M.; et al. Overview of the Mars Science Laboratory mission: Bradbury Landing to Yellowknife Bay and beyond. *J. Geophys. Res. Planets* **2014**, *119*, 1134–1161, doi:10.1002/2014je004622.

20. Forni, O.; Gaft, M.; Toplis, M.J.; Clegg, S.M.; Maurice, S.; Wiens, R.C.; Mangold, N.; Gasnault, O.; Sautter, V.; Le Mouélic, S.; et al. First detection of fluorine on Mars: Implications for Gale Crater's geochemistry. *Geophys. Res. Lett.* **2015**, *42*, 1020–1028, doi:10.1002/2014gl062742.

21. Cousin, A.; Meslin, P.; Wiens, R.; Rapin, W.; Mangold, N.; Fabre, C.; Gasnault, O.; Forni, O.; Tokar, R.; Ollila, A.; et al. Compositions of coarse and fine particles in martian soils at gale: A window into the production of soils. *Icarus* **2015**, *249*, 22–42, doi:10.1016/j.icarus.2014.04.052.

22. Payré, V.; Fabre, C.; Sautter, V.; Cousin, A.; Mangold, N.; Le Deit, L.; Forni, O.; Goetz, W.; Wiens, R.C.; Gasnault, O.; et al. Copper enrichments in the Kimberley formation in Gale crater, Mars: Evidence for a Cu deposit at the source. *Icarus* **2019**, *321*, 736–751, doi:10.1016/j.icarus.2018.12.015.

23. Wiens, R.C.; Sylvestre S. and the MSL Science Team Maurice; Reitz G. DLR Collaborator (MSL Science Team) ChemCam: Chemostratigraphy by the First Mars Microprobe. *Elements* **2015**, *11*, 33–38, doi:10.2113/gselements.11.1.33.

24. Fabre, C.; Bousquet, B. De chemcam à supercam: L'apport de la LIBS pour le spatial. *Photon* **2020**, 38–41, doi:10.1051/photon/202010338.

25. Maurice, S.; Wiens, R.C.; Bernardi, P.; Caïs, P.; Robinson, S.; Nelson, T.; Gasnault, O.; Reess, J.-M.; Deleuze, M.; Rull, F.; et al. The SuperCam Instrument Suite on the Mars 2020 Rover: Science Objectives and Mast-Unit Description. *Space Sci. Rev.* **2021**, *217*:47, doi:10.1007/s11214-021-00807-w.

26. Wiens, R.C.; Maurice, S.; Robinson, S.H.; Nelson, A.E.; Cais, P.; Bernardi, P.; Newell, R.T.; Clegg, S.; Sharma, S.K.; Storms, S.; et al. The SuperCam Instrument Suite on the NASA Mars 2020 Rover: Body Unit and Combined System Tests. *Space Sci. Rev.* **2021**, *217:4* doi:10.1007/s11214-020-00777-5.

27. Cuñat, J.; Palanco, S.; Carrasco, F.; Simón, M.D.; Laserna, J.J. Portable instrument and analytical method using laser-induced breakdown spectrometry for in situ characterization of speleothems in karstic caves. *J. Anal. At. Spectrom.* **2005**, *20*, 295–300, doi:10.1039/b417161f.

28. Rakovský, J.; Čermák, P.; Musset, O.; Veis, P. A review of the development of portable laser induced breakdown spectroscopy and its applications. *Spectrochim. Acta Part B At. Spectrosc.* **2014**, *101*, 269–287, doi:10.1016/j.sab.2014.09.015.

29. Connors, B.; Somers, A.; Day, D. Application of Handheld Laser-Induced Breakdown Spectroscopy (LIBS) to Geochemical Analysis. *Appl. Spectrosc.* **2016**, *70*, 810–815, doi:10.1177/0003702816638247.

30. Bennett, B.N.; Martin, M.Z.; Leonard, D.N.; Garlea, E. Calibration curves for commercial copper and aluminum alloys using handheld laser-induced breakdown spectroscopy. *Appl. Phys. A* **2018**, *124*, 42, doi:10.1007/s00340-018-6909-x.

31. Foucaud, Y.; Fabre, C.; Demeusy, B.; Filippova, I.; Filippov, L. Optimisation of fast quantification of fluorine content using handheld laser induced breakdown spectroscopy. *Spectrochim. Acta Part B At. Spectrosc.* **2019**, *158*, 105628, doi:10.1016/j.sab.2019.05.017.

32. Harmon, R.S.; Lawley, C.J.; Watts, J.; Harraden, C.L.; Somers, A.M.; Hark, R.R. Laser-Induced Breakdown Spectroscopy—An Emerging Analytical Tool for Mineral Exploration. *Minerals* **2019**, *9*, 718, doi:10.3390/min9120718.

33. Pochon, A.; Desaulty, A.-M.; Bailly, L. Handheld laser-induced breakdown spectroscopy (LIBS) as a fast and easy method to trace gold. *J. Anal. At. Spectrom.* **2020**, *35*, 254–264, doi:10.1039/c9ja00437h.

34. Senesi, G.S.; Harmon, R.S.; Hark, R.R. Field-portable and handheld laser-induced breakdown spectroscopy: Historical review, current status and future prospects. *Spectrochim. Acta Part B At. Spectrosc.* **2021**, *175*, 106013, doi:10.1016/j.sab.2020.106013.

35. Colao, F.; Fantoni, R.; Lazić, V.; Spizzichino, V. Laser-induced breakdown spectroscopy for semi-quantitative and quantitative analyses of artworks—application on multi-layered ceramics and copper based alloys. *Spectrochim. Acta Part B At. Spectrosc.* **2002**, *57*, 1219–1234, doi:10.1016/s0584-8547(02)00054-x.

36. El Haddad, J.; Canioni, L.; Bousquet, B. Good practices in LIBS analysis: Review and advices. *Spectrochim. Acta Part B At. Spectrosc.* **2014**, *101*, 171–182, doi:10.1016/j.sab.2014.08.039.

37. Shi, Q.; Niu, G.; Lin, Q.; Xu, T.; Li, F.; Duan, Y. Quantitative analysis of sedimentary rocks using laser-induced breakdown spectroscopy: comparison of support vector regression and partial least squares regression chemometric methods. *J. Anal. At. Spectrom.* **2015**, *30*, 2384–2393, doi:10.1039/c5ja00255a.

38. Ahmad, N.; Ahmed, R.; Umar, Z.A.; Liaqat, U.; Manzoor, U.; Baig, M.A. Qualitative and quantitative analyses of copper ores collected from Baluchistan, Pakistan using LIBS and LA-TOF-MS. *Appl. Phys. A* **2018**, *124*, 160, doi:10.1007/s00340-018-7032-8.

39. Maaza, M.; Mothudi, B.M. Laser-Induced Breakdown Spectroscopy (LIBS) on Geological Samples: Compositional Differentiation and Relative Hardness Quantification. Master Thesis, University of South Africa, Pretoria, South Africa, 2018.

40. Guezenoc, J.; Gallet-Budynek, A.; Bousquet, B. Critical review and advices on spectral-based normalization methods for LIBS quantitative analysis. *Spectrochim. Acta Part B At. Spectrosc.* **2019**, *160*, 105688, doi:10.1016/j.sab.2019.105688.

41. Sobron, P. Non-Linear Methods for Quantitative Elemental Analysis and Mineral Classification Using Laser-Induced Breakdown Spectroscopy (LIBS) 2019, https://patents.google.com/patent/US20190079019A1/en.

42. Syvilay, D.; Guezenoc, J.; Bousquet, B. Guideline for increasing the analysis quality in laser-induced breakdown spectroscopy. *Spectrochim. Acta Part B At. Spectrosc.* **2019**, *161*, 105696, doi:10.1016/j.sab.2019.105696.

43. Duponchel, L.; Bousquet, B.; Pelascini, F.; Motto-Ros, V. Should we prefer inverse models in quantitative LIBS analysis? *J. Anal. At. Spectrom.* **2020**, *35*, 794–803, doi:10.1039/c9ja00435a.

44. Rifai, K.; Paradis, M.-C.M.; Swierczek, Z.; Doucet, F.; Özcan, L.; Fayad, A.; Li, J.; Vidal, F. Emergences of New Technology for Ultrafast Automated Mineral Phase Identification

and Quantitative Analysis Using the CORIOSITY Laser-Induced Breakdown Spectroscopy (LIBS) System. *Minerals* **2020**, *10*, 918, doi:10.3390/min10100918.

45. Rifai, K.; Özcan, L.-Ç.; Doucet, F.R.; Rhoderick, K.; Vidal, F. Ultrafast Elemental Mapping of Platinum Group Elements and Mineral Identification in Platinum-Palladium Ore Using Laser Induced Breakdown Spectroscopy. *Minerals* **2020**, *10*, 207, doi:10.3390/min10030207.

46. Cardoso-Fernandes, J.; Silva, J.; Dias, F.; Lima, A.; Teodoro, A.; Barrès, O.; Cauzid, J.; Perrotta, M.; Roda-Robles, E.; Ribeiro, M. Tools for Remote Exploration: A Lithium (Li) Dedicated Spectral Library of the Fregeneda–Almendra Aplite–Pegmatite Field. *Data* **2021**, *6*, 33, doi:10.3390/data6030033.

47. Andrade, J.M.; Cristoforetti, G.; Legnaioli, S.; Lorenzetti, G.; Palleschi, V.; Shaltout, A. Classical univariate calibration and partial least squares for quantitative analysis of brass samples by laser-induced breakdown spectroscopy. *Spectrochim. Acta Part B At. Spectrosc.* **2010**, *65*, 658–663, doi:10.1016/j.sab.2010.04.008.

48. Wiens, R.; Maurice, S.; Lasue, J.; Forni, O.; Anderson, R.; Clegg, S.; Bender, S.; Blaney, D.; Barraclough, B.; Cousin, A.; et al. Preflight calibration and initial data processing for the ChemCam laser-induced breakdown spectroscopy instrument on the Mars Science Laboratory rover. *Spectrochim. Acta Part B At. Spectrosc.* **2013**, *82*, 1–27, doi:10.1016/j.sab.2013.02.003.

49. Fabre, C.; Cousin, A.; Wiens, R.; Ollila, A.; Gasnault, O.; Maurice, S.; Sautter, V.; Forni, O.; Lasue, J.; Tokar, R.; et al. In situ calibration using univariate analyses based on the onboard ChemCam targets: First prediction of Martian rock and soil compositions. *Spectrochim. Acta Part B At. Spectrosc.* **2014**, *99*, 34–51, doi:10.1016/j.sab.2014.03.014.

50. Payré, V.; Fabre, C.; Cousin, A.; Sautter, V.; Wiens, R.C.; Forni, O.; Gasnault, O.; Mangold, N.; Meslin, P.-Y.; Lasue, J.; et al. Alkali trace elements in Gale crater, Mars, with ChemCam: Calibration update and geological implications. *J. Geophys. Res. Planets* **2017**, *122*, 650–679, doi:10.1002/2016je005201.

51. Guezenoc, J.; Payré, V.; Fabre, C.; Syvilay, D.; Cousin, A.; Gallet-Budynek, A.; Bousquet, B. Variable selection in laser-induced breakdown spectroscopy assisted by multivariate analysis: An alternative to multi-peak fitting. *Spectrochim. Acta Part B At. Spectrosc.* **2019**, *152*, 6–13, doi:10.1016/j.sab.2018.12.001.

52. Gamela, R.R.; Costa, V.C.; Babos, D.V.; Araújo, A.S.; Pereira-Filho, E.R. Direct Determination of Ca, K, and Mg in Cocoa Beans by Laser-Induced Breakdown Spectroscopy (LIBS): Evaluation of Three Univariate Calibration Strategies for Matrix Matching. *Food Anal. Methods* **2020**, *13*, 1017–1026, doi:10.1007/s12161-020-01722-6.

53. Grew, E.S. The Minerals of Lithium. *Elements* **2020**, *16*, 235–240, doi:10.2138/gselements.16.4.235.

54. Cardoso-Fernandes, J.; Silva, J.; Lima, A.; Teodoro, A.C.; Perrotta, M.; Cauzid, J.; Roda-Robles, E.; Ribeiro, M. dos A. Reflectance Spectroscopy to Validate Remote Sensing Data/Algorithms for Satellite-Based Lithium (Li) Exploration (Central East Portugal). In Proceedings of the Earth Resources and Environmental Remote Sensing/GIS Applications XI, online conference, September 2020; Schulz, K., Nikolakopoulos, K.G., Michel, U., Eds.; SPIE: Bellingham, WA, USA, 2020; p. 19.

55. Cardoso-Fernandes, J.; Silva, J.; Lima, A.; Teodoro, A.C.; Perrotta, M.; Cauzid, J.; Roda-Robles, E. Characterization of Lithium (Li) Minerals from the Fregeneda-Almendra Region through Laboratory Spectral Measurements: A Comparative Study. In Proceedings of the Earth Resources and Environmental Remote Sensing/GIS Applications XI, online conference, September 2020; Schulz, K., Nikolakopoulos, K.G., Michel, U., Eds.; SPIE: Bellingham, WA, USA, 2020; p. 20.

56. Cousin, A.; Sautter, V.; Fabre, C.; Maurice, S.; Wiens, R.C. Textural and modal analyses of picritic basalts with ChemCam Laser-Induced Breakdown Spectroscopy. *J. Geophys. Res. Space Phys.* **2012**, *117*, 117, doi:10.1029/2012je004132.

57. Sweetapple, M.T.; Tassios, S. Laser-induced breakdown spectroscopy (LIBS) as a tool for in situ mapping and textural interpretation of lithium in pegmatite minerals. *Am. Miner.* **2015**, *100*, 2141–2151, doi:10.2138/am-2015-5165.

58. Linnen, R.L.; Van Lichtervelde, M.; Černý, P. Granitic Pegmatites as Sources of Strategic Metals. *Elements* **2012**, *8*, 275–280, doi:10.2113/gselements.8.4.275.

59. Popov, A.M.; Zaytsev, S.M.; Seliverstova, I.V.; Zakuskin, A.; Labutin, T.A. Matrix effects on laser-induced plasma parameters for soils and ores. *Spectrochim. Acta Part B At. Spectrosc.* **2018**, *148*, 205–210, doi:10.1016/j.sab.2018.07.005.

60. Maurice, S.; Wiens, R.C.; Saccoccio, M.; Barraclough, B.; Gasnault, O.; Forni, O.; Mangold, N.; Baratoux, D.; Bender, S.; Berger, G.; et al. The ChemCam Instrument Suite

on the Mars Science Laboratory (MSL) Rover: Science Objectives and Mast Unit Descriptn. *Space Sci. Rev.* **2012**, *170*, 95–166, doi:10.1007/s11214-012-9912-2.

61. Quarles, C.D.; Gonzalez, J.J.; East, L.J.; Yoo, J.H.; Morey, M.S.; Russo, R.E. Fluorine analysis using Laser Induced Breakdown Spectroscopy (LIBS). *J. Anal. At. Spectrom.* **2014**, *29*, 1238–1242, doi:10.1039/c4ja00061g.

62. McMillan, N.J.; Rees, S.; Kochelek, K.; E McManus, C. Geological Applications of Laser-Induced Breakdown Spectroscopy. *Geostand. Geoanalytical Res.* **2014**, *38*, 329–343, doi:10.1111/j.1751-908x.2014.00308.x.

63. Kochelek, K.A.; McMillan, N.J.; McManus, C.E.; Daniel, D.L. Provenance determination of sapphires and rubies using laserinduced breakdown spectroscopy and multivariate analysis. *Am. Miner.* **2015**, *100*, 1921–1931, doi:10.2138/am-2015-5185.

64. Farnsworth-Pinkerton, S.; McMillan, N.J.; Dutrow, B.L.; Henry, D.J. Provenance of detrital tourmalines from Proterozoic metasedimentary rocks in the Picuris Mountains, New Mexico, using Laser-Induced Breakdown Spectroscopy. *J. Geosci.* **2018**, *63*, 193–198, doi:10.3190/jgeosci.261

III.2. Interpretation of the reflectance spectra of Lithium (Li) minerals and pegmatites: a case study for mineralogical and lithological identification in the Fregeneda-Almendra area

Joana Cardoso-Fernandes, João Silva, Mônica Perrotta, Alexandre Lima, Ana C. Teodoro, Maria Anjos Ribeiro, Filipa Dias, Odile Barrès, Jean Cauzid, Encarnación Roda-Robles

Remote Sensing, 2021, **13 (18)**, 3688.

Abstract: Reflectance spectroscopy has been used to identify several deposit types. However, applications concerning lithium (Li)-pegmatites are still scarce. Reflectance spectroscopic studies complemented by microscopic and geochemical studies were employed in the Fregeneda–Almendra (Spain–Portugal) pegmatite field to analyze the spectral behavior of Li-minerals and field lithologies. The spectral similarity of the target class (Li-pegmatites) with other elements was also evaluated. Lepidolite was discriminated from other white micas and the remaining Li-minerals. No diagnostic feature of petalite and spodumene was identified, since their spectral curves are dominated by clays. Their presence was corroborated (by complementary techniques) in petalite relics and completely replaced crystals, although the clay-related absorption depths decrease with Li content. This implies that clays can be used as pathfinders only in areas where argillic alteration is not prevalent. All sampled lithologies present similar water and/or hydroxide features. The overall mineral assemblage is very distinct, with lepidolite, cookeite, and orthoclase exclusively identified in Li-pegmatite (being these minerals crucial targets for Li-pegmatite discrimination in real-life applications), while chlorite and biotite can occur in the remaining lithologies. Satellite data can be used to discriminate Li-pegmatites due to distinct reflectance magnitude and mineral assemblages, higher absorptions depths, and distinct Al–OH wavelength position. The potential use of multi- and hyperspectral data was evaluated; the main limitations and advantages were discussed. These new insights on the spectral behavior of Li-minerals and pegmatites may aid in new Li-pegmatite discoveries around the world.

Keywords: Remote sensing; reflectance spectroscopy; hyperspectral; geological exploration; spectral library; absorption features; spectral mineralogy; pegmatite; lithium

1. Introduction

Reflectance spectroscopy studies have shown a relevant economic potential to mineral exploration, either through the direct characterization and identification of the mineralogy of the deposits or through the identification of hydrothermal alteration zonation as a proxy to target mineralizations such as (i) porphyry copper deposits [1], (ii) volcanogenic massive sulfide (VMS) deposits [2,3], (iii) rare-earth element (REE) deposits [4,5], (iv) zinc-lead-silver deposits [6], (v) iron oxide-copper-gold (IOCG) deposits [7], and (vi) gold deposits [8].

Similar approaches have been applied to distinct deposit types like pegmatites that have a high economic interest for (i) ceramic components such as quartz and feldspar; (ii) rare, critical metals such as lithium (Li), tin (Sn), tantalum (Ta), cesium (Cs), beryllium (Be), and rubidium (Rb); as well as for (iii) colored gemstones [9-14]. Zhang et al. [15] developed a systematic spectroscopic characterization of tourmalines from the Koktokay No.3 pegmatite (northwestern China), the pegmatite contact wall zone, and from the host rocks, which included several methods, including reflectance spectroscopy. These methods, coupled with mineral chemistry analyses, allowed to better understand the magmatic to hydrothermal evolution of the pegmatite and the fluid interaction with the pegmatite and the country rocks. Carrino et al. [16] correlated an electron probe microanalysis (EPMA) with the reflectance spectra of elbaite (Li-tourmaline) gemstones from pegmatites of the Seridó Pegmatite Province (Northeastern Brazil). In the end, the application of statistical techniques, such as principal component analysis (PCA), discriminated tourmalines of different compositions based on the reflectance spectra. Bocchio et al. [17] used geochemical and spectroscopic techniques such as reflectance spectroscopy to achieve a gemological characterization of aquamarine (blue beryl) samples from granitic pegmatites of the Masino-Bregaglia Massif, Central Alps, Italy. Araújo Neto et al. [18] undertook a similar but more complete study to characterize emerald (green beryl) crystals from granitic aplite and pegmatite veins in the Paraná deposit (Northeastern Brazil), using mineral chemistry, absorption and reflectance spectroscopy, and thermal analysis. Silva et al. [19] explored the potential of reflectance spectroscopy to characterize the mineral phases of the Alto do Giz pegmatite in the Seridó Pegmatite Province (Northeastern Brazil). To complement the interpretation of the reflectance spectra, scanning electron microscopy (SEM) and X-ray diffraction (XRD) were used. Despite the intense kaolinization, hydrothermal-metasomatic and supergene alteration overprinting the rock bulk mineralogy, reflectance spectroscopy proved to be capable of defining the internal zonation of the pegmatite.

Although the literature shows that reflectance spectroscopy is successfully applicable to pegmatite deposits, study applications are still scarce. Moreover, this technique can be of considerable importance if applied to vector pegmatites with economic potential for rare and strategic metals like Li. The increasing economic significance of Li triggered several satellite-based exploration works that allowed identifying Li-pegmatites correctly worldwide and that lead to the discovery of pegmatite-hosted Li deposits [20-24]. Costa et al. [25] were the first authors to apply reflectance spectroscopy exclusively for Li-mineral identification and associated weathering alteration minerals in the Jequitinhonha region (Brazil). Despite showing promising results for minerals like spodumene or lepidolite, it was not possible to identify petalite and zinnwaldite through their spectral signatures. Moreover, the supergene alteration minerals seem to be related to the semi-arid climate of the region [25], which differs from Europe's climate conditions, highlighting the need for a similar approach in European territory.

Considering this, the study area chosen for this work is the Fregeneda–Almendra region, one of the largest European provinces in Li production [11]. In this region, the Li-bearing minerals with greater economic interest are spodumene ($LiAlSi_2O_6$; pyroxene; 8.03% Li_2O), petalite ($LiAlSi_4O_{10}$; feldspathoid; 4.5% Li_2O), and lepidolite ($K(Li,Al)_3(Si,Al)_4O_{10}(F,OH)_2$); mica; 7.7% Li_2O) [13,26,27]. This study delineated the following objectives: (i) build a spectral library dedicated to Li-bearing minerals and understand their respective spectral signatures, (ii) extend the spectral library to other lithologies that occur in the study area to enable satellite-based lithological classification, and (iii) evaluate if there can be any spectral confusion between the target class (Li-pegmatite) and other within-scene elements, as verified by Cardoso-Fernandes et al. [28]. Therefore, this research presents a complete view of the use of reflectance spectroscopy for laboratory identification of Li-bearing minerals and remote sensing mapping of Li-pegmatites, including spectral data acquired in a preliminary phase [29,30], as well as new spectral measurements and complementary geochemical, petrographic, and mineralogical studies. The combination of classical and uncommon analytical techniques allowed characterizing the mineral assemblage resulting from the alteration of petalite crystals, and the paragenesis of some of the collected rock samples. Overall, this study addresses different pertinent research questions: (i) Are Li-bearing minerals distinguishable from each other and other minerals? (ii) How can the alteration products affect the spectral signature of Li-bearing minerals? (iii) Can Li-pegmatites be spectrally discriminated from other lithologies in a supervised classification attempt? The results obtained are essential to better direct future remote sensing-based exploration studies. They provide new insights on the spectral behavior of Li-minerals and Li-pegmatites, allowing to identify

which minerals can be directly discriminated against while proposing, for the first time, relevant pathfinders to distinguish other Li-minerals, as well as Li-pegmatites. The main implications of this study may lead to new Li-pegmatite discoveries in Europe and worldwide.

2. Study Area and Field Surveys

The field surveys were conducted on the Fregeneda–Almendra aplite-pegmatite field (Figure 1), spreading from La Fregeneda (Spain) to Almendra (Portugal). The pegmatite field contains 11 different types of dikes ranging from barren to more evolved: Li, F, Sn, Rb, Nb > Ta, B, and P-enriched bodies [26,27,31]. Among the more evolved dikes, there are four types containing Li mineralization: (i) petalite-rich dikes (exploited in the Bajoca open-pit mine), (ii) spodumene-rich dikes (exploited in the Alberto open-pit mine), (iii) lepidolite-bearing dikes, and (iv) lepidolite + spodumene-bearing dikes (exploited in the Feli open-pit mine) [26,27,31]. All Li-rich pegmatite dikes are emplaced in a pre-Ordovician metasedimentary belt composed of a pelitic-sandy flysch series, Complexo Xisto-Grauváquico (CXG) [32-34]. Additionally, the fractionation degree of the pegmatite dikes increases with further distance to the syn-Variscan granitoid rocks (granites and granodiorite) of the Figueira de Castelo Rodrigo–Lumbrales Anatectic Complex [26-27,31,35-37] (Figure 1). These granitoids correspond to S-type, two-mica granites with several facies, showing distinct grain sizes (from fine to coarse-grained), and to a fine-to-medium-grained, essentially biotitic, granodiorite [36-38]. In the Fregeneda–Almendra region, there are also Ordovician phyllitic-quartzitic formations, as well as Cenozoic sedimentary deposits (Figure 1).

During the field surveys, samples were collected at several distinct field stations according to the aforementioned goals (Figure 1). To construct the Li-mineral database, petalite, spodumene, and lepidolite hand specimens were retrieved from different types of mineralized dikes either in open-pit mines or at unexploited locations. In general, spodumene was under-sampled in comparison with the other Li-minerals. To fill this gap, existing samples from Feli and Alberto mines (Figure 1), as well as from other locations in the Fregeneda–Almendra field, as part of a mineralogical collection at the University of Porto, were also included in this study, bringing the number of samples to a total of 28. Considering the future satellite-based lithological classification attempts, the various field lithologies (Li-pegmatite, metasediments, and granitoids) were also sampled to conduct further laboratory spectral analysis. The field stations included, whenever possible, several open-pit mines to ensure that the different lithologies presented large and fresh expositions to serve as possible training areas for supervised classification. These field campaigns allowed refining and improving the training

areas used in preliminary image classification attempts [28]. Additionally, some of the areas misclassified as Li-pegmatite in this preliminary classification were sampled to evaluate the degree of spectral similarity between these areas and Li-pegmatites. In the field, the exposed material in these misclassified areas was assessed, and a field description of each site was made.

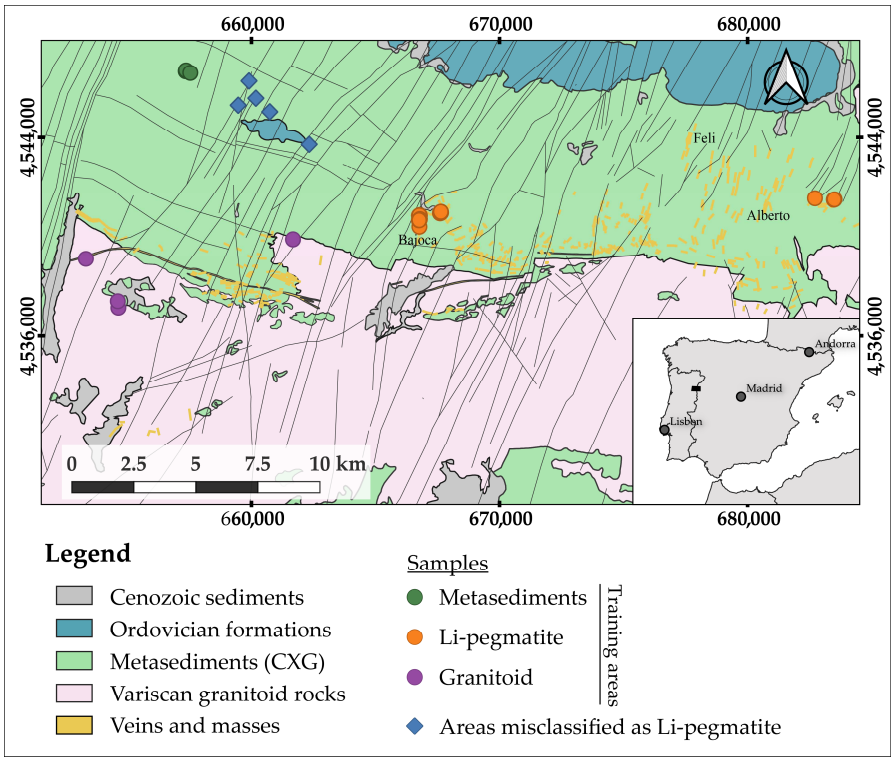

Figure 1. Location of the study area in the Iberian Peninsula and geological setting of the Fregeneda-Almendra pegmatite field (adapted from [26,39-40]). The field stations where the samples were collected are marked with a circle for the training areas (the color is dependent on the sample type) and with a diamond for the areas misclassified as Li-pegmatite using machine learning algorithms. Li-mineral specimens were also collected in Li-pegmatite sites. Map projection: Universal Transverse Mercator zone 29N from the WGS84 datum.

3. Methodology

3.1. Reflectance Spectroscopy Studies

The spectral studies were conducted in the laboratory employing two distinct spectroradiometers, both covering the spectral range between 350 and 2500 nm: (i) the ultra-high-resolution SR-6500 (Spectral Evolution, Inc.) equipment (1.5 nm @ 700 nm, 3.0 nm @ 1500 nm, and 3.8 nm @ 2100 nm) and (ii) the FieldSpec 4 (ASD, Inc.) standard resolution equipment (3.0 nm @ 700 nm, 10.0 nm @ 1400 nm, and 10.0 nm @ 2100 nm). In each case, the point spectral measurements were performed using a Contact Probe with similar

characteristics, namely an internal light source provided by a halogen bulb and spot size of 10 mm. For reflectance calibration, a Spectralon (Labsphere) plate with a maximum reflectance above 95% for the 250–2500-nm range and above 99% for the 400–1500-nm region. Small (less than 2 cm) or friable samples were analyzed over the white plate. When using either of the spectroradiometers, each measurement corresponded to an average of 40 scans. For the FieldSpec 4 equipment, four additional spectra were acquired in each analyzed spot, later averaged into a final spectrum, to increase the signal-to-noise ratio.

ASD ViewSpec Pro™ software [41] and SpectraGryph software [42] were used to individually analyze all spectra to exclude measurement errors or spectra with noticeable noise caused by vegetation fragments on the surface of the samples and for spectra averaging. Point measurements belonging to the same sample and with similar spectral behavior were averaged to aid visualization and allow fast interpretation of the spectra. The final Li-minerals spectral library contains reference data from 28 samples (five spodumene, 13 petalite, and ten lepidolite samples). Moreover, to complete the spectral studies for lithological classification, 45 samples from possible training areas were analyzed (five from CXG metasediments, 33 from distinct Li-pegmatite types, and seven from granitoid rocks), as well as 11 samples from four areas misclassified as Li-pegmatite. All samples and point measurements were photographed.

The laboratory acquired spectra were normalized through continuum removal [43] to compare the spectra obtained by both spectroradiometers and enhance the spectral absorption features. In this case, a hull quotient was calculated after automatically fitting a convex-hull to each spectrum in a Python environment using the *pysptools* library [44]. The extraction of the wavelength, depth, and other geometric parameters of the absorption features was made using SpectraGryph software and the *pysptools* library. The complete spectral library and additional information on the equipment used and spectra processing can be found in Cardoso-Fernandes et al. [45,46].

3.2. Complementary Petrographic and Geochemical Studies

Microscopic studies were conducted at the University of Porto, using a transmitted light Nikon petrographic microscope (Eclipse E 400 POL), coupled with a ZEISS Axiocam camera for both the petalite alteration products and the samples from the four areas misclassified as Li-pegmatite. Selected petalite samples with distinct degrees of alteration were crushed to quantify their Li content at Activation Laboratories Ltd. (Actlabs), ON, Canada, using the Code 8–Lithium Ore analytical package. Sample preparation and crushing were conducted at the

University of Porto using manual and automated mortar agate grinders (Retsch RM 200). Li quantification was achieved through inductively coupled plasma–optical emission spectrometry (ICP-OES) after four-acid digestion (detection limit 0.001%). Afterward, Li contents were converted to Li_2O (%) using a compound ratio of 2.1527. Mineralogical information was obtained through powder X-ray diffraction (XRD) for friable samples and through optical microscopy and Scanning Electron Microscopy with Energy Dispersive Spectroscopy (SEM-EDS) for hard rock samples. The XRD analysis was performed at the National Laboratory of Energy and Geology (LNEG, Portugal) using a Panalytical Diffractometer XPERT-PRO, equipped with a PW3050/60 goniometer, with a Theta-2Theta geometry and X-ray tube with a copper (Cu) anticathode. The tube voltage and current were set to 45 kV and 40 mA, respectively. Regarding the acquisition settings, a continuous scan mode with a scan range between 3° and 90° of 2teta, a step size of 0.0084°, and 4.960 s of counting time per step was used. The SEM-EDS studies were conducted at the University of Porto, in previously carbon-coated thin sections, using a Hitachi FlexSEM 1000 SEM coupled to a Bruker QUANTAX EDS system.

4. Results

In this section, selected spectra from the spectral library are presented, taking into account the previously designated goals. The main mineralogy inferred from the spectra is presented, but a detailed analysis spectrum per spectrum can be found in the Supplementary Materials (Tables S1–S3).

4.1. Li-Minerals Spectral Database

The spectral database was built for three distinct Li-minerals: lepidolite (Figure 2), spodumene (Figure 3), and petalite (Figure 4). For this study, monomineralic samples were preferred to rock samples to avoid the interference of other minerals. As can be seen in Figure 2, all lepidolite spectra show the white mica typical features due to the hydroxide ion (OH^-) absorption around ~1409 nm associated with the principal, sharp Al–OH absorption feature (between 2195 nm and 2205 nm) and the Al–OH secondaries (around ~2348 nm and ~2435 nm, respectively) [47,48,49]. Other white mica-related, weak absorption features located ~1537 nm, ~2002 nm, and ~2114 nm are due to OH^- and OH^- combined with lattice modes [49,50]. The depth of the water feature (~1909 nm) decreases from Figure 2 (a–c), and the slight inflection around ~1460 nm indicates that montmorillonite is also present, mixed with

white mica features [1,49]. The remaining spectra (d–k) have higher purity, allowing to characterize the lepidolite due to: (i) a peak in the red region, caused by lepidolite purple color and (ii) multiple absorption features in the visible and near-infrared (VNIR) region, together with the drop off to extreme blue observed in the raw reflectance curves (left panel of Figure 2). These features are interpreted to be related to ferric iron (Fe^{3+}) and manganese (Mn^{3+}) incorporated into the structure of lepidolite [50]. Ferrous iron (Fe^{2+}) may cause the absorption at 720 nm (Figure 2 (e)) [16,51].

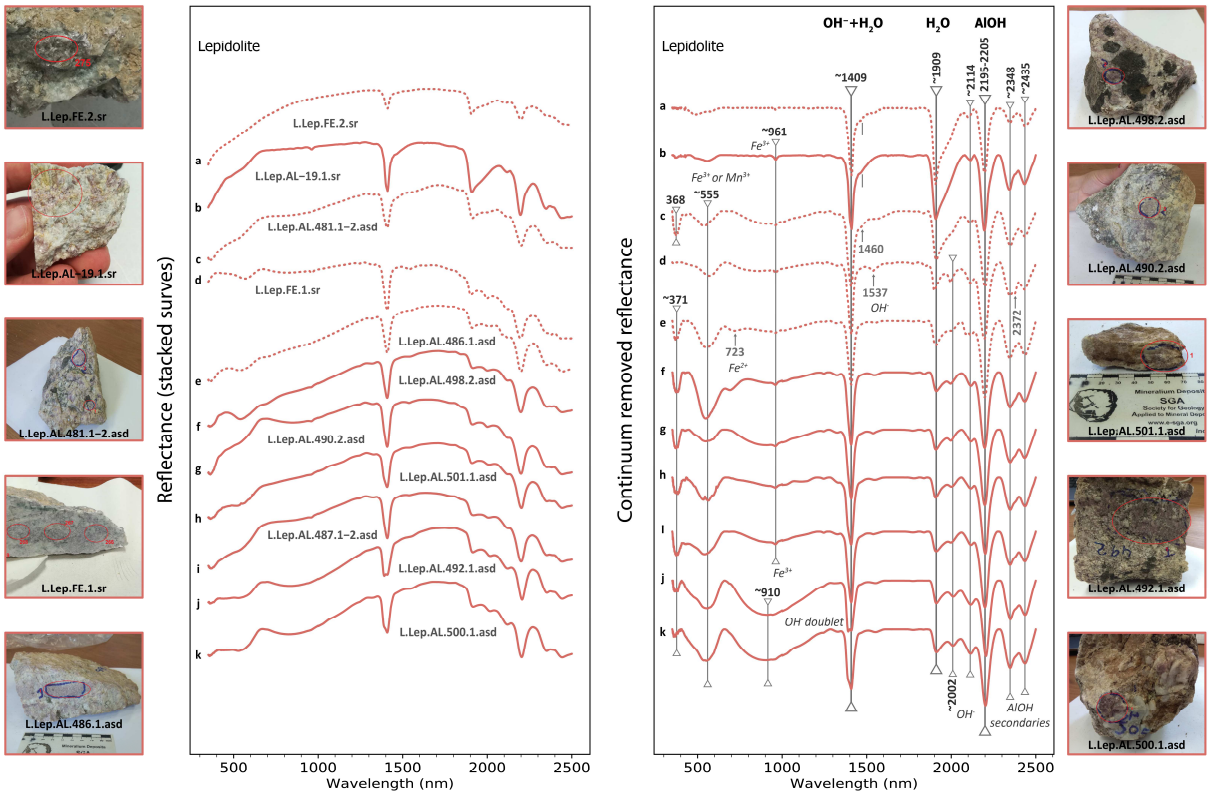

Figure 2. Spectral signature of lepidolite (Li-bearing mica): reflectance curves (to the left) and continuum removed curves (to the right). The main absorption features are highlighted, and sample photographs are provided. Each spectrum has a database code [45] providing information about the type of sample (L—Li-bearing minerals), mineralogy (Lep—lepidolite), sample provenance (FE—Feli mine and AL—Almendra), a three-digit numerical part representing the GPS code, a one- or two-digit code representing the spectra number or the averaged spectra numbers, and a reference to the spectroradiometer employed (sr—SR-6500; asd—FieldSpec 4). Dotted curves: fresh samples; full curves: samples with visible signs of weathering.

The reference spectral data of spodumene was acquired considering pure or spodumene intergrowth with quartz. Despite this, it is not expected that the associated quartz will obscure the spectral behavior of spodumene because the main diagnostic features of the former do not occur in the VNIR and shortwave infrared (SWIR) regions [47,52]. Figure 3 shows the main absorption features located around ~1414 nm, ~1910 nm, and ~2209 nm for spodumene + quartz samples and around ~1412 nm, ~1913 nm, and ~2205 nm for spodumene samples. The presence of molecular water is evidenced by the broader, asymmetric features

approximately at ~1410 nm (OH^- + H_2O) and ~1910 nm (H_2O) [48,52]. Molecular water associated with (i) higher depth of the water feature in comparison with the Al–OH fundamental absorption (around ~2200 nm) and (ii) a slight inflection around ~1467 nm are diagnostic of smectite minerals—in particular, of montmorillonite [1,48,49]. The shallow Al–OH secondaries at ~2350 nm and ~2437 nm for spodumene + quartz, and at ~2352 nm and ~2440 nm for spodumene, indicate the existence of illite mixed with montmorillonite and possibly kaolinite [48,49]. Iron incorporation (Fe^{3+} and possibly Fe^{2+}) into both spodumene and spodumene + quartz samples could be identified due to: (i) the drop off to the blue observed in the reflectance curves (left panel of Figure 3) [50] and (ii) a slight inflection around ~2240 nm related with the Fe-OH bond [49] (Figure 3 (a–h)). Spectra h–k show additional features diagnostic of kaolinite, such as (i) a small inflection around ~2165 nm and (ii) the presence of an Al–OH triplet at ~2312, ~2350, and ~2380 nm [8,48,49,53].

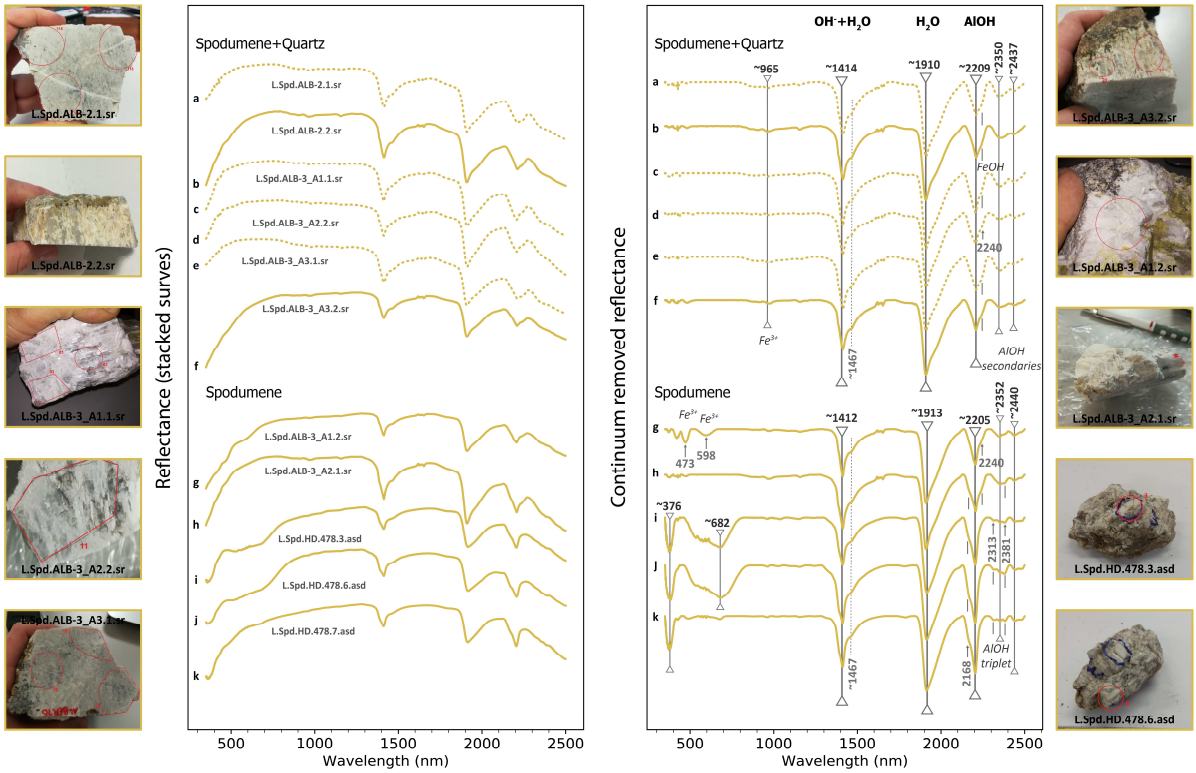

Figure 3. Spectral signature of spodumene (a Li-bearing pyroxene): reflectance curves (to the left) and continuum removed curves (to the right). The main absorption features are highlighted, and sample photographs are provided. Dotted curves: fresh samples; full curves: samples with visible signs of weathering. Each spectrum has a database code [45] providing information about the type of sample (L—Li-bearing minerals), mineralogy (Spd—spodumene), sample provenance (ALB—Alberto mine and HD—Hinojosa de Duero), a three-digit numerical part representing the GPS code, a one- or two-digit code representing the spectra number or the averaged spectra numbers, and a reference to the spectroradiometer employed (sr—SR-6500; asd—FieldSpec 4).

Most petalite spectra (Figure 4) are very similar to spodumene, showing the same main absorptions (Figure 4 (a–q)). Montmorillonite is identified in all samples by the broad,

asymmetric, and acute absorptions around ~1413 nm and ~1911 nm, associated with the Al–OH feature at ~2206 nm [48,49], shallower than the ~1911 nm one, and the slight inflection around ~1467 nm [1,49]. It is the sole mineral identified in spectra a–c, e, and o–q (Figure 4). Others (d and g–n) show additional shallow Al–OH secondary absorptions at ~2356 nm and ~2445 nm, indicating the mixture with illite [48,49]. The presence of the Al–OH triplet and the slight inflection around ~2165 nm allowed the identification of kaolinite in the spectra d and j (Figure 3) [8,48,49,53]. Figure 4 (l) shows a sharp absorption at ~2312 nm and a shallow feature at ~2390 nm, indicating that another smectite group mineral may be present, probably saponite, with diagnostic Mg-OH features at ~2310 nm and ~2380 nm [48,49]. The last three spectra of Figure 4 show distinct mineral assemblages. In spectra r and s, besides the montmorillonite features (broad, asymmetric water absorptions), it was possible to identify: (i) a deep symmetric but broad main Al–OH feature, (ii) two OH^- absorptions located at ~1574 nm and ~1834 nm, and (iii) a deep, broad, asymmetric Mg-OH feature at ~2355 nm that allowed the recognition of cookeite (Li-bearing chlorite) [19,25,54,55]. Spectrum t (Figure 4) shows illite/white mica features: (i) the sharp and symmetric OH^- and Al–OH features at ~1413 nm and 2198 nm, respectively and (ii) the well-pronounced Al–OH secondaries at 2345 nm and 2434 nm [47,48,49]. The water feature is deep and asymmetrical but shorter than the Al–OH, diagnosing the existence of illite [49]. Looking at the VNIR portion of the spectra, it was possible to notice a fall off to extreme blue in the reflectance curves (left panel of Figure 4), indicating that iron could be present in several samples [53]. Both ferric and ferrous iron were identified, the latter mainly through its characteristic ramp-like feature around ~1150 nm [56]. Notwithstanding, similar features around ~1150 nm were interpreted as water features in montmorillonite spectra by Hunt and Salisbury [47].

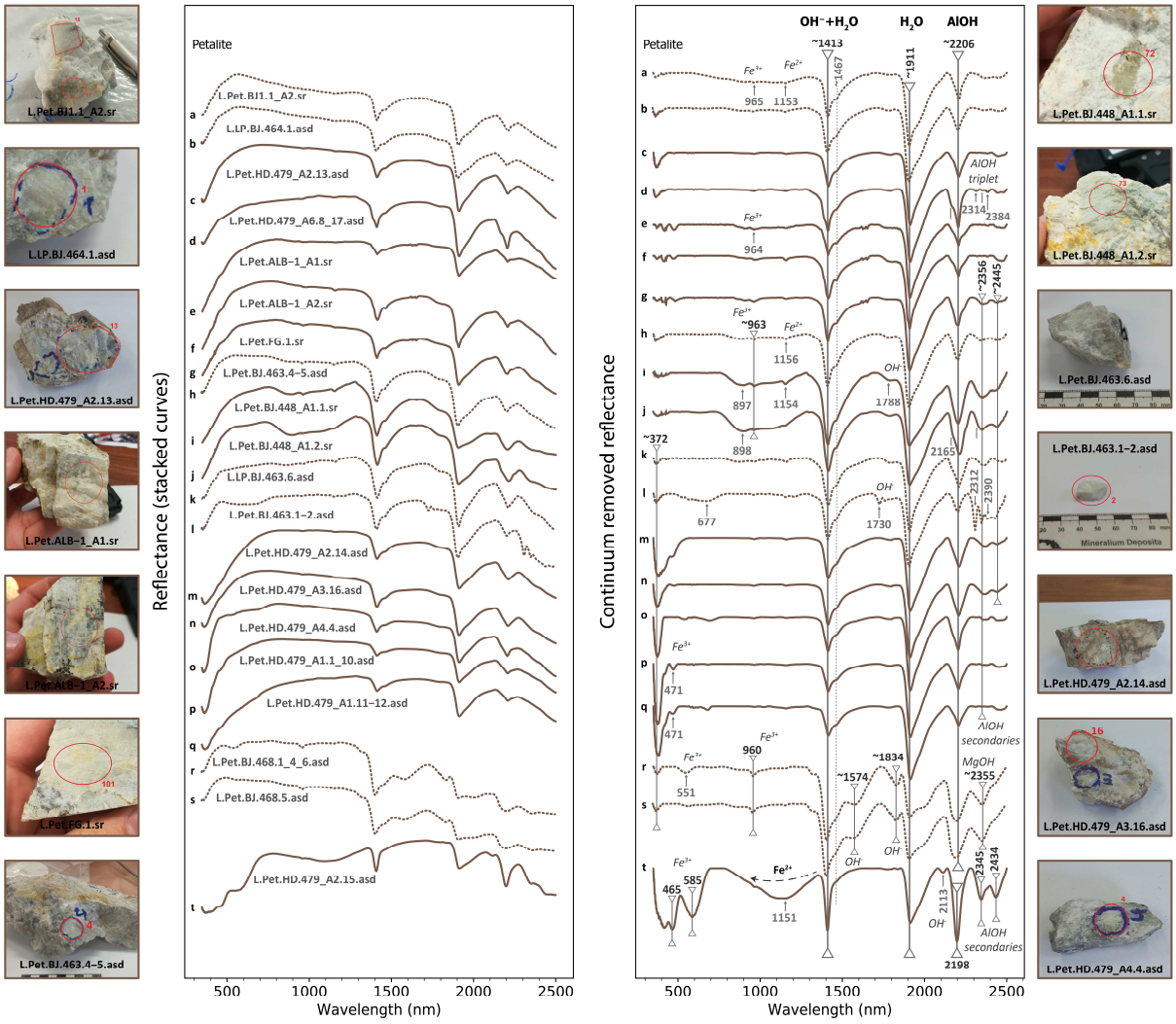

Figure 4. Spectral signature of petalite (a Li-bearing feldspathoid): reflectance curves (to the left) and continuum removed curves (to the right). The main absorption features are highlighted, and sample photographs are provided. Dotted curves: fresh samples; full curves: samples with visible signs of weathering. Each spectrum has a database code [45] providing information about the type of sample (L—Li-bearing minerals); mineralogy (Pet—petalite); sample provenance (ALB—Alberto mine and BJ—Bajoca mine, FG—Fregeneda, and HD—Hinojosa de Duero); a three-digit numerical part representing the GPS code; a one- or two-digit code representing the spectra number or the averaged spectra numbers; and a reference to the spectroradiometer employed (sr—SR-6500; asd—FieldSpec 4).

Lastly, the position of the ~2200 nm Al–OH feature was evaluated for all Li-minerals (Figure A1, Appendix A) as a possible factor for mineral discrimination.

Characterization of Petalite Alteration Products

The knowledge on the alteration associations can help to refine satellite image processing algorithms and to better understand the spectral behavior of fresh samples. During the field campaigns, it was possible to identify in the Bajoca mine front white to greenish clays preserving petalite cleavage (Figure 5a,b) [57] and yellow to greenish petalite crystals in Hinojosa de Duero. Additionally, in the Bajoca mine front, some petalite relics were found within the heavily altered portions, mainly consisted of friable clay-like minerals. Petalite relics and clayey alteration products were characterized through petrography, XRD, and reflectance spectroscopy. Table 1 summarizes these results and the ICP-OES Li quantification. Appendix A (Figure A6) provides the XRD diffractograms.

Table 1. Characterization and mineral identification of petalite's alteration products through petrography, XRD, and reflectance spectroscopy. Li quantification through ICP-OES is also shown. Alb—albite; Cok—cookeite (Li-chlorite); Il—illite; Kao—kaolinite; Mnt—montmorillonite; Msc—muscovite; Non—nontronite; Or—orthoclase; Pet—petalite; Pl—plagioclase; Qtz—quartz; Sap—saponite; Sep—sepiolite; Ser—sericite; WM—white mica. Sample provenance: BJ—Bajoca mine; HD—Hinojosa de Duero.

Sample	Friability	Petrography	XRD	Spectroscopy	Li_2O (%)
BJ.450	Friable	—	Qtz, Il, Mnt/Non, Kao	Mnt	0.116
BJ-20-12	Friable	—	—	Mnt, Il/WM	0.248
HD.479	Hard-rock	Pet, Ser, Pl, Qtz, WM	—	Mnt, Il/WM	4.585
BJ2-01	Friable	—	Qtz, Non, Msc, Il-Mnt	Mnt, Il/WM	0.082
BJ2-02	Friable	—	Qtz, Il/Sep, Msc, Or, Alb	Mnt, Il/WM	0.099
BJ3-01	Friable	—	Qtz, Il, Msc (phengitic), Alb	Mnt, Il/WM	0.062
BJ.451	Hard-rock	Cok, WM, Ser, Qtz	—	Mnt, Kao, Sap	0.409
BJ4-01	Hard-rock	Pet, Mnt*, WM, Pl	—	Mnt, Il/WM, Sap, Kao	4.628

* Identified through SEM-EDS

(**a**) (**b**)

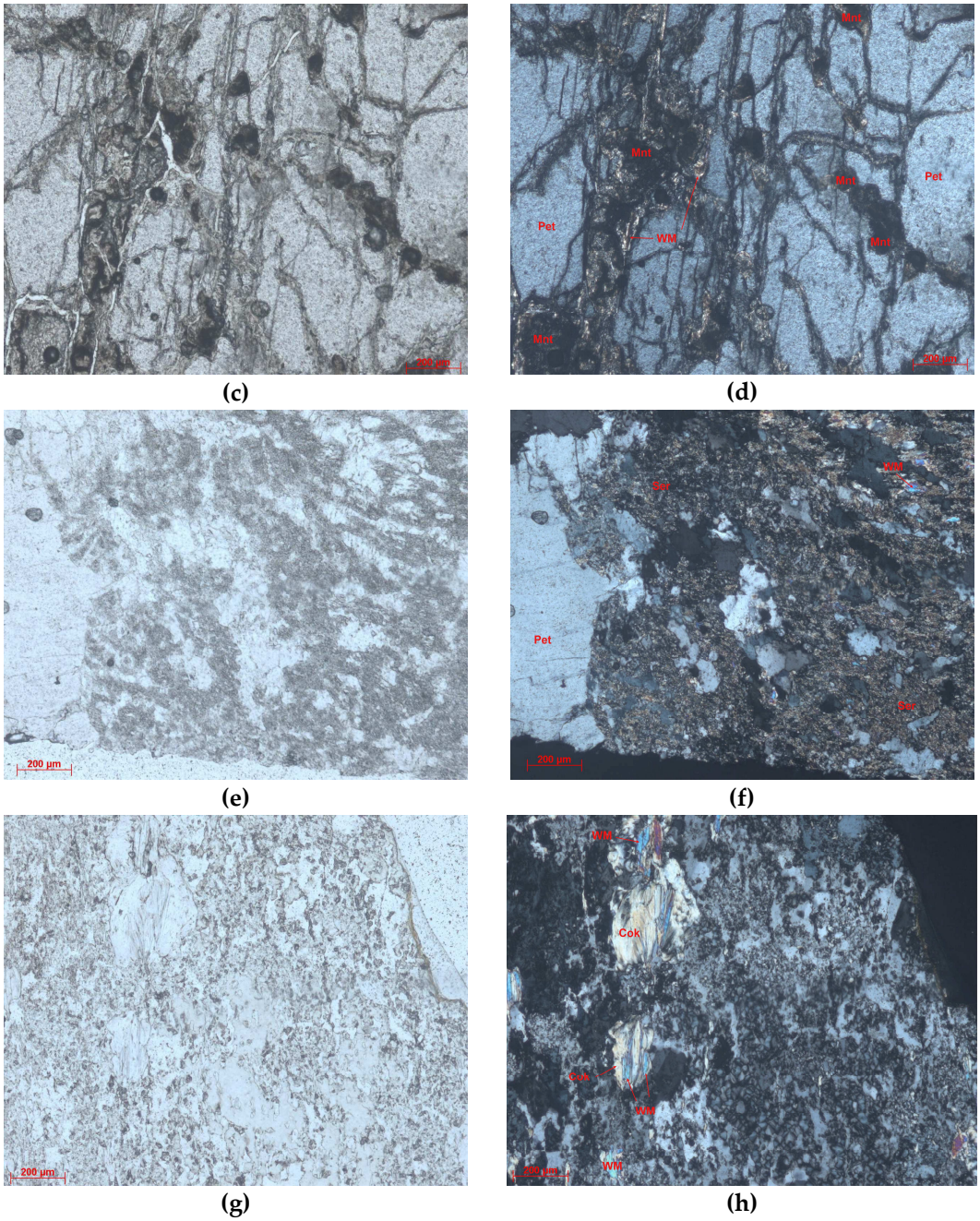

Figure 5. (a,b) Petalite altering to whitish and greenish clay minerals in the Bajoca mine front. **(b)** Former petalite crystal with preserved cleavage. **(c,d)** Photomicrographs of petalite relic with fractures filled by white mica and montmorillonite in parallel polarized light—ppl **(c)** and cross-polarized light—cpl **(d)**. **(e,f)** Photomicrographs of petalite altering to sericite, white mica, and quartz in ppl and cpl, respectively. **(g,h)** Former petalite replaced by cookeite associated with white mica, surrounded by quartz and pseudospherulitic clays in ppl and cpl, respectively. Cok—cookeite (Li-chlorite); Mnt—montmorillonite; Pet—petalite; Ser—sericite; WM—white mica.

Figure 5c–h shows representative photomicrographs of petalite's alteration minerals. Thin sections of the less altered samples allowed identifying petalite in two out of the three. In the third, petalite is completely replaced despite preserving its cleavage, as previously described by Cardoso-Fernandes et al. [57]. Petalite alteration concentrates along the cleavage (Figure

5c,d), filled by fine white mica and pale brown clays (under parallel polarized light–ppl; Figure 5c), identified as montmorillonite through SEM-EDS [57]. Montmorillonite also forms spherical aggregates more or less aligned (Figure 5c,d). Local sericitization was observed on the crystal borders (Figure 5e,f). Figure 5g,h shows the formation of cookeite (associated with white mica) and clay minerals with pseudospherulitic habit, often interpreted as crystals growing filling pre-existing voids [58].

Regarding the spectral behavior of the alteration assemblages (Figure 6), montmorillonite features such as the broad, asymmetric OH^- (~1413 nm) and H_2O (~1912 nm) absorptions with sharp minima, the Al–OH (~2200 nm) feature, and the small inflection around ~1467 nm [1,48,49] suggests its identification in spectra from a to j. The X-ray diffraction technique identified montmorillonite only in two of the four analyzed samples (Table 1 and Appendix A, Figure A6). In spectra from b to h, illite and/or white mica are also detected by (i) the Al–OH secondaries at ~2350 nm and ~2440 nm, (ii) the slight OH– feature at around ~1790 nm, and (iii) the proportion of Al–OH (~2200 nm) absorption depth to water absorption depth ranging around 1/2 [47-49]. The coexistence of illite and white mica was confirmed three samples analyzed through XRD (Table 1 and Appendix A, Figure A6). In Figure 6, the spectra i–k represent more complex mineral assemblages. Kaolinite can be present in spectra i and j because of the Al–OH absorption triplet (~2310 nm–~2350 nm–~2387 nm) and the slight inflection around ~2165 nm [8,48,49,53]. Nonetheless, the deeper 2311-nm absorption in spectra j indicates that a magnesium-bearing mineral such as saponite or sepiolite is also present [48,49]. Oppositely, spectrum k of Figure 6 is dominated by illite and/or white mica features: (i) deep, sharp, and symmetric main Al–OH feature (2196 nm) associated with a sharp, symmetric OH^- features (1409 nm); (ii) very pronounced Al–OH secondaries (at 2350 nm and 2433 nm); and (iii) minor OH^- feature at 2105 nm [47,48,49]. Most of the spectra of Figure 6 show iron-related absorption features, as observed in petalite fresh samples (Figure 4). The wavelength position allowed the discrimination of both ferrous and ferric iron [56].

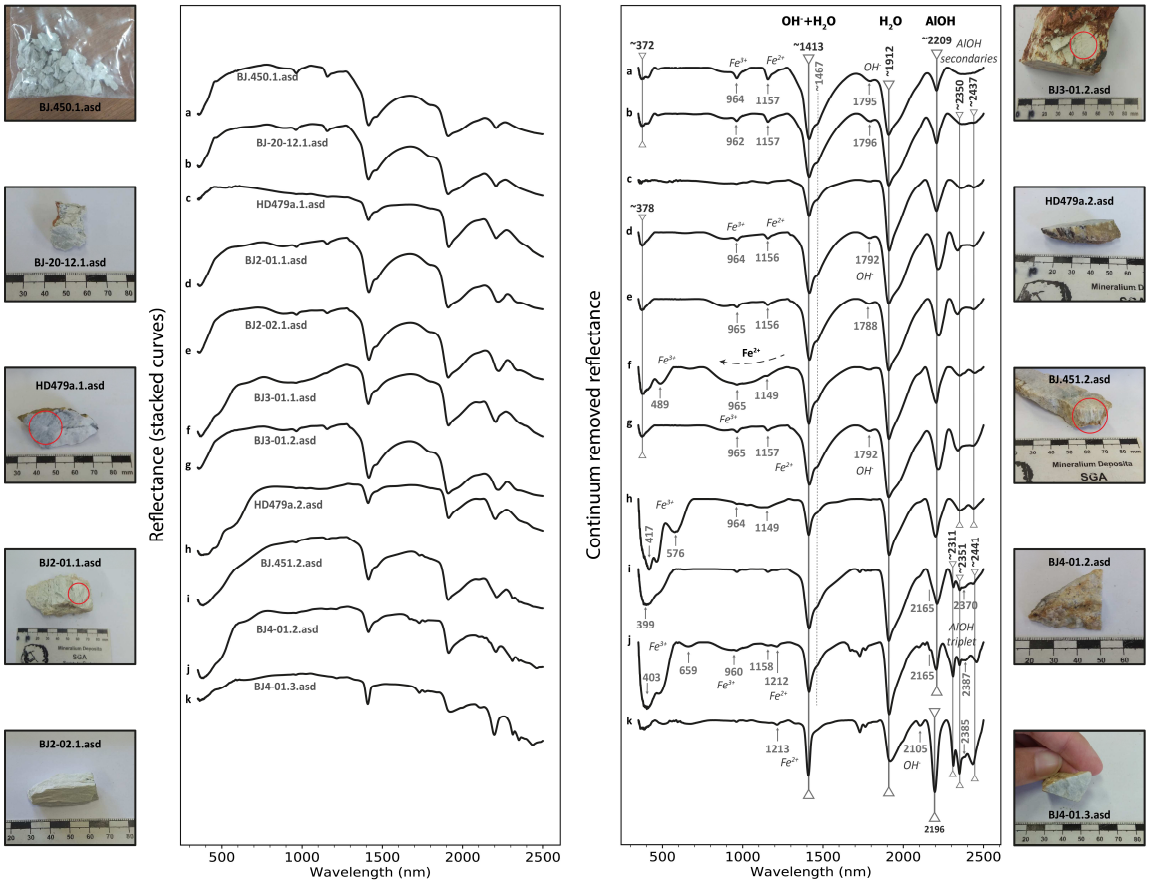

Figure 6. Spectral signature of the petalite's alteration products: reflectance curves (to the left) and continuum removed curves (to the right). The main absorption features are highlighted, and sample photographs are provided. Each spectrum name is composed by the sample provenance (BJ—Bajoca mine and HD—Hinojosa de Duero), a field code, a one-digit number representing the spectra, and the spectroradiometer employed (asd—FieldSpec 4).

As done for the spectra of Li-minerals, the position of the main Al–OH feature of the petalite alteration products was also assessed in Figure A1 (Appendix A). Additionally, any possible correlation between the Li content and the absorptions features in terms of wavelength, depth, area, and full-width at half maximum (FWHM) was evaluated (Figure 7).

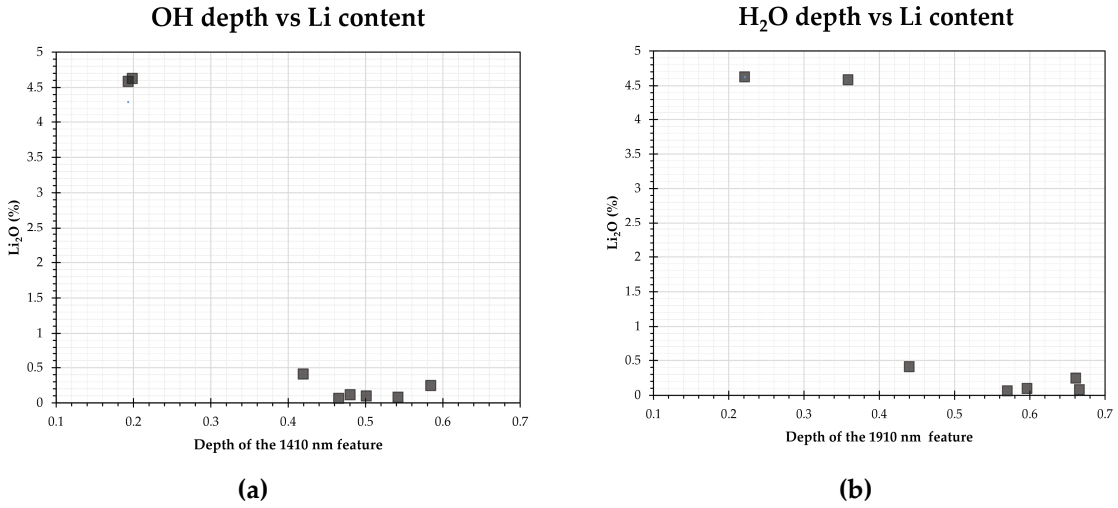

Figure 7. Relation between the depth of the hydroxyl **(a)** and water **(b)** absorption features and the Li content of altered petalite samples.

4.2. Spectral Studies for Lithological Classification

This section concerns the comparison of the spectral behavior of the main field lithologies. Additionally, a description of the areas misclassified as Li-pegmatite is presented, as well as the spectral behavior of the samples collected in each of the four areas.

Stacked reflectance and continuum removed curves of the metasedimentary formations from the CXG are presented in Figure 8 (a–g). White mica diagnostic features such as (i) deepest, sharp Al–OH feature around ~2214 nm, (ii) sharp and symmetric OH^- feature (~1413 nm) associated with the absence of a water feature (expected around ~1900 nm), and (iii) weak to pronounced Al–OH secondaries at ~2346 nm and ~2451 nm dominate the spectra of Figure 8 (a–c) [47-49]. The spectra of fresh samples (a–c) are also characterized by a ramp-like absorption feature due to the presence of ferrous iron (Fe^{2+}) [56], together with the ~750 nm, ~920 nm, and ~1150 nm Fe^{3+} and Fe^{2+} features [47,50,54]. These VNIR absorptions, associated with a slight inflection around ~2250 nm, related to the Fe-OH bonds [6,49] or Al(Mg, Fe)–OH bonds [59,60], and a slightly deeper 2350-nm absorption when comparing with the ~2451 nm Al–OH secondary, indicating the contribution of the Mg–OH bonds [48,49], are indicative of the presence of chlorite in fresh samples [47,49,54,59]. Despite the absorption features of spectra d–f of Figure 8 not being evident, there is (i) a weak, broad, rounded water absorption at ~1926 nm that may be associated with fluid inclusions in quartz [49] and (ii) ferric iron-related (Fe^{3+}) absorptions around ~942 nm evidencing sample oxidation (Figure 8) [49,56]. Finally, spectra g shows the calcite diagnostic features—namely, the carbonate ion (CO_3^{2-}) feature at 2339 nm and weaker carbonate features around ~1900–2000 nm [49].

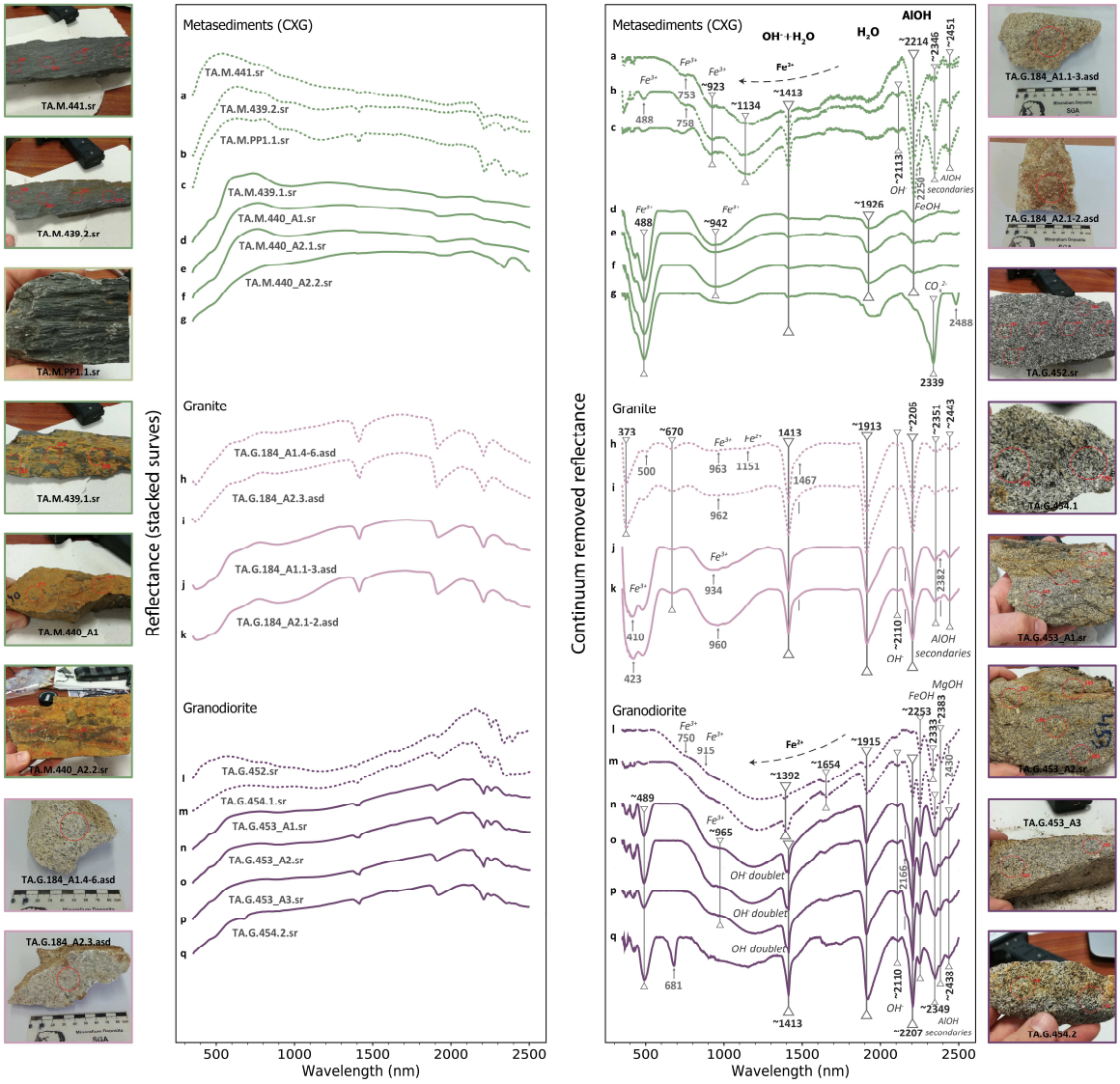

Figure 8. Spectral signature of the outcropping lithologies: reflectance curves (to the left) and continuum removed curves (to the right). The main absorption features are highlighted, and sample photographs are provided. Dotted curves: fresh samples; full curves: samples with visible signs of weathering. Each spectrum has a database code [45] providing information about the type of sample (TA—training areas), type of lithology (M—CXG metasediments, G—granite and granodiorite), a three-digit numerical part representing the GPS code, a one- or two-digit code representing the spectra number or the averaged spectra numbers, and a reference to the spectroradiometer employed (sr—SR-6500; asd—FieldSpec 4).

Regarding the granite samples, continuum removed curves (Figure 8 (h–k)), evidence a mixture of montmorillonite/illite and white mica features: (i) asymmetric OH^- (~1413 nm) and water (~1913 nm) features, (ii) broad water feature with sharp minima and similar depth to the Al–OH one (~2206 nm), (iii) a small inflection around ~1467 nm [1,48,49], (iv) Al–OH secondaries at ~2351 nm and ~2443 nm, and (v) weaker OH^- absorption at ~2110 nm [47-49]. Fresher samples (spectra h–i) show distinctive VNIR features at ~960 nm (Fe^{3+}) and ~1150 nm (Fe^{2+}), inferring the presence of biotite. Despite the dominance of montmorillonite and white

mica feature, which overlap with the main kandite group absorption features, altered samples (spectra j–k) show slight inflections at ~2165 nm and ~2382 nm that indicate that a kandite group mineral, like kaolinite or halloysite, is present in the mineral mixture [8,49]. Additionally, goethite was identified in altered samples through its diagnostic ferric iron features at ~670 nm and ~950 nm and peak in the red region (~750 nm) [49,56].

The granodiorite samples stacked reflectance and continuum removed curves are displayed in Figure 8 (l–q). White mica features dominate the spectra n to q, as evidenced by (i) the deep, narrow Al–OH absorption at ~2207 nm, (ii) the associated Al–OH secondaries (at ~2349 nm and ~2438 nm), and (iii) minor OH^- combined with lattice modes absorption features around ~2110 nm [47-49]. White mica is also present in Figure 8 (m). The ubiquitous biotite presence in all spectra (l to q) was confirmed by its diagnostic (i) ~2253-nm absorption feature, related to the either Fe–OH bonds [6,49] or Al(Mg, Fe)–OH bonds [59,60] and (ii) Mg–OH absorptions at ~2330–2350 nm and ~2380 nm [48,49]. The higher relative depth of the Mg–OH feature compared to the ~2250-nm absorption and the slight inflection/weak absorption around ~2430 nm indicate that biotite is Mg-rich (possibly mixed with phlogopite—for example, spectra q) [49,53]. Biotite also occurs mixed with chlorite in spectrum l, being chlorite identified through its diagnostic VNIR features (~750-nm, ~915-nm, and ~1150-nm ferric and ferrous iron absorptions) [47,50,54,56]. The existence of a doublet OH^- absorption in spectra o to q, associated with the slight inflection at ~2166 nm and the Al–OH absorptions at ~2349 nm and ~2383 nm is characteristic of the kandite group [8,48,49,53]. The prominent and deep water feature (~1915 nm) is diagnostic of halloysite [48,49]. Lastly, spectra q of Figure 8 shows a broad, asymmetric water feature that coupled with a unique OH^- feature (at ~1413 nm), and an Al–OH feature (at ~2207 nm) indicates that montmorillonite and/or illite may be present [48,49].

Finally, the Li-bearing pegmatites were separated according to the dominant mineralogy into (i) lepidolite-bearing and (ii) petalite-bearing. Stacked reflectance and continuum removed curves of both lepidolite- and petalite-bearing pegmatites are presented in Figure 9.

As shown in Figure 9 (a–f), white mica related absorptions dominate all spectra from lepidolite-bearing pegmatites (sharp and symmetric main OH^- and Al–OH, coupled with the associated secondaries at ~2347 nm and ~2434 nm and weaker OH^- combined with lattice modes absorptions at 1835 nm, ~1997 nm, and 2116 nm [47-49]). However, features in the VNIR region such as (i) the ~551-nm absorption, associated with the incorporation of Fe^{3+} and/or Mn^{3+}, and (ii) the peak in the red region (left panel of Figure 9), allowed discrimination of the white mica as lepidolite in spectra c–f [50]. In the VNIR region, another iron-related feature

was observed at ~960 nm (Fe^{3+}) [56]. Some clay minerals, such as montmorillonite and illite, may be present in spectra a, d, and f (Figure 9), identified by the relatively deep and/or asymmetric of the water feature at ~1912 nm and the slight inflection around ~1467 nm [1,49].

Like the petalite samples, mixtures of montmorillonite and illite dominate most of the spectra of the petalite-bearing pegmatites (Figure 9 (g,h,j–q)). The montmorillonite- related inflection at ~1467 nm is present in all the mentioned spectra [1]. In spectra g, i and j, montmorillonite features prevail over illite features: (i) higher asymmetry of the main OH^- feature (~1410 nm), (ii) higher depth of the water feature (~1912 nm) in comparison with the main Al–OH absorption (2192–2208 nm), and (iii) Al–OH secondaries (~2349 nm and ~2439 nm) absent or poorly developed [48,49]. In spectra o–q, the opposite happens, with illite being predominant due to: (i) narrower and/or more symmetric main OH^- feature, (ii) weaker OH^- absorptions 1620 nm and ~2108 nm, (iii) higher depth of the main Al–OH feature in relation to the water one, and (iv) well-developed Al–OH secondaries [48,49]. Spectra k–n represent a mixture of montmorillonite and illite. The rounded water absorption in spectra h indicates that free water is present, which could be due to fluid inclusions in minerals such as quartz [49]. White mica, which is discriminated from illite by the absence of a water feature [49], predominates spectra r–t, although the white mica present in spectra r is a hydrated white mica, probably sericite because the depth of the water feature is small than what would be expected for illite [49]. Figure 9 (w) shows diagnostic cookeite features, namely: (i) a broad, symmetric main Al–OH feature, (ii) OH^- absorptions at ~1581 nm and ~1835 nm, and (iii) a deep and broad Mg–OH feature at 2358 nm [19,25,54,55]. Cookeite also occurs mixed with white mica features in spectra t and mixed with montmorillonite/illite in spectra q. Kaolinite was identified in Figure 9 (g,j) through its characteristic Al–OH triplet and slight inflection at ~2166 nm [8,48,49,53]. Figure 9 (u,v) shows spectral behavior correspondent to orthoclase, where the absorptions at ~1410 nm and ~1912 nm may be the result of aqueous fluid inclusions [47,55]. Additionally, the ~2110-nm feature is diagnostic of ammonium (NH_4^+), but its relatively shallow depth can indicate only small amounts of NH_4^+ substituting K^+ and not the NH_4^+ feldspar (buddingtonite) [49,61,62]. When looking at the VNIR range, especially in the raw reflectance curves (left panel of Figure 9), goethite was identified in spectra g, h, l, and r, through its diagnostic ferric iron absorptions (Fe^{3+}) at ~960 nm and ~660 nm and peak in the red region around ~760 [49,56]. Other iron-related features were also observed.

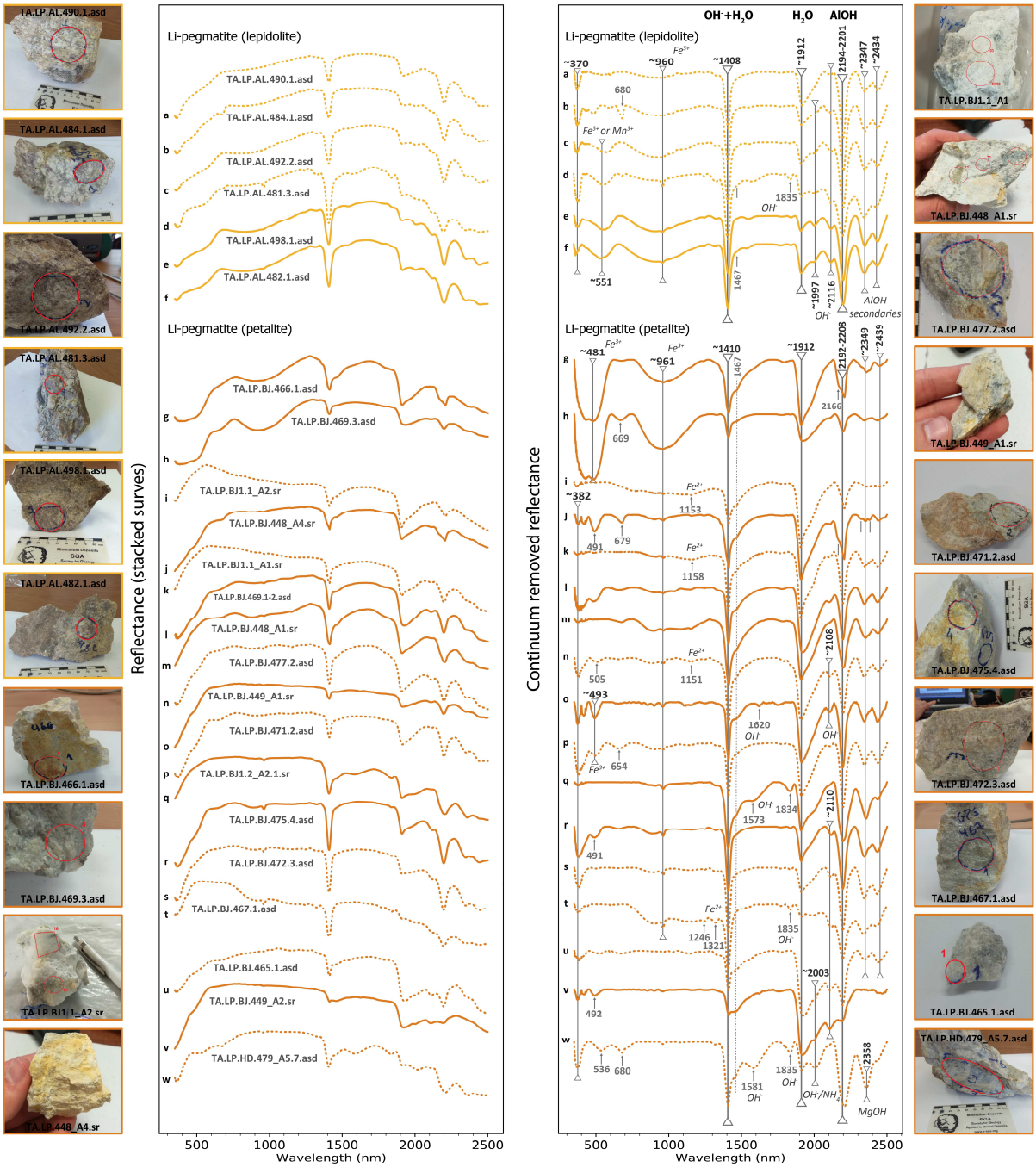

Figure 9. Spectral signature of the outcropping lithologies, namely lepidolite-bearing pegmatite and petalite-bearing pegmatite: reflectance curves (to the left) and continuum removed curves (to the right). The main absorption features are highlighted, and sample photographs are provided. Dotted curves: fresh samples; full curves: samples with visible signs of weathering. Each spectrum has a database code [45] providing information about the type of sample (TA—training areas); type of lithology (LP—Li-pegmatite); sample provenance (AL—Almendra, BJ—Bajoca mine, and HD—Hinojosa de Duero); a three-digit numerical part representing the GPS code; a one- or two-digit code representing the spectra number or the averaged spectra numbers; and a reference to the spectroradiometer employed (sr—SR-6500; asd—FieldSpec 4).

Overall, the misclassified regions correspond to (i) wine or olive plantations, where the agricultural activities exposed metasedimentary boulders, or (ii) hillside and slope areas, where many rock boulders are naturally exposed. Petrography and reflectance spectroscopy studies were conducted to fully characterize the collected samples and understand if there can be any spectral confusion with the target class (Li-pegmatite) and minerals. The results are summarized in Table A1 (Appendix A), while the spectral curves and photomicrographs are presented in Figure A2 and Figure A3, respectively.

As seen in Table A1, most of the samples correspond to CXG metasediments, although some quartzite and pegmatite samples were in some false-positive areas. The microscopic studies of CXG samples allowed characterization as interbed phyllites with metagraywacke layers, with well-preserved sedimentary features such as bedding and load casts (Figure A3a,b). The mineralogical assemblage identified, composed of quartz, white mica (detrital and metamorphic origin), biotite, chlorite, plagioclase, K-feldspar, detrital zircon, tourmaline, apatite, iron oxides, and other opaque minerals (Figure A3), is in line with the described in the literature [63]. Quartzite samples have tiny mica crystals in the matrix and exhibit an inherited clastic texture, compatible with the metapsamites described for the São Grabiel's Ordovician formation [37]. Lastly, no signs of Li mineralization were found in the pegmatite samples, which characterizes it as a barren pegmatite.

Figure A2 (Appendix A) shows the spectral signature of samples collected in false-positive sites. The continuum removed curves related to the area no. 1 (Figure A2 (a–e)) reveal white mica in spectra c (sharp, symmetric main OH^- and Al–OH absorptions at ~1414 nm and ~2210 nm, coupled with the Al–OH secondaries at ~2350 nm and ~2438 nm and the absence of water absorption). Illite was recognized in spectra b through similar features but with its typical more profound water feature (~1925 nm) [47-49]. In Figure A2 (e), montmorillonite deep water absorption is spectrally mixed with Mg-OH-related features at ~2350 nm and ~2383 nm (slight inflection), possibly due to the presence of chlorite or biotite (the VNIR features are not clear enough to discriminate the magnesium-bearing mineral) [48,49,54]. The wavelength position and rounded aspect of the water feature indicate the presence of free water, possibly related to fluid inclusions in quartz or the presence of iron oxides/hydroxides [49]. The ferric iron features at ~680 nm and ~960 nm and peak in the red region (~760 nm) allowed identifying the goethite in spectra a, while the remaining VNIR absorptions indicate that other iron oxides/hydroxides are present in spectra b, d, and e of Figure A2 [49,56].

In the case of the false-positive area no. 2 (Figure A2 (f,g)), it was possible to recognize hydrated kaolinite or kaosmectite due to the (i) slight inflections ~1407 nm and ~2197 nm indicative of the OH^- and Al–OH doublets; (ii) very shallow Al–OH triplet at (~2313 nm, ~2349

nm, and ~2384 nm); and (iii) the deep water feature at ~1921 nm [8,48,49,53]. Spectra g of Figure A2 is dominated by illite features, although there is a slight inflection at a wavelength characteristic of the Mg-OH bond (2379 nm) [47-49]. Identical OH^- and Al–OH features but with less profound water feature allowed to identify white mica in spectra h [47-49], while the rounded water feature has indicated the presence of quartz with fluid inclusions [49]. The remaining spectra (f and g) also show a distinctive wavelength position and roundness of the water feature, indicating free water. Based on the VNIR features, goethite was identified in Figure A2 (f,g), while spectra h also shows some ferric iron absorptions [49,56].

Regarding the spectra of the false-positive area no. 3 (Figure A2 (i–m)), the similar depth of the water (~1914 nm) and main Al–OH (~2208 nm) features indicate the spectral mixture montmorillonite (~1465-nm inflection and broad, deep, asymmetric water feature with sharp minima) and illite (typical Al–OH secondaries) in spectra i and k [1,48,49]. Montmorillonite also occurs mixed with chlorite/biotite in spectra j (well-pronounced Fe–OH or Al(Mg, Fe)–OH absorption at 2254 nm, associated with the deep Mg–OH absorption at ~2348 nm), but the VNIR features are not clear enough to discriminate the two minerals [6,48,49,59,60]. Figure A2 (l) shows a predominance of montmorillonite features (absence of Al–OH secondaries, inflection at 1467 nm, and deep water feature), but the shape of the 1914-nm (water) feature is not typical of the smectite group, with the rounded minima indicating the presence of free water [1,48,49]. Spectra m is dominated by chlorite features (diagnostic VNIR absorptions, inflection at ~2000 nm, and Mg–OH-related absorption at 2348 nm) [47-49,54,59] mixed with either white mica or illite [47,48,49]. Looking at the VNIR features in both reflectance and continuum removed curves, goethite can be present in spectra i, while other iron oxides and/or hydroxides (that not goethite or hematite) are present in spectra j–l [49,56].

Finally, in the false-positive area no. 4 (Figure A2 (n–q)), white mica (sharp, symmetric OH^- and Al–OH features, associated with the Al–OH secondaries and the absence of a prominent water feature), is mixed with chlorite (diagnostic VNIR absorptions and ~2000-nm inflection) in spectra n and q [47-49,54,59]. Spectra o and p show white mica features but a more pronounced, asymmetric water feature at ~1914 nm, indicating probable sericite (water absorption deeper than typical muscovite but not deep enough as illite) [49]. Ferric iron-related absorptions occur in spectra o and p of Figure A2.

The reflectance magnitude of the different classes is compared in Figure 10. Additionally, the minimum, maximum, and mean reflectance of each class are also compared in Figure A4 (Appendix A).

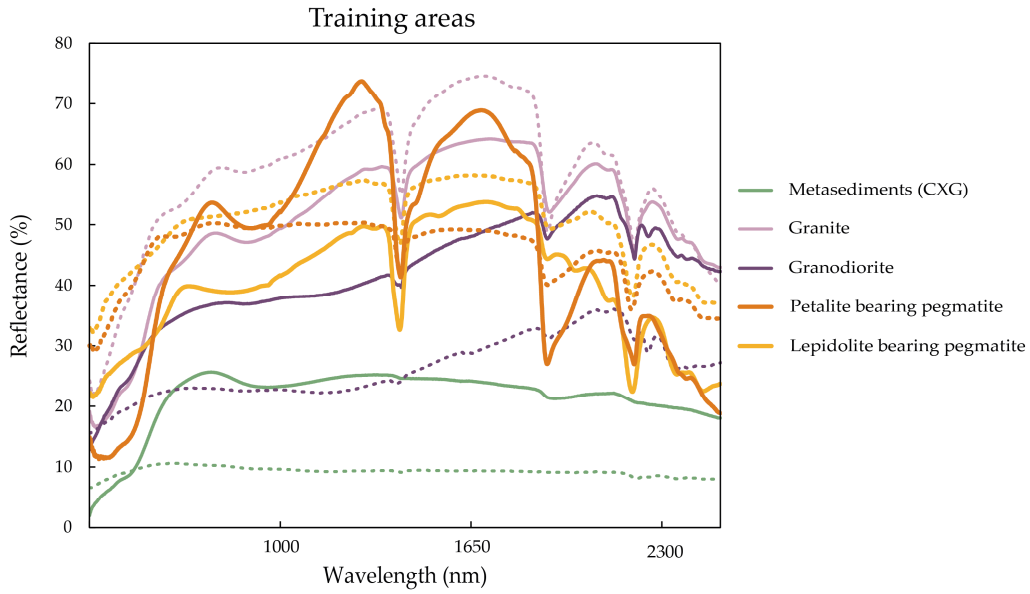

Figure 10. Comparison of the maximum reflectance magnitude of the different lithologies sampled at training area locations. Weathered samples (full lines) are discriminated from fresher samples (dotted lines).

Additionally, the wavelength position and depth of absorption features are among the most common criteria for lithological discrimination. Figure 11a shows the distribution of the wavelength of the main Al–OH feature according to the distinct types of samples containing white mica, and Figure 11b relates the position and depth of their Al–OH feature. To better discriminate the CXG metasediments from the granitoids based on the spectral mineralogy, the chlorite and/or biotite composition was evaluated through the Mg–OH wavelength position (Figure A5, Appendix A). Only the Mg–OH absorption was used, because not all spectra presented the ~2250-nm feature well-defined.

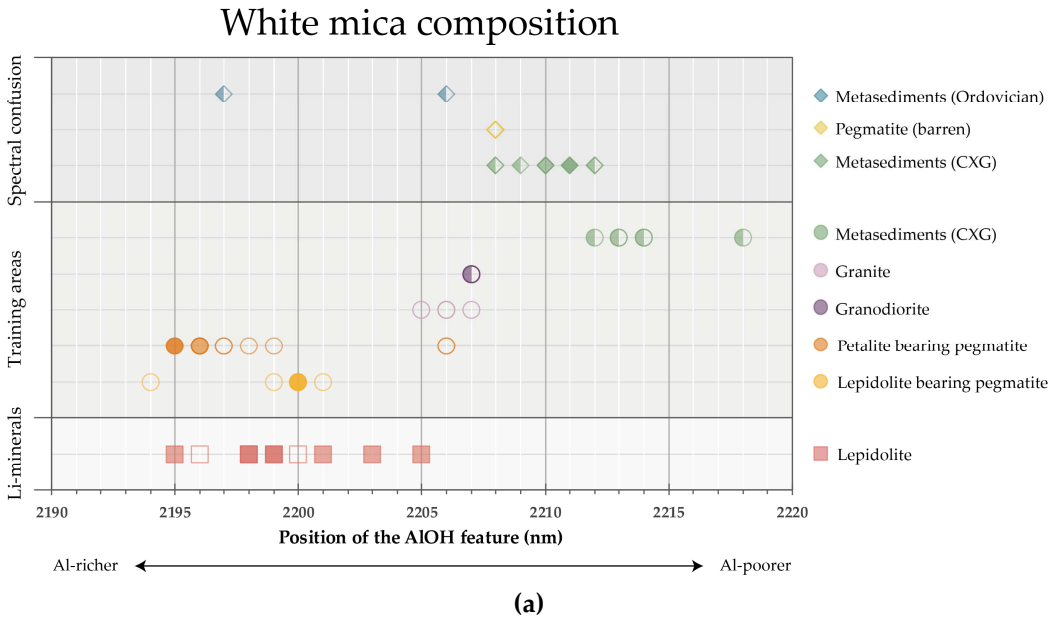

(a)

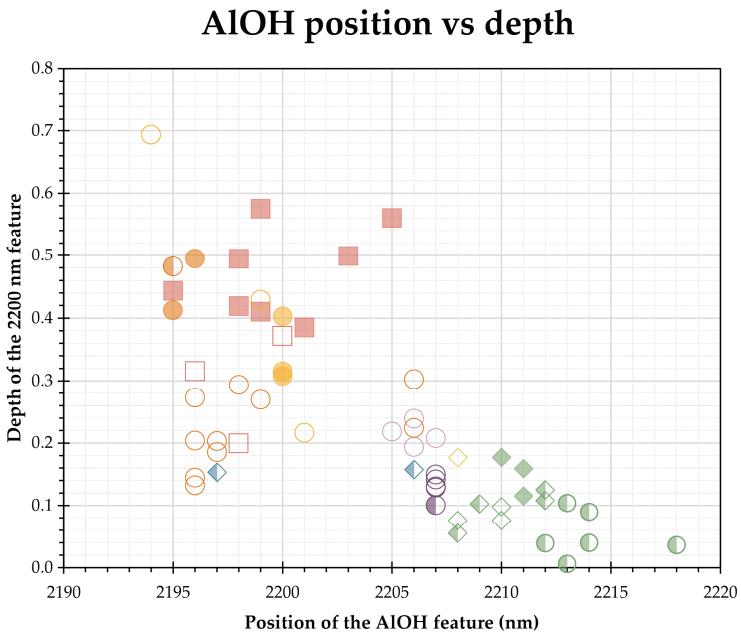

(b)

Figure 11. Wavelength position of the Al–OH feature in samples containing white mica: (a) relation between the wavelength and white mica composition (based on References [49,64]) and (b) relation between depth and position of the Al–OH feature. Lepidolite samples (squares) were plotted for comparison. Circles correspond to samples from training areas, while diamonds represent false-positive areas. Full symbols correspond to samples where white mica was exclusively identified; half-full symbols correspond to mixtures of white mica with minerals that do not overlap the main Al–OH absorption; symbols without fill represent spectra where white mica occurs mixed with minerals whose feature overlaps the Al–OH absorption.

Lastly, the spectral resolutions of different satellite or drone-borne sensors (such as Sentinel-2, Landsat-8 Operational Land Imager (OLI), Advanced Spaceborne Thermal Emission and Reflection Radiometer (ASTER), Prototype Research Instruments and Space Mission technology Advancement (PRISMA), and HySpex Mjolnir) were considered to evaluate the potential use of remote sensing data in Li-pegmatite exploration (Figure 12).

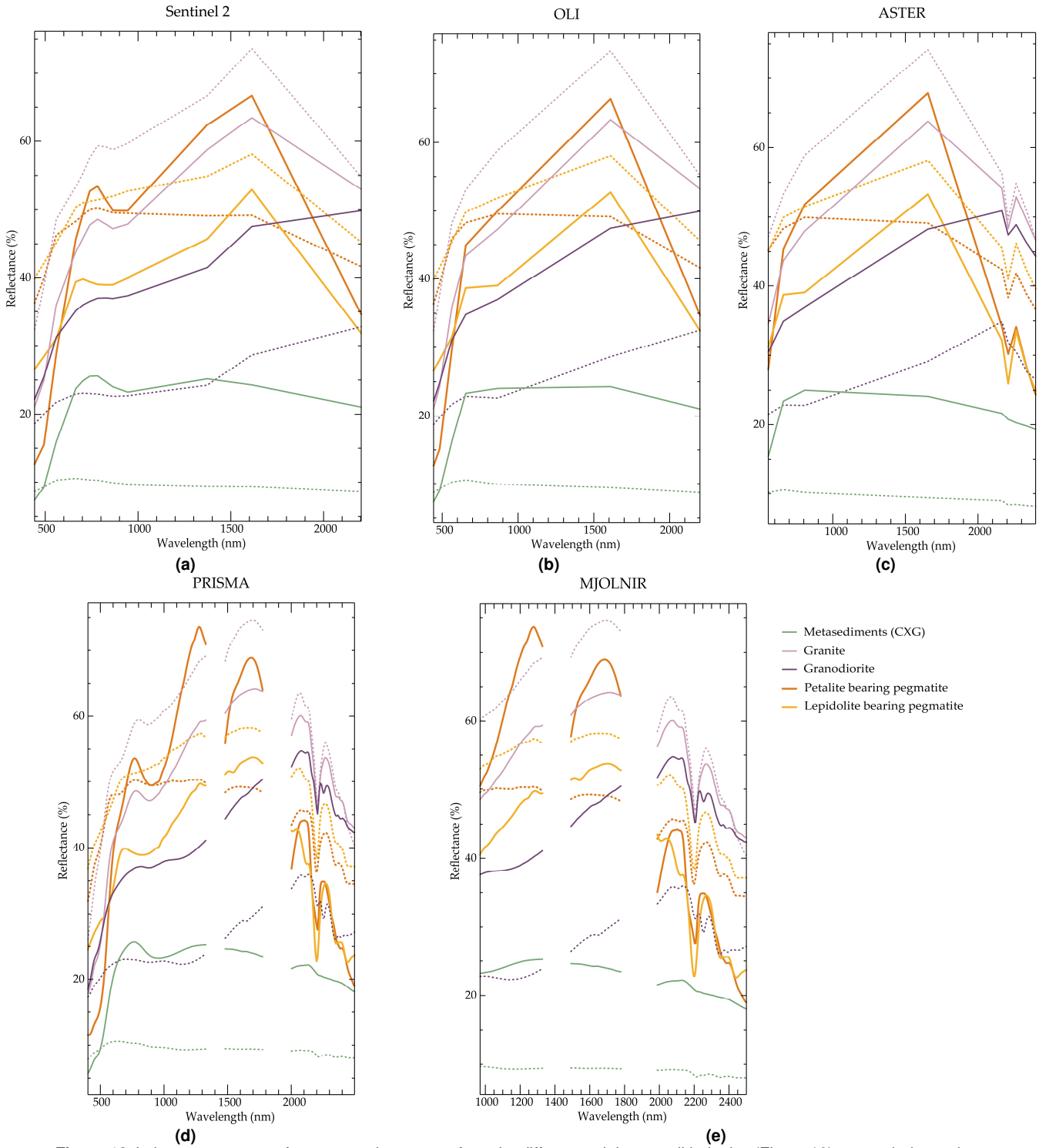

Figure 12. Laboratory spectra of representative spectra from the different training area lithologies (Figure 10) resampled to various multi- and hyperspectral sensors: (a) Sentinel-2, (b) Landsat-8 Operational Land Imager (OLI), (c) Advanced Spaceborne Thermal Emission and Reflection Radiometer (ASTER), (d) Prototype Research Instruments and Space Mission technology Advancement (PRISMA), and (e) Mjolnir. Weathered samples (full lines) are discriminated from fresher samples (dotted lines).

5. Discussion

5.1. Spectral Behavior of Li-Bearing Minerals

The collected lepidolite (Figure 2), spodumene (Figure 3), and petalite (Figure 4) spectra were compared, and, despite all three minerals showing significant absorption features in the same wavelength regions, the shape, symmetry, and relative depth of the features allowed differentiation of lepidolite from the remaining two Li-minerals. This is because lepidolite has diagnostic absorption features at around 550 nm and 960 nm, as well as a drop-off of the extreme blue (which reflect the purple color of lepidolite) and the white mica typical features due to the hydroxide ion (OH^-) absorption around ~1409 nm associated with the principal, sharp Al–OH absorption feature (between 2195 nm and 2205 nm) and the Al–OH secondaries (around ~2348 nm and ~2435 nm, respectively). These VNIR absorption features allow discriminating lepidolite from other white micas [50]. Since hyperspectral and multispectral air- or satellite-borne sensors cover the VNIR wavelength region, there is a high potential for lepidolite identification using remote sensing data. Previous studies where lepidolite was recognized and discriminated from other white micas using airborne HyMap hyperspectral data [65,66] corroborate this statement, although the position of the Al–OH features also played a fundamental part in that discrimination [66] (this topic will be further discussed below). All three Li-minerals show diagnostic iron-related features in the VNIR region, probably due, in part, to the substitution of aluminum in the minerals' structures (e.g., References [50,67]). In spodumene, iron substitution is observed, as well in the SWIR region (~2240 nm).

Concerning the petalite and spodumene, it was not possible to identify any diagnostic feature because the alteration minerals (montmorillonite with minor illite and kaolinite) dominate their spectral curves. Though, spodumene presents iron-related absorptions at ~2240 nm not visible in petalite. Conversely, some petalite samples showed additional cookeite (Li-chlorite) and saponite (Mg-smectite) features not recognized in spodumene samples. However, this is not enough to distinguish between the two Li-aluminosilicates, because cookeite and other clay minerals (such as kaolinite or smectites) can form from either petalite or spodumene alteration (e.g., [68-70] and references therein). These results also indicate that it would not be possible to spectrally discriminate spodumene or petalite from montmorillonite/illite, based on the absorption features.

Moreover, several authors have noticed a shift in the wavelength position of the main Al–OH absorption due to different Al contents in white micas [7,49,52,64]. As it can be seen in Figure A1 (Appendix A), the lepidolite samples show the Al–OH feature at shorter wavelengths (≤2005 nm), which indicates a higher Al content [7,49,64]. Although the Al–OH feature position

of spodumene and petalite overlaps the lepidolite range, there is a tendency for the Al–OH feature to be located at longer wavelengths (Figure A1). These wavelength differences could be caused by the spodumene and petalite substitution by montmorillonite and kaolinite instead of a higher Al content in white micas, especially because they are not present in all spectra.

Such subtle changes in wavelength positions are not detectable through multispectral sensors but are noticeable using hyperspectral data. For example, in the previous work conducted by Oshigami et al. [66], the wavelength position of the Al–OH absorptions allowed the distinction of lepidolite from Al-poor and Al-rich muscovite by applying different thresholds to the employed mineral indices. Despite some overlap in the position of the Al–OH feature between lepidolite and the other Li-minerals, a similar approach could be employed to hyperspectral data to map lepidolite- and spodumene/petalite-bearing areas.

5.2. Effects of Alteration in the Spectral Signature of Li-Bearing Minerals

Comparing the reflectance spectroscopy of altered petalite results (Figure 6) with the complementary petrographic/geochemical techniques (Table 1), it was possible to corroborate the presence of montmorillonite and illite in the same samples. Overall, the combination of methods was complementary, despite some contradictory mineral identification between XRD and reflectance spectroscopy. The XRD identified nontronite and Fe-bearing smectite, while the reflectance spectroscopy indicated montmorillonite and possibly saponite. Nonetheless, previous studies have shown that reflectance spectroscopy has a greater capacity to distinguish among different clay minerals and between clay minerals and illite and muscovite [48,52].

In general, the petalite alteration products' spectral behavior (Figure 6) is very similar to the one observed for petalite (Figure 4), with a dominance of montmorillonite and illite features. Kaolinite and saponite (Mg-smectite) were also observed. Regarding the main Al–OH feature (Figure A1, Appendix A), petalite alteration products show the widest range, reaching higher wavelengths than the ones observed for the three Li-bearing minerals.

There is also a spectral similarity between petalite relics (HD.479 and BJ4-01) and entirely replaced crystals. The petalite relics found within highly altered areas show Li contents compatible with unaltered petalite [13], which may be explained by superficial alteration cover and the concentration of alteration on fractures, cleavage, and crystal border, as observed in Figure 5c–f and Cardoso-Fernandes et al. [57]. Figure 7 shows an inverse correlation between the Li content and the hydroxyl and water features depth (Pearson's r = 0.95 and

0.88, respectively). However, it is not possible to estimate the Li content based on these parameters, because, at low Li concentrations, no trend was observed. From samples with preserved petalite relics to the wholly altered ones, there is an increase in the OH^- and H_2O absorption depth explained by higher amounts of alteration minerals since mineral abundance is related to the absorption intensity [56,64,71]. On its turn, a higher petalite substitution for alteration minerals such as clays leads to a decrease in Li content (Table 1 and Figure 7). The results indicate that the absorption intensity could be used to discriminate fresher petalite samples.

Despite the different climate, the resultant mineral alteration assemblage (montmorillonite and other smectite group minerals, illite, kaolinite) is very similar to the spodumene and petalite's supergene alteration paragenesis found in Brazil under tropical to subtropical climate [25]. Previous studies have shown that these alteration minerals can result from either supergene (weathering) or hydrothermal metasomatic alteration in the late stages of pegmatite crystallization [57,68,72,73], which would explain the occurrence of the same mineral paragenesis under distinct weathering conditions. At the same time, the presence of clay minerals in microfractures in spodumene was already described by Clark et al. [50], causing the spectral behavior of spodumene to be dominated by the clay's absorption features. Therefore, it is not surprising that spodumene and petalite samples show similar spectral curves because the two minerals seem to undergo the same alteration phenomena.

Taking this into account, it is indisputable that the alteration deeply affects the spectral behavior of Li-minerals even when clay minerals are present in minimal amounts. Therefore, any possible spectral signature of petalite or spodumene in the VNIR-SWIR spectral range is obscured by the very pronounced clay-related features. This poses advantages and limitations in satellite-based Li-exploration. Since spodumene and petalite's spectral features are similar and because different alteration degrees produce the same spectral signal, the ability to spectrally identify spodumene or petalite using the same methodology is not compromised. This is in line with the results obtained with classical and machine learning techniques in the study area [21,23]. Additionally, the results indicate no need for different methodological approaches worldwide since the same mineral assemblages could be found in distinct climates. The work of Santos et al. [22] corroborated this interpretation, because the methods developed for Li-pegmatite identification in the Fregeneda–Almendra area also showed potential for Li-exploration in the Minas Gerais region (Brazil). The main limitation is the impossibility of the spectral features allow discrimination between the areas where spodumene and/or petalite occur from the areas where the weathering of other materials produced the clay

minerals. This means that as in other deposits, clay minerals can be used as pathfinders for petalite or spodumene. Montmorillonite is identified through the diagnostic, broad, asymmetric, and acute absorptions around ~1413 nm and ~1911 nm; the Al–OH feature at ~2206 nm [48,49] shallower than the ~1911 nm one; and the slight inflection around ~1467 nm [1,49]. Kaolinite has also diagnostic features, such as (i) a small inflection around ~2165 nm; (ii) the presence of an Al–OH triplet at ~2312, ~2350, and ~2380 nm; and (iii) double OH^- and Al–OH absorptions (not visible in poorly crystalline kaolinite) [8,48,49,53]. However, this pathfinder approach would only work in areas where argillic alteration is not predominant. In future attempts, the variation of absorption intensity related to proportions of Li content could be used to try to discriminate Li-bearing minerals from barren, clay-bearing areas as observed in Figure 7. The co-occurrence of cookeite (formed after petalite or spodumene alteration) could also be used to highlight Li-bearing areas.

5.3. Discrimination of Li-Pegmatites from the Remaining Lithologies

The last objective of this work was to understand if Li-pegmatites can be discriminated from the remaining field lithologies. In general, it was possible to ascertain that all sampled lithologies present similar absorption features caused by water and/or hydroxyl present in the structure of rock-forming minerals (Figure 8 and Figure 9 and Figure A2). This is due to the presence of white mica/illite in samples from all field lithologies and false-positive areas or due to the presence of montmorillonite in some samples.

Lepidolite, cookeite, and orthoclase were exclusively identified in Li-pegmatite samples. These minerals can be used, therefore, as targets or pathfinders for Li-bearing pegmatites. Lepidolite diagnostic features were already described in Section 5.1, while cookeite shows several diagnostic features, namely: (i) a broad, symmetric main Al–OH feature, (ii) two OH^- absorptions at ~1580 nm and ~1835 nm, and (iii) a deep and broad Mg-OH feature at ~2355 nm [19,25,54,55]. Orthoclase can be indirectly identified through (i) aqueous fluid inclusions with absorptions at ~1410 nm and ~1912 nm [47,55] and (ii) NH_4^+ substituting K^+, with a diagnostic absorption at ~2110 nm [49,61,62]. Chlorite takes place in CXG and granodiorite samples. Biotite occurs in both granite and granodiorite samples, but the exclusive occurrence of phlogopite in the granodiorite allows discrimination between the two. Chlorite and/or biotite were also observed in false-positives areas 1, 3, and 4. Montmorillonite and minor kaolinite compound the alteration assemblage of Li-pegmatites, granite, granodiorite, and false-positive areas 1–3. Altered samples of Li-pegmatite, granite, CXG, and false-positive areas 1–3 present iron oxides, predominantly goethite.

As verified, except for certain exclusive minerals or distinct mineral assemblages, other factors may need to be considered to achieve lithological discrimination fully. When considering the reflectance magnitude of the different classes (Figure 10 and Figure A4), in general, altered samples show higher reflectance values when compared to the fresh ones, which is due to alteration minerals (such as clays and iron-oxides). Additionally, petalite- and lepidolite-bearing pegmatites present similar mean reflectance values, although the former can reach higher maximum values. The granite samples demonstrate the highest mean reflectance (Figure A4). These relative differences in magnitude help to discriminate between lithological types in data from multi- or hyperspectral sensors.

The wavelength position of given absorption features can also be helpful for lithological discrimination (Figure 11 and Figure A5). The metasediments samples of the CXG show the Al–OH absorption position at longer wavelengths which indicates that the white mica is Al-poor (Figure 11); Li-pegmatite samples present the main Al–OH absorption at shorter wavelengths, similar to lepidolite; granitoid samples show an intermediate wavelength position and, therefore, Al content [7,49,52,64]. Despite the correlation between white mica composition and the wavelength position of the Al–OH absorption, more recent studies have shown that Al-rich phengites can overlap the typical muscovite wavelength range [7,8]. Moreover, lepidolite and Li-rich micas are characterized by a lower Al content than muscovite due to Li substituting Al in octahedral sites [74]. This indicates that another factor is influencing the smaller wavelength of the ~2200 nm feature. Additional research, namely detailed mineral chemistry studies, is needed to fully understand this issue. Nonetheless, there is a clear 2205 nm threshold that is useful for remote sensing applications, at least in this study area. Figure 11b indicates that the Al–OH position varies within the different sampled lithologies as the depth of the Al–OH absorption, which is more profound in Li-pegmatite and shallower in CXG samples (either from the training or false-positive areas). Considering this, it is possible to differentiate the CXG metasediments (host rocks) from the target class (Li-pegmatites). The difference between the two classes is even more pronounced when only the most spectrally pure samples are considered (full and half-full symbols of Figure 11). Such wavelength and depth variations could be evaluated using a hyperspectral sensor.

In what concerns the Mg–OH wavelength position (Figure A5; Appendix A), it is not possible to discriminate between the metasedimentary rocks and granitoids due to the overlap of wavelengths. However, chlorite presents a similar wavelength position and possibly composition in both training and false-positive areas. Except for one Mg-rich chlorite/biotite in the granodiorite samples, all remaining features are compatible with intermediate Mg/Fe

compositions [49,59]. In the case of chlorite, the iron-related features in the VNIR range, the shape, position, and relative depth of the ~2250 nm and ~2350 nm absorptions are compatible with intermediate compositions with both Fe and Mg present. Nonetheless, it should be noted that the overlap with the white mica Al–OH secondaries can lead to shifts in the Mg–OH position.

5.4. Potential of Li-Exploration Using Satellite Data

The previous results indicate that the potential use of remote sensing data is highly dependent on the sensors. As seen in Figure 12, the spectral behavior of the CXG metasediments is very distinct from the remaining lithologies, even for the Sentinel-2 and Landsat-8 OLI. However, the Al–OH absorption around ~2200 nm is only recognized in higher resolution sensors (ASTER, PRISMA, and Mjolnir). The existence of a band in this region increases the separability of the CXG metasedimentary class. The granodiorite samples are also spectrally distinct from Li-bearing pegmatites. The most significant similarity is observed between granite and Li-pegmatite samples. The hyperspectral sensors can identify the same wavelength shifts observed in the laboratory (Figure 11) that can help to discriminate them. Nonetheless, PRISMA has advantages over the Mjolnir sensor since the VNIR features can increase the separability of the two classes. On the other hand, when on board aircraft and UAVs, the Mjolnir sensor has a better spatial resolution, reducing the components in spectral mixtures.

Considering the results, it is possible to infer that although the distinct lithologies present similar absorption features, it is possible to spectrally discriminate Li-pegmatites from other lithologies using remote sensing data due to (i) the higher reflectance magnitude, (ii) more profound Al–OH absorption depths, and (iii) shifts in the wavelength position of the Al–OH features. Furthermore, distinct mineral assemblages result in particular spectral behavior (e.g., Li-pegmatites lack chlorite/biotite features in the VNIR region while presenting important and exclusive target minerals). The false-positive areas, for example, despite showing similar clay-related absorptions, also display distinct VNIR features. Of course, the ability to discriminate the target class from the remaining outcropping lithologies increases with an increasing spectral resolution (Figure 12), showing the importance of hyperspectral sensors such as PRISMA or Mjolnir. The capability to spectrally discriminate Li-pegmatites using hyperspectral data needs to be validated in further studies in a real-life application and not only using simulated hyperspectral data (e.g., [8,65,66]).

6. Conclusions

Analyzing the wavelength, shape, and symmetry of diagnostic absorption features, as well as the overall reflectance magnitude and absorption depths of a Li-dedicated spectral library, allowed the identification of the spectral mineralogy and characterization of samples of (i) different Li-bearing minerals, (ii) several field lithologies of the study area, and (iii) samples from areas previously misclassified as Li-pegmatite using a machine learning algorithm. Ultimately, the results obtained allowed evaluation of the potential of remote sensing and spectral data in Li-exploration, thus fulfilling the proposed objectives and addressing the main research questions:

1. *Can Li-bearing minerals be distinguished from each other and other minerals*? The spectra obtained allowed the discrimination of lepidolite from spodumene, petalite, and other white micas. However, it was not possible to distinguish petalite from spodumene because clay-related absorption features dominate the spectra of both Li-minerals, thus obscuring any likely diagnostic spectral behavior. This implies that spodumene and petalite can only be indirectly identified. Several factors, such as the VNIR features or the position of the main Al–OH absorption, enable direct lepidolite identification through multi- or hyperspectral satellite data.

2. *How can the alteration products affect the spectral signature of Li-bearing minerals*? The complementary petrography and geochemical studies proved that the same alteration minerals observed in previous studies occur in either well-preserved or completely altered samples. However, the clay-related absorption depths are much smaller for petalite relics. Further studies are needed to understand if the clay minerals formed from petalite alteration in the Fregeneda–Almendra region are related to weathering or metasomatic processes. Therefore, the effect of alteration paragenesis is paramount in the spectral behavior of spodumene and petalite, thus limiting the possibility to discriminate areas where these Li-minerals occur from heavily altered, barren areas through multispectral data. On the other hand, using hyperspectral data could overcome this limitation, either through the possibility of recognizing variable absorption depths (distinct amounts of clay minerals) or by the identification of other alteration minerals exclusively related to Li-minerals such as cookeite. Notwithstanding, in areas where clay-related alteration is not prevalent, the same methodology can be employed, using montmorillonite and kaolinite as pathfinders to identify spodumene and petalite worldwide since the alteration paragenesis is similar to the described in tropical conditions.

3. *Can Li-pegmatites be spectrally discriminated from other lithologies in a supervised classification attempt*? Despite the similar absorption features, we conclude that the satellite data can map Li-pegmatites through several criteria such as (i) the distinctive reflectance magnitude, (ii) higher absorptions depths, (iii) distinct wavelength position of key absorption features, and (iv) particular overall spectral behavior reflecting different mineral assemblages. Minerals such as lepidolite, cookeite, and orthoclase can work as targets for Li-pegmatites. Further studies are needed to evaluate the performance of hyperspectral data in real-life conditions and compare it with the laboratory-simulated hyperspectral data.

The results and conclusions withdrawn in this work provide valuable insights on the spectral behavior of pegmatite-hosted Li mineralization and minerals, allowing for more reasoned and directed satellite-based approaches in the future, based on the proposed strategies and pathfinders. Additional studies are needed to continue improving the knowledge on the alteration paragenesis and to understand the smaller wavelength of the ~2200 nm feature in lepidolite and its relationship with the Li and Al contents in the octahedral layer.

Supplementary Materials

The following are available online at **https://www.mdpi.com/article/10.3390/rs13183688/s1**: Table S1: Spectral mineralogy of Li-minerals, Table S2: Spectral mineralogy of the training areas, and Table S3: Spectral mineralogy of the false-positive areas.

Author Contributions

Conceptualization, J.C.-F., A.L. and A.C.T.; methodology, J.C.-F., A.L. and A.C.T.; software, J.C.-F.; formal analysis, J.C.-F., J.S., M.M.P., A.L., M.A.R. and F.D.; investigation, J.C.-F., J.S., F.D., A.L., A.C.T., M.M.P. and M.A.R.; resources, A.L., E.R-R., O.B. and J.C.; data curation, J.C.-F., J.S. and F.D.; writing—original draft preparation, J.C.-F.; writing—review and editing, all the remaining authors; visualization, J.C.-F.; supervision, A.L., A.C.T., M.A.R., M.M.P., E.R.-R. and O.B.; project administration, J.C., A.L. and A.C.T.; and funding acquisition, J.C. and A.L. All authors have read and agreed to the published version of the manuscript.

Funding

The authors would like to thank the financial support provided by FCT–Fundação para a Ciência e a Tecnologia, I.P., with the ERA-MIN/0001/2017–LIGHTS project and, also, with the 869274—GREENPEG—H2020-SC5-2018-2019-2020 project. This work was also supported by national funds through the FCT project UIDB/04683/2020–ICT (Institute of Earth Sciences). Joana Cardoso-Fernandes and Filipa Dias were financially supported within the compass of their respective Ph.D. theses, ref. SFRH/BD/136108/2018 and ref. 2020.05534.BD, by national funds from MCTES through FCT and co-financed by the European Social Fund (ESF) through POCH–Programa Operacional Capital Humano and NORTE 2020 regional program. The Spanish Ministerio de Ciencia, Innovacion y Universidades (Project RTI2018-094097-B-100, with ERDF funds) and the University of Basque County (UPV/EHU) (grant GIU18/084) also contributed economically. The French National Research Agency (ANR–10–LABX 21–LABEX RESSOURCES 21) partly supported the Master Student personal grant, and the 776804–NEXT–H2020-SC5-2017 project participated in equipment purchasing.

Institutional Review Board Statement

Not applicable.

Informed Consent Statement

Not applicable.

Data Availability Statement

The data presented in this study are openly available in Zenodo at **http://doi.org/10.5281/zenodo.4575375**, accessed on 12 September 2021, reference number [46].

Conflicts of Interest

The authors declare no conflict of interest. The funders had no role in the design of the study; in the collection, analyses, or interpretation of the data; in the writing of the manuscript; or in the decision to publish the results.

Appendix A

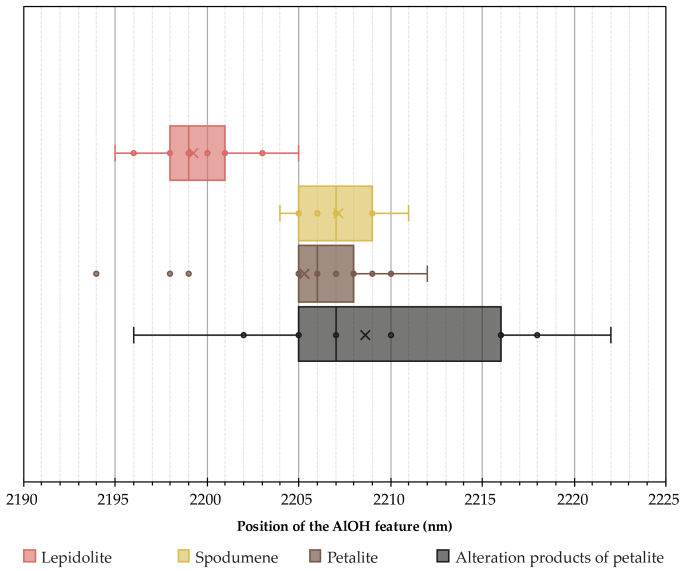

Figure A1. Boxplot diagrams of the main Al–OH absorption wavelength position for the Li minerals and associated alteration products.

Table A1. Description of each false-positive site and respective collected samples. Mineralogical information was collected with optical microscopy and reflectance spectroscopy. Ap—apatite; Bt—biotite; Chl—chlorite; Goe—goethite; Il—illite; IO—iron oxides/hydroxides; Mnt—montmorillonite; Pl—plagioclase; Qtz—quartz; Tur—tourmaline; Ser—sericite; WM—white mica; Zr—zircon.

False positive area	Site description	Lithology	Petrography	Spectroscopy
1 (GPS point 443)	Wine plantation; disturbed soil with many rock boulders	CXG metasediments: A1 *– striped phyllites interbed with metagraywacke benches; A2 – light-colored phyllite.	A1: WM/Ser, Qtz, IO, Bt, Pl, Chl, Tur, detrital WM, detrital Zr, opaque minerals	Il, Mnt, WM, Chl/Bt, Goe and other IO, Qtz?
2 (GPS point 444)	Hillside area; slope deposits	Ordovician metasediments: A1 – whitish impure quartzite (metapsamite) with a ferruginous crust; A2/A3 – reddish, ferruginous impure quartzite.	A1: Qtz, WM, IO, detrital Zr, Tur	WM, Qtz, Il, Goe, Kao
3 (GPS point 445)	Olive plantation; sparse rock boulders	CXG metasediments: A1/A2 – striped phyllites interbed with metagraywacke benches. A3 – pegmatite.	A2: WM/Ser, Qtz, Chl, detrital WM, Pl, IO, Ap, opaque minerals	Mnt, Il, Chl/Bt, Goe and other IO, Qtz?
4 (GPS point 446)	Almond plantation; disperse rock boulders	CXG metasediments: A1/A2 – striped phyllites interbed with metagraywacke benches	A1: Qtz, WM/Ser, Bt, Pl, detrital WM, Tur, IO, detrital Zr, Ap, opaque minerals	WM, Ser, Chl

* A1 to An: numeration given to different samples collected in the same area (where n equals to the total number of samples).

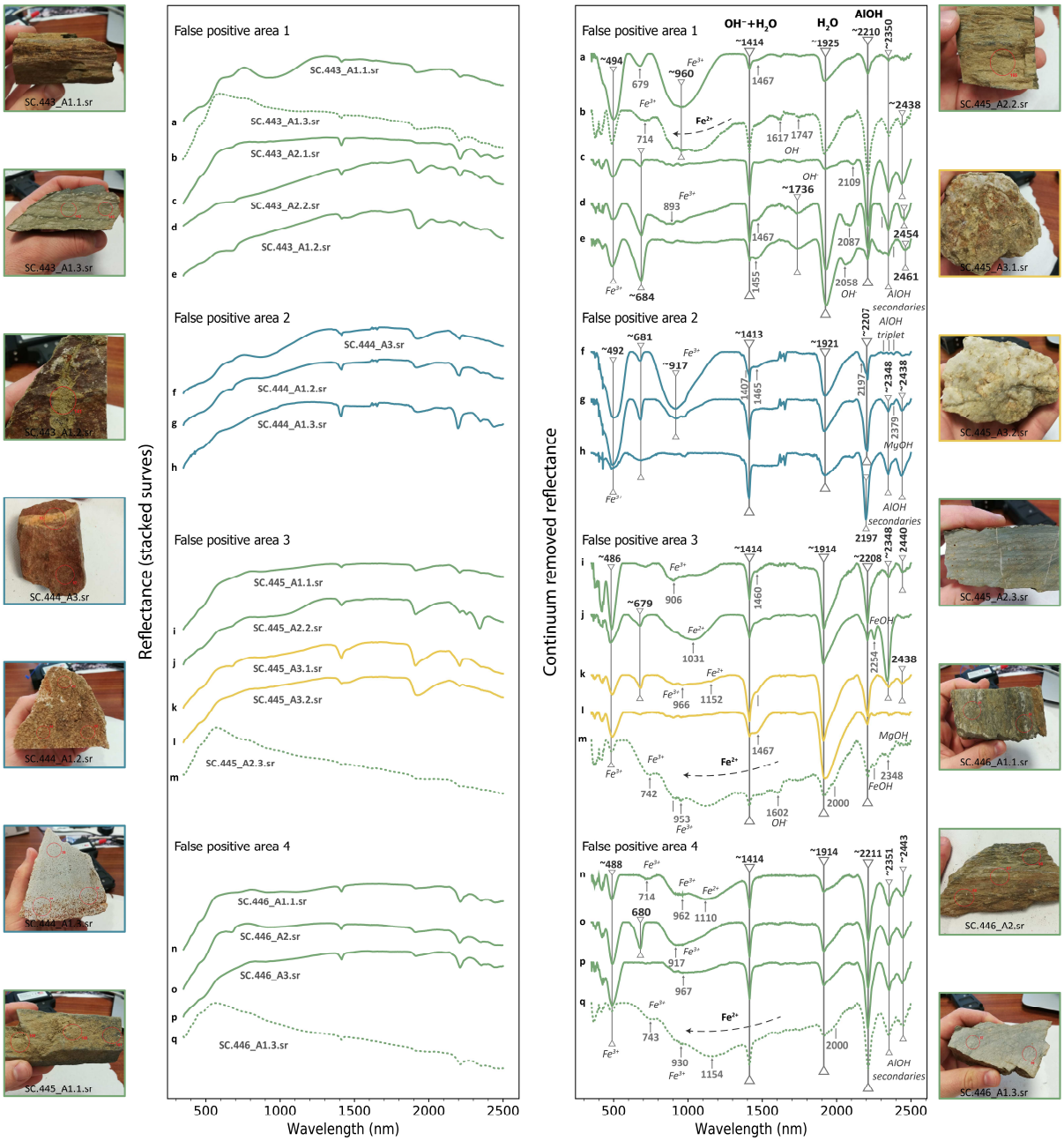

Figure A2. Spectral signature of samples collected in areas misclassified as Li-pegmatite in a previous classification attempt: reflectance curves (to the left) and continuum removed curves (to the right). The main absorption features are highlighted, and sample photographs are provided. Dotted curves: fresh samples; full curves: samples with visible signs of weathering. Each spectrum has a database code [45] providing information about the type of sample (SC—spectral confusion), a three-digit numerical part representing the GPS code, a one- or two-digit code representing the spectra number or the averaged spectra numbers, and a reference to the spectroradiometer employed (sr—SR-6500; asd—FieldSpec 4).

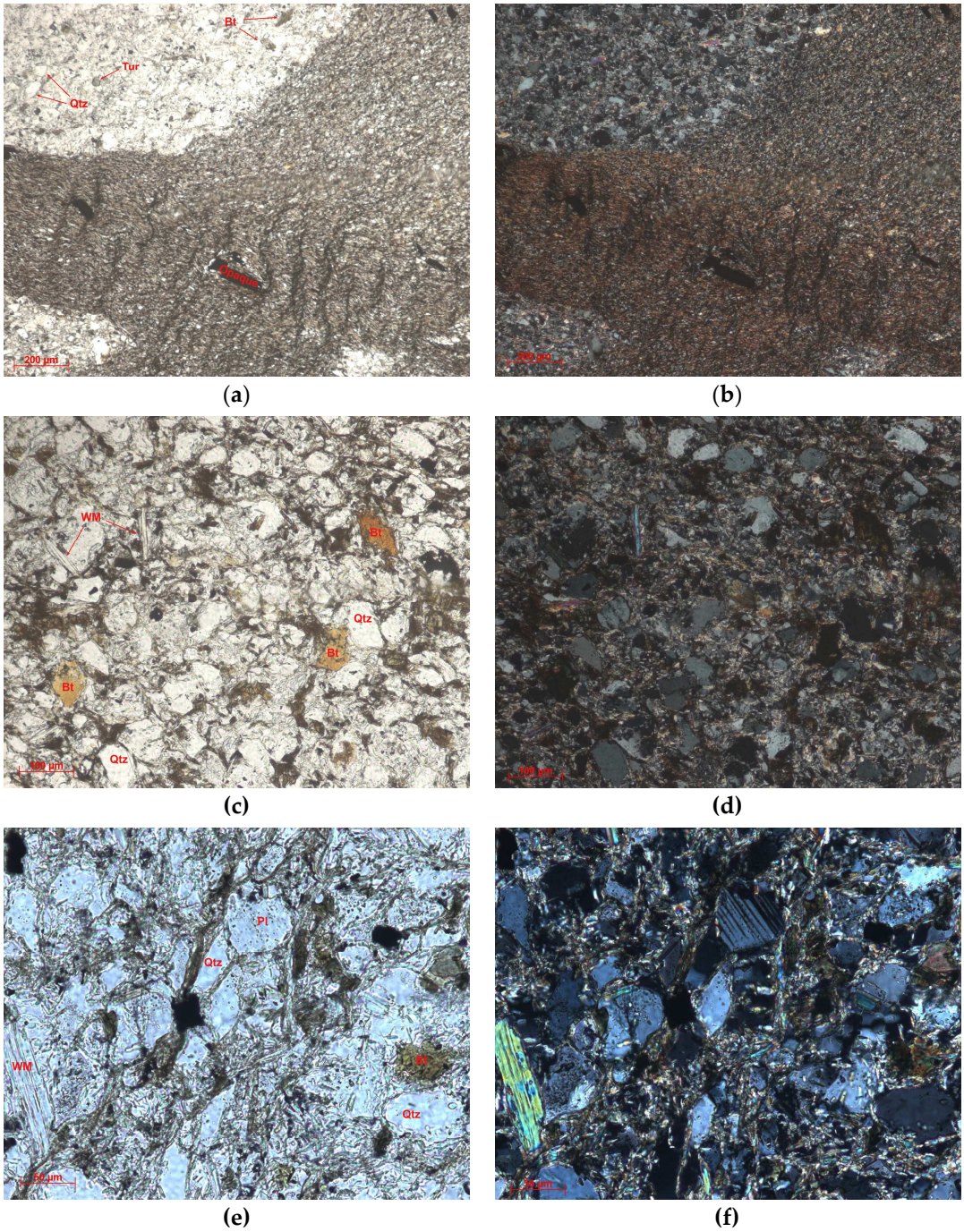

Figure A3. Photomicrographs of the CXG samples collected in the areas misclassified as Li-pegmatite. (**a**,**b**) Alternations of thin, micaceous layers and coarser metagraywacke beds (load cast structures) in parallel polarized light—ppl (**a**) and cross-polarized light—cpl (**b**). (**c**–**f**) The general aspects of the metagraywacke benches in ppl (**c**,**e**) and cpl (**d**,**f**). Bt—biotite; Pl—plagioclase; Qtz—quartz; Tur—tourmaline; WM—white mica.

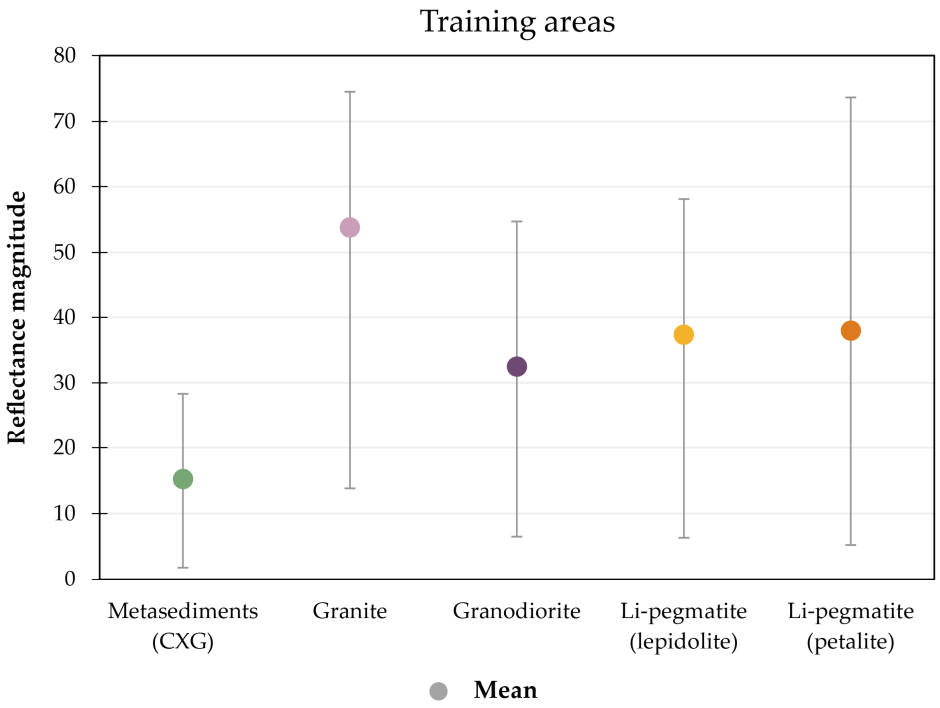

Figure A4. Minimum, maximum, and mean reflectance magnitudes of the different training area lithologies.

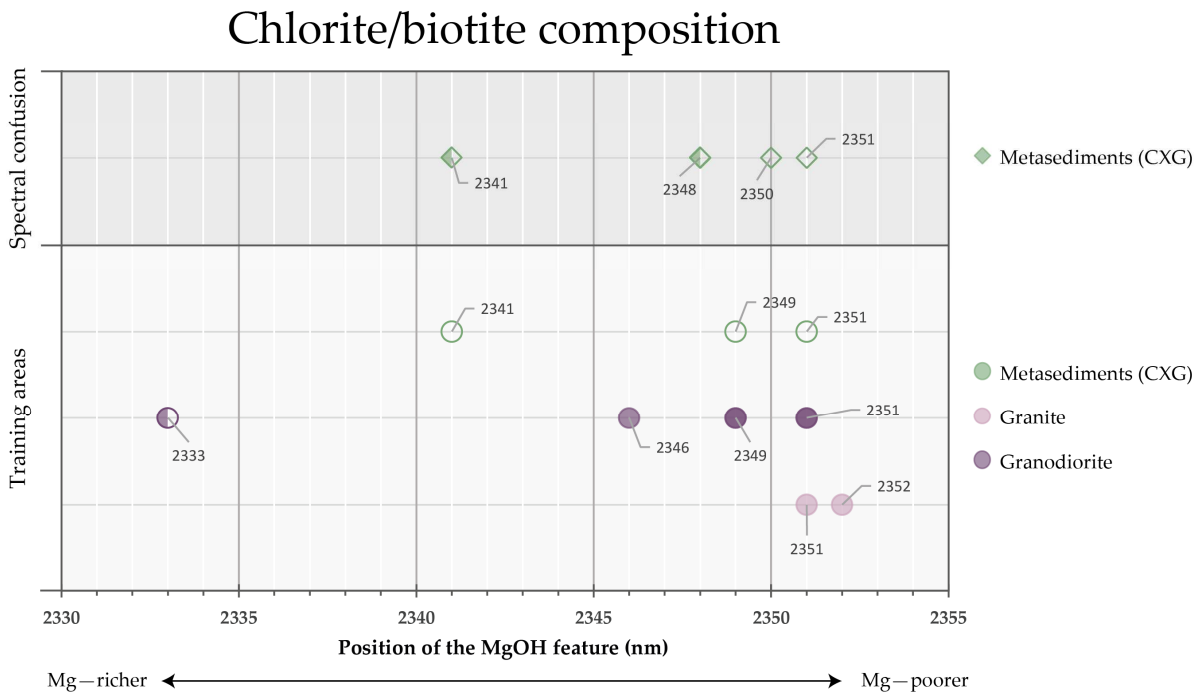

Figure A5. Comparison of the Mg–OH wavelength position of biotites and chlorites from the CXG metasediments and granitoid rocks. Full symbols correspond to biotite; empty symbols correspond to chlorite; half-full symbols represent chlorite and biotite mixtures or samples where it was not possible to discriminate between the two minerals.

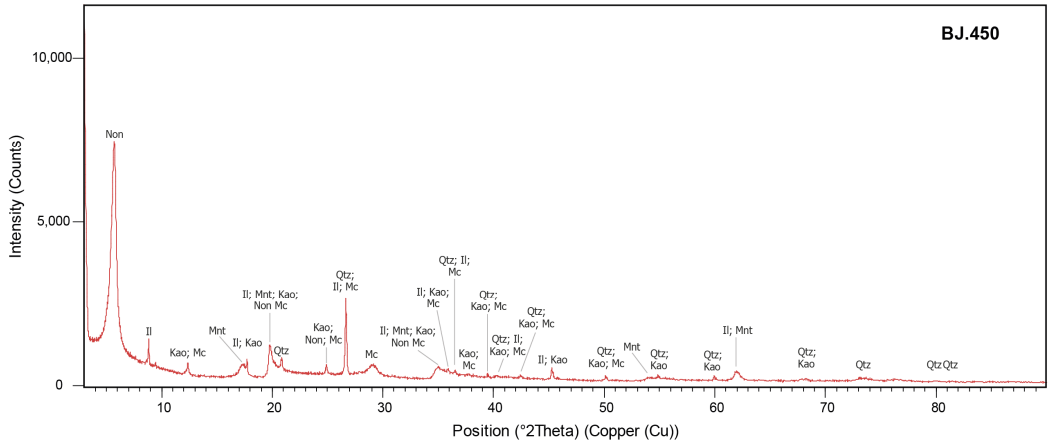
BJ.450
Intensity (Counts)
Position (°2Theta) (Copper (Cu))
Non
Il
Kao; Mc
Mnt
Il; Kao
Il; Mnt; Kao; Non Mc
Qtz
Kao; Non; Mc
Qtz; Il; Mc
Mc
Il; Mnt; Kao; Non Mc
Il; Kao; Mc
Qtz; Il; Mc
Kao; Mc
Qtz; Kao; Mc
Qtz; Il; Kao; Mc
Il; Kao
Qtz; Kao; Mc
Mnt
Qtz; Kao
Qtz; Kao
Il; Mnt
Qtz; Kao
Qtz
Qtz Qtz

(a)

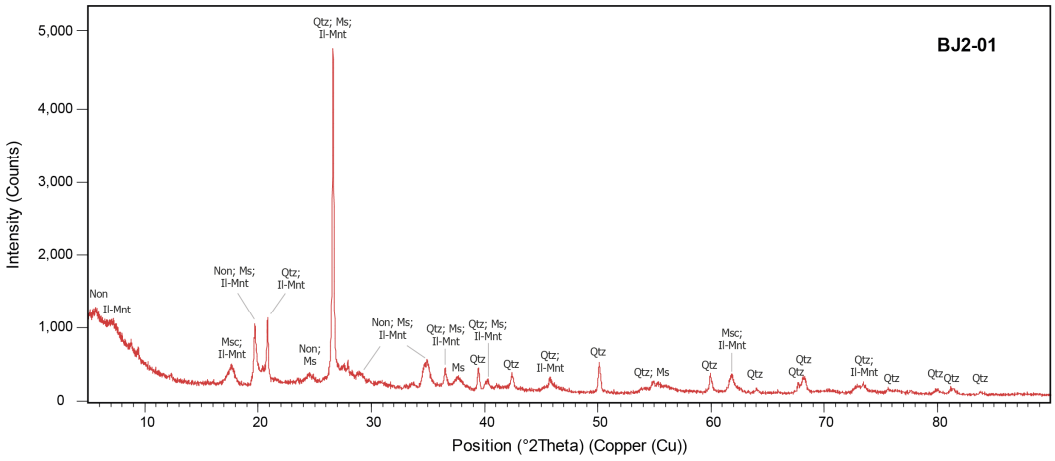
BJ2-01
Intensity (Counts)
Position (°2Theta) (Copper (Cu))
Non
Il-Mnt
Non; Ms; Il-Mnt
Qtz; Il-Mnt
Msc; Il-Mnt
Non; Ms
Qtz; Ms; Il-Mnt
Non; Ms; Il-Mnt
Qtz; Ms; Il-Mnt
Qtz; Ms; Qtz; Ms; Il-Mnt
Ms
Qtz
Qtz
Qtz; Il-Mnt
Qtz
Qtz; Ms
Qtz
Msc; Il-Mnt
Qtz
Qtz
Qtz
Qtz; Il-Mnt
Qtz
Qtz
Qtz
Qtz

(b)

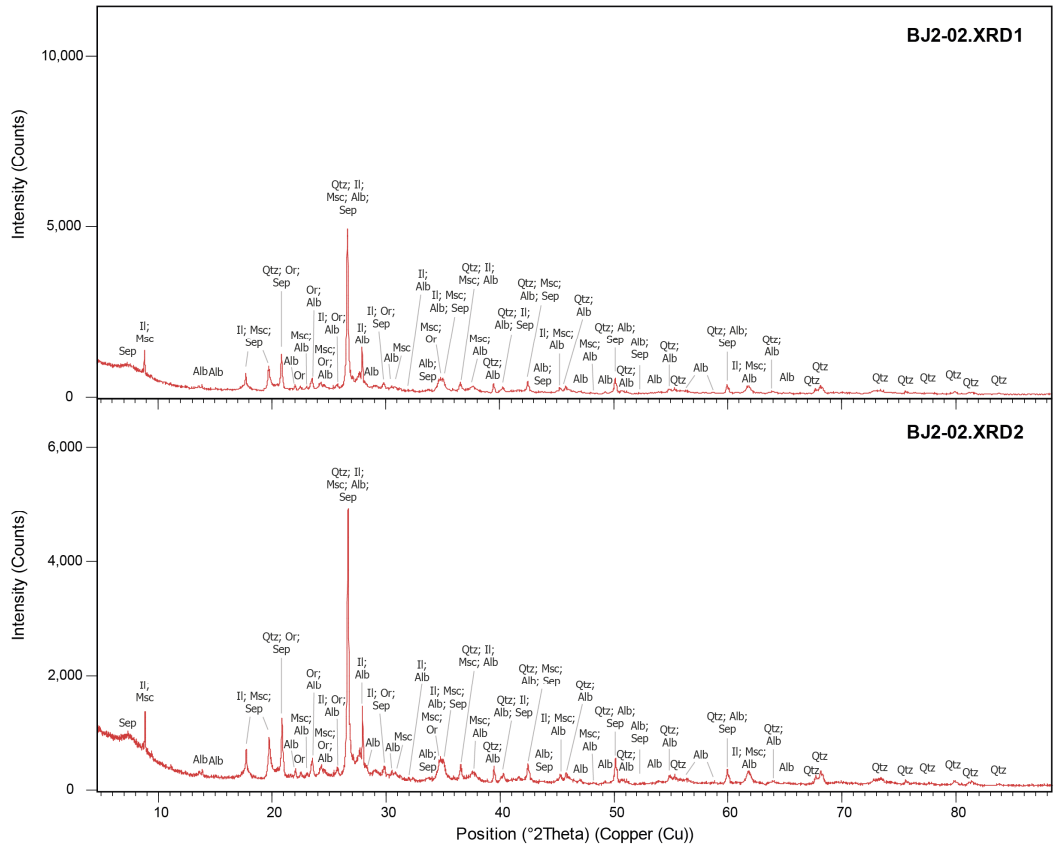

(c)

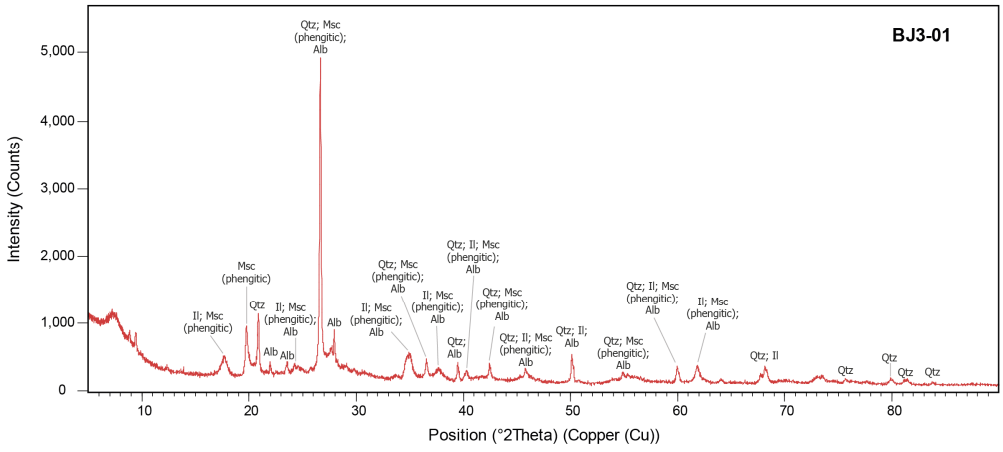

(d)

Figure A6. X-ray diffractograms of the selected samples of altered petalite crystals: (**a**) BJ.450, (**b**) BJ2-01, (**c**) BJ2-02, and (**d**) BJ3-01. Alb—albite; Il—illite; Kao—kaolinite; Mnt—montmorillonite; Msc—muscovite; Non—nontronite; Or—orthoclase; Qtz—quartz; Sep—sepiolite.

References

1. Lypaczewski, P.; Rivard, B.; Lesage, G.; Byrne, K.; D'Angelo, M.; Lee, R.G. Characterization of Mineralogy in the Highland Valley Porphyry Cu District Using Hyperspectral Imaging, and Potential Applications. *Minerals* **2020**, *10*, 473.

2. Laakso, K.; Peter, J.M.; Rivard, B.; Gloaguen, R. Combined hyperspectral and lithogeochemical estimation of alteration intensities in a volcanogenic massive sulfide deposit hydrothermal system: A case study from Northern Canada. In Proceedings of the 2016 8th Workshop on Hyperspectral Image and Signal Processing: Evolution in Remote Sensing (WHISPERS), Los Angeles, CA, USA, 21–24 August 2016; pp. 1–5.

3. Laakso, K.; Peter, J.M.; Rivard, B.; White, H.P. Short-Wave Infrared Spectral and Geochemical Characteristics of Hydrothermal Alteration at the Archean Izok Lake Zn-Cu-Pb-Ag Volcanogenic Massive Sulfide Deposit, Nunavut, Canada: Application in Exploration Target Vectoring. *Econ. Geol.* **2016**, *111*, 1223–1239.

4. Turner, D.; Rivard, B.; Groat, L. Rare earth element ore grade estimation of mineralized drill core from hyperspectral imaging spectroscopy. In Proceedings of the 2014 IEEE Geoscience and Remote Sensing Symposium, Quebec City, QC, Canada, 13–18 July 2014; pp. 4612–4615.

5. Möller, V.; Williams-Jones, A.E. A hyperspectral study (V-NIR-SWIR) of the Nechalacho REE-Nb-Zr deposit, Canada. *J. Geochem. Explor.* **2018**, *188*, 194–215.

6. Sun, Y.; Seccombe, P.K.; Yang, K. Application of short-wave infrared spectroscopy to define alteration zones associated with the Elura zinc–lead–silver deposit, NSW, Australia. *J. Geochem. Explor.* **2001**, *73*, 11–26.

7. Tappert, M.C.; Rivard, B.; Giles, D.; Tappert, R.; Mauger, A. The mineral chemistry, near-infrared, and mid-infrared reflectance spectroscopy of phengite from the Olympic Dam IOCG deposit, South Australia. *Ore Geol. Rev.* **2013**, *53*, 26–38.

8. Naleto, J.L.C.; Perrotta, M.M.; Costa, F.G.d.; de Souza Filho, C.R. Point and imaging spectroscopy investigations on the Pedra Branca orogenic gold deposit, Troia Massif, Northeast Brazil: Implications for mineral exploration in amphibolite metamorphic-grade terrains. *Ore Geol. Rev.* **2019**, *107*, 283–309.

9. Linnen, R.L.; Van Lichtervelde, M.; Černý, P. Granitic Pegmatites as Sources of Strategic Metals. *Elements* **2012**, *8*, 275–280.

10. Goodenough, K.M.; Shaw, R.A.; Smith, M.; Estrade, G.; Marqu, E.; Bernard, C.; Nex, P. Economic mineralization in pegmatites: Comparing and contrasting NYF and LCT examples. *Can. Mineral.* **2019**, *57*, 753–755.

11. Kesler, S.E.; Gruber, P.W.; Medina, P.A.; Keoleian, G.A.; Everson, M.P.; Wallington, T.J. Global lithium resources: Relative importance of pegmatite, brine and other deposits. *Ore Geol. Rev.* **2012**, *48*, 55–69.

12. Selway, J.B.; Breaks, F.W.; Tindle, A.G. A Review of Rare-Element (Li-Cs-Ta) Pegmatite Exploration Techniques for the Superior Province, Canada, and Large Worldwide Tantalum Deposits. *Explor. Min. Geol.* **2005**, *14*, 1–30.

13. Dill, H.G. Pegmatites and aplites: Their genetic and applied ore geology. *Ore Geol. Rev.* **2015**, *69*, 417–561.

14. Steiner, B.M. Tools and Workflows for Grassroots Li–Cs–Ta (LCT) Pegmatite Exploration. *Minerals* **2019**, *9*, 499.

15. Zhang, A.; Wang, R.; Li, Y.; Hu, H.; Lu, X.; Ji, J.; Zhang, H. Tourmalines from the Koktokay No.3 pegmatite, Altai, NW China: Spectroscopic characterization and relationships with the pegmatite evolution. *Eur. J. Mineral.* **2008**, *20*, 143–154.

16. Carrino, T.A.; de Brito Barreto, S.; de Oliveira, P.J.A.; de Araújo Neto, J.F.; de Lima Correia, A.M. Linking gemology and spectral geology: A case study of elbaites from Seridó Pegmatite Province, Northeastern Brazil. *Braz. J. Geol.* **2019**, *49*.

17. Bocchio, R.; Adamo, I.; Caucia, F. Aquamarine from the Masino-Bregaglia Massif, Central Alps, Italy. *Gems Gemol.* **2009**, *45*, 204–207.

18. de Araújo Neto, J.F.; de Brito Barreto, S.; Carrino, T.A.; Müller, A.; de Lira Santos, L.C.M. Mineralogical and gemological characterization of emerald crystals from Paraná deposit, NE Brazil: A study of mineral chemistry, absorption and reflectance spectroscopy and thermal analysis. *Braz. J. Geol.* **2019**, *49*.

19. da Silva, S.M.P.; Crósta, A.P.; Angélica, R.S.; Beurlen, H.; da Silva, M.R.R. Mineralogical characterization and mapping using reflectance spectroscopy: An experiment at Alto do Giz pegmatite in the south portion of Borborema Pegmatite Province (BPP), northeastern Brazil. *Estud. Geol.* **2009**, *19*, 337–342.

20. Cardoso-Fernandes, J.; Lima, A.; Roda-Robles, E.; Teodoro, A.C. Constraints and potentials of remote sensing data/techniques applied to lithium (Li)-pegmatites. *Can. Mineral.* **2019**, *57*, 723–725.

21. Cardoso-Fernandes, J.; Teodoro, A.C.; Lima, A. Remote sensing data in lithium (Li) exploration: A new approach for the detection of Li-bearing pegmatites. *Int. J. Appl. Earth Obs. Geoinf.* **2019**, *76*, 10–25.

22. Santos, D.; Teodoro, A.; Lima, A.; Cardoso-Fernandes, J. Remote sensing techniques to detect areas with potential for lithium exploration in Minas Gerais, Brazil. In Proceedings of the SPIE Remote Sensing, Strasbourg, France, 9–12 September 2019; Schulz, K., Michel, U., Nikolakopoulos, K.G., Eds.; SPIE: Bellingham, WA, USA, 2019.

23. Cardoso-Fernandes, J.; Teodoro, A.C.; Lima, A.; Roda-Robles, E. Semi-Automatization of Support Vector Machines to Map Lithium (Li) Bearing Pegmatites. *Remote Sens.* **2020**, *12*, 2319.

24. Gao, Y.; Bagas, L.; Li, K.; Jin, M.; Liu, Y.; Teng, J. Newly Discovered Triassic Lithium Deposits in the Dahongliutan Area, NorthWest China: A Case Study for the Detection of Lithium-Bearing Pegmatite Deposits in Rugged Terrains Using Remote-Sensing Data and Images. *Front. Earth Sci.* **2020**, *8*, 553.

25. Costa, M.A.C.; Perrotta, M.M.; Melo, T.G.; Turra, B. Estudos Espectrais. In *Avaliação do Potencial do Lítio no Brasil: Área do Médio Rio Jequitinhonha, Nordeste de Minas Gerais: Texto Explicativo e Mapas*; Paes, V.J.C., Santos, L.D., Tedeschi, M.F., Betiollo, L.M., Eds.; CPRM: Belo Horizonte, MG, Brazil, 2016; p. 276.

26. Vieira, R. Aplitopegmatitos com Elementos Raros da Região Entre Almendra (V.N. de Foz Côa) e Barca d'Alva (Figueira de Castelo Rodrigo). Campo Aplitopegmatítico da Fregeneda-Almendra. Ph.D. Thesis, Faculdade de Ciências da Universidade do Porto, Porto, Portugal, 2010.

27. Roda, E. Distribución, Caracteristicas y Petrogenesis de las Pegmatitas de La Fregeneda (Salamanca). Ph.D. Thesis, Facultad de Ciencia y Tecnología de la Universidad del País Vasco (UPV/EHU), Bilbao, Spain, 1993.

28. Cardoso-Fernandes, J.; Teodoro, A.C.; Lima, A.; Roda-Robles, E. Evaluating the performance of support vector machines (SVMs) and random forest (RF) in Li-pegmatite mapping: Preliminary results. In Proceedings of the SPIE Remote Sensing, Strasbourg,

France, 9–12 September 2019; Schulz, K., Michel, U., Nikolakopoulos, K.G., Eds.; SPIE: Bellingham, WA, USA, 2019.

29. Cardoso-Fernandes, J.; Silva, J.; Lima, A.; Teodoro, A.C.; Perrotta, M.; Cauzid, J.; Roda-Robles, E. Characterization of lithium (Li) minerals from the Fregeneda–Almendra region through laboratory spectral measurements: A comparative study. In *Earth Resources and Environmental Remote Sensing/GIS Applications XI*; SPIE: Bellingham, WA, USA, 2020.

30. Cardoso-Fernandes, J.; Silva, J.; Lima, A.; Teodoro, A.C.; Perrotta, M.; Cauzid, J.; Roda-Robles, E.; Ribeiro, M.A. Reflectance spectroscopy to validate remote sensing data/algorithms for satellite-based lithium (Li) exploration (Central East Portugal). In *Earth Resources and Environmental Remote Sensing/GIS Applications XI*; SPIE: Bellingham, WA, USA, 2020.

31. Roda-Robles, E.; Pesquera, A.; Velasco, F.; Fontan, F. The granitic pegmatites of the Fregeneda area (Salamanca, Spain): Characteristics and petrogenesis. *Mineral. Mag.* **1999**, *63*, 535–558.

32. da Costa, J.C.S. *Notícia Sobre Uma Carta Geológica do Buçaco, de Nery Delgado*; Serviços Geológicos de Portugal: Lisboa, Portugal, 1950.

33. Teixeira, C. *Notas Sobre Geologia de Portugal o Complexo Xisto-Grauváquico Ante-Ordoviciano*; Empresa Literaria Fluminense Lda.: Lisboa, Portugal, 1955; p. 48.

34. Rodríguez Alonso, M.D.; Díez Balda, M.A.; Perejón, A.; Pieren, A.; Liñán, E.; López Díaz, F.; Moreno, F.; Gámez Vintaned, J.A.; Gónzalez Lodeiro, F.; Martínez Poyatos, D.; et al. Domínio del Complejo Esquisto-Grauváquico: Estratigrafía. La secuencia litoestratigráfica del Neoproterozóico-Câmbrico Inferior. In *Geología de España*; Vera, J.A., Ed.; Geológica de España-Instituto Geológico y Minero de España (SGE-IGME): Madrid, Spain, 2004; pp. 78–81.

35. Pereira, I.; Dias, R.; Bento dos Santos, T.; Mata, J. Exhumation of a migmatite complex along a transpressive shear zone: Inferences from the Variscan Juzbado–Penalva do Castelo Shear Zone (Central Iberian Zone). *J. Geol. Soc.* **2017**, *174*, 1004.

36. Ferreira, J.A.; Bento dos Santos, T.; Pereira, I.; Mata, J. Tectonically assisted exhumation and cooling of Variscan granites in an anatectic complex of the Central Iberian Zone, Portugal: Constraints from LA-ICP-MS zircon and apatite U–Pb ages. *Int. J. Earth Sci.* **2019**, *108*, 2153–2175.

37. da Silva, A.F.; Ribeiro, M.L. *Notícia Explicativa da Folha 15-A: Vila Nova de Foz Côa*; Serviços Geológicos de Portugal: Lisboa, Portugal, 1991; p. 52.

38. da Silva, A.F.; Ribeiro, M.L. *Notícia Explicativa da Folha 15-B: Freixo de Espada à Cinta*; Instituto Geológico e Mineiro: Lisboa, Portugal, 1994; p. 48.

39. Silva, A.F.; Santos, A.J.; Ribeiro, A.; Cabral, J.; Ribeiro, M.L. *Carta Geológica de Portugal na Escala 1/50.000–Folha 15-B–Freixo de Espada à Cinta*; Serviços Geológicos de Portugal: Lisboa, Portugal, 1990.

40. Silva, A.F.; Santos, A.J.; Ribeiro, A.; Ribeiro, M.L. *Carta Geológica de Portugal na Escala 1/50.000–folha 15-A–Vila Nova de Foz Côa*; Serviços Geológicos de Portugal: Lisboa, Portugal, 1990.

41. ASD Inc. *ViewSpec Pro™ User Manual*; ASD Document 600555 Rev. A; ASD Inc.: Boulder, CO, USA, 2008.

42. Menges, F. Spectragryph–Optical Spectroscopy Software, Version 1.2.14. Available online: **http://www.effemm2.de/spectragryph/** (accessed on 22 July 2020).

43. Clark, R.N.; Roush, T.L. Reflectance spectroscopy: Quantitative analysis techniques for remote sensing applications. *J. Geophys. Res. Solid Earth* **1984**, *89*, 6329–6340.

44. Therien, C. Welcome to the PySptools Documentation. Available online: **https://pysptools.sourceforge.io/** (accessed on 22 July 2020).

45. Cardoso-Fernandes, J.; Silva, J.; Dias, F.; Lima, A.; Teodoro, A.C.; Barrès, O.; Cauzid, J.; Perrotta, M.; Roda-Robles, E.; Ribeiro, M.A. Tools for Remote Exploration: A Lithium (Li) Dedicated Spectral Library of the Fregeneda–Almendra Aplite–Pegmatite Field. *Data* **2021**, *6*, 33.

46. Cardoso-Fernandes, J.; Silva, J.; Dias, F.; Lima, A.; Teodoro, A.C.; Barrès, O.; Cauzid, J.; Perrotta, M.; Roda-Robles, E.; Ribeiro, M.A. *Tools for Remote Exploration: A Lithium (Li) Dedicated Spectral Library of the Fregeneda–Almendra Aplite-Pegmatite Field*; Zenodo: Meyrin, Switzerland, 2021.

47. Hunt, G.R.; Salisbury, J.W. Visible and near-infrared spectra of minerals and rocks: I Silicate minerals. *Mod. Geol.* **1970**, *1*, 283–300.

48. Clark, R.N.; King, T.V.V.; Klejwa, M.; Swayze, G.A.; Vergo, N. High spectral resolution reflectance spectroscopy of minerals. *J. Geophys. Res. Solid Earth* **1990**, *95*, 12653–12680.

49. Pontual, S.; Merry, N.J.; Gamson, P. *Spectral Interpretation Field Manual: GMEX Spectral Analysis Guides for Mineral Exploration*, 3rd ed.; AusSpec International Ltd.: Victoria, Australia, 2008; Volume 1.

50. Clark, R.N.; Swayze, G.A.; Gallagher, A.J.; King, T.V.V.; Calvin, W.M. *The U. S. Geological Survey, Digital Spectral Library: Version 1 (0.2 to 3.0 um)*; Open-File Report 93–592; Geological Survey: Reston, WV, USA, 1993.

51. Mattson, S.M.; Rossman, G.R. Fe^{2+}-Fe^{3+} interactions in tourmaline. *Phys. Chem. Miner.* **1987**, *14*, 163–171.

52. Clark, R.N. Chapter 1: Spectroscopy of rocks and minerals and principles of spectroscopy. In *Remote Sensing for the Earth Sciences: Manual of Remote Sensing*, 3rd ed.; Ryerson, R.A., Ed.; John Wiley & Sons, Inc.: Hoboken, NJ, USA, 1999.

53. Hunt, G.R. Spectral signatures of particulate minerals in the visible and near infrared. *Geophysics* **1977**, *42*, 501–513.

54. King, T.V.V.; Clark, R.N. Spectral characteristics of chlorites and Mg-serpentines using high-resolution reflectance spectroscopy. *J. Geophys. Res. Solid Earth* **1989**, *94*, 13997–14008.

55. Clark, R.N.; Swayze, G.A.; Wise, R.; Livo, K.E.; Hoefen, T.M.; Kokaly, R.F.; Sutley, S.J. USGS Digital Spectral Library splib05a. Available online: **https://pubs.usgs.gov/of/2003/ofr-03-395/** (accessed on 8 January 2021).

56. Hunt, G.R.; Ashley, R.P. Spectra of altered rocks in the visible and near infrared. *Econ. Geol.* **1979**, *74*, 1613–1629.

57. Cardoso-Fernandes, J.; Dias, F.; Lima, A.; Anjos Ribeiro, M.; Perrotta, M.; Roda-Robles, E.; Teodoro, A.C. Petalite alteration products from the Bajoca pegmatite (Central Portugal): A multiapproach for lithium exploration. In Proceedings of the EGU General Assembly 2021, Online, 19–30 April 2021.

58. Lima, A. Estrutura, Mineralogia e Génese dos Filões Aplitopegmatíticos com Espodumena da Região do Barroso-Alvão. Ph.D. Thesis, Universidade do Porto, Porto, Portugal, 2000.

59. Lypaczewski, P.; Rivard, B. Estimating the Mg# and AlVI content of biotite and chlorite from shortwave infrared reflectance spectroscopy: Predictive equations and recommendations for their use. *Int. J. Appl. Earth Obs. Geoinf.* **2018**, *68*, 116–126.

60. Bishop, J.L.; Lane, M.D.; Dyar, M.D.; Brown, A.J. Reflectance and emission spectroscopy study of four groups of phyllosilicates: Smectites, kaolinite-serpentines, chlorites and micas. *Clay Miner.* **2008**, *43*, 35–54.

61. Felzer, B.; Hauff, P.; Goetz, A.F.H. Quantitative reflectance spectroscopy of buddingtonite from the Cuprite mining district, Nevada. *J. Geophys. Res. Solid Earth* **1994**, *99*, 2887–2895.

62. Krohn, M.D.; Altaner, S.P. Near-infrared detection of ammonium minerals. *Geophysics* **1987**, *52*, 924–930.

63. Aires, S.C.M. Petrofísica e Litogeoquímica de Formações do "Complexo Xisto-Grauváquico" (Grupo do Douro) Estudo do Potencial do "Xisto" Para Exploração Como Pedra Natural. Ph.D. Thesis, Faculdade de Ciências da Universidade do Porto, Porto, Portugal, 2018.

64. Duke, E.F. Near infrared spectra of muscovite, Tschermak substitution, and metamorphic reaction progress: Implications for remote sensing. *Geology* **1994**, *22*, 621–624.

65. Ellis, R.J.; Scott, P.W. Evaluation of hyperspectral remote sensing as a means of environmental monitoring in the St. Austell China clay (kaolin) region, Cornwall, UK. *Remote Sens. Environ.* **2004**, *93*, 118–130.

66. Oshigami, S.; Yamaguchi, Y.; Uezato, T.; Momose, A.; Arvelyna, Y.; Kawakami, Y.; Yajima, T.; Miyatake, S.; Nguno, A. Mineralogical mapping of southern Namibia by application of continuum-removal MSAM method to the HyMap data. *Int. J. Remote Sens.* **2013**, *34*, 5282–5295.

67. Deer, W.A.; Howie, R.A.; Zussman, J. *Rock-Forming Minerals: Single-Chain Silicates*, 2nd ed.; The Geological Society: London, UK, 1978; Volume 2A, p. 668.

68. London, D.; Burt, D.M. Chemical models for lithium aluminosilicate stabilities in pegmatites and granites. *Am. Mineral.* **1982**, *67*, 494–509.

69. Dill, H.G. A geological and mineralogical review of clay mineral deposits and phyllosilicate ore guides in Central Europe—A function of geodynamics and climate change. *Ore Geol. Rev.* **2020**, *119*, 103304.

70. Cerny, P. The Tanco pegmatite at Bernic Lake, Manitoba; VIII, Secondary minerals from the spodumene-rich zones. *Can. Mineral.* **1972**, *11*, 714–726.

71. Asadzadeh, S.; Souza Filho, C.R. A review on spectral processing methods for geological remote sensing. *Int. J. Appl. Earth Obs. Geoinf.* **2016**, *47*, 69–90.

72. Quensel, P. Minerals of the Varuträsk Pegmatite: IV. Petalite and its Alteration Product, Montmorillonite. *Geol. Fören. Stockh. Förh.* **1937**, *59*, 150–156.

73. Quensel, P. Minerals of the Varuträsk Pegmatite: X. Spodumene and its Alteration Products. *Geol. Fören. Stockh. Förh.* **1938**, *60*, 201–215.

74. Foster, M.D. *Interpretation of the Composition of Lithium Micas*; United States Geological Survey Professional Paper: Washington, DC, USA, 1960; pp. 115–147.

Chapter IV: Geochemical exploration techniques as a complementary tool

Geochemical exploration tools are widely used in mineral exploration of gold (Au), copper (Cu), tungsten (W), and polymetallic deposits (Chandrajith *et al.*, 2001; Gonçalves *et al.*, 2001; Cheng, 2007; Shahrestani *et al.*, 2018; Ghezelbash *et al.*, 2019). Similar geochemical exploration campaigns can also be used for the identification of LCT pegmatites (Selway *et al.*, 2005; Steiner, 2019) through (i) soil sampling (Luecke, 1984; Galeschuk & Vanstone, 2007), (ii) stream sediment analysis (Fyzollahhi *et al.*, 2018; Steiner, 2018), (iii) whole-rock/mineral chemistry (Smeds, 1992; Dimmell & Morgan, 2005; Barros *et al.*, 2020) or (iv) a combination of multiple techniques (Nieder *et al.*, 2014).

The present chapter presents two distinct geochemical approaches that aim to complement and integrate the remote sensing results (Chapters II and III). The first (section IV.1.) concerns the reprocessing of historical stream sediment datasets, covering the case study area, for Li-pegmatite exploration. At first, it was fundamental to know and to evaluate the element distributions and lithological influence in each stream sediment sample. Descriptive and multivariate statistical techniques were employed to identify elemental associations in the whole dataset (Lima *et al.*, 2019) and considering sample location within granitic or metasedimentary rocks (Lima *et al.*, 2021). In a second stage, the same statistical techniques were employed to identify pathfinder elements for Li-exploration based on elemental associations observed in the whole-rock geochemical analysis of the Bajoca petalite dyke (Cardoso-Fernandes *et al.*, 2020a) and several Li-mineralized bodies in the CIZ (Cardoso-Fernandes *et al.*, 2020b). These works resulted in one extended abstract presented at an international conference, two abstracts presented at national conferences, and an abstract in a national journal (Appendix I.3). Most of the work was conducted in the framework of the LIGHTS project. The collaboration with the project partners resulted in a submitted peer-reviewed journal article comparing two distinct methodological approaches – spatial interpolation and catchment basins methods – for Li-pegmatite exploration (section IV.1.).

The second approach (section IV.2.) concerns the definition and characterization of exomorphic, metasomatic haloes in the metasedimentary host rocks caused by pegmatite installation. This work was conducted in collaboration with both LIGHTS and GREENPEG (https://www.greenpeg.eu/) projects. Two distinct sampling campaigns were conducted in the Fregeneda-Almendra area, at different stages, each one in the scope of a project, thus allowing

to improve the sampling methodology from one campaign to the other. Details on sampling, sample preparation, and analytical techniques can be found in Appendix II. In the first stage, it was necessary to comprehend the influence of lithology and mineralogy in the geochemical results. This was fundamental to ascertain if chemical variations are due to metasomatic processes or due to changes in lithology or even late weathering processes. Therefore, detailed petrographic and lithogeochemical analyses were employed (Appendix III and II, respectively). A parallel study was also conducted, resultant from the petrographic observations, in which biotite microstructures were investigated, and their implications for the tectonometamorphic history of the Bajoca region were accessed (Cardoso-Fernandes *et al*., 2019). Also, a preliminary analysis of the LIGHTS' campaign results allowed identifying the Li-correlated elements in the host rock samples while displaying the potential to use whole-rock geochemistry to discriminate between barren and Li-bearing dykes and vector possible buried pegmatites (Cardoso-Fernandes *et al*., 2021). These works resulted in two abstracts, the first presented at a national conference and the second at an international one (Appendix I.3). In collaboration with the GREENPEG project partners, a mass-balance study was conducted to understand element mobility during the pegmatite-induced metasomatism, as well as to understand the extent of the haloes and their implication to mineral exploration. This resulted in a work to be submitted in an international peer-reviewed journal (section IV.2.). The supplementary materials to this work are presented in Appendix II.5. Complementary, hyperspectral studies were also conducted to evaluate the possibility to use remote sensing data in the detection of the pegmatites' haloes (Appendix IV).

References

Barros, R., Kaeter, D., Menuge, J. F., & Škoda, R. (2020). Controls on chemical evolution and rare element enrichment in crystallising albite-spodumene pegmatite and wallrocks: Constraints from mineral chemistry. *Lithos, 352-353*, 105289. doi: https://doi.org/10.1016/j.lithos.2019.105289.

Cardoso-Fernandes, J., Lima, A., Roda-Robles, E., Ribeiro, M. A., & Teodoro, A. (2020b). *Geochemical pathfinder analysis for lithium (Li) exploration in the Iberian Peninsula.* Paper presented at the X Congresso Jovens Investigadores em Geociências, LEG, Estremoz, 12-15.

Cardoso-Fernandes, J.; Lima, A.; Roda-Robles, E.; Anjos Ribeiro, M.; Teodoro, A. (2020a). Associações elementares nos aplito-pegmatitos da mina da Bajoca (Almendra, Vila Nova de Foz Côa). *GeoCore 5*, 24-25.

Cardoso-Fernandes, J.; Lima, A.; Roda-Robles, E.; Ribeiro, M.A.; Teodoro, A. (2021; in press). *Vectoring lithium (Li) mineralizations: a first approach to pegmatite geochemical halo definition in the Fregeneda-Almendra area*. Abstract presented at Goldschmidt Virtual, 2021.

Cardoso-Fernandes, J.; Ribeiro, M.; Lima, A.; Roda-Robles, E.; Teodoro, A.; Lima, J. (2019). *Biotite porphyroblast microstructures in the Almendra (Vila Nova de Foz Côa) region*. Paper presented at IX Congresso Jovens Investigadores em Geociências, LEG 2019, Estremoz, 2019.

Chandrajith, R., Dissanayake, C. B., & Tobschall, H. J. (2001). Application of multi-element relationships in stream sediments to mineral exploration: a case study of Walawe Ganga Basin, Sri Lanka. *Applied Geochemistry, 16*(3), 339-350. doi: https://doi.org/10.1016/S0883-2927(00)00038-X.

Cheng, Q. (2007). Mapping singularities with stream sediment geochemical data for prediction of undiscovered mineral deposits in Gejiu, Yunnan Province, China. *Ore Geology Reviews, 32*(1-2), 314-324. doi: 10.1016/j.oregeorev.2006.10.002.

Dimmell, P. M., & Morgan, J. A. (2005). The Aubry Pegmatites: Exploration for Highly Evolved Lithium-Cesium-Tantalum Pegmatites in Northern Ontario. *Exploration and Mining Geology, 14*(1-4), 45-59. doi: 10.2113/gsemg.14.1-4.45.

Fyzollahhi, N., Torshizian, H., Afzal, P., & Jafari, M. R. (2018). Determination of lithium prospects using fractal modeling and staged factor analysis in Torud region, NE Iran. *Journal of Geochemical Exploration, 189*, 2-10. doi: https://doi.org/10.1016/j.gexplo.2017.09.017.

Galeschuk, C. R., & Vanstone, P. J. (2007). Exploration techniques for rare-element pegmatite in the Bird River greenstone belt, southeastern Manitoba. In B. Milkereit (Ed.), *Proceedings of Exploration 07: Fifth Decennial International Conference on Mineral Exploration* (pp. 823–839).

Ghezelbash, R., Maghsoudi, A., & Carranza, E. J. M. (2019). An Improved Data-Driven Multiple Criteria Decision-Making Procedure for Spatial Modeling of Mineral Prospectivity: Adaption of Prediction–Area Plot and Logistic Functions. *Natural Resources Research, 28*(4), 1299-1316. doi: 10.1007/s11053-018-9448-6.

Gonçalves, M. A., Mateus, A., & Oliveira, V. (2001). Geochemical anomaly separation by multifractal modelling. *Journal of Geochemical Exploration, 72*(2), 91-114. doi: https://doi.org/10.1016/S0375-6742(01)00156-X.

Lima, J.; Cardoso-Fernandes, J.; Lima, A. (2021). *Análise estatística da geoquímica de sedimentos de corrente em rochas graníticas e formações metassedimentares do Alto Douro (NE de Portugal)*. Abstract presented at Jornadas do ICT, Porto, 2021.

Lima, J.; Cardoso-Fernandes, J.; Lima, A.; Teodoro, A. (2019). *Statistical processing and principal component analysis of geochemical data from stream sediments for Li exploration*. Paper presented at XII Congresso Ibérico de Geoquímica (CIG), Évora, 2019.

Luecke, W. (1984). Soil Geochemistry above a Lithium Pegmatite Dyke at Aclare, Southeast Ireland. *Irish Journal of Earth Sciences, 6*(2), 205-211.

Nieder, R., Weber, T. K. D., Paulmann, I., Muwanga, A., Owor, M., Naramabuye, F.-X., Gakwerere, F., Biryabarema, M., Biester, H., & Pohl, W. (2014). The geochemical signature of rare-metal pegmatites in the Central Africa Region: Soils, plants, water and stream sediments in the Gatumba tin–tantalum mining district, Rwanda. *Journal of Geochemical Exploration, 144*, 539-551. doi: https://doi.org/10.1016/j.gexplo.2014.01.025.

Selway, J. B., Breaks, F. W., & Tindle, A. G. (2005). A Review of Rare-Element (Li-Cs-Ta) Pegmatite Exploration Techniques for the Superior Province, Canada, and Large Worldwide Tantalum Deposits. *Exploration and Mining Geology, 14*(1-4), 1-30. doi: 10.2113/gsemg.14.1-4.1.

Shahrestani, S., Mokhtari, A. R., & Hosseini-Dinani, H. (2018). How does sampling density affect mineralization detection in stream sediment geochemical exploration? A case study from NW of Iran. *Geochemistry: Exploration, Environment, Analysis, 18*(3), 196-203. doi: 10.1144/geochem2017-076.

Smeds, S. A. (1992). Trace elements in potassium-feldspar and muscovite as a guide in the prospecting for lithium- and tin-bearing pegmatites in Sweden. *Journal of Geochemical Exploration, 42*(2), 351-369. doi: https://doi.org/10.1016/0375-6742(92)90032-4.

Steiner, B. (2018). Using Tellus stream sediment geochemistry to fingerprint regional geology and mineralisation systems in Southeast Ireland. *Irish Journal of Earth Sciences, 36*, 45-61. doi: 10.3318/ijes.2018.36.45.

Steiner, B. M. (2019). Tools and Workflows for Grassroots Li–Cs–Ta (LCT) Pegmatite Exploration. *Minerals, 9*(8), 499. doi: 10.3390/min9080499.

IV.1. Stream sediment analysis for Lithium (Li) exploration in the Douro region (Portugal): a comparative study of the spatial interpolation and catchment basin approaches

Joana Cardoso-Fernandes, Jessica Lima, Alexandre Lima, Encarnación Roda-Robles, Martin Köhler, Stefan Schaefer, Andreas Barth, Andreas Knobloch, Mário A. Gonçalves, Filipe Gonçalves, Ana Cláudia Teodoro

Submitted to *Journal of Geochemical Exploration*

Abstract: Lithium (Li) was recently added to the list of critical raw materials by the European Union due to its significance for the green energy transition. Thus, the development of new toolchains to make Li exploration more economic and more effective is needed. Stream sediment analysis can play an important part in these new tool chains. In this work, two historical stream sediment datasets covering parts of the Fregeneda-Almendra pegmatite field in the Douro region (Portugal) were reprocessed considering two distinct approaches: spatial interpolation through inverse distance weighting (IDW) and the catchment basin approach using the concentration area (C-A) fractal analysis. The following objectives were delineated: (i) determine pathfinder elements for Li, considering relevant associations in the mineralization sources; (ii) compare the performance of both approaches; (iii) identify new target areas for Li. In the case of spatial interpolation, the highest Li values were associated to granites although the use of key elements allowed lithological discrimination and the delineation of target areas. In the catchment basin approach, fractal analysis proved to be effective in decreasing the number of areas of interest with high accuracy (>75%) when considering the previously mapped Li-pegmatites. One of the limitations identified was the number of anomalous basins related to the granites, despite the use of pathfinder elements allowing discriminating granite- from pegmatite-related Li anomalies. Comparing the two approaches, the spatial interpolation method is more adequate for the early stages of exploration (reconnaissance), while the catchment basin approach is more suited for prospect-scale exploration. Field validation of the results identified one pegmatite containing Li mineralization and three others with favorable signs for Li mineralization in the Douro region.

Keywords: geochemical exploration, pathfinder elements, inverse distance weighted (IDW), concentration-area (C-A) fractal analysis, portable LIBS, portable XRF

1. Introduction

Stream sediment analysis and separation of anomalous samples from the background are a common and well-accepted tool employed in mineral exploration, especially to target metallic mineral occurrences, namely gold (Au) and copper (Cu), where the pathfinder elements and their mobility are well-known (Carranza and Hale, 1997; Cheng et al., 1994; Ghezelbash and Maghsoudi, 2018; Hawkes, 1976; Mokhtari and Garousi Nezhad, 2015; Shahrestani and Mokhtari, 2017; Zuo, 2011). Stream sediment sampling is mainly employed in the reconnaissance stage of an exploration campaign allowing to delineate target areas and to reduce the number of favorable regions to conduct more detailed studies in the subsequent exploration stages (Carranza and Hale, 1997; Mokhtari and Garousi Nezhad, 2015). The analysis of this source of data can either rely on spatial interpolation techniques that include moving averages or kriging techniques, for example (Ghezelbash et al., 2019; Zuo, 2011), or on the sample catchment basin approach (Bonham-Carter et al., 1987; Mokhtari and Garousi Nezhad, 2015).

In the past decade, there has been an increasing demand for other raw materials that became essential for the green energy transition. This is the case of lithium (Li), which was recently considered critical by the European Union based on its economic importance and supply risk (European Commission: DG Internal Market Industry Entrepreneurship and SMEs, 2020). According to Kesler et al. (2012), the major hard-rock Li-deposits in Europe are hosted in pegmatites. Currently, there is only a few number of studies concerning the use of stream sediments to target pegmatite deposits, most of them related to lithium-cesium-tantalum (LCT) pegmatites (Dill et al., 2014; Frick and Strauss, 1987; Steiner, 2018). More recently, Fyzollahhi et al. (2018) and Saadati et al. (2020) have successfully used stream sediment data for Li exploration in Iran to identify prospects related to both granitic rocks and pegmatites and sedimentary hectorite deposits. However, Li is a mobile cation, in contrast with Sn, Nb, and Ta which are immobile ions in stream sediments which might pose a constraint for the use of this kind of geochemical exploration technique (Rose et al., 1979).

In the framework of the “Lightweight Integrated Ground and Airborne Hyperspectral Topological Solution” (LIGHTS; http://lights.univ-lorraine.fr/) project, one of the main aims is to

create a toolchain to make Li exploration more economically sustainable and effective (Cardoso-Fernandes et al., 2020b). To achieve this, historical stream sediment datasets covering the Douro region and the Portuguese portion of the Fregeneda-Almendra aplite-pegmatite field were reprocessed. Distinct methodological approaches employed by the project partners were confronted in this study. Additionally, to better understand the mobility of Li and related elements, this study compares for the first time the elemental associations observed in stream sediment samples with the ones observed at the mineralization source, i.e. pegmatite dykes and leucogranitic cupolas from the Iberian Peninsula. Taking this into account, the following objectives were defined for this study: (i) determine relevant pathfinder elements for Li in stream sediment samples; (ii) compare the results obtained with both spatial interpolation and catchment basins approaches and establish their utility in relation to traditional exploration stages; and (iii) delineate new Li prospects in the Douro region. Therefore, the findings presented in this work are a valuable contribution to the state of the art, since they can help in future and similar geochemical exploration campaigns for Li in other locations.

2. Study area and geological setting

The Li-mineralization in the Iberian Peninsula occurs along a belt with around 500 km in length and 150 km in width, mainly in aplite-pegmatite dykes but also in leucogranitic cupolas (Roda-Robles et al., 2016; Roda-Robles et al., 2018). This belt is located within the Central Iberian Zone (CIZ), which occupies a central portion of the Iberian Massif, one of the biggest and most complete fragments of the European Variscan Belt (Pérez-Estaún et al., 2004). The CIZ is mainly composed of a Neoproterozoic to Paleozoic metasedimentary succession, intruded by several Variscan granitoids (Martínez Catalán et al., 2004; Roda-Robles et al., 2018). Other important Li-occurrences are located in the Galicia-Trás-os-Montes Zone (GTMZ), a terrane accreted over the CIZ, that have similar ages and features to those in the CIZ (GTMZ: 310 ± 5 Ma; CIZ: 301 ± 3 Ma by U-Pb dating of columbite-group minerals) (Melleton et al., 2011; Roda-Robles et al., 2016; Roda-Robles et al., 2018).

The Fregeneda-Almendra aplite-pegmatite field corresponds to one of the Li-occurrences within the CIZ (Fig. 1). The field is divided into two sectors: an eastern side in the Salamanca province (Spain) and a western sector in Vila Nova de Foz Côa (Portugal). This study focuses on the Portuguese side of the field, where historical stream sediment geochemical data is available covering not only the Portuguese sector of the pegmatite field, but also a larger extent of the Douro region. The Li-pegmatites are emplaced in the Douro Group (Sousa, 1982; Sousa,

1983, 1984) of the Dúrico-Beirão Super Group (Silva et al., 1989), previously known as "Complexo Xisto-Grauváquico" (CXG) (Costa, 1950; Teixeira, 1955). The CXG corresponds to a monotonous pre-Ordovician pelitic-sandy flysch series of Upper Proterozoic to the Lower Cambrian age (Díez Balda et al., 1990; Rodríguez Alonso et al., 2004; Sousa, 1984). The series resulted from the accumulation of a thick sediment column (8000 m to 11000 m), under a regime of tectonic instability, in a foreland type basin created by the CIZ's compartmentation in fault-delimited blocks, during the Cadomian orogeny (Rodríguez Alonso et al., 2004; San José et al., 1990). In its turn, the Douro Group corresponds to a stratigraphic succession, characterized by interlayered phyllites and metagreywackes with turbiditic features, divided into six different formations that are, from the base to the top: Bateiras, Ervedosa, Rio Pinhão, Pinhão, Desejosa, and S. Domingos (Sousa, 1982; Sousa, 1983). Based on facies analysis, the basal formations present a distal turbiditic character, whilst the top formations present a proximal turbiditic character (Sousa, 1982; Sousa, 1983). At northeast, the Desejosa formation is overlayed by the Lower Ordovician quartzites from the Poiares' syncline and contacts with the alternating Ordovician quartzites and phyllites from the Castelo Melhor's syncline (Fig. 1) (Silva et al., 1990a; Silva et al., 1990b; Silva and Ribeiro, 1991, 1994). To the south of the study area, a more local CXG formation was also identified – the Excomungada formation (Ribeiro, 2001; Ribeiro and Silva, 2000). This formation belongs to the Arda-Marofa group proposed by Silva et al. (1995) and represents the culmination of the sedimentation in the basin and is characterized by the presence of modified-wave turbidites sedimented in a siliciclastic platform with strong subsidence (Silva, 2005). The Excomungada formation is mainly composed of chloritic phyllites and quartzphyllites overlaying, by sedimentary progradation, upon the Rio Pinhão formation (Ribeiro and Silva, 2000; Silva, 2005). North of the Lower Ordovician quartzites from Poiares-Figueira de Castelo Rodrigo formation and the Middle to Upper Ordovician grey to black phyllites of the Santo Antão formation, the Excomungada formation suffered intense metamorphism (ultrametamorphism) leading to the formation of migmatites (Carvalhosa, 1960; Ribeiro, 2001; Ribeiro and Silva, 2000).

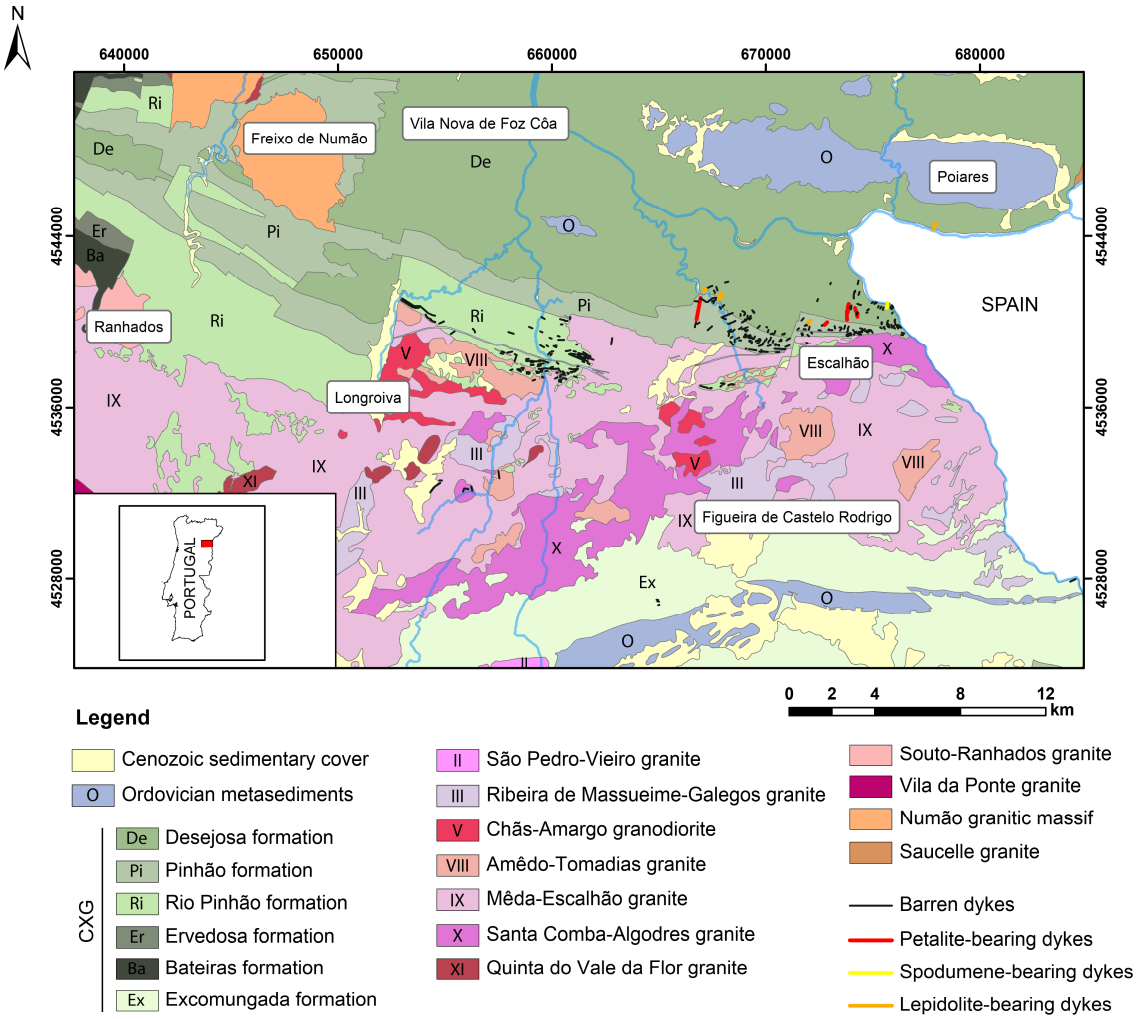

Fig. 1. Location of the study area and geological setting of the Portuguese side of the Fregeneda-Almendra aplite-pegmatite field, adapted from Carvalhosa (1960); Ribeiro and Silva (2000); Silva et al. (1990a); Silva et al. (1990b) and unpublished geological data at the scale of 1:25,000. Roman numerals are from Ribeiro and Silva (2000). Location and classification of the Portuguese aplite-pegmatite dykes from Vieira (2010). Map projection: Universal Transverse Mercator zone 29N from the WGS84 datum.

The metasedimentary sequences of the CXG were intruded by several granitoid rocks (Fig. 1), mainly in the south of the area, in the Figueira de Castelo Rodrigo–Lumbrales Anatectic Complex (FCR–LAC; Pereira et al. (2017)). These correspond essentially to syn-Variscan (concomitant with the third deformation phase – D3), S-type, two-mica granites ranging from fine- to coarse-grained, depending on the distinct facies (Ferreira et al., 2019; Pereira et al., 2017; Silva and Ribeiro, 1991, 1994). Fine-to-medium-grained, essentially biotitic, granodiorite is also present in the FCR–LAC (Ferreira et al., 2019; Ribeiro, 2001; Silva and Ribeiro, 1991, 1994), as well as some late-D3 two-mica granites with smaller cartographic expression (Silva and Ribeiro, 1991, 1994). Recent U-Pb zircon data show that the granitoids of the FCR-LAC yield ages between 300 and 317 Ma (Ferreira et al., 2019). The FCR-LAC exhumation was assisted by first-order shear zones (Ferreira et al., 2019; Pereira et al., 2017). In the northeast

and northwest of the study area, the late- to post-D3 Saucelle and Freixo de Numão two-mica granites crop out (Silva and Ribeiro, 1991, 1994). Finally, a non-outcropping, leucocratic, fine-to-medium-grained with muscovite >> biotite granite was detected by drilling surveys between the Riba D'Alva mine and Feli mine (305.0 ± 3.3 Ma) (Vieira, 2010). Locally, there are several Cenozoic sedimentary deposits including fluvial and slope deposits, alluvions, and fault-related arkoses covering both granitoids and metasediments (Silva and Ribeiro, 1991, 1994).

Regarding the Li-mineralization, there are four evolved dyke-types containing Li-minerals: (i) petalite-bearing aplite-pegmatites, (ii) spodumene-bearing aplite-pegmatites; (iii) lepidolite and spodumene-bearing aplite-pegmatites; and (iv) lepidolite-bearing aplite-pegmatites (Roda-Robles et al., 1999; Vieira, 2010). These are Li, F, Sn, Rb, Nb>Ta, B, and P enriched bodies (Roda-Robles et al., 1999; Roda, 1993; Vieira, 2010) that are emplaced in the CXG metasediments (Fig. 1). The mineral association includes quartz, feldspar, Li-muscovite, spodumene, petalite, cassiterite, montebrasite, and accessory apatite, Nb-Ta oxides, Fe-Mn phosphates, and eucryptite (Roda-Robles et al., 2018; Vieira, 2010; Vieira et al., 2011). Moreover, there are also several types of barren dykes, most emplaced within or near the granites of the FCR-LAC (Fig. 1). Therefore, there is an increasing fractionation degree to northwards as the distance to the granites increases (Vieira, 2010; Vieira et al., 2011). Similarly, since the metamorphic isograde are parallel to the granites' contact, barren dykes occur in the higher-grade metamorphic zones; petalite-bearing aplite-pegmatites only occur in the andalusite-sillimanite; and spodumene-bearing dykes are emplaced in the biotite and/or chlorite zones (Vieira, 2010; Vieira et al., 2011).

3. The geochemical dataset

In this work, a previous geochemical stream sediment campaign covering the study area (>1,250 km^2) was reprocessed. The historical dataset was acquired in the early 1980s by the Douro consortium composed by the French Bureau de Recherches Géologiques et Minières (BRGM) and the Portuguese institution, Serviço de Fomento Mineiro (SFM). The dataset is composed of a regional campaign containing 3 417 stream sediment samples, covering the 15-A, 15-B, and part of the 15-C and 15-D sheets of the Portuguese Geological Maps at the scale of 1:50 000 representing a density of four samples/km^2 (Viallefond, 1981; Viallefond and Angel, 1981). Moreover, there is a detailed, prospect-scale campaign in the Almendra region that was conducted for tin (Sn) and tungsten (W) exploration, where 298 samples were collected in a 43 km^2 area, representing an average density of about 7 samples/km^2 (Angel and Viallefond, 1981). This smaller, prospect scale campaign covers various lepidolite- and

petalite-bearing dykes including the Bajoca pegmatite (currently exploited as an open-pit mine), which corresponds to a petalite-bearing dyke that reaches 30 m in thickness and over 700 m in length (Almeida, 2003; Roda-Robles et al., 2010; Vieira, 2010). The regional campaign also covers known Li-mineralized dykes.

Similar sample collection and analytical procedures were employed in both regional and prospect scale campaigns. For the regional campaign, in each location, a sample of around 800 gr of fine sediments was collected off-stream. If the fine fraction was unavailable, gravel was sieved *in situ* to 1 mm particle size (Marroncle, 1980b). Each sample was divided into two equal parts, one for keeping and another to be dried at 30ºC in a muffle furnace. The dried part was then milled using a porcelain mortar and sieved to 100 mesh particle size (0.125 mm) in the laboratory (Marroncle, 1980b). From the sieved fraction, 20 gr were set aside for keeping while around 40 gr of the sample were destined for geochemical analysis. Regarding the prospect scale campaign, the samples were previously collected off-stream, dried, and sieved to a particle size less than 80 mesh (0.177 mm) (Marroncle, 1980a; Viegas et al., 1983-85). All samples from the SFM and BRGM datasets were analyzed at the BRGM facilities using optical emission spectrometry or quantometer (Angel and Viallefond, 1981; Viallefond, 1981; Viallefond and Angel, 1981). This multi-element technique provided the simultaneous quantification of 34 elements and compounds, namely SiO_2, Al_2O_3, Fe_2O_3, MgO, CaO, Na_2O, K_2O, TiO_2, MnO, P_2O_5, Ag, As, B, Ba, Be, Bi, Cd, Co, Cr, Cu, La, Li, Mo, Nb, Ni, Pb, Sb, Sn, Sr, V, W, Y, Zn and Zr. However, the reports do not specify details on the digestion methods and analytical precision of the analyses.

3.1. Pre-analysis of the dataset

Before basin delimitation and anomaly definition, exploratory data analysis (EDA) was conducted. First, descriptive statistics of measured and log-transformed data were computed to understand the element distribution of both campaigns separately and as a whole (Table 1). Additionally, graphic tools such as histograms, boxplots, and normal Q-Q plots were used. The analysis of the results shows that despite having similar trends for most elements, their distributions can differ between the two campaigns. Most of the elements/oxides have negatively skewed distributions (except Ba, SiO_2, Al_2O_3, Fe_2O_3, MgO, Na_2O, K_2O). However, BRGM shows element distributions more asymmetric than SFM except for Fe_2O_3, Na_2O, TiO_2, MnO, P_2O_5, Li, Be, and Nb. In both datasets, As, Sn, W, and Pb show a standard deviation higher than the mean. This is also the case of B, Cu, and Nb in the BRGM campaign. The SFM dataset shows: (i) a higher mean for Be, B, Cu, As, Sr, Sn, Ba, and W; (ii) higher standard

deviation for SiO_2, Al_2O_3, Fe_2O_3, TiO_2, MnO, B, Cu, As, Sn, and W; (iii) a higher maximum content for Fe_2O_3, MgO, TiO_2, and MnO; and (iv) a higher minimum content for Al_2O_3, Fe_2O_3, MgO, CaO, Na_2O, K_2O, MnO, Be, B, Cu, Zn, Sr, and Ba. Moreover, the analysis of the results obtained with the graphical tools allowed to observe two populations in the distributions of: (i) As, Ba, Cu, Li, Sn, Sr, and W for both datasets, (ii) Pb and Zn for the SMF campaign, and (iii) Nb for the BRGM campaign. In the case of As, Li, Pb, Nb, Sn, and W, the first population is associated with values near the detection limit. For Sn and W, this population near the detection limit corresponds to the largest one. Also, for CaO, MgO, and Be, their respective distributions are almost exclusively related to values around the detection limit. Compared with the raw data, most element distributions approached a normal-like shape distribution after the logarithmic transformation. However, Be, K_2O, Nb, Sn, and W distributions did not change significantly after the transformation, Li distribution changed to positively skewed, and Na_2O and SiO_2 distributions became more asymmetric.

Table 1. Descriptive statistics for all the stream sediment samples and separate datasets. Min – minimum; Max – maximum; St. Dev. – standard deviation; Skew. – skewness.

	All data					SFM					BRGM				
Element	**Min**	**Max**	**Mean**	**St. Dev.**	**Skew.**	**Min**	**Max**	**Mean**	**St. Dev.**	**Skew.**	**Min**	**Max**	**Mean**	**St. Dev.**	**Skew.**
SiO2	59.00	91.00	76.26	4.90	-0.32	59.00	84.00	72.62	5.56	-0.34	59.00	91.00	76.60	4.65	-0.23
Al2O3	4.00	24.00	12.20	3.12	0.49	6.00	23.00	13.66	3.53	0.34	4.00	24.00	12.03	3.03	0.49
Fe2O3	1.00	11.00	3.95	1.63	0.19	3.00	11.00	5.68	1.57	0.53	1.00	8.00	3.82	1.53	0.03
MgO	0.50	4.00	1.60	0.64	0.49	1.00	4.00	2.30	0.59	0.30	0.50	3.00	1.55	0.60	0.43
CaO	0.50	8.00	0.55	0.24	12.51	0.50	1.00	0.53	0.13	3.48	0.50	8.00	0.55	0.24	12.54
Na2O	0.10	3.60	1.88	0.62	-0.10	0.50	2.60	1.56	0.29	-0.20	0.10	3.60	1.89	0.63	-0.16
K2O	0.90	5.10	2.83	0.58	0.06	1.30	3.70	2.69	0.39	-0.81	0.90	5.10	2.84	0.58	0.07
TiO2	0.12	3.92	0.74	0.32	1.76	0.43	3.92	0.98	0.45	2.89	0.12	3.24	0.72	0.29	1.17
MnO	0.01	0.31	0.05	0.03	2.20	0.02	0.40	0.08	0.05	3.40	0.01	0.27	0.05	0.02	1.70
P2O5	0.01	1.20	0.18	0.11	1.22	0.01	0.73	0.10	0.07	3.92	0.02	1.20	0.18	0.11	1.17
Li	1.00	619.00	72.40	68.11	1.36	1.00	353.00	63.85	52.64	1.46	1.00	619.00	72.55	68.75	1.35
Be	0.50	12.00	0.93	0.62	5.33	1.00	7.00	1.12	0.53	6.67	0.50	12.00	0.92	0.63	5.44
B	7.00	1316.00	77.70	80.88	6.29	25.00	920.00	137.56	119.35	2.52	7.00	1316.00	74.41	76.61	6.94
Cu	1.00	608.00	21.97	24.73	7.58	8.00	209.00	52.41	36.95	1.16	1.00	608.00	20.97	23.81	8.47
Zn	32.00	2804.00	158.03	78.26	14.11	65.00	793.00	146.81	65.48	5.38	32.00	2804.00	158.01	78.25	14.62
As	1.00	1589.00	43.42	97.64	6.73	1.00	1379.00	150.45	238.31	2.33	1.00	1589.00	35.34	71.65	8.16
Sr	14.00	458.00	64.72	45.85	2.72	37.00	293.00	107.16	40.83	1.34	14.00	458.00	61.89	44.43	3.06
Nb	1.00	137.00	2.31	4.69	9.17	1.00	16.00	1.05	0.87	17.26	1.00	137.00	2.37	4.79	8.98
Sn	1.00	139.00	3.27	5.62	9.42	1.00	101.00	4.18	8.57	6.29	1.00	139.00	3.18	5.23	9.88
Ba	21.00	2017.00	285.79	148.65	0.86	141.00	667.00	396.83	101.20	0.47	21.00	2017.00	277.20	146.13	0.99
W	1.00	1034.00	4.17	32.60	19.46	1.00	786.00	20.58	67.99	6.71	1.00	1034.00	2.86	26.80	26.75
Pb	1.00	3000.00	19.14	77.08	33.00	1.00	724.00	24.80	51.76	9.18	1.00	3000.00	18.45	77.68	33.75

In a second stage, the same EDA tools were used to understand how the elementary distributions changed according to the lithology. Overall, granites have higher values of Na_2O, K_2O, Li, Nb, and Sn when compared to metasedimentary rocks. Oppositely, the metasediments show higher contents of Fe_2O_3, B, Cu, Sr, Ba, and W when compared with granitoid rocks. The difference among samples located on granites and metasedimentary rocks is more prominent on the BRGM campaign, which has a higher number of samples. These differences in average concentrations are critical for the correct anomaly definition as demonstrated in the following chapters.

Finally, association measures such as Pearson's and Spearman's correlation coefficients and multivariate analysis techniques such as Cluster analysis and Principal Component Analysis (PCA) were also employed to determine relevant element associations with Li. When considering the raw data from both datasets, for most elements the correlation with Li is negligible, but P_2O_5 showed a moderate correlation with Li ($0.5 \leq$ Pearson r < 0.7), while K_2O, Na_2O, Al_2O_3, Sn, Be, and As show weak correlations ($0.3 \leq$ Pearson r < 0.5). Nevertheless, the element associations are distinct for each campaign. In the SFM campaign, a weak correlation (based on Pearson's coefficient) was found between Li and Sn, As, Be, K_2O, B, and Pb. Considering Spearman's coefficient, the correlation with Sn, Pb, and As is moderate and there is an additional weak correlation between P_2O_5, W, and Li. For the BRGM campaign, there was only a moderate correlation between Li and P_2O_5, and weak correlations with K_2O, Na_2O, Al_2O_3, Sn, As, Be, when using the Spearman association measure. With Spearman's coefficient, there is also a weak correlation between Li and Zn, and the correlation with Sn, K_2O, and Na_2O increases to moderate.

The multivariate analysis was only employed for the Li-correlated elements, after standardization using the interquartile range (IQR). In the case of cluster analysis, the distance metric employed was always the Euclidian distance, but different linkage methods were tested (Ward's, single, complete, average, centroid, and median). The cophenetic correlation coefficient was computed to evaluate the hierarchical clustering. The dendrograms' cutoff value was set to the median of the third-from-last and second-from-last linkages. Moreover, PCA was employed on both Pearson's and Spearman's correlation matrices for Li-correlated elements. The dendrograms evidenced a Li-K_2O-B-As-P_2O_5 cluster for the SFM campaign and a Be-Al_2O_3-K_2O-Na_2O-Li-P_2O_5 for the BRGM dataset. PCA revealed more complex associations, but overall there are associations between Li and Pb, As, Sn, K_2O, and P_2O_5 in the SFM campaign, and associations between Li and P_2O_5, Na_2O, K_2O, Sn, Be, and As in the BRGM dataset.

3.2. Geochemical pathfinder analysis

The same multivariate statistical analysis (described in section 3.1.) was employed to determine relevant element associations in the Li-mineralization sources in the Iberian Peninsula, through a total of 168 whole-rock analyses from lepidolite-rich (n = 41), spodumene/petalite-rich (n = 25), and simple aplite-pegmatite dykes and leucogranitic cupolas (n = 102). The available geochemical dataset consists of 37 analyses performed by Roda-Robles et al. (2018), while the remaining analyses were compiled by the same authors based on existent research about the Argemela, Castillejo de Dos Casas, and Pinilla de Fermoselle lecogranitic cupolas, and about the Barroso-Alvão, Fregeneda-Almendra, Gonçalo, Lalín-Forcarei, Las Navas, Segura, Seixoso-Vieiros, Serra de Arga, Jalama, and Tres Arroyos pegmatite-fields (Almeida, 2003; Antunes et al., 2013; Charoy and Noronha, 1996; Fuertes Fuente and Martin Izard, 1998; Gallego Garrido, 1992; Helal, 1992; Leal Gomes, 1994; Martín-Izard et al., 1992; Neiva and Ramos, 2010; Roda-Robles et al., 2012; Von Knorring and Vidal Romani, 1981). As a consequence of the very heterogeneous whole-rock geochemistry dataset (distinct analytical packages for each studied location), two subsets were considered in the multivariate analysis to create a balance between preserving the largest number of samples and elements possible: i) 100 analysis for 16 elements (Al_2O_3, CaO, Fe_2O_3, K_2O, MgO, Na_2O, P_2O_5, SiO_2, Ba, Cs, Li, Nb, Rb, Sn, Sr, Ta); ii) 51 analysis for 22 elements (Al_2O_3, CaO, Fe_2O_3, K_2O, MgO, MnO, Na_2O, P_2O_5, SiO_2, TiO_2, Ba, Cs, F, Ga, Nb, Rb, Sn, Sr, Ta, Zn, Zr). The correlation analysis was employed on the entire whole-rock geochemical dataset.

The multivariate approach allowed defining a general Li-Rb-F-Sn-Cs-Al_2O_3-K_2O-MnO association. The multielement associations can vary according to the chosen subset and technique. For the first subset, cluster analysis evidenced a K_2O-Rb-Sn-Li-Al_2O_3-Na_2O association similar to the Rb-Cs-Li-Sn-(Al_2O_3) association identified through PCA (Fig. 2-A). In the second subset, an Al_2O_3-K_2O-MnO-Zn-Sn-Li-Rb-F cluster was observed (Fig. 2-B) while PCA highlighted an F-Cs-Li-Rb-Sn-MnO-(Zn) association. Spearman's measure also identified a weak correlation between Li and B. In a preliminary study where only Li-rich pegmatites and leucogranitic cupolas were considered (Cardoso-Fernandes et al., 2020a), a strong correlation was found with B, but the correlation between Li and Sn was not as relevant as the one observed using the whole dataset.

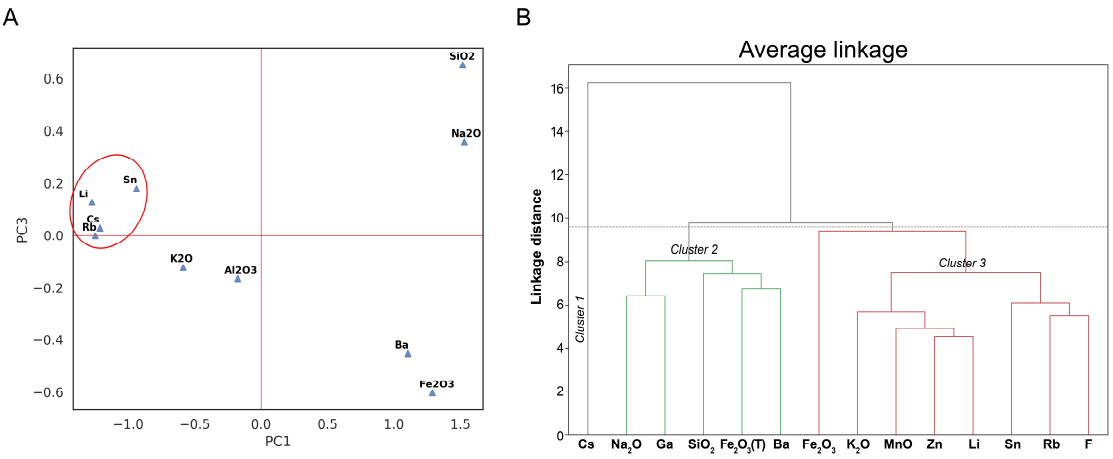

Fig. 2. Multivariate analysis for the identification of associations in Li-rich bodies from the CIZ: (A) Projection of the selected elements/oxides loadings on the plane PC3 vs PC1 for the first subset (n = 100); (B) Dendrogram showing the hierarchical clustering of selected elements/oxides for the second subset (n = 51).

Overall, B together with Rb, Sn, Cs, and F are common elements that define the geochemical signature of Rare-Element, Li-rich pegmatites worldwide (Černý and Ercit, 2005; Simmons and Webber, 2008). However, no association was found with other typical elements found in Li-rich bodies such as Ta and Nb (Černý and Ercit, 2005; Roda-Robles et al., 2018; Simmons and Webber, 2008). This could be explained by difficulties in acquiring representative samples for the accessory Ta-Nb phases or it could reflect the occurrence of a nugget effect (Cardoso-Fernandes et al., 2020a). Although Be could also be an important pathfinder element for Li-mineralizations, no association with Li was found through the multivariate approach which would be expected since beryl is less common in the Li-rich bodies of the Iberian Peninsula (Cardoso-Fernandes et al., 2020a; Roda-Robles et al., 2018). Finally, the association between Li and major oxides such as MnO, K_2O, and Al_2O_3 can be explained by the co-ocurrence of Mn oxides in Li-rich bodies of the CIZ-GTMZ and due to the presence of K and Al in the structure of Li-minerals (Cardoso-Fernandes et al., 2020a; Roda-Robles et al., 2018).

Comparing these results with the ones obtained in Section 3.1., it is evident that the Li association with elements such as Pb or As in the stream sediment samples do not represent the typical associations found in Li-rich bodies. Despite elements/oxides such as Be and P_2O_5 (that show a positive correlation with Li in the stream sediment dataset) may be present in Li-pegmatites, there was no significant correlation with Li in the CIZ's Li-rich bodies. Important pathfinders for Li-pegmatite exploration, namely Rb, Cs, and F were not analyzed in the stream sediment campaigns. Nonetheless, other relevant pathfinders can be used to pin-point Li-

pegmatites in the Douro region: Sn, B, Al_2O_3, MnO, and K_2O. All these pathfinder elements have shown correlations with Li in both CIZ's Li-rich bodies and the stream sediment samples.

4. Methods

4.1. Automatic extraction of drainage network and basin creation

The extraction of the drainage network was performed automatically using ArcGIS Spatial Analyst tools (Hydrology and Conditional menus) (Environmental Systems Research Institute, 2020). Different data sources covering the study area and methods were applied to determine which combination was more effective (Table 2).

Table 2. Description of the distinct data sources and drainage extraction methods employed.

Data Source	Resolution	Extraction method	Description
Digital Elevation Model (DEM)	20 m	Set Null	A threshold is applied to the flow accumulation model and only the cells with a flow accumulation higher than the stipulated threshold are classified as part of the drainage network.
Digital Flow Model (DFM)	25 m	Stream Order	The stream segments are classified based on the number of upstream tributaries (Strahler, 1952). Stream order only increases when streams of the same order intersect.

For each pair of data source/extraction method, the number of streams, total length of streams, and drainage density were calculated. The drainage density was calculated by dividing the total stream length by the area in which the drainage network was extracted. For the drainage networks extracted with the stream order method, it was also computed for each order the number of streams, their length, and the drainage density. In this case, the drainage density was calculated by dividing the length of streams in each order by total area. The drainage network chosen was the one obtained using the DFM and the Stream Order method, since it presented the least number of artifacts.

Each sampling point was manually corrected to intersect the extracted drainage network, but always considering the original sampling maps from the 1980s. Basin creation was made using the *Watershed* tool in the Hydrology menu (ArcGIS Spatial Analyst tools), which takes into account the flow direction as well as the stream sediment points. However, the automatically delineated catchment basins presented major topology problems (Fig. 3) such as: (i) polygons without true catchment area, (ii) existing polygons of major streams, and (iii) many polygon artifacts (irregular shapes or smaller catchment basins inside larger ones). Most of the identified problems are related to the resolution of the primary raster data set. The following

correction of catchment data was done through: (i) improvement of the drainage network and contour line creation for data validation; (ii) position correction of the stream sediment samples; (iii) manually correction of irregular polygons; and (iv) catchment basins related to major streams (>1.5 km^2) were excluded from the dataset due to their low representativeness since these samples correspond to a mixed signal and it is not possible to assign a source (due to a large number of tributaries in the upper course).

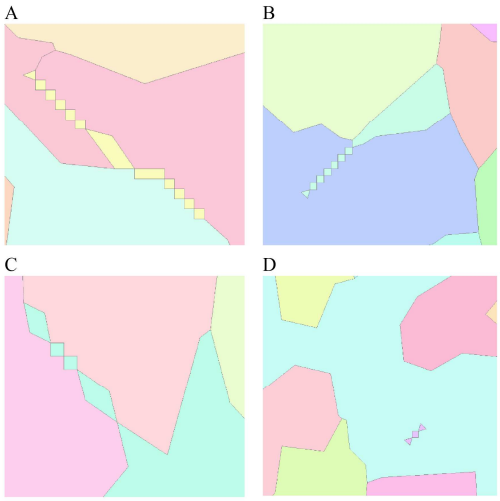

Fig. 3. Examples of basin artifacts that had to be manually corrected: (A-D) irregular polygon shapes; (D) smaller catchment basin inside a larger one.

4.2. The spatial interpolation method

Since the interpolation method is not dependent on the catchment area, it was possible to treat the two campaigns together. In preparation, the SFM and BRGM datasets were merged (after comparison of values) and overlapping polygons were adjusted. The values/units for the elements of interest (Li, Sn, W, As, etc.) were harmonized (% into mg/kg) and logarithmized. In the next step, the center of each polygon was projected using the Feature to Point-tool in ArcGIS v10.6 software.

In this work, to analyze the stream sediment data and estimate elemental concentrations in unsampled areas the inverse distance weighting (IDW) was employed. IDW is one of the most used moving-average interpolation techniques, with the advantage of intuitive and straightforward implementation (Carranza, 2009a; Ghezelbash and Maghsoudi, 2018; Spadoni, 2006; Zuo, 2011). The interpolation method estimates unknown values between known values based on the assumption that closer values are more related than distant values (Shepard, 1968). Taking this into account, a weight (power coefficient) is assigned to each

known point used in the prediction of unknown points that will decrease with the distance (equation 1):

$$\hat{Z}_j = \sum_{i=1}^{N} \frac{1}{{d_{i0}}^p} Z_i \Big/ \sum_{i=1}^{N} \frac{1}{{d_{i0}}^p} \quad (1)$$

where $\hat{Z}_j$ represents the estimation of the unknown value at point j, N is the number of points used in the prediction of the unknown value, Z_i is the value at point i, d_{i0} corresponds to the distance between point j and point i, and p represents the power factor that adjusts how the weight reduces as the distance increases (Johnston et al., 2004).

In this work, the IDW interpolation was conducted with a cell size of 20x20 m, exponent of distance (power) of 2, and a search radius of 20 m. The catchment centers represented the reference points for the interpolation using IDW. To limit the interpolation area, the center points were buffered by 1000 m, a polygon was assembled from all the single buffer polygons, and the edge of the resulting polygon was used as a mask. The interpolation itself was done using ArcPy running on ArcGIS 10.6 and the results were saved as a raster file format. Besides Li, other elements were interpolated via the IDW method, namely As, Sn, and Cu. These elements were selected based on the interrelationship with Li in the stream sediment dataset and the potential for lithological discrimination previously evaluated in Section 3.

4.3. The catchment basin method

Unlike the spatial interpolation approach, for the catchment basin method, the two campaigns (BRGM and SFM) were treated separately due to different sampling densities and distinct element distributions observed in the two populations. Since this approach relies on several area-dependent calculations, it is crucial to treat the campaigns independently.

4.3.1. Determination of the lithological background and dilution correction

Because lithological variations can have a great influence on element content in each sample, it is necessary to estimate the background concentration of each lithologic unit. This is particularly important since, as stated in Section 3.1., the granites are more enriched in elements such as Li, Cs, Rb, Nb, and Sn when compared to the metasedimentary units (Ferreira et al., 2020; Roda-Robles et al., 2018). The lithological background was estimated through the weighted average method which considers the area of lithologic units in every sample catchment basin (Bonham-Carter et al., 1987; Carranza, 2009b; Carranza and Hale, 1997). The local background content due to lithology in every sample catchment basin was

then estimated in two steps. First, a weighted average element concentration M_j (j = 1, 2… m) for the jth (j=1, 2… n) lithologic units was determined using equation 2 (Carranza, 2009b):

$$M_j = \sum_{i=1}^{n} C_i A_{ij} \Big/ \sum_{i=1}^{n} A_{ij} \quad (2)$$

where A_{ij} is the area of the jth lithologic unit in the sample catchment basin i (i=1, 2… n), C_i represents the element concentration of the sample at the basin outlet, and the sum term in the denominator is the total area of lithology j. Then, the local background concentration of the element (C'_i) due to lithology was estimated through equation 3 (Carranza, 2009b):

$$C'_i = \sum_{j=1}^{m} M_j A_{ij} \Big/ \sum_{j=1}^{m} A_{ij} \quad (3)$$

where the sum term in the denominator is equal to the total area of the ith sample catchment. The estimated local background values for every lithological unit in the SFM and BRGM campaigns are presented in Appendix A, Table A1 and Table A2, respectively.

Finally, another key aspect to consider when applying the catchment method is the dilution effect which results from the mixing of eroded sediments from non-anomalous locations with sediments from mineralized sources (Carranza and Hale, 1997; Hawkes, 1976; Mokhtari and Garousi Nezhad, 2015). Both the Hawkes' (equation 4, when n equals 0) and the Hawkes' modified methods (equation 4) were evaluated for the dilution correction, considering that the dilution effect is a function of the catchment area and that the area of the mineralized source (pegmatite) is negligible (0.01 km^2):

$$C_a = (100A_i)^{1+n}(C_i - C'_i) \quad (4)$$

where C_a represents element concentration due to anomalous sources, A_i is the area of the catchment basin, C_i corresponds to the measured concentration of the element at the basin outlet, C'_i represents the lithological background value of the element, and n corresponds to arbitrary equidistance values of 0, -0.25 and -0.5 (Carranza and Hale, 1997; Hawkes, 1976; Mokhtari and Garousi Nezhad, 2015). The final term of equation 4 represents the uni-element residuals. In this work, the residuals were standardized through the IQR method before the dilution correction as suggested by Carranza (2009b). The best results were obtained with the original Hawke's equation (n = 0).

4.3.1. Anomaly definition through fractal analysis

Several statistical techniques are available to separate and classify geochemical anomalies from the background population, namely the percentile method (Carranza, 2004), the median absolute deviation (Shahrestani and Mokhtari, 2017), or fractal analysis (Fyzollahhi et al., 2018; Mokhtari and Garousi Nezhad, 2015). However, the concentration area (C-A) fractal method proposed by Cheng et al. (1994) is one of the most popular methods for the definition of geochemical anomalies (Ghezelbash et al., 2019; Gonçalves et al., 2001). The C-A fractal theory is summarized in equation 5 (Cheng et al., 1994):

$$A(\rho \leq \upsilon) \propto \rho^{-\alpha_1};\ \ A(\rho > \upsilon) \propto \rho^{-\alpha_2} \quad (5)$$

where A(ρ) represents the occupied area with concentration values greater than the contour value ρ, υ corresponds to the threshold, α_1 and α_2 are the fractal dimensions of the anomalous and background populations, respectively, and ∝ denotes the proportionality between A(ρ) and ρ, with A(ρ) decreasing as a function of ρ. The fractal dimensions correspond to the slopes of the straight lines fitted by the least square method on the log-log plot of A(ρ) versus ρ (Carranza, 2009a). Breaks between straight-line segments on the log-log plot determine the thresholds between distinct geochemical populations (Carranza, 2009a; Cheng et al., 1994).

In this study, the C-A fractal method was employed to identify uni- and multi-elemental anomalies in each stream sediment dataset. For this, the diluted-corrected residuals of Li and the remaining pathfinder elements (defined in Section 3.2.) were used. The area was estimated through the box-counting method where a grid with distinct cells was superimposed on the areas covered by each campaign (Cheng et al., 1994). Different cell sizes were tested, ranging from the computed average nearest neighbor (avgnn) to a maximum of 2.5 times the avgnn, in equally spaced intervals. In the end, the chosen cell size was 443.32 m and 140.54 m, and the number of concentration classes was 35 and 30 for the BRGM and SFM campaigns, respectively. Different populations and thresholds were recognized in the C-A log-log plots (representative graphs are presented in Appendix B, Fig. B1-A, B).

In what concerns the multi-element anomaly definition, only the samples with positive diluted-corrected residuals at least for Li were selected, as suggested by Carranza (2009b). A rank-ordering approach was employed to the n positive diluted-corrected residuals, assigning descendent ranks from n to 1 (with averaged tied ranks) to after applying a Spearman rank correlation matrix on the rank-transformed diluted-corrected residuals (Carranza, 2009b; Carranza and Hale, 1997; George and Bonham-Carter, 1989). Finally, the PCA was carried out on the resultant Spearman correlation matrix. The existing multi-element associations on

each Principal Component (PC) were evaluated based on the resultant eigenvector loadings, allowing the selection of key PCs for Li-exploration (Appendix B, Table B1 and Table B2). The PC scores of the rank-transformed dilution-corrected residuals were computed according to equation 6 (George and Bonham-Carter, 1989):

$$S_{ci} = \sum_{j=1}^{k} L_{cj} r_{ij} \quad (6)$$

where S_{ci} corresponds to the score for sample i (=1,2,…,n) on PC c, L_{cj} is the loading of variable j (=1,2,…,k) on PC c, and r_{ij} is the rank of sample i for variable j. The resultant scores were then subject to the C-A fractal analysis. To better define multi-element anomalies, often two PCs of interest were integrated (through multiplication), after normalization of the individual scores, and before fractal analysis. The process to decompose the multi-elemental anomalies from the background was similar to the one employed for uni-element anomaly definition. The number of concentration classes was the same for each campaign, but due to a smaller number of samples, the cell size used in the box-counting method changed to 576.47 m and 192.56 m for the BRGM and SFM, respectively. The representative log-log plots are shown in Appendix B, Fig. B1-C, D.

4.4. Field validation

Two portable pieces of equipment were used to assess the dykes' potential to be mineralized in Li, namely the S1 Titan 600 portable X-Ray Fluorescence (XRF) from Brucker and Z300 Laser-Induced Breakdown Spectroscopy (LIBS) from SciAps© instruments. The former was employed to measure the content of Rb in potassium feldspar crystals since the enrichment in this metal during crystallization reflects the fractionation degree of the pegmatites and consequently, their economic potential for Li (Cerny et al., 1985; Smeds, 1992). A threshold of 2000 ppm was set to discriminate the more evolved dykes with the potential to bear Li minerals (Ribeiro et al., 2018). The XRF equipment works with a rhodium anode and an excitation source of 4 W, with a voltage of 15 to 50 kV and a current of 5 to 100 μA. A factory calibration for K_2O and Rb has a detection limit of 44 ppm and 1 ppm, respectively, when operating with the GeoMining mode according to the manufacturer. The XRF performance has been tested against certified samples in previous work (Ribeiro et al., 2018). On the other hand, the portable LIBS was employed to assess the Li content on micas and to confirm the existence of Li aluminum silicates (petalite or spodumene), using two specific in-house calibrations for the GeoChem mode, or phosphates (montebrasite-amblygonite), through the equipment's Element-Pro elemental detection method. The SciAps Z-300 spectrometer range goes from

190 to 950 nm (Li peaks are located around 610 and 670 nm), with a laser excitation source of 5 to 6 mJ/pulse, 10 to 50 Hz repetition rate and uses argon at 13 psi as a purge gas. More information on the use of the LIBS equipment and its use to analyze Li-rich minerals can be found in Fabre et al. (2021).

5. Results and discussion

5.1. The spatial interpolation approach

The final interpolation maps created with IDW are presented in Fig. 4. As visible in Fig. 4-A, the highest Li values are mainly related to the granites from the Numão Massif (top left corner) and the FCR-LAC (E-W belt), thus outlining a major structural feature – the Vilariça Fault zone. Nonetheless, there is also a high Li-value area near the Riba D'Alva mine, where lepidolite dykes are known (top right corner, below the Poiares syncline). In the Almendra region, covered by the SFM campaign (highest density of sampling), where several Li-rich dykes are mapped, an enrichment in Li is noticeable. However, this enrichment is overshadowed by the Li content of the granites to the south. Pathfinder elements, such as Sn (Fig. 4-B), proved to be useful in the delineation of target areas. Despite some anomalies related to granites (especially to the East), it is possible to delineate three smaller areas of interest: (i) near the Riba D'Alva mine, (ii) near Almendra (coinciding with a known petalite-rich dyke exploited in the Bajoca mine), and (iii) near Castelo Melhor (south of the area not sampled) where there are no known pegmatites. Important As enrichments were observed (Fig. 4-C) in the Castelo Melhor and Riba D'Alva areas, as well as in the granites to the East. Intermediate As contents were observed in Almendra. Finally, the interpolation of elements such as Cu (Fig. 4-D), proved to be helpful for lithological discrimination. As seen in Section 3.1., the metasedimentary rocks present higher Cu contents compared to granitoid rocks, thus allowing to properly discriminate the granites from the FAR-LAC. Oppositely, the granites from the Numão Massif show a higher Cu content not allowing their discrimination.

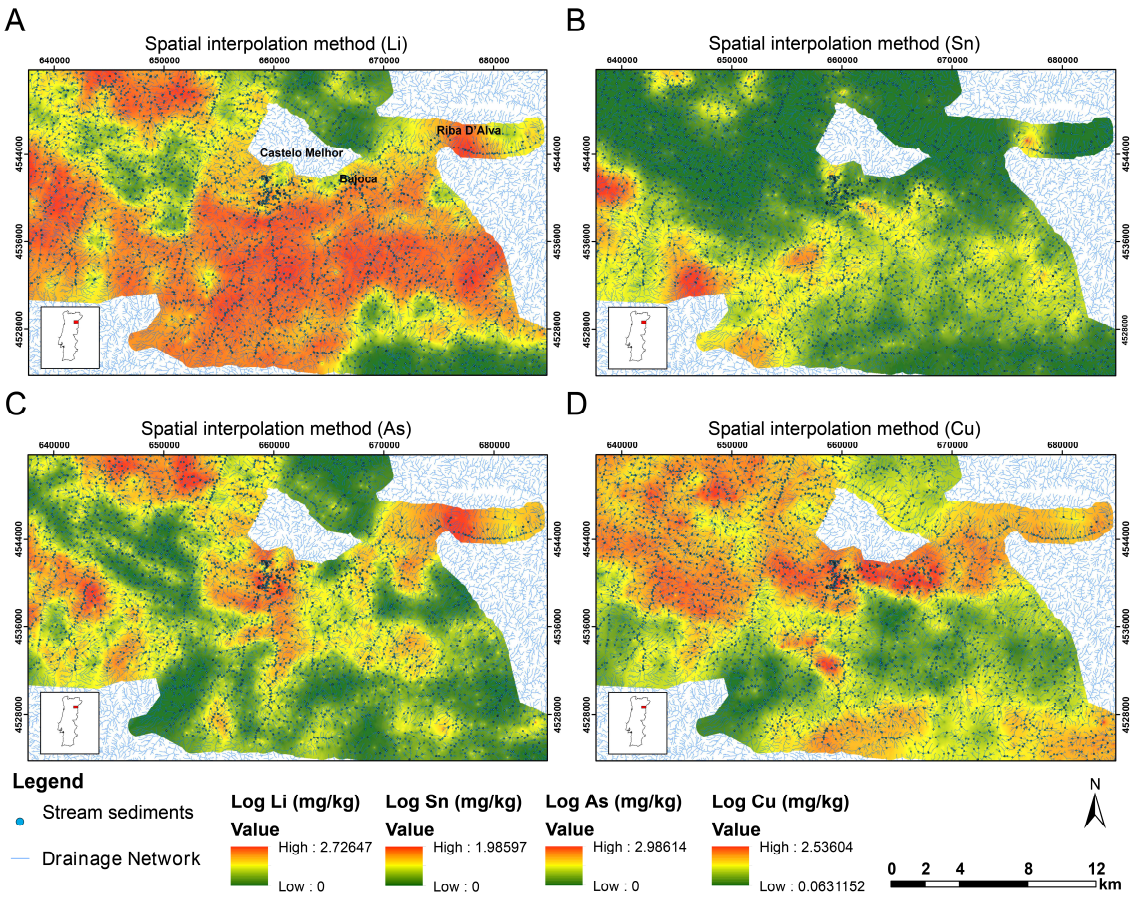

Fig. 4. Final interpolation maps obtained with the IDW: (A) Li; (B) Sn; (C) As; and (D) Cu.

Elemental interpolation using the IDW method turned out to be a simple and expeditious approach. Overall, the results show the influence that granitoids have on the Li content and proper definition of interest areas. This influence could be reduced through masking (using the existent geological maps) or the removal of lithological background (as performed in the catchment basin approach) prior to interpolation. Notwithstanding, the use of key pathfinder elements also allowed to decrease the granites' impact and was crucial to delineate target areas. In previous studies focusing on Li exploration through stream sediment analysis, interpolation techniques were also used to estimate the distribution of relevant factor scores of geochemical samples (Fyzollahhi et al., 2018; Saadati et al., 2020). The authors have concluded that such an approach is effective for reconnaissance campaigns and regional exploration (Saadati et al., 2020). The results obtained in this work also indicate that the interpolation approach is more suitable for early stages of exploration that focus on a regional (or district) scale since the inherent smoothing of the anomalies results in a loss of detail that is crucial in the final stages of exploration.

5.2. The catchment basin approach

As mentioned before, the two campaigns were treated separately in this approach. In the first stage, only uni-elemental anomalies were determined. The anomalous catchment basins for Li are depicted in Fig. 5, where both campaigns are presented. In the case of BRGM, 68 out of 3362 basins were identified as anomalous, which corresponds to approximately 2% of all basins. This indicates that the C-A fractal method was effective in reducing possible interest areas to visit in the field, and thus the duration and costs of field campaigns, which is of particular interest for exploration companies. Some of the anomalies shown in Fig. 5 correspond to the Riba D'Alva area or are related to known pegmatite dykes North of Escalhão (near the border with Spain). Table 3 summarizes the performance of the catchment basin approach, with the C-A fractal method achieving an overall accuracy (OA) of 93% considering the overlap of anomalous basins with known Li-pegmatites. Despite this, a large number of anomalous basins are still related to the outcropping granites, which is one of the main limitations found. After the removal of the lithological background, it was expected to eliminate the influence of granitoid rocks. Although it was not possible to eliminate their influence altogether, the impact of granites was reduced when compared with the spatial interpolation results (Fig. 4-A).

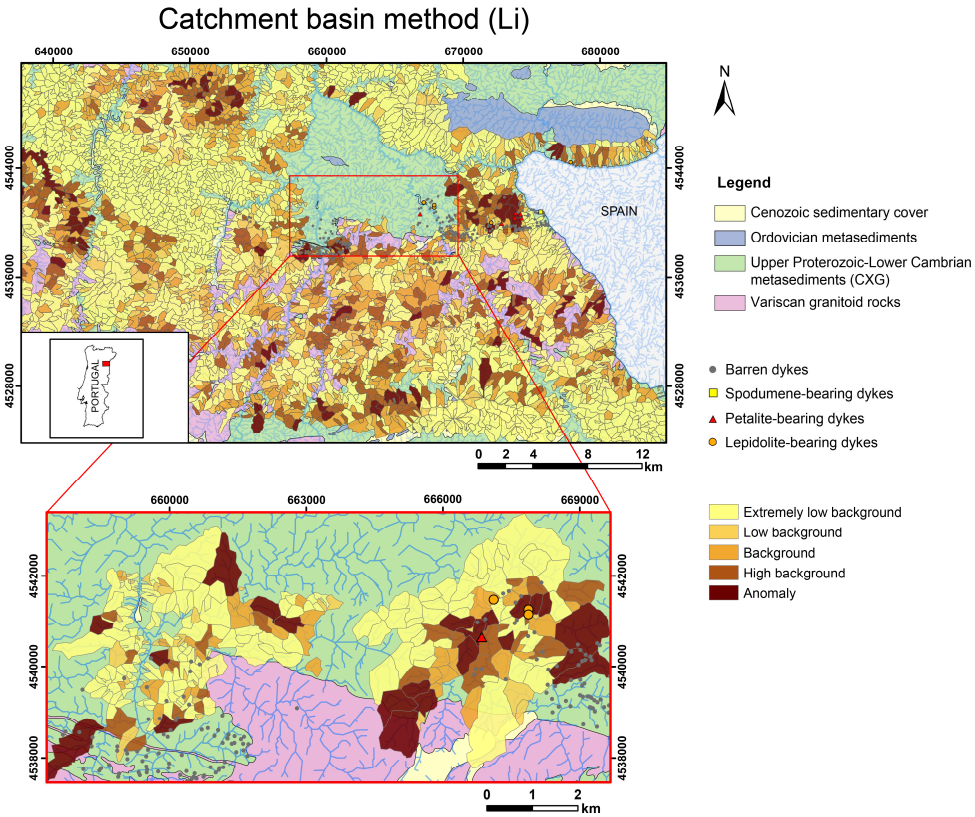

Fig. 5. Spatial distribution of diluted-corrected Li residuals for the BRGM (top) and SFM (bottom) campaigns. The thresholds used to identify distinct populations and define the anomalies are based on the log-log plots of Fig. B1. A simplified geological map is presented for reference.

For the SFM campaign, 22 out of 289 basins were identified as anomalous (approximately 7.6%). The higher percentage of anomalous basins is a consequence of the lower threshold identified in the log-log plot (Fig. B1-A). It also might be related to the smaller size of the basins, meaning that one source can contribute to multiple basins as observed around the Bajoca pegmatite (red triangle on the bottom of Fig. 5). There is still some influence of granitoid rocks (resulting in anomalous basins) that is a result of the lower estimated lithological backgrounds for granites (Table A1 and Table A2). This is linked with fewer availability of samples covering granites in the SFM campaign. Looking at Table 3, the OA of the fractal analysis drops to 75%. To improve these results, pathfinder elements were employed for multi-element definition.

Table 3. Performance matrix for uni- and multi-elemental anomaly definition considering the mapped pegmatites.

		BRGM (catchment basins = 3362)		**SFM (catchment basins = 289)**	
		Intersecting known pegmatites		Intersecting known pegmatites	
		Li-rich	Barren	Li-rich	Barren
Uni-elemental	Anomalous	4	5	5	6
	Non-anomalous	3	98	8	36
	Overall accuracy (OA)	93%		75%	
Multi-elemental	Highly Anomalous	1	4	7	1
	Other	6	99	6	41
	Overall accuracy (OA)	91%		87%	

The anomalous multi-element associations are represented in Fig. 6. For the BRGM campaign, the number of highly anomalous basins, representing a Sn-Li association, was 101 (around 3% of all catchment basins). The higher percentage of highlighted basins coupled with the lower OA of 91% indicates that the multi-elemental analysis did not produce the expected results, i.e., a decrease in the number of anomalous basins and reduce granite influence. However, intersecting anomalous Sn-Li basins with the previously identified Li-anomalous areas, the total number of highlighted catchments drops to 39.

Oppositely, in the SFM campaign, the number of highly anomalous basins, representing a Sn-Li-B association, was only 13 (around 4.5% of all catchment basins). This multi-element strategy not only allowed to eliminate anomalous areas related to the granites but also to increase the number of anomalous basins intersecting known Li-pegmatites (Fig. 6). Consequently, the OA of the C-A fractal method employed to the PCA results of Li pathfinder elements increased to 87% comparing to 75% obtained in the uni-elemental anomaly definition. The importance of using multi-elemental strategies for Li-exploration had already been demonstrated in the works of Fyzollahhi et al. (2018); Saadati et al. (2020), where the association with elements such as Cs, Rb, F, Be, Sn, and Nb not only allowed to identify Li

anomalous areas but also to discriminate two distinct Li-sources: (i) related to granites and pegmatites, and (ii) associated with Li-clays. The fact that the multi-elemental strategy was not equally successful in reducing the granites' influence in the BRGM campaign may indicate that in some cases the anomalous values are not just a consequence of the lithological background and that there can be anomalous areas inside the granites. This is out of the scope of this work, but it is worth further investigation in future studies to try to evaluate if there is any economic interest within the granites.

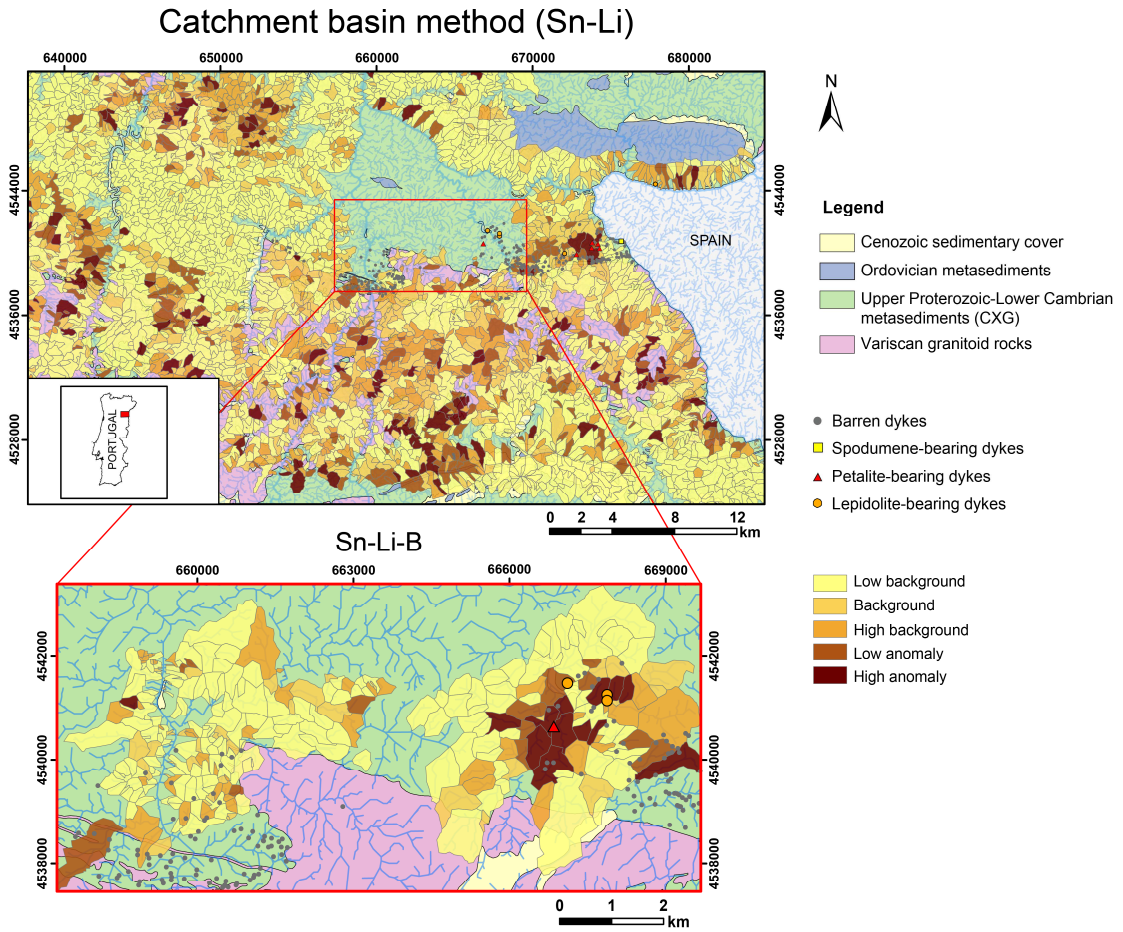

Fig. 6. Spatial distribution of integrated multi-elemental associations for the BRGM (top) and SFM (bottom) campaigns, obtained through the product of negated PC2 scores with PC4 scores, and the product of PC1 and PC2 scores, respectively (Table B1 and Table B2). The thresholds used to identify distinct populations and define the anomalies are based on the log-log plots of Fig. B1. A simplified geological map is presented for reference.

The OA reflects the ability of the employed approach to highlight anomalous basins with known Li-pegmatites and disregard areas with barren dykes. However, the anomalous basins intersecting barren pegmatites are of interest and should be validated in the field in the case of hidden Li-mineralization, that is, in the case that Li-minerals are not observed in the pegmatite surface but occur at depth.

Comparing both approaches, it is evident that the catchment basin approach is more suitable for prospect scale exploration, since it allows to only target the areas covered by the catchment basins (lesser area than the clusters of Fig. 5). Nonetheless, this catchment method proved to be very time-consuming, dependent on distinct processing steps, and the anomaly definition through fractal analysis was not straightforward. Ideally, such an approach could only be employed in the target areas defined through the spatial interpolation method, thus optimizing the chain process along the different stages of exploration.

5.3. Field validation

Two field campaigns were conducted to validate the results of the spatial interpolation and catchment basin approaches. This validation was affected by three main constraints: (i) poor road accesses to the interest areas (that implied traveling great distances to visit nearby places); (ii) several interest areas were located inside fenced private propriety; and (iii) the rough terrain of the region that did not allow to check every pegmatite dyke within anomalous basins. Despite this, eleven basins were checked in the field. Due to the time limitation, preference was given to anomalous basins where the existence of pegmatite dykes is known. Consequently, 17 pegmatite dykes were inspected for possible Li-mineralization.

In the region covered by the SFM campaign, it was possible to identify, in an anomalous area, one pegmatite dyke (previously mapped as barren) containing mineralization in Li and Sn. The first occurs mainly in pink microcrystalline masses of Li-micas with occasional petalite skeletal relics (boxworks) visible. The latter occurs in millimetric to centimetric cassiterite crystals containing small amounts of Nb and Ta. Iron and manganese phosphates were also found. Additionally, two other pegmatites in anomalous basins presented favorable evidence for Li-mineralization (Rb > 2000 ppm in K-feldspars), although no Li-mineralization was observed at the surface. Most pegmatite dykes were almost entirely covered by lichens which difficulted the recognition of possible Li-mineralization. It can also be the case that Li-minerals only occur in depth thus not allowing its recognition on outcrops even after using a hammer and sledgehammer to obtain vegetation-free samples. Moreover, the field campaigns allowed to identify a pegmatite dyke that was previously unknown. These findings show the importance of stream sediment analysis and the use of portable tools in Li-pegmatite exploration.

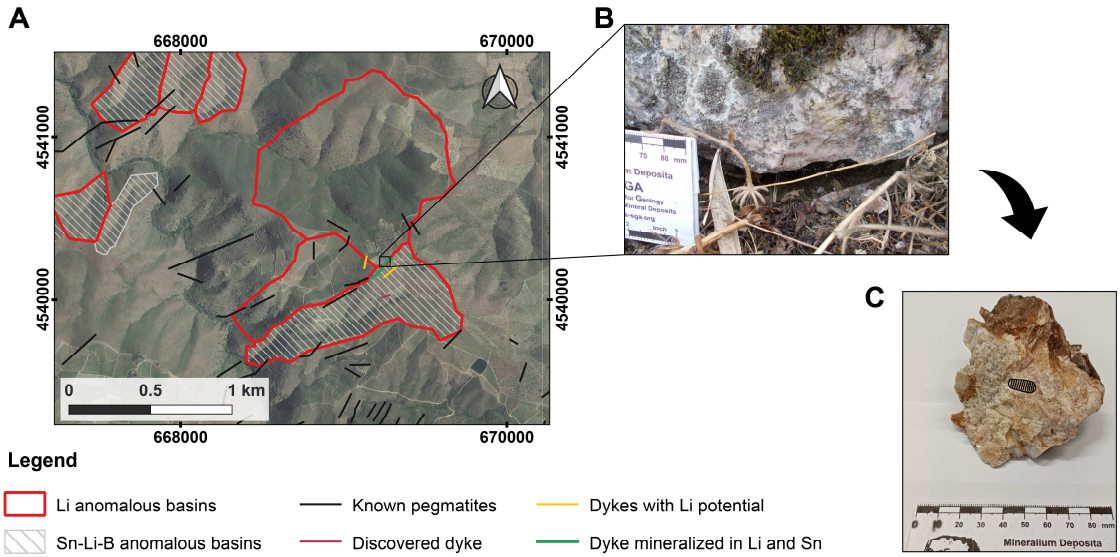

Fig. 7. A – Detail on three validated anomalous basins, where one pegmatite dyke was discovered (pink), two were highlighted as having Li potential (yellow), and where Li and Sn mineralization was found in a pegmatite previously considered as barren. B – Aspect of the Li mineralization in the outcrop (pink microcrystalline masses). C – Pink microcrystalline masses and boxworks of a previous petalite crystal in a hand sample.

For the BRGM campaign, less evidence of the source Li anomalies was found: all pegmatite dykes within anomalous basins visited in the field did not show favorable Rb and Li contents in K-feldspars and micas, respectively. Despite this, one pegmatite with the potential to be Li mineralized was identified within a catchment basin highlighted as high background through the uni-elemental C-A fractal analysis. To the south of the study area, the validated anomalous basins corresponded to: (i) urbanized areas, which may indicate human contamination, and (ii) granite-related areas. In the latter, intragranitic pegmatite dykes were observed, but presenting low Rb content in the K-feldspars and low Li content on the micas. Oppositely, the biotite in the granites showed higher relative Li contents than the ones observed in the pegmatites. Further studies may be employed in the future to assess the economic potential of Li within the granitoid rocks.

6. Conclusions

The performance of two distinct approaches to the geochemical exploration of Li-pegmatites was evaluated and the results have demonstrated their usefulness for this purpose:

1. The spatial interpolation method is a simple and expeditious approach for the early stages of mineral exploration (regional exploration). Despite the influence of granitoid rocks that can overshadow Li anomalous areas due to the occurrence of evolved pegmatites, it was

possible to delineate smaller areas of interest for detailed studies. Future works should consider masking or other techniques to decrease the granites' influence.

2. Oppositely, the catchment basin approach proved to be an important tool for prospect scale exploration, allowing to mark smaller areas for field verification. Removing the influence of the geological background reduced the anomalous areas related to granites. To optimize the exploration campaigns, this approach could be employed in the areas previously defined through the spatial interpolation method, due to the great computational cost and complexity involved in this catchment area approach.

3. In both approaches, the use of key pathfinder elements was crucial to delineate target areas and discriminate granite-related from pegmatite-related Li anomalies. This was particularly true for the SFM campaign, where the elements selected showed correlations with Li in both CIZ's Li-rich bodies and the stream sediment samples, highlighting an important Sn-Li-B association. Other pathfinder elements could be used for Li exploration worldwide, namely Rb, Cs, and F.

4. Finally, the C-A fractal method was very effective in reducing the number of catchment basins to validate in the field which can be of great interest for exploration companies, allowing to reduce the costs and duration of field campaigns. The accuracy of this approach was high (> 75%) when considering the previously mapped Li-pegmatites. The performance of the method was also confirmed through field validation. The fractal analysis allowed the identification of a pegmatite containing Li and Sn mineralization in one of the anomalous basins and highlight three other pegmatites with favorable evidence for possible hidden Li-mineralization.

5. Although multiple strategies were employed to reduce the granites' influence in the definition of anomalous basins, several areas persisted as anomalous. Therefore, further studies are needed to assess if there is any economic interest within the granites for Li.

Declaration of competing interest

The authors declare that they have no known competing financial interests or personal relationships that could have appeared to influence the work reported in this paper.

Acknowledgments

The authors would like to thank the financial support provided by FCT– Fundação para a Ciência e a Tecnologia, I.P. (Portugal) and BMBF Jülich – Bundesministerium für Bildung und Forschung (Germany), with the ERA-MIN/0001/2017 – LIGHTS project. The work was also supported by Portuguese National Funds through the FCT project UIDB/04683/2020 - ICT (Institute of Earth Sciences) and UIDB/50019/2020 – IDL (Instituto Dom Luiz). Joana Cardoso-Fernandes and Jéssica Lima are financially supported within the compass of their respective Ph.D. Thesis, ref. SFRH/BD/136108/2018 and ref. 2020.05793.BD, by national funds from MCTES through FCT, and co-financed by the European Social Fund (ESF) through POCH – Programa Operacional Capital Humano – and NORTE 2020 regional program. The Spanish Ministerio de Ciencia, Innovacion y Universidades (Project RTI2018-094097-B-100, with ERDF funds) and the University of the Basque Country (UPV/EHU) (grant GIU18/084) also contributed economically.

Author Contribution

Joana Cardoso-Fernandes: Conceptualization, Methodology, Software, Validation, Formal analysis, Investigation, Data Curation, Writing - Original Draft, Visualization; **Jessica Lima:** Conceptualization, Methodology, Software, Validation, Formal analysis, Investigation, Data Curation, Writing - Review & Editing; **Alexandre Lima:** Conceptualization, Methodology, Validation, Formal analysis, Resources, Writing - Review & Editing, Supervision, Project administration, Funding acquisition; **Encarnación Roda-Robles:** Conceptualization, Formal analysis, Resources, Writing - Review & Editing, Supervision, Funding acquisition; **Martin Köhler:** Methodology, Software, Formal analysis, Investigation, Data Curation, Writing - Review & Editing; **Stefan Schaefer:** Methodology, Software, Formal analysis, Investigation, Data Curation, Writing - Review & Editing; **Andreas Barth:** Methodology, Project administration; **Andreas Knobloch:** Methodology, Supervision, Project administration, Funding acquisition; **Mário Gonçalves:** Methodology, Software, Writing - Review & Editing; **Ana Cláudia Teodoro:** Conceptualization, Resources, Writing - Review & Editing, Supervision, Funding acquisition; **Filipe Gonçalves:** Validation, Investigation, Writing - Review & Editing.

Appendix A

Table A1. Estimated background values based on the weighted average method for different lithological units and for selected elements/oxides for the SFM campaign.

Lithology	Li (ppm)	Sn (ppm)	B (ppm)	Al_2O_3 (%)	MnO (%)	K_2O (%)
Alluviums and colluviums (Cenozoic sediments)	41.04	1.77	75.86	11.97	0.06	2.76
Desejosa formation (CXG)	42.87	1.67	75.52	12.54	0.06	2.78
Pinhão formation (CXG)	67.00	3.69	127.79	12.68	0.07	2.64
Rio Pinhão formation (CXG)	75.99	3.42	184.48	15.81	0.08	2.57
Mêda-Escalhão granite (CXG)	78.99	2.66	113.82	14.37	0.05	2.87

Table A2. Estimated background values based on the weighted average method for different lithological units and for selected elements/oxides for the BRGM campaign.

Lithology	Li (ppm)	Sn (ppm)	B (ppm)	Al_2O_3 (%)	MnO (%)	K_2O (%)
Alluviums and colluviums (Cenozoic sediments)	53.06	3.14	59.30	10.80	0.04	2.57
Slope deposits (Cenozoic sediments)	23.31	1.74	62.68	9.89	0.05	2.12
Ranha deposits (Cenozoic sediments)	100.78	4.52	49.98	12.08	0.04	3.15
Arkoses (Cenozoic sediments)	108.34	4.15	44.44	12.06	0.04	3.17
Santo Antão formation (Ordovician)	29.33	1.73	66.20	10.08	0.05	2.10
Poiares-Castelo Rodrigo (Ordovician)	20.97	1.40	69.71	10.42	0.05	2.13
Bateiras formation (CXG)	76.31	3.43	131.46	12.20	0.06	2.57
Desejosa formation (CXG)	41.80	1.66	92.97	11.51	0.06	2.66
Ervedosa formation (CXG)	68.39	2.73	130.34	11.67	0.06	2.61
Excomungada formation (CXG)	102.07	3.34	47.83	12.02	0.04	3.10
Pinhão formation (CXG)	98.59	5.20	54.54	12.24	0.04	3.25
Rio Pinhão formation (CXG)	86.14	4.15	84.04	11.93	0.05	3.01
Ribeira de Massueime-Galegos granite	111.40	4.19	43.71	12.15	0.04	3.18
Chãs-Amargo granodiorite	112.58	3.23	45.11	12.47	0.04	3.17
Amêdo-Tomadias granite	127.00	4.40	56.69	13.60	0.04	3.33
Mêda-Escalhão granite	103.41	4.88	50.49	12.21	0.04	3.23
Santa Comba-Algodres granite	108.29	4.44	46.36	12.18	0.04	3.20
Souto-Ranhados granite	163.31	13.79	172.99	11.06	0.04	2.91
Vila da Ponte granite	95.95	5.11	51.62	12.64	0.04	3.26
Freixo de Numão granite (Numão Massif)	78.51	2.64	53.46	13.99	0.06	2.97
Numão granite (Numão Massif)	0.00	5.39	41.67	14.62	0.05	3.32
Quinta da Silvã granite (Numão Massif)	49.00	7.95	44.95	12.74	0.05	3.02
Cachão do Arnozelo (Numão Massif)	0.00	3.99	45.45	13.69	0.05	3.05

Appendix B

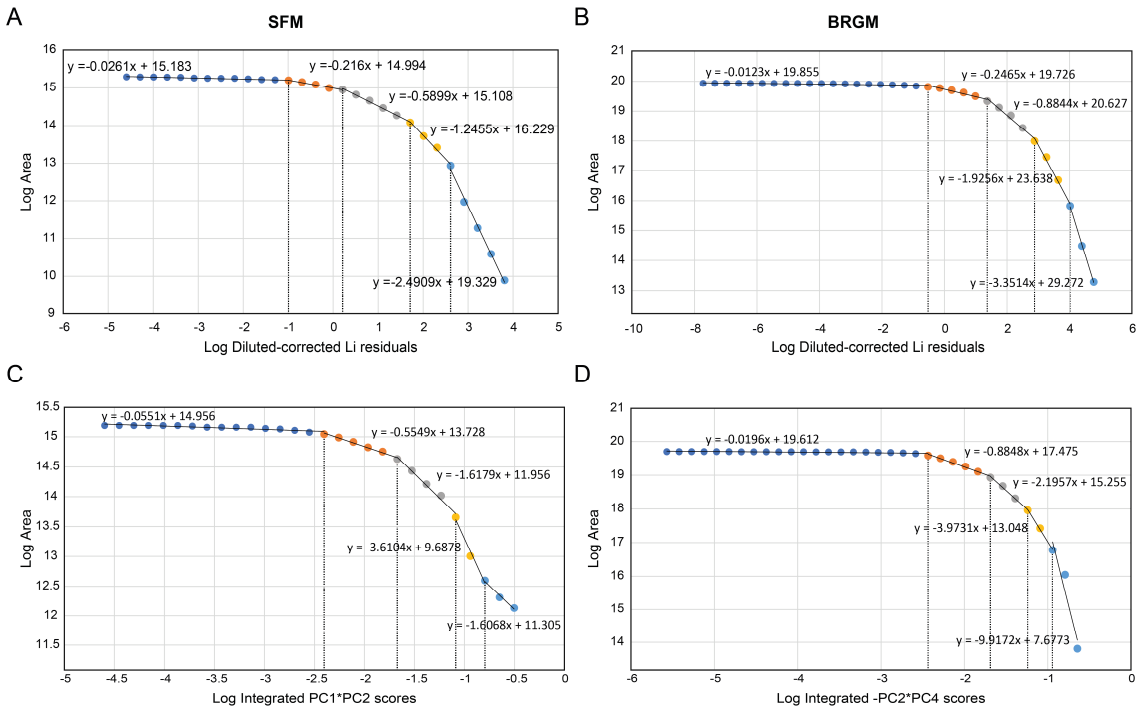

Fig. B1. Log-log plots of the concentration-area fractal analysis of diluted-correct Li residuals (A-B) and integrated PC scores of rank-transformed positive diluted-corrected residuals (C-D), representing Sn-Li-B and Sn-Li multi-elemental associations, respectively.

Table B1. PCA results of the rank-transformed positive diluted-corrected residuals of Li and associated pathfinder elements for the SFM campaign (n = 140).

	Li	Sn	B	K_2O	Al_2O_3	MnO	Variance	Eigenvalues
PC1	-0.1685	**0.6209**	**0.8456**	-0.8355	-0.8193	0.3569	0.5302	0.5251
PC2	**0.8216**	**0.3496**	-0.0916	0.0310	-0.3581	-0.7525	0.3031	0.3002
PC3	-0.2440	0.4260	-0.2926	0.1959	-0.1156	0.0302	0.0766	0.0758

Table B2. PCA results of the rank-transformed positive diluted-corrected residuals of Li and associated pathfinder elements for the BRGM campaign (n = 1674).

	Li	Sn	B	K_2O	Al_2O_3	MnO	Variance	Eigenvalues
PC1	-0.1057	-0.4137	-0.5288	0.7011	0.6119	-0.2648	0.3607	0.2796
PC2	**-0.2599**	**-0.6003**	0.0478	-0.1272	0.0997	0.8398	0.2997	0.2323
PC3	-0.0154	-0.3983	0.6307	-0.0107	0.1369	-0.3432	0.1789	0.1387
PC4	**0.5885**	-0.2347	-0.1625	-0.2358	0.0641	-0.0197	0.1259	0.0976

References

Almeida, C.M.P.d., 2003. Estudo do filão aplitopegmatítico da mina da Bajoca, Almendra: contribuição científico-tecnológica. Faculdade de Ciências da Universidade do Porto, Porto, pp. XIV, 120.

Angel, J.M., Viallefond, L. (1981). *Prospection géochimique Portugal. Résultats analytiques et interprétation de l'échantillonnage réalisé par le S.F.M. sur la feuille 15A, région de Almendra* (NOTE/GMX-748). p. 6.

Antunes, I.M.H.R., Neiva, A.M.R., Ramos, J.M.F., Silva, P.B., Silva, M.M.V.G., Corfu, F., 2013. Petrogenetic links between lepidolite-subtype aplite-pegmatite, aplite veins and associated granites at Segura (central Portugal). Geochemistry 73, 323-341. doi: https://doi.org/10.1016/j.chemer.2012.12.003.

Bonham-Carter, G.F., Rogers, P.J., Ellwood, D.J., 1987. Catchment basin analysis applied to surficial geochemical data, Cobequid Highlands, Nova Scotia. Journal of Geochemical Exploration 29, 259-278. doi: https://doi.org/10.1016/0375-6742(87)90081-1.

Cardoso-Fernandes, J., Lima, A., Roda-Robles, E., Ribeiro, M.A., Teodoro, A. (2020a). *Geochemical pathfinder analysis for lithium (Li) exploration in the Iberian Peninsula.* Paper presented at the X Congresso Jovens Investigadores em Geociências, LEG, Estremoz, 12-15.

Cardoso-Fernandes, J., Teodoro, A.C., Lima, A., Mielke, C., Körting, F., Roda-Robles, E., Cauzid, J. (2020b, 26 Sept.-2 Oct. 2020). *Multi-scale approach using remote sensing techniques for lithium pegmatite exploration: first results.* Paper presented at the IGARSS 2020 - 2020 IEEE International Geoscience and Remote Sensing Symposium, Waikoloa, HI, USA, 5226-5229. doi: 10.1109/IGARSS39084.2020.9323705.

Carranza, E.J.M., 2004. Usefulness of stream order to detect stream sediment geochemical anomalies. Geochemistry: Exploration, Environment, Analysis 4, 341-352. doi: 10.1144/1467-7873/03-040.

Carranza, E.J.M., 2009a. Chapter 4: Fractal analysis of geochemical anomalies, in: Carranza, E.J.M. (Ed.), Handbook of Exploration and Environmental Geochemistry. Elsevier Science B.V., pp. 85-114.

Carranza, E.J.M., 2009b. Chapter 5: Catchment Basin Analysis of Stream Sediment Anomalies, in: Carranza, E.J.M. (Ed.), Handbook of Exploration and Environmental Geochemistry. Elsevier Science B.V., pp. 115-144.

Carranza, E.J.M., Hale, M., 1997. A catchment basin approach to the analysis of reconnaissance geochemical - geological data from Albay province, Philippines. Journal of geochemical exploration 60, 151-171.

Carvalhosa, A., 1960. Carta Geológica de Portugal na escala 1/50.000 – folha 15-D – Figueira de Castelo Rodrigo. Serviços Geológicos de Portugal, Lisboa, Portugal.

Černý, P., Ercit, T.S., 2005. Classification of granitic pegmatites revisited. Can. Mineral. 43, 2005–2026.

Cerny, P., Meintzer, R.E., Anderson, A.J., 1985. Extreme fractionation in rare-element granitic pegmatites; selected examples of data and mechanisms. The Canadian Mineralogist 23, 381-421.

Charoy, B., Noronha, F., 1996. Multistage Growth of a Rare-Element, Volatile-Rich Microgranite at Argemela (Portugal). Journal of Petrology 37, 73-94. doi: 10.1093/petrology/37.1.73.

Cheng, Q., Agterberg, F.P., Ballantyne, S.B., 1994. The separation of geochemical anomalies from background by fractal methods. Journal of Geochemical Exploration 51, 109-130. doi: https://doi.org/10.1016/0375-6742(94)90013-2.

Costa, J.C.S.d., 1950. Notícia sobre uma carta geológica do Buçaco, de Nery Delgado. Serviços Geológicos de Portugal, Lisboa, Portugal.

Díez Balda, M.A., Vegas, R., Lodeiro, G., 1990. Central Iberian Zone: structure, in: Dallmeyer, R.D., Martinez Garcia, E. (Eds.), Pre-Mesozoic geology of the Iberian Peninsula. Springer Verlag, Berlim, pp. 172–188.

Dill, H.G., Weber, B., Melcher, F., Wiesner, W., Müller, A., 2014. Titaniferous heavy mineral aggregates as a tool in exploration for pegmatitic and aplitic rare-metal deposits (SE Germany). Ore Geology Reviews 57, 29-52. doi: https://doi.org/10.1016/j.oregeorev.2013.08.023.

Environmental Systems Research Institute, I. (2020). ArcMap Software. Retrieved from Available online: http://desktop.arcgis.com/en/arcmap/ (accessed on 27 July 2021).

European Commission: DG Internal Market Industry Entrepreneurship and SMEs. (2020). *Critical Raw Materials Resilience: Charting a Path towards greater Security and Sustainability* (COM(2020) 474 final). Brussels, p. 23.

Fabre, C., Ourti, N.E., Mercadier, J., Cardoso-Fernandes, J., Dias, F., Perrotta, M., Koerting, F., Lima, A., Kaestner, F., Koellner, N., Linnen, R., Benn, D., Martins, T., Cauzid, J., 2021.

Analyses of Li-Rich Minerals Using Handheld LIBS Tool. Data 6, 68. doi: 10.3390/data6060068.

Ferreira, J.A., Bento dos Santos, T., Pereira, I., Mata, J., 2019. Tectonically assisted exhumation and cooling of Variscan granites in an anatectic complex of the Central Iberian Zone, Portugal: constraints from LA-ICP-MS zircon and apatite U–Pb ages. International Journal of Earth Sciences 108, 2153-2175. doi: 10.1007/s00531-019-01755-1.

Ferreira, J.A., Mata, J., Bento dos Santos, T., Pereira, I., 2020. The role of melting on the geochemical evolution and isotopic variability of an anatectic complex in the Iberian Variscides. Lithos 378-379, 105769. doi: https://doi.org/10.1016/j.lithos.2020.105769.

Frick, C., Strauss, S.W., 1987. Geochemical evolution of the Richtersveld area, South Africa, as deduced from regional geochemical maps of stream sediments. Journal of Geochemical Exploration 28, 431-449. doi: https://doi.org/10.1016/0375-6742(87)90061-6.

Fuertes Fuente, M., Martin Izard, A., 1998. The Forcarei Sur rare-element granitic pegmatite field and associated mineralization, Galicia, Spain. The Canadian Mineralogist 36, 303-325.

Fyzollahhi, N., Torshizian, H., Afzal, P., Jafari, M.R., 2018. Determination of lithium prospects using fractal modeling and staged factor analysis in Torud region, NE Iran. Journal of Geochemical Exploration 189, 2-10. doi: https://doi.org/10.1016/j.gexplo.2017.09.017.

Gallego Garrido, M., 1992. Las mineralizaciones de Li asociadas a magmatismo ácido en Extremadura y su encuadre en la Zona Centro-Ibérica. Universidad Complutense de Madrid, Madrid, Spain, p. 323.

George, H., Bonham-Carter, G.F., 1989. Spatial modeling of geological data for gold exploration, Star Lake area, Saskatchewan, in: Agterberg, F.P., Bonham-Carter, G.F. (Eds.), Statistical Application in the Earth Sciences. Geological Survey of Canada Paper 89-9, pp. 157-169.

Ghezelbash, R., Maghsoudi, A., 2018. Comparison of U-spatial statistics and C–A fractal models for delineating anomaly patterns of porphyry-type Cu geochemical signatures in the Varzaghan district, NW Iran. Comptes Rendus Geoscience 350, 180-191. doi: https://doi.org/10.1016/j.crte.2018.02.003.

Ghezelbash, R., Maghsoudi, A., Carranza, E.J.M., 2019. An Improved Data-Driven Multiple Criteria Decision-Making Procedure for Spatial Modeling of Mineral Prospectivity: Adaption of

Prediction–Area Plot and Logistic Functions. Natural Resources Research 28, 1299-1316. doi: 10.1007/s11053-018-9448-6.

Gonçalves, M.A., Mateus, A., Oliveira, V., 2001. Geochemical anomaly separation by multifractal modelling. Journal of Geochemical Exploration 72, 91-114. doi: https://doi.org/10.1016/S0375-6742(01)00156-X.

Hawkes, H.E., 1976. The downstream dilution of stream sediment anomalies. Journal of Geochemical Exploration 6, 345-358. doi: https://doi.org/10.1016/0375-6742(76)90023-6.

Helal, B., 1992. Granitoïdes, granites à métaux rares et hydrothermalisme associé. Géologie, minéralogie et géochimie de plusieurs suites tardi-hercyniennes (Nord du Portugal). Ecole Nationale Supérieure des Mines de Paris, p. 507.

Johnston, K., Ver Hoef, J., Krivoruchko, K., Lucas, N., 2004. Using ArcGIS geostatistical analyst. ESRI Press.

Kesler, S.E., Gruber, P.W., Medina, P.A., Keoleian, G.A., Everson, M.P., Wallington, T.J., 2012. Global lithium resources: Relative importance of pegmatite, brine and other deposits. Ore Geology Reviews 48, 55-69. doi: https://doi.org/10.1016/j.oregeorev.2012.05.006.

Leal Gomes, C., 1994. Estudo estructural e paragenético de um sistema pegmatóide granítico. O campo aplito-pegmatítico de Arga Minho, Portugal. Universidade do Minho, p. 695.

Marroncle, J.L. (1980a). *Consórcio SPE / SEREM: Relatório semestral (Abril 1980 - Novembro 1980)*. Unpublished, p. 44.

Marroncle, J.L. (1980b). *Consórcio SPE / SEREM: Relatório semestral (Novembro 1979 - Abril 1980)*. Unpublished, p. 44.

Martín-Izard, A., Reguilón, R., Palero, F., 1992. Las mineralizaciones litiníferas del oeste de Salamanca y Zamora. Estudios Geológicos 48, 19-30.

Martínez Catalán, J.R., Martínez Poyatos, D., Bea, F., (Coords.), 2004. Zona Centroibérica: Introducción, in: Vera, J.A. (Ed.), Geología de España. Sociedad Geológica de España/ Instituto Geológico y Minero de España (SGE-IGME), Madrid, pp. 68-69.

Melleton, J., Gloaguen, E., Frei, D., Lima, A. (2011, 2011-08-14). *U-Pb dating of columbite-tantalite from Variscan rare-elements granites and pegmatites.* Paper presented at the Goldschmidt 2011, Prague, Czech Republic, 1452.

Mokhtari, A.R., Garousi Nezhad, S., 2015. A modified equation for the downstream dilution of stream sediment anomalies. Journal of Geochemical Exploration 159, 185-193. doi: 10.1016/j.gexplo.2015.09.007.

Neiva, A.M.R., Ramos, J.M.F., 2010. Geochemistry of granitic aplite-pegmatite sills and petrogenetic links with granites, Guarda-Belmonte area, central Portugal. European Journal of Mineralogy 22, 837-854. doi: 10.1127/0935-1221/2010/0022-2072.

Pereira, I., Dias, R., Bento dos Santos, T., Mata, J., 2017. Exhumation of a migmatite complex along a transpressive shear zone: inferences from the Variscan Juzbado–Penalva do Castelo Shear Zone (Central Iberian Zone). Journal of the Geological Society 174, 1004. doi: 10.1144/jgs2016-159.

Pérez-Estaún, A., Bea, F., Bastida, F., Marcos, A., Martínez Catalán, J.R., Martínez Poyatos, D., Arenas, R., Díaz García, F., Azor, A., Simancas, J.F., González Lodeiro, F., 2004. La cordillera varisca europea: el Macizo Ibérico, in: Vera, J.A. (Ed.), Geología de España. Sociedad Geológica de España/ Instituto Geológico y Minero de España (SGE-IGME), Madrid, pp. 21-25.

Ribeiro, M.L., 2001. Notícia explicativa da carta geológica simplificada do Parque Arqueológico do Vale do Côa. Parque Arqueológico do Vale do Côa, Vila Nova de Foz Côa, Portugal.

Ribeiro, M.L., Silva, A.F., 2000. Carta Geológica Simplificada do Parque Arqueológico do Vale do Côa. Instituto Geológico e Mineiro and Parque Arqueológico do Vale do Côa, Vila Nova de Foz Côa, Portugal.

Ribeiro, R., Lima, A., Guimarães, D. (2018). *Concentrations of Rb in K-Feldspar from the Pegmatite-aplite Barroso-Alvão Field.* Paper presented at the VIII Congresso Jovens Investigadores em Geociências, LEG, Livro de Actas Estremoz, 50-53.

Roda-Robles, E., Pesquera, A., Gil-Crespo, P., Torres-Ruiz, J., 2012. From granite to highly evolved pegmatite: A case study of the Pinilla de Fermoselle granite–pegmatite system (Zamora, Spain). Lithos 153, 192-207. doi: https://doi.org/10.1016/j.lithos.2012.04.027.

Roda-Robles, E., Pesquera, A., Gil-Crespo, P.P., Vieira, R., Lima, A., Garate-Olave, I., Martins, T., Torres-Ruiz, J., 2016. Geology and mineralogy of Li mineralization in the Central Iberian Zone (Spain and Portugal). Mineralogical Magazine 80, 103-126. doi: 10.1180/minmag.2016.080.049.

Roda-Robles, E., Pesquera, A., Velasco, F., Fontan, F., 1999. The granitic pegmatites of the Fregeneda area (Salamanca, Spain): characteristics and petrogenesis. Mineral. Mag. 63, 535–558.

Roda-Robles, E., Vieira, R., Pesquera, A., Lima, A., 2010. Chemical variations and significance of phosphates from the Fregeneda-Almendra pegmatite field, Central Iberian Zone (Spain and Portugal). Mineralogy and Petrology 100, 23-34. doi: 10.1007/s00710-010-0117-7.

Roda-Robles, E., Villaseca, C., Pesquera, A., Gil-Crespo, P.P., Vieira, R., Lima, A., Garate-Olave, I., 2018. Petrogenetic relationships between Variscan granitoids and Li-(F-P)-rich aplite-pegmatites in the Central Iberian Zone: Geological and geochemical constraints and implications for other regions from the European Variscides. Ore Geology Reviews 95, 408-430. doi: https://doi.org/10.1016/j.oregeorev.2018.02.027.

Roda, E., 1993. Distribución, Caracteristicas y Petrogenesis de las Pegmatitas de La Fregeneda (Salamanca), Dep. Min. y Petrol. . Facultad de Ciencia y Tecnología de la Universidad del País Vasco (UPV/EHU), Bilbao, Spain, p. 199.

Rodríguez Alonso, M.D., Díez Balda, M.A., Perejón, A., Pieren, A., Liñán, E., López Díaz, F., Moreno, F., Gámez Vintaned, J.A., Gónzalez Lodeiro, F., Martínez Poyatos, D., Vegas, R., 2004. Domínio del Complejo Esquisto-Grauváquico: Estratigrafía. La secuencia litoestratigráfica del Neoproterozóico-Câmbrico Inferior, in: Vera, J.A. (Ed.), Geología de España. Geol. España/Inst. Geol. Min. España (SGE-IGME), Madrid, pp. 78-81.

Rose, A.W., Hawkes, H.E., Webb, J.S., 1979. Geochemistry in mineral exploration. Academic Press, London.

Saadati, H., Afzal, P., Torshizian, H., Solgi, A., 2020. Geochemical exploration for lithium in NE Iran using the geochemical mapping prospectivity index, staged factor analysis, and a fractal model. Geochemistry: Exploration, Environment, Analysis 20, 461-472. doi: 10.1144/geochem2020-020.

San José, M.A., Pieren, A.P., Garcia-Hidalgo, J.F., Vilas, L., Herranz, P., Pelaez, J.R., Perejon, A., 1990. Central Iberian Zone. Autochthonous sequences: Ante-Ordovician stratigraphy, in: Dallmeyer, R.D., Martinez Garcia, E. (Eds.), Pre-Mesozoic Geology of Iberia. Springer-Verlag, Berlin, Heidelberg, pp. 147- 159.

Shahrestani, S., Mokhtari, A.R., 2017. Improved detection of anomalous catchment basins by incorporating drainage density in dilution correction of geochemical residuals. Geochemistry: Exploration, Environment, Analysis 17, 194-203. doi: 10.1144/geochem2016-015.

Shepard, D., 1968. A two-dimensional interpolation function for irregularly-spaced data, Proceedings of the 1968 23rd ACM national conference. Association for Computing Machinery, pp. 517–524.

Silva, A.F., 2005. A Litostratigrafia e Estrutura do Supergrupo Dúrico-Beirão (Complexo Xisto-Grauváquico), em Portugal, e sua Correlação com as Correspondentes Sucessões em Espanha. Instituto Nacional de Engenharia, Tecnologia e Inovação, IP, Alfragide, Portugal.

Silva, A.F., Romão, J.M.C., Sequeira, A.J.D., Oliveira, J.T. (1995). *A sucessão litostratigráfica anté-ordovícica na Zona Centro-Ibérica (ZCI), em Portugal: Ensaio de interpretação com base nos dados actuais.* Paper presented at the XIII Reunión de Geologia del Oeste Peninsular, RGOP/PICG, 319-320, Univ. Salamanca, Salamanca, 71-72.

Silva, A.F., Santos, A.J., Ribeiro, A., Cabral, J., Ribeiro, M.L., 1990a. Carta Geológica de Portugal na escala 1/50.000 – folha 15-B – Freixo de Espada à Cinta. Serviços Geológicos de Portugal, Lisboa, Portugal.

Silva, A.F., Santos, A.J., Ribeiro, A., Ribeiro, M.L., 1990b. Carta Geológica de Portugal na escala 1/50.000 – folha 15-A – Vila Nova de Foz Côa. Serviços Geológicos de Portugal, Lisboa, Portugal.

Silva, A.F.d., Rebelo, J.A., Ribeiro, M.L., 1989. Notícia Explicativa da folha 11-C Torre de Moncorvo. Serviços Geológicos de Portugal, Lisboa, Portugal.

Silva, A.F.d., Ribeiro, M.L., 1991. Notícia Explicativa da folha 15-A Vila Nova de Foz Côa. Serviços Geológicos de Portugal, Lisboa, Portugal.

Silva, A.F.d., Ribeiro, M.L., 1994. Notícia Explicativa da folha 15-B Freixo de Espada à Cinta. Instituto Geológico e Mineiro, Lisboa, Portugal.

Simmons, W.B.S., Webber, K.L., 2008. Pegmatite genesis: state of the art. European Journal of Mineralogy 20, 421-438. doi: 10.1127/0935-1221/2008/0020-1833.

Smeds, S.A., 1992. Trace elements in potassium-feldspar and muscovite as a guide in the prospecting for lithium- and tin-bearing pegmatites in Sweden. Journal of Geochemical Exploration 42, 351-369. doi: https://doi.org/10.1016/0375-6742(92)90032-4.

Sousa, M.B., 1982. Litostratigrafia e estrutura do “Complexo Xisto-Grauváquico Ante-Ordovícico” – Grupo do Douro (Nordeste de Portugal). Centro de Geociências da Universidade de Coimbra, Coimbra, Portugal, p. 222.

Sousa, M.B., 1983. Considerações paleogeográficas e ensaio de correlação das formações do Grupo do Douro (CXG) com as formações ante-Ordovícicas da Zona Centro-Ibérica. Memórias e Notícias, Publicações do Museu e Laboratório Mineralógico e Geológico da Universidade de Coimbra 65, 65-98.

Sousa, M.B., 1984. Considerações sobre a estratigrafia do Complexo Xisto-Grauváquico (CXG) e sua relação com o Paleozóico Inferior. Cuadernos de Geología Ibérica 9, 9-36.

Spadoni, M., 2006. Geochemical mapping using a geomorphologic approach based on catchments. Journal of Geochemical Exploration 90, 183-196. doi: 10.1016/j.gexplo.2005.12.001.

Steiner, B., 2018. Using Tellus stream sediment geochemistry to fingerprint regional geology and mineralisation systems in Southeast Ireland. Irish Journal of Earth Sciences 36, 45-61. doi: 10.3318/ijes.2018.36.45.

Strahler, A.N., 1952. Hypsometric (Area-Altitude) Analysis of Erosional Topography. GSA Bulletin 63, 1117-1142. doi: 10.1130/0016-7606(1952)63[1117:Haaoet]2.0.Co;2.

Teixeira, C., 1955. Notas sobre geologia de Portugal o complexo xisto-grauváquico ante-ordoviciano. Empresa Literaria Fluminense Lda., Lisboa, Portugal.

Viallefond, L. (1981). *Prospection géochimique Portugal : Résultats analytiques et interprétation de l'échantillonnage réalisé par le S.F.M. sur la feuille 15B* (NOTE/GMX-732). p. 27.

Viallefond, L., Angel, J.M. (1981). *Portugal Nord - Feuille 15A-15C - Interprétation des données analytiques* (NOTE/GMX-738). p. 17.

Viegas, L., Lima, L.P., Soares, J., Fonseca, E.C., 1983-85. Aplicação da análise estatística multi-variada ao estudo de amostras de sedimentos na região de Escalhão- Barca D'Alva (NE de Portugal). Boletim da Sociedade Geológica de Portugal XXIV, 161–169.

Vieira, R., 2010. Aplitopegmatitos com elementos raros da região entre Almendra (V.N. de Foz Côa) e Barca d'Alva (Figueira de Castelo Rodrigo). Campo aplitopegmatítico da Fregeneda-Almendra. Faculdade de Ciências da Universidade do Porto, Porto, Portugal, pp. XXVI, 273.

Vieira, R., Roda-Robles, E.n., Pesquera, A., Lima, A., 2011. Chemical variation and significance of micas from the Fregeneda-Almendra pegmatitic field (Central-Iberian Zone, Spain and Portugal). American Mineralogist 96, 637-645. doi: 10.2138/am.2011.3584.

Von Knorring, O., Vidal Romani, J.R., 1981. On the mineralogy of the O Casteliño spodumene pegmatite near Lalín, Galicia Spain. Cadernos do Laboratorio Xeolóxico de Laxe 2, 259-262.

Zuo, R., 2011. Identifying geochemical anomalies associated with Cu and Pb–Zn skarn mineralization using principal component analysis and spectrum–area fractal modeling in the Gangdese Belt, Tibet (China). Journal of Geochemical Exploration 111, 13-22. doi: 10.1016/j.gexplo.2011.06.012.

IV.2. Metasomatic effect of granitic aplite-pegmatite dykes in psammopelitic metasediments; mass-transfer quantification from whole-rock lithogeochemistry at La Fregeneda–Almendra (Central Iberian Zone)

Jon Errandonea-Martin, Idoia Garate-Olave, Encarnación Roda-Robles, Joana Cardoso-Fernandes, Alexandre Lima, Maria Anjos Ribeiro, Ana Cláudia Teodoro

To be submitted to *Ore Geology Reviews*

Abstract: Lithogeochemical studies of metasomatic haloes, caused by the intrusion of pegmatites, constitute a valuable tool in mineral resource exploration. Prospect scale systematic studies of geochemical aureoles carried out at the La Fregeneda–Almendra pegmatite field, in the Central Iberian zone of the Iberian Massif, provide practical data to consider in the development of innovative less-invasive exploration techniques. The selected different types of Li-bearing aplite-pegmatites intruded into fairly homogeneous psammitic and pelitic metasediments, derived principally from a felsic differentiated source, with a relatively lower compositional maturity than the Neoproterozoic Iberian Average Shale (NIBAS) and North-Central Iberian Zone (N-CIZ) slates. At a regional scale, F, B, Li, Rb, Cs, Sn, Be and Tl have been identified as highly mobile elements (metasomatized/non-metasomatized ratios of > 2.0), with Si, Al and Ti as the main immobile elements (metasomatized/non-metasomatized ratios of 1.00 ± 0.12) that constitute the reference frame for whole-rock mass-balance quantifications. The calculated decreasing trends (outwards the dykes) indicate that the extents of the metasomatic aureoles reach up to relative distances of about 4–5 times the thickness of the dykes, whereas significantly elevated enrichments are observed within a range of twice the width. The most evolved aplite-pegmatites (referred to as 'Li-mica' and 'spodumene' dykes) seem to generate the greatest haloes, with Cs and Li as the most mobile

elements followed by Rb and Sn (> F, B, Be, Tl). B and Cs show the highest relative gains (maximum values of ~160 and ~90, respectively), with lower ones in Sn (~60), Li (~40) and F (~20). For geochemical exploration, higher contents than 400 ppm (Li), 50 ppm (Cs), 300 ppm (Rb) and 15 ppm (Sn) in the metasedimentary samples would imply the proximity of a buried aplite-pegmatite, but samples with a high Chemical Index of Alteration (CIA) values (> 70) should be taken with caution, since they could have suffered a severe chloritization process that provoked the leaching of these highly mobile elements.

Keywords: Granitic pegmatite; psammopelitic metasediments; metasomatism; geochemical halo; lithogeochemistry

1. Introduction

Critical raw materials are of great economic and strategic relevance, since access to them may control technological progress and are closely related to green technologies (Blengini et al., 2020). In the last decade, lithium has become one of the main strategic metals, increasing significantly its demand on a global scale (Jaskula, 2017; Gourcerol et al., 2019). Subsequently, geological resource exploration has been focused on the discovery of new Li-deposits and/or the re-assessment of already known reservoirs (Kesler et al., 2012; Gourcerol et al., 2019; Pesquera et al., 2020). Among these reservoirs, granitic pegmatites represent an important source of not only Li, but also Sn, Ta, Nb, Be, Cs, Rb, Sc Th, U and Rare Earth Elements (REE) (Černý and Ercit, 2005; Linnen et al., 2012; London, 2018; Roda-Robles et al., 2018). During the last years, in line with sustainable mineral exploration, many research projects aim to redirect raw material exploration to innovative less-invasive techniques that allow reducing the environmental footprint (Cardoso-Fernandes et al., 2019; Kesselring et al., 2020; Ruiz-Coupeau et al., 2020). Since sustainability factors seem to be more decisive during the early stages of the natural resource extraction process (Kesselring et al., 2020), a complete understanding of the mineralization itself, and its effects on surrounding elements, can contribute to sustainable mineral exploration.

The intrusion of granitic–pegmatitic melts often result in the alteration of surrounding rocks and the development of metasomatic aureoles, causing a compositional change of pre-existing minerals and crystallization of new phases (Morgan and London, 1987; Lentz and Gregoire, 1995; Černý, 2005; Paoli et al., 2019; Pérez-Soba and Villaseca, 2019; Barros et al., 2020; Kaeter et al., 2021). The metasomatism of country rocks is originated from the influx of

pegmatitic melt and coexisting fluids, whose composition is controlled by the nature of the related pegmatite (e.g., Shearer et al., 1984; London, 1986; Migdisov and Williams-Jones, 2014). In this process associated with highly evolved fluids during late crystallization stages of granitic melts (*sensu lato*), the relevance of F and B is known to be of great importance (Shearer et al., 1984; Pollard et al., 1987; London et al., 1996; Thomas et al. 2000; Raith et al., 2004; Paoli et al., 2019). The enrichment of F and B in the pegmatite-related fluid phase enhances the transfer of highly mobile elements from the pegmatite to the surrounding host rocks (Shearer et al., 1984; Morgan and London, 1987; Lentz, 1996). This mass transfer in metasomatic systems is reflected in whole-rock elemental gains and losses, which vary depending on the chemical behavior of elements in specific conditions (Gresens, 1967; Grant, 1986; Ague, 1994; Lentz and Gregoire, 1995). The resultant distances (from the pegmatite dyke) to which gains of highly mobile elements reach, mark the thickness of the metasomatic aureole (for a single element or a group of elements), which is conditioned also by the type and size of the pegmatite (Morgan and London, 1987; Galeschuk and Vanstone, 2007). Other variables such as the structural relationship between the pegmatite dyke and host rocks (related also to P-T conditions), or the nature/composition of country rocks, determine also the thickness of the geochemical halo (Morgan and London, 1987; Ague, 1994). In the case of LCT pegmatites (Černý and Ercit, 2005), these alteration or metasomatic aureoles adjacent to the pegmatites are characterized by an enrichment of highly mobile elements such as Li, Cs, and Rb, and they can reach up to more than 150 m far away from the contact between the pegmatites and their country rocks (Černý, 1989; Galeschuk and Vanstone, 2007; Linnen et al., 2012). According to pioneering works, Li-aureoles tend to be thicker than those of Rb and Cs, and these geochemical haloes are bigger in the case of metasedimentary host rocks compared to those observed in igneous rocks (e.g., Trueman, 1978; Shearer et al., 1986; Morgan and London, 1987; Černý, 1989). More recent studies have revealed that despite occasional, W, In and Sn anomalies in host rocks could be good indicators of nearby pegmatites, as well as Th, U, Ni, Zn, Y, Zr, Hf (Galeschuk and Vanstone, 2007). Accordingly, the systematic lithogeochemical study of country rocks in pegmatite fields seems to be a useful and small-footprint exploration tool to identify buried pegmatites.

Abundant Li-pegmatites crop out in the Iberian Massif throughout a 500 km-long and NW–SSE striking belt, comprising different pegmatite fields that have been exploited during the last decades (Roda-Robles et al., 2016, 2018). These pegmatites would constitute a metallogenetic province related to the Variscan Orogeny, and considering geochemical, geochronological, and structural evidence they would be related to the main episode of granitic magmatism developed between 330 and 290 Ma (Roda-Robles et al., 2016, 2018 and

references therein). The Iberian pegmatites are characterized by 1) a more or less complex layering and textural variations (aplitic, pegmatitic and/or aplitic+pegmatitic), 2) an enrichment in Li and F (± Sn, P, Nb, Ta, Rb and Cs), 3) an overall absence of quartz cores, internal concentric zoning or graphic intergrowths, and 4) the occurrence of spodumene, petalite, Li-micas/lepidolite and montebrasite as main Li-bearing minerals (Roda-Robles et al., 2016, 2018). The La Fregeneda–Almendra pegmatite field is one of the main pegmatite fields of the Iberian Massif, which has been thoroughly studied in terms of mineralogical characterization of the distinguished pegmatite-types, their petrogenesis, and new exploration techniques (López-Plaza et al., 1982; Roda-Robles et al., 1995, 1996, 1999, 2010, in prep.; Vieira et al., 2011; Cardoso-Fernandes et al., 2019, 2020).

The main goal of this contribution is to exemplify, to the maximum possible extent and detail, metasomatic processes and related geochemical modifications associated with the intrusion of aplite-pegmatites from one of the most important Li-bearing pegmatite fields of the Iberian Massif: The La Fregeneda–Almendra pegmatite field. Accordingly, we present a prospect scale systematic study of geochemical haloes associated with several representative aplite-pegmatite bodies. The study of these aureoles relies on whole-rock geochemistry on the basis of mass-balance equations, providing more than sixty whole-rock major- and trace-element analyses of altered/unaltered country rocks and related aplite-pegmatites.

2. GEOLOGICAL SETTING

The La Fregeneda–Almendra pegmatite field is located in the Central Iberian Zone (CIZ) of the Iberian Massif, south of the allochthonous terranes of the Galicia–Trás-os-Montes Zone (Martínez Catalán et al., 2007 and references therein; Fig. 1a, b). Concretely, this pegmatite field occurs in the SW of the Tormes Dome, along a ~30 km-long and ~7 km-wide W–E belt delimited to the north by the Paleozoic successions of the Poiares Synform (Armorican Quartzite Formation), to the south by the Mêda–Escalhão–Penedono–Lumbrales (MEPL) Granitic Complex, to the east–northeast by the Saucelle Granite, and to the west by the Vilariça Segment of the Manteigas–Bragança Fault Zone (Roda-Robles et al., 1999, 2010, 2016, in prep.; Vieira et al., 2011; López-Moro et al., 2018; Cardoso-Fernandes et al., 2019; Fig. 1b, c).

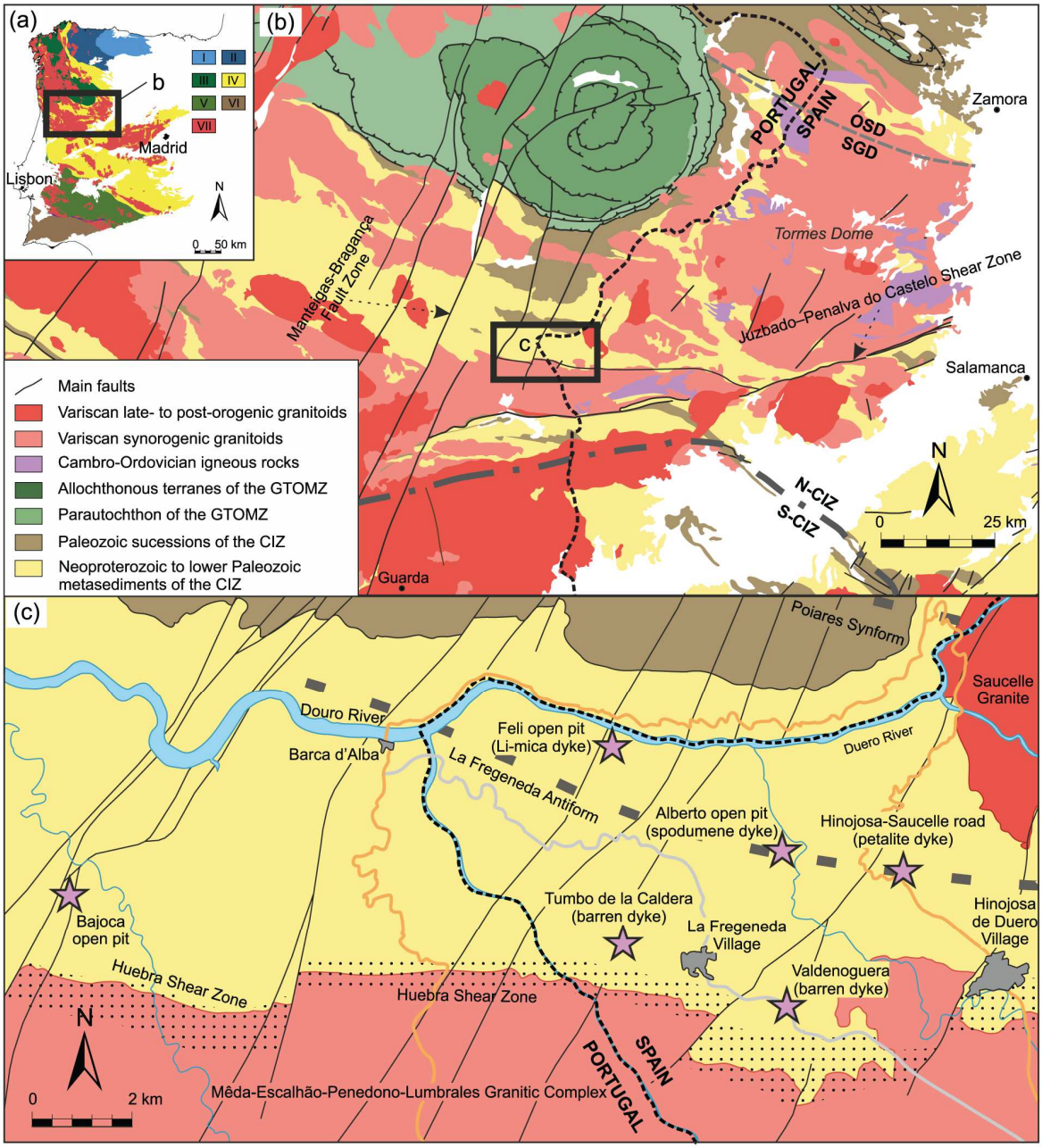

Fig. 1. (a) Geological map of the Iberian Massif, subdivision based on Julivert et al. (1972) and Variscan granitoids adapted from Rodríguez Fernández and Oliveira (2015). I: Cantabrian Zone, II: West Asturian-Leonese Zone, III: Galicia-Trás-os-Montes Zone (GTOMZ), IV: Central Iberian Zone (CIZ), V: Ossa-Morena Zone, VI: South Portuguese Zone, VII Variscan granitoids. (b) Regional geological map based on Rodríguez Fernández and Oliveira (2015), with subdivision of the Ollo de Sapo Domain (OSD) and Schist-Greywacke Domain (SGD), and showing also that of the Northern Central Iberian Zone (N-CIZ) and Southern Central Iberian Zone (S-CIZ; Talavera et al., 2012; Villaseca et al., 2014). (c) Detailed map of the La Fregeneda–Almendra pegmatite field, where locations of the selected dykes are emphasized (based on Silva and Ribeiro (1994) and Rodríguez Fernández et al. (2000)).

The stratigraphic record of the belt is constituted mainly by a thick Neoproterozoic to lower Paleozoic terrigenous metasedimentary sequence included in the Douro Group of Sousa

(1982), which represents, as other correlated pre-Ordovician metasediments of the CIZ, turbiditic flyschoid deposits of the northern continental margin of Gondwana (Silva and Ribeiro 1994; Rodríguez Fernández et al., 2000; Vallarades et al., 2002; Gutiérrez-Alonso et al., 2003; Rodríguez-Alonso et al., 2004; Ugidos et al., 2010; Talavera et al., 2012; Villaseca et al., 2014). This thick pile of pelitic and psammitic metasediments is characterized in the region by millimetre- to centimetre-scale alternations of phyllites (± lutites, slates, schists) and greywackes, with interbedded quartzite and calcsilicate layers (Silva and Ribeiro 1994; Rodríguez Fernández et al., 2000). Since the studied area has been included traditionally in the southern Schist Greywacke Domain of the CIZ according to stratigraphic bases, the pre-Ordovician metasediments of the area have been encompassed within the Schist–Greywacke Complex (Carrington da Costa, 1950; Silva and Ribeiro 1994; Rodríguez Fernández et al., 2000; Teixeira et al., 2011; Talavera et al., 2012). Nevertheless, more recently, based on geochemical evidence of Neoproterozoic metasediments and early Ordovician magmatism Villaseca et al. (2014) distinguished a southern CIZ, characterized by the presence of the abovementioned Schist–Greywacke Complex, and a northern CIZ with metasediments showing more mature and recycled crustal components (Fig. 1b). According to these authors, the studied aplite-pegmatite dykes would intrude into Neoproterozoic to lower Paleozoic metasediments of the northern CIZ that differ slightly from those of the Schist–Greywacke Complex *sensu stricto* (Fig. 1b).

The Neoproterozoic to lower Paleozoic metasediments of the studied area recorded a (very) low-grade Barrovian-type Variscan metamorphism and a polyphasic Variscan deformation (Escuder Viruete et al., 1994; Silva and Ribeiro, 1994; Rodríguez Fernández et al., 2000; Dias da Silva, 2014). The metamorphic grade decreases outwards the MEPL Granitic Complex and Tormes Dome (towards the W and NW), with extended areas belonging to the biotite zone (Silva and Ribeiro, 1994; Rodríguez Fernández et al., 2000; Vieira et al., 2011; Dias da Silva, 2014; Díez Fernández and Pereira, 2016). Apart from the regional metamorphism, the intrusion of Variscan granites generated narrow contact metamorphism aureoles that overprint the Barrovian metamorphism (Rodríguez Fernández et al., 2000; Dias da Silva, 2014; Díez Fernández and Pereira, 2016). The main structures in La Fregeneda–Almendra are WNW–ESE striking and NE vergent cartographic-scale antiforms and synforms, which have been related to the D1 deformation phase of the region and appear accompanied by an associated S1 slaty-cleavage (Escuder Viruete et al., 1994; Silva and Ribeiro 1994; Rodríguez Fernández et al., 2000; Dias da Silva, 2014; Fig. 1c). Late-Variscan tectonics in the studied area comprise NE–SW to NNE–SSW faults that cut previous W–E striking shear zones subsidiary to the large-scale Juzbado–Penalva do Castelo Shear Zone (Silva and Ribeiro 1994; Rodríguez

Fernández et al., 2000; Díez Fernández and Pereira, 2016; Dias da Silva et al., 2017; Fig. 1b, c).

Leaving aside minor Cambro–Ordovician crust-derived peraluminous magmatic rocks (Bea et al., 2007; Villaseca et al., 2014; García-Arias et al., 2018), the main magmatic representation in the area, by far, is comprised by the widespread Variscan granitic intrusions (Dias et al., 1998; López-Moro and López-Plaza, 2004; Valle-Aguado et al., 2005; Gutiérrez-Alonso et al., 2011; Teixeira et al., 2011, 2012; Díez Fernández and Pereira, 2016; López-Moro et al., 2017; Pereira et al., 2018; Ferreira et al., 2019, 2020; Fig. 1b, c). These granitic intrusions have been traditionally classified considering their temporal relationship with respect to the Variscan orogenic stages, distinguishing syn-tectonic intrusions (331–311 Ma) and late- to post-tectonic ones (308–300 Ma; U–Pb in zircon and monazite; Dias et al., 1998; Teixeira et al., 2011, 2012; Gutiérrez-Alonso et al., 2011; Díez Fernández and Pereira, 2016, 2017; López-Moro et al., 2018; Pereira et al., 2018; Ferreira et al., 2019, 2020). Consequently, the MEPL Granitic Complex (~319–313 Ma; U–Pb in zircon) has been defined as syn-orogenic, and the Saucelle Granite as late- to post-orogenic (Rodríguez Fernández et al., 2000; Díez Fernández and Pereira, 2016; Pereira et al., 2018; Ferreira et al., 2019; Fig. 1b, c). The MEPL Granitic Complex is composed mainly by coarse- to medium-grained two-mica peraluminous granites and biotite-rich porphyritic monzogranites, while the Saucelle Granite is constituted by homogeneous undeformed peraluminous two-mica leucogranites (Rodríguez Fernández et al., 2000; Díez Fernández and Pereira, 2016; Pereira et al., 2018; Ferreira et al., 2019, 2020).

2.1. Geology of the aplite-pegmatites from La Fregeneda-Almendra

Hundreds of pegmatite bodies have been identified in the La Fregeneda–Almendra pegmatite field, which have been classified in 11 groups (e.g., Roda-Robles et al., 1999, 2010, in prep.; Vieira et al., 2011). Four of the groups comprise concordant dykes that occur relatively close to the MEPL Granitic Complex and/or intragranitic bodies, while the rest of the groups are constituted by discordant dykes with a N10º–50ºE strike. Intermediate bodies are represented in two groups, whereas the remaining five types include evolved aplite-pegmatites (Roda-Robles et al., 1999, 2010, in prep; Vieira et al., 2011). Overall, the aplite-pegmatites display a spatial zonation from barren to evolved types by increasing the distance from the MEPL Granitic Complex (Roda-Robles et al., 1996, 1999, Vieira et al., 2011). Evolved aplite-pegmatites show enrichment in Li, F, Sn, Rb, Nb>Ta, B, P and Be, with spodumene, petalite, Li-micas and montebrasite as Li-bearing minerals (Roda-Robles et al., 1999, 2010; Vieira et al., 2011). According to Vieira et al. (2011), pegmatites from La Fregeneda–Almendra do not

correspond to a single crystallization path, and their possible petrogenetic linkage with the MEPL Granitic Complex is not completely understood.

3. MATERIALS AND METHODS

3.1. Sampling and petrography

A total of 66 rock samples were collected for the present study: 4 from representative aplite-pegmatites (covering the range of distinguished discordant pegmatite types; 8–12 Kg/sample), 51 from their host rocks, 4 from host metasediments of previous concordant barren dykes, and 7 control samples (2–3 Kg/sample for the control samples and ~1 Kg/sample for the rest). In five of the localities (Feli open pit, Alberto open pit, Hinojosa–Saucelle road, Tumbo de la Caldera, and Valdenoguera; Fig. 1c) a systematic sampling was allowed by the nature of the outcrops, where all samples were collected in a section perpendicular to the strike of the dykes and georeferenced (Supplementary Table 1). The length of the profiles for the halo sampling had to be, ideally, 10 times the width of the body, and based on that was established the number of samples per dyke, as well as the distance from the dyke for each sample. This minimum of samples was conditioned in all cases either by the absence of outcrop, by the degree of the weathering, and/or by the proximity of other dykes (that could potentially overprint the metasomatic effect of the selected body). Additionally, to complement this study, several samples of a drill core from the Bajoca open pit were included also. Control samples were collected from the surroundings of the selected dykes (more than 300 m away), attempting to avoid any possible effect external to the intrusion of the aplite-pegmatites. After hand sample observations, 60 thin sections were made for the petrographic study, which was carried out using a polarizing microscope Leica DM LP model fitted with a CCD camera at the Geology Department of the University of the Basque Country.

3.2. Whole-rock analyses

All collected samples were sent to Actlabs Laboratories (Ancaster, Ontario, Canada; https://actlabs.com) for whole-rock major- and trace-element analyses (complete results in Supplementary Table 1). Pegmatite samples were crushed to a nominal grain size of 1 cm at the Geology Department of the University of the Basque Country and then the resultant material was split to obtain representative sub-samples of 500 g. Similarly, in the case of host metasediments, samples were cut to obtain representative sub-samples of 300 g. Afterwards,

in Actlabs Laboratories, each sample was crushed up to 80% passing 2 mm, was split using a riffle splitter (250 g), and was pulverized to 95% passing 105 µm using a mild steel pulverizer. Major- and trace-element concentrations were obtained by different analytical techniques, which are listed together with respective detection limits in Supplementary Table 1. To obtain major element (SiO_2, TiO_2, Al_2O_3, $Fe_2O_3^t$, MnO, MgO, CaO, Na_2O, K_2O, P_2O_5) and Zr, Sc, Hf and Lu concentrations, a lithium metaborate/tetraborate fusion was performed to dissolve the entire sample. Major elements were measured using X-ray fluorescence whereas Sc and Zr were analyzed by Inductively Coupled Plasma - Optical Emission Spectrometer (ICP-OES) and Hf and Lu by Inductively Coupled Plasma - Mass Spectrometer (ICP-MS). The rest of trace element concentrations were measured also by ICP-MS, but with a previous sodium peroxide fusion, and F concentrations were analyzed by lithium borate fusion with Ion Selective Electrode (ISE).

3.3. Whole-rock calculations and mass-balance quantification

Whole-rock data handling and recalculations were carried out using the R software package GCDkit (Janoušek et al., 2006). The Chemical Index of Alteration (CIA; Nesbitt and Young, 1982) was applied as an estimation of later alterations, with values of < 70 as a proxy of fresh samples. CIA values were calculated as $CIA = [Al_2O_3 / (Al_2O_3 + CaO^* + Na_2O + K_2O)] \times 100$, where oxides are in molar proportions and CaO* represents the CaO of the silicate fraction (Fedo et al., 1995). Correction of CIA was carried out following McLennan (1993), with a first calculation of CaO in apatite considering whole-rock P_2O_5 data ($CaO_{ap} = CaO - 10/3 \times P_2O_5$), and a later comparison of CaO_{ap} with whole-rock Na_2O (if $CaO_{ap} > Na_2O$, then $CaO^* = Na_2O$; if $CaO_{ap} < Na_2O$, then $CaO^* = CaO_{ap}$). From now on, the term “weathered” will be restricted to meteoric weathering, “altered” will be used when referring to later events than the here studied metasomatic processes, and “metasomatized” would represent the consequence of intrusion of the studied aplite-pegmatite dykes.

Quantifications of chemical gains and losses were performed following the Isocon method proposed by Grant (1986) after Gresens’ (1967) equation for composition–volume relations in metasomatic alteration. In this study immobile elements (those with no differences in concentration between metasomatized and non-metasomatized samples; $\Delta C_i = C_i^a - C_i^0 = 0$) were considered as the reference frame, which were selected considering an ideal composition of a non-metasomatized metasedimentary sample (average of collected control samples) and based on 1) clusters of slopes, 2) the C^a vs. C^0 “Isocon diagram”, and 3) composition–volume diagrams (Gresen, 1967; Grant, 1986, 2005; Potdevin, 1993; López-Moro, 2012). Since an

ideal immobile element would display a slope (metasomatized/non-metasomatized; C_i^a / C_i^0) of 1 in the "Isocon diagram", in this work it has been considered at first glance as immobile any element with a slope of 1.0 ± 0.1. To make comparable numerical results of all samples (within the same locality), the same immobile elements were selected for the calculation of the isocon, which was assessed in each of the samples by means of least-squares regression using EASYGRESGRANT (López-Moro, 2012). Finally, the numerical gains and losses (relative to the initial non-metasomatized composition) were calculated for each of the metasomatized samples as: $\Delta C_i^a/C_i^0 = (1/M \times C_i^a / C_i^0) - 1$, where M is the slope of the isocon, C_i^a is the concentration of an element "i" (in wt% or ppm) from the metasomatized sample, and C_i^0 is the concentration of the element "i" (in wt% or ppm) from the ideal composition of a non-metasomatized sample (complete results in Supplementary Table 2).

4. FIELD DESCRIPTION AND PETROGRAPHY

4.1. Aplite-pegmatites dykes

The selected bodies for the systematic study from La Fregeneda–Almendra correspond to barren (Tumbo de la Caldera and Valdenoguera), petalite-bearing (Hinojosa–Saucelle road), spodumene-bearing (Alberto open pit), and Li-mica-bearing (Feli open pit) aplite-pegmatites (Fig. 1c). Excluding the concordant E–W trending vein from Valdenoguera, the rest of the bodies are subvertical dykes with a N–S strike that crosscut the regional foliation of the host rocks (Fig. 2a). These dykes are characterized by a marked variation in grain size, from few millimeters up to several centimeters, and variable thicknesses from 1.2 to 7.0 m (Table 1). A slight layering from border to border, parallel to the contact with the host rock, is observed in some cases, but within the selected bodies this feature is reduced to that from the Feli open pit. The complementary samples from the Bajoca open pit are from the 30 m-width subvertical petalite-bearing pegmatite where no layering is observed.

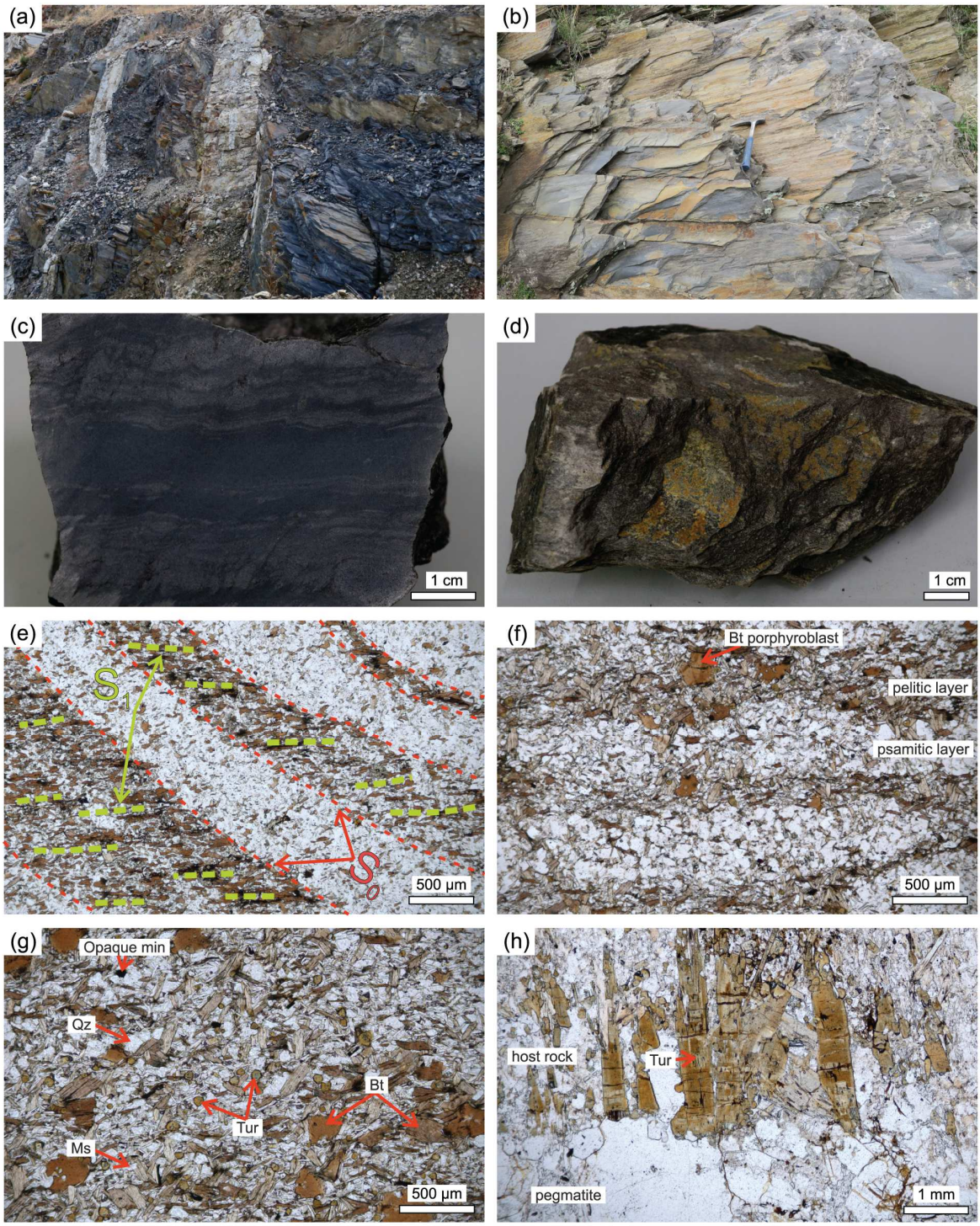

Fig. 2. (a) Outcrop photograph of the selected aplite-pegmatite dyke from the Alberto open pit (the width of the central dyke is of 2.6 m). (b) Representative field picture of the host psammitic and pelitic metasediments. (c) Section of a metasedimentary hand sample that display sedimentary structures in psammitic (lighter) layers. (d) Representative hand specimen of host psamopelitic metasediments (note the violetish tone). (e) Photomicrograph of alternating psammitic and pelitic layers in host metasediments (S0 sedimentary layering; S1 slaty-cleavage). (f) Photomicrograph of biotite (Bt) porphyroblasts developed in the more pelitic layers. (g) Photomicrograph of a relatively more pelitic sample with higher proportions of muscovite (Ms) and lower ones of quartz (Qz), showing small disperse tourmaline (Tur) crystals. (h) Photomicrograph of a contact between an aplite-pegmatite dyke and host metasediments with parallelly arranged tourmaline crystals.

The mineralogy of the selected barren dyke from Tumbo de la Caldera comprises mainly quartz, K-feldspar, albite, muscovite with minor Fe–Mn phosphates, montebrasite, tourmaline, cassiterite, and columbite-tantalite group minerals. Likewise, the vein from Valdenoguera is constituted by the same main mineral phases of the prior barren body, but with garnet, andalusite, and biotite as accessories. In the case of Hinojosa–Saucelle and Bajoca, the mineral phases correspond to quartz, petalite, albite, and K-feldspar, with minor muscovite and cassiterite, and Fe–Mn phosphates, montebrasite, and eucryptite as accessory. Similarly, the studied dyke from Alberto is composed of quartz, spodumene, albite, K-feldspar, muscovite, petalite, with occasional montebrasite and Fe–Mn phosphates. And finally, the selected body from Feli is formed by quartz albite, K-feldspar, Li-muscovite, muscovite, spodumene, montebrasite, cassiterite, columbite-tantalite group minerals, apatite, eucryptite, and Fe–Mn phosphates.

4.2. Host metasediments

The host rocks of the selected aplite-pegmatite dykes are part of a monotonous siliciclastic metasedimentary sequence with turbiditic features. This series comprehend a roughly rhythmic alternation (millimetric to centimetric) of phyllites and metagreywackes with minor calc-silicate rocks and no volcanic sections (Fig. 2a, b). Overall, the studied psammitic and pelitic metasediments are fine-grained, and they preserve, mainly in the most psammitic levels, sedimentary structures such as erosion surfaces, parallel lamination, ripples, load casts, and grain-size distribution (Fig. 2c). The colour scale of fresh samples includes grey to dark-grey tones, with slight greenish–bluish–violetish tints, which contrast with the light psammitic layers (Fig. 2c, d).

At microscope, the studied metasediments show granolepidoblastic texture. In the more pelitic layers, the metamorphic overprint is visible, with no-oriented porphyroblasts of biotite and a well-developed slaty-cleavage that cut the sedimentary structures (Fig. 2e, f, g). The main mineralogy of these metasediments comprises variable amounts of quartz, biotite, and muscovite, plus accessory plagioclase (± K-feldspar), apatite, zircon, and opaque phases (Fig. 2e, f, g). In general, the mineralogy of the selected samples is fairly homogeneous, but in some thin sections, in which later modifications are perceived, the occurrence of tourmaline or chlorite (± calcite, ± epidote and ± titanite) is common. In some samples an extensive chloritization is observed, where chlorite replaces partially or completely biotite crystals. The distribution of this later chloritization is totally heterogeneous at the outcrop scale, but is

present in all localities. Similarly, in samples principally close to the aplite-pegmatites, a strong tourmalinization occurs, resulting in the development of parallelly arranged tourmaline crystals in the pelitic layers (Fig. 2h). It seems that tourmalinization is stronger in the case of Hinojosa–Saucelle and Bajoca (thickest selected dykes and both petalite-bearing), where in the closest samples to the dyke tourmalinite layers could be discerned (tourmaline up to 80 % in vol). In the Hinojosa–Saucelle road later tourmaline crystals appear up to 15 m far from the dyke, but they are found as scattered small crystals or close to microfractures (Fig. 2g). It is outstanding also that host metasediments from Tumbo de la Caldera (barren aplite-pegmatite) and Bajoca (petalite-bearing aplite-pegmatite) are more micaceous than other localities, with lower proportions of quartz and higher muscovite.

5. WHOLE-ROCK GEOCHEMISTRY

5.1. Aplite-pegmatites dykes

The selected four aplite-pegmatite samples of the La Fregeneda–Almendra pegmatite field show high SiO_2 (70.84–74.29 wt%), Al_2O_3 (15.3–17.07 wt%), Na_2O (2.44–6.30 wt%), and P_2O_5 (0.37–0.87 wt%) contents (Table 1). On the contrary, MgO (0.01–0.15 wt%), $Fe_2O_3^t$ (0.36–0.50 wt%), TiO_2 (~0.02 wt%), CaO (0.21–0.43 wt%) and K_2O (2.15–3.78 wt%, excepting one sample) proportions are relatively low (Table 1). All selected samples are peraluminous to strongly peraluminous, with A/CNK values (Shand, 1943) from 1.11 to 1.99. They are perphosphorous, and they display K_2O/Na_2O ratios in the range of 0.34–2.17, with the lowest ratios in Feli (highest contents of Na_2O and P_2O_5; Table 1).

The studied samples are poor in Ba, Zr, Y, Th, As, W and REE, and are rich in Li, Rb, Cs, Nb, Ta, Sn, Be, Ge, and Tl (Table 1). Although F contents are relatively high in the Feli open pit (3100 ppm), where also occur the highest B proportions (50 ppm), overall F and B contents in these rocks are not significantly high (Table 1; Fig. 3a). In the cited locality Be, Ge, Cs, Nb, Ta, Sn and U also display maximum proportions, contrary to Li that is significantly richer in Alberto (9070 ppm), and Rb that shows the highest contents in the barren dyke from Tumbo de la Caldera (1310 ppm; Table 1). The Nb/Ta ratio decreases in the selected samples in the sense of barren → petalite → spodumene → Li-mica, similarly to the K/Rb ratio (Fig. 3b).

Table 1. Major- (wt%) and trace-element (ppm) whole-rock geochemical analyses of selected aplite-pegmatites from the La Fregeneda–Almendra pegmatite field.

Locality	**Feli**	**Alberto**	**Hinojosa-Saucelle**	**Tumbo de la Caldera**
Type	Li-mica	Spodumene	Petalite	Barren
Thickness (m)	1.8	2.6	7	1.2
Sample	FEL-02	ALB-01	PET-01	BAR-06
SiO_2	70.84	74.27	74.29	71.04
TiO_2	0.02	0.02	0.02	0.02
Al_2O_3	17.07	16.79	15.3	15.91
$Fe_2O_3^t$	0.45	0.36	0.38	0.5
MnO	0.03	0.017	0.027	0.041
MgO	0.04	0.15	0.01	0.05
CaO	0.32	0.21	0.43	0.3
Na_2O	6.3	2.44	5.41	3.44
K_2O	2.15	3.74	3.78	7.46
P_2O_5	0.82	0.37	0.48	0.67
LOI	1	0.86	0.71	0.63
Total	99.07	99.26	100.9	100.1
F	3100	< 100	100	200
As	7	< 5	7	< 5
B	50	20	50	< 10
Ba	27	20	52	29
Be	208	94	89	71
Bi	< 2	< 2	< 2	< 2
Cd	< 2	< 2	< 2	< 2
Co	1.3	0.6	0.6	0.9
Cr	70	70	100	70
Cs	379	57.2	28.5	40.7
Cu	27	10	8	12
Ga	38.2	15.1	15.7	19.6
Ge	13.6	4	4.1	4.1
Hf	4.8	< 0,2	0.6	0.4
In	< 0,2	< 0,2	< 0,2	< 0,2
Li	2600	9070	200	61
Mo	< 1	1	2	2
Nb	78.1	22.1	12.6	10.3
Ni	30	30	40	20
Pb	20.2	12.7	35	13.4
Rb	1080	772	640	1310
S	< 0,01	< 0,01	< 0,01	< 0,01
Sb	< 2	< 2	< 2	< 2
Sc	< 0,1	0.1	0.1	0.2
Se	< 8	< 8	< 8	< 8
Sn	768	93.2	61.1	34.6

Sr	75	50	82	45
Ta	118	14	6.7	3.5
Te	< 6	< 6	< 6	< 6
Th	3.1	0.4	0.2	0.2
Tl	7.7	6.2	4.3	10.4
U	8.9	1.5	1.7	1.2
V	< 5	< 5	< 5	< 5
W	3.9	< 0,7	0.9	3
Y	0.2	0.6	0.6	1.4
Zn	< 30	50	40	40
Zr	38	3	11	7
La	< 0,4	0.6	< 0,4	0.7
Ce	< 0,8	< 0,8	< 0,8	0.9
Pr	< 0,1	0.1	< 0,1	< 0,1
Nd	< 0,4	0.5	0.6	0.7
Sm	< 0,1	0.2	< 0,1	0.2
Eu	< 0,1	< 0,1	< 0,1	< 0,1
Gd	< 0,1	< 0,1	< 0,1	0.2
Tb	< 0,1	< 0,1	< 0,1	< 0,1
Dy	< 0,3	< 0,3	< 0,3	< 0,3
Ho	< 0,2	< 0,2	< 0,2	< 0,2
Er	< 0,1	< 0,1	< 0,1	< 0,1
Tm	< 0,1	< 0,1	< 0,1	< 0,1
Yb	< 0,1	< 0,1	< 0,1	0.2
Lu	0.02	0.08	< 0,01	0.01

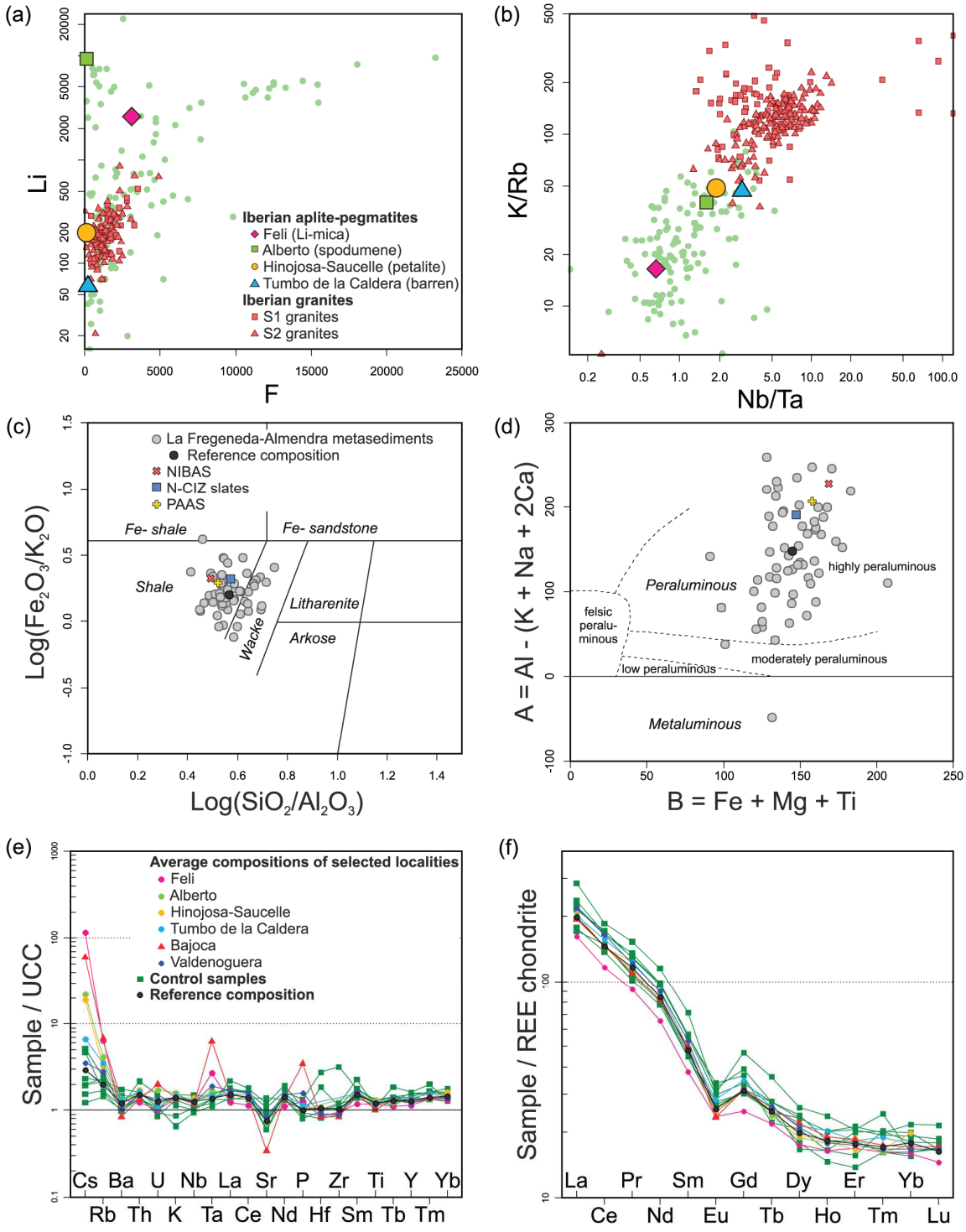

Fig. 3. (a) F vs. Li diagram emphasizing compositions of selected aplite-pegmatites (Iberian aplite-pegmatites, S1 granites and S2 granites taken from Roda-Robles et al., 2018). (b) Nb/Ta vs. K/Rb diagram for studied aplite-pegmatites (legend is the same of Fig. 3a). (c) Classification diagram for siliciclastic sediments (Herron 1988), showing compositions of studied metasedimentary host rocks (and the reference composition for La Fregeneda–Almendra). Compositions of the Neoproterozoic Iberian Average Shale (NIBAS; Ugidos et al., 2010), average of North-Central Iberian Zone (N-CIZ) slates (Villaseca et al., 2014) and the Post Archean Australian Shale (PAAS; Taylor and McLennan, 1985) are also displayed for comparison. (d) Maficity [B] vs. peraluminosity [A] diagram of Debon and Le Fort (1983) modified by Villaseca et al. (1998) the legend is the same of Fig. 3c. (e)

Upper Continental Crust (UCC; Rudnick and Gao, 2014) normalized spider plots for the studied metasediments. (f) Chondrite (McDonough and Sun, 1995) normalized REE diagrams for the studied metasediments (the legend is the same of Fig. 3e).

5.2. Host metasediments

5.2.1. Major elements

In the studied localities of La Fregeneda–Almendra, average SiO_2 contents of the host metasediments vary in the range of 60.49–66.05 (wt%), and average Al_2O_3 contents show values of 16,09–18,75 (wt%; Table 2). These SiO_2 and Al_2O_3 contents are relatively close to the Upper Continental Crust (UCC) of Taylor and McLennan (1995) and Rudnick and Gao (2014), but differ slightly from the Neoproterozoic Iberian Average Shale (NIBAS; Ugidos et al., 2010). Apart from SiO_2 and Al_2O_3 compositions, TiO_2, MgO and $Fe_2O_3^t$ contents display overall small dispersion, with total average values of 0.77, 2.26, and 6.29 (wt%), respectively (Table 2). The studied metasediments display low-CaO contents, with a reference value of 1.26 (wt%; excluding Ca-rich samples; Table 2). Discarding also anomalous P-rich samples, average Na_2O, K_2O, and P_2O_5 contents (1.86, 3.96, and 0.15 respectively, in wt%) approximate compositions of the NIBAS (Ugidos et al., 2010). Considering average values of different localities, the collected control samples, and excluding dissonant samples, a reference composition for the La Fregeneda–Almendra metasediments is given in Table 2. In terms of major elements the reference composition resembles average values of the studied localities.

Most of the studied samples plot into the field of shales in the classification diagram of Herron (1988), although some of them fall into the greywacke field (Fig. 3c), with SiO_2/Al_2O_3 values in the range of 2.57–5.59, and $Fe_2O_3^t/K_2O$ values from 0.24 to 4.19 (Supplementary Table 1). Dismissing the only metaluminous calc-silicate sample and Ca-rich samples, CaO/Na_2O ratios vary from 0.17 to 1.20, and K_2O/Na_2O proportion varies from 0.59 to 27.00. Values of A/CNK (Shand, 1943) fall within the range delimited by the low-peraluminous UCC of Rudnick and Gao (2014) and the NIBAS (Ugidos et al., 2010), showing moderate to strongly peraluminous compositions (A/CNK = 1.17–3.07; Supplementary Table 1). Overall, these metasediments show homogeneous Al_2O_3/TiO_2 ratios in the range of 20.99–24.36, and millicationic parameters of Debon and LeFort (1983) vary in the ranges of 40–260 (A parameter) and 90–210 (B parameter; Fig. 3d).

5.2.2. Trace elements

In terms of trace-elements, average contents of localities and compositions of control samples show that the studied metasediments are rich in Ni, Cr and Th, poor in V, Y, U and Hf, and have similar Zr and Co contents than the NIBAS (Table 2, Ugidos et al., 2010). Considering only the control samples, Ba, Rb and Sr contents are also slightly higher than the cited references, similarly to Cs contents compared with the UCC of Taylor and McLennan (1995) and Rudnick and Gao (2014). Ratios of Ti/Nb and La/Th are lower than the NIBAS, contrary to those of La/Y and Th/Yb. They show similar Ti/Zr ratios and compared to the UCC of Taylor and McLennan (1995) and Rudnick and Gao (2014) they show higher La/Sc, Th/Sc, and similar Zr/Sc proportions.

Excluding control samples, average compositions of the selected localities display significantly high contents of F, B, As, W, Li, Rb, Cs, Sn, Ta, Be, Ge and Tl (Table 2). In host metasediments of Li-mica, spodumene and petalite dykes, F and B contents reach up to extremely high contents of 7000 and >10000 ppm, respectively (Table 3). Similarly, these samples show significantly high Li (281–4120 ppm), Rb (163–1340 ppm), Cs (76.4–1280 ppm) and Sn (18.9–126 ppm) contents. Other trace-elements such as Be (up to 41.0 ppm), Ta (up to 20.2 ppm), Tl (up to 10.4 ppm) and Ge (up to 5.5 ppm), together with As, W, Mo and S also appear in high concentrations in some of the studied samples (Table 3 and Supplementary Table 1).

In the UCC (Rudnick and Gao, 2014) normalized diagram, average compositions of selected localities and control samples display flat patterns close to the UCC composition. The exceptions are marked by positive anomalies in Cs and Rb of the average compositions, as well as by Ta and P positive and Sr negative anomalies in the case of metasediments from Bajoca (Fig. 3e). Total Rare Earth Element (REE) contents in control samples and average compositions vary in the range of 172–286 ppm (Table 2), and chondrite-normalized REE patterns (normalization values from McDonough and Sun, 1995) exhibit segmented geometries, with La_N/Yb_N ratios (~11.2) higher than the NIBAS (Fig. 3f). Heavy Rare Earth Elements (HREE) show nearly flat patterns (Gd_N/Yb_N = ~1.76), contrary to Light Rare Earth Elements (LREE) that show moderate slopes (La_N/Sm_N = ~4.14), with a similar Eu anomaly ($Eu/Eu^* = Eu_N/[(Sm_N \times Gd_N)^{1/2}]$) in all cases (~0.66; Fig. 3f).

Table 2. Major- (wt%) and trace-element (ppm) whole-rock geochemical analyses of metasedimentary control samples, averages of selected localities, and the reference composition from the La Fregeneda–Almendra pegmatite field.

	Control samples							**Averages of localities**						**REFERENCE***
Sample	ALB-05	FEL-04	FEL-05	BAR-11	BAR-12	CXG3 438	CXG5 PP01	Feli	Alberto	Hinojosa-Saucelle	Tumbo de la Caldera	Bajoca	Valde-noguera	
SiO_2	63.50	67.12	61.24	65.29	63.18	65.38	69.74	66.05	65.20	60.49	62.95	64.23	65.50	63.63
TiO_2	0.72	0.70	0.81	0.73	0.81	0.82	0.84	0.74	0.74	0.83	0.80	0.65	0.75	0.77
Al_2O_3	15.18	15.43	18.04	16.06	17.12	16.99	14.00	16.09	16.34	18.75	17.30	17.80	17.16	17.27
$Fe_2O_3^t$	5.55	5.53	7.70	6.29	6.19	6.09	4.18	5.64	5.80	7.24	6.43	5.95	5.84	6.29
MnO	0.15	0.09	0.10	0.07	0.08	0.06	0.05	0.07	0.06	0.09	0.08	0.09	0.07	0.08
MgO	2.13	2.24	2.69	2.30	2.22	2.14	1.44	2.07	2.28	2.61	2.29	1.98	1.69	2.26
CaO	7.95	3.81	1.40	2.10	2.62	0.83	1.01	1.11	1.43	1.28	1.63	0.77	0.73	1.26
Na_2O	0.71	2.24	1.84	1.96	2.90	1.88	2.76	2.10	2.10	1.72	2.17	0.67	1.80	1.86
K_2O	1.84	2.41	4.01	3.72	4.02	4.28	3.20	3.87	4.40	3.89	4.22	3.92	3.89	3.96
P_2O_5	0.15	0.16	0.14	0.12	0.14	0.13	0.20	0.19	0.15	0.17	0.17	0.52	0.24	0.15
LOI	1.81	0.89	2.08	1.88	1.01	2.19	2.18	2.03	1.65	2.93	2.20	2.94	2.75	2.03
Total	99.74	100.7	100.1	100.60	100.30	100.80	99.61	99.96	100.15	100.00	100.24	99.52	100.42	99.55
F	300	400	400	300	100	400	300	2000	1200	700	500	3300	-	300
As	< 5	17	< 5	< 5	< 5	< 5	8	112	19.8	38.4	-	393	-	< 5
B	< 10	70	70	60	50	48	56	758	136	910	96.7	7485	-	60
Ba	642	611	827	633	1100	933	706	822	855	703	824	528	661	756
Be	4	3	4	5	4	3	2	8.70	6.70	6.56	6.63	21.6	6.75	3.5
Bi	< 2	< 2	< 2	< 2	< 2	1	< 0,4	-	-	-	-	-	-	< 2
Cd	< 2	< 2	< 2	< 2	< 2	NA	NA	-	-	-	-	-	-	< 2
Co	15.3	15.7	17.3	15.6	14.7	24	12	8.4	13.3	15	15.6	17	12.3	13.9
Cr	120	110	130	130	140	90	110	128	128	138	133	112	92.5	127
Cs	6	23	25.5	9.7	11.4	9.5	7.6	572	108	93.1	33	294	17.3	14.5
Cu	17	17	35	29	8	20	10	15.1	21.2	25.5	18.1	25	20	20.9
Ga	20.7	23.2	30.8	24.6	24	24	17	24.6	26.1	27.6	26.5	24.4	24.8	25.8
Ge	2.3	2.6	2.5	1.9	2.2	2	1	3.13	2.47	2.88	2.29	2.4	2.75	2.07
Hf	5.4	5.3	4.6	NA	9.8	4.3	14.6	4.53	-	-	-	4.46	4.88	5.74
In	< 0,2	< 0,2	< 0,2	< 0,2	< 0,2	< 0,2	< 0,2	-	-	-	-	-	-	< 0,2
Li	83	150	94	113	129	60	50	1572	1391	561	289	1060	125	97
Mo	2	< 1	< 1	< 1	< 1	< 2	3	-	-	-	-	-	-	< 1
Nb	11.4	12.9	15.5	13.2	15.1	18	12	14.8	14.5	16.9	15.4	14.2	15	15.3
Ni	40	40	60	50	50	30	30	46	56	67.6	55.6	46	< 20	52.4
Pb	28.3	22.4	24.2	23.3	34.7	21	21	20.7	23.1	31.3	22.1	17	23.5	24.6
Rb	121	138	207	197	185	182	141	537	350	275	299	574	235	167
S	0.02	< 0,01	0.02	< 0,01	< 0,01	NA	NA	-	-	-	-	-	-	< 0,01
Sb	< 2	< 2	< 2	< 2	< 2	< 2	< 2	-	-	-	-	-	-	< 2
Sc	12.1	11.6	15.7	NA	13.6	15	11	12.6	-	-	-	13.6	13.3	13.1
Se	11	< 8	20	11	11	NA	NA	9.6	12	8.53	13.4	-	-	10.8
Sn	2.7	1.9	3.7	1.9	2.8	4	3	30.7	23.9	16.7	17.1	84.2	18	2.86
Sr	448	381	190	294	343	191	228	252	231	241	255	109	268	240

Ta	1	1.1	1.4	1.2	1.4	1.3	1.2	2.45	1.52	1.32	1.34	5.62	1.73	1.23
Te	14	9	14	15	15	NA	NA	17.1	15.7	< 6	15.7	-	-	12
Th	14.3	14.5	16.5	15.8	16.9	14.7	22.7	13.1	15.6	18.1	17.2	14.2	16.1	16.1
Tl	0.5	0.7	0.9	0.6	1	0.9	1.1	4.76	2.04	1.52	1.66	3.78	1	0.81
U	2.9	2.5	3.2	2.3	2.9	2.7	4.1	2.72	4.66	2.9	2.93	5.38	3.65	3.41
V	75	75	101	82	86	97	74	82.5	82	105	88.4	92	87.8	90.7
W	1.5	1.2	2.2	1.6	2.4	3	2	6.68	6.61	3.41	2.6	9	4.5	1.99
Y	26.9	33.7	30.2	25.5	29.4	33	32	24.1	26.4	26.9	29	27.2	25.5	27
Zn	80	100	110	90	80	90	60	91	112	180	108	138	133	97.7
Zr	207	233	175	NA	214	171	612	184	-	-	-	163	172	199
La	42.2	67.7	56.2	40.7	53.1	46.1	51	38.3	47.2	49.3	47.9	46	52.2	47.1
Ce	84.3	114	103	91.3	102	90.2	106	71.3	89.5	88.6	96.1	89.7	101	89.1
Pr	9.4	14.2	12	9.9	12.6	10.2	11.9	8.55	10.6	11.5	11.5	10.1	11.3	10.8
Nd	35.4	52.5	45	36.7	44.8	37.3	44	30	38.6	40.8	41.1	37.3	41.3	38.7
Sm	6.6	10.6	8.3	6.6	8.4	6.8	8.2	5.65	7.09	7.27	7.27	7.34	7.83	7.1
Eu	1.4	1.7	1.9	1.5	1.8	1.56	1.68	1.33	1.46	1.4	1.59	1.32	1.46	1.45
Gd	6.3	9.3	7.3	6.1	7.8	6	6.7	5	6.29	6.14	6.91	6.26	6.1	6.2
Tb	1	1.3	0.8	0.9	1	0.9	1	0.79	0.86	0.924	0.944	0.94	0.95	0.905
Dy	4.1	6.4	5.1	4.4	5.9	5.7	5.7	4.31	4.66	4.76	5.28	5.42	5.2	4.89
Ho	0.9	1.3	0.9	0.8	1	1.1	1.1	0.9	0.97	0.994	1.11	1.04	0.975	1
Er	2.5	3.3	3.2	2.2	2.9	3.3	3.4	2.7	3.01	2.66	2.94	2.96	2.78	2.83
Tm	0.5	0.6	0.5	0.4	0.4	0.48	0.49	0.4	0.4	0.412	0.467	0.43	0.413	0.425
Yb	2.9	2.6	3.2	2.5	2.6	3.1	3.5	2.56	2.8	3.2	2.86	2.76	2.7	2.88
Lu	0.44	0.41	0.41	NA	0.42	0.46	0.53	0.357	-	-	-	0.422	0.41	0.4

*calculated from all samples, excluding anomalous analyses and enriched samples (see the discussion section)

**NA not analyzed

*** "-" not calculated

Table 3. Major- (wt%) and trace-element (ppm) whole-rock geochemical analyses of highly enriched (metasomatized) metasedimentary samples from the La Fregeneda–Almendra pegmatite field

Locality	**Feli**	**Feli**	**Feli**	**Alberto**	**Alberto**	**Alberto**	**Hinojosa -Saucelle**	**Hinojosa -Saucelle**	**Hinojosa-Saucelle**	**Bajoca**	**Bajoca**
Type	Li-mica	Li-mica	Li-mica	Spodumene	Spodumene	Spodumene	Petalite	Petalite	Petalite	Petalite	Petalite
Distance* (m)	0	1	1.8	0	0.5	0	0	0.5	12	0.5	0
Sample	FR-49	FR-51	FR-52	F-38	F-39	F-43	FR-18	FR-19	FR-24	BJ04-B-DD	BJ04-D-DD
SiO_2	67.59	58.46	66.23	66.85	63.52	65.32	53.9	61.76	58.89	68.05	64.64
TiO_2	0.67	0.95	0.71	0.76	0.77	0.76	0.91	0.8	0.89	0.551	0.584
Al_2O_3	14.4	20.79	15.07	15.7	17.44	15.87	20.98	17.79	20.47	14.68	16.77
$Fe_2O_3^t$	5.41	6.14	5.34	5.3	6.51	5.58	8.97	6.96	7.34	5.96	5.74
MnO	0.105	0.045	0.089	0.068	0.045	0.077	0.111	0.126	0.084	0.087	0.09
MgO	1.95	2.43	1.77	1.98	2.55	2.21	3.36	2.67	2.71	2.02	2.02
CaO	2.01	0.56	1.4	1.85	0.66	1.77	2.56	1.35	1.7	0.8	1.64
Na_2O	2.25	2.37	1.58	3	1.17	1.88	4	1.8	1.78	0.41	0.54

K_2O	2.62	5.09	4.42	3.74	5.28	3.33	3.77	3.5	1.75	3.22	2.97
P_2O_5	0.16	0.14	0.61	0.15	0.12	0.2	0.13	0.17	0.58	0.61	1.22
LOI	1.62	2.76	2.13	1.04	2.06	2.23	1.68	2.54	2.59	2.23	2.6
Total	98.82	99.76	99.41	100.5	100.2	99.27	100.5	99.52	98.82	98.6	98.83
F	0.34	0.31	0.7	0.24	0.07	0.18	0.16	0.13	0.27	0.31	0.34
As	45	73	148	31	7	26	41	18	281	466	1080
B	420	3900	910	250	220	110	470	2240	> 10000	6090	8880
Ba	972	1310	590	1000	894	681	620	850	566	294	280
Be	10.0	14.0	22	11.0	4.0	12.0	13.0	9.0	17.0	41.0	29
Bi	< 2	< 2	< 2	< 2	< 2	< 2	< 2	< 2	< 2	< 0,4	0.4
Cd	< 2	< 2	< 2	< 2	< 2	< 2	< 2	< 2	< 2	NA	NA
Co	7.8	9.4	8.3	11	15.2	11.3	11	15.5	8.8	11	15
Cr	100	160	110	120	140	130	140	140	140	90	100
Cs	1120	668	1280	169	107	130	270	157	76.4	306	230
Cu	7	17	11	6	31	30	16	18	22	10	10
Ga	21.3	35.2	24	23.4	27	27.5	29.3	25.2	29	18	20
Ge	2.5	3.9	4.5	2.6	2.3	2.9	3.5	2.8	5.5	2	3
Hf	5	4.2	6.7	NA	NA	NA	NA	NA	NA	3	3.8
In	< 0,2	0.3	< 0,2	< 0,2	< 0,2	< 0,2	< 0,2	< 0,2	< 0,2	< 0,2	< 0,2
Li	1990	2530	4120	1920	1530	1750	1450	1070	281	1270	1120
Mo	< 1	2	2	< 1	1	< 1	< 1	< 1	4	2	2
Nb	13.2	16.8	24.1	16.3	15.8	14.6	14.9	17.1	22.1	11	16
Ni	40	40	40	40	60	40	60	50	50	30	40
Pb	16.9	16.4	13.1	32	13.5	38.1	64	23.2	39.7	7	13
Rb	762	786	1340	417	342	507	523	378	163	665	557
S	< 0,01	0.12	< 0,01	< 0,01	< 0,01	0.02	< 0,01	< 0,01	0.02	NA	NA
Sb	< 2	< 2	< 2	< 2	< 2	< 2	< 2	< 2	< 2	< 2	< 2
Sc	10	18.2	10.5	NA	NA	NA	NA	NA	NA	10	11
Se	< 8	10	< 8	< 8	< 8	< 8	< 8	< 8	< 8	NA	NA
Sn	38.5	64.8	117	48	18.9	48.4	35.6	39.1	81.4	105	126
Sr	397	152	301	355	148	214	480	249	235	81	185
Ta	1.5	1.5	11.9	2.7	1.4	1.3	1.3	1.3	2	3.5	20.2
Te	15	18	13	20	20	16	< 6	< 6	< 6	NA	NA
Th	9.9	20.8	11.9	15.5	16.9	15.3	19.8	16.6	17.4	9.7	11
Tl	7.6	5.9	10.4	2.7	2	3	3.8	2.4	0.8	4.8	4.5
U	2.3	2.9	3.4	4.1	7.3	5.8	3.4	2.8	2.9	3.7	4.1
V	72	112	69	81	92	86	117	99	109	73	77
W	18.4	8.4	13.7	1.7	3	33.8	2	2.5	11.1	8	11
Y	14.7	28.8	24.7	22.7	27.9	31.5	17.5	28.4	24.5	24	27
Zn	80	80	100	190	80	190	180	730	170	130	200
Zr	206	154	261	NA	NA	NA	NA	NA	NA	127	140
La	20.4	56.5	38.7	48.3	51.8	48.8	54.1	46.1	45.1	32	33.7
Ce	36.8	114	63	92.1	97	91.2	95.3	82.8	84.2	63.5	64.9
Pr	4.5	13.2	8.2	10.8	11.3	10.9	12.2	11.2	10.2	7.2	7.55

Nd	16.9	46	32.2	39.7	39.1	41	41.3	39.5	36.8	26	27.6
Sm	2.8	8	5.1	6.4	8.3	7.6	6.3	7	5.7	5.3	5.8
Eu	1	2	1.5	1.4	1.4	1.5	1.6	1.2	1.3	0.86	1.17
Gd	2.8	6.5	6.1	5.6	6.3	6.4	5	6.2	5.5	5.2	5.4
Tb	0.3	1	0.9	0.9	0.9	1	0.6	0.9	0.9	0.9	0.8
Dy	2.7	4.7	4.5	4.4	5.2	5.3	3	5	4.7	5	4.8
Ho	0.6	1	0.9	0.8	0.9	1.1	0.5	1	1	1	0.9
Er	1.6	3	2.2	2.4	2.9	3.5	1.9	2.7	2.5	2.8	2.7
Tm	0.2	0.5	0.3	0.3	0.4	0.5	0.3	0.4	0.4	0.4	0.39
Yb	1.6	3.1	2.6	1.9	2.6	3.2	2	3.4	3.9	2.6	2.5
Lu	0.23	0.49	0.33	NA	NA	NA	NA	NA	NA	0.37	0.39

*Distance from the dyke

**NA not analyzed

6. DISCUSSION

6.1. Provenance of metasediments and later alterations

Coupled with petrographic observations, whole-rock geochemical constraints represent effective tracers for the provenance of sedimentary rocks (McLennan et al., 1993; Cox et al., 1995; Ugidos et al., 1997; Fuenlabrada et al., 2020). Major- and trace-element compositions of insoluble elements such as Fe, Al, Ti, REE, Y, Sc, Th, Zr, Hf, Cr, Co, Ni, Cu, Zn and their ratios are widely used to decipher source-rocks of clastic sedimentary rocks (Taylor and McLennan, 1985; Condie, 1993; Ugidos et al., 1997, 2003, 2010; Fuenlabrada et al., 2020). The Zr/Sc ratio can be used to assess the participation of felsic and mafic input since Zr is accommodated in zircon (abundant in felsic rocks) and Sc is associated with mafic terms (McLennan et al., 1993; Long et al., 2012). Similarly, Th/Sc, Cr/V and Y/Ni ratios are also used to discriminate felsic and mafic sources (McLennan et al., 1993; Ugidos et al., 1997, 2003). Zr/Sc ratios in La Fregeneda–Almendra metasediments vary in the range of 8.46–55.6, suggesting a zircon addition due to sorting and recycling processes (Fig. 4a; McLennan et al., 1993; Long et al., 2012). Similarly, high contents of Hf (up to 14.6 ppm) also point to old crust input (Fig. 4b; Floyd and Leveridge, 1987; Taylor and McLennan, 1995). These high Zr/Sc ratios and Hf contents are in accordance with high Y/Ni ratios (up to 1.56), low Cr/V (< 2) and La/Th (average of 2.89) ones, and those of Al_2O_3/TiO_2 (16.6–30.0), indicating (intermediate-) felsic source rocks (Fig. 4b, c; Floyd and Leveridge, 1987; McLennan et al., 1993). In agreement with the previous, higher La_N/Yb_N and Gd_N/Yb_N ratios than the NIBAS and N-CIZ slates, together with similar Eu/Eu* negative anomalies and flat HREE patterns, imply a principally felsic differentiated source (Fig. 3f; Ugidos et al., 2010; Villaseca et al., 2014). The reference composition of La Fregeneda–Almendra shows fairly similar Zr/Sc and La/Th, and

slightly higher Th/Sc and Cr/V ratios than the NIBAS, N-CIZ slates, and Post Archean Australian Shale (PAAS; Fig. 4a, b, c; Taylor and McLennan, 1985, 1995; Ugidos et al., 2010; Rudnick and Gao, 2014; Villaseca et al., 2014). Ti/Nb ratios of studied psamopelites (80 % of samples in the range 281–338) are lower than the NIBAS and N-CIZ slates, contrary to Th/Yb (3.44–9.90) and La/Y (up to 3.09) ratios that are higher. The degree of compositional maturity of clastic sediments is determined by the Index of Compositional Variability (ICV = (Fe_2O_3 + K_2O + Na_2O + CaO + MgO + TiO_2) / Al_2O_3; Cox et al., 1995). Overall, metasediments from La Fregeneda–Almendra display higher ICV values than the NIBAS, N-CIZ slates, and PAAS, indicating a lower maturity of the studied metasediments compared to those reference compositions (Fig. 4d; Taylor and McLennan, 1985; Ugidos et al., 2010; Villaseca et al., 2014). Although Nb and Th contents are higher in La Fregeneda, this observation of a less mature nature is supported also by lower Zr, Hf and Y contents in the studied area compared with the reference compositions of the NIBAS and N-CIZ slates (Ugidos et al., 2010; Villaseca et al., 2014). The decrease of ICV values is correlated with the increase of the CIA (Fig. 4d; Nesbitt and Young, 1982). The CIA values in La Fregeneda–Almendra (excluding Ca-rich samples; see the Materials and Methods section for calculation procedure) vary in the range of 55–80 (Supplementary Table 1). Samples with CIA values of > 70 are considered to be weakly to intensely weathered (Fig. 4d; e.g., Taylor and McLennan, 1985; Ugidos et al., 1997, 2003; Long et al., 2012; Fuenlabrada et al., 2020), values that in the case of the studied metasediments coincide with moderately- to extensively-chloritized samples. This chloritization would be later than the intrusion of the studied aplite-pegmatites, and so it would represent a younger alteration process (with relatively low P-T conditions and presence of fluids) than the here studied aplite-pegmatite related metasomatism. In addition, the enrichment in As, W and Mo observed in whole-rock compositions in some of the studied psamopelites can hardly be related to the intrusion of the aplite-pegmatites (significantly low contents of these elements in the selected aplite-pegmatites), and point also to a later hydrothermal process that could correspond to that developed during the Permian in the region (e.g., López-Moro et al., 2017 and references therein).

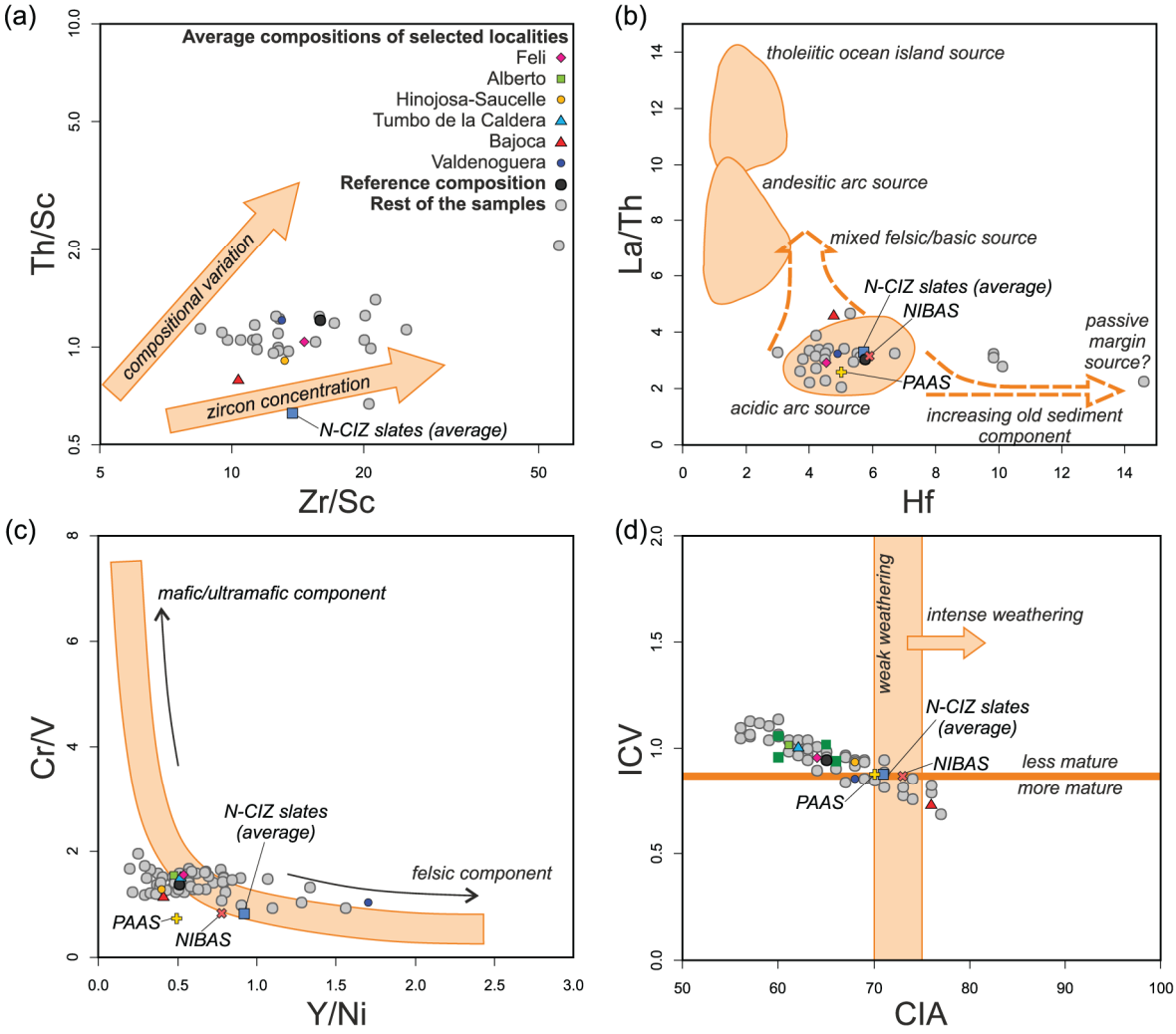

Fig. 4. (a) Zr/Sc vs. Th/Sc diagram for the psammopelitic metasediments of the La Fregeneda–Almendra pegmatite field (after McLennan et al., 1993). The legend serves for all diagrams. (b) Hf vs. La/Th diagram for the studied metasediments (after Floyd and Leveridge, 1987). (c) Y/Ni vs. Cr/V diagram for the set of studied samples (after McLennan et al., 1993). (d) Chemical Index of Alteration (CIA) vs. Index of Compositional Variability (ICV) diagram (after Long et al., 2012).

6.2. Metasomatism of metasediments by the intrusion of aplite-pegmatites

The intrusion of granitic-pegmatites often cause compositional changes in the surrounding rocks, where, depending on the nature of the dyke and that of the host rocks, distinct metasomatic aureoles can be developed (Shearer et al., 1984; Morgan and London, 1987; London et al., 1996; Barros et al., 2020). In this process related to the influx of pegmatitic melts and highly evolved coexisting fluids, the role of F and B as enablers of the transport of highly mobile elements is essential (Shearer et al., 1984; Morgan and London, 1987; Pollard et al., 1987; London et al., 1996; Thomas et al. 2000). In the case of LCT pegmatites (Černý and Ercit, 2005), this mass-transfer from pegmatites to host rocks leads to the enrichment of

elements such as Li, Cs, and Rb (±Sn, ±In, ±W) in the metasomatic haloes (Černý, 1989; Galeschuk and Vanstone, 2007; Linnen et al., 2012). To quantify the elemental mobility during metasomatic processes, whole-rock mass-balance equations have been extensively used to estimate chemical gains and losses (Gresens, 1967; Grant, 1986, Ague, 1994; Lentz and Gregoire, 1995). Accordingly, a detailed mass-balance study for the assessment of the metasomatic effect in host metasediments caused by the intrusion of aplite-pegmatites from La Fregeneda–Almendra will be addressed in the following sections. Since the structural relationship in the four principal localities (Feli, Alberto, Hinojosa–Saucelle road, and Tumbo de la Caldera) is reasonably the same between the selected dykes and host metasedimentary rocks, this variable can be omitted. As mentioned previously, results from Bajoca and Valdenoguera would complement the systematic study to broaden the discussion.

6.2.1. Selection of immobile elements

For the calculation of mass-transfer in whole-rock compositions, the assumption that at least one component behaves as immobile in a determined metasomatic system leads to the categorization of elements as relatively mobile or immobile (Gresen, 1967). Based on the equation formulated by Gresen (1967), and following Grant's method (Grant, 1986, 2005) if a single immobile element (or a set of elements) can be identified for which the difference in concentration between metasomatized and non-metasomatized samples ($\Delta C_i = C_i^a - C_i^0$) is 0, a straight line (the isocon line) can be calculated to consider as a reference (Fig. 5; see Materials and Methods section for abbreviations in formulas). Since an ideal immobile component would display a slope (C_i^a / C_i^0) of 1, in this work they have been considered as immobile, at a regional scale of the La Fregeneda–Almendra pegmatite field, those elements that show average slopes of 1.0 ± 0.1; Supplementary Table 2). In major elements, excepting P_2O_5, the rest of the elements show homogeneous slopes of 1.00 (± 0.01), while trace elements display significant dissimilarity. A number of High-Field Strength Elements (HFSE; Zr, Hf, Nb, Y, Ga, Sc, Th, U, Pb), Large Ion Lithophile Elements such as Sr and Ba, some transition metals (Ni, Cu, Co, Cr, V) and REE behave as immobile with slopes of 1.0 ± 0.1 (Supplementary Table 2). To assess the selection of immobile elements to calculate gains and losses in each of the studied localities (and in detail in each of the samples), the set of immobile elements had to be reduced in order to make comparable the obtained results. The best regression to constrain the fit of the isocon line in each of the samples (varying the set of immobile elements) deviates too much from the corresponding isocon line, which leads to the selection of Si, Al and Ti as the 'main' immobile elements for mass-balance equations.

Obtained slopes of the respective isocon lines in each of the samples (Supplementary Table 2) are worthy of comparison (1.00 ± 0.12), and therefore gains and losses of the different localities can be treated equally. The selection of Si, Al and Ti as the best immobile elements was tested by means of cluster of slopes (López-Moro, 2012), composition-volume diagrams (Gresen, 1967; Potdevin, 1993), and the isocon diagram (Grant, 1986, 2005).

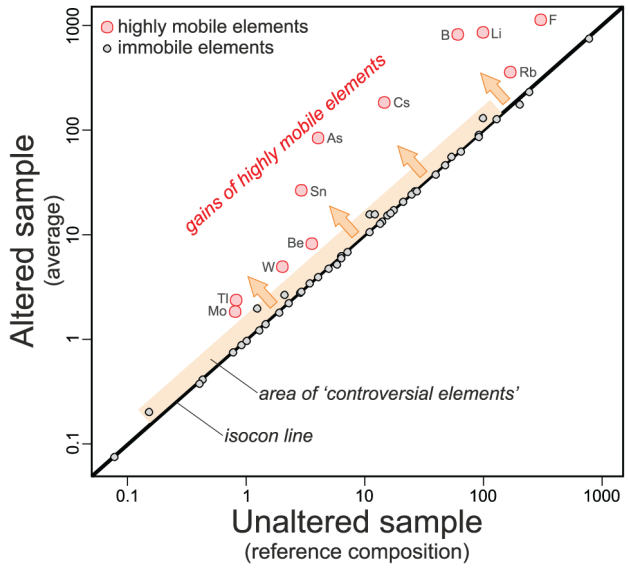

Fig.5. Isocon diagram (Grant, 1986, 2005) for the studied metasediments, considering the reference composition (Table 2) as the unaltered sample and total average contents of all selected localities (Supplementary Table 1) as the altered sample.

6.2.2. Determination of highly mobile elements

The selection of immobile elements allows identifying those elements that behave as highly mobile, but it must be considered that some components could show a variation due to the original composition, obscuring the recognition of those elements enriched by external (metasomatic) effects. These 'controversial elements' usually display higher C_i^a / C_i^0 slopes than immobile elements, but not high enough ones compared to highly mobile elements (e.g., Fig. 5). Concretely at La Fregeneda–Almendra, the minimum slope to discern between highly mobile elements and those suspect elements is marked by Rb. Due to the relatively high background contents of Rb in the studied metasediments (Table 2), the enrichment of Rb is defined by a slight average slope of 2.18 (Supplementary Table 2). In consequence, elements that display higher average slopes than 2.0 were considered as highly mobile in the studied samples, and the enrichment of these elements would be related to external processes (to the formation of the metasediments). The calculated average C_i^a / C_i^0 slopes conduce to consider F, B, Li, Rb, Cs, Sn, Be, Tl, As and W (±Mo) as highly mobile (Fig. 5; Supplementary Table 2), which should be contemplated in mass-balance equations to quantify whole-rock gains and

losses. Nonetheless, and as mentioned previously, the enrichment of As, W and Mo could hardly be related to the intrusion of the studied aplite-pegmatites, and will be excluded in mass-balance calculations. Apart from average values for slopes that define 'regional' highly mobile elements, in detail, it must be pointed out that other elements such as P_2O_5, Ge, Se, Ta and U also show higher slopes than 2 in a number of samples close to the studied dykes, and similarly, S displays greater slopes than 2 in some samples (but not related to the proximity of the dyke; Supplementary Table 2).

6.2.3. Quantification of gains and losses during mass-transfer

Whole-rock elemental gains and losses can be approached through absolute quantifications, where the concentration of an element "i" in the unaltered (C^0) sample is subtracted from the altered (C^a) samples ($C_i^a - C_i^0$; Fig. 6). In this sense, the highest gains considering the before mentioned highly mobile elements correspond to B (up to 9940 ppm), F (up to 6700 ppm) and Li (up to 4023 ppm), with lower absolute gains for Cs (up to 1266 ppm), Rb (up to 1173 ppm) and Sn (up to 167 ppm), and minor ones in the case of Be and Tl (Fig. 6; numerical results in Supplementary Table 2). Nevertheless, the most applied parameter to calculate mass-transfer in metasomatic systems is the gain and loss of an element "i" relative to its concentration prior to metasomatism, which, according to Grant (1986, 2005) is quantified as $\Delta C_i^a/C_i^0 = (1/M \times C_i^a / C_i^0) - 1$ (M is the slope of the isocon, C_i^a is the concentration of an element "i" in the metasomatized sample, and C_i^0 is the concentration of the element "i" from the non-metasomatized reference composition; Table 2). The obtained numerical results (Supplementary Table 2) indicate that the highest gains are those of B (up to 160), followed by Cs (up to 90), Sn (up to 60), and Li (up to 40), with lower F (up to 20), Be and Tl (up to ~10), and lowest ones of Rb (up to 7; Fig. 7). Those values would represent an approximation of how many times are richer the metasomatized samples in those elements compared with concentrations of the reference composition.

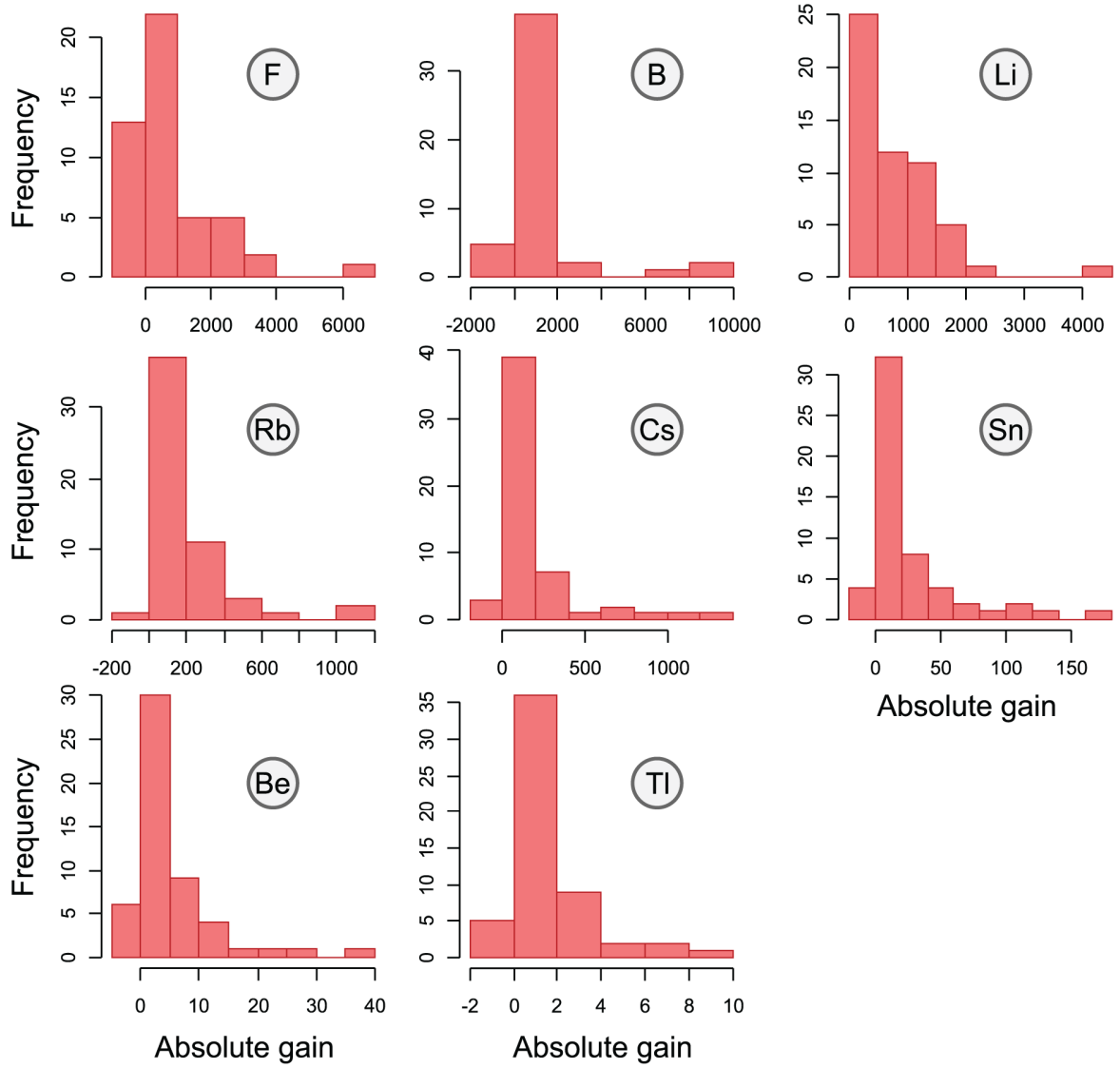

Fig. 6. Histogram of frequencies showing absolute gains (Cia - Ci0) for the determined highly mobile elements in La Fregeneda–Almendra pegmatite field.

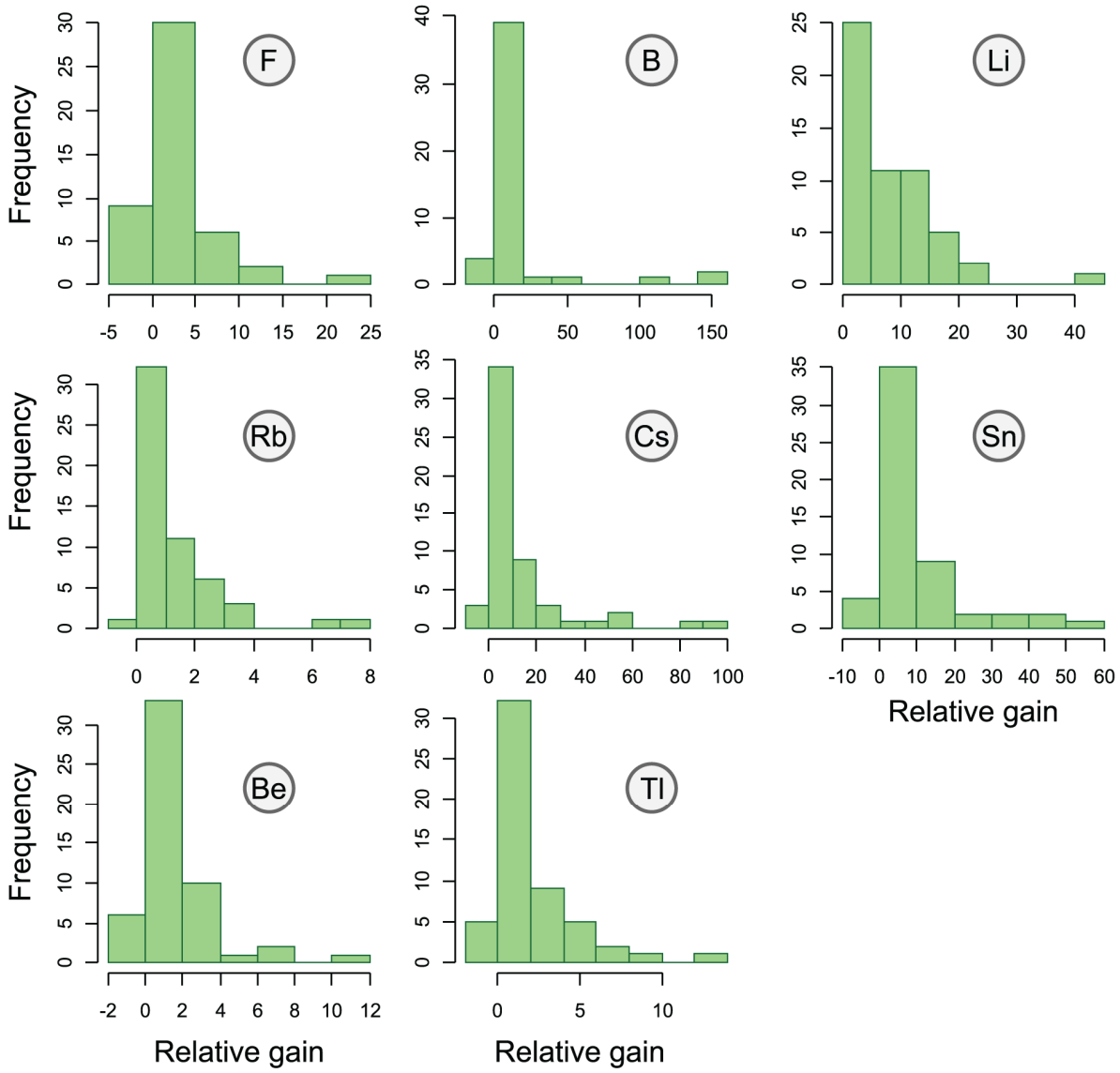

Fig. 7. Histogram of frequencies showing relative gains (ΔCia/Ci0 = [1/M × Cia / Ci0] – 1) for the determined highly mobile elements in La Fregeneda–Almendra pegmatite field.

Considering that the behavior of each of the selected elements differs in terms of absolute and relative gains, the observed variations must be examined considering possible correlations with the type of aplite-pegmatite and the distance from the dyke. To analyze the effect of the aplite-pegmatite types, the distances from the dyke (for each of the collected samples) have been normalized with the thickness of the related dyke (relative distance in Fig. 8 and Supplementary Table 2). In the case of Li, the observed decreasing trends of studied localities seem to get close to the reference composition in a relative distance of about 4–5 times the thickness of the dyke in Feli (Li-mica) and Alberto (spodumene; Fig. 8a). In Hinojosa–Saucelle (petalite) and Tumbo de la Caldera (barren), this approximation occurs at 2–3 times the width

of the dyke (Fig. 8a). Considerably high enrichment/relative gains seem to happen up to distances of twice the thickness of the dyke in all localities, with the highest gains in those samples from the Li-mica and spodumene dykes, and lower ones for the petalite dykes and barren dykes (Fig. 8a). It is outstanding that those samples that occur relatively close to another dyke (in between of two dykes) show superposed enrichments, falling out of the overall trend, similarly to those samples with high CIA values (extended chloritization) that display relatively low enrichments (empty circles that plot below the decreasing trends in Fig. 8). The behavior of Cs is similar to that of Li, with the highest gains in the Li-mica dyke (background values further than 6 times the thickness of the dyke). Nevertheless, in this case, higher gains appear related to the petalite dykes compared to the spodumene dyke (reaching background values in a relative distance of 3–4), with the lowest gains in samples from the barren dykes (Fig. 8b). The extent of the metasomatic halo for Rb is slightly lower than those of Li and Cs, with considerable gains up to twice the thickness of the dyke, and the highest ones in the Li-mica dyke of the Feli open pit (Fig. 8c). Gains of Sn differ a bit since the maximum enrichments are observed in Bajoca (petalite dyke), with two samples from barren dykes showing also elevated gains of 20–30 (Supplementary Table 2). In addition, there are no clear observable differences between the selected localities, leading to consider a general decreasing trend with relatively high gains up to twice the width of the dykes (Fig. 8d). In the same way, despite the absence of clear trends, the enrichment of F and B coincides with that of the determined highly mobile elements (Fig. 8e, f; Supplementary Table 2). This observation could lead to connecting, as in other similar cases, these “mass-transfer enablers” (F and B) with the extent of the enrichment of highly mobile elements (e.g., Shearer et al., 1984; Morgan and London, 1987). Related to this remark, it is outstanding that the selected aplite-pegmatites show relatively low F and B contents (with the Li-mica dyke with the highest contents; Fig. 3 a), which could suggest that these elements were almost completely drained from the dykes. To analyze deeply this connection between F-B and enrichments of Li, Cs, Rb and Sn, a detailed mineralogical study must be carried out, which is out of the scope of the present work. Anecdotally, a number of samples collected close to the aplite-pegmatites show also relative gains in P_2O_5, Ge, Se, Ta, and U.

6.3. Implication of metasomatic aureoles in mineral exploration

The characterized metasomatic haloes of the selected aplite-pegmatites from La Fregeneda–Almendra resemble those from other case studies of LCT pegmatites (Černý, 1989; Linnen et al., 2012), with elevated gains of Li, Cs, Rb and Sn (± Be, ± Tl; Fig. 7). In detail, the observed

decreasing trends in the studied localities indicate that each of the highly mobile elements behaves differently, with distinct enrichment degrees in a determined distance or reaching up to variable distances (Fig. 8). The elements that reach furthest from the dykes seem to be Cs, Li and > Rb, with minor haloes in the case of Sn, F, B, Be and Tl (Fig. 8; Supplementary Table 2). An important outcome from this work for mineral exploration is that an estimation of 'proximity indicator contents' could be calculated from the decreasing trends of Fig. 8. These contents, or higher values than these proposed, would indicate relative proximity of a buried dyke in La Fregeneda–Almendra, with Li and Cs as the most useful elements and Rb and Sn being more complex. Thus, Li contents of about 400 ppm (or higher) in the metasedimentary samples from the area (or equally ~50 ppm of Cs), would imply a relatively close mineralized dyke, with Rb (~300 ppm) and Sn (15 ppm) as complementary tracers. Despite the observed overall decreasing trends, F and B do not show clear trends in a certain dyke, and should be taken with caution in terms of geochemical exploration. Another observation that could be pointed out is that the CIA could be a key parameter in geochemical exploration. Greater CIA values than 70 in this type of siliciclastic metasediments could suggest a severe chloritization process that may cause significant leaching of highly mobile elements. Consequently, it has been noticed that these samples obscure the determination of the decreasing trend in a particular geochemical halo, originating an erroneous estimation of the proximity of a buried aplite-pegmatite. Similarly, some metasedimentary samples show extremely high enrichments in some highly mobile elements (e.g., ~4000 ppm of Li, ~1300 ppm of Cs, ~1300 ppm of Rb), with higher contents even than those from the related pegmatite dyke (Table 1; Table 3). This feature, displaying such high anomalous concentrations, would denote the superposition of metasomatic processes, and therefore, would be indicative of the presence of multiple evolved aplite-pegmatite dykes.

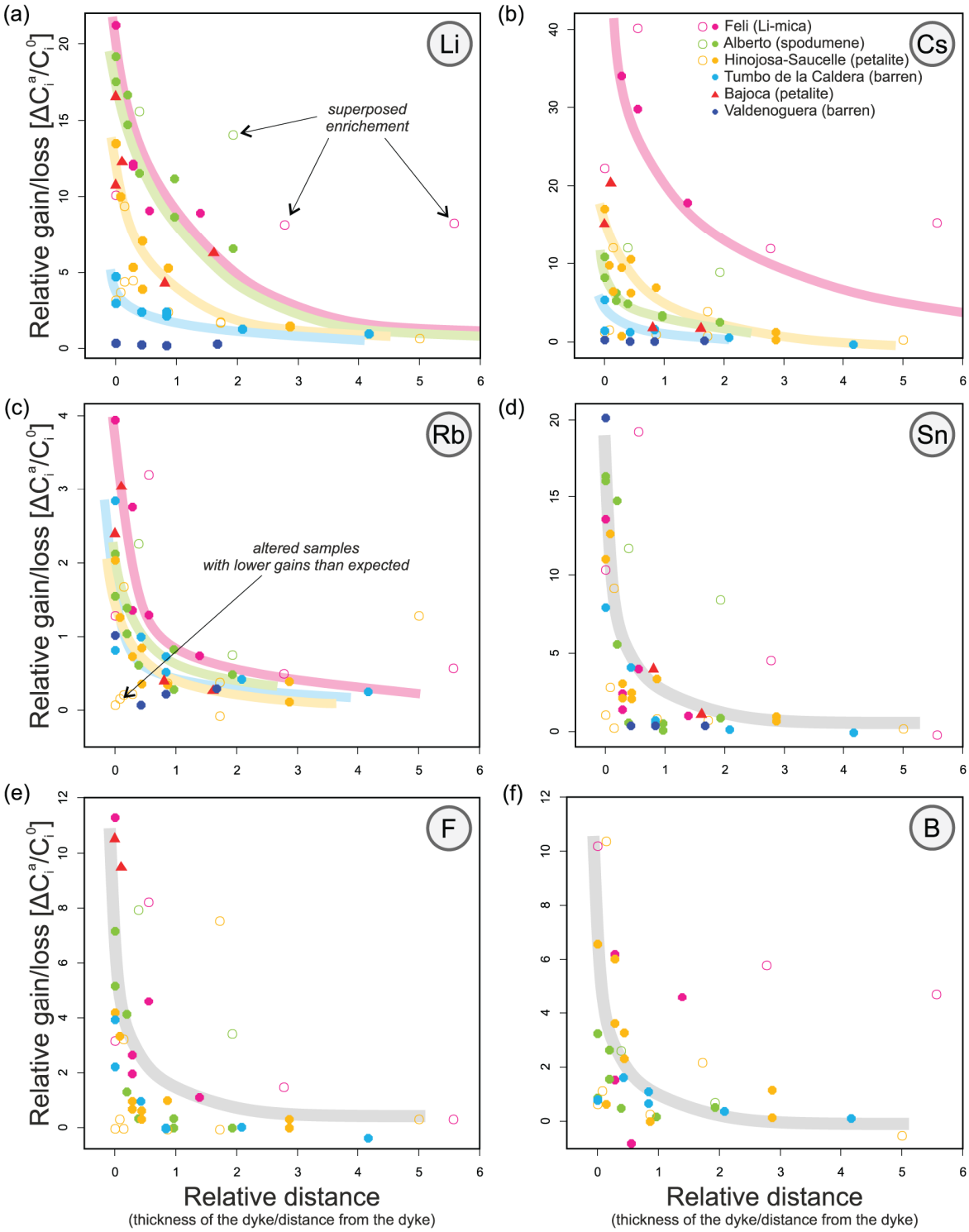

Fig. 8. Relative distance (thickness of the dyke/distance from the dyke) vs. relative gain/loss diagrams for (a) Li, (b) Cs, (c) Rb, (d) Sn, (e) F, (f) B. The legend for all diagrams is shown in Fig. 8b, with fulfilled symbols for representative samples and empty symbols for extremely enriched or altered samples.

Considering relative distances and calculated gains for the selected haloes, an economically interesting pegmatite dyke of about ~20 m wide would generate a metasomatic halo of ~40 m,

where significant enrichments of Li, Rb, Cs, Sn, F and B would be observed. Considering that at La Fregeneda–Almendra evolved pegmatite dykes are nearly subvertical and that the host metasediments show a similar structural relationship in those cases (Roda-Robles et al., 1999, 2010; Vieira et al., 2011), an interesting output from this work could be that in terms of superficial representation of a potentially interesting dyke and its geochemical halo would cover a longitudinal area of about 100 m wide (20 m dyke + [2 × 40 m halo]). The cartographic magnitude of such metasomatic haloes can make these anomalies detectable from space, which prompt new possibilities in mineral exploration, as remote sensing techniques, that have to be improved to constitute fundamental tools for geochemical exploration in the near future (e.g., Cardoso-Fernandes et al., 2019, 2020). Moreover, most of the highly mobile elements in the metasomatic haloes can be semi-quantitively analyzed in the field using portable tools such as X-Ray Fluorescence (XRF) and Laser-Induced Breakdown Spectroscopy (LIBS) equipment, thus expediting pegmatite exploration. Prospect scale studies, analogous to the provided for La Fregeneda–Almendra, with detailed characterizations of the metasomatic haloes, contribute to enhance the performance of these innovative techniques.

7. CONCLUSIONS

1) The psammitic and pelitic metasediments from the La Fregeneda–Almendra pegmatite field seem to be derived from a felsic differentiated (± intermediate) source and undergone subsequent sorting and recycling processes.

2) The compositional maturity of studied metasediments is slightly lower than the NIBAS and N-CIZ slates, with lower Zr, Hf and Y contents and CIA values of fresh samples ranging from 55 to 70.

3) The intrusion of the aplite-pegmatite dykes generated variable metasomatic haloes, with F, B, Li, Rb, Cs, Sn, Be and Tl as highly mobile elements and Si, Al and Ti as the main immobile elements. Observed enrichments of As, W and Mo could hardly be related to the intrusion of the studied aplite-pegmatites.

4) Calculated absolute and relative gains of highly mobile elements display decreasing trends related to the distance from the dyke, with first evidence of anomalous contents starting at distances of 4–5 times the thickness of the dyke and reaching up to high enrichments/gains in relative distances of 2.

5) The greatest geochemical haloes are those from the most evolved dykes (spodumene and Li-mica), with lower enrichments in petalite dykes and the lowest ones in the barren bodies. Cs seem to be, together with Li, the element that reaches furthest from the aplite-pegmatites, followed by Rb and Sn (> F, B, Be, Tl).

6) For mineral exploration, higher contents than 400 ppm (Li), 50 ppm (Cs), 300 ppm (Rb), and 15 ppm (Sn) in the metasedimentary samples from the area would indicate the proximity of a buried aplite-pegmatite. Samples with CIA values of > 70 should be avoided since they could imply a severe chloritization process that led to the leaching of highly mobile elements.

7) Considering the structural relationship between the aplite-pegmatites and host metasediments, in combination with estimated extents of metasomatic haloes of economically interesting bodies, suggest that the La Fregeneda–Almendra pegmatite field constitutes a suitable area to improve innovative exploration methods such as portable XRF and LIBS and remote sensing techniques, which would be a great contribution to exploration companies.

8. ACKNOWLEDGEMENTS

Financial support was provided by the Spanish Ministry of Economy, Industry and Competitiveness (Project RTI2018-094097-B-100, with ERDF funds), the University of the Basque Country UPV/ EHU (grant GIU18/084) and the European Commission's Horizon 2020 Innovation Programme (grant agreement No 869274, project GREENPEG: New Exploration Tools for European Pegmatite Green-Tech Resources). Work of I. Garate-Olave has been supported also by the UPV/EHU by means of the "Convocatoria de contratación para la especialización de personal investigador doctor en la UPV/EHU 2019". The authors would also like to thank the financial support provided by FCT– Fundação para a Ciência e a Tecnologia, I.P., with the ERA-MIN/0001/2017 – LIGHTS project and through the FCT project UIDB/04683/2020 - ICT (Institute of Earth Sciences). J. Cardoso-Fernandes has been financially supported within the compass of a Ph.D. Thesis, ref. SFRH/BD/136108/2018, by Portuguese national funds from MCTES through FCT, and co-financed by the European Social Fund (ESF) through POCH – Programa Operacional Capital Humano – and NORTE 2020 regional program.

9. REFERENCES

Ague, J. J. (1994). Mass transfer during Barrovian metamorphism of pelites, south-central Connecticut. I: Evidence for changes in composition and volume. *American Journal of Science* **294,** 989–1057. https://doi.org/10.2475/ajs.294.8.989

Barros, R., Kaeter, D., Menuge, J. F. & Škoda, R. (2020). Controls on chemical evolution and rare element enrichment in crystallising albite-spodumene pegmatite and wallrocks: Constraints from mineral chemistry. *Lithos* **352–353,** 105289. https://doi.org/10.1016/j.lithos.2019.105289

Bea, F., Montero, P., González-Lodeiro, F. & Talavera, C. (2007). Zircon inheritance reveals exceptionally fast crustal magma generation processes in Central Iberia during the Cambro-Ordovician. *Journal of Petrology* **48**, 2327–2339. https://doi.org/10.1093/petrology/egm061

Blengini, G. A., Latunussa, C. E. L., Eynard, U., Torres de Matos C., Wittmer, D., Georgitzikis, K., Pavel, C., Carrara, S., Mancini, L., Unguru, M., Blagoeva, D., Mathieux, F. & Pennington D. (2020). Study on the EU's list of Critical Raw Materials Final Report. *European Commission.* https://doi.org/10.2873/11619

Cardoso-Fernandes, J., Teodoro, A. C. & Lima, A. (2019). Remote sensing data in lithium (Li) exploration: A new approach for the detection of Li-bearing pegmatites. *International Journal of Applied Earth Observation and Geoinformation* **76**, 10–25. https://doi.org/10.1016/j.jag.2018.11.001

Cardoso-Fernandes, J., Teodoro, A. C., Lima, A. Perrotta, M. & Roda-Robles, E. (2020). Detecting Lithium (Li) Mineralizations from Space: Current Research and Future Perspectives. *Applied Sciences* **10**, 1785. https://doi.org/10.3390/app10051785

Carrington da Costa, M. (1950). Notícia sobre uma carta geológica do Buçaco de Nery Delgado. *Comunicações dos Serviços Geológicos de Portugal*, 1–28.

Černý, P. & Ercit, T. S. (2005). The classification of granitic pegmatites revisited. *Canadian Mineralogist* **43**, 2005–2026. http://doi.org/10.2113/gscanmin.43.6.2005

Černý, P. (1989). Exploration strategy and methods for pegmatite deposits of tantalum. In: Möller, P., Černý, P. & Saupé, F. (eds.) *Lanthanides, Tantalum and Niobium.* Springer-Verlag, Berlin, 274–302. https://doi.org/10.1007/978-3-642-87262-4

Černý, P. (2005). *The Tanco Rare-Element Pegmatite Deposit Manitoba: Regional Context, Internal Anatomy, and Global Comparisons*. In: Linnen, R. L. & Sampson, I. M. (eds.) *Rare–*

Element Geochemistry and Mineral Deposits; *GAC Short Course Notes*. Geological Association of Canada, St. Catharines **17**, 175–199

Condie, K. C. (1993). Chemical composition and evolution of the upper continental crust: Contrasting results from surface samples and shales. *Chemical Geology* **104**, 1–37. https://doi.org/10.1016/0009-2541(93)90140-E

Cox, R., Lowe, D. R. & Cullers, R. L. (1995). The influence of sediment recycling and basement composition on evolution of mudrock chemistry in the southwestern United States. *Geochimica et Cosmochimica Acta* **59**, 2919–2940. https://doi.org/10.1016/0016-7037(95)00185-9

Debon, F. & Le Fort, P. (1983). A chemical–mineralogical classification of common plutonic rocks and associations. *Transactions of the Royal Society of Edinburgh: Earth Sciences* **73**, 135–149. https://doi.org/10.1017/S0263593300010117

Dias da Silva, Í. (2014). Geología de las Zonas Centro Ibérica y Galicia-Trás-os-Montes en la parte oriental del Complejo de Morais, Portugal/España. PhD Thesis. Salamanca, Universidad de Salamanca, 424pp.

Dias da Silva, Í., Gómez-Barreiro, J., Martínez Catalán, J. R., Ayarza, P., Pohl, J. & Martínez, E. (2017). Structural and microstructural analysis of the Retortillo Syncline (Variscan belt, Central Iberia). Implications for the Central Iberian Orocline. *Tectonophysics* **717**, 99–115. https://doi.org/10.1016/j.tecto.2017.07.015

Dias, G., Leterrier, J., Mendes, A., Simões, P. P. & Bertrand, J. M. (1998). U–Pb zircon and monazite geochronology of post-collisional Hercynian granitoids from the Central Iberian Zone (Northern Portugal). *Lithos* **45**, 349–369. https://doi.org/10.1016/S0024-4937(98)00039-5

Díez Fernández, R. & Pereira, M. F. (2016). Extensional orogenic collapse captured by strike-slip tectonics: Constraints from structural geology and U–Pb geochronology of the Pinhel shear zone (Variscan orogen, Iberian Massif). *Tectonophysics* **691**, 290–310. https://doi.org/10.1016/j.tecto.2016.10.023

Díez Fernández, R. & Pereira, M. F. (2017). Strike-slip shear zones of the Iberian Massif: Are they coeval?. *Lithosphere* **9**, 726–744. https://doi.org/10.1130/L648.1

Escuder Viruete, J., Arenas, R. & Martínez Catalán, J. R. (1994). Tectonothermal evolution associated with Variscan crustal extension in the Tormes Gneiss Dome (NW Salamanca, Iberian Massif, Spain). *Tectonophysics* **238**, 117–138. https://doi.org/10.1016/0040-1951(94)90052-3

Fedo, C., Nesbitt, H. W. & Young, G. M. (1995). Unraveling the effects of potassium metasomatism in sedimentary rocks and paleosols, with implications for paleoweathering conditions and provenance. *Geology* **23,** 921–924. https://doi.org/10.1130/0091-7613(1995)023<0921:UTEOPM>2.3.CO;2

Ferreira, J. A., Bento dos Santos, T., Pereira, I. & Mata, J. (2019). Tectonically assisted exhumation and cooling of Variscan granites in an anatectic complex of the Central Iberian Zone, Portugal: constraints from LA-ICP-MS zircon and apatite U–Pb ages. *International Journal of Earth Sciences* **108**, 2153–2175. https://doi.org/10.1007/s00531-019-01755-1

Ferreira, J. A., Mata, J., Bento dos Santos, T. & Pereira, I. (2020). The role of melting on the geochemical evolution and isotopic variability of an anatectic complex in the Iberian Variscides. *Lithos* **378**–**379**, 105769. https://doi.org/10.1016/j.lithos.2020.105769

Floyd, P. A. & Leveridge, B. E. (1987). Tectonic environment of the Devonian Gramscatho basin, south Cornwall: framework mode and geochemical evidence from turbiditic sandstones. *Journal of the Geological Society* **144**, 531–542. https://doi.org/10.1144/gsjgs.144.4.0531

Fuenlabrada, J. M., Arenas, R., Sánchez Martínez, S., Díez Fernández, R., Pieren, A. P., Pereira, M. F., Chichorro, M. & Silva J. B. (2020). Geochemical and isotopic (Sm–Nd) provenance of Ediacaran-Cambrian metasedimentary series from the Iberian Massif. Paleoreconstruction of the North Gondwana margin. *Earth-Science Reviews* **201**, 103079. https://doi.org/10.1016/j.earscirev.2019.103079

Galeschuk, C. & Vanstone, P. (2007). *Exploration Techniques for Rare Element Pegmatite in the Bird River Greenstone Belt, Southeastern Manitoba*. In: Milkereit, B. (ed.) *Proceedings of Exploration 07*: *Fifth Decennial Conference on Mineral Exploration.* Toronto, Canada, 823–839.

García-Arias, M., Díez-Montes, A., Villaseca, C. & Blanco-Quintero, I. F. (2018). The Cambro-Ordovician Ollo de Sapo magmatism in the Iberian Massif and its Variscan evolution: A review. *Earth-Science Reviews* **176**, 345–372. https://doi.org/10.1016/j.earscirev.2017.11.004

Gourcerol, B., Gloaguen, E., Melleton, J., Tuduri, J. & Galieguea, X. (2019). Re-assessing the European lithium resource potential – A review of hard-rock resources and metallogeny. *Ore Geology Reviews* **109,** 494–519. https://doi.org/10.1016/j.oregeorev.2019.04.015

Grant, J. A. (1986). The Isocon Diagram—A Simple Solution to Gresens´ Equation for Metasomatic Alteration. *Economic Geology* **81**, 1976–1982. https://doi.org/10.2113/gsecongeo.81.8.1976

Grant, J. A. (2005). Isocon analysis: A brief review of the method and applications. *Physics and Chemistry of the Earth,* **30**, 997–1004. https://doi.org/10.1016/j.pce.2004.11.003

Gresens, R. L. (1967). Composition–volume relationships of metasomatism. *Chemical Geology* **2**, 47–55.

Gutiérrez-Alonso, G., Fernández-Suárez, J., Jeffries, T. E., Jenner, G. A., Tubrett, M. N., Cox, R. & Jackson, S. E. (2003). Terrane accretion and dispersal in the northern Gondwana margin. An Early Paleozoic analogue of a long-lived active margin. *Tectonophysics* **365**, 221–232. https://doi.org/10.1016/S0040-1951(03)00023-4

Gutiérrez-Alonso, G., Fernández-Suárez, J., Jeffries, T. E., Johnston, S. T., Pastor-Galán, D., Murphy, J. B., Franco, M. P. & Gonzalo, J. C. (2011). Diachronous post-orogenic magmatism within a developing orocline in Iberia, European Variscides. *Tectonics* **30**, TC5008. https://doi.org/10.1029/2010TC002845

Herron, M. M. (1988). Geochemical classification of terrigenous sands and shales from core or log data. *Journal of Sedimentary Petrology* **58**, 820–829. https://doi.org/10.1306/212F8E77-2B24-11D7-8648000102C1865D

Janoušek, V., Farrow, C. M. & Erban, V. (2006). Interpretation of whole-rock geochemical data in igneous geochemistry: introducing Geochemical Data Toolkit (GCDkit). *Journal of Petrology* **47**, 1255–1259. https://doi.org/10.1093/petrology/egl013

Jaskula, B. W. (2017). *Minerals Yearbook*: *Lithium.* U.S. Geological Survey.

Julivert, M., Marcos, A. & Truyols, J. (1972). L'évolution paléogéographique du NW de l'Espagne pendant l'Ordovicien-Silurien. *Bulletin de la Société Géologique et minéralogique de Bretagne* **4**, 1–7.

Kaeter, D., Barros, R. & Menuge, J. F. (2021). Metasomatic High Field Strength Element, Tin, and Base Metal Enrichment Processes in Lithium Pegmatites from Southeast Ireland. *Economic Geology* **116**, 169–198. https://doi.org/10.5382/econgeo.4784

Kesler, S. E., Gruber, P. W., Medina, P. A., Keoleian, G. A., Everson, M. P. & Wallington, T. J. (2012). Global lithium resources: Relative importance of pegmatite, brine and other deposits. *Ore Geology Reviews* **48**, 55–69. https://doi.org/10.1016/j.oregeorev.2012.05.006

Kesselring, M., Wagner, F., Kirsch, M., Ajjabou, L. & Gloaguen, R. (2020). Development of Sustainable Test Sites for Mineral Exploration and Knowledge Spillover for Industry. *Sustainability* **12**, 2016. https://doi.org/10.3390/su12052016

Lentz, D. R. & Gregoire, C. (1995). Petrology and mass-balance constraints on major-, trace-, and rare-earth-element mobility in porphyry– greisen alteration associated with the epizonal True Hill granite, southwestern New Brunswick, Canada. *Journal of Geochemical Exploration* **52**, 303–331. https://doi.org/10.1016/0375-6742(94)00059-K

Lentz, D. R. (1996). U, Mo, and REE mineralization in late-tectonic granitic pegmatites, southwestern Grenville Province, Canada. *Ore Geology Reviews* **11**, 197–227. https://doi.org/10.1016/0169-1368(95)00034-8

Linnen, R. L., Van Litchervelde, M. & Černý, P. (2012). Granitic pegmatites as sources of strategic metals. *Elements* **8**, 275–280. https://doi.org/10.2113/gselements.8.4.275

London, D. (1986). The magmatic-hydrothermal transition in the Tanco rare-element pegmatite: evidence from fluid inclusions and phase equilibrium experiments. *American Mineralogist* **71**, 376–395.

London, D. (2018). Ore-forming processes within granitic pegmatites. *Ore Geology Reviews* **101**, 349–383. https://doi.org/10.1016/j.oregeorev.2018.04.020

London, D., Morgan VI, G. B. & Wolf, M. B. (1996). *Boron in granitic rocks and their contact aureoles*. In: Grew, E. S. & Anovitz, L. M. (eds.) *Boron: Mineralogy, Petrology and Geochemistry*. Mineralogical Society of America, Reviews in Mineralogy **33**, 299–330.

Long, X., Yuan, C., Sun, M., Xiao, W., Wang, Y., Cai, K. & Jiang, Y. (2012). Geochemistry and Nd isotopic composition of the Early Paleozoic flysch sequence in the Chinese Altai, Central Asia: Evidence for a northward-derived mafic source and insight into Nd model ages in accretionary orogen. *Gondwana Research* **22**, 554–566. https://doi.org/10.1016/j.gr.2011.04.009

López-Moro, F. J. & López-Plaza, M. (2004). Monzonitic series from the Variscan Tormes Dome (Central Iberian Zone): petrogenetic evolution from monzogabbro to granite magmas. *Lithos* **72**, 19–44. https://doi.org/10.1016/j.lithos.2003.08.002

López-Moro, F. J. (2012). EASYGRESGRANT—A Microsoft Excel spreadsheet to quantity volume change and to perform mass-balance modeling in metasomatic systems. *Computers & Geosciences* **39**, 191–196. https://doi.org/10.1016/j.cageo.2011.07.014

López-Moro, F. J., López-Plaza, M., Gutiérrez-Alonso, G., Fernández-Suárez, J., López-Carmona, A., Hofmann, M. & Romer R. L. (2018). Crustal melting and recycling: geochronology and sources of Variscan syn-kinematic anatectic granitoids of the Tormes

Dome (Central Iberian Zone). A U–Pb LA-ICP-MS study. *International Journal of Earth Science* **107**, 985–1004. https://doi.org/10.1007/s00531-017-1483-8

López-Moro, F. J., Romer, R. L., López-Plaza, M. & Gónzalez Sánchez, M. (2017). Zircon and allanite U-Pb ID-TIMS ages of vaugnerites from the Calzadilla pluton, Salamanca (Spain): dating mantle-derived magmatism and post-magmatic subsolidus overprint. *Geologica Acta* **15,** 395–408. http://doi.org/10.1344/GeologicaActa2017.15.4.9

López-Plaza, M., Carnicero, A. & Gonzalo, J. C. (1982). Estudio geológico del campo filoniano de la Fregeneda (Salamanca). *Studia Geologica Salmanticensia* **17,** 89–98.

Martínez Catalán, J. R., Arenas, R., Díaz García, F., González Cuadra, P., Gómez-Barreiro, J., Abati, J., Castiñeiras, P., Fernández-Suárez, J., Sánchez-Martínez, S., Andonaegui, P., González Clavijo, E., Díez Montes, A., Rubio Pascual, F. J. & Valle Aguado, B. (2007). Space and time in the tectonic evolution of the northwestern Iberian Massif: Implications for the Variscan belt. *Geological Society of America, Memoir* **200**, 403–423. https://doi.org/10.1130/2007.1200(21)

McDonough, W. F. & Sun, S. -s. (1995). The composition of the Earth. *Chemical Geology* **120**, 223–253. https://doi.org/10.1016/0009-2541(94)00140-4

McLennan, S. M. (1993). Weathering and Global Denudation. *Journal of Geology* **101**, 295–303. http://doi.org/10.1086/648222

McLennan, S. M., Hemming, D. K. & Hanson, G. N. (1993). Geochemical approaches to sedimentation, provenance and tectonics. *Geological Society of America Special Papers* **284**, 21–40. https://doi.org/10.1130/SPE284-p21

Migdisov, A. A. & Williams-Jones, A. E. (2014). Hydrothermal transport and deposition of the rare earth elements by fluorine-bearing aqueous liquids. *Mineralium Deposita* **49**, 987–997. https://doi.org/10.1007/s00126-014-0554-z

Morgan VI, G. B. & London, D. (1987). Alteration of amphibolitic wallrocks around the Tanco rare-element pegmatite, Bernic Lake, Manitoba. *American Mineralogist* **72**, 1097–1121.

Nesbitt, H. W. & Young, G. M. (1982). Early Proterozoic climates and plate motions inferred from major element chemistry of lutites. *Nature* **299,** 715–717. https://doi.org/10.1038/299715a0

Paoli, G., Dini, A. & Rocchi, S. (2019). Footprints of element mobility during metasomatism linked to a late Miocene peraluminous granite intruding a carbonate host (Campiglia Marittima,

Tuscany). *International Journal of Earth Sciences* **108,** 1617–1641. https://doi.org/10.1007/s00531-019-01723-9

Pereira, M. F., Díez Fernández, R., Gama, C. Hofmann, M., Gärtner, A. & Linnemann, U. (2018). S-type granite generation and emplacement during a regional switch from extensional to contractional deformation (Central Iberian Zone, Iberian autochthonous domain, Variscan Orogeny). *International Journal of Earth Science* **107**, 251–267. https://doi.org/10.1007/s00531-017-1488-3

Pérez-Soba, C. & Villaseca, C. (2019). Li-Na-metasomatism related to I-type granite magmatism: A case study of the highly fractionated La Pedriza pluton (Iberian Variscan belt). *Lithos* **344–345**, 159–174. https://doi.org/10.1016/j.lithos.2019.06.008

Pesquera, A., Roda-Robles, E., Gil-Crespo, P. P., Valls, D. & Torres Ruiz, J. (2020). The metasomatic enrichment of Li in psammopelitic units at San José-Valdeflórez, Central Iberian Zone, Spain: a new type of lithium deposit. *Scientific Reports* **10**, 10828. https://doi.org/10.1038/s41598-020-67520-6

Pollard, P. J., Pichavant, M. & Charoy, B. (1987). Contrasting evolution of fluorine- and boron-rich tin systems. *Mineralium Deposita* **22**, 315–321.

Potdevin, J. L. (1993). Gresens 92: a simple Macintosh program of the Gresens method. *Computers & Geosciences* **19**, 1229–1238. https://doi.org/10.1016/0098-3004(93)90027-3

Raith, J. G., Riemer, née Schöner, N. & Meisel, T. (2004). Boron metasomatism and behaviour of rare earth elements during formation of tourmaline rocks in the eastern Arunta Inlier, central Australia. *Contributions to Mineralogy and Petrology* **147**, 91–109. https://doi.org/10.1007/s00410-003-0548-9

Roda-Robles, E., Pesquera, A. & Velasco, F. (1995). Micas of the muscovite-lepidolite series from the Fregeneda pegmatites (Salamanca, Spain). *Mineralogy and Petrology* **55**, 145–157.

Roda-Robles, E., Fontan, F., Pesquera, A. & Velasco, F. (1996). The phosphate mineral association of the granitic pegmatites of the Fregeneda area (Salamanca, Spain). *Mineralogical Magazine* **60**, 767–778. https://doi.org/10.1180/minmag.1996.060.402.06

Roda-Robles, E., Pesquera Pérez, A., Velasco Roldán, F. & Fontan, F. (1999). The granitic pegmatites of the Fregeneda area (Salamanca, Spain): characteristics and petrogenesis. *Mineralogical Magazine* **63**, 535–558. https://doi.org/10.1180/002646199548709

Roda-Robles, E., Pesquera, A., Gil-Crespo, P. P., Vieira, R., Lima, A., Garate-Olave, I., Martins, T. & Torres-Ruiz, J. (2016). Geology and mineralogy of Li mineralization in the Central Iberian Zone (Spain and Portugal). *Mineralogical Magazine* **80**, 103–126. https://doi.org/10.1180/minmag.2016.080.049

Roda-Robles, E., Vieira, R., Pesquera, A. & Lima, A. (2010). Chemical variations and significance of phosphates from the Fregeneda-Almendra pegmatite field, Central Iberian Zone (Spain and Portugal). *Mineralogy and Petrology* **100**, 23–34. https://doi.org/10.1007/s00710-010-0117-7

Roda-Robles, E., Villaseca, C., Pesquera, A., Gil-Crespo, P. P., Vieira, R., Lima, A. & Garate-Olave, I. (2018). Petrogenetic relationships between variscan granitoids and Li–(F–P)-rich aplite-pegmatites in the Central Iberian Zone: geological and geochemical constraints and implications for other regions from the European variscides. *Ore Geology Review* **95**, 408–430. https://doi.org/10.1016/j.oregeorev.2018.02.027

Roda-Robles, E., Vieira, R., Lima, A., Errandonea-Martin, J., Cardoso-Fernandes, J., Garate-Olave, I. & Pesquera, A. (in prep.). Petrogenesis of the granitic pegmatites from the Fregeneda – Almendra area (Central Iberian Zone, Spain - Portugal).

Rodríguez Fernández, L. R. & Oliveira, J. T. (2015). Mapa geológico de España y Portugal a escala 1:1.000.000. *Instituto Geológico y Minero de España, Laboratório Nacional de Energia e Geologia de Portugal*. http://info.igme.es/cartografiadigital/geologica/Geologicos1MMapa.aspx?Id=Geologico1000_(2015)

Rodríguez Fernández, L. R., Díez Montes, A., Escuder, J. & Carrasco, R. (2000). Hoja geológica número 448 (Vilvestre). Mapa Geológico de España a Escala 1:50.000 (2ª serie). Madrid: Instituto Geológico y Minero de España (IGME). Retrieved from http://info.igme.es/cartografiadigital/geologica/Magna50Hoja.aspx?intranet=false&id=448B

Rodríguez-Alonso, M. D., Peinado, M., López-Plaza, M., Franco, P., Carnicero, A. & Gonzalo, J. C. (2004). Neoproterozoic-Cambrian synsedimentary magmatism in the Central Iberian Zone (Spain): geology, petrology and geodynamic significance. *International Journal of Earth Science* **93**, 897–920. https://doi.org/10.1007/s00531-004-0425-4

Rudnick, R. L. & Gao, S. (2014). *Composition of the continental crust*. In: Holland, H. D., Turekian, K. K. (eds.) *Treatise on Geochemistry, 2nd edition Volume 4: The Crust*. Elsevier Science, Oxford, 1–51. https://doi.org/10.1016/B978-0-08-095975-7.00301-6

Ruiz-Coupeau, S., Jürgens, B., Keßelring, M. & Herrero-Solana, V. (2020). Sustainability in Mineral Exploration—Exploring Less Invasive Technologies via Patent Analysis. *Sustainability* **12,** 9761. https://doi.org/10.3390/su12229761

Shand, S. J. (1943). *Eruptive Rocks. Their Genesis, Composition, Classification, and Their Relation to Ore-Deposits with a Chapter on Meteorite*. John Wiley and Sons, New York.

Shearer, C. K., Papike, J. J., Simon, S. B. & Laul, J. C. (1986) Pegmatite-wallrock interactions, Black Hills, South Dakota: interaction between pegmatite-derived fluids and quartz-mica schist wallrock. *American Mineralogist* **71**, 518–539.

Shearer, C. K., Papike, J. J., Simon, S. B., Laul, J. C. & Christian, R. P. (1984). Pegmatite/wallrock interactions, Black Hills, South Dakota: Progressive boron metasomatism adjacent to the Tip Top pegmatite. *Geochimica et Cosmochimica Acta* **48**, 2563–2579. https://doi.org/10.1016/0016-7037(84)90306-5

Silva, A. F. & Ribeiro, M. L. (1994). Notícia explicativa da folha 15-B (Freixo de Espada à Cinta) da Carta Geológica de Portugal à Escala 1:50.000. Instituto Geológico e Mineiro.

Sousa, M.B. (1982). Litoestratigrafia e estrutura do Complexo Xisto-Grauváquico - Grupo do Douro (NE de Portugal). PhD Thesis. Coimbra, Universidade de Coimbra, unpublished, 222pp.

Talavera, C., Montero, P., Martínez Poyatos, D. & Williams, I. S. (2012). Ediacaran to Lower Ordovician age for rocks ascribed to the Schist–Graywacke Complex (Iberian Massif, Spain): Evidence from detrital zircon SHRIMP U–Pb geochronology. *Gondwana Research* **22**, 928–942. https://doi.org/10.1016/j.gr.2012.03.008

Taylor, S. R. & McLennan, S. M. (1985). *The Continental Crust: Its Composition and Evolution*. Blackwell Scientific Publications, Oxford.

Taylor, S. R. & McLennan, S. M. (1995). The geochemical evolution of the continental crust. *Reviews of Geophysics* **33***,* 241–265. https://doi.org/10.1029/95RG00262

Teixeira, R. J. S., Neiva, A. M. R., Gomes, M. E. P., Corfu, F., Cuesta, A. & Croudace, I. W. (2012). The role of fractional crystallization in the genesis of early syn-D_3, tin-mineralized Variscan two-mica granites from the Carrazeda de Ansiães area, northern Portugal. *Lithos* **153**, 177–191. https://doi.org/10.1016/j.lithos.2012.04.024

Teixeira, R. J. S., Neiva, A. M. R., Silva, P. B., Gomes, M. E. P., Andersen, T. & Ramos, J. M. F. (2011). Combined U–Pb geochronology and Lu–Hf isotope systematics by LAM–ICPMS of zircons from granites and metasedimentary rocks of Carrazeda de Ansiães and Sabugal

areas, Portugal, to constrain granite sources. *Lithos* **125**, 321–334. https://doi.org/10.1016/j.lithos.2011.02.015

Thomas, R., Webster, J. D. & Heinrich, W. (2000). Melt inclusions in pegmatite quartz: complete miscibility between silicate melts and hydrous fluids at low pressure. *Contributions to Mineralogy and Petrology* **139**, 394–401. https://doi.org/10.1007/s004100000120

Trueman, D. L. (1978). Exploration methods in the Tanco mine area of southeastern Manitoba, Canada. *Energy* **3**, 293–297. https://doi.org/10.1016/0360-5442(78)90025-7

Ugidos, J. M., Sánchez-Santos, J. M., Barba, P. & Valladares, M. I. (2010). Upper Neoproterozoic series in the Central Iberian, Cantabrian and West Asturian Leonese Zones (Spain): geochemical data and statistical results as evidence for a shared homogenised source area. *Precambrian Research* **178**, 51–58. https://doi.org/10.1016/j.precamres.2010.01.009

Ugidos, J. M., Valladares, M. I., Barba, P. & Ellam, R. M. (2003). The Upper Neoproterozoic-Lower Cambrian of the Central Iberian Zone, Spain: chemical and isotopic (Sm–Nd) evidence that the sedimentary succession records an inverted stratigraphy of its source. *Geochimica et Cosmochimica Acta* **67**, 2615–2629. https://doi.org/10.1016/S0016-7037(03)00027-9

Ugidos, J. M., Valladares, M. I., Recio, C., Rogers, G., Fallick, A. E. & Stephens, A. E. (1997). Provenance of Upper Precambrian-Lower Cambrian shales in the Central Iberian Zone, Spain: evidence from a chemical and isotopic study. *Chemical Geology* **136**, 55–70. https://doi.org/10.1016/S0009-2541(96)00138-6

Valladares, M. I., Ugidos, J. M., Barba, P. & Colmenero, J. R. (2002). Contrasting geochemical features of the Central Iberian Zone shales (Iberian Massif, Spain): implications for the evolution of Neoproterozoic–Lower Cambrian sediments and their sources in other peri-Gondwanan áreas. *Tectonophysics* **352**, 121–132. https://doi.org/10.1016/S0040-1951(02)00192-0

Valle-Aguado, B., Azevedo, M. R., Schaltegger, U., Martínez Catalán, J. R. & Nolan, J. (2005). U-Pb zircon and monazite geochronology of Variscan magmatism related to syn-convergence extension in Central Northern Portugal. *Lithos* **82**, 169–184. https://doi.org/10.1016/j.lithos.2004.12.012

Vieira, R., Roda-Robles, E., Pesquera, A. & Lima, A. (2011). Chemical variation and significance of micas from the Fregeneda-Almendra pegmatitic field (Central-Iberian Zone, Spain and Portugal). *American Mineralogist* **96**, 637–645. https://doi.org/10.2138/am.2011.3584

Villaseca, C., Barbero, L. & Herreros, V. (1998). A re-examination of the typology of peraluminous granite types in intracontinental orogenic belts. *Transactions of the Royal Society of Edinburgh: Earth Sciences* **89**, 113–119. https://doi.org/10.1017/S0263593300007045

Villaseca, C., Merino, E., Oyarzun, R., Orejana, D., Pérez-Soba, C. & Chicharro, E. (2014). Contrasting chemical and isotopic signatures from Neoproterozoic metasedimentary rocks in the Central Iberian Zone (Spain) of pre-Variscan Europe: Implications for terrane analysis and early Ordovician magmatic belts. *Precambrian Research* **245**, 131–145. https://doi.org/10.1016/j.precamres.2014.02.006

Chapter V: Data integration and prospectivity mapping

Mineral prospectivity mapping (MPM) is a fundamental step in mineral exploration that allows delineating favorable areas (regions of interest), for a given type of mineralization, from non-favorable areas, through the integration of distinct criteria such as geological, geophysical, geochemical, and remote sensing datasets, in a GIS environment (Zuo & Carranza, 2011; Abedi *et al.*, 2012; Shabankareh & Hezarkhani, 2017; Ghezelbash *et al.*, 2019a; Ghezelbash *et al.*, 2019b; Parsa, 2021). The highlighted areas are therefore indicated for further exploration studies (Shabankareh & Hezarkhani, 2017).

The approaches to MPM can be divided into two groups: (i) knowledge-driven; and (ii) data-driven methods (Zuo & Carranza, 2011; Abedi *et al.*, 2012; Rodriguez-Galiano *et al.*, 2015; Ghezelbash *et al.*, 2019a; Parsa, 2021; and references therein). The first type of these methods relies on the experience of a geoscientist regarding the genetic processes of mineral deposits and their spatial associations with distinct criteria, being more suited for poorly explored (i.e., greenfield) regions (Zuo & Carranza, 2011; Abedi *et al.*, 2012; Rodriguez-Galiano *et al.*, 2015; Ghezelbash *et al.*, 2019a). Oppositely, the parameters of data-driven approaches are estimated based on the quantification of the spatial relationships of the evidential features (geological, geochemical, geophysical, etc.) of the known mineralized areas that are used as training samples (Zuo & Carranza, 2011; Abedi *et al.*, 2012; Rodriguez-Galiano *et al.*, 2015). Thus, this approach is more applicable to well explored (i.e., brownfield) regions (Ghezelbash *et al.*, 2019a). In such cases, MPM is a classification process where each location is classified as prospective or non-prospective area (Zuo & Carranza, 2011; Abedi *et al.*, 2012; Ghezelbash *et al.*, 2019a). Similar to remote sensing applications, this classification can be either supervised or unsupervised. Data integration can be achieved through various geocomputational techniques including traditional data-driven methods such as weights of evidence and logistic regression or through MLAs (Abedi *et al.*, 2012; Parsa, 2021; and references therein). MLAs have been increasingly endorsed and are widely used in MPM since several studies have shown their ability to outperform traditional techniques (Rodriguez-Galiano *et al.*, 2015; Ghezelbash *et al.*, 2019a; Parsa, 2021; and references therein).

This chapter summarizes most of the work by integrating different datasets namely geological information, geochemical data from stream sediment samples, and the results of the application of image processing techniques to remotely sensed data, to delineate high potential

zones for Li-mineralization in the Fregeneda-Almendra area (Köhler *et al.*, 2021). This work was developed in collaboration with the LIGHTS project partners and resulted in a peer-reviewed journal article (section V.1.).

References

Abedi, M., Norouzi, G.-H., & Bahroudi, A. (2012). Support vector machine for multi-classification of mineral prospectivity areas. *Computers & Geosciences, 46*, 272-283. doi: https://doi.org/10.1016/j.cageo.2011.12.014.

Ghezelbash, R., Maghsoudi, A., & Carranza, E. J. M. (2019a). Performance evaluation of RBF- and SVM-based machine learning algorithms for predictive mineral prospectivity modeling: integration of S-A multifractal model and mineralization controls. *Earth Science Informatics, 12*(3), 277-293. doi: 10.1007/s12145-018-00377-6.

Ghezelbash, R., Maghsoudi, A., & Daviran, M. (2019b). Prospectivity modeling of porphyry copper deposits: recognition of efficient mono- and multi-element geochemical signatures in the Varzaghan district, NW Iran. *Acta Geochimica, 38*(1), 131-144. doi: 10.1007/s11631-018-0289-0.

Köhler, M., Hanelli, D., Schaefer, S., Barth, A., Knobloch, A., Hielscher, P., Cardoso-Fernandes, J., Lima, A., & Teodoro, A. C. (2021). Lithium Potential Mapping Using Artificial Neural Networks: A Case Study from Central Portugal. *Minerals, 11*(10), 1046. doi: 10.3390/min11101046.

Parsa, M. (2021). A data augmentation approach to XGboost-based mineral potential mapping: An example of carbonate-hosted ZnPb mineral systems of Western Iran. *Journal of Geochemical Exploration, 228*, 106811. doi: https://doi.org/10.1016/j.gexplo.2021.106811.

Rodriguez-Galiano, V., Sanchez-Castillo, M., Chica-Olmo, M., & Chica-Rivas, M. (2015). Machine learning predictive models for mineral prospectivity: An evaluation of neural networks, random forest, regression trees and support vector machines. *Ore Geology Reviews, 71*, 804-818. doi: https://doi.org/10.1016/j.oregeorev.2015.01.001.

Shabankareh, M., & Hezarkhani, A. (2017). Application of support vector machines for copper potential mapping in Kerman region, Iran. *Journal of African Earth Sciences, 128*, 116-126. doi: https://doi.org/10.1016/j.jafrearsci.2016.11.032.

Zuo, R., & Carranza, E. J. M. (2011). Support vector machine: A tool for mapping mineral prospectivity. *Computers & Geosciences, 37*(12), 1967-1975. doi: https://doi.org/10.1016/j.cageo.2010.09.014.

V.1. Lithium Potential Mapping Using Artificial Neural Networks: A Case Study from Central Portugal

Martin Köhler, Delira Hanelli, Stefan Schaefer, Andreas Barth, Andreas Knobloch, Peggy Hielscher, Joana Cardoso-Fernandes, Alexandre Lima and Ana C. Teodoro

Minerals, 2021, **11 (10)**, 1046.

Abstract: The growing importance and demand of lithium (Li) for industrial applications, in particular rechargeable Li-ion batteries, have led to a significant increase in exploration efforts for Li-bearing minerals. To ensure and expand a stable Li supply to the global economy, extensive research and exploration are necessary. Artificial neural networks (ANNs) provide powerful tools for exploration target identification. They can be cost-effectively applied in various geological settings. This article presents an integrated approach of Li exploration targeting using ANNs for data interpretation. Based on medium resolution geological maps (1:50,000) and stream sediment geochemical data (1 sample per 0.25 km^2), the Li potential was calculated for an area of approximately 1200 km^2 in the surroundings of Bajoca Mine (Northeast Portugal). Extensive knowledge about geological processes leading to Li mineralisation (such as weathering conditions and diverse Li minerals) proved to be a determining factor in the exploration model. Furthermore, Sentinel-2 satellite imagery was used in a separate ANN model to identify potential Li mine sites exposed on the ground surface by analysing the spectral signature of surface reflectance in well-known Li locations. Finally, the results were combined to design a final map of predicted Li mineralisation occurrences in the study area. The proposed approach reveals how remote sensing data in combination with geological and geochemical data can be used for delineating and ranking exploration targets of almost any deposit type.

Keywords: Lithium; Mineral Predictive Mapping; Exploration Targeting; Artificial Neural Networks; Portugal

1. Introduction

Lithium (Li) is on the European Union's (EU) list of critical raw materials [1], is an important element in modern technology applications, and plays a key role in the realisation of electromobility and effective energy storage. The supply of Li to the global industry depends on expanding the supply of resources. Therefore, the exploration of new Li deposits is vital to the establishment of a stable Li supply in the global economy. At present, about 50% of the global Li production is used in batteries, while 30% is used in the ceramics and glass sector. Minor shares are used in pharmaceuticals and the production of specialised lubricating grease [2]. Li-rich minerals (mainly from Li pegmatites) now account for more than half of the world's lithium production.

Li pegmatites have been extensively studied from an economic, petrographical, and geochemical point of view. The relative importance of pegmatite, brine, and other deposits is discussed by [3], leading to the conclusion that Li pegmatites, while certainly much smaller in tonnage than brine deposits, are a valuable asset to the global Li market due to their widespread occurrence. Li pegmatites could therefore lead to a geographical diversification in lithium production that would counteract the geopolitically restricted distribution of brine deposits [4]. General characteristics for such Li pegmatites are enrichment in distinct elements (Rb, Cs, Be, Ta, Nb, Sn, Li, P, F, and B) and distinct geochemical composition, but limited volumes. Economic pegmatitic lithium mineralisations are dominated by the minerals spodumene ($LiAlSi_2O_6$), petalite ($LiAlSi_4O_{10}$), and lepidolite group minerals ($K[Li,Al]_3[Si,Al]_4O_{10}[F,OH]_2$), and [5] improved the understanding of the crystallisation conditions of rare-element pegmatites by constructing a lithium aluminosilicate phase diagram. However, mechanisms for Li predictivity are only rarely addressed [5].

Portugal hosts considerable Li resources [3,6] and is the first Li-producing European country, but represents only 1.3% of world production [6]. Recent exploration by different mining companies increased the Portuguese reserves multiple times and significant research was performed to enhance the understanding of Li mineralisation types and deposits. An overview of Li-rich mineral occurrences in northern Portugal is provided by [7], and [8] covered the different styles of Li mineralisations (aplite–pegmatite dykes occurring in pegmatitic fields, Li mineralisation associated with leucogranitic cupolas, beryl–phosphate pegmatites, and quartz–montebrasite veins).

Artificial neural networks (ANNs) are powerful in the early stages of resource exploration. In recent years, several studies proved the potential of ANNs and their uses in geological contexts, e.g., [9–12]. Neural networks have several advantages over existing methods,

including the ability to respond to critical combinations of parameters, the combination of datasets without the loss of information inherent in existing methods, and results that are relatively unaffected by redundant data, spurious data, and data containing multiple populations [9]. A Geographic Information System (GIS), in concert with ANN software, offers great potential by providing a range of tools to query, manipulate, visualise, and analyse geological, geochemical, and geophysical data in mineral exploration applications [11]. Mineralisation potential maps can be easily produced to delineate areas for further exploration and therefore reduce the size of the actual fieldwork areas (thus time and expenditure) significantly.

This study aims to use ANNs to process classical geological data (maps and geochemical analyses) reliably and cost-effectively to enhance exploration targeting. As part of the LIGHTS project (Lightweight Integrated Ground and Airborne Hyperspectral Topological Solution; http://lights.univ-lorraine.fr/; accessed on 23 September 2021), this study aims to design a new exploration process chain at the target scale. Prospective areas with previously unknown Li mineralisations will then strengthen the geological understanding of the area and refine geological and minerogenetic maps. Moreover, this study assesses for the first time the potential use of different datasets and their combination according to known metallogenic aspects of the study area. Similar approaches could be extended to other areas of the Iberian Peninsula or even the European Variscides, allowing an increase in the knowledge on Li pegmatite distribution.

1.1. Geological Overview of the Test Area

Li mineralisation can be traced across the whole Central Iberian Zone (CIZ) of the Iberian Massif [8,13]. The CIZ represents parts of the westernmost segment of the Variscan Orogenic Belt of Europe, the latter extending from the Bohemian Massif across the Massif Central and the Armorican Massif to the north-western tip of the Iberian Peninsula, e.g., [14]. Geologically, the CIZ is dominated by S-type Variscan granitoid batholith complexes and adjacent metasedimentary zones (e.g., [13,15,16]). The main Li mineralisation in the CIZ is associated with pegmatitic to aplitic textured intrusive dykes of granitic composition [8]. The most Li-enriched dykes are unzoned and exhibit aplitic textures, often showing host-rock-contact parallel layering [13]. Additionally, Li occurrences of subsequent economic importance appear as quartz–phosphate veins and metasomatic modified cupolas of albite granites [8].

The approximate 1200 km^2 study area is located in north-western Portugal and covers major parts of the Fregenedra–Almendra pegmatitic field (FAF), CIZ (c.f. [17–19]) (Figure 1). The area is characterised by various pegmatite and aplite textured dykes hosted by Precambrian to Cambrian metasediments of the schist–metagreywacke complex (Complexo Xisto-Grauváquico, [20,21]) north of the Meda-Penedono-Lumbrales Granitoid Complex [22], recently designated as the Figueira de Castelo Rodrigo–Lumbrales Anatectic Complex [23,24]. The metasedimentary rocks of the schist–metagreywacke complex may contain quartz, white mica, biotite, plagioclase, K-feldspar, chlorite, zircon, apatite, tourmaline, calcite, epidote, sphene, actinolite, monazite, and opaque minerals [25]. The Granitoid Complex is mainly composed of syn-Variscan two mica granites [26,27] composed of quartz, plagioclase, potassic feldspar, biotite, muscovite, chlorite, sillimanite, zircon, apatite, rutile, and opaque minerals [24]. The Li-rich dykes are predominated by aplitic textures, with some exhibiting layering of Limica+quartz alternating with albite+quartz sequences [8]. The mainly sub-vertical bodies display simple mineralogy including albite, k-feldspar, quartz, and muscovite (barren type) associated with spodumene, petalite, and Li-micas in variable proportions (intermediate and rare-element type) [8]. Common accessory minerals are Li-phosphates, cassiterite, and Nb–Ta oxides [8]. The FAF is bounded at the northeast by the Lower Ordovician quartzites from the Poiares' syncline. Alternating Ordovician quartzites and phyllites occur in the smaller Castelo Melhor's syncline. Cenozoic sedimentary deposits of diverse origins occur throughout the region [26–31].

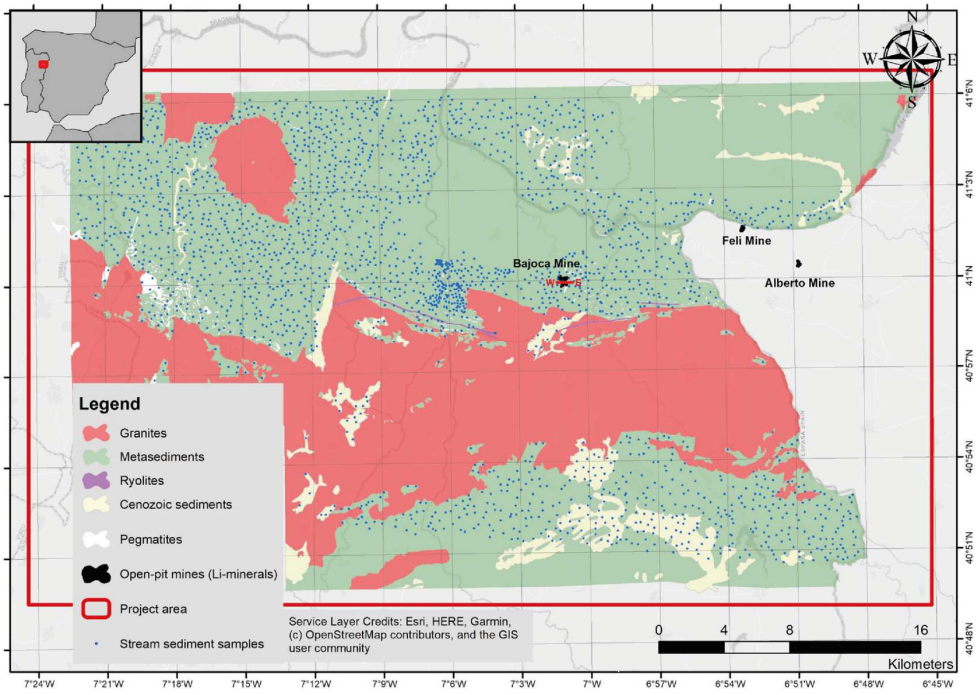

Figure 1. Extent of the simplified digitised geological maps, open-pit mines exploiting Li minerals, and the stream sediment data within the study area in NE Portugal (Coordinate System: Lisboa Hayford Transverse Mercator, Projection: Transverse Mercator).

1.2. Remote Sensing Data

Remote sensing is a powerful and cost-effective data source to collect up-to-date and historical information about the ground surface. In recent years, remote sensing data have been intensively used in geology applications for the exploration and identification of different mineralisation types and related mining activities, e.g., [32–34].

In the framework of the LIGHTS project, several methodological approaches have been developed to identify Li pegmatite areas through optical remote sensing data, including different types of satellite products such as ASTER, Landsat-5, Landsat-8, and Sentinel-2 [35,36]. In this regard, different machine learning algorithms have been employed to allow the automatic identification of Li pegmatites [37,38].

In this study, we elaborate on the potential of new Sentinel-2 derivatives to improve the automatic detection of Li-bearing mineralisation and introduce a new approach to differentiate Li-bearing mineralisation from other features with similar spectral signatures. The use of Sentinel-2 satellite imagery brings three main advantages compared to the other free-of-charge optical remote sensing data: (1) low-to-medium spatial resolution (4 × 10 m Bands, 6 × 20 m Bands, 3 × 60 m Bands); (2) multispectral data from the Visible (VNIR) and Near Infra-Red (NIR) to the Short Wave Infra-Red (SWIR), in 13 compressed JPEG-2000 images covering the total spectral range between 0.443 µm and 2.190 µm; (3) a temporal resolution of 5 days at the Equator since 2015. Additional information may be found in guides available on the ESA Sentinel website: https://sentinel.esa.int/web/sentinel/technical-guides/sentinel-2-msi (accessed on 23 September 2021).

2. Data and Processing

2.1. Geological Data

Geological maps of the study area [28–31] provide the geological framework for this study and were used to identify and digitise pegmatites using ArcGIS software (ArcGIS 10.6, Environmental Systems Research Institute, Redlands, CA, USA). Based on the Portuguese Geological Surveys 1:50,000 geological maps of Portugal [28–30], and, when not available, using the 1:80,000 geological map from the Côa Valley Archaeological Park [31], a unified geological map was created covering the entire study area. Afterwards, a simplified map (Figure 1) was produced by grouping the Variscan granitoids, the Precambrian and Paleozoic metasediments, and the Cenozoic sedimentary cover into distinct classes, to aid the masking

and processing stages. Finally, topological data analysis was performed to check any mistakes committed during all the processes created in ArcGIS software (ArcGIS 10.6, Environmental Systems Research Institutery, Redlands, CA, USA). These digital maps were used to create rastered data of individual geological units for further use in the prediction software.

2.2. Stream Sediment Data Processing

Stream sediment geochemical data (survey spot position and geochemical analysis) were obtained from earlier studies [39–41] carried out on campaigns in the early 1980s by the French Bureau de Recherches Géologiques et Minières (BRGM) with the Portuguese institution Serviço de Fomento Mineiro (SFM). A total of 3.715 stream sediment samples, including 298 samples from a more detailed campaign near Bajoca Mine, were collected in the FAF region covering an area of >1.250 km^2 in NE Portugal. The catchment creation was based on digital elevation model (DEM) data and the flow direction network. During the following procedure, center points of the catchment polygons were calculated using ArcGIS v10.6 software. Subsequently, raster datasets for various elements were created applying inverse distance weighting (IDW) interpolation on the catchment center points containing related geochemical information. Stream sediment data included analyses of the elements/compounds Ag, Al_2O_3, As, B, Ba, Be, Bi, CaO, Cd, Co, Cr, Cu, Fe_2O_3, K_2O, La, Li, MgO, MnO, Mo, Na_2O, Nb, Ni, P_2O_5, Pb, Sb, SiO_2, Sn, Sr, TiO_2, V, W, Y, Zn, and Zr. The multi-element quantification was achieved on the fine fraction below 60 mesh (250 microns or 0.25 mm) by optical emission spectrometry (quantometer studies, [39,40,42]). There is no information on the digestion methods and analytical precision of the analyses in the historical reports available.

2.3. Exploration Model

Li mineralisations in the study area occur principally in aplite–pegmatite bodies and hydrothermal veins [8], all with spatial relation to a granitic body (Figure 2). Regionally, Li mineralisation occurs in highly evolved aplite–pegmatite dykes hosted within metasedimentary rocks, with an increasing fractionation degree as the distance to the granite increases [8,42]. However, the regional granites are enriched in elements such as Li, P, or Rb when compared with the metasediments [13]. It is therefore important to separate these two lithologies, since Li signals could occur both in granites from their initial Li content (low Li content but huge volume) or Li pegmatites (high Li content but low volume), but cannot be clearly distinguished

in the stream sediment data (Figure A1; Appendix A). Hence, we excluded stream sediment data from granite areas since pegmatitic Li mineralisations (in the study area) are commonly hosted only by metasedimentary rocks and apical or marginal areas of granitic intrusions hosted by metasediments [42]. Therefore, the prediction models will not cover the granitic areas (which are of low interest for Li-bearing pegmatites).

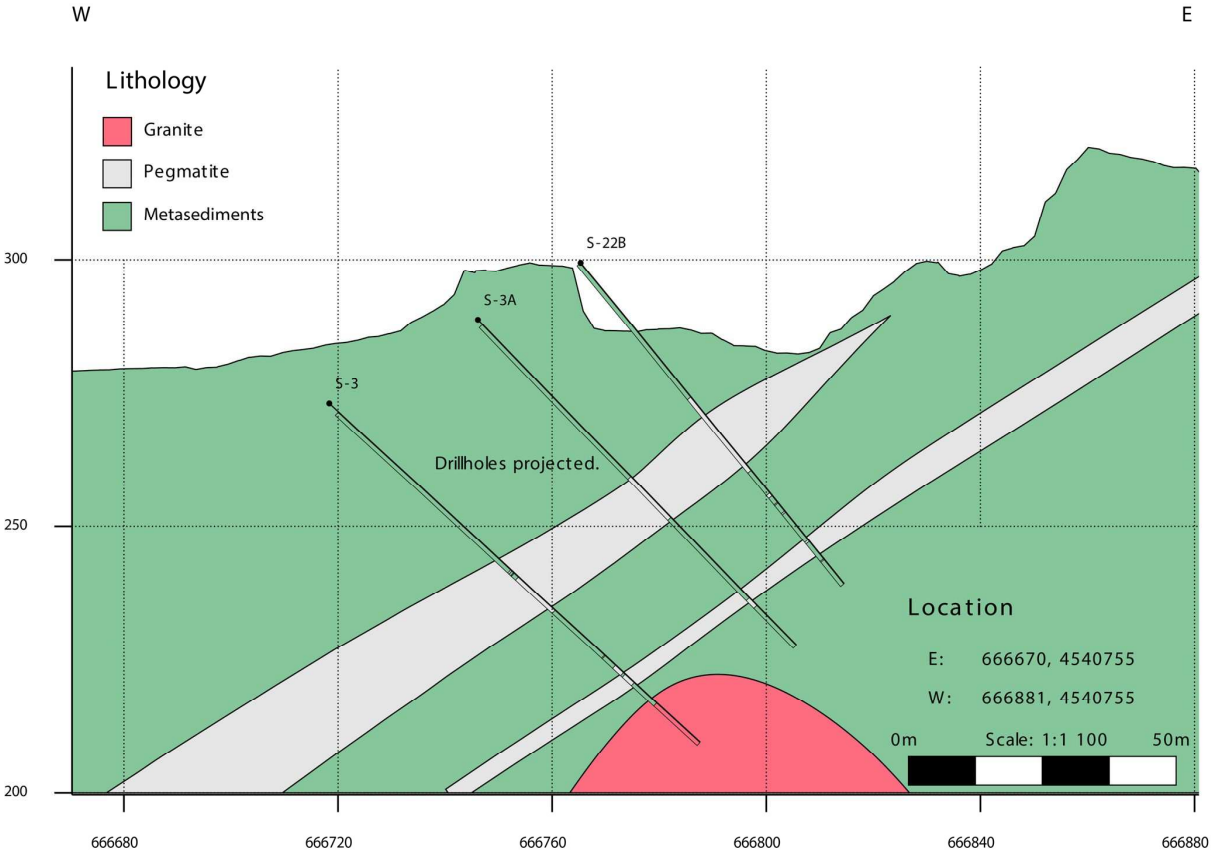

Figure 2. Geological profile of Bajoca Mine featuring Li-bearing pegmatite dykes with spatial relation to a granitic body hosted within metasedimentary rocks. The Li mineralisation is heterogeneously distributed within the dykes, since there is no internal zoning [13], while Sn mineralisation is concentrated along the aplite–pegmatite contact borders. The drillholes are projected in the profile, each one presenting variable directions and dips (from N115° E to N118° E; 39° to 45° S for S3; N125° E; 40° to 45° S for S3A; and from N124° E to N127° E; 41° to 45°S for S22B).

2.4. Unclassified Factor Analysis

Unclassified factor analyses of the stream sediment data were conducted using the statistical software Statgraphics Centurion XV to obtain a preliminary overview of the elements related to local Li mineralisation and to reduce the overall input data for the prediction software. The stream sediment data were clipped by the buffered extent of the mapped pegmatites (buffer 1000 m) to reduce the obscuring influence of samples from granitic and metamorphic rocks on pegmatitic samples.

Seven factor classes (with Eigenvalues > 1) could be identified and attributed: (1) metamorphic signature, (2) granitoid signature, (3) polymetallic signature, (4) siliceous signature, (5) Li-emphasised, (6) Sn(–Nb)-emphasised, and (7) W–Ti-emphasised. The Li-emphasised class has relatively high Li contents and shows coherent enrichments in Sn, As, Mo, Cu, and Ag. The data from these elements were subsequently used in the ANN model.

2.5. Sentinel-2 Imagery

Sentinel-2 image data were freely downloaded from the online data archive of the European Space Agency (ESA) (https://scihub.copernicus.eu/dhus; accessed on 23 September 2021). Their properties are described in Table 1. The selected acquisition meets the following criteria: (1) complete coverage of the study area; (2) cloud-free image over the study area; (3) good exposure of the Li mineralisation on the ground surface during the acquisition time.

Table 1. Downloaded Sentinel-2 satellite image data over the study area.

Tile	Data Product	Spatial Resolution	Data Source	Reference System	Time of Acquisition	Cloud Coverage
T29TPF	2A	10m, 20m, 60m	ESA	UTM29N / WGS84	20191002	2.3%

The proposed approach for the identification of Li-bearing pegmatites with optical images applies only to vegetation-free or -less areas, and ideally to regions with visually exposed bedrock. In the present study case, the study area is dominated by poor vegetation coverage and therefore represents adequate conditions for the identification of Li pegmatites exposed on the ground surface.

The selected satellite image is available as a Bottom-of-Atmosphere product (Level 2A), i.e., the reflectance values are already atmospherically corrected and refer to the surface reflectance. The raw spectral reflectance values were further pre-processed as denoted in the following steps:

1. Super-resolving Sentinel-2 Multispectral Imagery to 10 m spatial resolution

The low-resolution spectral reflectance bands (20 m and 60 m) were super-resolved to 10 m ground sample distance, using a convolutional neural network (CNN) as introduced by Lanaras et al. [43]. This approach extracts details from pixels with the highest resolution (four bands at 10 m resolution) and propagates these details to all other spectral bands (eight bands at 20 m and 60 m resolution) using the local consistency between neighbour pixels, to obtain an image

where all spectral bands have a resolution of 10 m while preserving the spectral characteristics. This preprocessing step is useful for detecting features at the size of 200–250 m^2.

2. Dimensionality Expansion for Sentinel-2 Multispectral Imagery

In order to increase the multispectral data dimensionality and the performance of analysis (see Section 3), a method described in [44] to generate nonlinearly correlated spectral band images is implemented. For this purpose, suitable Sentinel-2 spectral bands for geological applications [33] are taken into consideration (Table 2).

Table 2. Dimensionality expansion for Sentinel-2 multispectral imagery (√ = square root).

Dimensionality Expansion	Formula
eB01 – eB06	√ (B2, B3, B4, B8, B11, B12)
eB07 – eB12	Log (B2, B3, B4, B8, B11, B12)
eB13 – eB18	(B2, B3, B4, B8, B11, B12)2
eB19 – eB33	B02*B03, B02*B04, B02*B08, B02*B11, B02*B12 B03*B04, B03*B08, B03*B11, B03*B12 B04*B08, B04*B11, B04*B12 B08*B11, B08*B12 B11*B12

2.6. External Data

In order to reduce spectral variability, urban areas, transport infrastructure, and main water bodies were masked out using the Open Street Map (OSM) database. The OSM topographical dataset was downloaded at (https://download.geofabrik.de/; accessed 23 September 2021). The used OSM layers included:

- Polygon features of urban areas, stored in the “landuse” layer;
- Polygon features of water bodies, stored in the “water” layer, and;
- Polyline features of the road infrastructure, stored in the “roads” layer.

The OSM features in the study area were corrected accordingly using the underlying Sentinel-2 image. They were used as controlling parameters to mask out these features from the remote sensing models.

2.7. Training Patterns

The study area is well-known for the presence of Li-bearing mineralisation (pegmatites). Typically, training patterns of exposed Li pegmatites over the ground surface have been collected at three open-pit mines over the study area: the Bajoca (located in Portugal), Feli, and Alberto mines (located in Spain) (Figure 1). All data are projected to the

Lisboa_Hayford_Gauss_IGeoE coordinate system (WKID: 102164; EPSG:20790). A geographical grid projected into WGS_1984 is inserted into all presented maps for illustration purposes. The transformation succeeded with the transformation parameters integrated with the ArcGIS Software (ArcGIS 10.6, Environmental Systems Research Institutery, Redlands, CA, USA).

In this context, it is important to consider that the reflection intensity of Li-bearing pegmatites (albedo) is expected to be slightly different at various locations due to the dominance of diverse Li minerals (petalite in Bajoca Mine, lepidolite in Feli Mine, and spodumene in Alberto Mine). Furthermore, the sample colour, rock surface structure, and weathering conditions of Li minerals might represent controlling factors too. For example, reflectance spectroscopy studies of petalite, spodumene, and lepidolite from the Bajoca, Alberto, and Feli mines, respectively, have shown that even fresh petalite and spodumene samples present diagnostic features of illite and/or other clay minerals (Supplementary Figure S2) [45–47]. Oppositely, lepidolite presented diagnostic absorption features that allowed its identification in the collected spectra from Feli Mine. Detailed petrographic, mineralogical, and geochemical studies conducted in Bajoca Mine showed that the same alteration minerals can be present in samples with distinct degrees of alteration [48]. This is reflected in the spectral signatures (reflectance values as a function of the wavelength) for all three mines (Supplementary Figure S2). Obviously, the Li-bearing minerals in Alberto Mine depict slightly different properties, explained through the different exposure conditions of Li minerals in the mine, respectively. Nonetheless, it is noteworthy that Li-bearing minerals show relevant hydroxyl-related absorption features that coincide with Sentinel-2 Band 12 (Supplementary Figures S1 and S2). This absorption is also observed on the spectral signature collected in the pixels of the training areas (Supplementary Figure S2).

Taking this into account, the training patterns for the supervised machine learning algorithm were only collected in Bajoca Mine, due to its size and exposure on the ground surface and the representative spectra of the Li pegmatites. The polygons were digitised based on the Sentinel-2 image to represent the actual state of the mine site during the acquisition time of satellite imagery. For this purpose, different RGB combinations, suitable for geologic applications, were used as background images (Figure 3). The three stockpiles at the centre are from the Li pegmatite itself, whereas the two westernmost and the southmost piles are waste piles from the host rock and feature lower Li contents. Waste rock piles were used as additional training areas to simulate the metasomatism of host rocks.

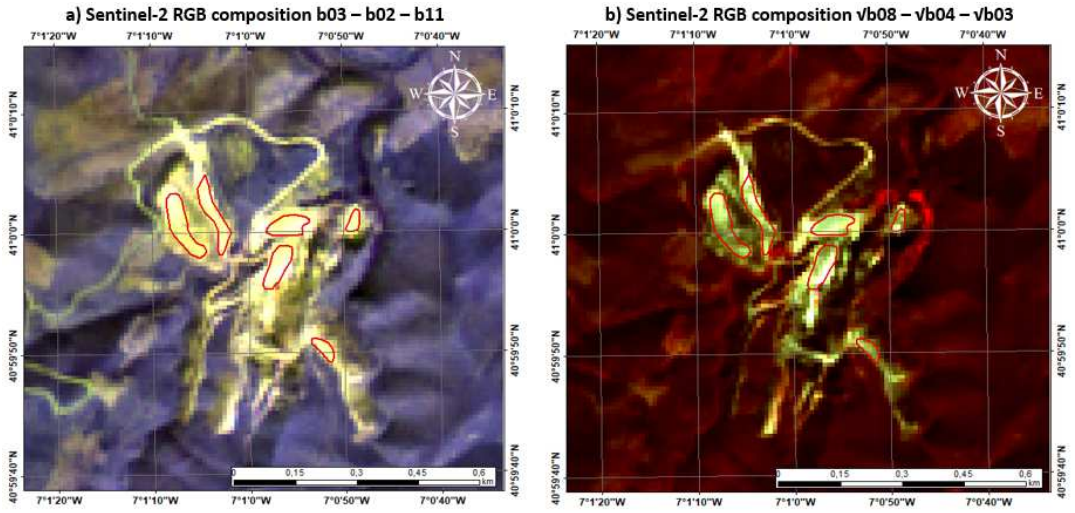

Figure 3. Training patterns (red outlines) with different RGB compositions in the background: (**a**) Sentinel-2 RGB composition b03–b02–b11, (**b**) Sentinel-2 RGB composition √b08–√b04–√b03. The yellow and greenish pixels in subfigure a and b, respectively, correspond to areas hosting Li mineralisation exposed on the ground surface.

3. Methods: Prediction Modelling

The ANNs of multilayer perceptron type are implemented in the advangeo® Prediction Software from Beak Consultants GmbH (www.advangeo.com; accessed on 23 September 2021). The modelling and prediction software is developed to model spatial data and analyse complex relationships between a wide variety of spatial influencing parameters and a given prognostic event or occurrence, by using methods of artificial intelligence within a familiar GIS environment. The base principle is the ability of artificial neural networks to generalise and learn from non-linear relationships and model natural complex processes and events, which are difficult or impossible to be described with analytical mathematics [49]. The software is available as a standalone application with a user-friendly interface, which enables the user to flexibly create and build parametrised models.

In this study, the prediction software is used to perform artificial neural networks of multilayer perceptron type to identify Li mineralisation over the given study area according to the processing schema in Figure 4.

The main workflow is described through the following steps:

1. Collection of model input data, i.e., data that control the modelled feature (here the Li mineralisation) including geological units and structures (e.g., granite bodies, metamorphic sequences, pegmatites), selected stream sediment data, cloud-free preprocessed Sentinel-2 satellite imagery, and OSM topographical data (settlements, infrastructure, water bodies, etc.).

2. Data processing of the spatial data to become suitable for use in analysing models, including the projection of input data to the project coordinate system, resampling to the specified spatial resolution according to project requirements, and clipping of input datasets to the extent of the project area as well as linear scaling of continuous raster data values between 0 and 1 and the conversion of discrete vector data into a binary raster with 0 and 1 value.

3. Design of ANN models in the prediction software for different use cases, i.e., using different controlling parameters and suitable training patterns. The training patterns for remote sensing modelling are ideally in obvious spectral contrast to the surrounding environment and with distinctive spectral reflectance characteristics. The training scenario comprises the controlling and the network parameters (number of hidden layers, number of neurons for each layer, the maximum number of training epochs, etc.).

4. Training of the ANN models using collected training patterns at the Bajoca Mine site, a well-known location for the presence of Li-bearing minerals. Other known locations (Feli and Alberto Mine) were used to validate the application model. The trained ANN will serve to identify similar Li-bearing pegmatite locations in unknown locations over the study area.

5. Validation of the trained ANNs: There are several possibilities to evaluate the accuracy and reliability of a trained ANN by the identification of known locations that have not been used for network training (Feli and Alberto Mine), considerations of the network (MSE) error including statistical evaluation (histograms, all pixels vs. the positive pixels), and analysis of the model parameter weights. Typically, MSE errors below 0.2, balanced parameter weights, and a high probability of modelled pixels are indicators of stable and good neural network quality.

6. Model application: After successful validation, the training network can be used in unknown locations for the prediction of similar events over the entire study area. The result is a distribution probability raster map.

7. Refinement and presentation: The ANN classification results are irregular pixelbased raster data. In many cases, the classification results have to be further refined and processed to improve the cartographic representation of the result.

8. The final distribution map of Li-bearing mineralisation: Combination of the distribution map result based on remote sensing data with the result obtained from modelling with geological and geochemical data. The combination of both geological and remote sensing data into one ANN model was tested, but it resulted in many false interpretations, as the controlling parameters refer to/explain different targets. Therefore, we chose the approach to merge the

two ANN models only as a final step once distribution maps of Li-bearing mineralisation were created.

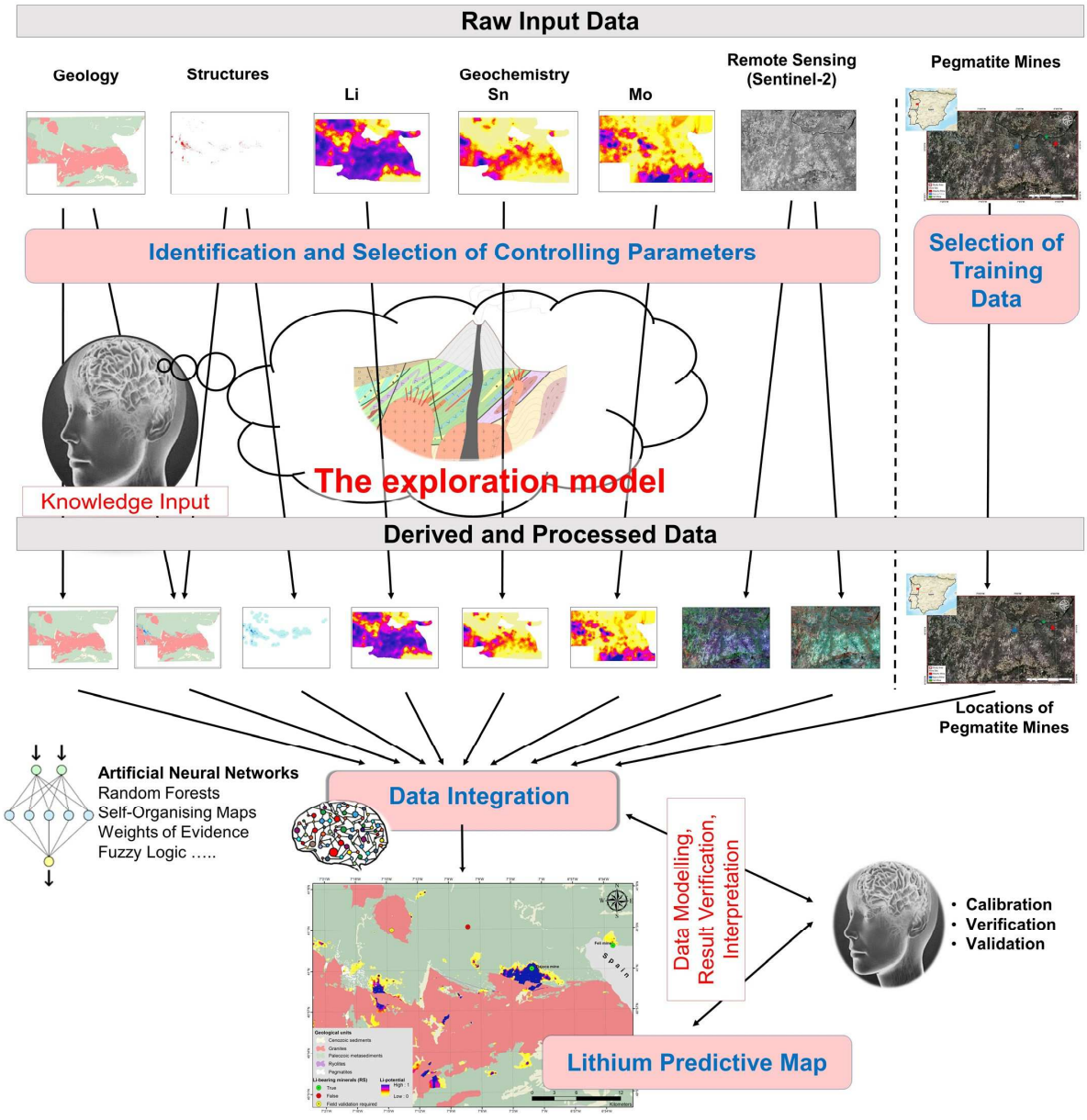

Figure 4. General processing schema in the advangeo® prediction software.

4. Results

Several prediction models with different controlling parameters have been designed with the described principles and workflow. Here, the most significant models and results are presented.

4.1. Geological Model

Controlling parameters of the geological model include digitised geological units (1:50,000), digitised pegmatites (1:50,000), and selected stream sediment data. The modelling was carried out using ANNs of multilayer perceptron type. The model accuracy is evaluated by the following quality parameters:

1. The network (MSE) error: The model error is shown in Supplementary Figure S3. Clearly, the model error converges after approximately 20 iterations and the final error is below 0.2, indicating that the neural network is stable and accurate. This means that the designed model was able to find correlations between the controlling parameters and the training data.

2. Statistical evaluation: Additionally, the histograms (Supplementary Figure S3) reveal that the algorithm was able to identify >80% of the pixels in the training patterns with a scale better than 0.9.

The prediction software delivers a distribution probability map in the value range of 0–1, illustrating the Li potential over the study area (Figure 5). Areas depicted with 1 or close to 1 are the areas with the highest probability of Li-bearing rocks. Within the study area (approximately 1200 km^2), 50 km^2 are mapped with Li potential between 0.1 and 1 (Figure 5). These areas are mainly located in regions of metamorphic rocks in the vicinity of granite intrusions, compatible with possible greisen cupolas or pegmatites and their host rocks. High predictive areas (>0.5 Li probability) extend over 6.4 km^2 and are mainly located directly to the south/southwest of Bajoca Mine (5.6 km^2) and to a lesser extent north of the town of Meda (0.47 km^2) as well as southwest of Santa Comba village (0.35 km^2).

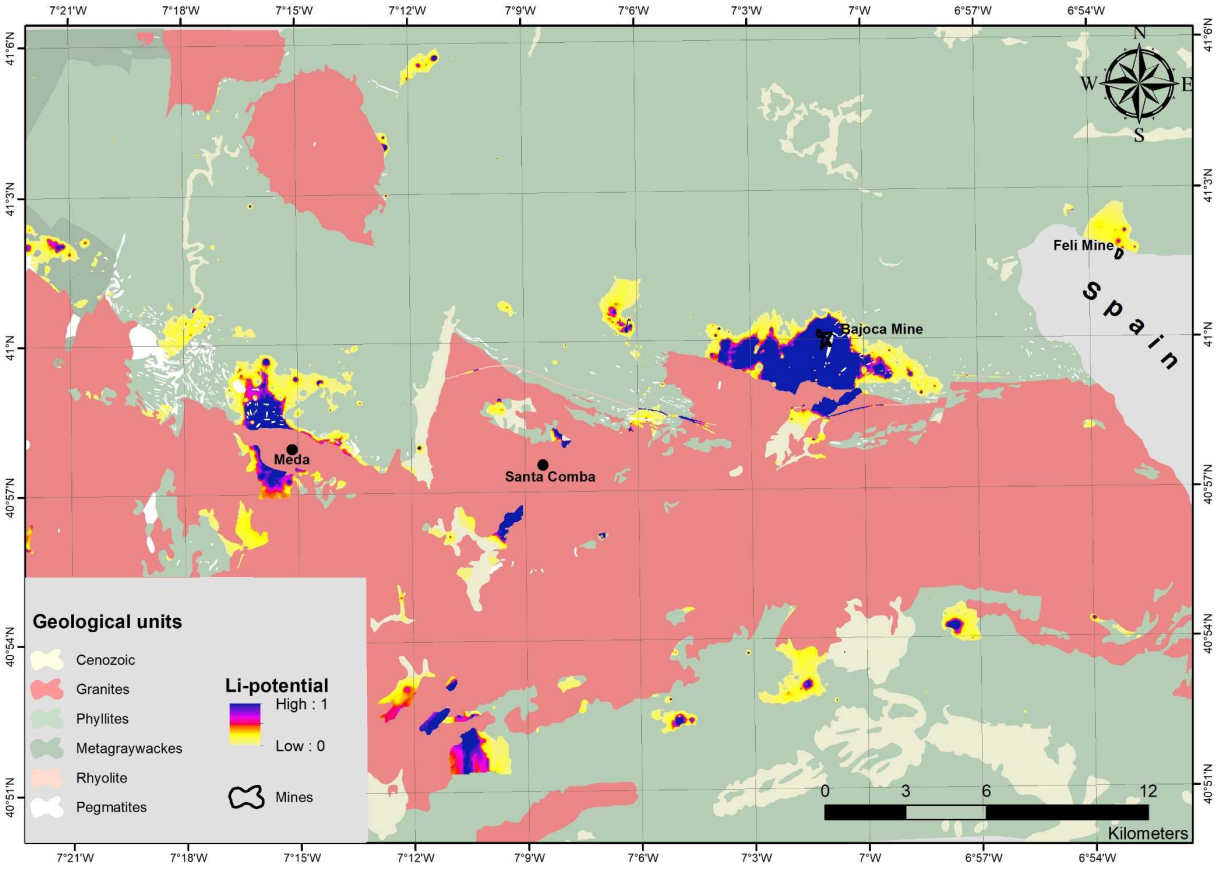

Figure 5. Probability map of Li mineralisation across the study area as a result of the geological/geochemical modelling approach (without remote sensing data).

4.2. Remote Sensing Models

4.2.1. Remote Sensing Model 1

Controlling parameters of Remote Sensing Model 1 include: Sentinel-2 superresolved spectral bands (visible, NIR, red-edge, and SWIR) and OSM topographical dataset.

The modelling was carried out using ANNs of multilayer perceptron type. The model accuracy is evaluated by the following quality parameters:

1. The network (MSE) error: The model error converges after approximately 40 iterations and the final error is below 0.2 (Supplementary Figure S4), indicating that the ANN is stable and accurate. This means that the designed model was able to find correlations between the controlling parameters and the training data.

2. Statistical evaluation: The histograms (Supplementary Figure S4) reveal that the algorithm was able to identify about 90% of the pixels in the training patterns with a scale better than 0.9.

3. The model parameter weights: The model weights confirm the Sentinel-2 visible (b2, b3, b4), NIR (b8, b8A), and SWIR (b11) spectral bands to be the most suitable for geological applications. On the other hand, the spectral bands in the red-edge part of the electromagnetic spectrum seem to be irrelevant for this application. The spectral bands with the highest weight contribution in the designed model are b2, b3, and b11. This is in accordance with Cardoso-Fernandes et al. (2019), who proposed the RGB combination Green–Blue–SWIR for the identification of Li mineralisation in the same region. The RGB composition out of b3–b2–b11 was further analysed in ArcGIS software 10.6 (Figure 6). Indeed, the well-known areas for Li mineralisation are successfully identified and highlighted compared to their surrounding environment. However, similar symbology is also assigned to other features with similar spectral properties as the target features.

4. The distribution probability raster map: The prediction software delivers a distribution probability map in the value range of 0–1, illustrating locations of potentially identified Li-bearing pegmatites in the study area (Figure 6). With 1 are depicted areas with the highest probability to represent Li-bearing mineralisation. In the resulting map, pixel values with a probability value higher than 95% were assigned as “positive” locations. The threshold value is defined based on the histograms in Supplementary Figure S4.

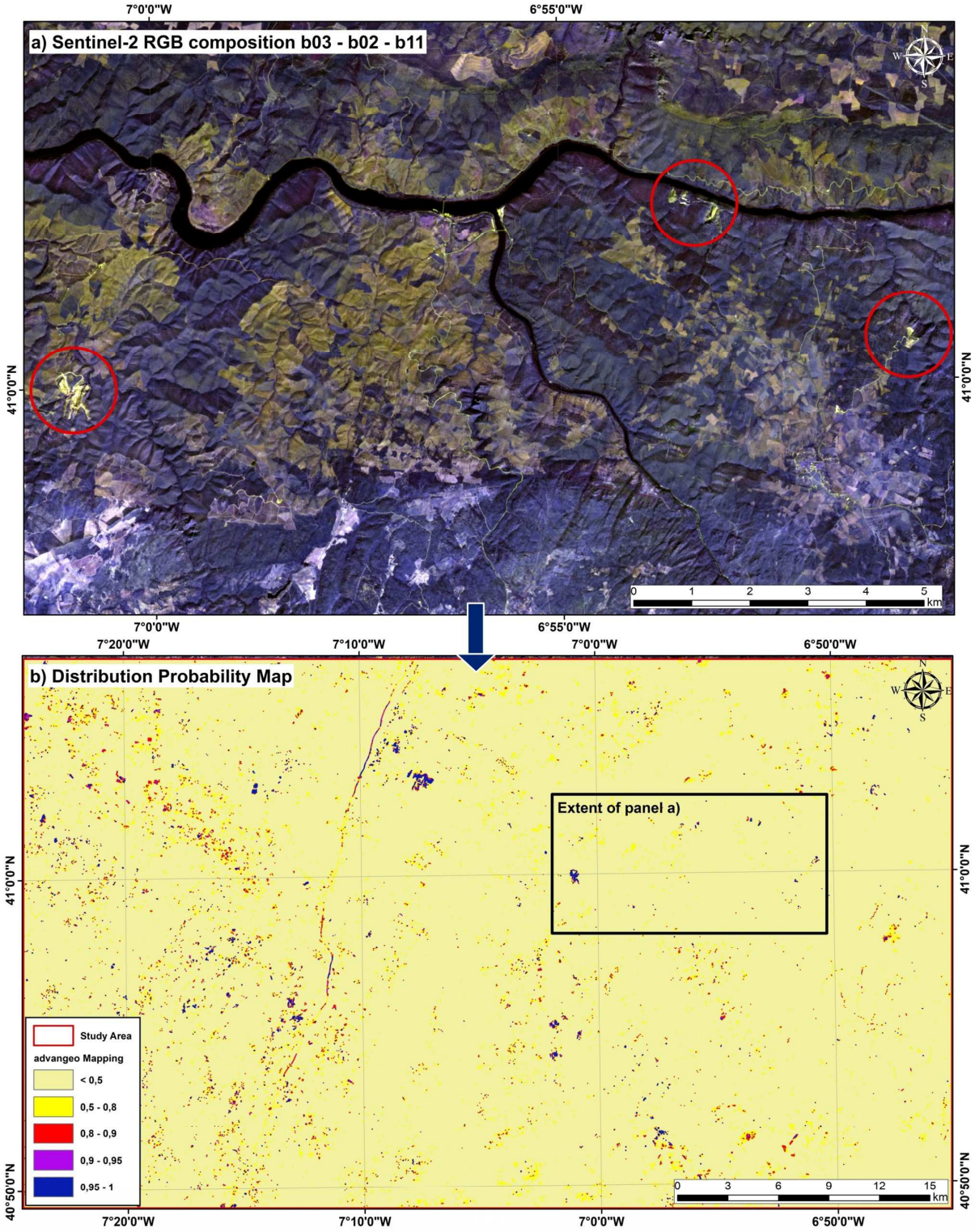

Figure 6. Results of Remote Sensing Model 1: (**a**) RGB composition detail using the super-resolved bands b3–b2–b11 in which mines with known Li mineralisation patterns are shown in light yellow, (**b**) Distribution probability map of Remote Sensing Model 1.

The validation of the identified areas in the resulting map with the underlying Sentinel-2 image revealed that all known locations of the open-pit mines with exposed Li pegmatites were successfully detected (Figure 7). As expected from the results of spectral analysis (Supplementary Figure S2), Li-bearing mineralisation at Alberto Mine was only partially detected due to the different mineralogical composition in contrast to Bajoca Mine.

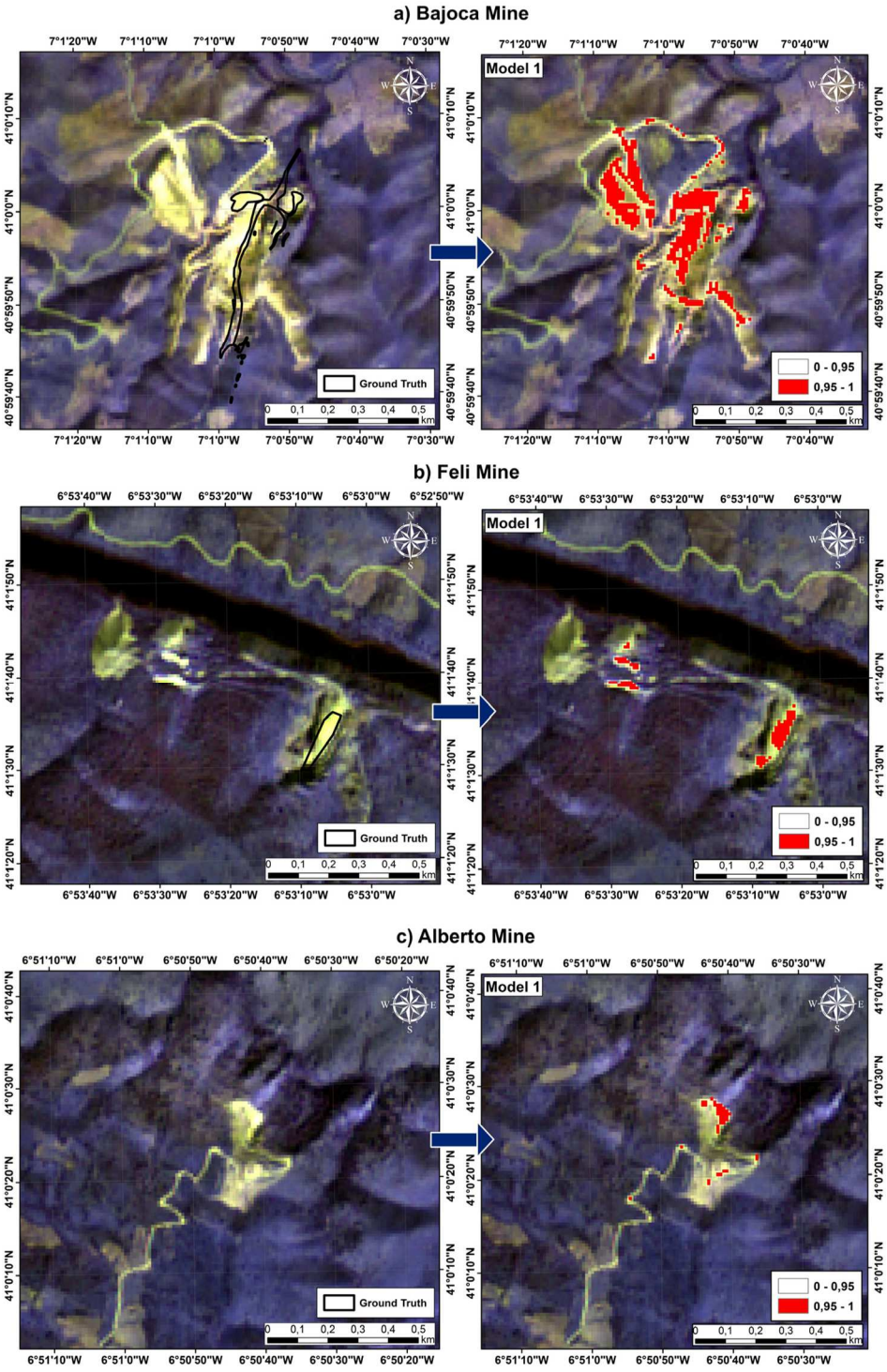

Figure 7. Li distribution probability map of Remote Sensing Model 1 for the three training areas: (**a**) Bajoca Mine, (**b**) Feli Mine, (**c**) Alberto Mine. High potentials are in red. Ground truths are marked with black polygons.

However, the validation of the distribution map over the entire study area revealed that other features with no evidence of Li presence (other mine sites, barren areas with exposed bedrock, etc.) but with similar spectral reflectance properties were also classified as “positive” pixels. Some examples are highlighted in Figure 8.

For a more detailed investigation, samples of “positive” classified pixels were randomly collected and their spectral reflectance properties were further analysed using the extended spectral bands described in Table 2.

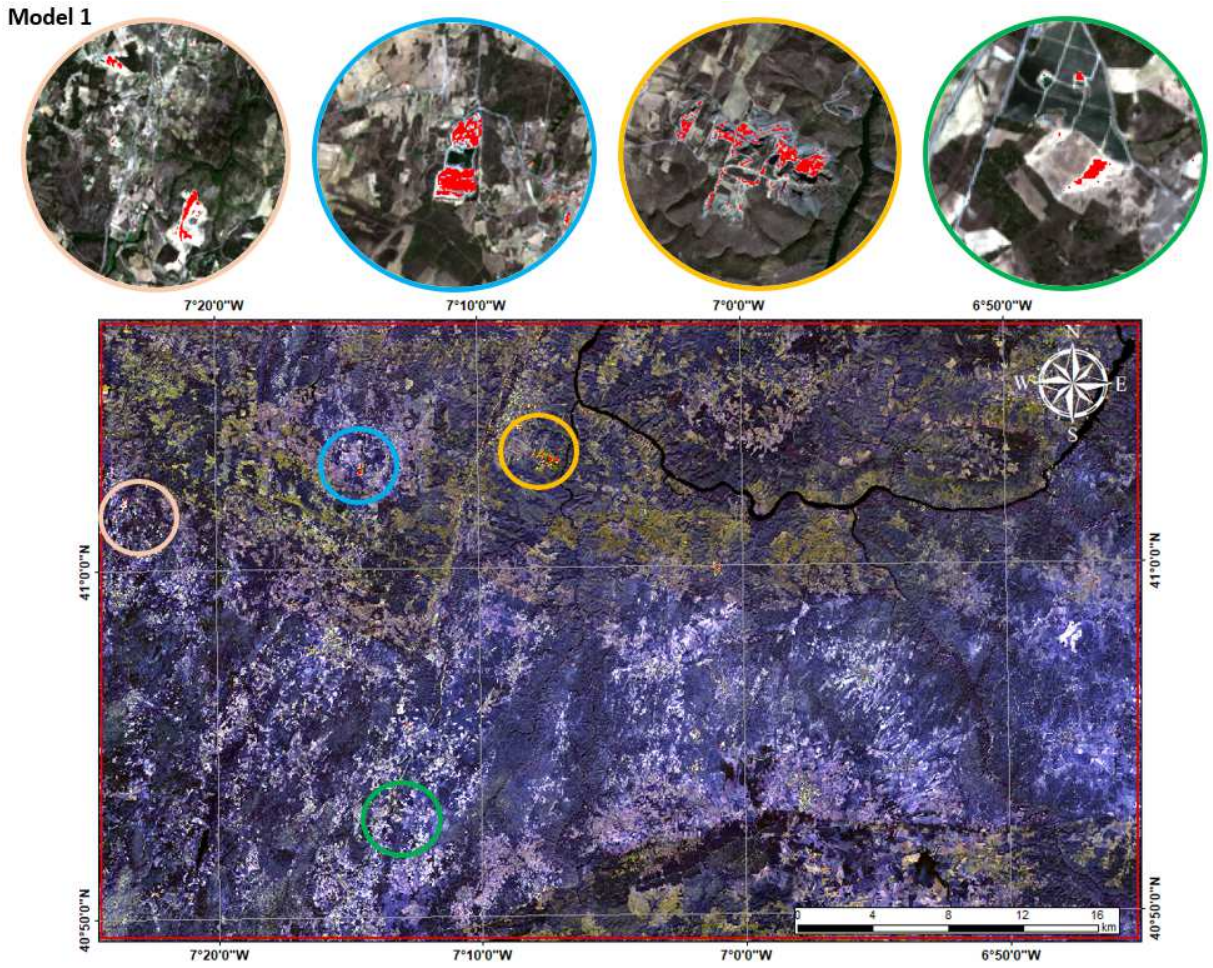

Figure 8. Example areas of possible false positives (misclassified pixels) from Remote Sensing Model 1: Póvoa de Penela, Touça (light brown), Touça (blue), Poio’s quarry (orange), and Marialva (green).

Analysis of spectral signatures

The misclassified areas with similar surface reflectance properties as the target features (Li pegmatites) were further analysed to depict the most suitable bands to differentiate them. For this purpose, samples of features with similar spectral properties based on Model 1 were

collected and their spectral signatures were graphically analysed and compared. These analyses revealed the most suitable extended bands to identify Li pegmatites and differentiate them from other features with similar spectral properties. The graphs are illustrated in Supplementary Figure S5. The reference spectral signature of the main outcropping lithologies (Li pegmatites, metasediments, and granitoid rocks) is presented in Supplemental Figure 6. In the case of the spectra of the metasedimentary rocks, they correspond to samples collected in the false positive area identified with an orange circle in Figure 8.

These analyses revealed that some of the extended bands were more likely to provide the best class separability between the selected patterns. The relevant bands are highlighted in Table 3 and were used in a second prediction model to better identify Li pegmatites.

Table 3. Suitable extended bands (eB) for automatic identification of Li-bearing pegmatites.

Extended Band	**eB14**	**eB15**	**eB16**	**eB24**	**eB25**	**eB28**	**eB29**	**eB31**
Formula	$b3^2$	$b4^2$	$b8^2$	b3*b4	b3*b8	b4*b8	b4*b11	b8*b11

4.2.2. Remote Sensing Model 2

Controlling parameters of Remote Sensing Model 2 include selected Sentinel-2 extended bands (Table 3), the distribution probability map from Model 1, and the OSM topographical dataset. The modelling was carried out using ANNs of multilayer perceptron type. The model accuracy is evaluated by the following quality parameters:

1. The network MSE error: A stable network MSE error that converges after 20 iterations and exceeds a final error lower than 0.001 (Supplementary Figure S7);

2. Statistical evaluation: Similar plausible histograms as shown in Supplementary Figure S7;

3. The model parameter weights: Distributed weights of controlling parameters. The combinations ($b3^2$), (b3 × b4), and (b8 × b11) were revealed to be significantly decisive for the prediction model.

Furthermore, the well-known locations for the presence of Li pegmatites were successfully detected in the distribution probability map of Remote Sensing Model 2 (Figure 9). The validation of the distribution map over the entire study area revealed that noises were drastically reduced compared to the results from Model 1. This is reflected through the following statistics (Table 4).

Table 4. Statistics of the identified "positive" pixels in Model 1 and 2.

Parameter	Model 1	Model 2
Number of "positive" pixels	12088	3526

Analogously to Model 1, the results were validated using the underlying Sentinel-2 RGB composition from the visible bands. The selected areas for the illustration of misclassified pixels in Figure 6 were re-validated with the results obtained from Model 2 (Figure 10). These sections show an obvious reduction/elimination of the misclassified pixels over the study area and thus an improved distribution map based only on remote sensing data.

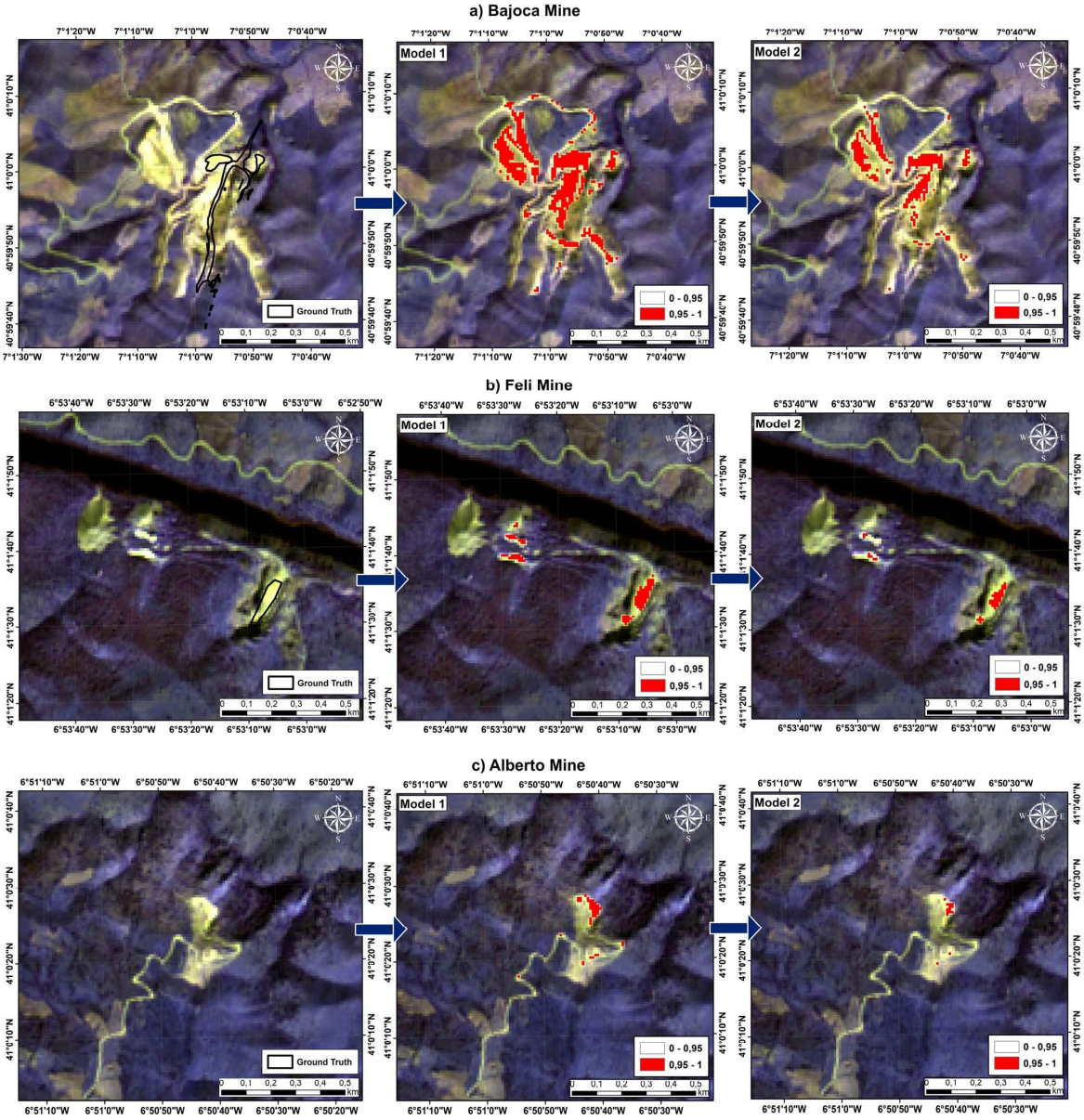

Figure 9. Reduction/elimination of misclassified pixels of Li distribution probabilities when comparing Remote Sensing Model 1 and 2 for the three training areas: (**a**) Bajoca Mine, (**b**) Feli Mine, (**c**) Alberto Mine.

The distribution raster map was further refined using GIS tools available in ArcGIS software, such as Boundary Clean, Majority Filter, etc., to remove the isolated pixels to improve the cartographic representation of the map.

The resulting raster was converted into vector data and further refined using tools such as Aggregate Polygons to cluster near-lying polygons representing the same physical feature.

The actual designed map (Figure 11) illustrates high-probability locations for Li mineralisation, exposed to the ground surface, based only on remote sensing data.

In the next step, this result was combined with the model based on geological datasets to finally conclude on the location of Li-bearing minerals over the study area. The final map result based only on remote sensing data is shown in Figure 11.

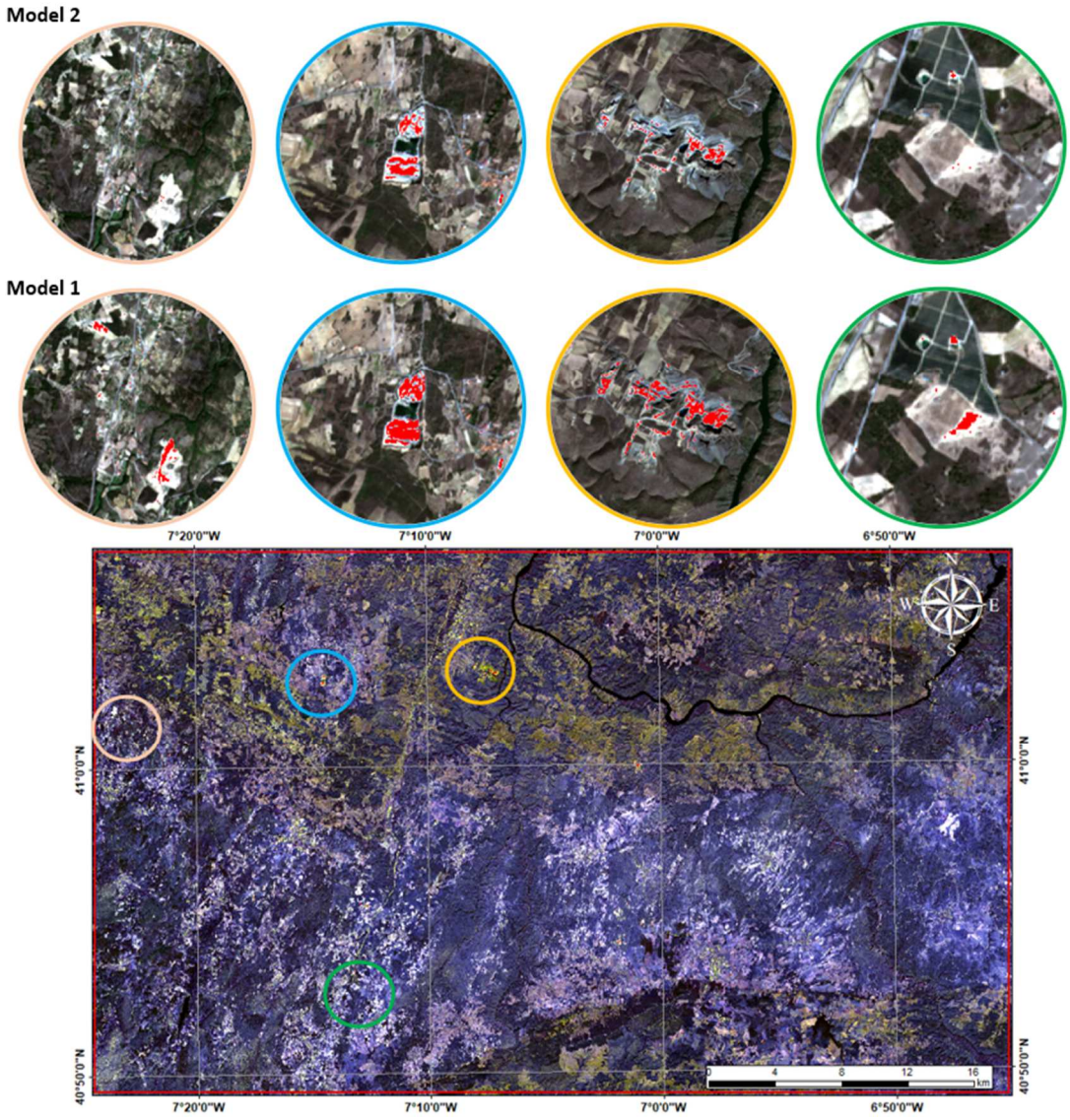

Figure 10. Reduction/elimination of misclassified pixels when comparing Remote Sensing Model 1 and 2.

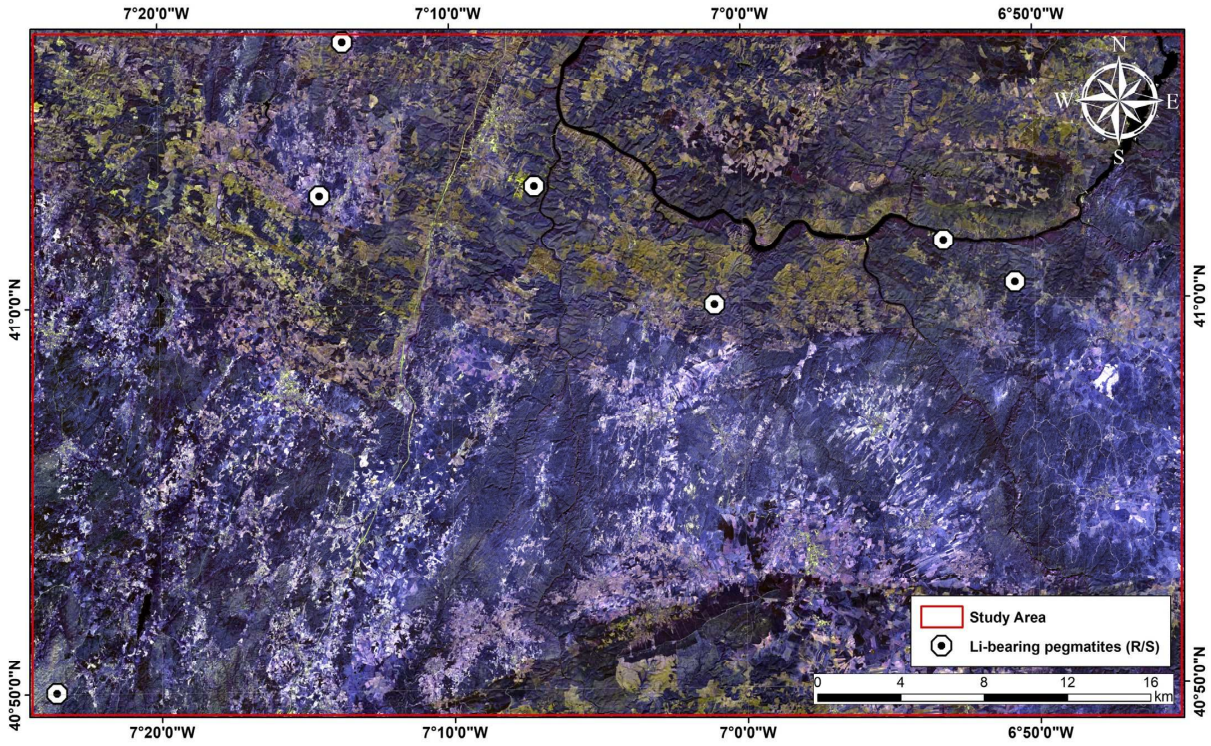

Figure 11. Result map of possible locations of Li-pegmatites based only on remote sensing data.

4.3. Combination of the Geological- and Remote Sensing Models

The prediction model result based on geological data (Figure 5) was further combined with the improved classification results based on remote sensing data to design a final map of Li mineralisation occurrences in the study area (Figure 12). The remote sensing models are limited to the detection of features of similar spectral characteristics exposed to the ground surface. On the other hand, the geological model is based on data related to the geological formations and geochemical characteristics (not always exposed on the ground surface). The combination of geological and remote sensing data into one ANN model resulted in many false interpretations, as the controlling parameters refer to/explain different targets. The results of the geological model and the knowledge from previous field campaigns helped us to exclude locations such as the Li-barren quarry at the Coa River (marked as False in Figure 12). The resulting map shows that the Bajoca and Feli mines, with a confirmed presence of Li pegmatites, could be successfully identified in both ANN models. Other potential areas identified from the geological-based model are not exposed to the ground surface and therefore could not be identified from the remote sensing data.

Through a combination of result maps, the identified location near the Coa River based on remote sensing data (marked as False in Figure 12) was automatically excluded. Further

research allied with a previous field campaign revealed that this is a schist quarry without the confirmed presence of Li at the mine site (https://www.solicel.pt/site/index.php/produtos; accessed on 02 February 2021). Additionally, in the case of the westernmost location identified using Sentinel-2 (Figure 11), the integration with available geological maps allowed us to identify it as another false positive since in the FAF the Li-bearing pegmatites are not emplaced within the granitoid rocks [17–19]. It is worth mentioning that a combination of the models based on geological data and remote sensing data could only succeed in areas where all data are available. The lack of geology information throughout the entire study area made it impossible to draw conclusions for the other identified locations in Figure 11.

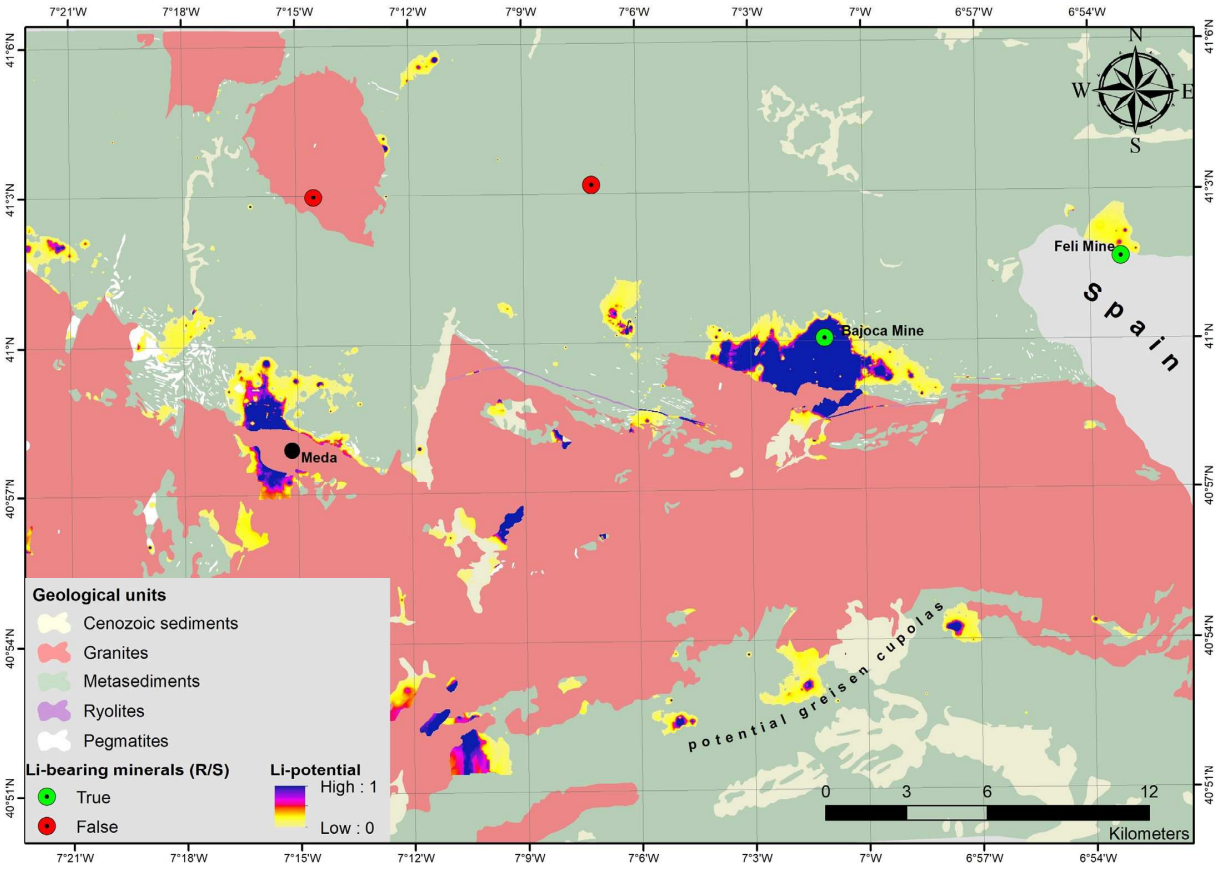

Figure 12. Predicted Li mineralisation based on geological and remote sensing data.

5. Discussion

The potential of low-to-medium resolution Sentinel-2 images was evaluated to automatically detect Li-bearing pegmatites exposed on the ground surface, depending on the weathering conditions of the Li-bearing rocks. Besides the raw spectral reflectance bands, dimensionality expansion techniques can be integrated to improve the classification workflows and distinguish features with similar spectral signatures to the Li-bearing minerals. Despite the potential to give

insights on other locations with similar surface reflectance to Li pegmatites, the remote sensing data only allowed the identification of Li-bearing rocks at known mines. These results show the limitations of the remote sensing data since most unexploited pegmatite bodies are often covered by vegetation, thus preventing their identification using only remote sensing data. On the other hand, integration with the geological and geochemical data was crucial to identify false positive areas resulting from the satellite-based approach. This indicates that the remote sensing model alone was not sufficient for prospectivity mapping. Field campaigns also helped to exclude some of the potential areas identified using the remote sensing models. The spectral signature of the rocks of one of the identified false positive areas (orange circle of Figure 8) was confronted with the spectra of Li-bearing pegmatites (Supplementary Figure S6c). Overall, the spectral behaviour of the two rocks is distinct enough to allow their spectral discrimination using hyperspectral data. Since this discrimination was not achieved using Sentinel-2 data, this may indicate that their spectral resolution may not be adequate. Moreover, even the spatial resolution of the images may have limited the identification of some of the smaller Li pegmatite bodies of the FAF that only reach less than 5 m in thickness [24].

These results are in line with previous research for the identification of Li pegmatites based only on remote sensing data and using traditional methods as well as machine learning algorithms such as ANN, Random Forest, Support Vector Machines, etc., [36–38] that have shown that the results are limited to features with similar spectral properties to Li-bearing mineralisations. For instance, Li mine sites could not be distinguished from the other within-scene elements in the study area using multispectral data due to their similar spectral properties. Despite this, field validation campaigns, the improvement of training areas, and algorithm parameterisation allowed us to decrease the number of false positive areas and increase the separability of Li mine sites [50]. In this paper, the knowledge acquired from previous field campaigns was integrated, including the insights provided by the reference spectra of the main outcropping lithologies (Supplementary Figure S6). Taking this into account, we investigated how the fusion of remote sensing data and geology knowledge improved the identification results and provided a more realistic approach, by allowing us to exclude false positive areas with no further interest for Li exploration

The presence of Li-bearing minerals is strongly related to specific geological formations such as pegmatites. For this reason, in this study, the prediction of Li mineralisation resulted in a combination of models based on remote sensing data (related to the ground surface) and geological/geochemical data (related to the geological formations at the ground surface). The proposed approach requires available geological data and remote sensing data over the entire

study area; otherwise, a combination of the models is not made possible. Geophysical data could further enhance the model, e.g., gravimetry could aid in the detection of hidden granite cupolas and related Li mineralisations, and pegmatite modelling could be enhanced by induced polarisation (IP) to measure contacts with the metasediments.

The prediction modelling based only on geological data was limited to the Portuguese side of the study area due to the availability of the geological and stream sediment data. The results shown in Figure 12 provide information on the spatial distribution of predicted Li mineralisation potential across the study area. The spatial distribution of Li-predictive areas in the transition of metasediments and granites could be a result of possible (hidden) greisen cupolas or pegmatites (Figure 5). As a result of the strong generalisation of geological units (metamorphics, intrusives, etc.), the areas with Li potential are mainly related to stream sediment geochemistry. Particularly straight area borders are caused by the boundaries of the main geological formations. Comparing the distribution of different elements across the study area (Sn, W, Li, Mo, As), several areas could be ruled out regarding Li mineralisation sensu stricto (pegmatites). As a result, only Bajoca Mine was used to validate the ANN model. However, the model was able to also predict the Li mineral deposits located near the cross-boundary of Portugal and Spain in the north-east part of the study area. The presence of Li mineralisation in this area is confirmed from the mining activities in the Riba D'Alva mine [51]. Further research is needed to validate the proposed approach in other areas, i.e., to check the high-potential areas identified through the mineral prospectivity mapping for the occurrence of unknown mineralisation. In the end, the resultant Li mineralisation prediction map (Figure 12) can be a useful tool for future exploration campaigns for exploration and mining companies, since it can help to delineate smaller interest areas in a large geographic area (>1.250 km^2). We recommend focusing future exploration activities on the following locations with high predicted Li potential: areas surrounding Bajoca Mine, Li anomalies in the west Meda, possible greisen cupolas in the south of the study area, and areas north of Feli Mine.

6. Conclusion

In this study, geological/geochemical data and remote sensing data (Sentinel-2 images) were used to create separate geological and remote sensing models using the ANN algorithm, respectively. In the end, the best remote sensing model was integrated with the geological one to delineate a Li mineralisation potential map for the FAF.

Using the ANN algorithm and Sentinel-2 multispectral data, it was possible to identify mine site locations and bare soil with similar reflectance properties to the training data. Overall, the Sentinel-2 data on their own are not enough to delineate other Li pegmatite occurrences, since only the known mine sites were correctly identified. The remaining highlighted areas corresponded to false positives. The exclusion of these false positive areas was only possible due to the knowledge obtained from field campaigns but also through the integration with the obtained geological model. The analysis of the reflectance spectra of selected pixels and reference samples (collected in field surveys) revealed that the coarse spectral resolution of Sentinel-2 is not able to reflect all significant characteristics of Li-bearing minerals and pegmatites. Therefore, the identification of Li pegmatite bodies specifically based only on Sentinel-2 data seems to be challenging due to the limited spectral and spatial resolution of the used satellite data and also the existing vegetation coverage (although sparse).

However, the combination of the satellite data with the geological model provides a potential approach to automatically predict the location of Li-bearing mineralisation using ANNs. Careful consideration of training patterns, spectral bands, and geological data proved to be key factors in establishing a working model. The proposed combined approach is a first step towards expeditious Li mineralisation prediction. The integration of the models allowed us to enrich the remote sensing classification results, since the geological prediction model gives insights on formations that are suitable to host Li pegmatites. Thus, the approach of combining the modelling results based on geological and remote sensing data is promising, not only to identify the known exposed Li pegmatites on the ground surface and exclude false features with similar signatures in the spectral reflectance, but also to reveal potential locations for further exploration. Nonetheless, Li pegmatite prediction needs to be improved in the future through the use of high spectral and spatial resolution data in the remote sensing modelling step. The proposed approach can also be used for other metals or raw materials and will make a cost-efficient contribution to raw material exploration in general.

Supplementary Materials

The following are available online at www.mdpi.com/article/10.3390/min11101046/s1, Figure S1: Reference spectral signatures of (a) petalite samples from Bajoca Mine, (b) spodumene samples from Alberto Mine, and (c) lepidolite samples from Feli Mine; Figure S2: Spectral signatures for Alberto, Bajoca and Feli mines based on Sentinel-2 data; Figure S3: Histogram (a) and Network MSE error (b) for the Geological Model; Figure S4: Histogram (a) and Network MSE error (b) for Remote Sensing Model 1; Figure S5: Spectral signatures for the extended

spectral bands: (a) 1–6, (b) 7–12, (c) 13–32; Figure S6: Reference spectral signatures of (a) lepidolite-bearing pegmatites, (b) pet-alite-bearing pegmatites (Bajoca Mine), (c) schist–metagreywacke complex (CXG) metasediments, and (d) granitoid rocks; Figure S7: Histogram (a) and Network MSE error (b) for Remote Sensing Model 2.

Author Contributions

Conceptualisation, M.K., D.H., A.B., and S.S.; methodology, M.K., D.H., and S.S.; software, P.H.; validation, M.K., D.H., S.S., J.C.-F., A.L., and A.C.T.; formal analysis, M.K., D.H., and S.S.; investigation, M.K., D.H., and S.S.; resources, M.K., D.H., S.S., and A.L.; data curation, M.K., D.H., S.S., J.C.-F., and A.L.; writing—original draft preparation, M.K., D.H., and S.S.; writing—review and editing, M.K., D.H., S.S., J.C.-F., A.L., and A.C.T.; visualisation, M.K. and D.H.; supervision, M.K.; project administration, S.S., A.K., and A.B.; funding acquisition, S.S., A.K., and A.B. All authors have read and agreed to the published version of the manuscript.

Funding

(1) The investigations in this paper were performed under the LIGHTS (Lightweight Integrated Ground and Airborne Hyperspectral Topological Solution; ERA-MIN/0001/2017– LIGHTS) research project funded by national research agencies under the EU H2020 ERAMIN-2 network. ERA-MIN2 is a global, innovative, and flexible pan-European network of research funding organisations, supported by EU Horizon 2020, that builds on the experience of the FP7ERANETERA-MIN (2011 to 2015). The national funding agencies supporting the project are: ANR— Agence Nationale de la Recherche (France), BMBF Jülich—Bundesministerium für Bildung und Forschung (Germany), and FCT—Fundação para a Ciência e a Tecnologia (Portugal). (2) The work was also supported by Portuguese National Funds through the FCT project UIDB/04683/2020—ICT (Institute of Earth Sciences). (3) Joana Cardoso-Fernandes is financially supported within the compass of a Ph.D. Thesis, ref. SFRH/BD/136108/2018, by national funds from MCTES through FCT, and co-financed by the European Social Fund (ESF) through POCH—Programa Operacional Capital Humano—and NORTE 2020 regional program.

Data Availability Statement

The spectral data presented in this study are openly available in Zenodo at http://doi.org/10.5481/zenodo.4575375, reference 45. Restrictions may apply to the availability of stream sediment data and to part of the geological data since they correspond to third party data obtained from the French Bureau de Recherches Géologiques et Minières (BRGM) and the Portuguese National Laboratory of Energy and Geology (LNEG), respectively.

Acknowledgments

The authors gratefully acknowledge the comments of three anonymous reviewers, which led to substantial improvement of the manuscript.

Conflicts of Interest

The authors declare no conflict of interest. The funders had no role in the design of the study; in the collection, analyses, or interpretation of data; in the writing of the manuscript, or in the decision to publish the results.

Appendix A

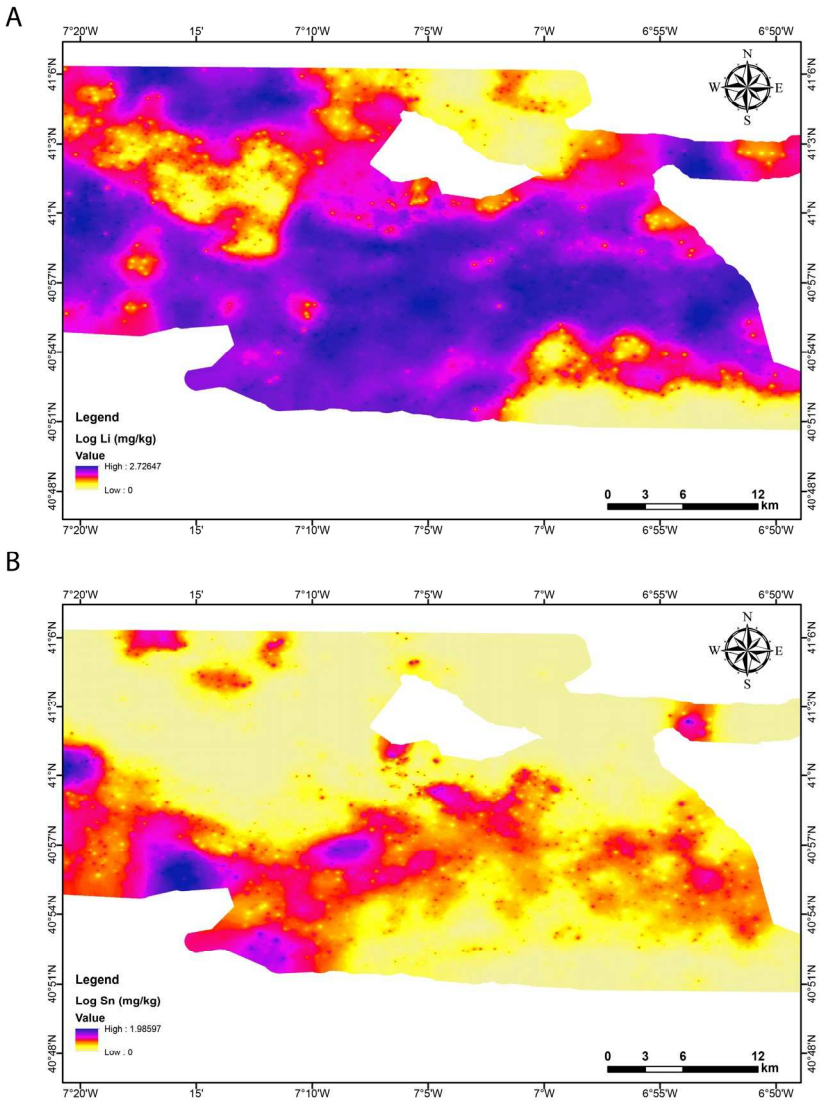

Figure A1. Geochemical anomaly maps for Li (**A**) and Sn (**B**) before excluding the granitic areas.

References

1. European Commission: DG Internal Market Industry Entrepreneurship and SMEs. *Critical Raw Materials Resilience: Charting a Path towards Greater Security and Sustainability*; COM(2020) 474 final; European Commission: DG Internal Market Industry Entrepreneurship and SMEs: Brussels, Belgium, 2020; p. 23.
2. Brooks, K. Lithium Minerals. *Geol. Today* **2020**, *36*, 192–197, doi:10.1111/gto.12326.
3. Kesler, S.E.; Gruber, P.W.; Medina, P.A.; Keoleian, G.A.; Everson, M.P.; Wallington, T.J. Global lithium resources: Relative importance of pegmatite, brine and other deposits. *Ore Geol. Rev.* **2012**, *48*, 55–69, doi:10.1016/j.oregeorev.2012.05.006.
4. Silva, D.; Lima, A.; Gumiaux, C.; Glouguen, E.; Deveaud, S. Spatial Geostatistical Analysis Applied to The Barroso-Alvão RareElements Pegmatite Field (Northern Portugal). In *GIS—An Overview of Applications*; Teodoro, A.C., Ed.; Bentham eBooks: Sharjah, United Arab Emirates, 2018.
5. Linnen, R.L.; Van Lichtervelde, M.; Černý, P. Granitic Pegmatites as Sources of Strategic Metals. *Elements* **2012**, *8*, 275–280, doi:10.2113/gselements.8.4.275.
6. Gourcerol, B.; Gloaguen, E.; Melleton, J.; Tuduri, J.; Galiegue, X. Re-assessing the European lithium resource potential—A review of hard-rock resources and metallogeny. *Ore Geol. Rev.* **2019**, *109*, 494–519, doi:10.1016/j.oregeorev.2019.04.015.
7. Carvalho, J.M.F.; Farinha, J.A.L.B. Lithium potentialities in Northern Portugal. In Proceedings of the 17th Industrial Minerals International Congress, Barcelona, Spain, 28–31 March 2004; pp. 1–10.
8. Roda-Robles, E.; Pesquera, A.; Gil-Crespo, P.P.; Vieira, R.; Lima, A.; Olave, I.G.; Martins, T.; Torres-Ruiz, J.; E., R.-R.; A., P.; et al. Geology and mineralogy of Li mineralization in the Central Iberian Zone (Spain and Portugal). *Miner. Mag.* **2016**, *80*, 103– 126, doi:10.1180/minmag.2016.080.049.
9. Brown, W.M.; Gedeon, T.D.; Groves, D.I.; Barnes, R.G. Artificial neural networks: A new method for mineral prospectivity mapping. *Aust. J. Earth Sci.* **2000**, *47*, 757–770, doi:10.1046/j.1440-0952.2000.00807.x.
10. Rigol-Sanchez, J.P.; Olmo, M.C.; Abarca-Hernández, F. Artificial neural networks as a tool for mineral potential mapping with GIS. *Int. J. Remote Sens.* **2003**, *24*, 1151–1156, doi:10.1080/0143116021000031791.
11. Oh, H.-J.; Lee, S. Application of Artificial Neural Network for Gold–Silver Deposits Potential Mapping: A Case Study of Korea. *Nat. Resour. Res.* **2010**, *19*, 103–124, doi:10.1007/s11053-010-9112-2.

12. Rodriguez-Galiano, V.; Sanchez-Castillo, M.; Olmo, M.C.; Chica-Rivas, M. Machine learning predictive models for mineral prospectivity: An evaluation of neural networks, random forest, regression trees and support vector machines. *Ore Geol. Rev.* **2015**, *71*, 804–818, doi:10.1016/j.oregeorev.2015.01.001.
13. Roda-Robles, E.; Villaseca, C.; Pesquera, A.; Gil-Crespo, P.P.; Vieira, R.; Lima, A.; Olave, I.G. Petrogenetic relationships between Variscan granitoids and Li-(F-P)-rich aplite-pegmatites in the Central Iberian Zone: Geological and geochemical constraints and implications for other regions from the European Variscides. *Ore Geol. Rev.* **2018**, *95*, 408–430, doi:10.1016/j.oregeorev.2018.02.027.
14. Catalán, J.R.M. The Central Iberian arc, an orocline centered in the Iberian Massif and some implications for the Variscan belt. *Acta Diabetol.* **2011**, *101*, 1299–1314, doi:10.1007/s00531-011-0715-6.
15. Dias, R.; Ribeiro, A. The Ibero-Armorican Arc: A collision effect against an irregular continent? *Tectonophys.* **1995**, *246*, 113–128, doi:10.1016/0040-1951(94)00253-6.
16. Bea, F.; Montero, P.; Zinger, T. The Nature, Origin, and Thermal Influence of the Granite Source Layer of Central Iberia. *J. Geol.* **2003**, *111*, 579–595, doi:10.1086/376767.
17. Roda, E. Distribución, Caracteristicas y Petrogenesis de las Pegmatitas de La Fregeneda (Salamanca). Ph.D. Thesis, UPV/EHU, Bilbao, Spain, 1993.
18. Roda-Robles, E.; Perez, A.P.; Roldan, F.V.; Fontan, F. The granitic pegmatites of the Fregeneda area (Salamanca, Spain): characteristics and petrogenesis. *Miner. Mag.* **1999**, *63*, 535–558, doi:10.1180/002646199548709.
19. Vieira, R. Aplitopegmatitos com Elementos Raros da Região Entre Almendra (V.N. de Foz Côa) e Barca d'Alva (Figueira de Castelo Rodrigo). Campo Aplitopegmatítico da Fregeneda-Almendra. Ph.D. Thesis, Faculdade de Ciências da Universidade do Porto, Porto, Portugal, 2010.
20. Costa, J.C.S. *Notícia Sobre uma Carta Geológica do Buçaco, de Nery Delgado*; Serviços Geológicos de Portugal: Lisboa, Portugal, 1950. 21. Teixeira, C. *Notas Sobre Geologia de Portugal o Complexo Xisto-Grauváquico ante-Ordoviciano*; Empresa Literaria Fluminense Lda.: Lisboa, Portugal, 1955; p. 48.
22. Bea, F.; Herrero, J.G.S.G.; Pinto, M.S.; Barrera, J.L.; Brandle, J.L.; Corretgé, L.G.; Suárez, O. Una compilación geoquímica (elementos mayores) para los granitóides del Macizo Hespérico. In *Geología de los Granitóides y Rocas Asociadas del Macizo Hesperico*; Bea, F., Carnicero, A., Gonzalo, J.C., López-Plaza, M., Rodríguez Alonso, M.D., Eds.; Libro de Homenaje a L. C. García de Figuerola, Editorial Rueda: Alcorcon, Madrid, Spain, 1987.

23. Pereira, I.; Dias, R.; Bento dos Santos, T.; Mata, J. Exhumation of a Migmatite Complex along a Transpressive Shear Zone: Inferences from the Variscan Juzbado–Penalva Do Castelo Shear Zone (Central Iberian Zone). *J. Geol. Soc.* **2017**, *174*, 1004–1018, doi:10.1144/jgs2016-159.
24. Ferreira, J.A.; Bento dos Santos, T.; Pereira, I.; Mata, J. Tectonically Assisted Exhumation and Cooling of Variscan Granites in an Anatectic Complex of the Central Iberian Zone, Portugal: Constraints from LA-ICP-MS Zircon and Apatite U–Pb Ages. *Int. J. Earth Sci.* **2019**, *108*, 2153–2175, doi:10.1007/s00531-019-01755-1.
25. Aires, S.C.M. Petrofísica e Litogeoquímica de Formações do "Complexo Xisto-Grauváquico" (Grupo do Douro) Estudo do Potencial do "Xisto" para Exploração como Pedra Natural. Ph.D. Thesis, Faculdade de Ciências da Universidade do Porto, Porto, Portugal, 2018.
26. Silva, A.F.d.; Ribeiro, M.L. *Notícia Explicativa da Folha 15-A Vila Nova de Foz Côa*; Serviços Geológicos de Portugal: Lisboa, Portugal, 1991; p. 52.
27. Silva, A.F.d.; Ribeiro, M.L. *Notícia Explicativa da Folha 15-B Freixo de Espada à Cinta*; Instituto Geológico e Mineiro: Lisboa, Portugal, 1994; p. 48.
28. Silva, A.F.; Santos, A.J.; Ribeiro, A.; Ribeiro, M.L. *Carta Geológica de Portugal na Escala 1/50.000—Folha 15-A—Vila Nova de Foz Côa*; Serviços Geológicos de Portugal: Lisboa, Portugal, 1990.
29. Silva, A.F.; Santos, A.J.; Ribeiro, A.; Cabral, J.; Ribeiro, M.L. *Carta Geológica de Portugal na Escala 1/50.000—Folha 15-B—Freixo de Espada à Cinta*; Serviços Geológicos de Portugal: Lisboa, Portugal, 1990.
30. Carvalhosa, A. *Carta Geológica de Portugal à Escala 1:50.000, Folha 15-D (Figueira de Castelo Rodrigo)*; Serviços Geológicos de Portugal: Lisboa, Portugal, 1960.
31. Ribeiro, M.L. *Carta Geológica Simplificada Do Parque Arqueológico Do Vale Do Côa Na Escala 1:80.000*; Parque Arqueológico do Vale do Côa: Vila Nova de Foz Côa, Portugal, 1990.
32. Al-Rawashdeh, S.; Saleh, B.; Hamzah, M. The Use of Remote Sensing Technology in Geological Investigation and Mineral Detection in El Azraq-Jordan. *Cybergeo Eur. J. Geogr.* **2006**, *358*, 1–17; doi:10.4000/cybergeo.2856.
33. van der Meer, F.D.; van der Werff, H.M.A.; van Ruitenbeek, F.J.A. Potential of ESA's Sentinel-2 for Geological Applications. *Remote Sens. Environ.* **2014**, *148*, 124–133,doi:10.1016/j.rse.2014.03.022.
34. Beiranvand Pour, A.; Park, T.-Y.; Park, Y.; Hong, J.; Zoheir, B.; Pradhan, B.; Ayoobi, I.; Hashim, M. Application of Multi-Sensor Satellite Data for Exploration of Zn–Pb Sulfide

Mineralization in the Franklinian Basin, North Greenland. *Remote Sens.* **2018**, *10*, 1186, doi:10.3390/rs10081186.

35. Cardoso-Fernandes, J.; Teodoro, A.; Lima, A. Potential of Sentinel-2 Data in the Detection of Lithium (Li)-Bearing Pegmatites: A Study Case. In Proceedings of the Earth Resources and Environmental Remote Sensing/GIS Applications IX, Berlin, Germany, 10–13 September 2018; doi:10.1117/12.2326285.
36. Cardoso-Fernandes, J.; Teodoro, A.C.; Lima, A. Remote Sensing Data in Lithium (Li) Exploration: A New Approach for the Detection of Li-Bearing Pegmatites. *Int. J. Appl. Earth Obs. Geoinf.* **2019**, *76*, 10–25, doi:10.1016/j.jag.2018.11.001.
37. Cardoso-Fernandes, J.; Teodoro, A.C.M.; Lima, A.; Roda-Robles, E. Evaluating the Performance of Support Vector Machines (SVMs) and Random Forest (RF) in Li-Pegmatite Mapping: Preliminary Results. In Proceedings of the Earth Resources and Environmental Remote Sensing/GIS Applications X, Strasbourg, France, 9–12 September 2019; doi:10.1117/12.2532577.
38. Cardoso-Fernandes, J.; Teodoro, A.C.; Lima, A.; Roda-Robles, E. Lithium (Li) Pegmatite Mapping Using Artificial Neural Networks (ANNs): Preliminary Results. In Proceedings of the IEEE International Geoscience and Remote Sensing Symposium, Waikoloa, HI, USA, 26 September–2 October 2020; pp. 557–560, doi:10.1109/IGARSS39084.2020.9323852.
39. Angel, J.M.; Viallefond, L. *Prospection Géochimique Portugal. Résultats Analytiques et Interprétation de l'échantillonnage Réalisé Par Le S.F.M. Sur La Feuille 15A, Région de Almendra*; NOTE/GMX-748; BRGM: Orléans, France, 1981; p. 6.
40. Viallefond, L. *Prospection Géochimique Portugal: Résultats Analytiques et Interprétation de l'Échantillonnage Réalisé par le S.F.M. sur la Feuille 15B*; NOTE/GMX-732; BRGM: Orléans, France, 1981; p. 27.
41. Viallefond, L.; Angel, J.M. *Portugal Nord—Feuille 15A-15C—Interprétation des Données Analytiques*; NOTE/GMX-738; BRGM: Orléans, France, 1981; p. 17.
42. Vieira, R.; Roda-Robles, E.n.; Pesquera, A.; Lima, A. Chemical variation and significance of micas from the Fregeneda-Almendra pegmatitic field (Central-Iberian Zone, Spain and Portugal). *Am. Mineral.* **2011**, *96*, 637–645, doi:10.2138/am.2011.3584.
43. Lanaras, C.; Bioucas-Dias, J.; Galliani, S.; Baltsavias, E.; Schindler, K. Super-Resolution of Sentinel-2 Images: Learning a Globally Applicable Deep Neural Network. *J. Photogramm. Remote Sens.* **2018**, *146*, 305–319, doi:10.1016/j.isprsjprs.2018.09.018.
44. Bahr, T.; Heinz, D.C. Creating Models Of Hyperspectral Classification Workflows Integrating Dimensionality Expansion For Multispectral Imagery. In Proceedings of the 10th Workshop on Hyperspectral Imaging and Signal Processing: Evolution in Remote

Sensing (WHISPERS), Amsterdam, The Netherlands, 24–26 September 2019; doi:10.1109/whispers.2019.8920946.

45. Cardoso-Fernandes, J.; Silva, J.; Lima, A.; Teodoro, A.C.; Perrotta, M.; Cauzid, J.; Roda-Robles, E.; Ribeiro, M.A. Reflectance spectroscopy to validate remote sensing data/algorithms for satellite-based lithium (Li) exploration (Central East Portugal). In Proceedings of the SPIE Remote Sensing, Earth Resources and Environmental Remote Sensing/GIS Applications XI, Online, 21–25 September 2020; https://doi.org/10.1117/12.2573929.
46. Cardoso-Fernandes, J.; Silva, J.; Lima, A.; Teodoro, A.C.; Perrotta, M.; Cauzid, J.; Roda-Robles, E. Characterization of lithium (Li) minerals from the Fregeneda-Almendra region through laboratory spectral measurements: A comparative study. In Proceedings of the SPIE Remote Sensing, Earth Resources and Environmental Remote Sensing/GIS Applications XI, Online, 21– 25 September 2020; https://doi.org/10.1117/12.2573941.
47. Cardoso-Fernandes, J.; Silva, J.; Dias, F.; Lima, A.; Teodoro, A.C.; Barrès, O.; Cauzid, J.; Perrotta, M.; Roda-Robles, E.; Ribeiro, M.A. Tools for remote exploration: A Lithium (Li) dedicated spectral library of the Fregeneda-Almendra aplite-pegmatite field. Version 1. Zenodo, 2021. Available online: https://zenodo.org/record/4575375#.YUGmx30RVPY (accessed on 9 March 2021).
48. Cardoso-Fernandes, J.; Dias, F.; Lima, A.; Anjos Ribeiro, M.; Perrotta, M.; Roda-Robles, E.; Teodoro, A.C. Petalite alteration products from the Bajoca pegmatite (Central Portugal): A multiapproach for lithium exploration. In Proceedings of the EGU General Assembly 2021, Online, 19–30 April 2021; doi:10.5194/egusphere-egu21-2364.
49. Haykin, S.S. *Neural Networks: A Comprehensive Foundation*; Prentice Hall: Englewood Cliffs, NJ, USA, 1999; ISBN 978-0-13273350-2.
50. Cardoso-Fernandes, J.; Teodoro, A.C.; Lima, A.; Roda-Robles, E. Semi-Automatization of Support Vector Machines to Map Lithium (Li) Bearing Pegmatites. *Remote. Sens.* **2020**, *12*, 2319, doi:10.3390/rs12142319
51. Gaspar, L.M.; Inverno, C.M.C. Mineralogy and Metasomatic Evolution of Distal Strata-BoundScheelite Skarns in the Riba de Alva Mine, Northeastern Portugal. *Econ. Geol.* **2000**, *95*, 1259–1275, doi:10.2113/gsecongeo.95.6.1259.

Discussion

The present thesis provides new algorithms and data for remote detection of Li-pegmatites. Moreover, the complementary geochemical tools investigated (LIBS data, stream sediments, metasomatic haloes) provide new insights for Li exploration.

Through a systematic review it was possible to identify four past approaches to Li exploration using remote sensing data and techniques, namely: (i) geobotanical mapping; (ii) lithological mapping; (iii) mineral alteration mapping; and (iv) direct discrimination of the mineralization source that could be employed to distinct types of Li-mineralization. In the case of Li-pegmatites, previous studies showed potential to discriminate them from their host rocks, although this discrimination may rely on the availability of TIR data according to the employed technique. The main difficulties of employing remote sensing data to identify Li-pegmatites were also assessed based on previous results: (i) lack of an automated process; (ii) spectral confusion between classes or spectral mixing at a pixel level (balance between spatial and spectral resolution); (iii) vegetation or other coverage; and (iv) lack of detailed knowledge on the specific alteration paragenesis and style of the related hydrothermal alteration. Several strategies were identified to overcome these shortcomings, and most of them were exploited in detail during this Ph.D. thesis.

First, several MLAs were evaluated for lithological discrimination in the case study area of Fregeneda-Almendra. Algorithms overfitting was the main limitation found. Therefore, several methodological improvements had to be made: (i) reducing the area to be classified and the number of classes through masking; (ii) a new strategy to split the training data into training and test subsets was proposed; and (iii) tailored metrics and strategies were developed to deal with class imbalance. In parallel, automatization of the SVM classification process was attempted. However, a blind automatization was not possible, because the intervention of the operator is a key for model training and parameterization. Despite this, and unlike previous studies (Noi & Kappas, 2017; Maxwell *et al.*, 2018; Cardoso-Fernandes *et al.*, 2019), the results showed the importance of ensuring the independency between the training and testing subsets and their effect on model overfit, as well as the sensitivity of the SVM algorithm to class imbalance. In the end, the discrimination between the Li-pegmatites and their host-rock was improved with the SVM models successfully mapping known areas where Li-pegmatites occur. However, pegmatite size and vegetation coverage of other unexploited dykes are still the main obstacles. Nonetheless, the methodological developments made are

a major contribution to Li-pegmatite exploration using remote sensing, but also to the field of MLAs applied to lithological mapping through remote sensing data.

Next, a spectral library was built, composed of field and laboratory spectra not only of Li-minerals (spodumene, petalite, lepidolite) but also from the main outcropping lithologies of the Fregeneda–Almendra area (granitoid rocks, CXG metasediments, Li-pegmatites). These reference spectra are crucial to delineate and improve future knowledge-based satellite image classification approaches and validate the previously obtained results while ground-checking the remotely sensed data (Teodoro & Veloso-Gomes, 2007; Rivard *et al.*, 2009; Pour & Hashim, 2018). Besides the spectrum acquisition settings, data curation is another important step that changes according to the spectroradiometer used. For example, a splice correction had to be applied to the spectra obtained with the FieldSpec 4 equipment to remove the offset between detectors (ASD Inc., 2008). A thorough inspection of each individual spectra was performed to check for measurement errors or vegetation interference. Moreover, to compare spectra collected with different spectroradiometers and to allow mineral identification, a normalization through the continuum removal process was employed (Van Der Meer, 2000; Carrino *et al.*, 2018). In this work, a Python improvement of the *pysptools* functions was made to automatically extract the main absorption features through batch processing, thus allowing to simultaneously treat hundreds or thousands of spectra. This could be very useful for researchers or companies in need of normalizing their own spectral libraries. It is also noteworthy that field spectra are expected to better match the spectral signatures acquired by satellite or airborne sensors due to similar illumination settings (natural sunlight exposure), but field spectra have the disadvantage of presenting sharp absorption bands around 1400 and 1800 nm caused by atmospheric water that must be removed.

Similarly, a LIBS database was built, since this tool is well-suited to analyze light elements. The LIBS spectral library is composed of distinct Li-rich materials, namely minerals, powder pellets, and rocks, thus allowing the evaluation of the matrix effect on the results. Overall, smooth, solid samples correspond to ones more suitable for this kind of analysis. The heterogeneity and granulometry of the samples have also a large impact on the geochemical results, in accordance with the previously demonstrated by Cousin *et al.* (2012); Fabre (2020), and cautionary measures should be employed. For example, the number of analyses on rock samples must be increased to obtain a reliable bulk composition estimation (Cousin *et al.*, 2012; Fabre, 2020). Alternatively, the samples can be crushed and homogenized by making pressed pellets. Afterward, a calibration curve can be obtained through the net

intensity under the peaks allowing to obtain a semi-quantification of the Li content on different sample types directly in the field. This is very appealing not only for academics but also to exploration and mining companies, allowing them to obtain fast results without the need for laboratory analysis. Moreover, multivariate techniques (such as partial least-squares regression) could be employed in the future for mineral discrimination or provenance recognition through the identification of major, minor, and trace elements (McMillan *et al.*, 2014; Kochelek *et al.*, 2015; Farnsworth-Pinkerton *et al.*, 2018). Therefore, both spectral libraries are of great importance and impact for mineral exploration not only in the case study area but also worldwide.

In what concerns the development of new tools and algorithms, for Li-pegmatite detection, the interpretation of key reflectance spectra is paramount. Regarding the Li-minerals, it was possible to discriminate lepidolite through its diagnostic absorption features from spodumene, petalite, and other white micas. However, spodumene and petalite do not have any diagnostic features because their spectral signature is dominated by clay-related absorptions. Detailed petrography and geochemical studies proved that these clays occur in either well-preserved or completely altered samples, as observed by Clark *et al.* (1993), although higher amounts of clays (and lower Li contents) may lead to increased absorption intensities of the OH^- and H_2O absorptions (Hunt & Ashley, 1979; Duke, 1994; Asadzadeh & Souza Filho, 2016). These findings limit the possibility to discriminate areas where these Li-minerals occur from clay-bearing barren areas. Notwithstanding, in areas where argillic alteration is not predominant, both spodumene and petalite can be identified through their pathfinder minerals. In what concerns the spectral behavior of the most widespread lithologies in the case study area, several criteria allow discriminating the Li-pegmatites despite the similar absorption features, namely: (i) the distinctive reflectance magnitude, (ii) higher absorptions depths, (iii) different wavelength position of key absorption features, and (iv) the specific overall spectral behavior of each lithology reflecting different mineral assemblages. The higher resolution sensors such as ASTER, PRISMA, and Mjolnir show the greatest ability to discriminate Li-pegmatites from the remaining lithologies. These insights on the spectral behavior of Li-minerals and pegmatites and the acquired mineral spectra can be employed in the future to delineate target areas for mineral occurrences, similar to the works of Laakso *et al.* (2015) and Naleto *et al.* (2019).

To complete the shortcomings of the remote sensing-based approaches, other geochemical tools were investigated. First, a historical stream sediment campaign covering the Portuguese side of the Fregeneda-Almendra aplite-pegmatite field was reprocessed. It is

noteworthy that working with such historical data also presents some difficulties due to a lack of critical information such as digestion methods used or the detection limits of the analysis, as pointed out by Steiner *et al.* (2019). Distinct approaches were considered and their applicability to mineral exploration was evaluated. Similar to previous studies (Saadati *et al.*, 2020), spatial interpolation proved to be a simple and expeditious approach for the early stages of mineral exploration, i.e. reconnaissance campaigns at a regional scale. This is due to the inherent smoothing of the anomalies that resulted in a loss of detail. Despite this and the influence of granitoid rocks, it was possible to delineate smaller areas of interest for detailed studies. Oppositely, the catchment basin approach is very time-consuming and a complex method. However, this approach is more suitable for prospect scale exploration since it allowed delineating smaller areas for field verification and reducing the anomalous areas related to granites. In both approaches, the use of key pathfinder elements was essential to delineate target areas and discriminate granite-related from pegmatite-related Li anomalies. The importance of using such multi-elemental strategies for Li-exploration had already been demonstrated in the works of Fyzollahhi *et al.* (2018); Saadati *et al.* (2020). Overall, the methodology employed was validated in the field as effective in the identification of Li-mineralized pegmatites. The findings presented in this work show the importance of stream sediment analysis and the use of portable tools in Li-pegmatite exploration, thus helping future and similar geochemical exploration campaigns for Li in other locations.

In parallel, a comprehensive study was developed to understand the effect of pegmatite intrusion into the metasedimentary host rocks of the case study area. As observed in previous works (Shearer *et al.*, 1984; Shearer *et al.*, 1986; Morgan & London, 1987; Barros *et al.*, 2020), the aplite-pegmatite dykes from Fregeneda-Almendra generated variable metasomatic haloes highly enriched in F, B, Li, Rb, Cs, Sn, Be, and Tl within relative distances of 2 times the dyke thickness and anomalous contents up to 4–5 times the thickness of the dyke. The results also show that the size of the halo is dependent on the pegmatite type (greater haloes observed for the most evolved dykes) and that element mobility is not the same with Cs and Li traveling to further distances than Rb and Sn (and even further than F, B, Be, Tl). Similar phenomena were also observed in previous studies (Shearer *et al.*, 1984; Shearer *et al.*, 1986; Galeschuk & Vanstone, 2007 and references therein). Other factors may influence the halo size, namely the type of host rock and the structural relation between pegmatite dykes and host rocks, as demonstrated by Galeschuk and Vanstone (2007). Overall, these findings are of great importance to mineral exploration. First, the metasomatic haloes can be used as a direct tool for Li-pegmatite identification as evidenced in past studies (Galeschuk & Vanstone, 2007; Martins *et al.*, 2017; Barros *et al.*,

2020). Higher contents than 400 ppm (Li), 50 ppm (Cs), 300 ppm (Rb), and 15 ppm (Sn) in the metasedimentary samples from the area would indicate the proximity of a buried aplite-pegmatite. All of these elements can be semi-quantitatively analyzed in the field with portable XRF and LIBS, which is of great interest to exploration companies. Secondly, a better understanding and characterization of the geochemical halo footprints is essential to improve the remote sensing detection of Li-pegmatites through the associated hydrothermal alteration. In the past decade, hyperspectral sensors have been employed with success to identify mineralogical and compositional changes related to the proximity to mineralized sources, thus allowing to vector towards distinct deposits types (Tappert *et al.*, 2013; Laakso *et al.*, 2015; Lypaczewski *et al.*, 2019). Preliminary spectral studies show that it is possible to detect changes in chlorite and muscovite composition along the sampling profiles (Appendix IV). Future studies are needed to understand if the composition changes are due to metasomatism or if they reflect the inherited whole-rock chemistry or even the pressure-temperature conditions of the metamorphism.

The final goal of mineral exploration is to integrate all available features into a model capable of highlighting the area with the highest potential for Li-mineralization. In this work, the integration of geological and geochemical data with the remote sensing data was achieved using ANNs. Careful selection of training patterns, spectral bands, and geological data was essential to establishing a sound model. Some limitations were found when only using satellite data, which were in line with the previous works. As stated before, high spectral and spatial resolution remote sensing data would improve the results. Nonetheless, the combination with other features was crucial to identify false-positive areas resultant from the satellite-based approach, enriching the prediction model and allowing to automatically predict areas with potential for Li-mineralization for further exploration. In one of these areas, Li-mineralization is confirmed by ancient mining activities in the Riba D'Alva mine (Gaspar & Inverno, 2000; Vieira, 2010). Further research is needed to validate and check the remaining high potential areas for the occurrence of unknown mineralization. Thus, the proposed combined approach is a significant first step towards reliable Li-prediction mineralization in large geographical areas that could be extended to other deposit types.

Although the findings of this thesis represent a great contribution to the state of the art of Li-pegmatite exploration, several open questions should be addressed in the future:

- Can remote sensing data and traditional algorithms/MLAs be used to target other types of Li-deposits?

- How can hyperspectral images and the reference spectral data be used to improve Li-pegmatite detection?
- Is there any economic potential for Li in the evolved granites of the region? If so, could remote sensing be employed to detect highly specialized granites?
- What are the main traps (i.e. minerals) responsible for the enrichment of highly mobile elements within the metasomatized host rocks?
- Can the mineral chemistry change within the haloes be detected through hyperspectral sensors? If so, what are the implications for remote sensing exploration of buried pegmatites?

References

Asadzadeh, S., & Souza Filho, C. R. (2016). A review on spectral processing methods for geological remote sensing. *International Journal of Applied Earth Observation and Geoinformation, 47*, 69-90. doi: https://doi.org/10.1016/j.jag.2015.12.004.

ASD Inc. (2008). *ViewSpec Pro™ User Manual. ASD Document 600555 Rev. A*. Boulder,

Barros, R., Kaeter, D., Menuge, J. F., & Škoda, R. (2020). Controls on chemical evolution and rare element enrichment in crystallising albite-spodumene pegmatite and wallrocks: Constraints from mineral chemistry. *Lithos, 352-353*, 105289. doi: https://doi.org/10.1016/j.lithos.2019.105289.

Cardoso-Fernandes, J., Teodoro, A. C., Lima, A., & Roda-Robles, E. (2019, 9–12 September 2019). *Evaluating the performance of support vector machines (SVMs) and random forest (RF) in Li-pegmatite mapping: preliminary results.* Paper presented at the SPIE Remote Sensing, Strasbourg, France, doi: 10.1117/12.2532577.

Carrino, T. A., Crósta, A. P., Toledo, C. L. B., & Silva, A. M. (2018). Hyperspectral remote sensing applied to mineral exploration in southern Peru: A multiple data integration approach in the Chapi Chiara gold prospect. *International Journal of Applied Earth Observation and Geoinformation, 64*, 287-300. doi: 10.1016/j.jag.2017.05.004.

Clark, R. N., Swayze, G. A., Gallagher, A. J., King, T. V. V., & Calvin, W. M. (1993). *The U. S. Geological Survey, Digital Spectral Library: Version 1 (0.2 to 3.0um)* (93-592). S. Geological, Retrieved from: http://pubs.er.usgs.gov/publication/ofr93592.

Cousin, A., Sautter, V., Fabre, C., Maurice, S., & Wiens, R. C. (2012). Textural and modal analyses of picritic basalts with ChemCam Laser-Induced Breakdown Spectroscopy.

Journal of Geophysical Research: Planets, 117(E10). doi: https://doi.org/10.1029/2012JE004132.

Duke, E. F. (1994). Near infrared spectra of muscovite, Tschermak substitution, and metamorphic reaction progress: Implications for remote sensing. *Geology, 22*(7), 621-624. doi: 10.1130/0091-7613(1994)022<0621:Nisomt>2.3.Co;2.

Fabre, C. (2020). Advances in Laser-Induced Breakdown Spectroscopy analysis for geology: A critical review. *Spectrochimica Acta Part B: Atomic Spectroscopy, 166*, 105799. doi: https://doi.org/10.1016/j.sab.2020.105799.

Farnsworth-Pinkerton, S., McMillan, N. J., Dutrow, B. L., & Henry, D. J. (2018). Provenance of detrital tourmalines from Proterozoic metasedimentary rocks in the Picuris Mountains, New Mexico, using Laser-Induced Breakdown Spectroscopy. *Journal of Geosciences, 63*(2), 193-198.

Fyzollahhi, N., Torshizian, H., Afzal, P., & Jafari, M. R. (2018). Determination of lithium prospects using fractal modeling and staged factor analysis in Torud region, NE Iran. *Journal of Geochemical Exploration, 189*, 2-10. doi: https://doi.org/10.1016/j.gexplo.2017.09.017.

Galeschuk, C. R., & Vanstone, P. J. (2007). Exploration techniques for rare-element pegmatite in the Bird River greenstone belt, southeastern Manitoba. In B. Milkereit (Ed.), *Proceedings of Exploration 07: Fifth Decennial International Conference on Mineral Exploration* (pp. 823–839).

Gaspar, L. M., & Inverno, C. M. C. (2000). Mineralogy and Metasomatic Evolution of Distal Strata-Bound Scheelite Skarns in the Riba de Alva Mine, Northeastern Portugal. *Economic Geology, 95*(6), 1259-1275. doi: 10.2113/gsecongeo.95.6.1259.

Hunt, G. R., & Ashley, R. P. (1979). Spectra of altered rocks in the visible and near infrared. *Economic Geology, 74*(7), 1613-1629. doi: 10.2113/gsecongeo.74.7.1613.

Kochelek, K. A., McMillan, N. J., McManus, C. E., & Daniel, D. L. (2015). Provenance determination of sapphires and rubies using laser-induced breakdown spectroscopy and multivariate analysis. *American Mineralogist, 100*(8-9), 1921-1931. doi: doi:10.2138/am-2015-5185.

Laakso, K., Rivard, B., Peter, J. M., White, H. P., Maloley, M., Harris, J., & Rogge, D. (2015). Application of Airborne, Laboratory, and Field Hyperspectral Methods to Mineral Exploration in the Canadian Arctic: Recognition and Characterization of Volcanogenic Massive Sulfide-Associated Hydrothermal Alteration in the Izok Lake Deposit Area,

Nunavut, Canada. *Economic Geology, 110*(4), 925-941. doi: 10.2113/econgeo.110.4.925.

Lypaczewski, P., Rivard, B., Gaillard, N., Perrouty, S., Piette-Lauzière, N., Bérubé, C. L., & Linnen, R. L. (2019). Using hyperspectral imaging to vector towards mineralization at the Canadian Malartic gold deposit, Québec, Canada. *Ore Geology Reviews, 111*, 102945. doi: https://doi.org/10.1016/j.oregeorev.2019.102945.

Martins, T., Linnen, R. L., Fedikow, M. A. F., & Singh, J. (2017). Whole-rock and mineral geochemistry as exploration tools for rare-element pegmatite in Manitoba: examples from the Cat Lake–Winnipeg River and Wekusko Lake pegmatite fields (parts of NTS 52L6, 63J13). In *Report of Activities 2017* (pp. 42–51). Manitoba Growth, Enterprise and Trade, Manitoba Geological Survey.

Maxwell, A. E., Warner, T. A., & Fang, F. (2018). Implementation of machine-learning classification in remote sensing: an applied review. *International Journal of Remote Sensing, 39*(9), 2784-2817. doi: 10.1080/01431161.2018.1433343.

McMillan, N. J., Rees, S., Kochelek, K., & McManus, C. (2014). Geological Applications of Laser-Induced Breakdown Spectroscopy. *Geostandards and Geoanalytical Research, 38*(3), 329-343. doi: https://doi.org/10.1111/j.1751-908X.2014.00308.x.

Morgan, G. B., & London, D. (1987). Alteration of amphibolitic wallrocks around the Tanco rare-element pegmatite, Bernic Lake, Manitoba. *American Mineralogist, 72*(11-12), 1097-1121.

Naleto, J. L. C., Perrotta, M. M., Costa, F. G. d., & Souza Filho, C. R. d. (2019). Point and imaging spectroscopy investigations on the Pedra Branca orogenic gold deposit, Troia Massif, Northeast Brazil: Implications for mineral exploration in amphibolite metamorphic-grade terrains. *Ore Geology Reviews, 107*, 283-309. doi: https://doi.org/10.1016/j.oregeorev.2019.02.019.

Noi, P. T., & Kappas, M. (2017). Comparison of Random Forest, k-Nearest Neighbor, and Support Vector Machine Classifiers for Land Cover Classification Using Sentinel-2 Imagery. *Sensors (Basel), 18*(1). doi: 10.3390/s18010018.

Pour, A. B., & Hashim, M. (2018). Hydrothermal alteration mapping from Landsat-8 data, Sar Cheshmeh copper mining district, south-eastern Islamic Republic of Iran. *Journal of Taibah University for Science, 9*(2), 155-166. doi: 10.1016/j.jtusci.2014.11.008.

Rivard, B., Zhang, J., Feng, J., & Sanchez-Azofeifa, G. A. (2009). Remote predictive lithologic mapping in the Abitibi Greenstone Belt, Canada, using airborne

hyperspectral imagery. *Canadian Journal of Remote Sensing, 35*(sup1), S95-S105. doi: 10.5589/m10-002.

Saadati, H., Afzal, P., Torshizian, H., & Solgi, A. (2020). Geochemical exploration for lithium in NE Iran using the geochemical mapping prospectivity index, staged factor analysis, and a fractal model. *Geochemistry: Exploration, Environment, Analysis, 20*(4), 461-472. doi: 10.1144/geochem2020-020.

Shearer, C. K., Papike, J. J., Simon, S. B., & Laul, J. C. (1986). Pegmatite-wallrock interactions, Black Hills, South Dakota: interaction between pegmatite-derived fluids and quartz-mica schist wallrock. *Am. Mineral.; (United States)*, Medium: X; Size: Pages: 518-539.

Shearer, C. K., Papike, J. J., Simon, S. B., Laul, J. C., & Christian, R. P. (1984). Pegmatite/wallrock interactions, Black Hills, South Dakota: Progressive boron metasomatism adjacent to the Tip Top pegmatite. *Geochimica et Cosmochimica Acta, 48*(12), 2563-2579.

Steiner, B. M., Rollinson, G. K., & Condron, J. M. (2019). An Exploration Study of the Kagenfels and Natzwiller Granites, Northern Vosges Mountains, France: A Combined Approach of Stream Sediment Geochemistry and Automated Mineralogy. *Minerals, 9*(12), 750. doi: 10.3390/min9120750.

Tappert, M. C., Rivard, B., Giles, D., Tappert, R., & Mauger, A. (2013). The mineral chemistry, near-infrared, and mid-infrared reflectance spectroscopy of phengite from the Olympic Dam IOCG deposit, South Australia. *Ore Geology Reviews, 53*, 26-38. doi: https://doi.org/10.1016/j.oregeorev.2012.12.006.

Teodoro, A. C., & Veloso-Gomes, F. (2007). Quantification of the Total Suspended Matter Concentration around the Sea Breaking Zone from In Situ Measurements and Terra/Aster Data. *Marine Georesources & Geotechnology, 25*(2), 67-80. doi: 10.1080/10641190701334164.

Van Der Meer, F. (2000). Spectral curve shape matching with a continuum removed CCSM algorithm. *International Journal of Remote Sensing, 21*(16), 3179-3185. doi: 10.1080/01431160050145063.

Vieira, R. (2010). *Aplitopegmatitos com elementos raros da região entre Almendra (V.N. de Foz Côa) e Barca d'Alva (Figueira de Castelo Rodrigo). Campo aplitopegmatítico da Fregeneda- Almendra.* (PhD thesis), Faculdade de Ciências da Universidade do Porto, Porto, Portugal, XXVI, 273.

Conclusions

1. After analyzing the past achievements made in Li-exploration using remote sensing methods and the main weaknesses of the approaches, it is expected that the number of studies concerning this topic will increase in the future and that remote sensing data/techniques will become an integrated and fundamental tool in the exploration of several types of Li-deposits.
2. The new methodological advances proposed to improve the SVM performance and decrease overfitting were successful in maximizing the discrimination of Li-pegmatites from the metasedimentary host rocks and identifying known Li-pegmatite occurrences as well as other target areas for Li-exploration.
3. The careful collection and construction of spectral libraries and large datasets proved to be essential, not only to validate previous results but also as a starting point for the development of new applications, allowing to have a better characterization of the specific signatures of Li-mineralization.
4. The interpretation of key reference spectra allowed to conclude that only lepidolite has diagnostic spectral features since the spectral curves of petalite and spodumene are dominated by clays. Nonetheless, the analysis of the spectral behavior of the different lithologies indicates that there is great potential to discriminate Li-pegmatites using hyperspectral sensors, which may aid in new discoveries around the world.
5. Geochemical tools can be employed to overcome the limitations of remote sensing techniques, namely the identification of buried or vegetation-covered pegmatites. The analysis of stream sediment samples allowed to identify pegmatites mineralized or with high Li potential. Distinct methodological approaches are more or less suitable depending on the exploration stage, while portable tools are fundamental to expedite field campaigns.
6. Pegmatite intrusion produced considerable enrichments in F, B, Li, Rb, Cs, Sn, Be, and Tl in the metasedimentary host rocks that can reach up to 4–5 times the thickness of the dykes. The size of the halo and degree of enrichment of certain elements is dependent on the pegmatite type. Such haloes can be used to identify buried pegmatites through analysis of fresh samples in the field using portable tools. The possibility to discriminate these haloes with remote sensing data needs to be evaluated in the future.
7. The integration of remote sensing data with key geological and geochemical features enabled the production of Li-target explorations maps and the identification of the

areas with the highest potential for Li-mineralization through MPM. Field campaigns are needed to check these high potential areas for the occurrence of unknown mineralization.

8. Overall, the proposed objectives for this thesis were fulfilled and new insights for Li-exploration were provided, thus allowing to contribute for increased efficiency and sustainability of mineral exploration. These outcomes have an important impact on the state of the art of Li-exploration and are of interest to exploration companies. Nonetheless, there is still room for new developments and improvements in this field and future studies should be conducted to address the open questions previously highlighted.

References

Introduction

Abrams, M., & Yamaguchi, Y. (2019). Twenty Years of ASTER Contributions to Lithologic Mapping and Mineral Exploration. *Remote Sensing, 11*(11), 1394.

Arrobas, D. L. P., Hund, K. L., Mccormick, M. S., Ningthoujam, J., & Drexhage, J. R. (2017). *The Growing Role of Minerals and Metals for a Low Carbon Future*. Washington, DC, USA: The World Bank,

Bea, F., Fershtater, G. & Corretgé, L. G. (1992). The geochemistry of phosphorus in granite rocks and effect of aluminium. *Lithos*, 29: 43–56. In: Vieira, R. (2010). Aplitopegmatitos com Elementos Raros da Região entre Almendra (V. N. de Foz-Côa) e Barca d'Alva (Figueira de Castelo Rodrigo). Campo Aplitopegmatítico da Fregeneda-Almendra. *phD Thesis*. Universidade do Porto, Portugal, p. 276.

Blengini, G. A., Latunussa, C. E. L., Eynard, U., Torres de Matos C., Wittmer, D., Georgitzikis, K., Pavel, C., Carrara, S., Mancini, L., Unguru, M., Blagoeva, D., Mathieux, F. & Pennington D. (2020). Study on the EU's list of Critical Raw Materials Final Report. *European Commission.* https://doi.org/10.2873/11619

Cardoso-Fernandes, J., Lima, A., Roda-Robles, E., & Teodoro, A. C. (2019a). Constraints and potentials of remote sensing data/techniques applied to lithium (Li)-pegmatites. *The Canadian Mineralogist, 57*(5), 723-725. doi: 10.3749/canmin.AB00004.

Cardoso-Fernandes, J., Silva, J., Dias, F., Lima, A., Teodoro, A. C., Barrès, O., Cauzid, J., Perrotta, M., Roda-Robles, E., & Ribeiro, M. A. (2021a). Tools for Remote Exploration: A Lithium (Li) Dedicated Spectral Library of the Fregeneda–Almendra Aplite–Pegmatite Field. *Data, 6*(3), 33. doi: 10.3390/data6030033.

Cardoso-Fernandes, J., Silva, J., Lima, A., Teodoro, A. C., Perrotta, M., Cauzid, J., & Roda-Robles, E. (2020a). *Characterization of lithium (Li) minerals from the Fregeneda-Almendra region through laboratory spectral measurements: a comparative study.* Paper presented at the SPIE Remote Sensing, Earth Resources and Environmental Remote Sensing/GIS Applications XI, doi: https://doi.org/10.1117/12.2573941.

Cardoso-Fernandes, J., Silva, J., Lima, A., Teodoro, A. C., Perrotta, M., Cauzid, J., Roda-Robles, E., & Ribeiro, M. A. (2020b). *Reflectance spectroscopy to validate remote sensing data/algorithms for satellite-based lithium (Li) exploration (Central East Portugal).* Paper

presented at the SPIE Remote Sensing, Earth Resources and Environmental Remote Sensing/GIS Applications XI, doi: https://doi.org/10.1117/12.2573929.

Cardoso-Fernandes, J., Silva, J., Perrotta, M. M., Lima, A., Teodoro, A. C., Ribeiro, M. A., Dias, F., Barrès, O., Cauzid, J., & Roda-Robles, E. (2021b). Interpretation of the Reflectance Spectra of Lithium (Li) Minerals and Pegmatites: A Case Study for Mineralogical and Lithological Identification in the Fregeneda–Almendra Area. *Remote Sensing, 13*(18), 3688. doi: 10.3390/rs13183688.

Cardoso-Fernandes, J., Teodoro, A. C., Lima, A., & Roda Robles, E. (2020f, 26 Sept.-2 Oct. 2020). *Lithium (Li) pegmatite mapping using Artificial Neural Networks (ANNs): preliminary results.* Paper presented at the IGARSS 2020 - 2020 IEEE International Geoscience and Remote Sensing Symposium, Waikoloa, HI, USA, 557-560. doi: 10.1109/IGARSS39084.2020.9323852.

Cardoso-Fernandes, J., Teodoro, A. C., Lima, A., & Roda-Robles, E. (2019b, 9–12 September 2019). *Evaluating the performance of support vector machines (SVMs) and random forest (RF) in Li-pegmatite mapping: preliminary results.* Paper presented at the SPIE Remote Sensing, Strasbourg, France, doi: 10.1117/12.2532577.

Cardoso-Fernandes, J., Teodoro, A. C., Lima, A., & Roda-Robles, E. (2020e). Semi-Automatization of Support Vector Machines to Map Lithium (Li) Bearing Pegmatites. *Remote Sensing, 12*(14), 2319. doi: 10.3390/rs12142319.

Cardoso-Fernandes, J., Teodoro, A. C., Lima, A., Mielke, C., Körting, F., Roda-Robles, E., & Cauzid, J. (2020c, 26 Sept.-2 Oct. 2020). *Multi-scale approach using remote sensing techniques for lithium pegmatite exploration: first results.* Paper presented at the IGARSS 2020 - 2020 IEEE International Geoscience and Remote Sensing Symposium, Waikoloa, HI, USA, 5226-5229. doi: 10.1109/IGARSS39084.2020.9323705.

Cardoso-Fernandes, J., Teodoro, A. C., Lima, A., Perrotta, M., & Roda-Robles, E. (2020d). Detecting Lithium (Li) Mineralizations from Space: Current Research and Future Perspectives. *Applied Sciences, 10*(5), 1785. doi: 10.3390/app10051785.

Carnicero, M. A. (1981). Granitoides del Centro Oeste de la Provincia de Salamanca. Clasificación y correlación. *Cuad. Lab. Xeol. Laxe,* 2: 45–49. In: Vieira, R. (2010). Aplitopegmatitos com Elementos Raros da Região entre Almendra (V. N. de Foz-Côa) e Barca d'Alva (Figueira de Castelo Rodrigo). Campo Aplitopegmatítico da Fregeneda-Almendra. *phD Thesis*. Universidade do Porto, Portugal, p. 276.

Carvalhosa, A., 1960. Carta Geológica de Portugal na escala 1/50.000 – folha 15-D – Figueira de Castelo Rodrigo. Serviços Geológicos de Portugal, Lisboa, Portugal.

Černý, P., & Ercit, T. S. (2005). Classification of granitic pegmatites revisited. *Can. Mineral., 43*, 2005–2026.

Christmann, P., Gloaguen, E., Labbé, J.-F., Melleton, J., & Piantone, P. (2015). Chapter 1 - Global Lithium Resources and Sustainability Issues. In A. Chagnes & J. Światowska (Eds.), *Lithium Process Chemistry* (pp. 1-40). Amsterdam: Elsevier.

Costa, J. C. S. d. (1950). *Notícia sobre uma carta geológica do Buçaco, de Nery Delgado*. Lisboa, Portugal: Serviços Geológicos de Portugal,

Dallmeyer, R. D., Catalán, J. R. M., Arenas, R., Gil Ibarguchi, J. I., Gutiérrez, Alonso, G., Farias, P., Bastida, F., & Aller, J. (1997). Diachronous Variscan tectonothermal activity in the NW Iberian Massif: Evidence from 40Ar/39Ar dating of regional fabrics. *Tectonophysics, 277*(4), 307-337. doi: https://doi.org/10.1016/S0040-1951(97)00035-8.

Dias da Silva, Í., Gómez-Barreiro, J., Martínez Catalán, J. R., Ayarza, P., Pohl, J., & Martínez, E. (2017). Structural and microstructural analysis of the Retortillo Syncline (Variscan belt, Central Iberia). Implications for the Central Iberian Orocline. *Tectonophysics, 717*, 99-115. doi: https://doi.org/10.1016/j.tecto.2017.07.015.

Dias, G., Noronha, F., & Ferreira, N. (2000). Variscan Plutonism in the Central Iberian Zone, Northern Portugal. In *Eurogranites 2000, Field Meeting, Guide Book* (pp. 1-15).

Díez Balda, M. A., Vegas, R., & Lodeiro, G. (1990). Central Iberian Zone: structure. In R. D. Dallmeyer & E. Martinez Garcia (Eds.), *Pre-Mesozoic geology of the Iberian Peninsula* (pp. 172–188). Berlim: Springer Verlag.

European Commission: DG Internal Market Industry Entrepreneurship and SMEs. (2020). *Critical Raw Materials Resilience: Charting a Path towards greater Security and Sustainability* (COM(2020) 474 final). Brussels. Retrieved from: https://eur-lex.europa.eu/legal-content/EN/ALL/?uri=COM:2020:474:FIN

Fabre, C., Ourti, N. E., Mercadier, J., Cardoso-Fernandes, J., Dias, F., Perrotta, M., Koerting, F., Lima, A., Kaestner, F., Koellner, N., Linnen, R., Benn, D., Martins, T., & Cauzid, J. (2021). Analyses of Li-Rich Minerals Using Handheld LIBS Tool. *Data, 6*(6), 68. doi: 10.3390/data6060068.

Ferreira, J. A., Bento dos Santos, T., Pereira, I., & Mata, J. (2019). Tectonically assisted exhumation and cooling of Variscan granites in an anatectic complex of the Central Iberian

Zone, Portugal: constraints from LA-ICP-MS zircon and apatite U–Pb ages. *International Journal of Earth Sciences, 108*(7), 2153-2175. doi: 10.1007/s00531-019-01755-1.

Ferreira, J. A., Mata, J., Bento dos Santos, T., & Pereira, I. (2020). The role of melting on the geochemical evolution and isotopic variability of an anatectic complex in the Iberian Variscides. *Lithos, 378-379*, 105769. doi: https://doi.org/10.1016/j.lithos.2020.105769.

Galeschuk, C. R., & Vanstone, P. J. (2007). Exploration techniques for rare-element pegmatite in the Bird River greenstone belt, southeastern Manitoba. In B. Milkereit (Ed.), *Proceedings of Exploration 07: Fifth Decennial International Conference on Mineral Exploration* (pp. 823–839).

Gaspar, L. (1997). *Contribuição para o estudo das mineralizações de volfrâmio (W), estanho (Sn) e lítio (Li) do sector Barca de Alva – Escalhão.* (Master thesis), Faculdade de Ciências da Universidade de Lisboa, Portugal, 267.

Gourcerol, B., Gloaguen, E., Melleton, J., Tuduri, J., & Galiegue, X. (2019). Re-assessing the European lithium resource potential – A review of hard-rock resources and metallogeny. *Ore Geology Reviews, 109*, 494-519. doi: https://doi.org/10.1016/j.oregeorev.2019.04.015.

Grosjean, C., Miranda, P. H., Perrin, M., & Poggi, P. (2012). Assessment of world lithium resources and consequences of their geographic distribution on the expected development of the electric vehicle industry. *Renewable and Sustainable Energy Reviews, 16*(3), 1735-1744. doi: https://doi.org/10.1016/j.rser.2011.11.023.

Gutiérrez-Alonso, G., Fernández-Suárez, J., Jeffries, T. E., Jenner, G. A., Tubrett, M. N., Cox, R., & Jackson, S. E. (2003). Terrane accretion and dispersal in the northern Gondwana margin. An Early Paleozoic analogue of a long-lived active margin. *Tectonophysics, 365*(1), 221-232. doi: https://doi.org/10.1016/S0040-1951(03)00023-4.

Gutiérrez-Alonso, G., Fernández-Suárez, J., López-Carmona, A., & Gärtner, A. (2018). Exhuming a cold case: The early granodiorites of the northwest Iberian Variscan belt—A Visean magmatic flare-up? *Lithosphere, 10*(2), 194-216. doi: 10.1130/l706.1.

Iglésias, M. & Ribeiro, A. (1981a). Zones de cisaillement ductile dans l'arc Ibéro-Armoricain. *Comun. Serv. Geol. Portugal*, 67 (1): 85–88.

Iglésias, M., & Ribeiro, A., (1981b). Position stratigraphique de la formation Ollo de Sapo dans la region de Zamora (Espagne) – Miranda do Douro (Portugal). *Comun. Serv. Geol. Portugal*, 67 (1): 141–146.

Julivert, M., Fontboté, J., Ribeiro, A., & Conde, L. (1974). Memória explicativa del Mapa Tectónico de la Península Ibérica y Baleares. Esc.: 1/ 1000000. In*st. Geol. Min. España,* Madrid. 133 pp.

Kesselring, M., Wagner, F., Kirsch, M., Ajjabou, L., & Gloaguen, R. (2020). Development of Sustainable Test Sites for Mineral Exploration and Knowledge Spillover for Industry. *Sustainability, 12*(5), 2016. doi: 10.3390/su12052016.

Köhler, M., Hanelli, D., Schaefer, S., Barth, A., Knobloch, A., Hielscher, P., Cardoso-Fernandes, J., Lima, A., & Teodoro, A. C. (2021). Lithium Potential Mapping Using Artificial Neural Networks: A Case Study from Central Portugal. *Minerals, 11*(10), 1046. doi: 10.3390/min11101046.

López-Plaza, M., Carnicero, A., & Gonzalo, J. C. (1982). Estudio geológico del campo filoniano de La Fregeneda (Salamanca). *STUDIA GEOLOGICA SALMANTICENSIA, XVII*, 89-98.

Martínez Catalán, J. R., Martínez Poyatos, D., Bea, F., & (Coords.). (2004). Zona Centroibérica: Introducción. In J. A. Vera (Ed.), *Geología de España* (pp. 68-69). Madrid: Sociedad Geológica de España/ Instituto Geológico y Minero de España (SGE-IGME).

Martínez Catalán, J. R., Rubio Pascual, F. J., Montes, A. D., Fernández, R. D., Barreiro, J. G., Dias Da Silva, Í., Clavijo, E. G., Ayarza, P., Alcock, J. E., Schulmann, K., Martínez Catalán, J. R., Lardeaux, J. M., Janoušek, V., & Oggiano, G. (2014). The late Variscan HT/LP metamorphic event in NW and Central Iberia: relationships to crustal thickening, extension, orocline development and crustal evolution. In *The Variscan Orogeny: Extent, Timescale and the Formation of the European Crust* (Vol. 405, pp. 0): Geological Society of London.

Martínez, F. J., Corretgé, L. G. & Suárez, O. (1990). The Central Iberian Zone (autochthonous sequences): distribution, characteristics and evolution of metamorphism. In: R. D. Dallmeyer & E. Martínez García (Eds), Pre-Mesozoic Geology of Iberia. Springer-Verlag. Berlim. p. 207–211.

Martín-Izard, A., Reguilón, R., & Palero, F. (1992). Las mineralizaciones litiníferas del oeste de Salamanca y Zamora. *Estudios Geológicos, 48*, 19-30.

Martins, T., Linnen, R. L., Fedikow, M. A. F., & Singh, J. (2017). Whole-rock and mineral geochemistry as exploration tools for rare-element pegmatite in Manitoba: examples from the Cat Lake–Winnipeg River and Wekusko Lake pegmatite fields (parts of NTS 52L6, 63J13). In *Report of Activities 2017* (pp. 42–51). Manitoba Growth, Enterprise and Trade, Manitoba Geological Survey.

Noronha, F., Ramos, J. M. F., Rebelo, J. A., Ribeiro, A., & Ribeiro, M. L. (1979). Essai de corrélation des phases de déformation hercynienne dans le Nord-Ouest Péninsulaire. *Bol. Soc. Geol. Portugal, 21*(2-3), 227-237.

Pereira, E. (1987). Estudo geológico estrutural da região de Celorico de Bastos e sua interpretação geodinâmica. *PhD thesis.* Fac. Ciências Univ. de Lisboa. 274 p. In: Dias, R., Ribeiro, A., Coke, C., Pereira, E., Rodrigues, J., Castro, P., Moreira, N., Rebelo, J. (2013). Evolução estrutural dos sectores setentrionais do Autóctone da Zona Centro-Ibérica. In: Dias, R., Araújo, A., terrinha, P., Kullberg, J.C. (Eds). *Geologia de Portugal. Volume I – Geologia Pré-mesozóica de Portugal*, Escolar Editora. pp. 73-147.

Pereira, E., Ribeiro, A. & Meireles, C. (1993). Cisalhamentos Hercínicos e controlo das mineralizações de Sn-W, Au e U na Zona Centro Ibérica, em Portugal. *Cuaderno Lab. Xeolóxico de Laxe*. Coruña. Vol. 18, pp.89-119.

Pereira, I., Dias, R., Bento dos Santos, T., & Mata, J. (2017). Exhumation of a migmatite complex along a transpressive shear zone: inferences from the Variscan Juzbado–Penalva do Castelo Shear Zone (Central Iberian Zone). *Journal of the Geological Society, 174*(6), 1004. doi: 10.1144/jgs2016-159.

Pereira, M. F., Díez Fernández, R., Gama, C., Hofmann, M., Gärtner, A., & Linnemann, U. (2018). S-type granite generation and emplacement during a regional switch from extensional to contractional deformation (Central Iberian Zone, Iberian autochthonous domain, Variscan Orogeny). *International Journal of Earth Sciences, 107*(1), 251-267. doi: 10.1007/s00531-017-1488-3.

Pérez-Estaún, A., Bea, F., Bastida, F., Marcos, A., Martínez Catalán, J. R., Martínez Poyatos, D., Arenas, R., Díaz García, F., Azor, A., Simancas, J. F., & González Lodeiro, F. (2004). La cordillera varisca europea: el Macizo Ibérico. In J. A. Vera (Ed.), *Geología de España* (pp. 21-25). Madrid: Sociedad Geológica de España/ Instituto Geológico y Minero de España (SGE-IGME).

Ribeiro, A. (1974). Contribution à l'étude tectonique de Trás-os-Montes oriental. *Mem. Serv. Geol. Portugal, Lisboa*, 24 (Nova Série). 168 p.

Ribeiro, A. (1990). Part IV – Central-Iberian Zone. Introduction. In: Dallmeyer, R. D. & Martinez Garcia, E. (Eds.) *Pre-Mesozoic Geology of Iberia*, Springer-Verlag, Berlin, Heidelberg, pp. 143-144.

Ribeiro, A., Antunes, M., Ferreira, M., Rocha, R., Soares, A., Zbyszewski, G., Almeida, F., Carvalho, D. & Monteiro, J. (1979). Introduction à la Géologie Générale du Portugal. *Serv. Geol. Portugal*, Lisboa.114 p.

Ribeiro, A., Pereira, E. & Dias, R. (1990). Structure in the Northwest of the Iberian Peninsula. In: Dallmeyer, R.D. & Martinez Garcia, E. (Eds.): *Pre-Mesozoic Geology of Iberia*, Springer-Verlag, Berlin, Heidelberg, pp. 220-236.

Ribeiro, A., Pereira, E., & Rodrigues, J. (2006). Tectónica. In: Pereira, E. (Coord.), Carta Geológica de Portugal na escala 1:200000 – Notícia explicativa da Folha 2, Lisboa, *Serv. Geol. Portugal*, 69-76.

Ribeiro, M. L. (2001). *Notícia explicativa da carta geológica simplificada do Parque Arqueológico do Vale do Côa*. Vila Nova de Foz Côa, Portugal: Parque Arqueológico do Vale do Côa, 71.

Ribeiro, M.L., Silva, A.F., 2000. Carta Geológica Simplificada do Parque Arqueológico do Vale do Côa. Instituto Geológico e Mineiro and Parque Arqueológico do Vale do Côa, Vila Nova de Foz Côa, Portugal.

Roda, E. (1993). *Distribución, Caracteristicas y Petrogenesis de las Pegmatitas de La Fregeneda (Salamanca).* (PhD thesis), Facultad de Ciencia y Tecnología de la Universidad del País Vasco (UPV/EHU), Bilbao, Spain, 199.

Roda-Robles, E., Pesquera, A., Gil-Crespo, P. P., Vieira, R., Lima, A., Garate-Olave, I., Martins, T., & Torres-Ruiz, J. (2016). Geology and mineralogy of Li mineralization in the Central Iberian Zone (Spain and Portugal). *Mineralogical Magazine, 80*(1), 103-126. doi: 10.1180/minmag.2016.080.049.

Roda-Robles, E., Pesquera, A., Velasco, F., & Fontan, F. (1999). The granitic pegmatites of the Fregeneda area (Salamanca, Spain): characteristics and petrogenesis. *Mineral. Mag., 63*(4), 535–558.

Roda-Robles, E., Villaseca, C., Pesquera, A., Gil-Crespo, P. P., Vieira, R., Lima, A., & Garate-Olave, I. (2018). Petrogenetic relationships between Variscan granitoids and Li-(F-P)-rich aplite-pegmatites in the Central Iberian Zone: Geological and geochemical constraints and implications for other regions from the European Variscides. *Ore Geology Reviews, 95*, 408-430. doi: https://doi.org/10.1016/j.oregeorev.2018.02.027.

Rodrigues, J., Pereira, E., & Ribeiro, A. (2011). Complexo de Mantos Parautóctones do NE de Portugal: Estrutura interna e Tectonoestratigrafia. In: Dias, R., Araújo, A., terrinha, P., Kullberg,

J.C. (Eds). *Geologia de Portugal. Volume I – Geologia Pré-mesozóica de Portugal*, Escolar Editora. pp. 269-325.

Rodríguez Alonso, M. D., Díez Balda, M. A., Perejón, A., Pieren, A., Liñán, E., López Díaz, F., Moreno, F., Gámez Vintaned, J. A., Gónzalez Lodeiro, F., Martínez Poyatos, D., & Vegas, R. (2004). Domínio del Complejo Esquisto-Grauváquico: Estratigrafía. La secuencia litoestratigráfica del Neoproterozóico-Câmbrico Inferior. In J. A. Vera (Ed.), *Geología de España* (pp. 78-81). Madrid: Geol. España/Inst. Geol. Min. España (SGE-IGME).

Rodríguez Fernández, L. R., Díez Montes, A., Escuder, J. & Carrasco, R. (2000). Hoja geológica número 448 (Vilvestre). Mapa Geológico de España a Escala 1:50.000 (2ª serie). Madrid: Instituto Geológico y Minero de España (IGME). Retrieved from http://info.igme.es/cartografiadigital/geologica/Magna50Hoja.aspx?intranet=false&id=448B

Ruiz-Coupeau, S., Jürgens, B., Keßelring, M., & Herrero-Solana, V. (2020). Sustainability in Mineral Exploration—Exploring Less Invasive Technologies via Patent Analysis. *Sustainability, 12*(22), 9761. doi: 10.3390/su12229761.

Sabins, F. F. (1999). Remote sensing for mineral exploration. *Ore Geology Reviews, 14*(3), 157-183. doi: https://doi.org/10.1016/S0169-1368(99)00007-4.

San José, M. A., Pieren, A. P., Garcia-Hidalgo, J. F., Vilas, L., Herranz, P., Pelaez, J. R., & Perejon, A. (1990). Central Iberian Zone. Autochthonous sequences: Ante-Ordovician stratigraphy. In R. D. Dallmeyer & E. Martinez Garcia (Eds.), *Pre-Mesozoic Geology of Iberia* (pp. 147- 159). Berlin, Heidelberg: Springer-Verlag.

Santos, D., Teodoro, A., Lima, A., & Cardoso-Fernandes, J. (2019, 9–12 September 2019). *Remote sensing techniques to detect areas with potential for lithium exploration in Minas Gerais, Brazil.* Paper presented at the SPIE Remote Sensing, Strasbourg, France, doi: https://doi.org/10.1117/12.2532744.

Silva, A. F. d., & Ribeiro, M. L. (1991). *Notícia Explicativa da folha 15-A Vila Nova de Foz Côa*. Lisboa, Portugal: Serviços Geológicos de Portugal, 52.

Silva, A. F. d., & Ribeiro, M. L. (1994). *Notícia Explicativa da folha 15-B Freixo de Espada à Cinta*. Lisboa, Portugal: Instituto Geológico e Mineiro, 48.

Silva, A. F., Santos, A. J., Ribeiro, A., & Ribeiro, M. L. (1990b). *Carta Geológica de Portugal na escala 1/50.000 – folha 15-A – Vila Nova de Foz Côa*. Lisboa, Portugal: Serviços Geológicos de Portugal, 1 map.

Silva, A. F., Santos, A. J., Ribeiro, A., Cabral, J., & Ribeiro, M. L. (1990a). *Carta Geológica de Portugal na escala 1/50.000 – folha 15-B – Freixo de Espada à Cinta*. Lisboa, Portugal: Serviços Geológicos de Portugal, 1 map.

Silva, I. (2013). *Geología de las zonas Centro Ibérica y Galicia – Trás-Os-Montes en la parte oriental del Complejo de Morais.* (phD thesis), Universidad de Salamanca, Spain, Portugal/España, 445.

Sousa, M. B. (1982). *Litostratigrafia e estrutura do "Complexo Xisto-Grauváquico Ante-Ordovícico" – Grupo do Douro (Nordeste de Portugal).* (PhD thesis), Centro de Geociências da Universidade de Coimbra, Coimbra, Portugal, 222.

Sousa, M. B. (1983). Considerações paleogeográficas e ensaio de correlação das formações do Grupo do Douro (CXG) com as formações ante-Ordovícicas da Zona Centro-Ibérica. *Memórias e Notícias, Publicações do Museu e Laboratório Mineralógico e Geológico da Universidade de Coimbra, 65*, 65-98.

Sousa, M. B. (1984). Considerações sobre a estratigrafia do Complexo Xisto-Grauváquico (CXG) e sua relação com o Paleozóico Inferior. *Cuadernos de Geología Ibérica, 9*, 9-36.

Teixeira, C. (1955). *Notas sobre geologia de Portugal o complexo xisto-grauváquico ante-ordoviciano*. Lisboa, Portugal: Empresa Literaria Fluminense Lda., 48.

Valladares, M. I., Ugidos, J. M., Barba, P., & Colmenero, J. R. (2002). Contrasting geochemical features of the Central Iberian Zone shales (Iberian Massif, Spain): implications for the evolution of Neoproterozoic–Lower Cambrian sediments and their sources in other peri-Gondwanan areas. *Tectonophysics, 352*(1), 121-132. doi: https://doi.org/10.1016/S0040-1951(02)00192-0.

Valle Aguado, B., Azevedo, M. R., Nolan, J., Medina, J., Costa, M. M., Corfu, F., & Martínez Catalán, J. R. (2017). Granite emplacement at the termination of a major Variscan transcurrent shear zone: The late collisional Viseu batholith. *Journal of Structural Geology, 98*, 15-37. doi: https://doi.org/10.1016/j.jsg.2017.04.002.

Van der Werff, H., & Van der Meer, F. (2016). Sentinel-2A MSI and Landsat 8 OLI Provide Data Continuity for Geological Remote Sensing. *Remote Sensing, 8*(11), 883. doi: 10.3390/rs8110883.

Viegas, L. (1983). *Recursos minerais de volfrâmio e estanho na região de Freixo-Escalhão*. Relatório interno do Serviço de Fomento Mineiro. Porto, 45. (Unpublished).

Vieira, R. (2010). *Aplitopegmatitos com elementos raros da região entre Almendra (V.N. de Foz Côa) e Barca d'Alva (Figueira de Castelo Rodrigo). Campo aplitopegmatítico da Fregeneda- Almendra.* (PhD thesis), Faculdade de Ciências da Universidade do Porto, Porto, Portugal, XXVI, 273.

Vieira, R., Roda-Robles, E. n., Pesquera, A., & Lima, A. (2011). Chemical variation and significance of micas from the Fregeneda-Almendra pegmatitic field (Central-Iberian Zone, Spain and Portugal). *American Mineralogist, 96*(4), 637-645. doi: 10.2138/am.2011.3584.

Villaseca, C. (2011). *On the origin of granite types in the Central Iberian Zone: contribution from integrated U-Pb and Hf isotope studies of zircon.* Paper presented at the VIII Congresso Ibérico de Geoquímica, Castelo Branco, Portugal, 271–276.

Villaseca, C., Merino, E., Oyarzun, R., Orejana, D., Pérez-Soba, C., & Chicharro, E. (2014). Contrasting chemical and isotopic signatures from Neoproterozoic metasedimentary rocks in the Central Iberian Zone (Spain) of pre-Variscan Europe: Implications for terrane analysis and Early Ordovician magmatic belts. *Precambrian Research, 245*, 131-145. doi: https://doi.org/10.1016/j.precamres.2014.02.006.

Chapter I: State of the art

Abbaszadeh, M.; Hezarkhani, A. Enhancement of hydrothermal alteration zones using the spectral feature fitting method in Rabor area, Kerman, Iran. *Arab. J. Geosci.* 2011, *6*, 1957–1964.

Abrams, M.; Yamaguchi, Y. Twenty years of ASTER contributions to lithologic mapping and mineral exploration. *Remote Sens.* 2019, *11*, 1394.

Ali, A.; Pour, A. Lithological mapping and hydrothermal alteration using Landsat 8 data: A case study in ariab mining district, red sea hills, Sudan. *Int. J. Basic Appl. Sci.* 2014, *3*.

Al-Nahmi, F.; Saddiqi, O.; Hilali, A.; Rhinane, H.; Baidder, L.; El arabi, H.; Khanbari, K. Application of remote sensing in geological mapping, case study Al Maghrabah Area—Hajjah Region, Yemen. *ISPRS Ann. Photogramm. Remote Sens. Spat. Inf. Sci.* 2017, 63–71.

Amer, R.; Kusky, T.; El Mezayen, A. Remote sensing detection of gold related alteration zones in Um Rus area, Central Eastern Desert of Egypt. *Adv. Space Res.* 2012, *49*, 121–134.

Arrobas, D.L.P.; Hund, K.L.; Mccormick, M.S.; Ningthoujam, J.; Drexhage, J.R. *The Growing Role of Minerals and Metals for a Low Carbon Future*; The World Bank: Washington, DC, USA, 2017.

Asadzadeh, S.; Souza Filho, C.R. A review on spectral processing methods for geological remote sensing. *Int. J. Appl. Earth Obs. Geoinf.* 2016, *47*, 69–90.

Bahrambeygi, B.; Moeinzadeh, H. Comparison of support vector machine and neutral network classification method in hyperspectral mapping of ophiolite mélanges–A case study of east of Iran. *Egypt. J. Remote Sens. Space Sci.* 2017, *20*, 1–10.

Bedini, E. Mineral mapping in the Kap Simpson complex, central East Greenland, using HyMap and ASTER remote sensing data. *Adv. Space Res.* 2011, *47*, 60–73.

Beiranvand Pour, A.; Park, T.-Y.; Park, Y.; Hong, J.; Zoheir, B.; Pradhan, B.; Ayoobi, I.; Hashim, M. Application of multi-sensor satellite data for exploration of Zn–Pb Sulfide mineralization in the franklinian basin, north greenland. *Remote Sens.* 2018, *10*, 1186.

Belgiu, M.; Drăguţ, L. Random forest in remote sensing: A review of applications and future directions. *ISPRS J. Photogramm. Remote Sens.* 2016, *114*, 24–31.

Berger, B.R.; King, T.V.V.; Morath, L.C.; Philli, J.D. Utility of high-altitude infrared spectral data in mineral exploration: Application to Northern Patagonia Mountains, Arizona. *Econ. Geol.* 2003, *98*, 1003–1018.

Bersi, M.; Saibi, H.; Chabou, M.C. Aerogravity and remote sensing observations of an iron deposit in Gara Djebilet, southwestern Algeria. *J. Afr. Earth Sci.* 2016, *116*, 134–150.

Bishop, C.A.; Liu, J.G.; Mason, P.J. Hyperspectral remote sensing for mineral exploration in Pulang, Yunnan Province, China. *Int. J. Remote Sens.* 2011, *32*, 2409–2426.

Breiman, L. Random forests. *Mach. Learn.* 2001, *45*, 5–32.

Bruzzone, L.; Chi, M.; Marconcini, M. A novel transductive SVM for semisupervised classification of remote-sensing images. *IEEE Trans. Geosci. Remote Sens.* 2006, *44*, 3363–3373.

Cardoso-Fernandes, J. "Detecting Lithium (Li) Mineralizations from Space". In *Scholarly Community Encyclopedia*, 2020. https://encyclopedia.pub/785.

Cardoso-Fernandes, J.; Lima, A.; Roda-Robles, E.; Teodoro, A.C. Constraints and potentials of remote sensing data/techniques applied to lithium (Li)-pegmatites. *Can. Mineral.* 2019, *57*, 723–725. doi: https://doi.org/10.3749/canmin.AB00004

Cardoso-Fernandes, J.; Teodoro, A.C.; Lima, A. Potential of Sentinel-2 data in the detection of lithium (Li)-bearing pegmatites: A study case. In Proceedings of the SPIE, SPIE Remote Sensing, Berlin, Germany, 10–13 September 2018; Michel, U., Schulz, K., Eds.; SPIE: Bellingham, WA, USA, 2018; p. 15.

Cardoso-Fernandes, J.; Teodoro, A.C.; Lima, A. Remote sensing data in lithium (Li) exploration: A new approach for the detection of Li-bearing pegmatites. *Int. J. Appl. Earth Obs. Geoinf.* 2019, *76*, 10–25.

Cardoso-Fernandes, J.; Teodoro, A.C.; Lima, A.; Perrotta, M.; Roda-Robles, E. Detecting Lithium (Li) Mineralizations from Space: Current Research and Future Perspectives. *Appl. Sci.* 2020, *10*, 1785.

Cardoso-Fernandes, J.; Teodoro, A.C.; Lima, A.; Perrotta, M.; Roda-Robles, E. Detecting Lithium (Li) Mineralizations from Space: Current Research and Future Perspectives. *Applied Sciences* 2020, *10* (5), 1785. doi: 10.3390/app10051785.

Cardoso-Fernandes, J.; Teodoro, A.C.; Lima, A.; Roda-Robles, E. Evaluating the performance of support vector machines (SVMs) and random forest (RF) in Li-pegmatite mapping: Preliminary results. In Proceedings of the SPIE, SPIE Remote Sensing, Strasbourg, France, 9–12 September 2019; Schulz, K., Michel, U., Nikolakopoulos, K.G., Eds.; SPIE: Bellingham, WA, USA, 2019.

Carrington da Costa, J.C.S. Notícia sobre uma carta geológica do Buçaco, de Nery Delgado. Serviços Geológicos de Portugal: Lisboa, Portugal, 1950.

Christmann, P.; Gloaguen, E.; Labbé, J.-F.; Melleton, J.; Piantone, P. Chapter 1—Global lithium resources and sustainability issues. In *Lithium Process Chemistry*; Chagnes, A., Światowska, J., Eds.; Elsevier: Amsterdam, The Netherlands, 2015; pp. 1–40.

Ciampalini, A.; Garfagnoli, F.; Antonielli, B.; Moretti, S.; Righini, G. Remote sensing techniques using Landsat ETM+ applied to the detection of iron ore deposits in Western Africa. *Arab. J. Geosci.* 2012, *6*, 4529–4546.

Cloutis, E.A. Review article hyperspectral geological remote sensing: Evaluation of analytical techniques. *Int. J. Remote Sens.* 1996, *17*, 2215–2242.

Cracknell, M.J.; Reading, A.M.; McNeill, A.W. Mapping geology and volcanic-hosted massive sulfide alteration in the Hellyer–Mt Charter region, Tasmania, using Random Forests™ and Self-Organising Maps. *Aust. J. Earth Sci.* 2014, *61*, 287–304.

Crósta, A.P.; Souza Filho, C.R.; Azevedo, F.; Brodie, C. Targeting key alteration minerals in epithermal deposits in Patagonia, Argentina, using ASTER imagery and principal component analysis. *Int. J. Remote Sens.* 2003, *24*, 4233–4240.

Cudahy, T. Mineral mapping for exploration: An Australian journey of evolving spectral sensing technologies and industry collaboration. *Geosciences* 2016, *6*, 52.

De Almeida, C.M.P. Estudo Do Filão Aplitopegmatítico Da Mina Da Bajoca, Almendra: Contribuição Científico-Tecnológica. MsC Thesis, Faculdade de Ciências da Universidade do Porto, Porto, Portugal, 2003.

Di Tommaso, I.; Rubinstein, N. Hydrothermal alteration mapping using ASTER data in the Infiernillo porphyry deposit, Argentina. *Ore Geol. Rev.* 2007, *32*, 275–290.

DigitalGlobe Inc. Data Sheet for WorldView 3. Available online: http://content.satimagingcorp.com.s3.amazonaws.com/media/pdf/WorldView-3-PDF-Download.pdf (accessed on 16 January 2020).

Ducart, D.F.; Silva, A.M.; Toledo, C.L.B.; Assis, L.M.D. Mapping iron oxides with Landsat-8/OLI and EO-1/Hyperion imagery from the Serra Norte iron deposits in the Carajás Mineral Province, Brazil. *Braz. J. Geol.* 2016, *46*, 331–349.

Duuring, P.; Hagemann, S.G.; Novikova, Y.; Cudahy, T.; Laukamp, C. Targeting iron ore in banded iron formations using aster data: Weld range greenstone belt, yilgarn craton, western australia. *Econ. Geol.* 2012, *107*, 585–597.

El-Baz, F. Remote sensing and mapping of Earth resources. *Terra Nova* 1990, *2*, 446–454.

Elhag, M.; Alshamsi, D. Integration of remote sensing and geographic information systems for geological fault detection on the island of Crete, Greece. *Geosci. Instrum. Methods Data Syst.* 2019, *8*, 45–54.

Ellis, R.J.; Scott, P.W. Evaluation of hyperspectral remote sensing as a means of environmental monitoring in the St. Austell China clay (kaolin) region, Cornwall, UK. *Remote Sens. Environ.* 2004, *93*, 118–130.

El-Magd, I.A.; Mohy, H.; Basta, F. Application of remote sensing for gold exploration in the Fawakhir area, Central Eastern Desert of Egypt. *Arab. J. Geosci.* 2014, *8*, 3523–3536.

Eslami, A.; Ghaderi, M.; Rajendran, S.; Pour, A.B.; Hashim, M. Integration of ASTER and landsat TM remote sensing data for chromite prospecting and lithological mapping in Neyriz ophiolite zone, south Iran. *Resour. Geol.* 2015, *65*, 375–388.

European Space Agency (ESA). Missions: Sentinel-2. Overview. Available online: https://sentinel.esa.int/web/sentinel/missions/sentinel-2/overview (accessed on 16 January 2020).

European Space Agency (ESA). Observing the Earth: Copernicus. Available online: http://www.esa.int/Our_Activities/Observing_the_Earth/Copernicus/Overview4 (accessed on 7 March 2018).

European Space Agency (ESA). Radiometric Resolutions. Available online: https://earth.esa.int/web/sentinel/user-guides/sentinel-2-msi/resolutions/radiometric (accessed on 16 January 2020).

Fal, S.; Maanan, M.; Baidder, L.; Rhinane, H. The contribution of sentinel-2 satellite images for geological mapping in the south of tafilalet Basin (Eastern Anti-Atlas, Morocco). *Int. Arch. Photogramm. Remote Sens. Spat. Inf. Sci.* 2019, 75–82.

Farahbakhsh, E.; Shirmard, H.; Bahroudi, A.; Eslamkish, T. Fusing ASTER and QuickBird-2 Satellite Data for detailed investigation of porphyry copper deposits using PCA.; Case study of Naysian Deposit, Iran. *J. Indian Soc. of Remote Sens.* 2016, *44*, 525–537.

Gabr, S.; Ghulam, A.; Kusky, T. Detecting areas of high-potential gold mineralization using ASTER data. *Ore Geol. Rev.* 2010, *38*, 59–69.

Gabr, S.S.; Hassan, S.M.; Sadek, M.F. Prospecting for new gold-bearing alteration zones at El-Hoteib area, South Eastern Desert, Egypt, using remote sensing data analysis. *Ore Geol. Rev.* 2015, *71*, 1–13.

Ge, W.; Cheng, Q.; Tang, Y.; Jing, L.; Gao, C. Lithological classification using sentinel-2A data in the shibanjing ophiolite complex in Inner Mongolia, China. *Remote Sens.* 2018, *10*, 638.

Gemail, K.; Abd-El Rahman, N.M.; Ghiath, B.M.; Aziz, R.N. Integration of ASTER and airborne geophysical data for mineral exploration and environmental mapping: A case study, Gabal Dara, North Eastern Desert, Egypt. *Environ. Earth Sci.* 2016, *75*.

Gemusse, U.; Lima, A.; Teodoro, A. Comparing different techniques of satellite imagery classification to mineral mapping pegmatite of Muiane and Naipa: Mozambique. In

Proceedings of the SPIE, SPIE Remote Sensing, Strasbourg, France, 9–12 September 2019; Schulz, K., Michel, U., Nikolakopoulos, K.G., Eds.; SPIE: Bellingham, WA, USA, 2019.

Gemusse, U.; Lima, A.; Teodoro, A. Pegmatite spectral behavior considering ASTER and Landsat 8 OLI data in Naipa and Muiane mines (Alto Ligonha, Mozambique). In Proceedings of the SPIE, SPIE Remote Sensing, Berlin, Germany, 10–13 September 2018; Michel, U., Schulz, K., Eds.; SPIE: Bellingham, WA, USA, 2018.

Géron, A. *Hands-On Machine Learning with Scikit-Learn and TensorFlow: Concepts, Tools, and Techniques to Build Intelligent Systems*; O'Reilly Media Inc.: Sebastopol, CA, USA, 2017; p. 568.

Grosjean, C.; Miranda, P.H.; Perrin, M.; Poggi, P. Assessment of world lithium resources and consequences of their geographic distribution on the expected development of the electric vehicle industry. *Renew. Sustain. Energy Rev.* 2012, *16*, 1735–1744.

Hassan, S.M.; Ramadan, T.M. Mapping of the late Neoproterozoic Basement rocks and detection of the gold-bearing alteration zones at Abu Marawat-Semna area, Eastern Desert, Egypt using remote sensing data. *Arab. J. Geosci.* 2014, *8*, 4641–4656.

Hosseinjani Zadeh, M.; Honarmand, M. A remote sensing-based discrimination of high- and low-potential mineralization for porphyry copper deposits; a case study from Dehaj–Sarduiyeh copper belt, SE Iran. *Eur. J. Remote Sens.* 2017, *50*, 332–342.

Hosseinjani Zadeh, M.; Tangestani, M.H.; Roldan, F.V.; Yusta, I. Sub-pixel mineral mapping of a porphyry copper belt using EO-1 Hyperion data. *Adv. Space Res.* 2014, *53*, 440–451.

Hosseinjani, M.; Tangestani, M.H. Mapping alteration minerals using sub-pixel unmixing of ASTER data in the Sarduiyeh area, SE Kerman, Iran. *Int. J. Digit. Earth* 2011, *4*, 487–504.

Hu, B.; Xu, Y.; Wan, B.; Wu, X.; Yi, G. Hydrothermally altered mineral mapping using synthetic application of Sentinel-2A MSI, ASTER and Hyperion data in the Duolong area, Tibetan Plateau, China. *Ore Geol. Rev.* 2018, *101*, 384–397.

Jet Propulsion Laboratory (JPL). ASTER User Advisory. Available online: https://asterweb.jpl.nasa.gov/swir-alert.asp (accessed on 16 January 2020).

Jet Propulsion Laboratory (JPL). ASTER: Advanced Spaceborne Thermal Emission and Reflection Radiometer. Available online: https://asterweb.jpl.nasa.gov/index.asp (accessed on 16 January 2020).

Jet Propulsion Laboratory (JPL). ASTER: Instrument Characteristics. Available online: https://asterweb.jpl.nasa.gov/characteristics.asp (accessed on 16 January 2020).

Kesler, S.E.; Gruber, P.W.; Medina, P.A.; Keoleian, G.A.; Everson, M.P.; Wallington, T.J. Global lithium resources: Relative importance of pegmatite, brine and other deposits. *Ore Geology Reviews* 2012, *48*, 55-69. doi: https://doi.org/10.1016/j.oregeorev.2012.05.006.

Kruse, F.A.; Boardman, J.W. Characterization and mapping of kimberlites and related diatremes using hyperspectral remote sensing. In Proceedings of the 2000 IEEE Aerospace Conference. Proceedings (Cat. No.00TH8484), Big Sky, MT, USA, 25 March 2000; Volume 3, pp. 299–304.

Kumar, A.; Ghosh, S.K.; Dadhwal, V.K. Full fuzzy land cover mapping using remote sensing data based on fuzzy c-means and density estimation. *Can. J. Remote Sens.* 2007, *33*, 81–87.

Latifovic, R.; Pouliot, D.; Campbell, J. Assessment of convolution neural networks for surficial geology mapping in the South Rae Geological Region, Northwest Territories, Canada. *Remote Sens.* 2018, *10*, 307.

Lefevre, M.J. Teledetection d'anomalies geobotaniques appliquee a la recherche miniere par la methode de traitement d'images, Echassieres (Allier). *Bull. Société Géologique Fr.* 1982, 127–130.

Li, Y.; Zhang, H.; Xue, X.; Jiang, Y.; Shen, Q. Deep learning for remote sensing image classification: A survey. *Wiley Interdiscip. Rev. Data Min. Knowl. Discov.* 2018, *8*, e1264.

Lightweight Integrated Ground and Airborne Hyperspectral Topological Solution. Available online: http://lights.univ-lorraine.fr/ (accessed on 29 January 2020).

Liu, L.; Zhou, J.; Han, L.; Xu, X. Mineral mapping and ore prospecting using Landsat TM and Hyperion data, Wushitala, Xinjiang, northwestern China. *Ore Geol. Rev.* 2017, *81*, 280–295.

Liu, L.; Zhou, J.; Yin, F.; Feng, M.; Zhang, B. The reconnaissance of mineral resources through aster data-based image processing, interpreting and ground inspection in the Jiafushaersu area, West Junggar, China. *J. Earth Sci.* 2014, *25*, 397–406.

Loughlin, W.P. Component analysis for alteration mapping. *Photogram. Eng. Rem. Sens.* 1991, *57*, 1163–1169.

Maxwell, A.E.; Warner, T.A.; Fang, F. Implementation of machine-learning classification in remote sensing: An applied review. *Int. J. Remote Sens.* 2018, *39*, 2784–2817.

Mazhari, N.; Malekzadeh Shafaroudi, A.; Ghaderi, M. Detecting and mapping different types of iron mineralization in Sangan mining region, NE Iran, using satellite image and airborne geophysical data. *Geosci. J.* 2017, *21*, 137–148.

Meer, V.D. Bakker validated surface mineralogy from high-spectral resolution remote sensing: A review and a novel approach applied to gold exploration using AVIRIS data. *Terra Nova* 1998, *10*, 112–119.

Mendes, D.; Perrotta, M.M.; Costa, M.A.C.; Paes, V.J.C. Mapeamento espectral para identificação de assinaturas espectrais de minerais de lítio em imagens ASTER (NE/MG). In Proceedings of the Anais do XVIII Simpósio Brasileiro de Sensoriamento Remoto, Santos-SP, Brasil, 28–29 May 2017; pp. 5273–5280.

Menze, B.H.; Kelm, B.M.; Splitthoff, D.N.; Koethe, U.; Hamprecht, F.A. On oblique random forests. In *Machine Learning and Knowledge Discovery in Databases*; Springer: Berlin/Heidelberg, Germany, 2011; pp. 453–469.

Mia, B.; Fujimitsu, Y. Mapping hydrothermal altered mineral deposits using Landsat 7 ETM+ image in and around Kuju volcano, Kyushu, Japan. *J. Earth Syst. Sci.* 2012, *121*, 1049–1057.

Mielke, C.; Bösche, N.; Rogass, C.; Segl, K.; Gauert, C.; Kaufmann, H. Potential applications of the Sentinel-2 multispectral sensor and the Enmap hyperspectral sensor in mineral exploration. *EARSeL eProceedings* 2014, *13*, 93–102.

Momose, A.; Miyatake, S.; Arvelyna, Y.; Nguno, A.; Mhopjeni, K.; Sibeso, M.; Muyongo, A.; Muvangua, E. Mapping pegmatite using HyMap data in southern Namibia. In Proceedings of the 2011 IEEE International Geoscience and Remote Sensing Symposium, Vancouver, BC, Canada, 24–29 July 2011; pp. 2216–2217.

Moradi, M.; Basiri, S.; Kananian, A.; Kabiri, K. Fuzzy logic modeling for hydrothermal gold mineralization mapping using geochemical, geological, ASTER imageries and other geo-data, a case study in Central Alborz, Iran. *Earth Sci. Inform.* 2014, *8*, 197–205.

Mountrakis, G.; Im, J.; Ogole, C. Support vector machines in remote sensing: A review. *ISPRS J. Photogramm. Remote Sens.* 2011, *66*, 247–259.

Mujabar, P.S.; Dajkumar, S. Mapping of bauxite mineral deposits in the northern region of Saudi Arabia by using advanced spaceborne thermal emission and reflection radiometer satellite data. *Geo Spat. Inf. Sci.* 2018, *22*, 35–44.

Ninomiya, Y.; Fu, B. Thermal infrared multispectral remote sensing of lithology and mineralogy based on spectral properties of materials. *Ore Geol. Rev.* 2019, *108*, 54–72.

Noi, P.T.; Kappas, M. Comparison of random forest, k-Nearest neighbor, and support vector machine classifiers for land cover classification using Sentinel-2 imagery. *Sensors* 2017, *18*, 18.

Oommen, T.; Misra, D.; Twarakavi, N.K.C.; Prakash, A.; Sahoo, B.; Bandopadhyay, S. An objective analysis of support vector machine based classification for remote sensing. *Math. Geosci.* 2008, *40*, 409–424.

Oshigami, S.; Yamaguchi, Y.; Uezato, T.; Momose, A.; Arvelyna, Y.; Kawakami, Y.; Yajima, T.; Miyatake, S.; Nguno, A. Mineralogical mapping of southern Namibia by application of continuum-removal MSAM method to the HyMap data. *Int. J. Remote Sens.* 2013, *34*, 5282–5295.

Othman, A.; Gloaguen, R. Improving Lithological Mapping by SVM classification of spectral and morphological features: The Discovery of a new chromite body in the mawat ophiolite complex (Kurdistan, NE Iraq). *Remote Sens.* 2014, *6*, 6867–6896.

Öztan, N.S.; Süzen, M.L. Mapping evaporate minerals by ASTER. *Int. J. Remote Sens.* 2011, *32*, 1651–1673.

Pal, M.; Mather, P.M. Support vector machines for classification in remote sensing. *Int. J. Remote Sens.* 2005, *26*, 1007–1011.

Parakh, K.; Thakur, S.; Chudasama, B.; Tirodkar, S.; Porwal, A.; Bhattacharya, A. Machine learning and spectral techniques for lithological classification. In Proceedings of the SPIE Asia-Pacific Remote Sensing, New Delhi, India, 4–7 April 2016.

Perrotta, M.M.; Souza Filho, C.R.; Leite, C.A.S. Mapeamento espectral de intrusões pegmatíticas relacionadas a mineralizações de lítio, gemas e minerais industriais na região do vale do Jequitinhonha (MG) a partir de imagens ASTER. In Proceedings of the Anais do XII Simpósio Brasileiro de Sensoriamento Remoto, Goiânia, Brasil, 16–21 April 2005; pp. 1855–1862.

Pesquera, A.; Torres-Ruiz, J.; Gil-Crespo, P.P.; Velilla, N. Chemistry and genetic implications of tourmaline and Li-F-Cs micas from the Valdeflores area (Caceres, Spain). *Am. Mineral.* 1999, *84*, 55–69.

Pour, A.B.; Hashim, M. Hydrothermal alteration mapping from Landsat-8 data, Sar Cheshmeh copper mining district, south-eastern Islamic Republic of Iran. *J. Taibah Univ. Sci.* 2015, *9*, 155–166.

Pour, A.B.; Hashim, M. Identification of hydrothermal alteration minerals for exploring of porphyry copper deposit using ASTER data, SE Iran. *J. Asian Earth Sci.* 2011, *42*, 1309–1323.

Pour, A.B.; Hashim, M. The application of ASTER remote sensing data to porphyry copper and epithermal gold deposits. *Ore Geol. Rev.* 2012, *44*, 1–9.

Pournamdari, M.; Hashim, M. Detection of chromite bearing mineralized zones in Abdasht ophiolite complex using ASTER and ETM+ remote sensing data. *Arab. J. Geosci.* 2013, *7*, 1973–1983.

Rajan Girija, R.; Mayappan, S. Mapping of mineral resources and lithological units: A review of remote sensing techniques. *Int. J. Image Data Fusion* 2019, *10*, 79–106.

Rajendran, S.; al-Khirbash, S.; Pracejus, B.; Nasir, S.; Al-Abri, A.H.; Kusky, T.M.; Ghulam, A. ASTER detection of chromite bearing mineralized zones in Semail Ophiolite Massifs of the northern Oman Mountains: Exploration strategy. *Ore Geol. Rev.* 2012, *44*, 121–135.

Rajendran, S.; Thirunavukkarasu, A.; Balamurugan, G.; Shankar, K. Discrimination of iron ore deposits of granulite terrain of Southern Peninsular India using ASTER data. *J. Asian Earth Sci.* 2011, *41*, 99–106.

Rajesh, H.M. Application of remote sensing and GIS in mineral resource mapping—An overview. *J. Mineral. Petrol. Sci.* 2004, *99*, 83–103.

Roda-Robles, E. Distribución, Caracteristicas y Petrogenesis de las Pegmatitas de La Fregeneda (Salamanca). PhD thesis, Facultad de Ciencia y Tecnología de la Universidad del País Vasco (UPV/EHU), Bilbao, Spain, 1993.

Roda-Robles, E.; Pesquera, A.; Velasco, F.; Fontan, F. The granitic pegmatites of the Fregeneda area (Salamanca, Spain): characteristics and petrogenesis. *Mineral. Mag.* 1999, *63* (4), 535–558.

Rodger, A.; Cudahy, T. Vegetation corrected continuum depths at 2.20µm: An approach for hyperspectral sensors. *Remote Sens. Environ.* 2009, *113*, 2243–2257.

Rossi, C.; Spittle, S.; Bayaraa, M.; Pandey, A.; Henry, N. An earth observation framework for the lithium exploration. In Proceedings of the IGARSS 2018—2018 IEEE International

Geoscience and Remote Sensing Symposium, Valencia, Spain, 22–27 July 2018; pp. 1616–1619.

Rowan, L.C.; Mars, J.C. Lithologic mapping in the Mountain Pass, California area using Advanced Spaceborne Thermal Emission and Reflection Radiometer (ASTER) data. *Remote Sens. Environ.* 2003, *84*, 350–366.

Rowan, L.C.; Mars, J.C.; Simpson, C.J. Lithologic mapping of the Mordor, NT, Australia ultramafic complex by using the Advanced Spaceborne Thermal Emission and Reflection Radiometer (ASTER). *Remote Sens. Environ.* 2005, *99*, 105–126.

Sabins, F.F. Remote sensing for mineral exploration. *Ore Geol. Rev.* 1999, *14*, 157–183.

Sabins, F.F. *Remote sensing principles and interpretation*. 3rd ed.; W. H. Freeman: New York, 1997; p 494.

Sabins, F.F. *Remote Sensing Principles and Interpretation*, 3rd ed.; W. H. Freeman: New York, NY, USA, 1997; p. 494.

Sabins, F.F.; Miller, R.M. Resource assessment—Salar Uyuni and vicinity. In Proceedings of the Tenth Thematic Conference on Geologic Remote Sensing (Ann Arbor, MI, Environmental Research Institute of Michigan), San Antonio, TX, USA, 9–12 May 1994; pp. 9–12.

Safari, M.; Maghsoudi, A.; Pour, A.B. Application of Landsat-8 and ASTER satellite remote sensing data for porphyry copper exploration: A case study from Shahr-e-Babak, Kerman, south of Iran. *Geocarto Int.* 2017, *33*, 1186–1201.

Salles, R.D.R.; Souza Filho, C.R.; Cudahy, T.; Vicente, L.E.; Monteiro, L.V.S. Hyperspectral remote sensing applied to uranium exploration: A case study at the Mary Kathleen metamorphic-hydrothermal U-REE deposit, NW, Queensland, Australia. *J. Geochem. Explor.* 2017, *179*, 36–50.

Santos, D.; Teodoro, A.; Lima, A.; Cardoso-Fernandes, J. Remote sensing techniques to detect areas with potential for lithium exploration in Minas Gerais, Brazil. In Proceedings of the SPIE, SPIE Remote Sensing, Strasbourg, France, 9–12 September 2019; Schulz, K., Michel, U., Nikolakopoulos, K.G., Eds.; SPIE: Bellingham, WA, USA, 2019.

Sarmah, D.K. A survey on the latest development of machine learning in genetic algorithm and particle swarm optimization. In *Optimization in Machine Learning and Applications*; Kulkarni, A.J., Satapathy, S.C., Eds.; Springer: Singapore, 2020; pp. 91–112.

Spatz, D.M. Remote sensing characteristics of the sediment- and volcanic-hosted precious metal systems: Imagery selection for exploration and development. *Int. J. Remote Sens.* 1997, *18*, 1413–1438.

Tavares, P.A.; Beltrão, N.; Guimarães, U.S.; Teodoro, A.; Gonçalves, P. Urban ecosystem services quantification through remote sensing approach: A systematic review. *Environments* 2019, *6*, 51.

Tavares, P.A.; Beltrão, N.E.S.; Guimarães, U.S.; Teodoro, A.C. Integration of Sentinel-1 and Sentinel-2 for Classification and LULC Mapping in the Urban Area of Belém, Eastern Brazilian Amazon. *Sensors* 2019, *19*, 1140.

Torres-Ruiz, J.; Pesquera, A.; Gil, P.P.; Casas, J. Tourmalinites and Sn-Li mineralization in the Valdeflores area (Cáceres, Spain). *Mineral. Petrol.* 1996, *56*, 209–223.

United States Geological Survey (USGS). Landsat 8 Band Designations. Available online: https://www.usgs.gov/media/images/landsat-8-band-designations (accessed on 16 January 2020).

United States Geological Survey (USGS). Landsat 8. Available online: https://www.usgs.gov/land-resources/nli/landsat/landsat-8 (accessed on 16 January 2020).

United States Geological Survey (USGS). Landsat Satellite Missions. Available online: https://www.usgs.gov/land-resources/nli/landsat/landsat-satellite-missions (accessed on 16 January 2020).

USGS Landsat Program. Comparison of #Landsat 7, 8, #Sentinel 2, #ASTER & #MODIS Bands. View Band Designations for All #Landsat Sensors. Available online: https://twitter.com/usgslandsat/status/837696716417687553 (accessed on 22 December 2017).

Van Der Meer, F.; Vazquez-Torres, M.; Van Dijk, P.M. Spectral characterization of ophiolite lithologies in the Troodos Ophiolite complex of Cyprus and its potential in prospecting for massive sulphide deposits. *Int. J. Remote Sens.* 2010, *18*, 1245–1257.

Van der Meer, F.D.; van der Werff, H.M.A.; van Ruitenbeek, F.J.A.; Hecker, C.A.; Bakker, W.H.; Noomen, M.F.; van der Meijde, M.; Carranza, E.J.M.; Smeth, J.B.D.; Woldai, T. Multi- and hyperspectral geologic remote sensing: A review. *Int. J. Appl. Earth Obs. Geoinf.* 2012, *14*, 112–128.

Van der Meer, F.D.; van der Werff, H.M.A.; van Ruitenbeek, F.J.A. Potential of ESA's Sentinel-2 for geological applications. *Remote Sens. Environ.* 2014, *148*, 124–133.

Van der Werff, H.; Van der Meer, F. Sentinel-2 for mapping iron absorption feature parameters. *Remote Sens.* 2015, *7*, 12635–12653.

Van der Werff, H.; Van der Meer, F. Sentinel-2A MSI and Landsat 8 OLI provide data continuity for geological remote sensing. *Remote Sens.* 2016, *8*, 883.

Vapnik, V.N. *The Nature of Statistical Learning Theory*; Springer: New York, NY, USA, 1995.

Vieira, R. Aplitopegmatitos com elementos raros da região entre Almendra (V.N. de Foz Côa) e Barca d'Alva (Figueira de Castelo Rodrigo). Campo aplitopegmatítico da Fregeneda-Almendra. PhD thesis, Faculdade de Ciências da Universidade do Porto, Porto, Portugal, 2010.

Wang, G.; Du, W.; Carranza, E.J.M. Remote sensing and GIS prospectivity mapping for magmatic-hydrothermal base- and precious-metal deposits in the Honghai district, China. *J. Afr. Earth Sci.* 2017, *128*, 97–115.

Xu, Y.; Chen, J.; Meng, P. Detection of alteration zones using hyperspectral remote sensing data from Dapingliang skarn copper deposit and its surrounding area, Shanshan County, Xinjiang Uygur autonomous region, China. *J. Vis. Commun. Image Represent.* 2019, *58*, 67–78.

Yu, L.; Liang, L.; Wang, J.; Zhao, Y.; Cheng, Q.; Hu, L.; Liu, S.; Yu, L.; Wang, X.; Zhu, P.; et al. Meta-discoveries from a synthesis of satellite-based land-cover mapping research. *Int. J. Remote Sens.* 2014, *35*, 4573–4588.

Yu, L.; Porwal, A.; Holden, E.-J.; Dentith, M.C. Towards automatic lithological classification from remote sensing data using support vector machines. *Comput. Geosci.* 2012, *45*, 229–239.

Zhang, N.; Zhou, K. Identification of hydrothermal alteration zones of the Baogutu porphyry copper deposits in northwest China using ASTER data. *J. Appl. Remote Sens.* 2017, *11*.

Zhang, X.; Pazner, M.; Duke, N. Lithologic and mineral information extraction for gold exploration using ASTER data in the south Chocolate Mountains (California). *ISPRS J. Photogramm. Remote Sens.* 2007, *62*, 271–282.

Zimmermann, R.; Brandmeier, M.; Andreani, L.; Mhopjeni, K.; Gloaguen, R. Remote sensing exploration of Nb-Ta-LREE-Enriched carbonatite (Epembe/Namibia). *Remote Sens.* 2016, *8*, 620.

Zoheir, B.A. Controls on lode gold mineralization, Romite deposit, South Eastern Desert, Egypt. *Geosci. Front.* 2012, *3*, 571–585.

Chapter II: Development of new remote sensing algorithms

1.4. Support Vector Machines—Scikit-Learn 0.20.4 Documentation. Available online: https://scikit-learn.org/0.20/modules/svm.html#svm-classification (accessed on 24 April 2020).

Abedi, M.; Norouzi, G.-H.; Bahroudi, A. Support vector machine for multi-classification of mineral prospectivity areas. *Comput. Geosci.* 2012, *46*, 272–283.

Abrams, M., & Yamaguchi, Y. (2019). Twenty Years of ASTER Contributions to Lithologic Mapping and Mineral Exploration. *Remote Sensing, 11*(11), 1394.

Cardoso-Fernandes, J., Teodoro, A. C., & Lima, A. (2019a). Remote sensing data in lithium (Li) exploration: A new approach for the detection of Li-bearing pegmatites. *International Journal of Applied Earth Observation and Geoinformation, 76*, 10-25. doi: https://doi.org/10.1016/j.jag.2018.11.001.

Cardoso-Fernandes, J., Teodoro, A. C., Lima, A., & Roda Robles, E. (2020b, 26 Sept.-2 Oct. 2020). *Lithium (Li) pegmatite mapping using Artificial Neural Networks (ANNs): preliminary results.* Paper presented at the IGARSS 2020 - 2020 IEEE International Geoscience and Remote Sensing Symposium, Waikoloa, HI, USA, 557-560. doi: 10.1109/IGARSS39084.2020.9323852.

Cardoso-Fernandes, J., Teodoro, A. C., Lima, A., & Roda-Robles, E. (2019b, 9–12 September 2019). *Evaluating the performance of support vector machines (SVMs) and random forest (RF) in Li-pegmatite mapping: preliminary results.* Paper presented at the SPIE Remote Sensing, Strasbourg, France, doi: 10.1117/12.2532577.

Cardoso-Fernandes, J., Teodoro, A. C., Lima, A., Mielke, C., Körting, F., Roda-Robles, E., & Cauzid, J. (2020a, 26 Sept.-2 Oct. 2020). *Multi-scale approach using remote sensing techniques for lithium pegmatite exploration: first results.* Paper presented at the IGARSS 2020

- 2020 IEEE International Geoscience and Remote Sensing Symposium, Waikoloa, HI, USA, 5226-5229. doi: 10.1109/IGARSS39084.2020.9323705.

Cardoso-Fernandes, J.; Lima, A.; Roda-Robles, E.; Teodoro, A.C. Constraints and potentials of remote sensing data/techniques applied to lithium (Li)-pegmatites. *Can. Miner.* 2019, *57*, 723–725.

Cardoso-Fernandes, J.; Teodoro, A.C.; Lima, A. Potential of Sentinel-2 data in the detection of lithium (Li)-bearing pegmatites: A study case. In Proceedings of the SPIE Remote Sensing, Berlin, Germany, 10–13 September 2018; p. 15.

Cardoso-Fernandes, J.; Teodoro, A.C.; Lima, A. Remote sensing data in lithium (Li) exploration: A new approach for the detection of Li-bearing pegmatites. *Int. J. Appl. Earth Obs. Geoinf.* 2019, *76*, 10–25.

Cardoso-Fernandes, J.; Teodoro, A.C.; Lima, A.; Mielke, C.; Körting, F.; Roda-Robles, E.; Cauzid, J. Multi-scale approach using remote sensing techniques for lithium pegmatite exploration: first results. In IGARSS 2020 - 2020 IEEE International Geoscience and Remote Sensing Symposium, Waikoloa, HI, USA, 26 Sept.-2 Oct. 2020; IEEE: 2020; pp 5226-5229.

Cardoso-Fernandes, J.; Teodoro, A.C.; Lima, A.; Perrotta, M.; Roda-Robles, E. Detecting Lithium (Li) Mineralizations from Space: Current Research and Future Perspectives. *Appl. Sci.* 2020, *10*, 1785.

Cardoso-Fernandes, J.; Teodoro, A.C.; Lima, A.; Roda Robles, E. Lithium (Li) pegmatite mapping using Artificial Neural Networks (ANNs): preliminary results. In IGARSS 2020 - 2020 IEEE International Geoscience and Remote Sensing Symposium, Waikoloa, HI, USA, 26 Sept.-2 Oct. 2020; IEEE: 2020; pp 557-560.

Cardoso-Fernandes, J.; Teodoro, A.C.; Lima, A.; Roda-Robles, E. Evaluating the performance of support vector machines (SVMs) and random forest (RF) in Li-pegmatite mapping: preliminary results. In Proceedings of SPIE, SPIE Remote Sensing, Strasbourg, France, 9–12 September 2019; Schulz, K.; Michel, U.; Nikolakopoulos, K. G., Eds. SPIE: Bellingham, WA; 2019.

Cardoso-Fernandes, J.; Teodoro, A.C.; Lima, A.; Roda-Robles, E. Semi-Automatization of Support Vector Machines to Map Lithium (Li) Bearing Pegmatites. *Remote Sensing* 2020, *12* (14), 2319. doi: 10.3390/rs12142319.

Cohen, J. A Coefficient of Agreement for Nominal Scales. *Educ. Psychol. Meas.* 1960, *20*, 37–46.

Congalton, R.G. A review of assessing the accuracy of classifications of remotely sensed data. *Remote Sens. Environ.* 1991, *37*, 35–46.

Cortes, C.; Vapnik, V. Support-vector networks. *Mach. Learn.* 1995, *20*, 273–297.

Costa, J.C.S.D. *Notícia sobre uma carta geológica do Buçaco, de Nery Delgado*; Serviços Geológicos de Portugal: Lisboa, Portugal, 1950.

Cracknell, M. J., Reading, A. M., & McNeill, A. W. (2014). Mapping geology and volcanic-hosted massive sulfide alteration in the Hellyer–Mt Charter region, Tasmania, using Random Forests™ and Self-Organising Maps. *Australian Journal of Earth Sciences, 61*(2), 287-304. doi: 10.1080/08120099.2014.858081.

De Boissieu, F.; Sevin, B.; Cudahy, T.; Mangeas, M.; Chevrel, S.; Ong, C.; Rodger, A.; Maurizot, P.; Laukamp, C.; Lau, I.; et al. Regolith-geology mapping with support vector machine: A case study over weathered Ni-bearing peridotites, New Caledonia. *Int. J. Appl. Earth Obs. Geoinf.* 2018, *64*, 377–385.

Esri World Imagery. Available online: https://www.arcgis.com/home/item.html?id=10df2279f9684e4a9f6a7f08febac2a9 (accessed on 9 May 2019).

Gasmi, A.; Gomez, C.; Zouari, H.; Masse, A.; Ducrot, D. PCA and SVM as geo-computational methods for geological mapping in the southern of Tunisia, using ASTER remote sensing data set. *Arab. J. Geosci.* 2016, *9*, 753.

Ge, W., Cheng, Q., Jing, L., Wang, F., Zhao, M., & Ding, H. (2020). Assessment of the Capability of Sentinel-2 Imagery for Iron-Bearing Minerals Mapping: A Case Study in the Cuprite Area, Nevada. *Remote Sensing, 12*(18), 3028. doi: 10.3390/rs12183028.

Gemusse, U., Cardoso-Fernandes, J., Santos, D., Teodoro, A., Lima, A. (2021). *Prospeção dos Pegmatitos de Muiane e Naipa (Moçambique) a partir de técnicas de Deteção Remota, usando imagens do sensor ASTER*. Abstract presented at *Jornadas do ICT*, *Porto*, 2021.

Geomatica 2018. Available online: https://www.pcigeomatics.com/ (accessed on 12 July 2019).

Geomatica Help. Available online: http://www.pcigeomatics.com/geomatica-help/ (accessed on 23 April 2019).

Geranian, H., Tabatabaei, S. H., Asadi, H. H., & Carranza, E. J. M. (2016). Application of Discriminant Analysis and Support Vector Machine in Mapping Gold Potential Areas for Further Drilling in the Sari-Gunay Gold Deposit, NW Iran. *Natural Resources Research, 25*(2), 145-159. doi: 10.1007/s11053-015-9271-2.

Géron, A. *Hands-On Machine Learning with Scikit-Learn and TensorFlow: Concepts, Tools, and Techniques to Build Intelligent Systems*; O'Reilly Media, Inc.: Sebastopol, CA, USA, 2017; p. 568.

Google Earth Pro. Available online: https://www.google.com/intl/en_uk/earth/desktop/ (accessed on 3 August 2018).

He, H.; Garcia, E.A. Learning from Imbalanced Data. *IEEE Trans. Knowl. Data Eng.* 2009, *21*, 1263–1284.

Knerr, S.; Personnaz, L.; Dreyfus, G. Single-layer learning revisited: A stepwise procedure for building and training a neural network. In *Neurocomputing*; Soulié, F.F., Hérault, J., Eds.; Springer: Berlin/Heidelberg, Germany, 1990; pp. 41–50.

Latifovic, R.; Pouliot, D.; Campbell, J. Assessment of Convolution Neural Networks for Surficial Geology Mapping in the South Rae Geological Region, Northwest Territories, Canada. *Remote Sens.* 2018, *10*, 307.

Li, Y.; Zhang, H.; Xue, X.; Jiang, Y.; Shen, Q. Deep learning for remote sensing image classification: A survey. *Wiley Interdiscip. Rev. Data Min. Knowl. Discov.* 2018, *8*, e1264.

Maxwell, A.E.; Warner, T.A.; Fang, F. Implementation of machine-learning classification in remote sensing: An applied review. *Int. J. Remote Sens.* 2018, *39*, 2784–2817.

Melgani, F.; Bruzzone, L. Classification of hyperspectral remote sensing images with support vector machines. *IEEE Trans. Geosci. Remote Sens.* 2004, *42*, 1778–1790.

Mendes, D.; Perrotta, M.M.; Costa, M.A.C.; Paes, V.J.C. Mapeamento espectral para identificação de assinaturas espectrais de minerais de lítio em imagens ASTER (NE/MG). In Proceedings of the Anais do XVIII Simpósio Brasileiro de Sensoriamento Remoto, Santos-SP, Brazil, 28–29 May 2017; pp. 5273–5280.

Missions: Sentinel-2. Available online: https://sentinel.esa.int/web/sentinel/missions/sentinel-2 (accessed on 20 April 2020).

Mountrakis, G.; Im, J.; Ogole, C. Support vector machines in remote sensing: A review. *ISPRS J. Photogramm. Remote Sens.* 2011, *66*, 247–259.

Müller, A.C.; Guido, S. Chapter 5. Model Evaluation and Improvement. In *Introduction to Machine Learning with Python: A Guide for Data Scientists*; Schanafelt, D., Ed.; O'Reilly Media, Inc.: Sebastopol, CA, USA, 2016; pp. 251–303.

MultiSpectral Instrument (MSI) Overview. Available online: https://sentinel.esa.int/web/sentinel/technical-guides/sentinel-2-msi/msi-instrument (accessed on 20 April 2020).

Noi, P. T., & Kappas, M. (2017). Comparison of Random Forest, k-Nearest Neighbor, and Support Vector Machine Classifiers for Land Cover Classification Using Sentinel-2 Imagery. *Sensors (Basel), 18*(1). doi: 10.3390/s18010018.

Oommen, T., Misra, D., Twarakavi, N. K. C., Prakash, A., Sahoo, B., & Bandopadhyay, S. (2008). An Objective Analysis of Support Vector Machine Based Classification for Remote Sensing. *Mathematical Geosciences, 40*(4), 409-424. doi: 10.1007/s11004-008-9156-6.

Othman, A.A.; Gloaguen, R. Improving Lithological Mapping by SVM Classification of Spectral and Morphological Features: The Discovery of a New Chromite Body in the Mawat Ophiolite Complex (Kurdistan, NE Iraq). *Remote Sens.* 2014, *6*, 6867–6896.

Pal, M.; Mather, P.M. Support vector machines for classification in remote sensing. *Int. J. Remote Sens.* 2005, *26*, 1007–1011.

Pedregosa, F.; Varoquaux, G.; Gramfort, A.; Michel, V.; Thirion, B.; Grisel, O.; Blondel, M.; Prettenhofer, P.; Weiss, R.; Dubourg, V.; et al. Scikit-learn: Machine Learning in Python. *J. Mach. Learn. Res.* 2012, *12*, 2825–2830.

Perrotta, M.M.; Souza Filho, C.R.; Leite, C.A.S. Mapeamento espectral de intrusões pegmatíticas relacionadas a mineralizações de lítio, gemas e minerais industriais na região do vale do Jequitinhonha (MG) a partir de imagens ASTER. In Proceedings of the Anais do XII Simpósio Brasileiro de Sensoriamento Remoto, Goiânia, Brazil, 16–21 April 2005; pp. 1855–1862.

Pour, A. B., & Hashim, M. (2015). Hydrothermal alteration mapping from Landsat-8 data, Sar Cheshmeh copper mining district, south-eastern Islamic Republic of Iran. *Journal of Taibah University for Science, 9*(2), 155-166. doi: 10.1016/j.jtusci.2014.11.008.

Roda, E. Distribución, Caracteristicas y Petrogenesis de las Pegmatitas de La Fregeneda (Salamanca). Ph.D. Thesis, UPV/EHU, Bilbao, Spain, 1993.

Roda-Robles, E.; Pesquera, A.; Velasco, F.; Fontan, F. The granitic pegmatites of the Fregeneda area (Salamanca, Spain): Characteristics and petrogenesis. *Miner. Mag.* 1999, *63*, 535–558.

Roda-Robles, E.; Vieira, R.; Pesquera, A.; Lima, A. Chemical variations and significance of phosphates from the Fregeneda-Almendra pegmatite field, Central Iberian Zone (Spain and Portugal). *Miner. Pet.* 2010, *100*, 23–34.

Rodriguez-Galiano, V.; Sanchez-Castillo, M.; Chica-Olmo, M.; Chica-Rivas, M. Machine learning predictive models for mineral prospectivity: An evaluation of neural networks, random forest, regression trees and support vector machines. *Ore Geol. Rev.* 2015, *71*, 804–818.

Santos, D., Teodoro, A., Lima, A., & Cardoso-Fernandes, J. (2019, 9–12 September 2019). *Remote sensing techniques to detect areas with potential for lithium exploration in Minas Gerais, Brazil.* Paper presented at the SPIE Remote Sensing, Strasbourg, France, doi: https://doi.org/10.1117/12.2532744.

Santos, D., Teodoro, A., Lima, A., Cardoso-Fernandes, J. (2021). *Aplicação de Métodos para Identificação de Novos Depósitos de Pegmatitos LCT e NYF: GREENPEG um Projeto Europeu*. Abstract presented at *Jornadas do ICT*, *Porto*, 2021.

Sentinel-2 MSI: Products and Algorithms. Available online: https://sentinel.esa.int/web/sentinel/technical-guides/sentinel-2-msi/products-algorithms (accessed on 20 April 2020).

Silva, A.F.d.; Rebelo, J.A.; Ribeiro, M.L. *Notícia Explicativa da folha 11-C Torre de Moncorvo*; Serviços Geológicos de Portugal: Lisboa, Portugal, 1989; p. 65.

Silva, A.F.d.; Ribeiro, M.L. *Notícia Explicativa da folha 15-A Vila Nova de Foz Côa*; Serviços Geológicos de Portugal: Lisboa, Portugal, 1991; p. 52.

SNAP. Available online: https://step.esa.int/main/toolboxes/snap/ (accessed on 20 April 2020).

Story, M.; Congalton, R. Accuracy assessment: A user's perspective. *Photogramm. Eng. Remote Sens.* 1986, *52*, 397–399.

Teixeira, C. *Notas sobre geologia de Portugal o complexo xisto-grauváquico ante-ordoviciano*; Empresa Literaria Fluminense Lda.: Lisboa, Portugal, 1955; p. 48.

Vapnik, V.N. *The Nature of Statistical Learning Theory*; Springer: New York, NY, USA, 1995.

Vieira, R. Aplitopegmatitos com elementos raros da região entre Almendra (V.N. de Foz Côa) e Barca d'Alva (Figueira de Castelo Rodrigo). Campo aplitopegmatítico da Fregeneda-Almendra. Ph.D. Thesis, Faculdade de Ciências da Universidade do Porto, Porto, Portugal, 2010.

Yu, L., Porwal, A., Holden, E.-J., & Dentith, M. C. (2012). Towards automatic lithological classification from remote sensing data using support vector machines. *Computers & Geosciences, 45*, 229-239. doi: https://doi.org/10.1016/j.cageo.2011.11.019.

Zuo, R.; Carranza, E.J.M. Support vector machine: A tool for mapping mineral prospectivity. *Comput. Geosci.* 2011, *37*, 1967–1975.

Chapter III: Spectral libraries for Li-exploration

Ahmad, N.; Ahmed, R.; Umar, Z.A.; Liaqat, U.; Manzoor, U.; Baig, M.A. Qualitative and quantitative analyses of copper ores collected from Baluchistan, Pakistan using LIBS and LA-TOF-MS. *Appl. Phys. A* 2018, *124*, 160, doi:10.1007/s00340-018-7032-8.

Aires, S.C.M. Petrofísica e litogeoquímica de formações do "Complexo Xisto- Grauváquico" (Grupo do Douro) estudo do potencial do "xisto" para exploração como pedra natural. PhD thesis, Faculdade de Ciências da Universidade do Porto, Porto, Portugal, 2018.

Akhmetzhanov, T.F.; Labutin, T.A.; Zaytsev, S.M.; Drozdova, A.N.; Popov, A.M. Determination of the Mn/Fe Ratio in Ferromanganese Nodules Using Calibration-Free Laser-Induced Breakdown Spectroscopy. *Opt. Spectrosc.* 2019, *126*, 316–320, doi:10.1134/s0030400x19040027.

Alvey, D.C.; Morton, K.; Harmon, R.S.; Gottfried, J.L.; Remus, J.J.; Collins, L.M.; Wise, M.A. Laser-induced breakdown spectroscopy-based geochemical fingerprinting for the rapid analysis and discrimination of minerals: The example of garnet. *Appl. Opt.* 2010, *49*, C168–C180, doi:10.1364/ao.49.00c168.

Andrade, J.M.; Cristoforetti, G.; Legnaioli, S.; Lorenzetti, G.; Palleschi, V.; Shaltout, A. Classical univariate calibration and partial least squares for quantitative analysis of brass samples by laser-induced breakdown spectroscopy. *Spectrochim. Acta Part B At. Spectrosc.* 2010, *65*, 658–663, doi:10.1016/j.sab.2010.04.008.

Araújo Neto, J.F.d.; Barreto, S.d.B.; Carrino, T.A.; Müller, A.; Santos, L.C.M.d.L. Mineralogical and gemological characterization of emerald crystals from Paraná deposit, NE Brazil: a study

of mineral chemistry, absorption and reflectance spectroscopy and thermal analysis. *Brazilian Journal of Geology* 2019, *49*. doi: 10.1590/2317-4889201920190014.

Asadzadeh, S.; Souza Filho, C.R. A review on spectral processing methods for geological remote sensing. *International Journal of Applied Earth Observation and Geoinformation* 2016, *47*, 69-90. doi: https://doi.org/10.1016/j.jag.2015.12.004.

ASD Inc. *ViewSpec Pro™ User Manual. ASD Document 600555 Rev. A*. Boulder, 2008.

Bennett, B.N.; Martin, M.Z.; Leonard, D.N.; Garlea, E. Calibration curves for commercial copper and aluminum alloys using handheld laser-induced breakdown spectroscopy. *Appl. Phys. A* 2018, *124*, 42, doi:10.1007/s00340-018-6909-x.

Bi, Y.; Yan, M.; Dong, X.; Li, Z.; Zhang, Y.; Li, Y. Recognition of 25 natural geological samples using a modified correlation analysis method and laser-induced breakdown spectroscopic data. *Optics* 2018, *158*, 1058–1062, doi:10.1016/j.ijleo.2017.12.167.

Bishop, J.L.; Lane, M.D.; Dyar, M.D.; Brown, A.J. Reflectance and emission spectroscopy study of four groups of phyllosilicates: smectites, kaolinite-serpentines, chlorites and micas. *Clay Minerals* 2008, *43* (1), 35-54. doi: 10.1180/claymin.2008.043.1.03.

Bocchio, R.; Adamo, I.; Caucia, F. Aquamarine from the Masino-Bregaglia Massif, Central Alps, Italy. *Gems & Gemology* 2009, *45*, 204-207. doi: 10.5741/GEMS.45.3.204.

Busser, B.; Moncayo, S.; Coll, J.-L.; Sancey, L.; Motto-Ros, V. Elemental imaging using laser-induced breakdown spectroscopy: A new and promising approach for biological and medical applications. *Coord. Chem. Rev.* 2018, *358*, 70–79, doi:10.1016/j.ccr.2017.12.006.

Cardoso-Fernandes, J., Dias, F., Lima, A., Anjos Ribeiro, M., Perrotta, M., Roda-Robles, E., & Teodoro, A. C. (2021a, 19–30 Apr). *Petalite alteration products from the Bajoca pegmatite (Central Portugal): a multiapproach for lithium exploration.* Paper presented at the EGU General Assembly 2021, online, doi: 10.5194/egusphere-egu21-2364.

Cardoso-Fernandes, J., Lima, A., Teodoro, A., Silva, J. (2021b). *Reflectance spectroscopy of minerals and rocks: a case study for lithological classification*. Abstract presented at *Jornadas do ICT*, *Porto*, 2021.

Cardoso-Fernandes, J., Silva, J., Dias, F., Lima, A., Teodoro, A. C., Barrès, O., Cauzid, J., Perrotta, M., Roda-Robles, E., & Ribeiro, M. A. (2021c). Tools for Remote Exploration: A Lithium (Li) Dedicated Spectral Library of the Fregeneda–Almendra Aplite–Pegmatite Field. *Data, 6*(3), 33. doi: 10.3390/data6030033.

Cardoso-Fernandes, J., Silva, J., Lima, A., Teodoro, A. C., Perrotta, M., Cauzid, J., & Roda-Robles, E. (2020a). *Characterization of lithium (Li) minerals from the Fregeneda-Almendra region through laboratory spectral measurements: a comparative study.* Paper presented at the SPIE Remote Sensing, Earth Resources and Environmental Remote Sensing/GIS Applications XI, doi: https://doi.org/10.1117/12.2573941.

Cardoso-Fernandes, J., Silva, J., Lima, A., Teodoro, A. C., Perrotta, M., Cauzid, J., Roda-Robles, E., & Ribeiro, M. A. (2020b). *Reflectance spectroscopy to validate remote sensing data/algorithms for satellite-based lithium (Li) exploration (Central East Portugal).* Paper presented at the SPIE Remote Sensing, Earth Resources and Environmental Remote Sensing/GIS Applications XI, doi: https://doi.org/10.1117/12.2573929.

Cardoso-Fernandes, J., Silva, J., Perrotta, M. M., Lima, A., Teodoro, A. C., Ribeiro, M. A., Dias, F., Barrès, O., Cauzid, J., & Roda-Robles, E. (2021d). Interpretation of the Reflectance Spectra of Lithium (Li) Minerals and Pegmatites: A Case Study for Mineralogical and Lithological Identification in the Fregeneda–Almendra Area. *Remote Sensing, 13*(18), 3688. doi: 10.3390/rs13183688.

Cardoso-Fernandes, J., Teodoro, A. C., Lima, A., & Roda-Robles, E. (2019, 9–12 September 2019). *Evaluating the performance of support vector machines (SVMs) and random forest (RF) in Li-pegmatite mapping: preliminary results.* Paper presented at the SPIE Remote Sensing, Strasbourg, France, doi: 10.1117/12.2532577.

Cardoso-Fernandes, J.; Dias, F.; Lima, A.; Anjos Ribeiro, M.; Perrotta, M.; Roda-Robles, E.; Teodoro, A.C. Petalite alteration products from the Bajoca pegmatite (Central Portugal): a multiapproach for lithium exploration. In EGU General Assembly 2021, online, 19–30 Apr; 2021. doi: 10.5194/egusphere-egu21-2364.

Cardoso-Fernandes, J.; Lima, A.; Roda-Robles, E.; Teodoro, A.C. Constraints and potentials of remote sensing data/techniques applied to lithium (Li)-pegmatites. *The Canadian Mineralogist* 2019, *57* (5), 723-725. doi: 10.3749/canmin.AB00004.

Cardoso-Fernandes, J.; Silva, J.; Dias, F.; Lima, A.; Teodoro, A.C.; Barrès, O.; Cauzid, J.; Perrotta, M.; Roda-Robles, E.; Ribeiro, M.A. Tools for Remote Exploration: A Lithium (Li) Dedicated Spectral Library of the Fregeneda–Almendra Aplite–Pegmatite Field. *Data* 2021, *6* (3), 33. doi: 10.3390/data6030033.

Cardoso-Fernandes, J.; Silva, J.; Dias, F.; Lima, A.; Teodoro, A.C.; Barrès, O.; Cauzid, J.; Perrotta, M.; Roda-Robles, E.; Ribeiro, M.A. Tools for remote exploration: a Lithium (Li)

dedicated spectral library of the Fregeneda-Almendra aplite-pegmatite field, Version 1; Zenodo: Available online: http://doi.org/10.5281/zenodo.4575375 (accessed 9 March 2021).

Cardoso-Fernandes, J.; Silva, J.; Lima, A.; Teodoro, A.C.; Perrotta, M.; Cauzid, J.; Roda-Robles, E. Characterization of lithium (Li) minerals from the Fregeneda-Almendra region through laboratory spectral measurements: a comparative study. In SPIE Remote Sensing, Earth Resources and Environmental Remote Sensing/GIS Applications XI, SPIE: 2020. doi: https://doi.org/10.1117/12.2573941.

Cardoso-Fernandes, J.; Silva, J.; Lima, A.; Teodoro, A.C.; Perrotta, M.; Cauzid, J.; Roda-Robles, E.; Ribeiro, M. dos A. Reflectance Spectroscopy to Validate Remote Sensing Data/Algorithms for Satellite-Based Lithium (Li) Exploration (Central East Portugal). In Proceedings of the Earth Resources and Environmental Remote Sensing/GIS Applications XI, online conference, September 2020; Schulz, K., Nikolakopoulos, K.G., Michel, U., Eds.; SPIE: Bellingham, WA, USA, 2020; p. 19.

Cardoso-Fernandes, J.; Silva, J.; Lima, A.; Teodoro, A.C.; Perrotta, M.; Cauzid, J.; Roda-Robles, E. Characterization of Lithium (Li) Minerals from the Fregeneda-Almendra Region through Laboratory Spectral Measurements: A Comparative Study. In Proceedings of the Earth Resources and Environmental Remote Sensing/GIS Applications XI, online conference, September 2020; Schulz, K., Nikolakopoulos, K.G., Michel, U., Eds.; SPIE: Bellingham, WA, USA, 2020; p. 20.

Cardoso-Fernandes, J.; Teodoro, A.C.; Lima, A. Remote sensing data in lithium (Li) exploration: A new approach for the detection of Li-bearing pegmatites. *International Journal of Applied Earth Observation and Geoinformation* 2019, *76*, 10-25. doi: https://doi.org/10.1016/j.jag.2018.11.001.

Cardoso-Fernandes, J.; Teodoro, A.C.; Lima, A.; Roda-Robles, E. Evaluating the performance of support vector machines (SVMs) and random forest (RF) in Li-pegmatite mapping: preliminary results. In Proceedings of SPIE, SPIE Remote Sensing, Strasbourg, France, 9–12 September 2019; Schulz, K.; Michel, U.; Nikolakopoulos, K. G., Eds. SPIE: Bellingham, WA; 2019. doi: 10.1117/12.2532577.

Cardoso-Fernandes, J.; Teodoro, A.C.; Lima, A.; Roda-Robles, E. Semi-Automatization of Support Vector Machines to Map Lithium (Li) Bearing Pegmatites. *Remote Sensing* 2020, *12* (14), 2319. doi: 10.3390/rs12142319.

Carrino, T.A.; Barreto, S.d.B.; Oliveira, P.J.A.d.; Araújo Neto, J.F.d.; Correia, A.M.d.L. Linking gemology and spectral geology: a case study of elbaites from Seridó Pegmatite Province, Northeastern Brazil. *Brazilian Journal of Geology* 2019, *49*. doi: 10.1590/2317-4889201920180113.

Castello, M.; Constantin, M.; Laflamme, M. Measurements of Gold in Ores by LIBS.; Quebec City, 23 August 2017. Available online: https://numerique.banq.qc.ca/patrimoine/details/52327/3081324 (accessed on 21 June 2021)

Cerny, P. The Tanco pegmatite at Bernic Lake, Manitoba; VIII, Secondary minerals from the spodumene-rich zones. *The Canadian Mineralogist* 1972, *11* (3), 714-726.

Clark, R.N. Spectroscopy of rocks and minerals and principles of spectroscopy: Chapter 1. In *Remote Sensing for the Earth Sciences: Manual of Remote Sensing,*, 3rd ed.; Ryerson, R. A., Ed. John Wiley & Sons, Inc.: 1999.

Clark, R.N.; King, T.V.V.; Klejwa, M.; Swayze, G.A.; Vergo, N. High spectral resolution reflectance spectroscopy of minerals. *Journal of Geophysical Research: Solid Earth* 1990, *95* (B8), 12653-12680. doi: 10.1029/JB095iB08p12653.

Clark, R.N.; Roush, T.L. Reflectance spectroscopy: Quantitative analysis techniques for remote sensing applications. *Journal of Geophysical Research: Solid Earth* 1984, *89* (B7), 6329-6340. doi: 10.1029/JB089iB07p06329.

Clark, R.N.; Swayze, G.A.; Gallagher, A.J.; King, T.V.V.; Calvin, W.M. *The U. S. Geological Survey, Digital Spectral Library: Version 1 (0.2 to 3.0um)*; 93-592; 1993.

Clark, R.N.; Swayze, G.A.; Wise, R.; Livo, K.E.; Hoefen, T.M.; Kokaly, R.F.; Sutley, S.J. USGS digital spectral library splib05a. Available online: https://pubs.usgs.gov/of/2003/ofr-03-395/ (accessed 8 January 2021).

Colao, F.; Fantoni, R.; Lazić, V.; Spizzichino, V. Laser-induced breakdown spectroscopy for semi-quantitative and quantitative analyses of artworks—application on multi-layered ceramics and copper based alloys. *Spectrochim. Acta Part B At. Spectrosc.* 2002, *57*, 1219–1234, doi:10.1016/s0584-8547(02)00054-x.

Connors, B.; Somers, A.; Day, D. Application of Handheld Laser-Induced Breakdown Spectroscopy (LIBS) to Geochemical Analysis. *Appl. Spectrosc.* 2016, *70*, 810–815, doi:10.1177/0003702816638247.

Costa, J.C.S.d. *Notícia sobre uma carta geológica do Buçaco, de Nery Delgado*. Serviços Geológicos de Portugal: Lisboa, Portugal, 1950.

Costa, M.A.C.; Perrotta, M.M.; Melo, T.G.; Turra, B. Estudos Espectrais. In *Avaliação do potencial do lítio no Brasil: área do Médio Rio Jequitinhonha, Nordeste de Minas Gerais: texto explicativo e mapas*, Paes, V. J. C.; Santos, L. D.; Tedeschi, M. F.; Betiollo, L. M., Eds. CPRM: Belo Horizonte, 2016; p 276.

Cousin, A.; Meslin, P.; Wiens, R.; Rapin, W.; Mangold, N.; Fabre, C.; Gasnault, O.; Forni, O.; Tokar, R.; Ollila, A.; et al. Compositions of coarse and fine particles in martian soils at gale: A window into the production of soils. *Icarus* 2015, *249*, 22–42, doi:10.1016/j.icarus.2014.04.052.

Cousin, A.; Sautter, V.; Fabre, C.; Maurice, S.; Wiens, R.C. Textural and modal analyses of picritic basalts with ChemCam Laser-Induced Breakdown Spectroscopy. *J. Geophys. Res. Space Phys.* 2012, *117*, 117, doi:10.1029/2012je004132.

Cremers, D.A.; Radziemski, L.J. History and fundamentals of LIBS. In *Laser Induced Breakdown Spectroscopy: Fundamentals and Applications*; Cambridge University Press: Cambridge, UK, 2006; pp. 9–16.

Cuñat, J.; Palanco, S.; Carrasco, F.; Simón, M.D.; Laserna, J.J. Portable instrument and analytical method using laser-induced breakdown spectrometry for in situ characterization of speleothems in karstic caves. *J. Anal. At. Spectrom.* 2005, *20*, 295–300, doi:10.1039/b417161f.

Deer, W.A.; Howie, R.A.; Zussman, J. *Rock-forming Minerals.* 2nd edition ed.; The Geological Society: London, 1978; Vol. 2A: Single-chain Silicates, p 668.

Díaz, D.; Hahn, D.W.; Molina, A. Quantification of gold and silver in minerals by laser-induced breakdown spectroscopy. *Spectrochim. Acta Part B At. Spectrosc.* 2017, *136*, 106–115, doi:10.1016/j.sab.2017.08.008.

Dill, H.G. A geological and mineralogical review of clay mineral deposits and phyllosilicate ore guides in Central Europe – A function of geodynamics and climate change. *Ore Geology Reviews* 2020, *119*, 103304. doi: https://doi.org/10.1016/j.oregeorev.2019.103304.

Dill, H.G. Pegmatites and aplites: Their genetic and applied ore geology. *Ore Geology Reviews* 2015, *69*, 417-561. doi: https://doi.org/10.1016/j.oregeorev.2015.02.022.

Duke, E.F. Near infrared spectra of muscovite, Tschermak substitution, and metamorphic reaction progress: Implications for remote sensing. *Geology* 1994, *22* (7), 621-624. doi: 10.1130/0091-7613(1994)022<0621:Nisomt>2.3.Co;2.

Duponchel, L.; Bousquet, B.; Pelascini, F.; Motto-Ros, V. Should we prefer inverse models in quantitative LIBS analysis? *J. Anal. At. Spectrom.* 2020, *35*, 794–803, doi:10.1039/c9ja00435a.

El Haddad, J.; Canioni, L.; Bousquet, B. Good practices in LIBS analysis: Review and advices. *Spectrochim. Acta Part B At. Spectrosc.* 2014, *101*, 171–182, doi:10.1016/j.sab.2014.08.039.

Ellis, R.J.; Scott, P.W. Evaluation of hyperspectral remote sensing as a means of environmental monitoring in the St. Austell China clay (kaolin) region, Cornwall, UK. *Remote Sensing of Environment* 2004, *93* (1), 118-130. doi: https://doi.org/10.1016/j.rse.2004.07.004.

Fabre, C. Advances in Laser-Induced Breakdown Spectroscopy analysis for geology: A critical review. *Spectrochim. Acta Part B At. Spectrosc.* 2020, *166*, 105799, doi:10.1016/j.sab.2020.105799.

Fabre, C., Ourti, N. E., Mercadier, J., Cardoso-Fernandes, J., Dias, F., Perrotta, M., Koerting, F., Lima, A., Kaestner, F., Koellner, N., Linnen, R., Benn, D., Martins, T., & Cauzid, J. (2021). Analyses of Li-Rich Minerals Using Handheld LIBS Tool. *Data, 6*(6), 68. doi: 10.3390/data6060068.

Fabre, C.; Bousquet, B. De chemcam à supercam: L'apport de la LIBS pour le spatial. *Photon* 2020, 38–41, doi:10.1051/photon/202010338.

Fabre, C.; Cousin, A.; Wiens, R.; Ollila, A.; Gasnault, O.; Maurice, S.; Sautter, V.; Forni, O.; Lasue, J.; Tokar, R.; et al. In situ calibration using univariate analyses based on the onboard ChemCam targets: First prediction of Martian rock and soil compositions. *Spectrochim. Acta Part B At. Spectrosc.* 2014, *99*, 34–51, doi:10.1016/j.sab.2014.03.014.

Fabre, C.; Devismes, D.; Moncayo, S.; Pelascini, F.; Trichard, F.; Lecomte, A.; Bousquet, B.; Cauzid, J.; Motto-Ros, V. Elemental imaging by laser-induced breakdown spectroscopy for the geological characterization of minerals. *J. Anal. At. Spectrom.* 2018, *33*, 1345–1353, doi:10.1039/c8ja00048d.

Farnsworth-Pinkerton, S.; McMillan, N.J.; Dutrow, B.L.; Henry, D.J. Provenance of detrital tourmalines from Proterozoic metasedimentary rocks in the Picuris Mountains, New Mexico,

using Laser-Induced Breakdown Spectroscopy. *J. Geosci.* 2018, *63*, 193–198, doi:10.3190/jgeosci.261

Felzer, B.; Hauff, P.; Goetz, A.F.H. Quantitative reflectance spectroscopy of buddingtonite from the Cuprite mining district, Nevada. *Journal of Geophysical Research: Solid Earth* 1994, *99* (B2), 2887-2895. doi: https://doi.org/10.1029/93JB02975.

Ferreira, J.A.; Bento dos Santos, T.; Pereira, I.; Mata, J. Tectonically assisted exhumation and cooling of Variscan granites in an anatectic complex of the Central Iberian Zone, Portugal: constraints from LA-ICP-MS zircon and apatite U–Pb ages. *International Journal of Earth Sciences* 2019, *108* (7), 2153-2175. doi: 10.1007/s00531-019-01755-1.

Forni, O.; Gaft, M.; Toplis, M.J.; Clegg, S.M.; Maurice, S.; Wiens, R.C.; Mangold, N.; Gasnault, O.; Sautter, V.; Le Mouélic, S.; et al. First detection of fluorine on Mars: Implications for Gale Crater's geochemistry. *Geophys. Res. Lett.* 2015, *42*, 1020–1028, doi:10.1002/2014gl062742.

Foster, M.D. *Interpretation of the composition of lithium micas*; 354E; United States Geological Survey Professional Paper: Washington, USA, 1960; pp 115-147.

Foucaud, Y.; Fabre, C.; Demeusy, B.; Filippova, I.; Filippov, L. Optimisation of fast quantification of fluorine content using handheld laser induced breakdown spectroscopy. *Spectrochim. Acta Part B At. Spectrosc.* 2019, *158*, 105628, doi:10.1016/j.sab.2019.05.017.

Gamela, R.R.; Costa, V.C.; Babos, D.V.; Araújo, A.S.; Pereira-Filho, E.R. Direct Determination of Ca, K, and Mg in Cocoa Beans by Laser-Induced Breakdown Spectroscopy (LIBS): Evaluation of Three Univariate Calibration Strategies for Matrix Matching. *Food Anal. Methods* 2020, *13*, 1017–1026, doi:10.1007/s12161-020-01722-6.

Gao, Y.; Bagas, L.; Li, K.; Jin, M.; Liu, Y.; Teng, J. Newly Discovered Triassic Lithium Deposits in the Dahongliutan Area, NorthWest China: A Case Study for the Detection of Lithium-Bearing Pegmatite Deposits in Rugged Terrains Using Remote-Sensing Data and Images. *Frontiers in Earth Science* 2020, *8* (553). doi: 10.3389/feart.2020.591966.

Goodenough, K.M.; Shaw, R.A.; Smith, M.; Estrade, G.; Marqu, E.; Bernard, C.; Nex, P. Economic mineralization in pegmatites: comparing and contrasting NYF and LCT examples. *The Canadian Mineralogist* 2019, *57* (5), 753-755. doi: 10.3749/canmin.AB00013.

Grew, E.S. The Minerals of Lithium. *Elements* 2020, *16*, 235–240, doi:10.2138/gselements.16.4.235.

Guezenoc, J.; Gallet-Budynek, A.; Bousquet, B. Critical review and advices on spectral-based normalization methods for LIBS quantitative analysis. *Spectrochim. Acta Part B At. Spectrosc.* 2019, *160*, 105688, doi:10.1016/j.sab.2019.105688.

Guezenoc, J.; Payré, V.; Fabre, C.; Syvilay, D.; Cousin, A.; Gallet-Budynek, A.; Bousquet, B. Variable selection in laser-induced breakdown spectroscopy assisted by multivariate analysis: An alternative to multi-peak fitting. *Spectrochim. Acta Part B At. Spectrosc.* 2019, *152*, 6–13, doi:10.1016/j.sab.2018.12.001.

Harhira, A.; Bouchard, P.; Rifai, K.; Haddad, J.E.; Sabsabi, M.; Blouin, A.; Laflamme, M. Advanced La-ser-Induced Breakdown Spectroscopy (LIBS) Sensor for Gold Mining. 2017. Available online: https://nrc-publications.canada.ca/eng/view/ft/?id=e302005a-66d5-4a1e-921d-d2cdb0ba0e77 (accessed on 1 April 2021)

Harmon, R.S.; De Lucia, F.C.; McManus, C.E.; McMillan, N.J.; Jenkins, T.F.; Walsh, M.E.; Miziolek, A. Laser-induced breakdown spectroscopy—An emerging chemical sensor technology for real-time field-portable, geochemical, mineralogical, and environmental applications. *Appl. Geochem.* 2006, *21*, 730–747, doi:10.1016/j.apgeochem.2006.02.003.

Harmon, R.S.; Lawley, C.J.; Watts, J.; Harraden, C.L.; Somers, A.M.; Hark, R.R. Laser-Induced Breakdown Spectroscopy—An Emerging Analytical Tool for Mineral Exploration. *Minerals* 2019, *9*, 718, doi:10.3390/min9120718.

Hunt, G.R. Spectral signatures of particulate minerals in the visible and near infrared. *Geophysics* 1977, *42* (3), 501-513. doi: 10.1190/1.1440721.

Hunt, G.R.; Ashley, R.P. Spectra of altered rocks in the visible and near infrared. *Economic Geology* 1979, *74* (7), 1613-1629. doi: 10.2113/gsecongeo.74.7.1613.

Hunt, G.R.; Salisbury, J.W. Visible and near-infrared spectra of minerals and rocks: I Silicate minerals. *Modern Geology* 1970, *1*, 283-300.

Jolivet, L.; Leprince, M.; Moncayo, S.; Sorbier, L.; Lienemann, C.-P.; Motto-Ros, V. Review of the recent advances and applications of LIBS-based imaging. *Spectrochim. Acta Part B At. Spectrosc.* 2019, *151*, 41–53, doi:10.1016/j.sab.2018.11.008.

Kesler, S.E.; Gruber, P.W.; Medina, P.A.; Keoleian, G.A.; Everson, M.P.; Wallington, T.J. Global lithium resources: Relative importance of pegmatite, brine and other deposits. *Ore Geology Reviews* 2012, *48*, 55-69. doi: https://doi.org/10.1016/j.oregeorev.2012.05.006.

King, T.V.V.; Clark, R.N. Spectral characteristics of chlorites and Mg-serpentines using high-resolution reflectance spectroscopy. *Journal of Geophysical Research: Solid Earth* 1989, *94* (B10), 13997-14008. doi: https://doi.org/10.1029/JB094iB10p13997.

Kochelek, K.A.; McMillan, N.J.; McManus, C.E.; Daniel, D.L. Provenance determination of sapphires and rubies using laserinduced breakdown spectroscopy and multivariate analysis. *Am. Miner.* 2015, *100*, 1921–1931, doi:10.2138/am-2015-5185.

Krohn, M.D.; Altaner, S.P. Near‐infrared detection of ammonium minerals. *Geophysics* 1987, *52* (7), 924-930. doi: 10.1190/1.1442362.

Laakso, K.; Peter, J.M.; Rivard, B.; Gloaguen, R. Combined hyperspectral and lithogeochemical estimation of alteration intensities in a volcanogenic massive sulfide deposit hydrothermal system: A case study from Northern Canada. In 2016 8th Workshop on Hyperspectral Image and Signal Processing: Evolution in Remote Sensing (WHISPERS), 21-24 Aug. 2016; 2016; pp 1-5. doi: 10.1109/WHISPERS.2016.8071707.

Laakso, K.; Peter, J.M.; Rivard, B.; White, H.P. Short-Wave Infrared Spectral and Geochemical Characteristics of Hydrothermal Alteration at the Archean Izok Lake Zn-Cu-Pb-Ag Volcanogenic Massive Sulfide Deposit, Nunavut, Canada: Application in Exploration Target Vectoring. *Economic Geology* 2016, *111* (5), 1223-1239. doi: 10.2113/econgeo.111.5.1223.

Lawley, C.J.; Somers, A.M.; Kjarsgaard, B.A. Rapid geochemical imaging of rocks and minerals with handheld laser induced breakdown spectroscopy (LIBS). *J. Geochem. Explor.* 2021, *222*, 106694, doi:10.1016/j.gexplo.2020.106694.

Lima, A. Estrutura, mineralogia e génese dos filões aplitopegmatíticos com espodumena da região do Barroso-Alvão. PhD thesis, Universidade do Porto, Porto, 2000.

Linnen, R.L.; Van Lichtervelde, M.; Černý, P. Granitic Pegmatites as Sources of Strategic Metals. *Elements* 2012, *8*, 275–280, doi:10.2113/gselements.8.4.275.

London, D.; Burt, D.M. Chemical models for lithium aluminosilicate stabilities in pegmatites and granites. *American Mineralogist* 1982, *67* (5-6), 494-509.

Lypaczewski, P.; Rivard, B. Estimating the Mg# and AlVI content of biotite and chlorite from shortwave infrared reflectance spectroscopy: Predictive equations and recommendations for their use. *International Journal of Applied Earth Observation and Geoinformation* 2018, *68*, 116-126. doi: https://doi.org/10.1016/j.jag.2018.02.003.

Lypaczewski, P.; Rivard, B.; Lesage, G.; Byrne, K.; D'Angelo, M.; Lee, R.G. Characterization of Mineralogy in the Highland Valley Porphyry Cu District Using Hyperspectral Imaging, and Potential Applications. *Minerals* 2020, *10* (5), 473. doi: 10.3390/min10050473.

Maaza, M.; Mothudi, B.M. Laser-Induced Breakdown Spectroscopy (LIBS) on Geological Samples: Compositional Differentiation and Relative Hardness Quantification. Master Thesis, University of South Africa, Pretoria, South Africa, 2018.

Mattson, S.M.; Rossman, G.R. Fe2+-Fe3+ interactions in tourmaline. *Physics and Chemistry of Minerals* 1987, *14* (2), 163-171. doi: 10.1007/BF00308220.

Maurice, S.; Wiens, R.C.; Bernardi, P.; Caïs, P.; Robinson, S.; Nelson, T.; Gasnault, O.; Reess, J.-M.; Deleuze, M.; Rull, F.; et al. The SuperCam Instrument Suite on the Mars 2020 Rover: Science Objectives and Mast-Unit Description. *Space Sci. Rev.* 2021, *217*:47, doi:10.1007/s11214-021-00807-w.

Maurice, S.; Wiens, R.C.; Saccoccio, M.; Barraclough, B.; Gasnault, O.; Forni, O.; Mangold, N.; Baratoux, D.; Bender, S.; Berger, G.; et al. The ChemCam Instrument Suite on the Mars Science Laboratory (MSL) Rover: Science Objectives and Mast Unit Descriptn. *Space Sci. Rev.* 2012, *170*, 95–166, doi:10.1007/s11214-012-9912-2.

McManus, C.E.; Dowe, J.; McMillan, N.J. Quantagenetics® analysis of laser-induced breakdown spectroscopic data: Rapid and accurate authentication of materials. *Spectrochim. Acta Part B At. Spectrosc.* 2018, *145*, 79–85, doi:10.1016/j.sab.2018.04.010.

McMillan, N.J.; Curry, J.; Dutrow, B.L.; Henry, D.J. Identification of the Host Lithology of Tourmaline Using Laser-Induced Breakdown Spectroscopy for Application in Sediment Provenance and Mineral Exploration. *Can. Miner.* 2018, *56*, 393–410, doi:10.3749/canmin.1800004.

McMillan, N.J.; Rees, S.; Kochelek, K.; E McManus, C. Geological Applications of Laser-Induced Breakdown Spectroscopy. *Geostand. Geoanalytical Res.* 2014, *38*, 329–343, doi:10.1111/j.1751-908x.2014.00308.x.

Menges, F. Spectragryph - optical spectroscopy software, Version 1.2.14. Available online: http://www.effemm2.de/spectragryph/ (accessed 22 July 2020).

Möller, V.; Williams-Jones, A.E. A hyperspectral study (V-NIR-SWIR) of the Nechalacho REE-Nb-Zr deposit, Canada. *Journal of Geochemical Exploration* 2018, *188*, 194-215. doi: https://doi.org/10.1016/j.gexplo.2018.01.011.

Naleto, J.L.C.; Perrotta, M.M.; Costa, F.G.d.; Souza Filho, C.R.d. Point and imaging spectroscopy investigations on the Pedra Branca orogenic gold deposit, Troia Massif, Northeast Brazil: Implications for mineral exploration in amphibolite metamorphic-grade terrains. *Ore Geology Reviews* 2019, *107*, 283-309. doi: https://doi.org/10.1016/j.oregeorev.2019.02.019.

Oshigami, S.; Yamaguchi, Y.; Uezato, T.; Momose, A.; Arvelyna, Y.; Kawakami, Y.; Yajima, T.; Miyatake, S.; Nguno, A. Mineralogical mapping of southern Namibia by application of continuum-removal MSAM method to the HyMap data. *International Journal of Remote Sensing* 2013, *34* (15), 5282-5295. doi: 10.1080/01431161.2013.789147.

Payré, V.; Fabre, C.; Cousin, A.; Sautter, V.; Wiens, R.C.; Forni, O.; Gasnault, O.; Mangold, N.; Meslin, P.-Y.; Lasue, J.; et al. Alkali trace elements in Gale crater, Mars, with ChemCam: Calibration update and geological implications. *J. Geophys. Res. Planets* 2017, *122*, 650–679, doi:10.1002/2016je005201.

Payré, V.; Fabre, C.; Sautter, V.; Cousin, A.; Mangold, N.; Le Deit, L.; Forni, O.; Goetz, W.; Wiens, R.C.; Gasnault, O.; et al. Copper enrichments in the Kimberley formation in Gale crater, Mars: Evidence for a Cu deposit at the source. *Icarus* 2019, *321*, 736–751, doi:10.1016/j.icarus.2018.12.015.

Pereira, I.; Dias, R.; Bento dos Santos, T.; Mata, J. Exhumation of a migmatite complex along a transpressive shear zone: inferences from the Variscan Juzbado–Penalva do Castelo Shear Zone (Central Iberian Zone). *Journal of the Geological Society* 2017, *174* (6), 1004. doi: 10.1144/jgs2016-159.

Pochon, A.; Desaulty, A.-M.; Bailly, L. Handheld laser-induced breakdown spectroscopy (LIBS) as a fast and easy method to trace gold. *J. Anal. At. Spectrom.* 2020, *35*, 254–264, doi:10.1039/c9ja00437h.

Pontual, S.; Merry, N.J.; Gamson, P. *Spectral interpretation field manual. GMEX Spectral analysis guides for mineral exploration*. 3rd ed.; AusSpec International Ltd.: Victoria, 2008; Vol. 1.

Popov, A.M.; Zaytsev, S.M.; Seliverstova, I.V.; Zakuskin, A.; Labutin, T.A. Matrix effects on laser-induced plasma parameters for soils and ores. *Spectrochim. Acta Part B At. Spectrosc.* 2018, *148*, 205–210, doi:10.1016/j.sab.2018.07.005.

Quarles, C.D.; Gonzalez, J.J.; East, L.J.; Yoo, J.H.; Morey, M.S.; Russo, R.E. Fluorine analysis using Laser Induced Breakdown Spectroscopy (LIBS). *J. Anal. At. Spectrom.* 2014, *29*, 1238–1242, doi:10.1039/c4ja00061g.

Quensel, P. Minerals of the Varuträsk Pegmatite. *Geologiska Föreningen i Stockholm Förhandlingar* 1937, *59* (2), 150-156. doi: 10.1080/11035893709444939.

Quensel, P. Minerals of the Varuträsk Pegmatite. *Geologiska Föreningen i Stockholm Förhandlingar* 1938, *60* (2), 201-215. doi: 10.1080/11035893809444995.

Radziemski, L.J. From LASER to LIBS, the path of technology development. *Spectrochim. Acta Part B At. Spectrosc.* 2002, *57*, 1109– 1113, doi:10.1016/s0584-8547(02)00052-6.

Rakovský, J.; Čermák, P.; Musset, O.; Veis, P. A review of the development of portable laser induced breakdown spectroscopy and its applications. *Spectrochim. Acta Part B At. Spectrosc.* 2014, *101*, 269–287, doi:10.1016/j.sab.2014.09.015.

Rifai, K.; Doucet, F.; Özcan, L.; Vidal, F. LIBS core imaging at kHz speed: Paving the way for real-time geochemical applications. *Spectrochim. Acta Part B At. Spectrosc.* 2018, *150*, 43–48, doi:10.1016/j.sab.2018.10.007.

Rifai, K.; Özcan, L.-Ç.; Doucet, F.R.; Rhoderick, K.; Vidal, F. Ultrafast Elemental Mapping of Platinum Group Elements and Mineral Identification in Platinum-Palladium Ore Using Laser Induced Breakdown Spectroscopy. *Minerals* 2020, *10*, 207, doi:10.3390/min10030207.

Rifai, K.; Paradis, M.-C.M.; Swierczek, Z.; Doucet, F.; Özcan, L.; Fayad, A.; Li, J.; Vidal, F. Emergences of New Technology for Ultrafast Automated Mineral Phase Identification and Quantitative Analysis Using the CORIOSITY Laser-Induced Breakdown Spectroscopy (LIBS) System. *Minerals* 2020, *10*, 918, doi:10.3390/min10100918.

Roda, E. Distribución, Caracteristicas y Petrogenesis de las Pegmatitas de La Fregeneda (Salamanca). PhD thesis, Facultad de Ciencia y Tecnología de la Universidad del País Vasco (UPV/EHU), Bilbao, Spain, 1993.

Roda-Robles, E.; Pesquera, A.; Velasco, F.; Fontan, F. The granitic pegmatites of the Fregeneda area (Salamanca, Spain): characteristics and petrogenesis. *Mineral. Mag.* 1999, *63* (4), 535–558.

Rodríguez Alonso, M.D.; Díez Balda, M.A.; Perejón, A.; Pieren, A.; Liñán, E.; López Díaz, F.; Moreno, F.; Gámez Vintaned, J.A.; Gónzalez Lodeiro, F.; Martínez Poyatos, D.; Vegas, R. Domínio del Complejo Esquisto-Grauváquico: Estratigrafía. La secuencia litoestratigráfica del

Neoproterozóico-Câmbrico Inferior. In *Geología de España*, Vera, J. A., Ed. Geol. España/Inst. Geol. Min. España (SGE-IGME): Madrid, 2004; pp 78-81.

Rossi, M.; Dell'Aglio, M.; De Giacomo, A.; Gaudiuso, R.; Senesi, G.S.; de Pascale, O.; Capitelli, F.; Nestola, F.; Ghiara, M.R. Multimethodological investigation of kunzite, hiddenite, alexandrite, elbaite and topaz, based on laser-induced breakdown spectroscopy and conventional analytical techniques for supporting mineralogical characterization. *Phys. Chem. Miner.* 2013, *41*, 127– 140, doi:10.1007/s00269-013-0631-3.

Santos, D.; Teodoro, A.; Lima, A.; Cardoso-Fernandes, J. Remote sensing techniques to detect areas with potential for lithium exploration in Minas Gerais, Brazil. In Proceedings of SPIE, SPIE Remote Sensing, Strasbourg, France, 9–12 September 2019; Schulz, K.; Michel, U.; Nikolakopoulos, K. G., Eds. SPIE: Bellingham, WA; 2019. doi: https://doi.org/10.1117/12.2532744.

Selway, J.B.; Breaks, F.W.; Tindle, A.G. A Review of Rare-Element (Li-Cs-Ta) Pegmatite Exploration Techniques for the Superior Province, Canada, and Large Worldwide Tantalum Deposits. *Exploration and Mining Geology* 2005, *14* (1-4), 1-30. doi: 10.2113/gsemg.14.1-4.1.

Senesi, G.S.; Harmon, R.S.; Hark, R.R. Field-portable and handheld laser-induced breakdown spectroscopy: Historical review, current status and future prospects. *Spectrochim. Acta Part B At. Spectrosc.* 2021, *175*, 106013, doi:10.1016/j.sab.2020.106013.

Shi, Q.; Niu, G.; Lin, Q.; Xu, T.; Li, F.; Duan, Y. Quantitative analysis of sedimentary rocks using laser-induced breakdown spectroscopy: comparison of support vector regression and partial least squares regression chemometric methods. *J. Anal. At. Spectrom.* 2015, *30*, 2384–2393, doi:10.1039/c5ja00255a.

Silva, A.F.; Santos, A.J.; Ribeiro, A.; Cabral, J.; Ribeiro, M.L. *Carta Geológica de Portugal na escala 1/50.000 – folha 15-B – Freixo de Espada à Cinta*. Serviços Geológicos de Portugal: Lisboa, Portugal, 1990; p 1 map.

Silva, A.F.; Santos, A.J.; Ribeiro, A.; Ribeiro, M.L. *Carta Geológica de Portugal na escala 1/50.000 – folha 15-A – Vila Nova de Foz Côa*. Serviços Geológicos de Portugal: Lisboa, Portugal, 1990; p 1 map.

Silva, A.F.d.; Ribeiro, M.L. *Notícia Explicativa da folha 15-A Vila Nova de Foz Côa*. Serviços Geológicos de Portugal: Lisboa, Portugal, 1991; p 52.

Silva, A.F.d.; Ribeiro, M.L. *Notícia Explicativa da folha 15-B Freixo de Espada à Cinta*. Instituto Geológico e Mineiro: Lisboa, Portugal, 1994; p 48.

Silva, J., Cardoso-Fernandes, J., Teodoro, A., Lima, A. (2020). "As Assinaturas Espectrais dos Minerais de Lítio do Campo Aplito-Pegmatítico de Fregeneda-Almendra". *GeoCore* 5, 22-23.

Silva, J., Teodoro, A., Lima, A., Cardoso-Fernandes, J., Cauzid, Jean (2021). *Espectroscopia de Reflectância no Campo Aplito-Pegmatítico de Fregeneda-Almendra: Estudo das Assinaturas Espectrais dos Minerais de Lítio*. Abstract presented at *Jornadas do ICT*, *Porto*, 2021.

Silva, S.M.P.d.; Crósta, A.P.; Angélica, R.S.; Beurlen, H.; Silva, M.R.R.d. Mineralogical characterization and mapping using reflectance spectroscopy: an experiment at Alto do Giz pegmatite in the south portion of Borborema Pegmatite Province (BPP), northeastern Brazil. *Estudos Geológicos* 2009, *19* (2), 337-342.

Sobron, P. Non-Linear Methods for Quantitative Elemental Analysis and Mineral Classification Using Laser-Induced Breakdown Spectroscopy (LIBS) 2019, https://patents.google.com/patent/US20190079019A1/en.

Steiner, B.M. Tools and Workflows for Grassroots Li–Cs–Ta (LCT) Pegmatite Exploration. *Minerals* 2019, *9* (8), 499. doi: 10.3390/min9080499.

Sun, Y.; Seccombe, P.K.; Yang, K. Application of short-wave infrared spectroscopy to define alteration zones associated with the Elura zinc–lead–silver deposit, NSW, Australia. *Journal of Geochemical Exploration* 2001, *73* (1), 11-26. doi: https://doi.org/10.1016/S0375-6742(01)00167-4.

Sweetapple, M.T.; Tassios, S. Laser-induced breakdown spectroscopy (LIBS) as a tool for in situ mapping and textural interpretation of lithium in pegmatite minerals. *Am. Miner.* 2015, *100*, 2141–2151, doi:10.2138/am-2015-5165.

Syvilay, D.; Guezenoc, J.; Bousquet, B. Guideline for increasing the analysis quality in laser-induced breakdown spectroscopy. *Spectrochim. Acta Part B At. Spectrosc.* 2019, *161*, 105696, doi:10.1016/j.sab.2019.105696.

Tappert, M.C.; Rivard, B.; Giles, D.; Tappert, R.; Mauger, A. The mineral chemistry, near-infrared, and mid-infrared reflectance spectroscopy of phengite from the Olympic Dam IOCG deposit, South Australia. *Ore Geology Reviews* 2013, *53*, 26-38. doi: https://doi.org/10.1016/j.oregeorev.2012.12.006.

Teixeira, C. *Notas sobre geologia de Portugal o complexo xisto-grauváquico ante-ordoviciano*. Empresa Literaria Fluminense Lda.: Lisboa, Portugal, 1955; p 48.

Therien, C. Welcome to the PySptools Documentation. Available online: https://pysptools.sourceforge.io/ (accessed 22 July 2020).

Turner, D.; Rivard, B.; Groat, L. Rare earth element ore grade estimation of mineralized drill core from hyperspectral imaging spectroscopy. In 2014 IEEE Geoscience and Remote Sensing Symposium, 13-18 July 2014; 2014; pp 4612-4615. doi: 10.1109/IGARSS.2014.6947520.

Vasavada, A.R.; Grotzinger, J.P.; Arvidson, R.E.; Calef, F.J.; Crisp, J.; Gupta, S.; A Hurowitz, J.; Mangold, N.; Maurice, S.; E Schmidt, M.; et al. Overview of the Mars Science Laboratory mission: Bradbury Landing to Yellowknife Bay and beyond. *J. Geophys. Res. Planets* 2014, *119*, 1134–1161, doi:10.1002/2014je004622.

Vieira, R. Aplitopegmatitos com elementos raros da região entre Almendra (V.N. de Foz Côa) e Barca d'Alva (Figueira de Castelo Rodrigo). Campo aplitopegmatítico da Fregeneda-Almendra. PhD thesis, Faculdade de Ciências da Universidade do Porto, Porto, Portugal, 2010.

Wiens, R.; Maurice, S.; Lasue, J.; Forni, O.; Anderson, R.; Clegg, S.; Bender, S.; Blaney, D.; Barraclough, B.; Cousin, A.; et al. Preflight calibration and initial data processing for the ChemCam laser-induced breakdown spectroscopy instrument on the Mars Science Laboratory rover. *Spectrochim. Acta Part B At. Spectrosc.* 2013, *82*, 1–27, doi:10.1016/j.sab.2013.02.003.

Wiens, R.C.; Maurice, S.; Robinson, S.H.; Nelson, A.E.; Cais, P.; Bernardi, P.; Newell, R.T.; Clegg, S.; Sharma, S.K.; Storms, S.; et al. The SuperCam Instrument Suite on the NASA Mars 2020 Rover: Body Unit and Combined System Tests. *Space Sci. Rev.* 2021, *217:4* doi:10.1007/s11214-020-00777-5.

Wiens, R.C.; Sylvestre S. and the MSL Science Team Maurice; Reitz G. DLR Collaborator (MSL Science Team) ChemCam: Chemostratigraphy by the First Mars Microprobe. *Elements* 2015, *11*, 33–38, doi:10.2113/gselements.11.1.33.

Zhang, A.; Wang, R.; Li, Y.; Hu, H.; Lu, X.; Ji, J.; Zhang, H. Tourmalines from the Koktokay No.3 pegmatite, Altai, NW China: spectroscopic characterization and relationships with the pegmatite evolution. *European Journal of Mineralogy* 2008, *20* (1), 143-154. doi: 10.1127/0935-1221/2008/0020-1779.

Chapter IV: Geochemical exploration techniques as a complementary tool

Ague, J. J. (1994). Mass transfer during Barrovian metamorphism of pelites, south-central Connecticut. I: Evidence for changes in composition and volume. *American Journal of Science* 294, 989–1057. https://doi.org/10.2475/ajs.294.8.989

Almeida, C.M.P.d., 2003. Estudo do filão aplitopegmatítico da mina da Bajoca, Almendra: contribuição científico-tecnológica. Faculdade de Ciências da Universidade do Porto, Porto, pp. XIV, 120.

Angel, J.M., Viallefond, L. (1981). *Prospection géochimique Portugal. Résultats analytiques et interprétation de l'échantillonnage réalisé par le S.F.M. sur la feuille 15A, région de Almendra* (NOTE/GMX-748). p. 6.

Antunes, I.M.H.R., Neiva, A.M.R., Ramos, J.M.F., Silva, P.B., Silva, M.M.V.G., Corfu, F., 2013. Petrogenetic links between lepidolite-subtype aplite-pegmatite, aplite veins and associated granites at Segura (central Portugal). Geochemistry 73, 323-341. doi: https://doi.org/10.1016/j.chemer.2012.12.003.

Barros, R., Kaeter, D., Menuge, J. F., & Škoda, R. (2020). Controls on chemical evolution and rare element enrichment in crystallising albite-spodumene pegmatite and wallrocks: Constraints from mineral chemistry. *Lithos, 352-353*, 105289. doi: https://doi.org/10.1016/j.lithos.2019.105289.

Bea, F., Montero, P., González-Lodeiro, F. & Talavera, C. (2007). Zircon inheritance reveals exceptionally fast crustal magma generation processes in Central Iberia during the Cambro-Ordovician. *Journal of Petrology* 48, 2327–2339. https://doi.org/10.1093/petrology/egm061

Blengini, G. A., Latunussa, C. E. L., Eynard, U., Torres de Matos C., Wittmer, D., Georgitzikis, K., Pavel, C., Carrara, S., Mancini, L., Unguru, M., Blagoeva, D., Mathieux, F. & Pennington D. (2020). Study on the EU's list of Critical Raw Materials Final Report. *European Commission.* https://doi.org/10.2873/11619

Bonham-Carter, G.F., Rogers, P.J., Ellwood, D.J., 1987. Catchment basin analysis applied to surficial geochemical data, Cobequid Highlands, Nova Scotia. Journal of Geochemical Exploration 29, 259-278. doi: https://doi.org/10.1016/0375-6742(87)90081-1.

Cardoso-Fernandes, J., Lima, A., Roda-Robles, E., Ribeiro, M. A., & Teodoro, A. (2020). *Geochemical pathfinder analysis for lithium (Li) exploration in the Iberian Peninsula.* Paper presented at the X Congresso Jovens Investigadores em Geociências, LEG, Estremoz, 12-15.

Cardoso-Fernandes, J., Teodoro, A. C. & Lima, A. (2019). Remote sensing data in lithium (Li) exploration: A new approach for the detection of Li-bearing pegmatites. *International Journal of Applied Earth Observation and Geoinformation* 76, 10–25. https://doi.org/10.1016/j.jag.2018.11.001

Cardoso-Fernandes, J., Teodoro, A. C., Lima, A. Perrotta, M. & Roda-Robles, E. (2020). Detecting Lithium (Li) Mineralizations from Space: Current Research and Future Perspectives. *Applied Sciences* 10, 1785. https://doi.org/10.3390/app10051785

Cardoso-Fernandes, J., Teodoro, A.C., Lima, A., Mielke, C., Körting, F., Roda-Robles, E., Cauzid, J. (2020, 26 Sept.-2 Oct. 2020). *Multi-scale approach using remote sensing techniques for lithium pegmatite exploration: first results.* Paper presented at the IGARSS 2020 - 2020 IEEE International Geoscience and Remote Sensing Symposium, Waikoloa, HI, USA, 5226-5229. doi: 10.1109/IGARSS39084.2020.9323705.

Cardoso-Fernandes, J.; Lima, A.; Roda-Robles, E.; Anjos Ribeiro, M.; Teodoro, A. (2020). Associações elementares nos aplito-pegmatitos da mina da Bajoca (Almendra, Vila Nova de Foz Côa). *GeoCore 5*, 24-25.

Cardoso-Fernandes, J.; Lima, A.; Roda-Robles, E.; Ribeiro, M.A.; Teodoro, A. (2021; in press). *Vectoring lithium (Li) mineralizations: a first approach to pegmatite geochemical halo definition in the Fregeneda-Almendra area*. Abstract presented at Goldschmidt Virtual, 2021.

Cardoso-Fernandes, J.; Ribeiro, M.; Lima, A.; Roda-Robles, E.; Teodoro, A.; Lima, J. (2019). *Biotite porphyroblast microstructures in the Almendra (Vila Nova de Foz Côa) region*. Paper presented at IX Congresso Jovens Investigadores em Geociências, LEG 2019, Estremoz, 2019.

Carranza, E.J.M., 2004. Usefulness of stream order to detect stream sediment geochemical anomalies. Geochemistry: Exploration, Environment, Analysis 4, 341-352. doi: 10.1144/1467-7873/03-040.

Carranza, E.J.M., 2009a. Chapter 4: Fractal analysis of geochemical anomalies, in: Carranza, E.J.M. (Ed.), Handbook of Exploration and Environmental Geochemistry. Elsevier Science B.V., pp. 85-114.

Carranza, E.J.M., 2009b. Chapter 5: Catchment Basin Analysis of Stream Sediment Anomalies, in: Carranza, E.J.M. (Ed.), Handbook of Exploration and Environmental Geochemistry. Elsevier Science B.V., pp. 115-144.

Carranza, E.J.M., Hale, M., 1997. A catchment basin approach to the analysis of reconnaissance geochemical - geological data from Albay province, Philippines. Journal of geochemical exploration 60, 151-171.

Carrington da Costa, M. (1950). Notícia sobre uma carta geológica do Buçaco de Nery Delgado. *Comunicações dos Serviços Geológicos de Portugal*, 1–28.

Carvalhosa, A., 1960. Carta Geológica de Portugal na escala 1/50.000 – folha 15-D – Figueira de Castelo Rodrigo. Serviços Geológicos de Portugal, Lisboa, Portugal.

Černý, P. & Ercit, T. S. (2005). The classification of granitic pegmatites revisited. *Canadian Mineralogist* 43, 2005–2026. http://doi.org/10.2113/gscanmin.43.6.2005

Černý, P. (1989). Exploration strategy and methods for pegmatite deposits of tantalum. In: Möller, P., Černý, P. & Saupé, F. (eds.) *Lanthanides, Tantalum and Niobium.* Springer-Verlag, Berlin, 274–302. https://doi.org/10.1007/978-3-642-87262-4

Černý, P. (2005). *The Tanco Rare-Element Pegmatite Deposit Manitoba: Regional Context, Internal Anatomy, and Global Comparisons*. In: Linnen, R. L. & Sampson, I. M. (eds.) *Rare–Element Geochemistry and Mineral Deposits*; *GAC Short Course Notes*. Geological Association of Canada, St. Catharines 17, 175–199

Černý, P., Ercit, T.S., 2005. Classification of granitic pegmatites revisited. Can. Mineral. 43, 2005–2026.

Cerny, P., Meintzer, R.E., Anderson, A.J., 1985. Extreme fractionation in rare-element granitic pegmatites; selected examples of data and mechanisms. The Canadian Mineralogist 23, 381-421.

Chandrajith, R., Dissanayake, C. B., & Tobschall, H. J. (2001). Application of multi-element relationships in stream sediments to mineral exploration: a case study of Walawe Ganga Basin, Sri Lanka. *Applied Geochemistry, 16*(3), 339-350. doi: https://doi.org/10.1016/S0883-2927(00)00038-X.

Charoy, B., Noronha, F., 1996. Multistage Growth of a Rare-Element, Volatile-Rich Microgranite at Argemela (Portugal). Journal of Petrology 37, 73-94. doi: 10.1093/petrology/37.1.73.

Cheng, Q. (2007). Mapping singularities with stream sediment geochemical data for prediction of undiscovered mineral deposits in Gejiu, Yunnan Province, China. *Ore Geology Reviews, 32*(1-2), 314-324. doi: 10.1016/j.oregeorev.2006.10.002.

Cheng, Q., Agterberg, F.P., Ballantyne, S.B., 1994. The separation of geochemical anomalies from background by fractal methods. Journal of Geochemical Exploration 51, 109-130. doi: https://doi.org/10.1016/0375-6742(94)90013-2.

Condie, K. C. (1993). Chemical composition and evolution of the upper continental crust: Contrasting results from surface samples and shales. *Chemical Geology* 104, 1–37. https://doi.org/10.1016/0009-2541(93)90140-E

Costa, J.C.S.d., 1950. Notícia sobre uma carta geológica do Buçaco, de Nery Delgado. Serviços Geológicos de Portugal, Lisboa, Portugal.

Cox, R., Lowe, D. R. & Cullers, R. L. (1995). The influence of sediment recycling and basement composition on evolution of mudrock chemistry in the southwestern United States. *Geochimica et Cosmochimica Acta* 59, 2919–2940. https://doi.org/10.1016/0016-7037(95)00185-9

Debon, F. & Le Fort, P. (1983). A chemical–mineralogical classification of common plutonic rocks and associations. *Transactions of the Royal Society of Edinburgh: Earth Sciences* 73, 135–149. https://doi.org/10.1017/S0263593300010117

Dias da Silva, Í. (2014). Geología de las Zonas Centro Ibérica y Galicia-Trás-os-Montes en la parte oriental del Complejo de Morais, Portugal/España. PhD Thesis. Salamanca, Universidad de Salamanca, 424pp.

Dias da Silva, Í., Gómez-Barreiro, J., Martínez Catalán, J. R., Ayarza, P., Pohl, J. & Martínez, E. (2017). Structural and microstructural analysis of the Retortillo Syncline (Variscan belt, Central Iberia). Implications for the Central Iberian Orocline. *Tectonophysics* 717, 99–115. https://doi.org/10.1016/j.tecto.2017.07.015

Dias, G., Leterrier, J., Mendes, A., Simões, P. P. & Bertrand, J. M. (1998). U–Pb zircon and monazite geochronology of post-collisional Hercynian granitoids from the Central Iberian Zone (Northern Portugal). *Lithos* 45, 349–369. https://doi.org/10.1016/S0024-4937(98)00039-5

Díez Balda, M.A., Vegas, R., Lodeiro, G., 1990. Central Iberian Zone: structure, in: Dallmeyer, R.D., Martinez Garcia, E. (Eds.), Pre-Mesozoic geology of the Iberian Peninsula. Springer Verlag, Berlim, pp. 172–188.

Díez Fernández, R. & Pereira, M. F. (2016). Extensional orogenic collapse captured by strike-slip tectonics: Constraints from structural geology and U–Pb geochronology of the Pinhel shear zone (Variscan orogen, Iberian Massif). *Tectonophysics* 691, 290–310. https://doi.org/10.1016/j.tecto.2016.10.023

Díez Fernández, R. & Pereira, M. F. (2017). Strike-slip shear zones of the Iberian Massif: Are they coeval?. *Lithosphere* 9, 726–744. https://doi.org/10.1130/L648.1

Dill, H.G., Weber, B., Melcher, F., Wiesner, W., Müller, A., 2014. Titaniferous heavy mineral aggregates as a tool in exploration for pegmatitic and aplitic rare-metal deposits (SE Germany). Ore Geology Reviews 57, 29-52. doi: https://doi.org/10.1016/j.oregeorev.2013.08.023.

Dimmell, P. M., & Morgan, J. A. (2005). The Aubry Pegmatites: Exploration for Highly Evolved Lithium-Cesium-Tantalum Pegmatites in Northern Ontario. *Exploration and Mining Geology, 14*(1-4), 45-59. doi: 10.2113/gsemg.14.1-4.45.

Environmental Systems Research Institute, I. (2020). ArcMap Software. Retrieved from Available online: http://desktop.arcgis.com/en/arcmap/ (accessed on 27 July 2021).

Escuder Viruete, J., Arenas, R. & Martínez Catalán, J. R. (1994). Tectonothermal evolution associated with Variscan crustal extension in the Tormes Gneiss Dome (NW Salamanca, Iberian Massif, Spain). *Tectonophysics* 238, 117–138. https://doi.org/10.1016/0040-1951(94)90052-3

European Commission: DG Internal Market Industry Entrepreneurship and SMEs. (2020). *Critical Raw Materials Resilience: Charting a Path towards greater Security and Sustainability* (COM(2020) 474 final). Brussels, p. 23.

Fabre, C., Ourti, N.E., Mercadier, J., Cardoso-Fernandes, J., Dias, F., Perrotta, M., Koerting, F., Lima, A., Kaestner, F., Koellner, N., Linnen, R., Benn, D., Martins, T., Cauzid, J., 2021. Analyses of Li-Rich Minerals Using Handheld LIBS Tool. Data 6, 68. doi: 10.3390/data6060068.

Fedo, C., Nesbitt, H. W. & Young, G. M. (1995). Unraveling the effects of potassium metasomatism in sedimentary rocks and paleosols, with implications for paleoweathering conditions and provenance. *Geology* 23, 921–924. https://doi.org/10.1130/0091-7613(1995)023<0921:UTEOPM>2.3.CO;2

Ferreira, J. A., Bento dos Santos, T., Pereira, I. & Mata, J. (2019). Tectonically assisted exhumation and cooling of Variscan granites in an anatectic complex of the Central Iberian

Zone, Portugal: constraints from LA-ICP-MS zircon and apatite U–Pb ages. *International Journal of Earth Sciences* 108, 2153–2175. https://doi.org/10.1007/s00531-019-01755-1

Ferreira, J. A., Mata, J., Bento dos Santos, T. & Pereira, I. (2020). The role of melting on the geochemical evolution and isotopic variability of an anatectic complex in the Iberian Variscides. *Lithos* 378–379, 105769. https://doi.org/10.1016/j.lithos.2020.105769

Ferreira, J.A., Bento dos Santos, T., Pereira, I., Mata, J., 2019. Tectonically assisted exhumation and cooling of Variscan granites in an anatectic complex of the Central Iberian Zone, Portugal: constraints from LA-ICP-MS zircon and apatite U–Pb ages. International Journal of Earth Sciences 108, 2153-2175. doi: 10.1007/s00531-019-01755-1.

Ferreira, J.A., Mata, J., Bento dos Santos, T., Pereira, I., 2020. The role of melting on the geochemical evolution and isotopic variability of an anatectic complex in the Iberian Variscides. Lithos 378-379, 105769. doi: https://doi.org/10.1016/j.lithos.2020.105769.

Floyd, P. A. & Leveridge, B. E. (1987). Tectonic environment of the Devonian Gramscatho basin, south Cornwall: framework mode and geochemical evidence from turbiditic sandstones. *Journal of the Geological Society* 144, 531–542. https://doi.org/10.1144/gsjgs.144.4.0531

Frick, C., Strauss, S.W., 1987. Geochemical evolution of the Richtersveld area, South Africa, as deduced from regional geochemical maps of stream sediments. Journal of Geochemical Exploration 28, 431-449. doi: https://doi.org/10.1016/0375-6742(87)90061-6.

Fuenlabrada, J. M., Arenas, R., Sánchez Martínez, S., Díez Fernández, R., Pieren, A. P., Pereira, M. F., Chichorro, M. & Silva J. B. (2020). Geochemical and isotopic (Sm–Nd) provenance of Ediacaran-Cambrian metasedimentary series from the Iberian Massif. Paleoreconstruction of the North Gondwana margin. *Earth-Science Reviews* 201, 103079. https://doi.org/10.1016/j.earscirev.2019.103079

Fuertes Fuente, M., Martin Izard, A., 1998. The Forcarei Sur rare-element granitic pegmatite field and associated mineralization, Galicia, Spain. The Canadian Mineralogist 36, 303-325.

Fyzollahhi, N., Torshizian, H., Afzal, P., & Jafari, M. R. (2018). Determination of lithium prospects using fractal modeling and staged factor analysis in Torud region, NE Iran. *Journal of Geochemical Exploration, 189*, 2-10. doi: https://doi.org/10.1016/j.gexplo.2017.09.017.

Galeschuk, C. & Vanstone, P. (2007). *Exploration Techniques for Rare Element Pegmatite in the Bird River Greenstone Belt, Southeastern Manitoba*. In: Milkereit, B. (ed.) *Proceedings of Exploration 07*: *Fifth Decennial Conference on Mineral Exploration.* Toronto, Canada, 823–839.

Gallego Garrido, M., 1992. Las mineralizaciones de Li asociadas a magmatismo ácido en Extremadura y su encuadre en la Zona Centro-Ibérica. Universidad Complutense de Madrid, Madrid, Spain, p. 323.

García-Arias, M., Díez-Montes, A., Villaseca, C. & Blanco-Quintero, I. F. (2018). The Cambro-Ordovician Ollo de Sapo magmatism in the Iberian Massif and its Variscan evolution: A review. *Earth-Science Reviews* 176, 345–372. https://doi.org/10.1016/j.earscirev.2017.11.004

George, H., Bonham-Carter, G.F., 1989. Spatial modeling of geological data for gold exploration, Star Lake area, Saskatchewan, in: Agterberg, F.P., Bonham-Carter, G.F. (Eds.), Statistical Application in the Earth Sciences. Geological Survey of Canada Paper 89-9, pp. 157-169.

Ghezelbash, R., Maghsoudi, A., & Carranza, E. J. M. (2019). An Improved Data-Driven Multiple Criteria Decision-Making Procedure for Spatial Modeling of Mineral Prospectivity: Adaption of Prediction–Area Plot and Logistic Functions. *Natural Resources Research, 28*(4), 1299-1316. doi: 10.1007/s11053-018-9448-6.

Ghezelbash, R., Maghsoudi, A., 2018. Comparison of U-spatial statistics and C–A fractal models for delineating anomaly patterns of porphyry-type Cu geochemical signatures in the Varzaghan district, NW Iran. Comptes Rendus Geoscience 350, 180-191. doi: https://doi.org/10.1016/j.crte.2018.02.003.

Gonçalves, M. A., Mateus, A., & Oliveira, V. (2001). Geochemical anomaly separation by multifractal modelling. *Journal of Geochemical Exploration, 72*(2), 91-114. doi: https://doi.org/10.1016/S0375-6742(01)00156-X.

Gourcerol, B., Gloaguen, E., Melleton, J., Tuduri, J. & Galieguea, X. (2019). Re-assessing the European lithium resource potential – A review of hard-rock resources and metallogeny. *Ore Geology Reviews* 109, 494–519. https://doi.org/10.1016/j.oregeorev.2019.04.015

Grant, J. A. (1986). The Isocon Diagram—A Simple Solution to Gresens´ Equation for Metasomatic Alteration. *Economic Geology* 81, 1976–1982. https://doi.org/10.2113/gsecongeo.81.8.1976

Grant, J. A. (2005). Isocon analysis: A brief review of the method and applications. *Physics and Chemistry of the Earth,* 30, 997–1004. https://doi.org/10.1016/j.pce.2004.11.003

Gresens, R. L. (1967). Composition–volume relationships of metasomatism. *Chemical Geology* 2, 47–55.

Gutiérrez-Alonso, G., Fernández-Suárez, J., Jeffries, T. E., Jenner, G. A., Tubrett, M. N., Cox, R. & Jackson, S. E. (2003). Terrane accretion and dispersal in the northern Gondwana margin. An Early Paleozoic analogue of a long-lived active margin. *Tectonophysics* 365, 221–232. https://doi.org/10.1016/S0040-1951(03)00023-4

Gutiérrez-Alonso, G., Fernández-Suárez, J., Jeffries, T. E., Johnston, S. T., Pastor-Galán, D., Murphy, J. B., Franco, M. P. & Gonzalo, J. C. (2011). Diachronous post-orogenic magmatism within a developing orocline in Iberia, European Variscides. *Tectonics* 30, TC5008. https://doi.org/10.1029/2010TC002845

Hawkes, H.E., 1976. The downstream dilution of stream sediment anomalies. Journal of Geochemical Exploration 6, 345-358. doi: https://doi.org/10.1016/0375-6742(76)90023-6.

Helal, B., 1992. Granitoïdes, granites à métaux rares et hydrothermalisme associé. Géologie, minéralogie et géochimie de plusieurs suites tardi-hercyniennes (Nord du Portugal). Ecole Nationale Supérieure des Mines de Paris, p. 507.

Herron, M. M. (1988). Geochemical classification of terrigenous sands and shales from core or log data. *Journal of Sedimentary Petrology* 58, 820–829. https://doi.org/10.1306/212F8E77-2B24-11D7-8648000102C1865D

Janoušek, V., Farrow, C. M. & Erban, V. (2006). Interpretation of whole-rock geochemical data in igneous geochemistry: introducing Geochemical Data Toolkit (GCDkit). *Journal of Petrology* 47, 1255–1259. https://doi.org/10.1093/petrology/egl013

Jaskula, B. W. (2017). *Minerals Yearbook*: *Lithium.* U.S. Geological Survey.

Johnston, K., Ver Hoef, J., Krivoruchko, K., Lucas, N., 2004. Using ArcGIS geostatistical analyst. ESRI Press.

Julivert, M., Marcos, A. & Truyols, J. (1972). L'évolution paléogéographique du NW de l'Espagne pendant l'Ordovicien-Silurien. *Bulletin de la Société Géologique et minéralogique de Bretagne* 4, 1–7.

Kaeter, D., Barros, R. & Menuge, J. F. (2021). Metasomatic High Field Strength Element, Tin, and Base Metal Enrichment Processes in Lithium Pegmatites from Southeast Ireland. *Economic Geology* 116, 169–198. https://doi.org/10.5382/econgeo.4784

Kesler, S.E., Gruber, P.W., Medina, P.A., Keoleian, G.A., Everson, M.P., Wallington, T.J., 2012. Global lithium resources: Relative importance of pegmatite, brine and other deposits. Ore Geology Reviews 48, 55-69. doi: https://doi.org/10.1016/j.oregeorev.2012.05.006.

Kesselring, M., Wagner, F., Kirsch, M., Ajjabou, L. & Gloaguen, R. (2020). Development of Sustainable Test Sites for Mineral Exploration and Knowledge Spillover for Industry. *Sustainability* 12, 2016. https://doi.org/10.3390/su12052016

Leal Gomes, C., 1994. Estudo estructural e paragenético de um sistema pegmatóide granítico. O campo aplito-pegmatítico de Arga Minho, Portugal. Universidade do Minho, p. 695.

Lentz, D. R. & Gregoire, C. (1995). Petrology and mass-balance constraints on major-, trace-, and rare-earth-element mobility in porphyry– greisen alteration associated with the epizonal True Hill granite, southwestern New Brunswick, Canada. *Journal of Geochemical Exploration* 52, 303–331. https://doi.org/10.1016/0375-6742(94)00059-K

Lentz, D. R. (1996). U, Mo, and REE mineralization in late-tectonic granitic pegmatites, southwestern Grenville Province, Canada. *Ore Geology Reviews* 11, 197–227. https://doi.org/10.1016/0169-1368(95)00034-8

Lima, J.; Cardoso-Fernandes, J.; Lima, A. (2021). *Análise estatística da geoquímica de sedimentos de corrente em rochas graníticas e formações metassedimentares do Alto Douro (NE de Portugal)*. Abstract presented at Jornadas do ICT, Porto, 2021.

Lima, J.; Cardoso-Fernandes, J.; Lima, A.; Teodoro, A. (2019). *Statistical processing and principal component analysis of geochemical data from stream sediments for Li exploration*. Paper presented at XII Congresso Ibérico de Geoquímica (CIG), Évora, 2019.

Linnen, R. L., Van Litchervelde, M. & Černý, P. (2012). Granitic pegmatites as sources of strategic metals. *Elements* 8, 275–280. https://doi.org/10.2113/gselements.8.4.275

London, D. (1986). The magmatic-hydrothermal transition in the Tanco rare-element pegmatite: evidence from fluid inclusions and phase equilibrium experiments. *American Mineralogist* 71, 376–395.

London, D. (2018). Ore-forming processes within granitic pegmatites. *Ore Geology Reviews* 101, 349–383. https://doi.org/10.1016/j.oregeorev.2018.04.020

London, D., Morgan VI, G. B. & Wolf, M. B. (1996). *Boron in granitic rocks and their contact aureoles*. In: Grew, E. S. & Anovitz, L. M. (eds.) *Boron: Mineralogy, Petrology and Geochemistry*. Mineralogical Society of America, Reviews in Mineralogy 33, 299–330.

Long, X., Yuan, C., Sun, M., Xiao, W., Wang, Y., Cai, K. & Jiang, Y. (2012). Geochemistry and Nd isotopic composition of the Early Paleozoic flysch sequence in the Chinese Altai, Central Asia: Evidence for a northward-derived mafic source and insight into Nd model ages in

accretionary orogen. *Gondwana Research* 22, 554–566. https://doi.org/10.1016/j.gr.2011.04.009

López-Moro, F. J. & López-Plaza, M. (2004). Monzonitic series from the Variscan Tormes Dome (Central Iberian Zone): petrogenetic evolution from monzogabbro to granite magmas. *Lithos* 72, 19–44. https://doi.org/10.1016/j.lithos.2003.08.002

López-Moro, F. J. (2012). EASYGRESGRANT—A Microsoft Excel spreadsheet to quantity volume change and to perform mass-balance modeling in metasomatic systems. *Computers & Geosciences* 39, 191–196. https://doi.org/10.1016/j.cageo.2011.07.014

López-Moro, F. J., López-Plaza, M., Gutiérrez-Alonso, G., Fernández-Suárez, J., López-Carmona, A., Hofmann, M. & Romer R. L. (2018). Crustal melting and recycling: geochronology and sources of Variscan syn-kinematic anatectic granitoids of the Tormes Dome (Central Iberian Zone). A U–Pb LA-ICP-MS study. *International Journal of Earth Science* 107, 985–1004. https://doi.org/10.1007/s00531-017-1483-8

López-Moro, F. J., Romer, R. L., López-Plaza, M. & Gónzalez Sánchez, M. (2017). Zircon and allanite U-Pb ID-TIMS ages of vaugnerites from the Calzadilla pluton, Salamanca (Spain): dating mantle-derived magmatism and post-magmatic subsolidus overprint. *Geologica Acta* 15, 395–408. http://doi.org/10.1344/GeologicaActa2017.15.4.9

López-Plaza, M., Carnicero, A. & Gonzalo, J. C. (1982). Estudio geológico del campo filoniano de la Fregeneda (Salamanca). *Studia Geologica Salmanticensia* 17, 89–98.

Luecke, W. (1984). Soil Geochemistry above a Lithium Pegmatite Dyke at Aclare, Southeast Ireland. *Irish Journal of Earth Sciences, 6*(2), 205-211.

Marroncle, J.L. (1980a). *Consórcio SPE / SEREM: Relatório semestral (Abril 1980 - Novembro 1980)*. Unpublished, p. 44.

Marroncle, J.L. (1980b). *Consórcio SPE / SEREM: Relatório semestral (Novembro 1979 - Abril 1980)*. Unpublished, p. 44.

Martínez Catalán, J. R., Arenas, R., Díaz García, F., González Cuadra, P., Gómez-Barreiro, J., Abati, J., Castiñeiras, P., Fernández-Suárez, J., Sánchez-Martínez, S., Andonaegui, P., González Clavijo, E., Díez Montes, A., Rubio Pascual, F. J. & Valle Aguado, B. (2007). Space and time in the tectonic evolution of the northwestern Iberian Massif: Implications for the Variscan belt. *Geological Society of America, Memoir* 200, 403–423. https://doi.org/10.1130/2007.1200(21)

Martínez Catalán, J.R., Martínez Poyatos, D., Bea, F., (Coords.), 2004. Zona Centroibérica: Introducción, in: Vera, J.A. (Ed.), Geología de España. Sociedad Geológica de España/ Instituto Geológico y Minero de España (SGE-IGME), Madrid, pp. 68-69.

Martín-Izard, A., Reguilón, R., Palero, F., 1992. Las mineralizaciones litiníferas del oeste de Salamanca y Zamora. Estudios Geológicos 48, 19-30.

McDonough, W. F. & Sun, S. -s. (1995). The composition of the Earth. *Chemical Geology* 120, 223–253. https://doi.org/10.1016/0009-2541(94)00140-4

McLennan, S. M. (1993). Weathering and Global Denudation. *Journal of Geology* 101, 295–303. http://doi.org/10.1086/648222

McLennan, S. M., Hemming, D. K. & Hanson, G. N. (1993). Geochemical approaches to sedimentation, provenance and tectonics. *Geological Society of America Special Papers* 284, 21–40. https://doi.org/10.1130/SPE284-p21

Melleton, J., Gloaguen, E., Frei, D., Lima, A. (2011, 2011-08-14). *U-Pb dating of columbite-tantalite from Variscan rare-elements granites and pegmatites.* Paper presented at the Goldschmidt 2011, Prague, Czech Republic, 1452.

Migdisov, A. A. & Williams-Jones, A. E. (2014). Hydrothermal transport and deposition of the rare earth elements by fluorine-bearing aqueous liquids. *Mineralium Deposita* 49, 987–997. https://doi.org/10.1007/s00126-014-0554-z

Mokhtari, A.R., Garousi Nezhad, S., 2015. A modified equation for the downstream dilution of stream sediment anomalies. Journal of Geochemical Exploration 159, 185-193. doi: 10.1016/j.gexplo.2015.09.007.

Morgan VI, G. B. & London, D. (1987). Alteration of amphibolitic wallrocks around the Tanco rare-element pegmatite, Bernic Lake, Manitoba. *American Mineralogist* 72, 1097–1121.

Neiva, A.M.R., Ramos, J.M.F., 2010. Geochemistry of granitic aplite-pegmatite sills and petrogenetic links with granites, Guarda-Belmonte area, central Portugal. European Journal of Mineralogy 22, 837-854. doi: 10.1127/0935-1221/2010/0022-2072.

Nesbitt, H. W. & Young, G. M. (1982). Early Proterozoic climates and plate motions inferred from major element chemistry of lutites. *Nature* 299, 715–717. https://doi.org/10.1038/299715a0

Nieder, R., Weber, T. K. D., Paulmann, I., Muwanga, A., Owor, M., Naramabuye, F.-X., Gakwerere, F., Biryabarema, M., Biester, H., & Pohl, W. (2014). The geochemical signature of

rare-metal pegmatites in the Central Africa Region: Soils, plants, water and stream sediments in the Gatumba tin–tantalum mining district, Rwanda. *Journal of Geochemical Exploration, 144*, 539-551. doi: https://doi.org/10.1016/j.gexplo.2014.01.025.

Paoli, G., Dini, A. & Rocchi, S. (2019). Footprints of element mobility during metasomatism linked to a late Miocene peraluminous granite intruding a carbonate host (Campiglia Marittima, Tuscany). *International Journal of Earth Sciences* 108, 1617–1641. https://doi.org/10.1007/s00531-019-01723-9

Pereira, I., Dias, R., Bento dos Santos, T., Mata, J., 2017. Exhumation of a migmatite complex along a transpressive shear zone: inferences from the Variscan Juzbado–Penalva do Castelo Shear Zone (Central Iberian Zone). Journal of the Geological Society 174, 1004. doi: 10.1144/jgs2016-159.

Pereira, M. F., Díez Fernández, R., Gama, C. Hofmann, M., Gärtner, A. & Linnemann, U. (2018). S-type granite generation and emplacement during a regional switch from extensional to contractional deformation (Central Iberian Zone, Iberian autochthonous domain, Variscan Orogeny). *International Journal of Earth Science* 107, 251–267. https://doi.org/10.1007/s00531-017-1488-3

Pérez-Estaún, A., Bea, F., Bastida, F., Marcos, A., Martínez Catalán, J.R., Martínez Poyatos, D., Arenas, R., Díaz García, F., Azor, A., Simancas, J.F., González Lodeiro, F., 2004. La cordillera varisca europea: el Macizo Ibérico, in: Vera, J.A. (Ed.), Geología de España. Sociedad Geológica de España/ Instituto Geológico y Minero de España (SGE-IGME), Madrid, pp. 21-25.

Pérez-Soba, C. & Villaseca, C. (2019). Li-Na-metasomatism related to I-type granite magmatism: A case study of the highly fractionated La Pedriza pluton (Iberian Variscan belt). *Lithos* 344–345, 159–174. https://doi.org/10.1016/j.lithos.2019.06.008

Pesquera, A., Roda-Robles, E., Gil-Crespo, P. P., Valls, D. & Torres Ruiz, J. (2020). The metasomatic enrichment of Li in psammopelitic units at San José-Valdeflórez, Central Iberian Zone, Spain: a new type of lithium deposit. *Scientific Reports* 10, 10828. https://doi.org/10.1038/s41598-020-67520-6

Pollard, P. J., Pichavant, M. & Charoy, B. (1987). Contrasting evolution of fluorine- and boron-rich tin systems. *Mineralium Deposita* 22, 315–321.

Potdevin, J. L. (1993). Gresens 92: a simple Macintosh program of the Gresens method. *Computers & Geosciences* 19, 1229–1238. https://doi.org/10.1016/0098-3004(93)90027-3

Raith, J. G., Riemer, née Schöner, N. & Meisel, T. (2004). Boron metasomatism and behaviour of rare earth elements during formation of tourmaline rocks in the eastern Arunta Inlier, central Australia. *Contributions to Mineralogy and Petrology* 147, 91–109. https://doi.org/10.1007/s00410-003-0548-9

Ribeiro, M.L., 2001. Notícia explicativa da carta geológica simplificada do Parque Arqueológico do Vale do Côa. Parque Arqueológico do Vale do Côa, Vila Nova de Foz Côa, Portugal.

Ribeiro, M.L., Silva, A.F., 2000. Carta Geológica Simplificada do Parque Arqueológico do Vale do Côa. Instituto Geológico e Mineiro and Parque Arqueológico do Vale do Côa, Vila Nova de Foz Côa, Portugal.

Ribeiro, R., Lima, A., Guimarães, D. (2018). *Concentrations of Rb in K-Feldspar from the Pegmatite-aplite Barroso-Alvão Field.* Paper presented at the VIII Congresso Jovens Investigadores em Geociências, LEG, Livro de Actas Estremoz, 50-53.

Roda, E., 1993. Distribución, Caracteristicas y Petrogenesis de las Pegmatitas de La Fregeneda (Salamanca), Dep. Min. y Petrol. . Facultad de Ciencia y Tecnología de la Universidad del País Vasco (UPV/EHU), Bilbao, Spain, p. 199.

Roda-Robles, E., Fontan, F., Pesquera, A. & Velasco, F. (1996). The phosphate mineral association of the granitic pegmatites of the Fregeneda area (Salamanca, Spain). *Mineralogical Magazine* 60, 767–778. https://doi.org/10.1180/minmag.1996.060.402.06

Roda-Robles, E., Pesquera Pérez, A., Velasco Roldán, F. & Fontan, F. (1999). The granitic pegmatites of the Fregeneda area (Salamanca, Spain): characteristics and petrogenesis. *Mineralogical Magazine* 63, 535–558. https://doi.org/10.1180/002646199548709

Roda-Robles, E., Pesquera, A. & Velasco, F. (1995). Micas of the muscovite-lepidolite series from the Fregeneda pegmatites (Salamanca, Spain). *Mineralogy and Petrology* 55, 145–157.

Roda-Robles, E., Pesquera, A., Gil-Crespo, P. P., Vieira, R., Lima, A., Garate-Olave, I., Martins, T. & Torres-Ruiz, J. (2016). Geology and mineralogy of Li mineralization in the Central Iberian Zone (Spain and Portugal). *Mineralogical Magazine* 80, 103–126. https://doi.org/10.1180/minmag.2016.080.049

Roda-Robles, E., Pesquera, A., Gil-Crespo, P., Torres-Ruiz, J., 2012. From granite to highly evolved pegmatite: A case study of the Pinilla de Fermoselle granite–pegmatite system (Zamora, Spain). Lithos 153, 192-207. doi: https://doi.org/10.1016/j.lithos.2012.04.027.

Roda-Robles, E., Pesquera, A., Gil-Crespo, P.P., Vieira, R., Lima, A., Garate-Olave, I., Martins, T., Torres-Ruiz, J., 2016. Geology and mineralogy of Li mineralization in the Central Iberian Zone (Spain and Portugal). Mineralogical Magazine 80, 103-126. doi: 10.1180/minmag.2016.080.049.

Roda-Robles, E., Pesquera, A., Velasco, F., Fontan, F., 1999. The granitic pegmatites of the Fregeneda area (Salamanca, Spain): characteristics and petrogenesis. Mineral. Mag. 63, 535–558.

Roda-Robles, E., Vieira, R., Lima, A., Errandonea-Martin, J., Cardoso-Fernandes, J., Garate-Olave, I. & Pesquera, A. (in prep.). Petrogenesis of the granitic pegmatites from the Fregeneda – Almendra area (Central Iberian Zone, Spain - Portugal).

Roda-Robles, E., Vieira, R., Pesquera, A. & Lima, A. (2010). Chemical variations and significance of phosphates from the Fregeneda-Almendra pegmatite field, Central Iberian Zone (Spain and Portugal). *Mineralogy and Petrology* 100, 23–34. https://doi.org/10.1007/s00710-010-0117-7

Roda-Robles, E., Vieira, R., Pesquera, A., Lima, A., 2010. Chemical variations and significance of phosphates from the Fregeneda-Almendra pegmatite field, Central Iberian Zone (Spain and Portugal). Mineralogy and Petrology 100, 23-34. doi: 10.1007/s00710-010-0117-7.

Roda-Robles, E., Villaseca, C., Pesquera, A., Gil-Crespo, P.P., Vieira, R., Lima, A., Garate-Olave, I., 2018. Petrogenetic relationships between Variscan granitoids and Li-(F-P)-rich aplite-pegmatites in the Central Iberian Zone: Geological and geochemical constraints and implications for other regions from the European Variscides. Ore Geology Reviews 95, 408-430. doi: https://doi.org/10.1016/j.oregeorev.2018.02.027.

Rodríguez Alonso, M.D., Díez Balda, M.A., Perejón, A., Pieren, A., Liñán, E., López Díaz, F., Moreno, F., Gámez Vintaned, J.A., Gónzalez Lodeiro, F., Martínez Poyatos, D., Vegas, R., 2004. Domínio del Complejo Esquisto-Grauváquico: Estratigrafía. La secuencia litoestratigráfica del Neoproterozóico-Cámbrico Inferior, in: Vera, J.A. (Ed.), Geología de España. Geol. España/Inst. Geol. Min. España (SGE-IGME), Madrid, pp. 78-81.

Rodríguez Fernández, L. R. & Oliveira, J. T. (2015). Mapa geológico de España y Portugal a escala 1:1.000.000. *Instituto Geológico y Minero de España, Laboratório Nacional de Energia e Geologia de Portugal*. http://info.igme.es/cartografiadigital/geologica/Geologicos1MMapa.aspx?Id=Geologico1000_(2015)

Rodríguez Fernández, L. R., Díez Montes, A., Escuder, J. & Carrasco, R. (2000). Hoja geológica número 448 (Vilvestre). Mapa Geológico de España a Escala 1:50.000 (2ª serie). Madrid: Instituto Geológico y Minero de España (IGME). Retrieved from http://info.igme.es/cartografiadigital/geologica/Magna50Hoja.aspx?intranet=false&id=448B

Rodríguez-Alonso, M. D., Peinado, M., López-Plaza, M., Franco, P., Carnicero, A. & Gonzalo, J. C. (2004). Neoproterozoic-Cambrian synsedimentary magmatism in the Central Iberian Zone (Spain): geology, petrology and geodynamic significance. *International Journal of Earth Science* 93, 897–920. https://doi.org/10.1007/s00531-004-0425-4

Rose, A.W., Hawkes, H.E., Webb, J.S., 1979. Geochemistry in mineral exploration. Academic Press, London.

Rudnick, R. L. & Gao, S. (2014). *Composition of the continental crust*. In: Holland, H. D., Turekian, K. K. (eds.) *Treatise on Geochemistry, 2nd edition Volume 4: The Crust*. Elsevier Science, Oxford, 1–51. https://doi.org/10.1016/B978-0-08-095975-7.00301-6

Ruiz-Coupeau, S., Jürgens, B., Keßelring, M. & Herrero-Solana, V. (2020). Sustainability in Mineral Exploration—Exploring Less Invasive Technologies via Patent Analysis. *Sustainability* 12, 9761. https://doi.org/10.3390/su12229761

Saadati, H., Afzal, P., Torshizian, H., Solgi, A., 2020. Geochemical exploration for lithium in NE Iran using the geochemical mapping prospectivity index, staged factor analysis, and a fractal model. Geochemistry: Exploration, Environment, Analysis 20, 461-472. doi: 10.1144/geochem2020-020.

San José, M.A., Pieren, A.P., Garcia-Hidalgo, J.F., Vilas, L., Herranz, P., Pelaez, J.R., Perejon, A., 1990. Central Iberian Zone. Autochthonous sequences: Ante-Ordovician stratigraphy, in: Dallmeyer, R.D., Martinez Garcia, E. (Eds.), Pre-Mesozoic Geology of Iberia. Springer-Verlag, Berlin, Heidelberg, pp. 147- 159.

Selway, J. B., Breaks, F. W., & Tindle, A. G. (2005). A Review of Rare-Element (Li-Cs-Ta) Pegmatite Exploration Techniques for the Superior Province, Canada, and Large Worldwide Tantalum Deposits. *Exploration and Mining Geology, 14*(1-4), 1-30. doi: 10.2113/gsemg.14.1-4.1.

Shahrestani, S., Mokhtari, A. R., & Hosseini-Dinani, H. (2018). How does sampling density affect mineralization detection in stream sediment geochemical exploration? A case study from NW of Iran. *Geochemistry: Exploration, Environment, Analysis, 18*(3), 196-203. doi: 10.1144/geochem2017-076.

Shahrestani, S., Mokhtari, A.R., 2017. Improved detection of anomalous catchment basins by incorporating drainage density in dilution correction of geochemical residuals. Geochemistry: Exploration, Environment, Analysis 17, 194-203. doi: 10.1144/geochem2016-015.

Shand, S. J. (1943). *Eruptive Rocks. Their Genesis, Composition, Classification, and Their Relation to Ore-Deposits with a Chapter on Meteorite*. John Wiley and Sons, New York.

Shearer, C. K., Papike, J. J., Simon, S. B. & Laul, J. C. (1986) Pegmatite-wallrock interactions, Black Hills, South Dakota: interaction between pegmatite-derived fluids and quartz-mica schist wallrock. *American Mineralogist* 71, 518–539.

Shearer, C. K., Papike, J. J., Simon, S. B., Laul, J. C. & Christian, R. P. (1984). Pegmatite/wallrock interactions, Black Hills, South Dakota: Progressive boron metasomatism adjacent to the Tip Top pegmatite. *Geochimica et Cosmochimica Acta* 48, 2563–2579. https://doi.org/10.1016/0016-7037(84)90306-5

Shepard, D., 1968. A two-dimensional interpolation function for irregularly-spaced data, Proceedings of the 1968 23rd ACM national conference. Association for Computing Machinery, pp. 517–524.

Silva, A. F. & Ribeiro, M. L. (1994). Notícia explicativa da folha 15-B (Freixo de Espada à Cinta) da Carta Geológica de Portugal à Escala 1:50.000. Instituto Geológico e Mineiro.

Silva, A.F., 2005. A Litostratigrafia e Estrutura do Supergrupo Dúrico-Beirão (Complexo Xisto-Grauváquico), em Portugal, e sua Correlação com as Correspondentes Sucessões em Espanha. Instituto Nacional de Engenharia, Tecnologia e Inovação, IP, Alfragide, Portugal.

Silva, A.F., Romão, J.M.C., Sequeira, A.J.D., Oliveira, J.T. (1995). *A sucessão litostratigráfica anté-ordovícica na Zona Centro-Ibérica (ZCI), em Portugal: Ensaio de interpretação com base nos dados actuais.* Paper presented at the XIII Reunión de Geologia del Oeste Peninsular, RGOP/PICG, 319-320, Univ. Salamanca, Salamanca, 71-72.

Silva, A.F., Santos, A.J., Ribeiro, A., Cabral, J., Ribeiro, M.L., 1990a. Carta Geológica de Portugal na escala 1/50.000 – folha 15-B – Freixo de Espada à Cinta. Serviços Geológicos de Portugal, Lisboa, Portugal.

Silva, A.F., Santos, A.J., Ribeiro, A., Ribeiro, M.L., 1990b. Carta Geológica de Portugal na escala 1/50.000 – folha 15-A – Vila Nova de Foz Côa. Serviços Geológicos de Portugal, Lisboa, Portugal.

Silva, A.F.d., Rebelo, J.A., Ribeiro, M.L., 1989. Notícia Explicativa da folha 11-C Torre de Moncorvo. Serviços Geológicos de Portugal, Lisboa, Portugal.

Silva, A.F.d., Ribeiro, M.L., 1991. Notícia Explicativa da folha 15-A Vila Nova de Foz Côa. Serviços Geológicos de Portugal, Lisboa, Portugal.

Silva, A.F.d., Ribeiro, M.L., 1994. Notícia Explicativa da folha 15-B Freixo de Espada à Cinta. Instituto Geológico e Mineiro, Lisboa, Portugal.

Simmons, W.B.S., Webber, K.L., 2008. Pegmatite genesis: state of the art. European Journal of Mineralogy 20, 421-438. doi: 10.1127/0935-1221/2008/0020-1833.

Smeds, S. A. (1992). Trace elements in potassium-feldspar and muscovite as a guide in the prospecting for lithium- and tin-bearing pegmatites in Sweden. *Journal of Geochemical Exploration, 42*(2), 351-369. doi: https://doi.org/10.1016/0375-6742(92)90032-4.

Sousa, M.B. (1982). Litoestratigrafia e estrutura do Complexo Xisto-Grauváquico - Grupo do Douro (NE de Portugal). PhD Thesis. Coimbra, Universidade de Coimbra, unpublished, 222pp.

Sousa, M.B., 1982. Litostratigrafia e estrutura do "Complexo Xisto-Grauváquico Ante-Ordovícico" – Grupo do Douro (Nordeste de Portugal). Centro de Geociências da Universidade de Coimbra, Coimbra, Portugal, p. 222.

Sousa, M.B., 1983. Considerações paleogeográficas e ensaio de correlação das formações do Grupo do Douro (CXG) com as formações ante-Ordovícicas da Zona Centro-Ibérica. Memórias e Notícias, Publicações do Museu e Laboratório Mineralógico e Geológico da Universidade de Coimbra 65, 65-98.

Sousa, M.B., 1984. Considerações sobre a estratigrafia do Complexo Xisto-Grauváquico (CXG) e sua relação com o Paleozóico Inferior. Cuadernos de Geología Ibérica 9, 9-36.

Spadoni, M., 2006. Geochemical mapping using a geomorphologic approach based on catchments. Journal of Geochemical Exploration 90, 183-196. doi: 10.1016/j.gexplo.2005.12.001.

Steiner, B. (2018). Using Tellus stream sediment geochemistry to fingerprint regional geology and mineralisation systems in Southeast Ireland. *Irish Journal of Earth Sciences, 36*, 45-61. doi: 10.3318/ijes.2018.36.45.

Steiner, B. M. (2019). Tools and Workflows for Grassroots Li–Cs–Ta (LCT) Pegmatite Exploration. *Minerals, 9*(8), 499. doi: 10.3390/min9080499.

Steiner, B., 2018. Using Tellus stream sediment geochemistry to fingerprint regional geology and mineralisation systems in Southeast Ireland. Irish Journal of Earth Sciences 36, 45-61. doi: 10.3318/ijes.2018.36.45.

Strahler, A.N., 1952. Hypsometric (Area-Altitude) Analysis of Erosional Topography. GSA Bulletin 63, 1117-1142. doi: 10.1130/0016-7606(1952)63[1117:Haaoet]2.0.Co;2.

Talavera, C., Montero, P., Martínez Poyatos, D. & Williams, I. S. (2012). Ediacaran to Lower Ordovician age for rocks ascribed to the Schist–Graywacke Complex (Iberian Massif, Spain): Evidence from detrital zircon SHRIMP U–Pb geochronology. *Gondwana Research* 22, 928–942. https://doi.org/10.1016/j.gr.2012.03.008

Taylor, S. R. & McLennan, S. M. (1985). *The Continental Crust: Its Composition and Evolution*. Blackwell Scientific Publications, Oxford.

Taylor, S. R. & McLennan, S. M. (1995). The geochemical evolution of the continental crust. *Reviews of Geophysics* 33*,* 241–265*.* https://doi.org/10.1029/95RG00262

Teixeira, C., 1955. Notas sobre geologia de Portugal o complexo xisto-grauváquico ante-ordoviciano. Empresa Literaria Fluminense Lda., Lisboa, Portugal.

Teixeira, R. J. S., Neiva, A. M. R., Gomes, M. E. P., Corfu, F., Cuesta, A. & Croudace, I. W. (2012). The role of fractional crystallization in the genesis of early syn-D_3, tin-mineralized Variscan two-mica granites from the Carrazeda de Ansiães area, northern Portugal. *Lithos* 153, 177–191. https://doi.org/10.1016/j.lithos.2012.04.024

Teixeira, R. J. S., Neiva, A. M. R., Silva, P. B., Gomes, M. E. P., Andersen, T. & Ramos, J. M. F. (2011). Combined U–Pb geochronology and Lu–Hf isotope systematics by LAM–ICPMS of zircons from granites and metasedimentary rocks of Carrazeda de Ansiães and Sabugal areas, Portugal, to constrain granite sources. *Lithos* 125, 321–334. https://doi.org/10.1016/j.lithos.2011.02.015

Thomas, R., Webster, J. D. & Heinrich, W. (2000). Melt inclusions in pegmatite quartz: complete miscibility between silicate melts and hydrous fluids at low pressure. *Contributions to Mineralogy and Petrology* 139, 394–401. https://doi.org/10.1007/s004100000120

Trueman, D. L. (1978). Exploration methods in the Tanco mine area of southeastern Manitoba, Canada. *Energy* 3, 293–297. https://doi.org/10.1016/0360-5442(78)90025-7

Ugidos, J. M., Sánchez-Santos, J. M., Barba, P. & Valladares, M. I. (2010). Upper Neoproterozoic series in the Central Iberian, Cantabrian and West Asturian Leonese Zones

(Spain): geochemical data and statistical results as evidence for a shared homogenised source area. *Precambrian Research* 178, 51–58. https://doi.org/10.1016/j.precamres.2010.01.009

Ugidos, J. M., Valladares, M. I., Barba, P. & Ellam, R. M. (2003). The Upper Neoproterozoic-Lower Cambrian of the Central Iberian Zone, Spain: chemical and isotopic (Sm–Nd) evidence that the sedimentary succession records an inverted stratigraphy of its source. *Geochimica et Cosmochimica Acta* 67, 2615–2629. https://doi.org/10.1016/S0016-7037(03)00027-9

Ugidos, J. M., Valladares, M. I., Recio, C., Rogers, G., Fallick, A. E. & Stephens, A. E. (1997). Provenance of Upper Precambrian-Lower Cambrian shales in the Central Iberian Zone, Spain: evidence from a chemical and isotopic study. *Chemical Geology* 136, 55–70. https://doi.org/10.1016/S0009-2541(96)00138-6

Valladares, M. I., Ugidos, J. M., Barba, P. & Colmenero, J. R. (2002). Contrasting geochemical features of the Central Iberian Zone shales (Iberian Massif, Spain): implications for the evolution of Neoproterozoic–Lower Cambrian sediments and their sources in other peri-Gondwanan áreas. *Tectonophysics* 352, 121–132. https://doi.org/10.1016/S0040-1951(02)00192-0

Valle-Aguado, B., Azevedo, M. R., Schaltegger, U., Martínez Catalán, J. R. & Nolan, J. (2005). U-Pb zircon and monazite geochronology of Variscan magmatism related to syn-convergence extension in Central Northern Portugal. *Lithos* 82, 169–184. https://doi.org/10.1016/j.lithos.2004.12.012

Viallefond, L. (1981). *Prospection géochimique Portugal : Résultats analytiques et interprétation de l'échantillonnage réalisé par le S.F.M. sur la feuille 15B* (NOTE/GMX-732). p. 27.

Viallefond, L., Angel, J.M. (1981). *Portugal Nord - Feuille 15A-15C - Interprétation des données analytiques* (NOTE/GMX-738). p. 17.

Viegas, L., Lima, L.P., Soares, J., Fonseca, E.C., 1983-85. Aplicação da análise estatística multi-variada ao estudo de amostras de sedimentos na região de Escalhão- Barca D'Alva (NE de Portugal). Boletim da Sociedade Geológica de Portugal XXIV, 161–169.

Vieira, R., 2010. Aplitopegmatitos com elementos raros da região entre Almendra (V.N. de Foz Côa) e Barca d'Alva (Figueira de Castelo Rodrigo). Campo aplitopegmatítico da Fregeneda-Almendra. Faculdade de Ciências da Universidade do Porto, Porto, Portugal, pp. XXVI, 273.

Vieira, R., Roda-Robles, E., Pesquera, A. & Lima, A. (2011). Chemical variation and significance of micas from the Fregeneda-Almendra pegmatitic field (Central-Iberian Zone, Spain and Portugal). *American Mineralogist* 96, 637–645. https://doi.org/10.2138/am.2011.3584

Villaseca, C., Barbero, L. & Herreros, V. (1998). A re-examination of the typology of peraluminous granite types in intracontinental orogenic belts. *Transactions of the Royal Society of Edinburgh: Earth Sciences* 89, 113–119. https://doi.org/10.1017/S0263593300007045

Villaseca, C., Merino, E., Oyarzun, R., Orejana, D., Pérez-Soba, C. & Chicharro, E. (2014). Contrasting chemical and isotopic signatures from Neoproterozoic metasedimentary rocks in the Central Iberian Zone (Spain) of pre-Variscan Europe: Implications for terrane analysis and early Ordovician magmatic belts. *Precambrian Research* 245, 131–145. https://doi.org/10.1016/j.precamres.2014.02.006

Von Knorring, O., Vidal Romani, J.R., 1981. On the mineralogy of the O Casteliño spodumene pegmatite near Lalín, Galicia Spain. Cadernos do Laboratorio Xeolóxico de Laxe 2, 259-262.

Zuo, R., 2011. Identifying geochemical anomalies associated with Cu and Pb–Zn skarn mineralization using principal component analysis and spectrum–area fractal modeling in the Gangdese Belt, Tibet (China). Journal of Geochemical Exploration 111, 13-22. doi: 10.1016/j.gexplo.2011.06.012.

Chapter V: Data integration and prospectivity mapping

Abedi, M., Norouzi, G.-H., & Bahroudi, A. (2012). Support vector machine for multi-classification of mineral prospectivity areas. *Computers & Geosciences, 46*, 272-283. doi: https://doi.org/10.1016/j.cageo.2011.12.014.

Aires, S.C.M. Petrofísica e Litogeoquímica de Formações do “Complexo Xisto-Grauváquico” (Grupo do Douro) Estudo do Potencial do “Xisto” para Exploração como Pedra Natural. Ph.D. Thesis, Faculdade de Ciências da Universidade do Porto, Porto, Portugal, 2018.

Al-Rawashdeh, S.; Saleh, B.; Hamzah, M. The Use of Remote Sensing Technology in Geological Investigation and Mineral Detection in El Azraq-Jordan. *Cybergeo Eur. J. Geogr.* 2006, *358*, 1–17; doi:10.4000/cybergeo.2856.

Al-Rawashdeh, S.; Saleh, B.; Hamzah, M. The Use of Remote Sensing Technology in Geological Investigation and Mineral Detection in El Azraq-Jordan. Cybergeo: European Journal of Geography 2006, doi:10.4000/cybergeo.2856.

Angel, J.M.; Viallefond, L. Prospection Géochimique Portugal. Résultats Analytiques et Interprétation de l'échantillonnage Réalisé Par Le S.F.M. Sur La Feuille 15A, Région de Almendra; NOTE/GMX-748; BRGM: Orléans, France, 1981; p. 6.

Bahr, T.; Heinz, D.C. Creating Models Of Hyperspectral Classification Workflows Integrating Dimensionality Expansion For Multispectral Imagery. 10th Workshop on Hyperspectral Imaging and Signal Processing: Evolution in Remote Sensing (WHISPERS) 2019, doi:10.1109/whispers.2019.8920946.

Bea, F.; Herrero, J.G.S.G.; Pinto, M.S.; Barrera, J.L.; Brandle, J.L.; Corretgé, L.G.; Suárez, O. Una compilación geoquímica (elementos mayores) para los granitóides del Macizo Hespérico. In Geología de los Granitóides y Rocas Asociadas del Macizo Hesperico; Bea, F., Carnicero, A., Gonzalo, J.C., López-Plaza, M., Rodríguez Alonso, M.D., Eds.; Libro de Homenaje a L. C. García de Figuerola, Editorial Rueda, 1987.

Bea, F.; Herrero, J.G.S.G.; Pinto, M.S.; Barrera, J.L.; Brandle, J.L.; Corretgé, L.G.; Suárez, O. Una compilación geoquímica (elementos mayores) para los granitóides del Macizo Hespérico. In *Geología de los Granitóides y Rocas Asociadas del Macizo Hesperico*; Bea, F., Carnicero, A., Gonzalo, J.C., López-Plaza, M., Rodríguez Alonso, M.D., Eds.; Libro de Homenaje a L. C. García de Figuerola, Editorial Rueda: Alcorcon, Madrid, Spain, 1987.

Bea, F.; Montero, P.; Zinger, T. The Nature, Origin, and Thermal Influence of the Granite Source Layer of Central Iberia. The Journal of Geology 2003, 111, doi:10.1086/376767.

Beiranvand Pour, A.; Park, T.-Y.; Park, Y.; Hong, J.; Zoheir, B.; Pradhan, B.; Ayoobi, I.; Hashim, M. Application of Multi-Sensor Satellite Data for Exploration of Zn–Pb Sulfide Mineralization in the Franklinian Basin, North Greenland. Remote Sensing 2018, 10, doi:10.3390/rs10081186.

Brooks, K. Lithium Minerals. Geology Today 2020, 36, doi:10.1111/gto.12326.

Brown, W.M.; Gedeon, T.D.; Groves, D.I.; Barnes, R.G. Artificial Neural Networks: A New Method for Mineral Prospectivity Mapping. Australian Journal of Earth Sciences 2000, 47, doi:10.1046/j.1440-0952.2000.00807.x.

Cardoso-Fernandes, J.; Dias, F.; Lima, A.; Anjos Ribeiro, M.; Perrotta, M.; Roda-Robles, E.; Teodoro, A.C. Petalite alteration products from the Bajoca pegmatite (Central Portugal): a multiapproach for lithium exploration. In EGU General Assembly 2021, online, 19–30 Apr; 2021. doi: 10.5194/egusphere-egu21-2364.

Cardoso-Fernandes, J.; Silva, J.; Dias, F.; Lima, A.; Teodoro, A.C.; Barrès, O.; Cauzid, J.; Perrotta, M.; Roda-Robles, E.; Ribeiro, M.A. Tools for remote exploration: A Lithium (Li) dedicated spectral library of the Fregeneda-Almendra aplite-pegmatite field. Version 1. Zenodo, 2021. Available online: https://zenodo.org/record/4575375#.YUGmx30RVPY (accessed on 9 March 2021).

Cardoso-Fernandes, J.; Silva, J.; Lima, A.; Teodoro, A.C.; Perrotta, M.; Cauzid, J.; Roda-Robles, E.; Ribeiro, M.A. Reflectance spectroscopy to validate remote sensing data/algorithms for satellite-based lithium (Li) exploration (Central East Portugal). In Proceedings of the SPIE Remote Sensing, Earth Resources and Environmental Remote Sensing/GIS Applications XI, Online, 21–25 September 2020; https://doi.org/10.1117/12.2573929.

Cardoso-Fernandes, J.; Silva, J.; Lima, A.; Teodoro, A.C.; Perrotta, M.; Cauzid, J.; Roda-Robles, E. Characterization of lithium (Li) minerals from the Fregeneda-Almendra region through laboratory spectral measurements: A comparative study. In Proceedings of the SPIE Remote Sensing, Earth Resources and Environmental Remote Sensing/GIS Applications XI, Online, 21– 25 September 2020; https://doi.org/10.1117/12.2573941.

Cardoso-Fernandes, J.; Teodoro, A.; Lima, A. Potential of Sentinel-2 Data in the Detection of Lithium (Li)-Bearing Pegmatites: A Study Case. In Proceedings of the Earth Resources and Environmental Remote Sensing/GIS Applications IX, Berlin, Germany, 10–13 September 2018; doi:10.1117/12.2326285.

Cardoso-Fernandes, J.; Teodoro, A.C.; Lima, A. Remote Sensing Data in Lithium (Li) Exploration: A New Approach for the Detection of Li-Bearing Pegmatites. International Journal of Applied Earth Observation and Geoinformation 2019, 76, doi:10.1016/j.jag.2018.11.001.

Cardoso-Fernandes, J.; Teodoro, A.C.; Lima, A.; Roda-Robles, E. Lithium (Li) Pegmatite Mapping Using Artificial Neural Networks (ANNs): Preliminary Results. IEEE International Geoscience and Remote Sensing Symposium, Waikoloa, HI, USA, 26 Sept.-2 Oct. 2020; IEEE 2020, pp 557-560. doi: 10.1109/IGARSS39084.2020.9323852.

Cardoso-Fernandes, J.; Teodoro, A.C.M.; Lima, A.; Roda-Robles, E. Evaluating the Performance of Support Vector Machines (SVMs) and Random Forest (RF) in Li-Pegmatite

Mapping: Preliminary Results. In Proceedings of the Earth Resources and Environmental Remote Sensing/GIS Applications X, Strasbourg, France, 9–12 September 2019; doi:10.1117/12.2532577.

Carvalho, J.M.F.; Farinha, J.A.L.B. Lithium potentialities in Northern Portugal. In 17th Industrial Minerals International Congress, Barcelona, Spain, 28–31 March 2004; pp 1-10.

Carvalhosa, A. Carta Geológica de Portugal à escala 1:50 000, folha 15-D (Figueira de Castelo Rodrigo); Serviços Geológicos de Portugal: Lisboa, Portugal, 1960.

Costa, J.C.S. Notícia sobre uma carta geológica do Buçaco, de Nery Delgado; Serviços Geológicos de Portugal: Lisboa, Por-tugal, 1950.

Dias, R.; Ribeiro, A. The Ibero-Armorican Arc: A Collision Effect against an Irregular Continent? Tectonophysics 1995, 246, doi:10.1016/0040-1951(94)00253-6.

European Commission, D.-G. for I.M., Industry, Entrepreneurship and SMEs Communication from the Commission to the European Parliament, the Council, the European Economic and Social Committee and the Committee of the Regions. Critical Raw Materials Resilience: Charting a Path towards Greater Security and Sustainability COM/2020/474 Final; 2020;

Ferreira, J.A.; Bento dos Santos, T.; Pereira, I.; Mata, J. Tectonically Assisted Exhumation and Cooling of Variscan Granites in an Anatectic Complex of the Central Iberian Zone, Portugal: Constraints from LA-ICP-MS Zircon and Apatite U–Pb Ages. In-ternational Journal of Earth Sciences 2019, 108, doi:10.1007/s00531-019-01755-1.

Gaspar, L.M.; Inverno, C.M.C. Mineralogy and Metasomatic Evolution of Distal Strata-BoundScheelite Skarns in the Riba de Alva Mine, Northeastern Portugal. Economic Geology 2000, 95, doi:10.2113/gsecongeo.95.6.1259.

Ghezelbash, R., Maghsoudi, A., & Carranza, E. J. M. (2019a). Performance evaluation of RBF- and SVM-based machine learning algorithms for predictive mineral prospectivity modeling: integration of S-A multifractal model and mineralization controls. *Earth Science Informatics, 12*(3), 277-293. doi: 10.1007/s12145-018-00377-6.

Ghezelbash, R., Maghsoudi, A., & Daviran, M. (2019b). Prospectivity modeling of porphyry copper deposits: recognition of efficient mono- and multi-element geochemical signatures in the Varzaghan district, NW Iran. *Acta Geochimica, 38*(1), 131-144. doi: 10.1007/s11631-018-0289-0.

Gourcerol, B.; Gloaguen, E.; Melleton, J.; Tuduri, J.; Galiegue, X. Re-Assessing the European Lithium Resource Potential – A Review of Hard-Rock Resources and Metallogeny. Ore Geology Reviews 2019, 109, doi:10.1016/j.oregeorev.2019.04.015.

Haykin, S.S. *Neural Networks: A Comprehensive Foundation*; Prentice Hall: Englewood Cliffs, NJ, USA, 1999; ISBN 978-0-13273350-2.

Kesler, S.E.; Gruber, P.W.; Medina, P.A.; Keoleian, G.A.; Everson, M.P.; Wallington, T.J. Global Lithium Resources: Relative Importance of Pegmatite, Brine and Other Deposits. Ore Geology Reviews 2012, 48, doi:10.1016/j.oregeorev.2012.05.006.

Köhler, M., Hanelli, D., Schaefer, S., Barth, A., Knobloch, A., Hielscher, P., Cardoso-Fernandes, J., Lima, A., & Teodoro, A. C. (2021). Lithium Potential Mapping Using Artificial Neural Networks: A Case Study from Central Portugal. *Minerals, 11*(10), 1046. doi: 10.3390/min11101046.

Lanaras, C.; Bioucas-Dias, J.; Galliani, S.; Baltsavias, E.; Schindler, K. Super-Resolution of Sentinel-2 Images: Learning a Globally Applicable Deep Neural Network. ISPRS Journal of Photogrammetry and Remote Sensing 2018, 146, doi:10.1016/j.isprsjprs.2018.09.018.

Linnen, R.L.; Van Lichtervelde, M.; Černý, P. Granitic Pegmatites as Sources of Strategic Metals. Elements 2012, 8, 275–280, doi:10.2113/gselements.8.4.275.

Martínez Catalán, J.R. The Central Iberian Arc, an Orocline Centered in the Iberian Massif and Some Implications for the Variscan Belt. International Journal of Earth Sciences 2011, 101, doi:10.1007/s00531-011-0715-6.

Oh, H.-J.; Lee, S. Application of Artificial Neural Network for Gold–Silver Deposits Potential Mapping: A Case Study of Korea. Natural Resources Research 2010, 19, doi:10.1007/s11053-010-9112-2.

Parsa, M. (2021). A data augmentation approach to XGboost-based mineral potential mapping: An example of carbonate-hosted ZnPb mineral systems of Western Iran. *Journal of Geochemical Exploration, 228*, 106811. doi: https://doi.org/10.1016/j.gexplo.2021.106811.

Pereira, I.; Dias, R.; Bento dos Santos, T.; Mata, J. Exhumation of a Migmatite Complex along a Transpressive Shear Zone: Inferences from the Variscan Juzbado–Penalva Do Castelo Shear Zone (Central Iberian Zone). Journal of the Geological So-ciety 2017, 174, doi:10.1144/jgs2016-159.

Ribeiro, M.L. Carta Geológica Simplificada Do Parque Arqueológico Do Vale Do Côa Na Escala 1:80.000; Parque Arqueológico do Vale do Côa: Vila Nova de Foz Côa, Portugal, 1990.

Rigol-Sanchez, J.P.; Chica-Olmo, M.; Abarca-Hernandez, F. Artificial Neural Networks as a Tool for Mineral Potential Map-ping with GIS. International Journal of Remote Sensing 2003, 24, doi:10.1080/0143116021000031791.

Roda Robles, E.; Pesquera Perez, A.; Velasco Roldan, F.; Fontan, F. The Granitic Pegmatites of the Fregeneda Area (Salamanca, Spain): Characteristics and Petrogenesis. Mineralogical Magazine 1999, 63, doi:10.1180/002646199548709.

Roda, E. Distribución, Caracteristicas y Petrogenesis de las Pegmatitas de La Fregeneda (Salamanca). PhD thesis, UPV/EHU, Bilbao, Spain, 1993.

Roda-Robles, E.; Pesquera, A.; Gil-Crespo, P.P.; Vieira, R.; Lima, A.; Garate-Olave, I.; Martins, T.; Torres-Ruiz, J. Geology and Mineralogy of Li Mineralization in the Central Iberian Zone (Spain and Portugal). Mineralogical Magazine 2016, 80, doi:10.1180/minmag.2016.080.049.

Roda-Robles, E.; Villaseca, C.; Pesquera, A.; Gil-Crespo, P.P.; Vieira, R.; Lima, A.; Garate-Olave, I. Petrogenetic Relationships between Variscan Granitoids and Li-(F-P)-Rich Aplite-Pegmatites in the Central Iberian Zone: Geological and Geochemical Constraints and Implications for Other Regions from the European Variscides. Ore Geology Reviews 2018, 95, doi:10.1016/j.oregeorev.2018.02.027.

Rodriguez-Galiano, V., Sanchez-Castillo, M., Chica-Olmo, M., & Chica-Rivas, M. (2015). Machine learning predictive models for mineral prospectivity: An evaluation of neural networks, random forest, regression trees and support vector machines. *Ore Geology Reviews, 71*, 804-818. doi: https://doi.org/10.1016/j.oregeorev.2015.01.001.

Shabankareh, M., & Hezarkhani, A. (2017). Application of support vector machines for copper potential mapping in Kerman region, Iran. *Journal of African Earth Sciences, 128*, 116-126. doi: https://doi.org/10.1016/j.jafrearsci.2016.11.032.

Silva, A.F.; Santos, A.J.; Ribeiro, A.; Cabral, J.; Ribeiro, M.L. Carta Geológica de Portugal na escala 1/50.000 – folha 15-B – Freixo de Espada à Cinta; Serviços Geológicos de Portugal: Lisboa, Portugal, 1990.

Silva, A.F.; Santos, A.J.; Ribeiro, A.; Ribeiro, M.L. Carta Geológica de Portugal na escala 1/50.000 – folha 15-A – Vila Nova de Foz Côa; Serviços Geológicos de Portugal: Lisboa, Portugal, 1990.

Silva, A.F.d.; Ribeiro, M.L. Notícia Explicativa da folha 15-A Vila Nova de Foz Côa; Serviços Geológicos de Portugal: Lisboa, Portugal, 1991; p. 52.

Silva, A.F.d.; Ribeiro, M.L. Notícia Explicativa da folha 15-B Freixo de Espada à Cinta; Instituto Geológico e Mineiro: Lisboa, Portugal, 1994; p 48.

Silva, D.; Lima, A.; Gumiaux, C.; Glouguen, E.; Deveaud, S. Spatial Geostatistical Analysis Applied to The Barroso-Alvão Rare-Elements Pegmatite Field (Northern Portugal). In GIS – An Overview of Applications; Teodoro, A.C., Ed.; Bentham eBooks: Sharjah, United Arab Emirates, 2018.

Teixeira, C. Notas sobre geologia de Portugal o complexo xisto-grauváquico ante-ordoviciano; Empresa Literaria Fluminense Lda.: Lisboa, Portugal, 1955; p 48.

van der Meer, F.D.; van der Werff, H.M.A.; van Ruitenbeek, F.J.A. Potential of ESA's Sentinel-2 for Geological Applications. Remote Sensing of Environment 2014, 148, doi:10.1016/j.rse.2014.03.022.

Viallefond, L. Prospection Géochimique Portugal: Résultats Analytiques et Interprétation de l'Échantillonnage Réalisé par le S.F.M. sur la Feuille 15B; NOTE/GMX-732; BRGM: Orléans, France, 1981; p. 27.

Viallefond, L.; Angel, J.M. Portugal Nord—Feuille 15A-15C—Interprétation des Données Analytiques; NOTE/GMX-738; BRGM: Orléans, France, 1981; p. 17.

Vieira, R. Aplitopegmatitos com elementos raros da região entre Almendra (V.N. de Foz Côa) e Barca d'Alva (Figueira de Castelo Rodrigo). Campo aplitopegmatítico da Fregeneda-Almendra. PhD thesis, Faculdade de Ciências da Universidade do Porto, Porto, Portugal, 2010.

Zuo, R., & Carranza, E. J. M. (2011). Support vector machine: A tool for mapping mineral prospectivity. *Computers & Geosciences, 37*(12), 1967-1975. doi: https://doi.org/10.1016/j.cageo.2010.09.014.

Discussion

Asadzadeh, S., & Souza Filho, C. R. (2016). A review on spectral processing methods for geological remote sensing. *International Journal of Applied Earth Observation and Geoinformation, 47*, 69-90. doi: https://doi.org/10.1016/j.jag.2015.12.004.

ASD Inc. (2008). *ViewSpec Pro™ User Manual. ASD Document 600555 Rev. A*. Boulder,

Barros, R., Kaeter, D., Menuge, J. F., & Škoda, R. (2020). Controls on chemical evolution and rare element enrichment in crystallising albite-spodumene pegmatite and wallrocks: Constraints from mineral chemistry. *Lithos, 352-353*, 105289. doi: https://doi.org/10.1016/j.lithos.2019.105289.

Cardoso-Fernandes, J., Teodoro, A. C., Lima, A., & Roda-Robles, E. (2019, 9–12 September 2019). *Evaluating the performance of support vector machines (SVMs) and random forest (RF) in Li-pegmatite mapping: preliminary results.* Paper presented at the SPIE Remote Sensing, Strasbourg, France, doi: 10.1117/12.2532577.

Carrino, T. A., Crósta, A. P., Toledo, C. L. B., & Silva, A. M. (2018). Hyperspectral remote sensing applied to mineral exploration in southern Peru: A multiple data integration approach in the Chapi Chiara gold prospect. *International Journal of Applied Earth Observation and Geoinformation, 64*, 287-300. doi: 10.1016/j.jag.2017.05.004.

Clark, R. N., Swayze, G. A., Gallagher, A. J., King, T. V. V., & Calvin, W. M. (1993). *The U. S. Geological Survey, Digital Spectral Library: Version 1 (0.2 to 3.0um)* (93-592). S. Geological, Retrieved from: http://pubs.er.usgs.gov/publication/ofr93592

Cousin, A., Sautter, V., Fabre, C., Maurice, S., & Wiens, R. C. (2012). Textural and modal analyses of picritic basalts with ChemCam Laser-Induced Breakdown Spectroscopy. *Journal of Geophysical Research: Planets, 117*(E10). doi: https://doi.org/10.1029/2012JE004132.

Duke, E. F. (1994). Near infrared spectra of muscovite, Tschermak substitution, and metamorphic reaction progress: Implications for remote sensing. *Geology, 22*(7), 621-624. doi: 10.1130/0091-7613(1994)022<0621:Nisomt>2.3.Co;2.

Fabre, C. (2020). Advances in Laser-Induced Breakdown Spectroscopy analysis for geology: A critical review. *Spectrochimica Acta Part B: Atomic Spectroscopy, 166*, 105799. doi: https://doi.org/10.1016/j.sab.2020.105799.

Farnsworth-Pinkerton, S., McMillan, N. J., Dutrow, B. L., & Henry, D. J. (2018). Provenance of detrital tourmalines from Proterozoic metasedimentary rocks in the Picuris Mountains, New Mexico, using Laser-Induced Breakdown Spectroscopy. *Journal of Geosciences, 63*(2), 193-198.

Fyzollahhi, N., Torshizian, H., Afzal, P., & Jafari, M. R. (2018). Determination of lithium prospects using fractal modeling and staged factor analysis in Torud region, NE Iran. *Journal of Geochemical Exploration, 189*, 2-10. doi: https://doi.org/10.1016/j.gexplo.2017.09.017.

Galeschuk, C. R., & Vanstone, P. J. (2007). Exploration techniques for rare-element pegmatite in the Bird River greenstone belt, southeastern Manitoba. In B. Milkereit (Ed.), *Proceedings of Exploration 07: Fifth Decennial International Conference on Mineral Exploration* (pp. 823–839).

Gaspar, L. M., & Inverno, C. M. C. (2000). Mineralogy and Metasomatic Evolution of Distal Strata-Bound Scheelite Skarns in the Riba de Alva Mine, Northeastern Portugal. *Economic Geology, 95*(6), 1259-1275. doi: 10.2113/gsecongeo.95.6.1259.

Hunt, G. R., & Ashley, R. P. (1979). Spectra of altered rocks in the visible and near infrared. *Economic Geology, 74*(7), 1613-1629. doi: 10.2113/gsecongeo.74.7.1613.

Kochelek, K. A., McMillan, N. J., McManus, C. E., & Daniel, D. L. (2015). Provenance determination of sapphires and rubies using laser-induced breakdown spectroscopy and multivariate analysis. *American Mineralogist, 100*(8-9), 1921-1931. doi: doi:10.2138/am-2015-5185.

Laakso, K., Rivard, B., Peter, J. M., White, H. P., Maloley, M., Harris, J., & Rogge, D. (2015). Application of Airborne, Laboratory, and Field Hyperspectral Methods to Mineral Exploration in the Canadian Arctic: Recognition and Characterization of Volcanogenic Massive Sulfide-Associated Hydrothermal Alteration in the Izok Lake Deposit Area, Nunavut, Canada. *Economic Geology, 110*(4), 925-941. doi: 10.2113/econgeo.110.4.925.

Lypaczewski, P., Rivard, B., Gaillard, N., Perrouty, S., Piette-Lauzière, N., Bérubé, C. L., & Linnen, R. L. (2019). Using hyperspectral imaging to vector towards mineralization at the Canadian Malartic gold deposit, Québec, Canada. *Ore Geology Reviews, 111*, 102945. doi: https://doi.org/10.1016/j.oregeorev.2019.102945.

Martins, T., Linnen, R. L., Fedikow, M. A. F., & Singh, J. (2017). Whole-rock and mineral geochemistry as exploration tools for rare-element pegmatite in Manitoba: examples from the Cat Lake–Winnipeg River and Wekusko Lake pegmatite fields (parts of NTS 52L6, 63J13). In *Report of Activities 2017* (pp. 42–51). Manitoba Growth, Enterprise and Trade, Manitoba Geological Survey.

Maxwell, A. E., Warner, T. A., & Fang, F. (2018). Implementation of machine-learning classification in remote sensing: an applied review. *International Journal of Remote Sensing, 39*(9), 2784-2817. doi: 10.1080/01431161.2018.1433343.

McMillan, N. J., Rees, S., Kochelek, K., & McManus, C. (2014). Geological Applications of Laser-Induced Breakdown Spectroscopy. *Geostandards and Geoanalytical Research, 38*(3), 329-343. doi: https://doi.org/10.1111/j.1751-908X.2014.00308.x.

Morgan, G. B., & London, D. (1987). Alteration of amphibolitic wallrocks around the Tanco rare-element pegmatite, Bernic Lake, Manitoba. *American Mineralogist, 72*(11-12), 1097-1121.

Naleto, J. L. C., Perrotta, M. M., Costa, F. G. d., & Souza Filho, C. R. d. (2019). Point and imaging spectroscopy investigations on the Pedra Branca orogenic gold deposit, Troia Massif, Northeast Brazil: Implications for mineral exploration in amphibolite metamorphic-grade terrains. *Ore Geology Reviews, 107*, 283-309. doi: https://doi.org/10.1016/j.oregeorev.2019.02.019.

Noi, P. T., & Kappas, M. (2017). Comparison of Random Forest, k-Nearest Neighbor, and Support Vector Machine Classifiers for Land Cover Classification Using Sentinel-2 Imagery. *Sensors (Basel), 18*(1). doi: 10.3390/s18010018.

Pour, A. B., & Hashim, M. (2018). Hydrothermal alteration mapping from Landsat-8 data, Sar Cheshmeh copper mining district, south-eastern Islamic Republic of Iran. *Journal of Taibah University for Science, 9*(2), 155-166. doi: 10.1016/j.jtusci.2014.11.008.

Rivard, B., Zhang, J., Feng, J., & Sanchez-Azofeifa, G. A. (2009). Remote predictive lithologic mapping in the Abitibi Greenstone Belt, Canada, using airborne hyperspectral imagery. *Canadian Journal of Remote Sensing, 35*(sup1), S95-S105. doi: 10.5589/m10-002.

Saadati, H., Afzal, P., Torshizian, H., & Solgi, A. (2020). Geochemical exploration for lithium in NE Iran using the geochemical mapping prospectivity index, staged factor analysis, and a fractal model. *Geochemistry: Exploration, Environment, Analysis, 20*(4), 461-472. doi: 10.1144/geochem2020-020.

Shearer, C. K., Papike, J. J., Simon, S. B., & Laul, J. C. (1986). Pegmatite-wallrock interactions, Black Hills, South Dakota: interaction between pegmatite-derived fluids and quartz-mica schist wallrock. *Am. Mineral.; (United States)*, Medium: X; Size: Pages: 518-539.

Shearer, C. K., Papike, J. J., Simon, S. B., Laul, J. C., & Christian, R. P. (1984). Pegmatite/wallrock interactions, Black Hills, South Dakota: Progressive boron metasomatism adjacent to the Tip Top pegmatite. *Geochimica et Cosmochimica Acta, 48*(12), 2563-2579.

Steiner, B. M., Rollinson, G. K., & Condron, J. M. (2019). An Exploration Study of the Kagenfels and Natzwiller Granites, Northern Vosges Mountains, France: A Combined Approach of Stream Sediment Geochemistry and Automated Mineralogy. *Minerals, 9*(12), 750. doi: 10.3390/min9120750.

Tappert, M. C., Rivard, B., Giles, D., Tappert, R., & Mauger, A. (2013). The mineral chemistry, near-infrared, and mid-infrared reflectance spectroscopy of phengite from the Olympic Dam

IOCG deposit, South Australia. *Ore Geology Reviews, 53*, 26-38. doi: https://doi.org/10.1016/j.oregeorev.2012.12.006.

Teodoro, A. C., & Veloso-Gomes, F. (2007). Quantification of the Total Suspended Matter Concentration around the Sea Breaking Zone from In Situ Measurements and Terra/Aster Data. *Marine Georesources & Geotechnology, 25*(2), 67-80. doi: 10.1080/10641190701334164.

Van Der Meer, F. (2000). Spectral curve shape matching with a continuum removed CCSM algorithm. *International Journal of Remote Sensing, 21*(16), 3179-3185. doi: 10.1080/01431160050145063.

Vieira, R. (2010). *Aplitopegmatitos com elementos raros da região entre Almendra (V.N. de Foz Côa) e Barca d'Alva (Figueira de Castelo Rodrigo). Campo aplitopegmatítico da Fregeneda- Almendra.* (PhD thesis), Faculdade de Ciências da Universidade do Porto, Porto, Portugal, XXVI, 273.

Appendices

Appendix I. Published materials 423

I.1. International, peer-reviewed journal articles 424

I.2. International, peer-reviewed conference proceedings 552

I.3. Conference abstracts and other publications 608

I.4. Supplementary materials to published journal articles 641

Appendix II. Geochemical studies 661

II.1. Sampling and sample preparation 662

II.2. Sample location and description 663

II.3. Analytical techniques 670

II.4. Geochemical results 671

II.5. Supplementary materials to section IV.2. 680

Appendix III. Petrographic studies 681

III.1. Sample preparation and equipment 682

III.2. Petalite alteration 683

III.3. Geochemical haloes 689

Appendix IV. Hyperspectral studies for halo detection 719

IV.1. Equipment and measurements.....720

IV.2. Sample list and selection of key spectra 721

IV.3. First results 737

Appendix I. Published materials

I.1. International, peer-reviewed journal articles

The Canadian Mineralogist
Vol. 57, pp. 723-725 (2019)
DOI: 10.3749/canmin.AB00004

CONSTRAINTS AND POTENTIALS OF REMOTE SENSING DATA/TECHNIQUES APPLIED TO LITHIUM (Li)-PEGMATITES

JOANA CARDOSO-FERNANDES[§] AND ALEXANDRE LIMA

Department of Geosciences, Environment and Land Planning, Faculty of Sciences, University of Porto, Rua Campo Alegre, Porto, Portugal
ICT (Institute of Earth Sciences) – Porto pole (Portugal)

ENCARNACIÓN RODA-ROBLES

Departamento de Mineralogía y Petrología, Univ. País Vasco (UPV/EHU), Apdo. 644, 48080-Bilbao, Spain

ANA CLÁUDIA TEODORO

Department of Geosciences, Environment and Land Planning, Faculty of Sciences, University of Porto, Rua Campo Alegre, Porto, Portugal
ICT (Institute of Earth Sciences) – Porto pole (Portugal)

Keywords: lithium, pegmatite, remote sensing, exploration, Fregeneda-Almendra, Portugal, Spain.

INTRODUCTION

Lithium (Li) is a mineral commodity increasingly sought after mainly because it is essential to the production of rechargeable Li-ion batteries mainly used in high-tech consumer electronics (like smartphones) and in the green-power industry. This increasing demand of Li is mainly driven by the electric car industry, in the pursuit for more environment-friendly means of transportation, and it will result in an intensive Li exploitation in the near future. Consequently, there is great pressure for mining and exploration companies to achieve fast but accurate results in targeting potentially economic areas. New and untraditional Li exploration methods are needed in order to meet the market expectations. One of these exploration methods could be remote sensing, which has shown good results in targeting gold and copper deposits for example. Remote sensing is the science which obtains, processes and interprets data that records the interaction between matter and electromagnetic energy at distance (Sabins 1997). Recently, the first steps towards its application in Li exploration were made.

In Europe the most important Li-bearing deposits are the ones hosted in pegmatites (Kesler *et al*. 2012), and one of the main areas of interest in Europe is the Iberian Peninsula where several aplite-pegmatite fields were already recognized. The Fregeneda-Almendra aplite-pegmatite field is one of these cases and was selected as the study area since the sparse vegetation allows the application of remote sensing techniques.

THE FREGENEDA-ALMENDRA APLITE-PEGMATITE FIELD

The Fregeneda-Almendra (FA) aplite-pegmatite field lies within the Central Iberian Zone, which occupies the central portion of the Iberian Massif. In the FA field different types of pegmatite veins were defined according to their mineralogy, morphology and internal structure (Roda-Robles 1993, Roda-Robles *et al*. 1999, Vieira 2010). These dikes intruded the pre-Ordovician metasediments of the schist-metagraywacke complex (Carrington da Costa 1950) and are located north of the syn-Variscan Mêda-Penedono-Lumbrales granitic complex. They show a zonal distribution from barren aplite-pegmatites to bodies enriched in Li, F, Sn, Rb, Nb > Ta, B, P and Be, with increasing fractionation degree as the

[§] *Corresponding author e-mail address*: joana.fernandes@fc.up.pt

distance to the granitic complex becomes greater. Within the evolved pegmatites, five types of dikes have been characterized: petalite-rich, spodumene-rich, lepidolite-spodumene-rich, lepidolite-rich and cassiterite-rich pegmatites.

Recently, in the FA area, some remote sensing algorithms such as RGB (red, green, blue) combinations, band ratios, principal component analysis (PCA) and image classification (using the Maximum Likelihood algorithm) were applied to identify Li-pegmatites (Cardoso-Fernandes *et al*. 2018, Cardoso-Fernandes *et al*. 2019).

Remote Sensing and Li-Pegmatites

In Li exploration, the previous works show that there are two main approaches to the application of the image processing methods: (i) the recognition of hydrothermally altered zones associated with the mineralized zones; (ii) the direct identification of Li-bearing minerals. These approaches were made using different types of multispectral products: Landsat 5 TM, Landsat 8 OLI, ASTER and Sentinel-2. In what concerns the first approach, the application of classic techniques with the known band combinations showed some contradictory results. On one hand, RGB combinations are capable of identifying some hydrothermal alteration near the Li-bearing pegmatites while the band ratio technique failed to identify minerals associated with hydrothermal alteration (like iron oxides and clays) near the open-pit mines where their presence was described. Also, the application of PCA, on only certain bands where the target minerals present characteristic absorption or reflectance features, allowed to identify the presence of iron minerals in some mines while only the ASTER sensor allowed to identify hydroxyl-bearing minerals like clays (Cardoso-Fernandes *et al*. 2019). All the existing RGB band combinations used in this approach were defined for other deposit types and therefore are not the most adequate to Li-exploration due to the different nature of the deposits and their associated mineralogy and alteration style. Detailed studies on the type of alteration associated with the Li-bearing pegmatites could help to develop new band combinations more robust to Li-exploration.

Regarding the second approach, different self-proposed RGB combinations were capable of discriminating Li-bearing pegmatites with good exposition from the host rocks for all sensors excepting the Sentinel-2 (Cardoso-Fernandes *et al*. 2019). The impossibility to discriminate the Li-pegmatites with Sentinel-2 images reflects the importance of thermal bands, which Sentinel-2 does not have available. Besides, other methods showed good results in highlighting Li-mineralizations, namely several band ratios and the application of PCA in certain subsets of bands. Finally, a first attempt to supervised image classification was made by Cardoso-Fernandes *et al*. (2018). In this study, a conventional classification algorithm Maximum Likelihood was employed and it positively identified the three open pit mines as Li-bearing areas. Nonetheless, this classification also produced several false positives and some confusion between the metasedimentary rocks and the granites.

Overall, we can identify the main difficulties/challenges in the application of remote sensing to Li-pegmatite exploration as being: (i) the vegetation coverage that even when sparse can mask out other spectral signals; (ii) the relation between the aplite-pegmatite dikes dimensions and the image pixel size which results in a small exposition; (iii) the spectral resolution of sensors due to the importance of the thermal infrared region in Li-mineral identification and due to the fact that a higher number of bands increases the capability of mineral discrimination; (iv) the spectral similarity of some classes mainly between the Li-bearing pegmatites and urbanized areas or agricultural fields.

Considering all this, even though some of the applied methodologies allowed a good discrimination of the Li-pegmatites, it is clear that more robust remote sensing techniques need to be applied and detailed spectral, petrographic and geochemical studies must be conducted in order to: (i) discriminate the areas with similar spectral behavior; (ii) identify the characteristics of hydrothermal alteration associated with the Li-bearing pegmatites and its spectral features.

To overcome the identified difficulties, several strategies are now being considered. The pixel size problem can be resolved by diminishing the pixel using very high-resolution images, namely World-View3. Also drone flights will allow to validate the results obtained with the satellite images. On the other hand, the construction of a spectral library of the different minerals and rocks will be the key to fully discriminate the spectral signatures obtained in the satellite products and also to validate the techniques applied. Lastly, to improve the image classification results, unconventional techniques such as machine learning algorithms are being used.

Acknowledgments

The authors would like to thank the financial support provided by FCT– Fundação para a Ciência e a Tecnologia with the ERA-MIN/0001/2017 – LIGHTS project and to FEDER through the operation POCI-01-0145-FEDER-007690 funded by the Pro-

grama Operacional Competitividade e Internacionalização – COMPETE2020 and by National Funds through FCT – Fundação para a Ciência e a Tecnologia within ICT, R&D Unit (reference UID/GEO/04683/2013). Joana Cardoso-Fernandes is financially supported by FCT within the compass of a Ph.D. Thesis, ref. SFRH/BD/136108/2018.

References

Cardoso-Fernandes, J., Lima, A., & Teodoro, A.C. (2018) Potential of Sentinel-2 data in the detection of lithium (Li)-bearing pegmatites: a study case. Proceedings Volume 10790, SPIE Remote Sensing, SPIE, 15 pp.

Cardoso-Fernandes, J., Teodoro, A.C., & Lima, A. (2019) Remote sensing data in lithium (Li) exploration: A new approach for the detection of Li-bearing pegmatites. *International Journal of Applied Earth Observation and Geoinformation* **76**, 10–25.

Carrington da Costa, J. (1950) Notícia sobre uma carta geológica do Buçaco, de Nery Delgado. Comunicações dos Serviços Geológicos de Portugal, Lisboa, 28 pp. (in Portuguese).

Kesler, S.E., Gruber, P.W., Medina, P.A., Keoleian, G.A., Everson, M.P., & Wallington, T.J. (2012) Global lithium resources: Relative importance of pegmatite, brine and other deposits. *Ore Geology Reviews* **48**, 55–69.

Roda-Robles, E. (1993) *Distribución, Caracteristicas y Petrogenesis de las Pegmatitas de La Fregeneda (Salamanca)*. Ph.D. Thesis, Department of Mineralogy & Petrology – UPV, Bilbao, Spain, 199 pp. (in Spanish).

Roda-Robles, E., Pesquera, A., Velasco, F., & Fontan, F. (1999) The granitic pegmatites of the Fregeneda area (Salamanca, Spain). characteristics and petrogenesis. *Mineralogical Magazine* **63**, 535–558.

Sabins, F.F. (1997) *Remote Sensing—Principles and Interpretation*. 3rd Edition, W.H. Freeman, New York City, New York.

Vieira, R. (2010) *Aplitopegmatitos com Elementos Raros da Região entre Almendra (V. N. de Foz-Côa) e Barca d'Alva (Figueira de Castelo Rodrigo). Campo Aplito-pegmatítico da Fregeneda-Almendra*. Ph.D. Thesis. Universidade do Porto, Porto, Portugal, 276 pp. (in Portuguese).

applied sciences

MDPI

Review

Detecting Lithium (Li) Mineralizations from Space: Current Research and Future Perspectives

Joana Cardoso-Fernandes [1,2,*], Ana C. Teodoro [1,2], Alexandre Lima [1,2], Mônica Perrotta [3] and Encarnación Roda-Robles [4]

1 Department of Geosciences, Environment and Land Planning, Faculty of Sciences, University of Porto, Rua Campo Alegre, 4169-007 Porto, Portugal; amteodor@fc.up.pt (A.C.T.); allima@fc.up.pt (A.L.)
2 Institute of Earth Sciences (ICT), Pole of University of Porto, 4169-007 Porto, Portugal
3 Geology and Mineral Resources Board of Directors, Geological Survey of Brazil (CPRM), Rua Costa, 01304-010 São Paulo, Brazil; monica.perrotta@cprm.gov.br
4 Departament of Mineralogía y Petrología, University of País Vasco (UPV/EHU), Barrio Sarriena, 48940 Leioa, Bilbao, Spain; encar.roda@ehu.es
* Correspondence: joana.fernandes@fc.up.pt

Received: 4 February 2020; Accepted: 2 March 2020; Published: 5 March 2020

check for updates

Abstract: Optical and thermal remote sensing data have been an important tool in geological exploration for certain deposit types. However, the present economic and technological advances demand the adaptation of the remote sensing data and image processing techniques to the exploration of other raw materials like lithium (Li). A bibliometric analysis, using a systematic review approach, was made to understand the recent interest in the application of remote sensing methods in Li exploration. A review of the application studies and developments in this field was also made. Throughout the paper, the addressed topics include: (i) achievements made in Li exploration using remote sensing methods; (ii) the main weaknesses of the approaches; (iii) how to overcome these difficulties; and (iv) the expected research perspectives. We expect that the number of studies concerning this topic will increase in the near future and that remote sensing will become an integrated and fundamental tool in Li exploration.

Keywords: satellite data; image processing algorithms; pegmatite; brine; lithological mapping; mineral alteration mapping; geobotanical mapping

1. Introduction

Optical and thermal remote sensing data, namely satellite-acquired images, have been an important tool in geological exploration allowing to target exploration areas for more than four decades. The major contribution that remote sensing offers to mineral exploration was reviewed in several works dedicated to this topic [1–5]: it provides information in a fairly quick, inexpensive, and non-intrusive way, which favors mining and exploration companies especially in inaccessible remote areas. However, Rajesh [3], in an overview of the use of remote sensing and Geographic Information Systems (GIS) in mineral exploration, points out the difficulty of directly pinpointing mineralizations using only remote sensing data, highlighting the importance of the integration with other types of geological data.

Sabins [6], in one of the first reviews about the types of data and image processing methods for mineral exploration, describes two main approaches to target mineral deposits: (i) structural and lithological mapping; and (ii) hydrothermal alteration mapping. Later, Rajesh [3] proposed three approaches: (i) lithological mapping; (ii) structural mapping; and (iii) alteration mapping. These approaches have been applied since the 1970s to identify very distinct types of mineral deposits. The more common applications include porphyry copper [7–17] and gold [18–28] deposits.

Other applications may include: iron ore deposits [19,29–32], volcanogenic massive sulfide ore (VMS) deposits [33–35], several skarn-hosted deposits [36–39], chromite deposits [40–43], uranium deposits [39,44], rare earth elements (REE) exploration [36,45], brine and evaporite deposits [46,47], porphyry molybdenum deposits [48,49], zinc-lead (Zn-Pb) deposits [50], diamond [51] and bauxite exploration [52].

Regarding the types of data used, multispectral products, namely Landsat and Advanced Spaceborne Thermal Emission and Reflection Radiometer (ASTER) sensor imagery, played an important part in geological remote sensing [4,5,53]. Abrams and Yamaguchi [54] reviewed ASTER's contributions to mineral exploration and lithological mapping. The success of the ASTER sensor in geological exploration was mainly due to a higher spectral resolution in the short-wave infrared (SWIR) and thermal infrared (TIR), specially designed for geological applications, which improved its lithological and mineral mapping capabilities, particularly in the identification of alteration minerals [4,53–55]. The importance of TIR (including ASTER's TIR subsystem) in the discrimination of minerals and rocks was revised by Ninomiya and Fu [55]. These authors highlight several studies in which the TIR region was fundamental for mineral discrimination, namely where silicate minerals occur, and reviewed the spectral indices proposed for lithological mapping using ASTER-TIR data. Nonetheless, the advent of hyperspectral remote sensing allowed the direct identification and quantification of specific minerals which represented a key contribution to mineral exploration [3,53]. Cudahy [4] in a review on mineral mapping projects for exploration led by Commonwealth Scientific and Industrial Research Organization (CSIRO) in Australia, pointed out that hyperspectral remote sensing can be less popular among exploration companies because of limited spatial coverage, the relatively high-cost of quality datasets, and the inherent complexity of hyperspectral data.

Despite the successful application of different types of remote sensing data to distinct mineral deposits, the current growing economic and technological advances, which rely on other mineral commodities, highlights the need to use and adapt remote sensing data and image processing techniques on new deposit types. Nowadays, green technologies, like electric vehicles, represent an important sector of the economy [56] and lithium (Li) has become a critical metal to the green-power industry [57,58]. However, Li exploration with the resource of remote sensing data and techniques represents an emergent field, with several difficulties and unknown possibilities. Taking this into account, this review aims at (i) providing information about what can be accomplished in Li exploration using remote sensing methods; (ii) identifying the main difficulties associated with this kind of deposits; and (iii) providing insights on how to overcome these difficulties as well as future research perspectives. This paper presents the first summary of the developments made in the field of remote sensing applied to Li exploration and we consider it to be timely and appropriate due to the high global demand of this metal to the production of Li-ion batteries [58]. Additionally, this review can help to promote new applications and to solve new exploration problems.

2. Li Exploration Using Remote Sensing

This section aims at summarizing past and current applications of remote sensing data and image processing techniques to Li exploration at first, and then highlights the main weaknesses associated with each methodology already proposed.

2.1. Advancements in Satellite-Based Remote Sensing

Despite the latest interest in this topic, the first application of remote sensing to Li mineralizations started in 1982. Lefevre [59] conducted a multitemporal study (from 1975 to 1976) using Landsat Multispectral Scanner System (MSS) images to detect geobotanical anomalies caused by dispersal halos of metals, such as lithium, tungsten, and arsenic, associated with the Collete granite and the Beauvoir domes. To extract the spectral signature of the circular anomaly, band ratios 7/5 and 7/6 (band 5: 0.6 to 0.7μm; band 6: 0.7 to 0.8 μm; band 7: 0.8 to 1.1 μm) were applied to the images. Comparing the spectral anomalies of the vegetation with the soil geochemical maps, the author concluded that there was a clear

correspondence between spectral and geochemical anomalies. However, such spectral anomalies could be related to the presence of the other metals in the vegetation's leaves and not necessarily due to the presence of Li.

Over a decade ago, Perrotta et al. [60] used ASTER images for a trial mapping of Li-bearing pegmatites in the Vale do Jequitinhonha region, Brazil. The authors used visible, near-infrared (VNIR), and SWIR data to evaluate the spectral signatures of gem- and Li pegmatites, and related alteration minerals. For that, the target spectra were determined through the estimation of the pixel purity index (PPI) either directly in the atmospherically-corrected images or after applying a minimum noise fraction (MNF) transformation of the data. PPI was estimated since the mean spectra of each sample group, where the pixel samples were identified in ASTER images, failed as reference spectra. The obtained reference spectra were used to classify the ASTER image using the spectral angle mapper (SAM) and the mixture-tuned matched filtering (MTMF), having the last supervised method outperform the first since SAM was also sensible to roads, agricultural fields, or areas around the main drainage lines.

Mendes et al. [61] applied a similar methodology in the identification of Li minerals' spectral signatures in view of future identification of unknown ore deposits in the Vale do Jequitinhonha region, Brazil. To achieve that goal, reference spectra of Li-bearing minerals, as well as associated alteration minerals and soils, were collected in the laboratory. However, only the open-pit mines delimited in image data were used as training areas after the spectra obtained in the laboratory failed to serve as a reference for the classification process. Similar to before, an MNF transformation was applied to the ASTER VNIR and SWIR bands in order to segregate the noise. Statistical analysis was applied to the MNF to determine the reference pixels with the highest PPI, from which tree reference signatures were selected. Afterward, two supervised classification methods were employed, SAM and MTMF, only where the location of metasediment outcrops, while the other lithologies where masked. Although both methods were able to correctly identify the spectral features of pegmatite intrusions, the SAM classifier also mapped other features, like roads or agricultural fields, while MTMF only identified a small number of pixels to have similar spectral behavior to the reference spectra. The solution proposed by Mendes et al. [61] was to produce a final target potential map through the Boolean intersection of the results obtained from the application of MTMF and SAM techniques.

Another remote sensing approach to Li pegmatite exploration was made recently in the Fregeneda-Almendra (Salamanca, Spain–Vila Nova de Foz Côa, Portugal) pegmatite field. Cardoso-Fernandes et al. [62], in a preliminary stage, presented the potential of the Sentinel-2 Multispectral Instrument (MSI) in Li mapping. The study attempted to identify Li pegmatites mainly based on the recognition of the associated alteration halos. To achieve that goal, several methods applied to other deposit types were adapted to the Sentinel-2 images, including RGB (red, green, blue) combinations, band ratios and principal component analysis (PCA). These methodologies allowed to predict the occurrence of iron oxides and clay minerals, and to discriminate between non-altered and hydrothermally-altered zones. The authors also tried to directly identify Li pegmatites based on their spectral behavior. Using the reference spectra of spodumene (a Li-bearing mineral), the band ratio 3/8 was proposed to discriminate the presence of Li-bearing minerals. Another approach was to use a supervised image classification to map Li-bearing pegmatites. The classification was performed on the resultant bands from the application of PCA, using the land cover signature classification (LCS) and the maximum likelihood (ML) algorithms simultaneously. The reference spectral curves used to classify the image were the ones collected in training sites identified in the Sentinel-2 images. The training areas included open-pit mines exploiting Li minerals. Although the algorithm employed allowed to correctly identify the Li pegmatites in exploitation, it also generated some false positives and misclassified some metasedimentary areas. The authors [62] also highlighted the need and importance of the acquisition of mineral spectra to improve the classification output. Considering the results given in this work, Cardoso-Fernandes et al. [63] presented two new different approaches: (i) identification of hydrothermal alteration minerals associated with the Li-bearing pegmatites; and (ii) direct identification of Li minerals. These methods were applied in different types of multispectral

cloud-free products, namely, Landsat-5 Thematic Mapper (TM), Landsat-8 Operational Land Imager (OLI) and Thermal Infrared Sensor (TIRS), ASTER, and Sentinel-2 MSI. The alteration mapping results differ from one image processing method to another [63]: while RGB combinations highlighted hydrothermally-altered areas near the Li-bearing pegmatites, the common band ratios applied were unsuccessful in the identification of iron oxides and clay minerals in the open-pit mines where they were described [64]. Additionally, Selective PCA, i.e., PCA applied in a subset of bands chosen based on characteristic absorption or reflectance features of the target minerals, only identified the occurrence of iron minerals in some of the open pits. The ASTER sensor was the one that showed better performance since hydroxyl-bearing minerals like clays were solely identified in the ASTER image [63], reflecting the higher mapping capabilities of ASTER due to its better spectral resolution. On the other hand, some spectral confusion with areas affected by wildfires and with agricultural fields hindered the results. In what concerns the approach to directly identify Li minerals, Cardoso-Fernandes et al. [63] proposed new algorithms capable of identifying the Li pegmatites with better exposition (i.e., outcropping area) (see Appendix A). In the case of RGB combinations (ASTER 5-1-14 and 2-1-13; Landsat-8 7-3-11 and 2-1-11; Landsat-5 7-2-6 and 2-1-6), it was possible to discriminate the Li-bearing pegmatites from the host rocks (metapelites) [63]. However, this discrimination could not be achieved using Sentinel-2 images due to the lack of TIR bands and the importance of this region of the electromagnetic spectrum in silicate minerals [55,65] like the Li-bearing silicates (spodumene and petalite) that occur in the Fregeneda-Almendra area. The proposed band ratios (ASTER 7/6 and 1/3, Landsat-8 3/5, Landsat-5 2/4, Sentinel-2 3/8) and selective PCA based on subsets of two and four bands were also able to highlight the Li pegmatites, isolating the related spectral inputs, although the authors recommend the use of the two-band subset for PCA since it reduces unnecessary noise [63]. Despite the success in Li pegmatite discrimination, all methods manifested spectral confusion with urbanized areas and agricultural fields. These spectral confusions are consistent with the ones reported by other authors in different regions of the world [60,61], pointing to the need to spectrally separate the classes.

In follow-up work, Santos et al. [66] applied the algorithms proposed by Cardoso-Fernandes et al. [63] to evaluate their performance in drawing potential exploration areas in other Li pegmatites occurrences, namely in the pegmatite fields of Araçuaí and São João Del Rei in Brazil. The methods (RGB combinations, band ratios, and selective PCA) and the algorithms employed (see Appendix A) showed variable performances in the two pegmatite fields. Additionally, Li pegmatite identification was more accurate in the São João Del Rei region than in Araçuaí, having the vegetation coverage in the second area negatively influenced the results according to the authors [66]. It is worth mentioning the ability of RGB combinations to discriminate Li pegmatites from both host rocks and associated tailings and mine dumps, with the exception of the Landsat-5 images [66]. Additionally, in the São João Del Rei area, the most successful band ratios were the ones proposed based on the reference spectrum of lepidolite (a Li-bearing mica): Landsat-5 3/7, Landsat-8 4/7 and Sentinel-2 4/7 [63]. Regarding the ratios proposed for spodumene, only ASTER 1/3 was able to highlight Li mineralized areas. In the Araçuaí area, the spodumene based ratios were the most accurate in Li pegmatite identification. In what concerns selective PCA, the two-band subset produced better results in the São João Del Rei pegmatite field while the four-band subset worked better in Araçuaí [66]. Overall, selective PCA presented the most accurate results while band rationing was the least efficient method in Li pegmatite identification [66]. On the other hand, no limitations were found in the use of Sentinel-2 images, unlike that reported in other works [63]. This may suggest that the ability to discriminate Li pegmatites using Sentinel-2 images might rely on the composition of the host rocks. Nevertheless, the results obtained were very significant, contributing to the state of the art of this field, since not only did it confirm the methodology proposed by Cardoso-Fernandes et al. [63] but also showed its ability to detect other pegmatite occurrences with Li potential besides the known target areas. Currently, field validation is in progress to check if Li mineralization is in fact present in the potential areas identified.

Moreover, in the Alto Ligonha province (Mozambique), Gemusse et al. [67] used ASTER and Landsat-8 images to map hydrothermal alteration minerals associated with Li-bearing pegmatites,

since several pegmatites in the region present a thick kaolinitic weathering crust. The two satellite products were used to produce land cover classification maps with the SAM supervised algorithm. Although the ASTER image classification obtained a higher overall accuracy, both products allowed to identify the spectral signatures of hydrothermal clay alteration (kaolin occurrences) associated with pegmatites [67]. This identification was also supported by published spectral libraries. Additionally, field samples of Li minerals, such as lepidolite and spodumene, were collected and analyzed using an ASD HandHeld2 spectroradiometer [67]. However, the spectroradiometer only covers the VNIR region of the spectra, so it was not possible to discriminate the two Li minerals in these wavelengths. Nonetheless, the classification results, using the target signatures collected in the satellite products, were able to identify two potential areas for future pegmatite exploration [67]. The authors also concluded that ASTER and Landsat-8 provide complementary information on mineral composition. Still in the Alto Ligonha region, different satellite products (namely ASTER, Landsat-8, and Sentinel-2) and different remote sensing algorithms were compared to target Li pegmatites [68]. The algorithms include three supervised classification methods—minimum distance, SAM, and ML—and one unsupervised algorithm: k-means clustering. The land cover classifications maps were compared as well as the performance accuracy of each classifier. Contrary to expected, the minimum distance attained the best accuracy while ML showed the worst performance [68] but no explanation to the fact is given. Perhaps these results reflect the quality of the training data. Despite the disparity between the results obtained with the different classifiers, Gemusse et al. [68] stated that the classification maps show clay minerals, such as kaolinite and montmorillonite, resultant from pegmatite alteration. These maps were validated through field investigations, geological maps and previous works and reports [68]. The authors also noted that the satellite product that achieves the best accuracy for the SAM and minimum distance algorithm was the Sentinel-2. More work is necessary, since the results may indicate a positive contribution from the increased spatial resolution of the sensor.

In a work focused on the application of image classification in Li pegmatite exploration, Cardoso-Fernandes et al. [69] compared the performance between two machine learning algorithms (MLAs), support vector machine (SVM) and random forest (RF), in the Fregeneda-Almendra area, using Sentinel-2A images. For details on model selection and parametrization, the original publication should be consulted [69]. This work represents the first application of MLAs in Li pegmatite mapping. Both algorithms (SVM and RF) correctly mapped the occurrence of Li pegmatites in the open-pit mines [69]. Although SVM achieved a higher overall accuracy (98.54%), the RF model (built using class balancing strategies; overall accuracy of 97.70%) was able to correctly classify a larger number of mapped Li-bearing pegmatites [69]. Additionally, some of the areas classified by SVM and RF as Li pegmatites correspond with the regions of interest delimited in previous studies [63] or to barren mapped pegmatites. Despite the potential shown by this type of approach, these techniques still produced several false positives resultant from the spectral similarity of Li pegmatites with other lithologies, namely metasedimentary rocks [69]. This may indicate that more high spatial resolution images are needed. Moreover, other difficulties were encountered (see Section 2.2), mainly associated with the high number of classes defined in the image, having the authors [69] concluded that both SVM and RF were overfitting at a class level, despite this kind of algorithms being less prone to overfit than other machine learning techniques [70–73]. This illustrates that this kind of approach can be optimized.

All the developments mentioned so far concerned the application of remote sensing the hard-rock Li deposits. However, new applications in other Li deposits are emerging. One example is the "Space enabled exploration and monitoring of Cornwall Lithium resources" research project dedicated to Li brine exploration [74]. The project aims at targeting underground geothermal Li brines through the integration of several multispectral and SAR products to produce geological, active faulting, and vegetation maps [74]. The geological mapping will be achieved in two stages: (i) the first consists on geological mapping using Landsat-8 and Sentinel-2 images with subsequent integration of geophysical data; and (ii) the second will focus on mineral alteration mapping using multispectral (ASTER and Worldview-3) and airborne hyperspectral data (HyMAp) [74]. On its turn, SAR data, namely Sentinel-1

scenes, will be used to map in detail fault systems that may structurally control Li brines. Another approach will consist of the detection of vegetation with possible Li anomalies [74].

Another deposit type that may have big potential for remote sensing applications are metasediment-hosted Li deposits like the Valdeflores (Cáceres, Spain) case where the mineralization occurs in Li-bearing micas [75,76]. This deposit would have been formed by a pervasive metasomatism that resulted in a target area of approximately 250 × 500 m [75] which means that the spatial resolution of the sensors would no longer be a problem as in pegmatite deposits. Additionally, the metasomatic formation of white mica in other mineral deposits is usually accompanied by wavelength changes of the 2200 nm absorption feature that can be used to target mineralizations using hyperspectral sensors [4]. A similar approach could be applied to detect Li micas in metasedimentary rocks.

2.1.1. Brief Overview

To understand the recent interest in the application of remote sensing methods in Li exploration and to provide an overall picture of the state of the research, we searched the number of publications in the Scopus bibliographic database using specific keywords ("Remot * sens *" AND "Lithium" AND "Mineral *"; "Satellite" AND "Lithium" AND "Mineral *"; "Remot * sens *" AND "Lithium").

After search refinement, title and abstract screening and eligibility check, a total of nine publications from the initial 261 were included in the analysis (representing 3.4% of the total). Despite this number being considered low for bibliographic analysis [77], it highlights the existent gap in the literature in Li exploration using remote sensing data/techniques. All documents were analyzed by type, country, and citations. The co-occurrence of keywords was also analyzed considering their frequency. The VOSviewer software was employed for network visualization of the data through clustered density maps. Table 1 presents a summary of information on the nine publications included in the analysis.

Table 1. SCOPUS search results concerning publications related to Li exploration using remote sensing data and techniques.

Authors (Year)	Title	Citations
Cardoso-Fernandes et al. (2019)	Constraints and potentials of remote sensing data/techniques applied to lithium (Li) pegmatites	-
Cardoso-Fernandes et al. (2019)	Remote sensing data in lithium (Li) exploration: A new approach for the detection of Li-bearing pegmatites	6
Santos et al. (2019)	Remote sensing techniques to detect areas with potential for lithium exploration in Minas Gerais, Brazil	-
Cardoso-Fernandes et al. (2019)	Evaluating the performance of support vector machines (SVMs) and random forest (RF) in Li pegmatite mapping: Preliminary results	-
Rossi et al. (2018)	An earth observation framework for the lithium exploration	-
Cardoso-Fernandes et al. (2018)	Potential of Sentinel-2 data in the detection of lithium (Li)-bearing pegmatites: A study case	4
Gemusse et al. (2018)	Pegmatite spectral behavior considering ASTER and Landsat 8 OLI data in Naipa and Muiane mines (Alto Ligonha, Mozambique)	1
Dai et al. (2017)	Geological mapping and ore-prospecting study using remote sensing technology in Jiajika area of Western Sichuan Province	1
Lefevre (1982)	Remote sensing of geobotanical anomalies in mineral exploration: a Landsat 1 processing methodology - Echassieres, Allier, France	-

The average publication year is 2014, with eight documents (88.9%) published after 2016, which reflects the recent interest in this field. Almost all documents were published in English (7; 77.8%), with the exception of one document published in Chinese (11.1%) and another one in French (11.1%) (Figure 1a). When analyzing the type of document, five publications (55.6%) correspond to conference papers while the remaining four documents (44.4%) correspond to journal articles (Figure 1b). The publications received a total of 12 citations, with an average of 1.3 citations per document since there are four documents (44.4%) with at least one citation (Table 1).

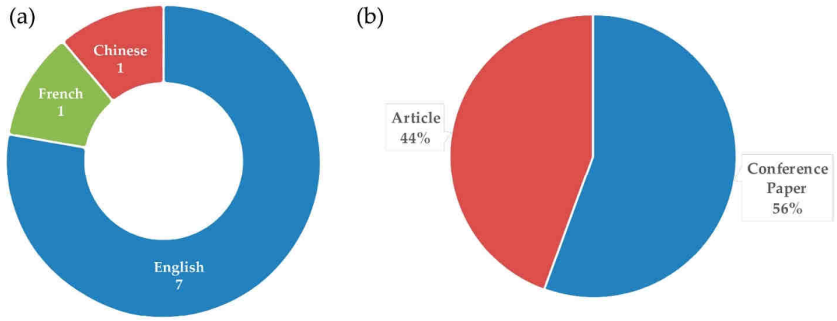

Figure 1. (**a**) Donut chart showing the distribution of the documents' language. (**b**) Pie chart with the distribution of the documents' type.

The co-occurrence of author and index keywords was also analyzed (Figure 2), being "remote sensing", "lithium", and "granite" the most frequent keywords occurring eight, seven, and four times, respectively.

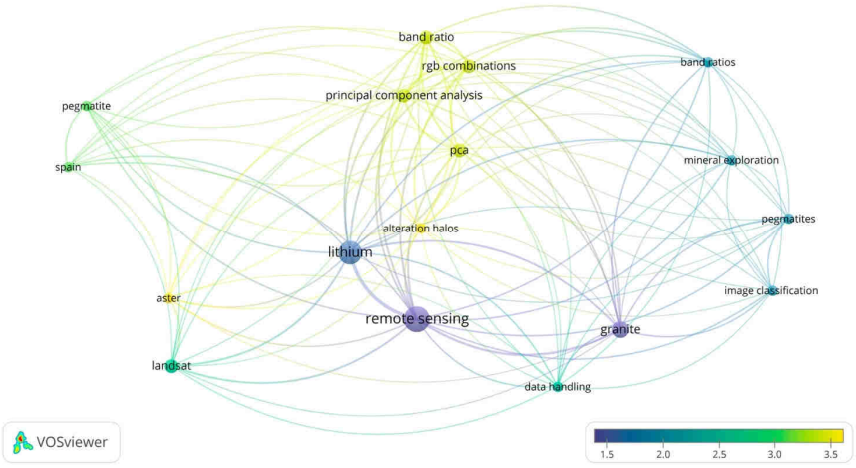

Figure 2. Co-occurrence of author and index keywords. Each circle represents a different keyword, being the size proportional to the respective number of occurrences. The color represents the average citation associated with each keyword, while the lines represent the link strength between different keywords. The minimum number of occurrences of a keyword considered was two, with 17 keywords having met the criteria.

Regarding the geographic distribution of the publications, most of the studies were conducted by researchers with European affiliations (Figure 3a): Portugal ranked first with six publications (66.7% of the total), followed by Spain with two studies (22.2% of the total), and by France and the United Kingdom with one document each (representing 11.1% of the total). On the other hand, as can be seen in Figure 3, the study area considered in each work not always corresponds to the affiliation country of the authors. Despite most studies areas being located in Europe, other applications were made in the American, African, and Asian continents (Figure 3b).

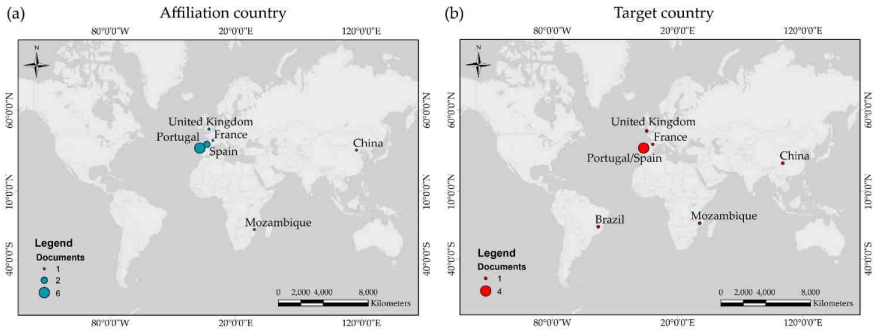

Figure 3. (**a**) Geographic distribution of the retrieved publications taking into account the affiliation country. (**b**) Geographic distribution of the analyzed publications considering the study area of the work. In some cases, the study area encompasses more than one country (Portugal/Spain).

2.2. Main Challenges

The difficulties encountered in the previously mentioned applications are mainly related to the inherent characteristics of Li deposits, especially in the case of Li pegmatites which are characterized by low areas of exposition due to their dimensions (pegmatites are relatively narrow bodies).

Mendes et al. [61] reported difficulties in the direct application of the spectral signatures of Li-bearing minerals obtained in the laboratory to identify similar targets in the ASTER images. The authors [61] attributed this challenge to: (i) the low spatial resolution of the images when compared to the target area; (ii) spectral noise resultant from mixture of the materials presented in a pixel; and (iii) the low spectral resolution of the ASTER sensor when compared to the laboratory spectroradiometer.

Cardoso-Fernandes et al. [63] highlighted that the main problem associated with the identification by the hydrothermal alteration approach is that the applied RGB combinations, band ratios, and the subsets used for selective PCA correspond to algorithms proposed for the identification of other deposit types with distinct alteration styles and mineral assemblages. Thus, in order to optimize alteration mapping associated with Li pegmatites is fundamental to characterize the associated alteration minerals and possible alteration halos in the host rocks. The knowledge on the alteration halos would allow directing the image processing methods to specific minerals and it could help to discriminate between barren and Li-mineralized pegmatites. Furthermore, the possible recognition of the associated alteration halos from satellite sensors would also allow increasing the target exposition area, allowing to overcome the pegmatite thickness problem.

Based on the works conducted in the Fregeneda-Almendra area, Cardoso-Fernandes et al. [78] made a preliminary attempt to identify the main constraints in Li pegmatite exploration using satellite remote sensing as being: (i) the vegetation coverage that masks the target spectral signatures; (ii) the small pegmatite size when compared to pixel size (the exposition problem); (iii) the small number of bands and/or the lack of thermal bands in some satellite sensors (the spectral resolution problem); and (iv) the spectral resemblance between the Li pegmatites and urbanized areas or agricultural fields. These challenges are in line with the difficulties identified in other pegmatite locations [60,61,66].

In what concerns the vegetation coverage, Cudahy [4] stated, for other applications, that even when green vegetation is sparse, dry vegetation can negatively influence the spectral signature of each image pixel. At least in the Fregeneda-Almendra region, dry vegetation is more abundant than green vegetation. However, no attempts to minimize its influence were made (only green vegetation was masked). On the other hand, Cudahy [4] adverted that unmixing the spectral signatures of both green and dry vegetation is preferred than masking them. For that, Rodger and Cudahy [79] developed an unmixing method for hyperspectral sensors in which a vegetation corrected continuum depth is obtained. Despite multispectral products such as ASTER not being the most adequate to measure the spectral features of dry vegetation, it is still possible to obtain an approximate dry vegetation index [4].

Nonetheless, the compromise between spatial and spectral resolution is, in our opinion, the principal challenge in Li pegmatite exploration. This is best exemplified in the work that attempted to classify Sentinel-2 images using MLAs [69]. Although Sentinel-2 represents the free multispectral product with better spatial resolution and, therefore, the one with the best capability to overcome the pegmatite exposition problem, several misclassification errors resulted from the absence of bands in the TIR region. These misclassifications include the spectral mixing between Li pegmatites and the metasedimentary host rocks [69]. Additionally, the relatively high number of classes, identified in the image for the classification process, contributed to a higher data complexity that may have hindered the obtained results. The reduction of the number of classes, through masking of classes with no interest in Li exploration, will certainly help to optimize the algorithm performance, as recognized by the authors [69].

Another critical challenge to Li exploration based on satellite data is that in spite of the many diagnostic spectral features of Li minerals, to the best of our knowledge, it was not possible to identify so far, a unique spectral feature solely caused by the presence of Li in the structure of minerals.

Taking all this into account, it is our opinion that there are yet several developments to be made in the field of remote sensing applied to Li-mineralizations, and new algorithms and methodologies to be developed in space and Earth sciences. More insights on other remote sensing data products are given in Chapter 3.

3. Future Perspectives

A discussion on the available data products and image classification algorithms is made in the attempt to solve some of the problems identified (Section 2.2). The special requirements of Li exploration are taken into account. New types of approaches and applications to other Li deposits are addressed.

3.1. Data Products Used for the Research

Past applications (Section 2.1) included products such as ASTER, Landsat-5, Landsat-8, and Sentinel-2 images. For the purpose of this review, we will only consider the more recent products since our goal is to help in choosing the best product for future studies.

The ASTER is an imaging instrument onboard of Terra satellite, the flagship satellite of NASA's Earth Observing System (EOS), launched in December 1999 [80]. It resulted from a collaboration between NASA and Japan's Ministry of Economy Trade and Industry—METI [80]. ASTER captures medium-high spectral resolution data in 14 bands whose spatial resolution varies with wavelength: 15 m in the VNIR, 30 m in the SWIR, and 90 m in the TIR [81]. ASTER also provides a stereo viewing capability for digital elevation model creation [80,81]. The temporal resolution is 16 days. Due to sensor failure, SWIR data acquired since April of 2008 is not available [82]. Nonetheless, as mentioned before, ASTER's specific characteristics greatly contributed to mineral exploration, especially in alteration mapping associated with gold and porphyry copper deposits [53,54]. A review of the different "on-demand" ASTER products can be found in the work of Pour and Hashim [83].

The Landsat program represents the world's longest continuously acquired collection of space-based moderate-resolution multispectral land remote sensing data [84]. It is the result of a joint effort of the United States Geological Survey (USGS) and the National Aeronautics and Space Administration (NASA). Until now, Landsat counts with seven successful and one failed mission [84]. The last mission corresponds to Landsat-8, which was launched in 2013. Landsat-9 is planned to be launched in December 2020 [84]. Landsat-8 carries two different instruments: (i) the Operational Land Imager (OLI); and (ii) the Thermal Infrared Sensor (TIRS). Each image product contains nine spectral bands with a spatial resolution of 30 m for bands 1–7 and 9, and 15 m for band 8 (panchromatic); and two thermal bands (10 and 11) are collected at 100 m, but resampled for 30 m [85]. Each band consists of a 16-bit grayscale image. The scene size is 170 km × 185 km [85]. The temporal resolution is 16 days. Key publications in geological remote sensing (at least until the time of publication) from both the Landsat and the ASTER eras can be found in van der Meer et al. [53].

The Sentinel-2 mission includes the recent twin satellites Sentinel-2A and Sentinel-2B launched in the frame of the European Union's Copernicus Program [86]. Since the satellites are out of phase with each other, the temporal resolution is five days at the equator [87]. Both satellites acquire information in 13 spectral bands in the VNIR-SWIR regions: four bands at 10 m spatial resolution, six bands at 20 m, and three bands at 60 m [87]. The orbital swath width is 290 km. A comparison between Landsat-8, Sentinel-2 and ASTER bands is established in Table 2 and in Figure 2.

Table 2. Characteristics of sensors with potential for remote sensing of Li deposits [81,85,88,89].

Sensor Name		Spectral Region (μm)			Nr. of Bands	Spatial Resolution (m)		
		VNIR	SWIR	TIR		VNIR	SWIR	TIR
Landsat-8 OLI/TIRS		0.43–0.88	1.57–2.29	10.60–12.51	11	30	30	100
ASTER		0.52–0.86	1.60–2.43	8.13–10.95	14	15	30	90
Sentinel-2 MSI	A	0.42–0.94	1.52–2.38	-	12	10	20	-
	B	0.42–0.94	1.52–2.37					
WorldView-3		0.40–1.04	1.20–2.37	-	16	1.24	3.70	-

Van der Meer et al. [53] refer to the importance of the Sentinel-2 mission to ensure data continuity, especially after the failure of ASTER's SWIR module. However, the application of Sentinel-2 images for geological studies is scarce when compared to the previously mentioned satellite sensors, especially when it comes to geological exploration. The first articles in the literature regarding this satellite address their potential to alteration and iron/gossan mapping, while others highlight the correspondence between ASTER, Landsat 8, and Sentinel-2 VNIR and SWIR bands [90–93]. More recent studies highlight the possible contribution and suitability of Sentinel-2 images for geological mapping [94,95] and for geological fault detection [96]. Ge et al. [97] applied different MLAs, Artificial Neural Network (ANN), k-Nearest Neighbor (k-NN), RF and SVM, to Sentinel-2 images in order to perform lithological classification in an ophiolite complex in Inner Mongolia, China. Hu et al. [98] compared the use of Sentinel-2, ASTER, and Hyperion in hydrothermally-altered mineral mapping associated with porphyry copper deposits. Cardoso-Fernandes et al. [62] and Cardoso-Fernandes et al. [63] already showed some potentialities and limitations of the use of Sentinel-2 in Li pegmatite identification. Overall, some of these works show that, on the contrary of what it was thought, Sentinel-2 might not be able to replace ASTER in the acquisition of data for geological applications, due to the lack of a TIR sensor. Until now there is no free or commercial product capable of responding to the necessities of geological mapping and exploration, so other solutions need to be explored. The potential of the combined use of multi- and hyperspectral satellite data in mineral exploration was already discussed by Mielke et al. [93].

In what concerns the compromise between spatial and spectral resolution, the answer may rely on commercial satellites such as WorldView-3. Launched in 2014 by DigitalGlobe, World-View-3 is a high-resolution multispectral sensor that measures reflected radiance in eight VNIR bands (at 1.24 m

spatial resolution) and eight SWIR bands (at 3.70 m resolution) although SWIR data is resampled to a 7.5 m pixel size for commercial distribution [99] (Table 2; Figure 4). WorldView-3 also has a panchromatic band with 0.31 m of spatial resolution [99]. The swath width is 13.1 km. Despite lacking a TIR sensor, WorldView-3 has good potential for mineral mapping since its bandpasses are very similar to the ASTER VNIR-SWIR ones [4,54]. Additionally, such high resolution can help to tackle the vegetation problems due to the sensors' ability to map between trees [4].

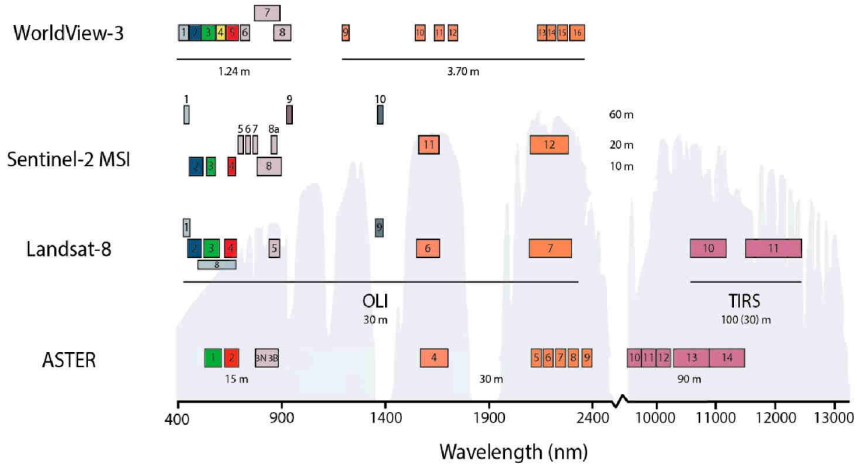

Figure 4. Comparison between ASTER, Landsat 8, Sentinel-2, and WorldView-3 bands. Adapted from USGS Landsat Program [100]. ASTER [81]: 1 green; 2 red; 3N/3B—NIR nadir-looking/NIR backward-looking; 4–9 SWIR; 10–14 TIR. Landsat-8 [89]: 1 coastal aerosol; 2 blue; 3 green; 4 red; 5 NIR; 6 SWIR 1; 7 SWIR 2; 8 Panchromatic; 9 cirrus; 10 TIRS 1; 11 TIRS 2. Sentinel-2 [88]: 1 coastal aerosol; 2 blue; 3 green; 4 red; 5, 6, 7, and 9 vegetation red edge; 8 NIR; 10 cirrus; 11 and 12 SWIR. WorldView-3 [99]: 1 coastal; 2 blue; 3 green; 4 yellow; 5 red; 6 red edge; 7 NIR 1; 8 NIR 2; 9–16 SWIR.

To overcome the remaining inherent difficulties of Li exploration, other types of remote sensing platforms should be considered. Nowadays, drone-borne hyperspectral sensors are a reality. In fact, such an approach is being used to quickly identifying target areas for Li exploration within the "Lightweight Integrated Ground and Airborne Hyperspectral Topological Solution" (LIGHTS) project [101]. However, this kind of data has one big limitation due to the high associated cost of mounting the equipment in the drone, of around 200,000 USD. Nonetheless, it is our opinion this kind of approach will be highly sought after in the future, once the drone and hyperspectral camera prices go down.

3.2. *Image Processing Algorithms*

In the past, several authors have reviewed the different techniques and image processing algorithms that can be applied to geological remote sensing in general [102,103] or in mineral exploration [5,6]. Some even group the image processing methods into functional categorization schemes. Sabins [104] defined three categories: (i) image restoration; (ii) image enhancement; and (iii) information extraction. Later, in 2016, Asadzadeh and Souza Filho [103] proposed a new scheme in which the techniques are divided into knowledge-based and data-driven approaches.

Common image processing algorithms employed in mineral exploration are: (i) RGB combinations [105,106]; (ii) band ratios [6,105]; (iii) PCA [28,107]; (iv) MNF [21,105,106]; (v) matched filtering (MF) [24,105]; (vi) linear spectral unmixing (LSU) [11,51]; (vii) constrained energy minimization

(CEM) [17,21]; (viii) least square fitting method [105]; (ix) independent component analysis [50]. and supervised algorithms such as (x) SAM [8,108], and (xi) MTNF [8,15]. Methods such as MNF, PPI, and SAM have already been applied to pegmatite detection in Southern Namibia using airborne hyperspectral data (HyMap) [109]. For the same region, Oshigami et al. [110] proposed a new classification method named continuum-removal MSAM that combined the Modified Spectral Angle Mapper (MSAM) and continuum-removal methods. Using HyMap images, the authors produced mineral index maps to target common pegmatite minerals such as lepidolite and other white micas. In the Cornwall region, United Kingdom, Ellis and Scott [111] used lepidolite as a pathfinder for topaz-bearing granites in an environmental monitoring study. For that, HyMap airborne images were used and methods like MNF, PPI, and MTMF were employed.

Recently, great attention has been given to non-parametric classifiers such as machine and deep learning algorithms. These techniques have been applied in land-use/land-cover (LULC) problems with great success, outperforming classical algorithms [112–115]. In 2014, Yu et al. [116] conducted a meta-analysis and synthesis of satellite-based land-cover mapping studies, concluding that, from all classification methods (used more than 10 times out of the 1651 analyzed studies), MLAs, namely ensemble classifiers, ANN and SVM, are the methods that achieved a performance better than the average accounted in the 1651 experiments.

Although the number of applications is smaller when compared to the LULC studies, similar results have been obtained in lithological mapping and mineral exploration [40,117–121]. Yu et al. [117], in 2012, developed an automated approach to lithological mapping in Northwestern India where different SVMs with the radial basis function (RBF) kernel were trained using ASTER, ASTER-derived digital elevation model (DEM), and aeromagnetic data. The tested number of input features ranged from 14 to 33, having the classification accuracy increased with the increasing number of layers. When compared with a classical classifier, SVM clearly outperformed ML, achieving a much higher accuracy [117]. Cracknell et al. [118] applied RF and self-organizing maps (SOM) to map lithology and volcanic-hosted massive sulfide (VHMS) alteration in Tasmania. The input data included airborne geophysical, soil geochemical and Landsat-7 Enhanced Thematic Mapper Plus (ETM+) spectral data. The approach provided new geological detail and allowed to identify areas of interest for geological and VHMS alteration mapping. According to the authors [118], the combination of supervised and unsupervised MLAs delivered a robust mean to analyze and map complex, challenging terrains. In 2016, Parakh et al. [119] compared the performance between RF and SVM in lithological mapping in India using Landsat-8, ASTER, and DEM data. Additionally, band-depth images from the analysis of laboratory spectra were used as input for the fuzzy inference system (FIS) to further discriminate between amphibolite and mica-schist. Overall, the performance of RF and SVM was similar although RF provided a higher accuracy for the minor class [119]. Bahrambeygi and Moeinzadeh [120] compared SVM and ANN in hyperspectral mapping of ophiolite terrains in Iran using Hyperion images, the ANN having achieved higher accuracy. Latifovic et al. [121], in 2018, assessed the performance of convolutional neural networks (CNN) in lithological mapping in Northwestern Canada. Different data layers were used to train the network including Landsat TM/ETM+ scenes, aerial photos, and high-resolution DEM data. The performance of CNN was evaluated in two sampling scenarios: the first uses samples collected over the area to be mapped, while the second scenario corresponds to an independent test area. Secondly, the performance of CNN was confronted with the one attained using the more widely used RF algorithm [121]. In the first scenario, both algorithms showed similar results with an average accuracy of around 76%. However, in the independent test sets, CNN outperformed RF by 4%.

Most of these works show that the classification accuracy is improved when additional data is added to the satellite-acquired one. This follows the line of thought of Rajesh [3] that remote sensing data by itself may not be sufficient to identify new mineral deposits. Therefore, it would be important to try to integrate satellite data with other types of data in Li exploration. This type of logic could also be applied to techniques employed, that is, several classifiers could be combined to form a better

predictor (using ensemble methods like AdaBoost or bagging). Such an approach can help to overcome the weaknesses of single classifiers [122].

In the past recent years, several reviews have been published on either the use of a specific MLA or on the comparison of a set of machine and/or deep learning algorithms. Mountrakis et al. [72] presented various applications of SVM in remote sensing as well as several algorithmic advances and SVM variants developed. Belgiu and Drăguţ [70] reviewed the use of RF as a classifier in remote sensing. The authors also highlight developments made and new applications in the field of remote sensing, besides pointing out future directions. Maxwell et al. [123] reviewed MLAs from an applied perspective, focusing on SVM, decision trees (DTs), boosted DTs, RF, ANNs, and k-NN, the choice of proper algorithms, their implementation, training data requirements (class balancing problems for example), parameter tuning, computational costs, and availability of MLAs in remote sensing software packages. Li et al. [124] survey and compare the performances achieved by typical deep learning (DL) methods, such as model CNNs, stacked auto-encoders (SAEs), and deep belief networks (DBNs). The authors also presented a systematic review of developments made in pixel-wise and scene wise approaches using DL methods.

Despite the great performance achieved by MLAs in the field of computer vision and image processing [122,124], some difficulties are expected in what concerns their application to Li exploration. The first and most obvious obstacle is the in-depth knowledge about the MLAs and DL required for any geoscientist/geologist to conduct such an approach. The second is related to the nature of the classification problem since mineral exploration in general, and Li exploration in particular, inherently differ from classical applications, such as LULC problems. Finally, the amount of training associated with each algorithm and the need to parameterize the algorithms are another major obstacle. This parametrization can be more difficult in some MLAs like SVM but, overall, past studies show that the parameters tend to be case sensitive and therefore fundamental [112,123]. New developments on how to transfer learning from one case study to another are needed and they will definitely increase the importance and usage of MLAs and DL in mineral exploration. On the other hand, there are still a great number of potentialities to explore in Li exploration that are constantly increasing with the new models and algorithms being proposed. These include adaptations of the original algorithms (e.g., oblique RF classification [125] or transductive SVM [126]) and the use of non-traditional optimization algorithms, such as genetic algorithms and particle swarm optimization, with MLAs [127]. The application of MLAs in sub-pixel classification (e.g., [128]) could also help to decrease the impact of mixed pixels in medium spatial resolution images.

4. Summary and Conclusions

Despite the early attempt to target Li mineralizations with the launch of the Landsat missions, there is an unequivocal exponential growth on the publication numbers in the last decades. Nonetheless, since it still is an emergent field, the studies are limited to a small number of research groups, mainly based in Europe. However, considering the market demand for this raw material, we expect that many other studies will flourish in the near future all around the globe.

In general, past application studies relied on four distinct approaches: (i) geobotanical mapping; (ii) lithological mapping; (iii) mineral alteration mapping; and (iv) Li minerals/Li pegmatite discrimination. Different types of satellite products with distinct characteristics were employed as well as diverse image processing algorithms ranging from simple logical or mathematical operations (band ratios) to more evolved and complex algorithms like MLAs.

Overall, the objectives and the research questions addressed in this review were successfully accomplished/answered:

1. What can be accomplished in Li exploration using remote sensing methods? The reviewed publications show that it is possible to identify the spectral features of pegmatite intrusions and to discriminate the Li-bearing pegmatites from the host rocks (despite the misclassification errors in the lithological mapping approach). Depending on the type of host rock, this discrimination may

not be possible without using TIR data. The proposed approach to directly identify Li minerals/Li pegmatites was confirmed in other areas of the globe. To some extent, the alteration mapping approach works to target Li pegmatites, although it is more promising in highly weathered areas such as in the Alto Ligonha region (Mozambique).

2. What are the main difficulties? Both the alteration mapping and Li pegmatite mapping results differ regarding the area or the image processing method applied, which points to the lack of an automated proceeding to target Li-mineralizations. Other noted difficulties are related to the spectral confusion with urbanized areas and agricultural fields or spectral noise resultant from mixing at the pixel level. From our knowledge, these problems are inherently caused by low spectral and spatial resolution, respectively. The vegetation coverage is another difficulty since it masks the Li minerals/Li pegmatites spectral signatures. In specific areas of the world, there may be problems in the hydrothermal alteration approach since the Li pegmatites may present distinct alteration styles and mineral assemblages not detected by the common techniques.

3. How to overcome these difficulties? Currently, there is no existing or expected satellite product capable of responding to all the necessities of Li exploration. Despite lacking thermal bands, WorldView-3 is probably the closest product available capable of dealing with the spatial and spectral resolution compromise. Additionally, WorldView-3 high spatial resolution can help to tackle the vegetation difficulties. Another solution to dampen the effects of vegetation is the spectral unmixing of both green and dry vegetation. To optimize the alteration mapping approach, a detailed geological characterization of the associated alteration minerals and possible alteration halos in the host rocks can lead to the development of specific, more efficient algorithms. Other types of remote sensing data, namely drone-borne hyperspectral sensors, may constitute a more efficient Li exploration tool in the future. For now, such an approach is not feasible due to the high associated costs.

4. What are the future research perspectives? We believe that there are several developments to be made in the field of remote sensing applied to Li mineralizations in the future. The constant increase and development of MLAs, in specific, offers unlimited possibilities to be explored. Less common techniques, such as the adaptation of the original MLAs or the combination of several classifiers into one single predictor, can help to achieve a better performance in Li exploration. The integration of remote sensing data with geological information (mineral prospectivity) will increase the ability to target new deposits. The development and improvement of the geobotanical approach may enable Li exploration using remote sensing in highly vegetated areas, which for now is unthinkable. The generalization of the mentioned approaches to other Li deposit types (e.g., brines) will also contribute to establishing remote sensing as a fundamental tool in Li exploration.

Author Contributions: All the authors designed and schematized the manuscript; J.C.-F. wrote the original draft; A.C.T., A.L., M.P., and E.R.-R. revised and edited the paper. All authors have read and agreed to the published version of the manuscript.

Funding: The authors would like to thank the financial support provided by FCT—Fundação para a Ciência e a Tecnologia with the ERA-MIN/0001/2017—LIGHTS project, FEDER through operation POCI-01-0145-FEDER-007690 funded by the Programa Operacional Competitividade e Internacionalização—COMPETE2020 and by National Funds through FCT within the ICT, R and D Unit (reference UIDB/04683/2020). The University of the Basque Country (UPV/EHU) contributed economically with grant GIU18/084. Joana Cardoso-Fernandes is financially supported within the compass of a Ph.D. Thesis, ref. SFRH/BD/136108/2018, by national funds from MCTES through FCT, and co-financed by the European Social Fund (ESF) through POCH—Programa Operacional Capital Humano.

Conflicts of Interest: The authors declare no conflict of interest.

Appendix A. Spectral Indices

Appendix A.1. RGB Combinations

In 2019, Cardoso-Fernandes et al. [63] proposed different RGB combinations to target Li-bearing pegmatites using atmospherically corrected, surface reflectance ASTER, Landsat-5, Landsat-8, and Sentinel-2 products (Table A1).

Table A1. Proposed RGB combinations for Li pegmatite detection [63].

Sensor	RGB Combination
ASTER	5-1-14
	2-1-13
Landsat-5 TM	7-2-6
	2-1-6
Landsat-8 OLI/TIRS	7-3-11
	2-1-11
Sentinel-2 MSI	3-2-12

Appendix A.2. Band Ratios

Band ratios were also proposed to identify Li pegmatites [62,63]. These ratios were based on spectral absorption features of Li minerals, such as spodumene and lepidolite (Table A2).

Table A2. Band ratios proposed to identify Li pegmatites [62,63].

Sensor	Band Ratio
ASTER	7/6
	1/3
Landsat-5 TM	2/4
	3/7
Landsat-8 OLI/TIRS	3/5
	4/7
Sentinel-2 MSI	3/8
	4/12

Appendix A.3. PCA

Cardoso-Fernandes et al. [63] also selected two- and four-band subsets for the application of selective PCA to isolate target spectral signatures of Li pegmatites (Table A3). Input data were the ASTER, Landsat-5, Landsat-8, and Sentinel-2 raw bands.

Table A3. Band subsets for selective PCA in Li pegmatite identification.

Sensor	Band Subset
ASTER	1, 3
	1, 3, 11, 14
Landsat-5 TM	2, 4
	1, 2, 4, 6
Landsat-8 OLI/TIRS	3, 5
	2, 3, 5, 11
Sentinel-2 MSI	3, 8
	2, 3, 8, 11

References

1. El-Baz, F. Remote sensing and mapping of Earth resources. *Terra Nova* **1990**, *2*, 446–454. [CrossRef]
2. Meer, V.D. Bakker validated surface mineralogy from high-spectral resolution remote sensing: A review and a novel approach applied to gold exploration using AVIRIS data. *Terra Nova* **1998**, *10*, 112–119. [CrossRef]
3. Rajesh, H.M. Application of remote sensing and GIS in mineral resource mapping—An overview. *J. Mineral. Petrol. Sci.* **2004**, *99*, 83–103. [CrossRef]
4. Cudahy, T. Mineral mapping for exploration: An Australian journey of evolving spectral sensing technologies and industry collaboration. *Geosciences* **2016**, *6*, 52. [CrossRef]
5. Rajan Girija, R.; Mayappan, S. Mapping of mineral resources and lithological units: A review of remote sensing techniques. *Int. J. Image Data Fusion* **2019**, *10*, 79–106. [CrossRef]
6. Sabins, F.F. Remote sensing for mineral exploration. *Ore Geol. Rev.* **1999**, *14*, 157–183. [CrossRef]
7. Abbaszadeh, M.; Hezarkhani, A. Enhancement of hydrothermal alteration zones using the spectral feature fitting method in Rabor area, Kerman, Iran. *Arab. J. Geosci.* **2011**, *6*, 1957–1964. [CrossRef]
8. Bishop, C.A.; Liu, J.G.; Mason, P.J. Hyperspectral remote sensing for mineral exploration in Pulang, Yunnan Province, China. *Int. J. Remote Sens.* **2011**, *32*, 2409–2426. [CrossRef]
9. Di Tommaso, I.; Rubinstein, N. Hydrothermal alteration mapping using ASTER data in the Infiernillo porphyry deposit, Argentina. *Ore Geol. Rev.* **2007**, *32*, 275–290. [CrossRef]
10. Farahbakhsh, E.; Shirmard, H.; Bahroudi, A.; Eslamkish, T. Fusing ASTER and QuickBird-2 Satellite Data for detailed investigation of porphyry copper deposits using PCA.; Case study of Naysian Deposit, Iran. *J. Indian Soc. of Remote Sens.* **2016**, *44*, 525–537. [CrossRef]
11. Hosseinjani, M.; Tangestani, M.H. Mapping alteration minerals using sub-pixel unmixing of ASTER data in the Sarduiyeh area, SE Kerman, Iran. *Int. J. Digit. Earth* **2011**, *4*, 487–504. [CrossRef]
12. Hosseinjani Zadeh, M.; Honarmand, M. A remote sensing-based discrimination of high- and low-potential mineralization for porphyry copper deposits; a case study from Dehaj–Sarduiyeh copper belt, SE Iran. *Eur. J. Remote Sens.* **2017**, *50*, 332–342. [CrossRef]
13. Hosseinjani Zadeh, M.; Tangestani, M.H.; Roldan, F.V.; Yusta, I. Sub-pixel mineral mapping of a porphyry copper belt using EO-1 Hyperion data. *Adv. Space Res.* **2014**, *53*, 440–451. [CrossRef]
14. Pour, A.B.; Hashim, M. Identification of hydrothermal alteration minerals for exploring of porphyry copper deposit using ASTER data, SE Iran. *J. Asian Earth Sci.* **2011**, *42*, 1309–1323. [CrossRef]
15. Pour, A.B.; Hashim, M. Hydrothermal alteration mapping from Landsat-8 data, Sar Cheshmeh copper mining district, south-eastern Islamic Republic of Iran. *J. Taibah Univ. Sci.* **2015**, *9*, 155–166. [CrossRef]
16. Safari, M.; Maghsoudi, A.; Pour, A.B. Application of Landsat-8 and ASTER satellite remote sensing data for porphyry copper exploration: A case study from Shahr-e-Babak, Kerman, south of Iran. *Geocarto Int.* **2017**, *33*, 1186–1201. [CrossRef]
17. Zhang, N.; Zhou, K. Identification of hydrothermal alteration zones of the Baogutu porphyry copper deposits in northwest China using ASTER data. *J. Appl. Remote Sens.* **2017**, *11*. [CrossRef]
18. Amer, R.; Kusky, T.; El Mezayen, A. Remote sensing detection of gold related alteration zones in Um Rus area, Central Eastern Desert of Egypt. *Adv. Space Res.* **2012**, *49*, 121–134. [CrossRef]

19. Ciampalini, A.; Garfagnoli, F.; Antonielli, B.; Moretti, S.; Righini, G. Remote sensing techniques using Landsat ETM+ applied to the detection of iron ore deposits in Western Africa. *Arab. J. Geosci.* **2012**, *6*, 4529–4546. [CrossRef]
20. El-Magd, I.A.; Mohy, H.; Basta, F. Application of remote sensing for gold exploration in the Fawakhir area, Central Eastern Desert of Egypt. *Arab. J. Geosci.* **2014**, *8*, 3523–3536. [CrossRef]
21. Gabr, S.; Ghulam, A.; Kusky, T. Detecting areas of high-potential gold mineralization using ASTER data. *Ore Geol. Rev.* **2010**, *38*, 59–69. [CrossRef]
22. Gabr, S.S.; Hassan, S.M.; Sadek, M.F. Prospecting for new gold-bearing alteration zones at El-Hoteib area, South Eastern Desert, Egypt, using remote sensing data analysis. *Ore Geol. Rev.* **2015**, *71*, 1–13. [CrossRef]
23. Hassan, S.M.; Ramadan, T.M. Mapping of the late Neoproterozoic Basement rocks and detection of the gold-bearing alteration zones at Abu Marawat-Semna area, Eastern Desert, Egypt using remote sensing data. *Arab. J. Geosci.* **2014**, *8*, 4641–4656. [CrossRef]
24. Liu, L.; Zhou, J.; Han, L.; Xu, X. Mineral mapping and ore prospecting using Landsat TM and Hyperion data, Wushitala, Xinjiang, northwestern China. *Ore Geol. Rev.* **2017**, *81*, 280–295. [CrossRef]
25. Moradi, M.; Basiri, S.; Kananian, A.; Kabiri, K. Fuzzy logic modeling for hydrothermal gold mineralization mapping using geochemical, geological, ASTER imageries and other geo-data, a case study in Central Alborz, Iran. *Earth Sci. Inform.* **2014**, *8*, 197–205. [CrossRef]
26. Zhang, X.; Pazner, M.; Duke, N. Lithologic and mineral information extraction for gold exploration using ASTER data in the south Chocolate Mountains (California). *ISPRS J. Photogramm. Remote Sens.* **2007**, *62*, 271–282. [CrossRef]
27. Zoheir, B.A. Controls on lode gold mineralization, Romite deposit, South Eastern Desert, Egypt. *Geosci. Front.* **2012**, *3*, 571–585. [CrossRef]
28. Crósta, A.P.; Souza Filho, C.R.; Azevedo, F.; Brodie, C. Targeting key alteration minerals in epithermal deposits in Patagonia, Argentina, using ASTER imagery and principal component analysis. *Int. J. Remote Sens.* **2003**, *24*, 4233–4240. [CrossRef]
29. Bersi, M.; Saibi, H.; Chabou, M.C. Aerogravity and remote sensing observations of an iron deposit in Gara Djebilet, southwestern Algeria. *J. Afr. Earth Sci.* **2016**, *116*, 134–150. [CrossRef]
30. Ducart, D.F.; Silva, A.M.; Toledo, C.L.B.; Assis, L.M.D. Mapping iron oxides with Landsat-8/OLI and EO-1/Hyperion imagery from the Serra Norte iron deposits in the Carajás Mineral Province, Brazil. *Braz. J. Geol.* **2016**, *46*, 331–349. [CrossRef]
31. Duuring, P.; Hagemann, S.G.; Novikova, Y.; Cudahy, T.; Laukamp, C. Targeting iron ore in banded iron formations using aster data: Weld range greenstone belt, yilgarn craton, western australia. *Econ. Geol.* **2012**, *107*, 585–597. [CrossRef]
32. Rajendran, S.; Thirunavukkarasu, A.; Balamurugan, G.; Shankar, K. Discrimination of iron ore deposits of granulite terrain of Southern Peninsular India using ASTER data. *J. Asian Earth Sci.* **2011**, *41*, 99–106. [CrossRef]
33. Berger, B.R.; King, T.V.V.; Morath, L.C.; Philli, J.D. Utility of high-altitude infrared spectral data in mineral exploration: Application to Northern Patagonia Mountains, Arizona. *Econ. Geol.* **2003**, *98*, 1003–1018. [CrossRef]
34. Van Der Meer, F.; Vazquez-Torres, M.; Van Dijk, P.M. Spectral characterization of ophiolite lithologies in the Troodos Ophiolite complex of Cyprus and its potential in prospecting for massive sulphide deposits. *Int. J. Remote Sens.* **2010**, *18*, 1245–1257. [CrossRef]
35. Wang, G.; Du, W.; Carranza, E.J.M. Remote sensing and GIS prospectivity mapping for magmatic-hydrothermal base- and precious-metal deposits in the Honghai district, China. *J. Afr. Earth Sci.* **2017**, *128*, 97–115. [CrossRef]
36. Rowan, L.C.; Mars, J.C. Lithologic mapping in the Mountain Pass, California area using Advanced Spaceborne Thermal Emission and Reflection Radiometer (ASTER) data. *Remote Sens. Environ.* **2003**, *84*, 350–366. [CrossRef]
37. Mazhari, N.; Malekzadeh Shafaroudi, A.; Ghaderi, M. Detecting and mapping different types of iron mineralization in Sangan mining region, NE Iran, using satellite image and airborne geophysical data. *Geosci. J.* **2017**, *21*, 137–148. [CrossRef]

38. Xu, Y.; Chen, J.; Meng, P. Detection of alteration zones using hyperspectral remote sensing data from Dapingliang skarn copper deposit and its surrounding area, Shanshan County, Xinjiang Uygur autonomous region, China. *J. Vis. Commun. Image Represent.* **2019**, *58*, 67–78. [CrossRef]
39. Salles, R.D.R.; Souza Filho, C.R.; Cudahy, T.; Vicente, L.E.; Monteiro, L.V.S. Hyperspectral remote sensing applied to uranium exploration: A case study at the Mary Kathleen metamorphic-hydrothermal U-REE deposit, NW, Queensland, Australia. *J. Geochem. Explor.* **2017**, *179*, 36–50. [CrossRef]
40. Othman, A.; Gloaguen, R. Improving Lithological Mapping by SVM classification of spectral and morphological features: The Discovery of a new chromite body in the mawat ophiolite complex (Kurdistan, NE Iraq). *Remote Sens.* **2014**, *6*, 6867–6896. [CrossRef]
41. Eslami, A.; Ghaderi, M.; Rajendran, S.; Pour, A.B.; Hashim, M. Integration of ASTER and landsat TM remote sensing data for chromite prospecting and lithological mapping in Neyriz ophiolite zone, south Iran. *Resour. Geol.* **2015**, *65*, 375–388. [CrossRef]
42. Pournamdari, M.; Hashim, M. Detection of chromite bearing mineralized zones in Abdasht ophiolite complex using ASTER and ETM+ remote sensing data. *Arab. J. Geosci.* **2013**, *7*, 1973–1983. [CrossRef]
43. Rajendran, S.; al-Khirbash, S.; Pracejus, B.; Nasir, S.; Al-Abri, A.H.; Kusky, T.M.; Ghulam, A. ASTER detection of chromite bearing mineralized zones in Semail Ophiolite Massifs of the northern Oman Mountains: Exploration strategy. *Ore Geol. Rev.* **2012**, *44*, 121–135. [CrossRef]
44. Gemail, K.; Abd-El Rahman, N.M.; Ghiath, B.M.; Aziz, R.N. Integration of ASTER and airborne geophysical data for mineral exploration and environmental mapping: A case study, Gabal Dara, North Eastern Desert, Egypt. *Environ. Earth Sci.* **2016**, *75*. [CrossRef]
45. Zimmermann, R.; Brandmeier, M.; Andreani, L.; Mhopjeni, K.; Gloaguen, R. Remote sensing exploration of Nb-Ta-LREE-Enriched carbonatite (Epembe/Namibia). *Remote Sens.* **2016**, *8*, 620. [CrossRef]
46. Sabins, F.F.; Miller, R.M. Resource assessment—Salar Uyuni and vicinity. In Proceedings of the Tenth Thematic Conference on Geologic Remote Sensing (Ann Arbor, MI, Environmental Research Institute of Michigan), San Antonio, TX, USA, 9–12 May 1994; pp. 9–12.
47. Öztan, N.S.; Süzen, M.L. Mapping evaporate minerals by ASTER. *Int. J. Remote Sens.* **2011**, *32*, 1651–1673. [CrossRef]
48. Bedini, E. Mineral mapping in the Kap Simpson complex, central East Greenland, using HyMap and ASTER remote sensing data. *Adv. Space Res.* **2011**, *47*, 60–73. [CrossRef]
49. Liu, L.; Zhou, J.; Yin, F.; Feng, M.; Zhang, B. The reconnaissance of mineral resources through aster data-based image processing, interpreting and ground inspection in the Jiafushaersu area, West Junggar, China. *J. Earth Sci.* **2014**, *25*, 397–406. [CrossRef]
50. Beiranvand Pour, A.; Park, T.-Y.; Park, Y.; Hong, J.; Zoheir, B.; Pradhan, B.; Ayoobi, I.; Hashim, M. Application of multi-sensor satellite data for exploration of Zn–Pb Sulfide mineralization in the franklinian basin, north greenland. *Remote Sens.* **2018**, *10*, 1186. [CrossRef]
51. Kruse, F.A.; Boardman, J.W. Characterization and mapping of kimberlites and related diatremes using hyperspectral remote sensing. In Proceedings of the 2000 IEEE Aerospace Conference. Proceedings (Cat. No.00TH8484), Big Sky, MT, USA, 25 March 2000; Volume 3, pp. 299–304.
52. Mujabar, P.S.; Dajkumar, S. Mapping of bauxite mineral deposits in the northern region of Saudi Arabia by using advanced spaceborne thermal emission and reflection radiometer satellite data. *Geo Spat. Inf. Sci.* **2018**, *22*, 35–44. [CrossRef]
53. Van der Meer, F.D.; van der Werff, H.M.A.; van Ruitenbeek, F.J.A.; Hecker, C.A.; Bakker, W.H.; Noomen, M.F.; van der Meijde, M.; Carranza, E.J.M.; Smeth, J.B.D.; Woldai, T. Multi- and hyperspectral geologic remote sensing: A review. *Int. J. Appl. Earth Obs. Geoinf.* **2012**, *14*, 112–128. [CrossRef]
54. Abrams, M.; Yamaguchi, Y. Twenty years of ASTER contributions to lithologic mapping and mineral exploration. *Remote Sens.* **2019**, *11*, 1394. [CrossRef]
55. Ninomiya, Y.; Fu, B. Thermal infrared multispectral remote sensing of lithology and mineralogy based on spectral properties of materials. *Ore Geol. Rev.* **2019**, *108*, 54–72. [CrossRef]
56. Christmann, P.; Gloaguen, E.; Labbé, J.-F.; Melleton, J.; Piantone, P. Chapter 1—Global lithium resources and sustainability issues. In *Lithium Process Chemistry*; Chagnes, A., Światowska, J., Eds.; Elsevier: Amsterdam, The Netherlands, 2015; pp. 1–40.

57. Grosjean, C.; Miranda, P.H.; Perrin, M.; Poggi, P. Assessment of world lithium resources and consequences of their geographic distribution on the expected development of the electric vehicle industry. *Renew. Sustain. Energy Rev.* **2012**, *16*, 1735–1744. [CrossRef]
58. Arrobas, D.L.P.; Hund, K.L.; Mccormick, M.S.; Ningthoujam, J.; Drexhage, J.R. *The Growing Role of Minerals and Metals for a Low Carbon Future*; The World Bank: Washington, DC, USA, 2017.
59. Lefevre, M.J. Teledetection d'anomalies geobotaniques appliquee a la recherche miniere par la methode de traitement d'images, Echassieres (Allier). *Bull. Société Géologique Fr.* **1982**, 127–130. [CrossRef]
60. Perrotta, M.M.; Souza Filho, C.R.; Leite, C.A.S. Mapeamento espectral de intrusões pegmatíticas relacionadas a mineralizações de lítio, gemas e minerais industriais na região do vale do Jequitinhonha (MG) a partir de imagens ASTER. In Proceedings of the Anais do XII Simpósio Brasileiro de Sensoriamento Remoto, Goiânia, Brasil, 16–21 April 2005; pp. 1855–1862.
61. Mendes, D.; Perrotta, M.M.; Costa, M.A.C.; Paes, V.J.C. Mapeamento espectral para identificação de assinaturas espectrais de minerais de lítio em imagens ASTER (NE/MG). In Proceedings of the Anais do XVIII Simpósio Brasileiro de Sensoriamento Remoto, Santos-SP, Brasil, 28–29 May 2017; pp. 5273–5280.
62. Cardoso-Fernandes, J.; Teodoro, A.C.; Lima, A. Potential of Sentinel-2 data in the detection of lithium (Li)-bearing pegmatites: A study case. In Proceedings of the SPIE, SPIE Remote Sensing, Berlin, Germany, 10–13 September 2018; Michel, U., Schulz, K., Eds.; SPIE: Bellingham, WA, USA, 2018; p. 15.
63. Cardoso-Fernandes, J.; Teodoro, A.C.; Lima, A. Remote sensing data in lithium (Li) exploration: A new approach for the detection of Li-bearing pegmatites. *Int. J. Appl. Earth Obs. Geoinf.* **2019**, *76*, 10–25. [CrossRef]
64. De Almeida, C.M.P. Estudo Do Filão Aplitopegmatítico Da Mina Da Bajoca, Almendra: Contribuição Científico-Tecnológica. MsC Thesis, Faculdade de Ciências da Universidade do Porto, Porto, Portugal, 2003.
65. Spatz, D.M. Remote sensing characteristics of the sediment- and volcanic-hosted precious metal systems: Imagery selection for exploration and development. *Int. J. Remote Sens.* **1997**, *18*, 1413–1438. [CrossRef]
66. Santos, D.; Teodoro, A.; Lima, A.; Cardoso-Fernandes, J. Remote sensing techniques to detect areas with potential for lithium exploration in Minas Gerais, Brazil. In Proceedings of the SPIE, SPIE Remote Sensing, Strasbourg, France, 9–12 September 2019; Schulz, K., Michel, U., Nikolakopoulos, K.G., Eds.; SPIE: Bellingham, WA, USA, 2019.
67. Gemusse, U.; Lima, A.; Teodoro, A. Pegmatite spectral behavior considering ASTER and Landsat 8 OLI data in Naipa and Muiane mines (Alto Ligonha, Mozambique). In Proceedings of the SPIE, SPIE Remote Sensing, Berlin, Germany, 10–13 September 2018; Michel, U., Schulz, K., Eds.; SPIE: Bellingham, WA, USA, 2018.
68. Gemusse, U.; Lima, A.; Teodoro, A. Comparing different techniques of satellite imagery classification to mineral mapping pegmatite of Muiane and Naipa: Mozambique. In Proceedings of the SPIE, SPIE Remote Sensing, Strasbourg, France, 9–12 September 2019; Schulz, K., Michel, U., Nikolakopoulos, K.G., Eds.; SPIE: Bellingham, WA, USA, 2019.
69. Cardoso-Fernandes, J.; Teodoro, A.C.; Lima, A.; Roda-Robles, E. Evaluating the performance of support vector machines (SVMs) and random forest (RF) in Li-pegmatite mapping: Preliminary results. In Proceedings of the SPIE, SPIE Remote Sensing, Strasbourg, France, 9–12 September 2019; Schulz, K., Michel, U., Nikolakopoulos, K.G., Eds.; SPIE: Bellingham, WA, USA, 2019.
70. Belgiu, M.; Drăguţ, L. Random forest in remote sensing: A review of applications and future directions. *ISPRS J. Photogramm. Remote Sens.* **2016**, *114*, 24–31. [CrossRef]
71. Breiman, L. Random forests. *Mach. Learn.* **2001**, *45*, 5–32. [CrossRef]
72. Mountrakis, G.; Im, J.; Ogole, C. Support vector machines in remote sensing: A review. *ISPRS J. Photogramm. Remote Sens.* **2011**, *66*, 247–259. [CrossRef]
73. Vapnik, V.N. *The Nature of Statistical Learning Theory*; Springer: New York, NY, USA, 1995.
74. Rossi, C.; Spittle, S.; Bayaraa, M.; Pandey, A.; Henry, N. An earth observation framework for the lithium exploration. In Proceedings of the IGARSS 2018—2018 IEEE International Geoscience and Remote Sensing Symposium, Valencia, Spain, 22–27 July 2018; pp. 1616–1619.
75. Pesquera, A.; Torres-Ruiz, J.; Gil-Crespo, P.P.; Velilla, N. Chemistry and genetic implications of tourmaline and Li-F-Cs micas from the Valdeflores area (Caceres, Spain). *Am. Mineral.* **1999**, *84*, 55–69. [CrossRef]
76. Torres-Ruiz, J.; Pesquera, A.; Gil, P.P.; Casas, J. Tourmalinites and Sn-Li mineralization in the Valdeflores area (Cáceres, Spain). *Mineral. Petrol.* **1996**, *56*, 209–223. [CrossRef]
77. Tavares, P.A.; Beltrão, N.; Guimarães, U.S.; Teodoro, A.; Gonçalves, P. Urban ecosystem services quantification through remote sensing approach: A systematic review. *Environments* **2019**, *6*, 51. [CrossRef]

78. Cardoso-Fernandes, J.; Lima, A.; Roda-Robles, E.; Teodoro, A.C. Constraints and potentials of remote sensing data/techniques applied to lithium (Li)-pegmatites. *Can. Mineral.* **2019**, *57*, 723–725. [CrossRef]
79. Rodger, A.; Cudahy, T. Vegetation corrected continuum depths at 2.20μm: An approach for hyperspectral sensors. *Remote Sens. Environ.* **2009**, *113*, 2243–2257. [CrossRef]
80. Jet Propulsion Laboratory (JPL). ASTER: Advanced Spaceborne Thermal Emission and Reflection Radiometer. Available online: https://asterweb.jpl.nasa.gov/index.asp (accessed on 16 January 2020).
81. Jet Propulsion Laboratory (JPL). ASTER: Instrument Characteristics. Available online: https://asterweb.jpl.nasa.gov/characteristics.asp (accessed on 16 January 2020).
82. Jet Propulsion Laboratory (JPL). ASTER User Advisory. Available online: https://asterweb.jpl.nasa.gov/swir-alert.asp (accessed on 16 January 2020).
83. Pour, A.B.; Hashim, M. The application of ASTER remote sensing data to porphyry copper and epithermal gold deposits. *Ore Geol. Rev.* **2012**, *44*, 1–9. [CrossRef]
84. United States Geological Survey (USGS). Landsat Satellite Missions. Available online: https://www.usgs.gov/land-resources/nli/landsat/landsat-satellite-missions (accessed on 16 January 2020).
85. United States Geological Survey (USGS). Landsat 8. Available online: https://www.usgs.gov/land-resources/nli/landsat/landsat-8 (accessed on 16 January 2020).
86. European Space Agency (ESA). Observing the Earth: Copernicus. Available online: http://www.esa.int/Our_Activities/Observing_the_Earth/Copernicus/Overview4 (accessed on 7 March 2018).
87. European Space Agency (ESA). Missions: Sentinel-2. Overview. Available online: https://sentinel.esa.int/web/sentinel/missions/sentinel-2/overview (accessed on 16 January 2020).
88. European Space Agency (ESA). Radiometric Resolutions. Available online: https://earth.esa.int/web/sentinel/user-guides/sentinel-2-msi/resolutions/radiometric (accessed on 16 January 2020).
89. United States Geological Survey (USGS). Landsat 8 Band Designations. Available online: https://www.usgs.gov/media/images/landsat-8-band-designations (accessed on 16 January 2020).
90. Van der Meer, F.D.; van der Werff, H.M.A.; van Ruitenbeek, F.J.A. Potential of ESA's Sentinel-2 for geological applications. *Remote Sens. Environ.* **2014**, *148*, 124–133. [CrossRef]
91. Van der Werff, H.; Van der Meer, F. Sentinel-2 for mapping iron absorption feature parameters. *Remote Sens.* **2015**, *7*, 12635–12653. [CrossRef]
92. Van der Werff, H.; Van der Meer, F. Sentinel-2A MSI and Landsat 8 OLI provide data continuity for geological remote sensing. *Remote Sens.* **2016**, *8*, 883. [CrossRef]
93. Mielke, C.; Bösche, N.; Rogass, C.; Segl, K.; Gauert, C.; Kaufmann, H. Potential applications of the Sentinel-2 multispectral sensor and the Enmap hyperspectral sensor in mineral exploration. *EARSeL eProceedings* **2014**, *13*, 93–102. [CrossRef]
94. Fal, S.; Maanan, M.; Baidder, L.; Rhinane, H. The contribution of sentinel-2 satellite images for geological mapping in the south of tafilalet Basin (Eastern Anti-Atlas, Morocco). *Int. Arch. Photogramm. Remote Sens. Spat. Inf. Sci.* **2019**, 75–82. [CrossRef]
95. Al-Nahmi, F.; Saddiqi, O.; Hilali, A.; Rhinane, H.; Baidder, L.; El arabi, H.; Khanbari, K. Application of remote sensing in geological mapping, case study Al Maghrabah Area—Hajjah Region, Yemen. *ISPRS Ann. Photogramm. Remote Sens. Spat. Inf. Sci.* **2017**, 63–71. [CrossRef]
96. Elhag, M.; Alshamsi, D. Integration of remote sensing and geographic information systems for geological fault detection on the island of Crete, Greece. *Geosci. Instrum. Methods Data Syst.* **2019**, *8*, 45–54. [CrossRef]
97. Ge, W.; Cheng, Q.; Tang, Y.; Jing, L.; Gao, C. Lithological classification using sentinel-2A data in the shibanjing ophiolite complex in Inner Mongolia, China. *Remote Sens.* **2018**, *10*, 638. [CrossRef]
98. Hu, B.; Xu, Y.; Wan, B.; Wu, X.; Yi, G. Hydrothermally altered mineral mapping using synthetic application of Sentinel-2A MSI, ASTER and Hyperion data in the Duolong area, Tibetan Plateau, China. *Ore Geol. Rev.* **2018**, *101*, 384–397. [CrossRef]
99. DigitalGlobe Inc. Data Sheet for WorldView 3. Available online: http://content.satimagingcorp.com.s3.amazonaws.com/media/pdf/WorldView-3-PDF-Download.pdf (accessed on 16 January 2020).
100. USGS Landsat Program. Comparison of #Landsat 7, 8, #Sentinel 2, #ASTER & #MODIS Bands. View Band Designations for All #Landsat Sensors. Available online: https://twitter.com/usgslandsat/status/837696716417687553 (accessed on 22 December 2017).
101. Lightweight Integrated Ground and Airborne Hyperspectral Topological Solution. Available online: http://lights.univ-lorraine.fr/ (accessed on 29 January 2020).

102. Cloutis, E.A. Review article hyperspectral geological remote sensing: Evaluation of analytical techniques. *Int. J. Remote Sens.* **1996**, *17*, 2215–2242. [CrossRef]
103. Asadzadeh, S.; Souza Filho, C.R. A review on spectral processing methods for geological remote sensing. *Int. J. Appl. Earth Obs. Geoinf.* **2016**, *47*, 69–90. [CrossRef]
104. Sabins, F.F. *Remote Sensing Principles and Interpretation*, 3rd ed.; W. H. Freeman: New York, NY, USA, 1997; p. 494.
105. Mia, B.; Fujimitsu, Y. Mapping hydrothermal altered mineral deposits using Landsat 7 ETM+ image in and around Kuju volcano, Kyushu, Japan. *J. Earth Syst. Sci.* **2012**, *121*, 1049–1057. [CrossRef]
106. Ali, A.; Pour, A. Lithological mapping and hydrothermal alteration using Landsat 8 data: A case study in ariab mining district, red sea hills, Sudan. *Int. J. Basic Appl. Sci.* **2014**, *3*. [CrossRef]
107. Loughlin, W.P. Component analysis for alteration mapping. *Photogram. Eng. Rem. Sens.* **1991**, *57*, 1163–1169.
108. Rowan, L.C.; Mars, J.C.; Simpson, C.J. Lithologic mapping of the Mordor, NT, Australia ultramafic complex by using the Advanced Spaceborne Thermal Emission and Reflection Radiometer (ASTER). *Remote Sens. Environ.* **2005**, *99*, 105–126. [CrossRef]
109. Momose, A.; Miyatake, S.; Arvelyna, Y.; Nguno, A.; Mhopjeni, K.; Sibeso, M.; Muyongo, A.; Muvangua, E. Mapping pegmatite using HyMap data in southern Namibia. In Proceedings of the 2011 IEEE International Geoscience and Remote Sensing Symposium, Vancouver, BC, Canada, 24–29 July 2011; pp. 2216–2217.
110. Oshigami, S.; Yamaguchi, Y.; Uezato, T.; Momose, A.; Arvelyna, Y.; Kawakami, Y.; Yajima, T.; Miyatake, S.; Nguno, A. Mineralogical mapping of southern Namibia by application of continuum-removal MSAM method to the HyMap data. *Int. J. Remote Sens.* **2013**, *34*, 5282–5295. [CrossRef]
111. Ellis, R.J.; Scott, P.W. Evaluation of hyperspectral remote sensing as a means of environmental monitoring in the St. Austell China clay (kaolin) region, Cornwall, UK. *Remote Sens. Environ.* **2004**, *93*, 118–130. [CrossRef]
112. Noi, P.T.; Kappas, M. Comparison of random forest, k-Nearest neighbor, and support vector machine classifiers for land cover classification using Sentinel-2 imagery. *Sensors* **2017**, *18*, 18. [CrossRef]
113. Tavares, P.A.; Beltrão, N.E.S.; Guimarães, U.S.; Teodoro, A.C. Integration of Sentinel-1 and Sentinel-2 for Classification and LULC Mapping in the Urban Area of Belém, Eastern Brazilian Amazon. *Sensors* **2019**, *19*, 1140. [CrossRef] [PubMed]
114. Pal, M.; Mather, P.M. Support vector machines for classification in remote sensing. *Int. J. Remote Sens.* **2005**, *26*, 1007–1011. [CrossRef]
115. Oommen, T.; Misra, D.; Twarakavi, N.K.C.; Prakash, A.; Sahoo, B.; Bandopadhyay, S. An objective analysis of support vector machine based classification for remote sensing. *Math. Geosci.* **2008**, *40*, 409–424. [CrossRef]
116. Yu, L.; Liang, L.; Wang, J.; Zhao, Y.; Cheng, Q.; Hu, L.; Liu, S.; Yu, L.; Wang, X.; Zhu, P.; et al. Meta-discoveries from a synthesis of satellite-based land-cover mapping research. *Int. J. Remote Sens.* **2014**, *35*, 4573–4588. [CrossRef]
117. Yu, L.; Porwal, A.; Holden, E.-J.; Dentith, M.C. Towards automatic lithological classification from remote sensing data using support vector machines. *Comput. Geosci.* **2012**, *45*, 229–239. [CrossRef]
118. Cracknell, M.J.; Reading, A.M.; McNeill, A.W. Mapping geology and volcanic-hosted massive sulfide alteration in the Hellyer–Mt Charter region, Tasmania, using Random Forests™ and Self-Organising Maps. *Aust. J. Earth Sci.* **2014**, *61*, 287–304. [CrossRef]
119. Parakh, K.; Thakur, S.; Chudasama, B.; Tirodkar, S.; Porwal, A.; Bhattacharya, A. Machine learning and spectral techniques for lithological classification. In Proceedings of the SPIE Asia-Pacific Remote Sensing, New Delhi, India, 4–7 April 2016.
120. Bahrambeygi, B.; Moeinzadeh, H. Comparison of support vector machine and neutral network classification method in hyperspectral mapping of ophiolite mélanges–A case study of east of Iran. *Egypt. J. Remote Sens. Space Sci.* **2017**, *20*, 1–10. [CrossRef]
121. Latifovic, R.; Pouliot, D.; Campbell, J. Assessment of convolution neural networks for surficial geology mapping in the South Rae Geological Region, Northwest Territories, Canada. *Remote Sens.* **2018**, *10*, 307. [CrossRef]
122. Géron, A. *Hands-On Machine Learning with Scikit-Learn and TensorFlow: Concepts, Tools, and Techniques to Build Intelligent Systems*; O'Reilly Media Inc.: Sebastopol, CA, USA, 2017; p. 568.
123. Maxwell, A.E.; Warner, T.A.; Fang, F. Implementation of machine-learning classification in remote sensing: An applied review. *Int. J. Remote Sens.* **2018**, *39*, 2784–2817. [CrossRef]

124. Li, Y.; Zhang, H.; Xue, X.; Jiang, Y.; Shen, Q. Deep learning for remote sensing image classification: A survey. *Wiley Interdiscip. Rev. Data Min. Knowl. Discov.* **2018**, *8*, e1264. [CrossRef]
125. Menze, B.H.; Kelm, B.M.; Splitthoff, D.N.; Koethe, U.; Hamprecht, F.A. On oblique random forests. In *Machine Learning and Knowledge Discovery in Databases*; Springer: Berlin/Heidelberg, Germany, 2011; pp. 453–469.
126. Bruzzone, L.; Chi, M.; Marconcini, M. A novel transductive SVM for semisupervised classification of remote-sensing images. *IEEE Trans. Geosci. Remote Sens.* **2006**, *44*, 3363–3373. [CrossRef]
127. Sarmah, D.K. A survey on the latest development of machine learning in genetic algorithm and particle swarm optimization. In *Optimization in Machine Learning and Applications*; Kulkarni, A.J., Satapathy, S.C., Eds.; Springer: Singapore, 2020; pp. 91–112.
128. Kumar, A.; Ghosh, S.K.; Dadhwal, V.K. Full fuzzy land cover mapping using remote sensing data based on fuzzy c-means and density estimation. *Can. J. Remote Sens.* **2007**, *33*, 81–87. [CrossRef]

© 2020 by the authors. Licensee MDPI, Basel, Switzerland. This article is an open access article distributed under the terms and conditions of the Creative Commons Attribution (CC BY) license (http://creativecommons.org/licenses/by/4.0/).

remote sensing

MDPI

Article

Semi-Automatization of Support Vector Machines to Map Lithium (Li) Bearing Pegmatites

Joana Cardoso-Fernandes [1,2,*], Ana C. Teodoro [1,2], Alexandre Lima [1,2] and Encarnación Roda-Robles [3]

1 Department of Geosciences, Environment and Land Planning, Faculty of Sciences, University of Porto, Rua Campo Alegre, 4169-007 Porto, Portugal; amteodor@fc.up.pt (A.C.T.); allima@fc.up.pt (A.L.)
2 Institute of Earth Sciences (ICT), Pole of University of Porto, 4169-007 Porto, Portugal
3 Departamento de Mineralogía y Petrología, University of País Vasco (UPV/EHU), Barrio Sarriena, Leioa, 48940 Bilbao, Spain; encar.roda@ehu.es
* Correspondence: joana.fernandes@fc.up.pt

Received: 5 June 2020; Accepted: 17 July 2020; Published: 19 July 2020

Abstract: Machine learning (ML) algorithms have shown great performance in geological remote sensing applications. The study area of this work was the Fregeneda–Almendra region (Spain–Portugal) where the support vector machine (SVM) was employed. Lithium (Li)-pegmatite exploration using satellite data presents some challenges since pegmatites are, by nature, small, narrow bodies. Consequently, the following objectives were defined: (i) train several SVM's on Sentinel-2 images with different parameters to find the optimal model; (ii) assess the impact of imbalanced data; (iii) develop a successful methodological approach to delineate target areas for Li-exploration. Parameter optimization and model evaluation was accomplished by a two-staged grid-search with cross-validation. Several new methodological advances were proposed, including a region of interest (ROI)-based splitting strategy to create the training and test subsets, a semi-automatization of the classification process, and the application of a more innovative and adequate metric score to choose the best model. The proposed methodology obtained good results, identifying known Li-pegmatite occurrences as well as other target areas for Li-exploration. Also, the results showed that the class imbalance had a negative impact on the SVM performance since known Li-pegmatite occurrences were not identified. The potentials and limitations of the methodology proposed are highlighted and its applicability to other case studies is discussed.

Keywords: machine learning; remote sensing; lithological mapping; supervised classification; Sentinel-2; mineral exploration; Lithium; pegmatite

1. Introduction

Recently, there has been an increasing demand for lithium (Li) as a mineral commodity driven by the electric car industry, in which Li is one of the batteries' main components. This increasing demand will result in an intensive Li exploitation soon, and untraditional Li-exploration methods that allow exploration companies to quickly delineate potentially economic areas are to meet the market expectations. With that goal in mind, some authors have attempted to identify Li-bearing pegmatites with different remote sensing data (ASTER, Landsat-5, Landsat-8, and Sentinel-2) and different image processing techniques [1–6]. Cardoso-Fernandes, et al. [7] recently reviewed the approaches and developments made to Li-exploration using remote sensing data and image processing techniques, pointing out their weaknesses and strengths.

The study area of this work is the Fregeneda–Almendra (Salamanca, Spain—Vila Nova de Foz Côa, Portugal) region, where different Li-bearing pegmatites were mapped using ASTER, Landsat-5,

Landsat-8, and Sentinel-2 data, and several image processing algorithms, such as RGB combinations, band ratios, and principal component analysis (PCA) were employed [1,2]. Although these techniques allowed to vector known Li-pegmatites and other potential areas, spectral confusion with urbanized areas or agricultural fields was noticeable. Therefore, a more powerful technique capable of vectoring Li-pegmatites with more confidence is needed, to make the use of remote sensing data in Li-exploration more significant for exploration companies.

During the last decades, there has also been a growing application of machine learning (ML) in the field of geology, either in satellite-based geological mapping [8–12] or in mineral prospectivity mapping [13–16]. Their growing popularity is due to their ability to outperform classical classification algorithms (e.g., [8,16]). While the use of ML to map Li-pegmatites may seem promising, two main problems can be identified beforehand: (i) pegmatites are relatively small bodies and (ii) generally have low exposition. This means that in an image classification approach, Li-pegmatites correspond to a scarce class with few training samples, and some ML algorithms are sensitive to training data size and class imbalance. Furthermore, the objectives of geological exploration are different from the objectives of Land Use/Land Cover (LULC) classification. In a LULC classification problem, all classes bear the same importance and both false positives and false negatives need to be avoided. In a geological exploration, and in this case, the Li-bearing pegmatite class is the target class. Consequently, misclassifications affecting other classes are less important. Besides, false positives (i.e., over-estimating the Li-pegmatite class) may not constitute a problem while false negatives (i.e., not identifying pixels that correspond in fact to Li-pegmatites on the ground) are serious and should be avoided.

Taking this into account, the choice of correct ML algorithms is paramount to successfully map and identify Li-pegmatites. That is why in a preliminary study in the Fregeneda–Almendra region, ML algorithms like support vector machines (SVM's) and random forest (RF) were employed to classify Sentinel-2 images [5]. According to several authors, these algorithms, when compared with classical and other ML techniques, are less sensitive to the training size [17,18] and more capable of dealing with imbalanced datasets [19]. The preliminary results obtained in this study area [5] were unsatisfactory. Both algorithms presented overfitting problems, achieving perfect to almost perfect accuracy scores at a class level, but then failing to correctly map some classes in the whole image [5]. Moreover, the discrimination between Li-pegmatites and the host-rocks was very low which ultimately resulted in a large number of Li-pegmatite false positives [5].

Moreover, algorithm parameterization is still a major difficulty in the sense that most of the time ML algorithms cannot achieve good performance without optimization [18,19]. Therefore, we believe that the previous results can be improved through better algorithm parameterization and improvement of training data. For this improved approach, SVM's were chosen due to their challenging optimization when compared with RF. Several models were optimized and tested, including kernelized and non-kernelized SVM. The objectives of this study were then to (i) train several SVM's on Sentinel-2 images with different parameters to find the optimal model; (ii) assess the impact of imbalanced data through the comparison of different class-balancing strategies; and (iii) improve the previously employed methodology and delineate target areas for Li-exploration. This work also aimed to answer distinct research questions, namely: (i) how to overcome the overfitting challenges; (ii) which factors most influence the SVM performance; (iii) can the SVM classification process be automatized; (iv) what are the main challenges and benefits of using SVM in Li-pegmatite mapping; and (v) can the methodology be extrapolated to other study areas. Ultimately, this research intends to fill the literature gap by contributing to the state of the art regarding the use of ML in Li-pegmatite mapping, by clarifying how SVM can be helpful in Li-pegmatite exploration.

The Fregeneda–Almendra Pegmatite Field

The Fregeneda–Almendra (FA) pegmatite field lies within the Central Iberian Zone of the Iberian Massif, spreading from Portugal (Almendra) to Spain (La Fregeneda). The border is materialized by the Águeda river, and the pegmatite field is delimitated to the north by the Douro river and to the east by

the Variça's fault. The study area of this work comprises most of the FA field where different types of pegmatite dykes were defined (Figure 1) taking into account their mineralogy, morphology, and internal structure [20–22]. These bodies intruded on the metasedimentary rocks of the Schist-Graywacke Complex (SGC) [23,24]. To the south the syn-Variscan Mêda-Penedono-Lumbrales granitic complex outcrops. Within the more evolved aplite–pegmatites, there are four dyke-types containing Li-bearing minerals: petalite-rich, spodumene-rich, lepidolite–spodumene-rich, and lepidolite-rich. All the Li-pegmatites are discordant from the host-rock main foliation and are emplaced in the same fracture set, striking from N-S to N30 °E. The petalite-rich dykes can reach a maximum thickness of 5 m to 30 m [22,25]. The spodumene-rich dykes are very similar to the petalite ones in terms of mineralogy, attitude, and dimension, with a thickness ranging from 4 m to 15 m [22,25]. Both dyke-types present no internal zonation. The lepidolite–spodumene-rich dykes present a common internal layering and thickness usually less than 15 m [22,25]. The thinner dykes are the lepidolite-rich, with a thickness lesser than 3 m and occasionally with internal banded structure (where lepidolite-rich layers alternate with albite-rich ones) [22,25].

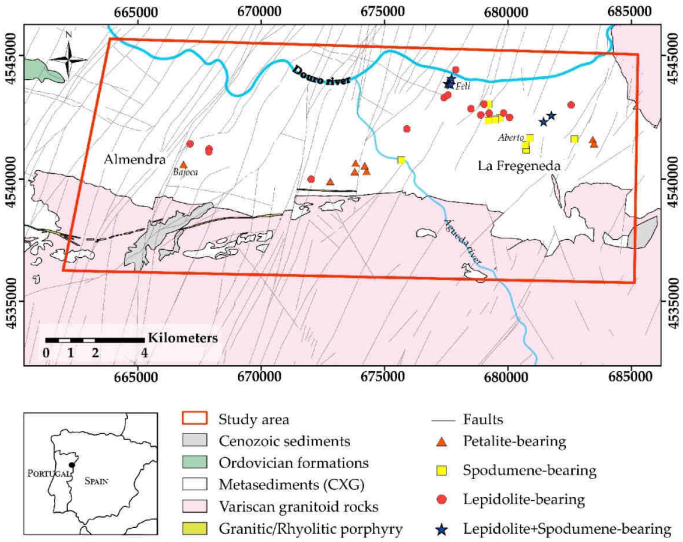

Figure 1. Location and geological map of the study area where the different aplite–pegmatite dykes outcrop (adapted from [22,26,27]). Open-pit mines of Bajoca, Feli and Alberto are also highlighted. The map projection is Universal Transverse Mercator zone 29 N from the WGS84 datum.

In the FA area, there are three locations were these Li-dykes are being exploited in open-pit mines (Figure 1). This type of excavation favors the application of remote sensing data/techniques, because it increases pegmatite exposition at the surface. Moreover, each open-pit mine exploits a different pegmatite dyke-type. The Bajoca mine, located near Almendra in the Portuguese side of the field, exploits a petalite-rich dyke with up to 30 m of thickness [22]. The Alberto mine, near La Fregeneda in Spain, exploits several spodumene-rich dykes with varying thicknesses. Despite spodumene being the predominant Li-bearing phase, primary petalite can also be found in these dykes [22]. Finally, in the Feli mine, located near the Douro river on the Spanish side of the pegmatite field, a lepidolite–spodumene-rich dike is exploited.

Currently, other complementary studies are being developed in the FA area to help target Li-mineralizations. Stream sediment analysis of more than 3000 samples is being employed on the

Portuguese side to identify areas with Li-potential. Spectral studies are being conducted using a laboratory spectroradiometer to build a spectral database of Li-bearing minerals. Moreover, as stated by Cardoso-Fernandes, et al. [7], the knowledge on the alteration halos associated with Li-pegmatites could favor alteration mapping techniques, thus increasing the size of the target areas and possibly allowing to vector near-surface hidden dykes. For that, more than 70 host-rocks samples are being characterized through geochemical studies. Overall, the expected results will help to improve Li-pegmatite remote mapping capabilities. The ability to recognize Li-pegmatites remotely is of great interest to the exploration/mining industry. Firstly, it would allow to decrease the time and costs of field campaigns. Secondly, the social acceptance of mineral exploration is becoming a major concern in Europe. Consequently, less intrusive exploration methods such as remote sensing are increasingly becoming an integral part of the companies' exploration strategies.

2. Support Vector Machines (SVM's)

Support vector machines (SVM's) are a non-parametric classification technique based on statistical learning theory [28], and therefore no assumption on the distribution of the data is made. The SVM technique tries to find an optimal hyperplane that separates the dataset into a defined number of classes. This optimal hyperplane is the decision boundary that maximizes the distance of the margin between the class bounding hyperplanes (also called supporting hyperplanes). The bounding hyperplanes are parallel to the optimal hyperplane and are defined by the training samples that are closest to the boundary—the support vectors (Figure 2).

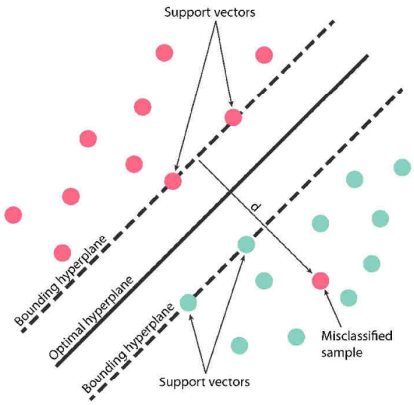

Figure 2. The support vector machines (SVM) method: the optimal hyperplane separates the two classes and is parallel to the bounding hyperplanes on which the support vectors lie. The distance between these two bounding hyperplanes is called the margin, and the distance *d* between the bounding hyperplane and the outlier (misclassified sample) indicates that there are slack variables (modified from [8]).

SVM is by nature a binary classifier, but it can be extended for multiclass classification, using the 'one-against-all' or 'one-against-one' strategies [8,17]. In the 'one-against-all' strategy, k SVM models are built (where k is equal to the number of classes), each of them separating one class from the remaining. In the 'one-against-one' approach, k(k-1)/2 SVM classifiers are built and trained for all possible two-class combinations out of k classes [29]. In other words, a sample is classified as one of two classes for each model and the output class label is decided by the majority votes.

Since the SVM is inherently a linear classifier, it assumes that the multispectral feature data are linearly separable in the input space [17]. However, in practice, the data can be noisy and different

classes may not be entirely separable due to class overlap [8,17]. This limitation can be overcome using techniques like the soft margin method [30] and the kernel trick that map the data into a higher dimension known as feature space and add additional variables called slack variables to accommodate outliers. This projection is done under the assumption that a linear boundary may exist in that higher-dimensional feature space [18]. In what concerns the soft-margin technique, the training samples are allowed to fall on the opposite side of the decision boundary (the optimal hyperplane) and the limit of the violation of the bounding hyperplanes is set by the slack variables. To each sample classified on the wrong side of the boundary, there is a penalty associated, in this case, it is the cost hyperparameter C [30]. A smaller C value will result in a larger margin that will allow for more violations, but this may lead to an inappropriate (large) number of support vectors [8,18]. Oppositely, a higher C value means a narrower margin that will limit violations. This can result in a more complex decision boundary and may cause the model to lose its generalization capability and even overfit the data [8,18]. In remote sensing, an overfitting model can explain very well the variance of the training data, while having a low capability to generalize to the whole image. Consequently, a classical sign that a model is overfitting the data is when the performance on the training set is notably better than in the testing/validation dataset [31]. In the kernel trick case, some of the more popular kernel functions(K) are, for two input vectors x_i e x_j:

$$\text{Linear: } K(x_i,x_j) = \gamma x_i x_j; \quad (1)$$

$$\text{Polynomial of degree d: } K(x_i,x_j) = (\gamma x_i x_j + r)^d, \gamma > 0; \quad (2)$$

$$\text{Radial basis function (RBF): } K(x_i,x_j) = \exp\{-\gamma||x_i - x_j||^2, \gamma > 0; \quad (3)$$

$$\text{Sigmoid: } K(x_i,x_j) = \tanh(\gamma x_i x_j + r), \gamma > 0; \quad (4)$$

where the γ (gamma parameter) serves as an inner product coefficient in the polynomial function (Equation (2)) and in the hyperbolic tangent function of the sigmoid kernel (Equation (4)), while controlling the kernel width in RBF (Equation (3)) [13,31]. In the specific case of the RBF kernel (Equation (3)), the γ parameter defines the range of influence of each training sample. A higher γ decreases the range of influence of sample which results in a more irregular decision boundary, while a smaller γ increases the range of influence of each sample, leading to a smoother boundary [31]. The parameter *d* corresponds to the degree of the polynomial function (Equation (2)). The parameter *r* is used for both the polynomial (Equation (2)) and sigmoid (Equation (4)) kernels, and controls in Equation (2) how much the model is influenced by high-degree polynomials versus low-degree polynomials [31].

3. Data and Methodology

3.1. Dataset

As mentioned before, pegmatite exposition can be very small when compared with the spatial resolution of several free satellite products [7,32]. Despite the fact that lack of thermal band can limit the applicability of Sentinel-2 images in Li-pegmatite identification [2], its medium to high spatial resolution (10–60 m) may be crucial in a classification exercise where the target class presents the lowest exposition. Therefore, a Sentinel-2B satellite product, acquired on 07/09/2019 (tile number T29TPF), was used. The product's processing level is 2A and its projection is Universal Transverse Mercator zone 29 N, WGS84 datum.

The Sentinel-2 mission includes a constellation of two twin satellites placed in the same sun-synchronous orbit, phased at 180° to each other: Sentinel-2A and Sentinel-2B [33]. On-board, the Multispectral Instrument (MSI) acquires information in 13 spectral bands from the visible-near infrared (VNIR) to the short-wave infrared (SWIR), but only the bands in bold in Table 1 were used in the image classification approach. These bands are the most adequate for geological purposes since minerals and rocks have important absorption features in the correspondent wavelengths. Additionally,

the remaining Sentinel-2 bands have specific applications, such as detecting coastal aerosols (band 1), vegetation (bands 5, 6 and 7), water vapor (band 9), and clouds (band 10).

Table 1. Sentinel-2B Band's Characteristics [34].

Band Number	Central Wavelength (nm)	Bandwidth (nm)	Spatial Resolution (m)
1	442.3	21	60
2	492.1	66	10
3	559.0	36	10
4	665.0	31	10
5	703.8	16	20
6	739.1	15	20
7	779.7	20	20
8	833.0	106	10
8A	864.0	22	20
9	943.2	21	60
10	1376.9	30	60
11	1610.4	94	20
12	2185.7	185	20

Since it is a Level 2A product, the bands were already provided in surface reflectance [35]. Basic pre-processing operations such as resampling all bands to a 10-m spatial resolution, as well as spectral and geographic sub-setting were performed using the Sentinel Application Platform (SNAP) software [36].

3.1.1. Sampling and Training Areas Definition

The training areas were defined based on (i) areas directly identified by visual inspection of the Sentinel-2 images, namely of a natural color composite (RGB combination 4-3-2) and the calculation of the Normalized Burn Ratio (NBR) index; (ii) extremely high-resolution images provided by Google Earth [37], Esri World Imagery [38] and by drone flights made over a known outcropping Li-pegmatite (0.025 m resolution); (iii) the Portuguese Geological Map at 1:50,000 [26,27]; and (iv) field reconnaissance.

The definition of training areas corresponded to an iterative process: for each set of training samples, class separability measurements (see Section 3.1.2) and spectral analysis were made until satisfactory results were obtained in order to select the best training areas and therefore proceed with the classification process. To improve the classification results and class separability, the number of user-defined classes was diminished when compared to previous attempts [5]. Urbanized and vegetated areas as well as the water bodies were masked out from the image, using the information provided by the Portuguese and Spanish LULC Maps (COS 2015; COS 2018; SIOSE 2014) and the Scene Classification maps provided in the Sentinel-2 Level 2A products [35]. In addition, some lithological units were deliberately left out from the classification due to small exposition (Ordovician Formations; Figure 1) or to great spatial correlation with other classes (Cenozoic sediments; Figure 1). The selected training areas contain 3053 pixels distributed by 5 classes and 33 regions of interest (ROIs) as presented in Table 2.

Table 2. Distribution of Training Pixels by Classes and regions of interest (ROIs).

Class name	Total Pixel Number	Training Pixels	Testing Pixels	ROI Number
Agricultural fields	1230	894	336	8
Burned areas	205	80	125	2
Granite	1231	987	244	9
Li-bearing pegmatite	43	17	26	5
Metasediments	344	166	178	9

Since different classes occupy different areas on the ground, sample acquisition was not even between classes. The major problem was in the identification of samples from the Li-bearing pegmatite class because of their small exposition. Although the training areas included samples not only from the outcropping dykes, but also from ore stockpiles, the resulting dataset was still very imbalanced as can be seen in Table 2. The spectral responses of the classes for the training pixel samples were computed directly from the Sentinel-2B image—Figure 3.

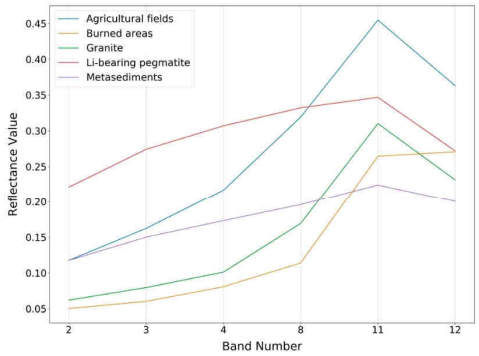

Figure 3. Mean spectral signatures based on the training pixels selected for each class.

3.1.2. Class Separability

As referred before, the evaluation of the spectral separability between pairs of training classes is an important step of the training areas refinement process. Therefore, a quantitative measurement of class separation was made using the Jeffries–Matusita (JM) distance and transformed divergence (TD) matrix. These spectral distances were computed using PCI's Geomatica 2018 software [39] and the values obtained are presented in Table 3. Both distances present values between 0 and 2, where 0 means a complete overlap between the signatures of two classes, and 2 indicates a complete separation between classes [40]. In general, values higher than 1.9 indicate a very good class separability, values between 1.7 and 1.9 correspond to a good class separability, while values below 1.7 indicate that the classes are difficult to separate. These measurements can give an insight into the classification accuracy: a higher-class separability should indicate a better classification result.

Table 3. Jeffries–Matusita (JM) (Blue) and transformed divergence (TD) (Orange) Separability Measures for Each Pair of Classes.

	Li-Bearing Pegmatite	Metasediments	Granite	Burned Areas	Agricultural Fields
Li-bearing pegmatite		2.000	2.000	2.000	2.000
Metasediments	1.977		2.000	2.000	2.000
Granite	2.000	1.998		2.000	1.994
Burned areas	2.000	2.000	2.000		2.000
Agricultural fields	1.998	1.994	1.865	2.000	

Table 3 shows that all classes have a good separability, with exception of the pair Granite–Agricultural fields which is the one with minimum separability. Using the JM distance, the average separability obtained was 1.983, the minimum separability obtained was 1.865, while the maximum separability achieved was 2.000. Similarly, minimum and maximum separability obtained with the TD matrix were between 1.994 and 2.000, with an average separability of 1.999.

3.2. Parameter Tuning, Cross-Validation, and Model Evaluation

To achieve high accuracy, optimization of the parameters and kernel functions is required, because they are site-sensitive [18,19]. Parameter tuning and model evaluation was achieved using the open-source library scikit-learn [41] (version 0.20.1) for Python programming language.

Initially, all training samples were shuffled and randomly divided into training and test sets (25% for testing and 75% for training) using a stratified iterator to ensure that both sets contained samples from Li-bearing pegmatites. However, after a considerable number of trials, all the models presented the same signs of overfitting with almost perfect training scores and very high-test scores. In a classical overfitting example, the test score should be very low in comparison to the training score. However, when analyzing the results, it was possible to conclude that the training and test subsets were not independent. This means that the variance of the training and test data were very similar. Consequently, SVM not only learned very well the patterns of the training data, but also from the test subset. Only when applying the models to the whole image (i.e., when introducing new, independent data), the performance score would drop drastically as typical in overfitting models. Thus, a different strategy had to be employed to ensure that the training and testing data were independent. Considering that all samples from the same ROI would have similar spectral behavior, instead of randomly splitting the individual samples, a procedure to randomly split the ROIs into training and test subsets was adopted (Figure 4). Additional information, as well as the source code employed in this procedure, is available in Section 1 of the Supplementary Materials.

The choice of the best kernel (among linear, polynomial and RBF) and of best parameters was accomplished by a two-staged grid-search with cross-validation (CV). Besides the kernelized SVM models, the Linear model (that assumes the data is linearly separable without using any kernel function [31]) was also evaluated (Figure 4). While scikit-learn's kernelized SVM classifier uses a 'one-against-one' multiclass strategy, the Linear model employs "one-vs-the-rest" [42].

The first stage grid-search represents a coarser grid-search: the Linear model (non-kernelized SVM) and all the different kernels were tested separately, using several ranges for the parameters, which either increased in a logarithmic or exponential fashion (see for example [19,43]). Each parameter range was cross-validated using a stratified 5-fold CV. This means that the original training set was split into five groups (maintaining the original proportion of samples per class), and in each fold, one group was retained in turn to use as a validation set, while the model was trained in the remaining 4/5 of the data. After the 5 folds were completed, the score obtained in each fold was averaged, obtaining the mean test score for every parameter input or combination. The best parameter(s) were the ones that obtained a higher mean CV test score. In this step, to optimize the discrimination between the target class (Li-bearing pegmatite) and the host rocks (Metasediments) the employed metric score was the F1-score of these two classes. The F1-score is the harmonic mean of precision and recall, where precision measures the accuracy of positive predictions and recall measures how many positive samples are correctly detected by the classifier [31].

The first stage grid-search is mainly based on the knowledge of the operator since different ranges will return very distinct optimal parameter(s). The sensitivity of SVM to the setting of the parameter range was already described by other authors [44]. Therefore, the results of each range should be interpreted carefully and an increase or decrease of the search space may be necessary to improve the grid-search outputs. When choosing the best range, several criteria must be considered besides the CV test score, namely the values of the returned parameter(s). This means that when the obtained scores are similar, the operator should opt for the one with a smaller C and/or gamma, for example, to avoid choosing a rigid model that may overfit the data [31].

To try to balance the dataset, three different approaches were applied: (i) use a built-in class-weight parameter; (ii) downsampling; and (iii) upsampling. In the first case, a weight is attributed to each class during the training phase to account for class imbalance: this weight can be user-defined, or it can be set automatically to the inversely proportional to class frequency (the so-called "balanced" mode). In this work, we decided to use the "balanced" option. In what concerns the downsampling

process, the classes with more observations are randomly sampled without replacement, to obtain several samples equal to the size of the smallest class. On the other hand, upsampling is the process that for each observation of the largest class, randomly selects from the other classes with replacement. For more information on the first stage grid-search, see Section 2 of the Supplementary Materials.

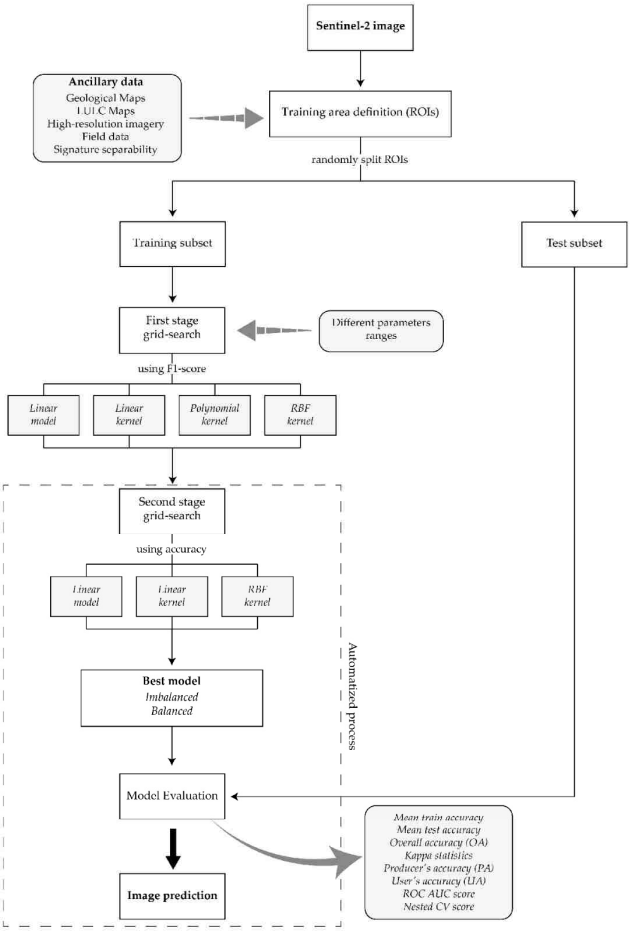

Figure 4. Flowchart of the image classification process.

In the second stage grid-search, a stratified 5-fold CV was again implemented, but this time with linear increments around the best parameter values returned in the first step. Whenever possible, the incremental steps employed were the same used by Oommen, et al. [43]. In this second stage, the polynomial kernel was not included, since the best degree obtained in the first stage was always equal to one, and the first-degree polynomial corresponds to the linear kernel when the parameter r equals to zero (Equations (1) and (2)). The downsampling and upsampling strategies were also excluded from the second stage, because the introduction of a random sampling process (that did not consider the ROIs) leads to overtraining problems. Consequently, in the second stage grid-search, only three models were trained for both the imbalanced and balanced data using the class-weight

parameter. The choice of the best model was automatized (see Section 3 of the Supplementary Materials) and in the end, two models, one built on the imbalanced data and one using the class-weight option, were applied to the whole image (Figure 4). This means that on the contrary of what happened in the first stage (where each model was trained separately), in the second stage the three models were confronted in the same grid-search and the best model was automatically return. Only the best model returned were subjected to the "Model evaluation" step of Figure 4.

In what concerns the model evaluation, the metric score employed to choose the best model in the second stage was the accuracy. Besides the mean train accuracy and mean test accuracy obtained in the CV, the overall accuracy and the Kappa statistics were also computed. To evaluate the classification at the class level, the producer's and user's accuracy were calculated. Knowing the true and predicted classes of the test data, the confusion matrix gives insight for each class on how many samples were correctly classified, how many were misclassified, and on which class the samples were incorrectly classified. The matrix diagonal represents the samples that were correctly classified in the respective class and the OA is calculated by dividing the sum of the correctly classified instances by the total number of pixels [45]. The producer's accuracy (PA) is obtained by dividing the number of correct pixels in a given class by the total number of pixels of that class in the test set, and indicates the probability of a training sample being correctly classified [46]. On the other hand, the user's accuracy (UA) can be computed by dividing the number of correct pixels in a determined class by the total number of pixels that were classified in that class. It indicates the reliability of the map and gives the probability that a pixel classified as of belonging to a certain class actually belongs to that class on the ground [45,46]. The Kappa statistic corresponds to a measure of agreement between the classifier output and reference data [47]. To access the influence of the correct choice of model in the Li-pegmatite class, receiver operating characteristic (ROC) curves were computed for all the models tested during the second stage grid-search. The ROC curve plots the true positive rate (or for recall) against the false positive rate (fraction of negative samples misclassified as positive) [31]. The area under the curve (AUC) score was calculated to compare the different classifiers.

The ability of each model to generalize to unknown data was evaluated by applying a nested CV. This procedure allows multiple splits of CV instead of just one (the training-validation split), thus reducing the risk of biasing model evaluations by using different portions of the data for parameter selection and model evaluation. In practice, the procedure corresponds to a CV of the first CV: the inner loop is for parameter tuning and model selection, the outer loop is dedicated to evaluating the model's performance. In this work, the outer loop consisted of a 3-fold CV. The source code employed in this procedure is available in Section 3 of the Supplementary Materials.

4. Results

The automatized process allowed to choose the best model for both the imbalanced and balanced datasets. Data balancing had an impact on SVM performance since the best model found was the Linear model (non-kernelized SVM) for the imbalanced data and the RBF kernel for the dataset balanced using the class weight option.

The results from the second stage grid-search with CV and from the model evaluation step are presented in Table 4. In general, both models reached a similar performance, although the Linear-SVM obtained a higher train score. The RBF-SVM was the model that achieved a higher test score during the CV process, but the Linear-SVM attained a better OA and Kappa hat statistics. The models' generalization capability (nested CV score) was also very similar.

Based on the metrics, especially on the attained OA and Kappa hat, the Linear-SVM appears to be the best model. Plotting the ROC curves for each model tested in the second stage grid-search and computing the respective AUC score allowed to assess the models' performance exclusively on the Li-pegmatite class (Figure 5). The results show that the use of class balancing strategies improved the performance on the Li-pegmatite class for the Linear model and for the Linear kernel. In the balanced dataset, the best model found through the automatized process, the RBF kernel, was the

one that achieved a higher AUC. However, in the case of imbalanced data, the RBF kernel was still the one with the highest AUC, despite the Linear model being chosen as the best model with the automatized process. This happened because the automatized process selects the best model based on the performance in all classes while the AUC score only accounts for the Li-pegmatite class.

Table 4. Classification Performance Summary for the Two Models Built.

Model	Imbalanced	Balanced
	Linear Model	RBF Kernel
Parameter(s)	C = 32	C = 0.2 γ = 4.4
Mean train score (CV)	0.980643	0.941802
Mean test score (CV)	0.917444	0.93750
Overall accuracy (OA)	0.852585	0.832783
Kappa hat	0.801678	0.777337
Nested CV score	0.906241	0.906229

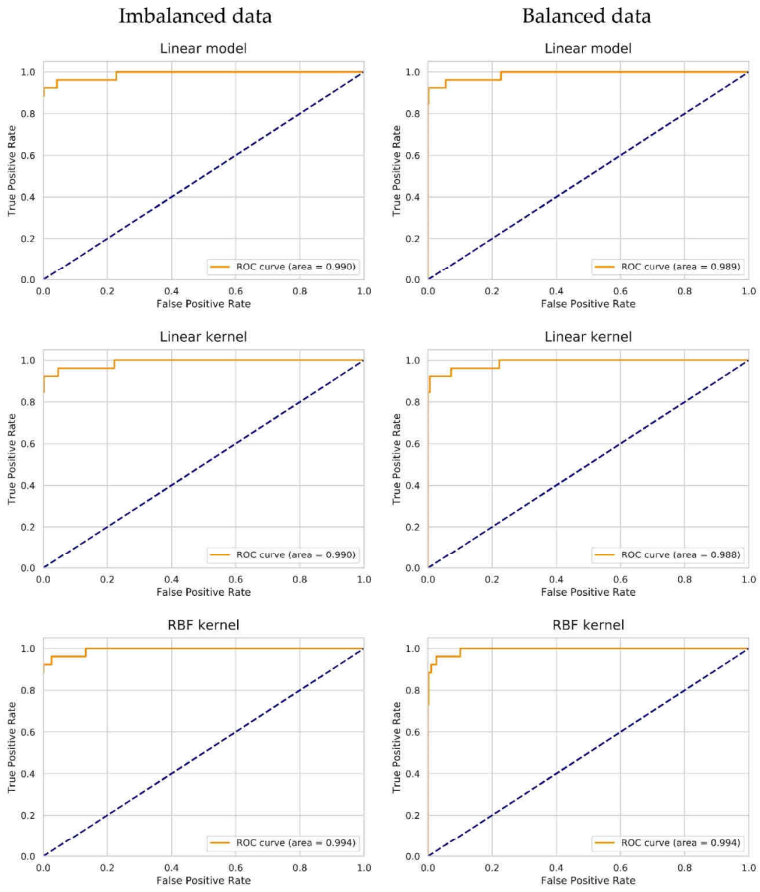

Figure 5. Receiver operating characteristic (ROC) curves and area under the curve (AUC) scores for each of the models tested in the second stage grid-search for both the imbalanced and balanced data.

To analyze and compare in detail the accuracy performance on each class the confusion matrices were computed for the Linear-SVM (Figure A1) and the RBF-SVM (Figure 6). The UA and PA were computed considering the respective confusion matrix and are presented in Table 5.

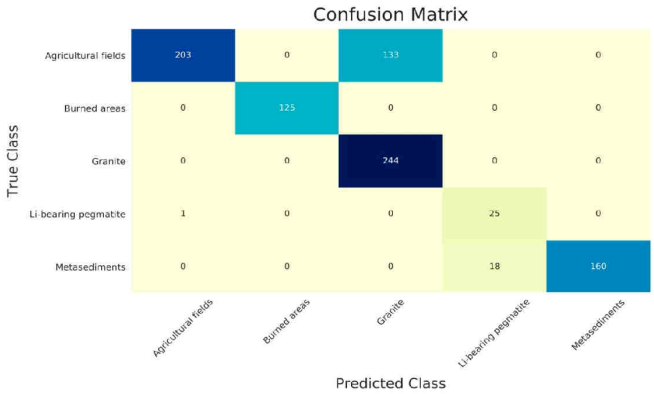

Figure 6. Confusion matrix for the RBF-SVM model built on the balanced dataset.

Table 5. User's and producer's accuracy (UA and PA) for Both the Linear-SVM and Radial Basis Function (RBF)-SVM Models. Values in percentage (%).

Class	Imbalanced		Balanced	
	PA	UA	PA	UA
Agricultural fields	64.58	93.53	61.01	99.51
Burned areas	100.00	100.00	100.00	100.00
Granite	98.77	66.94	100.00	65.07
Li-bearing pegmatite	88.46	100.00	96.15	59.52
Metasediments	94.94	100.00	90.45	100.00

As can be observed, in both models, the greater misclassification errors happened between the Agricultural fields and Granite classes. Regarding the Li-bearing pegmatite class, the Linear-SVM model was the one that maximized the discrimination between the mineralized dykes and the host rocks, but this was done at a cost—a higher number of false negatives. Conversely, the RBF-SVM model minimized the misclassification of true samples from the Li-bearing pegmatite class at the cost of a higher confusion with the metasedimentary host-rocks. These results are in line with the interpretations with the final classification maps obtained for Linear-SVM (Figure 7) and for RBF-SVM (Figure 8).

The comparison between the two classification maps indicated that the overall performance of each class changed from one model to the other. For example, the RBF-SVM model was able to correctly classify all the areas affected by wildfires while the Linear-SVM model misclassified some of these areas as Metasediments. On the other hand, the Linear-SVM model was the one that better identified the Agricultural Fields, whereas the RBF-model only showed good performance in the classification of the Agricultural Fields located over a granitic basement. Both models showed problems in the classification of the Metasediments that were often classified as Granites.

In what concerns the target class, Li-bearing pegmatite, the Linear-SVM was able to minimize the occurrence of false positives. Therefore, the pixels classified as belonging to the Li-class were limited, almost exclusively, to small areas inside the known open-pit mines. On the other hand, the RBF-SVM was able to identify other possible target areas beyond the known occurrences. As this is the final goal of mineral exploration, the results obtained with RBF-SVM are preferred even though some areas where Metasediments outcrop were classified as Li-bearing pegmatite (top left corner and top center

of the classified image—Figure 8). These results are contradictory to the quantitative model analysis achieved with the OA and Kappa statistics. That is why it is fundamental to evaluate the models using distinct statistical methods. Moreover, the results obtained with each model were qualitatively analyzed and evaluated.

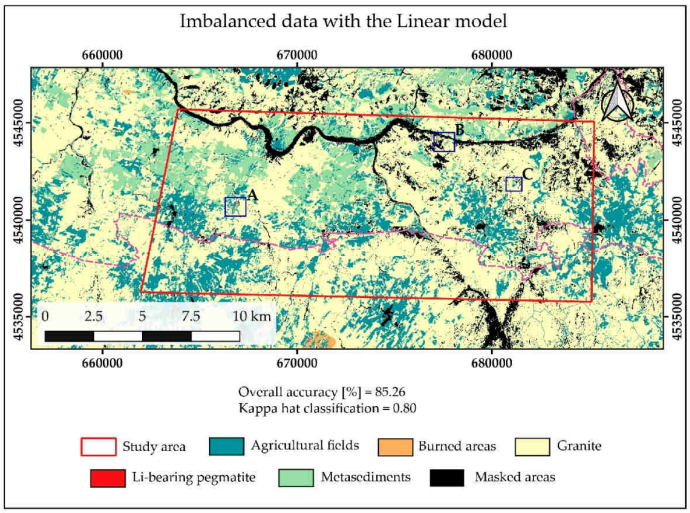

Figure 7. Final classification map based on the Linear-SVM model built with imbalanced data. Three open-pit mines exploiting Li-minerals are identified: A—Bajoca, B—Feli, and C—Alberto. The dashed purple line represents the simplified contact between the Metasediments and the Granite. Zoom images of the open-pit mines can be found in Figure 9.

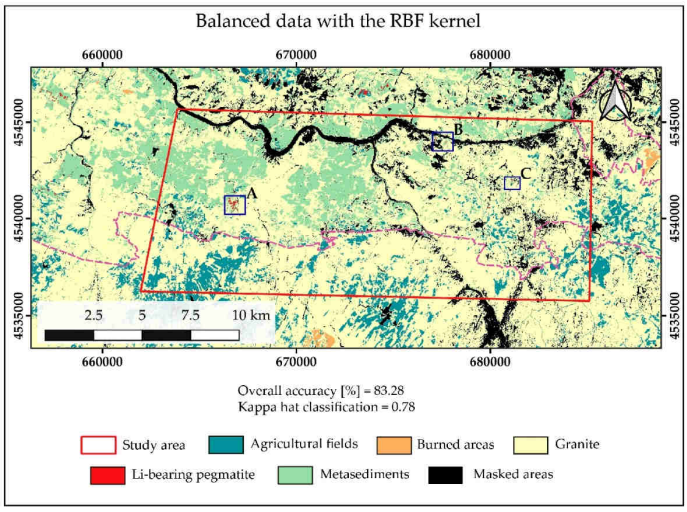

Figure 8. Final classification map based on the RBF-SVM model built with the balanced data. A—Bajoca mine, B—Feli mine, and C—Alberto mine. Dashed purple line: simplified contact between the Metasediments and the Granite. Zoom images of the open-pit mines can be found in Figure 9.

The performance of the models was evaluated in their capacity to correctly identify known target areas. As mentioned before, in the Fregenda–Almendra area there are three open-pit mines currently exploiting Li-bearing pegmatites: the Bajoca mine on the Portuguese side, and the Feli and Alberto mines in Spain. From the 43 Li-pegmatite samples defined for training and evaluation, 42 of those samples belonged to the Bajoca mine (outcropping pegmatite and ore stockpile). The remaining sample was collected from one outcropping pegmatite in the Alberto mine. The classification results obtained for these three target areas using both algorithms are presented in Figure 9.

The results obtained for the Feli mine were similar using the two algorithms, identifying the presence of Li-bearing pegmatite in the open-pit and next to the two waste piles (to the left of the open-pit). However, in the case of the Bajoca and Alberto mines, the Linear-SVM classified a much smaller area as being Li-bearing pegmatite when compared to the RBF model. Oppositely, the RBF-SVM identifies some false positives like in the dirt road that leads to the Bajoca mine (Figure 9). Regarding the other classes, both models overestimated the occurrence of Granite where in fact metasedimentary rocks occur. Moreover, the Linear-SVM misclassified some pixels inside the open-pits as being Agricultural Fields. This misclassification was less frequent with the RBF model.

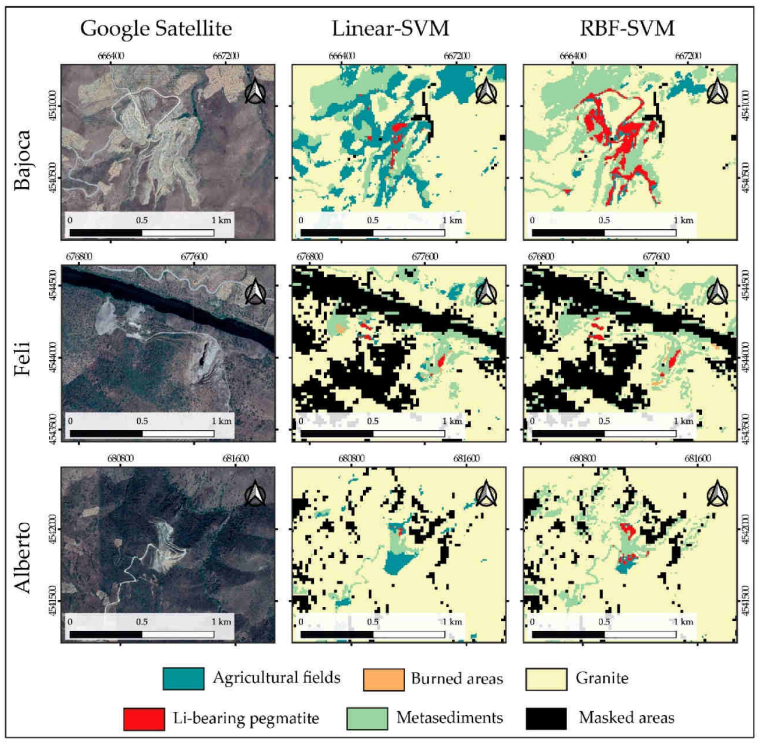

Figure 9. Evaluation of the models' performance in the known open-pit mines exploiting Li-bearing pegmatite.

On the contrary to what happens in the Bajoca mine, the ore stockpiles, where the extracted Li-pegmatite from the Feli and Alberto mines are stored, are not located near the open-pits. Therefore, these two known stockpiles were also used to verify the models' performance in the classification of the Li-bearing pegmatite class (Figure 10). Field campaigns allowed to verify that Li-minerals are present

in these stockpiles (Figure 10b). In the case of the Feli stockpile, both models were able to identify the occurrence of Li-bearing pegmatite. Inversely, on the Alberto stockpile, only the RBF-SVM correctly identified most of the areas where Li-pegmatite is present. In what concerns the remaining classes, besides the areas misclassified as Granite, the Linear-SVM was the model that correctly identified most of the Agricultural Fields.

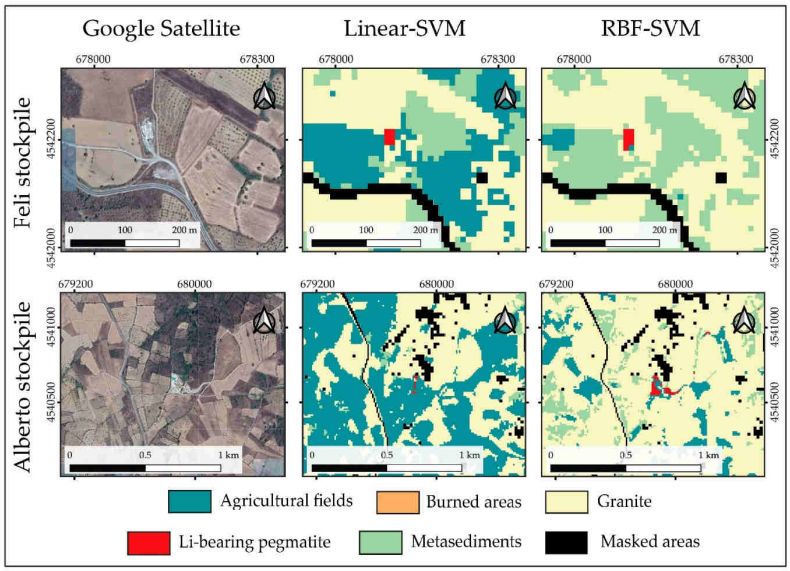

(**a**)

(**b**)

Figure 10. Evaluation of the models' performance in known ore stockpiles containing Li-bearing minerals (**a**). (**b**) Field photograph of a spodumene crystal (a Li-bearing mineral) from the Alberto stockpile.

5. Discussion

A previous attempt to use ML algorithms in Li-bearing pegmatite identification showed that the model parameterization and optimization were not enough to avoid overfitting, which ultimately led to a large number of Li-pegmatite false positives [5]. In this study, several methodological improvements were made. Besides reducing the area to be classified and the number of classes through masking of undesired classes, a new strategy to split the training data into training and test subsets was proposed. This new strategy resulted in a higher independency between the two subsets, since sample location was taken into consideration in the split. Inevitably, the random sampling process introduced when using the downsampling and upsampling strategies made the developed ROI-based splitting strategy infeasible. This led to overfitting problems and, therefore, these strategies were excluded from the classification. The proper definition of the range of the tested parameters was crucial to optimize the models during the first stage grid-search, and several literature-based ranges were tested. While several authors have also employed grid-search techniques to determine the best parameter(s) [8,18,19,43,48], this step is not always employed, with some authors achieving parameterization through the trial and error method [14]. Other authors have opted to not optimize the models and used the default parameters or other specific sets of parameters [9,10,12,49]. The observation of the first stage results allowed to select the right parameters, but also to exclude the polynomial kernel, reinforcing the importance of the intervention of the operator at the beginning of the classification process.

The second stage grid-search automatically returned two different models respectively for the imbalanced and balanced datasets, which is the first indication that class imbalance may affect the obtained results. The Linear-SVM trained on the imbalance data and the RBF-SVM trained using the class-weight option showed, at turn, better performance depending on the class. Both models achieved a better ability to discriminate the target class (Li-pegmatite) from the host rocks, thus reducing the number of false positives when compared to the SVM model trained in the previous work of Cardoso-Fernandes, et al. [5]. This corroborates that the methodological adjustments made in the current study helped to improve the SVM performance.

Nonetheless, the results obtained with each model for the Li-bearing pegmatite class were very distinct. The Linear-SVM presented the best discrimination between Li-pegmatite and Metasediments, while missing to correctly classify pixels with known Li-pegmatite exposition. Oppositely, the RBF-SVM avoided the occurrence of Li-pegmatite false negatives while classifying Metasediments and dirt roads as areas with Li-potential. Increasing the discrimination between Metasediments and Li-pegmatites may only be achieved with a better spatial resolution data. In the Fregeneda–Almendra pegmatite field, dyke thickness can range between 4 m and 15 m in the case of the spodumene-bearing dykes, and between 5 m and 30 m in the petalite-bearing ones [25]. Even in the largest dyke that outcrops in the Bajoca mine, metasedimentary enclaves can be found in the middle of the pegmatite, which contributes to pixel mixing, since the Sentinel-2 bands used in this work have between 10 m to 20 m of spatial resolution. In addition, the slightly different mineral paragenesis of the Feli mine (with lepidolite), when compared with Alberto or Bajoca, may have influenced the performance of Linear-SVM.

The interpretations of the final classification maps (Figures 7 and 8) are supported by the computed statistical metrics and respective confusion matrices (Figures 6 and A1). When looking at the performance metrics at a class level, Linear-SVM reached a better performance on the test set (Figure A1), which may indicate more overtraining and fewer ability to generalize to unknown data, when compared with RBF-SVM. When dealing with imbalanced datasets, special attention should be given when interpreting the results obtained with global metrics such as OA and Kappa hat, since the influence that minor classes such as Li-pegmatite have on the final output can be masked by the majority class(es) [44,50]. That is why it is important to qualitatively assess the performance of the models. Zoom images concerning known Li-pegmatite expositions (Figures 9 and 10) support the previous interpretations that the RBF-SVM performs better in Li-pegmatite identification, when compared with the Linear-SVM. Moreover, the results obtained highlight that the developed methodology can identify Li-pegmatite occurrences beyond those that were used as training instances.

In what concerns the remaining lithological classes, both models overestimated the occurrence of Granite in areas where Metasediments occur. This can be mainly explained by the spectral confusion with the Agricultural fields class, especially in the case of the RBF-model. The phenomenon is not only corroborated by the computed confusion matrices, but also by the signature separability measures (see Section 3.1.2.). The overestimation of the Granite class can also be linked to the difficulty to correctly classify the metasedimentary rocks since (i) they outcrop in less extent when compared with the granites, (ii) are often covered by vegetation or (iii) serve for olive/almond tree plantations. This happens because granites are not so easily weathered as the metasediments, and regolith tends to form over the latter. Taking this into account, a regolith–geology mapping approach like the one employed by De Boissieu, et al. [9] could help improve the results.

On the other hand, considering that in geological exploration false negatives should be avoided, the RBF-SVM built using a class balancing strategy is therefore the preferred model to define areas with Li-potential. In satellite image classification, the RBF is often the preferred kernel, commonly showing good performance [12,19,43,49]. Melgani and Bruzzone [51] concluded that the RBF-kernel achieved higher OA than the Linear-model in hyperspectral image classification. Geranian, et al. [16] have compared the performance attained with different kernels in mineral prospectivity mapping and concluded the RBF achieved the best results. However, in a similar study, Zuo and Carranza [13] found the sigmoid kernel to be the optimal function.

Contrary to the expected and opposed to previous studies [5], the results also show that the class imbalance had a higher impact on the SVM performance (Figures 5 and 7–10). This is of particular interest and importance, since Maxwell, et al. [18] stated that, for SVM, balancing the data had a negligible effect on UA and PA of the rare classes of the Indian pine dataset, Indiana (USA). Noi and Kappas [19] also concluded that SVM was less impacted by sample size and class imbalance than other ML algorithms. However, despite its robustness to data imbalance, the SVM algorithm works by minimizing the overall error (that is inherently biased toward the majority class) which can lead to the underprediction of the less-abundant class [18,50]. In this work, the Li-class was underpredicted using the imbalanced dataset when compared to the balanced one. Ultimately, class imbalance affected the ability to predict the Li-pegmatite class not only in possibly target areas, but also where Li-pegmatite occurrences are known.

Overall, the methodological developments made in this study represent a major contribution not only to the state of the art of Li-pegmatite satellite-based exploration, but also to the application of ML algorithms to remote sensing lithological mapping. The step-by-step optimization made in this study is proof that ML algorithms, particularly SVM, are not easy and ready to apply (at least to some specific applications such as mineral exploration). The major difficulty in Li-pegmatite exploration using remote sensing data is their relatively small size and exposition. This means that, in an image classification problem, the target class is by nature a small, underrepresented class. Therefore, the adaptations proposed to achieve the optimal parameters proved to be fundamental to successfully deal with class imbalance. Detailed insights on algorithm parameterization were given, so that the methodology can be replicated in other case studies. Algorithm optimization was reached at several levels, namely: (i) data splitting for training and testing; (ii) strategy do deal with data imbalance; (iii) type of SVM model and kernel function; (iv) associated hyperparameter(es); and (v) metric score employed in the CV process. When using a grid-search with CV to find the best parameters, commonly used metrics are the OA and Kappa statistics [8,18,19]. As part of the algorithm optimization, a more innovative strategy was employed in the first stage grid-search where the parameters were chosen based on the F1-score of just two classes: the Li-pegmatite and the Metasediments. Moreover, the semi-automatization of the SVM classification process allowed to simplify the choice of the best model among several options. In this case, the results obtained with the RBF-SVM allowed to delineate target areas for Li-exploration.

However, the developed methodology still has some shortcomings. The main limitation is that some smaller pegmatite occurrences and other potential areas for Li-exploration were missed while trying to increase the discrimination between the Li-pegmatite class and the Metasediments. This can

be related or accentuated by the low ratio between pegmatite size and the satellite image spatial resolution. This issue was vastly explained in previous studies [7,32]. Another major concern in ML and deep learning (DL) remote sensing applications is the ability to transfer learning between case studies [52]. Unfortunately, there is no current solution for this problem, but in this study, we wanted to ensure that the improved methodology and SVM optimization could be applied to other datasets and study areas. To achieve this goal, the first stage grid-search was optimized to discriminate the target area from the host-rocks. Thus, when applying to another area, the operator should adapt the source code available in Section 2 of Supplementary Materials, to create a personalized metric score concerning the Li-bearing pegmatite and the existing host-rocks. In this metric score, a *beta* coefficient can be added to the F1-score, thus creating an F-beta score that allows the operator to adjust the relative importance of precision and recall, according to characteristics of the study area.

6. Conclusions

In this study, untraditional approaches were developed and employed to improve SVM performance in Li-pegmatite mapping. Several kernelized and non-kernelized SVM's models with different parameter ranges were trained to find the optimal model. Overall, the objectives of this work were accomplished, and the research questions proposed were addressed with the new methodological advances proposed:

1. To overcome and avoid overfitting, a new splitting strategy based on the regions of interest (ROIs) was developed and applied with success to create the training and test subsets.
2. The choice of an adequate metric score proved to be essential not only in the parameter optimization but also in the model evaluation step. To maximize the discrimination between the target (Li-pegmatites) and the host rocks, a customized metric score was created for the first stage grid-search with CV.
3. A semi-automatized process allowed to choose the best model among several options. However, a blind automatization of the SVM classification is not yet possible, since the intervention of the operator is fundamental at the beginning of the model training and parameterization.
4. The methodological adjustments proposed in this study improved the previously obtained results with SVM for the same study area, by reducing model overfitting and improving the discrimination between Li-pegmatites and their host-rock. The best model found with the semi-automatized process was the one built with the RBF kernel and using the class-weight option to account for imbalanced data.
5. Contrary to the results obtained by other authors, this study shows that the class imbalance had a negative impact on the SVM performance, and the adaptations made to account for the imbalanced nature of the data were crucial for successfully delineating Li-pegmatite occurrences.
6. On the other hand, the qualitative assessment of the SVM models' performance highlighted the success and potential of the methodology in the identification of known Li-pegmatite occurrences beyond those used for training. Other target areas for Li-exploration were also delineated using the RBF-SVM model.
7. The main limitation found was that some smaller pegmatite occurrences and other potential areas for Li-exploration were missed while trying to optimize class separability and reduce overfitting. Therefore, the right balance between increasing the separability of Li-pegmatite/host-rocks and minimizing false negatives needs to be found. This can be achieved with higher resolution satellite images. Different ML algorithms can also be compared.
8. Furthermore, the methodological optimization made in this study already provides tools to personalize and help generalize its application to other locations. This approach could also be modified to map remotely other types of pegmatites containing important mineral commodities like rare elements and gemstones.

Despite the encountered limitations, these results still represent a major contribution to the state of art regarding the use of ML in Li-pegmatite mapping. Moreover, the newly developed methodological approach can be very helpful for the exploration/mining industry, since the ability to remotely map mineralized pegmatites can reduce the costs of exploration campaigns while increasing the social acceptance of mineral exploration through the use of more conscientious environmental practices.

Supplementary Materials: The source code developed in this study is available online at http://www.mdpi.com/2072-4292/12/14/2319/s1, Section 1: Splitting the data into training and test subsets; Section 2: First stage grid-search; Section 3: Second stage grid-search, model evaluation and image prediction.

Author Contributions: All the authors conceived and designed the experiments; J.C.-F. performed the experiments and conducted the research; all the authors analyzed the data; J.C.-F. wrote the paper; A.C.T., A.L., and E.R.-R. revised the paper. All authors have read and agreed to the published version of the manuscript.

Funding: The authors would like to thank the financial support provided by FCT—Fundação para a Ciência e a Tecnologia, I.P., with the ERA-MIN/0001/2017—LIGHTS project. The work was also supported by National Funds through the FCT project UIDB/04683/2020—ICT (Institute of Earth Sciences). Joana Cardoso-Fernandes is financially supported within the compass of a Ph.D. Thesis, ref. SFRH/BD/136108/2018, by national funds from MCTES through FCT, and co-financed by the European Social Fund (ESF) through POCH—Programa Operacional Capital Humano. The Spanish Ministerio de Ciencia, Innovacion y Universidades (Project RTI2018-094097-B-100, with ERDF funds) and the University of the Basque Country (UPV/EHU) (grant GIU18/084) also contributed economically.

Acknowledgments: The authors would like to thank N. Pires (University of Porto) for helping with Python coding.

Conflicts of Interest: The authors declare no conflict of interest. The funders had no role in the design of the study; in the collection, analyses, or interpretation of data; in the writing of the manuscript, or in the decision to publish the results.

Appendix A

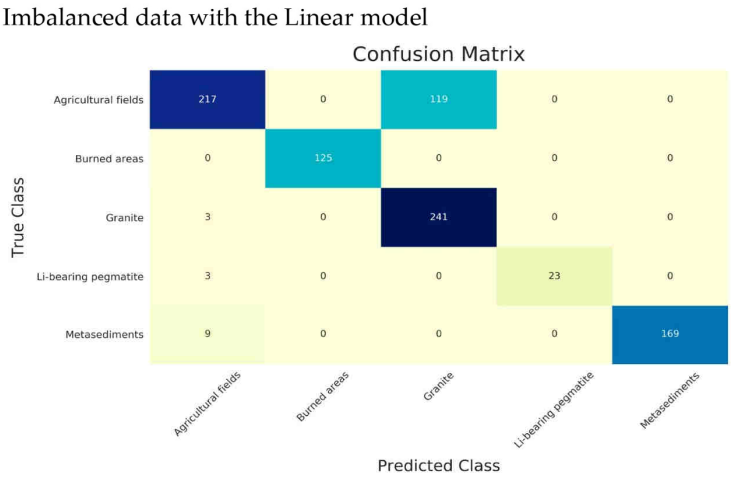

Figure A1. Confusion matrix for the Linear-SVM model built on the imbalanced dataset.

References

1. Cardoso-Fernandes, J.; Teodoro, A.C.; Lima, A. Potential of Sentinel-2 data in the detection of lithium (Li)-bearing pegmatites: A study case. In Proceedings of the SPIE Remote Sensing, Berlin, Germany, 10–13 September 2018; p. 15.
2. Cardoso-Fernandes, J.; Teodoro, A.C.; Lima, A. Remote sensing data in lithium (Li) exploration: A new approach for the detection of Li-bearing pegmatites. *Int. J. Appl. Earth Obs. Geoinf.* **2019**, *76*, 10–25. [CrossRef]

3. Perrotta, M.M.; Souza Filho, C.R.; Leite, C.A.S. Mapeamento espectral de intrusões pegmatíticas relacionadas a mineralizações de lítio, gemas e minerais industriais na região do vale do Jequitinhonha (MG) a partir de imagens ASTER. In Proceedings of the Anais do XII Simpósio Brasileiro de Sensoriamento Remoto, Goiânia, Brazil, 16–21 April 2005; pp. 1855–1862.
4. Mendes, D.; Perrotta, M.M.; Costa, M.A.C.; Paes, V.J.C. Mapeamento espectral para identificação de assinaturas espectrais de minerais de lítio em imagens ASTER (NE/MG). In Proceedings of the Anais do XVIII Simpósio Brasileiro de Sensoriamento Remoto, Santos-SP, Brazil, 28–29 May 2017; pp. 5273–5280.
5. Cardoso-Fernandes, J.; Teodoro, A.C.; Lima, A.; Roda-Robles, E. Evaluating the performance of support vector machines (SVMs) and random forest (RF) in Li-pegmatite mapping: Preliminary results. In Proceedings of the SPIE Remote Sensing, Strasbourg, France, 9–12 September 2019.
6. Santos, D.; Teodoro, A.; Lima, A.; Cardoso-Fernandes, J. Remote sensing techniques to detect areas with potential for lithium exploration in Minas Gerais, Brazil. In Proceedings of the SPIE Remote Sensing, Strasbourg, France, 9–12 September 2019.
7. Cardoso-Fernandes, J.; Teodoro, A.C.; Lima, A.; Perrotta, M.; Roda-Robles, E. Detecting Lithium (Li) Mineralizations from Space: Current Research and Future Perspectives. *Appl. Sci.* **2020**, *10*, 1785. [CrossRef]
8. Yu, L.; Porwal, A.; Holden, E.-J.; Dentith, M.C. Towards automatic lithological classification from remote sensing data using support vector machines. *Comput. Geosci.* **2012**, *45*, 229–239. [CrossRef]
9. De Boissieu, F.; Sevin, B.; Cudahy, T.; Mangeas, M.; Chevrel, S.; Ong, C.; Rodger, A.; Maurizot, P.; Laukamp, C.; Lau, I.; et al. Regolith-geology mapping with support vector machine: A case study over weathered Ni-bearing peridotites, New Caledonia. *Int. J. Appl. Earth Obs. Geoinf.* **2018**, *64*, 377–385. [CrossRef]
10. Othman, A.A.; Gloaguen, R. Improving Lithological Mapping by SVM Classification of Spectral and Morphological Features: The Discovery of a New Chromite Body in the Mawat Ophiolite Complex (Kurdistan, NE Iraq). *Remote Sens.* **2014**, *6*, 6867–6896. [CrossRef]
11. Latifovic, R.; Pouliot, D.; Campbell, J. Assessment of Convolution Neural Networks for Surficial Geology Mapping in the South Rae Geological Region, Northwest Territories, Canada. *Remote Sens.* **2018**, *10*, 307. [CrossRef]
12. Gasmi, A.; Gomez, C.; Zouari, H.; Masse, A.; Ducrot, D. PCA and SVM as geo-computational methods for geological mapping in the southern of Tunisia, using ASTER remote sensing data set. *Arab. J. Geosci.* **2016**, *9*, 753. [CrossRef]
13. Zuo, R.; Carranza, E.J.M. Support vector machine: A tool for mapping mineral prospectivity. *Comput. Geosci.* **2011**, *37*, 1967–1975. [CrossRef]
14. Abedi, M.; Norouzi, G.-H.; Bahroudi, A. Support vector machine for multi-classification of mineral prospectivity areas. *Comput. Geosci.* **2012**, *46*, 272–283. [CrossRef]
15. Rodriguez-Galiano, V.; Sanchez-Castillo, M.; Chica-Olmo, M.; Chica-Rivas, M. Machine learning predictive models for mineral prospectivity: An evaluation of neural networks, random forest, regression trees and support vector machines. *Ore Geol. Rev.* **2015**, *71*, 804–818. [CrossRef]
16. Geranian, H.; Tabatabaei, S.H.; Asadi, H.H.; Carranza, E.J.M. Application of Discriminant Analysis and Support Vector Machine in Mapping Gold Potential Areas for Further Drilling in the Sari-Gunay Gold Deposit, NW Iran. *Nat. Resour. Res.* **2016**, *25*, 145–159. [CrossRef]
17. Mountrakis, G.; Im, J.; Ogole, C. Support vector machines in remote sensing: A review. *ISPRS J. Photogramm. Remote Sens.* **2011**, *66*, 247–259. [CrossRef]
18. Maxwell, A.E.; Warner, T.A.; Fang, F. Implementation of machine-learning classification in remote sensing: An applied review. *Int. J. Remote Sens.* **2018**, *39*, 2784–2817. [CrossRef]
19. Noi, P.T.; Kappas, M. Comparison of Random Forest, k-Nearest Neighbor, and Support Vector Machine Classifiers for Land Cover Classification Using Sentinel-2 Imagery. *Sensors* **2017**, *18*, 18. [CrossRef]
20. Roda, E. Distribución, Caracteristicas y Petrogenesis de las Pegmatitas de La Fregeneda (Salamanca). Ph.D. Thesis, UPV/EHU, Bilbao, Spain, 1993.
21. Roda-Robles, E.; Pesquera, A.; Velasco, F.; Fontan, F. The granitic pegmatites of the Fregeneda area (Salamanca, Spain): Characteristics and petrogenesis. *Miner. Mag.* **1999**, *63*, 535–558. [CrossRef]
22. Vieira, R. Aplitopegmatitos com elementos raros da região entre Almendra (V.N. de Foz Côa) e Barca d'Alva (Figueira de Castelo Rodrigo). Campo aplitopegmatítico da Fregeneda- Almendra. Ph.D. Thesis, Faculdade de Ciências da Universidade do Porto, Porto, Portugal, 2010.

23. Costa, J.C.S.D. *Notícia sobre uma carta geológica do Buçaco, de Nery Delgado*; Serviços Geológicos de Portugal: Lisboa, Portugal, 1950.
24. Teixeira, C. *Notas sobre geologia de Portugal o complexo xisto-grauváquico ante-ordoviciano*; Empresa Literaria Fluminense Lda.: Lisboa, Portugal, 1955; p. 48.
25. Roda-Robles, E.; Vieira, R.; Pesquera, A.; Lima, A. Chemical variations and significance of phosphates from the Fregeneda-Almendra pegmatite field, Central Iberian Zone (Spain and Portugal). *Miner. Pet.* **2010**, *100*, 23–34. [CrossRef]
26. Silva, A.F.d.; Rebelo, J.A.; Ribeiro, M.L. *Notícia Explicativa da folha 11-C Torre de Moncorvo*; Serviços Geológicos de Portugal: Lisboa, Portugal, 1989; p. 65.
27. Silva, A.F.d.; Ribeiro, M.L. *Notícia Explicativa da folha 15-A Vila Nova de Foz Côa*; Serviços Geológicos de Portugal: Lisboa, Portugal, 1991; p. 52.
28. Vapnik, V.N. *The Nature of Statistical Learning Theory*; Springer: New York, NY, USA, 1995.
29. Knerr, S.; Personnaz, L.; Dreyfus, G. Single-layer learning revisited: A stepwise procedure for building and training a neural network. In *Neurocomputing*; Soulié, F.F., Hérault, J., Eds.; Springer: Berlin/Heidelberg, Germany, 1990; pp. 41–50.
30. Cortes, C.; Vapnik, V. Support-vector networks. *Mach. Learn.* **1995**, *20*, 273–297. [CrossRef]
31. Géron, A. *Hands-On Machine Learning with Scikit-Learn and TensorFlow: Concepts, Tools, and Techniques to Build Intelligent Systems*; O'Reilly Media, Inc.: Sebastopol, CA, USA, 2017; p. 568.
32. Cardoso-Fernandes, J.; Lima, A.; Roda-Robles, E.; Teodoro, A.C. Constraints and potentials of remote sensing data/techniques applied to lithium (Li)-pegmatites. *Can. Miner.* **2019**, *57*, 723–725. [CrossRef]
33. Missions: Sentinel-2. Available online: https://sentinel.esa.int/web/sentinel/missions/sentinel-2 (accessed on 20 April 2020).
34. MultiSpectral Instrument (MSI) Overview. Available online: https://sentinel.esa.int/web/sentinel/technical-guides/sentinel-2-msi/msi-instrument (accessed on 20 April 2020).
35. Sentinel-2 MSI: Products and Algorithms. Available online: https://sentinel.esa.int/web/sentinel/technical-guides/sentinel-2-msi/products-algorithms (accessed on 20 April 2020).
36. SNAP. Available online: https://step.esa.int/main/toolboxes/snap/ (accessed on 20 April 2020).
37. Google Earth Pro. Available online: https://www.google.com/intl/en_uk/earth/desktop/ (accessed on 3 August 2018).
38. Esri World Imagery. Available online: https://www.arcgis.com/home/item.html?id=10df2279f9684e4a9f6a7f08febac2a9 (accessed on 9 May 2019).
39. Geomatica 2018. Available online: https://www.pcigeomatics.com/ (accessed on 12 July 2019).
40. Geomatica Help. Available online: http://www.pcigeomatics.com/geomatica-help/ (accessed on 23 April 2019).
41. Pedregosa, F.; Varoquaux, G.; Gramfort, A.; Michel, V.; Thirion, B.; Grisel, O.; Blondel, M.; Prettenhofer, P.; Weiss, R.; Dubourg, V.; et al. Scikit-learn: Machine Learning in Python. *J. Mach. Learn. Res.* **2012**, *12*, 2825–2830.
42. 1.4. Support Vector Machines—Scikit-Learn 0.20.4 Documentation. Available online: https://scikit-learn.org/0.20/modules/svm.html#svm-classification (accessed on 24 April 2020).
43. Oommen, T.; Misra, D.; Twarakavi, N.K.C.; Prakash, A.; Sahoo, B.; Bandopadhyay, S. An Objective Analysis of Support Vector Machine Based Classification for Remote Sensing. *Math. Geosci.* **2008**, *40*, 409–424. [CrossRef]
44. Müller, A.C.; Guido, S. Chapter 5. Model Evaluation and Improvement. In *Introduction to Machine Learning with Python: A Guide for Data Scientists*; Schanafelt, D., Ed.; O'Reilly Media, Inc.: Sebastopol, CA, USA, 2016; pp. 251–303.
45. Story, M.; Congalton, R. Accuracy assessment: A user's perspective. *Photogramm. Eng. Remote Sens.* **1986**, *52*, 397–399.
46. Congalton, R.G. A review of assessing the accuracy of classifications of remotely sensed data. *Remote Sens. Environ.* **1991**, *37*, 35–46. [CrossRef]
47. Cohen, J. A Coefficient of Agreement for Nominal Scales. *Educ. Psychol. Meas.* **1960**, *20*, 37–46. [CrossRef]
48. Cracknell, M.J.; Reading, A.M.; McNeill, A.W. Mapping geology and volcanic-hosted massive sulfide alteration in the Hellyer–Mt Charter region, Tasmania, using Random Forests™ and Self-Organising Maps. *Aust. J. Earth Sci.* **2014**, *61*, 287–304. [CrossRef]

49. Pal, M.; Mather, P.M. Support vector machines for classification in remote sensing. *Int. J. Remote Sens.* **2005**, *26*, 1007–1011. [CrossRef]
50. He, H.; Garcia, E.A. Learning from Imbalanced Data. *IEEE Trans. Knowl. Data Eng.* **2009**, *21*, 1263–1284. [CrossRef]
51. Melgani, F.; Bruzzone, L. Classification of hyperspectral remote sensing images with support vector machines. *IEEE Trans. Geosci. Remote Sens.* **2004**, *42*, 1778–1790. [CrossRef]
52. Li, Y.; Zhang, H.; Xue, X.; Jiang, Y.; Shen, Q. Deep learning for remote sensing image classification: A survey. *Wiley Interdiscip. Rev. Data Min. Knowl. Discov.* **2018**, *8*, e1264. [CrossRef]

© 2020 by the authors. Licensee MDPI, Basel, Switzerland. This article is an open access article distributed under the terms and conditions of the Creative Commons Attribution (CC BY) license (http://creativecommons.org/licenses/by/4.0/).

data

MDPI

Data Descriptor

Tools for Remote Exploration: A Lithium (Li) Dedicated Spectral Library of the Fregeneda–Almendra Aplite–Pegmatite Field

Joana Cardoso-Fernandes [1,2,*], João Silva [1], Filipa Dias [1,2], Alexandre Lima [1,2], Ana C. Teodoro [1,2], Odile Barrès [3], Jean Cauzid [3], Mônica Perrotta [4], Encarnación Roda-Robles [5] and Maria Anjos Ribeiro [1,2]

[1] Department of Geosciences, Environment and Spatial Plannings, Faculty of Sciences, University of Porto, Rua Campo Alegre, 4169-007 Porto, Portugal; jpc.silva1996@gmail.com (J.S.); filipa.dias@fc.up.pt (F.D.); allima@fc.up.pt (A.L.); amteodor@fc.up.pt (A.C.T.); maribeir@fc.up.pt (M.A.R.)
[2] ICT (Institute of Earth Sciences)—Porto Pole (Portugal), Rua Campo Alegre, 4169-007 Porto, Portugal
[3] CNRS, GeoRessources Laboratory, Université de Lorraine, F-54000 Nancy, France; odile.barres@univ-lorraine.fr (O.B.); jean.cauzid@univ-lorraine.fr (J.C.)
[4] Remote Sensing and Mineral Spectroscopy Laboratory, Geological Survey of Brazil (CPRM), Rua Costa, 55, São Paulo 01304-010, Brazil; monica.perrotta@cprm.gov.br
[5] Departamento de Geología, Universidad del País Vasco (UPV/EHU), Barrio Sarriena, Leioa, 48940 Bilbao, Spain; encar.roda@ehu.es
* Correspondence: joana.fernandes@fc.up.pt

check for updates

Citation: Cardoso-Fernandes, J.; Silva, J.; Dias, F.; Lima, A.; Teodoro, A.C.; Barrès, O.; Cauzid, J.; Perrotta, M.; Roda-Robles, E.; Ribeiro, M.A. Tools for Remote Exploration: A Lithium (Li) Dedicated Spectral Library of the Fregeneda–Almendra Aplite–Pegmatite Field. *Data* **2021**, *6*, 33. https://doi.org/10.3390/data6030033

Academic Editor: Vladimir Sreckovic

Received: 3 March 2021
Accepted: 14 March 2021
Published: 16 March 2021

Publisher's Note: MDPI stays neutral with regard to jurisdictional claims in published maps and institutional affiliations.

Copyright: © 2021 by the authors. Licensee MDPI, Basel, Switzerland. This article is an open access article distributed under the terms and conditions of the Creative Commons Attribution (CC BY) license (https://creativecommons.org/licenses/by/4.0/).

Abstract: The existence of diagnostic features in the visible and infrared regions makes it possible to use reflectance spectra not only to identify mineral assemblages but also for calibration and classification of satellite images, considering lithological and/or mineral mapping. For this purpose, a consistent spectral library with the target spectra of minerals and rocks is needed. Currently, there is big market pressure for raw materials including lithium (Li) that has driven new satellite image applications for Li exploration. However, there are no reference spectra for petalite (a Li mineral) in large, open spectral datasets. In this work, a spectral library was built exclusively dedicated to Li minerals and Li pegmatite exploration through satellite remote sensing. The database includes field and laboratory spectra collected in the Fregeneda–Almendra region (Spain–Portugal) from (i) distinct Li minerals (spodumene, petalite, lepidolite); (ii) several Li pegmatites and other outcropping lithologies to allow satellite-based lithological mapping; (iii) areas previously misclassified as Li pegmatites using machine learning algorithms to allow comparisons between these regions and the target areas. Ancillary data include (i) sample location and coordinates, (ii) sample conditions, (iii) sample color, (iv) type of face measured, (v) equipment used, and for the laboratory spectra, (vi) sample photographs, (vii) continuum removed spectra files, and (viii) statistics on the main absorption features automatically extracted. The potential future uses of this spectral library are reinforced by its major advantages: (i) data is provided in a universal file format; (ii) it allows users to compare field and laboratory spectra; (iii) a large number of complementary data allow the comparison of shape, asymmetry, and depth of the absorption features of the distinct Li minerals.

Dataset: http://doi.org/10.5281/zenodo.4575375.

Dataset License: CC-BY.

Keywords: reflectance spectroscopy; spectrometer; geological exploration; remote sensing; pegmatite; lithium

1. Summary

The use of reflectance spectroscopy to identify minerals through diagnostic absorption features in the visible and infrared regions has been described by several authors in recent

decades [1–4]. Due to these diagnostic features, the acquired mineral spectra can be employed in several knowledge-based satellite image classification approaches to delineate target areas for mineral occurrences [5,6]. Moreover, field spectra allows ground-checking of the remotely sensed data (e.g., [7–9]) and validation of the atmospheric corrections made to satellite images.

The recent growing economic importance of lithium (Li), mainly due to its application in batteries for electric cars, has triggered several attempts to use satellite images to target the occurrence of Li minerals and Li pegmatites [10–14]. Reference spectra for some of the most important Li minerals, such as spodumene and lepidolite, can be found in the United States Geological Survey (USGS) [15] and ECOSTRESS [16] spectral libraries. Nonetheless, there are no reference spectra for petalite in these open domain spectral libraries. The Geological Survey of Brazil (CPRM) has been trying to address this issue by compiling a spectral database with a Li minerals' dedicated section, but so far the petalite diagnostic features have not been identified [17].

To fill in this gap and to complement the development of image classification algorithms for Li exploration, a spectral database was built in this work based on samples collected in the Fregeneda–Almendra aplite–pegmatite field (Figure 1). In this region, spodumene, petalite, and lepidolite minerals occur in evolved pegmatites [18,19] that intruded metasedimentary rocks belonging to the "Complexo Xisto–Grauváquico" (CXG) [20].

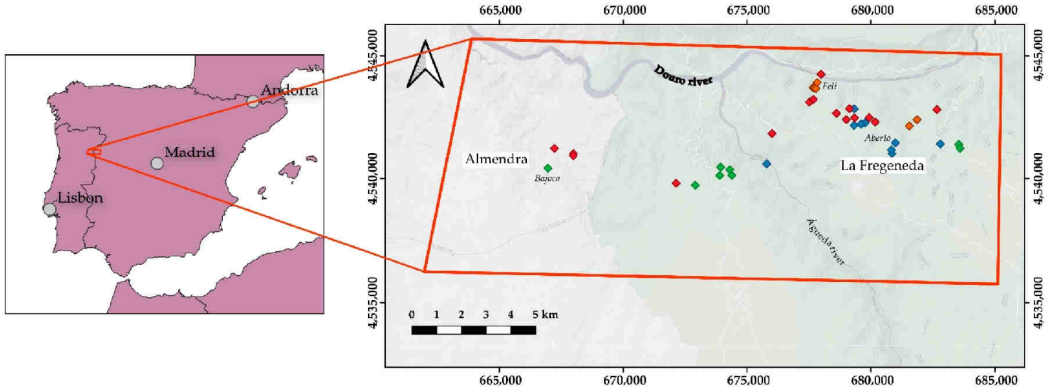

Figure 1. Location of the Fregeneda–Almendra pegmatite field in the Iberian Peninsula. Diamonds represent pegmatites containing Li minerals: green–petalite; blue–spodumene; red–lepidolite; orange–spodumene + lepidolite [18,19]. The map projection is Universal Transverse Mercator zone 29N from the WGS84 datum.

The spectral library is composed of field and laboratory spectra not only of Li minerals (spodumene, petalite, lepidolite) but also from the main outcropping lithologies of the Fregeneda–Almendra area (granitoid rocks, CXG metasediments, Li pegmatite). These rock spectra were mainly acquired in areas of good exposition so they could be used as training areas for satellite-based lithological mapping. Additionally, to allow further investigation on the ability to discriminate Li minerals and Li pegmatites from other lithologies, the spectra from areas misclassified as Li pegmatites using machine learning algorithms [13] are also provided. The comparison of the aforementioned data can allow users to evaluate the degree of spectral similarity between the target minerals/rocks and the remaining within-scene elements.

Complementary data such as (i) the sample location and coordinates (when available), (ii) degree of alteration of the sample, (iii) sample color, (iv) type of face measured, and (v) equipment used, are provided for each spectrum. Spectra acquisition and curation are described thoroughly. For the laboratory spectra, also available are (i) sample photographs,

(ii) respective continuum removed spectra files, and (iii) details on the main absorption features automatically extracted.

This spectral database was established in the ambit of the "Lightweight Integrated Ground and Airborne Hyperspectral Topological Solution" (LIGHTS) project, whose goal is to develop a tool that combines remote sensing data acquired at different scales with geological and geochemical data to rapidly identify target areas for Li exploration [21,22]. However, such a database could be useful for other ongoing research projects, namely: (i) the fiber laser plasma spectroscopy system for real-time element analysis (FLaPsys) project, which aims at developing an advanced spectroscopy system capable of real-time element identification and quantification mainly applied to Li mineralizations [23], and in which laser-induced breakdown spectroscopy (LIBS) will be correlated with the visible and infrared data acquired; (ii) new exploration tools for a European pegmatite green-tech resources (GREENPEG) project which aims at improving responsible exploration in Europe for pegmatites through the development of integrated, multi-method exploration toolsets that include satellite image processing and airborne and ground-based geophysics and geochemical approaches [24]. Part of this spectral database was already the basis for some publications [25,26], but more works are expected in the future since there is great potential in this dataset whose main advantages include: (i) that the data are provided in a universal text file format that is not dependent on software; (ii) the ability to compare field and laboratory spectra for 52 coincident spots; (iii) finally, the details and statistics of the extracted features provided allow the user to compare the shape, asymmetry, and depth of the absorption features of the distinct Li minerals, including petalite.

2. Data Description

The spectral database is divided into two subsets; the first concerning the spectra collected in the laboratory and the second corresponding to the spectra acquired in the field. The spectra were organized into categories within each subset according to their application purpose (Table 1). To allow a rapid and easy identification of the spectra, the spectrum naming was made considering logical codes embedded in the spectrum title (Table 1). Consequently, information such as the location of the sample and analyzed lithology/mineralogy can be readily extracted based just on the spectrum name. Besides the codes of Table 1, each spectrum has its associated measurement number.

Table 1. String, numerical, and alphanumerical codes used for spectrum naming and identification.

	Code	Observation
Purpose of the sample	L	Li mineral database
	TA	Training areas
	SC	Spectral confusion (represents false positive areas)
Lithology	G	Granitoid rock
	LP	Li pegmatite
	M	Metasedimentary rock
Mineralogy	Lep	Lepidolite
	Pet	Petalite
	Spd	Spodumene
Location	AL	Almendra
	ALB	Alberto open pit mine
	BJ	Bajoca open pit mine
	FE	Feli open pit mine
	FG	Fregeneda
	HD	Hinojosa de Duero
	999	3-digit numbers represent the GPS point number
Multiple samples	A1 to An	Code given to distinct hand samples collected at the same location (where n = number of samples)
Equipment used	sr	SR-6500 (Spectral Evolution, Inc., Haverhill, MA, USA)
	asd	FieldSpec 4 (ASD, Inc., untsville, AL, USA)
Other	f	Spectra collected in the field under real conditions

All spectra are provided in a universal UTF-8 text file format that can be read in any proprietary or open-source software, representing measurements made in the visible and near-infrared (VNIR) and shortwave infrared (SWIR) regions. From a total of 340 spectra collected in the laboratory, 84 represent Li minerals, 196 correspond to the outcropping lithologies of the Fregeneda–Almendra area that can be used as training areas for satellite image classification, and 60 spectra were collected from samples in Li pegmatite false-positive areas identified in previous satellite image classification attempts [13]. Additionally, 75 field spectra are presented in the spectral database (35 measurements of Li minerals and 40 measurements of distinct Li pegmatites). As mentioned in Table 1, two spectrometers were used for spectral measurements. For the data acquired with the SR-6500 equipment, the UTF-8 text files are composed of a 28 line-header containing information about the equipment and acquisition settings and two columns, the first with the wavelength (in nanometers or nm) and the second with the measured reflectance (in percentage). In the case of the spectra acquired with the ASD FieldSpec 4, there are just two columns, one with the wavelength (in nm) and the other with absolute reflectance values. For each subset (field and laboratory spectra) there is a *.xlsx table containing important ancillary data:

- Spectrum name
- Acquisition equipment
- Sample type
- Sample conditions
- Sample face type
- Sample color
- Location
- Coordinates (Universal Transverse Mercator zone 29N from the WGS84 datum).

The coordinates are only available for samples collected in situ and, therefore, samples collected in ore stockpiles (for example) do not have this kind of information registered. For the spectra acquired in the laboratory, additional information is also provided, namely: (i) sample photographs with the analyzed spots highlighted, (ii) a UTF-8 text file with the respective continuum removed spectra (with absolute reflectance values); (iii) PNG files showing for each spectrum the main absorption features and a CSV file summarizing the main statistics of each feature (Section 3.2).

3. Methods

3.1. Spectra Acquisition

Two field campaigns were carried out in February and July of 2020 to collect the data to build the spectral library. At the time of the first campaign, there was no portable spectrometer available in the University of Porto to collect spectra in situ, therefore representative samples from 25 locations were taken to the GeoRessources laboratory (University of Lorraine). The spectral measurements were performed with the SR-6500 equipment. Due to difficulties in accessing pegmatites containing spodumene on the field, samples from an existing Li mineral collection at the University of Porto were also analyzed. In the second field survey, favorable weather conditions (absence of clouds) allowed collection of spectra from several Li pegmatites and the different Li minerals in 35 locations dispersed along the Fregeneda–Almendra pegmatite field. In this case, the ASD FieldSpec 4 spectrometer was used. Samples were retrieved in 28 of these 35 locations to collect further spectra under a controlled environment at the University of Porto, using the same equipment. Either in the field or the laboratory, the two spectrometers were calibrated using a Spectralon (Labsphere) plate with a maximum reflectance higher than 95% for the 250–2500 nm region, and higher than 99% for 400–1500 nm interval. In the field, the calibration was repeated every time the solar lighting conditions changed (about each 30′). Regarding the acquisition settings, to improve the signal-to-noise ratio, each of the spectra acquired in the laboratory represented the average of 40 scans. To expedite spectra acquisition in the field, this value was lowered to 30 scans. However, when using the ASD FieldSpec 4 equipment, five spectra were acquired in each analyzed spot. These five

spectra were averaged afterward (Section 3.2) and only the final spectrum was provided in the spectral library. The characteristics of each spectrometer are compared in Table 2. The major differences are observed in terms of the spectral resolution with the SR-6500 outperforming the ASD FieldSpec 4.

Table 2. Comparison of the main characteristics of the employed spectrometers [27,28].

	Spectral Evolution SR-6500	**ASD FieldSpec 4**
Spectral Range	350–2500 nm Ultra-High Resolution	350–2500 nm Standard resolution
Spectral Resolution	1.5 nm @ 700 nm 3.0 nm @ 1500 nm 3.8 nm @ 2100 nm	3 nm @ 700 nm 10 nm @ 1400 nm 10 nm @ 2100 nm
Spectral sampling (bandwidth)	1 nm increments	1.4 nm @ 350–1000 nm 1.1 nm @ 1001–2500 nm
Wavelength reproducibility	0.1 nm	0.1 nm
Wavelength accuracy	0.5 nm	0.5 nm
Channels	2151	2151
Detectors	1024 element TE-cooled silicon photodiode array detector (VNIR) 512 element TE-cooled InGaAs photodiode array detector (SWIR 1) 512 element TE-cooled extended InGaAs photodiode array detector (SWIR 2)	VNIR detector: 512 element silicon array SWIR 1 detector: Graded Index InGaAs Photodiode, Two-Stage TE Cooled SWIR 2 detector: Graded Index InGaAs Photodiode, Two-Stage TE Cooled
Noise Equivalent Radiance (NEdL)	0.8×10^{-9} W/cm^2/nm/sr @ 400 nm 0.3×10^{-9} W/cm^2/nm/sr @ 1500 nm 5.8×10^{-9} W/cm^2/nm/sr @ 2100 nm	1.0×10^{-9} W/cm^2/nm/sr @ 700 nm 1.2×10^{-9} W/cm^2/nm/sr @ 1400 nm 1.9×10^{-9} W/cm^2/nm/sr @ 2100 nm
Weight	4.99 kg (11 pounds)	5.44 kg (12 lbs)
Contact probe	Internal light source: Halogen bulb: 4.25 V, 1.06 A Spot size: 10 mm	Internal light source: Halogen bulb: 12–18 V, 6.5 W Spot size: 10 mm Natural lighting
Field pistol grip	—	Spot size as a function of distance to the sample

3.2. Spectra Curation and Treatment

The spectra acquired with ASD FieldSpec 4 were post-processed using the ASD ViewSpec Pro™ software [29]. The first step included averaging each of the five spectra collected for each spot. To the averaged spectrum, a splice correction was applied to remove the offset between detectors that is caused by differences in their sensibility [29] (Figure 2). Finally, the final spectra were exported to UTF-8 text files. In the case of the spectra collected using the SR-6500, a simple conversion from SED to the UTF-8 text file was necessary. The SpectraGryph software [30] was used to analyze each spectrum individually to exclude the ones with measurement errors or with noticeable noise caused by the presence of vegetation, for example.

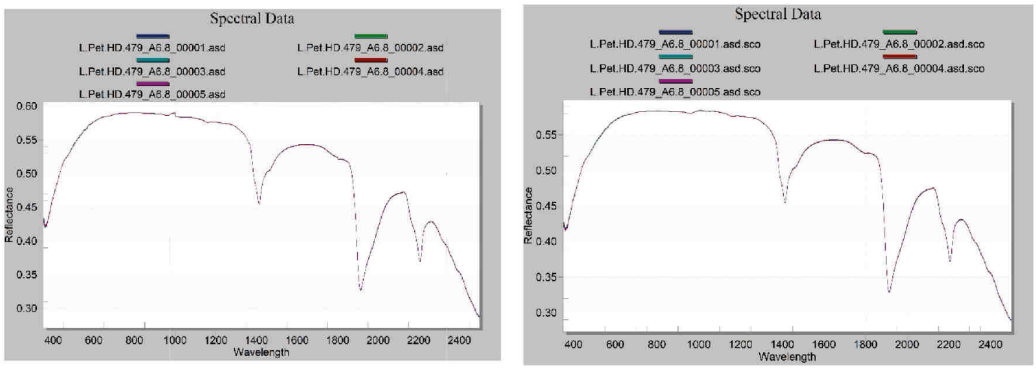

(**a**) (**b**)

Figure 2. Splice correction process: (**a**) before and (**b**) after applying the correction. The VNIR and SWIR2 ranges are adjusted using the endpoints (~1000 to 1800 nm) and shape of the curve of the SWIR1 range since this detector is more stable to temperature changes [29].

To allow a more detailed analysis of each spectrum, a hull quotient procedure was applied to remove the continuum and normalize the spectra (Figure 3). This was accomplished in a Python environment using the *pysptools* library [31] based on the technique proposed by Clark and Roush [2]. First, a convex hull was fitted to the spectrum (Figure 3a) connecting the hull points (corresponding to local maxima) [32]. Afterwards, the convex hull (continuum) was removed through a hull-quotient process and the measured reflectance values were divided by the convex hull [2,33,34]. The continuum removal process is of great importance because it not only allows the comparison of the data obtained with different spectrometers but also allows the enhancement and correct determination of the absorption features [32–34]. The *pysptools* library was used to automatically extract the main absorption features (Figure 3b–d) and to calculate their associated statistics according to the work of Kokaly [35]. To avoid the extraction of non-significant features, a baseline value of 0.93 was employed: all features below the baseline were kept and the ones above it were rejected [31] (Figure 3). For each spectrum, a CSV file was automatically created summarizing the statistics of each absorption feature. Table 3 shows a list of the extracted statistics and the respective abbreviation used in the CSV files. The Supplementary Materials provided shows the adaptation of the *pysptools* functions to batch process this particular spectral library.

Table 3. List of the statistics automatically extracted for each spectrum and respective abbreviations used in the resultant CSV file.

Abbreviation	Extracted Statistics
id	feature number
area	area
cstart_wvl	continuum start wavelength
cstop_wvl	continuum stop wavelength
cslope	continuum slope
abs_wvl	center wavelength
abs_depth	absorption depth
FWHM_delta	full-width at half maximum

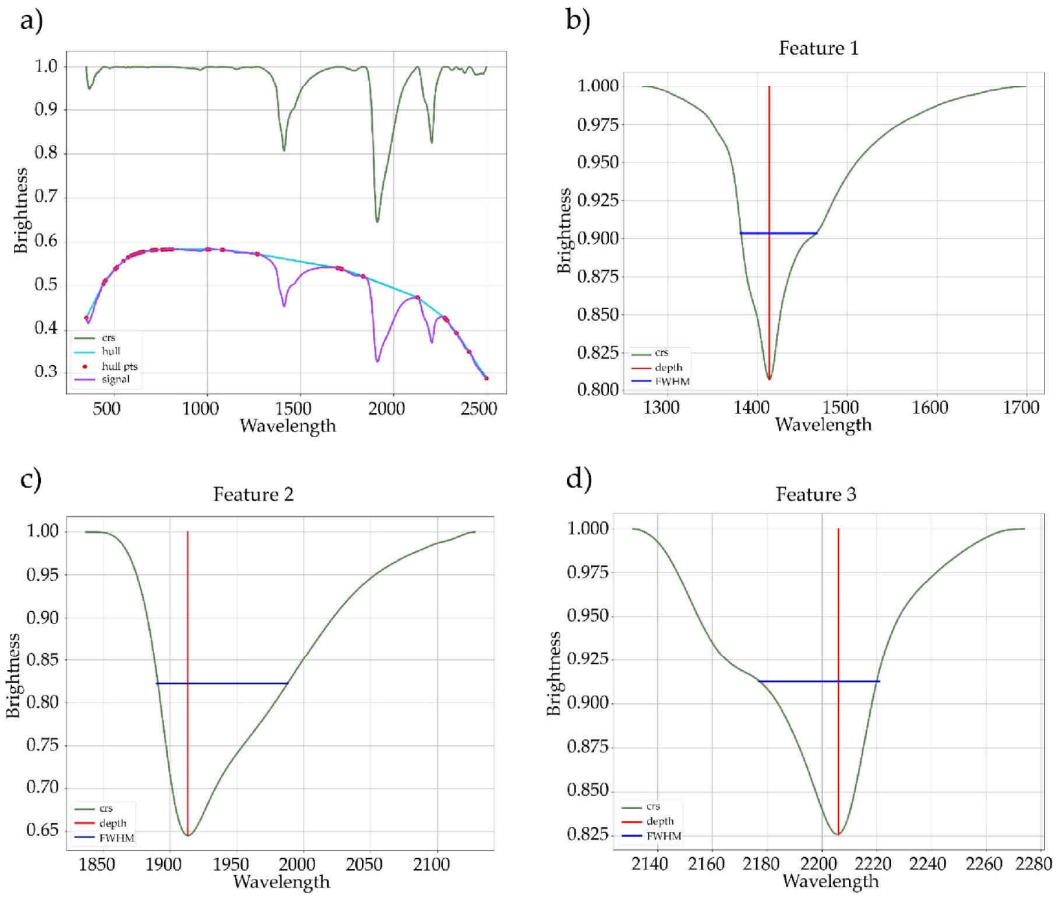

Figure 3. (**a**) Convex hull fitting to the original signal and the respective continuum removed spectrum (crs); (**b**–**d**) automatic extraction of the main absorption features using the *pysptools* library [31]. pts–points; FWHM–full width at half maximum.

4. User Notes

This spectral database has the advantage of presenting field and laboratory spectra for 52 analyzed spots, allowing comparisons and evaluation of the influence of the acquisition conditions on the final spectra. Additionally, field spectra are expected to better match the spectral signatures acquired by airborne sensors. However, as can be seen in Figure 4, field spectra present additional sharp bands around 1400 and 1800 nm caused by atmospheric water that should be removed before additional processing.

A final note on the usage of the automatically extracted features that are available for all spectra acquired in the laboratory. As aforementioned, a baseline value was set to determine which absorption features to extract. Therefore, setting a different baseline may produce different results and change the features' statistics. Additionally, different results can be obtained if the features are extracted considering the whole spectrum or spectra subset matching a given region of interest [34]. According to the user's objectives, one of the two methods may be more appropriate.

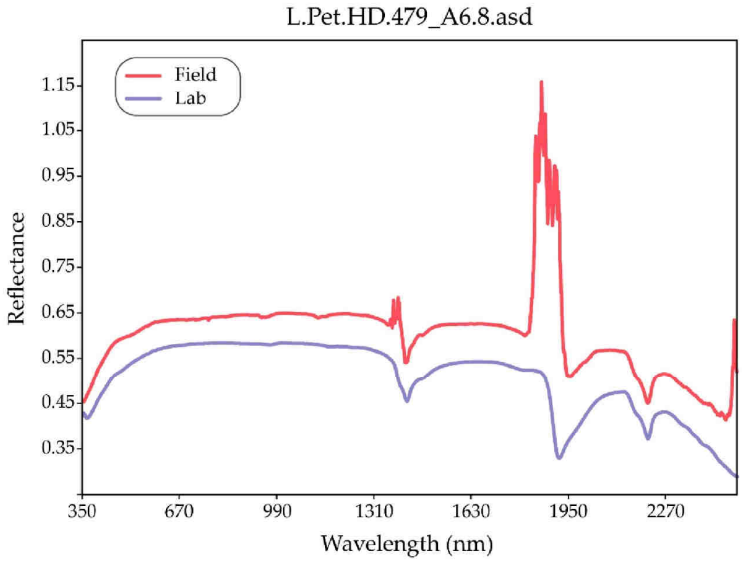

Figure 4. Comparison of laboratory and field spectra obtained for the same petalite sample. Notice the spikes in the field spectrum caused by the presence of water in the atmosphere.

Supplementary Materials: The source code adapted in this study to remove the continuum and automatically extract the main absorption features is available online at https://www.mdpi.com/2306-5729/6/3/33/s1.

Author Contributions: Conceptualization, J.C.-F., A.L., and A.C.T.; methodology, J.C.-F., A.L., and A.C.T.; software, J.C.-F.; formal analysis J.C.-F., J.S., M.P., and M.A.R.; investigation, J.C.-F., J.S., F.D., A.L., A.C.T., M.P., and M.A.R.; resources A.L., E.R.-R., O.B., and J.C.; data curation, J.C.-F., J.S., and F.D.; writing—original draft preparation, J.C.-F.; writing—review and editing, all remaining authors; visualization, J.C.-F., J.S., and F.D.; supervision, A.L., A.C.T., M.A.R., M.P., E.R.-R., and O.B.; project administration, J.C., A.L., and A.C.T.; funding acquisition, J.C. and A.L. All authors have read and agreed to the published version of the manuscript.

Funding: The authors are grateful for the financial support provided by FCT– Fundação para a Ciência e a Tecnologia, I.P., through the ERA-MIN/0001/2017–LIGHTS project and also the 869274–GREENPEG–H2020-SC5-2018-2019-2020 project. The work was also supported by National Funds through the FCT project UIDB/04683/2020–ICT (Institute of Earth Sciences). Joana Cardoso-Fernandes and Filipa Dias are financially supported within the compass of their respective Ph.D. theses, ref. SFRH/BD/136108/2018 and ref. 2020.05534.BD, by national funds from MCTES through FCT, and cofinanced by the European Social Fund (ESF) through POCH—Programa Operacional Capital Humano—and NORTE 2020 regional program. The Spanish Ministerio de Ciencia, Innovacion y Universidades (Project RTI2018-094097-B-100, with ERDF funds) and the University of the Basque Country (UPV/EHU) (grant GIU18/084) also contributed economically. The French National Research Agency (ANR–10–LABX 21–LABEX RESSOURCES 21) partly supported Master Student personal grant and the 776804–NEXT– H2020-SC5-2017 project participated to equipment purchase.

Data Availability Statement: The data presented in this study are publicly archived in the Zenodo platform: https://zenodo.org/record/4575375#.YFAgGNwRVPY (accessed on 16 March 2021).

Conflicts of Interest: The authors declare no conflict of interest.

Abbreviations

The following abbreviations are used in this manuscript:

CPRM	Geological Survey of Brazil
crs	continuum removed spectra
CSV	comma-separated values
CXG	Complexo Xisto–Grauváquico (Schist–graywacke complex)
FWHM	full-width at half maximum
Lab	laboratory
LIBS	laser-induced breakdown spectroscopy
Li	lithium
NEdL	noise equivalent radiance
PNG	portable network graphics
pts	points
SWIR	shortwave infrared
TE	thermoelectrically
USGS	United States Geological Survey
UTF	unicode transformation format
VNIR	visible and near-infrared
WGS	World Geodetic System

References

1. Hunt, G.R.; Salisbury, J.W. Visible and near-infrared spectra of minerals and rocks: I Silicate minerals. *Modern Geol.* **1970**, *1*, 283–300.
2. Clark, R.N.; Roush, T.L. Reflectance spectroscopy: Quantitative analysis techniques for remote sensing applications. *J. Geophys. Res. Space Phys.* **1984**, *89*, 6329–6340. [CrossRef]
3. Clark, R.N.; King, T.V.V.; Klejwa, M.; Swayze, G.A.; Vergo, N. High spectral resolution reflectance spectroscopy of minerals. *J. Geophys. Res. Space Phys.* **1990**, *95*, 12653–12680. [CrossRef]
4. Pontual, S.; Merry, N.J.; Gamson, P. Spectral interpretation field manual. In *GMEX Spectral Analysis Guides for Mineral Exploration*, 3rd ed.; AusSpec International Ltd.: Queenstown, New Zealand, 2008; Volume 1.
5. Asadzadeh, S.; Filho, C.R.D.S. A review on spectral processing methods for geological remote sensing. *Int. J. Appl. Earth Obs. Geoinf.* **2016**, *47*, 69–90. [CrossRef]
6. Naleto, J.L.C.; Perrotta, M.M.; da Costa, F.G.; Filho, C.R.D.S. Point and imaging spectroscopy investigations on the Pedra Branca orogenic gold deposit, Troia Massif, Northeast Brazil: Implications for mineral exploration in amphibolite metamorphic-grade terrains. *Ore Geol. Rev.* **2019**, *107*, 283–309. [CrossRef]
7. Pour, A.B.; Hashim, M. Hydrothermal alteration mapping from Landsat-8 data, Sar Cheshmeh copper mining district, south-eastern Islamic Republic of Iran. *J. Taibah Univ. Sci.* **2015**, *9*, 155–166. [CrossRef]
8. Teodoro, A.C.; Veloso-Gomes, F. Quantification of the Total Suspended Matter Concentration around the Sea Breaking Zone from In Situ Measurements and Terra/Aster Data. *Mar. Georesour. Geotechnol.* **2007**, *25*, 67–80. [CrossRef]
9. Rivard, B.; Zhang, J.; Feng, J.; Sanchez-Azofeifa, A.G. Remote predictive lithologic mapping in the Abitibi Greenstone Belt, Canada, using airborne hyperspectral imagery. *Can. J. Remote Sens.* **2009**, *35*, 95. [CrossRef]
10. Cardoso-Fernandes, J.; Teodoro, A.C.; Lima, A.; Perrotta, M.; Roda-Robles, E. Detecting Lithium (Li) Mineralizations from Space: Current Research and Future Perspectives. *Appl. Sci.* **2020**, *10*, 1785. [CrossRef]
11. Cardoso-Fernandes, J.; Teodoro, A.C.; Lima, A. Remote sensing data in lithium (Li) exploration: A new approach for the detection of Li-bearing pegmatites. *Int. J. Appl. Earth Obs. Geoinf.* **2019**, *76*, 10–25. [CrossRef]
12. Cardoso-Fernandes, J.; Lima, A.; Roda-Robles, E.; Teodoro, A.C. Constraints and potentials of remote sensing data/techniques applied to lithium (Li)-pegmatites. *Can. Mineral.* **2019**, *57*, 723–725. [CrossRef]
13. Cardoso-Fernandes, J.; Teodoro, A.C.M.; Lima, A.; Roda-Robles, E. Evaluating the performance of support vector machines (SVMs) and random forest (RF) in Li-pegmatite mapping: Preliminary results. In *Earth Resources and Environmental Remote Sensing/GIS Applications X*; SPIE: Bellingham, DC, USA, 2019; Volume 11156, p. 111560Q.
14. Cardoso-Fernandes, J.; Teodoro, A.C.; Lima, A.; Roda-Robles, E. Semi-Automatization of Support Vector Machines to Map Lithium (Li) Bearing Pegmatites. *Remote Sens.* **2020**, *12*, 2319. [CrossRef]
15. Kokaly, R.F.; Clark, R.N.; Swayze, G.A.; Livo, K.E.; Hoefen, T.M.; Pearson, N.C.; Wise, R.A.; Benzel, W.M.; Lowers, H.A.; Driscoll, R.L.; et al. *USGS Spectral Library Version 7, 1035*; USGS: Reston, VA, USA, 2017; p. 68.
16. Meerdink, S.K.; Hook, S.J.; Roberts, D.A.; Abbott, E.A. The ECOSTRESS spectral library version 1.0. *Remote Sens. Environ.* **2019**, *230*, 111196. [CrossRef]
17. Costa, M.A.C.; Perrotta, M.M.; Melo, T.G.; Turra, B. Estudos Espectrais. In *Avaliação do Potencial do Lítio no Brasil: Área do Médio Rio Jequitinhonha, Nordeste de Minas Gerais: Texto Explicativo e Mapas*; Paes, V.J.C., Santos, L.D., Tedeschi, M.F., Betiollo, L.M., Eds.; CPRM: Belo Horizonte, Brazil, 2016; p. 276.

18. Roda, E.; Fontan, F.; Pesquera, A.; Velasco, F. The phosphate mineral association of the granitic pegmatites of the Fregeneda area (Salamanca, Spain). *Mineral. Mag.* **1996**, *60*, 767–778. [CrossRef]
19. Vieira, R. Aplitopegmatitos com Elementos Raros da Região Entre Almendra (V.N. de Foz Côa) e Barca d'Alva (Figueira de Castelo Rodrigo). Campo Aplitopegmatítico da Fregeneda-Almendra. Ph.D. Thesis, Faculdade de Ciências da Universidade do Porto, Porto, Portugal, 2010.
20. Costa, J.C.S. *Notícia Sobre uma Carta Geológica do Buçaco, de Nery Delgado*; Serviços Geológicos de Portugal: Lisboa, Portugal, 1950.
21. LIGHTS (Lightweight Integrated Ground and Airborne Hyperspectral Topological Solution). Available online: http://lights.univ-lorraine.fr/ (accessed on 9 November 2020).
22. Cardoso-Fernandes, J.; Teodoro, A.C.; Lima, A.; Mielke, C.; Korting, F.; Roda-Robles, E.; Cauzid, J. Multi-Scale Approach using Remote Sensing Techniques for Lithium Pegmatite Exploration: First Results. *IGARSS* **2020**, 5226–5229. [CrossRef]
23. PROJECTS: FLAPSYS. Available online: https://www.inesctec.pt/pt/projetos/flapsys (accessed on 9 November 2020).
24. GREENPEG. Available online: https://www.greenpeg.eu/ (accessed on 9 November 2020).
25. Cardoso-Fernandes, J.; Silva, J.; Lima, A.; Teodoro, A.C.; Perrotta, M.; Cauzid, J.; Roda-Robles, E. Characterization of lithium (Li) minerals from the Fregeneda–Almendra region through laboratory spectral measurements: A comparative study. In *Earth Resources and Environmental Remote Sensing/GIS Applications XI*; SPIE: Bellingham, DC, USA, 2020; Volume 11534, p. 115340N.
26. Cardoso-Fernandes, J.; Silva, J.; Lima, A.; Teodoro, A.C.; Perrotta, M.; Cauzid, J.; Roda-Robles, E.; Ribeiro, M.D.A. Reflectance spectroscopy to validate remote sensing data/algorithms for satellite-based lithium (Li) exploration (Central East Portugal). In *Earth Resources and Environmental Remote Sensing/GIS Applications XI*; SPIE: Bellingham, DC, USA, 2020; Volume 11534, p. 115340M.
27. Full Range Photodiode Array UV-VIS-NIR-SWIR. Available online: https://spectralevolution.com/products/hardware/compact-lab-spectroradiometers/ (accessed on 5 November 2020).
28. ASD FieldSpec 4 Standard-Res Spectroradiometer. Available online: https://www.malvernpanalytical.com/en/products/product-range/asd-range/fieldspec-range/fieldspec-4-standard-res-spectroradiometer#specs (accessed on 5 November 2020).
29. ASD Inc. ViewSpec Pro™ User Manual. ASD Document 600555 Rev. A. Boulder, 2008. Available online: http://geoinfo.amu.edu.pl/geoinf/m/spektr/viewspecpro.pdf (accessed on 4 November 2020).
30. Menges, F. Spectragryph Optical Spectroscopy Software, Version 1.2.14. Available online: http://www.effemm2.de/spectragryph/ (accessed on 22 July 2020).
31. Therien, C. Welcome to the PySptools Documentation. Available online: https://pysptools.sourceforge.io/ (accessed on 22 July 2020).
32. Van Der Meer, F. Spectral curve shape matching with a continuum removed CCSM algorithm. *Int. J. Remote Sens.* **2000**, *21*, 3179–3185. [CrossRef]
33. Carrino, T.A.; Crósta, A.P.; Toledo, C.L.B.; Silva, A.M. Hyperspectral remote sensing applied to mineral exploration in southern Peru: A multiple data integration approach in the Chapi Chiara gold prospect. *Int. J. Appl. Earth Obs. Geoinf.* **2018**, *64*, 287–300. [CrossRef]
34. Continuum Removal. Available online: https://www.l3harrisgeospatial.com/docs/ContinuumRemoval.html (accessed on 6 November 2020).
35. Kokaly, R.F. PRISM: Processing Routines in IDL for Spectroscopic Measurements (Installation Manual and User's Guide, Version 1.0); 2011-1155; Reston, VA, 2011. Available online: https://pubs.usgs.gov/of/2011/1155/pdf/ofr2011-1155-17oct2011.pdf (accessed on 6 November 2020).

data

MDPI

Data Descriptor

Analyses of Li-Rich Minerals Using Handheld LIBS Tool

Cécile Fabre [1,*], Nour Eddine Ourti [1], Julien Mercadier [1], Joana Cardoso-Fernandes [2,3], Filipa Dias [2,3], Mônica Perrotta [4], Friederike Koerting [5], Alexandre Lima [2,3], Friederike Kaestner [5], Nicole Koellner [5], Robert Linnen [6], David Benn [6], Tania Martins [7] and Jean Cauzid [1]

1 Geosciences Department, GeoRessources CNRS-Université de Lorraine, BP 70239, 54506 Vandoeuvre-les-Nancy, France; Nour-eddine.ourti@univ-lorraine.fr (N.E.O.); julien.mercadier@univ-lorraine.fr (J.M.); jean.cauzid@univ-lorraine.fr (J.C.)
2 Department of Geosciences, Environment and Spatial Plannings, Faculty of Sciences, University of Porto, Rua Campo Alegre, 4169-007 Porto, Portugal; joana.fernandes@fc.up.pt (J.C.-F.); filipa.dias@fc.up.pt (F.D.); allima@fc.up.pt (A.L.)
3 ICT (Institute of Earth Sciences)–Porto pole (Portugal), Rua Campo Alegre, 4169-007 Porto, Portugal
4 Remote Sensing Division, Geological Survey of Brazil (CPRM), Rua Costa, São Paulo 01304-010, Brazil; monica.perrotta@cprm.gov.br
5 Helmholtz Centre Potsdam, GFZ, 14473 Potsdam, Germany; koerting@gfz-potsdam.de (F.K.); klos@gfz-potsdam.de (F.K.); nicolek@gfz-potsdam.de (N.K.)
6 Department of Earth Sciences, University of Western Ontario, BGS 1000B, London, ON N6A 5B7, Canada; rlinnen@uwo.ca (R.L.); dbenn2@uwo.ca (D.B.)
7 Manitoba Geological Survey, 360-1395 Ellice Avenue, Winnipeg, MB R3G 3P2, Canada; Tania.Martins@gov.mb.ca
* Correspondence: cecile.fabre@univ-lorraine.fr

check for updates

Citation: Fabre, C.; Ourti, N.E.; Mercadier, J.; Cardoso-Fernandes, J.; Dias, F.; Perrotta, M.; Koerting, F.; Lima, A.; Kaestner, F.; Koellner, N.; et al. Analyses of Li-Rich Minerals Using Handheld LIBS Tool. *Data* **2021**, *6*, 68. https://doi.org/10.3390/data6060068

Academic Editor: Vladimir Sreckovic

Received: 2 April 2021
Accepted: 17 June 2021
Published: 21 June 2021

Publisher's Note: MDPI stays neutral with regard to jurisdictional claims in published maps and institutional affiliations.

Copyright: © 2021 by the authors. Licensee MDPI, Basel, Switzerland. This article is an open access article distributed under the terms and conditions of the Creative Commons Attribution (CC BY) license (https://creativecommons.org/licenses/by/4.0/).

Abstract: Lithium (Li) is one of the latest metals to be added to the list of critical materials in Europe and, thus, lithium exploration in Europe has become a necessity to guarantee its mid- to long-term stable supply. Laser-induced breakdown spectroscopy (LIBS) is a powerful analysis technique that allows for simultaneous multi-elemental analysis with an excellent coverage of light elements ($Z < 13$). This data paper provides more than 4000 LIBS spectra obtained using a handheld LIBS tool on approximately 140 Li-content materials (minerals, powder pellets, and rocks) and their Li concentrations. The high resolution of the spectrometers combined with the low detection limits for light elements make the LIBS technique a powerful option to detect Li and trace elements of first interest, such as Be, Cs, F, and Rb. The LIBS spectra dataset combined with the Li content dataset can be used to obtain quantitative estimation of Li in Li-rich matrices. This paper can be utilized as technical and spectroscopic support for Li detection in the field using a portable LIBS instrument.

Dataset: https://doi.org/10.24396/ORDAR-65.

Dataset License: CC-BY

Keywords: lithium; LIBS; handheld tool; exploration; Li-mineral

1. Summary

Since the emergence of laser-induced breakdown spectroscopy (LIBS) [1,2], it has been utilized in numerous geological studies. This is due to the large range of potentially detected elements, which makes it a promising technique for the future. For a better overview, one can read the numerous papers and reviews on the applications of LIBS for geological purposes [3–18]. One may recall that the Perseverance rover on Mars, similar to the previous Curiosity rover, uses the LIBS technique (with the ChemCam and SuperCam instruments, respectively). Since 2012, the ChemCam tool has provided several thousand LIBS analyses on Martian soils and rocks for the geological interpretation of the Gale crater [19–23]. The SuperCam instrument, which arrived on Mars in February 2021, has

already obtained remote LIBS–Raman–VNIR analyses of calibration targets and Martian rocks and soils [24–26].

More recently, portable LIBS tools have been widely used for the analysis of rocks, minerals, economic elements, and light elements [18,27–34]. Although quantitative data are mainly obtained from metal studies [30,35], for more complex materials such as geological mineral mixtures or rocks, standards and calibrations need to be designed to obtain consistent data when using the LIBS technique and, thus, the handheld LIBS tools [6,17,36–43]. The LIGHTS (Lightweight Integrated Ground and airborne Hyperspectral Topological Solutions) project aims at facilitating the exploration of new lithium (Li) resources, which mainly consist of pegmatites (http://lights.univ-lorraine.fr accessed on 1 May 2021). One of the richest regions in Europe is in Northern Portugal and North-Western Spain. These outcrops were specially selected to test the simultaneous acquisition of hyperspectral imaging data (HSI) and in situ analyses using handheld tools (LIBS, VNIR, SWIR). The project is dedicated to recognizing the most favorable targets from remotely sensed data and immediately following these up with ground measurements. In fact, by avoiding lab interpretation after the remote sensing work and the ground-truthing, the duration of exploration processes could be considerably shortened. This would require near real-time data processing based on chemometrics and artificial intelligence [44,45]. One previous data paper reported the acquisition of VNIR and SWIR spectra in the field from outcrops and various reference minerals [46] within the same project. As the LIBS handheld tool provides fast identification of trace elements, i.e., Li (Figure 1); here we aimed to establish the calibration curve of Li content in different matrices. These univariate calibrations can be used in LIBS applications [42,47–52].

(**a**) (**b**)

Figure 1. (**a**) Full portable LIBS operating on a pegmatite outcrop; some of the detected elements and the LIBS spectra can be seen on the screen; (**b**) transfer of the data from the Z300 to the laptop using the Profile Builder interface.

2. Data Description

The database mainly includes laboratory LIBS spectra obtained from homogeneous Li-bearing minerals such as spodumene ($LiAlSi_2O_6$), petalite ($LiAlSi_4O_{10}$), amblygonite or montebrasite ($LiAl(PO_4)(F,OH)$), lepidolite ($K_2(Li,Al)_{5\text{-}6}(Si_{6\text{-}7}Al_{2\text{-}1}O_{20})(OH,F)_4$), zinnwaldite ($KLiFeAl(AlSi_3)O_{10}(OH,F)_2$), and altered Li minerals [53]. Various LIBS analyses

were also directly performed on Li-rich pegmatites at fresh outcrops in the field in Portugal by our Portuguese colleagues [46,54,55]. LIBS analyses were additionally performed on different powder pellets (obtained from the FAME project) and glasses made up of crushed powders from homogenized minerals. These samples (pellets and glasses) were specially tested to check the potential matrix effect that occurs during plasma formation and its emission.

In this study, 134 samples were analyzed using the handheld LIBS tool, covering the main minerals investigated during the LIGHTS project. In order to help the users of our dataset, the Li concentrations of minerals, calculated using bulk analysis such as ICP-OES, are available on the LIBS_database_file.csv with other important information, such as (i) the name of sample/spectra; (ii) sample matrix: mineral/rock, pressed pellet, synthetic glass; (iii) mineralogy if known; (iv) main trace elements detected by LIBS; (v) number of point analysis (mean number of available spectra) by sample; (vi) Li concentration (%). A first description of the samples is reported in the Table 1.

Table 1. Description of the samples with their providers, their geological origin if known, and matrix. More information is available in the LIBS_database_file (.csv) (see data reference).

Partners	Samples	Minerals
Université de Lorraine, France	Rocks, minerals, glasses, pellets	Lepidolite, spodumene, Kunzite, petalite, hindenite
University of Western Ontario and MGS, Canada	Rocks, thin sections, glass	Lepidolite, spodumene, petalite
Geological Service of Brazil, Brazil	Rocks	Spodumene, amblygonite
GFZ, Germany	Powders	Li-rich pegmatite

According to the rock mineralogy, the number of LIBS spectra acquired in each area (higher than 45) is sufficient to provide consistent data that reveal the mean composition of the rock. The relationship between the granulometry of the rock and the LIBS analyses is detailed in [17,56]. Thus, all the LIBS spectra presented in this data paper are representative of each composition. The relative standard deviations that were obtained from the different samples, and particularly for the lithium emission peaks, were between 7% for the powder pellets and 15% for the minerals. Previous studies have already reported the potential of handheld LIBS for lithium applications [18,32,57].

2.1. Format of the LIBS Spectra Files

Concerning data acquisition, the spectra can be directly displayed on the portable tool just after the analyses and the mean spectra are provided on the Profile Builder (internal software). These LIBS data (spectra) can be exported from the device to the user's computer by opening the communication between the LIBS and the computer (USB connection or Wi-Fi). Different options are possible such as raw LIBS spectra, mean raw spectra, or all individual and/or mean spectra calibrated in wavelength. Here, two different kinds of spectra, obtained after cleaning the laser shots to avoid any dust contamination, are available in this dataset (as downloaded from the LIBS tool):

(i) Firstly, 4362 LIBS files correspond to the raw LIBS spectra with no processing treatment; thus, each spectra value corresponds to a point (corresponding to several laser shots) on the samples. These spectra values are not calibrated in wavelengths; thus, the identification of the elements is difficult due to potential shifts in nm as a result of the detectors. The raw spectra correspond to the LIBS spectra obtained at each point, are recorded in csv format, and they correspond to three columns: the first for pixels, the second for the wavelengths, and the last for the intensity (arbitrary intensity, counts on the detector), with the column titles being "pixel", "wavelength", and "intensity". For the raw data, the initial format was built as IDmineral_yearmonthday_hour_PM_Spectrumnumber_PixelData.csv. These spectra can be downloaded from seven separate folders with explicit names that

correspond to the providers and/or matrices (i.e., Univ. Lorraine, Canada, Brazil, GFZ, thin sections, powders, etc.). The open access website of ORDaR (OTELo Research Data Repository) is https://doi.org/10.24396/ORDAR-65 (accessed on 21 June 2021).

(ii) Secondly, 369 average LIBS spectra values calculated for each area are available. It should be highlighted that these LIBS spectra were directly recorded from the handheld LIBS tool and the spectra were calibrated in wavelength in order to facilitate element identification (as the element peaks are very narrow) by adding artificial pixels. The LIBS mean spectra values also correspond to .csv files. These calibrated spectra are the mean spectra obtained at several points, and they correspond to two columns: the first for wavelengths and the second for the intensity (arbitrary intensity, counts on the detector), with the column titles being "wavelength" and "intensity". The initial format was built as IDmineral_yearmonthday_hour_AM_AverageSpectrum.csv; for the spectra associated with the analysis number, IDmineral_yearmonthday_hour_PM_Spectrumnumber.csv was used. In this study, the AverageSpectrum.csv was always kept for the major part of the spectra, and the beginning of the filename corresponds to the mineral ID. A typical name of these spectra is "IDMineral_20190417_041453_PM_AverageSpectrum" with the ID mineral at the beginning, the YearMonthDay_hourminutesecond time of the acquisition, and the notification of the AverageSpectrum. These spectra can be downloaded from the LIBS LIBS_spectra_DATAPAPER.zip.

2.2. Mineral Samples

The sample collection is composed of 128 minerals (spodumene ($LiAlSi_2O_6$), petalite ($LiAlSi_4O_{10}$), amblygonite ($LiAl(PO_4)(F,OH)$), lepidolite ($K_2(Li,Al)_{5\text{-}6}(Si_{6\text{-}7}Al_{2\text{-}1}O_{20})(OH,F)_4$), zinnwaldite ($KLiFeAl(AlSi_3)O_{10}(OH,F)_2$)), and rock samples: 51 samples correspond to outcrop minerals/rocks from the Fregenda–Almendra pegmatite field, 30 minerals correspond to reference minerals from official suppliers, personal collections, or partners (MGS, Univ. Ontario, Suffel Collection, GeoRessources), and 41 LIBS spectra located on 24 different thick sections (provided by Univ. Ontario) correspond to individual minerals analyzed using LIBS. Nine rock samples were provided by Monica Perrotta from the Brazilian Geological Survey.

2.3. Thin Rock Sections

The analyzed thin rock sections (1 cm × 2 cm × 0.5 mm) correspond to muscovite samples where LA-ICP-MS analyses (individual points) on different micas were already performed, and the LIBS analysis was performed to compare the two techniques (not presented in this paper). In these minerals, the main elements detected using LIBS were obviously Al, Si, Mg, K, Na, Fe, Ca, and Li, but numerous trace elements were also detected such as Cs, Rb, Ta, Be, and Sr [58].

2.4. Powder Pellets

One portion of the samples corresponds to powder pellets with low Li content. One portion of the powders was provided by the FAME project (from the lepidolite pegmatite of Gonçalo in Portugal (GLi and TPR samples)), and the other portion of the pellets was from Bajoca outcrop rocks (the location can be found on the Bajoca_sample_location.csv file). These powders are less enriched in lithium than the Li-mineral samples. The particulate size of the powders used for the pellets was approximately 150 ± 10 µm. The powders were poured into steel molds with a diameter of 26 mm and a thickness of 2 mm to be finally compacted under 6.5 ton cm^{-2} for 1 min, since a pressure below 3 ton cm^{-2} can disturb the LIBS intensities [31,59].

2.5. Best Conditions for LIBS Analysis

Solid samples are more suitable for LIBS, and marked asperities on the sample surface can lead to a loss of ablation and problems with the plasma emission. However, for classical LIBS element detection, the signal is usually sufficient for identification even if

the sample is not strictly flat (for the scale of the window 3 mm × 4 mm). For quantitative applications, a strict flatness is required, which can be compensated for by normalization if the matrix is the same [36,40,42]. If bulk estimation is the aim of the study, samples must be homogeneous at the laser beam scale (or on the area analyzed by several laser shots). The granulometry of the rock is the most critical point to be investigated before any geochemical interpretation, especially for analyses performed on micrometric areas (μLIBS, μXRF, Raman, VNIR, etc.). Multiplying the number of analyses on the rock is required in order to obtain the bulk composition [17,39,56]. Crushed and homogenized samples can be investigated by making pressed pellets. LIBS analysis is slightly destructive with an ablated layer of several to dozens of micrometers per laser shot depending on the smoothness of the material. As a series of laser shots is usually emitted, the sample thickness should be a minimum of 40 micrometers (corresponding to common thin rock sections). Finely grained samples may be homogeneous enough and provide good data but there is no way of knowing if there is a hidden feature below the sample surface, shallow enough to contribute to the signal. As such, confidence in results from such samples is not at the level it would be for homogenized ones.

3. Methods

3.1. Laser-Induced Breakdown Spectroscopy Technique

More information can be obtained through various specific papers as regards the spectroscopic aspects of the LIBS technique and its application in geology and more recently on Martian soil and rock ChemCam analyses [2,3,17,23,29,34,60]. The portable LIBS tool has a very safe design and avoids any laser operating in the air, allowing the geologists to perform analyses safely in the field. A pre-ablation shot at very low intensity is always emitted and if low or no plasma emission is detected, the device automatically stops. These devices now rely on Li batteries, which may require transportation authorization when traveling by road, boat, or plane. The batteries are usually below the threshold for road transportation. They should, however, be declared for boat or plane trips. The normal regulation, based on risk mitigation, is to avoid transporting Li batteries in the hold and to keep them with the traveler. A maximum number of batteries per traveler may be imposed by the transport company.

3.2. LIBS Spectra Acquisition (Z300 Instrument)

All LIBS spectra acquisitions were obtained using one unique handheld instrument (Z300 SciAps © instruments). Depending on the samples and the size of the minerals, the number of mean spectra values acquired can be from 3 to 5 different analyzed zones corresponding to 9 and 15 points, respectively. Thus, the most relevant information regarding acquisition is available in the LIBS_Database_file.csv file.

3.2.1. Laser Parameters and Ablation

When using the portable Z300 LIBS instrument, the parameters of the laser cannot be modified. For Z300 analyses, the characteristics for all the spectra were 5–6 mJ/pulse, 10 Hz repetition rate for the analysis and for the cleaning shot, and a 1064 nm pulsed Nd-YAG laser source. The use of laser ablation allows one to "clean" the first micrometers of the surface to avoid any dust contamination. Here, we used cleaning mode firing and made only one laser cleaning shot that was not recorded.

3.2.2. Wavelength Range of the Detectors

LIBS analysis does not require a prerequisite of the detected elements, and their detection only depends on the wavelength. Here, Z300 provides an extended spectrometer range from 190 to 950 nm, allowing for the detection of the major and trace elements present in the rocks such as F, N, O, Br, Cl, Rb, Cs, and S.

3.2.3. Number of Measurements

The Z300 tool provides an image of the sample through a camera to optimize the correct location of the sampled points. As repeating the measurement can improve the error bars, a 2D raster of 15 points can be used to obtain a kind of bulk content. Therefore, the laser is fired in discreet increments in two dimensions (X-Y) with a number of points/locations depending on the samples.

- For Li minerals, which were reported as reference minerals and analyzed in GeoRessources laboratory of Université de Lorraine, the LIBS rasters were centered along a three points by five points rectangle with four laser shots at each point (with one laser cleaning shot to avoid any dust contamination). This grid was duplicated for each sample and 30 LIBS spectra were obtained to mimic a bulk composition. Then, the mean average LIBS spectra values were recorded and they corresponded to the database reported here (258 mean spectra). To ensure that we were on a non-altered mineral, the selected zones were based on the selection of the most color-homogenized zone observed on the entire sample (larger than 3 mm square). This protocol was also followed for the bulk analysis.
- For powder pellets, which were realized at GeoRessources and analyzed there, the grid was three points by three points with five laser shots at each point (one cleaning laser shot). Five different random locations were studied and 45 LIBS spectra were recorded. For this data paper, each LIBS reference spectrum on each pellet corresponds to the mean LIBS of 45 spectra (Figure 2).

Figure 2. (**a**) Schematic representation of the analytical protocol for the LIBS analysis on powder pellets, with the five different random zones, nine points for each; (**b**) images of powder pellets with random areas of analysis; the nine craters can be seen as a square, and the crater size is around 100 µm due to the smoothness of the material.

3.2.4. Atmosphere and Time Gating Measurement

All of the LIBS analyses were performed under ambient air added to a constant argon purge (13 mPsi), yielding enhancement in signal particularly for emissions in the deep UV (190 to 300 nm). Here, concerning the temporal conditions of the plasma analysis, the delay time was fixed as follows: the beginning of the acquisition of the LIBS emission was

400 ns and the acquisition time window was fixed to 1 ms. Then, in case of molecular recombination during the plasma emission (such as CaF or AlO), the large bands could be detected [31,61]. For the LIBS acquisition parameters, no file can be downloaded directly, but the information is available on the panel control of the Profile Builder interface.

3.3. LIBS Spectra Analysis

The reading and the interpretation of the LIBS spectra can be done using the Profile Builder for the recognition of the detected element emission lines. It is possible to explore the spectra and to normalize the spectra to the total area if necessary (in the case of a change in the ablated volume, point by point), and it is possible to obtain the net intensity under the peaks to provide a calibration curve directly using the Profile Builder software after defining standards. All the detected and non-detected elements can be downloaded in a .csv format if necessary. Various different software programs can be used to treat the spectra or to establish calibration curves [36,43]. In the following for example, we use SpectraGryph (http://spectroscopy.ninja, accessed on 1 May 2021).

3.3.1. Detected Elements

The major elements detected by the handheld LIBS tool for all the minerals mainly corresponded to Al, Si, O, Mg, Ca, Li, Na, K, and Fe (Figure 3). Minor and trace elements depending on the mineral origins, such as Be, Sr, Ba, Cs, Sn, Cs, Ta, W, etc., were also identified in numerous LIBS spectra provided in this database. The main trace elements detected in these Li-rich materials are reported in the LIBS_database_file.csv. The reference emission lines can also be obtained online from various websites and, for example, from the NIST LIBS database (https://physics.nist.gov/PhysRefData/ASD/LIBS/libs-form.html, accessed on 1 May 2021).

3.3.2. Spectra Treatment

For the LIBS spectra treatment, a qualitative comparison between different samples can be performed by looking at the peak areas under the selected emission with an individual baseline. The relative standard deviations obtained for the Li emission lines were approximately 18% for the Li minerals and 13% for the pellets. These values can be linked to the heterogeneity of the rocks, to their granulometry regarding the beam size of the laser (approximately 50 µm), and to a possible change in the ablated volume point by point. Ratios between different emission lines can also be proposed for comparison. A careful selection of the emission spectra for such a treatment is necessary to avoid any overlapping of other emission lines or saturation of the detector. The use of the mean value obtained from various spectra is preferred in order to provide a bulk vision of the elements detected in the minerals. When bulk analysis is available or if the concentration of the element in the sample can be obtained, a calibration curve can be established to obtain the contents of unknown samples, associating each analyzed area with its element content [43]. Normalization of the LIBS spectra (for example, normalization to the entire spectra or using the standard normal variate (SNV) method) can also be performed if the matrices are very different from each other in terms of chemistry or hardness [17,40]. Multivariate techniques can also be applied to the LIBS spectra to classify the samples or to obtain calibration curves of the different elements [62–64].

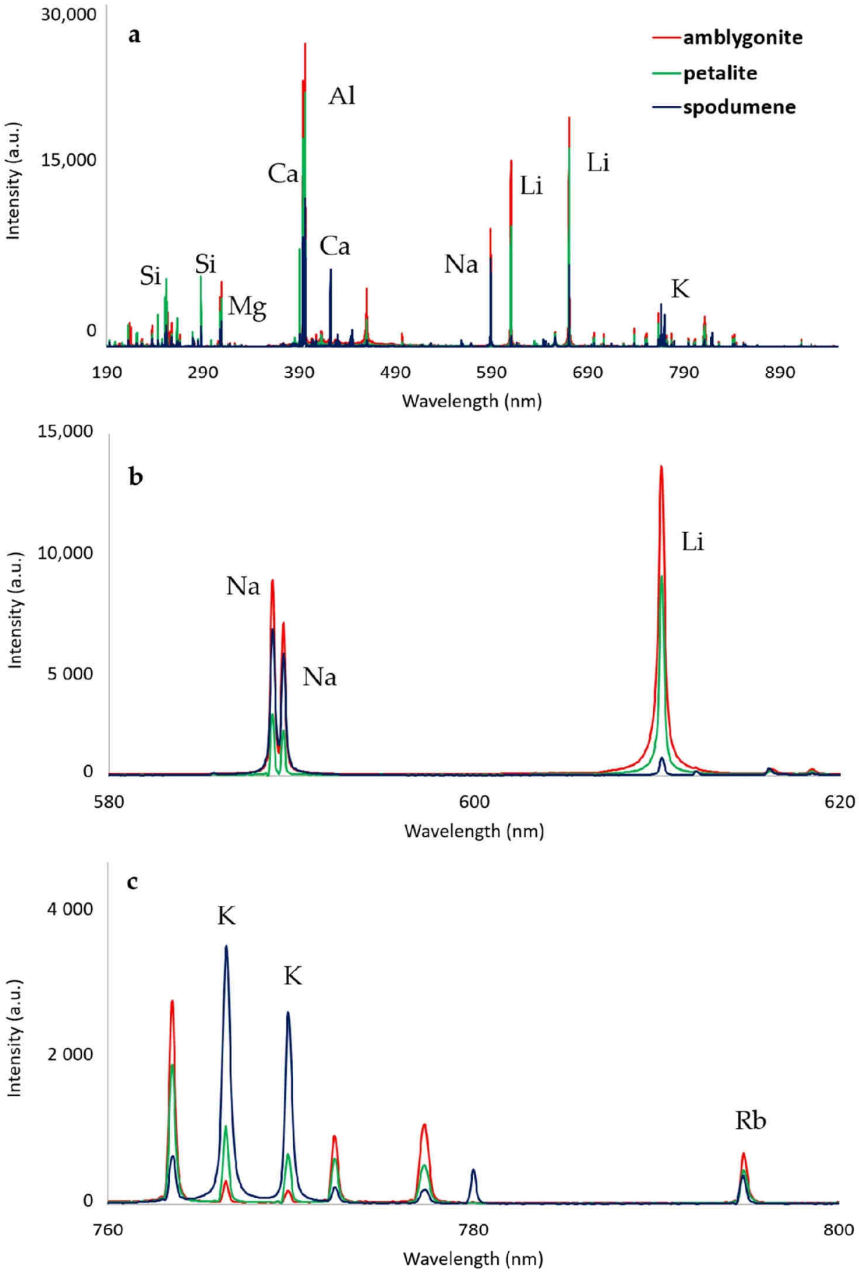

Figure 3. LIBS spectra obtained from different Li-rich minerals: amblygonite (4371-ambly-PF-M-0031-A2_2_20191), petalite (4183-peta-LB-R-0013-A_3_2019112), and spodumene (Boa-RS-Spo-M_20190417_043329_PM). (**a**) Spectra in the entire wavelength range; (**b**) zoomed image of the Na doublet and Li emission lines; (**c**) zoomed image of the K and Rb emissions lines from the VNIR. The major element emission lines are shown on the spectra; the LIBS spectra are not normalized.

Author Contributions: Conceptualization, C.F. and J.C.; methodology, C.F., N.E.O., and J.C.; validation, C.F. and N.E.O.; formal analysis, N.E.O., J.C.-F., and C.F.; investigation, C.F.; resources, A.L., M.P., F.K. (Friederike Kaestner), N.K., F.K. (Friederike Koerting), J.C.-F., R.L., T.M., D.B., and J.M.; data curation, C.F. and N.E.O.; writing—original draft preparation, C.F.; writing—review and editing, C.F., N.E.O., F.K. (Friederike Koerting), and J.C.-F.; visualization, C.F.; supervision, C.F. and J.C.; project administration, J.C.; funding acquisition, J.C.; F.D. contributed to the Resources of this paper. All authors have read and agreed to the published version of the manuscript.

Funding: This research was funded by the ERA-MIN/0001/2017–LIGHTS project. The work was also supported by Portuguese National Funds through the FCT– Fundação para a Ciência e a Tecnologia, I.P., project UIDB/04683/2020-ICT (Institute of Earth Sciences). Joana Cardoso-Fernandes and Filipa Dias are financially supported within the compass of their respective Ph.D. Theses, ref. SFRH/BD/136108/2018 and ref. 2020.05534.BD, by national funds from MCTES through FCT, and co-financed by the European Social Fund (ESF) through POCH–Programa Operacional Capital Humano–and NORTE 2020 regional program.

Institutional Review Board Statement: Not applicable.

Informed Consent Statement: Not applicable.

Data Availability Statement: All of the files mentioned on this study can be found in open access at the following address: https://doi.org/10.24396/ORDAR-65 (accessed on 21 June 2021).

Acknowledgments: We acknowledge Robert Linnen for his synthetized glasses and also Tania Martin and Marc Binnen for their mineral investigation. We thank the Suffel Collection, department of Ontario, for providing some of the Li-rich minerals. We acknowledge SciAps Company for technical support. Pierre-Yves Arnould is acknowledged for his technical support for ORDaR (OTELo Research Data Repository) website.

Conflicts of Interest: The authors declare no conflict of interest. The funders had no role in the design of the study; in the collection, analyses, or interpretation of data; in the writing of the manuscript, or in the decision to publish the results.

References

1. Radziemski, L.J. From LASER to LIBS, the path of technology development. *Spectrochim. Acta Part B At. Spectrosc.* **2002**, *57*, 1109–1113. [CrossRef]
2. Cremers, D.A.; Radziemski, L.J. History and fundamentals of LIBS. In *Laser Induced Breakdown Spectroscopy: Fundamentals and Applications*; Cambridge University Press: Cambridge, UK, 2006; pp. 9–16.
3. Harmon, R.S.; De Lucia, F.C.; McManus, C.E.; McMillan, N.J.; Jenkins, T.F.; Walsh, M.E.; Miziolek, A. Laser-induced breakdown spectroscopy—An emerging chemical sensor technology for real-time field-portable, geochemical, mineralogical, and environmental applications. *Appl. Geochem.* **2006**, *21*, 730–747. [CrossRef]
4. Alvey, D.C.; Morton, K.; Harmon, R.S.; Gottfried, J.L.; Remus, J.J.; Collins, L.M.; Wise, M.A. Laser-induced breakdown spectroscopy-based geochemical fingerprinting for the rapid analysis and discrimination of minerals: The example of garnet. *Appl. Opt.* **2010**, *49*, C168–C180. [CrossRef]
5. Rossi, M.; Dell'Aglio, M.; De Giacomo, A.; Gaudiuso, R.; Senesi, G.S.; de Pascale, O.; Capitelli, F.; Nestola, F.; Ghiara, M.R. Multi-methodological investigation of kunzite, hiddenite, alexandrite, elbaite and topaz, based on laser-induced breakdown spectroscopy and conventional analytical techniques for supporting mineralogical characterization. *Phys. Chem. Miner.* **2013**, *41*, 127–140. [CrossRef]
6. Díaz, D.; Hahn, D.W.; Molina, A. Quantification of gold and silver in minerals by laser-induced breakdown spectroscopy. *Spectrochim. Acta Part B At. Spectrosc.* **2017**, *136*, 106–115. [CrossRef]
7. Castello, M.; Constantin, M.; Laflamme, M. Measurements of Gold in Ores by LIBS.; Quebec City, 23 August 2017. Available online: https://numerique.banq.qc.ca/patrimoine/details/52327/3081324 (accessed on 21 June 2021).
8. Harhira, A.; Bouchard, P.; Rifai, K.; Haddad, J.E.; Sabsabi, M.; Blouin, A.; Laflamme, M. Advanced La-ser-Induced Breakdown Spectroscopy (LIBS) Sensor for Gold Mining. 2017. Available online: https://nrc-publications.canada.ca/eng/view/ft/?id=e302005a-66d5-4a1e-921d-d2cdb0ba0e77 (accessed on 1 April 2021).
9. McMillan, N.J.; Curry, J.; Dutrow, B.L.; Henry, D.J. Identification of the Host Lithology of Tourmaline Using Laser-Induced Breakdown Spectroscopy for Application in Sediment Provenance and Mineral Exploration. *Can. Miner.* **2018**, *56*, 393–410. [CrossRef]
10. Rifai, K.; Doucet, F.; Özcan, L.; Vidal, F. LIBS core imaging at kHz speed: Paving the way for real-time geochemical applications. *Spectrochim. Acta Part B At. Spectrosc.* **2018**, *150*, 43–48. [CrossRef]

11. Fabre, C.; Devismes, D.; Moncayo, S.; Pelascini, F.; Trichard, F.; Lecomte, A.; Bousquet, B.; Cauzid, J.; Motto-Ros, V. Elemental imaging by laser-induced breakdown spectroscopy for the geological characterization of minerals. *J. Anal. At. Spectrom.* **2018**, *33*, 1345–1353. [CrossRef]
12. Jolivet, L.; Leprince, M.; Moncayo, S.; Sorbier, L.; Lienemann, C.-P.; Motto-Ros, V. Review of the recent advances and applications of LIBS-based imaging. *Spectrochim. Acta Part B At. Spectrosc.* **2019**, *151*, 41–53. [CrossRef]
13. Bi, Y.; Yan, M.; Dong, X.; Li, Z.; Zhang, Y.; Li, Y. Recognition of 25 natural geological samples using a modified correlation analysis method and laser-induced breakdown spectroscopic data. *Optics* **2018**, *158*, 1058–1062. [CrossRef]
14. McManus, C.E.; Dowe, J.; McMillan, N.J. Quantagenetics® analysis of laser-induced breakdown spectroscopic data: Rapid and accurate authentication of materials. *Spectrochim. Acta Part B At. Spectrosc.* **2018**, *145*, 79–85. [CrossRef]
15. Busser, B.; Moncayo, S.; Coll, J.-L.; Sancey, L.; Motto-Ros, V. Elemental imaging using laser-induced breakdown spectroscopy: A new and promising approach for biological and medical applications. *Coord. Chem. Rev.* **2018**, *358*, 70–79. [CrossRef]
16. Akhmetzhanov, T.F.; Labutin, T.A.; Zaytsev, S.M.; Drozdova, A.N.; Popov, A.M. Determination of the Mn/Fe Ratio in Ferromanganese Nodules Using Calibration-Free Laser-Induced Breakdown Spectroscopy. *Opt. Spectrosc.* **2019**, *126*, 316–320. [CrossRef]
17. Fabre, C. Advances in Laser-Induced Breakdown Spectroscopy analysis for geology: A critical review. *Spectrochim. Acta Part B At. Spectrosc.* **2020**, *166*, 105799. [CrossRef]
18. Lawley, C.J.; Somers, A.M.; Kjarsgaard, B.A. Rapid geochemical imaging of rocks and minerals with handheld laser induced breakdown spectroscopy (LIBS). *J. Geochem. Explor.* **2021**, *222*, 106694. [CrossRef]
19. Vasavada, A.R.; Grotzinger, J.P.; Arvidson, R.E.; Calef, F.J.; Crisp, J.; Gupta, S.; A Hurowitz, J.; Mangold, N.; Maurice, S.; E Schmidt, M.; et al. Overview of the Mars Science Laboratory mission: Bradbury Landing to Yellowknife Bay and beyond. *J. Geophys. Res. Planets* **2014**, *119*, 1134–1161. [CrossRef]
20. Forni, O.; Gaft, M.; Toplis, M.J.; Clegg, S.M.; Maurice, S.; Wiens, R.C.; Mangold, N.; Gasnault, O.; Sautter, V.; Le Mouélic, S.; et al. First detection of fluorine on Mars: Implications for Gale Crater's geochemistry. *Geophys. Res. Lett.* **2015**, *42*, 1020–1028. [CrossRef]
21. Cousin, A.; Meslin, P.; Wiens, R.; Rapin, W.; Mangold, N.; Fabre, C.; Gasnault, O.; Forni, O.; Tokar, R.; Ollila, A.; et al. Compositions of coarse and fine particles in martian soils at gale: A window into the production of soils. *Icarus* **2015**, *249*, 22–42. [CrossRef]
22. Payré, V.; Fabre, C.; Sautter, V.; Cousin, A.; Mangold, N.; Le Deit, L.; Forni, O.; Goetz, W.; Wiens, R.C.; Gasnault, O.; et al. Copper enrichments in the Kimberley formation in Gale crater, Mars: Evidence for a Cu deposit at the source. *Icarus* **2019**, *321*, 736–751. [CrossRef]
23. Wiens, R.C.; Sylvestre, S.; the MSL Science Team Maurice; Reitz, G. DLR Collaborator (MSL Science Team) ChemCam: Chemostratigraphy by the First Mars Microprobe. *Elements* **2015**, *11*, 33–38. [CrossRef]
24. Fabre, C.; Bousquet, B. De chemcam à supercam: L'apport de la LIBS pour le spatial. *Photon* **2020**, 38–41. [CrossRef]
25. Maurice, S.; Wiens, R.C.; Bernardi, P.; Caïs, P.; Robinson, S.; Nelson, T.; Gasnault, O.; Reess, J.-M.; Deleuze, M.; Rull, F.; et al. The SuperCam Instrument Suite on the Mars 2020 Rover: Science Objectives and Mast-Unit Description. *Space Sci. Rev.* **2021**, *217*, 47. [CrossRef]
26. Wiens, R.C.; Maurice, S.; Robinson, S.H.; Nelson, A.E.; Cais, P.; Bernardi, P.; Newell, R.T.; Clegg, S.; Sharma, S.K.; Storms, S.; et al. The SuperCam Instrument Suite on the NASA Mars 2020 Rover: Body Unit and Combined System Tests. *Space Sci. Rev.* **2021**, *217*, 4. [CrossRef]
27. Cuñat, J.; Palanco, S.; Carrasco, F.; Simón, M.D.; Laserna, J.J. Portable instrument and analytical method using laser-induced breakdown spectrometry for in situ characterization of speleothems in karstic caves. *J. Anal. At. Spectrom.* **2005**, *20*, 295–300. [CrossRef]
28. Rakovský, J.; Čermák, P.; Musset, O.; Veis, P. A review of the development of portable laser induced breakdown spectroscopy and its applications. *Spectrochim. Acta Part B At. Spectrosc.* **2014**, *101*, 269–287. [CrossRef]
29. Connors, B.; Somers, A.; Day, D. Application of Handheld Laser-Induced Breakdown Spectroscopy (LIBS) to Geochemical Analysis. *Appl. Spectrosc.* **2016**, *70*, 810–815. [CrossRef] [PubMed]
30. Bennett, B.N.; Martin, M.Z.; Leonard, D.N.; Garlea, E. Calibration curves for commercial copper and aluminum alloys using handheld laser-induced breakdown spectroscopy. *Appl. Phys. A* **2018**, *124*, 42. [CrossRef]
31. Foucaud, Y.; Fabre, C.; Demeusy, B.; Filippova, I.; Filippov, L. Optimisation of fast quantification of fluorine content using handheld laser induced breakdown spectroscopy. *Spectrochim. Acta Part B At. Spectrosc.* **2019**, *158*, 105628. [CrossRef]
32. Harmon, R.S.; Lawley, C.J.; Watts, J.; Harraden, C.L.; Somers, A.M.; Hark, R.R. Laser-Induced Breakdown Spectroscopy—An Emerging Analytical Tool for Mineral Exploration. *Minerals* **2019**, *9*, 718. [CrossRef]
33. Pochon, A.; Desaulty, A.-M.; Bailly, L. Handheld laser-induced breakdown spectroscopy (LIBS) as a fast and easy method to trace gold. *J. Anal. At. Spectrom.* **2020**, *35*, 254–264. [CrossRef]
34. Senesi, G.S.; Harmon, R.S.; Hark, R.R. Field-portable and handheld laser-induced breakdown spectroscopy: Historical review, current status and future prospects. *Spectrochim. Acta Part B At. Spectrosc.* **2021**, *175*, 106013. [CrossRef]
35. Colao, F.; Fantoni, R.; Lazić, V.; Spizzichino, V. Laser-induced breakdown spectroscopy for semi-quantitative and quantitative analyses of artworks—application on multi-layered ceramics and copper based alloys. *Spectrochim. Acta Part B At. Spectrosc.* **2002**, *57*, 1219–1234. [CrossRef]

36. El Haddad, J.; Canioni, L.; Bousquet, B. Good practices in LIBS analysis: Review and advices. *Spectrochim. Acta Part B At. Spectrosc.* **2014**, *101*, 171–182. [CrossRef]
37. Shi, Q.; Niu, G.; Lin, Q.; Xu, T.; Li, F.; Duan, Y. Quantitative analysis of sedimentary rocks using laser-induced breakdown spectroscopy: Comparison of support vector regression and partial least squares regression chemometric methods. *J. Anal. At. Spectrom.* **2015**, *30*, 2384–2393. [CrossRef]
38. Ahmad, N.; Ahmed, R.; Umar, Z.A.; Liaqat, U.; Manzoor, U.; Baig, M.A. Qualitative and quantitative analyses of copper ores collected from Baluchistan, Pakistan using LIBS and LA-TOF-MS. *Appl. Phys. A* **2018**, *124*, 160. [CrossRef]
39. Maaza, M.; Mothudi, B.M. Laser-Induced Breakdown Spectroscopy (LIBS) on Geological Samples: Compositional Differentiation and Relative Hardness Quantification. Master's Thesis, University of South Africa, Pretoria, South Africa, 2018.
40. Guezenoc, J.; Gallet-Budynek, A.; Bousquet, B. Critical review and advices on spectral-based normalization methods for LIBS quantitative analysis. *Spectrochim. Acta Part B At. Spectrosc.* **2019**, *160*, 105688. [CrossRef]
41. Sobron, P. Non-Linear Methods for Quantitative Elemental Analysis and Mineral Classification Using Laser-Induced Breakdown Spectroscopy (LIBS) 2019. Available online: https://patents.google.com/patent/US20190079019A1/en (accessed on 21 June 2021).
42. Syvilay, D.; Guezenoc, J.; Bousquet, B. Guideline for increasing the analysis quality in laser-induced breakdown spectroscopy. *Spectrochim. Acta Part B At. Spectrosc.* **2019**, *161*, 105696. [CrossRef]
43. Duponchel, L.; Bousquet, B.; Pelascini, F.; Motto-Ros, V. Should we prefer inverse models in quantitative LIBS analysis? *J. Anal. At. Spectrom.* **2020**, *35*, 794–803. [CrossRef]
44. Rifai, K.; Paradis, M.-C.M.; Swierczek, Z.; Doucet, F.; Özcan, L.; Fayad, A.; Li, J.; Vidal, F. Emergences of New Technology for Ultrafast Automated Mineral Phase Identification and Quantitative Analysis Using the CORIOSITY Laser-Induced Breakdown Spectroscopy (LIBS) System. *Minerals* **2020**, *10*, 918. [CrossRef]
45. Rifai, K.; Özcan, L.-Ç.; Doucet, F.R.; Rhoderick, K.; Vidal, F. Ultrafast Elemental Mapping of Platinum Group Elements and Mineral Identification in Platinum-Palladium Ore Using Laser Induced Breakdown Spectroscopy. *Minerals* **2020**, *10*, 207. [CrossRef]
46. Cardoso-Fernandes, J.; Silva, J.; Dias, F.; Lima, A.; Teodoro, A.; Barrès, O.; Cauzid, J.; Perrotta, M.; Roda-Robles, E.; Ribeiro, M. Tools for Remote Exploration: A Lithium (Li) Dedicated Spectral Library of the Fregeneda–Almendra Aplite–Pegmatite Field. *Data* **2021**, *6*, 33. [CrossRef]
47. Andrade, J.M.; Cristoforetti, G.; Legnaioli, S.; Lorenzetti, G.; Palleschi, V.; Shaltout, A. Classical univariate calibration and partial least squares for quantitative analysis of brass samples by laser-induced breakdown spectroscopy. *Spectrochim. Acta Part B At. Spectrosc.* **2010**, *65*, 658–663. [CrossRef]
48. Wiens, R.; Maurice, S.; Lasue, J.; Forni, O.; Anderson, R.; Clegg, S.; Bender, S.; Blaney, D.; Barraclough, B.; Cousin, A.; et al. Pre-flight calibration and initial data processing for the ChemCam laser-induced breakdown spectroscopy instrument on the Mars Science Laboratory rover. *Spectrochim. Acta Part B At. Spectrosc.* **2013**, *82*, 1–27. [CrossRef]
49. Fabre, C.; Cousin, A.; Wiens, R.; Ollila, A.; Gasnault, O.; Maurice, S.; Sautter, V.; Forni, O.; Lasue, J.; Tokar, R.; et al. In situ calibration using univariate analyses based on the onboard ChemCam targets: First prediction of Martian rock and soil compositions. *Spectrochim. Acta Part B At. Spectrosc.* **2014**, *99*, 34–51. [CrossRef]
50. Payré, V.; Fabre, C.; Cousin, A.; Sautter, V.; Wiens, R.C.; Forni, O.; Gasnault, O.; Mangold, N.; Meslin, P.-Y.; Lasue, J.; et al. Alkali trace elements in Gale crater, Mars, with ChemCam: Calibration update and geological implications. *J. Geophys. Res. Planets* **2017**, *122*, 650–679. [CrossRef]
51. Guezenoc, J.; Payré, V.; Fabre, C.; Syvilay, D.; Cousin, A.; Gallet-Budynek, A.; Bousquet, B. Variable selection in laser-induced breakdown spectroscopy assisted by multivariate analysis: An alternative to multi-peak fitting. *Spectrochim. Acta Part B At. Spectrosc.* **2019**, *152*, 6–13. [CrossRef]
52. Gamela, R.R.; Costa, V.C.; Babos, D.V.; Araújo, A.S.; Pereira-Filho, E.R. Direct Determination of Ca, K, and Mg in Cocoa Beans by Laser-Induced Breakdown Spectroscopy (LIBS): Evaluation of Three Univariate Calibration Strategies for Matrix Matching. *Food Anal. Methods* **2020**, *13*, 1017–1026. [CrossRef]
53. Grew, E.S. The Minerals of Lithium. *Elements* **2020**, *16*, 235–240. [CrossRef]
54. Cardoso-Fernandes, J.; Silva, J.; Lima, A.; Teodoro, A.C.; Perrotta, M.; Cauzid, J.; Roda-Robles, E.; Ribeiro, M.A. Reflectance Spectroscopy to Validate Remote Sensing Data/Algorithms for Satellite-Based Lithium (Li) Exploration (Central East Portugal). In Proceedings of the Earth Resources and Environmental Remote Sensing/GIS Applications XI, Online Conference, 20 September 2020; Schulz, K., Nikolakopoulos, K.G., Michel, U., Eds.; SPIE: Bellingham, WA, USA, 2020; p. 19.
55. Cardoso-Fernandes, J.; Silva, J.; Lima, A.; Teodoro, A.C.; Perrotta, M.; Cauzid, J.; Roda-Robles, E. Characterization of Lithium (Li) Minerals from the Fregeneda-Almendra Region through Laboratory Spectral Measurements: A Comparative Study. In Proceedings of the Earth Resources and Environmental Remote Sensing/GIS Applications XI, Online Conference, 20 September 2020; Schulz, K., Nikolakopoulos, K.G., Michel, U., Eds.; SPIE: Bellingham, WA, USA, 2020; p. 20.
56. Cousin, A.; Sautter, V.; Fabre, C.; Maurice, S.; Wiens, R.C. Textural and modal analyses of picritic basalts with ChemCam Laser-Induced Breakdown Spectroscopy. *J. Geophys. Res. Space Phys.* **2012**, *117*, 117. [CrossRef]
57. Sweetapple, M.T.; Tassios, S. Laser-induced breakdown spectroscopy (LIBS) as a tool for in situ mapping and textural interpretation of lithium in pegmatite minerals. *Am. Miner.* **2015**, *100*, 2141–2151. [CrossRef]
58. Linnen, R.L.; Van Lichtervelde, M.; Černý, P. Granitic Pegmatites as Sources of Strategic Metals. *Elements* **2012**, *8*, 275–280. [CrossRef]

59. Popov, A.M.; Zaytsev, S.M.; Seliverstova, I.V.; Zakuskin, A.; Labutin, T.A. Matrix effects on laser-induced plasma parameters for soils and ores. *Spectrochim. Acta Part B At. Spectrosc.* **2018**, *148*, 205–210. [CrossRef]
60. Maurice, S.; Wiens, R.C.; Saccoccio, M.; Barraclough, B.; Gasnault, O.; Forni, O.; Mangold, N.; Baratoux, D.; Bender, S.; Berger, G.; et al. The ChemCam Instrument Suite on the Mars Science Laboratory (MSL) Rover: Science Objectives and Mast Unit Descriptn. *Space Sci. Rev.* **2012**, *170*, 95–166. [CrossRef]
61. Quarles, C.D.; Gonzalez, J.J.; East, L.J.; Yoo, J.H.; Morey, M.S.; Russo, R.E. Fluorine analysis using Laser Induced Breakdown Spectroscopy (LIBS). *J. Anal. At. Spectrom.* **2014**, *29*, 1238–1242. [CrossRef]
62. McMillan, N.J.; Rees, S.; Kochelek, K.; E McManus, C. Geological Applications of Laser-Induced Breakdown Spectroscopy. *Geostand. Geoanal. Res.* **2014**, *38*, 329–343. [CrossRef]
63. Kochelek, K.A.; McMillan, N.J.; McManus, C.E.; Daniel, D.L. Provenance determination of sapphires and rubies using laser-induced breakdown spectroscopy and multivariate analysis. *Am. Miner.* **2015**, *100*, 1921–1931. [CrossRef]
64. Farnsworth-Pinkerton, S.; McMillan, N.J.; Dutrow, B.L.; Henry, D.J. Provenance of detrital tourmalines from Proterozoic metasedimentary rocks in the Picuris Mountains, New Mexico, using Laser-Induced Breakdown Spectroscopy. *J. Geosci.* **2018**, *63*, 193–198. [CrossRef]

remote sensing

MDPI

Article

Interpretation of the Reflectance Spectra of Lithium (Li) Minerals and Pegmatites: A Case Study for Mineralogical and Lithological Identification in the Fregeneda-Almendra Area

Joana Cardoso-Fernandes [1,2,*], João Silva [1], Mônica M. Perrotta [3], Alexandre Lima [1,2], Ana C. Teodoro [1,2], Maria Anjos Ribeiro [1,2], Filipa Dias [1,2], Odile Barrès [4], Jean Cauzid [4] and Encarnación Roda-Robles [5]

[1] Department of Geosciences, Environment and Spatial Plannings, Faculty of Sciences, University of Porto, Rua Campo Alegre, 4169-007 Porto, Portugal; up201503357@fc.up.pt (J.S.); allima@fc.up.pt (A.L.); amteodor@fc.up.pt (A.C.T.); maribeir@fc.up.pt (M.A.R.); filipa.dias@fc.up.pt (F.D.)
[2] ICT (Institute of Earth Sciences)–Porto pole (Portugal), Rua Campo Alegre, 4169-007 Porto, Portugal
[3] Remote Sensing and Mineral Spectroscopy Laboratory, Geological Survey of Brazil (CPRM), Rua Costa, 55, São Paulo 01304-010, Brazil; monica.perrotta@cprm.gov.br
[4] GeoRessources Laboratory, Université de Lorraine, CNRS, F-54000 Nancy, France; odile.barres@univ-lorraine.fr (O.B.); jean.cauzid@univ-lorraine.fr (J.C.)
[5] Departamento de Geología, Universidad del País Vasco (UPV/EHU), Barrio Sarriena s/n, 48940 Leioa, Spain; encar.roda@ehu.es
* Correspondence: joana.fernandes@fc.up.pt

Abstract: Reflectance spectroscopy has been used to identify several deposit types. However, applications concerning lithium (Li)-pegmatites are still scarce. Reflectance spectroscopic studies complemented by microscopic and geochemical studies were employed in the Fregeneda–Almendra (Spain–Portugal) pegmatite field to analyze the spectral behavior of Li-minerals and field lithologies. The spectral similarity of the target class (Li-pegmatites) with other elements was also evaluated. Lepidolite was discriminated from other white micas and the remaining Li-minerals. No diagnostic feature of petalite and spodumene was identified, since their spectral curves are dominated by clays. Their presence was corroborated (by complementary techniques) in petalite relics and completely replaced crystals, although the clay-related absorption depths decrease with Li content. This implies that clays can be used as pathfinders only in areas where argillic alteration is not prevalent. All sampled lithologies present similar water and/or hydroxide features. The overall mineral assemblage is very distinct, with lepidolite, cookeite, and orthoclase exclusively identified in Li-pegmatite (being these minerals crucial targets for Li-pegmatite discrimination in real-life applications), while chlorite and biotite can occur in the remaining lithologies. Satellite data can be used to discriminate Li-pegmatites due to distinct reflectance magnitude and mineral assemblages, higher absorptions depths, and distinct Al–OH wavelength position. The potential use of multi- and hyperspectral data was evaluated; the main limitations and advantages were discussed. These new insights on the spectral behavior of Li-minerals and pegmatites may aid in new Li-pegmatite discoveries around the world.

Keywords: remote sensing; reflectance spectroscopy; hyperspectral; geological exploration; spectral library; absorption features; spectral mineralogy; pegmatite; lithium

check for updates

Citation: Cardoso-Fernandes, J.; Silva, J.; Perrotta, M.M.; Lima, A.; Teodoro, A.C.; Ribeiro, M.A.; Dias, F.; Barrès, O.; Cauzid, J.; Roda-Robles, E. Interpretation of the Reflectance Spectra of Lithium (Li) Minerals and Pegmatites: A Case Study for Mineralogical and Lithological Identification in the Fregeneda-Almendra Area. *Remote Sens.* **2021**, *13*, 3688. https://doi.org/10.3390/rs13183688

Academic Editors: Prasad S. Thenkabail and Amin Beiranvand Pour

Received: 30 May 2021
Accepted: 12 September 2021
Published: 15 September 2021

Publisher's Note: MDPI stays neutral with regard to jurisdictional claims in published maps and institutional affiliations.

Copyright: © 2021 by the authors. Licensee MDPI, Basel, Switzerland. This article is an open access article distributed under the terms and conditions of the Creative Commons Attribution (CC BY) license (https://creativecommons.org/licenses/by/4.0/).

1. Introduction

Reflectance spectroscopy studies have shown a relevant economic potential to mineral exploration, either through the direct characterization and identification of the mineralogy of the deposits or through the identification of hydrothermal alteration zonation as a proxy to target mineralizations such as (i) porphyry copper deposits [1], (ii) volcanogenic massive sulfide (VMS) deposits [2,3], (iii) rare-earth element (REE) deposits [4,5], (iv)

zinc-lead-silver deposits [6], (v) iron oxide-copper-gold (IOCG) deposits [7], and (vi) gold deposits [8].

Similar approaches have been applied to distinct deposit types like pegmatites that have a high economic interest for (i) ceramic components such as quartz and feldspar; (ii) rare, critical metals such as lithium (Li), tin (Sn), tantalum (Ta), cesium (Cs), beryllium (Be), and rubidium (Rb); as well as for (iii) colored gemstones [9–14]. Zhang et al. [15] developed a systematic spectroscopic characterization of tourmalines from the Koktokay No.3 pegmatite (northwestern China), the pegmatite contact wall zone, and from the host rocks, which included several methods, including reflectance spectroscopy. These methods, coupled with mineral chemistry analyses, allowed to better understand the magmatic to hydrothermal evolution of the pegmatite and the fluid interaction with the pegmatite and the country rocks. Carrino et al. [16] correlated an electron probe microanalysis (EPMA) with the reflectance spectra of elbaite (Li-tourmaline) gemstones from pegmatites of the Seridó Pegmatite Province (Northeastern Brazil). In the end, the application of statistical techniques, such as principal component analysis (PCA), discriminated tourmalines of different compositions based on the reflectance spectra. Bocchio et al. [17] used geochemical and spectroscopic techniques such as reflectance spectroscopy to achieve a gemological characterization of aquamarine (blue beryl) samples from granitic pegmatites of the Masino-Bregaglia Massif, Central Alps, Italy. Araújo Neto et al. [18] undertook a similar but more complete study to characterize emerald (green beryl) crystals from granitic aplite and pegmatite veins in the Paraná deposit (Northeastern Brazil), using mineral chemistry, absorption and reflectance spectroscopy, and thermal analysis. Silva et al. [19] explored the potential of reflectance spectroscopy to characterize the mineral phases of the Alto do Giz pegmatite in the Seridó Pegmatite Province (Northeastern Brazil). To complement the interpretation of the reflectance spectra, scanning electron microscopy (SEM) and X-ray diffraction (XRD) were used. Despite the intense kaolinization, hydrothermal-metasomatic and supergene alteration overprinting the rock bulk mineralogy, reflectance spectroscopy proved to be capable of defining the internal zonation of the pegmatite.

Although the literature shows that reflectance spectroscopy is successfully applicable to pegmatite deposits, study applications are still scarce. Moreover, this technique can be of considerable importance if applied to vector pegmatites with economic potential for rare and strategic metals like Li. The increasing economic significance of Li triggered several satellite-based exploration works that allowed identifying Li-pegmatites correctly worldwide and that lead to the discovery of pegmatite-hosted Li deposits [20–24]. Costa et al. [25] were the first authors to apply reflectance spectroscopy exclusively for Li-mineral identification and associated weathering alteration minerals in the Jequitinhonha region (Brazil). Despite showing promising results for minerals like spodumene or lepidolite, it was not possible to identify petalite and zinnwaldite through their spectral signatures. Moreover, the supergene alteration minerals seem to be related to the semi-arid climate of the region [25], which differs from Europe's climate conditions, highlighting the need for a similar approach in European territory.

Considering this, the study area chosen for this work is the Fregeneda–Almendra region, one of the largest European provinces in Li production [11]. In this region, the Li-bearing minerals with greater economic interest are spodumene ($LiAlSi_2O_6$; pyroxene; 8.03% Li_2O), petalite ($LiAlSi_4O_{10}$; feldspathoid; 4.5% Li_2O), and lepidolite ($K(Li,Al)_3(Si,Al)_4O_{10}(F,OH)_2$); mica; 7.7% Li_2O) [13,26,27]. This study delineated the following objectives: (i) build a spectral library dedicated to Li-bearing minerals and understand their respective spectral signatures, (ii) extend the spectral library to other lithologies that occur in the study area to enable satellite-based lithological classification, and (iii) evaluate if there can be any spectral confusion between the target class (Li-pegmatite) and other within-scene elements, as verified by Cardoso-Fernandes et al. [28]. Therefore, this research presents a complete view of the use of reflectance spectroscopy for laboratory identification of Li-bearing minerals and remote sensing mapping of Li-pegmatites, including spectral data acquired in a preliminary phase [29,30], as well as new spectral measurements and complementary

geochemical, petrographic, and mineralogical studies. The combination of classical and uncommon analytical techniques allowed characterizing the mineral assemblage resulting from the alteration of petalite crystals, and the paragenesis of some of the collected rock samples. Overall, this study addresses different pertinent research questions: (i) Are Li-bearing minerals distinguishable from each other and other minerals? (ii) How can the alteration products affect the spectral signature of Li-bearing minerals? (iii) Can Li-pegmatites be spectrally discriminated from other lithologies in a supervised classification attempt? The results obtained are essential to better direct future remote sensing-based exploration studies. They provide new insights on the spectral behavior of Li-minerals and Li-pegmatites, allowing to identify which minerals can be directly discriminated against while proposing, for the first time, relevant pathfinders to distinguish other Li-minerals, as well as Li-pegmatites. The main implications of this study may lead to new Li-pegmatite discoveries in Europe and worldwide.

2. Study Area and Field Surveys

The field surveys were conducted on the Fregeneda–Almendra aplite-pegmatite field (Figure 1), spreading from La Fregeneda (Spain) to Almendra (Portugal). The pegmatite field contains 11 different types of dikes ranging from barren to more evolved: Li, F, Sn, Rb, Nb > Ta, B, and P-enriched bodies [26,27,31]. Among the more evolved dikes, there are four types containing Li mineralization: (i) petalite-rich dikes (exploited in the Bajoca open-pit mine), (ii) spodumene-rich dikes (exploited in the Alberto open-pit mine), (iii) lepidolite-bearing dikes, and (iv) lepidolite + spodumene-bearing dikes (exploited in the Feli open-pit mine) [26,27,31]. All Li-rich pegmatite dikes are emplaced in a pre-Ordovician metasedimentary belt composed of a pelitic-sandy flysch series, Complexo Xisto-Grauváquico (CXG) [32–34]. Additionally, the fractionation degree of the pegmatite dikes increases with further distance to the syn-Variscan granitoid rocks (granites and granodiorite) of the Figueira de Castelo Rodrigo–Lumbrales Anatectic Complex [26,27,31,35–37] (Figure 1). These granitoids correspond to S-type, two-mica granites with several facies, showing distinct grain sizes (from fine to coarse-grained), and to a fine-to-medium-grained, essentially biotitic, granodiorite [36–38]. In the Fregeneda–Almendra region, there are also Ordovician phyllitic-quartzitic formations, as well as Cenozoic sedimentary deposits (Figure 1).

During the field surveys, samples were collected at several distinct field stations according to the aforementioned goals (Figure 1). To construct the Li-mineral database, petalite, spodumene, and lepidolite hand specimens were retrieved from different types of mineralized dikes either in open-pit mines or at unexploited locations. In general, spodumene was under-sampled in comparison with the other Li-minerals. To fill this gap, existing samples from Feli and Alberto mines (Figure 1), as well as from other locations in the Fregeneda–Almendra field, as part of a mineralogical collection at the University of Porto, were also included in this study, bringing the number of samples to a total of 28. Considering the future satellite-based lithological classification attempts, the various field lithologies (Li-pegmatite, metasediments, and granitoids) were also sampled to conduct further laboratory spectral analysis. The field stations included, whenever possible, several open-pit mines to ensure that the different lithologies presented large and fresh expositions to serve as possible training areas for supervised classification. These field campaigns allowed refining and improving the training areas used in preliminary image classification attempts [28]. Additionally, some of the areas misclassified as Li-pegmatite in this preliminary classification were sampled to evaluate the degree of spectral similarity between these areas and Li-pegmatites. In the field, the exposed material in these misclassified areas was assessed, and a field description of each site was made.

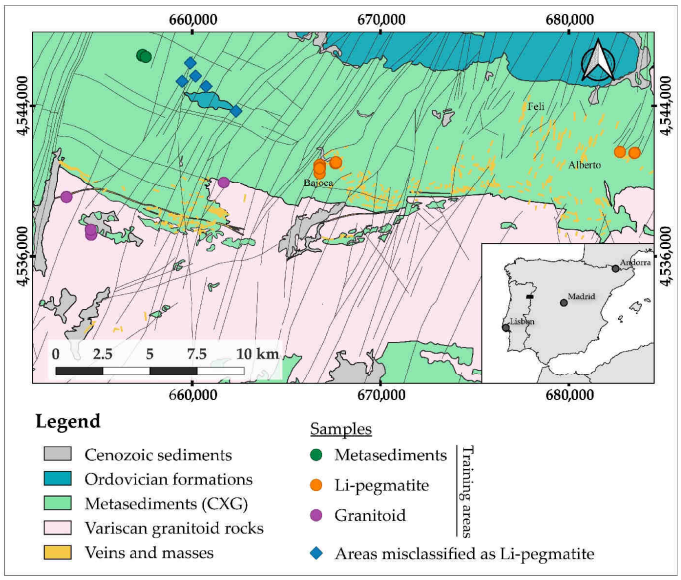

Figure 1. Location of the study area in the Iberian Peninsula and geological setting of the Fregeneda–Almendra pegmatite field (adapted from References [26,39,40]). The field stations where the samples were collected are marked with a circle for the training areas (the color is dependent on the sample type) and with a diamond for the areas misclassified as Li-pegmatite using machine learning algorithms. Li-mineral specimens were also collected in Li-pegmatite sites. Map projection: Universal Transverse Mercator zone 29N from the WGS84 datum.

3. Methodology

3.1. Reflectance Spectroscopy Studies

The spectral studies were conducted in the laboratory employing two distinct spectroradiometers, both covering the spectral range between 350 and 2500 nm: (i) the ultra-high-resolution SR-6500 (Spectral Evolution, Inc.) equipment (1.5 nm @ 700 nm, 3.0 nm @ 1500 nm, and 3.8 nm @ 2100 nm) and (ii) the FieldSpec 4 (ASD, Inc.) standard resolution equipment (3.0 nm @ 700 nm, 10.0 nm @ 1400 nm, and 10.0 nm @ 2100 nm). In each case, the point spectral measurements were performed using a Contact Probe with similar characteristics, namely an internal light source provided by a halogen bulb and spot size of 10 mm. For reflectance calibration, a Spectralon (Labsphere) plate with a maximum reflectance above 95% for the 250–2500-nm range and above 99% for the 400–1500-nm region. Small (less than 2 cm) or friable samples were analyzed over the white plate. When using either of the spectroradiometers, each measurement corresponded to an average of 40 scans. For the FieldSpec 4 equipment, four additional spectra were acquired in each analyzed spot, later averaged into a final spectrum, to increase the signal-to-noise ratio.

ASD ViewSpec Pro™ software [41] and SpectraGryph software [42] were used to individually analyze all spectra to exclude measurement errors or spectra with noticeable noise caused by vegetation fragments on the surface of the samples and for spectra averaging. Point measurements belonging to the same sample and with similar spectral behavior were averaged to aid visualization and allow fast interpretation of the spectra. The final Li-minerals spectral library contains reference data from 28 samples (five spodumene, 13 petalite, and ten lepidolite samples). Moreover, to complete the spectral studies for lithological classification, 45 samples from possible training areas were analyzed (five from CXG metasediments, 33 from distinct Li-pegmatite types, and seven from granitoid rocks),

as well as 11 samples from four areas misclassified as Li-pegmatite. All samples and point measurements were photographed.

The laboratory acquired spectra were normalized through continuum removal [43] to compare the spectra obtained by both spectroradiometers and enhance the spectral absorption features. In this case, a hull quotient was calculated after automatically fitting a convex-hull to each spectrum in a Python environment using the *pysptools* library [44]. The extraction of the wavelength, depth, and other geometric parameters of the absorption features was made using SpectraGryph software and the *pysptools* library. The complete spectral library and additional information on the equipment used and spectra processing can be found in Cardoso-Fernandes et al. [45,46].

3.2. Complementary Petrographic and Geochemical Studies

Microscopic studies were conducted at the University of Porto, using a transmitted light Nikon petrographic microscope (Eclipse E 400 POL), coupled with a ZEISS Axiocam camera for both the petalite alteration products and the samples from the four areas misclassified as Li-pegmatite. Selected petalite samples with distinct degrees of alteration were crushed to quantify their Li content at Activation Laboratories Ltd. (Actlabs), ON, Canada, using the Code 8–Lithium Ore analytical package. Sample preparation and crushing were conducted at the University of Porto using manual and automated mortar agate grinders (Retsch RM 200). Li quantification was achieved through inductively coupled plasma–optical emission spectrometry (ICP-OES) after four-acid digestion (detection limit 0.001%). Afterward, Li contents were converted to Li_2O (%) using a compound ratio of 2.1527. Mineralogical information was obtained through powder X-ray diffraction (XRD) for friable samples and through optical microscopy and Scanning Electron Microscopy with Energy Dispersive Spectroscopy (SEM-EDS) for hard rock samples. The XRD analysis was performed at the National Laboratory of Energy and Geology (LNEG, Portugal) using a Panalytical Diffractometer XPERT-PRO, equipped with a PW3050/60 goniometer, with a Theta-2Theta geometry and X-ray tube with a copper (Cu) anticathode. The tube voltage and current were set to 45 kV and 40 mA, respectively. Regarding the acquisition settings, a continuous scan mode with a scan range between 3° and 90° of 2teta, a step size of 0.0084°, and 4.960 s of counting time per step was used. The SEM-EDS studies were conducted at the University of Porto, in previously carbon-coated thin sections, using a Hitachi FlexSEM 1000 SEM coupled to a Bruker QUANTAX EDS system.

4. Results

In this section, selected spectra from the spectral library are presented, taking into account the previously designated goals. The main mineralogy inferred from the spectra is presented, but a detailed analysis spectrum per spectrum can be found in the Supplementary Materials (Tables S1–S3).

4.1. Li-Minerals Spectral Database

The spectral database was built for three distinct Li-minerals: lepidolite (Figure 2), spodumene (Figure 3), and petalite (Figure 4). For this study, monomineralic samples were preferred to rock samples to avoid the interference of other minerals. As can be seen in Figure 2, all lepidolite spectra show the white mica typical features due to the hydroxide ion (OH^-) absorption around ~1409 nm associated with the principal, sharp Al–OH absorption feature (between 2195 nm and 2205 nm) and the Al–OH secondaries (around ~2348 nm and ~2435 nm, respectively) [47–49]. Other white mica-related, weak absorption features located ~1537 nm, ~2002 nm, and ~2114 nm are due to OH^- and OH^- combined with lattice modes [49,50]. The depth of the water feature (~1909 nm) decreases from Figure 2 (a–c), and the slight inflection around ~1460 nm indicates that montmorillonite is also present, mixed with white mica features [1,49]. The remaining spectra (d–k) have higher purity, allowing to characterize the lepidolite due to: (i) a peak in the red region, caused by lepidolite purple color and (ii) multiple absorption features

in the visible and near-infrared (VNIR) region, together with the drop off to extreme blue observed in the raw reflectance curves (left panel of Figure 2). These features are interpreted to be related to ferric iron (Fe^{3+}) and manganese (Mn^{3+}) incorporated into the structure of lepidolite [50]. Ferrous iron (Fe^{2+}) may cause the absorption at 720 nm (Figure 2 (e)) [16,51].

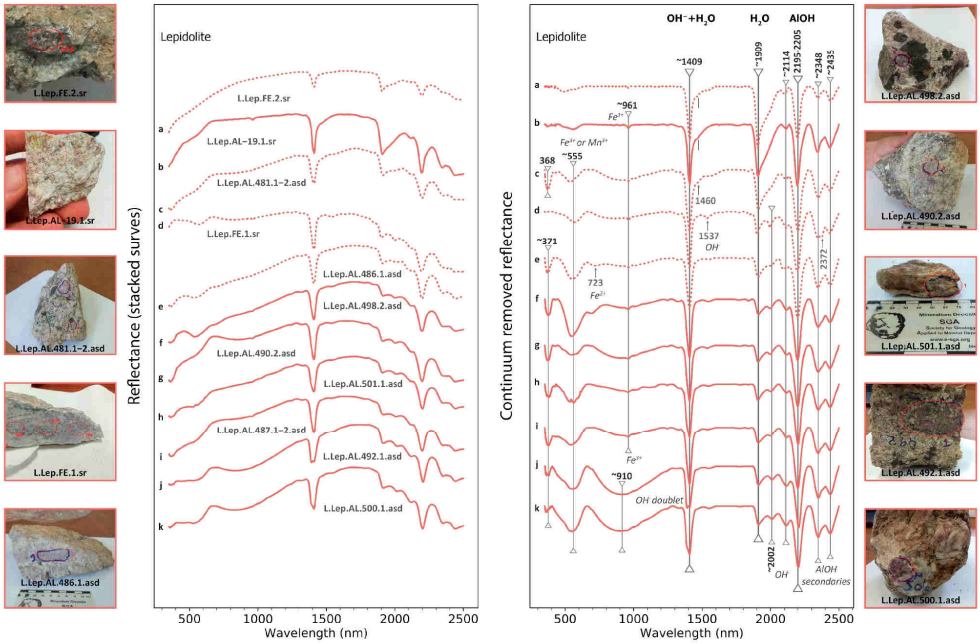

Figure 2. Spectral signature of lepidolite (Li-bearing mica): reflectance curves (to the left) and continuum removed curves (to the right). The main absorption features are highlighted, and sample photographs are provided. Each spectrum has a database code [45] providing information about the type of sample (L—Li-bearing minerals), mineralogy (Lep—lepidolite), sample provenance (FE—Feli mine and AL—Almendra), a three-digit numerical part representing the GPS code, a one- or two-digit code representing the spectra number or the averaged spectra numbers, and a reference to the spectroradiometer employed (sr—SR-6500; asd—FieldSpec 4). Dotted curves: fresh samples; full curves: samples with visible signs of weathering.

The reference spectral data of spodumene was acquired considering pure or spodumene intergrowth with quartz. Despite this, it is not expected that the associated quartz will obscure the spectral behavior of spodumene because the main diagnostic features of the former do not occur in the VNIR and shortwave infrared (SWIR) regions [47,52]. Figure 3 shows the main absorption features located around ~1414 nm, ~1910 nm, and ~2209 nm for spodumene + quartz samples and around ~1412 nm, ~1913 nm, and ~2205 nm for spodumene samples. The presence of molecular water is evidenced by the broader, asymmetric features approximately at ~1410 nm (OH^- + H_2O) and ~1910 nm (H_2O) [48,52]. Molecular water associated with (i) higher depth of the water feature in comparison with the Al–OH fundamental absorption (around ~2200 nm) and (ii) a slight inflection around ~1467 nm are diagnostic of smectite minerals—in particular, of montmorillonite [1,48,49]. The shallow Al–OH secondaries at ~2350 nm and ~2437 nm for spodumene + quartz, and at ~2352 nm and ~2440 nm for spodumene, indicate the existence of illite mixed with montmorillonite and possibly kaolinite [48,49]. Iron incorporation (Fe^{3+} and possibly Fe^{2+}) into both spodumene and spodumene + quartz samples could be identified due to: (i) the drop off to the blue observed in the reflectance curves (left panel of Figure 3) [50] and

(ii) a slight inflection around ~2240 nm related with the Fe-OH bond [49] (Figure 3 (a–h)). Spectra h–k show additional features diagnostic of kaolinite, such as (i) a small inflection around ~2165 nm and (ii) the presence of an Al–OH triplet at ~2312, ~2350, and ~2380 nm [8,48,49,53].

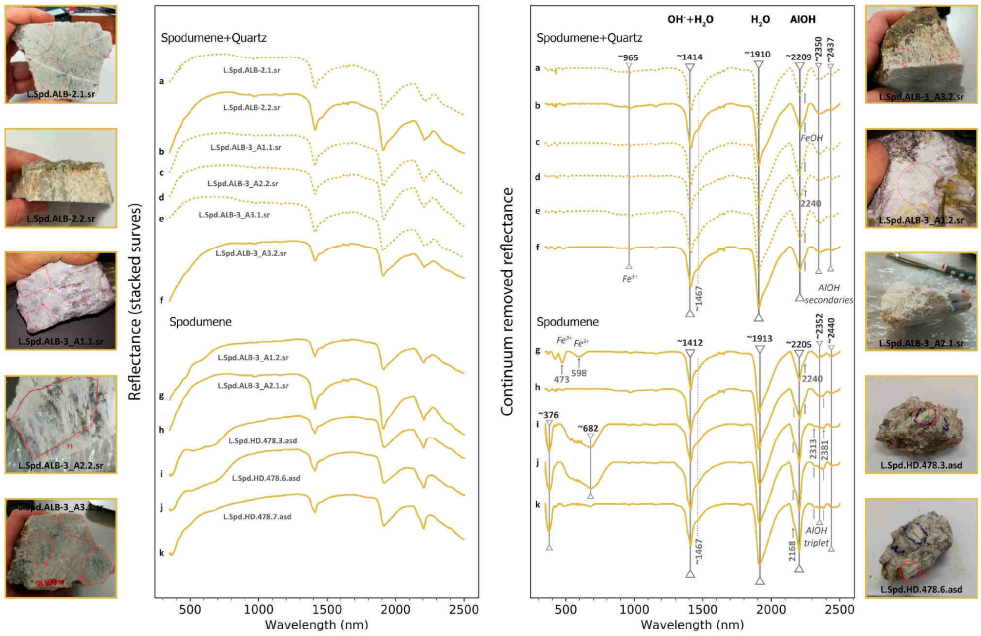

Figure 3. Spectral signature of spodumene (a Li-bearing pyroxene): reflectance curves (to the left) and continuum removed curves (to the right). The main absorption features are highlighted, and sample photographs are provided. Dotted curves: fresh samples; full curves: samples with visible signs of weathering. Each spectrum has a database code [45] providing information about the type of sample (L—Li-bearing minerals), mineralogy (Spd—spodumene), sample provenance (ALB—Alberto mine and HD—Hinojosa de Duero), a three-digit numerical part representing the GPS code, a one- or two-digit code representing the spectra number or the averaged spectra numbers, and a reference to the spectroradiometer employed (sr—SR-6500; asd—FieldSpec 4).

Most petalite spectra (Figure 4) are very similar to spodumene, showing the same main absorptions (Figure 4 (a–q)). Montmorillonite is identified in all samples by the broad, asymmetric, and acute absorptions around ~1413 nm and ~1911 nm, associated with the Al–OH feature at ~2206 nm [48,49], shallower than the ~1911 nm one, and the slight inflection around ~1467 nm [1,49]. It is the sole mineral identified in spectra a–c, e, and o–q (Figure 4). Others (d and g–n) show additional shallow Al–OH secondary absorptions at ~2356 nm and ~2445 nm, indicating the mixture with illite [48,49]. The presence of the Al–OH triplet and the slight inflection around ~2165 nm allowed the identification of kaolinite in the spectra d and j (Figure 3) [8,48,49,53]. Figure 4 (l) shows a sharp absorption at ~2312 nm and a shallow feature at ~2390 nm, indicating that another smectite group mineral may be present, probably saponite, with diagnostic Mg-OH features at ~2310 nm and ~2380 nm [48,49]. The last three spectra of Figure 4 show distinct mineral assemblages. In spectra r and s, besides the montmorillonite features (broad, asymmetric water absorptions), it was possible to identify: (i) a deep symmetric but broad main Al–OH feature, (ii) two OH^- absorptions located at ~1574 nm and ~1834 nm, and (iii) a deep, broad, asymmetric Mg-OH feature at ~2355 nm that allowed the recognition of cookeite (Li-bearing chlorite) [19,25,54,55]. Spectrum t (Figure 4) shows illite/white mica features: (i) the

sharp and symmetric OH^- and Al–OH features at ~1413 nm and 2198 nm, respectively and (ii) the well-pronounced Al–OH secondaries at 2345 nm and 2434 nm [47–49]. The water feature is deep and asymmetrical but shorter than the Al–OH, diagnosing the existence of illite [49]. Looking at the VNIR portion of the spectra, it was possible to notice a fall off to extreme blue in the reflectance curves (left panel of Figure 4), indicating that iron could be present in several samples [53]. Both ferric and ferrous iron were identified, the latter mainly through its characteristic ramp-like feature around ~1150 nm [56]. Notwithstanding, similar features around ~1150 nm were interpreted as water features in montmorillonite spectra by Hunt and Salisbury [47].

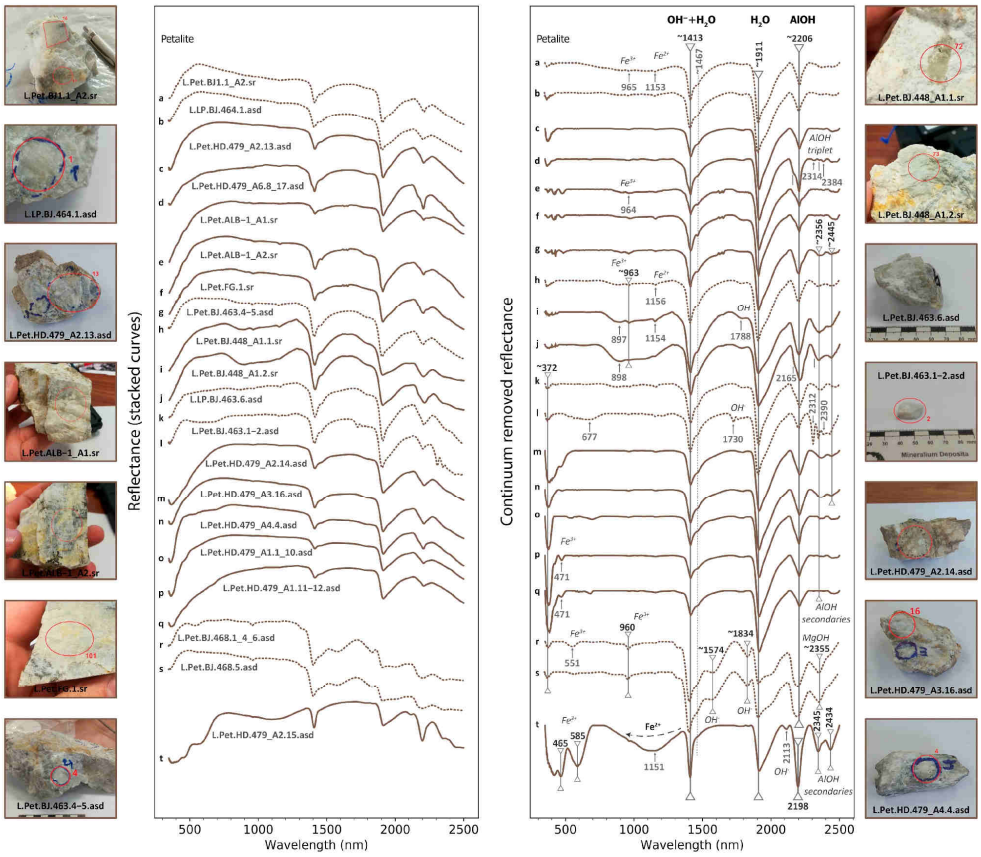

Figure 4. Spectral signature of petalite (a Li-bearing feldspathoid): reflectance curves (to the left) and continuum removed curves (to the right). The main absorption features are highlighted, and sample photographs are provided. Dotted curves: fresh samples; full curves: samples with visible signs of weathering. Each spectrum has a database code [45] providing information about the type of sample (L—Li-bearing minerals); mineralogy (Pet—petalite); sample provenance (ALB—Alberto mine and BJ—Bajoca mine, FG—Fregeneda, and HD—Hinojosa de Duero); a three-digit numerical part representing the GPS code; a one- or two-digit code representing the spectra number or the averaged spectra numbers; and a reference to the spectroradiometer employed (sr—SR-6500; asd—FieldSpec 4).

Lastly, the position of the ~2200 nm Al–OH feature was evaluated for all Li-minerals (Figure A1, Appendix A) as a possible factor for mineral discrimination.

Characterization of Petalite Alteration Products

The knowledge on the alteration associations can help to refine satellite image processing algorithms and to better understand the spectral behavior of fresh samples. During the field campaigns, it was possible to identify in the Bajoca mine front white to greenish clays preserving petalite cleavage (Figure 5a,b) [57] and yellow to greenish petalite crystals in Hinojosa de Duero. Additionally, in the Bajoca mine front, some petalite relics were found within the heavily altered portions, mainly consisted of friable clay-like minerals. Petalite relics and clayey alteration products were characterized through petrography, XRD, and reflectance spectroscopy. Table 1 summarizes these results and the ICP-OES Li quantification. Appendix A (Figure A6) provides the XRD diffractograms.

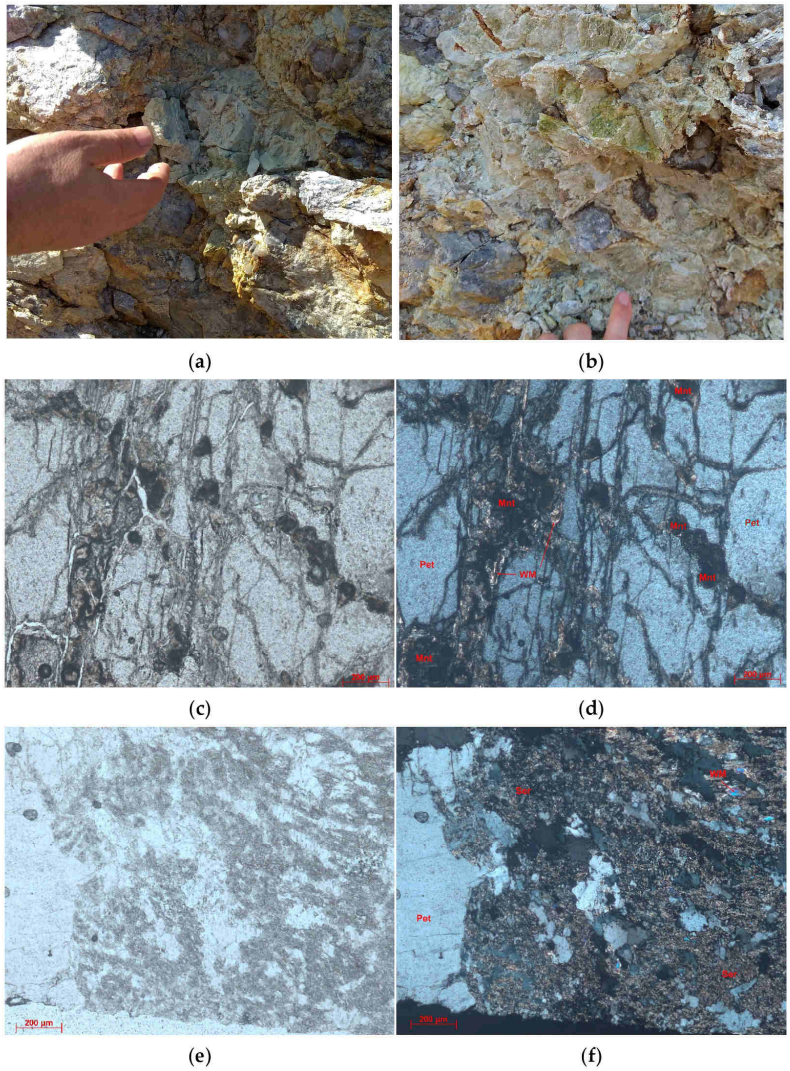

Figure 5. *Cont.*

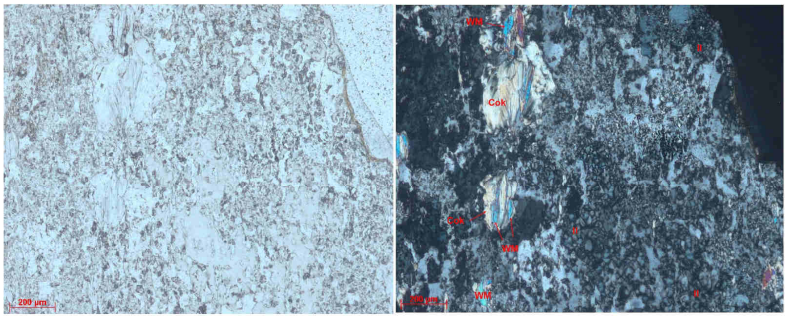

(**g**) (**h**)

Figure 5. (**a**,**b**) Petalite altering to whitish and greenish clay minerals in the Bajoca mine front. (**b**) Former petalite crystal with preserved cleavage. (**c**,**d**) Photomicrographs of petalite relic with fractures filled by white mica and montmorillonite in parallel polarized light—ppl (**c**) and cross-polarized light—cpl (**d**). (**e**,**f**) Photomicrographs of petalite altering to sericite, white mica, and quartz in ppl and cpl, respectively. (**g**,**h**) Former petalite replaced by cookeite associated with white mica, surrounded by quartz and pseudospherulitic clays in ppl and cpl, respectively. Cok—cookeite (Li-chlorite); Mnt—montmorillonite; Pet—petalite; Ser—sericite; WM—white mica.

Table 1. Characterization and mineral identification of petalite's alteration products through petrography, XRD, and reflectance spectroscopy. Li quantification through ICP-OES is also shown. Alb—albite; Cok—cookeite (Li-chlorite); Il—illite; Kao—kaolinite; Mnt—montmorillonite; Msc—muscovite; Non—nontronite; Or—orthoclase; Pet—petalite; Pl—plagioclase; Qtz—quartz; Sap—saponite; Sep—sepiolite; Ser—sericite; WM—white mica. Sample provenance: BJ—Bajoca mine; HD—Hinojosa de Duero.

Sample	Friability	Petrography	XRD	Spectroscopy	Li_2O (%)
BJ.450	Friable	—	Qtz, Il, Mnt/Non, Kao	Mnt	0.116
BJ-20-12	Friable	—	—	Mnt, Il/WM	0.248
HD.479	Hard rock	Pet, Ser, Pl, Qtz, WM	—	Mnt, Il/WM	4.585
BJ2-01	Friable	—	Qtz, Non, Msc, Il-Mnt	Mnt, Il/WM	0.082
BJ2-02	Friable	—	Qtz, Il/Sep, Msc, Or, Alb	Mnt, Il/WM	0.099
BJ3-01	Friable	—	Qtz, Il, Msc (phengitic), Alb	Mnt, Il/WM	0.062
BJ.451	Hard rock	Cok, WM, Ser, Qtz	—	Mnt, Kao, Sap	0.409
BJ4-01	Hard rock	Pet, Mnt *, WM, Pl	—	Mnt, Il/WM, Sap, Kao	4.628

* Identified through SEM-EDS.

Figure 5c–h shows representative photomicrographs of petalite's alteration minerals. Thin sections of the less altered samples allowed identifying petalite in two out of the three. In the third, petalite is completely replaced despite preserving its cleavage, as previously described by Cardoso-Fernandes et al. [57]. Petalite alteration concentrates along the cleavage (Figure 5c,d), filled by fine white mica and pale brown clays (under parallel polarized light–ppl; Figure 5c), identified as montmorillonite through SEM-EDS [57]. Montmorillonite also forms spherical aggregates more or less aligned (Figure 5c,d). Local sericitization was observed on the crystal borders (Figure 5e,f). Figure 5g,h shows the formation of cookeite (associated with white mica) and clay minerals with pseudospherulitic habit, often interpreted as crystals growing filling pre-existing voids [58].

Regarding the spectral behavior of the alteration assemblages (Figure 6), montmorillonite features such as the broad, asymmetric OH^- (~1413 nm) and H_2O (~1912 nm) absorptions with sharp minima, the Al–OH (~2200 nm) feature, and the small inflection around ~1467 nm [1,48,49] suggests its identification in spectra from a to j. The X-ray diffraction technique identified montmorillonite only in two of the four analyzed samples (Table 1 and Appendix A, Figure A6). In spectra from b to h, illite and/or white

mica are also detected by (i) the Al–OH secondaries at ~2350 nm and ~2440 nm, (ii) the slight OH^- feature at around ~1790 nm, and (iii) the proportion of Al–OH (~2200 nm) absorption depth to water absorption depth ranging around 1/2 [47–49]. The coexistence of illite and white mica was confirmed three samples analyzed through XRD (Table 1 and Appendix A, Figure A6). In Figure 6, the spectra i–k represent more complex mineral assemblages. Kaolinite can be present in spectra i and j because of the Al–OH absorption triplet (~2310 nm–~2350 nm–~2387 nm) and the slight inflection around ~2165 nm [8,48,49,53]. Nonetheless, the deeper 2311-nm absorption in spectra j indicates that a magnesium-bearing mineral such as saponite or sepiolite is also present [48,49]. Oppositely, spectrum k of Figure 6 is dominated by illite and/or white mica features: (i) deep, sharp, and symmetric main Al–OH feature (2196 nm) associated with a sharp, symmetric OH^- features (1409 nm); (ii) very pronounced Al–OH secondaries (at 2350 nm and 2433 nm); and (iii) minor OH^- feature at 2105 nm [47–49]. Most of the spectra of Figure 6 show iron-related absorption features, as observed in petalite fresh samples (Figure 4). The wavelength position allowed the discrimination of both ferrous and ferric iron [56].

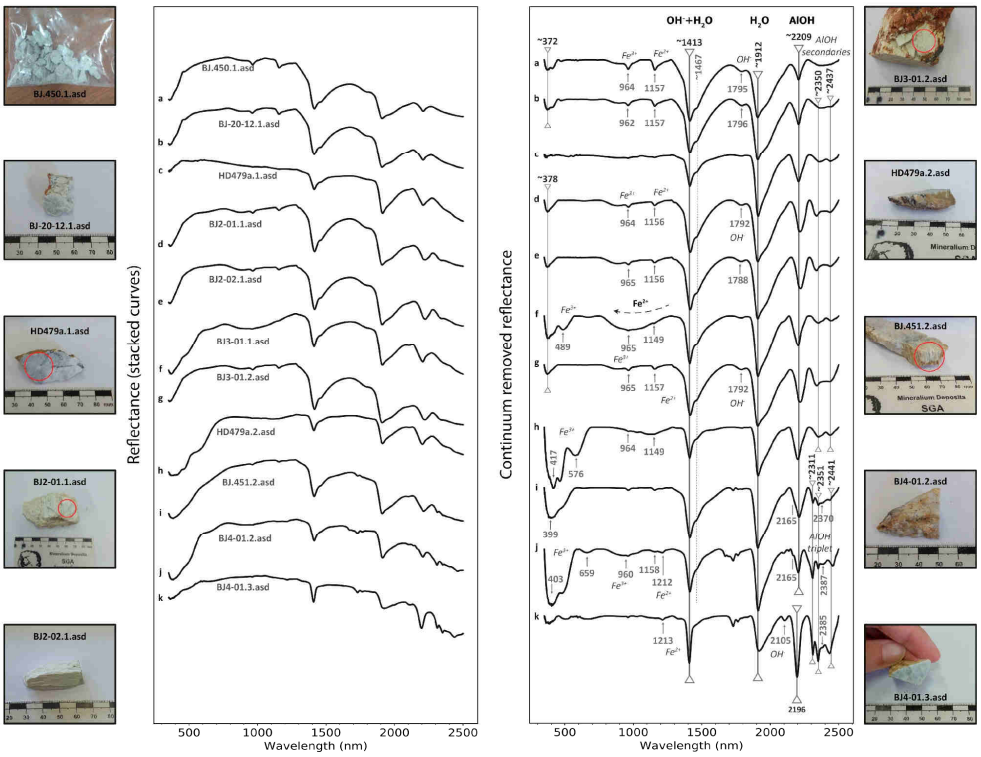

Figure 6. Spectral signature of the petalite's alteration products: reflectance curves (to the left) and continuum removed curves (to the right). The main absorption features are highlighted, and sample photographs are provided. Each spectrum name is composed by the sample provenance (BJ—Bajoca mine and HD—Hinojosa de Duero), a field code, a one-digit number representing the spectra, and the spectroradiometer employed (asd—FieldSpec 4).

As done for the spectra of Li-minerals, the position of the main Al–OH feature of the petalite alteration products was also assessed in Figure A1 (Appendix A). Additionally, any possible correlation between the Li content and the absorptions features in terms

of wavelength, depth, area, and full-width at half maximum (FWHM) was evaluated (Figure 7).

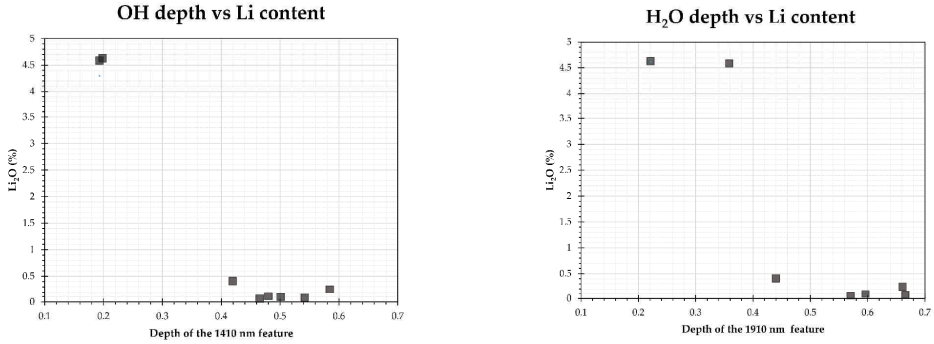

(**a**) (**b**)

Figure 7. Relation between the depth of the hydroxyl (**a**) and water (**b**) absorption features and the Li content of the altered petalite samples.

4.2. Spectral Studies for Lithological Classification

This section concerns the comparison of the spectral behavior of the main field lithologies. Additionally, a description of the areas misclassified as Li-pegmatite is presented, as well as the spectral behavior of the samples collected in each of the four areas.

Stacked reflectance and continuum removed curves of the metasedimentary formations from the CXG are presented in Figure 8 (a–g). White mica diagnostic features such as (i) deepest, sharp Al–OH feature around ~2214 nm, (ii) sharp and symmetric OH^- feature (~1413 nm) associated with the absence of a water feature (expected around ~1900 nm), and (iii) weak to pronounced Al–OH secondaries at ~2346 nm and ~2451 nm dominate the spectra of Figure 8 (a–c) [47–49]. The spectra of fresh samples (a–c) are also characterized by a ramp-like absorption feature due to the presence of ferrous iron (Fe^{2+}) [56], together with the ~750 nm, ~920 nm, and ~1150 nm Fe^{3+} and Fe^{2+} features [47,50,54]. These VNIR absorptions, associated with a slight inflection around ~2250 nm, related to the Fe-OH bonds [6,49] or Al(Mg, Fe)–OH bonds [59,60], and a slightly deeper 2350-nm absorption when comparing with the ~2451 nm Al–OH secondary, indicating the contribution of the Mg–OH bonds [48,49], are indicative of the presence of chlorite in fresh samples [47,49,54,59]. Despite the absorption features of spectra d–f of Figure 8 not being evident, there is (i) a weak, broad, rounded water absorption at ~1926 nm that may be associated with fluid inclusions in quartz [49] and (ii) ferric iron-related (Fe^{3+}) absorptions around ~942 nm evidencing sample oxidation (Figure 8) [49,56]. Finally, spectra g shows the calcite diagnostic features—namely, the carbonate ion (CO_3^{2-}) feature at 2339 nm and weaker carbonate features around ~1900–2000 nm [49].

Regarding the granite samples, continuum removed curves (Figure 8 (h–k)), evidence a mixture of montmorillonite/illite and white mica features: (i) asymmetric OH– (~1413 nm) and water (~1913 nm) features, (ii) broad water feature with sharp minima and similar depth to the Al–OH one (~2206 nm), (iii) a small inflection around ~1467 nm [1,48,49], (iv) Al–OH secondaries at ~2351 nm and ~2443 nm, and (v) weaker OH– absorption at ~2110 nm [47–49]. Fresher samples (spectra h–i) show distinctive VNIR features at ~960 nm (Fe^{3+}) and ~1150 nm (Fe^{2+}), inferring the presence of biotite. Despite the dominance of montmorillonite and white mica feature, which overlap with the main kandite group absorption features, altered samples (spectra j–k) show slight inflections at ~2165 nm and ~2382 nm that indicate that a kandite group mineral, like kaolinite or halloysite, is present in the mineral mixture [8,49]. Additionally, goethite was identified in altered samples

through its diagnostic ferric iron features at ~670 nm and ~950 nm and peak in the red region (~750 nm) [49,56].

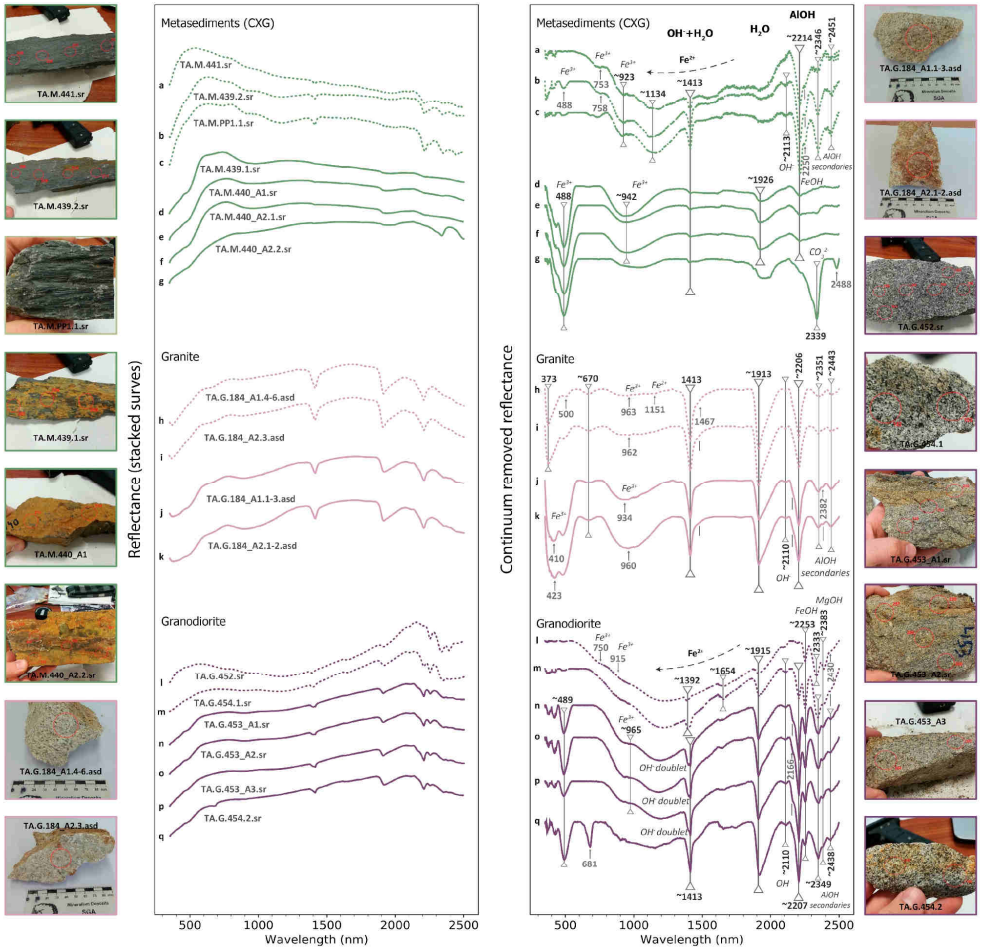

Figure 8. Spectral signature of the outcropping lithologies: reflectance curves (to the left) and continuum removed curves (to the right). The main absorption features are highlighted, and sample photographs are provided. Dotted curves: fresh samples; full curves: samples with visible signs of weathering. Each spectrum has a database code [45] providing information about the type of sample (TA—training areas), type of lithology (M—CXG metasediments, G—granite and granodiorite), a three-digit numerical part representing the GPS code, a one- or two-digit code representing the spectra number or the averaged spectra numbers, and a reference to the spectroradiometer employed (sr—SR-6500; asd—FieldSpec 4).

The granodiorite samples stacked reflectance and continuum removed curves are displayed in Figure 8 (l–q). White mica features dominate the spectra n to q, as evidenced by (i) the deep, narrow Al–OH absorption at ~2207 nm, (ii) the associated Al–OH secondaries (at ~2349 nm and ~2438 nm), and (iii) minor OH^- combined with lattice modes absorption features around ~2110 nm [47–49]. White mica is also present in Figure 8 (m). The ubiquitous biotite presence in all spectra (l to q) was confirmed by its diagnostic (i) ~2253-nm absorption feature, related to the either Fe–OH bonds [6,49] or Al(Mg, Fe)–OH

bonds [59,60] and (ii) Mg–OH absorptions at ~2330–2350 nm and ~2380 nm [48,49]. The higher relative depth of the Mg–OH feature compared to the ~2250-nm absorption and the slight inflection/weak absorption around ~2430 nm indicate that biotite is Mg-rich (possibly mixed with phlogopite—for example, spectra q) [49,53]. Biotite also occurs mixed with chlorite in spectrum l, being chlorite identified through its diagnostic VNIR features (~750-nm, ~915-nm, and ~1150-nm ferric and ferrous iron absorptions) [47,50,54,56]. The existence of a doublet OH^- absorption in spectra o to q, associated with the slight inflection at ~2166 nm and the Al–OH absorptions at ~2349 nm and ~2383 nm is characteristic of the kandite group [8,48,49,53]. The prominent and deep water feature (~1915 nm) is diagnostic of halloysite [48,49]. Lastly, spectra q of Figure 8 shows a broad, asymmetric water feature that coupled with a unique OH^- feature (at ~1413 nm), and an Al–OH feature (at ~2207 nm) indicates that montmorillonite and/or illite may be present [48,49].

Finally, the Li-bearing pegmatites were separated according to the dominant mineralogy into (i) lepidolite-bearing and (ii) petalite-bearing. Stacked reflectance and continuum removed curves of both lepidolite- and petalite-bearing pegmatites are presented in Figure 9.

As shown in Figure 9 (a–f), white mica related absorptions dominate all spectra from lepidolite-bearing pegmatites (sharp and symmetric main OH^- and Al–OH, coupled with the associated secondaries at ~2347 nm and ~2434 nm and weaker OH^- combined with lattice modes absorptions at 1835 nm, ~1997 nm, and 2116 nm [47–49]). However, features in the VNIR region such as (i) the ~551-nm absorption, associated with the incorporation of Fe^{3+} and/or Mn^{3+}, and (ii) the peak in the red region (left panel of Figure 9), allowed discrimination of the white mica as lepidolite in spectra c–f [50]. In the VNIR region, another iron-related feature was observed at ~960 nm (Fe^{3+}) [56]. Some clay minerals, such as montmorillonite and illite, may be present in spectra a, d, and f (Figure 9), identified by the relatively deep and/or asymmetric of the water feature at ~1912 nm and the slight inflection around ~1467 nm [1,49].

Like the petalite samples, mixtures of montmorillonite and illite dominate most of the spectra of the petalite-bearing pegmatites (Figure 9 (g,h,j–q)). The montmorillonite-related inflection at ~1467 nm is present in all the mentioned spectra [1]. In spectra g, i and j, montmorillonite features prevail over illite features: (i) higher asymmetry of the main OH^- feature (~1410 nm), (ii) higher depth of the water feature (~1912 nm) in comparison with the main Al–OH absorption (2192–2208 nm), and (iii) Al–OH secondaries (~2349 nm and ~2439 nm) absent or poorly developed [48,49]. In spectra o–q, the opposite happens, with illite being predominant due to: (i) narrower and/or more symmetric main OH^- feature, (ii) weaker OH^- absorptions 1620 nm and ~2108 nm, (iii) higher depth of the main Al–OH feature in relation to the water one, and (iv) well-developed Al–OH secondaries [48,49]. Spectra k–n represent a mixture of montmorillonite and illite. The rounded water absorption in spectra h indicates that free water is present, which could be due to fluid inclusions in minerals such as quartz [49]. White mica, which is discriminated from illite by the absence of a water feature [49], predominates spectra r–t, although the white mica present in spectra r is a hydrated white mica, probably sericite because the depth of the water feature is small than what would be expected for illite [49]. Figure 9 (w) shows diagnostic cookeite features, namely: (i) a broad, symmetric main Al–OH feature, (ii) OH^- absorptions at ~1581 nm and ~1835 nm, and (iii) a deep and broad Mg–OH feature at 2358 nm [19,25,54,55]. Cookeite also occurs mixed with white mica features in spectra t and mixed with montmorillonite/illite in spectra q. Kaolinite was identified in Figure 9 (g,j) through its characteristic Al–OH triplet and slight inflection at ~2166 nm [8,48,49,53]. Figure 9 (u,v) shows spectral behavior correspondent to orthoclase, where the absorptions at ~1410 nm and ~1912 nm may be the result of aqueous fluid inclusions [47,55]. Additionally, the ~2110-nm feature is diagnostic of ammonium (NH_4^+), but its relatively shallow depth can indicate only small amounts of NH_4^+ substituting K^+ and not the NH_4^+ feldspar (buddingtonite) [49,61,62]. When looking at the VNIR range, especially in the raw reflectance curves (left panel of Figure 9), goethite was identified in

spectra g, h, l, and r, through its diagnostic ferric iron absorptions (Fe^{3+}) at ~960 nm and ~660 nm and peak in the red region around ~760 [49,56]. Other iron-related features were also observed.

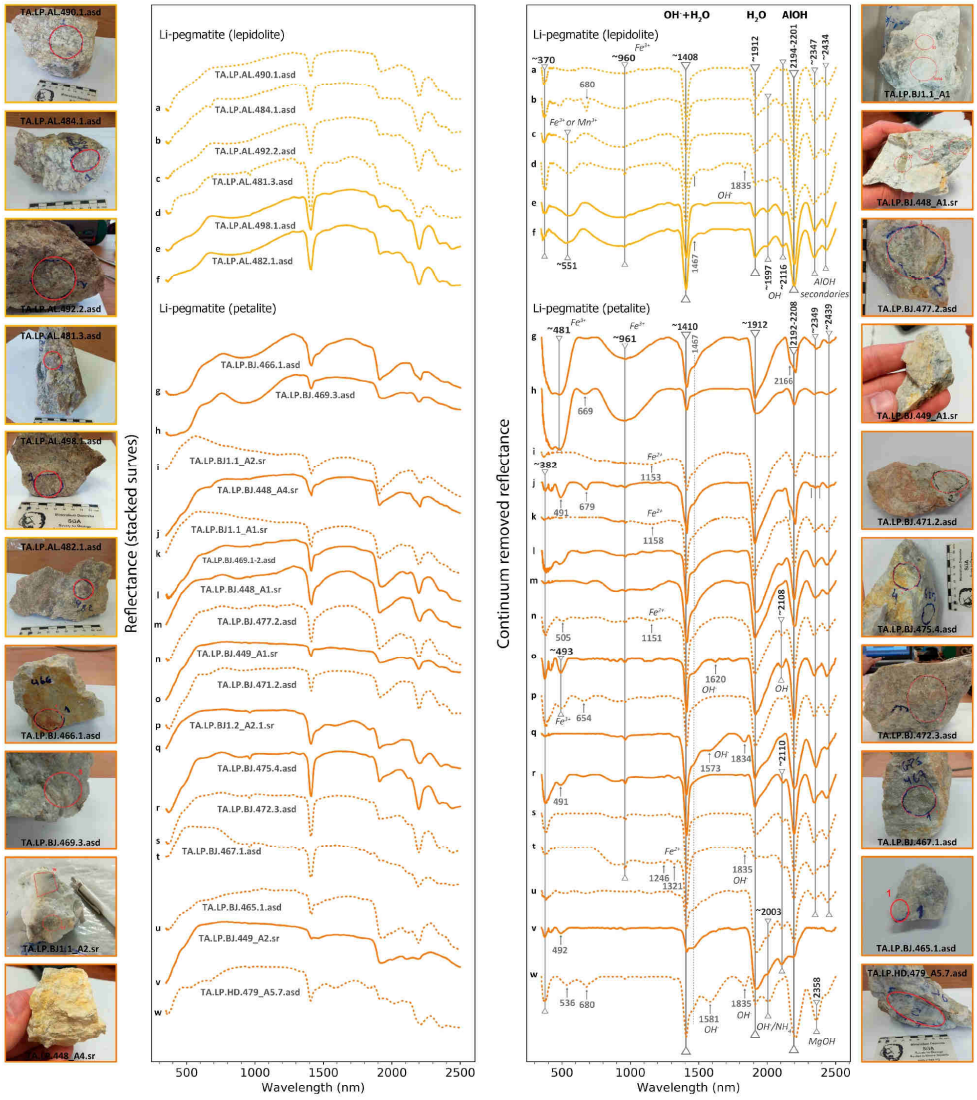

Figure 9. Spectral signature of the outcropping lithologies, namely lepidolite-bearing pegmatite and petalite-bearing pegmatite: reflectance curves (to the left) and continuum removed curves (to the right). The main absorption features are highlighted, and sample photographs are provided. Dotted curves: fresh samples; full curves: samples with visible signs of weathering. Each spectrum has a database code [45] providing information about the type of sample (TA—training areas); type of lithology (LP—Li-pegmatite); sample provenance (AL—Almendra, BJ—Bajoca mine, and HD—Hinojosa de Duero); a three-digit numerical part representing the GPS code; a one- or two-digit code representing the spectra number or the averaged spectra numbers; and a reference to the spectroradiometer employed (sr—SR-6500; asd—FieldSpec 4).

Overall, the misclassified regions correspond to (i) wine or olive plantations, where the agricultural activities exposed metasedimentary boulders, or (ii) hillside and slope areas, where many rock boulders are naturally exposed. Petrography and reflectance spectroscopy studies were conducted to fully characterize the collected samples and understand if there can be any spectral confusion with the target class (Li-pegmatite) and minerals. The results are summarized in Table A1 (Appendix A), while the spectral curves and photomicrographs are presented in Figures A2 and A3, respectively.

As seen in Table A1, most of the samples correspond to CXG metasediments, although some quartzite and pegmatite samples were in some false-positive areas. The microscopic studies of CXG samples allowed characterization as interbed phyllites with metagraywacke layers, with well-preserved sedimentary features such as bedding and load casts (Figure A3a,b). The mineralogical assemblage identified, composed of quartz, white mica (detrital and metamorphic origin), biotite, chlorite, plagioclase, K-feldspar, detrital zircon, tourmaline, apatite, iron oxides, and other opaque minerals (Figure A3), is in line with the described in the literature [63]. Quartzite samples have tiny mica crystals in the matrix and exhibit an inherited clastic texture, compatible with the metapsamites described for the São Grabiel's Ordovician formation [37]. Lastly, no signs of Li mineralization were found in the pegmatite samples, which characterizes it as a barren pegmatite.

Figure A2 (Appendix A) shows the spectral signature of samples collected in false-positive sites. The continuum removed curves related to the area no. 1 (Figure A2 (a–e)) reveal white mica in spectra c (sharp, symmetric main OH^- and Al–OH absorptions at ~1414 nm and ~2210 nm, coupled with the Al–OH secondaries at ~2350 nm and ~2438 nm and the absence of water absorption). Illite was recognized in spectra b through similar features but with its typical more profound water feature (~1925 nm) [47–49]. In Figure A2 (e), montmorillonite deep water absorption is spectrally mixed with Mg-OH-related features at ~2350 nm and ~2383 nm (slight inflection), possibly due to the presence of chlorite or biotite (the VNIR features are not clear enough to discriminate the magnesium-bearing mineral) [48,49,54]. The wavelength position and rounded aspect of the water feature indicate the presence of free water, possibly related to fluid inclusions in quartz or the presence of iron oxides/hydroxides [49]. The ferric iron features at ~680 nm and ~960 nm and peak in the red region (~760 nm) allowed identifying the goethite in spectra a, while the remaining VNIR absorptions indicate that other iron oxides/hydroxides are present in spectra b, d, and e of Figure A2 [49,56].

In the case of the false-positive area no. 2 (Figure A2 (f,g)), it was possible to recognize hydrated kaolinite or kaosmectite due to the (i) slight inflections ~1407 nm and ~2197 nm indicative of the OH^- and Al–OH doublets; (ii) very shallow Al–OH triplet at (~2313 nm, ~2349 nm, and ~2384 nm); and (iii) the deep water feature at ~1921 nm [8,48,49,53]. Spectra g of Figure A2 is dominated by illite features, although there is a slight inflection at a wavelength characteristic of the Mg-OH bond (2379 nm) [47–49]. Identical OH^- and Al–OH features but with less profound water feature allowed to identify white mica in spectra h [47–49], while the rounded water feature has indicated the presence of quartz with fluid inclusions [49]. The remaining spectra (f and g) also show a distinctive wavelength position and roundness of the water feature, indicating free water. Based on the VNIR features, goethite was identified in Figure A2 (f,g), while spectra h also shows some ferric iron absorptions [49,56].

Regarding the spectra of the false-positive area no. 3 (Figure A2 (i–m)), the similar depth of the water (~1914 nm) and main Al–OH (~2208 nm) features indicate the spectral mixture montmorillonite (~1465-nm inflection and broad, deep, asymmetric water feature with sharp minima) and illite (typical Al–OH secondaries) in spectra i and k [1,48,49]. Montmorillonite also occurs mixed with chlorite/biotite in spectra j (well-pronounced Fe–OH or Al(Mg, Fe)–OH absorption at 2254 nm, associated with the deep Mg–OH absorption at ~2348 nm), but the VNIR features are not clear enough to discriminate the two minerals [6,48,49,59,60]. Figure A2 (l) shows a predominance of montmorillonite features (absence of Al–OH secondaries, inflection at 1467 nm, and deep water feature),

but the shape of the 1914-nm (water) feature is not typical of the smectite group, with the rounded minima indicating the presence of free water [1,48,49]. Spectra m is dominated by chlorite features (diagnostic VNIR absorptions, inflection at ~2000 nm, and Mg–OH-related absorption at 2348 nm) [47–49,54,59] mixed with either white mica or illite [47–49]. Looking at the VNIR features in both reflectance and continuum removed curves, goethite can be present in spectra i, while other iron oxides and/or hydroxides (that not goethite or hematite) are present in spectra j–l [49,56].

Finally, in the false-positive area no. 4 (Figure A2 (n–q)), white mica (sharp, symmetric OH^- and Al–OH features, associated with the Al–OH secondaries and the absence of a prominent water feature), is mixed with chlorite (diagnostic VNIR absorptions and ~2000-nm inflection) in spectra n and q [47–49,54,59]. Spectra o and p show white mica features but a more pronounced, asymmetric water feature at ~1914 nm, indicating probable sericite (water absorption deeper than typical muscovite but not deep enough as illite) [49]. Ferric iron-related absorptions occur in spectra o and p of Figure A2.

The reflectance magnitude of the different classes is compared in Figure 10. Additionally, the minimum, maximum, and mean reflectance of each class are also compared in Figure A4 (Appendix A).

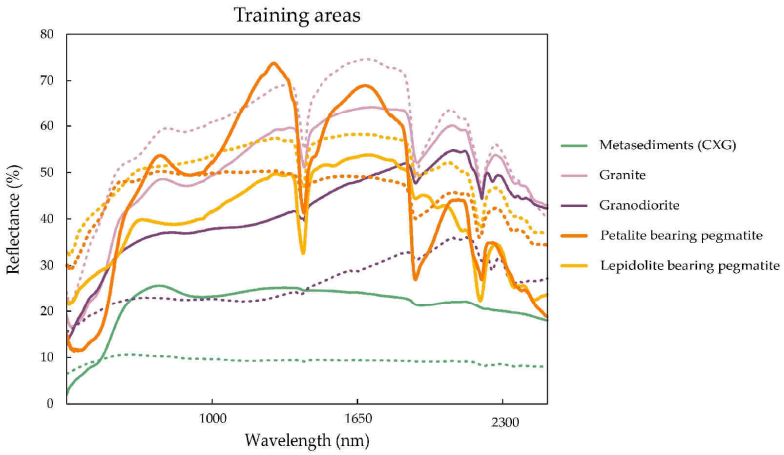

Figure 10. Comparison of the maximum reflectance magnitude of the different lithologies sampled at training area locations. Weathered samples (full lines) are discriminated from fresher samples (dotted lines).

Additionally, the wavelength position and depth of absorption features are among the most common criteria for lithological discrimination. Figure 11a shows the distribution of the wavelength of the main Al–OH feature according to the distinct types of samples containing white mica, and Figure 11b relates the position and depth of their Al–OH feature. To better discriminate the CXG metasediments from the granitoids based on the spectral mineralogy, the chlorite and/or biotite composition was evaluated through the Mg–OH wavelength position (Figure A5, Appendix A). Only the Mg–OH absorption was used, because not all spectra presented the ~2250-nm feature well-defined.

Lastly, the spectral resolutions of different satellite or drone-borne sensors (such as Sentinel-2, Landsat-8 Operational Land Imager (OLI), Advanced Spaceborne Thermal Emission and Reflection Radiometer (ASTER), Prototype Research Instruments and Space Mission technology Advancement (PRISMA), and HySpex Mjolnir) were considered to evaluate the potential use of remote sensing data in Li-pegmatite exploration (Figure 12).

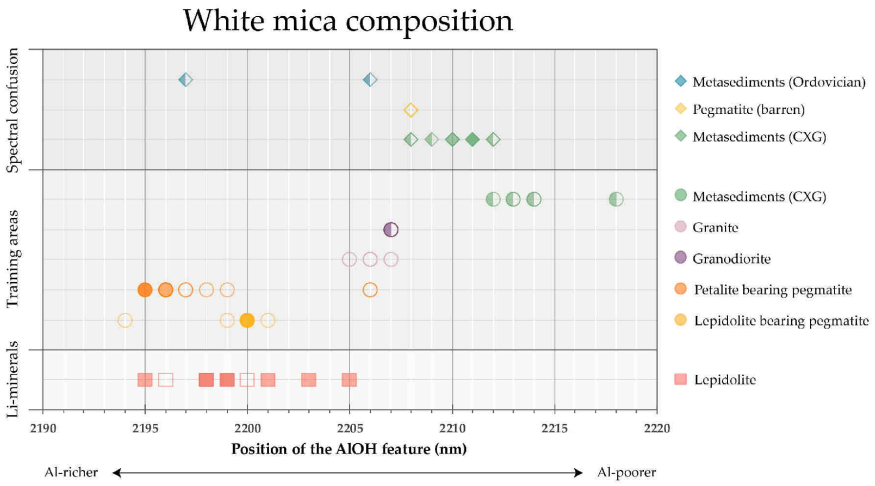

(**a**)

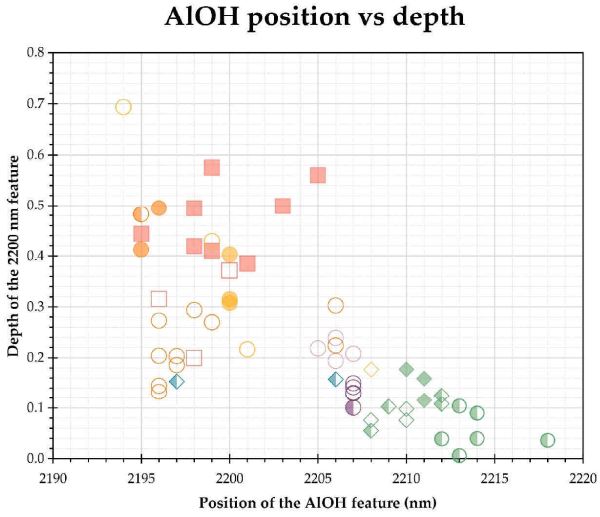

(**b**)

Figure 11. Wavelength position of the Al–OH feature in samples containing white mica: (**a**) relation between the wavelength and white mica composition (based on References [49,64]) and (**b**) relation between depth and position of the Al–OH feature. Lepidolite samples (squares) were plotted for comparison. Circles correspond to samples from training areas, while diamonds represent false-positive areas. Full symbols correspond to samples where white mica was exclusively identified; half-full symbols correspond to mixtures of white mica with minerals that do not overlap the main Al–OH absorption; symbols without fill represent spectra where white mica occurs mixed with minerals whose feature overlaps the Al–OH absorption.

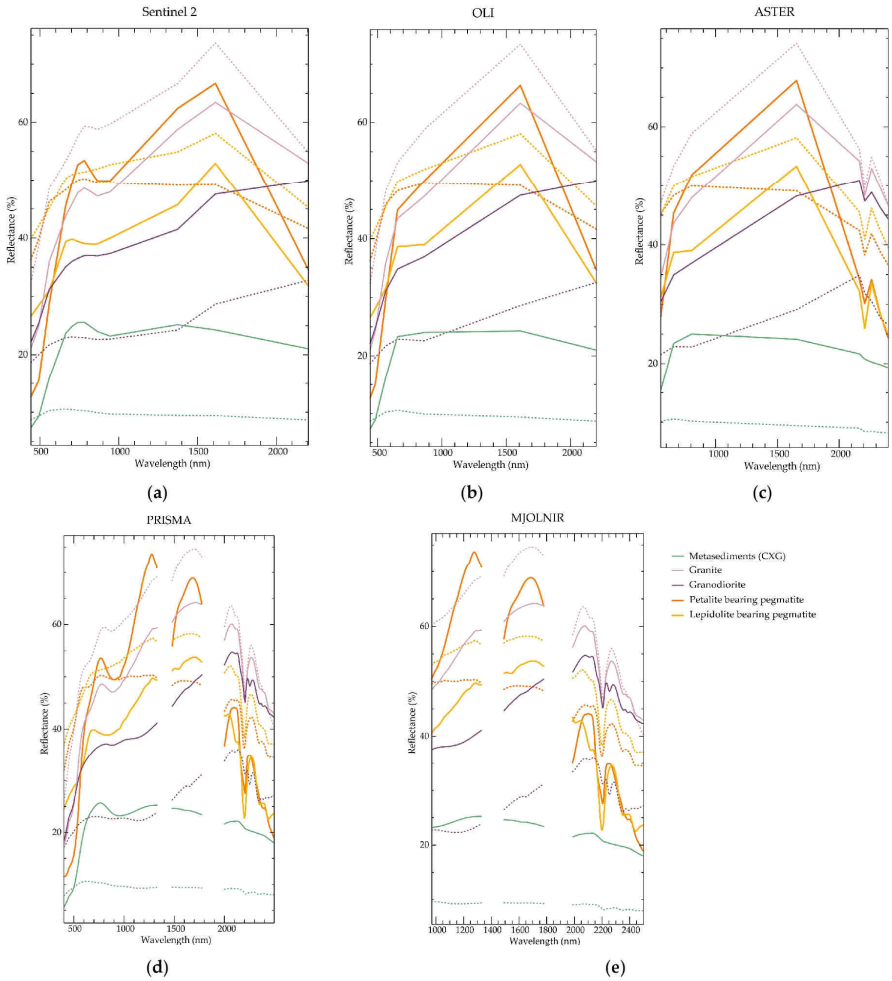

Figure 12. Laboratory spectra of representative spectra from the different training area lithologies (Figure 10) resampled to various multi- and hyperspectral sensors: (**a**) Sentinel-2, (**b**) Landsat-8 Operational Land Imager (OLI), (**c**) Advanced Spaceborne Thermal Emission and Reflection Radiometer (ASTER), (**d**) Prototype Research Instruments and Space Mission technology Advancement (PRISMA), and (**e**) Mjolnir. Weathered samples (full lines) are discriminated from fresher samples (dotted lines).

5. Discussion

5.1. Spectral Behavior of Li-Bearing Minerals

The collected lepidolite (Figure 2), spodumene (Figure 3), and petalite (Figure 4) spectra were compared, and, despite all three minerals showing significant absorption features in the same wavelength regions, the shape, symmetry, and relative depth of the features allowed differentiation of lepidolite from the remaining two Li-minerals. This is because lepidolite has diagnostic absorption features at around 550 nm and 960 nm, as well as a drop-off of the extreme blue (which reflect the purple color of lepidolite) and the white mica typical features due to the hydroxide ion (OH^-) absorption around ~1409 nm associated with the principal, sharp Al–OH absorption feature (between 2195 nm and

2205 nm) and the Al–OH secondaries (around ~2348 nm and ~2435 nm, respectively). These VNIR absorption features allow discriminating lepidolite from other white micas [50]. Since hyperspectral and multispectral air- or satellite-borne sensors cover the VNIR wavelength region, there is a high potential for lepidolite identification using remote sensing data. Previous studies where lepidolite was recognized and discriminated from other white micas using airborne HyMap hyperspectral data [65,66] corroborate this statement, although the position of the Al–OH features also played a fundamental part in that discrimination [66] (this topic will be further discussed below). All three Li-minerals show diagnostic iron-related features in the VNIR region, probably due, in part, to the substitution of aluminum in the minerals' structures (e.g., References [50,67]). In spodumene, iron substitution is observed, as well in the SWIR region (~2240 nm).

Concerning the petalite and spodumene, it was not possible to identify any diagnostic feature because the alteration minerals (montmorillonite with minor illite and kaolinite) dominate their spectral curves. Though, spodumene presents iron-related absorptions at ~2240 nm not visible in petalite. Conversely, some petalite samples showed additional cookeite (Li-chlorite) and saponite (Mg-smectite) features not recognized in spodumene samples. However, this is not enough to distinguish between the two Li-aluminosilicates, because cookeite and other clay minerals (such as kaolinite or smectites) can form from either petalite or spodumene alteration (e.g., [68–70] and references therein). These results also indicate that it would not be possible to spectrally discriminate spodumene or petalite from montmorillonite/illite, based on the absorption features.

Moreover, several authors have noticed a shift in the wavelength position of the main Al–OH absorption due to different Al contents in white micas [7,49,52,64]. As it can be seen in Figure A1 (Appendix A), the lepidolite samples show the Al–OH feature at shorter wavelengths ($\leq$2005 nm), which indicates a higher Al content [7,49,64]. Although the Al–OH feature position of spodumene and petalite overlaps the lepidolite range, there is a tendency for the Al–OH feature to be located at longer wavelengths (Figure A1). These wavelength differences could be caused by the spodumene and petalite substitution by montmorillonite and kaolinite instead of a higher Al content in white micas, especially because they are not present in all spectra.

Such subtle changes in wavelength positions are not detectable through multispectral sensors but are noticeable using hyperspectral data. For example, in the previous work conducted by Oshigami et al. [66], the wavelength position of the Al–OH absorptions allowed the distinction of lepidolite from Al-poor and Al-rich muscovite by applying different thresholds to the employed mineral indices. Despite some overlap in the position of the Al–OH feature between lepidolite and the other Li-minerals, a similar approach could be employed to hyperspectral data to map lepidolite- and spodumene/petalite-bearing areas.

5.2. Effects of Alteration in the Spectral Signature of Li-Bearing Minerals

Comparing the reflectance spectroscopy of altered petalite results (Figure 6) with the complementary petrographic/geochemical techniques (Table 1), it was possible to corroborate the presence of montmorillonite and illite in the same samples. Overall, the combination of methods was complementary, despite some contradictory mineral identification between XRD and reflectance spectroscopy. The XRD identified nontronite and Fe-bearing smectite, while the reflectance spectroscopy indicated montmorillonite and possibly saponite. Nonetheless, previous studies have shown that reflectance spectroscopy has a greater capacity to distinguish among different clay minerals and between clay minerals and illite and muscovite [48,52].

In general, the petalite alteration products' spectral behavior (Figure 6) is very similar to the one observed for petalite (Figure 4), with a dominance of montmorillonite and illite features. Kaolinite and saponite (Mg-smectite) were also observed. Regarding the main Al–OH feature (Figure A1, Appendix A), petalite alteration products show the widest range, reaching higher wavelengths than the ones observed for the three Li-bearing minerals.

There is also a spectral similarity between petalite relics (HD.479 and BJ4-01) and entirely replaced crystals. The petalite relics found within highly altered areas show Li contents compatible with unaltered petalite [13], which may be explained by superficial alteration cover and the concentration of alteration on fractures, cleavage, and crystal border, as observed in Figure 5c–f and Cardoso-Fernandes et al. [57]. Figure 7 shows an inverse correlation between the Li content and the hydroxyl and water features depth (Pearson's r = 0.95 and 0.88, respectively). However, it is not possible to estimate the Li content based on these parameters, because, at low Li concentrations, no trend was observed. From samples with preserved petalite relics to the wholly altered ones, there is an increase in the OH^- and H_2O absorption depth explained by higher amounts of alteration minerals since mineral abundance is related to the absorption intensity [56,64,71]. On its turn, a higher petalite substitution for alteration minerals such as clays leads to a decrease in Li content (Table 1 and Figure 7). The results indicate that the absorption intensity could be used to discriminate fresher petalite samples.

Despite the different climate, the resultant mineral alteration assemblage (montmorillonite and other smectite group minerals, illite, kaolinite) is very similar to the spodumene and petalite's supergene alteration paragenesis found in Brazil under tropical to subtropical climate [25]. Previous studies have shown that these alteration minerals can result from either supergene (weathering) or hydrothermal metasomatic alteration in the late stages of pegmatite crystallization [57,68,72,73], which would explain the occurrence of the same mineral paragenesis under distinct weathering conditions. At the same time, the presence of clay minerals in microfractures in spodumene was already described by Clark et al. [50], causing the spectral behavior of spodumene to be dominated by the clay's absorption features. Therefore, it is not surprising that spodumene and petalite samples show similar spectral curves because the two minerals seem to undergo the same alteration phenomena.

Taking this into account, it is indisputable that the alteration deeply affects the spectral behavior of Li-minerals even when clay minerals are present in minimal amounts. Therefore, any possible spectral signature of petalite or spodumene in the VNIR-SWIR spectral range is obscured by the very pronounced clay-related features. This poses advantages and limitations in satellite-based Li-exploration. Since spodumene and petalite's spectral features are similar and because different alteration degrees produce the same spectral signal, the ability to spectrally identify spodumene or petalite using the same methodology is not compromised. This is in line with the results obtained with classical and machine learning techniques in the study area [21,23]. Additionally, the results indicate no need for different methodological approaches worldwide since the same mineral assemblages could be found in distinct climates. The work of Santos et al. [22] corroborated this interpretation, because the methods developed for Li-pegmatite identification in the Fregeneda–Almendra area also showed potential for Li-exploration in the Minas Gerais region (Brazil). The main limitation is the impossibility of the spectral features allow discrimination between the areas where spodumene and/or petalite occur from the areas where the weathering of other materials produced the clay minerals. This means that as in other deposits, clay minerals can be used as pathfinders for petalite or spodumene. Montmorillonite is identified through the diagnostic, broad, asymmetric, and acute absorptions around ~1413 nm and ~1911 nm; the Al–OH feature at ~2206 nm [48,49] shallower than the ~1911 nm one; and the slight inflection around ~1467 nm [1,49]. Kaolinite has also diagnostic features, such as (i) a small inflection around ~2165 nm; (ii) the presence of an Al–OH triplet at ~2312, ~2350, and ~2380 nm; and (iii) double OH^- and Al–OH absorptions (not visible in poorly crystalline kaolinite) [8,48,49,53]. However, this pathfinder approach would only work in areas where argillic alteration is not predominant. In future attempts, the variation of absorption intensity related to proportions of Li content could be used to try to discriminate Li-bearing minerals from barren, clay-bearing areas as observed in Figure 7. The co-occurrence of cookeite (formed after petalite or spodumene alteration) could also be used to highlight Li-bearing areas.

5.3. Discrimination of Li-Pegmatites from the Remaining Lithologies

The last objective of this work was to understand if Li-pegmatites can be discriminated from the remaining field lithologies. In general, it was possible to ascertain that all sampled lithologies present similar absorption features caused by water and/or hydroxyl present in the structure of rock-forming minerals (Figures 8 and 9 and Figure A2). This is due to the presence of white mica/illite in samples from all field lithologies and false-positive areas or due to the presence of montmorillonite in some samples.

Lepidolite, cookeite, and orthoclase were exclusively identified in Li-pegmatite samples. These minerals can be used, therefore, as targets or pathfinders for Li-bearing pegmatites. Lepidolite diagnostic features were already described in Section 5.1, while cookeite shows several diagnostic features, namely: (i) a broad, symmetric main Al–OH feature, (ii) two OH^- absorptions at ~1580 nm and ~1835 nm, and (iii) a deep and broad Mg-OH feature at ~2355 nm [19,25,54,55]. Orthoclase can be indirectly identified through (i) aqueous fluid inclusions with absorptions at ~1410 nm and ~1912 nm [47,55] and (ii) NH_4^+ substituting K^+, with a diagnostic absorption at ~2110 nm [49,61,62]. Chlorite takes place in CXG and granodiorite samples. Biotite occurs in both granite and granodiorite samples, but the exclusive occurrence of phlogopite in the granodiorite allows discrimination between the two. Chlorite and/or biotite were also observed in false-positives areas 1, 3, and 4. Montmorillonite and minor kaolinite compound the alteration assemblage of Li-pegmatites, granite, granodiorite, and false-positive areas 1–3. Altered samples of Li-pegmatite, granite, CXG, and false-positive areas 1–3 present iron oxides, predominantly goethite.

As verified, except for certain exclusive minerals or distinct mineral assemblages, other factors may need to be considered to achieve lithological discrimination fully. When considering the reflectance magnitude of the different classes (Figures 10 and A4), in general, altered samples show higher reflectance values when compared to the fresh ones, which is due to alteration minerals (such as clays and iron-oxides). Additionally, petalite- and lepidolite-bearing pegmatites present similar mean reflectance values, although the former can reach higher maximum values. The granite samples demonstrate the highest mean reflectance (Figure A4). These relative differences in magnitude help to discriminate between lithological types in data from multi- or hyperspectral sensors.

The wavelength position of given absorption features can also be helpful for lithological discrimination (Figures 11 and A5). The metasediments samples of the CXG show the Al–OH absorption position at longer wavelengths which indicates that the white mica is Al-poor (Figure 11); Li-pegmatite samples present the main Al–OH absorption at shorter wavelengths, similar to lepidolite; granitoid samples show an intermediate wavelength position and, therefore, Al content [7,49,52,64]. Despite the correlation between white mica composition and the wavelength position of the Al–OH absorption, more recent studies have shown that Al-rich phengites can overlap the typical muscovite wavelength range [7,8]. Moreover, lepidolite and Li-rich micas are characterized by a lower Al content than muscovite due to Li substituting Al in octahedral sites [74]. This indicates that another factor is influencing the smaller wavelength of the ~2200 nm feature. Additional research, namely detailed mineral chemistry studies, is needed to fully understand this issue. Nonetheless, there is a clear 2205 nm threshold that is useful for remote sensing applications, at least in this study area. Figure 11b indicates that the Al–OH position varies within the different sampled lithologies as the depth of the Al–OH absorption, which is more profound in Li-pegmatite and shallower in CXG samples (either from the training or false-positive areas). Considering this, it is possible to differentiate the CXG metasediments (host rocks) from the target class (Li-pegmatites). The difference between the two classes is even more pronounced when only the most spectrally pure samples are considered (full and half-full symbols of Figure 11). Such wavelength and depth variations could be evaluated using a hyperspectral sensor.

In what concerns the Mg–OH wavelength position (Figure A5; Appendix A), it is not possible to discriminate between the metasedimentary rocks and granitoids due to the overlap of wavelengths. However, chlorite presents a similar wavelength position and

possibly composition in both training and false-positive areas. Except for one Mg-rich chlorite/biotite in the granodiorite samples, all remaining features are compatible with intermediate Mg/Fe compositions [49,59]. In the case of chlorite, the iron-related features in the VNIR range, the shape, position, and relative depth of the ~2250 nm and ~2350 nm absorptions are compatible with intermediate compositions with both Fe and Mg present. Nonetheless, it should be noted that the overlap with the white mica Al–OH secondaries can lead to shifts in the Mg–OH position.

5.4. Potential of Li-Exploration Using Satellite Data

The previous results indicate that the potential use of remote sensing data is highly dependent on the sensors. As seen in Figure 12, the spectral behavior of the CXG metasediments is very distinct from the remaining lithologies, even for the Sentinel-2 and Landsat-8 OLI. However, the Al–OH absorption around ~2200 nm is only recognized in higher resolution sensors (ASTER, PRISMA, and Mjolnir). The existence of a band in this region increases the separability of the CXG metasedimentary class. The granodiorite samples are also spectrally distinct from Li-bearing pegmatites. The most significant similarity is observed between granite and Li-pegmatite samples. The hyperspectral sensors can identify the same wavelength shifts observed in the laboratory (Figure 11) that can help to discriminate them. Nonetheless, PRISMA has advantages over the Mjolnir sensor since the VNIR features can increase the separability of the two classes. On the other hand, when on board aircraft and UAVs, the Mjolnir sensor has a better spatial resolution, reducing the components in spectral mixtures.

Considering the results, it is possible to infer that although the distinct lithologies present similar absorption features, it is possible to spectrally discriminate Li-pegmatites from other lithologies using remote sensing data due to (i) the higher reflectance magnitude, (ii) more profound Al–OH absorption depths, and (iii) shifts in the wavelength position of the Al–OH features. Furthermore, distinct mineral assemblages result in particular spectral behavior (e.g., Li-pegmatites lack chlorite/biotite features in the VNIR region while presenting important and exclusive target minerals). The false-positive areas, for example, despite showing similar clay-related absorptions, also display distinct VNIR features. Of course, the ability to discriminate the target class from the remaining outcropping lithologies increases with an increasing spectral resolution (Figure 12), showing the importance of hyperspectral sensors such as PRISMA or Mjolnir. The capability to spectrally discriminate Li-pegmatites using hyperspectral data needs to be validated in further studies in a real-life application and not only using simulated hyperspectral data (e.g., [8,65,66]).

6. Conclusions

Analyzing the wavelength, shape, and symmetry of diagnostic absorption features, as well as the overall reflectance magnitude and absorption depths of a Li-dedicated spectral library, allowed the identification of the spectral mineralogy and characterization of samples of (i) different Li-bearing minerals, (ii) several field lithologies of the study area, and (iii) samples from areas previously misclassified as Li-pegmatite using a machine learning algorithm. Ultimately, the results obtained allowed evaluation of the potential of remote sensing and spectral data in Li-exploration, thus fulfilling the proposed objectives and addressing the main research questions:

1. *Can Li-bearing minerals be distinguished from each other and other minerals*? The spectra obtained allowed the discrimination of lepidolite from spodumene, petalite, and other white micas. However, it was not possible to distinguish petalite from spodumene because clay-related absorption features dominate the spectra of both Li-minerals, thus obscuring any likely diagnostic spectral behavior. This implies that spodumene and petalite can only be indirectly identified. Several factors, such as the VNIR features or the position of the main Al–OH absorption, enable direct lepidolite identification through multi- or hyperspectral satellite data.

2. *How can the alteration products affect the spectral signature of Li-bearing minerals*? The complementary petrography and geochemical studies proved that the same alteration minerals observed in previous studies occur in either well-preserved or completely altered samples. However, the clay-related absorption depths are much smaller for petalite relics. Further studies are needed to understand if the clay minerals formed from petalite alteration in the Fregeneda–Almendra region are related to weathering or metasomatic processes. Therefore, the effect of alteration paragenesis is paramount in the spectral behavior of spodumene and petalite, thus limiting the possibility to discriminate areas where these Li-minerals occur from heavily altered, barren areas through multispectral data. On the other hand, using hyperspectral data could overcome this limitation, either through the possibility of recognizing variable absorption depths (distinct amounts of clay minerals) or by the identification of other alteration minerals exclusively related to Li-minerals such as cookeite. Notwithstanding, in areas where clay-related alteration is not prevalent, the same methodology can be employed, using montmorillonite and kaolinite as pathfinders to identify spodumene and petalite worldwide since the alteration paragenesis is similar to the described in tropical conditions.
3. *Can Li-pegmatites be spectrally discriminated from other lithologies in a supervised classification attempt*? Despite the similar absorption features, we conclude that the satellite data can map Li-pegmatites through several criteria such as (i) the distinctive reflectance magnitude, (ii) higher absorptions depths, (iii) distinct wavelength position of key absorption features, and (iv) particular overall spectral behavior reflecting different mineral assemblages. Minerals such as lepidolite, cookeite, and orthoclase can work as targets for Li-pegmatites. Further studies are needed to evaluate the performance of hyperspectral data in real-life conditions and compare it with the laboratory-simulated hyperspectral data.

The results and conclusions withdrawn in this work provide valuable insights on the spectral behavior of pegmatite-hosted Li mineralization and minerals, allowing for more reasoned and directed satellite-based approaches in the future, based on the proposed strategies and pathfinders. Additional studies are needed to continue improving the knowledge on the alteration paragenesis and to understand the smaller wavelength of the ~2200 nm feature in lepidolite and its relationship with the Li and Al contents in the octahedral layer.

Supplementary Materials: The following are available online at https://www.mdpi.com/article/10.3390/rs13183688/s1: Table S1: Spectral mineralogy of Li-minerals, Table S2: Spectral mineralogy of the training areas, and Table S3: Spectral mineralogy of the false-positive areas.

Author Contributions: Conceptualization, J.C.-F., A.L. and A.C.T.; methodology, J.C.-F., A.L. and A.C.T.; software, J.C.-F.; formal analysis, J.C.-F., J.S., M.M.P., A.L., M.A.R. and F.D.; investigation, J.C.-F., J.S., F.D., A.L., A.C.T., M.M.P. and M.A.R.; resources, A.L., E.R-R., O.B. and J.C.; data curation, J.C.-F., J.S. and F.D.; writing—original draft preparation, J.C.-F.; writing—review and editing, all the remaining authors; visualization, J.C.-F.; supervision, A.L., A.C.T., M.A.R., M.M.P., E.R.-R. and O.B.; project administration, J.C., A.L. and A.C.T.; and funding acquisition, J.C. and A.L. All authors have read and agreed to the published version of the manuscript.

Funding: The authors would like to thank the financial support provided by FCT–Fundação para a Ciência e a Tecnologia, I.P., with the ERA-MIN/0001/2017–LIGHTS project and, also, with the 869274—GREENPEG—H2020-SC5-2018-2019-2020 project. This work was also supported by national funds through the FCT project UIDB/04683/2020–ICT (Institute of Earth Sciences). Joana Cardoso-Fernandes and Filipa Dias were financially supported within the compass of their respective Ph.D. theses, ref. SFRH/BD/136108/2018 and ref. 2020.05534.BD, by national funds from MCTES through FCT and co-financed by the European Social Fund (ESF) through POCH–Programa Operacional Capital Humano and NORTE 2020 regional program. The Spanish Ministerio de Ciencia, Innovacion y Universidades (Project RTI2018-094097-B-100, with ERDF funds) and the University of Basque County (UPV/EHU) (grant GIU18/084) also contributed economically. The French National Research

Agency (ANR–10–LABX 21–LABEX RESSOURCES 21) partly supported the Master Student personal grant, and the 776804–NEXT–H2020-SC5-2017 project participated in equipment purchasing.

Institutional Review Board Statement: Not applicable.

Informed Consent Statement: Not applicable.

Data Availability Statement: The data presented in this study are openly available in Zenodo at http://doi.org/10.5281/zenodo.4575375, accessed on 12 September 2021, reference number [46].

Conflicts of Interest: The authors declare no conflict of interest. The funders had no role in the design of the study; in the collection, analyses, or interpretation of the data; in the writing of the manuscript; or in the decision to publish the results.

Appendix A

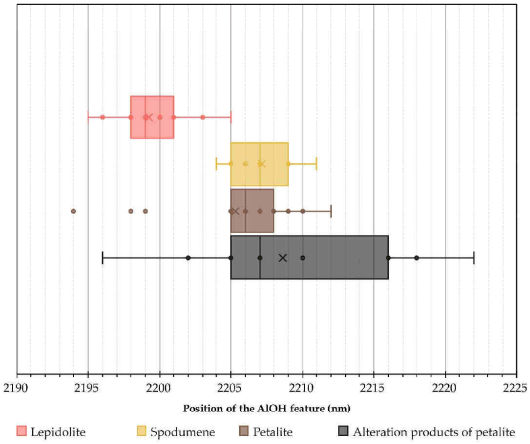

Figure A1. Boxplot diagrams of the main Al–OH absorption wavelength position for the Li minerals and associated alteration products.

Table A1. Description of each false-positive site and respective collected samples. Mineralogical information was collected with optical microscopy and reflectance spectroscopy. Ap—apatite; Bt—biotite; Chl—chlorite; Goe—goethite; Il—illite; IO—iron oxides/hydroxides; Mnt—montmorillonite; Pl—plagioclase; Qtz—quartz; Tur—tourmaline; Ser—sericite; WM—white mica; Zr—zircon.

False-Positive Area	Site Description	Lithology	Petrography	Spectroscopy
1 (GPS point 443)	Wine plantation; disturbed soil with many rock boulders	CXG metasediments: A1 *–striped phyllites interbed with metagraywacke benches; A2–light-colored phyllite.	A1: WM/Ser, Qtz, IO, Bt, Pl, Chl, Tur, detrital WM, detrital Zr, opaque minerals	Il, Mnt, WM, Chl/Bt, Goe and other IO, Qtz?
2 (GPS point 444)	Hillside area; slope deposits	Ordovician metasediments: A1–whitish impure quartzite (metapsamite) with a ferruginous crust; A2/A3–reddish, ferruginous impure quartzite.	A1: Qtz, WM, IO, detrital Zr, Tur	WM, Qtz, Il, Goe, Kao
3 (GPS point 445)	Olive plantation; sparse rock boulders	CXG metasediments: A1/A2–striped phyllites interbed with metagraywacke benches. A3–pegmatite.	A2: WM/Ser, Qtz, Chl, detrital WM, Pl, IO, Ap, opaque minerals	Mnt, Il, Chl/Bt, Goe and other IO, Qtz?
4 (GPS point 446)	Almond plantation; disperse rock boulders	CXG metasediments: A1/A2–striped phyllites interbed with metagraywacke benches	A1: Qtz, WM/Ser, Bt, Pl, detrital WM, Tur, IO, detrital Zr, Ap, opaque minerals	WM, Ser, Chl

* A1 to An: numeration given to different samples collected in the same area (where n equals to the total number of samples).

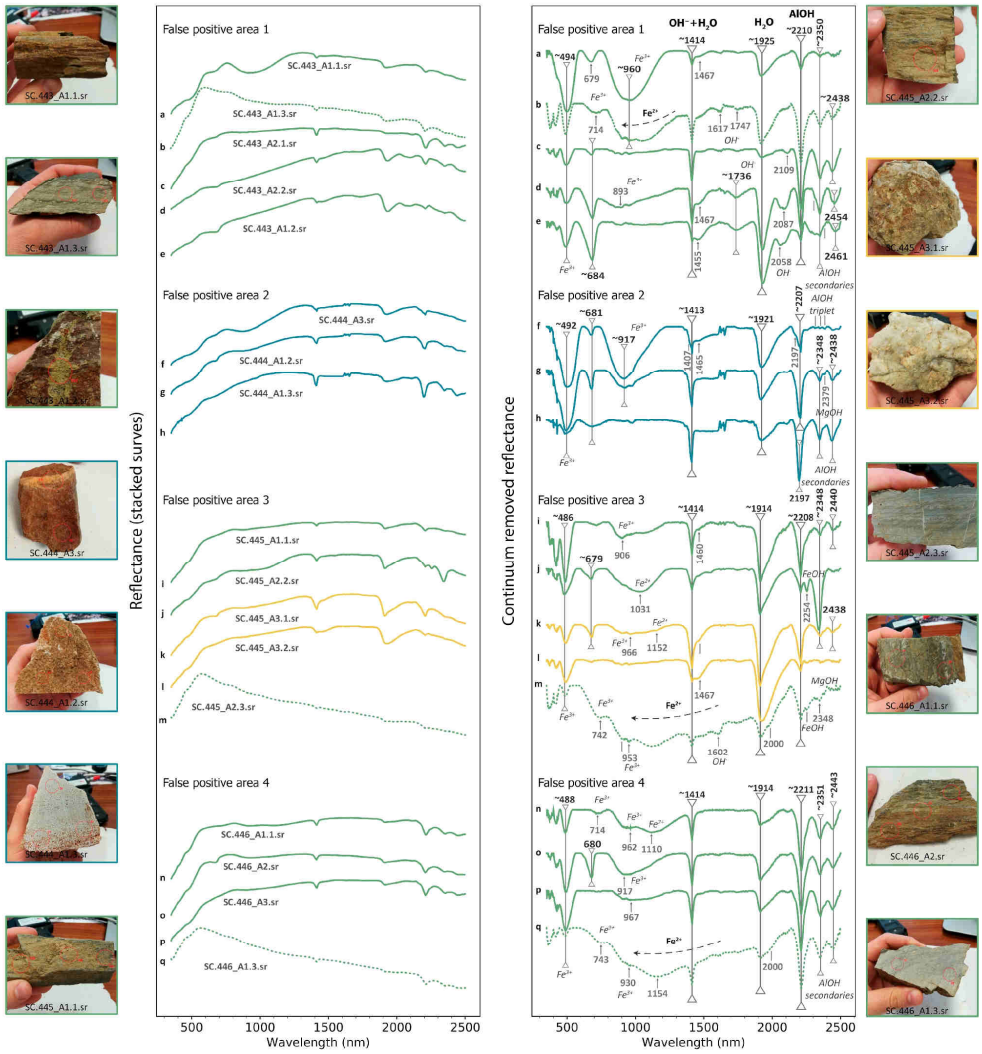

Figure A2. Spectral signature of samples collected in areas misclassified as Li-pegmatite in a previous classification attempt: reflectance curves (to the left) and continuum removed curves (to the right). The main absorption features are highlighted, and sample photographs are provided. Dotted curves: fresh samples; full curves: samples with visible signs of weathering. Each spectrum has a database code [45] providing information about the type of sample (SC—spectral confusion), a three-digit numerical part representing the GPS code, a one- or two-digit code representing the spectra number or the averaged spectra numbers, and a reference to the spectroradiometer employed (sr—SR-6500; asd—FieldSpec 4).

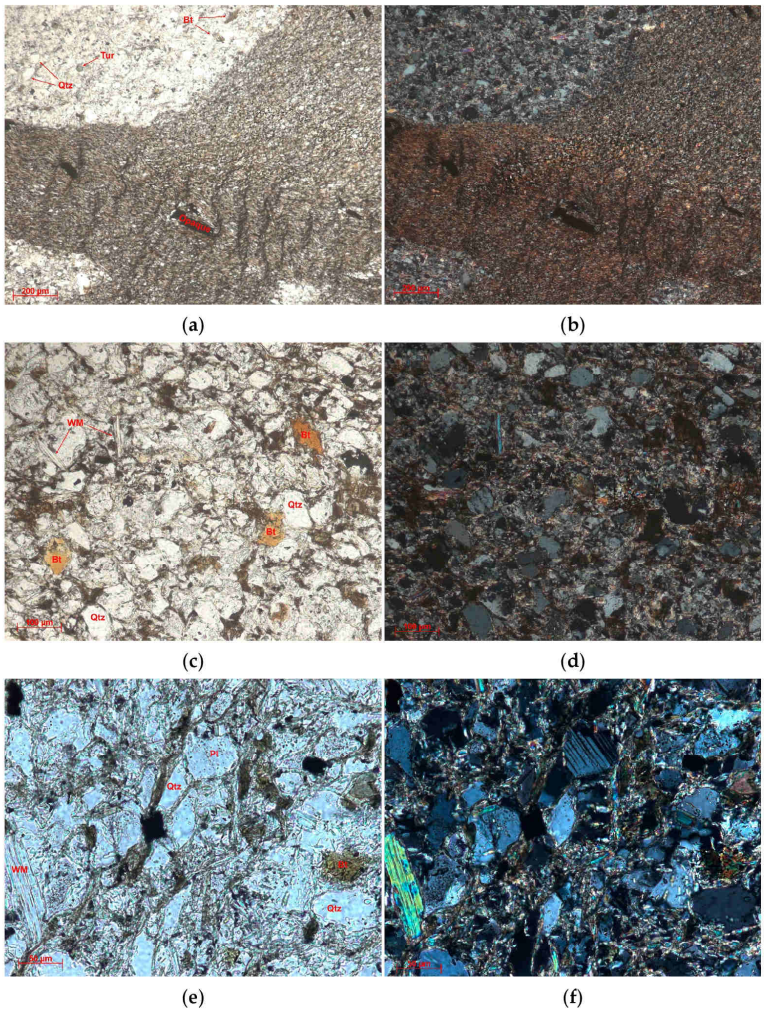

Figure A3. Photomicrographs of the CXG samples collected in the areas misclassified as Li-pegmatite. (**a**,**b**) Alternations of thin, micaceous layers and coarser metagraywacke beds (load cast structures) in parallel polarized light—ppl (**a**) and cross-polarized light—cpl (**b**). (**c**–**f**) The general aspects of the metagraywacke benches in ppl (**c**,**e**) and cpl (**d**,**f**). Bt—biotite; Pl—plagioclase; Qtz—quartz; Tur—tourmaline; WM—white mica.

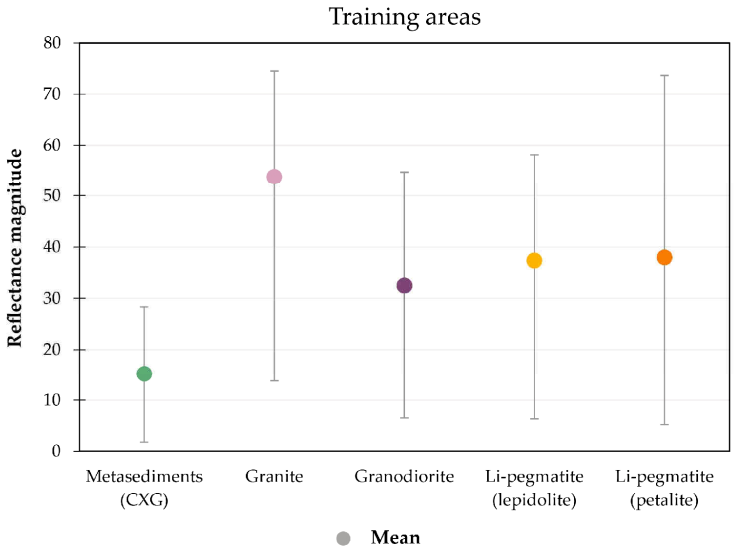

Figure A4. Minimum, maximum, and mean reflectance magnitudes of the different training area lithologies.

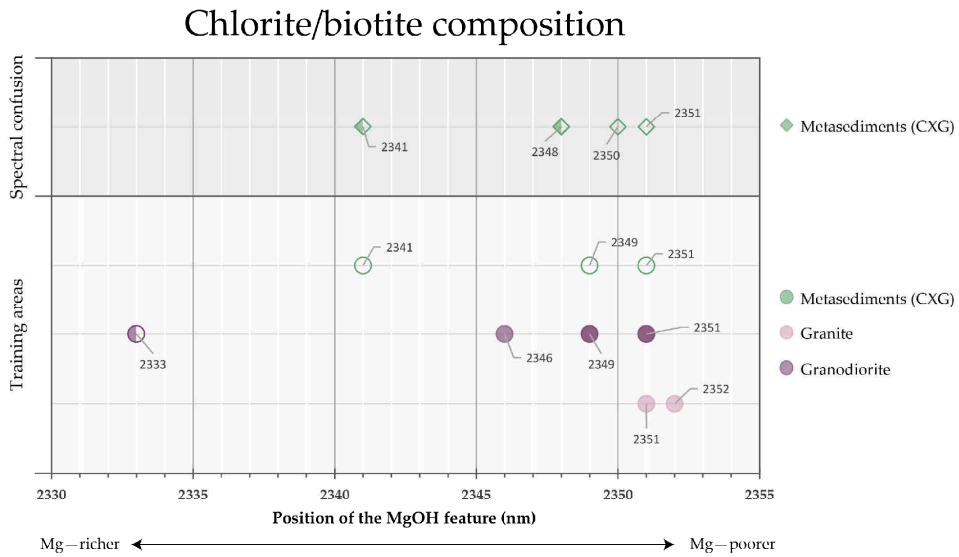

Figure A5. Comparison of the Mg–OH wavelength position of biotites and chlorites from the CXG metasediments and granitoid rocks. Full symbols correspond to biotite; empty symbols correspond to chlorite; half-full symbols represent chlorite and biotite mixtures or samples where it was not possible to discriminate between the two minerals.

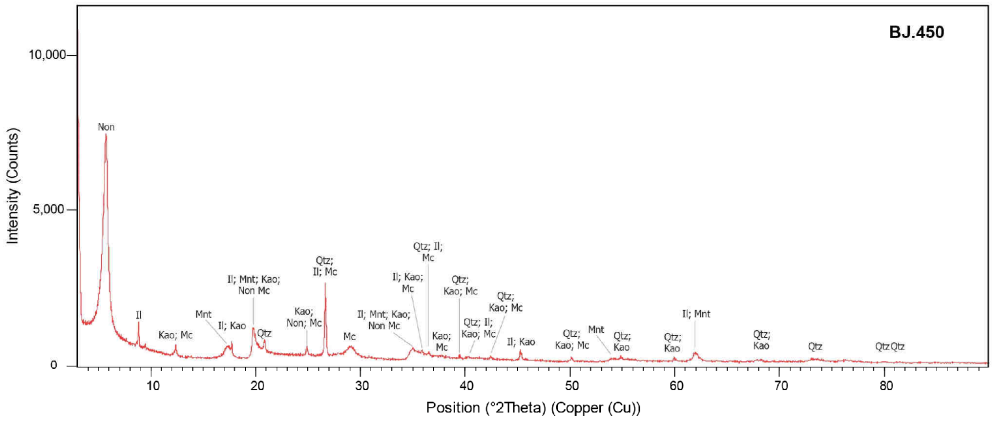

(**a**)

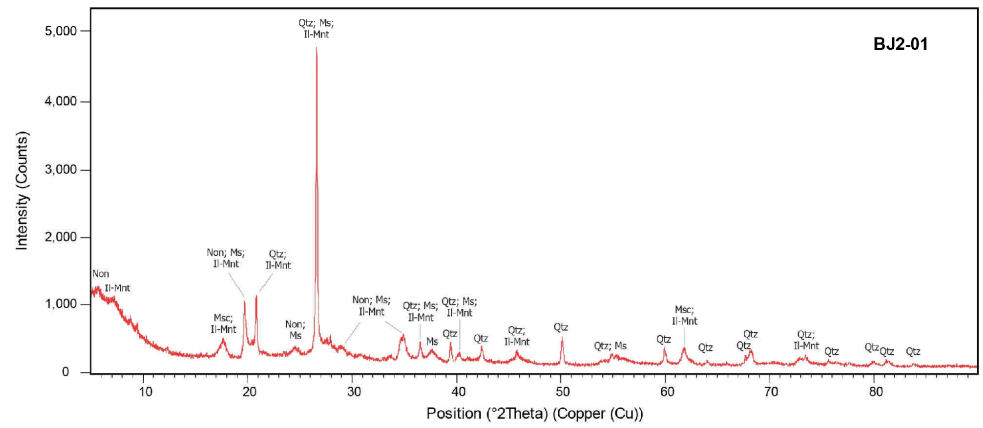

(**b**)

Figure A6. *Cont.*

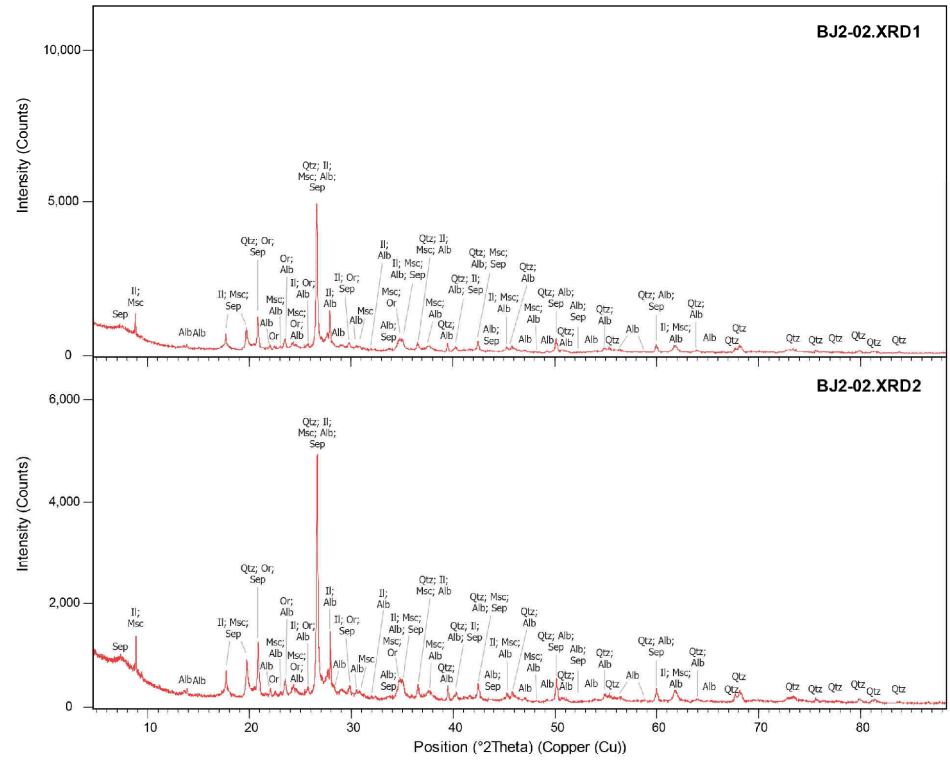

(**c**)

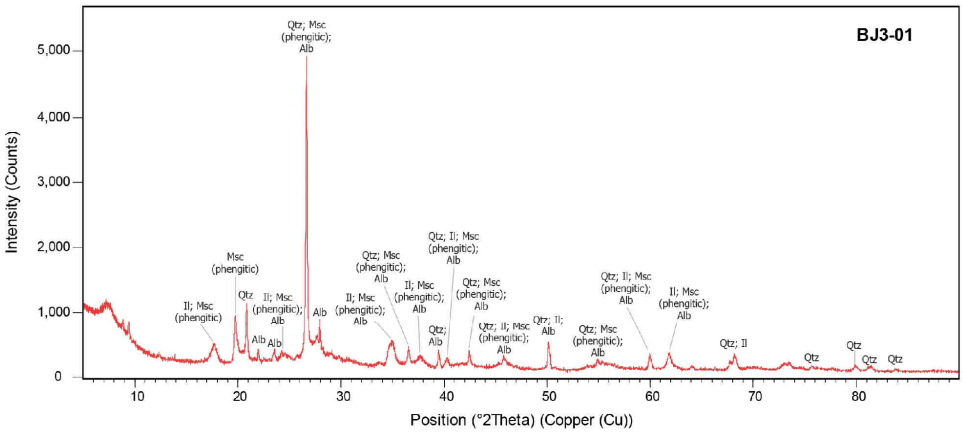

(**d**)

Figure A6. X-ray diffractograms of the selected samples of altered petalite crystals: (**a**) BJ.450, (**b**) BJ2-01, (**c**) BJ2-02, and (**d**) BJ3-01. Alb—albite; Il—illite; Kao—kaolinite; Mnt—montmorillonite; Msc—muscovite; Non—nontronite; Or—orthoclase; Qtz—quartz; Sep—sepiolite.

References

1. Lypaczewski, P.; Rivard, B.; Lesage, G.; Byrne, K.; D'Angelo, M.; Lee, R.G. Characterization of Mineralogy in the Highland Valley Porphyry Cu District Using Hyperspectral Imaging, and Potential Applications. *Minerals* **2020**, *10*, 473. [CrossRef]
2. Laakso, K.; Peter, J.M.; Rivard, B.; Gloaguen, R. Combined hyperspectral and lithogeochemical estimation of alteration intensities in a volcanogenic massive sulfide deposit hydrothermal system: A case study from Northern Canada. In Proceedings of the 2016 8th Workshop on Hyperspectral Image and Signal Processing: Evolution in Remote Sensing (WHISPERS), Los Angeles, CA, USA, 21–24 August 2016; pp. 1–5. [CrossRef]
3. Laakso, K.; Peter, J.M.; Rivard, B.; White, H.P. Short-Wave Infrared Spectral and Geochemical Characteristics of Hydrothermal Alteration at the Archean Izok Lake Zn-Cu-Pb-Ag Volcanogenic Massive Sulfide Deposit, Nunavut, Canada: Application in Exploration Target Vectoring. *Econ. Geol.* **2016**, *111*, 1223–1239. [CrossRef]
4. Turner, D.; Rivard, B.; Groat, L. Rare earth element ore grade estimation of mineralized drill core from hyperspectral imaging spectroscopy. In Proceedings of the 2014 IEEE Geoscience and Remote Sensing Symposium, Quebec City, QC, Canada, 13–18 July 2014; pp. 4612–4615. [CrossRef]
5. Möller, V.; Williams-Jones, A.E. A hyperspectral study (V-NIR-SWIR) of the Nechalacho REE-Nb-Zr deposit, Canada. *J. Geochem. Explor.* **2018**, *188*, 194–215. [CrossRef]
6. Sun, Y.; Seccombe, P.K.; Yang, K. Application of short-wave infrared spectroscopy to define alteration zones associated with the Elura zinc–lead–silver deposit, NSW, Australia. *J. Geochem. Explor.* **2001**, *73*, 11–26. [CrossRef]
7. Tappert, M.C.; Rivard, B.; Giles, D.; Tappert, R.; Mauger, A. The mineral chemistry, near-infrared, and mid-infrared reflectance spectroscopy of phengite from the Olympic Dam IOCG deposit, South Australia. *Ore Geol. Rev.* **2013**, *53*, 26–38. [CrossRef]
8. Naleto, J.L.C.; Perrotta, M.M.; Costa, F.G.d.; de Souza Filho, C.R. Point and imaging spectroscopy investigations on the Pedra Branca orogenic gold deposit, Troia Massif, Northeast Brazil: Implications for mineral exploration in amphibolite metamorphic-grade terrains. *Ore Geol. Rev.* **2019**, *107*, 283–309. [CrossRef]
9. Linnen, R.L.; Van Lichtervelde, M.; Černý, P. Granitic Pegmatites as Sources of Strategic Metals. *Elements* **2012**, *8*, 275–280. [CrossRef]
10. Goodenough, K.M.; Shaw, R.A.; Smith, M.; Estrade, G.; Marqu, E.; Bernard, C.; Nex, P. Economic mineralization in pegmatites: Comparing and contrasting NYF and LCT examples. *Can. Mineral.* **2019**, *57*, 753–755. [CrossRef]
11. Kesler, S.E.; Gruber, P.W.; Medina, P.A.; Keoleian, G.A.; Everson, M.P.; Wallington, T.J. Global lithium resources: Relative importance of pegmatite, brine and other deposits. *Ore Geol. Rev.* **2012**, *48*, 55–69. [CrossRef]
12. Selway, J.B.; Breaks, F.W.; Tindle, A.G. A Review of Rare-Element (Li-Cs-Ta) Pegmatite Exploration Techniques for the Superior Province, Canada, and Large Worldwide Tantalum Deposits. *Explor. Min. Geol.* **2005**, *14*, 1–30. [CrossRef]
13. Dill, H.G. Pegmatites and aplites: Their genetic and applied ore geology. *Ore Geol. Rev.* **2015**, *69*, 417–561. [CrossRef]
14. Steiner, B.M. Tools and Workflows for Grassroots Li–Cs–Ta (LCT) Pegmatite Exploration. *Minerals* **2019**, *9*, 499. [CrossRef]
15. Zhang, A.; Wang, R.; Li, Y.; Hu, H.; Lu, X.; Ji, J.; Zhang, H. Tourmalines from the Koktokay No.3 pegmatite, Altai, NW China: Spectroscopic characterization and relationships with the pegmatite evolution. *Eur. J. Mineral.* **2008**, *20*, 143–154. [CrossRef]
16. Carrino, T.A.; de Brito Barreto, S.; de Oliveira, P.J.A.; de Araújo Neto, J.F.; de Lima Correia, A.M. Linking gemology and spectral geology: A case study of elbaites from Seridó Pegmatite Province, Northeastern Brazil. *Braz. J. Geol.* **2019**, *49*. [CrossRef]
17. Bocchio, R.; Adamo, I.; Caucia, F. Aquamarine from the Masino-Bregaglia Massif, Central Alps, Italy. *Gems Gemol.* **2009**, *45*, 204–207. [CrossRef]
18. de Araújo Neto, J.F.; de Brito Barreto, S.; Carrino, T.A.; Müller, A.; de Lira Santos, L.C.M. Mineralogical and gemological characterization of emerald crystals from Paraná deposit, NE Brazil: A study of mineral chemistry, absorption and reflectance spectroscopy and thermal analysis. *Braz. J. Geol.* **2019**, *49*. [CrossRef]
19. da Silva, S.M.P.; Crósta, A.P.; Angélica, R.S.; Beurlen, H.; da Silva, M.R.R. Mineralogical characterization and mapping using reflectance spectroscopy: An experiment at Alto do Giz pegmatite in the south portion of Borborema Pegmatite Province (BPP), northeastern Brazil. *Estud. Geol.* **2009**, *19*, 337–342.
20. Cardoso-Fernandes, J.; Lima, A.; Roda-Robles, E.; Teodoro, A.C. Constraints and potentials of remote sensing data/techniques applied to lithium (Li)-pegmatites. *Can. Mineral.* **2019**, *57*, 723–725. [CrossRef]
21. Cardoso-Fernandes, J.; Teodoro, A.C.; Lima, A. Remote sensing data in lithium (Li) exploration: A new approach for the detection of Li-bearing pegmatites. *Int. J. Appl. Earth Obs. Geoinf.* **2019**, *76*, 10–25. [CrossRef]
22. Santos, D.; Teodoro, A.; Lima, A.; Cardoso-Fernandes, J. Remote sensing techniques to detect areas with potential for lithium exploration in Minas Gerais, Brazil. In Proceedings of the SPIE Remote Sensing, Strasbourg, France, 9–12 September 2019; Schulz, K., Michel, U., Nikolakopoulos, K.G., Eds.; SPIE: Bellingham, WA, USA, 2019. [CrossRef]
23. Cardoso-Fernandes, J.; Teodoro, A.C.; Lima, A.; Roda-Robles, E. Semi-Automatization of Support Vector Machines to Map Lithium (Li) Bearing Pegmatites. *Remote Sens.* **2020**, *12*, 2319. [CrossRef]
24. Gao, Y.; Bagas, L.; Li, K.; Jin, M.; Liu, Y.; Teng, J. Newly Discovered Triassic Lithium Deposits in the Dahongliutan Area, NorthWest China: A Case Study for the Detection of Lithium-Bearing Pegmatite Deposits in Rugged Terrains Using Remote-Sensing Data and Images. *Front. Earth Sci.* **2020**, *8*, 553. [CrossRef]
25. Costa, M.A.C.; Perrotta, M.M.; Melo, T.G.; Turra, B. Estudos Espectrais. In *Avaliação do Potencial do Lítio no Brasil: Área do Médio Rio Jequitinhonha, Nordeste de Minas Gerais: Texto Explicativo e Mapas*; Paes, V.J.C., Santos, L.D., Tedeschi, M.F., Betiollo, L.M., Eds.; CPRM: Belo Horizonte, MG, Brazil, 2016; p. 276.

26. Vieira, R. Aplitopegmatitos com Elementos Raros da Região Entre Almendra (V.N. de Foz Côa) e Barca d'Alva (Figueira de Castelo Rodrigo). Campo Aplitopegmatítico da Fregeneda-Almendra. Ph.D. Thesis, Faculdade de Ciências da Universidade do Porto, Porto, Portugal, 2010.
27. Roda, E. Distribución, Caracteristicas y Petrogenesis de las Pegmatitas de La Fregeneda (Salamanca). Ph.D. Thesis, Facultad de Ciencia y Tecnología de la Universidad del País Vasco (UPV/EHU), Bilbao, Spain, 1993.
28. Cardoso-Fernandes, J.; Teodoro, A.C.; Lima, A.; Roda-Robles, E. Evaluating the performance of support vector machines (SVMs) and random forest (RF) in Li-pegmatite mapping: Preliminary results. In Proceedings of the SPIE Remote Sensing, Strasbourg, France, 9–12 September 2019; Schulz, K., Michel, U., Nikolakopoulos, K.G., Eds.; SPIE: Bellingham, WA, USA, 2019. [CrossRef]
29. Cardoso-Fernandes, J.; Silva, J.; Lima, A.; Teodoro, A.C.; Perrotta, M.; Cauzid, J.; Roda-Robles, E. Characterization of lithium (Li) minerals from the Fregeneda–Almendra region through laboratory spectral measurements: A comparative study. In *Earth Resources and Environmental Remote Sensing/GIS Applications XI*; SPIE: Bellingham, WA, USA, 2020. [CrossRef]
30. Cardoso-Fernandes, J.; Silva, J.; Lima, A.; Teodoro, A.C.; Perrotta, M.; Cauzid, J.; Roda-Robles, E.; Ribeiro, M.A. Reflectance spectroscopy to validate remote sensing data/algorithms for satellite-based lithium (Li) exploration (Central East Portugal). In *Earth Resources and Environmental Remote Sensing/GIS Applications XI*; SPIE: Bellingham, WA, USA, 2020. [CrossRef]
31. Roda-Robles, E.; Pesquera, A.; Velasco, F.; Fontan, F. The granitic pegmatites of the Fregeneda area (Salamanca, Spain): Characteristics and petrogenesis. *Mineral. Mag.* **1999**, *63*, 535–558. [CrossRef]
32. da Costa, J.C.S. *Notícia Sobre Uma Carta Geológica do Buçaco, de Nery Delgado*; Serviços Geológicos de Portugal: Lisboa, Portugal, 1950.
33. Teixeira, C. *Notas Sobre Geologia de Portugal o Complexo Xisto-Grauváquico Ante-Ordoviciano*; Empresa Literaria Fluminense Lda.: Lisboa, Portugal, 1955; p. 48.
34. Rodríguez Alonso, M.D.; Díez Balda, M.A.; Perejón, A.; Pieren, A.; Liñán, E.; López Díaz, F.; Moreno, F.; Gámez Vintaned, J.A.; Gónzalez Lodeiro, F.; Martínez Poyatos, D.; et al. Domínio del Complejo Esquisto-Grauváquico: Estratigrafía. La secuencia litoestratigráfica del Neoproterozóico-Cámbrico Inferior. In *Geología de España*; Vera, J.A., Ed.; Geológica de España-Instituto Geológico y Minero de España (SGE-IGME): Madrid, Spain, 2004; pp. 78–81.
35. Pereira, I.; Dias, R.; Bento dos Santos, T.; Mata, J. Exhumation of a migmatite complex along a transpressive shear zone: Inferences from the Variscan Juzbado–Penalva do Castelo Shear Zone (Central Iberian Zone). *J. Geol. Soc.* **2017**, *174*, 1004. [CrossRef]
36. Ferreira, J.A.; Bento dos Santos, T.; Pereira, I.; Mata, J. Tectonically assisted exhumation and cooling of Variscan granites in an anatectic complex of the Central Iberian Zone, Portugal: Constraints from LA-ICP-MS zircon and apatite U–Pb ages. *Int. J. Earth Sci.* **2019**, *108*, 2153–2175. [CrossRef]
37. da Silva, A.F.; Ribeiro, M.L. *Notícia Explicativa da Folha 15-A: Vila Nova de Foz Côa*; Serviços Geológicos de Portugal: Lisboa, Portugal, 1991; p. 52.
38. da Silva, A.F.; Ribeiro, M.L. *Notícia Explicativa da Folha 15-B: Freixo de Espada à Cinta*; Instituto Geológico e Mineiro: Lisboa, Portugal, 1994; p. 48.
39. Silva, A.F.; Santos, A.J.; Ribeiro, A.; Cabral, J.; Ribeiro, M.L. *Carta Geológica de Portugal na Escala 1/50.000–Folha 15-B–Freixo de Espada à Cinta*; Serviços Geológicos de Portugal: Lisboa, Portugal, 1990.
40. Silva, A.F.; Santos, A.J.; Ribeiro, A.; Ribeiro, M.L. *Carta Geológica de Portugal na Escala 1/50.000–folha 15-A–Vila Nova de Foz Côa*; Serviços Geológicos de Portugal: Lisboa, Portugal, 1990.
41. ASD Inc. *ViewSpec Pro™ User Manual*; ASD Document 600555 Rev. A; ASD Inc.: Boulder, CO, USA, 2008.
42. Menges, F. Spectragryph–Optical Spectroscopy Software, Version 1.2.14. Available online: http://www.effemm2.de/spectragryph/ (accessed on 22 July 2020).
43. Clark, R.N.; Roush, T.L. Reflectance spectroscopy: Quantitative analysis techniques for remote sensing applications. *J. Geophys. Res. Solid Earth* **1984**, *89*, 6329–6340. [CrossRef]
44. Therien, C. Welcome to the PySptools Documentation. Available online: https://pysptools.sourceforge.io/ (accessed on 22 July 2020).
45. Cardoso-Fernandes, J.; Silva, J.; Dias, F.; Lima, A.; Teodoro, A.C.; Barrès, O.; Cauzid, J.; Perrotta, M.; Roda-Robles, E.; Ribeiro, M.A. Tools for Remote Exploration: A Lithium (Li) Dedicated Spectral Library of the Fregeneda–Almendra Aplite–Pegmatite Field. *Data* **2021**, *6*, 33. [CrossRef]
46. Cardoso-Fernandes, J.; Silva, J.; Dias, F.; Lima, A.; Teodoro, A.C.; Barrès, O.; Cauzid, J.; Perrotta, M.; Roda-Robles, E.; Ribeiro, M.A. *Tools for Remote Exploration: A Lithium (Li) Dedicated Spectral Library of the Fregeneda–Almendra Aplite-Pegmatite Field*; Zenodo: Meyrin, Switzerland, 2021. [CrossRef]
47. Hunt, G.R.; Salisbury, J.W. Visible and near-infrared spectra of minerals and rocks: I Silicate minerals. *Mod. Geol.* **1970**, *1*, 283–300.
48. Clark, R.N.; King, T.V.V.; Klejwa, M.; Swayze, G.A.; Vergo, N. High spectral resolution reflectance spectroscopy of minerals. *J. Geophys. Res. Solid Earth* **1990**, *95*, 12653–12680. [CrossRef]
49. Pontual, S.; Merry, N.J.; Gamson, P. *Spectral Interpretation Field Manual: GMEX Spectral Analysis Guides for Mineral Exploration*, 3rd ed.; AusSpec International Ltd.: Victoria, Australia, 2008; Volume 1.
50. Clark, R.N.; Swayze, G.A.; Gallagher, A.J.; King, T.V.V.; Calvin, W.M. *The U. S. Geological Survey, Digital Spectral Library: Version 1 (0.2 to 3.0 um)*; Open-File Report 93–592; Geological Survey: Reston, WV, USA, 1993.
51. Mattson, S.M.; Rossman, G.R. Fe^{2+}-Fe^{3+} interactions in tourmaline. *Phys. Chem. Miner.* **1987**, *14*, 163–171. [CrossRef]

52. Clark, R.N. Chapter 1: Spectroscopy of rocks and minerals and principles of spectroscopy. In *Remote Sensing for the Earth Sciences: Manual of Remote Sensing*, 3rd ed.; Ryerson, R.A., Ed.; John Wiley & Sons, Inc.: Hoboken, NJ, USA, 1999.
53. Hunt, G.R. Spectral signatures of particulate minerals in the visible and near infrared. *Geophysics* **1977**, *42*, 501–513. [CrossRef]
54. King, T.V.V.; Clark, R.N. Spectral characteristics of chlorites and Mg-serpentines using high-resolution reflectance spectroscopy. *J. Geophys. Res. Solid Earth* **1989**, *94*, 13997–14008. [CrossRef]
55. Clark, R.N.; Swayze, G.A.; Wise, R.; Livo, K.E.; Hoefen, T.M.; Kokaly, R.F.; Sutley, S.J. USGS Digital Spectral Library splib05a. Available online: https://pubs.usgs.gov/of/2003/ofr-03-395/ (accessed on 8 January 2021).
56. Hunt, G.R.; Ashley, R.P. Spectra of altered rocks in the visible and near infrared. *Econ. Geol.* **1979**, *74*, 1613–1629. [CrossRef]
57. Cardoso-Fernandes, J.; Dias, F.; Lima, A.; Anjos Ribeiro, M.; Perrotta, M.; Roda-Robles, E.; Teodoro, A.C. Petalite alteration products from the Bajoca pegmatite (Central Portugal): A multiapproach for lithium exploration. In Proceedings of the EGU General Assembly 2021, Online, 19–30 April 2021. [CrossRef]
58. Lima, A. Estrutura, Mineralogia e Génese dos Filões Aplitopegmatíticos com Espodumena da Região do Barroso-Alvão. Ph.D. Thesis, Universidade do Porto, Porto, Portugal, 2000.
59. Lypaczewski, P.; Rivard, B. Estimating the Mg# and AlVI content of biotite and chlorite from shortwave infrared reflectance spectroscopy: Predictive equations and recommendations for their use. *Int. J. Appl. Earth Obs. Geoinf.* **2018**, *68*, 116–126. [CrossRef]
60. Bishop, J.L.; Lane, M.D.; Dyar, M.D.; Brown, A.J. Reflectance and emission spectroscopy study of four groups of phyllosilicates: Smectites, kaolinite-serpentines, chlorites and micas. *Clay Miner.* **2008**, *43*, 35–54. [CrossRef]
61. Felzer, B.; Hauff, P.; Goetz, A.F.H. Quantitative reflectance spectroscopy of buddingtonite from the Cuprite mining district, Nevada. *J. Geophys. Res. Solid Earth* **1994**, *99*, 2887–2895. [CrossRef]
62. Krohn, M.D.; Altaner, S.P. Near-infrared detection of ammonium minerals. *Geophysics* **1987**, *52*, 924–930. [CrossRef]
63. Aires, S.C.M. Petrofísica e Litogeoquímica de Formações do "Complexo Xisto-Grauváquico" (Grupo do Douro) Estudo do Potencial do "Xisto" Para Exploração Como Pedra Natural. Ph.D. Thesis, Faculdade de Ciências da Universidade do Porto, Porto, Portugal, 2018.
64. Duke, E.F. Near infrared spectra of muscovite, Tschermak substitution, and metamorphic reaction progress: Implications for remote sensing. *Geology* **1994**, *22*, 621–624. [CrossRef]
65. Ellis, R.J.; Scott, P.W. Evaluation of hyperspectral remote sensing as a means of environmental monitoring in the St. Austell China clay (kaolin) region, Cornwall, UK. *Remote Sens. Environ.* **2004**, *93*, 118–130. [CrossRef]
66. Oshigami, S.; Yamaguchi, Y.; Uezato, T.; Momose, A.; Arvelyna, Y.; Kawakami, Y.; Yajima, T.; Miyatake, S.; Nguno, A. Mineralogical mapping of southern Namibia by application of continuum-removal MSAM method to the HyMap data. *Int. J. Remote Sens.* **2013**, *34*, 5282–5295. [CrossRef]
67. Deer, W.A.; Howie, R.A.; Zussman, J. *Rock-Forming Minerals: Single-Chain Silicates*, 2nd ed.; The Geological Society: London, UK, 1978; Volume 2A, p. 668.
68. London, D.; Burt, D.M. Chemical models for lithium aluminosilicate stabilities in pegmatites and granites. *Am. Mineral.* **1982**, *67*, 494–509.
69. Dill, H.G. A geological and mineralogical review of clay mineral deposits and phyllosilicate ore guides in Central Europe—A function of geodynamics and climate change. *Ore Geol. Rev.* **2020**, *119*, 103304. [CrossRef]
70. Cerny, P. The Tanco pegmatite at Bernic Lake, Manitoba; VIII, Secondary minerals from the spodumene-rich zones. *Can. Mineral.* **1972**, *11*, 714–726.
71. Asadzadeh, S.; Souza Filho, C.R. A review on spectral processing methods for geological remote sensing. *Int. J. Appl. Earth Obs. Geoinf.* **2016**, *47*, 69–90. [CrossRef]
72. Quensel, P. Minerals of the Varuträsk Pegmatite: IV. Petalite and its Alteration Product, Montmorillonite. *Geol. Fören. Stockh. Förh.* **1937**, *59*, 150–156. [CrossRef]
73. Quensel, P. Minerals of the Varuträsk Pegmatite: X. Spodumene and its Alteration Products. *Geol. Fören. Stockh. Förh.* **1938**, *60*, 201–215. [CrossRef]
74. Foster, M.D. *Interpretation of the Composition of Lithium Micas*; United States Geological Survey Professional Paper: Washington, DC, USA, 1960; pp. 115–147.

minerals

MDPI

Article

Lithium Potential Mapping Using Artificial Neural Networks: A Case Study from Central Portugal

Martin Köhler [1,*], Delira Hanelli [1], Stefan Schaefer [1], Andreas Barth [1], Andreas Knobloch [1], Peggy Hielscher [1], Joana Cardoso-Fernandes [2,3], Alexandre Lima [2,3] and Ana C. Teodoro [2,3]

[1] Beak Consultants GmbH, Am St. Niclas Schacht 13, 09599 Freiberg, Germany; delira.hanelli@beak.de (D.H.); st.schaefer.geo@googlemail.com (S.S.); andreas.barth@beak.de (A.B.); andreas.knobloch@beak.de (A.K.); peggy.hielscher@beak.de (P.H.)
[2] Department of Geosciences, Environment and Spatial Planning, Faculty of Sciences, University of Porto, 4169-007 Porto, Portugal; joana.fernandes@fc.up.pt (J.C.-F.); allima@fc.up.pt (A.L.); amteodor@fc.up.pt (A.C.T.)
[3] Institute of Earth Sciences (ICT), Pole of University of Porto, 4169-007 Porto, Portugal
* Correspondence: martin.koehler@beak.de

Abstract: The growing importance and demand of lithium (Li) for industrial applications, in particular rechargeable Li-ion batteries, have led to a significant increase in exploration efforts for Li-bearing minerals. To ensure and expand a stable Li supply to the global economy, extensive research and exploration are necessary. Artificial neural networks (ANNs) provide powerful tools for exploration target identification. They can be cost-effectively applied in various geological settings. This article presents an integrated approach of Li exploration targeting using ANNs for data interpretation. Based on medium resolution geological maps (1:50,000) and stream sediment geochemical data (1 sample per 0.25 km^2), the Li potential was calculated for an area of approximately 1200 km^2 in the surroundings of Bajoca Mine (Northeast Portugal). Extensive knowledge about geological processes leading to Li mineralisation (such as weathering conditions and diverse Li minerals) proved to be a determining factor in the exploration model. Furthermore, Sentinel-2 satellite imagery was used in a separate ANN model to identify potential Li mine sites exposed on the ground surface by analysing the spectral signature of surface reflectance in well-known Li locations. Finally, the results were combined to design a final map of predicted Li mineralisation occurrences in the study area. The proposed approach reveals how remote sensing data in combination with geological and geochemical data can be used for delineating and ranking exploration targets of almost any deposit type.

Keywords: lithium; mineral predictive mapping; exploration targeting; artificial neural networks; Portugal

Citation: Köhler, M.; Hanelli, D.; Schaefer, S.; Barth, A.; Knobloch, A.; Hielscher, P.; Cardoso-Fernandes, J.; Lima, A.; Teodoro, A.C. Lithium Potential Mapping Using Artificial Neural Networks: A Case Study from Central Portugal. *Minerals* **2021**, *11*, 1046. https://doi.org/10.3390/min11101046

Academic Editors: Maarit Middleton and Veronika Kopačková-Strandová

Received: 13 August 2021
Accepted: 22 September 2021
Published: 27 September 2021

Publisher's Note: MDPI stays neutral with regard to jurisdictional claims in published maps and institutional affiliations.

Copyright: © 2021 by the authors. Licensee MDPI, Basel, Switzerland. This article is an open access article distributed under the terms and conditions of the Creative Commons Attribution (CC BY) license (http://creativecommons.org/licenses/by/4.0/).

1. Introduction

Lithium (Li) is on the European Union's (EU) list of critical raw materials [1], is an important element in modern technology applications, and plays a key role in the realisation of electromobility and effective energy storage. The supply of Li to the global industry depends on expanding the supply of resources. Therefore, the exploration of new Li deposits is vital to the establishment of a stable Li supply in the global economy. At present, about 50% of the global Li production is used in batteries, while 30% is used in the ceramics and glass sector. Minor shares are used in pharmaceuticals and the production of specialised lubricating grease [2]. Li-rich minerals (mainly from Li pegmatites) now account for more than half of the world's lithium production.

Li pegmatites have been extensively studied from an economic, petrographical, and geochemical point of view. The relative importance of pegmatite, brine, and other

deposits is discussed by [3], leading to the conclusion that Li pegmatites, while certainly much smaller in tonnage than brine deposits, are a valuable asset to the global Li market due to their widespread occurrence. Li pegmatites could therefore lead to a geographical diversification in lithium production that would counteract the geopolitically restricted distribution of brine deposits [4]. General characteristics for such Li pegmatites are enrichment in distinct elements (Rb, Cs, Be, Ta, Nb, Sn, Li, P, F, and B) and distinct geochemical composition, but limited volumes. Economic pegmatitic lithium mineralisations are dominated by the minerals spodumene ($LiAlSi_2O_6$), petalite ($LiAlSi_4O_{10}$), and lepidolite group minerals ($K[Li,Al]_3[Si,Al]_4O_{10}[F,OH]_2$), and [5] improved the understanding of the crystallisation conditions of rare-element pegmatites by constructing a lithium aluminosilicate phase diagram. However, mechanisms for Li predictivity are only rarely addressed [5].

Portugal hosts considerable Li resources [3,6] and is the first Li-producing European country, but represents only 1.3% of world production [6]. Recent exploration by different mining companies increased the Portuguese reserves multiple times and significant research was performed to enhance the understanding of Li mineralisation types and deposits. An overview of Li-rich mineral occurrences in northern Portugal is provided by [7], and [8] covered the different styles of Li mineralisations (aplite–pegmatite dykes occurring in pegmatitic fields, Li mineralisation associated with leucogranitic cupolas, beryl–phosphate pegmatites, and quartz–montebrasite veins).

Artificial neural networks (ANNs) are powerful in the early stages of resource exploration. In recent years, several studies proved the potential of ANNs and their uses in geological contexts, e.g., [9–12]. Neural networks have several advantages over existing methods, including the ability to respond to critical combinations of parameters, the combination of datasets without the loss of information inherent in existing methods, and results that are relatively unaffected by redundant data, spurious data, and data containing multiple populations [9]. A Geographic Information System (GIS), in concert with ANN software, offers great potential by providing a range of tools to query, manipulate, visualise, and analyse geological, geochemical, and geophysical data in mineral exploration applications [11]. Mineralisation potential maps can be easily produced to delineate areas for further exploration and therefore reduce the size of the actual fieldwork areas (thus time and expenditure) significantly.

This study aims to use ANNs to process classical geological data (maps and geochemical analyses) reliably and cost-effectively to enhance exploration targeting. As part of the LIGHTS project (Lightweight Integrated Ground and Airborne Hyperspectral Topological Solution; http://lights.univ-lorraine.fr/; accessed on 23 September 2021), this study aims to design a new exploration process chain at the target scale. Prospective areas with previously unknown Li mineralisations will then strengthen the geological understanding of the area and refine geological and minerogenetic maps. Moreover, this study assesses for the first time the potential use of different datasets and their combination according to known metallogenic aspects of the study area. Similar approaches could be extended to other areas of the Iberian Peninsula or even the European Variscides, allowing an increase in the knowledge on Li pegmatite distribution.

1.1. Geological Overview of the Test Area

Li mineralisation can be traced across the whole Central Iberian Zone (CIZ) of the Iberian Massif [8,13]. The CIZ represents parts of the westernmost segment of the Variscan Orogenic Belt of Europe, the latter extending from the Bohemian Massif across the Massif Central and the Armorican Massif to the north-western tip of the Iberian Peninsula, e.g., [14]. Geologically, the CIZ is dominated by S-type Variscan granitoid batholith complexes and adjacent metasedimentary zones (e.g., [13,15,16]). The main Li mineralisation in the CIZ is associated with pegmatitic to aplitic textured intrusive dykes of granitic composition [8]. The most Li-enriched dykes are unzoned and exhibit aplitic textures, often showing host-rock-contact parallel layering [13]. Additionally, Li occurrences of

subsequent economic importance appear as quartz–phosphate veins and metasomatic modified cupolas of albite granites [8].

The approximate 1200 km² study area is located in north-western Portugal and covers major parts of the Fregenedra–Almendra pegmatitic field (FAF), CIZ (c.f. [17–19]) (Figure 1). The area is characterised by various pegmatite and aplite textured dykes hosted by Precambrian to Cambrian metasediments of the schist–metagreywacke complex (Complexo Xisto-Grauváquico, [20,21]) north of the Meda-Penedono-Lumbrales Granitoid Complex [22], recently designated as the Figueira de Castelo Rodrigo–Lumbrales Anatectic Complex [23,24]. The metasedimentary rocks of the schist–metagreywacke complex may contain quartz, white mica, biotite, plagioclase, K-feldspar, chlorite, zircon, apatite, tourmaline, calcite, epidote, sphene, actinolite, monazite, and opaque minerals [25]. The Granitoid Complex is mainly composed of syn-Variscan two-mica granites [26,27] composed of quartz, plagioclase, potassic feldspar, biotite, muscovite, chlorite, sillimanite, zircon, apatite, rutile, and opaque minerals [24]. The Li-rich dykes are predominated by aplitic textures, with some exhibiting layering of Li-mica+quartz alternating with albite+quartz sequences [8]. The mainly sub-vertical bodies display simple mineralogy including albite, k-feldspar, quartz, and muscovite (barren type) associated with spodumene, petalite, and Li-micas in variable proportions (intermediate and rare-element type) [8]. Common accessory minerals are Li-phosphates, cassiterite, and Nb–Ta oxides [8]. The FAF is bounded at the northeast by the Lower Ordovician quartzites from the Poiares' syncline. Alternating Ordovician quartzites and phyllites occur in the smaller Castelo Melhor's syncline. Cenozoic sedimentary deposits of diverse origins occur throughout the region [26–31].

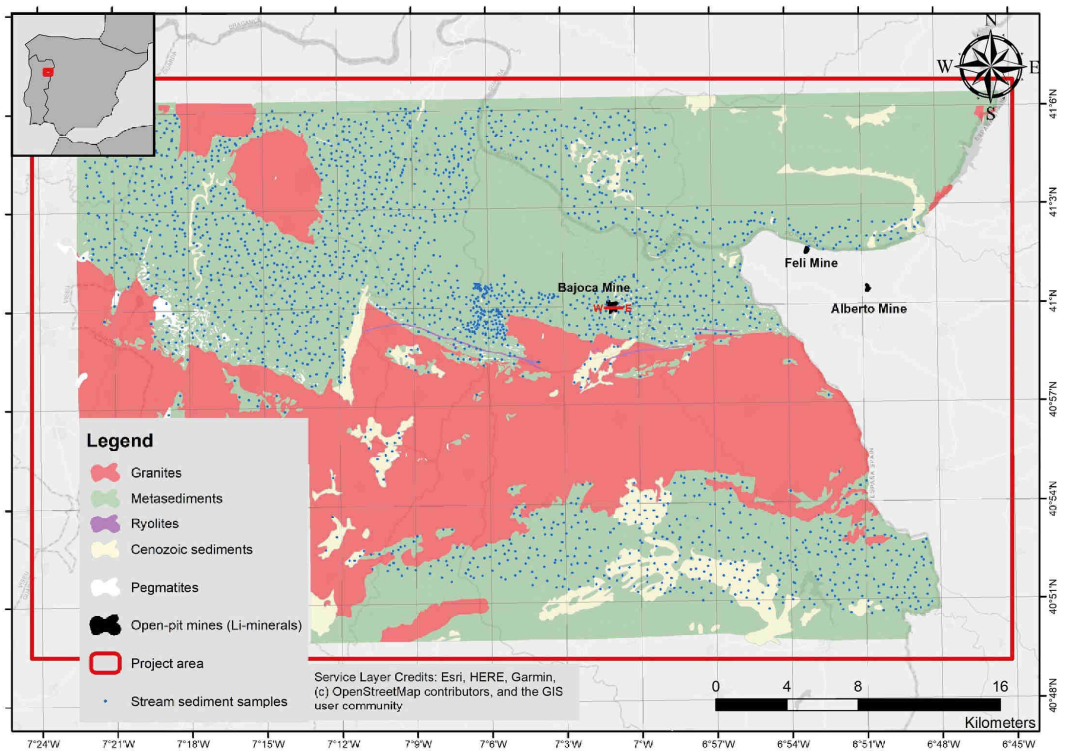

Figure 1. Extent of the simplified digitised geological maps, open-pit mines exploiting Li minerals, and the stream sediment data within the study area in NE Portugal (Coordinate System: Lisboa Hayford Transverse Mercator, Projection: Transverse Mercator).

1.2. Remote Sensing Data

Remote sensing is a powerful and cost-effective data source to collect up-to-date and historical information about the ground surface. In recent years, remote sensing data have been intensively used in geology applications for the exploration and identification of different mineralisation types and related mining activities, e.g., [32–34].

In the framework of the LIGHTS project, several methodological approaches have been developed to identify Li pegmatite areas through optical remote sensing data, including different types of satellite products such as ASTER, Landsat-5, Landsat-8, and Sentinel-2 [35,36]. In this regard, different machine learning algorithms have been employed to allow the automatic identification of Li pegmatites [37,38].

In this study, we elaborate on the potential of new Sentinel-2 derivatives to improve the automatic detection of Li-bearing mineralisation and introduce a new approach to differentiate Li-bearing mineralisation from other features with similar spectral signatures. The use of Sentinel-2 satellite imagery brings three main advantages compared to the other free-of-charge optical remote sensing data: (1) low-to-medium spatial resolution (4 × 10 m Bands, 6 × 20 m Bands, 3 × 60 m Bands); (2) multispectral data from the Visible (VNIR) and Near Infra-Red (NIR) to the Short Wave Infra-Red (SWIR), in 13 compressed JPEG-2000 images covering the total spectral range between 0.443 μm and 2.190 μm; (3) a temporal resolution of 5 days at the Equator since 2015. Additional information may be found in guides available on the ESA Sentinel website: https://sentinel.esa.int/web/sentinel/technical-guides/sentinel-2-msi (accessed on 23 September 2021).

2. Data and Processing

2.1. Geological Data

Geological maps of the study area [28–31] provide the geological framework for this study and were used to identify and digitise pegmatites using ArcGIS software (ArcGIS 10.6, Environmental Systems Research Institute, Redlands, CA, USA). Based on the Portuguese Geological Surveys 1:50,000 geological maps of Portugal [28–30], and, when not available, using the 1:80,000 geological map from the Côa Valley Archaeological Park [31], a unified geological map was created covering the entire study area. Afterwards, a simplified map (Figure 1) was produced by grouping the Variscan granitoids, the Precambrian and Paleozoic metasediments, and the Cenozoic sedimentary cover into distinct classes, to aid the masking and processing stages. Finally, topological data analysis was performed to check any mistakes committed during all the processes created in ArcGIS software (ArcGIS 10.6, Environmental Systems Research Institutery, Redlands, CA, USA). These digital maps were used to create rastered data of individual geological units for further use in the prediction software.

2.2. Stream Sediment Data Processing

Stream sediment geochemical data (survey spot position and geochemical analysis) were obtained from earlier studies [39–41] carried out on campaigns in the early 1980s by the French Bureau de Recherches Géologiques et Minières (BRGM) with the Portuguese institution Serviço de Fomento Mineiro (SFM). A total of 3.715 stream sediment samples, including 298 samples from a more detailed campaign near Bajoca Mine, were collected in the FAF region covering an area of >1.250 km^2 in NE Portugal. The catchment creation was based on digital elevation model (DEM) data and the flow direction network. During the following procedure, center points of the catchment polygons were calculated using ArcGIS v10.6 software. Subsequently, raster datasets for various elements were created

applying inverse distance weighting (IDW) interpolation on the catchment center points containing related geochemical information. Stream sediment data included analyses of the elements/compounds Ag, Al_2O_3, As, B, Ba, Be, Bi, CaO, Cd, Co, Cr, Cu, Fe_2O_3, K_2O, La, Li, MgO, MnO, Mo, Na_2O, Nb, Ni, P_2O_5, Pb, Sb, SiO_2, Sn, Sr, TiO_2, V, W, Y, Zn, and Zr. The multi-element quantification was achieved on the fine fraction below 60 mesh (250 microns or 0.25 mm) by optical emission spectrometry (quantometer studies, [39,40,42]). There is no information on the digestion methods and analytical precision of the analyses in the historical reports available.

2.3. Exploration Model

Li mineralisations in the study area occur principally in aplite–pegmatite bodies and hydrothermal veins [8], all with spatial relation to a granitic body (Figure 2). Regionally, Li mineralisation occurs in highly evolved aplite–pegmatite dykes hosted within metasedimentary rocks, with an increasing fractionation degree as the distance to the granite increases [8,42]. However, the regional granites are enriched in elements such as Li, P, or Rb when compared with the metasediments [13]. It is therefore important to separate these two lithologies, since Li signals could occur both in granites from their initial Li content (low Li content but huge volume) or Li pegmatites (high Li content but low volume), but cannot be clearly distinguished in the stream sediment data (Figure A1; Appendix A). Hence, we excluded stream sediment data from granite areas since pegmatitic Li mineralisations (in the study area) are commonly hosted only by metasedimentary rocks and apical or marginal areas of granitic intrusions hosted by metasediments [42]. Therefore, the prediction models will not cover the granitic areas (which are of low interest for Li-bearing pegmatites).

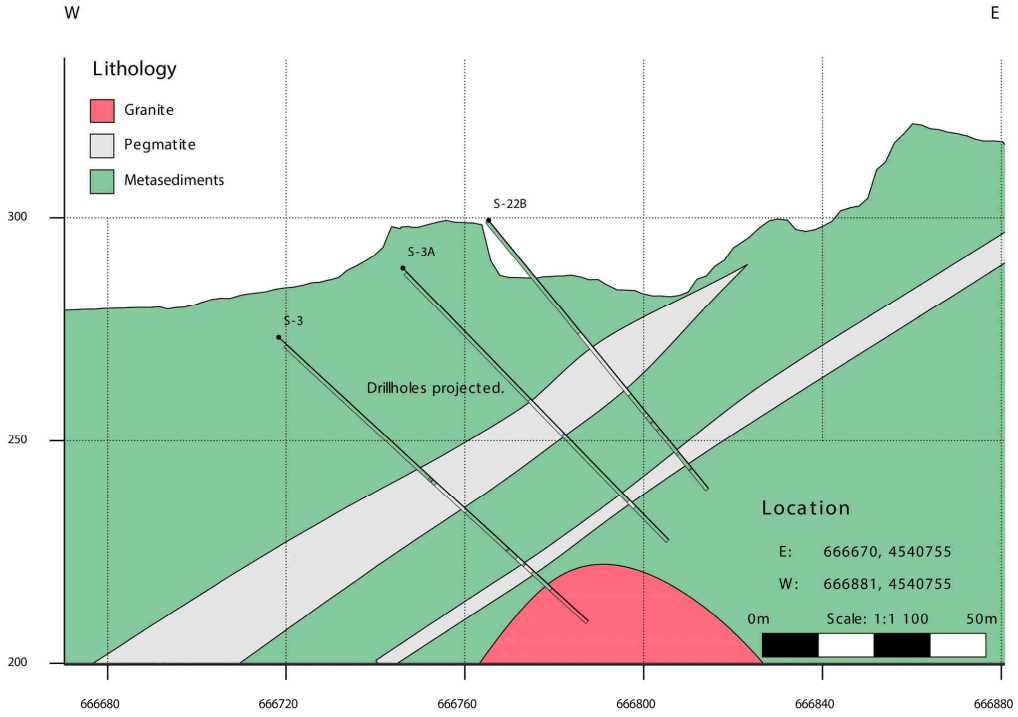

Figure 2. Geological profile of Bajoca Mine featuring Li-bearing pegmatite dykes with spatial relation to a granitic body hosted within metasedimentary rocks. The Li mineralisation is heterogeneously distributed within the dykes, since there is no internal zoning [13], while Sn mineralisation is concentrated along the aplite–pegmatite contact borders. The drillholes are projected in the profile, each one presenting variable directions and dips (from N115° E to N118° E; 39° to 45° S for S3; N125° E; 40° to 45° S for S3A; and from N124° E to N127° E; 41° to 45°S for S22B).

2.4. Unclassified Factor Analysis

Unclassified factor analyses of the stream sediment data were conducted using the statistical software Statgraphics Centurion XV to obtain a preliminary overview of the elements related to local Li mineralisation and to reduce the overall input data for the prediction software. The stream sediment data were clipped by the buffered extent of the mapped pegmatites (buffer 1000 m) to reduce the obscuring influence of samples from granitic and metamorphic rocks on pegmatitic samples.

Seven factor classes (with Eigenvalues > 1) could be identified and attributed: (1) metamorphic signature, (2) granitoid signature, (3) polymetallic signature, (4) siliceous signature, (5) Li-emphasised, (6) Sn(–Nb)-emphasised, and (7) W–Ti-emphasised. The Li-emphasised class has relatively high Li contents and shows coherent enrichments in Sn, As, Mo, Cu, and Ag. The data from these elements were subsequently used in the ANN model.

2.5. Sentinel-2 Imagery

Sentinel-2 image data were freely downloaded from the online data archive of the European Space Agency (ESA) (https://scihub.copernicus.eu/dhus; accessed on 23 September 2021). Their properties are described in Table 1. The selected acquisition meets the following criteria: (1) complete coverage of the study area; (2) cloud-free image over the study area; (3) good exposure of the Li mineralisation on the ground surface during the acquisition time.

Table 1. Downloaded Sentinel-2 satellite image data over the study area.

Tile	Data Product	Spatial Resolution	Data Source	Reference System	Date of Acquisition	Cloud Coverage
T29TPF	2A	10m, 20m, 60m	ESA	UTM29N / WGS84	20191002	2.3%

The proposed approach for the identification of Li-bearing pegmatites with optical images applies only to vegetation-free or -less areas, and ideally to regions with visually exposed bedrock. In the present study case, the study area is dominated by poor vegetation coverage and therefore represents adequate conditions for the identification of Li pegmatites exposed on the ground surface.

The selected satellite image is available as a Bottom-of-Atmosphere product (Level 2A), i.e., the reflectance values are already atmospherically corrected and refer to the surface reflectance. The raw spectral reflectance values were further pre-processed as denoted in the following steps:

1. Super-resolving Sentinel-2 Multispectral Imagery to 10 m spatial resolution

   The low-resolution spectral reflectance bands (20 m and 60 m) were super-resolved to 10 m ground sample distance, using a convolutional neural network (CNN) as introduced by Lanaras et al. [43]. This approach extracts details from pixels with the highest resolution (four bands at 10 m resolution) and propagates these details to all other spectral bands (eight bands at 20 m and 60 m resolution) using the local consistency between neighbour pixels, to obtain an image where all spectral bands have a resolution of 10 m while preserving the spectral characteristics. This pre-processing step is useful for detecting features at the size of 200–250 m^2.
2. Dimensionality Expansion for Sentinel-2 Multispectral Imagery

In order to increase the multispectral data dimensionality and the performance of analysis (see Section 3), a method described in [44] to generate nonlinearly correlated spectral band images is implemented. For this purpose, suitable Sentinel-2 spectral bands for geological applications [33] are taken into consideration (Table 2).

Table 2. Dimensionality expansion for Sentinel-2 multispectral imagery (√ = square root).

Dimensionality Expansion	Formula
eB01–eB06	√ (B2, B3, B4, B8, B11, B12)
eB07–eB12	Log (B2, B3, B4, B8, B11, B12)
eB13–eB18	(B2, B3, B4, B8, B11, B12)2
eB19–eB33	B02 × B03, B02 × B04, B02 × B08, B02 × B11, B02 × B12 B03 × B04, B03 × B08, B03 × B11, B03 × B12 B04 × B08, B04 × B11, B04 × B12 B08 × B11, B08 × B12 B11 × B12

2.6. External Data

In order to reduce spectral variability, urban areas, transport infrastructure, and main water bodies were masked out using the Open Street Map (OSM) database. The OSM topographical dataset was downloaded at (https://download.geofabrik.de/; accessed 23 September 2021). The used OSM layers included:

- Polygon features of urban areas, stored in the "landuse" layer;
- Polygon features of water bodies, stored in the "water" layer, and;
- Polyline features of the road infrastructure, stored in the "roads" layer.

The OSM features in the study area were corrected accordingly using the underlying Sentinel-2 image. They were used as controlling parameters to mask out these features from the remote sensing models.

2.7. Training Patterns

The study area is well-known for the presence of Li-bearing mineralisation (pegmatites). Typically, training patterns of exposed Li pegmatites over the ground surface have been collected at three open-pit mines over the study area: the Bajoca (located in Portugal), Feli, and Alberto mines (located in Spain) (Figure 1). All data are projected to the Lisboa_Hayford_Gauss_IGeoE coordinate system (WKID: 102164; EPSG:20790). A geographical grid projected into WGS_1984 is inserted into all presented maps for illustration purposes. The transformation succeeded with the transformation parameters integrated with the ArcGIS Software (ArcGIS 10.6, Environmental Systems Research Institutery, Redlands, CA, USA).

In this context, it is important to consider that the reflection intensity of Li-bearing pegmatites (albedo) is expected to be slightly different at various locations due to the dominance of diverse Li minerals (petalite in Bajoca Mine, lepidolite in Feli Mine, and spodumene in Alberto Mine). Furthermore, the sample colour, rock surface structure, and weathering conditions of Li minerals might represent controlling factors too. For example, reflectance spectroscopy studies of petalite, spodumene, and lepidolite from the Bajoca, Alberto, and Feli mines, respectively, have shown that even fresh petalite and spodumene samples present diagnostic features of illite and/or other clay minerals (Supplementary Figure S2) [45–47]. Oppositely, lepidolite presented diagnostic absorption features that allowed its identification in the collected spectra from Feli Mine. Detailed petrographic, mineralogical, and geochemical studies conducted in Bajoca Mine showed that the same alteration minerals can be present in samples with distinct degrees of alteration [48]. This is reflected in the spectral signatures (reflectance values as a function of the wavelength) for all three mines (Supplementary Figure S2). Obviously, the Li-bearing minerals in

Alberto Mine depict slightly different properties, explained through the different exposure conditions of Li minerals in the mine, respectively. Nonetheless, it is noteworthy that Li-bearing minerals show relevant hydroxyl-related absorption features that coincide with Sentinel-2 Band 12 (Supplementary Figures S1 and S2). This absorption is also observed on the spectral signature collected in the pixels of the training areas (Supplementary Figure S2).

Taking this into account, the training patterns for the supervised machine learning algorithm were only collected in Bajoca Mine, due to its size and exposure on the ground surface and the representative spectra of the Li pegmatites. The polygons were digitised based on the Sentinel-2 image to represent the actual state of the mine site during the acquisition time of satellite imagery. For this purpose, different RGB combinations, suitable for geologic applications, were used as background images (Figure 3). The three stockpiles at the centre are from the Li pegmatite itself, whereas the two westernmost and the southmost piles are waste piles from the host rock and feature lower Li contents. Waste rock piles were used as additional training areas to simulate the metasomatism of host rocks.

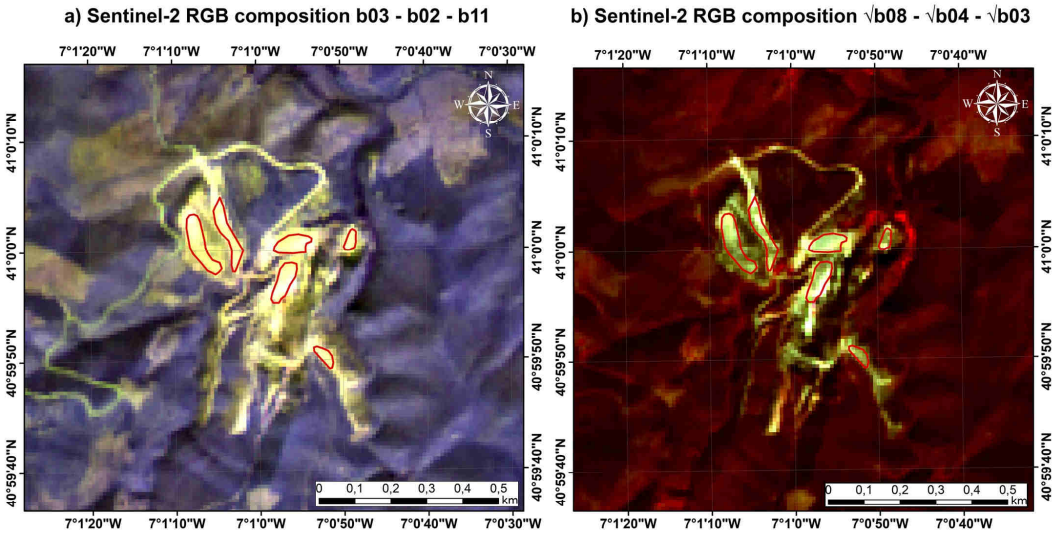

Figure 3. Training patterns (red outlines) with different RGB compositions in the background: (**a**) Sentinel-2 RGB composition b03–b02–b11, (**b**) Sentinel-2 RGB composition √b08–√b04–√b03. The yellow and greenish pixels in subfigure a and b, respectively, correspond to areas hosting Li mineralisation exposed on the ground surface.

3. Methods: Prediction Modelling

The ANNs of multilayer perceptron type are implemented in the advangeo® Prediction Software from Beak Consultants GmbH (www.advangeo.com; accessed on 23 September 2021). The modelling and prediction software is developed to model spatial data and analyse complex relationships between a wide variety of spatial influencing parameters and a given prognostic event or occurrence, by using methods of artificial intelligence within a familiar GIS environment. The base principle is the ability of artificial neural networks to generalise and learn from non-linear relationships and model natural complex processes and events, which are difficult or impossible to be described with analytical mathematics [49]. The software is available as a standalone application with a

user-friendly interface, which enables the user to flexibly create and build parametrised models.

In this study, the prediction software is used to perform artificial neural networks of multilayer perceptron type to identify Li mineralisation over the given study area according to the processing schema in Figure 4.

The main workflow is described through the following steps:

1. Collection of model input data, i.e., data that control the modelled feature (here the Li mineralisation) including geological units and structures (e.g., granite bodies, metamorphic sequences, pegmatites), selected stream sediment data, cloud-free pre-processed Sentinel-2 satellite imagery, and OSM topographical data (settlements, infrastructure, water bodies, etc.).
2. Data processing of the spatial data to become suitable for use in analysing models, including the projection of input data to the project coordinate system, resampling to the specified spatial resolution according to project requirements, and clipping of input datasets to the extent of the project area as well as linear scaling of continuous raster data values between 0 and 1 and the conversion of discrete vector data into a binary raster with 0 and 1 value.
3. Design of ANN models in the prediction software for different use cases, i.e., using different controlling parameters and suitable training patterns. The training patterns for remote sensing modelling are ideally in obvious spectral contrast to the surrounding environment and with distinctive spectral reflectance characteristics. The training scenario comprises the controlling and the network parameters (number of hidden layers, number of neurons for each layer, the maximum number of training epochs, etc.).
4. Training of the ANN models using collected training patterns at the Bajoca Mine site, a well-known location for the presence of Li-bearing minerals. Other known locations (Feli and Alberto Mine) were used to validate the application model. The trained ANN will serve to identify similar Li-bearing pegmatite locations in unknown locations over the study area.
5. Validation of the trained ANNs: There are several possibilities to evaluate the accuracy and reliability of a trained ANN by the identification of known locations that have not been used for network training (Feli and Alberto Mine), considerations of the network (MSE) error including statistical evaluation (histograms, all pixels vs. the positive pixels), and analysis of the model parameter weights. Typically, MSE errors below 0.2, balanced parameter weights, and a high probability of modelled pixels are indicators of stable and good neural network quality.
6. Model application: After successful validation, the training network can be used in unknown locations for the prediction of similar events over the entire study area. The result is a distribution probability raster map.
7. Refinement and presentation: The ANN classification results are irregular pixel-based raster data. In many cases, the classification results have to be further refined and processed to improve the cartographic representation of the result.
8. The final distribution map of Li-bearing mineralisation: Combination of the distribution map result based on remote sensing data with the result obtained from modelling with geological and geochemical data. The combination of both geological and remote sensing data into one ANN model was tested, but it resulted in many false interpretations, as the controlling parameters refer to/explain different targets. Therefore, we chose the approach to merge the two ANN models only as a final step once distribution maps of Li-bearing mineralisation were created.

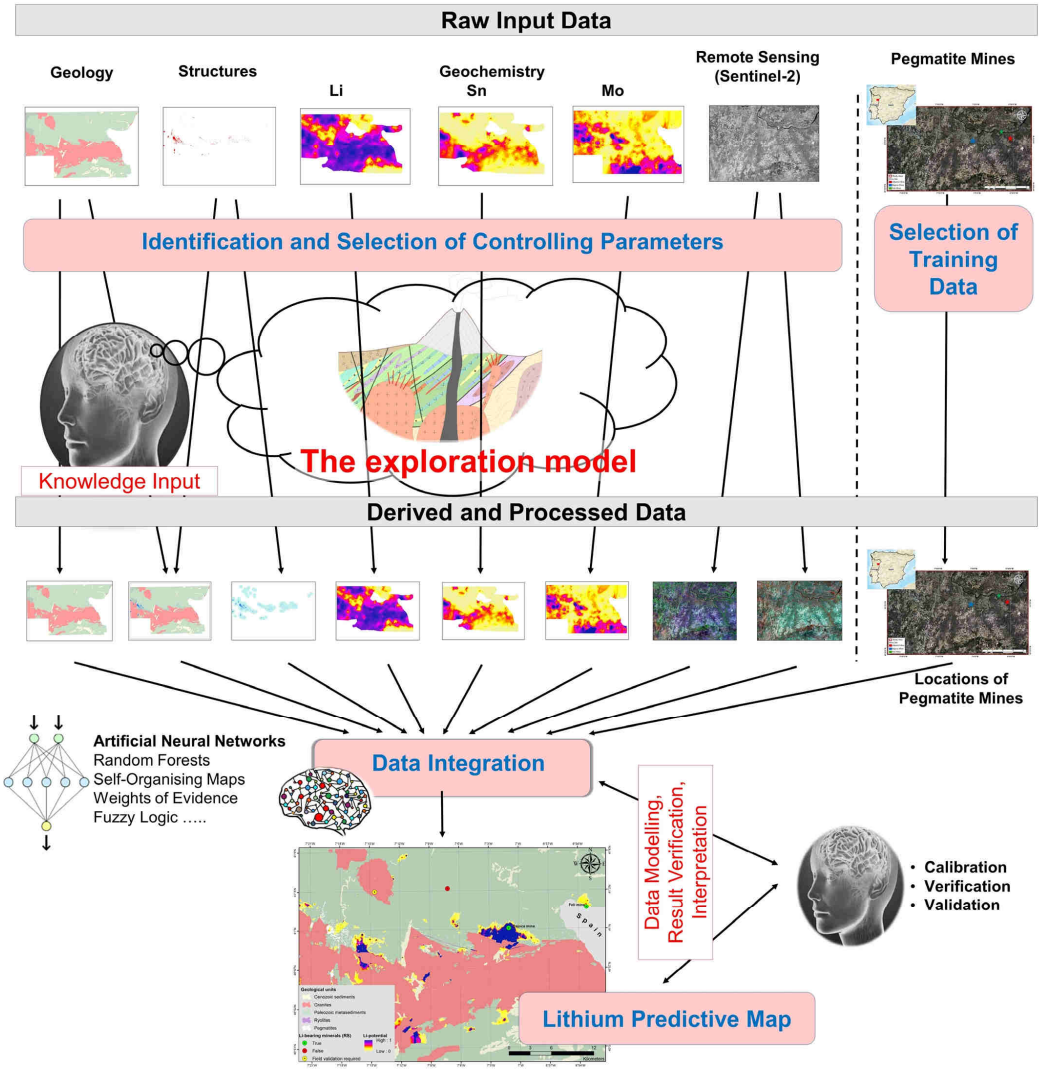

Figure 4. General processing schema in the advangeo® prediction software.

4. Results

Several prediction models with different controlling parameters have been designed with the described principles and workflow. Here, the most significant models and results are presented.

4.1. Geological Model

Controlling parameters of the geological model include digitised geological units (1:50,000), digitised pegmatites (1:50,000), and selected stream sediment data. The modelling was carried out using ANNs of multilayer perceptron type. The model accuracy is evaluated by the following quality parameters:

1. The network (MSE) error: The model error is shown in Supplementary Figure S3. Clearly, the model error converges after approximately 20 iterations and the final error is below 0.2, indicating that the neural network is stable and accurate. This means that the designed model was able to find correlations between the controlling parameters and the training data.
2. Statistical evaluation: Additionally, the histograms (Supplementary Figure S3) reveal that the algorithm was able to identify >80% of the pixels in the training patterns with a scale better than 0.9.

The prediction software delivers a distribution probability map in the value range of 0–1, illustrating the Li potential over the study area (Figure 5). Areas depicted with 1 or close to 1 are the areas with the highest probability of Li-bearing rocks. Within the study area (approximately 1200 km^2), 50 km^2 are mapped with Li potential between 0.1 and 1 (Figure 5). These areas are mainly located in regions of metamorphic rocks in the vicinity of granite intrusions, compatible with possible greisen cupolas or pegmatites and their host rocks. High predictive areas (>0.5 Li probability) extend over 6.4 km^2 and are mainly located directly to the south/southwest of Bajoca Mine (5.6 km^2) and to a lesser extent north of the town of Meda (0.47 km^2) as well as southwest of Santa Comba village (0.35 km^2).

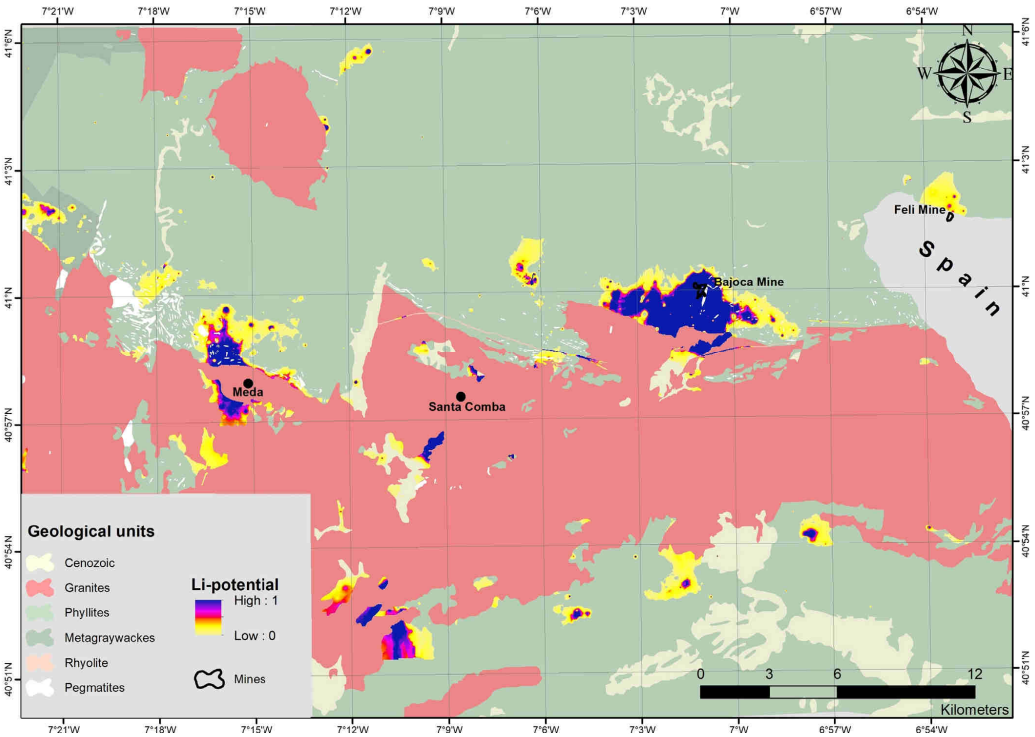

Figure 5. Probability map of Li mineralisation across the study area as a result of the geological/geochemical modelling approach (without remote sensing data).

4.2. Remote Sensing Models

4.2.1. Remote Sensing Model 1

Controlling parameters of Remote Sensing Model 1 include: Sentinel-2 super-resolved spectral bands (visible, NIR, red-edge, and SWIR) and OSM topographical dataset.

The modelling was carried out using ANNs of multilayer perceptron type. The model accuracy is evaluated by the following quality parameters:

1. The network (MSE) error: The model error converges after approximately 40 iterations and the final error is below 0.2 (Supplementary Figure S4), indicating that the ANN is stable and accurate. This means that the designed model was able to find correlations between the controlling parameters and the training data.
2. Statistical evaluation: The histograms (Supplementary Figure S4) reveal that the algorithm was able to identify about 90% of the pixels in the training patterns with a scale better than 0.9.
3. The model parameter weights: The model weights confirm the Sentinel-2 visible (b2, b3, b4), NIR (b8, b8A), and SWIR (b11) spectral bands to be the most suitable for geological applications. On the other hand, the spectral bands in the red-edge part of the electromagnetic spectrum seem to be irrelevant for this application. The spectral bands with the highest weight contribution in the designed model are b2, b3, and b11. This is in accordance with Cardoso-Fernandes et al. (2019), who proposed the RGB combination Green–Blue–SWIR for the identification of Li mineralisation in the same region. The RGB composition out of b3–b2–b11 was further analysed in ArcGIS software 10.6 (Figure 6). Indeed, the well-known areas for Li mineralisation are successfully identified and highlighted compared to their surrounding environment. However, similar symbology is also assigned to other features with similar spectral properties as the target features.
4. The distribution probability raster map: The prediction software delivers a distribution probability map in the value range of 0–1, illustrating locations of potentially identified Li-bearing pegmatites in the study area (Figure 6). With 1 are depicted areas with the highest probability to represent Li-bearing mineralisation. In the resulting map, pixel values with a probability value higher than 95% were assigned as "positive" locations. The threshold value is defined based on the histograms in Supplementary Figure S4.

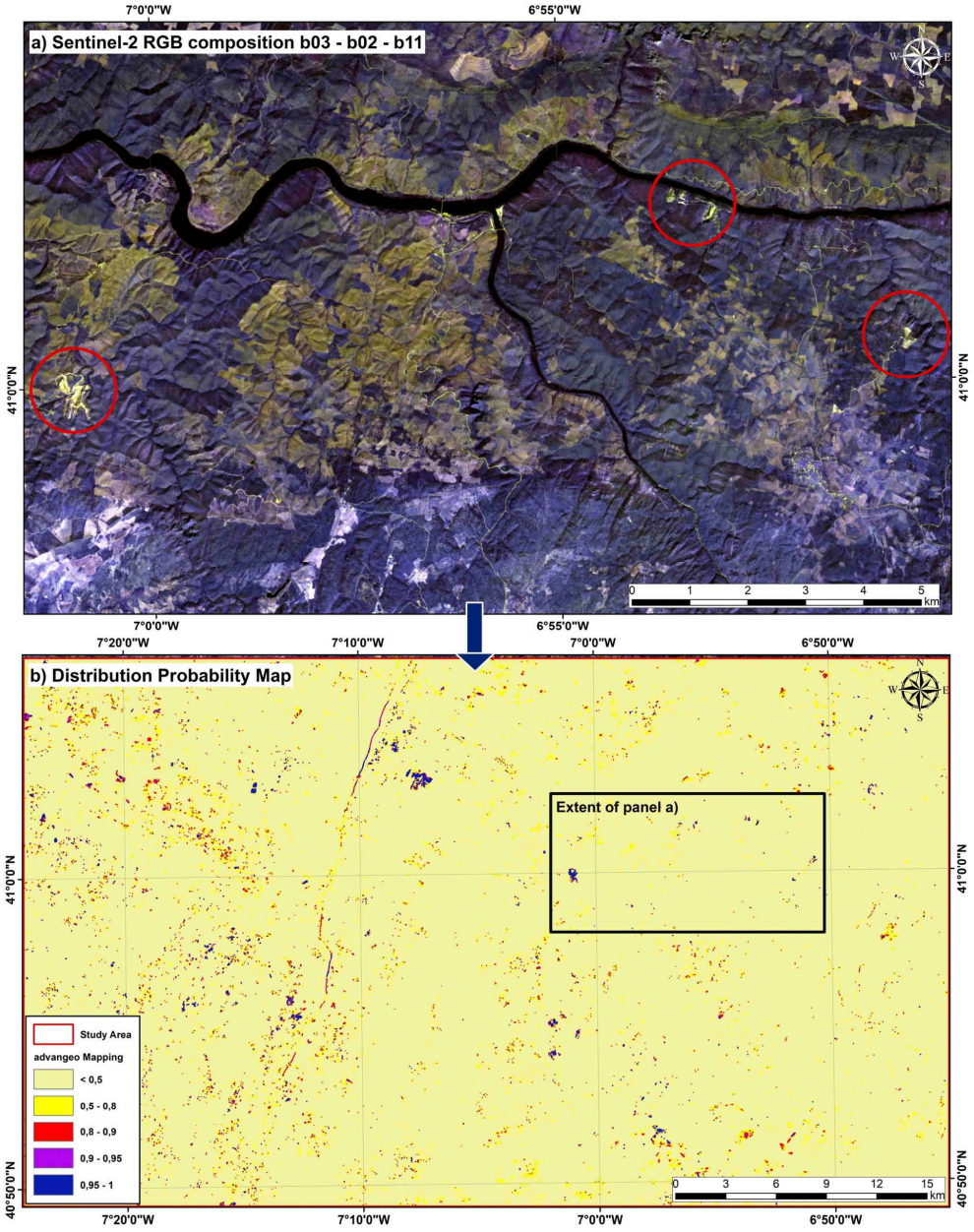

Figure 6. Results of Remote Sensing Model 1: (**a**) RGB composition detail using the super-resolved bands b3–b2–b11 in which mines with known Li mineralisation patterns are shown in light yellow, (**b**) Distribution probability map of Remote Sensing Model 1.

The validation of the identified areas in the resulting map with the underlying Sentinel-2 image revealed that all known locations of the open-pit mines with exposed Li pegmatites were successfully detected (Figure 7). As expected from the results of spectral analysis (Supplementary Figure S2), Li-bearing mineralisation at Alberto Mine was only partially detected due to the different mineralogical composition in contrast to Bajoca Mine.

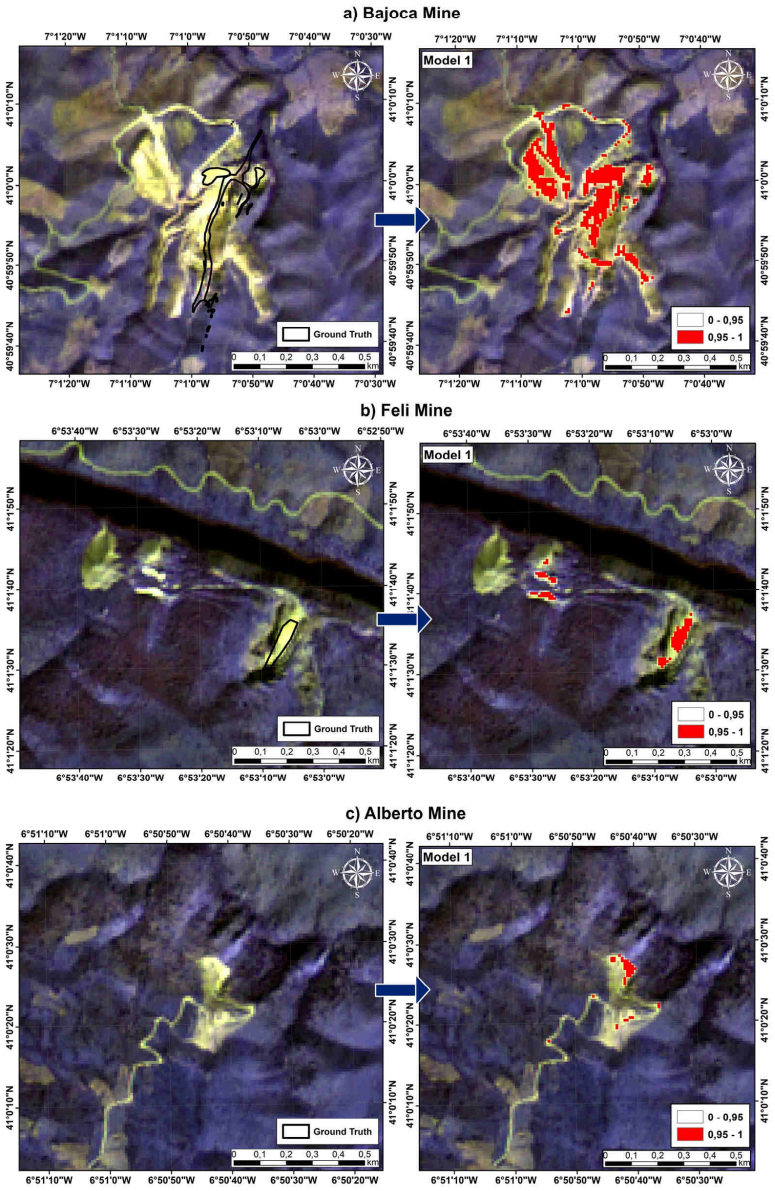

Figure 7. Li distribution probability map of Remote Sensing Model 1 for the three training areas: (**a**) Bajoca Mine, (**b**) Feli Mine, (**c**) Alberto Mine. High potentials are in red. Ground truths are marked with black polygons.

However, the validation of the distribution map over the entire study area revealed that other features with no evidence of Li presence (other mine sites, barren areas with exposed bedrock, etc.) but with similar spectral reflectance properties were also classified as "positive" pixels. Some examples are highlighted in Figure 8.

For a more detailed investigation, samples of "positive" classified pixels were randomly collected and their spectral reflectance properties were further analysed using the extended spectral bands described in Table 2.

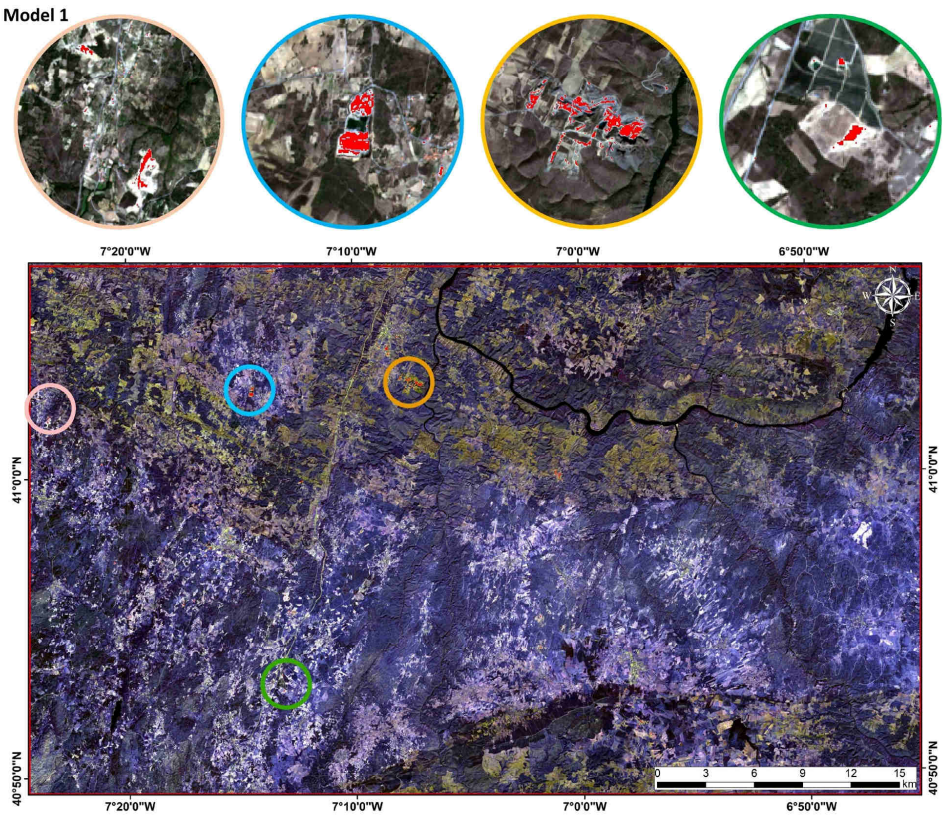

Figure 8. Example areas of possible false positives (misclassified pixels) from Remote Sensing Model 1: Póvoa de Penela, Touça (light brown), Touça (blue), Poio's quarry (orange), and Marialva (green).

Analysis of Spectral Signatures

The misclassified areas with similar surface reflectance properties as the target features (Li pegmatites) were further analysed to depict the most suitable bands to differentiate them. For this purpose, samples of features with similar spectral properties based on Model 1 were collected and their spectral signatures were graphically analysed and compared. These analyses revealed the most suitable extended bands to identify Li pegmatites and differentiate them from other features with similar spectral properties.

The graphs are illustrated in Supplementary Figure S5. The reference spectral signature of the main outcropping lithologies (Li pegmatites, metasediments, and granitoid rocks) is presented in Supplemental Figure 6. In the case of the spectra of the metasedimentary rocks, they correspond to samples collected in the false positive area identified with an orange circle in Figure 8.

These analyses revealed that some of the extended bands were more likely to provide the best class separability between the selected patterns. The relevant bands are highlighted in Table 3 and were used in a second prediction model to better identify Li pegmatites.

Table 3. Suitable extended bands (eB) for automatic identification of Li-bearing pegmatites.

Extended Band	eB14	eB15	eB16	eB24	eB25	eB28	eB29	eB31
Formula	$b3^2$	$b4^2$	$b8^2$	b3 × b4	b3 × b8	b4 × b8	b4 × b11	b8 × b11

4.2.2. Remote Sensing Model 2

Controlling parameters of Remote Sensing Model 2 include selected Sentinel-2 extended bands (Table 3), the distribution probability map from Model 1, and the OSM topographical dataset. The modelling was carried out using ANNs of multilayer perceptron type. The model accuracy is evaluated by the following quality parameters:

1. The network MSE error: A stable network MSE error that converges after 20 iterations and exceeds a final error lower than 0.001 (Supplementary Figure S7);
2. Statistical evaluation: Similar plausible histograms as shown in Supplementary Figure S7;
3. The model parameter weights: Distributed weights of controlling parameters. The combinations ($b3^2$), (b3 × b4), and (b8 × b11) were revealed to be significantly decisive for the prediction model.

Furthermore, the well-known locations for the presence of Li pegmatites were successfully detected in the distribution probability map of Remote Sensing Model 2 (Figure 9). The validation of the distribution map over the entire study area revealed that noises were drastically reduced compared to the results from Model 1. This is reflected through the following statistics (Table 4).

Table 4. Statistics of the identified "positive" pixels in Models 1 and 2.

Parameter	Model 1	Model 2
Number of "positive" pixels	12,088	3526

Analogously to Model 1, the results were validated using the underlying Sentinel-2 RGB composition from the visible bands. The selected areas for the illustration of misclassified pixels in Figure 6 were re-validated with the results obtained from Model 2 (Figure 10). These sections show an obvious reduction/elimination of the misclassified pixels over the study area and thus an improved distribution map based only on remote sensing data.

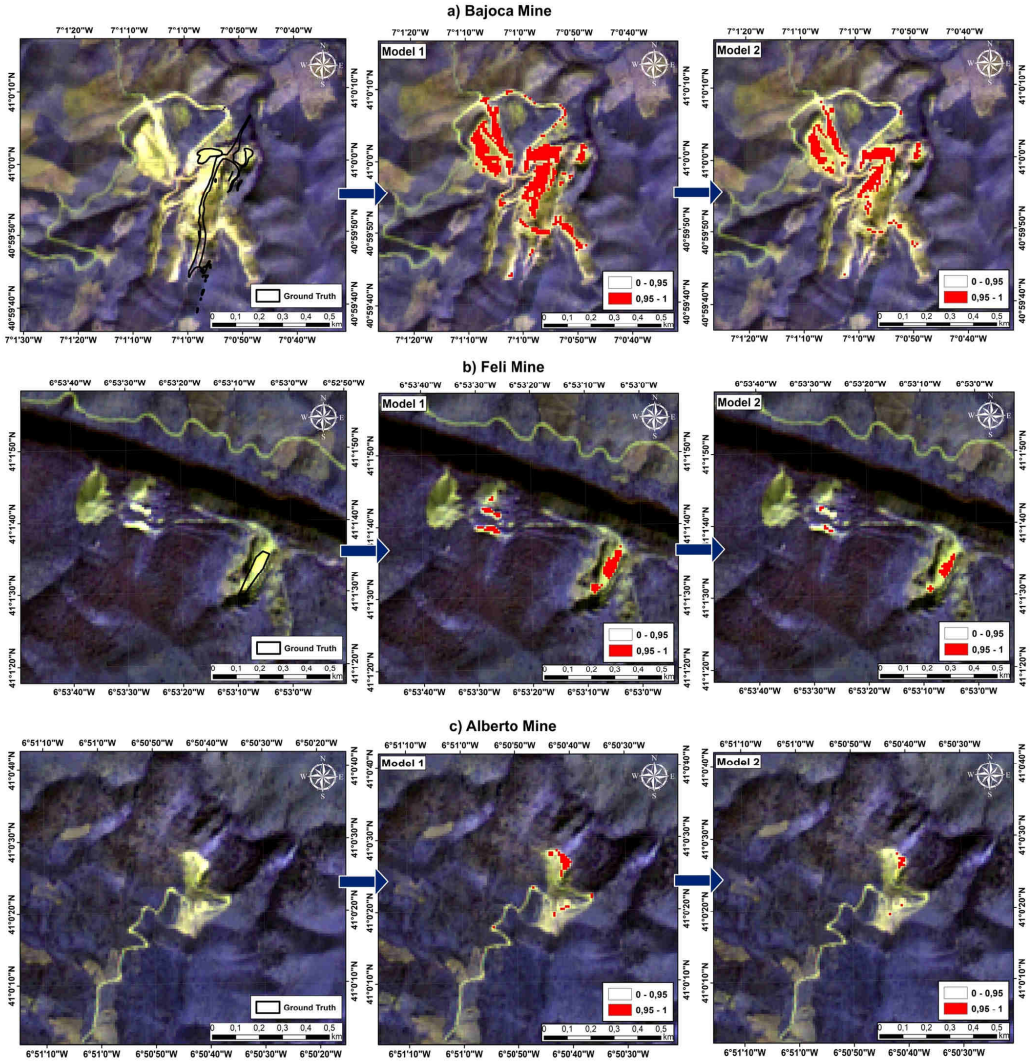

Figure 9. Reduction/elimination of misclassified pixels of Li distribution probabilities when comparing Remote Sensing Model 1 and 2 for the three training areas: (**a**) Bajoca Mine, (**b**) Feli Mine, (**c**) Alberto Mine.

The distribution raster map was further refined using GIS tools available in ArcGIS software, such as Boundary Clean, Majority Filter, etc., to remove the isolated pixels to improve the cartographic representation of the map.

The resulting raster was converted into vector data and further refined using tools such as Aggregate Polygons to cluster near-lying polygons representing the same physical feature.

The actual designed map (Figure 11) illustrates high-probability locations for Li mineralisation, exposed to the ground surface, based only on remote sensing data.

In the next step, this result was combined with the model based on geological datasets to finally conclude on the location of Li-bearing minerals over the study area. The final map result based only on remote sensing data is shown in Figure 11.

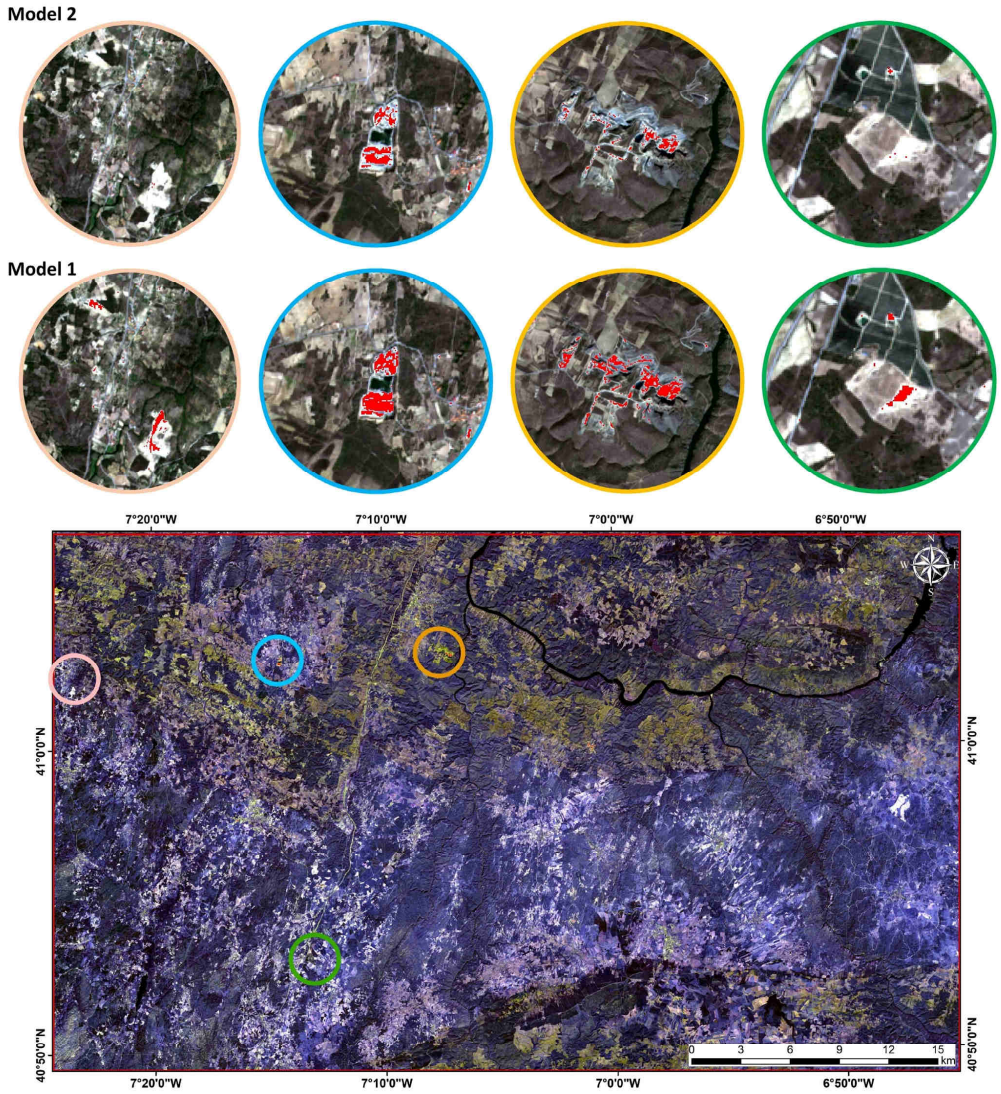

Figure 10. Reduction/elimination of misclassified pixels when comparing Remote Sensing Model 1 and 2.

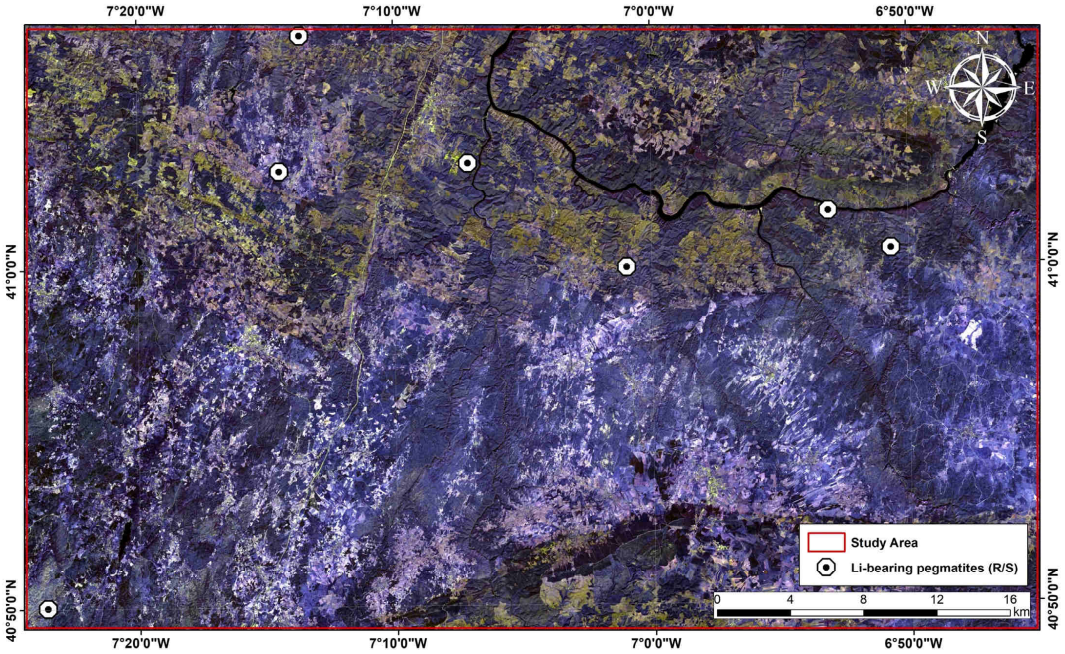

Figure 11. Result map of possible locations of Li pegmatites based only on remote sensing data.

4.3. Combination of the Geological- and Remote Sensing Models

The prediction model result based on geological data (Figure 5) was further combined with the improved classification results based on remote sensing data to design a final map of Li mineralisation occurrences in the study area (Figure 12). The remote sensing models are limited to the detection of features of similar spectral characteristics exposed to the ground surface. On the other hand, the geological model is based on data related to the geological formations and geochemical characteristics (not always exposed on the ground surface). The combination of geological and remote sensing data into one ANN model resulted in many false interpretations, as the controlling parameters refer to/explain different targets. The results of the geological model and the knowledge from previous field campaigns helped us to exclude locations such as the Li-barren quarry at the Coa River (marked as False in Figure 12). The resulting map shows that the Bajoca and Feli mines, with a confirmed presence of Li pegmatites, could be successfully identified in both ANN models. Other potential areas identified from the geological-based model are not exposed to the ground surface and therefore could not be identified from the remote sensing data.

Through a combination of result maps, the identified location near the Coa River based on remote sensing data (marked as False in Figure 12) was automatically excluded. Further research allied with a previous field campaign revealed that this is a schist quarry without the confirmed presence of Li at the mine site (https://www.solicel.pt/site/index.php/produtos; accessed on 02 February 2021). Additionally, in the case of the westernmost location identified using Sentinel-2 (Figure 11), the integration with available geological maps allowed us to identify it as another false positive since in the FAF the Li-bearing pegmatites are not emplaced within the granitoid rocks [17–19]. It is worth mentioning that a combination of the models based on geological data and remote sensing data could only succeed in areas where all data are

available. The lack of geology information throughout the entire study area made it impossible to draw conclusions for the other identified locations in Figure 11.

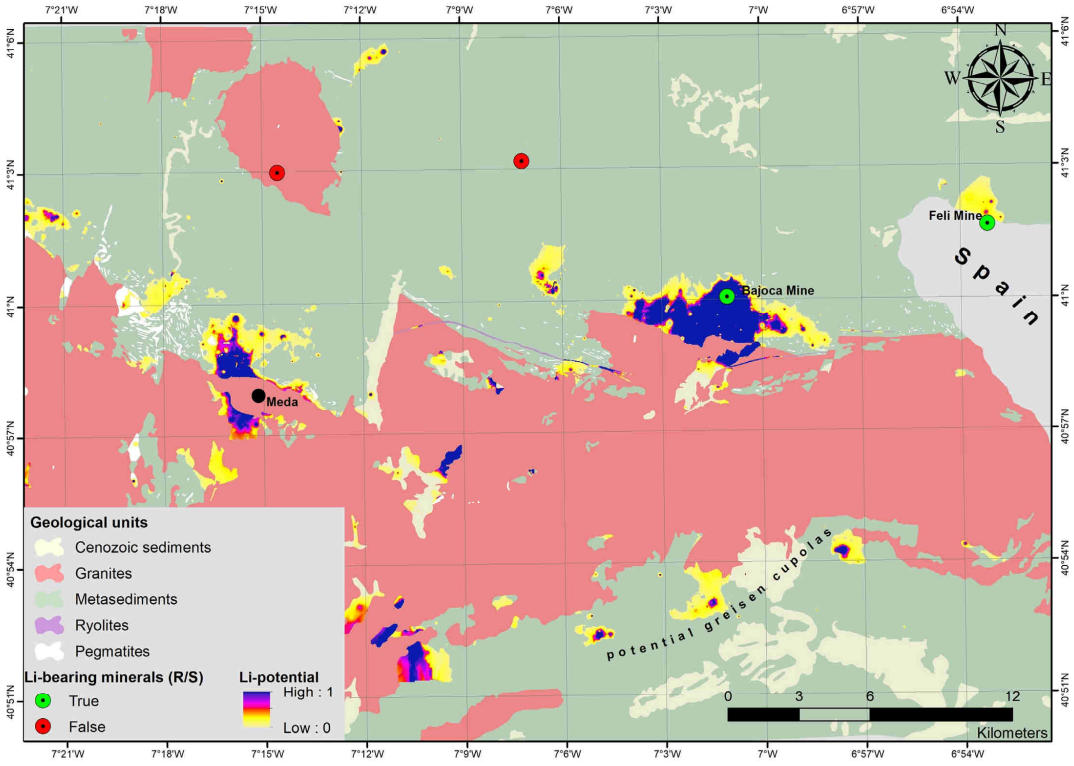

Figure 12. Predicted Li mineralisation based on geological and remote sensing data.

5. Discussion

The potential of low-to-medium resolution Sentinel-2 images was evaluated to automatically detect Li-bearing pegmatites exposed on the ground surface, depending on the weathering conditions of the Li-bearing rocks. Besides the raw spectral reflectance bands, dimensionality expansion techniques can be integrated to improve the classification workflows and distinguish features with similar spectral signatures to the Li-bearing minerals. Despite the potential to give insights on other locations with similar surface reflectance to Li pegmatites, the remote sensing data only allowed the identification of Li-bearing rocks at known mines. These results show the limitations of the remote sensing data since most unexploited pegmatite bodies are often covered by vegetation, thus preventing their identification using only remote sensing data. On the other hand, integration with the geological and geochemical data was crucial to identify false positive areas resulting from the satellite-based approach. This indicates that the remote sensing model alone was not sufficient for prospectivity mapping. Field campaigns also helped to exclude some of the potential areas identified using the remote sensing models. The spectral signature of the rocks of one of the identified false positive areas (orange circle of Figure 8) was confronted with the spectra of Li-bearing pegmatites (Supplementary Figure S6c). Overall, the spectral behaviour of the two rocks is distinct enough to allow their spectral discrimination using hyperspectral data. Since this

discrimination was not achieved using Sentinel-2 data, this may indicate that their spectral resolution may not be adequate. Moreover, even the spatial resolution of the images may have limited the identification of some of the smaller Li pegmatite bodies of the FAF that only reach less than 5 m in thickness [24].

These results are in line with previous research for the identification of Li pegmatites based only on remote sensing data and using traditional methods as well as machine learning algorithms such as ANN, Random Forest, Support Vector Machines, etc., [36–38] that have shown that the results are limited to features with similar spectral properties to Li-bearing mineralisations. For instance, Li mine sites could not be distinguished from the other within-scene elements in the study area using multispectral data due to their similar spectral properties. Despite this, field validation campaigns, the improvement of training areas, and algorithm parameterisation allowed us to decrease the number of false positive areas and increase the separability of Li mine sites [50]. In this paper, the knowledge acquired from previous field campaigns was integrated, including the insights provided by the reference spectra of the main outcropping lithologies (Supplementary Figure S6). Taking this into account, we investigated how the fusion of remote sensing data and geology knowledge improved the identification results and provided a more realistic approach, by allowing us to exclude false positive areas with no further interest for Li exploration

The presence of Li-bearing minerals is strongly related to specific geological formations such as pegmatites. For this reason, in this study, the prediction of Li mineralisation resulted in a combination of models based on remote sensing data (related to the ground surface) and geological/geochemical data (related to the geological formations at the ground surface). The proposed approach requires available geological data and remote sensing data over the entire study area; otherwise, a combination of the models is not made possible. Geophysical data could further enhance the model, e.g., gravimetry could aid in the detection of hidden granite cupolas and related Li mineralisations, and pegmatite modelling could be enhanced by induced polarisation (IP) to measure contacts with the metasediments.

The prediction modelling based only on geological data was limited to the Portuguese side of the study area due to the availability of the geological and stream sediment data. The results shown in Figure 12 provide information on the spatial distribution of predicted Li mineralisation potential across the study area. The spatial distribution of Li-predictive areas in the transition of metasediments and granites could be a result of possible (hidden) greisen cupolas or pegmatites (Figure 5). As a result of the strong generalisation of geological units (metamorphics, intrusives, etc.), the areas with Li potential are mainly related to stream sediment geochemistry. Particularly straight area borders are caused by the boundaries of the main geological formations. Comparing the distribution of different elements across the study area (Sn, W, Li, Mo, As), several areas could be ruled out regarding Li mineralisation sensu stricto (pegmatites). As a result, only Bajoca Mine was used to validate the ANN model. However, the model was able to also predict the Li mineral deposits located near the cross-boundary of Portugal and Spain in the north-east part of the study area. The presence of Li mineralisation in this area is confirmed from the mining activities in the Riba D'Alva mine [51]. Further research is needed to validate the proposed approach in other areas, i.e., to check the high-potential areas identified through the mineral prospectivity mapping for the occurrence of unknown mineralisation. In the end, the resultant Li mineralisation prediction map (Figure 12) can be a useful tool for future exploration campaigns for exploration and mining companies, since it can help to delineate smaller interest areas in a large geographic area (>1.250 km^2). We recommend focusing future exploration activities on the following locations with high predicted Li potential: areas surrounding Bajoca Mine, Li anomalies in the west Meda, possible greisen cupolas in the south of the study area, and areas north of Feli Mine.

6. Conclusions

In this study, geological/geochemical data and remote sensing data (Sentinel-2 images) were used to create separate geological and remote sensing models using the ANN algorithm, respectively. In the end, the best remote sensing model was integrated with the geological one to delineate a Li mineralisation potential map for the FAF.

Using the ANN algorithm and Sentinel-2 multispectral data, it was possible to identify mine site locations and bare soil with similar reflectance properties to the training data. Overall, the Sentinel-2 data on their own are not enough to delineate other Li pegmatite occurrences, since only the known mine sites were correctly identified. The remaining highlighted areas corresponded to false positives. The exclusion of these false positive areas was only possible due to the knowledge obtained from field campaigns but also through the integration with the obtained geological model. The analysis of the reflectance spectra of selected pixels and reference samples (collected in field surveys) revealed that the coarse spectral resolution of Sentinel-2 is not able to reflect all significant characteristics of Li-bearing minerals and pegmatites. Therefore, the identification of Li pegmatite bodies specifically based only on Sentinel-2 data seems to be challenging due to the limited spectral and spatial resolution of the used satellite data and also the existing vegetation coverage (although sparse).

However, the combination of the satellite data with the geological model provides a potential approach to automatically predict the location of Li-bearing mineralisation using ANNs. Careful consideration of training patterns, spectral bands, and geological data proved to be key factors in establishing a working model. The proposed combined approach is a first step towards expeditious Li mineralisation prediction. The integration of the models allowed us to enrich the remote sensing classification results, since the geological prediction model gives insights on formations that are suitable to host Li pegmatites. Thus, the approach of combining the modelling results based on geological and remote sensing data is promising, not only to identify the known exposed Li pegmatites on the ground surface and exclude false features with similar signatures in the spectral reflectance, but also to reveal potential locations for further exploration. Nonetheless, Li pegmatite prediction needs to be improved in the future through the use of high spectral and spatial resolution data in the remote sensing modelling step. The proposed approach can also be used for other metals or raw materials and will make a cost-efficient contribution to raw material exploration in general.

Supplementary Materials: The following are available online at www.mdpi.com/article/10.3390/min11101046/s1, Figure S1: Reference spectral signatures of (a) petalite samples from Bajoca Mine, (b) spodumene samples from Alberto Mine, and (c) lepidolite samples from Feli Mine; Figure S2: Spectral signatures for Alberto, Bajoca and Feli mines based on Sentinel-2 data; Figure S3: Histogram (a) and Network MSE error (b) for the Geological Model; Figure S4: Histogram (a) and Network MSE error (b) for Remote Sensing Model 1; Figure S5: Spectral signatures for the extended spectral bands: (a) 1–6, (b) 7–12, (c) 13–32; Figure S6: Reference spectral signatures of (a) lepidolite-bearing pegmatites, (b) pet-alite-bearing pegmatites (Bajoca Mine), (c) schist–metagreywacke complex (CXG) metasediments, and (d) granitoid rocks; Figure S7: Histogram (a) and Network MSE error (b) for Remote Sensing Model 2.

Author Contributions: Conceptualisation, M.K., D.H., A.B., and S.S.; methodology, M.K., D.H., and S.S.; software, P.H.; validation, M.K., D.H., S.S., J.C.-F., A.L., and A.C.T.; formal analysis, M.K., D.H., and S.S.; investigation, M.K., D.H., and S.S.; resources, M.K., D.H., S.S., and A.L.; data curation, M.K., D.H., S.S., J.C.-F., and A.L.; writing—original draft preparation, M.K., D.H., and S.S.; writing—review and editing, M.K., D.H., S.S., J.C.-F., A.L., and A.C.T.; visualisation, M.K. and D.H.; supervision, M.K.; project administration, S.S., A.K., and A.B.; funding acquisition, S.S., A.K., and A.B. All authors have read and agreed to the published version of the manuscript.

Funding: (1) The investigations in this paper were performed under the LIGHTS (Lightweight Integrated Ground and Airborne Hyperspectral Topological Solution; ERA-MIN/0001/2017–LIGHTS) research project funded by national research agencies under the EU H2020 ERAMIN-2 network. ERA-MIN2 is a global, innovative, and flexible pan-European network of research funding

organisations, supported by EU Horizon 2020, that builds on the experience of the FP7ERA-NETERA-MIN (2011 to 2015). The national funding agencies supporting the project are: ANR—Agence Nationale de la Recherche (France), BMBF Jülich—Bundesministerium für Bildung und Forschung (Germany), and FCT—Fundação para a Ciência e a Tecnologia (Portugal). (2) The work was also supported by Portuguese National Funds through the FCT project UIDB/04683/2020—ICT (Institute of Earth Sciences). (3) Joana Cardoso-Fernandes is financially supported within the compass of a Ph.D. Thesis, ref. SFRH/BD/136108/2018, by national funds from MCTES through FCT, and co-financed by the European Social Fund (ESF) through POCH—Programa Operacional Capital Humano—and NORTE 2020 regional program

Data Availability Statement: The spectral data presented in this study are openly available in Zenodo at http://doi.org/10.5481/zenodo.4575375, reference 45. Restrictions may apply to the availability of stream sediment data and to part of the geological data since they correspond to third party data obtained from the French Bureau de Recherches Géologiques et Minières (BRGM) and the Portuguese National Laboratory of Energy and Geology (LNEG), respectively.

Acknowledgments: The authors gratefully acknowledge the comments of three anonymous reviewers, which led to a substantial improvement in the manuscript.

Conflicts of Interest: The authors declare no conflict of interest. The funders had no role in the design of the study; in the collection, analyses, or interpretation of data; in the writing of the manuscript, or in the decision to publish the results.

Appendix A

A

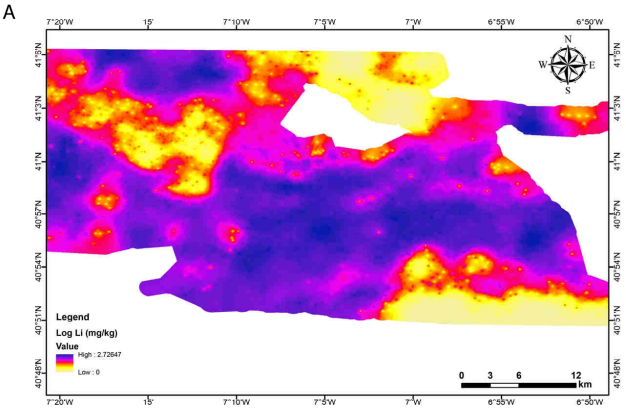

B

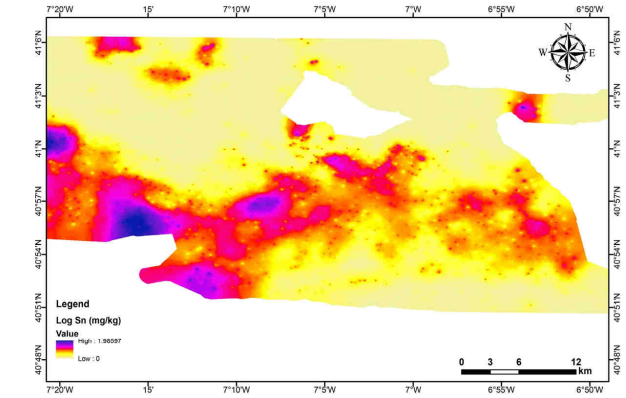

Figure A1. Geochemical anomaly maps for Li (**A**) and Sn (**B**) before excluding the granitic areas.

References

1. European Commission: DG Internal Market Industry Entrepreneurship and SMEs. *Critical Raw Materials Resilience: Charting a Path towards Greater Security and Sustainability*; COM(2020) 474 final; European Commission: DG Internal Market Industry Entrepreneurship and SMEs: Brussels, Belgium, 2020; p. 23.
2. Brooks, K. Lithium Minerals. *Geol. Today* **2020**, *36*, 192–197, doi:10.1111/gto.12326.
3. Kesler, S.E.; Gruber, P.W.; Medina, P.A.; Keoleian, G.A.; Everson, M.P.; Wallington, T.J. Global lithium resources: Relative importance of pegmatite, brine and other deposits. *Ore Geol. Rev.* **2012**, *48*, 55–69, doi:10.1016/j.oregeorev.2012.05.006.
4. Silva, D.; Lima, A.; Gumiaux, C.; Glouguen, E.; Deveaud, S. Spatial Geostatistical Analysis Applied to The Barroso-Alvão Rare-Elements Pegmatite Field (Northern Portugal). In *GIS—An Overview of Applications*; Teodoro, A.C., Ed.; Bentham eBooks: Sharjah, United Arab Emirates, 2018.
5. Linnen, R.L.; Van Lichtervelde, M.; Černý, P. Granitic Pegmatites as Sources of Strategic Metals. *Elements* **2012**, *8*, 275–280, doi:10.2113/gselements.8.4.275.
6. Gourcerol, B.; Gloaguen, E.; Melleton, J.; Tuduri, J.; Galiegue, X. Re-assessing the European lithium resource potential—A review of hard-rock resources and metallogeny. *Ore Geol. Rev.* **2019**, *109*, 494–519, doi:10.1016/j.oregeorev.2019.04.015.
7. Carvalho, J.M.F.; Farinha, J.A.L.B. Lithium potentialities in Northern Portugal. In Proceedings of the 17th Industrial Minerals International Congress, Barcelona, Spain, 28–31 March 2004; pp. 1–10.
8. Roda-Robles, E.; Pesquera, A.; Gil-Crespo, P.P.; Vieira, R.; Lima, A.; Olave, I.G.; Martins, T.; Torres-Ruiz, J.; E., R.-R.; A., P.; et al. Geology and mineralogy of Li mineralization in the Central Iberian Zone (Spain and Portugal). *Miner. Mag.* **2016**, *80*, 103–126, doi:10.1180/minmag.2016.080.049.
9. Brown, W.M.; Gedeon, T.D.; Groves, D.I.; Barnes, R.G. Artificial neural networks: A new method for mineral prospectivity mapping. *Aust. J. Earth Sci.* **2000**, *47*, 757–770, doi:10.1046/j.1440-0952.2000.00807.x.
10. Rigol-Sanchez, J.P.; Olmo, M.C.; Abarca-Hernández, F. Artificial neural networks as a tool for mineral potential mapping with GIS. *Int. J. Remote Sens.* **2003**, *24*, 1151–1156, doi:10.1080/0143116021000031791.
11. Oh, H.-J.; Lee, S. Application of Artificial Neural Network for Gold–Silver Deposits Potential Mapping: A Case Study of Korea. *Nat. Resour. Res.* **2010**, *19*, 103–124, doi:10.1007/s11053-010-9112-2.
12. Rodriguez-Galiano, V.; Sanchez-Castillo, M.; Olmo, M.C.; Chica-Rivas, M. Machine learning predictive models for mineral prospectivity: An evaluation of neural networks, random forest, regression trees and support vector machines. *Ore Geol. Rev.* **2015**, *71*, 804–818, doi:10.1016/j.oregeorev.2015.01.001.
13. Roda-Robles, E.; Villaseca, C.; Pesquera, A.; Gil-Crespo, P.P.; Vieira, R.; Lima, A.; Olave, I.G. Petrogenetic relationships between Variscan granitoids and Li-(F-P)-rich aplite-pegmatites in the Central Iberian Zone: Geological and geochemical constraints and implications for other regions from the European Variscides. *Ore Geol. Rev.* **2018**, *95*, 408–430, doi:10.1016/j.oregeorev.2018.02.027.
14. Catalán, J.R.M. The Central Iberian arc, an orocline centered in the Iberian Massif and some implications for the Variscan belt. *Acta Diabetol.* **2011**, *101*, 1299–1314, doi:10.1007/s00531-011-0715-6.
15. Dias, R.; Ribeiro, A. The Ibero-Armorican Arc: A collision effect against an irregular continent? *Tectonophys.* **1995**, *246*, 113–128, doi:10.1016/0040-1951(94)00253-6.
16. Bea, F.; Montero, P.; Zinger, T. The Nature, Origin, and Thermal Influence of the Granite Source Layer of Central Iberia. *J. Geol.* **2003**, *111*, 579–595, doi:10.1086/376767.
17. Roda, E. Distribución, Caracteristicas y Petrogenesis de las Pegmatitas de La Fregeneda (Salamanca). Ph.D. Thesis, UPV/EHU, Bilbao, Spain, 1993.
18. Roda-Robles, E.; Perez, A.P.; Roldan, F.V.; Fontan, F. The granitic pegmatites of the Fregeneda area (Salamanca, Spain): characteristics and petrogenesis. *Miner. Mag.* **1999**, *63*, 535–558, doi:10.1180/002646199548709.
19. Vieira, R. Aplitopegmatitos com Elementos Raros da Região Entre Almendra (V.N. de Foz Côa) e Barca d'Alva (Figueira de Castelo Rodrigo). Campo Aplitopegmatítico da Fregeneda-Almendra. Ph.D. Thesis, Faculdade de Ciências da Universidade do Porto, Porto, Portugal, 2010.
20. Costa, J.C.S. *Notícia Sobre uma Carta Geológica do Buçaco, de Nery Delgado*; Serviços Geológicos de Portugal: Lisboa, Portugal, 1950.
21. Teixeira, C. *Notas Sobre Geologia de Portugal o Complexo Xisto-Grauváquico ante-Ordoviciano*; Empresa Literaria Fluminense Lda.: Lisboa, Portugal, 1955; p. 48.
22. Bea, F.; Herrero, J.G.S.G.; Pinto, M.S.; Barrera, J.L.; Brandle, J.L.; Corretgé, L.G.; Suárez, O. Una compilación geoquímica (elementos mayores) para los granitóides del Macizo Hespérico. In *Geología de los Granitóides y Rocas Asociadas del Macizo Hesperico*; Bea, F., Carnicero, A., Gonzalo, J.C., López-Plaza, M., Rodríguez Alonso, M.D., Eds.; Libro de Homenaje a L. C. García de Figuerola, Editorial Rueda: Alcorcon, Madrid, Spain, 1987.
23. Pereira, I.; Dias, R.; Bento dos Santos, T.; Mata, J. Exhumation of a Migmatite Complex along a Transpressive Shear Zone: Inferences from the Variscan Juzbado–Penalva Do Castelo Shear Zone (Central Iberian Zone). *J. Geol. Soc.* **2017**, *174*, 1004–1018, doi:10.1144/jgs2016-159.

24. Ferreira, J.A.; Bento dos Santos, T.; Pereira, I.; Mata, J. Tectonically Assisted Exhumation and Cooling of Variscan Granites in an Anatectic Complex of the Central Iberian Zone, Portugal: Constraints from LA-ICP-MS Zircon and Apatite U–Pb Ages. *Int. J. Earth Sci.* **2019**, *108*, 2153–2175, doi:10.1007/s00531-019-01755-1.
25. Aires, S.C.M. Petrofísica e Litogeoquímica de Formações do "Complexo Xisto-Grauváquico" (Grupo do Douro) Estudo do Potencial do "Xisto" para Exploração como Pedra Natural. Ph.D. Thesis, Faculdade de Ciências da Universidade do Porto, Porto, Portugal, 2018.
26. Silva, A.F.d.; Ribeiro, M.L. *Notícia Explicativa da Folha 15-A Vila Nova de Foz Côa*; Serviços Geológicos de Portugal: Lisboa, Portugal, 1991; p. 52.
27. Silva, A.F.d.; Ribeiro, M.L. *Notícia Explicativa da Folha 15-B Freixo de Espada à Cinta*; Instituto Geológico e Mineiro: Lisboa, Portugal, 1994; p. 48.
28. Silva, A.F.; Santos, A.J.; Ribeiro, A.; Ribeiro, M.L. *Carta Geológica de Portugal na Escala 1/50.000—Folha 15-A—Vila Nova de Foz Côa*; Serviços Geológicos de Portugal: Lisboa, Portugal, 1990.
29. Silva, A.F.; Santos, A.J.; Ribeiro, A.; Cabral, J.; Ribeiro, M.L. *Carta Geológica de Portugal na Escala 1/50.000—Folha 15-B—Freixo de Espada à Cinta*; Serviços Geológicos de Portugal: Lisboa, Portugal, 1990.
30. Carvalhosa, A. *Carta Geológica de Portugal à Escala 1:50.000, Folha 15-D (Figueira de Castelo Rodrigo)*; Serviços Geológicos de Portugal: Lisboa, Portugal, 1960.
31. Ribeiro, M.L. *Carta Geológica Simplificada Do Parque Arqueológico Do Vale Do Côa Na Escala 1:80.000*; Parque Arqueológico do Vale do Côa: Vila Nova de Foz Côa, Portugal, 1990.
32. Al-Rawashdeh, S.; Saleh, B.; Hamzah, M. The Use of Remote Sensing Technology in Geological Investigation and Mineral Detection in El Azraq-Jordan. *Cybergeo Eur. J. Geogr.* **2006**, *358*, 1–17; doi:10.4000/cybergeo.2856.
33. van der Meer, F.D.; van der Werff, H.M.A.; van Ruitenbeek, F.J.A. Potential of ESA's Sentinel-2 for Geological Applications. *Remote Sens. Environ.* **2014**, *148*, 124–133,doi:10.1016/j.rse.2014.03.022.
34. Beiranvand Pour, A.; Park, T.-Y.; Park, Y.; Hong, J.; Zoheir, B.; Pradhan, B.; Ayoobi, I.; Hashim, M. Application of Multi-Sensor Satellite Data for Exploration of Zn–Pb Sulfide Mineralization in the Franklinian Basin, North Greenland. *Remote Sens.* **2018**, *10*, 1186, doi:10.3390/rs10081186.
35. Cardoso-Fernandes, J.; Teodoro, A.; Lima, A. Potential of Sentinel-2 Data in the Detection of Lithium (Li)-Bearing Pegmatites: A Study Case. In Proceedings of the Earth Resources and Environmental Remote Sensing/GIS Applications IX, Berlin, Germany, 10–13 September 2018; doi:10.1117/12.2326285.
36. Cardoso-Fernandes, J.; Teodoro, A.C.; Lima, A. Remote Sensing Data in Lithium (Li) Exploration: A New Approach for the Detection of Li-Bearing Pegmatites. *Int. J. Appl. Earth Obs. Geoinf.* **2019**, *76*, 10–25, doi:10.1016/j.jag.2018.11.001.
37. Cardoso-Fernandes, J.; Teodoro, A.C.M.; Lima, A.; Roda-Robles, E. Evaluating the Performance of Support Vector Machines (SVMs) and Random Forest (RF) in Li-Pegmatite Mapping: Preliminary Results. In Proceedings of the Earth Resources and Environmental Remote Sensing/GIS Applications X, Strasbourg, France, 9–12 September 2019; doi:10.1117/12.2532577.
38. Cardoso-Fernandes, J.; Teodoro, A.C.; Lima, A.; Roda-Robles, E. Lithium (Li) Pegmatite Mapping Using Artificial Neural Networks (ANNs): Preliminary Results. In Proceedings of the IEEE International Geoscience and Remote Sensing Symposium, Waikoloa, HI, USA, 26 September–2 October 2020; pp. 557–560, doi:10.1109/IGARSS39084.2020.9323852.
39. Angel, J.M.; Viallefond, L. *Prospection Géochimique Portugal. Résultats Analytiques et Interprétation de l'échantillonnage Réalisé Par Le S.F.M. Sur La Feuille 15A, Région de Almendra*; NOTE/GMX-748; BRGM: Orléans, France, 1981; p. 6.
40. Viallefond, L. *Prospection Géochimique Portugal: Résultats Analytiques et Interprétation de l'Échantillonnage Réalisé par le S.F.M. sur la Feuille 15B*; NOTE/GMX-732; BRGM: Orléans, France, 1981; p. 27.
41. Viallefond, L.; Angel, J.M. *Portugal Nord—Feuille 15A-15C—Interprétation des Données Analytiques*; NOTE/GMX-738; BRGM: Orléans, France, 1981; p. 17.
42. Vieira, R.; Roda-Robles, E.n.; Pesquera, A.; Lima, A. Chemical variation and significance of micas from the Fregeneda-Almendra pegmatitic field (Central-Iberian Zone, Spain and Portugal). *Am. Mineral.* **2011**, *96*, 637–645, doi:10.2138/am.2011.3584.
43. Lanaras, C.; Bioucas-Dias, J.; Galliani, S.; Baltsavias, E.; Schindler, K. Super-Resolution of Sentinel-2 Images: Learning a Globally Applicable Deep Neural Network. *J. Photogramm. Remote Sens.* **2018**, *146*, 305–319, doi:10.1016/j.isprsjprs.2018.09.018.
44. Bahr, T.; Heinz, D.C. Creating Models Of Hyperspectral Classification Workflows Integrating Dimensionality Expansion For Multispectral Imagery. In Proceedings of the 10th Workshop on Hyperspectral Imaging and Signal Processing: Evolution in Remote Sensing (WHISPERS), Amsterdam, The Netherlands, 24–26 September 2019; doi:10.1109/whispers.2019.8920946.
45. Cardoso-Fernandes, J.; Silva, J.; Lima, A.; Teodoro, A.C.; Perrotta, M.; Cauzid, J.; Roda-Robles, E.; Ribeiro, M.A. Reflectance spectroscopy to validate remote sensing data/algorithms for satellite-based lithium (Li) exploration (Central East Portugal). In Proceedings of the SPIE Remote Sensing, Earth Resources and Environmental Remote Sensing/GIS Applications XI, Online, 21–25 September 2020; https://doi.org/10.1117/12.2573929.
46. Cardoso-Fernandes, J.; Silva, J.; Lima, A.; Teodoro, A.C.; Perrotta, M.; Cauzid, J.; Roda-Robles, E. Characterization of lithium (Li) minerals from the Fregeneda-Almendra region through laboratory spectral measurements: A comparative study. In Proceedings of the SPIE Remote Sensing, Earth Resources and Environmental Remote Sensing/GIS Applications XI, Online, 21–25 September 2020; https://doi.org/10.1117/12.2573941.
47. Cardoso-Fernandes, J.; Silva, J.; Dias, F.; Lima, A.; Teodoro, A.C.; Barrès, O.; Cauzid, J.; Perrotta, M.; Roda-Robles, E.; Ribeiro, M.A. Tools for remote exploration: A Lithium (Li) dedicated spectral library of the Fregeneda-Almendra aplite-pegmatite field. Version 1. Zenodo, 2021. Available online: https://zenodo.org/record/4575375#.YUGmx30RVPY (accessed on 9 March 2021).

48. Cardoso-Fernandes, J.; Dias, F.; Lima, A.; Anjos Ribeiro, M.; Perrotta, M.; Roda-Robles, E.; Teodoro, A.C. Petalite alteration products from the Bajoca pegmatite (Central Portugal): A multiapproach for lithium exploration. In Proceedings of the EGU General Assembly 2021, Online, 19–30 April 2021; doi:10.5194/egusphere-egu21-2364.
49. Haykin, S.S. *Neural Networks: A Comprehensive Foundation*; Prentice Hall: Englewood Cliffs, NJ, USA, 1999; ISBN 978-0-13-273350-2.
50. Cardoso-Fernandes, J.; Teodoro, A.C.; Lima, A.; Roda-Robles, E. Semi-Automatization of Support Vector Machines to Map Lithium (Li) Bearing Pegmatites. *Remote. Sens.* **2020**, *12*, 2319, doi:10.3390/rs12142319
51. Gaspar, L.M.; Inverno, C.M.C. Mineralogy and Metasomatic Evolution of Distal Strata-BoundScheelite Skarns in the Riba de Alva Mine, Northeastern Portugal. *Econ. Geol.* **2000**, *95*, 1259–1275, doi:10.2113/gsecongeo.95.6.1259.

I.2. International, peer-reviewed conference proceedings

Credits to the original publication:

PROCEEDINGS OF SPIE

SPIEDigitalLibrary.org/conference-proceedings-of-spie

Remote sensing techniques to detect areas with potential for lithium exploration in Minas Gerais, Brazil

D. Santos, A. Teodoro, A. Lima, J. Cardoso-Fernandes

D. Santos, A. Teodoro, A. Lima, J. Cardoso-Fernandes, "Remote sensing techniques to detect areas with potential for lithium exploration in Minas Gerais, Brazil," Proc. SPIE 11156, Earth Resources and Environmental Remote Sensing/GIS Applications X, 111561F (3 October 2019); doi: 10.1117/12.2532744

SPIE.

Event: SPIE Remote Sensing, 2019, Strasbourg, France

Downloaded From: https://www.spiedigitallibrary.org/conference-proceedings-of-spie on 08 Oct 2019 Terms of Use: https://www.spiedigitallibrary.org/terms-of-use

Remote Sensing techniques to Detect Areas with Potential for Lithium Prospection in Minas Gerais, Brazil.

D. Santos[a], A.Teodoro[b,c], A. Lima[b,c], J. Cardoso-Fernandes[b,c]

[a]Dep. Of Geography, Faculty of Arts, University of Porto, Portugal
[b]Dep. Geosciences, Environment and Land Planning Faculty of Sciences, Rua Campo Alegre, 4169-007, Porto, University of Porto, Porto, Portugal
[c]Earth Sciences Institute (ICT), Faculty of Sciences, Rua Campo Alegre, 4169-007, Porto, University of Porto, Porto, Portugal

ABSTRACT

Lithium (Li) is defined as an alkaline metal which does not exist in nature in its free form. Moreover, it has properties that make it possible to be applied in several manners, such as industrial use, especially in the ceramic and glass industries, as well as the battery industry which has had an increase in this element consumption. It is crucial to use less expensive and faster techniques, compared to classical and intrusive methods, to identify new Li deposits. Remote sensing as proved to be a powerful tool to identify areas with potential for Li exploration. The objective of this work is to apply several images processing techniques, such as RGB band combinations, Band Ratios and Principal Components Analysis (PCA) to identify potential areas for Li prospection in the pegmatite district of São João Del Rei, located in the south of the state of Minas Gerais, Brazil. In these areas, two study zones were defined: the zone A, with approximately 323 km² in the pegmatite district of São João Del Rei and the zone B with approximately 90 km² in the pegmatite district of Araçuaí. The results of the techniques applied in this study are very promising since, in addition to ease and low cost, these techniques can be applied to several locations. This approach is highly valuable for the Li mining industry.

Keywords: Lithium, Remote sensing, RGB combinations, Band ratio, PCA.

1. INTRODUCTION

In the last decade a great growth in the global demand for lithium (Li), caused mostly by the increasing introduction of electric vehicles in the market, besides the increase of batteries consumption, were observed. Thereby, Li, which was traditionally used by the ceramics and glass industries, has become a strategic raw material for the 21st century, especially with regard to its application in energy storage technologies[1,2]. In order to meet this growing demand, it is necessary to identify new Li deposits. The use of remote sensing methods has proved to be a powerful tool not only for its efficiency in the targets' identification but also because it is a fast and less expensive method than traditional techniques[3].

With a technological advance in the use of remote sensing data/techniques to map terrestrial resources, it was inevitable to use these data/techniques for exploration purposes, for instances in studies aimed at the exploration of hydrothermal gold.[3,4] Remote sensing has been also used to study other types of deposits.[5,6,7] In relation to Li deposits, we can highlight the work of Perrota,[8] which used ASTER images in the spectral mapping of pegmatite intrusions hosting Li mineralization's and, more recently, Cardoso-Fernandes et al.[3] that presents a new approach in using remote sensing data in the detection of Li pegmatites considering three methods: RGB Combinations, Band Ratios and Principal Component Analysis (PCA).

The objective of this study is to apply the methods proposed by Cardoso-Fernandes et al.[3] to draw potential areas to Li exploration in the pegmatite district of Araçuaí and in the pegmatite district of São João Del Rei, located in the northeast and south of the state of Minas Gerais, respectively, in Brazil. The results of the techniques applied in this work are very promising, since in addition to the low cost, they can still be applied to other locations. Thus, they are highly valuable techniques for the Li mining industry.

Earth Resources and Environmental Remote Sensing/GIS Applications X, edited by Karsten Schulz, Ulrich Michel, Konstantinos G. Nikolakopoulos, Proc. of SPIE Vol. 11156, 111561F
© 2019 SPIE · CCC code: 0277-786X/19/$21 · doi: 10.1117/12.2532744

Downloaded From: https://www.spiedigitallibrary.org/conference-proceedings-of-spie on 08 Oct 2019
Terms of Use: https://www.spiedigitallibrary.org/terms-of-use

2. STUDY AREA

The study area is divided in two zones: (i) the pegmatite district of Araçuaí and; (ii) the pegmatite district of São João Del Rei located respectively in the northeast and south of the state of Minas Gerais, respectively, in Brazil (Fig.1).
The pegmatites of the district of Araçuaí intruded the metasedimentary rocks of the Salinas formation or the parental granites themselves, and are usually tabular or lenticular in this district. In order to achieve better results, we delimited our study area to a zone (zone B) of approximately 90 km^2 [9]. Zone B has four mines exploiting Li minerals: three spodumene mines (Zué, Oscar and Monte Alto 2) and one lepidolite mine (Monte Alto 1)[10].
The province of São João del Rei is located in the center-south portion of the state of Minas Gerais. It covers the municipalities of Nazareno, São Tiago, Resende Costa, Cassiterita (current Conception of Barra de Minas), São João del Rei, Ritápolis and Coronel Xavier Chaves, encompassing an area of 1,400 km². The size of the pegmatites of the region of São João del Rei can range from a few meters to more than 1 km, and the bodies considered large are more than 100 m long and more than 5 meters wide [11]. In this area, a study zone (zone A) with approximately 323 km² was defined. Both areas were defined by taking into account the geological factors of the local and the already known locations of important exploration points of Li minerals in the region. The zone A has the Volta Grande mine [12] and other pegmatite occurences as target points for Li minerals in the analyzes. At first, the target area was only the Volta Grande mine, but by applying these methodologies it was possible to highlight some areas of interest, which when compared to geological cartography correspond to occurrences of pegmatites.

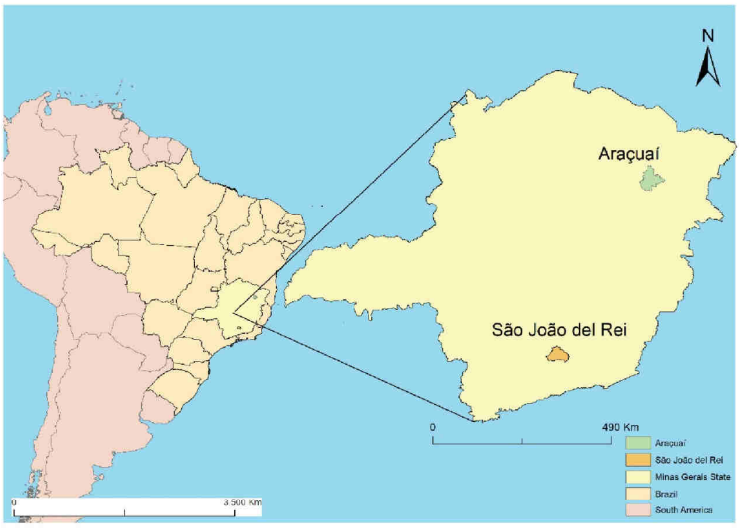

Figure 1. Study area location (Araçuaí and São João Del Rei) in Minas Gerais State, Brazil.

3. METHODOLOGY

3.1.1 Image Acquisition

As the spectral range of the ASTER, Landsat-5 TM, Landsat-8 OLI and Sentinel-2 MSI satellites sensors are more suitable for geology purposes than the products of other missions, due to the availability of SWIR bands, these data were used for image processing and interpretation[13,14]. These data are more suitable due to the absorption of mineral characteristics in near infrared (NIR) and short-wave infrared (SWIR) part of the electromagnetic spectrum. All downloaded images have a cloud cover less than 10%. Considering that the study area belongs to the Atlantic forest biome, it naturally has a high vegetation cover, so images in months of drought were prioritized in the selection, with the objective of obtaining images with the lowest vegetation cover.

Downloaded From: https://www.spiedigitallibrary.org/conference-proceedings-of-spie on 08 Oct 2019
Terms of Use: https://www.spiedigitallibrary.org/terms-of-use

The Landsat-5 images acquired were from 16/09/1986 in zone A and 11/10/1986 in zone B. Landsat-5 images have a spatial resolution of 30 m and their data file consists of 7 spectral bands, being three bands in the visible, one in the NIR and two in the SWIR[13]. The Landsat-8 images were from 05/09/2017 in zone A and 08/08/2016 in zone B. Landsat-8 OLI has nine spectral bands with a spatial resolution of 30 m for bands 1-7 and 9 (five bands in the visible and NIR, and two in the SWIR); 15 m for band 8 (panchromatic). This satellite carried out another sensor –TIRS- with two thermal bands (10 and 11) collected at 100 m, and resampled at 30 m[3,15]. The Sentinel-2 images were from 09/19/2017 in zone A and 09/21/2018 for zone B. The Sentinel-2 Multispectral Instrument (MSI) had 13 spectral bands: four bands at 10 m, six bands at 20 m and three bands at 60 m spatial resolution[16]. Due to a problem with the SWIR band in 2008, it became necessary to acquire the ASTER images before 2008. The ASTER had three bands in the visible and NIR with 15 m of spatial resolution, six bands in the SWIR with a spatial resolution of 30 m and four bands in the TIR with 90 m[17]. This information is summarized in Table 1. All data were geometrically corrected[18].

Table 1. Characteristics of the data used.

Satellites/Sensor	Image dates	Bands	Spatial Resolution (m)
ASTER	14/06/2007 – zone A 24/08/2004 – zone B	3 VNIR 6 SWIR 5 TIR	15 30 90
Landsat-5 TM	16/09/1986 - zone A 11/10/1986 - zone B	3 Visible 1 NIR 2 SWIR	 30
Landsat-8 OLI	05/09/2017 – zone A 08/08/2016 – zone B	5 VNIR 2 SWIR 2 TIR	30 (15 for Band 8) 30 100
Sentinel-2 MSI	09/19/2017 – zone A 09/21/2018 - zone B	10 VNIR 3 SWIR	10 (B2, B3, B4, B8), 20 (B5, B6, B7, B8a) 60 (B1, B9) 20 (B11, B12) 60 (B10)

3.1.2 Image pre-processing

After downloading the images and delimiting the study areas, some corrections such as atmospheric corrections need to be applied. The atmospheric phenomena of scattering, absorption and refraction of the electromagnetic energy, end up affecting the radiance reflected by the surface, which in turn is captured by the sensor[19]. Thus, atmospheric correction is necessary to minimize these atmospheric effects. Sentinel-2 images are already supplied in surface reflectance. In the Landsat-5, Landsat-8 and ASTER satellites images it was necessary to convert the digital numbers (DNs) to the top of the atmosphere reflectance (TOA) and after applying an atmospheric correction algorithm. The atmospheric correction method applied was the Dark Object Subtraction (DOS1), that is a method that corrects the atmospheric scattering in which the atmospheric interference is estimated directly from DN of the satellite image, was considered[19]. This method was applied, with the exception of thermal bands, to convert TOA reflectance into surface reflectance. The atmospheric correction was performed using the Semi-Automatic Classification Plugin (SCP) tool version 6.2.9 available in the QGIS software version 3.2.1.

The pansharpening process is defined when high-resolution panchromatic and lower multispectral resolution images are merged to create a single high-resolution image[17]. The Brovey Transform available in SCP (Equation 1) was applied to the Landsat 8 images resulting in the resampling of bands 2 to 7 from 30 m to 15 m.

$$MS_{out} = \frac{MS_i}{MS_{tot}} \cdot PAN \quad (1)$$

Downloaded From: https://www.spiedigitallibrary.org/conference-proceedings-of-spie on 08 Oct 2019
Terms of Use: https://www.spiedigitallibrary.org/terms-of-use

3.1.3 Image processing

The image processing consisted of applying the techniques used by Cardoso-Fernandes et al.[3], in the study areas defined for this work. These techniques correspond to: RGB combination, Band Ratios and Selective PCA. ArcGIS software (version 10.6.1) was used to complement the tools of SPC. Using information derived from Normalized Difference Vegetation (NDVI), a mask was created to reduce noise contamination and spectral variability of major water bodies and areas with vegetation.

3.1.4 RGB Combinations

Combining different bands, it is possible to produce different color combinations that can be used for different objectives[20]. In order to identify possible areas of interest for Li minerals exploration, different RGB combinations already tested by Cardoso-Fernandes et al.[3] in each satellite dataset were applied, according to Table 2.

Table 2. RGB combinations applied.

Satellites	RGB Combinations
ASTER	5-1-14
	2-1-13
Landsat-5 TM	7-2-6
	2-1-6
Landsat-8 OLI	7-3-11
	3-2-11
Sentinel-2 MSI	3-2-12

Following the procedure of Cardoso-Fernandes et al.[3], the RGB combinations were divided into two sets. The first is a composed by a SWIR, a visible band and a thermal band, respectively; and the second consists of two visible bands and a thermal band, respectively. Regarding Sentinel-2, the thermal band was replaced by a SWIR band.

3.1.5 Band ratios

For the lithological discrimination, band ratio combinations are one of the most useful image processing methods, where two bands are divided in order to highlight specific spectral differences [3,21]. The band ratios applied according to Table 3 were based on the Cardoso-Fernandes et al. [3] work.

Table 3. Band ratios tested.

Satellites	Band Ratios/Pegmatite identified
ASTER	1/3 Spodumene
	7/6 Lepidolite
Landsat-5 TM	2/4 Spodumene
	3/7 Lepidolite
Landsat-8 OLI	3/5 Spodumene
	4/7 Lepidolite
Sentinel-2 MSI	3/8 Spodumene
	4/12 Lepidolite

To identify pegmatites with Li, Cardoso-Fernandes et al.[3] considers the Li minerals reflectance curves peaks, using different band ratios for spodumene and lepidolite, as presented in Table 3.

Downloaded From: https://www.spiedigitallibrary.org/conference-proceedings-of-spie on 08 Oct 2019
Terms of Use: https://www.spiedigitallibrary.org/terms-of-use

3.1.6 Principal Component Analysis (PCA)

PCA is a multivariate statistical technique used to enhance and separate certain types of spectral signatures from the background [22]. Table 4 shows the bands used to compute the PCA, which according to Cardoso-Fernandes et al.[3] were processed considering two and four components.

Table 4. PCA for Li-bearing minerals processed.

Satellites	PC
ASTER	1,3 1,3,11,14
Landsat-5 TM	2,4 1,2,4,6
Landsat-8 OLI	3,5 2,3,5,11
Sentinel-2 MSI	3,8 2,3,8,11

4. RESULTS

Only the best results of the methods used (RGB combinations, band ratios and PCA) to identify Li minerals will be presented in this paper. Results will be divided into two Zones (A and B).

Zone A

4.1.1 RGB Combination

The RGB combinations that best identified Li minerals were applied. For ASTER, the combination 2-1-13 (Figure 2) Li minerals in the training areas and other pegmatite occurrences are highlighting in yellowish colors. This combination has less interference from water, which appears in greenish color, unlike the RGB 5-1-14 combination where there was a signal mixing with water bodies near to the areas containing pegmatites (not showed). The Landsat-5 TM gave a good result for the combination 7-2-6, detecting Li minerals in known Li-mineralized areas and other pegmatite occurrences, highlighting these areas in bright yellow color (Figure 3). In combination 2-1-6 for Landsat-5 TM, both metasediments and pegmatite occurrences appear in yellowish pixels, which makes impossible to distinguish it (not showed). The Landsat-8 images show an excellent result, where we can observe, in both combinations 7-3-11 (Figure 4) and 3-2-11 (not showed), that the sensor could not only detect Li minerals in yellow and greenish pixels, but was also is able to distinguish them from the associated tailings and mine dumps that appear in bright pixels in the mineralized Li's Volta Grande mine. Finally, the 3-2-12 (Figure 5) combination for Sentinel-2 was also able to distinguish Li mineralized areas (appearing in yellowish pixels) from the mine dumps (which appear in bright pixels).

Downloaded From: https://www.spiedigitallibrary.org/conference-proceedings-of-spie on 08 Oct 2019
Terms of Use: https://www.spiedigitallibrary.org/terms-of-use

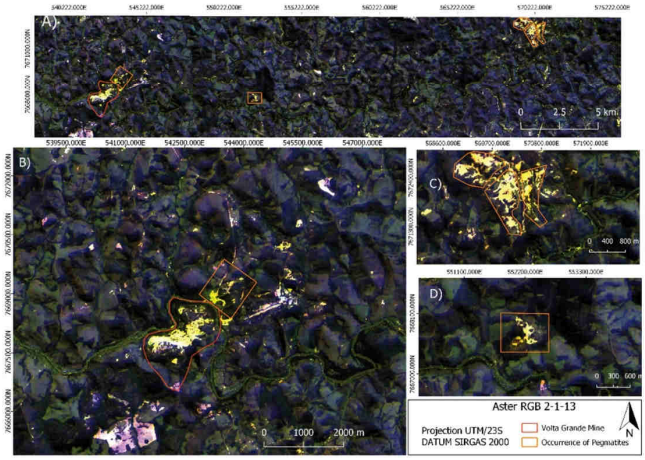

Figure 2. RGB Combination 2-1-13 for ASTER. A) Zone A. The known Li-mineralized areas appear in a yellow color, water bodies appear in green color and the granites appear in purple; B) Detailed image of Volta Grande Mine and surrounding area of pegmatite occurrences; C) Detailed image of pegmatite occurrences; D) Detailed image of pegmatite occurrences.

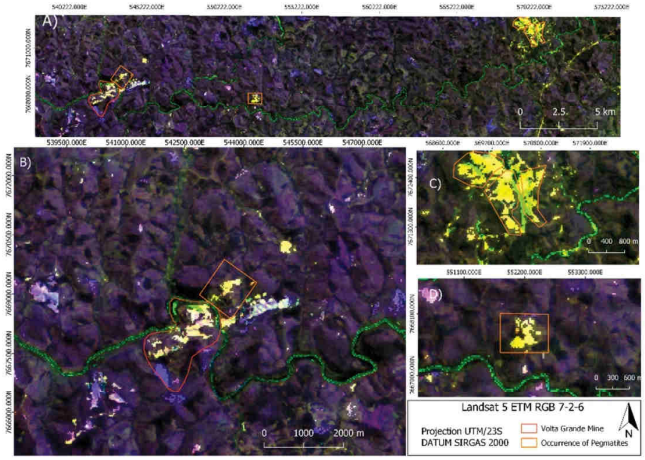

Figure 3. RGB Combination 7-2-6 for Landsat-5. A) Zone A. The known Li-mineralized areas appear in yellow color, water bodies appear in green color and granites appear in purple; B) Detailed image of Volta Grande Mine and surrounding area of pegmatite occurrences; C) Detailed image of pegmatite occurrences; D) Detailed image of pegmatite occurrences.

Downloaded From: https://www.spiedigitallibrary.org/conference-proceedings-of-spie on 08 Oct 2019
Terms of Use: https://www.spiedigitallibrary.org/terms-of-use

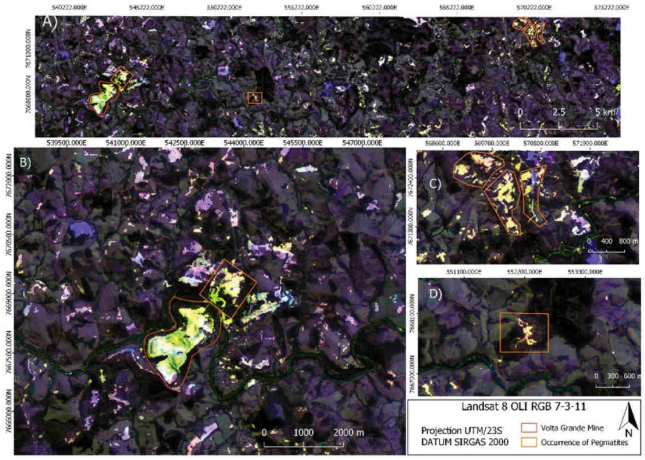

Figure 4. RGB Combination 7-3-11 for Landsat - 8. A) Zone A. The known Li-mineralized areas appear in yellow and greenish color, water bodies appear in dark green color and granites appear in purple; B) Detailed image of Volta Grande Mine and surrounding area of pegmatite occurrences; C) Detailed image of pegmatite occurrences; D) Detailed image of pegmatite occurrences.

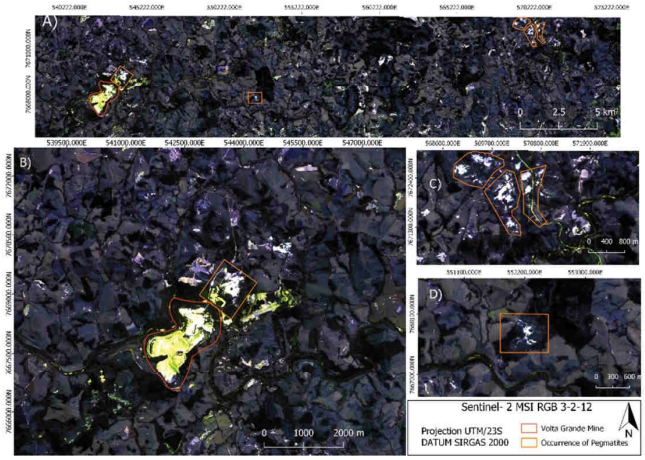

Figure 5. RGB Combination 3-2-12 for Sentinel-2. A) Zone A. The known Li-mineralized areas appear in a yellow color, water bodies appear in greenish color and granites appear in purple; B) Detailed image of Volta Grande Mine and surrounding area of pegmatite occurrences; C) Detailed image of pegmatite occurrences; D) Detailed image of pegmatite occurrences.

4.1.2 Band ratios

The band ratios used to identify lepidolite (ratio 3/7 for Landsat-5, ratio 4/7 for Landsat-8 and ratio 4/12 for Sentinel-2) (Table 3) were the most successful in detecting known pegmatite occurrences and known Li-mineralized areas like the Volta Grande mine. Meanwhile, the band ratios that focused on identifying spodumene had only one acceptable result (ratio 1/3 for ASTER). The ASTER sensor was the only one that did not show good results for lepidolite (Figure 6), unlike the other sensors that showed good results for lepidolite but not for spodumene. The ratio 1/3 for ASTER shows the Volta

Downloaded From: https://www.spiedigitallibrary.org/conference-proceedings-of-spie on 08 Oct 2019
Terms of Use: https://www.spiedigitallibrary.org/terms-of-use

Grande mine area in bright gray pixels and the other pegmatite occurrences appear in gray. The ratio 3/7 for Landsat-5 (Figure 7) show Volta Grande mine area in grayish pixels, and the other pegmatite occurrences appear in bright pixels. In the ratio 4/7 for Landsat-8 (Figure 8), we can observe bright and grayish pixels in the Volta Grande mine area, while the pegmatite occurrences appear in gray, however, this ratio was not able to identify one of these areas (highlighted in Figure 8 - D).
The ratio 4/12 for Sentinel-2 identifies the Volta Grande mine in bright gray pixels and the known pegmatite occurrences in gray color (Figure 9).

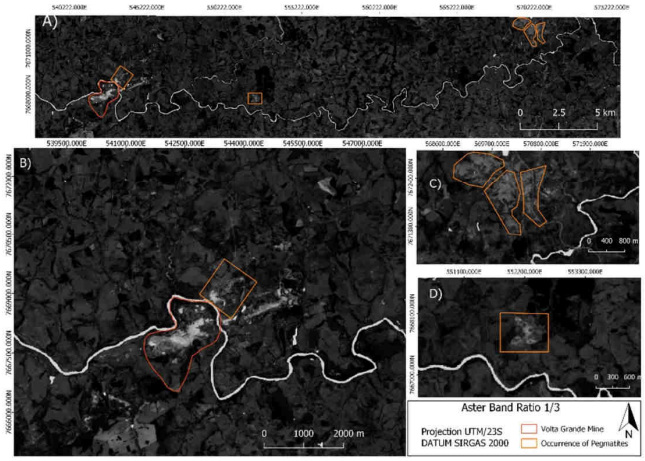

Figure 6. ASTER ratio 1/3. A) Zone A. The known Li-mineralized areas appear in light gray color, water bodies appear white; B) Detailed image of Volta Grande Mine and surrounding area of pegmatite occurrences; C) Detailed image of pegmatite occurrences; D) Detailed image of pegmatite occurrences.

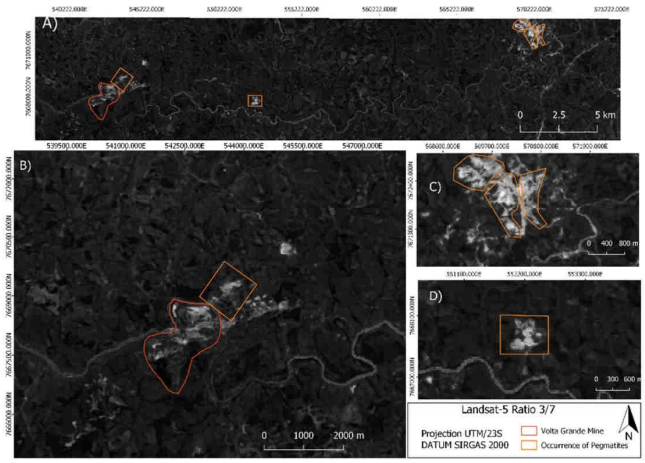

Figure 7. Landsat-5 ratio 3/7. A) Zone A. The known Li-mineralized areas appear in light gray color, water bodies appear in dark gray; B) Detailed image of Volta Grande Mine and surrounding area of pegmatite occurrences; C) Detailed image of pegmatite occurrences; D) Detailed image of pegmatite occurrences.

Downloaded From: https://www.spiedigitallibrary.org/conference-proceedings-of-spie on 08 Oct 2019
Terms of Use: https://www.spiedigitallibrary.org/terms-of-use

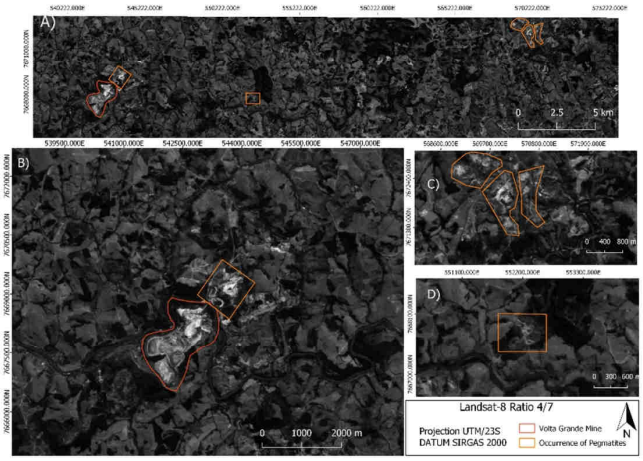

Figure 8. Landsat-8 ratio 4/7. A) Zone A. The known Li-mineralized areas appear in light gray color, water bodies appear in black color; B) Detailed image of Volta Grande Mine and surrounding area of pegmatite occurrences; C) Detailed image of pegmatite occurrences; D) Detailed image of pegmatite occurrences.

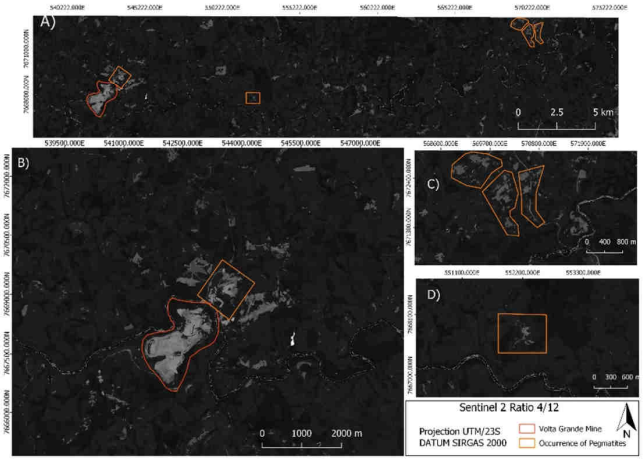

Figure 9. Sentinel-2 ratio 4/12. A) Zone A. The known Li-mineralized areas appear in gray color, water bodies appear in dark gray color; B) Detailed image of Volta Grande Mine and surrounding area of pegmatite occurrences; C) Detailed image of pegmatite occurrences; D) Detailed image of pegmatite occurrences.

4.1.3 PCA

From the applied PCA (Table 4), only those that showed the best results will be presented in this work. The selective PC on 2 components (Table 5) for ASTER showed a very good result, highlighting in bright pixels both the Volta Grande Mine and the other pegmatite occurrences (Figure 10).

Downloaded From: https://www.spiedigitallibrary.org/conference-proceedings-of-spie on 08 Oct 2019
Terms of Use: https://www.spiedigitallibrary.org/terms-of-use

The 4 PCs combinations that presented best results was for Landsat-5 (1,2,4,6) and for Landsat-8 (2,3,5,8). In the 4 PCs for Landsat-5, both the Li mineralized areas and pegmatite occurrences appear in bright pixels (Figure 11), but for the Landsat 8 the pixels appear in bright in the Volta Grande mine while the other pegmatite occurrences appear in gray color (Figure 12), as occurs in 2 PCs combination for the same sensor.
Considering 2 PCs, in Landsat-5 (2,4) (not showed), and Sentinel-2 (3,8) the bright pixels correspond to pegmatite occurrences and known Li mineralized areas (Figure 13). However, in Landsat-8 2 PCs (3,5) the pixels appear bright in the Volta Grande mine, while other pegmatite occurrences appear in gray color (not showed).

Table 5. Eigenvector and eigenvalues matrix for the two PCs for Li-bearing minerals processed considering ASTER sensor.

	PC1	PC2
Bands 1	0,16112	0,98693
Bands 3	0,98693	-0,16112
Eigenvalues	0,00127	0,00015
Percent of EigenValues	89,4041	10,5959
Accumulative of EigenValues	89,4041	100,0000

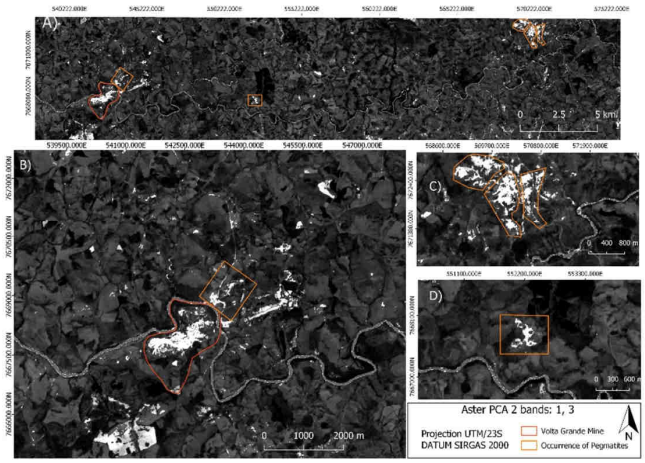

Figure 10. ASTER selective PCA (2 PCs). A) Zone A. The known Li-mineralized areas appear in bright pixels, water bodies appear in dark gray color; B) Detailed image of Volta Grande Mine and surrounding area of pegmatite occurrences; C) Detailed image of pegmatite occurrences; D) Detailed image of pegmatite occurrences.

Downloaded From: https://www.spiedigitallibrary.org/conference-proceedings-of-spie on 08 Oct 2019
Terms of Use: https://www.spiedigitallibrary.org/terms-of-use

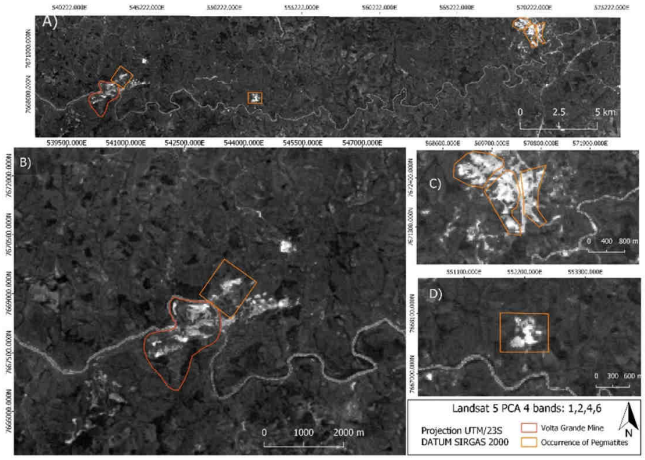

Figure 11. Landsat-5 selective PCA (4 PCs). A) Zone A. The known Li-mineralized areas appear in white pixels, water bodies appear in dark gray color; B) Detailed image of Volta Grande Mine and surrounding area of pegmatite occurrences; C) Detailed image of pegmatite occurrences; D) Detailed image of pegmatite occurrences.

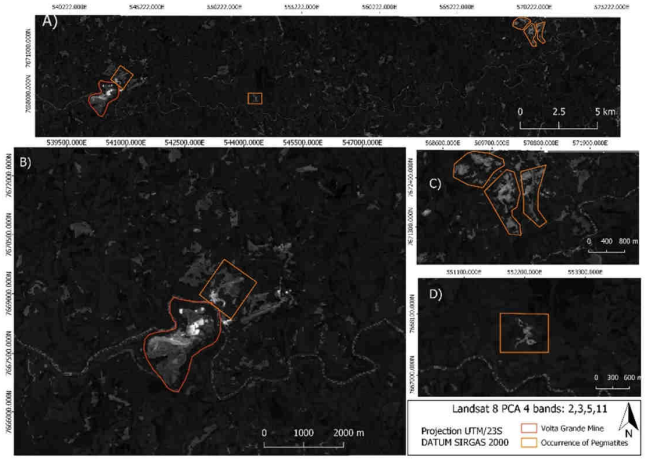

Figure 12. Landsat-8 selective PCA (4 PCs). A) Zone A. The Known Li-mineralized areas appear in white for Volta Grande Mine and greyish pixels for the other areas, water bodies appear in dark gray color; B) Detailed image of Volta Grande Mine and surrounding area of pegmatite occurrences; C) Detailed image of pegmatite occurrences; D) Detailed image of pegmatite occurrences.

Downloaded From: https://www.spiedigitallibrary.org/conference-proceedings-of-spie on 08 Oct 2019
Terms of Use: https://www.spiedigitallibrary.org/terms-of-use

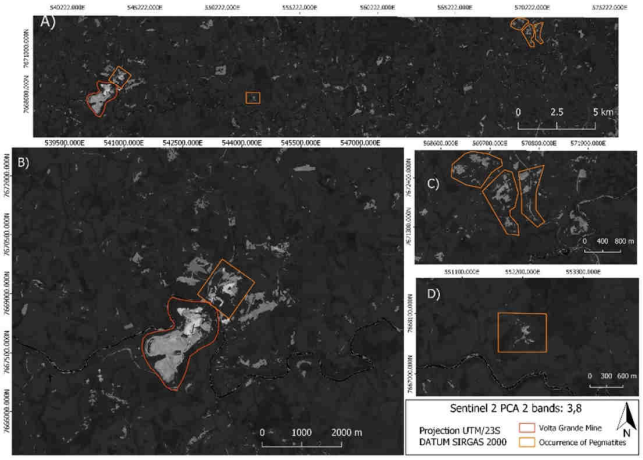

Figure 13. Selective PCA (2 PCs) for Sentinel-2. A) Zone A. The known Li-mineralized areas appear in bright gray for Volta Grande Mine and greyish pixels for the other areas, water bodies appear in dark gray color; B) Detailed image of Volta Grande Mine and surrounding area of pegmatite occurrences; C) Detailed image of pegmatite occurrences; D) Detailed image of pegmatite occurrences.

Zone B

4.1.4 RGB combinations

The RGB combinations that give a better result were the ASTER 2-1-13, Landsat-8 7-3-11 and Sentinel-2 3-2-12 (Figure 14). The results considering this approach were not satisfactory for Landsat-5 image. This can be justified by several factors, such as the highest vegetation coverage of the images that may have interfered with the spectral signal. In Figure 15, is presented in detail the result obtained from each sensor for known Li-bearing areas. The ASTER 2-1-13 was the only one capable of identifying all Li-bearing areas (yellow pixels). The combination 3-2-12 for Landsat-8 was able to identify the Monte Alto 1 and Zué mining areas (also in yellow pixels). The Oscar mine also appears in yellow, but the signal is very weak. Monte Alto 2 was not identified by this sensor. Like Landsat-8, Sentinel-2 also presents a very weak signal for the Oscar mine. The Monte Alto 1 and Zué mining areas were well identified in yellow pixels. Monte Alto 2 was also not identified by this sensor.

Downloaded From: https://www.spiedigitallibrary.org/conference-proceedings-of-spie on 08 Oct 2019
Terms of Use: https://www.spiedigitallibrary.org/terms-of-use

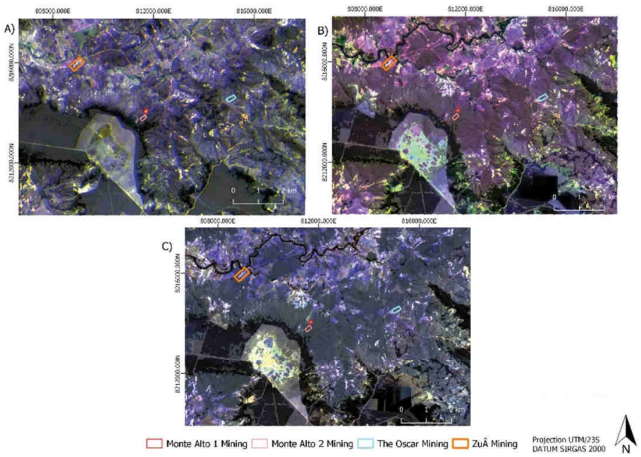

Figure 14. A) In RGB combination 2-1-13 for ASTER, the known Li-mineralized areas appear in a yellow color, water bodies appear in dark blue color and granites appear in blue; B) In RGB Combination 7-3-11 for Landsat-8, the known Li-mineralized areas appear in a yellow and greenish color, water bodies appear in dark green color and granites appear in purple; C) In RGB Combination 3-2-12 for Sentinel-2, the known Li-mineralized areas appear in a yellow color, water bodies appear black and granites appear in blue.

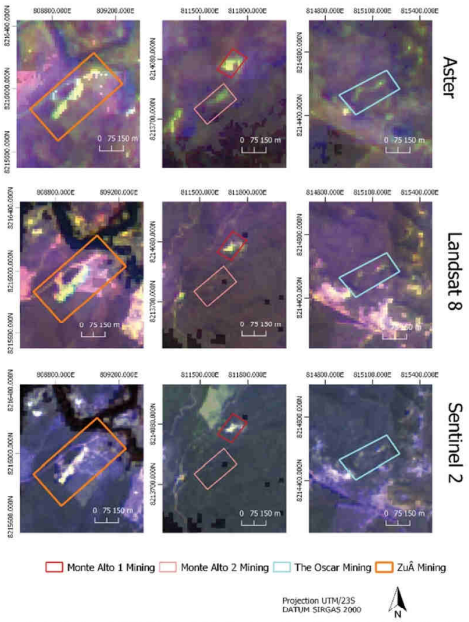

Figure 15. RGB Combinations: 2-1-13 for ASTER; 7-3-11 for Landsat-8, and 3-2-12 for Sentinel-2, detailed results.

Downloaded From: https://www.spiedigitallibrary.org/conference-proceedings-of-spie on 08 Oct 2019
Terms of Use: https://www.spiedigitallibrary.org/terms-of-use

4.1.5 Band ratios

Unlike Zone A, the band ratios used to identify spodumene (Table 3) were the most successful approach in detecting the knowing Li-bearing areas. The ratio 1/3 for ASTER detected all mines that exploit Li minerals with exception of Monte Alto 2 and Oscar mines that have a very weak signal. In ratio 3/5 for Landsat-8, we can observe the Monte Alto 1 and Zué mines in bright pixels. The Oscar mine appears with a very weak signal. Monte Alto 2 was not identified by this sensor. The ratio 3/8 for Sentinel-2 identifies the Monte Alto 1 and Zué mines in bright pixels as well. The Oscar mine appears with a very weak signal. Monte Alto 2 was also not identified by this sensor (Figure 16).

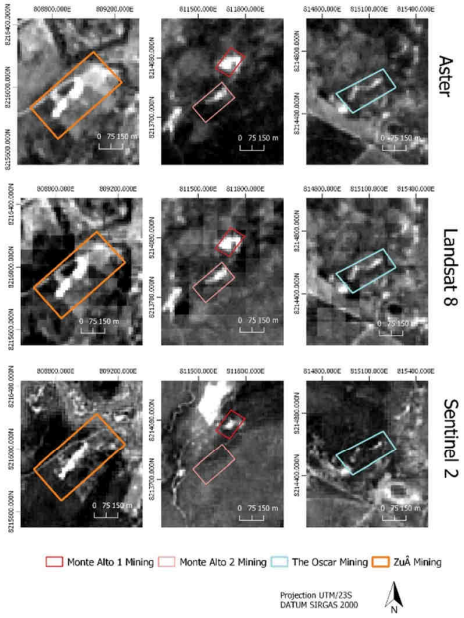

Figure 16. Band ratios: 1/3 for ASTER; 3/5 for Landsat-8, and 3/8 for Sentinel-2, detailed results.

4.1.6 PCA

For Zone B, the PC's that best identified Li mining areas were selective 4 PCs. The best result was obtained for ASTER sensor (1, 3, 11, 14). As we can see in Table 5, the PC that is best suited according to the method used by Cardoso-Fernandes et al.[3], is the PC4, which had to be multiplied by -1, so that the pixels in Li known areas appear in bright pixels. This sensor was again able to detect all known Li-bearing areas. The PCA on 4 bands for Landsat-8 (2, 3, 5,11) showed the Monte Alto 1 and Zué mines in bright pixels. The Oscar mine appears with a very weak signal. Monte Alto 2 has not been identified. The PCA on 4 selective bands for Sentinel- 2 (2, 3, 8, 11) shows the Monte Alto 1 and Zué mines in bright pixels as well. The Oscar mine appears with a very weak signal. Monte Alto 2 has not been identified (Figure 17).

Downloaded From: https://www.spiedigitallibrary.org/conference-proceedings-of-spie on 08 Oct 2019
Terms of Use: https://www.spiedigitallibrary.org/terms-of-use

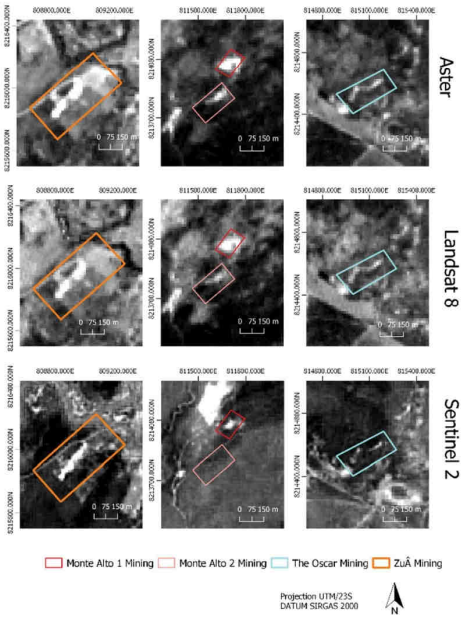

Figure 17. Selective 4 PCs: 1,3,11,14 for ASTER; 8 2,3,5,11 for Landsat-8, and 2,3,8,11 for Sentinel-2, detailed results.

Table 6. PCA on 4 bands for Li-bearing minerals processed for ASTER. Eigenvector and eigenvalues matrix.

	PC1	PC2	PC3	PC4
Bands 1	0,00282	0,00907	0,03974	-0,99917
Bands 3	0,00031	0,00667	0,99919	0,39801
Bands 11	0,72254	-0,72252	0,00478	-0,00442
Bands 14	89,4041	0,69126	-0,00516	0,00811
Eigenvalues	15,59852	0,05840	0,00115	0,00011
Percent of EigenValues	99,6190	0,3729	0,0074	0,0007
Accumulative of EigenValues	99,6190	99,9919	99,9993	100,0000

5. DISCUSSION

All the approaches applied in this study[3] presented better results in zone A. This may be justified by several factors, from the difference in soil composition to the high amount of vegetation coverage in zone B, which results in signal interference, which degrade the results.

5.1.1 RGB combinations

Cardoso-Fernandes et al.[3], divided the RGB combinations into 2 sets: the first set considers the SWIR, the visible and the thermal band, respectively, and the second set considers two visible bands and a thermal band.
In zone A, the Landsat-8 RGB combinations show excellent results in both sets, where we can observe, in both combinations 7-3-11 (Figure 4) and 3-2-11 (Figure 5), that the sensor could not only detect the Li-mineralized areas, but was also able to distinguish them from the waste pile in the Volta Grande mine. In zone B, the first set presents the best

Downloaded From: https://www.spiedigitallibrary.org/conference-proceedings-of-spie on 08 Oct 2019
Terms of Use: https://www.spiedigitallibrary.org/terms-of-use

result, but only the ASTER RGB combinations (2, 1, 13) was able to identify all known areas where Li minerals occur. The other sensors had difficulty in the identification of the Oscar mine. The Monte Alto 2 mine was not detected by the other sensors (Figure 19). Despite the difficulties in interpretation caused by mixing signals from other minerals, RGB combinations have proved to be an effective technique for identifying Li minerals in the two study areas considered, especially in zone A.

5.1.2 Band ratio

Band ratios were also divided into two sets, one for spodumene and other for lepidolite (Table 3). In zone A, band ratios were used to identify lepidolite (Table 3) and know Li-mineralized areas like the Volta Grande mine. Meanwhile, considering the band ratios focused on identifying spodumene, only one had an acceptable result: band ratio 1/3 for the ASTER sensor. Zone B, when compared to zone A, presented better results considering spodumene specific ratios (Table 3). Nevertheless, all ratios had difficulty or did not identify the Oscar and Monte Alto 2 mines. Even for the ratios applied to ASTER images, which obtained the best results among all the ratios tested, the signal was very weak for the Oscar and Monte Alto 2 mines. In spite of being able to identify areas with Li minerals, the band ratio technique presents several fragilities, especially in zone B.

5.1.3 PCA

The PCA presents the best results considering the 2 PCs, for ASTER (1, 3). Moreover, and for both 2 PCs and 4 PCs, Landsat-5 (2, 4 and 1, 2, 4, 6) showed good results, highlighting the areas of pegmatite occurrences and the Volta Grande Mine. The PCA applied to the images for Landsat-8 and Sentinel-2 showed a very weak signal in the pegmatite occurrences. The 4 PCs presents better results for zone B, especially the PCs applied to ASTER and Landsat-8 that allowed to detect all known Li mining areas. The 4 PCs for Sentinel-2 was not able to detect the Monte Alto 2 mine. PCA proved to be the most efficient method for detecting Li minerals, regarding the two study areas considered in this work. Although 4 PCs applied to Sentinel-2 images could not identify Monte Alto 2 mine in zone B, this technique identified all other areas with known Li minerals and had less signal interference from other mineral, when compared to RGB combinations.

6. CONCLUSIONS

The objective of this study is to apply three different approaches already proposed in the literature to identify potential areas for Li exploration in the Araçuaí pegmatite district and the São João Del Rei pegmatite district. Three techniques were applied: RGB combinations, band ratios and PCA. PCA has proven to be the most effective techniques for recognizing mineralized areas in study zones selected. The RGB combination, in spite some signs of mixing of other minerals, was able to identify areas of Li minerals, especially in ASTER and Landsat-8 images. On the other hand, band ratios proved to be the less effective technique for identifying Li minerals. Regarding the sensors, ASTER and Landsat-8 stand out, presenting the best results for all the techniques used. The Landsat-5 reached good results in the zone A, but it could not recognize effectively small mineralized areas, which contributed to the poor results for zone B. Although the nonexistence of a thermal band, Sentinel-2 has proved to be effective in the identification of Li minerals. Concluding, the sensor that achieve best results was the ASTER and the most suitable approach for the identification of Li minerals was the PCA technique. The results of the techniques applied in this study are very promising, identifying occurrences of pegmatites beyond expected, since in addition to ease and low cost, they can be applied to several locations. Thus, this approach is highly valuable for the Li mining industry.

ACKNOWLEGMENTS

The authors would like to thank the financial support provided by FCT with the ERA-MIN/0001/2017 – LIGHTS project and to FEDER through the operation POCI-01-0145-FEDER-007690 funded by the Programa Operacional Competitividade e Internacionalização – COMPETE2020 and by National Funds through FCT – Fundação para a Ciência e a Tecnologia within ICT, R&D Unit (reference UID/GEO/04683/2013). The authors would also like to thank Bruna Piva for their helpful support. J. Cardoso-Fernandes is financially supported by FCT within the compass of a Ph.D. Thesis, ref. SFRH/BD/136108/2018.

Downloaded From: https://www.spiedigitallibrary.org/conference-proceedings-of-spie on 08 Oct 2019
Terms of Use: https://www.spiedigitallibrary.org/terms-of-use

REFERENCES

[1] Martins, L., "Aspectos da geoestratégia global do lítio. O contexto ibero-americano," Miniforum Valorização de Pegmatitos Litiníferos, 1-3 (2011).
[2] Lima, A., Martins, T., Vieira, R., Noronha, F., "Campo aplitopegmatítico litinífero do Barroso-Alvão. Os seus diferentes minerais de lítio e sua melhor aplicação futura," Miniforum Valorização de Pegmatitos Litiníferos, 19-22 (2011).
[3] Cardoso-Fernandes, J., Teodoro, A.C., Lima, A.,"Remote sensing data in lithium (Li) exploration: A new approach for the detection of Li-bearing pegmatites," International Journal of Applied Earth Observation and Geoinformation 76(1), 10-25 (2019).
[4] Moradi, M., Basiri, S., Kananian, A., Kabiri, K., "Fuzzy logic modeling for hydrothermal gold mineralization mapping using geochemical, geological, ASTER imageries and other geo-data, a case study in Central Alborz, Iran," Earth Sci Informatics 8(1), 1997-205 (2014).
[5] Pascholati, E.M., Silva, C.L., Costa, S.S., Osak, L.S., Amaral, G., Rodriguez, I.P., "Novas ocorrências de urânio na região de lagoa real, a partir da superposição de dados geofísicos, geológicos e de sensoriamento remoto," Revista Brasileira de Geociências 3(2), 91-98 (2003).
[6] Almeida, T., "Modelos exploratórios para a prospecção de pb/zn utilizandoí dados de sensoriamento remoto: estudo de caso do prospecto salobro (porteirinha- mg)," Master Thesis UNICAMP, 122 (2000).
[7] Sabins, F.F., Miller, R.M., "Resource assessment—Salar uyuni and vicinity," Proceedings of Tenth Thematic Conference on Geologic Remote Sensing Environmental Research Institute of Michigan 2(1), 8-12 (1994).
[8] Perrotta, M.M., Filho, C.R.S., Leite, C.A.S., "Mapeamento espectral de intrusões pegmatíticas relacionadas a mineralizações de lítio, gemas e minerais industriais na região do Vale do Jequitinhonha (MG) a partir de imagens ASTER," Anais XII Simpósio Brasileiro de Sensoriamento Remoto INPE, 1855-1862 (2005).
[9] Soares, P.A.C., Marciano, V.R.P.R.O., "A Província Pegmatítica Oriental do Brasil à Luz dos Conhecimentos Atuais," Revista Brasileira de Geociências 16(1), 106-118 (1986).
[10] Francesconi, R. "Pegmatitos da região de São João del Rey, MG," Master Thesis USP, 98 (1972).
[11] Assumpção, C.S.," Caracterização mineralógica e geoquímica do pegmatito da mina de volta grande, provincia pegmatítica de são joão del rei, nazareno, minas gerais.," Master Thesis UFOP, 87 (2015).
[12] Tedechi, M.F., Paes, V.J.C., "Avaliação do potencial do lítio no brasil: área do médio rio Jequitinhonha, nordeste de minas gerais," Minerais Estratégicos 3(1), 196-202 (2016).
[13] Teodoro, A.C., and Veloso-Gomes, F., "Quantification of the Total Suspended Matter concentration around the sea breaking zone from in situ measurements and TERRA/ASTER data," Marine Georesources and Geotechnology. 25(2), 67-80 (2007).
[14] Teodoro, A.C., Pais-Barbosa, J., Gonçalves, H., Veloso-Gomes, F., and Taveira-Pinto, F., "Identification of beach features/patterns through image classification techniques applied to remotely sensed data," International Journal of Remote Sensing. 32(22), 7399-7422 (2011).
[15] U.S. Geological Survey. "Landsat—Earth observation satellites," U.S. Geological Survey Fact Sheet august 2016. < https://pubs.usgs.gov/fs/2015/3081/fs20153081.pdf> (23 March 2019).
[16] User Guides: Sentinel-2 < https://earth.esa.int/web/sentinel/user-guides/sentinel-2-msi/resolutions/spatial > (23 March 2019)
[17] ASTER Mission. < https://asterweb.jpl.nasa.gov/characteristics.asp > (24 March 2019)
[18] Gonçalves, H., Gonçalves, J.A., Corte-Real, L., and Teodoro, A.C., "CHAIR: Automatic image registration based on correlation and Hough transform," International Journal of Remote Sensing. 33(24), 7936-7968 (2012).
[19] Sanches, I.D.A., Andrade, R.G., Quartaroli, C.F., Rodrigues, C.A.G., "Análise comparativa de três métodos de correção atmosférica de imagens Landsat 5 – TM para obtenção de reflectância de superfície e NDVI," Anais XV Simpósio Brasileiro de Sensoriamento Remoto INPE, 7564-7570 (2011).
[20] Divate, D.D., "Extraction of feature from satellite images- using pan Chromatic sharpening," Proc. ICCCES-16, 1-7 (2016)
[21] Simon, N., Ali, C.A., Mohamed, K.R., Sharir, K., "Best Band Ratio Combinations for the Lithological Discrimination of the Dayang Bunting and Tuba Islands, Langkawi, Malaysia," Sains Malaysiana 45(5), 659-667 (2016).
[22] Loughlint W.P., "Principal Component Analysis for Alteration Mapping" Photogrammetric Engineering & Remote Sensing 57(9), 1663-1669 (1991).

Downloaded From: https://www.spiedigitallibrary.org/conference-proceedings-of-spie on 08 Oct 2019
Terms of Use: https://www.spiedigitallibrary.org/terms-of-use

In reference to IEEE copyrighted material which is used with permission in this thesis, the IEEE does not endorse any of University of Porto's products or services. Internal or personal use of this material is permitted. If interested in reprinting/republishing IEEE copyrighted material for advertising or promotional purposes or for creating new collective works for resale or redistribution, please go to http://www.ieee.org/publications_standards/publications/rights/rights_link.html to learn how to obtain a License from RightsLink. If applicable, University Microfilms and/or ProQuest Library, or the Archives of Canada may supply single copies of the dissertation.

MULTI-SCALE APPROACH USING REMOTE SENSING TECHNIQUES FOR LITHIUM PEGMATITE EXPLORATION: FIRST RESULTS

Joana Cardoso-Fernandes[1,2], Ana Cláudia Teodoro[1,2], Alexandre Lima[1,2], Christian Mielke[3], Friederike Körting[3], Encarnación Roda-Robles[4], Jean Cauzid[5]

[1]Department of Geosciences, Environment and Land Planning, Faculty of Sciences, University of Porto, Porto, Portugal
[2]ICT (Institute of Earth Sciences) – Porto pole (Portugal)
[3]Helmholtz Center Potsdam, German Research Center for Geosciences, Potsdam, Germany
[4]Departamento de Mineralogía y Petrología, Univ. País Vasco (UPV/EHU), Bilbao, Spain
[5]Laboratoire GeoRessources, Université de Lorraine-CNRS-CREGU, Vandœuvre-lès-Nancy, France
joana.fernandes@fc.up.pt; amteodor@fc.up.pt; allima@fc.up.pt; chmielke@gfz-potsdam.de, koerting@gfz-potsdam.de, encar.roda@ehu.es, jean.cauzid@univ-lorraine.fr

ABSTRACT

Raw-materials like lithium (Li) are crucial to the current global decarbonization, but Li-exploration presents some technical challenges. Therefore, new solutions for Li-exploration are needed. Consequently, the aim of this study is to present a unique multi-scale remote sensing approach for Li-pegmatite exploration integrated within the LIGHTS project, considering as study area the Bajoca mine (Portugal). Satellite data allowed the identification of the spectral signatures of Li-pegmatites at a district scale, while drone-borne hyperspectral measurements provided data at the target scale. Handheld spectroscopy and in situ hyperspectral scans of the mine walls were carried out to validate the satellite and drone data. Hyperspectral field and laboratory scans also aim to collect information at the mineral scale, to distinguish different lithological materials, and to identify the Li-rich areas. In the future, machine learning algorithms will deliver an automated integration of all acquired data.

Index Terms— Satellite, drone, hyperspectral scan, data integration, field validation

1. INTRODUCTION

The current path to global decarbonization cannot be achieved without the use of specific raw-materials that contribute in diverse ways to changing our economic models and lifestyles. One of these raw-materials is lithium (Li) that when incorporated in compounds such as Li Hydroxide (LiOH) is essential to produce rechargeable batteries that are increasingly used in electric vehicles. This shift in the motorization industry leads to big pressure to meet market demands. However, Li-exploration presents some difficulties since Li is difficult to identify and quantify and new exploration techniques will be crucial to target new deposits.

To address and overcome the inherent exploration difficulties, the "Lightweight Integrated Ground and Airborne Hyperspectral Topological Solution" (LIGHTS) project was implemented. LIGHTS is a consortium between academic and industrial partners from Portugal, Spain, France, Germany, and Brazil. The main aim of the project is to deliver a unique, cost-efficient and robust system capable of rapidly identifying target areas for Li-exploration through the integration of remote sensing data acquired at different scales (from district to mineral scale) and supporting geological and geochemical data. Remotely sensed data includes satellite- and drone-borne sensors as well as *in situ* spectroscopic measurements. Such an exploration system aims to be easily operated by any geoscientist and therefore it aims to help revolutionizing and stimulating Li-exploration, reducing the dependency on imported Li.

The relevance of this project is reinforced by the lack of remote sensing applications to Li-bearing pegmatites [1]. The first applications began with ASTER images in Brazil [2, 3]. Recently, in the ambit of the LIGHTS project, some approaches to the detection of Li-pegmatites were made [4-7]. It is worth mentioning that the innovative methodology proposed is capable of detecting the spectral signatures of Li-bearing pegmatites [5]. The objective of the present work is to show how remote sensing data acquired at the different scales will be integrated within the LIGHTS project by showing some preliminary results.

2. STUDY AREA

The study area is the Bajoca mine of the Fregeneda-Almendra (Spain, Portugal) pegmatite field, located within the Iberian Massif, more precisely in the Central Iberian Zone. The mine

© 2020 IEEE. Reprinted, with permission, from Cardoso- Fernandes, J., Teodoro, A.C., Lima, A., Mielke, C., Körting, F., Roda- Robles, E., & Cauzid, J. (2020, 26 Sept.- 2 Oct. 2020). *Multi-scale approach using remote sensing techniques for lithium pegmatite exploration: first results*. Paper presented at the IGARSS 2020- IEEE International Geoscience and Remote Sensing Symposium, Waikoloa, HI, USA, 5226- 5229. doi: 10.1109/IGARSS39084.2020.9323705.

is located 4 km East of Almendra, in the Vila Nova de Foz Côa Municipality, north of Portugal (Fig. 1).

The pegmatite field has different types of veins, with distinct mineralogical, morphological and structural characteristics, including four types of Li-bearing dikes [8, 9]: petalite-rich, spodumene-rich, lepidolite-spodumene-rich, lepidolite-rich pegmatites. Therefore, this pegmatite field has a high economic potential for Li [10].

In the Bajoca mining concession barren, lepidolite-rich and petalite-rich dikes outcrop [9]. All these dikes are emplaced in the pre-Ordovician metasediments of the schist-metagraywacke complex [11]. The dike with the highest economic interest is the petalite-rich one, which is currently being exploited for glass and ceramic industries. Its average thickness can reach 30 m [12].

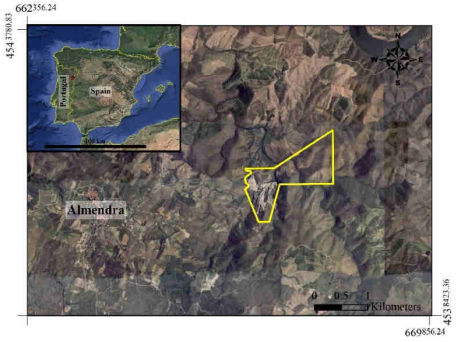

Fig. 1. Location of the Bajoca mining concession (yellow polygon). The map projection is Universal Transverse Mercator zone 29 N, WGS84 datum.

3. METHODOLOGY

This study encompasses several innovative approaches to define the specific mineralogical and geochemical signatures of the Li-pegmatites at different scales, especially in the visible, near infrared (VNIR) and short-wave infrared (SWIR) domains. The multi-source remote sensing data will allow detecting the Li-pegmatite signatures from the district to target scales. Mapping at a district scale will be achieved through satellite images. Cross-referencing satellite data and geological information will allow to select target areas. The gap between the satellite and field data will be overcome through drone-borne hyperspectral surveys at the target scale, with pixels sizes ranging from centimeters to decimeters. This step is fundamental since Li-pegmatites present limited lateral extension in this area. Drone-borne data will be preprocessed and classified into mineral anomaly maps. Moreover, handheld spectroscopy and *in situ* hyperspectral scans of the open-pit mine will provide a strong calibration source and ground-check of the satellite- and drone-sensed data, with information acquired at the mineral grain scale.

3.1. Satellite

Classical remote sensing techniques, namely RGB (red, green, blue) combinations, band rationing and principal component analysis (PCA) were employed to several satellite products with different spatial and spectral resolutions, as in ASTER, Landsat 5, Landsat 8 and Sentinel-2 [5]. The methods were proposed considering the laboratory spectra of Li-minerals. PCA was also applied in subsets of four and two-bands to reduce noise influence.

3.2. Drone measurements

Data takes are carried out by the HySpex Mjolnir S-620 camera, which is mounted on an octocopter system. The data may be preprocessed by PARGE [13] and ATCOR-4 [14]. The resulting reflectance data covers the spectral region from 1000 nm up until 2500 nm.

3.3. Hyperspectral scanning

Hyperspectral scans of the mine walls were acquired using the HySpex Mjolnir system from a rotation stage set up. A GFZ in-house reflectance retrieval is used to calculate at object (at outcrop) reflectance using reference plates distributed throughout the scene for reflectance retrieval.

Rock samples have been collected at different validation sites throughout the image scene for further geochemical analysis. At these sampling sites, in-situ handheld LIBS measurements (laser induced breakdown spectroscopy, via a the SciApsZ300, 180 – 906nm) and in-situ spectra were collected (via a handheld point spectrometer PSR+ 3500 in the spectral range of 350 – 2500nm).

4. RESULTS

This section presents some preliminary results from the multi-scale approaches applied to target Li-minerals.

4.1. Satellite

Several potential target areas were selected using the proposed methodology. Also, the acquisition of images before the opening of the Bajoca mine (Landsat 5, acquired in 1990) and during the exploitation process (Landsat 8, acquired in 2014) evidence changes in the detection of spectral signals. This means that, through the years, with an increasing exposition of the pegmatite area, the unique target signature of the Li-pegmatite can be sensed. Fig. 2 shows the clear spectral difference between PC4 of Landsat 5 (1, 2, 4, 6 band-subset) and PC4 of Landsat 8 (2, 3, 5, 11).

4.2. Hyperspectral drone and outcrop scanning

Results from the airborne Mjolnir acquisitions are currently under validation. An example scan of the Bajoca Mine and a classification of different rock types is shown in Fig. 3.

Fig. 3-a shows an image composite from the Mjolnir data. Fig. 3-b shows the result of a lithological classification, which has been achieved by building a site-specific spectral library from the rock samples that have been collected for further geochemical work. They have been grouped into four different spectral-geological classes according to their image spectrum from laboratory scans. Group A is based on 3 different samples with similar spectral fingerprints, Group B is based on 2 samples, Group C and D are based on 4 samples each. These spectra are further used as input for the classification result. If possible, the spectra groups were color-coded internally based on the Li content of the geochemical analyses based on ICP_ES/ ICP_MS analyses performed by the Bureau Veritas. Stronger colors indicate samples that showed a Li content above 500 ppm.

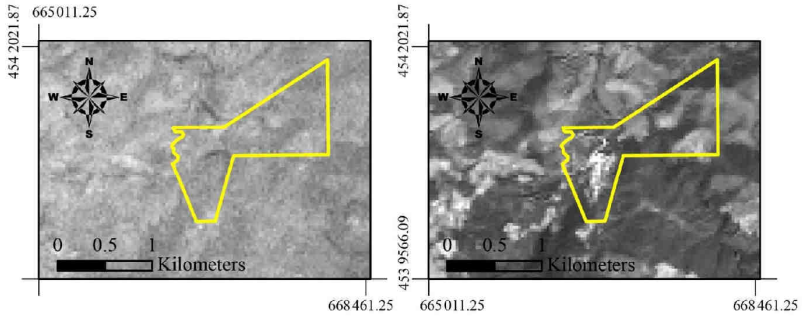

Fig. 2. Selective PCA on four-band subsets show the spectral differences caused by the Li-pegmatite before (left) and after (right) the opening of the Bajoca mine. Left: Landsat 5 image (1990). Right: Landsat 8 image (2014).

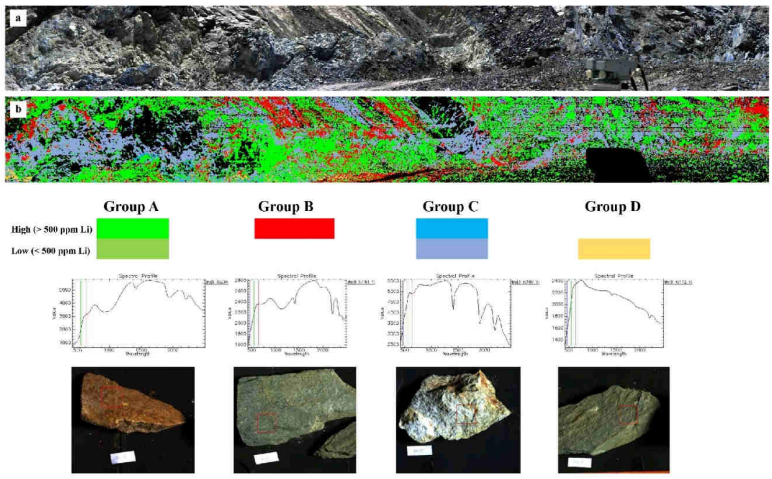

Fig. 3. Scan of the Bajoca Mine (May 2019), using HySpex Mjolnir S620. SWIR combination of 985nm, 1113nm and 1317nm for (RGB) (a). Classification (b) based on the collected samples shown below. Group A: Aplite-pegmatite with hematite crust. Group B: Schist from the contact with the pegmatite. Group C: Aplite-pegmatite. Group D: Schist.

5. DISCUSSION AND CONCLUSIONS

This study presents the first results obtained in the ambit of the LIGHTS project which aims at establishing a quick, cost-efficient system capable of targeting potential areas for Li-exploration. The novelty and relevance of the LIGHTS project reside in the unique multi-scale approach to target Li-pegmatite mineralizations from the district to target and mineral scales. Similar approaches are being conducted in other regions of the world, namely in South Africa.

Satellite data proved to be helpful in delineating regions of interest at a district scale. Multi-temporal image acquisition recognized the target signature of Li-pegmatites. Drone hyperspectral data allowed to sense information at the target scale. In the future, such drone flights will allow a quick check of the areas of interest recognized at the district scale using satellite data. Field validation is crucial to calibrate and ground-check the satellite- and airborne-data. Hyperspectral scans of the mine walls also played an important part in the data validation. In addition, these hyperspectral scans provided important information on the mineral grain scale. Not only did the scans allow to distinguish different lithological materials, but also to identify areas with the highest Li content. This ability can be particularly appealing to exploration and mining companies.

Nonetheless, LIGHTS is still an ongoing project and therefore more advances are expected in the future. The final goal of LIGHTS is to attain an automated analysis and a seamless integration of remote sensing and field data using machine learning algorithms. This analysis can be extended to various types of mineral deposits worldwide.

6. ACKNOWLEDGMENTS

The authors would like to thank the financial support provided by FCT with the ERA-MIN/0001/2017 – LIGHTS project and to ICT through the project COMPETE 2020 (UIDB/04683/2020), ref. POCI-01-0145-FEDER-007690. J. Cardoso-Fernandes is financially supported with a Ph.D. grant, ref. SFRH/BD/136108/2018, by national funds through FCT, and co-financed by the ESF through POCH.

7. REFERENCES

[1] J. Cardoso-Fernandes, A. C. Teodoro, A. Lima, M. Perrotta, and E. Roda-Robles, "Detecting Lithium (Li) Mineralizations from Space: Current Research and Future Perspectives," *Applied Sciences,* vol. 10, no. 5, p. 1785, 2020.

[2] D. Mendes, M. M. Perrotta, M. A. C. Costa, and V. J. C. Paes, "Mapeamento espectral para identificação de assinaturas espectrais de minerais de lítio em imagens ASTER (NE/MG)," in *Anais do XVIII Simpósio Brasileiro de Sensoriamento Remoto*, Santos, Brasil, 2017, pp. 5273-5280.

[3] M. M. Perrotta, C. R. Souza Filho, and C. A. S. Leite, "Mapeamento espectral de intrusões pegmatíticas relacionadas a mineralizações de lítio, gemas e minerais industriais na região do vale do Jequitinhonha (MG) a partir de imagens ASTER," in *Anais do XII Simpósio Brasileiro de Sensoriamento Remoto*, Goiânia, Brasil, 2005, pp. 1855-1862.

[4] J. Cardoso-Fernandes, A. C. Teodoro, and A. Lima, "Potential of Sentinel-2 data in the detection of lithium (Li)-bearing pegmatites: a study case," in *SPIE Remote Sensing*, 2018, vol. 10790, p. 15: SPIE, 2018.

[5] J. Cardoso-Fernandes, A. C. Teodoro, and A. Lima, "Remote sensing data in lithium (Li) exploration: A new approach for the detection of Li-bearing pegmatites,"*International Journal of Applied Earth Observation and Geoinformation,* vol. 76, pp. 10-25, 2019/04/01/ 2019.

[6] J. Cardoso-Fernandes, A. C. Teodoro, A. Lima, and E. Roda-Robles, "Evaluating the performance of support vector machines (SVMs) and random forest (RF) in Li-pegmatite mapping: preliminary results," in *SPIE Remote Sensing*, 2019, vol. 11156: SPIE.

[7] J. Cardoso-Fernandes, A. Lima, E. Roda-Robles, and A. C. Teodoro, "Constraints and potentials of remote sensing data/techniques applied to lithium (Li)-pegmatites," *The Canadian Mineralogist,* vol. 57, no. 5, pp. 723-725, 2019.

[8] E. Roda-Robles, A. Pesquera, F. Velasco, and F. Fontan, "The granitic pegmatites of the Fregeneda area (Salamanca, Spain): characteristics and petrogenesis," *Mineral. Mag.,* vol. 63, no. 4, pp. 535–558, 1999.

[9] R. Vieira, "Aplitopegmatitos com elementos raros da região entre Almendra (V.N. de Foz Côa) e Barca d'Alva (Figueira de Castelo Rodrigo). Campo aplitopegmatítico da Fregeneda- Almendra," PhD thesis, Faculdade de Ciências da Universidade do Porto, Porto, 2010.

[10] E. Roda-Robles *et al.*, "Geology and mineralogy of Li mineralization in the Central Iberian Zone (Spain and Portugal)," *Mineralogical Magazine,* vol. 80, no. 1, pp. 103-126, 2016.

[11] J. C. S. d. Costa, *Notícia sobre uma carta geológica do Buçaco, de Nery Delgado*. Lisboa: Serviços Geológicos de Portugal, 1950.

[12] E. Roda-Robles, R. Vieira, A. Pesquera, and A. Lima, "Chemical variations and significance of phosphates from the Fregeneda-Almendra pegmatite field, Central Iberian Zone (Spain and Portugal)," *Mineralogy and Petrology,* vol. 100, no. 1, pp. 23-34, 2010/09/01 2010.

[13] D. Schlaepfer, M. E. Schaepman, and K. I. Itten, "PARGE: parametric geocoding based on GCP-calibrated auxiliary data," in *SPIE's International Symposium on Optical Science, Engineering, and Instrumentation*, 1998, vol. 3438: SPIE.

[14] D. Schläpfer and R. Richter, "Recent Developments in ATCOR For Atmospheric Compensation and Radiometric Processing of Imaging Spectroscopy Data," in *EARSeL eProceedings*, 2016, vol. 14, no. 2, pp. 40-48.

Credits to the original publication:

PROCEEDINGS OF SPIE

SPIEDigitalLibrary.org/conference-proceedings-of-spie

Evaluating the performance of support vector machines (SVMs) and random forest (RF) in Li-pegmatite mapping: preliminary results

J. Cardoso-Fernandes, A. C. Teodoro, A. Lima, E. Roda-Robles

J. Cardoso-Fernandes, A. C. Teodoro, A. Lima, E. Roda-Robles, "Evaluating the performance of support vector machines (SVMs) and random forest (RF) in Li-pegmatite mapping: preliminary results," Proc. SPIE 11156, Earth Resources and Environmental Remote Sensing/GIS Applications X, 111560Q (3 October 2019); doi: 10.1117/12.2532577

SPIE.

Event: SPIE Remote Sensing, 2019, Strasbourg, France

Downloaded From: https://www.spiedigitallibrary.org/conference-proceedings-of-spie on 08 Oct 2019 Terms of Use: https://www.spiedigitallibrary.org/terms-of-use

Best Student Paper Award

Evaluating the performance of support vector machines (SVMs) and random forest (RF) in Li-pegmatite mapping: preliminary results

J. Cardoso-Fernandes*[a,b], A. C. Teodoro[a,b], A. Lima[a,b], E. Roda-Robles[c]

[a]Dep. of Geosciences, Environment and Land Planning, Faculty of Sciences, University of Porto, Rua Campo Alegre, Porto, Portugal; [b]ICT (Institute of Earth Sciences) – Porto pole (Portugal); [c]Departamento Mineralogía y Petrología, Univ. País Vasco (UPV/EHU), Bilbao, Spain

ABSTRACT

Machine learning algorithms (MLAs) have gained great importance in remote sensing-based applications, and also in mineral prospectivity mapping. Studies show that MLAs can outperform classical classification techniques. So, MLAs can be useful in the exploration of strategical raw materials like lithium (Li), which is used in consumer electronics and in the green-power industry. The study area of this work is the Fregeneda-Almendra region (between Spain and Portugal), where Li occurs in pegmatites. However, their smaller exposition can be regarded as a problem to the application of remote sensing methods. To overcome this, Support Vector Machine (SVM) and Random Forest (RF) algorithms were applied to. This study aims at: (i) comparing the performance accuracy in lithological mapping achieved by SVM and by RF; (ii) evaluating the sensitivity of both classifiers to class imbalance and; (iii) compare the results achieved with previously obtained results. For these, the same Level 1-C Sentinel-2 images (October 2017) were used. SVM showed slightly better accuracy, but RF was able to correctly classify a larger number of mapped Li-bearing pegmatites. The performance of the models was not equal for all classes, having all underperformed in some classes. Also, RF was affected by class imbalanced, while SVM prove to be more insensitive. The potential of this kind of approach in Li-exploration was confirmed since both algorithms correctly identified the presence of Li-bearing pegmatites in the three open-pit mines where they outcrop as well in areas where Li-pegmatites were mapped. Also, some of the areas classified as Li-bearing pegmatites are corroborated by the interest areas delimited in previous studies.

Keywords: Machine learning, Support Vector Machine (SVM), Random Forest (RF), Remote Sensing, Image Classification, Lithium (Li), Pegmatites

1. INTRODUCTION

In geology, mineral exploration is a multidisciplinary task whose purpose is to discover new mineral deposits through the integration of several datasets [1, 2]. The correct definition of target areas with economic potential in the early stages of exploration can lead to a significant decrease in the cost of the exploration campaigns, especially when low-cost methods with high ground-coverage such as remote sensing are applied.

Traditional remote sensing methods applied in geological exploration include RGB (red, green, blue) combinations (e.g. [3, 4]), band ratios (e.g. [3, 5]), principal component analysis (PCA) (e.g. [6-8]), minimum noise fraction (MNF) (e.g. [3, 4, 9]), matched-filtering (MF) (e.g. [3]), constrained energy minimization (CEM) (e.g. [9]), and classification algorithms since lithological mapping is, in a remote sensing perspective, a classification problem. Image classification can be defined as an image processing technique that automatically assigns pixels into classes based on similar spectral properties [5]. Image classification algorithms can be supervised or unsupervised whether or not the user specifies the classes and their respective representative pixels (training pixels). The main issue with unsupervised classification is that the target classes may have subtle spectral differences and the resultant classification may not be of interest. In lithological classification, common supervised algorithms are the spectral angle mapper (SAM) (e.g. [10]), mixture-tuned matched-filtering (MTNF) (e.g. [11]) and the maximum likelihood (ML) (e.g. [12]).

*joana.fernandes@fc.up.pt

Earth Resources and Environmental Remote Sensing/GIS Applications X, edited by Karsten Schulz, Ulrich Michel, Konstantinos G. Nikolakopoulos, Proc. of SPIE Vol. 11156, 111560Q
© 2019 SPIE · CCC code: 0277-786X/19/$21 · doi: 10.1117/12.2532577

Downloaded From: https://www.spiedigitallibrary.org/conference-proceedings-of-spie on 08 Oct 2019
Terms of Use: https://www.spiedigitallibrary.org/terms-of-use

In the last decades, non-parametric methods, such as machine learning algorithms (MLAs), not only have gained great importance in remote sensing-based applications (e.g. [13-16]), but also in the geological area (e.g. [12, 17]), especially in mineral exploration (e.g. [1, 2]). Several studies show that MLAs can outperform classical techniques either in satellite-based lithological mapping or in prospectivity mapping (e.g. [12, 18]). It becomes clear that it is necessary to apply MLAs in the geological exploration of strategical raw materials like lithium (Li), which is mainly used in consumer electronics and in the green-power industry.

1.1 Study area

The study area of the present work is the Fregeneda-Almendra (Salamanca, Spain - Vila Nova de Foz Côa, Portugal) region (Figure 1), where Li mineralization occurs in dyke-like rocks called pegmatites. These pegmatites present differences in their mineralogy, morphology and internal structure and were divided into several different types of dykes based in these characteristics [19-21]. The dykes intruded a pre-Ordovician E-W metasedimentary belt located to the north of the syn-Variscan Mêda-Penedono-Lumbrales granitic complex. Four types of pegmatites with Li bearing minerals were described: petalite-bearing, spodumene-bearing, lepidolite+spodumene-bearing, and lepidolite-bearing. All Li-pegmatites belong to the LCT (lithium, cesium, tantalum) family, REE-Li subclass and Complex type of the Černý & Ercit [22] classification [21]. The dykes have a zoned spatial distribution with the barren dykes outcropping closest to the granites, emplaced in the tectonic foliation from the third Variscan deformation phase (WNW-ESE general trend), while the Li-rich pegmatites are discordant and emplaced along the regional fracture system N-S to N30° E [21]. However, these Li-pegmatites have a much smaller exposition when compared to the other outcropping lithologies (metasediments and granitoid rocks) contributing to class imbalance.

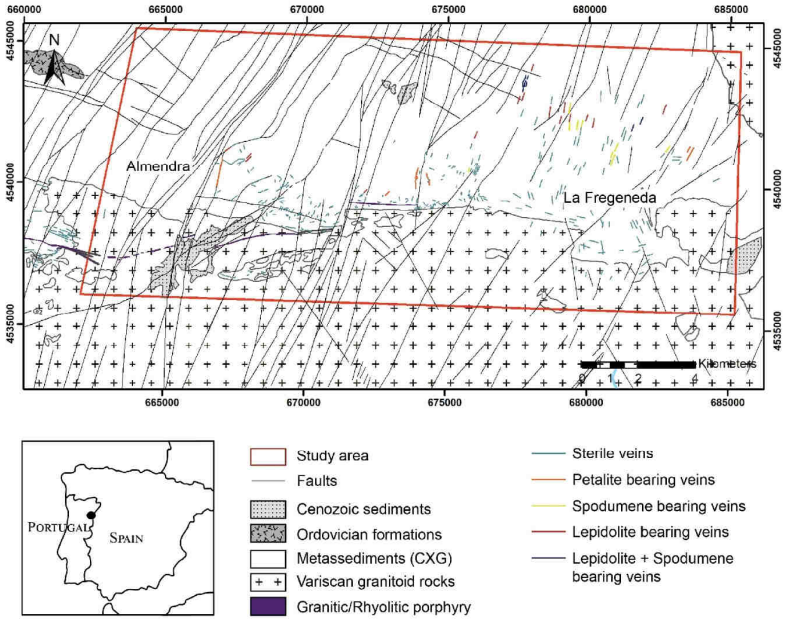

Figure 1. Location and geology of the study area with the different aplite-pegmatite dykes mapped (adapted from [21, 23, 24]). Map projection: Universal Transverse Mercator zone 29N, WGS84 datum.

1.2 Previous work

Recently, Cardoso-Fernandes et al. [25] classified a Sentinel-2 image covering the study area considered in this work using a parametric image classification method: the Maximum Likelihood (ML) algorithm. Although ML performed

Downloaded From: https://www.spiedigitallibrary.org/conference-proceedings-of-spie on 08 Oct 2019
Terms of Use: https://www.spiedigitallibrary.org/terms-of-use

relatively well for the major lithoclasses, it produced a considerable number of false positives while classifying the small class represented by Li-pegmatites. The solution to improve the classification results can be the application of MLA: for example, support vector machines (SVMs) and ensemble methods like random forest (RF) which are less sensitive to the training size [26, 27] and have more ability in dealing with unbalanced data [13]. Additionally, other remote sensing algorithms such as RGB combinations, band ratios, and PCA were also applied to this area [28].

1.3 Data used

In this study, the same Level 1-C cloud-free Sentinel-2 images processed in the previous works [25, 28] were used. The satellite image covering the study area was acquired on 27/10/2017 (tile number T29TPF) and its map projection is Universal Transverse Mercator zone 29 N, WGS84 datum. The bands were previously pre-processed using the Semi-Automatic Classification Plugin (SCP) developed by Congedo [29]. Details about the pre-processing can be found in [25].

Sentinel-2 Multispectral Instrument (MSI) has 13 spectral bands from the visible-near infrared (VNIR) to the short-wave infrared (SWIR): four bands at 10 m, six bands at 20 m and three bands at 60 m spatial resolution [30, 31]. Only the most adequate bands for geological applications were used for the image classification process: band 2 – blue (10 m), band 3 – green (10 m), band 4 – red (10 m), band 8 – NIR (10 m), bands 11 and 12 – SWIR (20 m) [30, 31].

2. METHODOLOGY

2.1 Support vector machine (SVM)

SVM is a supervised learning technique to solve regression and classification problems, based statistic learning theory [32]. SVM acts by finding an optimal hyperplane separating two classes and maximizing the distance between them. This distance is the so-called margin that is delimited by two hyperplanes parallel to the optimal hyperplane – the bounding hyperplanes. The support vectors are the training samples that lie on these bounding hyperplanes. Usually, the hyperplane is found using a subset of the data – the training set –, and the hyperplane's power to generalize is evaluated in another set of data – the testing set [16].

In a classification problem, a support vector classifier is used (SVC). When the two classes are clearly separable, a hard-margin hyperplane can be used. However, in most of the cases, data is not entirely separable so, a soft-margin allowing some outliers is the best strategy. For each outlier, a penalty C for the misclassification error is attributed. SVC is inherently a two-class classifier, but it can be employed for multiclass classification if the 'one-against-all' or 'one-against-one' are used [12, 26]. In addition to linear classification, SVC can be applied in non-linear classification by transforming the input space into a higher dimension using a mathematical kernel function, in order that the training samples become separable by a linear hyperplane (the "kernel trick"). Besides the linear kernel, other non-linear kernels are: the polynomial kernel and the gaussian kernel also called radial basis function (RBF). For the linear kernel, only the hyperparameter C needs to be tuned. When employing the polynomial kernel, besides the C parameter, the degree of the polynomial function d also needs to be optimized. A parameter r, controlling the effect of the polynomial degree on the model, can also be adjusted. For the RBF kernel, it is necessary to optimize the C hyperparameter as well as the gamma (γ) hyperparameter that controls the width of the kernel.

2.2 Random forest (RF)

RF is an ensemble learning method that combines a large number of randomized decision trees in order to avoid overfitting [33]. To make a prediction using this method, the prediction of all individual trees in the ensemble is taken into account: (i) if a hard-voting strategy is used, the final predicted class will be determined by the majority votes; (ii) if a soft-voting strategy is used instead, then the probabilistic prediction of all trees is averaged and the final predicted class is the one with the highest probability [34]. On the other hand, to ensure the randomness and avoid the correlation between trees, each tree is grown with a different training data subset generated through the bootstrap aggregation method or bagging [35], which allows to randomly resample the dataset with replacement. This means that for each predictor (i.e. tree) only about two-thirds of the samples are used for training, and the remaining one-third of the samples are the so-called out-of-bag (OOB) data [34]. The generalization accuracy can be then estimated either in a left-out set – the training set (similarly to the described for the SVM) – or on the OOB samples [36]. Another mechanism that ensures the randomness of the trees in the RF is to select a different subset of input features (bands in this case) to use in each node when determining the best split: the lower the number the features, the greater the difference between trees. So, when compared with SVMs, RF has fewer user-defined parameters to optimize, as it only requires two [13]: the number of trees in the ensemble and the number of features used in each node for splitting. The reduction of training data as well of the features contributes to a higher tree

Downloaded From: https://www.spiedigitallibrary.org/conference-proceedings-of-spie on 08 Oct 2019
Terms of Use: https://www.spiedigitallibrary.org/terms-of-use

diversity, that results in a slight increase in the bias of the RF usually compensated by the resultant decrease in variance, thus yielding an overall better model [34, 36]. Another advantage of RF is that also allows to evaluate the relative importance of each band, which can indicate which spectral contribution is crucial in Li-pegmatite identification.

Accordingly, the objectives of this study were: (i) a comparison between the performance accuracy in lithological mapping, especially in Li-pegmatite mapping, achieved by the best SVM model and by the best of RF model; (ii) evaluate the sensitivity to imbalanced dataset and to training data size of both classifiers and; (iii) compare the results of this work with previously obtained results.

2.3 Model selection and evaluation

In what concerns model selection, presently, most commercial software packages do not provide methods to automatically optimize the user-defined parameters associated with each MLA. Thus, in this work, parameter tuning and model evaluation was accomplished using the free open-source library *scikit-learn* [37] for Python programming language. Before building the respective models, 25% of all training samples were selected for testing, while the remaining 75% were used for training. The split of the data was made in a randomly stratified manner to ensure Li-bearing pegmatites samples were present in both sets. In the case of SVC, a two-staged grid-search with stratified 5-fold cross-validation (CV) was employed to choose the best kernel as well as the best parameters. For the linear kernel, it was observed that the CV accuracy tends to plateau when C is high enough (as recognized by [27]), but the grid-search always returns the highest C in the tested parameter range. For the RF, only one-stage grid-search with stratified 5-fold CV was enough to find the optimal parameters since the ranges applied in the search (number of tress = 10, 50, 100, 150, 200, 250; number of features = 1-6) were smaller when compared to SVM (C and $\gamma = 2^{-2}, 2^{-1}, 2^{0}, 2^{1}, 2^{2}, 2^{3}, 2^{4}, 2^{5}, 2^{6}, 2^{7}$).

Since one of the objectives of this study was also to compare the effect of data imbalance in each classifier, the previously mentioned grid-searches were repeated but this time using a built-in class-weight parameter in both algorithms to account for class imbalance. The class-weight was set automatically as the inverse of each class frequency.

The metric score employed for model evaluation and to choose the best model was the CV accuracy. Overall accuracy (OA), producer's and user's accuracy (PA and UA, respectively), and Kappa statistics were also computed to evaluate the classification result.

3. RESULTS AND DISCUSSION

Before model selection, class separability quantitative studies were made using the Transformed Divergence (TD) matrix in order to evaluate the quality of the training data (Table 1). All the classes present a good separability (>1.7) with exception of the pair Metasediments–Li-bearing pegmatite that presents a lower value, which may reflect the difficulty to isolate Li-pegmatites in one pixel since Sentinel-2's pixel size is bigger than the average pegmatite thickness (3 to 30 m [19-21].

Table 1. TD separability measure for each pair of classes identified in this work.

	Ga	Ms	QD	LiP	BA	VA	Bu	AF
Ms	2.000							
QD	2.000	2.000						
LiP	2.000	1.654	2.000					
BA	2.000	2.000	2.000	2.000				
VA	2.000	2.000	2.000	2.000	2.000			
Bu	2.000	1.999	2.000	2.000	2.000	2.000		
AF	1.882	1.999	2.000	2.000	2.000	2.000	2.000	
Wt	2.000	2.000	2.000	2.000	2.000	2.000	2.000	2.000

Ga – Granite; Ms – Metasediments; QD – Quaternary deposits; LiP – Li-bearing pegmatites; BA – Burned areas; VA – Vegetated areas; Bu – Built-up; AF – Agricultural fields; Wt – Water

Downloaded From: https://www.spiedigitallibrary.org/conference-proceedings-of-spie on 08 Oct 2019
Terms of Use: https://www.spiedigitallibrary.org/terms-of-use

The classification results obtained with each algorithm using imbalanced data are compared in Table 2. The RF classifier returns an OA slightly smaller (97.28%) than the one attained by SVM (98.33%). The same happens for the kappa statistics, although both results are equally high (0.97 and 0.98).

Table 2. Classification accuracies for the SVM and RF algorithms for the imbalanced dataset (producer's and user's accuracy: PA and UA, respectively).

	SVM		RF	
Class	**PA (%)**	**UA (%)**	**PA (%)**	**UA (%)**
Agricultural fields	97.50	97.50	95.63	96.23
Built-up	94.79	97.85	93.75	95.74
Burned areas	100.00	100.00	100.00	100.00
Fluvial deposits	100.00	96.97	100.00	100.00
Granite	98.98	95.10	95.92	90.38
Li-bearing pegmatite	70.00	100.00	60.00	100.00
Metasediments	95.65	94.29	92.75	92.75
Vegetated areas	100.00	100.00	100.00	98.90
Water	100.00	100.00	100.00	100.00
Overall accuracy [%]	98.33		97.28	
Kappa hat classification	0.98		0.97	

Observing the classification results at a class level, we can conclude that most of the samples in the test set were not misclassified due to the high PA achieved. The main exception concerns the Li-bearing pegmatite class which achieved the lowest PA, having SVM outperformed the RF with respectively 70% and 60% of PA. The two algorithms were also compared using the models built with the class weight option. The classification accuracies obtained are listed in Table 3.

Table 3. Classification accuracies for the SVM and RF algorithms using the class weight option to balance the data (producer's and user's accuracy: PA and UA, respectively).

	SVM		RF	
Class	**PA (%)**	**UA (%)**	**PA (%)**	**UA (%)**
Agricultural fields	97.50	98.11	96.88	97.48
Built-up	92.71	100.00	93.75	96.77
Burned areas	100.00	100.00	100.00	100.00
Fluvial deposits	100.00	100.00	100.00	100.00
Granite	100.00	95.15	96.94	92.23
Li-bearing pegmatite	90.00	90.00	70.00	100.00
Metasediments	97.10	93.06	92.75	92.75
Vegetated areas	100.00	100.00	100.00	97.83
Water	100.00	100.00	100.00	100.00
Overall accuracy [%]	98.54		97.70	
Kappa hat classification	0.98		0.97	

Downloaded From: https://www.spiedigitallibrary.org/conference-proceedings-of-spie on 08 Oct 2019
Terms of Use: https://www.spiedigitallibrary.org/terms-of-use

The results were quite similar, with SVM outperforming RF, especially in the Li-bearing pegmatite class. The OA increased very slightly with the class weight option, although the kappa statistics remained the same. PA for the Li-bearing pegmatite class increase with class balancing, especially for the SVM model. In contrast, UA decreased for this class with SVM, since a sample from the metasediments class was misclassified as Li-bearing pegmatite. It is also noteworthy that the burned areas, fluvial deposits, water and vegetation classes achieved the maximum value of PA and UA with at least one of the two classifiers. The final classification maps obtained with SVM and RF are presented in Figure 2 and in Figure 3, respectively.

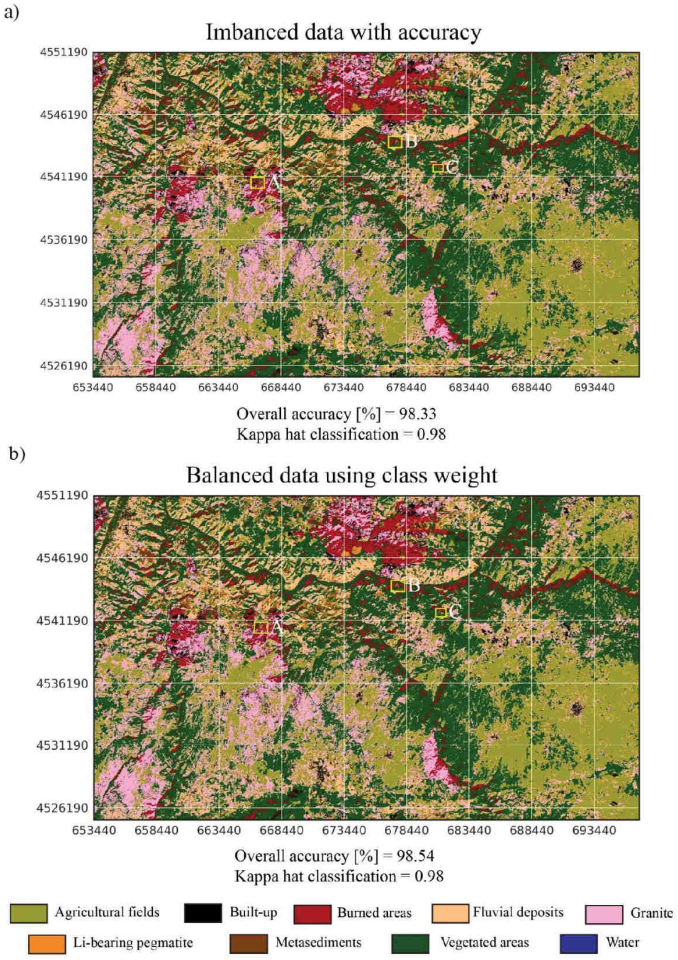

Figure 2. Final classification maps using SVM with the imbalanced (a) and balanced data (b). Three open-pit mines currently exploiting Li-minerals are identified: A – Bajoca, B – Feli, C – Alberto.

Downloaded From: https://www.spiedigitallibrary.org/conference-proceedings-of-spie on 08 Oct 2019
Terms of Use: https://www.spiedigitallibrary.org/terms-of-use

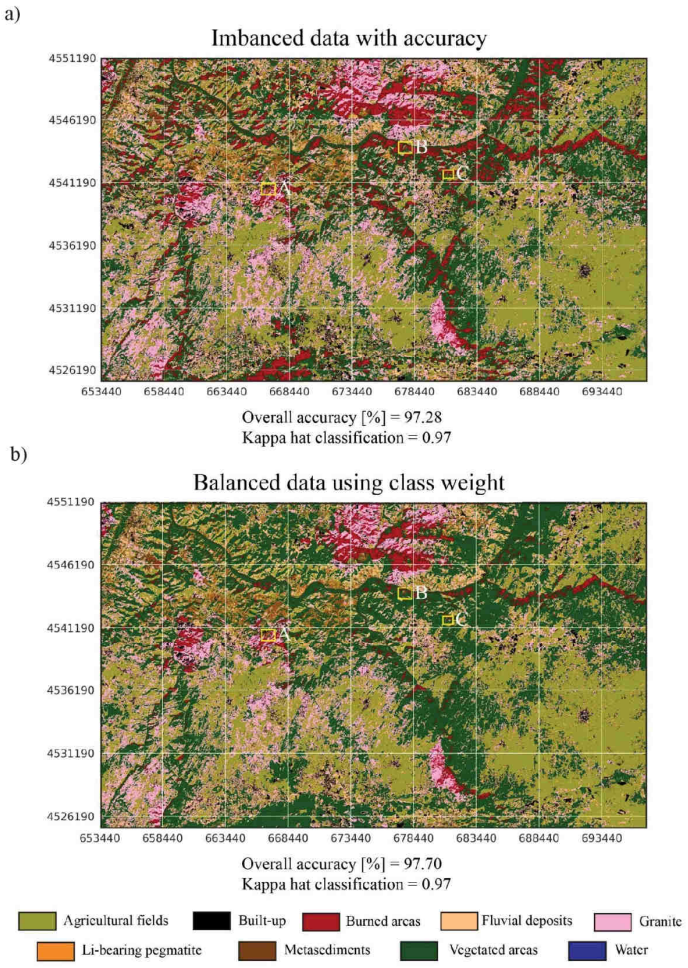

Figure 3. Final classification maps using RF with the imbalanced (a) and balanced data (b). Three open-pit mines currently exploiting Li-minerals are identified: A – Bajoca, B – Feli, C – Alberto.

As it can be seen in the classification maps presented in Figure 2 and Figure 3, the performance of the MLAs is not equal for all classes: while the areas mapped as granite or agricultural fields seem acceptable, both algorithms were incapable of correctly classify any of the water bodies. In fact, most of the rivers were classified as vegetated areas. Also, both SVM and RF showed some difficulties in mapping all the areas where metasedimentary rocks outcrop, as well as all the areas affected by wildfires since some relatively large burned areas, were partially or entirely classified as granites. More local misclassifications, common to the four models, include: (i) burned areas recognized as built-up; (ii) vegetated areas and metasediments that were classified as granitic rocks; (iii) agricultural fields classified as granite or fluvial deposits, mainly

Downloaded From: https://www.spiedigitallibrary.org/conference-proceedings-of-spie on 08 Oct 2019
Terms of Use: https://www.spiedigitallibrary.org/terms-of-use

in the south part of the images; (iv) vegetation identified as burned areas, especially in regions with a higher slope (near the rivers). Taking into account the performance of the models for the burned and vegetated areas, the fluvial deposits and the water classes (Figure 2 and Figure 3) as well as the respective PA and UA achieved, it is possible to conclude that the models fit very well the training data but have problems classifying the rest of the image, i.e., the models may be overfitting the mentioned classes.

When comparing the differences between the two models, SVM (Figure 2) clearly underperformed in the classification of fluvial deposits since this class, with small representativeness in the geological map, occupies a considerable portion of the images, mainly due to spectral confusion with metasediments and agricultural fields. Comparing Figure 2-a and Figure 3-a, the RF model built with the imbalanced dataset presents more difficulties on correctly classifying vegetated areas. The misclassification of vegetation as burned areas corresponds to some of the areas highlighted by the Burned Area Index (BAI) in a previous study [28], but not to the areas highlighted using the Normalized Burn Ratio (NBR). Considering that the NBR is not affected by topographic effects, we can conclude that topography has a large influence on the classification results obtained in the present work. The RF model also maps larger areas as Li-bearing pegmatites reflecting more spectral confusion between metasediments and the Li-class. Oppositely, RF better discriminates the metasediments and urban areas (even recognizing some main paved streets) and performs better in the fluvial deposits class, showing fewer overestimation, although there are more vegetated areas classified as granites instead.

The performance between balanced and imbalanced models was compared. In general, the outputs of the two SVM models (Figure 2) were very similar to the exception of the Li-bearing class. Major differences were encountered in the RF models: the balanced RF model (Figure 3-b) classifies vegetated areas more accurately, and there are less vegetated areas misclassified as burned areas. However, it also maps incorrectly a larger area as fluvial deposits when compared to the imbalanced model (Figure 3-a). Concerning the Li-pegmatite class, balanced SVM (Figure 2-b) classified more pixels as Li-pegmatites while balanced RF (Figure 3-b) identified Li-bearing areas in different spots not classified as such using imbalanced data (Figure 3-a). Opposing the balanced models of the two algorithms, balanced SVM (Figure 2-b) performs worst on the fluvial deposits class and balanced RF (Figure 3-b) performs better in the agricultural fields, vegetated areas, and especially in the metasediments and Li-bearing classes, identifying much less Li-pegmatite false positives.

Nonetheless, the objective of this work is not to obtain an accurate land cover/geological map but to identify and map the Li-bearing pegmatites. With that in mind, close-up images of interest areas (Figure 4) show that all four models correctly identified the presence of Li-bearing pegmatites in the three open-pit mines, where these dyke types are being exploited: the Bajoca, Feli and Alberto mines. Considering Figure 4, we can see that RF maps less pixels as Li-bearing areas in the Bajoca and Feli mines when compared to SVM.

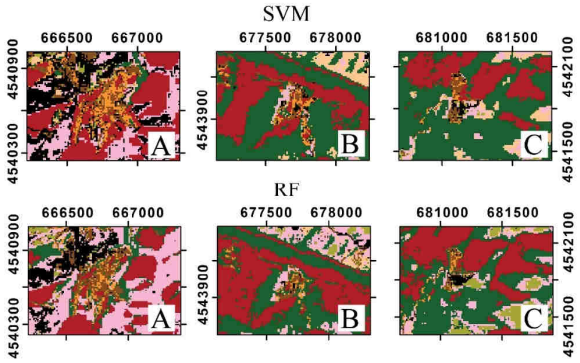

Figure 4. Close-up view of the Bajoca (A), Feli (B) and Alberto (C) mines in the imbalanced data classification maps of Figure 2-a and Figure 3-a.

Some of the remaining areas identified as Li-bearing pegmatite in all models coincide with the interest areas delimited in previous studies using other methods [25, 28]; some spots coincide with barren pegmatites or Li-pegmatites mapped; other areas do not coincide with either the mapped pegmatites or the identified regions of interest. Overall, the balanced RF model was the one that could recognize a larger number of mapped Li-bearing pegmatites.

Downloaded From: https://www.spiedigitallibrary.org/conference-proceedings-of-spie on 08 Oct 2019
Terms of Use: https://www.spiedigitallibrary.org/terms-of-use

On the other hand, for the SVM algorithm, the application of a balancing strategy only resulted in increased accuracy for the Li-pegmatite class in the test set, and not improved the results of the final classification. Thus, it is possible to conclude that SVM performance was not affected by class imbalance. Inversely, the results obtained with the RF algorithm improved very much when a class weight was applied, in particular for the Li-pegmatite class.

Despite these good results, many false positives can be identified in all models, even though balanced SVM presents more than the others. The identification of false positives is mainly due to spectral confusion with the metasedimentary rocks. This constitutes a problem aggravated by a large number of mixed pixels. In previous works, Cardoso-Fernandes et al. [28] documented the importance of the thermal band in the discrimination of Li-pegmatites from the metasedimentary in RGB combinations. So, the strategy to fully separate these two classes might be the use of the thermal band. Since Sentinel-2 does not acquire data in this region of the electromagnetic spectrum, MLAs should be employed in other types of remote sensing data. Furthermore, increasing class separability in general, and between metasediments and Li-pegmatites in particular, may only be achieved with data with a better spatial resolution.

In what concerns the previously mentioned underperformance of the models, improvement of the quality of training samples is required to refine the classification results. Other strategies like reducing the size of the classified image in order to reach a ratio of training pixels/total image pixels of 1:4, as mentioned by Noi and Kappas [13], may also be considered to attain better results. Another approach could be reducing the number of classes, which can be accomplished by: (i) deleting the class of fluvial deposits or merging it with the metasediments; (ii) creating and applying masks for the vegetation and water bodies, thus eliminating the need to classify these areas and reducing misclassification errors.

Regardless of the limitations and weakness found, the obtained results can still be of great importance for mineral exploration. In a land cover classification problem both false positives and false negatives need to be avoided and all classes bear the same importance. In a geological exploration, and in this particular case, the Li-bearing pegmatite class is the most important one, and misclassifications affecting other classes have little importance. Besides, false positives (i.e. over-estimating the Li-pegmatite class) may not constitute a problem while false negatives (i.e. not identifying pixels that correspond in fact to Li-pegmatites on the ground) are serious and should be avoided.

Finally, the relative importance of each band determined by the RF algorithm for both balanced and imbalanced data is presented in Table 4. As it can be seen, when a class weight option is used to account for class imbalance, band 3 (green) and 4 (red) are less important, and band 2 (blue) becomes more relevant. In both datasets, the SWIR bands (11 and 12) are determinant for class separability, which is not surprising since minerals have importance absorption features in this region of the electromagnetic spectrum.

Table 4. Relative importance of each Sentinel-2 band (%) assessed by the RF algorithm.

	Imbalanced dataset	**Balanced dataset**
Band 2	10.71	22.65
Band 3	13.83	5.96
Band 4	10.79	8.00
Band 8	15.97	16.34
Band 11	27.52	24.62
Band 12	21.18	22.44

4. CONCLUSIONS

In this study, a first attempt to map Li-bearing pegmatites using machine learning algorithms was made. The objective of this study to compare the performance accuracy of SVM and RF in lithological mapping, especially in Li-pegmatite mapping, as well as to evaluate each classifiers' sensitivity to imbalanced data while comparing with previously obtained results. To achieve that goal, Sentinel-2A images covering the study area were used. SVM showed slightly better accuracy in the test set but the best performance in Li-mapping was achieved by the balanced RF because it correctly classified a larger number of mapped Li-bearing pegmatites. Overall, the results obtained confirm the potential of this kind of approach in Li-exploration since both algorithms correctly identified the presence of Li-bearing pegmatites in the three open-pit

Downloaded From: https://www.spiedigitallibrary.org/conference-proceedings-of-spie on 08 Oct 2019
Terms of Use: https://www.spiedigitallibrary.org/terms-of-use

mines where Li-minerals outcrop as well as in areas Li-pegmatites have been mapped. Some of the spots classified as Li-bearing pegmatites also coincide with barren pegmatites or with some of the interest areas delimited in previous studies using other methods. Nonetheless, the image classification needs to be improved through the acquisition of mineral spectra and it is necessary to validate the results in the field. Also, the large number of Li-bearing pegmatite false positives found in the final classification maps demonstrates the difficulty to spectrally separate between metasedimentary rocks and Li-pegmatites. This can be overcome through the collection of new and better training samples. Previous works show that the use of a thermal band may also help the classification results.

In general, the performance of the models was not equal for all classes, having all underperformed in the classification of the water, burned areas, vegetation and metasediments classes. SVM also underperformed in fluvial deposits class. Taking into account the performance accuracy attained on the test set, we conclude that overfit may occur at class level, thus explaining the bad performance in the mentioned classes. So, reducing the size of the classified image and reducing the number of classes may also help improve the classification output.

The results were also relatively consistent between the SVM models, which points to the fact that class imbalance may have a neglectable effect in SVM performance. Oppositely, RF was affected by class imbalance and the results obtained were improved when a strategy to deal with data imbalanced was applied.

Regardless of the limitations found, the obtained results can still be a major contribute for Li mineral exploration since the occurrence of false positives is preferred to the occurrence of false negatives because the latter implies missing possible areas with high economic potential.

ACKNOWLEDGMENTS

The authors would like to thank the financial support provided by FCT– Fundação para a Ciência e a Tecnologia with the ERA-MIN/0001/2017 – LIGHTS project and to FEDER through the operation POCI-01- 0145-FEDER-007690 funded by the Programa Operacional Competitividade e Internacionalização – COMPETE2020 and by National Funds through FCT within ICT, R&D Unit (reference UID/GEO/04683/2013). J. Cardoso-Fernandes is financially supported by FCT within the compass of a Ph.D. Thesis, ref. SFRH/BD/136108/2018.

REFERENCES

[1] R. Zuo, and E. J. M. Carranza, "Support vector machine: A tool for mapping mineral prospectivity," Computers & Geosciences, 37(12), 1967-1975 (2011).
[2] M. Abedi, G.-H. Norouzi, and A. Bahroudi, "Support vector machine for multi-classification of mineral prospectivity areas," Computers & Geosciences, 46, 272-283 (2012).
[3] B. Mia, and Y. Fujimitsu, "Mapping hydrothermal altered mineral deposits using Landsat 7 ETM+ image in and around Kuju volcano, Kyushu, Japan," Journal of Earth System Science, 121(4), 1049-1057 (2012).
[4] A. Ali, and A. Pour, "Lithological mapping and hydrothermal alteration using Landsat 8 data: a case study in ariab mining district, red sea hills, Sudan," International Journal of Basic and Applied Sciences, 3(3), (2014).
[5] F. F. Sabins, "Remote sensing for mineral exploration," Ore Geology Reviews, 14(3), 157-183 (1999).
[6] W. P. Loughlin, "Component Analysis for Alteration Mapping," Photogram. Eng. Rem. Sens., 57, 1163-1169 (1991).
[7] A. P. Crósta, C. R. De Souza Filho, F. Azevedo, and C. Brodie, "Targeting key alteration minerals in epithermal deposits in Patagonia, Argentina, using ASTER imagery and principal component analysis," International Journal of Remote Sensing, 24(21), 4233-4240 (2003).
[8] A. Singh, and A. Harrison, "Standardized principal components," International Journal of Remote Sensing, 6(6), 883-896 (1985).
[9] S. Gabr, A. Ghulam, and T. Kusky, "Detecting areas of high-potential gold mineralization using ASTER data," Ore Geology Reviews, 38(1-2), 59-69 (2010).

Downloaded From: https://www.spiedigitallibrary.org/conference-proceedings-of-spie on 08 Oct 2019
Terms of Use: https://www.spiedigitallibrary.org/terms-of-use

[10] L. C. Rowan, J. C. Mars, and C. J. Simpson, "Lithologic mapping of the Mordor, NT, Australia ultramafic complex by using the Advanced Spaceborne Thermal Emission and Reflection Radiometer (ASTER)," Remote Sensing of Environment, 99(1), 105-126 (2005).
[11] A. B. Pour, and M. Hashim, "Hydrothermal alteration mapping from Landsat-8 data, Sar Cheshmeh copper mining district, south-eastern Islamic Republic of Iran," Journal of Taibah University for Science, 9(2), 155-166 (2015).
[12] L. Yu, A. Porwal, E.-J. Holden, and M. C. Dentith, "Towards automatic lithological classification from remote sensing data using support vector machines," Computers & Geosciences, 45, 229-239 (2012).
[13] P. T. Noi, and M. Kappas, "Comparison of Random Forest, k-Nearest Neighbor, and Support Vector Machine Classifiers for Land Cover Classification Using Sentinel-2 Imagery," Sensors (Basel), 18(1), (2017).
[14] P. A. Tavares, N. E. S. Beltrão, U. S. Guimarães, and A. C. Teodoro, "Integration of Sentinel-1 and Sentinel-2 for Classification and LULC Mapping in the Urban Area of Belém, Eastern Brazilian Amazon," Sensors, 19(5), 1140 (2019).
[15] M. Pal, and P. M. Mather, "Support vector machines for classification in remote sensing," International Journal of Remote Sensing, 26(5), 1007-1011 (2005).
[16] T. Oommen, D. Misra, N. K. C. Twarakavi, A. Prakash, B. Sahoo, and S. Bandopadhyay, "An Objective Analysis of Support Vector Machine Based Classification for Remote Sensing," Mathematical Geosciences, 40(4), 409-424 (2008).
[17] M. J. Cracknell, A. M. Reading, and A. W. McNeill, "Mapping geology and volcanic-hosted massive sulfide alteration in the Hellyer–Mt Charter region, Tasmania, using Random Forests™ and Self-Organising Maps," Australian Journal of Earth Sciences, 61(2), 287-304 (2014).
[18] H. Geranian, S. H. Tabatabaei, H. H. Asadi, and E. J. M. Carranza, "Application of Discriminant Analysis and Support Vector Machine in Mapping Gold Potential Areas for Further Drilling in the Sari-Gunay Gold Deposit, NW Iran," Natural Resources Research, 25(2), 145-159 (2016).
[19] E. Roda, [Distribución, Caracteristicas y Petrogenesis de las Pegmatitas de La Fregeneda (Salamanca)], PhD thesis, UPV, Bilbau, 199 (1993).
[20] E. Roda, A. Pesquera, F. Velasco, and F. Fontan, "The granitic pegmatites of the Fregeneda area (Salamanca, Spain): characteristics and petrogenesis," Mineral. Mag., 63(4), 535–558 (1999).
[21] R. Vieira, [Aplitopegmatitos com elementos raros da região entre Almendra (V.N. de Foz Côa) e Barca d'Alva (Figueira de Castelo Rodrigo). Campo aplitopegmatítico da Fregeneda- Almendra], PhD thesis, Faculdade de Ciências da Universidade do Porto, Porto, XXVI, 273 (2010).
[22] P. Černý, and T. S. Ercit, "Classification of granitic pegmatites revisited," Can. Mineral., 43, 2005–2026 (2005).
[23] A. F. Silva, A. J. Santos, A. Ribeiro, J. Cabral, and M. L. Ribeiro, [Carta Geológica de Portugal na escala 1/50.000 – folha 15-B – Freixo de Espada à Cinta] Serv. Geol. Portugal, (1990).
[24] A. F. Silva, A. J. Santos, A. Ribeiro, and M. L. Ribeiro, [Carta Geológica de Portugal na escala 1/50.000 – folha 15-A – Vila Nova de Foz Côa] Serv. Geol. Portugal (1990).
[25] J. Cardoso-Fernandes, A. Lima, and A. C. Teodoro, "Potential of Sentinel-2 data in the detection of lithium (Li)-bearing pegmatites: a study case." Proc. SPIE 10790, Earth Resources and Environmental Remote Sensing/GIS Applications IX 107900T (9 October 2018), 15 (2018).
[26] G. Mountrakis, J. Im, and C. Ogole, "Support vector machines in remote sensing: A review," ISPRS Journal of Photogrammetry and Remote Sensing, 66(3), 247-259 (2011).
[27] A. E. Maxwell, T. A. Warner, and F. Fang, "Implementation of machine-learning classification in remote sensing: an applied review," International Journal of Remote Sensing, 39(9), 2784-2817 (2018).
[28] J. Cardoso-Fernandes, A. C. Teodoro, and A. Lima, "Remote sensing data in lithium (Li) exploration: A new approach for the detection of Li-bearing pegmatites," International Journal of Applied Earth Observation and Geoinformation, 76, 10-25 (2019).
[29] L. Congedo, [Semi-Automatic Classification Plugin Documentation], (2016).
[30] European Space Agency (ESA), "User Guides: Sentinel-2 - Overview," < Available online: https://sentinel.esa.int/web/sentinel/user-guides/sentinel-2-msi/overview> (January 2018)
[31] European Space Agency (ESA), "Missions: Sentinel-2 - Overview," < Available online: https://sentinel.esa.int/web/sentinel/missions/sentinel-2/overview> (January 2018)
[32] V. N. Vapnik, [The Nature of Statistical Learning Theory] Springer-Verlag, New York (1995).
[33] L. Breiman, "Random Forests," Machine Learning, 45(1), 5-32 (2001).

Downloaded From: https://www.spiedigitallibrary.org/conference-proceedings-of-spie on 08 Oct 2019
Terms of Use: https://www.spiedigitallibrary.org/terms-of-use

[34] A. Géron, [Hands-On Machine Learning with Scikit-Learn and TensorFlow: Concepts, Tools, and Techniques to Build Intelligent Systems] O'Reilly Media, Inc., Sebastopol, CA, USA (2017).
[35] L. Breiman, "Bagging Predictors," Machine Learning, 24(2), 123-140 (1996).
[36] scikit-learn developers, "1.11. Ensemble methods — scikit-learn 0.21.2 documentation", 2019, <Available online: https://scikit-learn.org/stable/modules/ensemble.html#b2001> (July 2019)
[37] F. Pedregosa, G. Varoquaux, A. Gramfort, V. Michel, B. Thirion, O. Grisel, M. Blondel, P. Prettenhofer, R. Weiss, V. Dubourg, J. Vanderplas, A. Passos, D. Cournapeau, M. Brucher, M. Perrot, E. Duchesnay, and G. Louppe, "Scikit-learn: Machine Learning in Python," Journal of Machine Learning Research, 12, 2825-2830 (2012).

Downloaded From: https://www.spiedigitallibrary.org/conference-proceedings-of-spie on 08 Oct 2019
Terms of Use: https://www.spiedigitallibrary.org/terms-of-use

LITHIUM (LI) PEGMATITE MAPPING USING ARTIFICIAL NEURAL NETWORKS (ANNS): PRELIMINARY RESULTS

Joana Cardoso-Fernandes[1,2], Ana Cláudia Teodoro[1,2], Alexandre Lima[1,2], Encarnación Roda-Robles[3]

[1]Department of Geosciences, Environment and Land Planning, Faculty of Sciences, University of Porto, Porto, Portugal
[2]ICT (Institute of Earth Sciences) – Porto pole (Portugal)
[3]Departamento de Mineralogía y Petrología, Univ. País Vasco (UPV/EHU), Bilbao, Spain
joana.fernandes@fc.up.pt; amteodor@fc.up.pt; allima@fc.up.pt; encar.roda@ehu.es

ABSTRACT

Satellite-based mineral exploration will be increasingly relevant in the future to achieve more conscious exploration models. Therefore, new applications to high-demand mineral commodities such as lithium (Li) are emerging. Previous applications to the study area of Fregeneda (Spain) – Almendra (Portugal) showed a high number of false positives despite their ability to identify Li pegmatites. So, the objective of the present work is to improve the classification results using Artificial Neural Networks (ANNs). For that, the same Sentinel-2A images were used and a three-layer feedforward network was computed using the backpropagation method. The ANN created was able to identify all the open-pit mines exploiting Li pegmatites in the area. However, the high number of Li false positives persisted. Future applications may include Convolutional Neural Networks (CNNs) to improve these results.

Index Terms— Remote Sensing, deep learning, image classification, lithium, pegmatites

1. INTRODUCTION

Nowadays, social acceptance of mineral exploration is a big concern in Europe, because local populations fear for the security of their homes, animals, and crops. This fear results from a lack of knowledge about what is, in fact, mineral exploration, leading people to mistake it for mining activities. So, to obtain the confidence of local populations is now crucial for exploration companies to start exploration using less intrusive methods which are more and more sought-after.

Remote sensing represents one of the less intrusive exploration methods, especially when the sensors are satellite-born. Satellite images can be very helpful to target gold and porphyry-copper deposits (e.g. [1, 2]). However, it is necessary to apply remote sensing methods on new mineral deposit types so a more conscious, environmental-friendly exploration can be achieved.

One example of a new area of application is lithium (Li) exploration. Cardoso-Fernandes, et al. [3] proposed an approach to Li pegmatite identification in the Fregeneda-Almendra area using classical image processing techniques (RGB combination, band ratios, principal component analysis (PCA)). The same methodology was tested in Brazil proving its capability to discriminate Li pegmatites [4]. Building on this successful approach, new algorithms are being tested. The main achievements and weaknesses of the approaches made to Li exploration using remote sensing data were recently reviewed [5]. Cardoso-Fernandes, et al. [6] evaluated the performance of random forest (RF) and support vector machine (SVM) algorithms in Li pegmatite mapping in the Fregeneda-Almendra area. However, some difficulties were encountered, and the classification results showed a high number of false positives. So, the objective of this work is to improve the classification output using, for the first time, Artificial Neural Networks (ANNs) in Li identification. Different metrics were employed to access the results.

2. DATA AND METHODS

2.1. Study area

The study area corresponds to the Fregeneda (Spain) – Almendra (Portugal) aplite-pegmatite field (Fig. 1). The field, located in the Central Iberian Zone of the Iberian Massif, is delimitated by the Douro river at the north, and by the Vilariça's fault valley at east. Also, the Douro and Águeda rivers materialize the border between Portugal and Spain.

The aplite-pegmatite dikes intruded a pre-Ordovician E-W metasedimentary belt and can be divided into several types according to their internal structure, morphology and mineral assemblages [7, 8]. The dikes show an increasing fractionation degree away from the syn-tectonic granites that outcrop to the south, being the more evolved aplite-pegmatites rich in Li [7, 8]. Four types of Li-rich dikes were described (Fig. 1): petalite-bearing, spodumene-bearing, lepidolite+spodumene-bearing, and lepidolite-bearing.

© 2020 IEEE. Reprinted, with permission, from Cardoso-Fernandes, J., Teodoro, A. C., Lima, A., & Roda Robles, E. (2020, 26 Sept.-2 Oct. 2020). *Lithium (Li) pegmatite mapping using Artificial Neural Networks (ANNs): preliminary results.* Paper presented at the IGARSS 2020 - 2020 IEEE International Geoscience and Remote Sensing Symposium, Waikoloa, HI, USA, 557-560. doi: 10.1109/IGARSS39084.2020.9323852.

2.2. Data

Since the aim of this study is to compare the performance of ANN with a previous RF and SVM classification, the same Level 1-C cloud-free Sentinel-2 images were used [6]. The images acquired in 2017 are already pre-processed and atmospherically corrected [3].

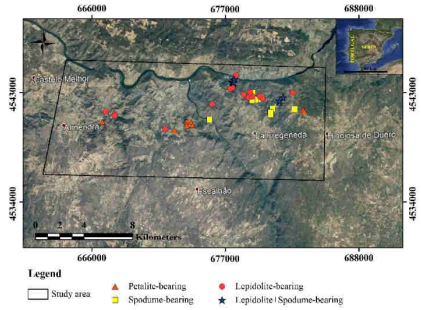

Fig. 1. Location of the study area. Lithium pegmatites are also marked. The map projection is Universal Transverse Mercator zone 29 N, WGS84 datum.

For comparison reasons, the same training areas and classes were used [6]: AF – Agricultural fields; Bu – Built-up; BA – Burned areas; FD – Fluvial deposits; Ga – Granite; LiP – Li pegmatites; Ms – Metasediments; VA – Vegetated areas; Wt – Water. Details on class separability measures as well as on the RF and SVM algorithms can be found in [6].

2.3. Methods

ANNs [9] were chosen for this work because their versatile and powerful nature is ideal to resolve highly complex tasks, frequently outperforming conventional classification techniques and even other machine learning algorithms [10-13]. The ANN corresponds to a large class of models and learning methods inspired in the human brain since they acquire knowledge through a learning process, storing the information in simple processing units (neurons or nodes) distributed in parallel consecutive layers [10, 14, 15]. These layers include an input and an output layer as well as one or more hidden layers between them. All nodes in the different layers are interconnected and the strength of the connections or links is usually called weights [15]. At the start, the weights have randomly assigned values that are iteratively adjusted during the learning process to achieve the desired output [14, 15]. Therefore, the connection weights that contribute to the correct prediction are reinforced [10]. Overall, an ANN corresponds to a nonlinear generalization of the linear model [14] since after computing the linear combiner output of the input signals (weighted by the connection weights), a non-linear function – the activation function – is applied [15]. In general, an external bias is also added to the model to control the net input of the activation function [15].

In this study, PCI Geomatica 2018 software was used to create and train the ANNs and to classify the image. The training dataset (comprising 3821 labeled samples) was randomly divided into training (75% of each class) and test (25% of each class) subsets. The classifier created corresponds to a multilayer feedforward network and the connection weights of the ANN were estimated using the back-propagation method [16]. The default activation function is the sigmoid function. The number of nodes in the input layer is equal to the number of bands (input features) that in this case are six: blue, green, red, near-infrared (NIR), and two short-wave infrared (SWIR) bands. Accordingly, the number of nodes in the output layer is determined by the number of previously defined classes, nine classes in this case. Just one hidden layer was used to create the model. One of the most important parameters in ANNs is the number of nodes in the hidden layer, so different literature-based recommendations were considered. Ultimately, the number of nodes was calculated as the number of pairwise separating hyperplanes over the number of classes [17].

Since the amount of training influences the ability of an ANN model to generalize [18], the network training was stopped when one of three cutoff limits imposed was reached: (i) a maximum normalized total error equal to 0.01; (ii) a maximum individual error of 0.001; (iii) a maximum number of epochs equal to 1000. In this study, training stopped after 1000 iterations.

In the post-classification analysis, overall accuracy (OA), producer's and user's accuracy (PA and UA, respectively), and Kappa statistics were computed to evaluate the network performance. These statistical techniques were based on the error matrix of the true versus the predicted classes of the test subset. The OA is calculated by dividing the sum of the correct classifications by the total number of pixels in the error matrix [19]. The PA indicates the probability of a training sample being correctly classified and the UA indicates the probability that a pixel classified as of belonging to a certain class actually belongs to that class on the ground [19, 20]. The Kappa statistic expresses the level of agreement between the classifier output and reference data [21].

3. RESULTS AND DISCUSSION

After training, the network reached a total normalized error of 0.075 and a maximum individual error of 1.797. The OA reached by ANN was 93% (Table 1). PA and UA for the LiP class are also showed in Table 1. The results are compared with the ones attained by SVM and RF [6].

In general, ANN showed the worst performance in comparison with SVM and RF. In what concerns the target class (LiP), although ANN presents a perfect PA, the UA is very small indicating low reliability and a high number of false positives.

Table 1. Performance metrics of ANN in comparison with SVM and RF.

Algorithm		OA (%)	kappa value	PA LiP (%)	UA LiP (%)
ANN		93.00	0.92	100.00	18.75
SVM*	Imbalanced	98.33	0.98	70.00	100.00
	Balanced	98.54	0.98	90.00	90.00
RF*	Imbalanced	97.28	0.97	60.00	100.00
	Balanced	97.70	0.97	70.00	100.00

* Classification results from Cardoso-Fernandes, et al. [6].

The classification results obtained after the application of the created ANN model is given in Fig. 2. As can be seen, some confusion between vegetated areas and burned areas near the rivers, and the misclassification of burned areas as granites also occurs, similar to SVM and RF [6].

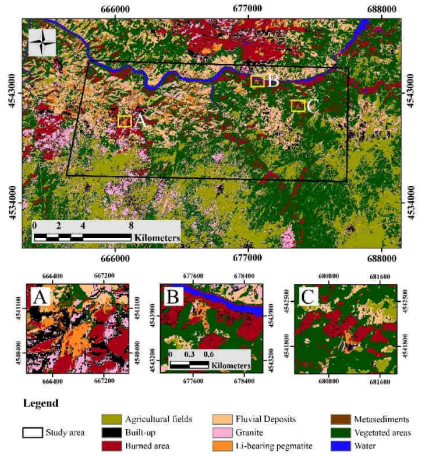

Fig. 2. ANN classification of the Sentinel-2 image. A, B and C represent open-pit mines were LiP occur. Zoom images at the same scale.

In what concerns the lithological units of the region, FD were once again overestimated, representing the largest classified lithology (Table 2) when in fact it is one of the units with fewer expression. Comparing the area of the image classified as lithological units by the three algorithms (Table 2), ANN was the one that classified fewer pixels as granites.

ANN was also the algorithm that classified more pixels as LiP instead of the Ms class, which explains the low UA reached for the LiP class. However, ANN was the algorithm with better performance in the classification of the three open-pit mines that exploit LiP (Fig. 2 – A, B, C). This suggests the potential of this kind of approach, which certainly needs to be improved to reduce false positives.

Table 2. Area of the image classified as a lithological unit in percentage (%).

Algorithm		FD	Ga	LiP	Ms
ANN		11.13	9.28	2.12	1.06
SVM*	Imbalanced	12.41	19.94	0.54	1.32
	Balanced	9.63	20.29	1.18	1.00
RF*	Imbalanced	4.42	24.94	0.80	1.84
	Balanced	6.96	19.51	1.03	1.96

* Classification results from Cardoso-Fernandes, et al. [6].

4. CONCLUSIONS

This study represents the first application of ANN to LiP exploration. The objective of the work was to reduce the number of false positives produced in the classification process in comparison with other machine learning techniques such as RF and SVM. For that, the same Sentinel-2 images and the same training areas were used.

Although ANN achieves an acceptable OA, the performance on the target class (LiP) produced even more false positives than the other two algorithms. Therefore, the main objective of this work could not be accomplished. Despite a large number of false positives, ANN allowed to correctly identify the three open-pit mines exploiting Li-minerals in the region. Therefore, we conclude that there is potential to identify LiPs using a similar approach, but future studies should be dedicated to spectrally discriminate LiP from the host rocks (metasediments). A better optimization of the training areas and classes could improve the results.

Other methodology improvements could also be made, namely different activation functions, number of hidden layers and other stopping mechanisms/parameters that can be tried. Future works will include an improved approach through the application of more powerful networks such as Convolutional Neural Networks (CNNs) that are very effective in learning complex features and in computer vision tasks like image classification [22]. Also, CNNs have the advantage of being less prone to overfitting than ANN.

5. ACKNOWLEDGMENTS

The authors would like to thank the financial support provided by FCT with the ERA-MIN/0001/2017 – LIGHTS project and to ICT through the project COMPETE 2020 (UIDB/04683/2020), ref. POCI-01-0145-FEDER-007690. Joana Cardoso-Fernandes is financially supported by a Ph.D. grant, ref. SFRH/BD/136108/2018, by national funds through FCT, and co-financed by the ESF through POCH.

6. REFERENCES

[1] S. Gabr, A. Ghulam, and T. Kusky, "Detecting areas of high-potential gold mineralization using ASTER data," *Ore Geology Reviews,* vol. 38, no. 1-2, pp. 59-69, 2010.

[2] M. Hosseinjani Zadeh, M. H. Tangestani, F. Velasco Roldan, and I. Yusta, "Mineral Exploration and Alteration Zone Mapping Using Mixture Tuned Matched Filtering Approach on ASTER Data at the Central Part of Dehaj-Sarduiyeh Copper Belt, SE Iran," *IEEE Journal of Selected Topics in Applied Earth Observations and Remote Sensing,* vol. 7, no. 1, pp. 284-289, 2014.

[3] J. Cardoso-Fernandes, A. C. Teodoro, and A. Lima, "Remote sensing data in lithium (Li) exploration: A new approach for the detection of Li-bearing pegmatites," *International Journal of Applied Earth Observation and Geoinformation,* vol. 76, pp. 10-25, 2019/04/01/2019.

[4] D. Santos, A. Teodoro, A. Lima, and J. Cardoso-Fernandes, "Remote sensing techniques to detect areas with potential for lithium exploration in Minas Gerais, Brazil," in *SPIE Remote Sensing*, 2019, vol. 11156: SPIE.

[5] J. Cardoso-Fernandes, A. C. Teodoro, A. Lima, M. Perrotta, and E. Roda-Robles, "Detecting Lithium (Li) Mineralizations from Space: Current Research and Future Perspectives," *Applied Sciences,* vol. 10, no. 5, p. 1785, 2020.

[6] J. Cardoso-Fernandes, A. C. Teodoro, A. Lima, and E. Roda-Robles, "Evaluating the performance of support vector machines (SVMs) and random forest (RF) in Li-pegmatite mapping: preliminary results," in *SPIE Remote Sensing*, 2019, vol. 11156: SPIE.

[7] E. Roda-Robles, A. Pesquera, F. Velasco, and F. Fontan, "The granitic pegmatites of the Fregeneda area (Salamanca, Spain): characteristics and petrogenesis," *Mineral. Mag.,* vol. 63, no. 4, pp. 535–558, 1999.

[8] R. Vieira, "Aplitopegmatitos com elementos raros da região entre Almendra (V.N. de Foz Côa) e Barca d'Alva (Figueira de Castelo Rodrigo). Campo aplitopegmatítico da Fregeneda- Almendra," PhD thesis, Faculdade de Ciências da Universidade do Porto, Porto, 2010.

[9] W. S. McCulloch and W. Pitts, "A logical calculus of the ideas immanent in nervous activity," *The bulletin of mathematical biophysics,* journal article vol. 5, no. 4, pp. 115-133, December 01 1943.

[10] A. Géron, *Hands-On Machine Learning with Scikit-Learn and TensorFlow: Concepts, Tools, and Techniques to Build Intelligent Systems.* Sebastopol, CA, USA: O'Reilly Media, Inc., 2017, p. 568.

[11] G. F. Hepner, T. Logan, N. Pitter, and N. Bryant, "Artificial neural network classification using a minimal training set: Comparison to conventional supervised classification," *Photogrammetric Engineering and Remote Sensing,* vol. 56, pp. 469-473, 1990.

[12] A. C. Teodoro, F. Veloso-Gomes, and H. Goncalves, "Retrieving TSM Concentration From Multispectral Satellite Data by Multiple Regression and Artificial Neural Networks," *IEEE Transactions on Geoscience and Remote Sensing,* vol. 45, no. 5, pp. 1342-1350, 2007.

[13] J. A. Benediktsson, P. H. Swain, and O. K. Ersoy, "Neural Network Approaches Versus Statistical Methods In Classification Of Multisource Remote Sensing Data," *IEEE Transactions on Geoscience and Remote Sensing,* vol. 28, no. 4, pp. 540-552, 1990.

[14] T. Hastie, R. Tibshirani, and J. Friedman, "Neural Networks," in *The Elements of Statistical Learning: Data Mining, Inference, and Prediction,* New York, NY: Springer New York, 2009, pp. 389-416.

[15] S. Haykin, *Neural Networks: A Comprehensive Foundation*, 2nd ed. Prentice Hall PTR, 1998, p. 842.

[16] D. E. Rumelhart and J. L. McClelland, "Learning Internal Representations by Error Propagation," in *Parallel Distributed Processing: Explorations in the Microstructure of Cognition: Foundations*: MITP, 1987, pp. 318-362.

[17] R. A. Dunne and N. A. Campbell, "Some practical aspects of pruning multi-layer perceptron models applied to remotely sensed data," Technical Report 94/06, Murdoch University, 1994.

[18] C. M. Bishop, *Neural Networks for Pattern Recognition*. New York, USA: Oxford University Press, Inc., 1995, p. 482.

[19] M. Story and R. Congalton, "Accuracy assessment: a user's perspective," Photogrammetric Engineering and Remote Sensing, vol. 52, no. 3, pp. 397-399, 1986.

[20] R. G. Congalton, "A review of assessing the accuracy of classifications of remotely sensed data," Remote Sensing of Environment, vol. 37, no. 1, pp. 35-46, 1991/07/01/ 1991.

[21] J. Cohen, "A Coefficient of Agreement for Nominal Scales," Educational and Psychological Measurement, vol. 20, no. 1, pp. 37-46, 1960.

[22] I. Gogul and V. S. Kumar, "Flower species recognition system using convolution neural networks and transfer learning," in *2017 Fourth International Conference on Signal Processing, Communication and Networking (ICSCN)*, 2017, pp. 1-6.

Credits to the original publication:

PROCEEDINGS OF SPIE

SPIEDigitalLibrary.org/conference-proceedings-of-spie

Reflectance spectroscopy to validate remote sensing data/algorithms for satellite-based lithium (Li) exploration (Central East Portugal)

Cardoso-Fernandes, J., Silva, J., Lima, A., Teodoro, A. C., Perrotta, M., et al.

J. Cardoso-Fernandes, J. Silva, A. Lima, A. C. Teodoro, M. Perrotta, J. Cauzid, E. Roda-Robles, M. A. Ribeiro, "Reflectance spectroscopy to validate remote sensing data/algorithms for satellite-based lithium (Li) exploration (Central East Portugal)," Proc. SPIE 11534, Earth Resources and Environmental Remote Sensing/GIS Applications XI, 115340M (20 September 2020); doi: 10.1117/12.2573929

SPIE.

Event: SPIE Remote Sensing, 2020, Online Only

Downloaded From: https://www.spiedigitallibrary.org/conference-proceedings-of-spie on 20 Sep 2020 Terms of Use: https://www.spiedigitallibrary.org/terms-of-use

Reflectance spectroscopy to validate remote sensing data/algorithms for satellite-based lithium (Li) exploration (Central East Portugal)

J. Cardoso-Fernandes*[a,b], J. Silva[a], A. Lima[a,b], A. C. Teodoro[a,b], M. Perrotta[c], J. Cauzid[d], E. Roda-Robles[e], M. A. Ribeiro[a,b]

[a]Department of Geosciences, Environment and Land Planning, Faculty of Sciences, University of Porto, Rua Campo Alegre, Porto, Portugal; [b]Institute of Earth Sciences (ICT), Pole of University of Porto, Porto, Portugal; [c]Geology and Mineral Resources Board of Directors, Geological Survey of Brazil (CPRM), Rua Costa, São Paulo, Brazil; [d]Laboratoire GeoRessources, Université de Lorraine, CNRS, GeoRessources, F-54000 Nancy, France; [e]Departament of Mineralogía y Petrología, University of País Vasco (UPV/EHU), Barrio Sarriena, Leioa, Bilbao, Spain

ABSTRACT

The acquisition of field data plays an important role in the calibration of the remotely sensed data, especially when combined with reflectance spectroscopy studies. The study area of this work is the Fregeneda-Almendra pegmatite field (spreading from Portugal to Spain) where different lithium (Li)-pegmatites are known. Several image processing techniques were applied to satellite images for Li exploration in the region, including machine learning classifiers. However, these algorithms identified several zones as Li-pegmatites false positives. Taking this into account, the following objectives were delineated: (i) validate the training areas used in previous studies and collect field data for training area refinement; (ii) assess the reason for the false positives previously obtained through field surveys. For that, various outcropping lithologies (Li-pegmatite, metasediments, granite) were sampled for laboratory spectral analysis. The spectral signature of Li-pegmatite was compared with the remaining outcropping lithologies. Also, the spectral signature of the sampled false positive areas was confronted with the spectra of Li-minerals. It was possible to conclude that these two classes present similar water/hydroxide and Al–OH-related features. The sampled granitic and metasedimentary rocks also presented water and/or hydroxide absorption features that can lead to some spectral confusion. However, Li-pegmatites can be discriminated from the remaining lithologies either in the training areas and the false positive areas due to the absence of iron-related absorption features and to the distinct reflectance magnitudes.

Keywords: Remote sensing; spectral library; geology; field validation; pegmatite; lithium

1. INTRODUCTION

Reflectance spectroscopy is an extensively used technique to identify minerals mainly due to the existence of diagnostic absorption wavelengths intervals in the visible and infrared regions [1, 2]. This technique is mainly applied to characterize the products of hydrothermal alteration, with increasing economic applications in the mineral industry [3]. Field data acquisition is important to calibrate the remotely sensed data: the reflectance spectroscopy studies, either made in the laboratory or directly in the field, provide a calibration source (ground-check) of the remotely sensed data and allow to validate the atmospheric corrections made to satellite-acquired images.

In this study, field validation and sample collection were made in the Portuguese side of the Fregeneda-Almendra pegmatite field that spreads from Salamanca (Spain) to Vila Nova de Foz Côa (Portugal). In recent years, several image processing techniques were applied to satellite images covering this region to identify lithium (Li)-pegmatites [4-6]. These techniques included machine learning algorithms such as Support Vector Machine (SVM) and Random Forest (RF) [6]. Although these algorithms were able to identify the presence of Li-pegmatite in areas where its occurrence is known, they also identified several zones as Li-pegmatites false positives. Therefore, it is fundamental to develop detailed studies to understand if the misclassifications obtained using satellite images are due to a similar spectral behavior between lithologies or to a flaw in the methodology developed.

*joana.fernandes@fc.up.pt

Earth Resources and Environmental Remote Sensing/GIS Applications XI, edited by Karsten Schulz, Proc. of SPIE Vol. 11534, 115340M · © 2020 SPIE · CCC code: 0277-786X/20/$21 · doi: 10.1117/12.2573929

Downloaded From: https://www.spiedigitallibrary.org/conference-proceedings-of-spie on 20 Sep 2020
Terms of Use: https://www.spiedigitallibrary.org/terms-of-use

Taking this into account, the following objectives were delineated: (i) validation of the training areas used in previous studies and collection of new field data for training area improvement and refinement; (ii) assessment of the reason of the false positives previously obtained with SVM and RF [6] through field surveys.

2. FIELD SURVEYS AND REFLECTANCE SPECTROSCOPY

2.1 Study area and fieldwork

The Fregeneda-Almendra pegmatite field spreads from Portugal to Spain, in the central part of the Iberian Massif. In this field, several barren and Li-mineralized pegmatites were identified [7, 8]. The Li-mineralized pegmatites were divided into four distinct types of dikes: petalite-bearing, spodumene-bearing, lepidolite+spodumene-bearing, and lepidolite-bearing. The pegmatite dikes intruded the pre-Ordovician metasediments of the Complexo Xisto-Grauváquico (CXG) [9], located to the north of the Figueira de Castelo Rodrigo–Lumbrales Anatectic Complex [10] where several syn-Variscan two-mica granites outcrop (Figure 1). In the region, there are also phyllitic-quartzitic formations of Ordovician age as well as some Cenozoic sedimentary deposits.

To achieve the previously delineated goals, a field campaign was carried out in February of 2020 to sample various outcropping lithologies for laboratory spectral analysis. The fieldwork was conducted on the Portuguese side of the pegmatite field (in the Guarda district). The sample locations included some of the training areas used in the previous classification process [6] as well as several open-pit mines where the different lithologies (Li-pegmatite, metasediments, granite) present larger and fresher expositions (Figure 1). Some areas identified as Li-pegmatite considering SVM and RF were also visited in the field to assess the exposed material in these targets (Figure 1). Field description of each site was made, and samples were collected for the spectral studies.

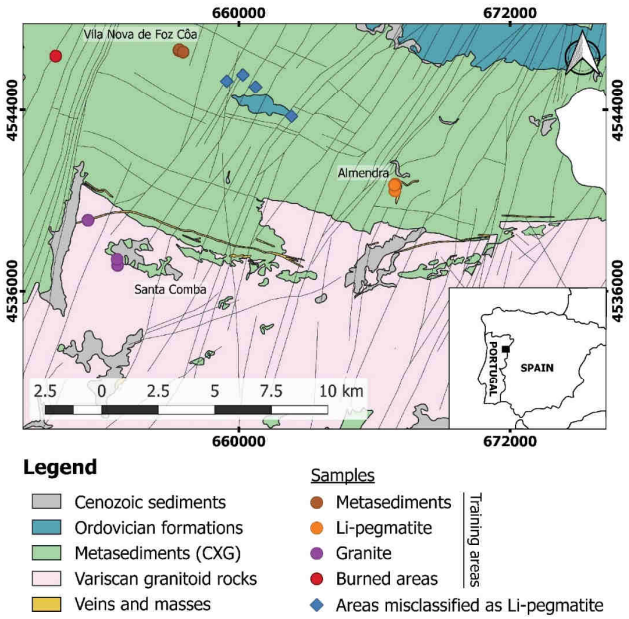

Figure 1. Location of the study area and geological setting of the Portuguese side of the Fregeneda-Almendra pegmatite field (adapted from [11, 12]). The location of the samples collected in the field surveys is marked with a circle for the training areas and with a diamond for the areas misclassified as Li-pegmatite using SVM and RF. Map projection: Universal Transverse Mercator zone 29N, WGS84 datum.

Downloaded From: https://www.spiedigitallibrary.org/conference-proceedings-of-spie on 20 Sep 2020
Terms of Use: https://www.spiedigitallibrary.org/terms-of-use

2.2 Laboratory reflectance studies

A total of 220 point analyses were made to build a spectral library for each lithological class and Li-minerals identified. The equipment used for the measurements was the ultra-high-resolution SR-6500A spectroradiometer (Spectral Evolution, Inc.) with a spectral range between 350 and 2500 nm, and 1.5 nm resolution in the visible and near-infrared (VNIR), and 3-3.8 nm resolution in the shortwave infrared (SWIR). All spectral measurements were made in the laboratory using a Handheld Contact Probe with an internal light source (halogen bulb: 4.25 V, 1.06 A). The reflectance values were calibrated using a Spectralon (Labsphere) plate with a maximum reflectance of 95% for the 250-2500 nm region.

All spectra were individually analyzed in order to exclude irregular values caused by measurement errors or by the presence of vegetation in the surface of the samples. In the end, 198 valid spectra were retained, each one corresponding to an analyzed spot of a total of 42 samples collected. The point analyses were averaged by lithology or by location in the case of the false positive areas. Fresh and altered samples were treated separately to evaluate if there is any difference. Further spectra processing was conducted in a Python environment where the *pysptools* library [13] was used to remove the spectra continuum and to identify and extract the main absorption features. The SpectraGryph software [14] was also used as a complementary tool.

3. RESULTS AND DISCUSSION

3.1 Validation and improvement of the training areas

Most of the training areas used in the previous works regarding image classification [6], as well as new locations were visited in the field to collect reference spectra for the main outcropping lithologies of the area (granite, Li-pegmatite, metasediments). Their (reflectance) mean spectral signature is compared in Figure 2. Also, the mean spectra of petalite, a Li-mineral, is shown. The respective continuum removed spectra and the identified absorption features are presented in Figure 3.

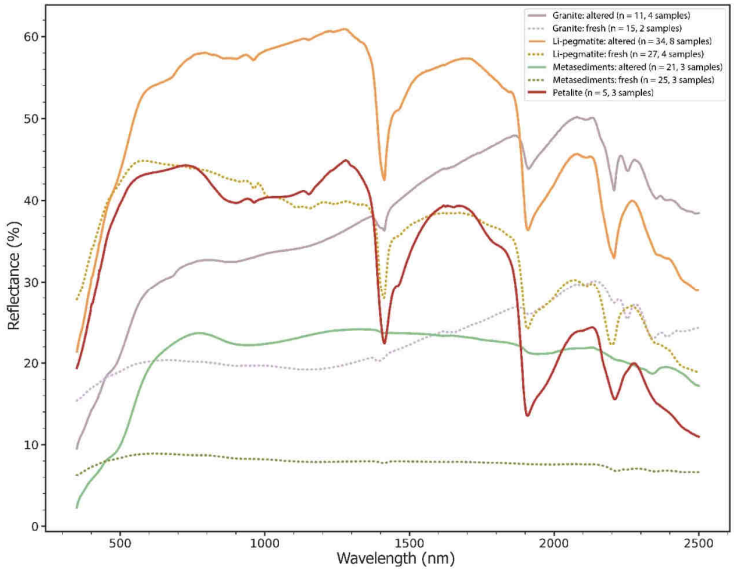

Figure 2. Raw mean spectral signature of the different outcropping lithologies. Dotted lines represent fresh samples. The mean spectrum of petalite (a Li-mineral) is plotted for comparison.

Downloaded From: https://www.spiedigitallibrary.org/conference-proceedings-of-spie on 20 Sep 2020
Terms of Use: https://www.spiedigitallibrary.org/terms-of-use

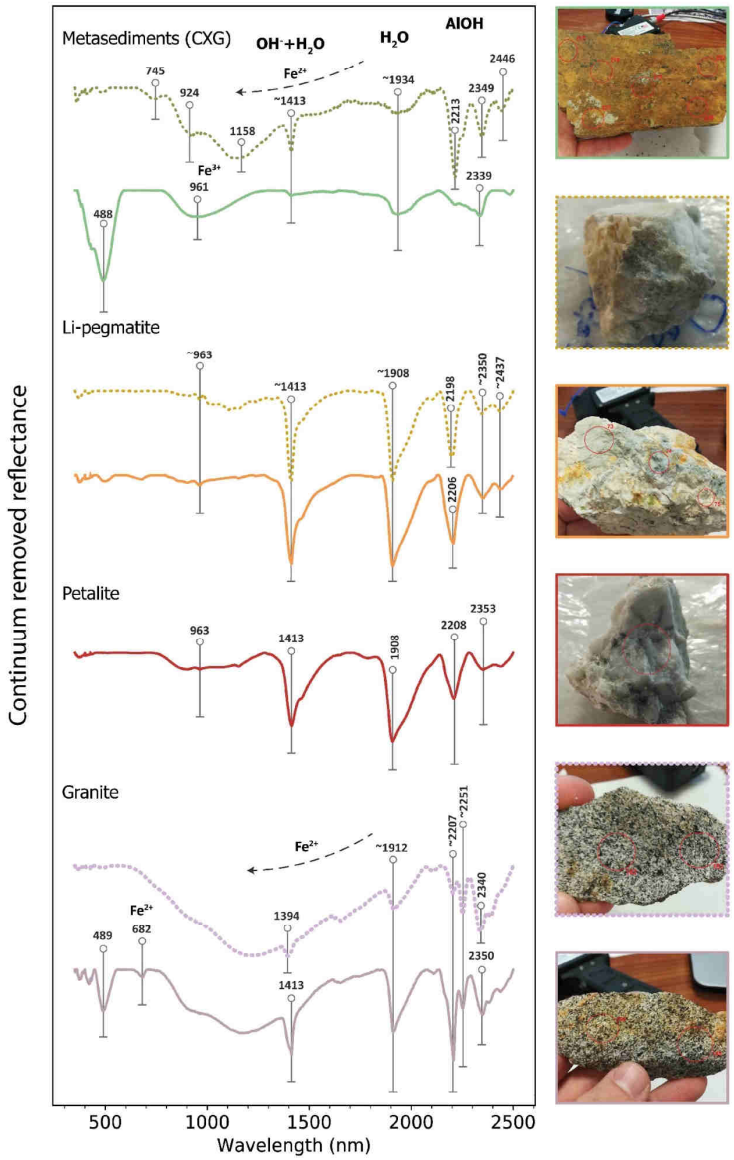

Figure 3. Mean spectral signatures of the outcropping lithologies with the continuum removed. Dotted lines represent fresh samples while full lines represent altered samples. The mean spectrum of petalite is also shown.

Downloaded From: https://www.spiedigitallibrary.org/conference-proceedings-of-spie on 20 Sep 2020
Terms of Use: https://www.spiedigitallibrary.org/terms-of-use

Analyzing the spectra from the different lithologies (Figure 2), it is observed, as expected, that the reflectance of the fresh samples is always lower than the one from the altered samples. Regarding the Li-pegmatite spectra, the main absorption features appear to coincide with the features present in the petalite spectrum. Also, the altered samples of granite and metasediments show less pronounced but similar absorption features around ~1400 and ~2200 nm, and around ~1900 nm in the case of the altered granite (Figure 2). This is again visible in the continuum removed spectra of Figure 3, however, the magnitude of the reflectance is distinct in each lithology. The position of the absorption features was identified after the removal of the continuum, and some of these features are diagnostic of the presence of certain ions/molecules in the samples.

The fresh samples of metasediments show a typical broad (ramp-like) ferrous iron (Fe^{2+}) feature that disappears in the altered samples probably as a result of the oxidation process and the passage to ferric iron (Fe^{3+}) [15]. The 745, 924, and 1158 nm iron diagnostic absorptions, which also don´t persist in altered samples, may correspond to mixtures between chlorite and biotite, as well as evidenced by the SWIR absorption feature in 2349 nm associated to the inflection in ~2240 nm [16]. The weak absorption around ~1934 nm indicates that only a small amount of water (H_2O) is present, and the feature around ~1413 nm, mainly due to the hydroxide ion (OH^-) [1], when associated to the Al–OH 2213 nm absorption, indicates the presence of white mica, also evidenced by the secondaries 2349 nm and 2446 nm absorptions, despite the deeper 2349 nm feature because of the chlorite/biotite presence effect. These features almost disappear in the altered samples (Figure 3).

Oppositely, the Li-pegmatite and petalite spectra present a deep, asymmetrical feature around ~1910 nm indicating the presence of water. In the case of Li-pegmatite, the molecular water indicated by the ~1413 nm (OH^-+H_2O) feature and the main Al–OH absorption by around 2200 nm, with the associated secondaries in 2350 and 2437 nm, are diagnostic of the presence of illite (and/or white mica) probably in mixtures with clay-minerals from the smectite group, mainly in altered samples, where the 2200 nm feature moves to slightly longer wavelengths [1]. Similarly, petalite shows important features in these same main positions, but, the OH^- feature more asymmetric, the water absorption significantly deeper than the main A–OH absorption, and the almost absent Al–OH secondaries features, indicate that smectite dominates the spectra [1] (Figure 3).

In what concerns the granite, the broad Fe^{2+} absorption is present in both altered and fresh samples, although more pronounced in the fresh ones (Figure 3). Also, in both cases, the absorption pair ~2251 nm/2340-2350 nm, related to the Fe–OH and Mg–OH bonds, respectively [17], is due to the presence of biotite. The Al–OH feature, also present, indicates the presence of white mica or sericite, and maybe a clay mineral in altered samples (Figure 3).

Ultimately, the field validation allowed to define important areas where these different lithologies outcrop clear of vegetation. The new field data were used with good results in a new classification attempt in the study area [18].

3.2 Areas misclassified as Li-pegmatite

Four areas misclassified as Li-pegmatite by both the SVM and RF algorithms were also sampled. These false positive areas mainly correspond to regions where the soil was disturbed and plowed for wine or olive plantations, exposing boulders of metasedimentary rocks. Other areas correspond to slope areas where this type of rocks are naturally exposed. Figure 4 shows the mean spectral signature of these false positive areas. The identified absorption features are compared with the ones from Li-minerals.

In general, the samples collected in the false positive areas present the same absorption features related to OH^- +/- H_2O (~1414 nm), H_2O (~1910 nm) and Al–OH (~2208 nm) [1]. However, the spectra from the misclassified areas present clear distinct features in the VNIR region associated with the presence of ferrous and ferric iron (Figure 4). Additionally, the distinct absorptions depths of the SWIR features indicate the occurrence of different mineral assemblages. For example, the spectra from the false positive areas no. 2 and no.4 show a deeper absorption around ~2200 nm when compared with the water feature at ~1910 nm. This is diagnostic of the presence of illite [3, 16]. On the opposite, the altered samples from false positives areas no. 1 and no. 3 have the ~1910 nm feature deeper than the Al–OH (~2208 nm), indicating the presence of clay minerals. These features were not identified in the samples collected in the training areas for the metasediments lithological class.

The presence of illite may occur in the metasedimentary rocks interstratified with muscovite or, more commonly, can be formed in retrograde metamorphic conditions linked to meteoric alteration. At this stage, the presence of clay minerals is not yet fully understood. Additional geological data will be acquired through petrographic and geochemical analysis to

Downloaded From: https://www.spiedigitallibrary.org/conference-proceedings-of-spie on 20 Sep 2020
Terms of Use: https://www.spiedigitallibrary.org/terms-of-use

complement and explain the obtained results. More field campaigns are scheduled to complete the spectral library, including spectral measurements made in the field to better match the solar conditions verified when acquiring satellite images.

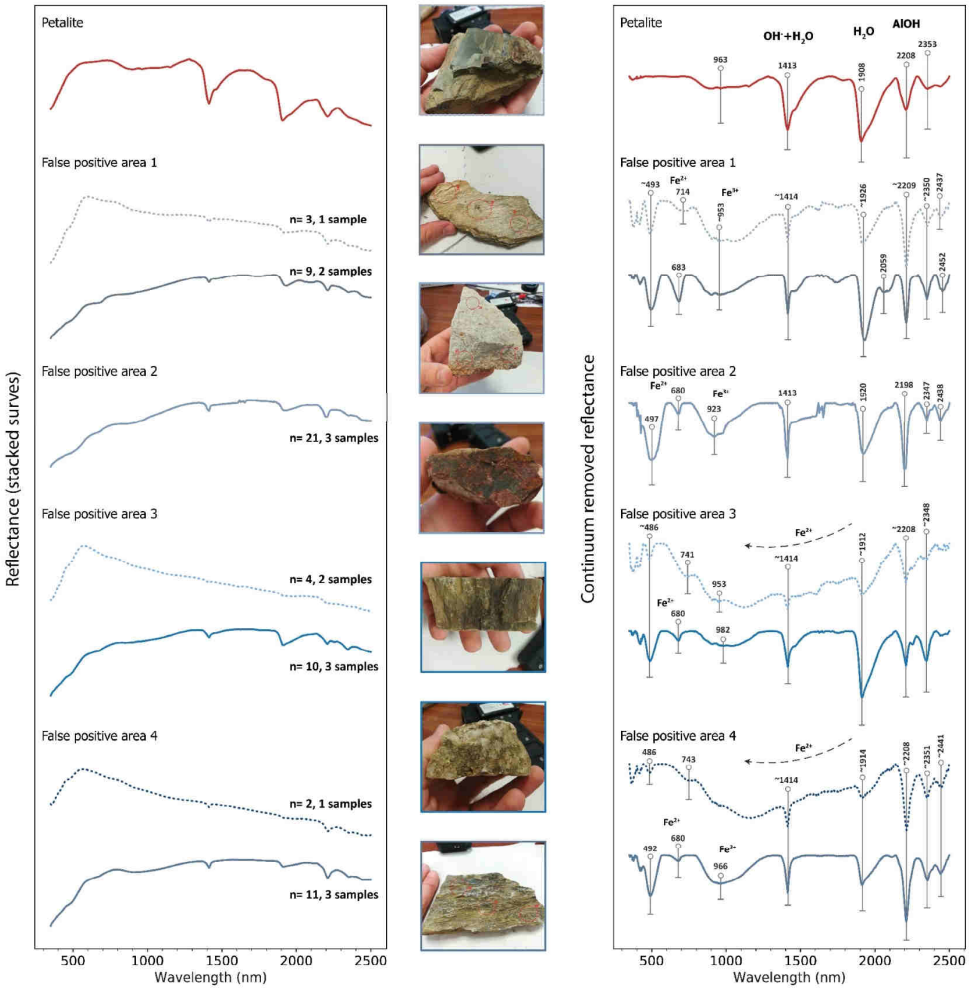

Figure 4. Mean spectral signature of the areas misclassified as Li-pegmatite in previous studies (reflectance spectra to the left; continuum removed spectra to the right). Dotted lines represent fresh samples while full lines represent altered samples. The mean spectral signal of petalite is also shown.

Downloaded From: https://www.spiedigitallibrary.org/conference-proceedings-of-spie on 20 Sep 2020
Terms of Use: https://www.spiedigitallibrary.org/terms-of-use

4. CONCLUSIONS

This study aimed at obtaining field and laboratory data for satellite-based Li exploration. Overall, the proposed objectives were fulfilled:

1. A reference spectra of main outcropping lithologies was obtained. Despite all lithologies presenting similar features related to the presence of water/hydroxide in the structure of rock-constituent minerals, the absorptions depths are higher in the Li-pegmatites probably due to the occurrence of clay minerals. These absorptions depths differences aligned with the presence of iron-related features in the VNIR region and the distinct reflectance magnitudes of each lithology should be enough to spectrally discriminate them using satellite data. Also important is the variation in Al–OH absorption position, showing longer wavelengths in metasediments (probably due to relatively Al-poorer white mica), shorter in Li-pegmatite, and intermediate in granite, petalite, and altered rocks. Moreover, due to the distinct spectral behaviors, the fresh and altered samples were treated separately. The higher reflectance of the altered samples, when compared to the fresh ones, may be related to the presence of alteration minerals like clays and iron-oxides.
2. The spectra of the metasedimentary rocks from the false positive areas were confronted with the spectra of Li-minerals. The results show that, in fact, the outcropping rocks from these areas have similar water/hydroxide and Al–OH-related features to ones observed in the Li-minerals. This is due to the presence of clays/illite not observed in the samples from the training areas. Nonetheless, as before, the metasediments show iron-related absorption features that are not observed in the Li-minerals/pegmatites. Thus, it is necessary to improve the previous methodology employed in lithological classification.

Future studies will include the collection of more spectral and geological data for further analysis and interpretation. The spectra will be analyzed sample by sample, instead of the mean spectral signal, to identify the mineral assemblages in each lithology through the characterization of their respective diagnostic features.

ACKNOWLEDGEMENTS

The authors would like to thank the financial support provided by FCT– Fundação para a Ciência e a Tecnologia, I.P., with the ERA-MIN/0001/2017 – LIGHTS project. The work was also supported by National Funds through the FCT project UIDB/04683/2020 - ICT (Institute of Earth Sciences). Joana Cardoso-Fernandes is financially supported within the compass of a Ph.D. Thesis, ref. SFRH/BD/136108/2018, by national funds from MCTES through FCT, and co-financed by the European Social Fund (ESF) through POCH – Programa Operacional Capital Humano. The Spanish Ministerio de Ciencia, Innovacion y Universidades (Project RTI2018-094097-B-100, with ERDF funds) and the University of the Basque Country (UPV/EHU) (grant GIU18/084) also contributed economically. Odile Barrès is thanked for the help handling the spectroradiometer at Université de Lorraine (France).

REFERENCES

[1] R. N. Clark, T. V. V. King, M. Klejwa, G. A. Swayze, and N. Vergo, “High spectral resolution reflectance spectroscopy of minerals,” Journal of Geophysical Research: Solid Earth, 95(B8), 12653-12680 (1990).
[2] R. N. Clark, and T. L. Roush, “Reflectance spectroscopy: Quantitative analysis techniques for remote sensing applications,” Journal of Geophysical Research: Solid Earth, 89(B7), 6329-6340 (1984).
[3] J. L. C. Naleto, M. M. Perrotta, F. G. d. Costa, and C. R. d. Souza Filho, “Point and imaging spectroscopy investigations on the Pedra Branca orogenic gold deposit, Troia Massif, Northeast Brazil: Implications for mineral exploration in amphibolite metamorphic-grade terrains,” Ore Geology Reviews, 107, 283-309 (2019).
[4] J. Cardoso-Fernandes, A. C. Teodoro, and A. Lima, "Potential of Sentinel-2 data in the detection of lithium (Li)-bearing pegmatites: a study case." 10790, 15 (2018).
[5] J. Cardoso-Fernandes, A. C. Teodoro, and A. Lima, “Remote sensing data in lithium (Li) exploration: A new approach for the detection of Li-bearing pegmatites,” International Journal of Applied Earth Observation and Geoinformation, 76, 10-25 (2019).

Downloaded From: https://www.spiedigitallibrary.org/conference-proceedings-of-spie on 20 Sep 2020
Terms of Use: https://www.spiedigitallibrary.org/terms-of-use

[6] J. Cardoso-Fernandes, A. C. Teodoro, A. Lima, and E. Roda-Robles, "Evaluating the performance of support vector machines (SVMs) and random forest (RF) in Li-pegmatite mapping: preliminary results." 11156.
[7] R. Vieira, [Aplitopegmatitos com elementos raros da região entre Almendra (V.N. de Foz Côa) e Barca d'Alva (Figueira de Castelo Rodrigo). Campo aplitopegmatítico da Fregeneda- Almendra], PhD thesis, Faculdade de Ciências da Universidade do Porto, Porto, XXVI, 273 (2010).
[8] E. Roda-Robles, A. Pesquera, F. Velasco, and F. Fontan, "The granitic pegmatites of the Fregeneda area (Salamanca, Spain): characteristics and petrogenesis," Mineral. Mag., 63(4), 535–558 (1999).
[9] J. C. S. d. Costa, [Notícia sobre uma carta geológica do Buçaco, de Nery Delgado] Serviços Geológicos de Portugal, Lisboa (1950).
[10] I. Pereira, R. Dias, T. Bento dos Santos, and J. Mata, "Exhumation of a migmatite complex along a transpressive shear zone: inferences from the Variscan Juzbado–Penalva do Castelo Shear Zone (Central Iberian Zone)," Journal of the Geological Society, 174(6), 1004 (2017).
[11] A. F. Silva, A. J. Santos, A. Ribeiro, J. Cabral, and M. L. Ribeiro, [Carta Geológica de Portugal na escala 1/50.000 – folha 15-B – Freixo de Espada à Cinta], Serv. Geol. Portugal, Lisboa (1990).
[12] A. F. Silva, A. J. Santos, A. Ribeiro, and M. L. Ribeiro, [Carta Geológica de Portugal na escala 1/50.000 – folha 15-A – Vila Nova de Foz Côa],Serv. Geol. Portugal Lisboa (1990).
[13] C. Therien, "Welcome to the PySptools Documentation," <https://pysptools.sourceforge.io/> (22 July 2020)
[14] F. Menges, "Spectragryph - optical spectroscopy software, Version 1.2.14," 2020, <http://www.effemm2.de/spectragryph/>
[15] G. R. Hunt, and R. P. Ashley, "Spectra of altered rocks in the visible and near infrared," Economic Geology, 74(7), 1613-1629 (1979).
[16] S. Pontual, N. J. Merry, and P. Gamson, [Spectral interpretation field manual. GMEX Spectral analysis guides for mineral exploration], 1, 3rd, AusSpec International Ltd., Victoria, 189 (2008).
[17] Y. Sun, P. K. Seccombe, and K. Yang, "Application of short-wave infrared spectroscopy to define alteration zones associated with the Elura zinc–lead–silver deposit, NSW, Australia," Journal of Geochemical Exploration, 73(1), 11-26 (2001).
[18] J. Cardoso-Fernandes, A. C. Teodoro, A. Lima, and E. Roda-Robles, "Semi-Automatization of Support Vector Machines to Map Lithium (Li) Bearing Pegmatites," Remote Sensing, 12(14), 2319 (2020).

Downloaded From: https://www.spiedigitallibrary.org/conference-proceedings-of-spie on 20 Sep 2020
Terms of Use: https://www.spiedigitallibrary.org/terms-of-use

Credits to the original publication:

PROCEEDINGS OF SPIE

SPIEDigitalLibrary.org/conference-proceedings-of-spie

Characterization of lithium (Li) minerals from the Fregeneda-Almendra region through laboratory spectral measurements: a comparative study

Cardoso-Fernandes, J., Silva, J., Lima, A., Teodoro, A. C., Perrotta, M., et al.

J. Cardoso-Fernandes, J. Silva, A. Lima, A. C. Teodoro, M. Perrotta, J. Cauzid, E. Roda-Robles, "Characterization of lithium (Li) minerals from the Fregeneda-Almendra region through laboratory spectral measurements: a comparative study," Proc. SPIE 11534, Earth Resources and Environmental Remote Sensing/GIS Applications XI, 115340N (20 September 2020); doi: 10.1117/12.2573941

SPIE.

Event: SPIE Remote Sensing, 2020, Online Only

Downloaded From: https://www.spiedigitallibrary.org/conference-proceedings-of-spie on 20 Sep 2020 Terms of Use: https://www.spiedigitallibrary.org/terms-of-use

Characterization of lithium (Li) minerals from the Fregeneda-Almendra region through laboratory spectral measurements: a comparative study

J. Cardoso-Fernandes*[a,b], J. Silva[a], A. Lima[a,b], A. C. Teodoro[a,b], M. Perrotta[c], J. Cauzid[d], E. Roda-Robles[e]

[a]Department of Geosciences, Environment and Land Planning, Faculty of Sciences, University of Porto, Rua Campo Alegre, Porto, Portugal; [b]Institute of Earth Sciences (ICT), Pole of University of Porto, Porto, Portugal; [c]Geology and Mineral Resources Board of Directors, Geological Survey of Brazil (CPRM), Rua Costa, São Paulo, Brazil; [d]Laboratoire GeoRessources, Université de Lorraine, CNRS, GeoRessources, F-54000 Nancy, France; [e]Departament of Mineralogía y Petrología, University of País Vasco (UPV/EHU), Barrio Sarriena, Leioa, Bilbao, Spain

ABSTRACT

Although several lithium (Li) bearing minerals have already been spectrally characterized, there are no current reference spectra for petalite in large and public access spectral libraries. This fact is aggravated by the difficulty in the identification of petalite's diagnostic features. The study area of this work is the Fregeneda (Spain) – Almendra (Portugal) region, where distinct Li bearing minerals occur in several types of enriched pegmatite dikes. Accordingly, the objectives delineated for this work were: (i) improve the existing knowledge on the spectral signatures of Li bearing minerals (lepidolite, spodumene, petalite); (ii) compare the spectra obtained for petalite and spodumene in the study area; (iii) and compare the spectra of the Li bearing minerals from the Fregeneda-Almendra area with the reference spectra from the United States Geological Survey (USGS), the ECOSTRESS and the Geological Survey of Brazil (CPRM) spectral libraries. For that, spectral measurements were conducted in the laboratory using the SR-6500A (Spectral Evolution, Inc.) spectrometer. The results only allowed to discriminate lepidolite, since that, both, petalite and spodumene, present absorption features typical of montmorillonite and illite, or a combination between these two minerals. This is also verified in samples of corresponding minerals in other spectral libraries. No diagnostic features of these two Li bearing minerals were identified, highlighting the difficulty to spectrally discriminate them from each other and from clay minerals.

Keywords: Geological exploration, remote sensing, reflectance spectroscopy, pegmatite, lithium

1. INTRODUCTION

Nowadays, satellite-based lithium (Li) exploration represents an emergent field with applications in Li brines and pegmatite-hosted hard rock Li deposits [1]. Most of the remote sensing data and techniques focus on the last type of deposit where the most common Li bearing minerals are spodumene (a Li bearing pyroxene), petalite (a Li bearing feldspathoid), and lepidolite (a Li bearing mica). However, there are no current reference spectra for petalite in large and public access spectral libraries such as the United States Geological Survey (USGS) [2] and ECOSTRESS [3] spectral libraries. Therefore, it is important to fill this gap and to develop new application studies. In the last decade, the Geological Survey of Brazil (CPRM) has been building a spectral library with a section specially dedicated to Li bearing minerals constantly updated and with more than 1500 reference spectra. However, they have experienced difficulties in the identification of petalite's diagnostic features [4].

The study area of this work corresponds to the Fregeneda (Spain) – Almendra (Portugal) region where distinct Li bearing minerals occur in rare-element enriched pegmatite dikes. In the region, several attempts to identify and map Li bearing pegmatites were made using several image processing techniques and employing different types of free satellite data [5-7].

* joana.fernandes@fc.up.pt

Earth Resources and Environmental Remote Sensing/GIS Applications XI,
edited by Karsten Schulz, Proc. of SPIE Vol. 11534, 115340N · © 2020
SPIE · CCC code: 0277-786X/20/$21 · doi: 10.1117/12.2573941

Downloaded From: https://www.spiedigitallibrary.org/conference-proceedings-of-spie on 20 Sep 2020
Terms of Use: https://www.spiedigitallibrary.org/terms-of-use

The results obtained are promising but can be improved through the acquisition of reference spectral data to use as a target. Taking this into consideration, the objectives of this work are: (i) improve the existing knowledge on the spectral signatures of Li bearing minerals; (ii) compare the spectra obtained for petalite and spodumene in the study area; (iii) and compare the spectral characteristics and diagnostic features of the Li bearing minerals from the Fregeneda-Almendra area with the reference spectra from the USGS, the ECOSTRESS and the CPRM spectral libraries.

1.1 The Fregeneda-Almendra area

The study area spreads from La Fregeneda in Spain to the Almendra parish in Portugal (Figure 1). In the region, both barren and rare-element pegmatite bodies were identified and classified into several types according to their distinct mineralogical, morphological, and structural properties [8, 9]. All the rare-element pegmatites were emplaced in pre-Ordovician metasediments of the Complexo Xisto-Grauváquico (CXG) [10] and show enrichment in Li, F, Sn, Rb, Nb>Ta, B, P and Be with increasing fractionation degree. The fractionation degree tends to increase with further distance to syn-Variscan Mêda-Penedono-Lumbrales granites of the Figueira de Castelo Rodrigo–Lumbrales Anatectic Complex [11]. Among the more evolved pegmatite dikes, there are four-types mineralized in Li [8, 9]: i) petalite-bearing dikes (exploited in the Bajoca mine), ii) spodumene-bearing dikes (exploited in the Alberto mine), iii) lepidolite-bearing dikes, and iv) lepidolite+spodumene-bearing dikes (exploited in the Feli mine) – Figure 1.

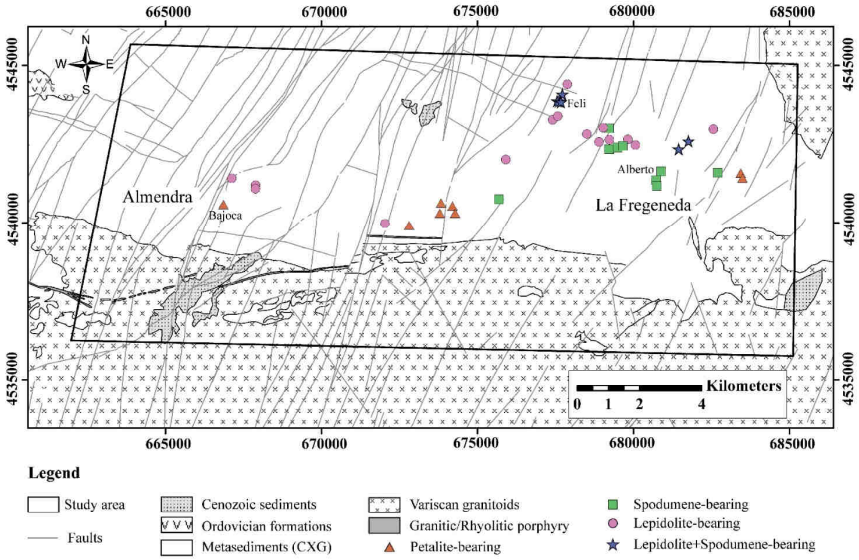

Figure 1. Geological setting of the Fregeneda-Almendra area (Spain-Portugal), adapted from [8, 12, 13]. The location of Li-rich dikes is highlighted. Map projection: Universal Transverse Mercator zone 29N, WGS84 datum.

2. METHODS

A spectral database was built with 12 samples of Li bearing minerals (including petalite, spodumene, and lepidolite) collected in different types of mineralized dikes, accounting for a total of 49 analyzed spots. Most of the samples were acquired in Bajoca, Feli, and Alberto mines (Figure 1). The remaining samples were acquired in other unexploited pegmatite dikes. In the end, the spectra were averaged according to the respective Li bearing mineral.

Downloaded From: https://www.spiedigitallibrary.org/conference-proceedings-of-spie on 20 Sep 2020
Terms of Use: https://www.spiedigitallibrary.org/terms-of-use

All spectral studies were conducted in the laboratory in a controlled lighting environment using a halogen bulb (4.25 V, 1.06 A). The employed spectroradiometer was the SR-6500A (Spectral Evolution, Inc.) that acquires information in the visible and near-infrared (VNIR) to the shortwave infrared (SWIR) spectral range (350-2500 nm) with ultra-high-resolution (1.5 nm @ 700 nm, 3.0 nm @ 1500 nm, 3.8 nm @ 2100 nm) – Figure 2. Before performing the spectral measurements, a Spectralon reflectance standard (from Labsphere) was used to calibrate the equipment.

Figure 2. Laboratory equipment used for spectral measurements. Spectroradiometer model: SR-6500A.

The arithmetic operations between spectra were performed using the SpectraGryph software [14]. The mean spectra of each Li bearing mineral were then normalized through the continuum removal (hull quotient) process using the *pysptools* library [15] for the Python programming language (Figure 3-a). The analysis and identification of the absorption features were made using both the SpectraGryph software and the *pysptools* library (Figure 3-b, c, d).

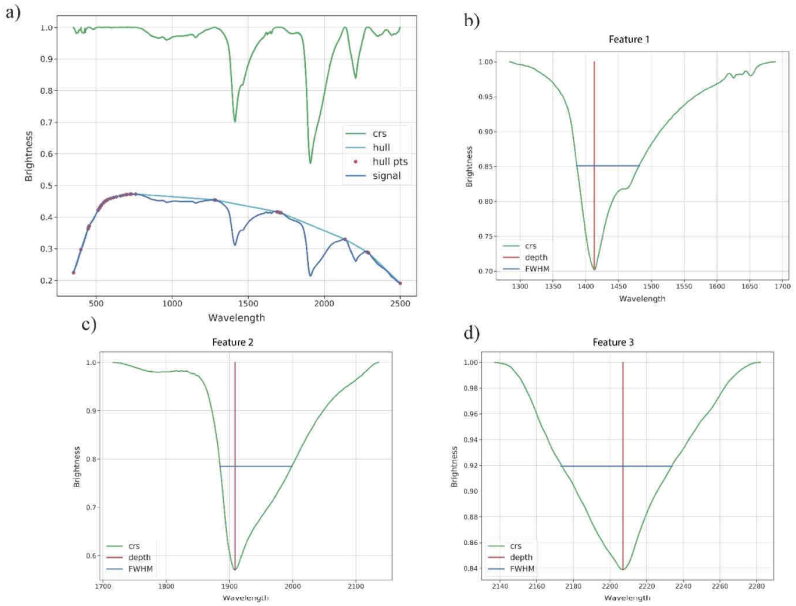

Figure 3. The continuum removal (hull quotient) process (a) and the extraction of the main absorption features (b-d) using the *pysptools* library. crs – continuum removed spectra; pts – points; FWHM – full width at half maximum.

Downloaded From: https://www.spiedigitallibrary.org/conference-proceedings-of-spie on 20 Sep 2020
Terms of Use: https://www.spiedigitallibrary.org/terms-of-use

Afterward, the obtained mean spectra of each Li bearing mineral was compared with the USGS and ECOSTRESS spectral libraries using the "spectral similarity" algorithm of SpectraGryph [16]. This algorithm calculates the Pearson correlation coefficient for the full-spectrum and returns the highest-rating matching reference spectra [16]. Also, the mean spectra obtained in this work were visually compared with the corresponding minerals from the CPRM spectral library.

3. RESULTS AND DISCUSSION

The graphic presented in Figure 4 shows the lepidolite, petalite, and spodumene+quartz mean spectral signatures. It was not possible to acquire an isolated spectrum of spodumene because it is intergrown with quartz. However, the diagnostic features of quartz do not occur in the VNIR-SWIR range [17, 18] and, therefore, should not have great interference in the overall resultant spectrum. Comparing both the petalite and spodumene signatures (Figure 4-a), it is easily understandable that the percentage of reflectance has an identical evolutive trend throughout the spectra. Starting by rapidly increasing and getting to the maximum percentages of reflectance in the first third of the spectrum (350 to 850 nm), for then initiate a decrease for the remaining wavelengths. Although they might seem to have the same trend, spodumene has a slightly more continuous trend after the initial increase, staying longer in the top reflectance percentages, showing only a decrease in the second half of the spectrum (1350 to 2500 nm) – Figure 4-a. In the case of lepidolite, the reflectance values increase more slowly in the VNIR region, with two gentle absorptions around ~550 nm and ~950 nm that are caused by its the purple color. The reflectance also drops after the absorption around ~1900 nm (Figure 4-a), but showing more peaks and troughs than spodumene and petalite.

The main absorption features were identified in Figure 4-b, and, as can be seen, the three Li bearing minerals present coincident features around ~1410 nm, ~1910 nm, and ~2200 nm. These absorption features are related to $OH^{+}H_2O$, H_2O, and Al–OH, respectively [17, 19]. Despite this, it is possible to distinguish lepidolite from spodumene and petalite: the first shows narrow, symmetric absorption features at 1410 nm and 2196 nm, while petalite and spodumene show broader, asymmetric features around ~1413 nm and ~2207 nm (Figure 4-b). Also, lepidolite presents features characteristic of white mica such as the absorption around 2346 nm and 2433 nm (Al–OH secondary features), as well as a deeper Al–OH absorption feature when compared to the H_2O one [18, 20, 21]. The location of the main Al–OH feature at 2196 nm may point to higher Al contents [20, 21].

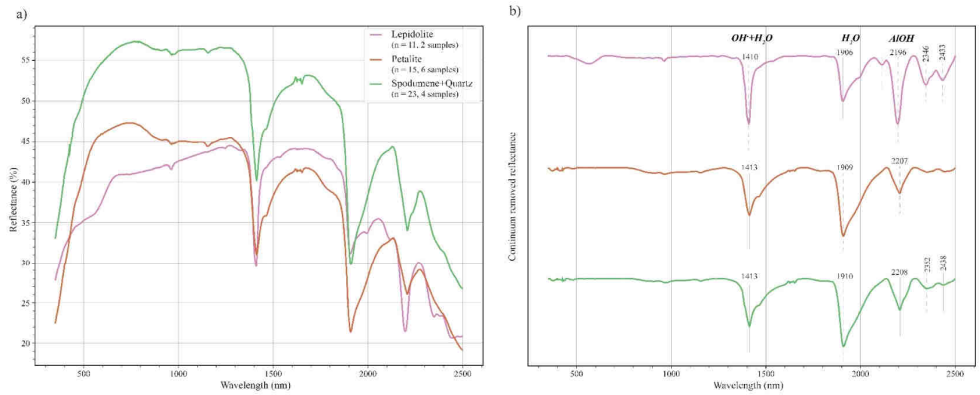

Figure 4. Raw (a) and continuum removed (b) mean reflectance spectra of the three Li bearing minerals: lepidolite, petalite and spodumene. The main absorption features were identified in the continuum removed spectra.

In what concerns the petalite and spodumene, and similarly to what happened with the raw spectra, the continuum removed spectra of both minerals is very similar, with visible noise present between 1610 nm and 1670 nm (Figure 4-b). The Al–OH feature in these minerals is much less pronounced than in lepidolite and the very deep absorption features around ~1910 nm indicate the presence of free molecular H_2O [22]. These are diagnostic features of the smectite group, probably montmorillonite since it is the only smectite that readily absorbs water from the air [19, 22]. The only main difference, of these two minerals spectral signatures, is the existence of shallow Al–OH secondary absorption features at

Downloaded From: https://www.spiedigitallibrary.org/conference-proceedings-of-spie on 20 Sep 2020
Terms of Use: https://www.spiedigitallibrary.org/terms-of-use

2352 nm and 2438 nm in the spodumene spectrum (Figure 4-b). This shows that besides montmorillonite, illite is also present. It was not possible to identify any diagnostic feature of petalite or spodumene, and their spectral signal is mostly dominated by the alteration minerals.

When comparing the raw spectra of the Li bearing minerals with the reference spectra from the USGS and ECOSTRESS spectral libraries (Table 1), the existence of clay minerals diagnostic features clearly influenced the results. Table 1 shows for each mineral the top 5 highest-rating spectral matches (hit percentage above 96.82%).

Table 1. Highest-rating matching reference spectra from the USGS and ECOSTRESS spectral libraries for each Li bearing mineral raw spectrum. The matches are presented by decreasing hit percentage.

Mineral	Spectral match USGS	Spectral match ECOSTRESS
Lepidolite	Endellite; Kaolinite; Illite; Halloysite; Dickite	Muscovite; Microcline; Lepidolite
Petalite	Saponite; Montmorillonite	Scheelite; Montmorillonite; Illite/smectite
Spodumene (with quartz intergrowths)	Montmorillonite	Illite/smectite; Montmorillonite

Most of the matches correspond to clay minerals or to white micas. The match of petalite with the ECOSTRESS's scheelite (calcium tungstate) reference spectrum is unexpected. For petalite and spodumene, both spectral libraries returned matches of montmorillonite reference spectra. In the case of lepidolite, the best matches were obtained in the ECOSTRESS spectral library (Table 1). Figure 5 shows the reference spectra of the USGS spectral library that matched the raw spectrum of lepidolite (Figure 5-a), petalite (Figure 5-b, -c), and spodumene (Figure 5-b). In the future, it would be important to assess the influence of the chosen matching algorithm in the spectral match results. Perhaps, a Li-mineral dedicated method could be developed using machine learning techniques.

Finally, the mean spectra of each Li bearing mineral were visually compared with the correspondent spectra of the CPRM spectral library. The same diagnostic features of clay minerals are present in the petalite and spodumene samples of the CPRM database. However, the lepidolite from the Fregeneda-Almendra area presents deeper H_2O features, while the spodumene does not show any of the iron absorption features that seem to be very common in the CPRM samples.

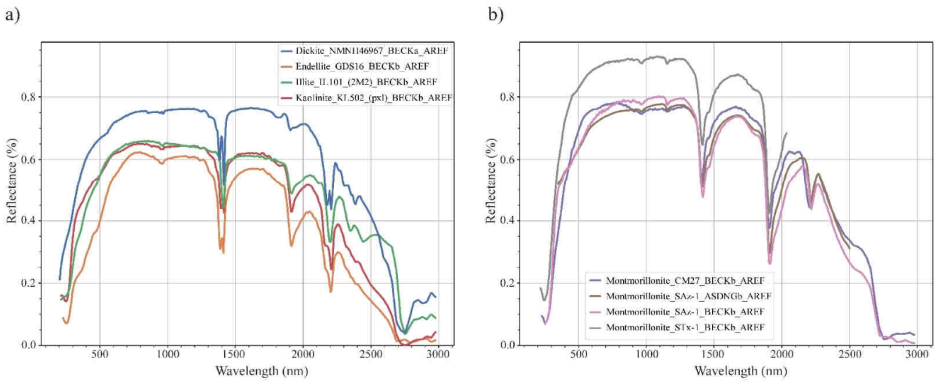

Downloaded From: https://www.spiedigitallibrary.org/conference-proceedings-of-spie on 20 Sep 2020
Terms of Use: https://www.spiedigitallibrary.org/terms-of-use

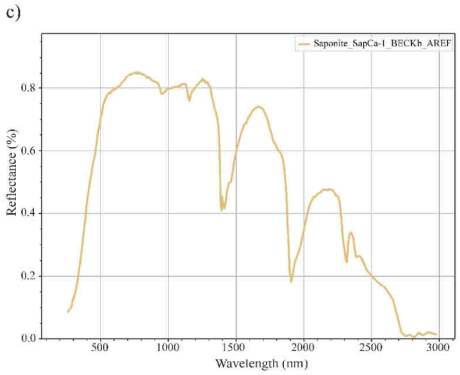

Figure 5. Reference spectra extracted from the USGS spectral library [2]. These spectra represent the top 5 highest-rating spectral matches with the lepidolite (a), petalite (b and c) and spodumene (b) from the Fregeneda-Almendra area.

4. CONCLUSIONS

In this study, a characterization of three different Li bearing minerals (lepidolite, petalite, and spodumene) was made through laboratory spectral measurements. It was only possible to discriminate lepidolite based on its spectral signature since the spectra obtained for spodumene and petalite were very similar. The analysis and interpretation of the results indicate that both the petalite and spodumene from the Fregeneda-Almendra area present absorption features typical of clay minerals such as smectite (characteristically montmorillonite) and illite, or a combination between both. No diagnostic features of these two Li bearing minerals were identified at this stage. The presence of clays' diagnostic features is also verified in samples of corresponding minerals in other spectral libraries. Taking this into account, all the objectives delineated for this work were accomplished.

Although detailed geological studies are needed to fully understand the obtained results, namely petrographic and geochemical analysis, this work may represent a relevant contribution to the field of spectroscopy studies of Li bearing minerals. The results highlight the difficulty to spectrally discriminate petalite and spodumene because they constantly show signs of alteration minerals. This could also difficult the discrimination of Li bearing minerals from clays through satellite remote sensing. Future studies will include spectral measurements of Li bearing minerals' alteration products currently being characterized using X-ray diffraction (XRD).

ACKNOWLEDGEMENTS

The authors would like to thank the financial support provided by FCT– Fundação para a Ciência e a Tecnologia, I.P., with the ERA-MIN/0001/2017 – LIGHTS project. The work was also supported by National Funds through the FCT project UIDB/04683/2020 - ICT (Institute of Earth Sciences). Joana Cardoso-Fernandes is financially supported within the compass of a Ph.D. Thesis, ref. SFRH/BD/136108/2018, by national funds from MCTES through FCT, and co-financed by the European Social Fund (ESF) through POCH – Programa Operacional Capital Humano. The Spanish Ministerio de Ciencia, Innovacion y Universidades (Project RTI2018-094097-B-100, with ERDF funds) and the University of the Basque Country (UPV/EHU) (grant GIU18/084) also contributed economically. Odile Barrès is thanked for the help handling the spectroradiometer at Université de Lorraine (France).

Downloaded From: https://www.spiedigitallibrary.org/conference-proceedings-of-spie on 20 Sep 2020
Terms of Use: https://www.spiedigitallibrary.org/terms-of-use

REFERENCES

[1] J. Cardoso-Fernandes, A. C. Teodoro, A. Lima, M. Perrotta, and E. Roda-Robles, "Detecting Lithium (Li) Mineralizations from Space: Current Research and Future Perspectives," Applied Sciences, 10(5), 1785 (2020).
[2] R. F. Kokaly, R. N. Clark, G. A. Swayze, K. E. Livo, T. M. Hoefen, N. C. Pearson, R. A. Wise, W. M. Benzel, H. A. Lowers, R. L. Driscoll, and A. J. Klein, [USGS Spectral Library Version 7], Reston, VA (2017).
[3] S. K. Meerdink, S. J. Hook, D. A. Roberts, and E. A. Abbott, "The ECOSTRESS spectral library version 1.0," Remote Sensing of Environment, 230, 111196 (2019).
[4] M. A. C. Costa, M. M. Perrotta, T. G. Melo, and B. Turra, "Estudos Espectrais", [Avaliação do potencial do lítio no Brasil: área do Médio Rio Jequitinhonha, Nordeste de Minas Gerais: texto explicativo e mapas], V. J. C. Paes, L. D. Santos, M. F. Tedeschi and L. M. Betiollo, Ed., CPRM, Belo Horizonte, 276 (2016).
[5] J. Cardoso-Fernandes, A. C. Teodoro, and A. Lima, "Remote sensing data in lithium (Li) exploration: A new approach for the detection of Li-bearing pegmatites," International Journal of Applied Earth Observation and Geoinformation, 76, 10-25 (2019).
[6] J. Cardoso-Fernandes, A. C. Teodoro, A. Lima, and E. Roda-Robles, "Evaluating the performance of support vector machines (SVMs) and random forest (RF) in Li-pegmatite mapping: preliminary results." 11156.
[7] J. Cardoso-Fernandes, A. C. Teodoro, A. Lima, and E. Roda-Robles, "Semi-Automatization of Support Vector Machines to Map Lithium (Li) Bearing Pegmatites," Remote Sensing, 12(14), 2319 (2020).
[8] R. Vieira, [Aplitopegmatitos com elementos raros da região entre Almendra (V.N. de Foz Côa) e Barca d'Alva (Figueira de Castelo Rodrigo). Campo aplitopegmatítico da Fregeneda- Almendra], PhD thesis, Faculdade de Ciências da Universidade do Porto, Porto, XXVI, 273 (2010).
[9] E. Roda-Robles, A. Pesquera, F. Velasco, and F. Fontan, "The granitic pegmatites of the Fregeneda area (Salamanca, Spain): characteristics and petrogenesis," Mineral. Mag., 63(4), 535–558 (1999).
[10] J. C. S. d. Costa, [Notícia sobre uma carta geológica do Buçaco, de Nery Delgado], Serviços Geológicos de Portugal, Lisboa (1950).
[11] I. Pereira, R. Dias, T. Bento dos Santos, and J. Mata, "Exhumation of a migmatite complex along a transpressive shear zone: inferences from the Variscan Juzbado–Penalva do Castelo Shear Zone (Central Iberian Zone)," Journal of the Geological Society, 174(6), 1004 (2017).
[12] A. F. d. Silva, and M. L. Ribeiro, [Notícia Explicativa da folha 15-A Vila Nova de Foz Côa], Serviços Geológicos de Portugal, Lisboa (1991).
[13] A. F. d. Silva, and M. L. Ribeiro, [Notícia Explicativa da folha 15-B Freixo de Espada à Cinta], Instituto Geológico e Mineiro, Lisboa (1994).
[14] F. Menges, "Spectragryph - optical spectroscopy software, Version 1.2.14," 2020, <http://www.effemm2.de/spectragryph/>
[15] C. Therien, "Welcome to the PySptools Documentation," <https://pysptools.sourceforge.io/> (22 July 2020)
[16] F. Menges, "Functions of the Identify ribbon," 2019, <https://www.effemm2.de/spectragryph/about_help_manual_identify.html> (10 August 2020)
[17] R. N. Clark, "Spectroscopy of rocks and minerals and principles of spectroscopy: Chapter 1", [Remote Sensing for the Earth Sciences: Manual of Remote Sensing,], R. A. Ryerson, Ed., John Wiley & Sons, Inc., (1999).
[18] G. R. Hunt, and J. W. Salisbury, "Visible and near-infrared spectra of minerals and rocks: I Silicate minerals," Modern Geology, 1, 283-300 (1970).
[19] R. N. Clark, T. V. V. King, M. Klejwa, G. A. Swayze, and N. Vergo, "High spectral resolution reflectance spectroscopy of minerals," Journal of Geophysical Research: Solid Earth, 95(B8), 12653-12680 (1990).
[20] J. L. C. Naleto, M. M. Perrotta, F. G. d. Costa, and C. R. d. Souza Filho, "Point and imaging spectroscopy investigations on the Pedra Branca orogenic gold deposit, Troia Massif, Northeast Brazil: Implications for mineral exploration in amphibolite metamorphic-grade terrains," Ore Geology Reviews, 107, 283-309 (2019).
[21] K. M. Scott, and K. Yang, [Spectral reflectance studies of white micas], CSIRO Division of Exploration and Mining, (1997), <ftp://ftp.arrc.csiro.au/arrc/AMIRA%20P435%20Project%20Reports/Emr439r%20White%20Mica.pdf> (31 July 2020)
[22] G. R. Hunt, and R. P. Ashley, "Spectra of altered rocks in the visible and near infrared," Economic Geology, 74(7), 1613-1629 (1979).

Downloaded From: https://www.spiedigitallibrary.org/conference-proceedings-of-spie on 20 Sep 2020
Terms of Use: https://www.spiedigitallibrary.org/terms-of-use

I.3. Conference abstracts and other publications

Detecting Lithium Mineralizations from Space

Subjects: Space Science

Submitted by: Joana Cardoso-Fernandes

Definition

Optical and thermal remote sensing data have been an important tool in geological exploration for certain deposit types. However, the present economic and technological advances demand the adaptation of the remote sensing data and image processing techniques to the exploration of other raw materials like lithium (Li). A review of the application studies and developments in this field was also made. The addressed topics include: (i) achievements made in Li exploration using remote sensing methods; (ii) the main weaknesses of the approaches; (iii) how to overcome these difficulties; and (iv) the expected research perspectives. We expect that the number of studies concerning this topic will increase in the near future and that remote sensing will become an integrated and fundamental tool in Li exploration.

1. Introdcution

Optical and thermal remote sensing data, namely satellite-acquired images, have been an important tool in geological exploration allowing to target exploration areas for more than four decades. The major contribution that remote sensing offers to mineral exploration was reviewed in several works dedicated to this topic [1][2][3][4][5]: it provides information in a fairly quick, inexpensive, and non-intrusive way, which favors mining and exploration companies especially in inaccessible remote areas. However, Rajesh [3], in an overview of the use of remote sensing and Geographic Information Systems (GIS) in mineral exploration, points out the difficulty of directly pinpointing mineralizations using only remote sensing data, highlighting the importance of the integration with other types of geological data.

Sabins [6], in one of the first reviews about the types of data and image processing methods for mineral exploration, describes two main approaches to target mineral deposits: (i) structural and lithological mapping; and (ii) hydrothermal alteration mapping. Later, Rajesh [3] proposed three approaches: (i) lithological mapping; (ii) structural mapping; and (iii) alteration mapping. These approaches have been applied since the 1970s to identify very distinct types of mineral deposits. The more common applications include porphyry copper [7][8][9][10][11][12][13][14][15][16][17] and gold [18][19][20][21][22][23][24][25][26][27][28] deposits. Other applications may include: iron ore deposits [19],[29][30][31][32], volcanogenic massive sulfide ore (VMS) deposits [33][34][35], several skarn-hosted deposits [36][37][38][39], chromite deposits [40][41][42][43], uranium deposits [39],[44], rare earth elements (REE) exploration[36][45], brine and evaporite deposits [46][47], porphyry molybdenum deposits [48][49], zinc-lead (Zn-Pb) deposits [50], diamond [51] and bauxite exploration [52].

Regarding the types of data used, multispectral products, namely Landsat and Advanced Spaceborne Thermal Emission and Reflection Radiometer (ASTER) sensor imagery, played an important part in geological remote sensing [4],[5][53]. Abrams and Yamaguchi [54] reviewed ASTER's contributions to mineral exploration and lithological mapping. The success of the ASTER sensor in geological exploration was mainly due to a higher spectral resolution in the short-wave infrared (SWIR) and thermal infrared (TIR), specially designed for geological applications, which improved its lithological and mineral mapping capabilities, particularly in the identification of alteration minerals [4][55][54],[55]. The importance of TIR (including ASTER's TIR subsystem) in the discrimination of minerals and rocks was revised by Ninomiya and Fu [55]. These authors highlight several studies in which the TIR region was fundamental for mineral discrimination, namely where silicate minerals occur, and reviewed the spectral indices proposed for lithological mapping using ASTER-TIR data. Nonetheless, the advent of hyperspectral remote sensing allowed the direct identification and quantification of specific minerals which represented a key contribution to mineral exploration [3][53]. Cudahy [4] in a review on mineral mapping projects for exploration led by Commonwealth Scientific and Industrial Research Organization (CSIRO) in Australia, pointed out that hyperspectral remote sensing can be less popular among exploration companies because of limited spatial coverage, the relatively high-cost of quality datasets, and the inherent complexity of hyperspectral data.

2. Influence and application

Despite the successful application of different types of remote sensing data to distinct mineral deposits, the current growing economic and technological advances, which rely on other mineral commodities, highlights the need to use and adapt remote sensing data and image processing techniques on new deposit types. Nowadays, green technologies, like electric vehicles, represent an important sector of the economy [56] and lithium (Li) has become a critical metal to the green-power industry [57][58]. However, Li exploration with the resource of remote sensing data and techniques represents an emergent field, with several difficulties and unknown possibilities. Taking this into account, this review aims at (i) providing information about what can be accomplished in Li exploration using remote sensing methods; (ii) identifying the main difficulties associated with this kind of deposits; and (iii) providing insights on how to overcome these difficulties as well as future research perspectives. This paper presents the first summary of the developments made in the field of remote sensing applied to Li exploration and we consider it to be timely and appropriate due to the high global demand of this metal to the production of Li-ion batteries [58]. Additionally, this review can help to promote new applications and to solve new exploration problems.

In general, past application studies relied on four distinct approaches: (i) geobotanical mapping; (ii) lithological mapping; (iii) mineral alteration mapping; and (iv) Li minerals/Li pegmatite discrimination. Different types of satellite products with distinct characteristics were employed as well as diverse image processing algorithms ranging from simple logical or mathematical operations (band ratios) to more evolved and complex algorithms like machine learning algorithms.

Despite the early attempt to target Li mineralizations with the launch of the Landsat missions, there is an unequivocal exponential growth on the publication numbers in the last decades. Nonetheless, since it still is an emergent field, the studies are limited to a small number of research groups, mainly based in Europe. However, considering the market demand for this raw material, we expect that many other studies will flourish in the near future all around the globe.

References

1. Stefan Saradeth; Thomas Weißmann; AQUIFER – Remote Sensing as Support for the Management of Internationally Shared Transboundary Aquifers in Africa. *The Future of Drylands* **2008**, *null*, 217-228, 10.1007/978-1-4020-6970-3_26.
2. Meer, V.D. Bakker validated surface mineralogy from high-spectral resolution remote sensing: A review and a novel approach applied to gold exploration using AVIRIS data. Terra Nova 1998, 10, 112–119.
3. H.M. Rajesh; Application of remote sensing and GIS in mineral resource mapping-An overview. *Journal of Mineralogical and Petrological Sciences* **2004**, *99*, 83-103, 10.2465/jmps.99.83.
4. Tom Cudahy; Mineral Mapping for Exploration: An Australian Journey of Evolving Spectral Sensing Technologies and Industry Collaboration. *Geosciences* **2016**, *6*, 52, 10.3390/geosciences6040052.
5. Rejith Rajan Girija; Sundararajan Mayappan; Mapping of mineral resources and lithological units: a review of remote sensing techniques. *International Journal of Image and Data Fusion* **2019**, *10*, 79-106, 10.1080/19479832.2019.1589585.
6. Floyd F Sabins; Remote sensing for mineral exploration. *Ore Geology Reviews* **1999**, *14*, 157-183, 10.1016/s0169-1368(99)00007-4.
7. Maliheh Abbaszadeh; Ardeshir Hezarkhani; Enhancement of hydrothermal alteration zones using the spectral feature fitting method in Rabor area, Kerman, Iran. *Arabian Journal of Geosciences* **2011**, *6*, 1957-1964, 10.1007/s12517-011-0495-0.
8. Charlotte A. Bishop; Jian Guo Liu; Philippa Mason; Hyperspectral remote sensing for mineral exploration in Pulang, Yunnan Province, China. *International Journal of Remote Sensing* **2011**, *32*, 2409-2426, 10.1080/01431161003698336.
9. Inés Di Tommaso; Nora Rubinstein; Hydrothermal alteration mapping using ASTER data in the Infiernillo porphyry deposit, Argentina. *Ore Geology Reviews* **2007**, *32*, 275-290, 10.1016/j.oregeorev.2006.05.004.
10. Ehsan Farahbakhsh; Hodjat Shirmard; Abbas Bahroudi; Taymor Eslamkish; Fusing ASTER and QuickBird-2 Satellite Data for Detailed Investigation of Porphyry Copper Deposits Using PCA; Case Study of Naysian Deposit, Iran. *Journal of the Indian Society of Remote Sensing* **2016**, *44*, 525-537, 10.1007/s12524-015-0516-7.
11. Mahdieh Hosseinjanizadeh; Majid H. Tangestani; Mapping alteration minerals using sub-pixel unmixing of ASTER data in the Sarduiyeh area, SE Kerman, Iran. *International Journal of Digital Earth* **2011**, *4*, 487-504, 10.1080/17538947.2010.550937.
12. Mahdieh Hosseinjanizadeh; Mehdi Honarmand; A remote sensing-based discrimination of high- and low-potential mineralization for porphyry copper deposits; a case study from Dehaj–Sarduiyeh copper belt, SE Iran. *European Journal of Remote Sensing* **2017**, *50*, 332-342, 10.1080/22797254.2017.1328646.
13. Mahdieh Hosseinjanizadeh; Majid H. Tangestani; Francisco Velasco Roldán; Iñaki Yusta; Sub-pixel mineral mapping of a porphyry copper belt using EO-1 Hyperion data. *Advances in Space Research* **2014**, *53*, 440-451, 10.1016/j.asr.2013.11.029.
14. Amin Beiranvnd Pour; M. Hashim; Identification of hydrothermal alteration minerals for exploring of porphyry copper deposit using ASTER data, SE Iran. *Journal of Asian Earth Sciences* **2011**, *42*, 1309-1323, 10.1016/j.jseaes.2011.07.017.
15. Amin Beiranvand Pour; M. Hashim; Hydrothermal alteration mapping from Landsat-8 data, Sar Cheshmeh copper mining district, south-eastern Islamic Republic of Iran. *Journal of Taibah University for Science* **2015**, *9*, 155-166, 10.1016/j.jtusci.2014.11.008.

16. Morteza Safari; Abbas Maghsoudi; Amin Beiranvand Pour; Application of Landsat-8 and ASTER satellite remote sensing data for porphyry copper exploration: a case study from Shahr-e-Babak, Kerman, south of Iran. *Geocarto International* **2017**, *33*, 1186-1201, 10.1080/10106049.2017.1334834.
17. Nannan Zhang; Kefa Zhou; Identification of hydrothermal alteration zones of the Baogutu porphyry copper deposits in northwest China using ASTER data. *Journal of Applied Remote Sensing* **2017**, *11*, 15016, 10.1117/1.jrs.11.015016.
18. Reda Amer; Timothy Kusky; Ahmed El Mezayen; Remote sensing detection of gold related alteration zones in Um Rus area, Central Eastern Desert of Egypt. *Advances in Space Research* **2012**, *49*, 121-134, 10.1016/j.asr.2011.09.024.
19. Andrea Ciampalini; Francesca Garfagnoli; Benedetta Antonielli; Sandro Moretti; Gaia Righini; Remote sensing techniques using Landsat ETM+ applied to the detection of iron ore deposits in Western Africa. *Arabian Journal of Geosciences* **2012**, *6*, 4529-4546, 10.1007/s12517-012-0725-0.
20. Islam Abou El-Magd; Hassan Mohy; Fawzy Basta; Application of remote sensing for gold exploration in the Fawakhir area, Central Eastern Desert of Egypt. *Arabian Journal of Geosciences* **2014**, *8*, 3523-3536, 10.1007/s12517-014-1429-4.
21. Safwat Gabr; Abduwasit Ghulam; Timothy M. Kusky; Detecting areas of high-potential gold mineralization using ASTER data. *Ore Geology Reviews* **2010**, *38*, 59-69, 10.1016/j.oregeorev.2010.05.007.
22. Safwat Gabr; Safaa M. Hassan; Mohamed F. Sadek; Prospecting for new gold-bearing alteration zones at El-Hoteib area, South Eastern Desert, Egypt, using remote sensing data analysis. *Ore Geology Reviews* **2015**, *71*, 1-13, 10.1016/j.oregeorev.2015.04.021.
23. Safaa M. Hassan; T. M. Ramadan; Mapping of the late Neoproterozoic Basement rocks and detection of the gold-bearing alteration zones at Abu Marawat-Semna area, Eastern Desert, Egypt using remote sensing data. *Arabian Journal of Geosciences* **2014**, *8*, 4641-4656, 10.1007/s12517-014-1562-0.
24. Lei Liu; Jun Zhou; Ling Han; Xinliang Xu; Mineral mapping and ore prospecting using Landsat TM and Hyperion data, Wushitala, Xinjiang, northwestern China. *Ore Geology Reviews* **2017**, *81*, 280-295, 10.1016/j.oregeorev.2016.10.007.
25. Masoud Moradi; Sedigheh Basiri; Ali Kananian; Keivan Kabiri; Fuzzy logic modeling for hydrothermal gold mineralization mapping using geochemical, geological, ASTER imageries and other geo-data, a case study in Central Alborz, Iran. *Earth Science Informatics* **2014**, *8*, 197-205, 10.1007/s12145-014-0151-9.
26. Zhang, X.; Pazner, M.; Duke, N. Lithologic and mineral information extraction for gold exploration using ASTER data in the south Chocolate Mountains (California). ISPRS J. Photogramm. Remote Sens. 2007, 62, 271–282.
27. Basem Zoheir; Controls on lode gold mineralization, Romite deposit, South Eastern Desert, Egypt. *Geoscience Frontiers* **2012**, *3*, 571-585, 10.1016/j.gsf.2012.03.003.
28. Alvaro Crosta; Carlos Roberto Souza Filho; F. Azevedo; C. Brodie; Targeting key alteration minerals in epithermal deposits in Patagonia, Argentina, using ASTER imagery and principal component analysis. *International Journal of Remote Sensing* **2003**, *24*, 4233-4240, 10.1080/0143116031000152291.
29. Mohand Bersi; Hakim Saibi; Moulley Charaf Chabou; Aerogravity and remote sensing observations of an iron deposit in Gara Djebilet, southwestern Algeria. *Journal of African Earth Sciences* **2016**, *116*, 134-150, 10.1016/j.jafrearsci.2016.01.004.
30. Diego Fernando Ducart; Adalene Silva; Catarina Labouré Bemfica Toledo; Luciano Mozer De Assis; Mapping iron oxides with Landsat-8/OLI and EO-1/Hyperion imagery from the Serra Norte iron deposits in the Carajás Mineral Province, Brazil. *Brazilian Journal of Geology* **2016**, *46*, 331-349, 10.1590/2317-4889201620160023.
31. P. Duuring; S. G. Hagemann; Y. Novikova; T. Cudahy; Carsten Laukamp; Targeting Iron Ore in Banded Iron Formations Using ASTER Data: Weld Range Greenstone Belt, Yilgarn Craton, Western Australia. *Economic Geology* **2012**, *107*, 585-597, 10.2113/econgeo.107.4.585.
32. Sankaran Rajendran; A. Thirunavukkarasu; G. Balamurugan; K. Shankar; Discrimination of iron ore deposits of granulite terrain of Southern Peninsular India using ASTER data. *Journal of Asian Earth Sciences* **2011**, *41*, 99-106, 10.1016/j.jseaes.2011.01.004.
33. Byron R. Berger; Trude V. V. King; Laurie C. Morath; Jeffrey Phillips; Utility of High-Altitude Infrared Spectral Data in Mineral Exploration: Application to Northern Patagonia Mountains, Arizona. *Economic Geology* **2003**, *98*, 1003-1018, 10.2113/gsecongeo.98.5.1003.
34. F. Van Der Meer; M. Vazquez-Torres; P. M. Van Dijk; Spectral characterization of ophiolite lithologies in the Troodos Ophiolite complex of Cyprus and its potential in prospecting for massive sulphide deposits. *International Journal of Remote Sensing* **1997**, *18*, 1245-1257, 10.1080/014311697218395.
35. Gongwen Wang; Wenhui Du; E. J. M. Carranza; Remote sensing and GIS prospectivity mapping for magmatic-hydrothermal base- and precious-metal deposits in the Honghai district, China. *Journal of African Earth Sciences* **2017**, *128*, 97-115, 10.1016/j.jafrearsci.2016.06.020.
36. Lawrence C Rowan; John C Mars; Lithologic mapping in the Mountain Pass, California area using Advanced Spaceborne Thermal Emission and Reflection Radiometer (ASTER) data. *Remote Sensing of Environment* **2003**, *84*, 350-366, 10.1016/s0034-4257(02)00127-x.
37. Nazi Mazhari; Azadeh Malekzadeh Shafaroudi; Majid Ghaderi; Detecting and mapping different types of iron mineralization in Sangan mining region, NE Iran, using satellite image and airborne geophysical data. *Geosciences Journal* **2017**, *21*, 137-148, 10.1007/s12303-016-0018-9.

38. Yuanjin Xu; Jianguo Chen; Pengyan Meng; Detection of alteration zones using hyperspectral remote sensing data from Dapingliang skarn copper deposit and its surrounding area, Shanshan County, Xinjiang Uygur autonomous region, China. *Journal of Visual Communication and Image Representation* **2019**, *58*, 67-78, 10.1016/j.jvcir.2018.11.032.
39. Rodrigo Salles; Carlos Roberto Souza Filho; Tom Cudahy; Luiz E. Vicente; Lena Virgínia Soares Monteiro; Hyperspectral remote sensing applied to uranium exploration: A case study at the Mary Kathleen metamorphic-hydrothermal U-REE deposit, NW, Queensland, Australia. *Journal of Geochemical Exploration* **2017**, *179*, 36-50, 10.1016/j.gexplo.2016.07.002.
40. Othman, A.; Gloaguen, R. Improving Lithological Mapping by SVM classification of spectral and morphological features: The Discovery of a new chromite body in the mawat ophiolite complex (Kurdistan, NE Iraq). Remote Sens. 2014, 6, 6867–6896.
41. Alireza Eslami; Majid Ghaderi; Sankaran Rajendran; Amin Beiranvand Pour; M. Hashim; Integration of ASTER and landsat TM remote sensing data for chromite prospecting and lithological mapping in Neyriz ophiolite zone, south Iran. *Resource Geology* **2015**, *65*, 375-388, 10.1111/rge.12076.
42. Mohsen Pournamdari; M. Hashim; Detection of chromite bearing mineralized zones in Abdasht ophiolite complex using ASTER and ETM+ remote sensing data. *Arabian Journal of Geosciences* **2013**, *7*, 1973-1983, 10.1007/s12517-013-0927-0.
43. Sankaran Rajendran; Salah Al-Khirbash; Bernhard Pracejus; Sobhi Nasir; Amani Humaid Al-Abri; Timothy Kusky; Abduwasit Ghulam; ASTER detection of chromite bearing mineralized zones in Semail Ophiolite Massifs of the northern Oman Mountains: Exploration strategy. *Ore Geology Reviews* **2012**, *44*, 121-135, 10.1016/j.oregeorev.2011.09.010.
44. Khaled S. Gemail; Naglaa Adb Elrahman; B. M. Ghiath; R. N. Aziz; Integration of ASTER and airborne geophysical data for mineral exploration and environmental mapping: a case study, Gabal Dara, North Eastern Desert, Egypt. *Environmental Earth Sciences* **2016**, *75*, ., 10.1007/s12665-016-5368-0.
45. Robert Zimmermann; Melanie Brandmeier; Louis Andreani; Kombada Mhopjeni; Richard Gloaguen; Remote Sensing Exploration of Nb-Ta-LREE-Enriched Carbonatite (Epembe/Namibia). *Remote Sensing* **2016**, *8*, 620, 10.3390/rs8080620.
46. Sabins, F.F.; Miller, R.M. Resource assessment—Salar Uyuni and vicinity. In Proceedings of the Tenth Thematic Conference on Geologic Remote Sensing (Ann Arbor, MI, Environmental Research Institute of Michigan), San Antonio, TX, USA, 9–12 May 1994; pp. 9–12.
47. N. Serkan Öztan; Mehmet Lütfi Süzen; Mapping evaporate minerals by ASTER. *International Journal of Remote Sensing* **2011**, *32*, 1651-1673, 10.1080/01431160903586799.
48. Enton Bedini; Mineral mapping in the Kap Simpson complex, central East Greenland, using HyMap and ASTER remote sensing data. *Advances in Space Research* **2011**, *47*, 60-73, 10.1016/j.asr.2010.08.021.
49. Lei Liu; Jun Zhou; Fang Yin; Min Feng; Bing Zhang; The reconnaissance of mineral resources through aster data-based image processing, interpreting and ground inspection in the Jiafushaersu area, West Junggar, China. *Journal of Earth Science* **2014**, *25*, 397-406, 10.1007/s12583-014-0423-9.
50. Amin Beiranvand Pour; Tae-Yoon S. Park; Yongcheol Park; Jong Kuk Hong; Basem Zoheir; Biswajeet Pradhan; Iman Ayoobi; M. Hashim; Application of Multi-Sensor Satellite Data for Exploration of Zn–Pb Sulfide Mineralization in the Franklinian Basin, North Greenland. *Remote Sensing* **2018**, *10*, 1186, 10.3390/rs10081186.
51. Kruse, F.A.; Boardman, J.W. Characterization and mapping of kimberlites and related diatremes using hyperspectral remote sensing. In Proceedings of the 2000 IEEE Aerospace Conference. Proceedings (Cat. No.00TH8484), Big Sky, MT, USA, 25 March 2000; Volume 3, pp. 299–304.
52. P. Sheik Mujabar; S. Dajkumar; Mapping of bauxite mineral deposits in the northern region of Saudi Arabia by using Advanced Spaceborne Thermal Emission and Reflection Radiometer satellite data. *Geo-spatial Information Science* **2018**, *22*, 35-44, 10.1080/10095020.2018.1530857.
53. Freek D. Van Der Meer; Harald Van Der Werff; Frank J.A. Van Ruitenbeek; Christoph Hecker; Wim H. Bakker; Marleen Noomen; Mark Van Der Meijde; E. J. M. Carranza; J. Boudewijn De Smeth; Tsehaie Woldai; et al. Multi- and hyperspectral geologic remote sensing: A review. *International Journal of Applied Earth Observation and Geoinformation* **2012**, *14*, 112-128, 10.1016/j.jag.2011.08.002.
54. Michael Abrams; Y. Yamaguchi; Twenty Years of ASTER Contributions to Lithologic Mapping and Mineral Exploration. *Remote Sensing* **2019**, *11*, 1394, 10.3390/rs11111394.
55. Ninomiya, Y.; Fu, B.; Thermal infrared multispectral remote sensing of lithology and mineralogy based on spectral properties of materials. *Ore Geol. Rev.* **2019**, *108*, 54–72.
56. Christmann, P.; Gloaguen, E.; Labbé, J.-F.; Melleton, J.; Piantone, P. Chapter 1—Global lithium resources and sustainability issues. In Lithium Process Chemistry; Chagnes, A., Świątowska, J., Eds.; Elsevier: Amsterdam, The Netherlands, 2015; pp. 1–40.
57. Camille Grosjean; Pamela Herrera Miranda; Marion Perrin; Philippe Poggi; Assessment of world lithium resources and consequences of their geographic distribution on the expected development of the electric vehicle industry. *Renewable and Sustainable Energy Reviews* **2012**, *16*, 1735-1744, 10.1016/j.rser.2011.11.023.
58. Arrobas, D.L.P.; Hund, K.L.; Mccormick, M.S.; Ningthoujam, J.; Drexhage, J.R. The Growing Role of Minerals and Metals for a Low Carbon Future; The World Bank: Washington, DC, USA, 2017. [Google Scholar]

Keywords

satellite data;image processing algorithms;pegmatite;brine;lithological mapping;mineral alteration mapping;geobotanical mapping

Retrieved from https://encyclopedia.pub/785

JORNADAS DO ICT
11 e 12 de fevereiro de 2021
Faculdade de Ciências da Universidade do Porto

Aplicação de Métodos para Identificação de Novos Depósitos de Pegmatitos LCT e NYF: GREENPEG um Projeto Europeu

Douglas Santos[1*], Ana Cláudia Teodoro[1,2], Alexandre Lima[1,2], Joana Cardoso-Fernandes[1,2]

[1] Departamento de Geociências, Ambiente e Ordenamento do Território, Faculdade de Ciências, Universidade do Porto, Porto, Portugal
[2] ICT (Instituto de Ciências da Terra) – Porto (Portugal)
[*]douglas.santos@fc.up.pt

Resumo

Os depósitos de pegmatitos, apesar de comuns na Europa, são um tipo de recurso pouco explorado. Tendo em vista o enorme potencial para se encontrar mais depósitos, o Projeto GREENPEG procura desenvolver ferramentas de prospeção inovadoras, competitivas e mais amigas do meio ambiente, para a prospeção de pegmatitos do tipo Lithium-Caesium-Tantalum (LCT) e Niobium-Yttrium-Fluorine (NYF).

Com o objetivo de identificar esses depósitos de pegmatitos, uma série de técnicas e tecnologias de deteção remota foram aplicadas. As técnicas de deteção remota que são aplicada no âmbito desta investigação podem ser divididas em quatro etapas: (i) seleção e aquisição de imagens de satélite e delimitação das áreas de estudo; (ii) processamento das imagens de satélite; (iii) aquisição de dados espectrorradiométricos das áreas de estudo; e (iv) Integração dos resultados dos metodologias anteriormente referidas para elaboração de mapas de prospeção.

Seis áreas de estudo foram determinadas para o projeto. Três delas são consideradas áreas principais: Leinster (Irlanda do Sul), Wolfsberg (Áustria) e Tysfjord (Noruega); e três áreas consideradas áreas de estudo adicionais: Adagói (Portugal), Valdeflórez (Espanha) e Kitee (Finlândia). As imagens de três satélites (Landsat 8– OLI e TIRS, Sentinel-2 MSI e Terra/ASTER) foram obtidas através do serviço Earth Explorer da USGS. Todas as imagens possuem cobertura de nuvens inferior a 10% e a menor cobertura vegetal possível.

O processamento das imagens de satélite, por sua vez, pode ser dividido em duas etapas: (i) Aplicação de abordagens convencionais de processamento de imagem (Combinações RGB (Red, Green, Blue), Band Ratios (BR) e Principal Component Analysis (PCA)) e; (ii) Aplicação de algoritmos de classificação de imagens mais avançados, baseados em técnicas de machine learning.

A combinação RGB é um método onde, três bandas são inseridas nos canais vermelho, verde ou azul para gerar imagens com diferentes combinações das unidades hidrotermais e litológicas das rochas. O BR, consiste na divisão de bandas com o objetivo de destacar diferenças espetrais específicas. Já a PCA corresponde a uma técnica estatística multivariada, usada para melhorar a identificação e separar certos tipos de assinaturas espetrais.

As etapas de aquisição de imagens de satélites e definição das áreas de estudo juntamente com a aplicação dos métodos convencionais do processamento de imagens, estão concluídos e, apesar de alguns resultados animadores, é percetível a necessidade de

aplicação métodos mais robustos, como algoritmos machine learning, para se obter melhores resultados. Esses métodos serão aplicados nas próximas etapas do projeto.

Palavras chave: Prospeção; Combinações RGB; Band Ratios; Principal Component Analysis; Machine Learning.

JORNADAS DO ICT
11 e 12 de fevereiro de 2021
Faculdade de Ciências da Universidade do Porto

Prospeção dos Pegmatitos de Muiane e Naipa (Moçambique) a partir de técnicas de Deteção Remota, usando imagens do sensor ASTER.

U. Gemusse[1,2*], Joana Cardoso-Fernandes[2], Douglas Santos[2], A.C. Teodoro[2], A. Lima[2]
[1] Faculdade de Ciências e Tecnologia, Universidade Licungo, PO Box 2025, Beira, Moçambique
[2] Instituto Ciências da Terra - Polo da Universidade do Porto e Departamento de Geociências, Ambiente e Ordenamento do Território, Faculdade de Ciências, Universidade do Porto, Rua do Campo Alegre 687, 4169-007 Porto, Portugal
[*]ugemusse@gmail.com

Resumo

Os pegmatitos alvos neste trabalho localizam-se na Província de Zambézia (Moçambique), distrito de Gilé. Pretendeu-se com este trabalho, demostrar o potencial da deteção remota na prospeção de filões pegmatíticos com minerais de lítio em Moçambique, através da análise de assinaturas espetrais, identificadas em imagens processadas do sensor ASTER, que possam indicar a presença de pegmatitos mineralizados através de um suporte Sistema de Informação Geográfica (SIG), usando o software ENVI 4.8.

As imagens de satélite usadas encontram-se disponíveis gratuitamente. Foram selecionadas imagens de várias séries, entre as que combinam menor cobertura de nuvens e com baixa cobertura de vegetação. Neste caso de estudo, usou-se a imagem ASTER de 27/05/2005, que satisfaz as condições anteriormente referidas. O pré-processamento envolveu a conversão de refletância no topo da atmosfara para refletância de superfície (correção atmosférica). As principais ações de campo, envolveram os seguintes pegmatitos: Naipa (3.703 km^2); Nuaparra (18.75 km^2) e Muiane (15.63 km^2), todos localizados no Complexo de Nampula, região de Alto Ligonha, uma subdivisão estratigráfica tectônica do Cinturão de Moçambique. Os métodos de processamento de imagem incluíram análise de componentes principais (ACP), combinações RGB (vermelho, verde, azul), razão de bandas, classificação supervisionada e algoritmos de machine learning. Esta combinação de técnicas permitiu prever a ocorrência de pegmatitos nessas regiões. As razões de bandas e combinações RGB e ACP propostas, permitiram a discriminação dos pegmatitos supostos portadores de Li das rochas encaixantes. Foram efetuadas amostragens dos pegmatitos de Muiane e Naipa e das suas rochas encaixantes para estudos espetrais e geoquímicos, nomeadamente utilizando um espetroradiómetro. Foram classificados 687 pixéis, para classe dos pegmatitos, usando Spectral Angle Mapping (SAM) com uma exatidão do utilizador (EU) de 97% e com uma exatidão produtor (EP) de 92%. Para o algoritmo Distância Mínima, a classe de Pegmatito apresentou 256 pixéis, atingindo uma EU de 100%, uma EP de 95,5% e um kappa de 1, significando que a classe de pegmatitos foi perfeitamente identificada, enquanto que para o algoritmo Máxima Verossimilhança, a classe Pegmatito apresentou 356 pixéis, uma EU de 97% e uma EP de 99,16%. Para o algoritmo Suporte Vetorial Machine (SVM), a classe Pegmatito apresentou 359 pixéis, com um erro de comissão de 1,10% e um erro de omissão de 2,18%.

Os resultados demostraram que a classe dos Pegmatitos aparece evidenciada em todas as técnicas aplicadas nesse trabalho. A informação obtida por deteção remota tem vindo a ser aplicada em diversos sectores de estudo e torna-se nesta fase relevante compreender qual a potencialidade dessa informação para Moçambique, mais especificamente, para os pegmatitos de Alto Ligonha.

Palavras-chave: Deteção remota, classificação de imagens, razão de bandas, ACP, Combinação RGB, assinaturas espectrais, pegmatitos.

Agradecimentos: U. Gemusse, beneficiou de uma Bolsa financiado pelo Instituto de Bolsas de Moçambique (IBE) no âmbito da bolsa de doutoramento com a referência D101/2016-2028. J. Cardoso-Fernandes agradece o suporte da FCT, através do programa regional NORTE 2020, para o desenvolvimento da tese de doutoramento, ref. SFRH/BD/136108/2018.Os autores agradecem a Agência Espacial Europeia (ESA) e os Serviços Geológicos norte americanos (USGS) pela disponibilidade das imagens orbitais multiespectrais utilizadas.

As Assinaturas Espectrais dos Minerais de Lítio do Campo Aplito-Pegmatítico de Fregeneda-Almendra

João Silva[1*], Joana Cardoso-Fernandes[1,2], Ana Claúdia Teodoro[1,2], Alexandre Lima[1,2]
[1] Faculdade de Ciências da Universidade do Porto
[2] Instituto de Ciências da Terra – Pólo Porto
*up201503357@fc.up.pt

Resumo

No decorrer da última década, a procura por tecnologias e energias ambientalmente mais amigáveis, levou ao aumento da procura por Lítio (Li), por esta razão, técnicas de deteção remota têm vindo a ser aplicadas na identificação de novos depósitos litiníferos. Com isto, para uma mais fácil identificação destes depósitos, existe a necessidade de se obter um maior conhecimento das assinaturas espectrais dos minerais de Li.

O campo aplito-pegmatítico de Fregeneda (Espanha)-Almendra (Portugal) constitui a área de estudo deste trabalho, sendo esta uma região onde se conhece a ocorrência de diversos minerais de Li (petalite, espodumena, lepidolite, zinnwaldite e montebrasite), associados a quatro diferentes tipos de filões aplito-pegmatíticos enriquecidos em Li (Roda et al., 1993; Roda et al., 1999; Vieira, 2010). Esta região encontra-se integrada na Zona Centro Ibérica (Farias et al., 1987; Julivert, 1972; Lotze, 1945), tendo como principais características a presença de formações metassedimentares autóctones, do pré-Mesozoico, intruídas por granitos Variscos (Dias et al., 2000; Martínez Catalán et al., 2004).

Um total de 25 amostras coletadas na área de estudo, em diferentes tipos de filões aplito-pegmatíticos enriquecidos em Li, foram estudas, resultando em 170 espetros medidos e analisados. Todas estas medições foram realizadas em um ambiente de luz controlada, através de uma lâmpada de halogénio (4.25 V, 1.06 A). O SR-6500 (Spectral Evolution, Inc.) foi o espetrorradiómetro utilizado no estudo, sendo este um aparelho com uma resolução espetral entre os 350 nm e os 2500 nm (VIS-NIR-SWIR).

Os resultados obtidos demonstraram grandes similaridades nas assinaturas espectrais da petalite e da espodumena, apresentando feições de absorção idênticas (~1412 nm, ~1910 nm, ~2206 nm). Um estudo mais minucioso destas assinaturas, mostrou que as feições de absorção apresentadas são diagnósticas para a presença de minerais de argila, do grupo da esmectite (Clark et al., 1990; Clark, 1999), nomeadamente montmorillonite. Feições típicas da ilite são também detetadas, sobretudo no espetro da espodumena, porém é percetível a dominância da montmorillonite. Também a lepidolite apresenta feições diagnósticas de minerais de argila, que associadas à presença de feições secundárias de Al-OH podem indicar características diagnósticas de micas brancas (Hunt and Salisbury, 1970; Scott and Yang, 1997; Naleto et al., 2019). Estas mesmas feições diagnósticas são as encontradas na assinatura espetral da zinnwaldite. A assinatura espetral da montebrasite, dos 1300 nm aos 2500 nm (SWIR), encontra-se intensamente marcada pela presença de feições de absorção, sendo que as principais zonas de absorção possíveis de detetar são distintas quando comparadas com as dos restantes minerais de Li estudados.

Na Figura 1 é possível observar a representação gráfica das assinaturas espectrais obtidas neste estudo.

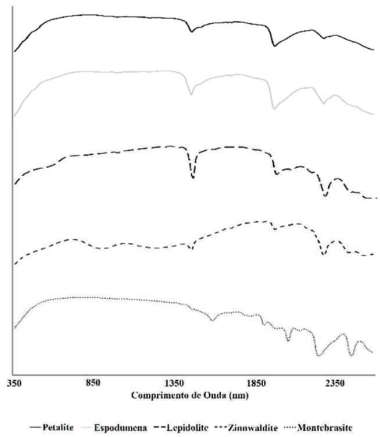

Figura 1 – Representação gráfica das assinaturas espetrais obtidas no estudo dos minerais de Li do campo aplito-pegmatítico de Fregeneda-Almendra.

Palavras chaves: Lítio, Petalite, Espodumena, Lepidolite, Assinatura Espetral

Referências bibliográficas

Clark R. M., King T. V. V., Klejwa M., Swayze G. A., and Vergo N., 1990. High spectral resolution reflectance spectroscopy of minerals. Journal of Geophysical Research: Solid Earth, 95(B8), 12653-12680.

Clark R. N., 1999. Spectroscopy of rocks and minerals and principles of spectroscopy: Chapter 1. Remote Sensing for the Earth Sciences: Manual of Remote Sensing. R. A. Ryerson, Ed., John Wiley & Sons, Inc.

Dias, G., Noronha, F., Ferreira, N., 2000. Variscan Plutonism in the Central Iberian Zone, Northern Portugal. Eurogranites 2000, Field Meeting, Guidebook. pp. 1–15.

Farias, P., Gallastegui, G., Gonzalez Lodeiro, F., Marquinez, J., Martin Parra, L.M., Martinez Catalan, J.R., Pablo Maciá, J.G. De & Rodriguez Fernandez, L.R., 1987. Aportaciones al conocimiento de la litoestratigrafia y estructura de Galícia Central. In: IX Reunião de Geologia do Oeste Peninsular, Porto, 1985. Mem. Mus. Labor. Miner. Geol. Fac. Ciênc. Univ. Porto, 1: 411-431.

Hunt, G.R., Salisbury, J.W., 1970. Visible and near-infrared spectra of minerals and rocks: I Silicate minerals. Modern Geology. 1, pp. 283–300.

Julivert, M., 1972. Mapa tectónico de la Península Ibérica y Baleares Escala 1:1.000.000. Ministerio de Industria y Energía, Servicio de Publicaciones, Madrid p 1 mapa.

Lotze, F., 1945. Zur gliederung der Varisziden der Iberischen Meseta. s.n. Berlin. pp. 15.

Martínez Catalán, J.R., Fernández-Suárez, J., Jenner, G.A., Belousova, E. and Díez Montes, A. 2004. Provenance constraints from detrital zircon U-Pb ages in the NW Iberian Massif: implications for Paleozoic plate configuration and Variscan evolution. Journal of the Geological Society, London, 161, 461-473.

Naleto J. L. C., Perrotta M. M., Costa F. G. and Souza Filho C. R., 2019. Point and imaging spectroscopy investigations on the Pedra Branca orogenic gold deposit, Troia Massif, Northeast Brazil: Implications for mineral exploration in amphibolite metamorphic-grade terrains. Ore Geology Reviews, 107, pp.283-309.

Roda, E., 1993. Distribución, Caracteristicas y Petrogenesis de las Pegmatitas de La Fregeneda (Salamanca). Tese de Doctoramento. UPV, Bilbau.

Roda, E., Pesquera, A., Velasco, F., Fontan, F., 1999. The granitic pegmatites of the Fregeneda area (Salamanca, Spain): characteristics and petrogenesis. Mineral. Mag. 63 (4), 535–558.

Scott, K.M., Yang, K., 1997. Spectral reflectance studies of white micas. Exploration and Mining Report 439R. CSIRO Division of Exploration and Mining, pp. 41.

Vieira, R., 2010. Aplitopegmatitos com elementos raros da região entre Almendra (V.N. de Foz Côa) e Barca d'Alva (Figueira de Castelo Rodrigo). Campo aplitopegmatítico da Fregeneda- Almendra. Tese de Doutoramento. Faculdade de Ciências da Universidade do Porto, Porto.

JORNADAS DO ICT
11 e 12 de fevereiro de 2021
Faculdade de Ciências da Universidade do Porto

Reflectance spectroscopy of minerals and rocks: a case study for lithological classification

Joana Cardoso-Fernandes[1*], Alexandre Lima[1], Ana Cláudia Teodoro[1], João Silva[1]
[1] Departamento de Geociências, Ambiente e Ordenamento do Território, Faculdade de Ciências, Universidade do Porto, Instituto de Ciências da Terra, Polo-Porto, Rua do Campo Alegre 4169-007 Porto, Portugal
[*]joana.fernandes@fc.up.pt

Abstract

Reflectance spectroscopy is a fundamental tool for remote lithological classification. Diagnostic absorption features allow for mineral identification and rock discrimination. This study concerns the use of reflectance spectroscopy to improve lithological classification in the Fregeneda-Almendra aplite-pegmatite field. The main aim is to highlight the potentials of this kind of non-destructive technique to obtain a quick understanding of rock composition and evolution. The mineral interpretations were based on reflectance spectra acquired in the 350-2500 nm region. Overall, it was possible to identify several of the rock-forming minerals: (i) white mica, mixtures of chlorite (dominant) and biotite, and quartz with fluid inclusions in samples from the Desejosa Formation of the Complexo Xisto-Grauváquico (CXG); (ii) white mica and biotite were also ubiquitous in granitoid samples, but the presence of phlogopite and the larger quantities of biotite allowed to distinguish the Chãs granodiorite from the Medas granite. In the case of lithium (Li)-pegmatites, the only Li-minerals undoubtedly identified were lepidolite and cookeite. White mica, quartz with fluid inclusions, sericite, and orthoclase (possibly containing ammonia) were also observed. Spodumene and petalite showed spectral signatures of illite and/or montmorillonite. Moreover, for each lithology, it was possible to identify the associated alteration minerals: (i) montmorillonite and a kandite group mineral (like kaolinite or halloysite) in granite samples; (ii) illite/montmorillonite and halloysite in granodiorite; (iii) kaolinite and illite/montmorillonite in Li-pegmatite. The collected spectra also allowed to readily distinguish iron oxides and to determine the iron oxidation state in several samples. Goethite was described for altered samples of granite, pegmatite, and CXG. Oppositely, fresh CXG samples are characterized by the presence of ferrous iron (Fe^{2+}) which corroborates that sample alteration led to oxidation and formation of ferric iron (Fe^{3+}). The spectra of fresh granite pointed to the coexistence of both oxidation states. Both fresh and altered granodiorite samples show the presence of ferrous iron. Finally, reflectance spectroscopy provided insightful interpretations regarding mica crystallinity degree and on white mica/chlorite composition. For example, the depth of the water feature allowed to distinguish illite from highly crystalline micas. Compositionally, white mica in CXG is consistently compatible with phengite, while micas from Li-pegmatites range from muscovite to paragonite. Granitoid samples show a muscovitic composition. Chlorites from CXG show intermediate compositions with both iron and magnesium. These results proved the reflectance spectroscopy potential not only to discriminate distinct lithologies in remote classification but also to promptly obtain mineralogical and crystallographic information.

Key words: Remote sensing; spectral library; absorption features; mineral composition; mineral crystallinity

Acknowledgments: The authors would like to thank the financial support provided by FCT– Fundação para a Ciência e a Tecnologia, I.P., with the ERA-MIN/0001/2017 – LIGHTS project, and also with the 869274 — GREENPEG — H2020-SC5-2018-2019-2020 project. The work was also supported by National Funds through the FCT project UIDB/04683/2020 - ICT (Institute of Earth Sciences). Joana Cardoso-Fernandes is financially supported within the compass of a Ph.D. Thesis, ref. SFRH/BD/136108/2018, by national funds from MCTES, through FCT, and co-financed by the European Social Fund (ESF) through POCH and NORTE 2020 regional program.

JORNADAS DO ICT
11 e 12 de fevereiro de 2021
Faculdade de Ciências da Universidade do Porto

Espectroscopia de Reflectância no Campo Aplito-Pegmatítico de Fregeneda-Almendra: Estudo das Assinaturas Espectrais dos Minerais de Lítio

João Silva[1*], Ana Cláudia Teodoro[1], Alexandre Lima[1], Joana Cardoso-Fernandes[1], Jean Cauzid[2]

[1] Departamento de Geociências, Ambiente e Ordenamento do Território, Faculdade de Ciências da Universidade do Porto, Instituto de Ciências da Terra – Pólo Porto, Rua Campo Alegre, Porto, Portugal
[2] Laboratoire GeoRessources, Université de Lorraine, CNRS, GeoRessources, F-54000 Nancy, France
*up201503357@fc.up.pt

Resumo

No decorrer dos últimos anos, diversas técnicas de deteção remota, como a espectroscopia de reflectância, têm vindo a ser praticadas no estudo e identificação de novos depósitos de Lítio (Li), possibilitando um mais rápido e menos dispendioso mapeamento deste recurso. Com a aplicação destas técnicas, surge a necessidade de um maior conhecimento das assinaturas espectrais dos vários minerais de Li, dado que são as suas características de absorção que os permitem identificar e mapear.

Atualmente, no campo aplito-pegmatítico de Fregeneda (Espanha)-Almendra (Portugal), encontram-se mapeados mais de 800 corpos aplito-pegmatíticos classificados em 11 diferentes tipos. Em 4 destes tipos, verifica-se a ocorrência de minerais de Li (petalite; espodumena; lepidolite; zinnwaldite; montebrasite). Para este estudo, foram analisadas 25 amostras de filões aplito-pegmatíticos enriquecidos em Li, tendo resultado em 170 espectros de reflectância medidos na região dos 350 nm aos 2500 nm, com os quais se procedeu ao estudo das assinaturas espectrais destes minerais.

As assinaturas espectrais obtidas para a petalite e espodumena, apresentam-se com 3 principais zonas de absorção (~1410 nm; ~1910 nm; ~2200 nm), correspondentes a feições de OH^-+H_2O, H_2O, e Al–OH, respetivamente, condizentes com características espectrais de minerais de argila do grupo da esmectite. Em ambas as assinaturas constata-se que é a feição de H_2O que manifesta maior profundidade, sugerindo assim, uma predominância de montmorilonite, o único mineral do grupo da esmectite que é conhecido por absorver água da atmosfera. Para além destas características, a espodumena apresenta ainda feições de Al-OH secundárias (~2346 nm; ~2437 nm), diagnósticas para a ilite. Desta forma, percebe-se que estas duas assinaturas estão intensamente marcadas pela presença de minerais de alteração, sendo difícil encontrar características próprias destes minerais de Li. A assinatura da lepidolite apresenta-se com as mesmas feições características de minerais de argila, contudo, nesta, é a feição de H_2O que manifesta menor profundidade. As feições de Al-OH secundárias estão também presentes, surgindo bem mais marcadas do que na espodumena. Deste modo, as feições exibidas pela lepidolite mostram características espectrais de micas brancas. A assinatura da zinnwaldite apresenta estas mesmas características da lepidolite, diferenciando-se pela presença de feições relativas a óxidos de ferro. A montebrasite é um mineral com propriedades discordantes das dos restantes minerais apresentados, e como tal, a sua assinatura surge também diferente das restantes. A comparação destas assinaturas com os espectros de referência das bibliotecas espectrais do USGS e ECOSTRESS, permitiram corroborar em pleno os resultados obtidos.

Palavras chave: Lítio, Petalite, Espodumena, Lepidolite, Assinatura Espectral

Agradecimentos: Os autores gostariam de agradecer o suporte financeiro concedido pelo projeto ERA-MIN/0001/2017 – LIGHTS.

EGU21-2364
https://doi.org/10.5194/egusphere-egu21-2364
EGU General Assembly 2021
© Author(s) 2021. This work is distributed under
the Creative Commons Attribution 4.0 License.

Petalite alteration products from the Bajoca pegmatite (Central Portugal): a multiapproach for lithium exploration

Joana Cardoso-Fernandes[1,2], Filipa Dias[1,2], Alexandre Lima[1,2], Maria Anjos Ribeiro[1,2], Mônica Perrotta[3], Encarnación Roda-Robles[4], and Ana Cláudia Teodoro[1,2]

[1]Department of Geosciences, Environment and Spatial Plannings, Faculty of Sciences, University of Porto , Porto, Portugal (joana.fernandes@fc.up.pt)

[2]Institute of Earth Sciences (ICT), Pole of University of Porto, Porto, Portugal

[3]Geology and Mineral Resources Board of Directors, Geological Survey of Brazil (CPRM), São Paulo, Brazil

[4]Department of Mineralogía y Petrología, University of País Vasco, Bilbao, Spain

Key hydrothermal or supergene alteration minerals are crucial in the remote detection of several mineral deposit types using satellite images. Hydrothermal metasomatic alteration of spodumene and petalite can form eucryptite, albite, K-feldspar and/or micas, and cookeite in more acidic conditions [1, 2]. Moreover, either hydrothermal or supergene alteration of petalite and spodumene lead to the formation of clay minerals like kaolinite, halloysite, pink montmorillonite, and greenish illite-montmorillonite aggregates [1, 3, 4].

This study aims at describing for the first time the petalite alteration products from the Bajoca pegmatite (Central Portugal, Fregeneda-Almendra pegmatite field). Field campaigns allowed to identify white to greenish alteration products with increasing alteration degree respectively, but often with a pseudomorphic character preserving the petalite shape and cleavage. Despite being exploited for more than two decades, hitherto such green clayey assemblage was not described. This alteration was not observed at the surface and is restricted to a sector in the base of the open-pit, with intense fracturing.

A multidisciplinary study was employed to characterize the alteration products through optical microscopy, XRD, SEM-EDS, and reflectance spectroscopy (350-2500 nm). Petrographic studies show that petalite alteration started along the cleavage, fractures, and crystal borders. Fine white mica and pale brown clays were observed in fractures. Compositional data and spectra obtained with SEM-EDS are compatible with white mica and montmorillonite. Eucryptite was also identified. More heavily altered samples show a complete pseudomorph replacement of petalite, widening of the cleavage and quartz precipitation, the formation of cookeite in close association with white mica, and pseudospherulitic illite filling voids. Locally, a later sericitization is observed superimposed on the previous alteration. The clay agglomerates analyzed with XRD consisted of quartz, illite, montmorillonite/nontronite association with occasional muscovite, albite, kaolinite, and orthoclase. The reflectance spectra show the presence of montmorillonite (ubiquitous), illite and/or white mica, and kaolinite (in two samples).

The results seem to indicate at least two stages of petalite alteration: one consistent with the formation of kaolinite in acidic conditions, and another in an alkaline environment that favored illite-montmorillonite [1]. Intense fracturing associated with a known fault-zone was key for fluid circulation. Further investigations are needed to establish the succession of the alteration stages and their relationship with the late-magmatic hydrothermal alteration of petalite to form albite, orthoclase, and eucryptite. Nonetheless, these findings will help to improve satellite detection of lithium-minerals.

Acknowledgment

The work was financial supported by FCT with the ERA-MIN/0001/2017–LIGHTS project, the UIDB/04683/2020–ICT project, and through Ph.D. Thesis, ref. SFRH/BD/136108/2018 and 2020.05534.BD (ESF, NORTE2020).

1. London, D. and D.M. Burt, Chemical models for lithium aluminosilicate stabilities in pegmatites and granites. American Mineralogist, 1982. 67(5-6): p. 494-509.

2. Charoy, B., F. Noronha, and A. Lima, Spodumene-petalite-eucryptite: mutual relationships and pattern of alteration in Li-rich aplite-pegmatite dykes from northern Portugal. The Canadian Mineralogist, 2001. 39(3): p. 729-746.

3. Quensel, P., Minerals of the Varuträsk Pegmatite. Geologiska Föreningen i Stockholm Förhandlingar, 1937. 59(2): p. 150-156.

4. Quensel, P., Minerals of the Varuträsk Pegmatite. Geologiska Föreningen i Stockholm Förhandlingar, 1938. 60(2): p. 201-215.

XII Congresso Ibérico de Geoquímica | XX Semana da Geoquímica

Processamento estatístico e análise de componentes principais de dados geoquímicos de sedimentos de corrente para prospecção de Li

Statistical processing and principal component analysis of geochemical data from stream sediments for Li exploration

Lima, J.[1,2]*, Cardoso-Fernandes, J. [1,2], Lima, A.[1,2], Teodoro, A.C.[1,2], Roda-Robles, E.[3]

[1] Universidade do Porto, Faculdade de Ciências, DGAOT, Rua Campo Alegre, Porto, Portugal
[2] ICT (Instituto de Ciências da Terra) – Polo do Porto, Portugal
[3] Dpto. Mineralogía y Petrología, Universidad del País Vasco UPV/EHU, Barrio Sarriena s/n, 48940 Leioa, Spain
* jlima.geol@gmail.com

Resumo: Dados geoquímicos de sedimentos de corrente da região de Fregeneda-Almendra foram preliminarmente analisados por meio de estatística elementar e análise de componentes principais (PCA) para avaliar a associação entre sete elementos selecionados (Li, Sn, As, B, Ba, Sr e Nb) com a finalidade de prospeção de lítio em pegmatitos. Foi aplicada transformação logarítimica aos dados brutos a fim de reduzir a sua assimetria e o método de padronização foi utilizado para evitar erros de interpretação devido à presença de subconjuntos não identificados dentro da população. Além disso, um dendrograma, com os dados de 34 elementos transformados logariticamente e padronizados, foi construído de modo a tentar agrupar as variáveis correlacionadas e posteriormente foi comparado com os resultados da PCA. Duas associações principais foram interpretadas com os métodos referidos: Sn-Li-Nb e Ba-Sr, com relação antipatética entre si. Outra associação foi B-As, embora menos prontamente observada pela PCA. Precisam ser feitas investigações adicionais antes que estes resultados possam ser aplicados com precisão na prospeção de Li.

Palavras-chave: estatística elementar, PCA, sedimentos de corrente, geoquímica, lítio

Abstract: Geochemical stream sediment data from Fregeneda-Almendra region were preliminary analyzed through elementary statistics and principal component analysis (PCA) to assess the association among seven selected elements (Li, Sn, As, B, Ba, Sr and Nb) for purposes of lithium exploration in pegmatites. Log-transformation was applied to the raw data in order to reduce their asymmetry and the method of standardization was employed to avoid misinterpretations due to the presence of unidentified subsets inside the data. In addition, a dendrogram with the standardized log- transformed data of 34 elements was built as an attempt of grouping the correlated variables and was later compared to the PCA results. Two main associations were interpreted with the referred methods: Sn-Li-Nb and Ba-Sr, with an antipathetic relation between each other. Another association was B-As, though less readily observed through PCA. Further investigations need to be done before these results can be accurately applied in Li exploration.

Keywords: elementary statistics, PCA, stream sediments, geochemistry, lithium

1. Introduction

The analysis of stream sediment geochemistry is widely applied to exploration and environmental surveys, both for regional investigation and for well-known mineralized regions.

Various techniques have been used to identify the background influence in the chemical composition of stream sediments and to delineate geochemical anomalies of mineralized rocks (Carranza and Hale 1997; Spadoni 2006; Shahrestani and Mokhtari 2017). In order to do that, a previous important task is to understand the data distribution and the factors which determine its variability (e.g. lithology).

This study is a preliminary attempt of recognizing the geochemical data from 3,598 stream sediment samples from the Fregeneda-Almendra region, East of Portugal, using elementary statistics and principal component analysis (PCA) aiming at Li exploration in pegmatites.

2. Geology and Samples

The study area of Fregeneda-Almendra mainly consists of pre-Ordovician metamorphic rocks from the schist-metagraywacke complex, located north of the Mêda-Penedono-Lumbrales granitic complex. Numerous occurrences of aplitic-pegmatitic veins are reported, some bearing Li minerals (Vieira 2010).

The stream sediment samples were collected in an area of approximately 1040 km² during the 1980s by the consortium "Bureau de Recherches Géologiques et Minières" (BRGM; France) – "Sociedade Portuguesa de Empreendimentos" (SPE; Portugal), in collaboration with the Mining Development Service of Portugal, currently known as "Laboratório Nacional de Energia e Geologia" (LNEG).

3. Methodology

Data were manipulatedthrough elementary statistics in order to define the best approach for PCA, a multivariate method to assess multi-element associations and to identify geochemical anomalies.

Among the 34 elements analyzed in the BRGM-SPE campaign, seven of them were chosen for the PCA analysis due to their expected association with Li (Černý *et al*. 1985). Thus, the target elements of this study were: Li, Sn, As, B, Ba, Sr and Nb. Although Ta is an important element to be studied in pegmatites, it was not analyzed in the aforementioned campaign. Moreover, dendrograms were obtained by Hierarchical Cluster Analysis and the Ward's method Eucledean Distance. Since they represent diagrams which organize the variables according to the association among each other, they were produced with the whole set of data to be compared to the PCA results.

All treatment of geochemical data was achieved using the numpy, matplotlib, seaborn, pandas, scipy and scikit-learn modules for Python programing language.

4. Results and Discussion

4.1. Elementary Statistics

Statistics are widely used for modeling uni- and multi-element geochemical anomalies (Carranza 2009) and represent important tools to understand data behaviour and its distribution. Since multivariate analytical techniques such as PCA require symmetry of the data, logarithmic transformation is often applied when raw data show an asymmetric distribution.

In addition, the method of standardization (Carranza 2009) is appropriate to recognize multiple populations inside the data, specially when they are not subdivided according to controlling features (e.g. lithology). Considering that noticing and defining the existing subsets is not straightforward, all data were standardized based on their arithmetic mean and standard deviation to prevent misinterpretations.

Elementary statistics of raw and log-transformed data and their standardized values are shown in Tables 1a, 1b, 1c and 1d. It is noteworthy that log-transformed data skewness is smaller than the raw data, which demonstrates that the former is, to some extent, more symmetric. However, the process of standardizing the data did not change the skewness of neither raw or log-transformed values.

The histograms of standardized log-transformed data for the selected elements are presented in Figure 1. The Nb histogram is not displayed due to an odd asymmetry of data, since most

analyzes are possibly near the detection limit.

4.2. Dendrograms

Dendrograms obtained with unstandardized raw and log-transformed data showed unexpected associations of Li with elements such as Cr, Ni and V, which is not in agreement with paragenesis found in pegmatites, extensively described in the literature (Černý *et al*. 1985; Selway *et al*. 2005; Roda-Robles *et al*. 2018). Since this study is a preliminar approach and does not yet consider the effect of element mobility in stream sediments, it was chosen not to use this type of data. Therefore, the dendrograms analyzed were the ones obtained from standardized data. For both standardized raw and standardized log-transformed data, Li is in association with K_2O, Na_2O and P_2O_5. However, the dendrogram of standardized log-transformed data (Fig. 2) is the only approach which provides a close Li-Sn relationship, which are largely correlated elements in Portuguese aplites and pegmatites in the Central Iberian Zone (Roda-Robles *et al*. 2018). Other relevant associations can be noticed among the elements used for PCA: Nb shows some relation to Li-Sn, B is related to As and Ba to Sr.

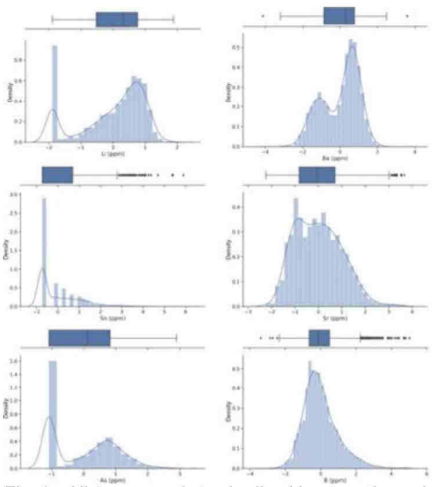

Fig. 1 – Histograms of standardized log-transformed data.

Tab. 1a – Elementary statistics for raw data

Element	Min	Max	Mean	St. dev.	Skew.
Li	1	619	72.40	68.11	1.36
B	7	1316	77.70	80.88	6.29
As	1	1589	43.42	97.64	6.73
Sr	14	458	64.72	45.85	2.72
Nb	1	137	2.31	4.69	9.17
Sn	1	139	3.27	5.62	9.42
Ba	21	2017	285.79	148.65	0.86

Tab. 1b – Elementary statistics for log-transformed data

Element	Min	Max	Mean	St. dev.	Skew.
Li	0.69	6.43	3.57	1.52	-0.83
B	2.08	7.18	4.14	0.61	0.94
As	0.69	7.37	2.50	1.67	0.25
Sr	2.71	6.13	4.01	0.58	0.41
Nb	0.69	4.93	0.90	0.58	2.79
Sn	0.69	4.94	1.16	0.64	1.48
Ba	3.09	7.61	5.51	0.59	-0.47

Tab.1c – Elementary statistics analyzed for standardized raw data

Element	Min	Max	Mean	St. dev.	Skew.
Li	-1.05	8.03	3.95E-17	1	1.36
B	-0.87	15.31	4.74E-17	1	6.29
As	-0.43	15.83	7.90E-18	1	6.73
Sr	-1.11	8.58	3.95E-17	1	2.72
Nb	-0.28	28.74	4.74E-17	1	9.17
Sn	-0.40	24.16	0.00E+00	1	9.42
Ba	-1.78	11.65	1.58E-16	1	0.86

Tab. 1d – Elementary statistics analyzed for standardized log-transformed data

Element	Min	Max	Mean	St. dev.	Skew.
Li	-1.89	1.88	-2.29E-14	1	-0.83
B	-3.39	5.03	-5.04E-14	1	0.94
As	-1.08	2.91	-3.89E-14	1	0.25
Sr	-2.24	3.67	-5.94E-14	1	0.41
Nb	-0.36	6.89	-6.01E-14	1	2.79
Sn	-0.73	5.90	-1.02E-14	1	1.48
Ba	-4.12	3.59	3.75E-14	1	-0.47

4.3. PCA

As previously mentioned, principal component analysis requires a somewhat symmetric set of data. However, log-transformation could only decrease asymmetry to a certain degree, both for raw and standardized data (see histograms in Fig. 1). According to Carranza and Hale (1997), another way to approach this issue is by using the Spearman rank correlation matrix instead of Pearson's. This method was used with standardized log-transformed data, showing a high PC1 variance and good associations between Li and the chosen elements.

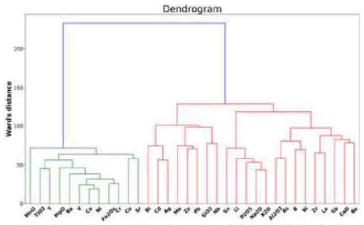

Fig. 2 – Dendrogram showing hierarchical cluster analysis of standardized log- transformed data

PCA results are shown in Table 2. PC1 accounts for 75% of the total variance and two strong correlations can be observed, Sn-Li-Nb and Ba-Sr, which are inversely associated. Another relation is B-As, though less prominent than the previous two. PC2, with 16% of the total variance, has two more difficult eigen values As-Li-B and Nb-Ba, which are also antipathetic between each other. The other 4 principal components cannot be readily interpreted and thus are not discussed.

Overall, these results agree with the elemental association showed on the standardized log-transformed dendrogram to the point it includes the Sn-Li-Nb inversely correlated to Ba-Sr, though with different degrees of affinities, and the B-As association.

Tab. 2 – Results of PCA of standardized log-transformed data

	As	B	Ba	Li	Sn	Nb	Sr	Variance
PC1	-0.13	-0.58	-1.39	1.00	1.41	0.93	-1.25	0.75
PC2	-0.66	-0.20	0.33	-0.41	-0.09	0.94	0.07	0.16
PC3	0.10	0.56	-0.23	-0.26	-0.10	0.16	-0.23	0.05
PC4	0.27	-0.15	-0.06	0.04	-0.25	0.17	-0.01	0.02
PC5	-0.14	0.08	-0.10	0.20	-0.14	0.02	0.10	0.01
PC6	0.02	-0.03	-0.14	-0.09	0.06	0.01	0.17	0.01

5. Conclusions and future work

The preliminary data treatment and processing results suggest that log-transformation and standardization are viable approaches to study the geochemistry of stream sediment samples. The dendrograms and principal component analysis (using the Spearman rank correlation matrix) indicate the associations Sn-Li-Nb and Ba-Sr, and the antipathetic relation between them. These elemental grouping are extremely helpful for assessing the metal distribution, delineating anomalies and targeting mineralized areas, but still need to be evaluated in more detail. Further work includes analyzing each element mobility,the influence of lithology in data behavior, the identification of data subsets and the association with catchment basins.

Acknowledgements

The authors would like to thank the financial support provided by FCT – Fundação para a Ciência e a Tecnologia with the ERA-MIN/0001/2017 – LIGHTS project and FEDER through the operation POCI-01-0145-FEDER-007690 funded by the Programa Operacional Competitividade e Internacionalização – COMPETE2020 and by National Funds through FCT within ICT, R&D Unit (reference UID/GEO/04683/2013). Joana Cardoso-Fernandes is financially supported by FCT within the compass of a PhD. Thesis, ref. SFRH/BD/136108/2018.

The authors also acknowledge LNEG for making the data available for this study.

References

Carranza, E.J.M., 2009. Geochemical Anomaly and Mineral Prospectivity Mapping in GIS. In: Hale, M. (Ed). Handbook of Exploration and Environmental Geochemistry. Elsevier, Hungary, 51-84.

Carranza, E.J.M., Hale, M., 1997. A catchment basin approach to the analysis of reconnaissance geochemical-geological data from Ably Province, Philippines. J. Geochem. Explor. 60, 157–171.

Černý, P., Meintzer, R.E., Anderson, A.J., 1985. Extreme fractionation in rare-element granitic pegmatites: selected examples of data and mechanisms. Can. Mineral. 23, 381–421.

Roda-Robles, E., Villaseca, C., Pesquera, A., Gil-Crespo, P.P., Vieira, R., Lima, A., Garate-Olave, I., 2018. Petrogenetic relationships between Variscan granitoids and Li-(F-P)-rich aplite-pegmatites in the Central Iberian Zone: Geological and geochemical constraints and implications for other regions from the European Variscides. Ore Geol. Rev. 95, 408-430.

Selway, J.B., Breaks, F.W. and Tindle, A.G., 2005. A Review of Rare-Element (Li-Cs-Ta) Pegmatite Exploration Techniques for the Superior Province, Canada, and Large Worldwide Tantalum Deposits. Expl. Min. Geol. 14(1–4), 1–30.

Shahrestani, S., Mokhtari, A.R., 2017. Improved detection of anomalous catchment basins by incorporating drainage density in dilution correction of geochemical residuals. Geochem. Explor. Env. A. 17, 194-203.

Spadoni, M., 2006. Geochemical mapping using a geomorphologic approach based on catchments.
J. Geochem. Explor. 90, 183–196.

Vieira, R., 2010. Aplitopegmatitos com elementos raros da região entre Almendra (V.N. de Foz Côa) e Barca d'Alva (Figueira de Castelo Rodrigo). Campo aplitopegmatítico da Fregeneda- Almendra. PhD thesis, Faculdade de Ciências da Universidade do Porto, Porto, 306 p.

JORNADAS DO ICT
11 e 12 de fevereiro de 2021
Faculdade de Ciências da Universidade do Porto

Análise estatística da geoquímica de sedimentos de corrente em rochas graníticas e formações metassedimentares do Alto Douro (NE de Portugal)

J. Lima[1*], J. Cardoso-Fernandes[1], A. Lima[1]
[1] Departamento de Geociências, Ambiente e Ordenamento do Território, Faculdade de Ciências da Universidade do Porto; Instituto de Ciências da Terra, Polo-Porto, Rua Campo Alegre, Porto, Portugal
*jessica.torres@fc.up.pt

Resumo

A partir de dados geoquímicos de 3.713 pontos de amostragem relativos às campanhas de sedimentos de corrente realizadas na década de 80 pelo consórcio BRGM–SPE–LNEG na região do Alto Douro (NE de Portugal), foram realizadas análises de estatística exploratória com um grupo selecionado de elementos associados ao lítio em ambientes pegmatíticos, a saber: As, B, Ba, Be, Li, Sn, W e P_2O_5. O banco de dados foi dividido em dois subconjuntos (SFM e BRMG) e tratados separadamente, uma vez que as campanhas possuem diferentes malhas de amostragem e distribuições distintas. Utilizando ferramentas de programação no software R, foram produzidos histogramas, boxplots, QQ-plots e matrizes de correlação para as distribuições desses elementos, considerando também as possíveis diferenças entre amostras localizadas em granitos e rochas metassedimentares do Complexo Xisto-Grauváquico e do Ordovício (Formação Santo Antão).

Foi possível perceber que o conjunto de dados SFM apresenta menores valores de B, Ba e Be, maior média para As, B, Ba, Be, Sn e W, maior mediana para As, B e Ba, maior assimetria para Be, Li e P_2O_5, e maior desvio padrão (superior à média) para As, B, Sn e W. No geral, após a transformação logarítmica e remoção de valores censurados (menores que o limite de deteção), os histogramas de dados SFM mostram uma distribuição um pouco mais simétrica para As, mas a maioria dos elementos nas duas campanhas são distorcidos negativamente (exceto Li) e contêm mais de uma população. A diferença entre as amostras localizadas em granitos e em rochas metassedimentares é mais proeminente na campanha BRGM, que apresenta um maior número de amostras. O lítio é o elemento com maior diferença: os granitos têm valor médio de 111,8 ppm e as rochas metassedimentares de 41,31 ppm. A estatística descritiva para rochas metassedimentares entre as duas campanhas difere especialmente para os dados de As, B, Be e Li, embora a mediana seja bastante semelhante para todos os elementos, exceto para o Be. Porém, a subdivisão dos dados por formações de rochas metassedimentares permite ver as diferenças para todos os elementos (exceto W) nas formações Pinhão, Rinho Pinhão e Santo Antão. Dados de Ba, Li e P_2O_5 também mostram diferenças na formação Desejosa.

Palavras chave: lítio, geoquímica exploratória, estatística descritiva, programação.

Agradecimentos: Os autores agradecem o financiamento obtido por meio da Fundação para a Ciência e a Tecnologia (FCT) com o projeto ERA-MIN2/0001/2017 – LIGHTS e FEDER (operação POCI-01-0145-FEDER-007690) financiada pelo Programa

Operacional Competitividade e Internacionalização – COMPETE2020 e por Fundos Nacionais do ICT, R&D Unit (referência UID/GEO/04683/2013). Joana Cardoso-Fernandes agradece o suporte da FCT para o desenvolvimento da tese de doutoramento, ref. SFRH/BD/136108/2018. Os autores também agradecem ao LNEG pela disponibilização dos dados para este estudo.

Associações elementares nos aplito-pegmatitos da mina da Bajoca (Almendra, Vila Nova de Foz Côa)

Joana Cardoso-Fernandes[1,2*], Alexandre Lima[1,2], Encarnación Roda-Robles[3], Maria dos Anjos Ribeiro[1,2], Ana Teodoro[1,2]

[1] Faculdade de Ciências da Universidade do Porto

[2] Instituto de Ciências da Terra – Pólo Porto

[3] Universidad del País Vasco

*joana.fernandes@fc.up.pt

Resumo

Recentemente, tem-se verificado uma crescente procura por comodidades minerais provenientes de aplito-pegmatitos, destacando-se o papel do lítio (Li) no processo de descarbonização em curso. Tendo isto em conta, o objetivo deste trabalho é avaliar as associações elementares existentes nos aplito-pegmatitos da mina da Bajoca (Almendra, Vila Nova de Foz Côa) de forma a comparar com as associações elementares observadas em amostras de sedimentos de corrente na mesma região (Lima et al., 2019). A área de estudo insere-se no campo aplito-pegmatítico de Fregeneda-Almendra onde foram descritos vários tipos de diques ricos em elementos raros (Vieira, 2010; Roda-Robles et al., 1999). No caso da mina da Bajoca, observam-se três diques aplito-pegmatíticos, dois deles discordantes da foliação da rocha encaixante (Complexo Xisto-Grauváquico) e mineralizados em Li. No âmbito deste estudo, foram aplicadas técnicas estatísticas multivariadas às análises de elementos maiores (realizadas pela Felmica S.A.) em 96 amostras de aplito-pegmatito recolhidas ao longo de oito sondagens distintas. As técnicas aplicadas incluíram os coeficientes de correlação de Pearson e de Spearman, assim como a análise de *clusters* através do método do dendrograma. Tendo em conta as duas medidas de associação utilizadas, observa-se uma correlação muito forte positiva entre P_2O_5-CaO, correlação moderada a forte positiva MgO-Fe_2O_3, e correlação moderada a forte negativa entre Al_2O_3-SiO_2. As duas primeiras correlações são corroboradas pelo dendrograma da Figura 1: o primeiro *cluster* é formado apenas pelo TiO_2, o segundo corresponde à associação Fe_2O_3-MgO, e o terceiro *cluster* corresponde aos restantes elementos maiores. A associação P_2O_5-CaO está relacionada com a presença de apatite, enquanto que a correlação MgO-Fe_2O_3 poderá ser resultado das zonas de alteração causadas pela falha do Barril que afeta o corpo principal da mina da Bajoca (Almeida, 2003). A correlação negativa entre Al_2O_3-SiO_2 foi também observada em trabalhos anteriores (Almeida, 2003), e pode dever-se à existência de zonas mais ricas em quartzo e zonas mais ricas em aluminossilicatos como feldspato potássico e petalite (mineral de Li) dentro dos diques aplito-pegmatíticos. No caso da análise de *clusters* realizada para as amostras de sedimentos de corrente (Lima et al., 2019), verifica-se que o SiO_2 forma um *cluster* separado dos restantes óxidos, e que as associações Fe_2O_3-MgO e P_2O_5-CaO se mantêm apesar de as distâncias de ligação aumentarem. Conclui-se, portanto, que, no caso dos elementos maiores, apesar das diferentes mobilidades dos elementos, as associações verificadas na fonte (aplito-pegmatitos) tendem a persistir nas amostras de sedimentos de corrente. Estudos futuros incluirão a análise das associações elementares entre os elementos menores e traço para os aplito-pegmatitos do campo de Fregeneda-Almendra.

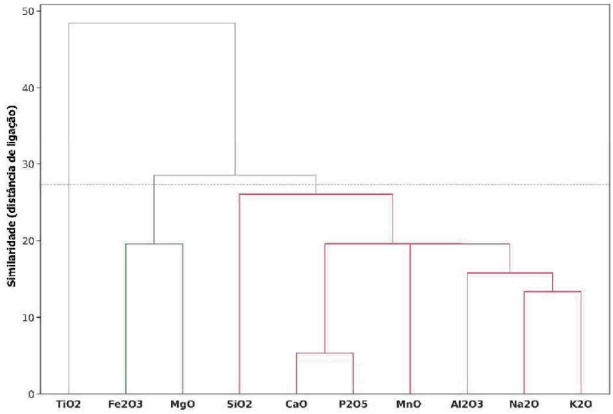

Figura 1 – Dendrograma demonstrando a análise de *clusters* hierárquica (*average linkage*, distância Euclidiana).

Palavras chaves: Geoquímica, prospeção, estatística multivariada, análise de *clusters*, pegmatito.

Referências bibliográficas

Almeida, C., 2003. Estudo do filão aplitopegmatítico da mina da Bajoca, Almendra: contribuição científico-tecnológica. (tese de Mestrado), Faculdade de Ciências da Universidade do Porto, Porto (120 pp.).

Lima, J., Cardoso-Fernandes, J., Lima, A., Teodoro, A.C., Roda-Robles, E., 2019. Statistical processing and principal component analysis of geochemical data from stream sediments for Li exploration, XII Congresso Ibérico de Geoquímica (CIG), Évora, 273-276.

Roda-Robles, E., Pesquera, A., Velasco, F., Fontan, F., 1999. The granitic pegmatites of the Fregeneda area (Salamanca, Spain): characteristics and petrogenesis. Mineral. Mag., 63(4), 535–558.

Vieira, R., 2010. Aplitopegmatitos com elementos raros da região entre Almendra (V.N. de Foz Côa) e Barca d'Alva (Figueira de Castelo Rodrigo). Campo aplitopegmatítico da Fregeneda-Almendra. (tese de doutoramento), Faculdade de Ciências da Universidade do Porto, Porto (273 pp.).

X Congresso Jovens Investigadores em Geociências, LEG 2020
Estremoz, 20-22 Novembro 2020
Livro de Actas

Geochemical pathfinder analysis for lithium (Li) exploration in the Iberian Peninsula

Análise de elementos-guia para a prospeção de lítio (Li) na Península Ibérica

J. Cardoso-Fernandes[1*], A. Lima[1], E. Roda-Robles[2], M. Ribeiro[1], A.C. Teodoro[1]

[1] University of Porto, Faculty of Sciences, DGAOT, ICT (Institute of Earth Sciences), Rua Campo Alegre s/n, Porto, Portugal
[2] Universidad del País Vasco (UPV/EHU), Departamento Mineralogía y Petrología, Bilbao, Spain
[*] joana.fernandes@fc.up.pt

Abstract: The Central Iberian Zone (CIZ) and Galicia-Trás-os-Montes Zone (GTMZ) contain several important Li-mineralizations. A multivariate statistical approach, including correlation, cluster, and principal component analysis, was employed to define geochemical pathfinders for Li exploration. A total of 66 geochemical analyses of Li-bearing pegmatites and leucogranitic cupolas from the CIZ-GTMZ, available from the literature, were used. The main pathfinder elements identified were Rb, Cs, Sn, F, and B. Oppositely, no association with Ta and Nb was observed contrary to the expected. Further sampling is needed to understand these results. Other element associations (K_2O, MnO, Al_2O_3) can be explained by the mineral paragenesis but the Li correlation with Tl, In and Ge needs to be investigated. These results can help to better direct future geochemical exploration campaigns in the CIZ-GTMZ, especially when using semi-quantitative portable analytical devices.

Key-words: Multivariate analysis; cluster analysis; principal component analysis (PCA); Li-rich pegmatite

Resumo: A Zona Centro-Ibérica (ZCI) e Zona Galiza-Trás-os-Montes (ZGTM) contêm importantes mineralizações de Li. Para determinar elementos-guia para a prospeção geoquímica de Li, foi aplicada uma abordagem de estatística multivariada que incluiu análise de correlações, *clusters* e componentes principais. Para tal, foram usadas 66 análises geoquímicas de pegmatitos e cúpulas leucograníticas ricas em Li da ZCI-ZGTM, disponíveis na literatura. Os principais elementos-guia identificados foram Rb, Cs, Sn, F, e B. Ao contrário do esperado, não foi possível observar nenhuma correlação com Ta e Nb. Amostragem complementar é necessária para compreender os resultados. Outras associações geoquímicas (K_2O, MnO, Al_2O_3) podem ser explicadas pela paragénese mineral descrita. Contudo, a correlação entre Li e Tl, In e Ge precisam de ser estudadas. Os resultados obtidos podem ajudar a direcionar futuras campanhas de prospeção geoquímica na ZCI-ZGTM, especialmente aquando da utilização de equipamentos analíticos semi-quantitativos portáteis.

Palavras-chave: Análise multivariada; análise de *clusters*; análise de componentes principais (ACP); pegmatito de Lítio

INTRODUCTION

The Central Iberian Zone (CIZ), occupying a central position on the Iberian Massif, is composed of Neoproterozoic to Paleozoic metasedimentary succession, intruded by Variscan granitoids (Martínez Catalán et al., 2004; Roda-Robles et al., 2018). The lithium (Li)-mineralization in the CIZ occurs along a belt with around 500 km in length and 150 km in width, mainly in aplite-pegmatite dykes but also in leucogranitic cupolas (Roda-Robles et al., 2016; 2018). There are also important Li-occurrences in the Galicia-Trás-Os-Montes Zone (GTMZ), a terrane accreted over CIZ , that have similar ages and features to those in the CIZ (GTMZ: 310 ± 5 Ma; CIZ: 301 ± 3 Ma by U-Pb dating of columbite-group minerals) (Roda-Robles et al., 2016; 2018; Melleton et al., 2011). Recently, the economic importance

and demand of Li have been increasing, reinforced by its role in the global decarbonization process and, consequently, it is crucial to develop new exploration tools. Taking this into account, the goals of this study are to use available whole-rock geochemical data to i) evaluate if the element associations agree with the known mineral paragenesis of Li-rich bodies; and ii) establish geochemical pathfinders that could be used for exploration of Li in the CIZ-GTMZ.

DATA AND METHODS

A total of 66 geochemical analyses of lepidolite-rich (n = 41) and spodumene/petalite-rich (n = 25) dykes and leucogranitic cupolas from 12 Li-rich fields in the CIZ-GTMZ were used in this study. Of all the analysis, 22 were performed by Roda-Robles et al. (2018), while the remaining analyses were compiled by the same authors based on published research from the Argemela, Castillejo de Dos Casas and Pinilla de Fermoselle leucogranitic cupolas, and from the Barroso-Alvão, Fregeneda-Almendra, Gonçalo, Lalín-Forcarei, Las Navas, Segura, Seixoso-Vieiros, Serra de Arga and Tres Arroyos pegmatite-fields. The results of the analyses were treated and evaluated with the resource Python programming language. The statistical analyses included descriptive statistics, Pearson and Spearman correlation measures, and multivariate techniques such as cluster analysis (dendrograms) and principal component analysis (PCA), enabling to evaluate the most relevant element associations with Li. Before employing the multivariate analysis for Li-correlated elements, the data was standardized using the interquartile range (IQR). In the case of cluster analysis, the distance metric employed was always the Euclidian distance, but different linkage methods were tested (Ward's, single, complete, average, centroid, and median). The dendrogram's cutoff value was set to the median of the third-from-last and second-from-last linkages. Moreover, PCA was employed to Pearson's correlation matrix for Li-correlated elements.

RESULTS AND DISCUSSION

The results from Pearson's and Spearman's association measures are presented in Table 1. The correlation analysis was performed between all available variables (58 oxides or elements) but the table only shows relevant element associations with Li (correlation coefficient > 0.3). A strong to moderate positive correlation is verified for Rb, F, B, Cs, Tl, In, and Ge, as well as a moderate (to weak) correlation with K_2O and MnO. Strong negative associations are observed between Li and Bi, and moderate with Na_2O and Ba. No correlation with Sn, Ta or Nb was verified. As observed in Table 1, the dataset is very heterogeneous since that for each studied locality the packages of elements analyzed were distinct. Consequently, in the multivariate analysis, an attempt was made to create a balance between preserving the largest number of samples and elements possible. Two subsets were then considered: i) 48 analysis for 16 elements (Al_2O_3, CaO, Fe_2O_3, K_2O, MgO, Na_2O, P_2O_5, SiO_2, Ba, Cs, Li, Nb, Rb, Sn, Sr, Ta); ii) 22 analysis for 22 elements (Al_2O_3, CaO, Fe_2O_3, K_2O, MgO, MnO, Na_2O, P_2O_5,

SiO_2, TiO_2, Ba, Cs, F, Ga, Nb, Rb, Sn, Sr, Ta, Zn, Zr). Figure 1 summarizes the cluster analysis and PCA results for both subsets. For the first subset, both methods identified a Li-Rb-K_2O-Cs-Al_2O_3 association. For the second subset, cluster analysis allowed to identify an Li-F-Cs-Rb-Sn-Zn association while PCA identified an Li-F-Cs-Al_2O_3-Rb-Sn-Zr association. Most of these associations are in line with the geochemical signature identified for rare-element, Li-rich pegmatites worldwide: Li, Rb, Cs, Be, Ga, Sn, Nb, Ta, B, P, and F (Černý & Ercit, 2005; Simmons & Webber, 2008). However, no correlation with Ta or Nb was identified which is unexpected since Nb-Ta oxides are commonly found within the Li-rich pegmatites/cupolas (Roda-Robles et al., 2018). This may indicate that the sampling is not representative for this kind of accessory phases and that the nugget effect may occur in some samples. Similarly, no correlation between Li and Be was verified, but this would be expected since beryl is less common in the Li-rich bodies of CIZ-GTMZ (Roda-Robles et al., 2018). The correlation between Li and MnO, K_2O, and Al_2O_3 can also be explained by the presence of Mn oxides and because K and Al can be found in the structure of Li-minerals. At the time, no explanation for the moderate Li correlation with Tl, In, and Ge is found but this is worth further investigation.

Table 1. Pearson's and Spearman's correlation coefficients with Li. Bold: strong association; italic: moderate association; regular: weak association; n: number of analysis for each analyzed element/oxide.
Tabela 1. Coeficientes de correlação de Pearson e Spearman com o Li. Negrito: associação forte; itálico: associação moderada; regular: associação fraca; n: número de análises existentes para cada elemento/óxido.

Pearson's correlation coefficient						**Spearman's correlation coefficient**					
	Positive	**n**		**Negative**	**n**		**Positive**	**n**		**Negative**	**n**
Rb	**0.7426**	**60**	**Bi**	**-0.8601**	11	*Tl*	*0.6727*	*11*	**Bi**	**-0.7073**	**11**
F	**0.7379**	**40**	*Na_2O*	*-0.6580*	*66*	*B*	*0.6000*	*6*	*Na_2O*	*-0.6555*	*66*
B	**0.7061**	**6**	*Ba*	*-0.4270*	*63*	*Rb*	*0.5717*	*60*	*Ba*	*-0.5706*	*63*
Cs	*0.6919*	*55*	SiO_2	-0.3666	66	*Ge*	*0.5709*	*12*	Pb	-0.3775	27
Tl	*0.6719*	*11*	TiO_2	-0.3483	52	*F*	*0.5507*	*40*	Lu	-0.3466	13
K_2O	*0.6113*	*66*				*Cs*	*0.5412*	*55*	Be	-0.3385	29
In	*0.5923*	*11*				*In*	*0.5218*	*11*	Sr	-0.3282	63
MnO	*0.5619*	*55*				*W*	*0.5110*	*13*	TiO_2	-0.3001	52
Ge	*0.5405*	*12*				K_2O	0.4740	66			
Al_2O_3	*0.5272*	*66*				Cu	0.4425	22			
Zn	0.4666	44				MnO	0.4332	55			
Th	0.4479	27				Zn	0.3309	44			
Co	0.3510	15				Th	0.3202	27			
Cu	0.3149	22				Sc	0.3048	14			

CONCLUSIONS

In this study, by applying multivariate statistical analysis to an existent whole-rock geochemical dataset of Li-rich bodies in the CIZ-GTMZ, it was possible to identify pathfinder elements for Li exploration, namely Rb, Cs, Sn, F, and B. These elements are characteristic of Li-rich pegmatites worldwide. Other element associations were also verified: most correlations can be explained by the mineral paragenesis but the association with Tl, In and Ge in the CIZ-GTMZ pegmatites needs to be studied in detail in the future. Contrary to the observed around the world and to the mineral paragenesis described for the CIZ-GTMZ's Li-rich bodies, no association with Ta or Nb was observed. Complementary geochemical sampling is needed to further interpret these results. These results are

crucial to better direct future geochemical exploration campaigns in the CIZ-GTMZ through either stream/soil sampling or pegmatite metasomatic halo definition. Also, the identified geochemical pathfinders can be semi-quantitively analyzed in the field using portable XRF or LIBS equipment.

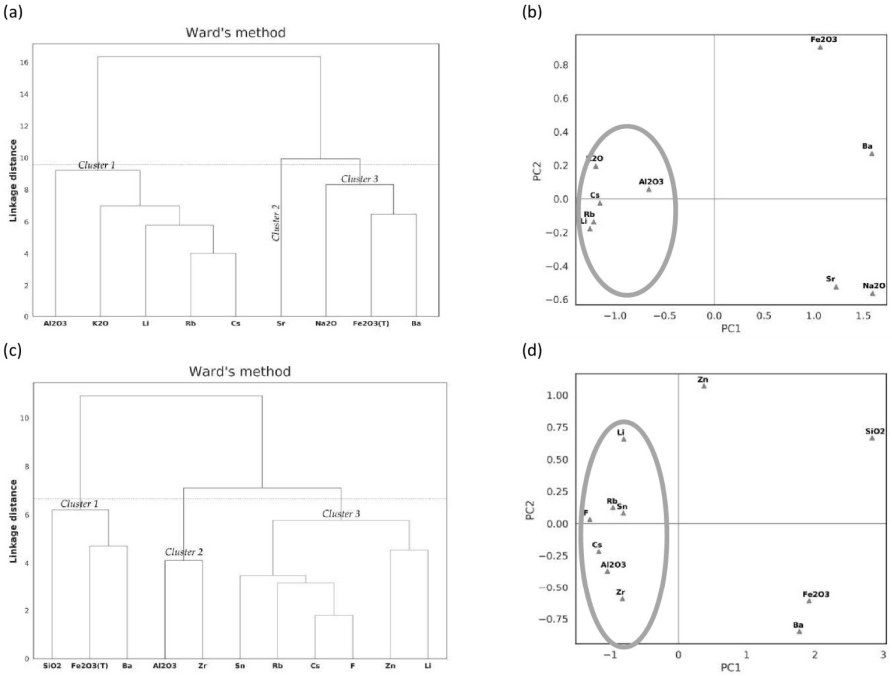

Figure 1. Dendrograms showing the hierarchical clustering of selected elements/oxides: (a) n = 48; (c) n = 22. Projection of the selected elements/oxides loadings on the plane PC2 vs PC1: (b) n = 48; (d): n = 22.
Figura 1. Dendrograma ilustrativo da análise de clusters hierárquica para os elementos/óxidos selecionados: (a) n = 48; (c) n = 22. b) Projeção dos *loadings* dos elementos/óxidos selecionados no plano PC2 vs. PC1: (b) n = 48; (d) n = 22.

ACKNOWLEDGEMENTS
The authors would like to thank the financial support provided by FCT, with the ERA-MIN/0001/2017 – LIGHTS project and through the UIDB/04683/2020 - ICT (Institute of Earth Sciences) project. J. Cardoso-Fernandes is financially supported within the compass of a Ph.D. Thesis, ref. SFRH/BD/136108/2018, through FCT, and co-financed by the ESF through POCH.

References

- ČERNÝ, P., & ERCIT, T.S. (2005) - Classification of granitic pegmatites revisited. *Can. Mineral.*, vol. 43: 2005–2026.
- MARTÍNEZ CATALÁN, J. R., MARTÍNEZ POYATOS, D., BEA, F., & (Coords.). (2004) - Zona Centroibérica: Introducción. In: J. A. VERA (Ed.), *Geología de España*. Madrid: Geol. España/Inst. Geol. Min. España (SGE-IGME), 68-69 pp.
- MELLETON, J., GLOAGUEN, E., FREI, D., LIMA, A. (2011) - U-Pb dating of columbite–tantalite from Variscan rare-elements granites and pegmatites. *Mineral. Mag.*, vol. 75: 1452.
- RODA-ROBLES, E., PESQUERA, A., GIL-CRESPO, P. P., VIEIRA, R., LIMA, A., GARATE-OLAVE, I., MARTINS, T., & TORRES-RUIZ, J. (2016) - Geology and mineralogy of Li mineralization in the Central Iberian Zone (Spain and Portugal). *Mineralogical Magazine*, vol. 80(1): 103-126.
- RODA-ROBLES, E., VILLASECA, C., PESQUERA, A., GIL-CRESPO, P.P., VIEIRA, R., LIMA, A., GARATE-OLAVE, I. (2018) - Petrogenetic relationships between Variscan granitoids and Li-(F-P)-rich aplite-pegmatites in the Central Iberian Zone: Geological and geochemical constraints and implications for other regions from the European Variscides. *Ore Geology Reviews*, vol. 95: 408-430.
- SIMMONS, W. B. S., & WEBBER, K. L. (2008) - Pegmatite genesis: state of the art. *European Journal of Mineralogy*, vol. 20(4): 421-438.

IX Congresso Jovens Investigadores em Geociências, LEG 2019
Estremoz, 23-24 Novembro 2019
Livro de Actas

Biotite porphyroblast microstructures in the Almendra (Vila Nova de Foz Côa) region

Microstruturas de porfiroblastos de biotite na região de Almendra (Vila Nova de Foz Côa)

J. Cardoso-Fernandes[1 *], M. Ribeiro[1], A. Lima[1], E. Roda-Robles[2], A. C. Teodoro[1], J. Lima[1]

[1] University of Porto, Faculty of Sciences, DGAOT, ICT (Institute of Earth Sciences), Rua Campo Alegre s/n, Porto, Portugal
[2] Universidad del País Vasco (UPV/EHU), Departamento Mineralogía y Petrología, Bilbao, Spain
[*] joana.fernandes@fc.up.pt

Abstract: Porphyroblasts can give significant insights about the tectonometamorphic history of a region. Metapelite samples from the Almendra (Vila Nova de Foz Côa) region were investigated and the associated microstructures documented allowing to conclude that biotite porhyroblastesis was pre- to sin- a later deformation phase (probably D_3). Smaller, mimetic biotite crystals also occur in the matrix. Most porphyroblasts present unzoned inclusion patterns, but zoned patterns were also observed. The most frequent type of inclusions was interpreted to be the product of the biotite-forming chemical reaction. A second type of inclusions probably reflects later matrix overgrowth.

K**ey-words:** Inclusions; Blastesis; Deformation

Resumo: Os porfiroblastos podem ajudar a compreender a história tectono-metamórfico de uma região. As microestruturas analisadas em amostras de metapelitos da zona de Almendra (Vila Nova de Foz Côa) permitiram concluir que a blastese de porfiroblastos de biotite é ante- a sin- um episódio de deformação tardio (provavelmente D_3). Na matriz ocorre também biotite mais pequena e mimética. A maioria dos porfiroblastos não apresenta padrões de inclusões zonados, apesar de existirem cristais com padrões zonados. O tipo de inclusões mais frequente foi interpretado como sendo o produto da reação química que forma biotite. O segundo tipo de inclusões provavelmente reflete um crescimento tardio sobre a matriz.

Palavras-chave: Inclusões; Blastese; Deformação

INTRODUCTION

The nature and geometry of porphyroblast inclusion trails, especially passive inclusions, can be very important in assessing the tectonometamorphic history of orogenic belts, since they provide information about the blastesis process, the previous matrix fabric and the style of strain at the time of porphyroblast growth (Lister *et al*., 1986; Miyake, 1993; Kim & Cho, 2008; Camilleri, 2009). In upper greenschist to lower amphibolite facies, biotite porphyroblast growth follows a two-stage constructive phase: the first, dominated by chemical replacement of the matrix with incorporation of passive inclusions, and the second dominated by blastesis of inclusion-free biotite in extensional cracks and dilating pressure shadows (Lister *et al*., 1986; Miyake, 1993; Kim & Cho, 2008; Camilleri, 2009). These are followed by a destructive phase with fracturing, residual growth, and rotation (Camilleri, 2009). The focus of this study was biotite growth and associated microstructures in metapelites from the Almendra region (Central Iberian Zone). The samples were collected along a transverse section of the Bajoca Li-pegmatite (host rock and metapelite enclaves) to study the associated alteration halos, but the microstructures found are also noteworthy.

IX Congresso Jovens Investigadores em Geociências, LEG 2019
Estremoz, 23-24 Novembro 2019
Livro de Actas

GEOLOGICAL SETTING

The area is dominated by metasedimentary rocks, of Upper Proterozoic to the Lower Cambrian age (Díez Balda *et al*., 1990), belonging to the Schist-Greywacke Complex (SGC), more precisely the Douro Group, limited to the north by the Lower Ordovician quartzites from the Poiares' syncline and to the south by the Figueira de Castelo Rodrigo–Lumbrales Anatectic Complex (FCR–LAC; Pereira *et al*., 2017). The metasediments were affected by a pre-D_3 prograde metamorphism that did not overcome the chlorite zone, and in the vicinities of the FCR–LAC sin- to late-D_3 thermal peak reached the sillimanite zone (Silva & Ribeiro, 1991, 1994). The metamorphic grade increases progressively to the south, in the direction of the FCR-LAC. The metamorphic isograde have a W-E trend, parallel to the granites (Silva & Ribeiro, 1991, 1994). The Bajoca pegmatite is in the andalusite zone near the transition to the biotite zone (Silva *et al*., 1990).

BIOTITE MICROSTRUCTURES AND INCLUSION TRAILS

Biotite microstructures were investigated in thin sections normal to the foliation, allowing the identification of two types of crystals: (i) mostly poikiloblastic porphyroblasts (1-1.5 mm); (ii) biotite crystals disperse in the matrix, of smaller dimensions. The matrix crystals are essentially inclusion-free, randomly oriented, but often concordant with the main foliation (S_n). Most of these crystals were interpreted as mimetic over a previous foliation. The biotite porphyroblasts show random orientations, although most of the porphyroblasts are oriented with the (001) cleavages at a high angle with S_n. The random orientation of biotite can be the result of nucleation under static conditions (Kim & Cho, 2008). This random distribution allied to (i) the adaptation of the external foliation (S_e) around some porphyroblasts (Fig. 1-A), and (ii) the existence of deformed porphyroblasts, indicate that biotite blastesis began after the deformation phase (D_n), responsible for the formation of S_n, being biotite growth pre- to sin- a later deformation phase (D_{n+1}, probably D_3), responsible for a generally incipient crenulation.

The inclusions of the porphyroblasts are mainly quartz, and can be divided into two types (Fig. 1): (i) Type 1 corresponds to quartz of very small dimensions when compared to the matrix, with ellipsoidal to drop-like form, forming gently- to well-defined inclusions trails (S_i), mostly showing an oblique to normal relationship with the (001) cleavage, with several trends and dips, but often sub-concordant with S_e (Fig.1-A); (ii) Type 2 consists of quartz with bigger dimensions, less frequent, with often random orientations, occasionally aligned parallel or oblique to the (001) cleavage, and sometimes concentrated in the porphyroblast edges (Fig. 1-B). The majority of the porphyroblasts is unzoned (Fig. 1-A) indicating growth in a static environment with low or no strain (Camilleri, 2009). Zoned porphyroblasts are also observed (Fig. 1-B; C), normally with included cores and inclusion-free borders parallel to the (001) faces. The zoning patterns can result from sin-tectonic growth of biotite in pressure shadows of porphyroblasts with (001) at high angle with S_n (Lister *et al*., 1986; Miyake, 1993; Camilleri, 2009).

IX Congresso Jovens Investigadores em Geociências, LEG 2019
Estremoz, 23-24 Novembro 2019
Livro de Actas

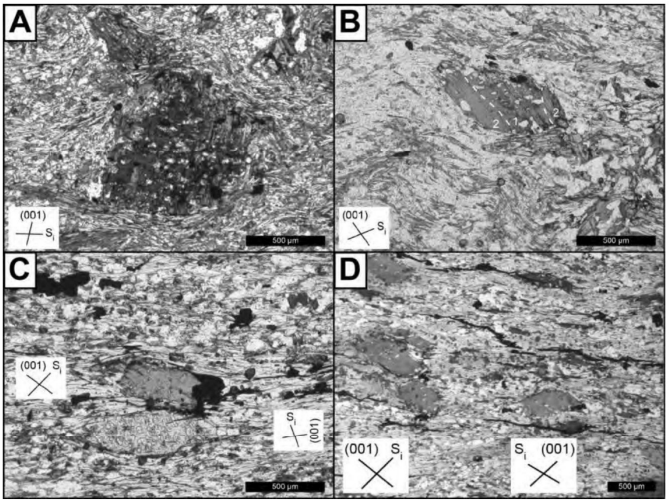

Figure 1 – Photomicrographs of biotite microstructures under plane-polarized light. A: Unzoned porphyroblast with poikiloblastic rim. Adaption of S_n around the crystal is visible. B: Zoned porphyroblast with an included core (1) and less-included borders (2). Two inclusions types are visible. Top right corner of the crystal appears to have suffered dissolution. C: Bottom porphyroblast with the cleavage parallel to S_e, while S_i is oblique to S_e. Top porphyroblast with opposite S_i and (001) orientations. D: Deformation corridor with porphyroblasts showing opposition trends and dips of S_i and (001) cleavage.

Figura 1 – Microfotografias de microstruturas de biotite em luz plana-polarizada. A: Porfiroblasto não zonado com bordo poiciloblástico. É visível a adaptação de S_n em torno do cristal. B: Porfiroblasto zonado com núcleo com inclusões (1) e bordos menos incluídos (2). Dois tipos de inclusões visíveis. Canto superior direito do cristal parece ter sofrido dissolução. C: Porfiroblasto em baixo com clivagem paralela a S_e, enquanto S_i é oblíqua a S_e. D: Corredor de deformação com porfiroblastos a evidenciar direções e inclinações opostas de S_i e de (001).

Inclusion trails similar to Type 1 inclusions, with the same oblique to normal relationship with (001) cleavage, were interpreted in other regions as passive inclusions composed by matrix grains defining a pre-existing foliation (Lister *et al.*, 1986; Kim & Cho, 2008; Camilleri, 2009). The systematic transverse character with the crystal cleavage can be explained by preferential growth, under static conditions, of porphyroblast with (001) at a high angle with the foliation, and the varying orientation and dips of the inclusion trails as the result of different initial crystallographic orientations (Lister *et al.*, 1986; Camilleri, 2009). However, in this study it was possible to observe a small number of porphyroblasts with the (001) cleavage parallel to sub-parallel to S_e, but with inclusion trails still oblique or normal to (001) and, therefore, to S_e (Fig. 1-C). This could be explained by passive incorporation of inclusions from the matrix in porphyroblasts that originally growth with (001) at high angle with the S_n, that were subsequently rotated. This rotation would also help explain the varying trends and dips of inclusion trails (Miyake, 1993; Camilleri, 2009). Nevertheless, the existence of adjacent porphyroblasts in the same deformation corridor with the (001) cleavages and inclusion trails oriented in opposing directions (Fig. 1-C; D) is incompatible with the rotation theory. It is also necessary to explain the granularity difference between Type 1 inclusions and the matrix quartz. This granularity difference coupled with the often drop-like morphology of the inclusions, and the consistent oblique to normal

relations with the (001) cleavage, points that Type 1 inclusions are not passive inclusions but instead the product of the metamorphic reaction that forms biotite (Miyashiro, 1978):

$$\text{phengite + chlorite = biotite + muscovite + quartz + } H_2O$$

The resultant quartz would be then incorporated into the growing porphyroblast, and this incorporation would be conditioned crystallographically by the biotite cleavage.

In what concerns the Type 2 inclusions, they may represent small inclusions that grew during the metamorphic process or matrix grains that were later included. These inclusions may be linked with the final stage of the biotite constructive phase in which occurs matrix overgrowth in all directions (Camilleri, 2009). The final stage is evidenced by poikiloblastic or dendritic rims (Fig. 1-A).

Some indication of biotite deformation was also found, namely, porphyroblast rotation, the local formation of extension fractures parallel to the (001) cleavage and dissolution of porphyroblast corners that endured rotation representing a destructive phase (Fig. 1-B).

FINAL CONSIDERATIONS

Two types of biotite were identified: (i) pre- to sin-Dn+1 (probably D_3) poikiloblastic porphyroblasts; (ii) smaller biotite crystals, mimetic over the matrix S_n foliation. Most porphyroblasts present unzoned inclusion trails. The inclusions can be divided into two types. Type 1 corresponds to a product of the metamorphic reaction instead of passive inclusions as documented in other studies. Type 2 corresponds to matrix inclusions due to overgrowth. The porphyroblasts are not the result of a classic Barrovian metamorphism but instead of a low-pressure and high-temperature static metamorphism.

ACKNOWLEDGMENTS

The authors would like to thank the financial support provided by FCT with the ERA-MIN/0001/2017 - LIGHTS project and to FEDER through the operation POCI-01- 0145-FEDER-007690 funded by COMPETE2020 and by National Funds through FCT within ICT, R&D Unit (reference UID/GEO/04683/2013). J. Cardoso-Fernandes is financially supported within the compass of a Ph.D. Thesis, ref. SFRH/BD/136108/2018, by national funds through FCT, and co-financed by ESF through POCH.

References

- CAMILLERI, P.A. (2009) – Growth, behavior, and textural sector zoning of biotite porphyroblasts during regional metamorphism and the implications for interpretation of inclusion trails: Insights from the Pequop Mountains and Wood Hills, Nevada, USA. *Geosphere,* vol. 5 (3): 215–251.
- DÍEZ BALDA, M.A., VEGAS, R., & LODEIRO, G. (1990) – Central Iberian Zone: structure. In R. D. Dallmeyer & E. Martinez Garcia (Eds.), *Pre-Mesozoic geology of the Iberian Peninsula* (pp. 172–188). Springer Verlag.
- KIM, Y., CHO, M. (2008) – Two-stage growth of porphyroblastic biotite and garnet in the Barrovian metapelites of the Imjingang belt, central Korea. *Journal of Metamorphic Geology*, vol. 26: 385-399.
- LISTER, G.S., BOLAND, J.N., ZWART, H.J. (1986) – Step-wise growth of biotite porphyroblasts in pelitic schists of the western Lys-Caillaouas massif (Pyrenees). *Journal of Structural Geology*, vol. 8 (5): 543-562.
- MIYAKE, A. (1993) – Rotation of biotite porphyroblasts in pelitic schist from the Nukata area, central Japan. *Journal of Structural Geology*, vol. 15 (11): 1303-1313.
- MIYASHIRO, A. (1978) – *Metamorphism and metamorphic belts*. George Allen & Unwin Ed., London, 492.
- PEREIRA, I., DIAS, R., BENTO DOS SANTOS, T., & MATA, J. (2017) – Exhumation of a migmatite complex along a transpressive shear zone: inferences from the Variscan Juzbado–Penalva do Castelo Shear Zone (Central Iberian Zone). *Journal of the Geological Society,* vol. 174 (6): 1004–1018.
- SILVA, A.F., & RIBEIRO, M.L. (1991) – Notícia *Explicativa da folha 15-A*. Lisboa: Serviços Geológicos de Portugal, 52.
- SILVA, A.F., & RIBEIRO, M.L. (1994) – *Notícia Explicativa da folha 15-B*. Lisboa: Instituto Geológico e Mineiro, 48.
- SILVA, A.F., SANTOS, A.J., RIBEIRO, A., & RIBEIRO, M.L. (1990) – *Carta Geológica de Portugal na escala 1/50.000 – folha 15-A*. Lisboa: Serv. Geol. Portugal 1 map.

I.4. Supplementary materials to published journal articles

Remote Sens. **2020**, *12*, x FOR PEER REVIEW 1 of 7

Supplementary Materials: Semi-automatization of support vector machines to map lithium (Li) bearing pegmatites

Joana Cardoso-Fernandes*[1,2], Ana C. Teodoro[1,2], Alexandre Lima[1,2] and Encarnación Roda-Robles[3]

[1] Department of Geosciences, Environment and Land Planning, Faculty of Sciences, University of Porto, Rua Campo Alegre, 4169-007 Porto, Portugal; amteodor@fc.up.pt (A.C.T.); allima@fc.up.pt (A.L.)
[2] Institute of Earth Sciences (ICT), Pole of University of Porto, 4169-007 Porto, Portugal
[3] Departamento Mineralogía y Petrología, Univ. País Vasco (UPV/EHU), Barrio Sarriena, 48940 Leioa, Bilbao, Spain; encar.roda@ehu.es
* Correspondence: joana.fernandes@fc.up.pt

1. Splitting the data into training and test subsets

To ensure the independence between the training and test subsets, the samples were randomly divided according to their respective region of interest (ROI). This means that the samples belonging to the same ROI will either belong to the training or the test set. Unlike the scikit-learn's `train_test_split` function, the `GroupShuffleSplit` iterator does not allow to stratify the sample splitting, i.e., `GroupShuffleSplit` does not guarantee that all classes will be present in both subsets. Therefore, it is necessary to find, by trial and error method, a random state seed that satisfies this condition (in this work the random seed found was 1020).

The data for this example can be found here: https://drive.google.com/drive/folders/1K43om-5XMh0DBwSqwDF-Tz4CEW2ul92a?usp=sharing.

The Sentinel-2 image (S2B_MSIL2A_20190907T112119_N0213_R037_T29TPF_20190907T144322) can be downloaded here: https://scihub.copernicus.eu/dhus/#/home.

```
## The scikit-learn version is 0.20.1
# Start with the general imports
import numpy as np
import pandas as pd

# Load the data
path = '/user/…/'
S2_dataset = pd.read_csv(path, sep='\t')

# Load the ROI information of every sample
path2 = '/user/…/'
groups = pd.read_csv(path2, sep='\t')
groups = groups['Groups'] # remove second column
groups = np.array(groups)

# Create features
X_S2 = S2_dataset.drop('Classname', axis=1)
X_S2 = np.array(X_S2)
print("Features shape: {}".format(X_S2.shape))
```

```
# Create target
y_S2 = S2_dataset['Classname']
y_S2= np.array(y_S2)
print("Target shape: {}".format(y_S2.shape))
# Use GroupShuffleSplit to create train/test set
from sklearn.model_selection import GroupShuffleSplit

train_inds, test_inds = next(GroupShuffleSplit(test_size=0.25,
     random_state=1020).split(X_S2, y_S2, groups))

X_train, X_test, y_train, y_test = X_S2[train_inds],
     X_S2[test_inds], y_S2[train_inds], y_S2[test_inds]

print("X_train shape: {}".format(X_train.shape))
print("y_train shape: {}".format(y_train.shape))
print("X_test shape: {}".format(X_test.shape))
print("y_test shape: {}".format(y_test.shape))
```

2. First stage grid-search

Having the data loaded and the training/test subsets created, it is possible to instantiate the grid-search process. Since the first stage requires more control from the operator, each model was addressed separately. In practice, the first stage grid-search was repeated every time one of the following variables changed: (i) type of data (imbalanced/balanced); (ii) type of model (Linear model, linear kernel, polynomial kernel, and RBF kernel); (iii) parameter range.

As mentioned, the metric score employed in this first stage was the harmonic mean of the precision and recall, i.e., the F1-score of the selected classes (Li-bearing pegmatite and Metasediments). For that, it was necessary to create a personalized metric score to pass was one of the `GridSearchCV` attributes. Instead of using the `f1_score` function directly, we decided to use the `fbeta_score` since it gives the operator the ability to attribute a bigger weight to precision or to recall according to the final goal.

For demonstration purposes, only the source code employed for the Linear model using the class-weight balancing strategy is shown.

```
# General imports
import matplotlib.pyplot as plt
import seaborn as sns; sns.set()
from sklearn.svm import LinearSVC
from sklearn.model_selection import GridSearchCV
from sklearn.metrics import fbeta_score
from sklearn.metrics import make_scorer

# Make notebook stable across runs
np.random.seed(42)
```

```
# Make a personalized score (F1-score), where precision and recall
have the same weight
score_beta = make_scorer(fbeta_score, beta=1,
     labels = ['Li-bearing pegmatite','Metasediments'],
     average = 'micro')

# Specify the parameter range (search space) using a dictionary
    # using the parameters used by Noi & Kappas 2018
param_grid = {'C':[0.25, 0.5, 1, 2, 4, 8, 16, 32, 64, 128]}
print("Parameter grid:\n{}".format(param_grid))

# Create grid-search
grid_search = GridSearchCV(LinearSVC(class_weight='balanced'),
     param_grid, cv=5, n_jobs=-1, verbose=1, scoring=score_beta,
     return_train_score=True)

# Fit grid-search
grid_search.fit(X_train, y_train)

# View best hyperparameters
print('Best C:',  grid_search.best_estimator_.get_params()['C'])

# Show best cross-validation F1-score
print("Best CV F1-score: {:.6f}".format(grid_search.best_score_))

# Show the results of the grid search
results = pd.DataFrame(grid_search.cv_results_)
results

# Show results in an image
scores = np.array(results.mean_test_score)
C_param = [0.25, 0.5, 1, 2, 4, 8, 16, 32, 64, 128]
plt.plot(C_param, scores)
plt.xlabel('C')
plt.ylabel('scores')
```

3. Second stage grid-search, model evaluation and image prediction

This section corresponds to the automatized part of the image classification process. During the second stage grid-search, the Linear model, linear kernel and RBF kernel are confronted, and the best model is automatically returned. The best model is evaluated using the test subset and used to predict the whole image.

The following source code exemplifies the automated process of model selection, evaluation and classification for the imbalanced dataset. As before, the training/test subsets are already loaded.

```
# General imports
import matplotlib.pyplot as plt
import seaborn as sns; sns.set()
import pandas as pd
from sklearn.svm import SVC
from sklearn.svm import LinearSVC
from sklearn.model_selection import GridSearchCV
from sklearn.pipeline import Pipeline
import rasterio as rio
from rasterio import plot
import geopandas as gpd


# Make notebook stable accross runs
np.random.seed(42)

# Create a pipeline
pipe = Pipeline([("classifier", SVC())])

# Create dictionary with candidate algorithms and their parameters
search_space = [{"classifier": [LinearSVC()],
    "classifier__max_iter": [2500],
    "classifier__C": [30.5, 31, 31.5, 32, 32.5, 33, 33.5]},
    {"classifier": [SVC()],
     "classifier__kernel":['linear'],
    "classifier__C": [6.5, 7, 7.5, 8, 8.5, 9, 9.5]},
    {"classifier": [SVC()],
     "classifier__kernel":['rbf'],
     "classifier__C": [0.5, 1, 1.5, 2, 2.5, 3, 3.5],
     "classifier__gamma": [1.4,1.6,1.8,2,2.2,2.4,2.6]}]

# Create grid-search
grid_search = GridSearchCV(pipe, search_space, cv=5, n_jobs=-1,
    verbose=1, scoring= 'accuracy', return_train_score=True)

# Fit grid-search
best_model = grid_search.fit(X_train, y_train)

print("Best parameters: {}".format(best_model.best_params_))
print("Best CV score: {:.6f}".format(best_model.best_score_))
print("Test-score: {:.6f}".format(best_model.score(X_test,y_test)))
```

```
# Show the results of the grid search
results = pd.DataFrame(best_model.cv_results_)

# Nested cross-validation to evaluate the best model
from sklearn.model_selection import cross_val_score
scores= cross_val_score(grid_search, X_S2, y_S2)
print("Cross-validation scores: ", scores)
print("Mean cross-validation score: ", scores.mean())


### Evaluate the classifier predictions
# Predict labels for new data
y_predicted = best_model.predict(X_test)

# Get classification report
from sklearn.metrics import classification_report
print(classification_report(y_test, y_predicted))

# Show confusion matrix
from sklearn.metrics import confusion_matrix
matrix = confusion_matrix(y_test, y_predicted)
class_names = np.unique(S2_dataset["Classname"])
dataframe = pd.DataFrame(matrix, index=class_names,
    columns=class_names)

plt.figure(figsize = (16,10))
sns.heatmap(dataframe, annot=True, cbar=None,
    fmt='g',cmap='YlGnBu', annot_kws={"size": 15})
plt.title("Confusion Matrix",fontsize=32, pad=15),
    plt.tight_layout()
plt.ylabel("True Class",fontsize=25, labelpad=15),
    plt.xlabel("Predicted Class",fontsize=25, labelpad=15)
plt.xticks(fontsize=16,rotation = 45)
plt.yticks(fontsize=16)
plt.show()

# Compute kappa statistics
from sklearn.metrics import cohen_kappa_score
kappa = cohen_kappa_score(y_test, y_predicted)
print("kappa statistics: ", kappa)
```

```
## Predict the whole image
#Load the Sentinel-2 bands
b2 = rio.open('/user/…/B2.tif')
b3 = rio.open('/user/…/B3.tif')
b4 = rio.open('/user/…/B4.tif')
b8 = rio.open('/user/…/B8.tif')
b11 = rio.open('/user/…/B11.tif')
b12 = rio.open('/user/…/B12.tif')

B2 = b2.read(1).astype('float32')
B3 = b3.read(1).astype('float32')
B4 = b4.read(1).astype('float32')
B8 = b8.read(1).astype('float32')
B11 = b11.read(1).astype('float32')
B12 = b12.read(1).astype('float32')

# Write image to stack
reshaped_img = np.dstack([B2, B3, B4, B8, B11, B12])
print(reshaped_img.shape)

# Predict image
class_prediction = best_model.predict(reshaped_img.reshape(-1, 6))

# Reshape image back into a 2D matrix
class_prediction =
    class_prediction.reshape(reshaped_img[:, :, 0].shape)

# Convert the classes' string labels to a numpy array
class_prediction[class_prediction == 'Agricultural fields'] = 0
class_prediction[class_prediction == 'Burned areas'] = 1
class_prediction[class_prediction == 'Granite'] = 2
class_prediction[class_prediction == 'Li-bearing pegmatite'] = 3
class_prediction[class_prediction == 'Metasediments'] = 4

class_prediction = class_prediction.astype(float)
```

```
# Export final image
Imb_acc = rio.open('/user/…/Final_classified_map.tiff','w',
                           driver='Gtiff',
                           width = b4.width,
                           height = b4.height,
                           count=1,
                           crs = b4.crs,
                           transform = b4.transform,
                           dtype='float64')
Imb_acc.write(class_prediction,1)
Imb_acc.close()
```

data

MDPI

Supplementary Materials: Tools for remote exploration: a Lithium (Li) dedicated spectral library of the Fregeneda-Almendra aplite-pegmatite field

Joana Cardoso-Fernandes [1,2,*], João Silva [1], Filipa Dias [1,2], Alexandre Lima [1,2], Ana C. Teodoro [1,2], Odile Barrès [3], Jean Cauzid [3], Mônica Perrotta [4], Encarnación Roda-Robles [5], Maria Anjos Ribeiro [1,2]

[1] Department of Geosciences, Environment and Spatial Plannings, Faculty of Sciences, University of Porto, Rua Campo Alegre, 4169-007 Porto, Portugal; joana.fernandes@fc.up.pt (J.C-F.); .); jpc.silva1996@gmail.com (J.S); filipa.dias@fc.up.pt (F.D); allima@fc.up.pt (A.L.); amteodor@fc.up.pt (A.C.T.); maribeir@fc.up.pt (M.A.R.)
[2] ICT (Institute of Earth Sciences) – Porto pole (Portugal), Rua Campo Alegre, 4169-007 Porto, Portugal
[3] Université de Lorraine, CNRS, GeoRessources Laboratory, F-54000 Nancy, France; odile.barres@univ-lorraine.fr (O.B.); jean.cauzid@univ-lorraine.fr (J.C.)
[4] Remote Sensing Division, Geological Survey of Brazil (CPRM), Rua Costa, 01304-010, São Paulo, Brazil; monica.perrotta@cprm.gov.br
[5] Departamento de Geología, Universidad del País Vasco (UPV/EHU), Barrio Sarriena, 48940 Leioa, Bilbao, Spain; encar.roda@ehu.es
* joana.fernandes@fc.up.pt

Continuum removal and feature extraction

The source code employed to remove the continuum and extract the main absorption features for the spectra collected using the SR-6500A equipment is given as an example. The process is similar for the spectra acquired with the ASD FieldSpec 4 and only minor changes are required: (i) when reading the original spectra files, only one header line needs to be skipped; (ii) these spectra already show absolute reflectance values, so there is no need to make the conversion.

```
# General imports
import numpy as np
import pandas as pd
import matplotlib.pyplot as plt
import os
from pysptools.spectro import FeaturesConvexHullQuotient
from pysptools.spectro import SpectrumConvexHullQuotient

# State where to save the resultant spectra
path_results = '/.../results/'

# Create function to save the spectra
def save_fig(fig_id, tight_layout=True, fig_extension="tif", resolution=300):
    path = os.path.join(path_results, fig_id + "." + fig_extension)
    print("Saving figure", fig_id)
    if tight_layout:
        plt.tight_layout()
    plt.savefig(path, format=fig_extension, dpi=resolution)
```

```
# Specify the path the folder containing the raw spectra
path_folder = '/.../'

# Find every file in the folder directory
spectra_paths = [os.path.join(path_folder, f) for f in os.listdir(path_folder) if
os.path.isfile(os.path.join(path_folder, f))]
spectra_paths.sort()
spectra_paths

# Get the name of the files
names = [os.path.splitext(os.path.basename(x))[0] for x in spectra_paths]

# Create a dictionary with all the spectra
spectra = [1]
for i in range(len(names)):
    spectra[names[i]] = pd.read_table(spectra_paths[i],
           delim_whitespace=True, names = ('Wvl', 'Reflect. %'), skiprows=28)

# Plot the spectra and save the figure
for key, value in spectra.items():
    plt.figure()
    ax = plt.gca()
    spectra[key].plot(kind='line',x='Wvl',y='Reflect. %',ax=ax)
    plt.xlabel('Wavelength (nm)',fontsize=14)
    plt.xticks(size=14)
    plt.ylabel('Reflectance (%)',fontsize=14)
    plt.yticks(size=14)
    plt.title(key, fontsize=16, pad=10)
    ax.get_legend().remove()
    plt.show()
    save_fig(key)
    plt.pause(1)
    plt.close()

# Change the parameters for plotting the figures
params = {'legend.fontsize': 'xx-large',
         'lines.linewidth': 3,
         'lines.markersize': 13,
         'figure.figsize': (14,11),
         'figure.dpi':300,
         'figure.titlesize': 'xx-large',
```

```
        'axes.labelsize': 'xx-large',
        'axes.titlesize':'xx-large',
        'axes.labelpad':15,
        'axes.titlepad':15,
        'xtick.labelsize':'x-large',
        'ytick.labelsize':'x-large'}
plt.rcParams.update(params)

# Remove the continnum
""" The FeaturesConvexHullQuotient function removes the convex-hull of the signal by hull
quotient"""
spectrum = list()
wvl_list = list()

for key, value in spectra.items():
    pixel = value['Reflect. %']
    pixel = pixel/100 # get absolute reflectance values
    wvl = value['Wvl']
    spectrum = pixel.tolist()
    wvl_list = wvl.tolist()
    spectra_features = FeaturesConvexHullQuotient(spectrum=spectrum,
            wvl = wvl_list, baseline=0.93)
    # plot the extracted features
    spectra_features.plot(path= path_results,plot_name= key, feature='all')
    # plot side by side original and corrected spectrum
    spectra_features.plot_convex_hull_quotient(path= path_results,
           plot_name= key + '_comparison')

# Get the statistics associated with each feature
b = {}
spectrum = list()
wvl_list = list()
for key, value in spectra.items():
    pixel = value['Reflect. %']
    pixel = pixel/100
    wvl = value['Wvl']
    spectrum = pixel.tolist()
    wvl_list = wvl.tolist()
    spectra_features = FeaturesConvexHullQuotient(spectrum=spectrum,
            wvl = wvl_list, baseline=0.93)
    b = spectra_features.features_all
    b_stats = pd.DataFrame(b)
```

```
    is_keep = b_stats['state']=='keep'
    b_stats_keep = b_stats[is_keep]
    b_stats_keep.to_csv(path_results+key+'.csv', sep=',', index =False)

# Export the continuum removed spectrum as *.txt, plot and save the spectra
b = {}
spectrum = list()
wvl_list = list()
plt.rcParams.update(plt.rcParamsDefault)
for key, value in spectra.items():
    pixel = value['Reflect. %']
    pixel = pixel/100
    wvl = value['Wvl']
    spectrum = pixel.tolist()
    wvl_list = wvl.tolist()
    spectra_remov = SpectrumConvexHullQuotient(spectrum=spectrum, wvl = wvl_list)
    conti_rem = spectra_remov.get_continuum_removed_spectrum()
    cont_corr = pd.DataFrame({'Reflectance':conti_rem})
    cont_corr.insert(0, 'Wvl', wvl)
    cont_corr['Wvl']=wvl
    cont_corr.to_csv(path_results+key+'_continuum_corr_spectra.txt',
           sep= '\t', index=False, header=False)
    plt.figure()
    ax = plt.gca()
    cont_corr.plot(kind='line',color= 'g', x='Wvl',y='Reflectance', ax=ax)
    plt.xlabel('Wavelength (nm)', fontsize=14)
    plt.xticks(size=14)
    plt.ylabel('Continuum removed reflectance',fontsize=14)
    plt.yticks(size=14)
    plt.title(key,fontsize=16, pad=10)
    ax.get_legend().remove()
    plt.show()
    save_fig(key + "_continuum_removed")
    plt.pause(1)
    plt.close()
```

The supplementary materials for “Interpretation of the reflectance spectra of Lithium (Li) minerals and pegmatites: a case study for mineralogical and lithological identification in the Fregeneda-Almendra area” are available at:
https://www.mdpi.com/article/10.3390/rs13183688/s1

minerals

MDPI

Supplementary Material for

Lithium Potential Mapping Using Artificial Neural Networks: A Case Study from Central Portugal

Martin Köhler [1,*], Delira Hanelli [1], Stefan Schaefer [1], Andreas Barth [1], Andreas Knobloch [1], Peggy Hielscher [1], Joana Cardoso-Fernandes [2,3], Alexandre Lima [2,3] and Ana C. Teodoro [2,3]

Supplemental Figure S1

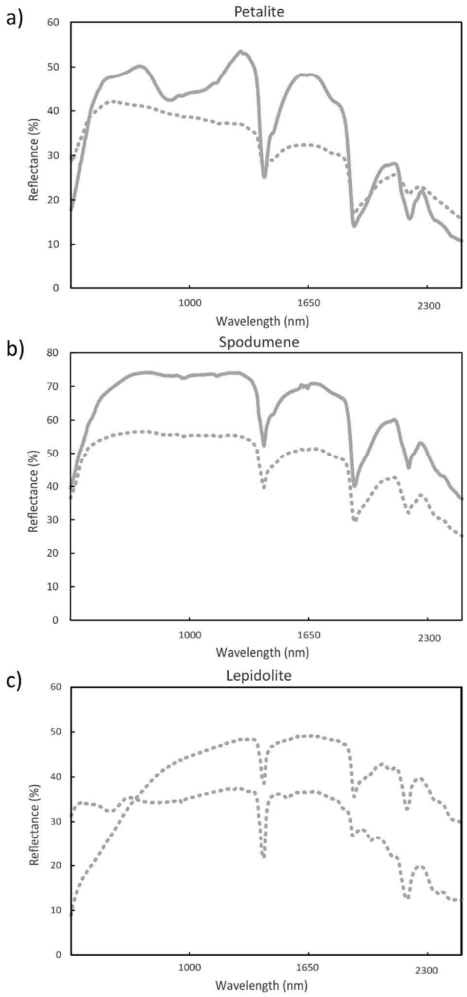

Figure S1. Reference spectral signatures of (**a**) petalite samples from Bajoca mine, (**b**) spodumene samples from the Alberto mine, and (**c**) lepidolite samples from the Feli mines [45]. Dotted curves correspond to fresh samples. Full curves represent weathered samples.

Supplemental Figure S2

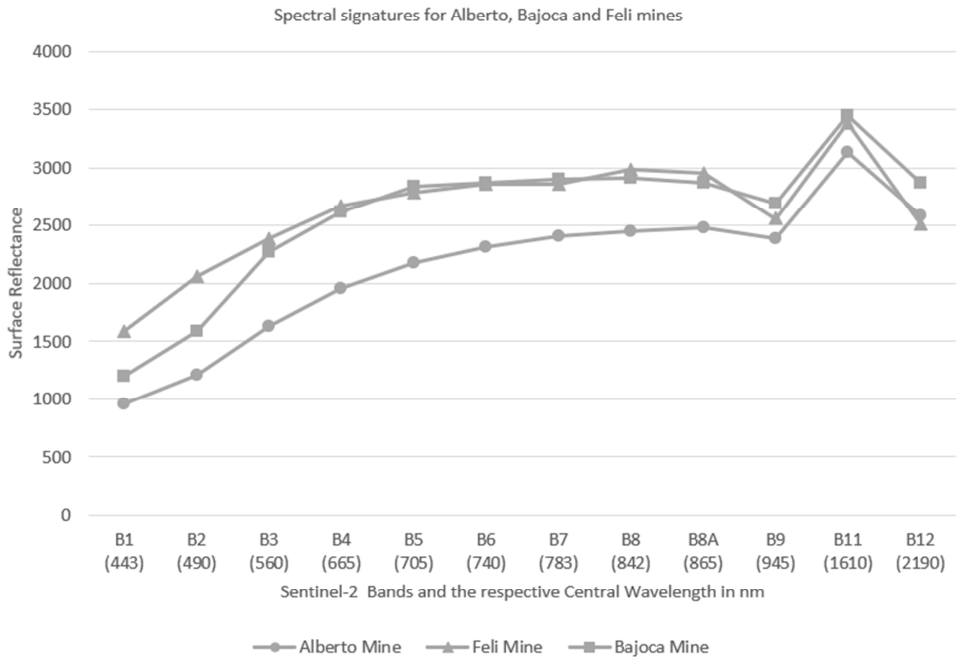

Figure S2. Spectral signatures for Alberto, Bajoca and Feli mines based on Sentinel-2 data.

Supplemental Figure S3

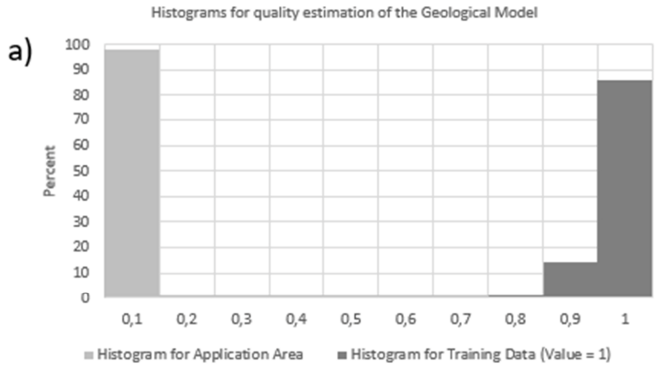

Histograms for the quality estimation of the Geological Model indicating that the ANN is able to identify >80% of the pixels in the training patterns with a scale better than 0.9, resulting in a reliable model.

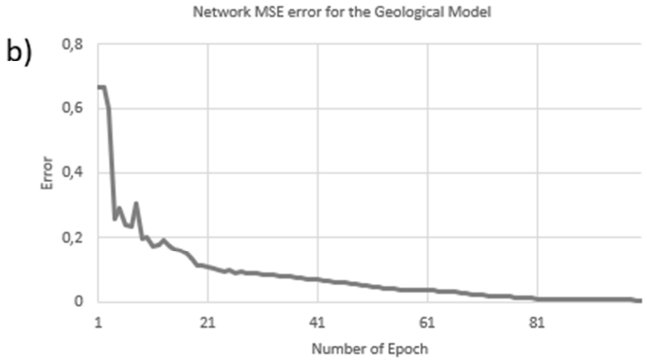

Network MSE error for the Geological Model indicating a stable ANN able to find correlations between the controlling parameters and the training data. The final Network MSE error is 0,0054175.

Figure S3. Histogram (**a**) and Network MSE error (**b**) for the Geological Model.

Supplemental Figure S4

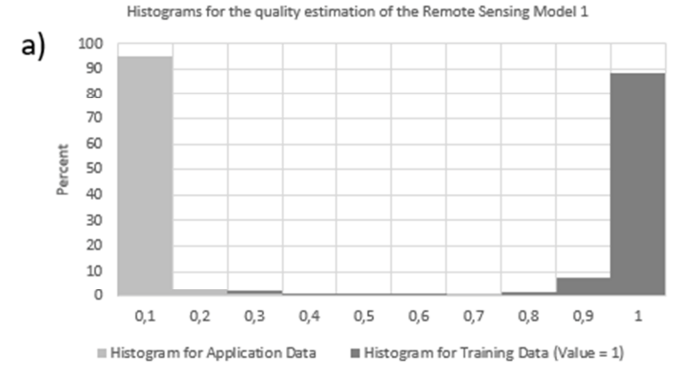

Histograms for the quality estimation of the Remote Sensing Model 1 indicating that the ANN is able to identify >90% of the pixels in the training patterns with a scale better than 0.9, resulting in a reliable model.

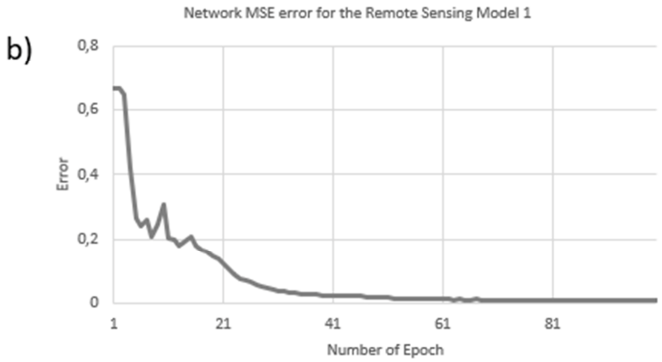

Network MSE error for the Remote Sensing Model 1 indicating a stable ANN able to find correlations between the controlling parameters and the training data. The final Network MSE error is 0,0082843.

Figure S4. Histogram (**a**) and Network MSE error (**b**) for the Remote Sensing Model 1.

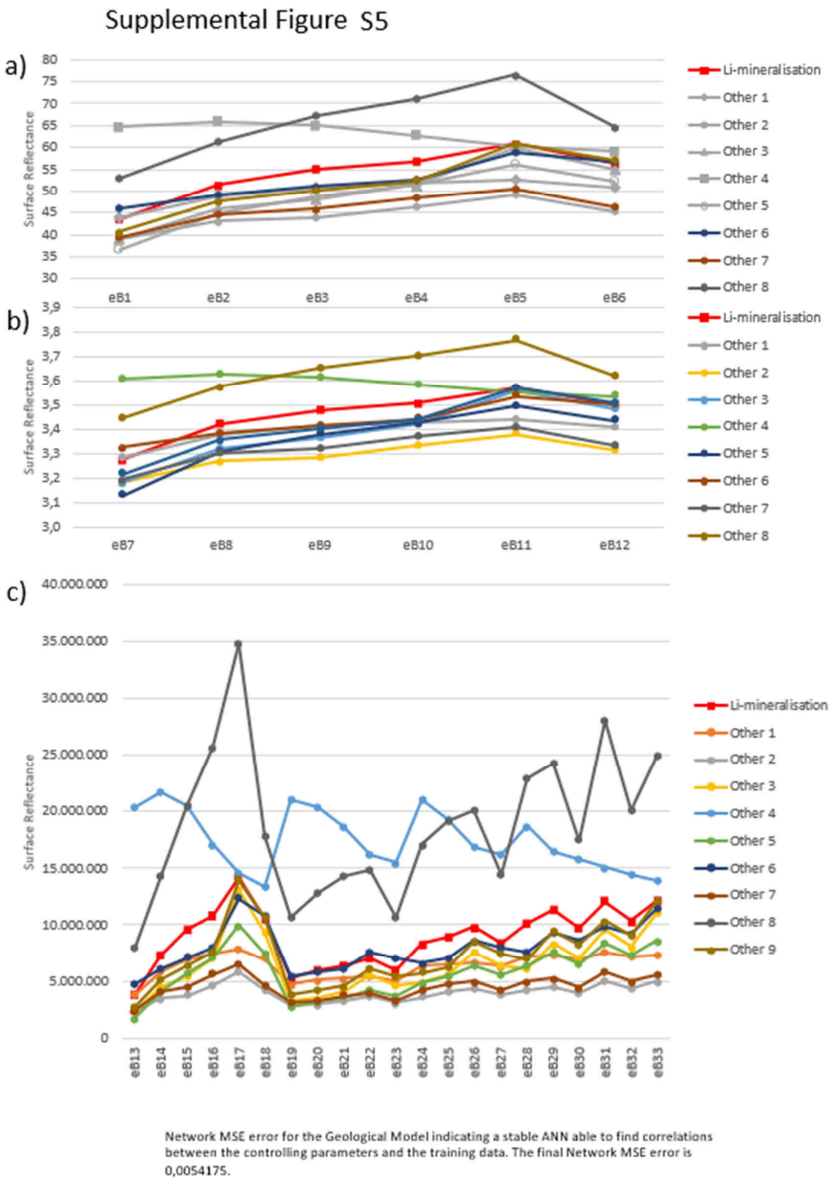

Figure S5. Spectral signatures for the extended spectral bands: (**a**) 1–6, (**b**) 7–12, (**c**) 13–32.

Supplemental Figure S6

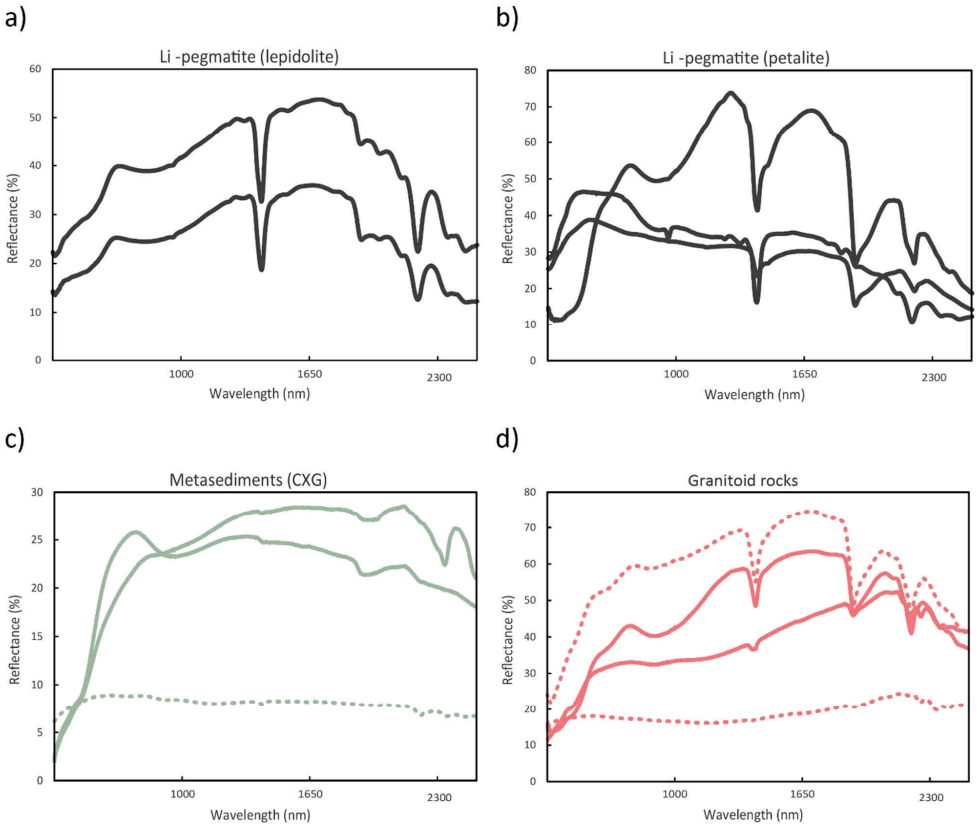

Figure S6. Reference spectral signatures of (**a**) lepidolite-bearing pegmatites, (**b**) petalite-bearing pegmatites (Bajoca mine), (**c**) schist-metagreywacke complex (CXG) metasediments, and (**d**) granitoid rocks [45]. Dotted curves correspond to fresh samples. Full curves represent weathered samples.

Supplemental Figure S7

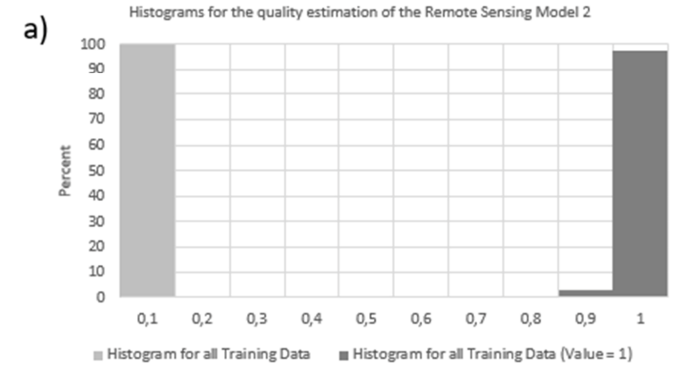

Histograms for the quality estimation of the Remote Sensing Model 2 indicating that the ANN is able to identify >90% of the pixels in the training patterns with a scale better than 0.9, resulting in a reliable model.

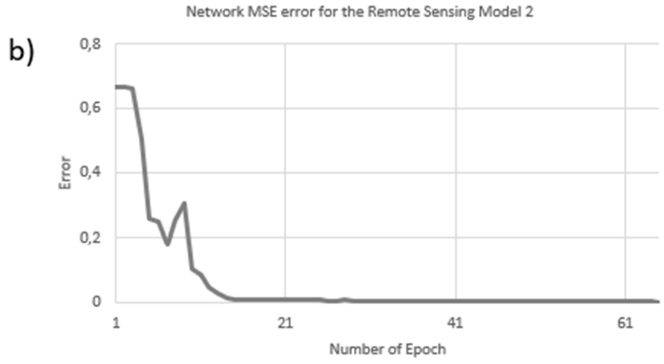

Network MSE error for the Remote Sensing Model 2 indicating a stable ANN able to find correlations between the controlling parameters and the training data. The final Network MSE error is 0,00097011.

Figure S7. Histogram (**a**) and Network MSE error (**b**) for the Remote Sensing Model 2.

Appendix II. Geochemical studies

II.1. Sampling and sample preparation

As previously mentioned, two distinct sampling campaigns were conducted in the scope of the LIGHTS and GREENPEG projects, respectively. The first corresponded to an exploratory campaign where samples were collected at relatively similar intervals increasing further away from pegmatite dykes. Since the preliminary results showed that the most important enrichments occurred at closer distances from the dykes, in the scope of the GREENPEG project a logarithmic sampling scheme was employed, with a higher sample density close to the dykes and fewer samples with increasing distance. In both cases, the samples were collected using appropriate geological hammers and sledgehammers as well as chisels. Several aspects were taken into account in the field, namely evidence of rock alteration (weathering) or the existence of smaller pegmatite dykes or quartz veins. All samples were named and individually bagged *in situ*.

Sample preparation for the whole-rock geochemical analyses was conducted at the Faculty of Sciences of the University of Porto (FCUP) in the case of the LIGHTS campaign, while for the GREENPEG campaign the samples were prepared at the University of the Basque Country (UPV/EHU) as described in Chapter 4 (Section IV.2). At FCUP, the samples were first crushed with a jaw crusher and ground with a hammer mill to a particle size of <0.5 mm. Afterward, they were sorted and ground with an automated agate mortar (Retsch RM 200) to a fraction size of +/- 125 microns.

II.2. Sample location and description

This section provides the location (Table II. 2; Figure II. 1) and description of the samples collected in the LIGHTS campaign. The same information for the GREENPEG campaign is found in Appendix II.5.

The following sampling codes were used (Table II. 1):

Table II. 1. Employed sampling codes.

T4	—	Simple, concordant pegmatite dykes
T5	—	Potassium feldspar-bearing aplite-pegmatite dykes
T6	—	Simple, discordant aplite-pegmatite dykes
TC	Tumbo de la Caldera	
T7	—	Petalite-bearing aplite-pegmatite dykes
BJ	Bajoca	
BJ-DD	Bajoca (drill-core)	
ALB	Alberto	Spodumene-bearing aplite-pegmatite dykes
AL	Almendra	Li-mica-rich aplite-pegmatite dykes
FE	Feli	Li-mica and spodumene-bearing aplite-pegmatite dykes

Table II. 2. Coordinate list for the LIGHTS samples.

Group	Sample	X (UTM)	Y (UTM)
Control	CXG1 436	690404.60	4540924.57
	CXG2 437	690870.87	4540187.44
	CXG3 438	690966.91	4539993.74
	CXG5 PP01	657273.35	4546519.52
T4	T4-19-01	681145.68	4538892.12
	T4-19-02	681145.95	4538891.47
	T4-19-03	681146.25	4538890.87
	T4-19-04	681146.58	4538890.20
	T4-19-05	681145.41	4538892.58
	T4-19-06	681144.84	4538893.48
	T4-19-07	681126.48	4538902.53
T5	T5-19-01a	678268.78	4540036.68
	T5-19-02	678269.20	4540036.68
	T5-19-03	678271.01	4540036.59
	T5-19-04	678266.98	4540010.20
T6	T6-19-01	678393.94	4541972.40
	T6-19-02	678386.15	4541973.55
	T6-19-03	678385.66	4541973.59
	T6-19-04	678384.66	4541973.61
	T6-19-05	678378.09	4541974.32
	T6-19-06	678375.18	4541974.24
	T6-19-07	678373.12	4541974.22
TC	TC-19-01	677939.79	4539979.83
	TC-19-02	677939.31	4539979.82
	TC-19-03	677938.85	4539979.85
	TC-19-04	677940.06	4539979.83
	TC-19-05	677941.54	4539979.84
	TC-19-06	678014.00	4539991.73
	TC-19-07	678015.09	4539991.73
	TC-19-08	678016.08	4539991.73
	TC-19-09	678017.11	4539991.70
	TC-19-10	678018.30	4539991.73
	TC-19-11	678018.98	4539991.81
	TC-19-12	678019.63	4539991.87
T7	T7-19-01	681059.87	4541862.71
	T7-19-02	681058.48	4541862.75
	T7-19-03	681057.39	4541862.71
	T7-19-04	681056.21	4541862.73
BJ	BJ-01-385	666849.60	4540501.25
	BJ-02-LT1	666847.56	4540502.20
	BJ-03-384	666842.69	4540505.31
	BJ-04-383	666840.34	4540508.82

Group	Sample	X (UTM)	Y (UTM)
	BJ-05-382	666837.60	4540510.75
	BJ-06-381	666834.38	4540511.79
	BJ-07-377	666832.26	4540512.41
	BJ-09-379	666832.78	4540515.53
	BJ-10-378b	666831.25	4540516.38
	BJ-10-LT3/378	666831.25	4540516.38
	BJ-11-376	666832.02	4540519.40
	BJ-12-LT6	666746.16	4540516.90
	BJ-13-390	666742.62	4540509.82
	BJ-14-388	666753.72	4540502.74
	BJ-15-386	666757.34	4540491.38
	BJ-16-387	666762.75	4540493.84
	BJ-19-01	666768.65	4540708.46
	BJ-19-02	666758.79	4540512.63
	BJ-19-03	—	—
	BJ-19-04	666736.00	4540886.55
	BJ-19-05	666804.81	4540831.91
	BJ-19-06	666804.81	4540831.91
	BJ-19-07	666784.00	4540333.00
	BJ-19-08	666783.00	4540287.00
	BJ-19-09	—	—
	BJ-19-12	666760.00	4540410.00
	BJ-20-04	666762.70	4540507.05
	BJ-20-05	666753.19	4540507.39
	BJ-20-06	666744.81	4540505.86
	BJ-20-07	666731.73	4540503.80
	BJ-20-08	666723.52	4540509.50
	BJ-20-09	666701.80	4540506.34
	BJ-20-10	666686.84	4540509.11
	BJ-20-11	666672.72	4540508.45
	BJ-20-14	666144.83	4540485.72
	BJ-X-LT4	666800.15	4540496.13
BJ-DD	BJ03-A-DD	—	—
	BJ03-B-DD	—	—
	BJ03-D-DD	—	—
	BJ04-A-DD	—	—
	BJ04-B-DD	—	—
	BJ04-C-DD	—	—
	BJ04-D-DD	—	—
	BJ04-E-DD	—	—
	BJ04-F-DD	—	—
ALB	ALB-19-01	681074.49	4541938.95
	ALB-19-02	681074.54	4541938.39
	ALB-19-03	681074.76	4541936.83
	ALB-19-04	681075.09	4541935.07
	ALB-19-05	681074.76	4541945.06
	ALB-19-06	681074.46	4541946.83
AL	AL-19-10	667627.00	4540970.00
	AL-19-11b	667578.89	4540928.40
FE	FE-19-01	677626.14	4543837.34
	FE-19-02	677626.67	4543837.34
	FE-19-03	677627.09	4543837.34
	FE-19-04	677627.80	4543837.27
	FE-19-05	677628.54	4543837.29
	FE-19-06	677630.63	4543837.25
	FE-19-07	677632.77	4543837.21
	FE-19-08	677636.69	4543837.59
	FE-19-09	677643.36	4543842.68
	FE-20-01	677816.98	4543880.40
	FE-20-02	677646.55	4543848.94
	FE-20-03	677657.29	4543832.87
	FE-20-04	677688.60	4543814.86
	FE-20-05	677712.15	4543825.64

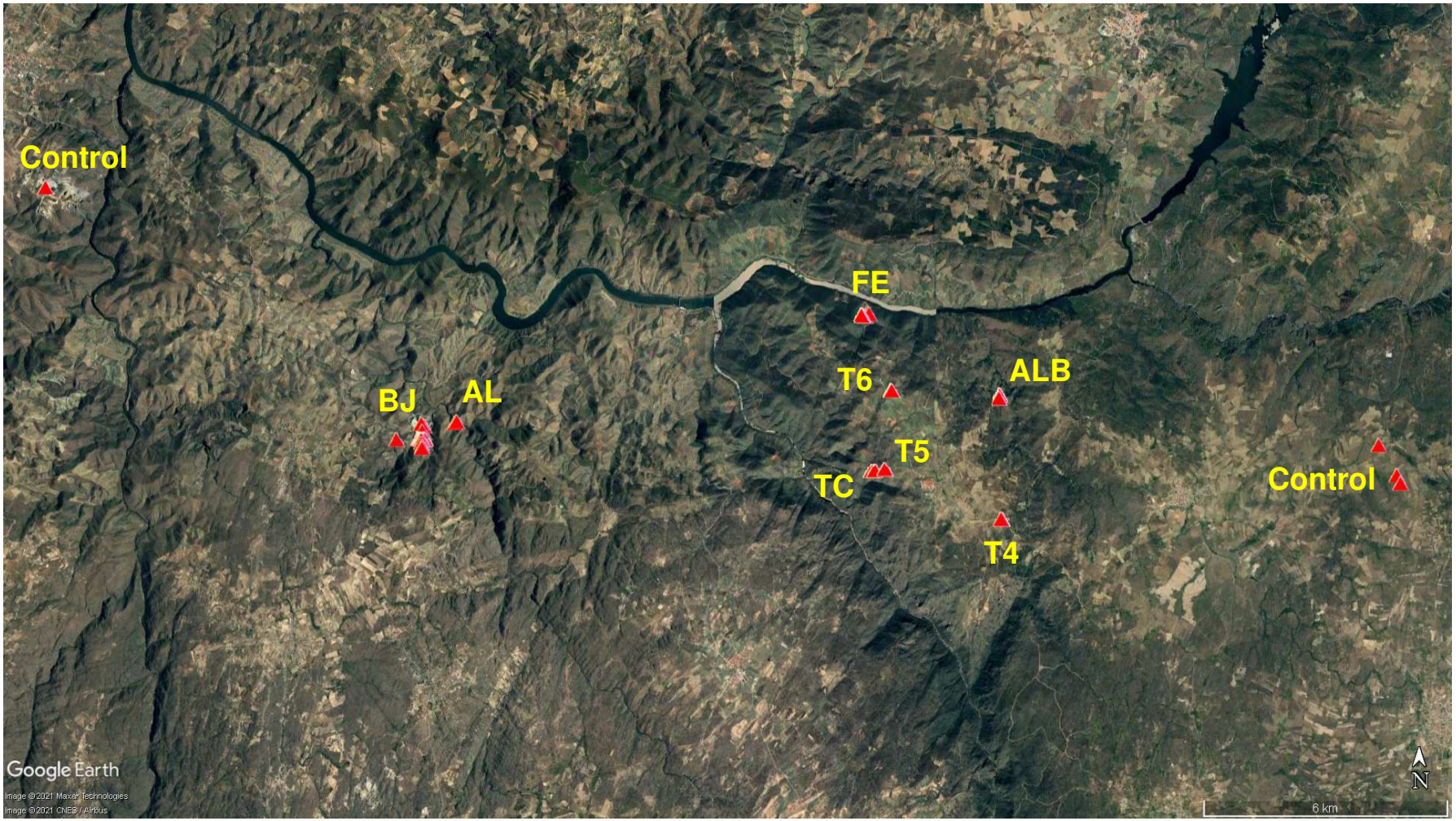

Figure II. 1. Geographic location of the LIGHTS samples according to the previously defined sample groups: T4 – Simple, concordant pegmatite dykes; T5 – Potassium feldspar-bearing aplite-pegmatite dykes; T6/TC – Simple, discordant aplite-pegmatite dykes; T7/BJ-DD/BJ – Petalite-bearing aplite-pegmatite dykes; ALB – Spodumene-bearing aplite-pegmatite dykes; AL – Li-mica-rich aplite-pegmatite dykes; FE – Li-mica and spodumene-bearing aplite-pegmatite dykes.

Table II. 3. Sample list and short description for the LIGHTS campaign. Sample naming was made according to the previously defined sample groups: T4 – Simple, concordant pegmatite dykes; T5 – Potassium feldspar-bearing aplite-pegmatite dykes; T6/TC – Simple, discordant aplite-pegmatite dykes; T7/BJ-DD/BJ – Petalite-bearing aplite-pegmatite dykes; ALB – Spodumene-bearing aplite-pegmatite dykes; AL – Li-mica-rich aplite-pegmatite dykes; FE – Li-mica and spodumene-bearing aplite-pegmatite dykes.

Sample	Date	Local	Description	Borehole depth	Distance (m)
CXG1 436	12/11/19	Hinojosa-Saucelle	CXG control sample (Desejosa formation)	—	—
CXG2 437	12/11/19	Hinojosa-Saucelle	CXG control sample (Desejosa formation)	—	—
CXG3 438	12/11/19	Hinojosa-Saucelle	CXG control sample (Desejosa formation)	—	—
CXG4 441	06/02/20	Poio's quarry	CXG control sample (Desejosa formation)	—	—
CXG5 PP01	06/0/220	Poio's quarry	CXG control sample (Desejosa formation)	—	—
BJ-20-14	26/09/20	Almendra	CXG control sample (Pinhão formation); outside the Bajoca concession (600 m from the Bajoca pegmatite but near small barren dykes)	—	600
T4-19-01	12/11/19	Valdenoguera	Contact footwall	—	0
T4-19-02	12/11/19		Footwall	—	+/- 0.7
T4-19-03	12/11/19		Footwall	—	+/- 0.7
T4-19-04	12/11/19		Footwall	—	+/- 2
T4-19-05	12/11/19		Contact hanging wall	—	0.10
T4-19-06	12/11/19		Hanging wall	—	+/- 1
T4-19-07	12/11/19	Valdenoguera	Metasedimentary enclave (barren, discordant dyke)	—	—
T5-19-01	12/11/19	On the road between La Fregeneda and Tumbo de la Caldera	W contact	—	0
T5-19-02	12/11/19		W profile	—	+/- 0.5
T5-19-03	12/11/19		W profile	—	+/- 2
T5-19-04	12/11/19	On the road between La Fregeneda and Tumbo de la Caldera	Metasedimentary enclave	—	—
T6-19-01	12/11/19	Main road between Barca D'Alva and La Fregeneda, near the entrance to the Feli stockpile	E contact	—	0
T6-19-02	12/11/19		E profile	—	1
T6-19-03	12/11/19		E profile	—	1.5
T6-19-04	12/11/19		E profile	—	9.75
T6-19-05	12/11/19		W contact	—	0
T6-19-06	12/11/19		W profile	—	2.95
T6-19-07	12/11/19		W profile	—	4.9

Sample	Date	Local	Description	Borehole depth	Distance (m)
TC-19-01	12/11/19	Tumbo de la Caldera	W contact	—	0
TC-19-02	12/11/19		W profile	—	0.55
TC-19-03	12/11/19		W profile	—	1.15
TC-19-04	12/11/19		E contact (visible psammitic and calcsilicated layers)	—	0
TC-19-05	12/11/19		E profile	—	1.4
TC-19-06	12/11/19	Tumbo de la Caldera	W profile for the first dyke to the left	—	+/- 2.5
TC-19-07	12/11/19		W profile for the first dyke to the left	—	+/-1
TC-19-08	12/11/19		W contact for the first dyke to the left	—	0
TC-19-09	12/11/19		E contact for the first dyke to the left (between dykes)	—	0
TC-19-10	12/11/19		W contact for the second dyke to the right (between dykes)	—	0
TC-19-11	12/11/19		E contact for the second dyke to the right	—	0
TC-19-12	12/11/19		E profile for the second dyke to the right	—	+/- 1
T7-19-01	12/11/19	Entrance to Alberto Mine	NW contact	—	0
T7-19-02	12/11/19		NW profile	—	+/- 1
T7-19-03	12/11/19		NW profile	—	+/- 2
T7-19-04	12/11/19		NW profile	—	+/- 3
BJ-01-385	20/07/18	Bajoca Mine	E profile	—	30
BJ-02-LT1	20/07/18		E profile	—	28
BJ-03-384	20/07/18		E profile	—	23
BJ-04-383	20/07/18		E profile	—	19
BJ-05-382	20/07/18		E profile	—	15
BJ-06-381	20/07/18		E profile	—	13
BJ-07-377	20/07/18		E profile	—	11
BJ-09-379	20/07/18		E profile	—	9
BJ-10-378b	20/07/18		E profile	—	8
BJ-10-LT3/378	20/07/18		E profile	—	7
BJ-11-376	20/07/18		E profile	—	5
BJ-12-LT6	20/07/18		W profile	—	29
BJ-13-390	20/07/18		W profile	—	27
BJ-14-388	20/07/18		W profile	—	14

Sample	Date	Local	Description	Borehole depth	Distance (m)
BJ-15-386	20/07/18		W profile	—	6
BJ-16-387	20/07/18		W profile	—	1.5
BJ-19-01	09/05/19	Bajoca Mine	W contact	—	0
BJ-19-02	09/05/19	Bajoca Mine	Loose sample; quartzitic layers	—	—
BJ-19-03	09/05/19	Bajoca Mine	Loose sample; psammitic level with arsenopyrite in the contact	—	—
BJ-19-04	10/05/19	Bajoca Mine	Contact with the barren E-W branch	—	0
BJ-19-05 (a, b)	10/05/19	Bajoca Mine	Loose samples near the stockpile with intense tourmalinization	—	—
BJ-19-06	10/05/19	Bajoca Mine	Loose samples near the stockpile with sulfides	—	—
BJ-19-07	11/05/19	Bajoca Mine	Top contact (natural outcrop to S)	—	0
BJ-19-08	11/05/19	Bajoca Mine	Top contact (natural outcrop to S)	—	0
BJ-19-09	12/05/19	Bajoca Concession	Loose sample; barren dyke	—	—
BJ-19-12	12/05/19	Bajoca Mine	W contact	—	0
BJ-20-01	26/09/20	Bajoca Mine	E profile	—	+/-10
BJ-20-02	26/09/20		E profile	—	+/- 20
BJ-20-03	26/09/20		E profile	—	+/- 30
BJ-20-04	26/09/20		W contact	—	0
BJ-20-05	26/09/20		W profile	—	10
BJ-20-06	26/09/20		W profile	—	20
BJ-20-07	26/09/20		W profile	—	30
BJ-20-08	26/09/20		W profile	—	40
BJ-20-09	26/09/20		W profile	—	60
BJ-20-10	26/09/20		W profile; near inverse fault (N10º; 60ºW)	—	80
BJ-20-11	26/09/20		W profile	—	100
BJ04-A-DD	16/04/19	Bajoca Mine (Drill core samples)	Top of upper contact	4.40-4.50 m	0.15
BJ04-B-DD	16/04/19		Bottom of upper contact (metasedimentary enclave)	9.80-9.85 m	0.4
BJ04-C-DD	16/04/19		Middle of the metasedimentary enclave	18.75-18.95 m	—
BJ04-D-DD	16/04/19		Top of lower contact (metasedimentary enclave)	28.85-28.90 m	0.1
BJ04-E-DD	16/04/19		Bottom of lower contact	35.20-35.35 m	0.05
BJ04-F-DD	16/04/19		End of borehole	39.80-40.00 m	4.65

Sample	Date	Local	Description	Borehole depth	Distance (m)
BJ03-A-DD	15/07/20	Bajoca Mine (Drill core samples)	Metasedimentary enclave (more psammitic)	7-8.60 m	—
BJ03-B-DD	15/07/20		Metasedimentary enclave (more pelitic)	7-8.60 m	—
BJ03-D-DD	15/07/20		End of borehole	50 m	4.30
ALB-19-01	12/11/19	Alberto Mine	SE contact	—	0
ALB-19-02	12/11/19		SE profile	—	+/- 0.5
ALB-19-03	12/11/19		SE profile	—	+/- 1.5
ALB-19-04	12/11/19		SE profile	—	4
ALB-19-05	12/11/19		NW contact	—	0
ALB-19-06	12/11/19		NW profile	—	1.8
AL-19-10	12/05/19	Bajoca Concession	Contact with Li-mica dyke	—	0
AL-19-11 (a, b)	12/05/19		Loose samples	—	—
FE-19-01	11/11/19	Feli Mine	E contact	—	0
FE-19-02	11/11/19		E profile	—	0.4
FE-19-03	11/11/19		E profile	—	0.7
FE-19-04	11/11/19		E profile (calcsilicated level)	—	1.35
FE-19-05	11/11/19		E profile	—	2.05
FE-19-06	11/11/19		E profile	—	4
FE-19-07	11/11/19		E profile	—	5.95
FE-19-08	11/11/19		E profile (near four smaller dykes)	—	9.85
FE-19-09	11/11/19		E profile	—	17.65
FE-20-01	25/09/20	Feli Mine	E profile	—	20
FE-20-02	25/09/20		E profile (near a quartz vein and small aplite-pegmatite dyke)	—	30
FE-20-03	25/09/20		E profile (near a spodumene-bearing aplite-pegmatite dyke)	—	40
FE-20-04	25/09/20		E profile (near barren, concordant pegmatite dyke)	—	70
FE-20-05	25/09/20		E profile	—	95

A detailed description of each sample is provided in Appendix IV.

II.3. Analytical techniques

The analytical techniques employed to obtain whole-rock concentrations of the GREENPEG samples and their correspondent detection limits are presented in Chapter 4 (Section IV.2) and Appendix II.5., respectively.

In the case of the LIGHTS campaign, all samples were also analyzed at Activation Laboratories Ltd. (Actlabs), Ontario, Canada, through the 4LITHO(4B2), 8-Lithium Ore, 4F-B(2ppm), 4F-F, and 8-Peroxide ICP analytical packages. In the first case, a Li metaborate/tetraborate fusion was performed to dissolve the entire sample with the major and trace elements analyzed by Inductively Coupled Plasma - Optical Emission Spectrometer (ICP-OES) and Inductively Coupled Plasma - Mass Spectrometer (ICP-MS). In the case of Li, the assays were first made by peroxide fusion ICP-OES (detection limit 0.01%) and later by 4-Acid Digestion ICP-OES (detection limit 0.001%). For halogens, F concentrations were analyzed by a lithium borate fusion with Ion Selective Electrode (ISE), while B concentrations were measured by Prompt Gamma Neutron Activation Analysis (PGNAA) and by sodium peroxide fusion ICP-OES for samples with high B contents.

Mineral chemistry studies were also initiated, namely trace element measurement at UPV/EHU by Quadropolar Laser-Ablation Inductively Coupled Plasma Mass Spectrometry (LA-Q-ICP-MS) (iCAP-Qc model) and Electron-microprobe analyses using a CAMECA SX100 at the research center of the University of Oviedo (Spain). These results are not available yet.

II.4. Geochemical results

The major and trace element whole-rock geochemical analyses of metasedimentary samples collected in the scope of the LIGHTS campaign are available in Table II.4. in the following link: https://docs.google.com/spreadsheets/d/1BwfvetmfLCeTmZ9iiYh4KIRWD7gzRXv6/edit?usp=sharing&ouid=109284842719792190654&rtpof=true&sd=true

A litogeochemical study was employed to the resultant whole-rock analyses to try to ascertain relevant geochemical signatures, as well as possible distinct sedimentary sources, sedimentary evolution, or hydrothermal metasomatic processes between the samples collected in the different profiles. As observed in hand samples and field descriptions, most of the FE samples plot in the field of Wacke or Graywackes while most of the BJ samples plot in the field of shales in the Herron[1], Moine[2] , and La Roche[3] classification diagrams (Figure II. 2-a, -b, and -c, respectively).

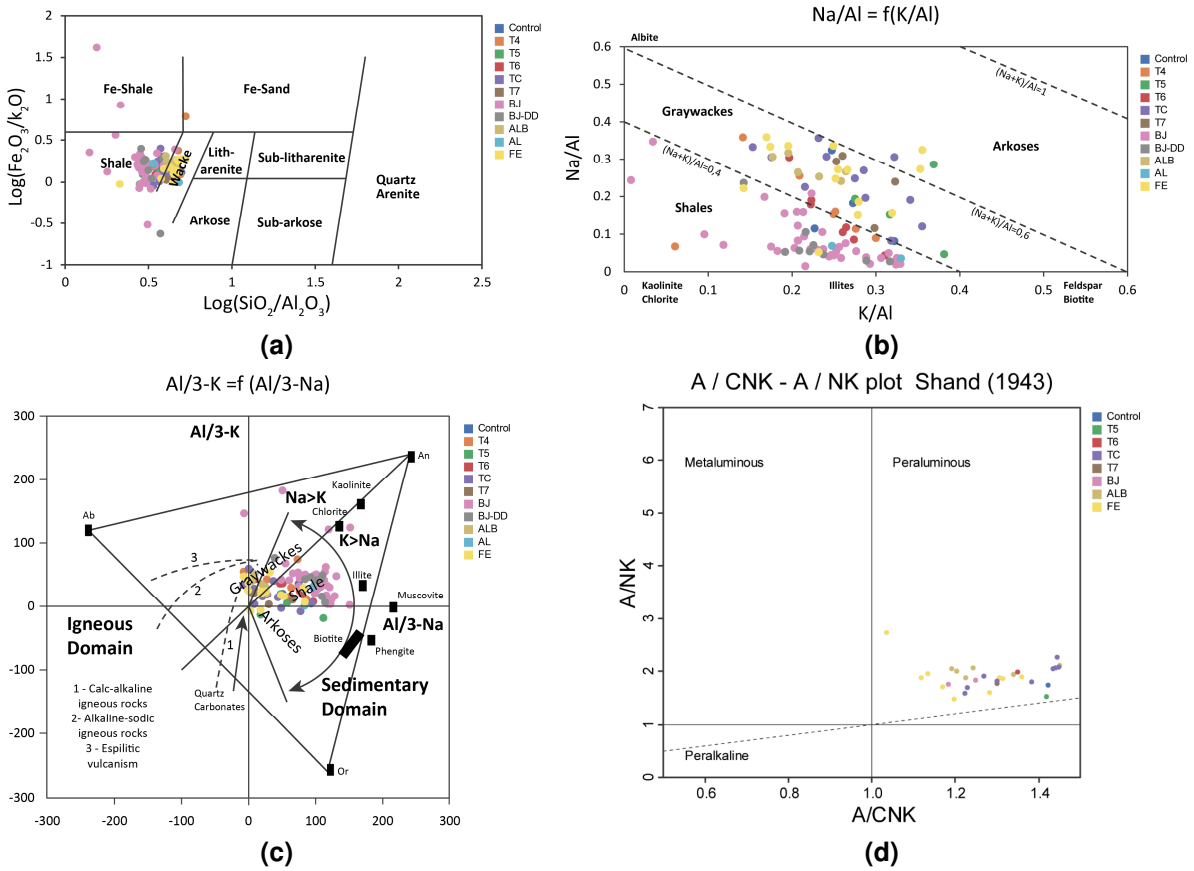

Figure II. 2. (a) Herron (1988) classification of siliciclastic sediments; (b) Na/Al = f(K/Al) diagram of Moine (1974); (c) A1/3-K = f(Al/3-Na) diagram of La Roche (1968); (d) A/CNK-A/NK diagram of Shand (1943) applied to the LIGHTS samples colored according to the previously defined sampling codes.

[1] Herron, M. M. (1988). Geochemical classification of terrigenous sands and shales from core or log data. *Journal of Sedimentary Petrology* 58, 820–829. https://doi.org/10.1306/212F8E77-2B24-11D7-8648000102C1865D
[2] Moine, B. (1974). Caracteres de sedimentation et de métamorphisme des séries précambriennes épizonales à catazonales du centre de Madagascar (Région d'Ambatofinandrahana). *Sci. Terre, Mémoire* 31.
[3] La Roche, M. H. (1968). Comportement géochimique différentiel de Na, K et Al dans les formations volcaniques et sédimentaires: un guide pour l'étude des formations métamorphiques et plutoniques.. *C.R. Acad. Sci., Paris,* Sér.D, 267: 39-42.

However, it should be noted that despite the tempted approximation through the whole-rock geochemical data, the wacke/shale classification is more granulometric than compositional.

In the Moine diagram (Figure II. 2-b), a few samples plot in the field of Arkoses, but this only implies that the respective samples are Na-rich. The same is true for the samples that plot in the negative quadrants of the X-axis of the La Roche diagram (Figure II. 2-c). The La Roche diagram also allows evaluating an igneous or sedimentary source for a certain lithological unit as well as the degree of chemical-mineralogical maturity of the sediments. Accordingly, the Na-rich sediments plot in the igneous domain. The samples that plot in the origin point to a high compositional or mineralogical maturity of the sediments, while there are a few outliers from BJ (some representing Ca-rich samples) that may indicate the influence of metasomatic processes in their whole-rock composition. Finally, all samples show a peraluminous composition according to the Shand[4] diagram of Figure II. 2-d.

The sedimentary chemical differences of the distinct sampling groups are more evidenced in the triangular A-CN-K diagram of Figure II. 3. This diagram allows evaluating the textural and compositional maturity and evolution resultant from the sedimentary processes: (i) the wider, full arrow represents the compositional evolution from an igneous source with progressive weathering; (ii) the A-K axis represents the late stages of weathering alteration, from illite towards kaolinite compositions; and (iii) the dotted arrows represent the two possible trends resultant from sedimentary sorting, where clays and quartz/feldspar follow distinct concentration paths.

As observed in Figure II. 3, the FE and ALB samples present a composition closer to the one of the igneous protolith (tonalite/gabbro), while the BJ samples present a higher compositional maturity, with some samples already evidencing late stages of weathering alteration (plotted along the A-K line). Moreover, the BJ samples plot near the pole of pelitic sediments while the FE and ALB samples are more poorly sorted or tending to the psammitic pole. Therefore, all evidence points that the textural and compositional differences are due to a primary differentiation. It is also noteworthy the existence of outliers from the BJ and T4 sampling groups that do not follow the trend observed for the remaining samples.

[4] Shand, S. J. (1943). *Eruptive Rocks. Their Genesis, Composition, Classification, and Their Relation to Ore-Deposits with a Chapter on Meteorite*. John Wiley and Sons, New York.

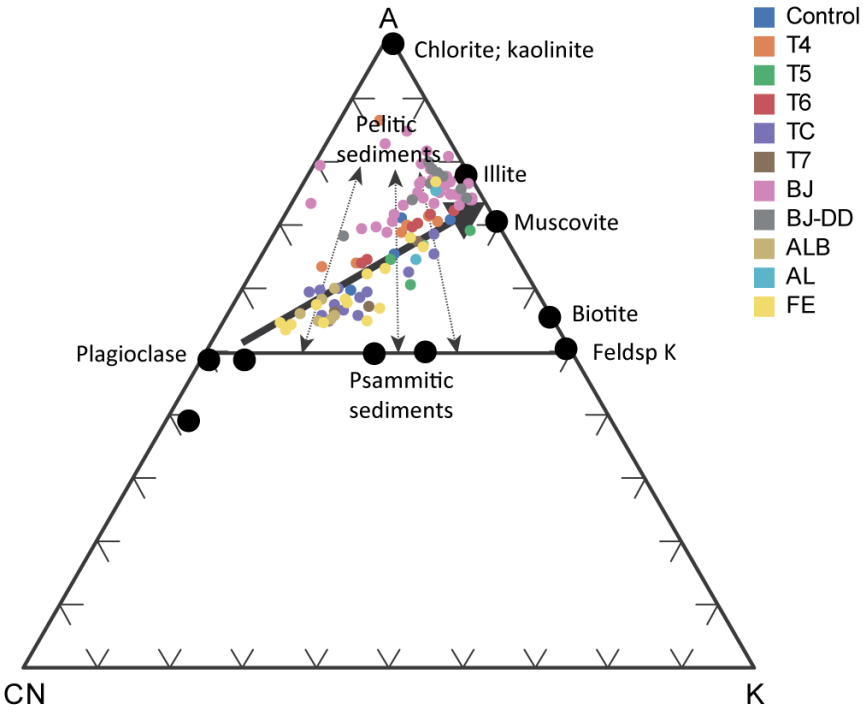

Figure II. 3. A-CN-K diagram (A= Al_2O_3; CN= CaO^*+Na_2O; K=K_2O, where oxides are in molar proportions and CaO* represents the CaO only from the silicate fraction) from Nesbitt *et al.* (1996)[5]. The LIGHTS samples are colored according to the previously defined sampling codes.

The A vertex of the A-CN-K diagram has a direct correlation with the Chemical Index of Alteration (CIA)[6]. This index as well as the Chemical Index of Weathering (CIW)[7] when compared with the SiO_2 content of clastic sediments (parameter representative of the sedimentary sorting), can provide information on the chemical maturity of the protolith sediments of metasedimentary rocks[8,9]. The respective bivariate diagrams are presented in Figure II. 4. Although the BJ samples present higher CIA and CIW values when compared with the FE and ALB samples, there is no marked distinction between sampling groups with the differences reflecting the sedimentary processes. Figure II. 4-c shows the sedimentary sorting through the negative correlation between Al_2O_3 and SiO_2. On the other hand, Figure II. 4-d shows two different trends of variation of K_2O and Al_2O_3 within the different sampling groups. As K_2O and Al_2O_3 are more correlated in clays, these trends represent different percentages of quartz mixed with clays. In all diagrams of Figure II. 4, the outliers are marked with red

[5] Nesbitt, H. W., Young, G. M., Mclennan, S. M. & Keays, R. R. (1996). Effects of chemical weathering and sorting on the petrogenesis of siliciclastic sediments, with implications for provenance studies. *J.Geol,* 104: 525-542.
[6] Nesbitt, H. W. & Young, G. M. (1982). Early Proterozoic climates and plate motions inferred from major element chemistry of lutites. *Nature* 299**,** 715–717. https://doi.org/10.1038/299715a0
[7] Harnois, L. (1988). The CIW index: A new chemical index of weathering. *Sediment.Geol,* 55: 319-322.
[8] Beetsma, J. J. (1995). The late Proterozoic/ Paleozoic and hercynian crustal evolution of the Iberian Massif, N. Portugal, (as traced by geochemistry and Sr-Nd-Pb isotope systematics of pre-Hercynian terrigenous sediments and Hercynian granitoids, PhD thesis, Vrije Universiteit, Amsterdam, 223 pp..
[9] Ribeiro, M.A.M. (1998). Estudo litogeoquímico das formações metassedimentares encaixantes e Trás-os-Montes Ocidental: implicações metalogénicas. PhD thesis, Faculdade de Ciências da Universidade do Porto, 231 pp.

dotted circles. These are the same outliers observed in the A1/3-K = f(Al/3-Na) and A-CN-K diagrams, corresponding to Si-poor samples with variable K contents. This shows that the samples in question present geochemical compositions that do not reflect the sedimentary processes. Further studies are worthy to understand if these outliers represent highly metasomatized samples.

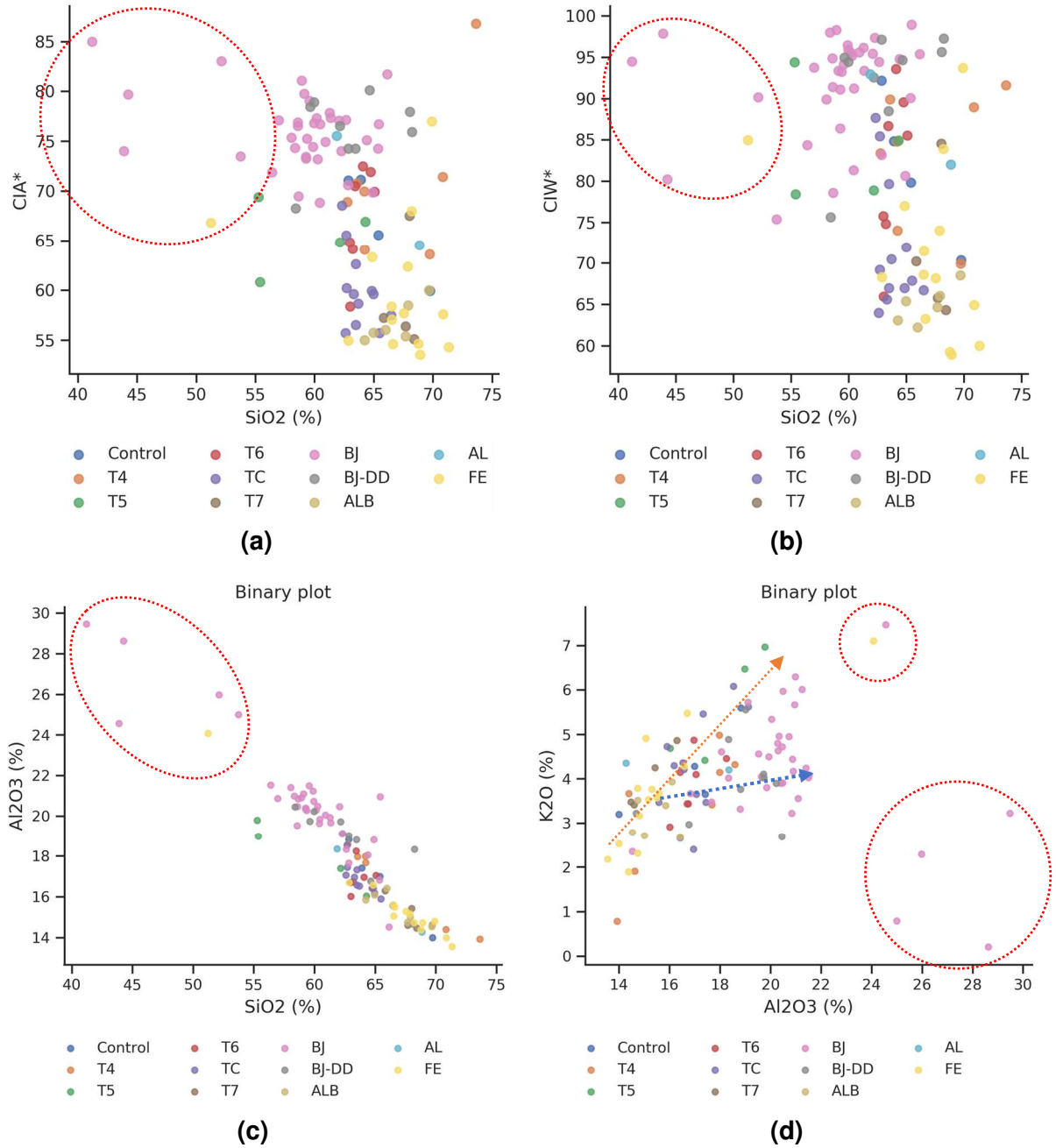

Figure II. 4. (a) CIA = ([Al_2O_3 / (Al_2O_3 + CaO* + Na_2O + K_2O)] 100) vs SiO_2, where CaO* represents the CaO only from the silicate fraction in molar proportions; (b) CIW = ([Al_2O_3 / (Al_2O_3 + CaO* - Na_2O)] × 100) vs SiO_2, where CaO* represents the CaO only from the silicate fraction in molar proportions; (c) variation diagram of Al_2O_3 vs SiO_2; (d) variation diagram of K_2O vs Al_2O_3. The LIGHTS samples are colored according to the previously defined sampling codes.

Finally, all samples were normalized to the North American Shale Composite (NASC)[10] and Upper Continental Crust (UCC)[11]. Trace element normalization is presented in Figure II. 5 and Figure II. 7, respectively. REE-normalized diagrams are also presented separately in Figure II. 6 and Figure II. 8.

These figures also highlight some differences between the sampling groups. For example, FE samples are more enriched in Ba and Sr due to the presence of plagioclase, which confirms the higher sedimentary immaturity of the sediments. Also, FE samples show a depletion of LREE when compared to both NASC and UCC. This could be linked to an igneous source as observed in other diagrams.

Overall, all sampling groups are enriched in Cs, W, and Rb, and depleted in Sb, Co, and Ni when compared with NASC. There is also enrichment in As, more accentuated in BJ, BJ-DD, and FE. Similarly, when compared with the UCC, all sampling groups are enriched in Tl, Cs, W, Rb, B, As, Be, Ta, Nb, Sn, Li, and Ag, while depleted in F, Cu, and Ni.

[10] Rudnick, R. L. & Gao, S. (2014). *Composition of the continental crust*. In: Holland, H. D., Turekian, K. K. (eds.) *Treatise on Geochemistry, 2nd edition Volume 4: The Crust*. Elsevier Science, Oxford, 1–51. https://doi.org/10.1016/B978-0-08-095975-7.00301-6.

[11] Gromet, L. P., Dymek, R. F., Haskin, L. A. & Korotev, R. L. (1984). The "North American shale composite": Its compilation, major and trace element characteristic. *Geochim. Cosmochim. Acta,* 48: 2469-2482.

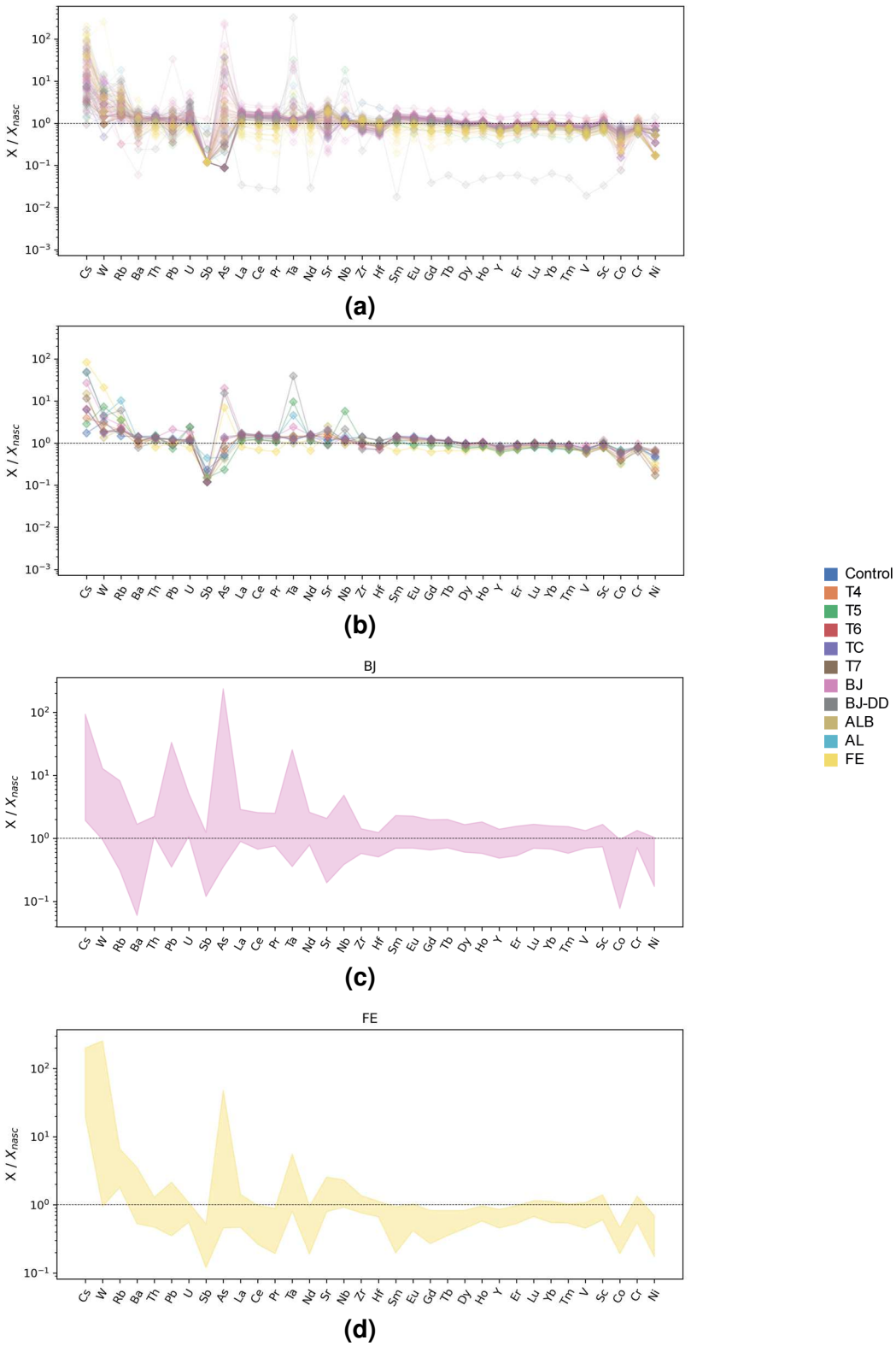

Figure II. 5. NASC-normalized trace element diagram for: (a) all samples according to sampling group; (b) average composition of each group; (c) variation range of BJ samples; (d) variation range of FE samples.

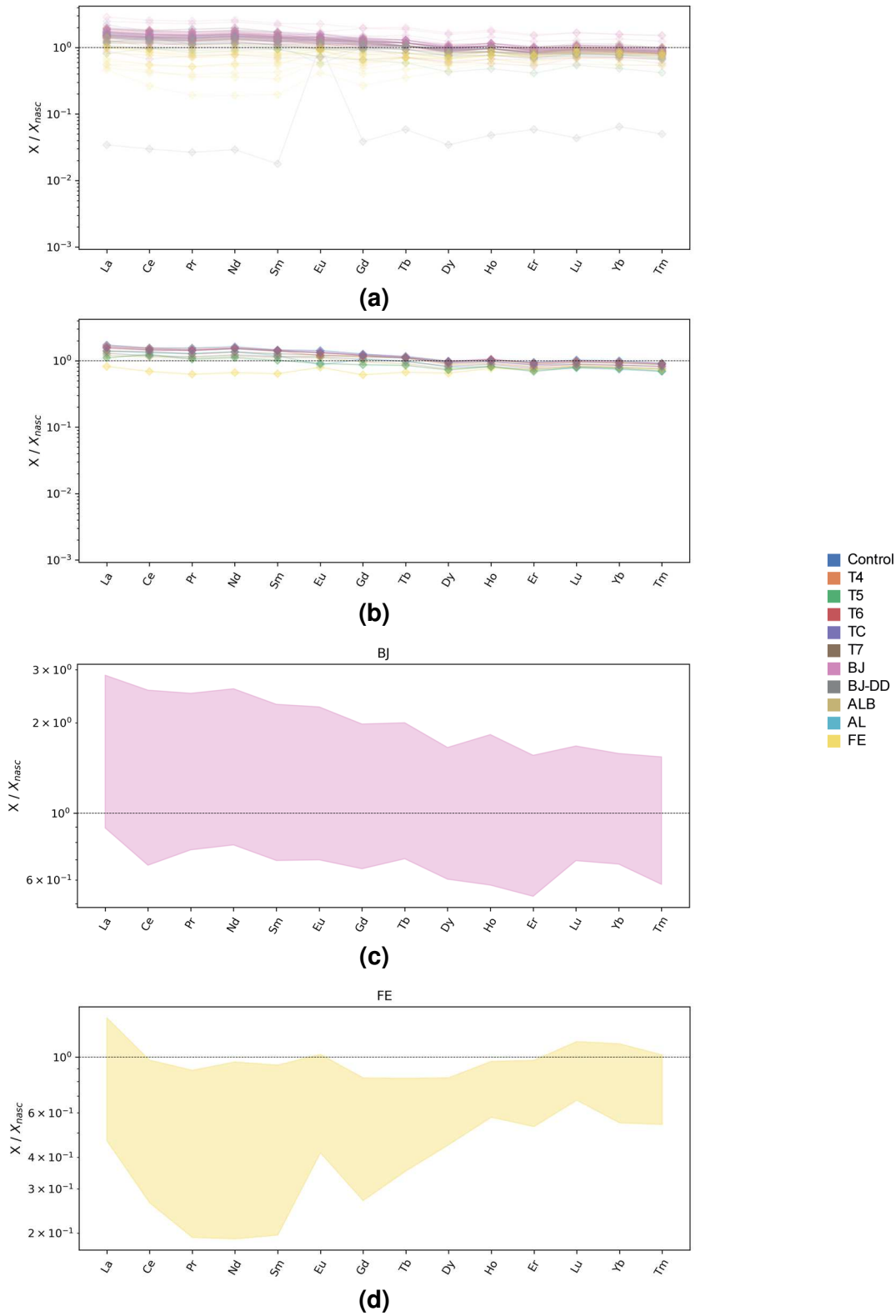

Figure II. 6. NASC-normalized REE diagram for: (a) all samples according to sampling group; (b) average composition of each group; (c) variation range of BJ samples; (d) variation range of FE samples.

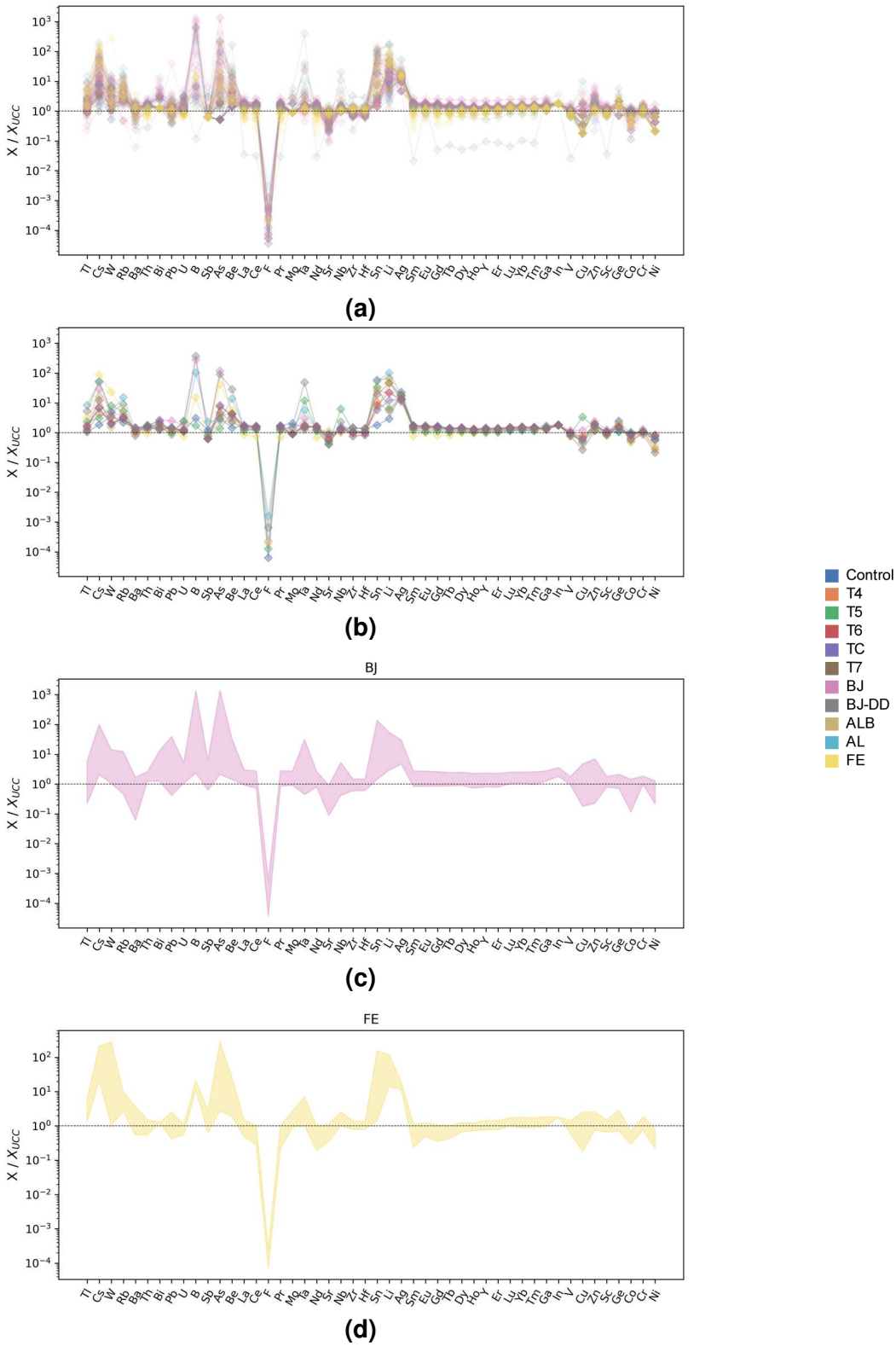

Figure II. 7. UCC-normalized trace element diagram for: (a) all samples according to sampling group; (b) average composition of each group; (c) variation range of BJ samples; (d) variation range of FE samples.

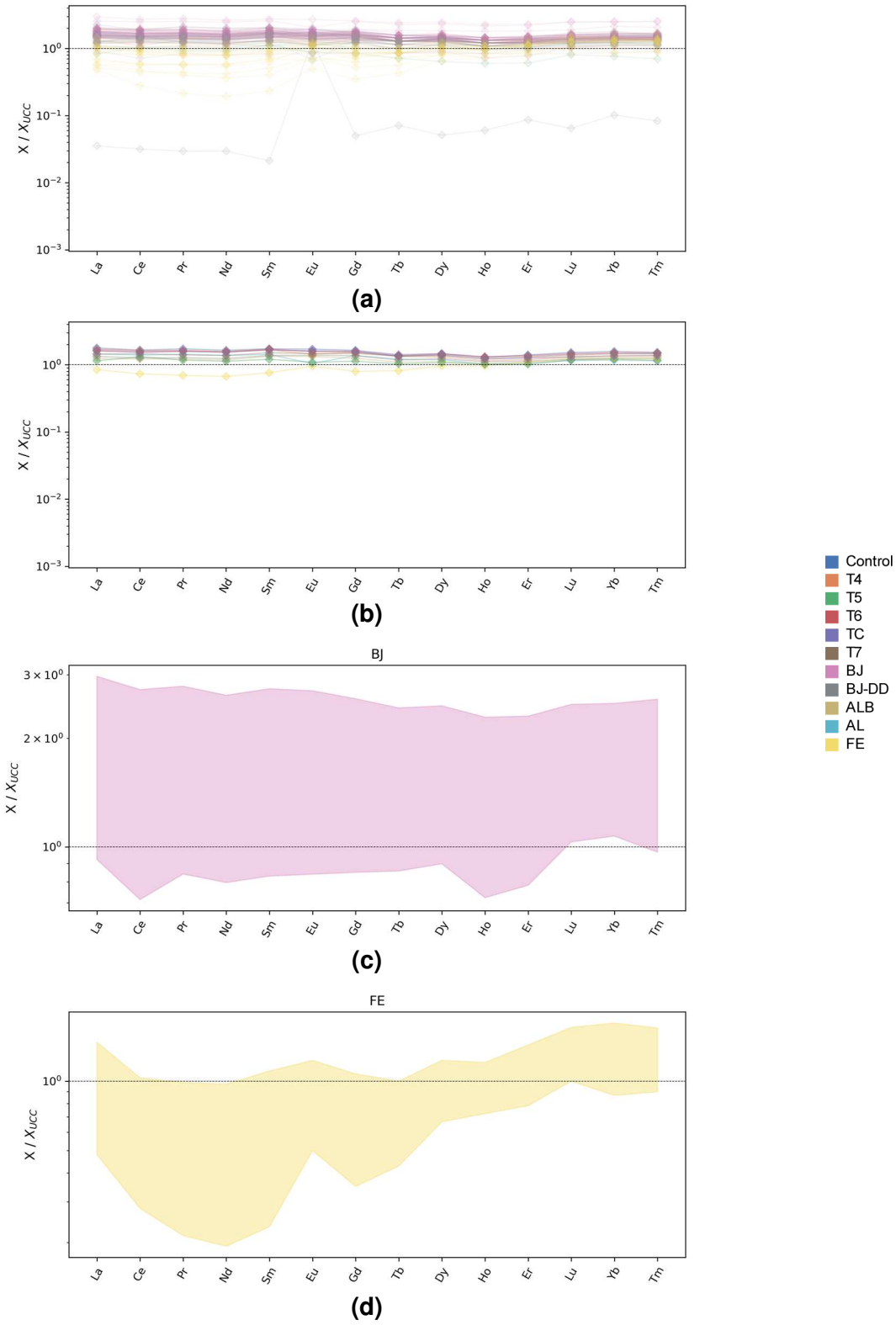

Figure II. 8. UCC-normalized REE diagram for: (a) all samples according to sampling group; (b) average composition of each group; (c) variation range of BJ samples; (d) variation range of FE samples.

II.5. Supplementary materials to section IV.2.

The supplementary tables are available at the following link: https://docs.google.com/spreadsheets/d/1PasvOJnevQ-9Wjs1TuVE39aL9YI-bZ9O/edit?usp=sharing&ouid=109284842719792190654&rtpof=true&sd=true

Appendix III. Petrographic studies

III.1. Sample preparation and equipment

In what concerns the samples collected in the scope of the LIGHTS project, sample preparation was conducted at FCUP. A total of 67 polished thin sections were produced, part in the thin section preparation laboratory of FCUP and the remaining at the Geology Department of the University of Trás-os-Montes and Alto Douro (UTAD).

The microscopic studies were conducted at FCUP, using (i) a transmitted light Nikon petrographic microscope (Eclipse E 400 POL), coupled with a ZEISS Axiocam camera; (ii) a transmitted light Leica petrographic microscope (DM4000), coupled with a DFC295 or FLEXACAM C1 Leica cameras; and (iii) a Citl cold cathode cathodoluminescence, Cl 8200 Mk4 model, coupled with a Nikon polarizing microscope (OPTIPHOT-POL) and a DinoEye eyepiece camera. Complementary Scanning Electron Microscopy with Energy Dispersive Spectroscopy (SEM-EDS) studies were also conducted at the FCUP, using a Hitachi FlexSEM 1000 SEM, coupled to a Bruker QUANTAX EDS system.

Regarding the samples collected in the scope of the GREENPEG project, 60 thin sections were prepared at UPV/EHU. As described in Chapter 4 (section IV.2.), a Leica polarizing microscope, DM LP model, coupled with a mounted NIKON D90 camera was employed for the petrographic studies. Also, 15 additional thick sections (100 microns) were prepared and studied at UPV/EHU as part of the mineral chemistry studies (EPMA, LA-ICP-MS).

III.2. Petalite alteration

Figure III.1.

Petrographic aspects of petalite alteration in the Bajoca open pit mine.

(a, c) Pale brown clays were observed in parallel polarized light (ppl) filling fractures or along the petalite cleavage.

(b, d) In cross-polarized light (cpl), the clays present low birefringence with polarization colors of the first order.

(e, f) Clays under the electronic microscope (SEM), backscattered electron image (BSE). (e) corresponds to the are marked with a red rectangle in (a), rotated to the left. (f) corresponds to the area in (c-d) rotated 90º to the right. SEM-EDS studies indicate that these clays correspond to montmorillonite.

Figure III.1.

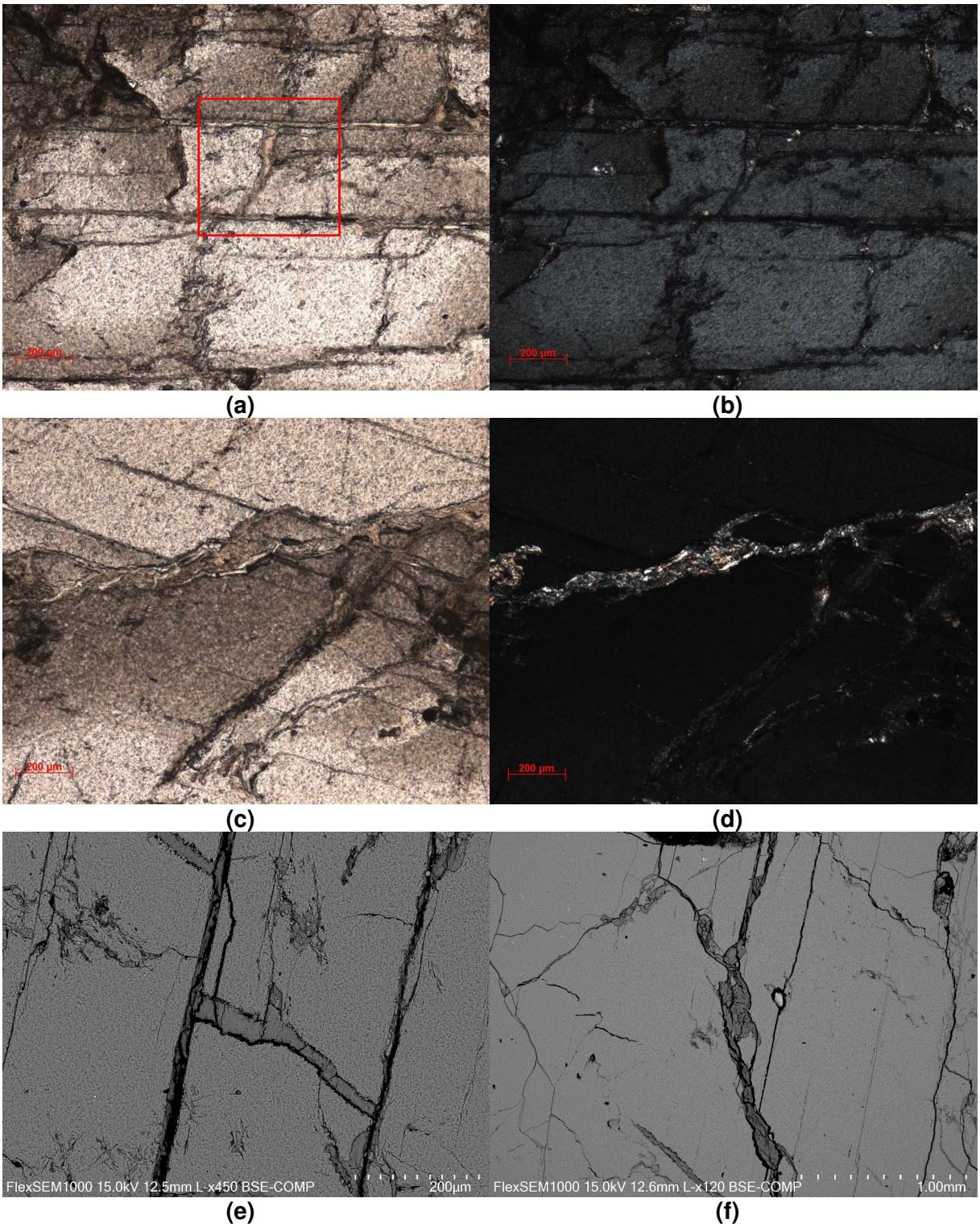
200 µm
200 µm
(a)
(b)
200 µm
200 µm
(c)
(d)
FlexSEM1000 15.0kV 12.5mm L-x450 BSE-COMP
200µm
FlexSEM1000 15.0kV 12.6mm L-x120 BSE-COMP
1.00mm
(e)
(f)

Figure III.2.

Petrographic aspects of petalite alteration in an aplite-pegmatite dyke from Hinojosa de Duero.

(a-b) Petalite fractures can also be filling by micas. Eucrypite (Euc) also occurs associated along the fractures.

(c-d) Eucrypite (Euc) was identified through SEM-EDS surrounding quartz and albite inclusions in petalite.

Figure III.2.

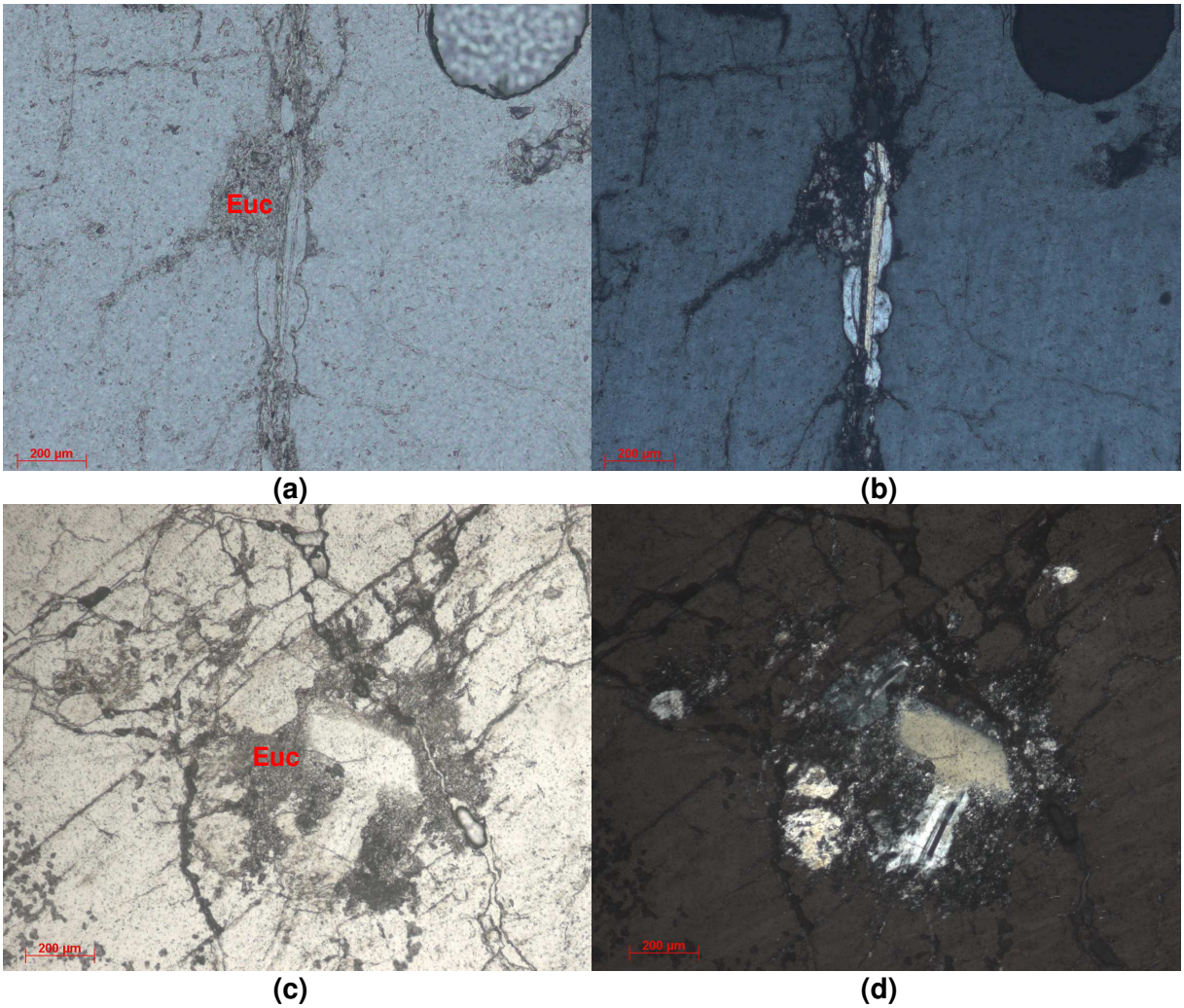

Figure III.3.

Petrographic aspects of petalite alteration in the Bajoca open pit mine.

Further petalite alteration led to (i) widening and quartz (Qtz) precipitation along the petalite cleavage **(a, b)**; (ii) the formation of pseudospherulitic clay minerals filling pre-existing voids **(c,d)**; and (iii) the formation of cookeite (Cok), displaying fan-like extinction in cpl, intergrown or surrounding white mica (WM) crystals **(e, f)**.

A later event led to sericitization (Ser) locally superimposed on the quartz-filled cleavage, pseudospherulitic clays, and cookeite **(a, b)**.

Figure III.3.

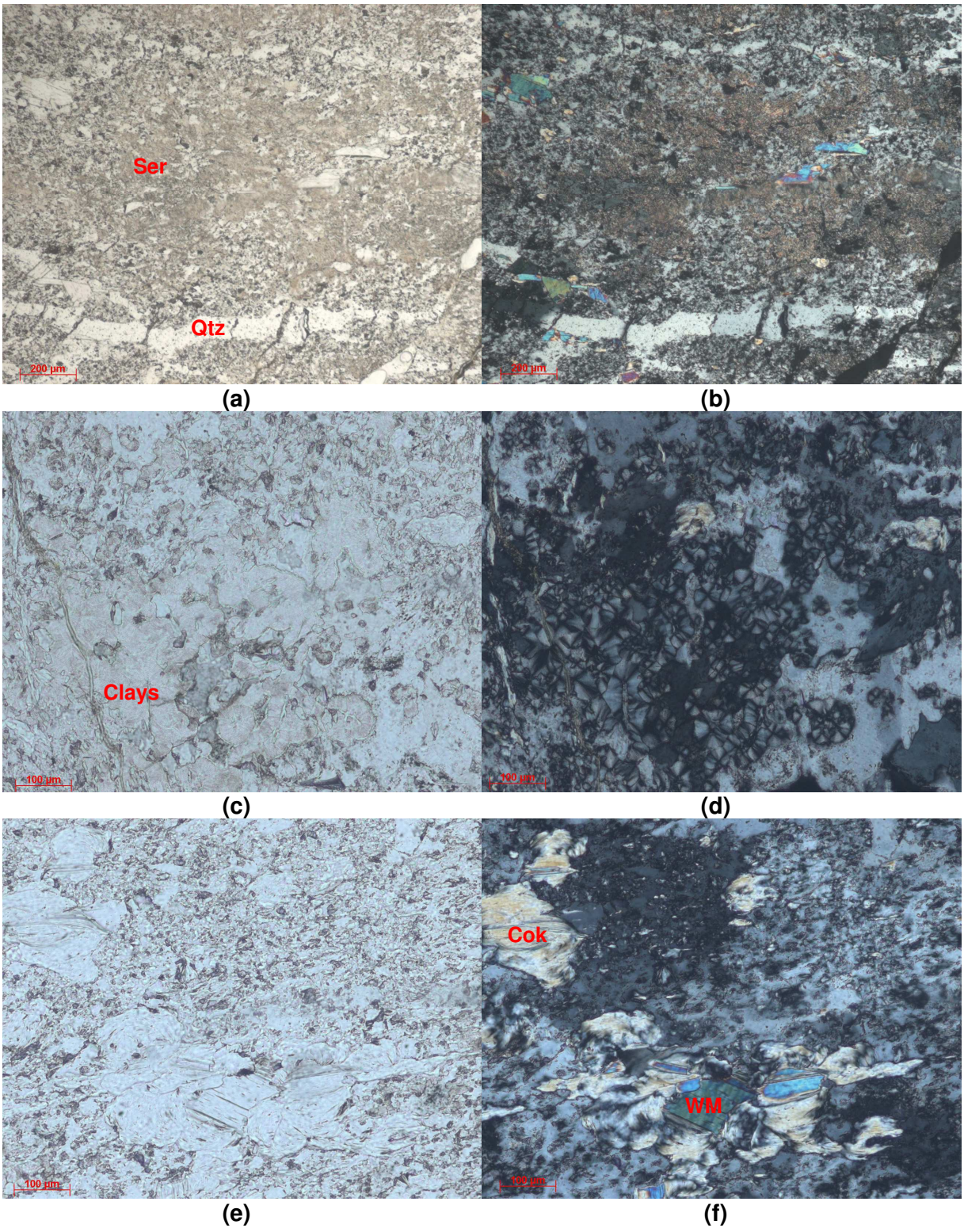
Ser
Qtz
200 µm
(a)
200 µm
(b)
Clays
100 µm
(c)
100 µm
(d)
100 µm
(e)
Cok
WM
100 µm
(f)

III.3. Geochemical haloes

Figure III.4.

Petrographic aspects of the more psammitic samples.

Although the samples generally present a well-evidenced compositional layering (millimetric to centimetric rhythmic alternation between pelitic, semi-pelitic and psammitic levels), there is a predominance of quartz in relation to micas. Also, plagioclase can be observed in minor quantities (metagreywackes). These samples are characterized by a fine granularity and a granolepidoblastic texture. Biotite occurs mostly disperse in the matrix, with rare porphyroblasts usually of small dimensions. Biotite is mimetic over a pre-existent foliation (Sn).

(a, b) Mimetic character of biotite, growing in multiple directions. The matrix is mainly composed of quartz (Qtz) and biotite (Bt) but is also possible to observe tourmaline (Turm), apatite (Ap) and fine white mica (WM) crystals.

(c-f) Foliation transposition: oblique relation between the main foliation (Sn) and primary foliation or stratification (S0). It is also noticeable the transition between semi-pelitic layers of granolepidoblastic texture and psammitic levels of granoblastic texture. Small biotite porphyroblasts with different orientations are observed in (e, f),

Figure III.4.

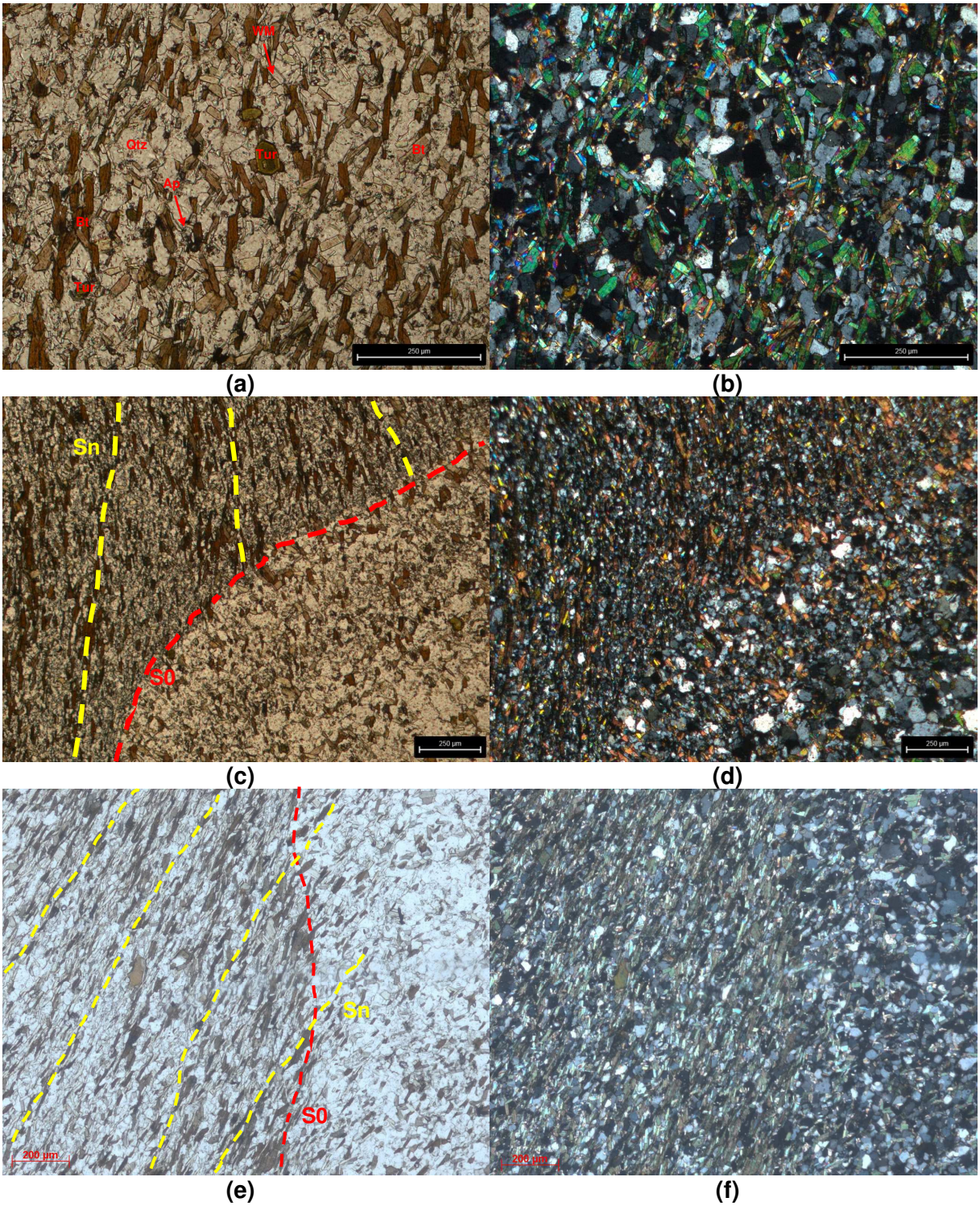
Wht
Qtz
Tur
Bt
Ap
Bt
Tur
250 µm
(a)
250 µm
(b)
Sn
S0
250 µm
(c)
250 µm
(d)
Sn
S0
200 µm
(e)
200 µm
(f)

Figure III.5.

Petrographic aspects of the more psammitic samples.

The more psammitic levels often preserve sedimentary features such as load casts, typical of turbiditic sequences.

(a, b) Alternating pelitic and psammitic layers (load cast) in thick section (magnification of 5x).

(c, d) Psammitic lenses and σ-type porphyroclasts in thick section, typical of the Desejosa formation (magnification of 5x).

Figure III.5.

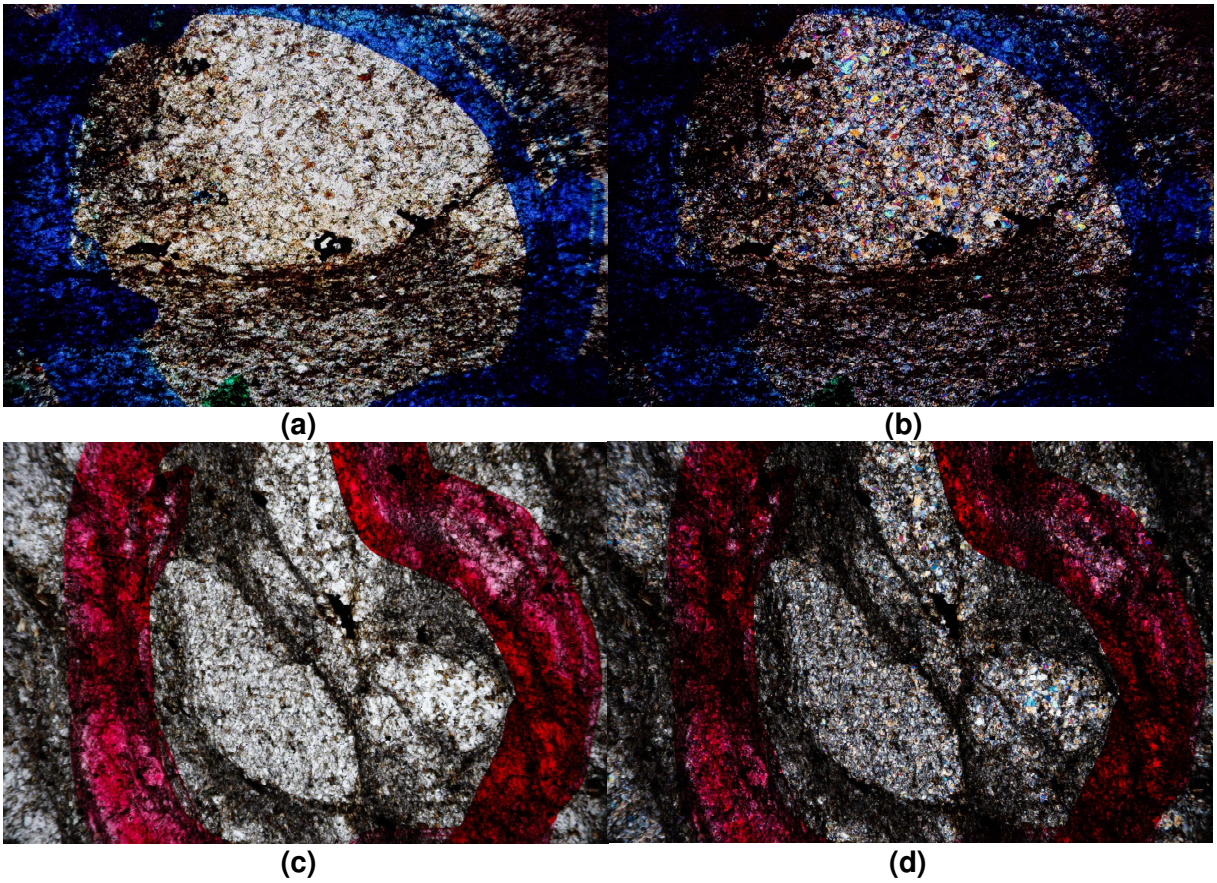

Figure III.6.

Petrographic aspects of the more pelitic samples.

Unlike the more psammitic samples, the more pelitic ones are characterized by (i) larger grain size, (ii) a higher relative quantity of white mica (and a lower proportion of quartz), and (iii) frequent, large biotite porphyroblasts in a granolepidoblastic matrix, typical of the Pinhão formation. Biotite is mimetic over a previous foliation (Sn), but Sn crenulation and adaptation around the biotite porphyroblasts indicate that there was another deformation event (Dn+1).

(a, b) Biotite (Bt) porphyroblasts over a semi-pelitic matrix. The inclusion trails on the larger porphyroblast form an internal foliation (Si) normal to the (001) cleavage. The same porphyroblast shows a dextral sense of rotation. Also, the main foliation is adapted around the biotite porphyroblasts. Intense tourmanilization (Tur) is observed over the micaceous levels.

(c, d) Granolepidoblastic texture with biotite (Bt) disperse in the matrix, as well as quartz (Qtz), white mica (WM), tourmaline (Turm), and opaque minerals.

(e, f) Compositional layering with alternating micaceous and quartzo-micaceous levels. In this case, the micaceous layers are mostly composed of white mica (WM) intergrown with chlorite (Chl).

Figure III.6.

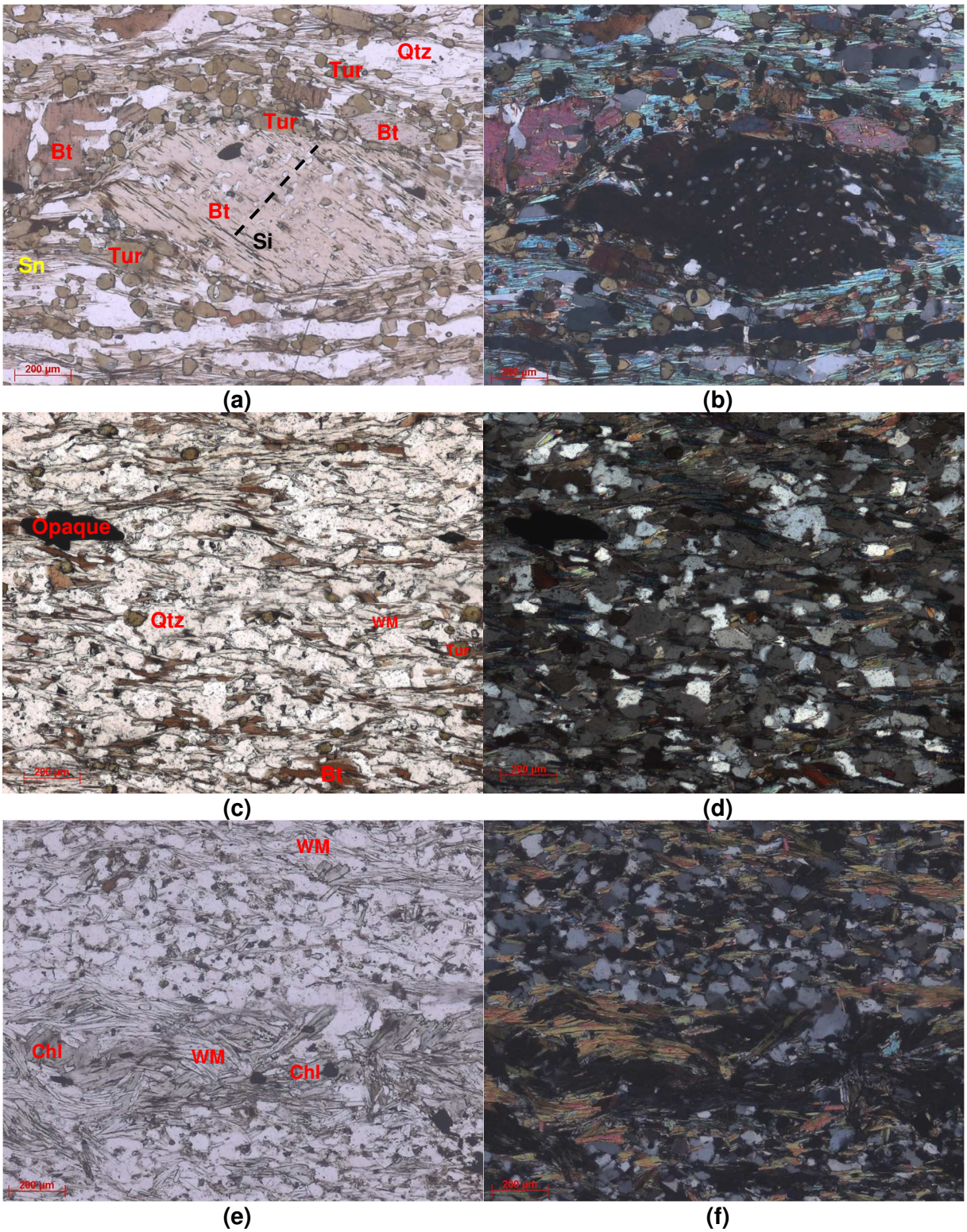
Qtz
Tur
Tur
Bt
Bt
Bt
Si
Sn
Tur
200 µm
(a)
(b)
Opaque
Qtz
WM
Tur
Bt
(c)
(d)
WM
Chl
WM
Chl
(e)
(f)

Figure III.7.

Petrographic aspects of the more pelitic samples.

Often the compositional layering is not so evident in the more pelitic samples, due to the increased thickness of the layers.

(a, b) Biotite porphyroblasts in a granolepidoblastic matrix, with a visible adaptation of Sn around the porphyroblasts. Moreover, Sn transposes S0 (thick section; magnification of 5x).

(c, d) Biotite porphyroblasts in semi-pelitic layer with interbedded σ-type psammitic porphyroclast (thick section; magnification of 5x).

Figure III.7.

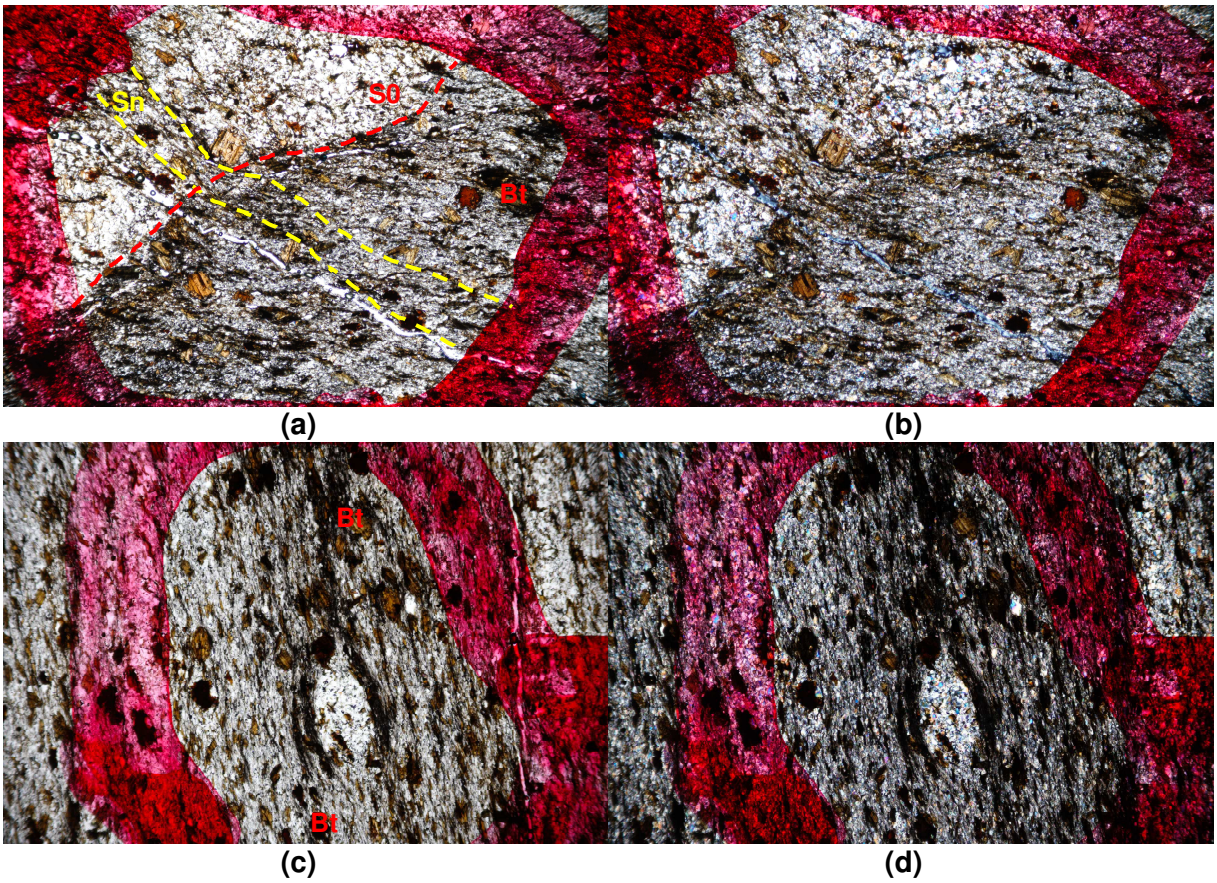

Figure III.8.

Petrographic aspects of biotite microstructures.

Biotite microstructures provide meaningful insights into the blastesis process. Mimetic crystals indicate that the blastesis began after the deformation phase (Dn), responsible for the development of Sn, while the existence of deformed crystals and inclusion zoning patterns indicate that biotite growth was pre- to sin- a later deformation phase (Dn+1, probably D3), responsible for a generally incipient crenulation.

(a) Deformed porphyroblast presenting unzoned inclusion trails, compatible with growth in a static environment with low or no strain. The inclusion trails (Si) are composed of ellipsoidal to drop-like shape quartz inclusions (Type 1), sub-concordant with the external foliation (Se).

(b) Porphyroblast with two inclusions types. Type 2 inclusions present bigger dimensions and are concentrated in the porphyroblast rims.

(c, d) Biotite with zoned inclusion patterns with an included core (1) and less-included borders (2). These zoning patterns are typical of syn-tectonic growth of biotite.

(e) Deformation corridor with biotite porphyroblasts showing opposition trends and dips of Si and (001) cleavage.

(f) Biotite porphyroblast showing a sinistral sense of rotation.

Figure III.8.

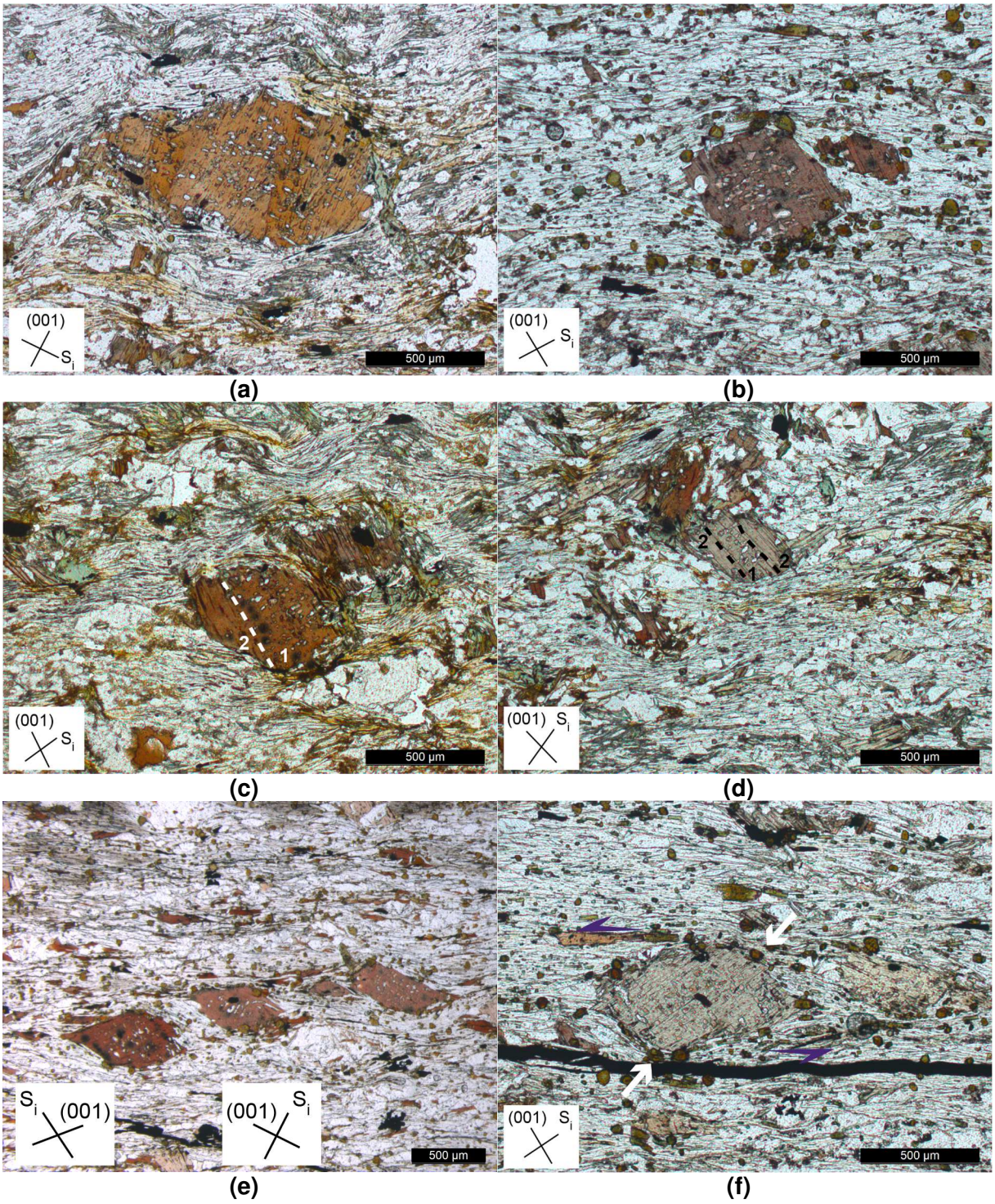
(001)
Si
500 µm
(a)
(001)
Si
500 µm
(b)
2
1
(001)
Si
500 µm
(c)
2
1
2
(001)
Si
500 µm
(d)
Si
(001)
(001)
Si
500 µm
(e)
(001)
Si
500 µm
(f)

Figure III.9.

Petrographic aspects of the chloritization of biotite in more pelitic samples.

Biotite chloritization represents a late event (post Dn+1), heterogenous at the thin section scale. Chlorite can either completely **(a)** or only partially **(b-d)** replace biotite. In the last case, chlorite starts to form along the (001) cleavage or in crystal borders.

In **(c)** the passage of biotite to chlorite is accompanied by rutile exsolution (filling the cleavage).

(d) Kinks in biotite as a result of brittle-ductile deformation, with more intense chloritization in the resultant pressure shadows.

Figure III.9.

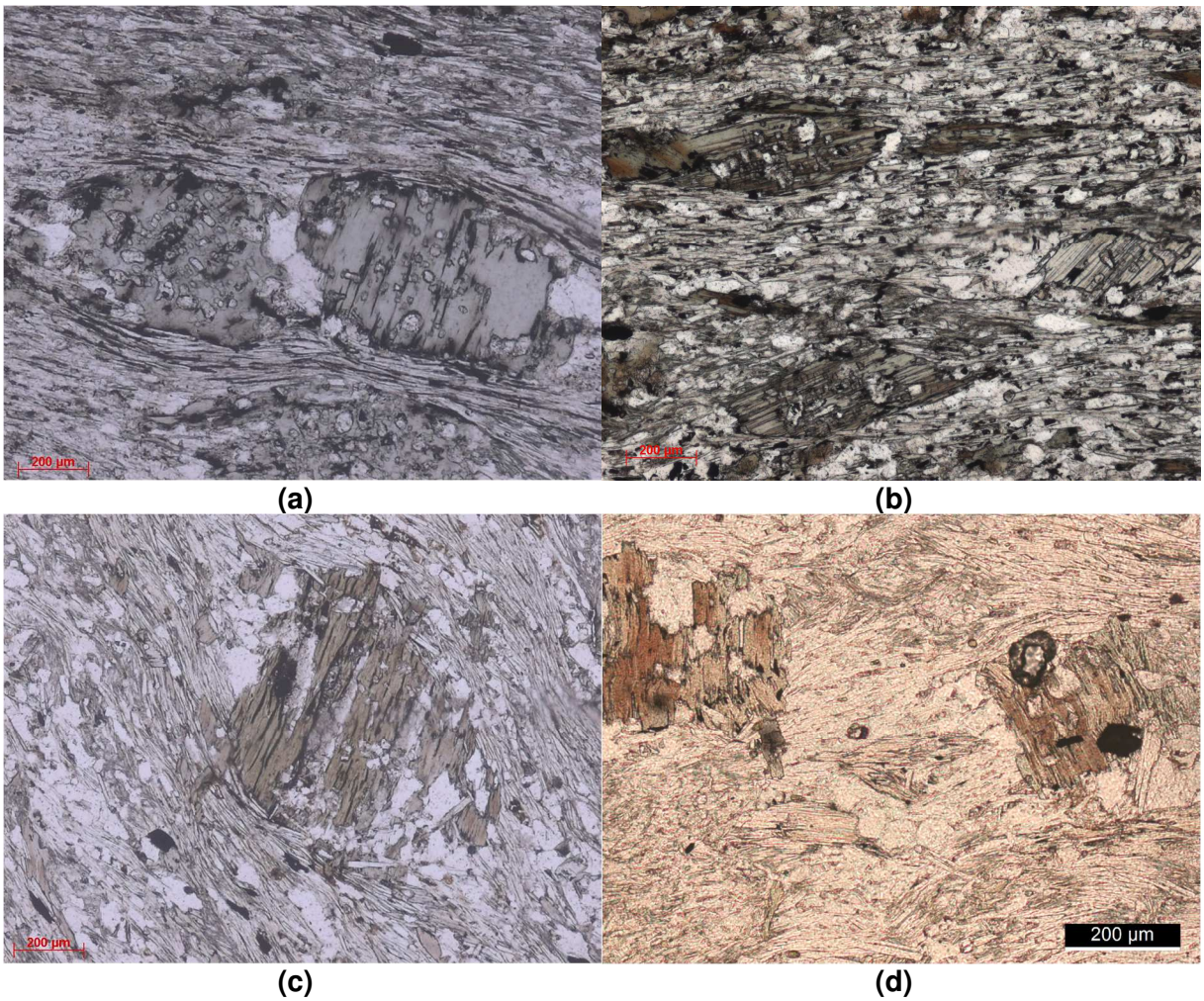

(a) **(b)**

(c) **(d)**

Figure III.10.

Petrographic aspects of the tourmalinization.

As previously mentioned, the tourmalinization event is heterogeneous, mainly controlled by the host-rock permeability. This means that tourmalinization is more intense in the pelitic layers than in the psammitic ones **(a-f)**, thus accentuating the stratification (S0). In the more heavily tourmalinized samples, biotite (Bt) tends to be scarce, which may indicate biotite consumption to form tourmaline (Tur), although they can coexist **(a-b)**.

(a, b) Compositional layering with alternating micaceous and quartzo-micaceous levels. This layering is emphasized by the intense tourmalinization in the more micaceous levels.

(c, d) Intense tourmalinization in the micaceous layers is associated with fosfatization (apatite – Ap – development). The quartzose levels present a polygonal granoblastic texture (triple points at quartz grain boundary).

(e, f) Quartzose level, mainly composed of quartz (Qtz) with minor plagioclase (Pl), displaying a granoblastic heterogranular texture with a polygonal tendency, indicating static heating. Tourmaline (Tur) is rare in this layer. Sphene (or titanite; Sph) is also visible.

Figure III.10.

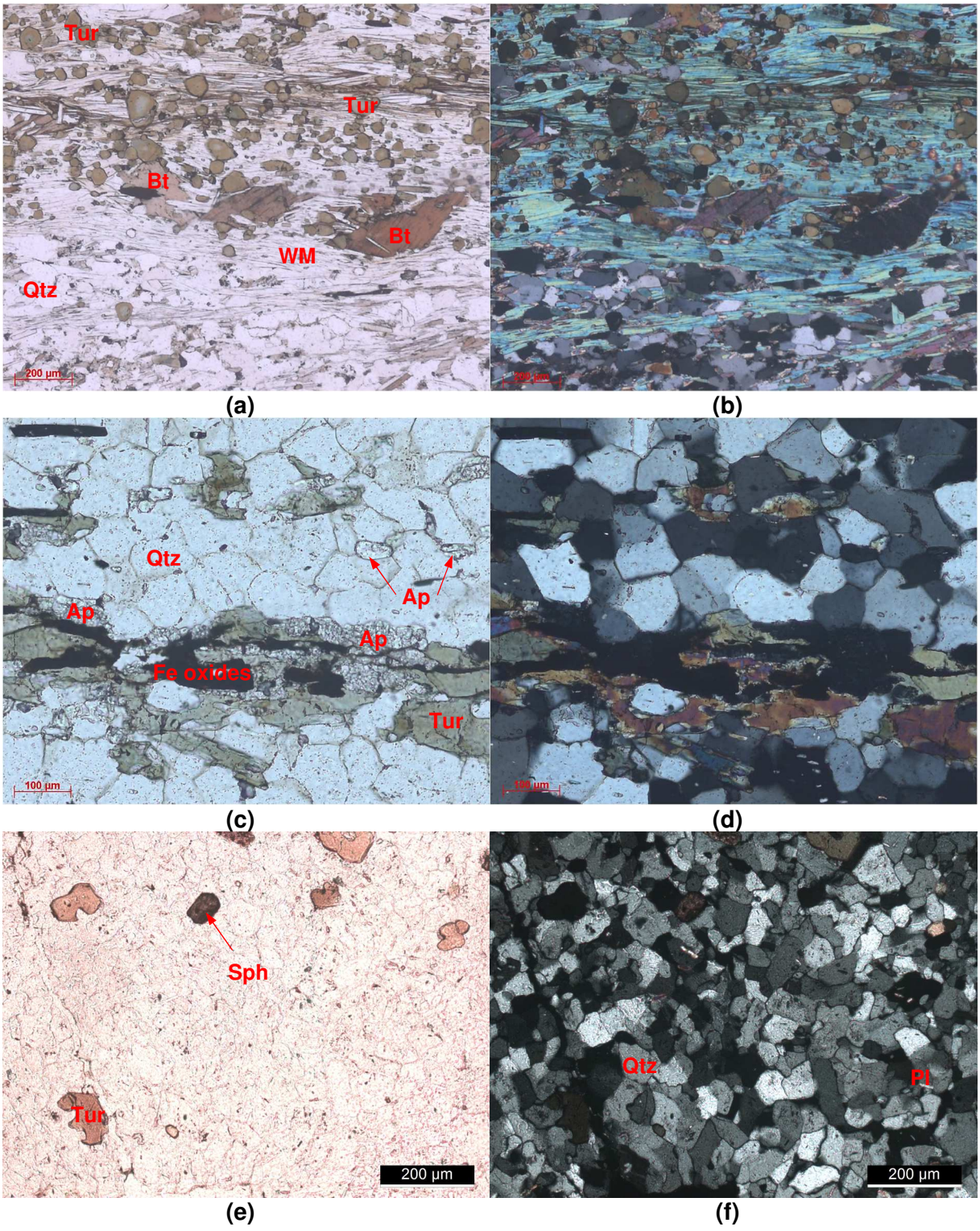

Figure III.11.

Petrographic aspects of tourmalinite samples from the host-rock enclave of the Bajoca aplite-pegmatite. Similar samples were also described in tourmalinized levels parallel to S0 in the western transverse sampling profile.

The samples are characterized by intense tourmaline (Turm) growth **(a-b)**, often aligned with a previous foliation, white mica (WM; **a-f**), large, frequently euhedral apatite (Ap) crystals **(a-d)**, hydrothermal, fibro-radiated chlorite (Chl; **e-f**), and quartz with intergranular fluid inclusion planes. Chlorite presents the typical Berlin blue color in cpl.

Some tourmalinite samples are cross-cut by secant aplite injections, causing an abrupt contact, although aplite injections also occurred parallel with the previous foliation creating smooth transition zones. The aplitic zones are characterized by euhedral crystals of apatite, white mica growing in fibro-radiated nuclei, quartz, and plagioclase.

Figure III.11.

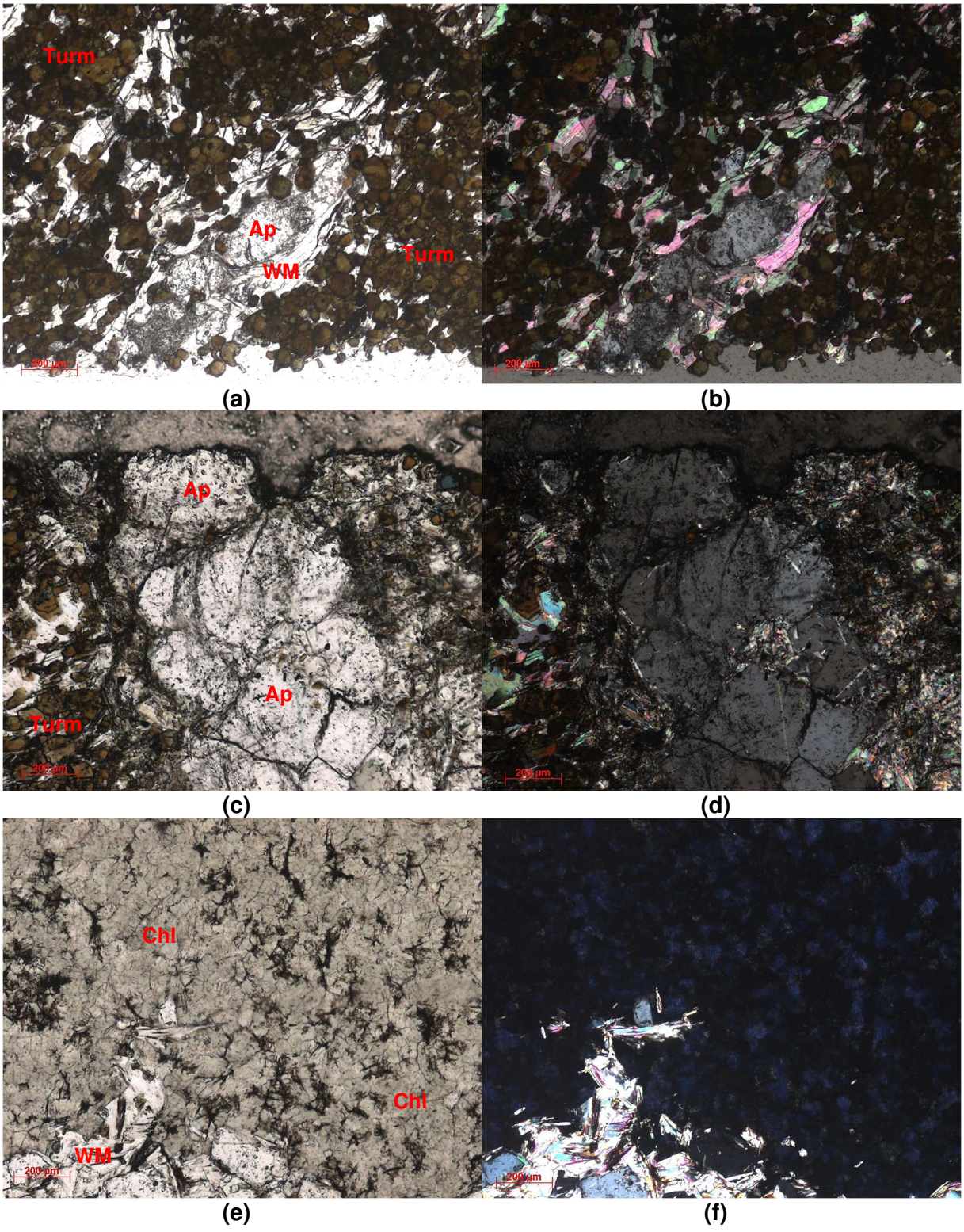

Figure III.12.

Petrographic aspects of apatite in the tourmalinized samples.

Cathodoluminescence studies not only allowed to identify apatite within samples but also to observe growth zoning in each crystal. All apatites show strong luminescence in a greenish-yellow color and weak luminescence in a brownish color **(a-d)**, as a consequence of enrichments in manganese and iron, respectively. Similar signatures are often attributed to a magmatic origin for apatite.

(a-c) show concentric zoning patterns while **(d)** presents more complex patterns.

Figure III.12.

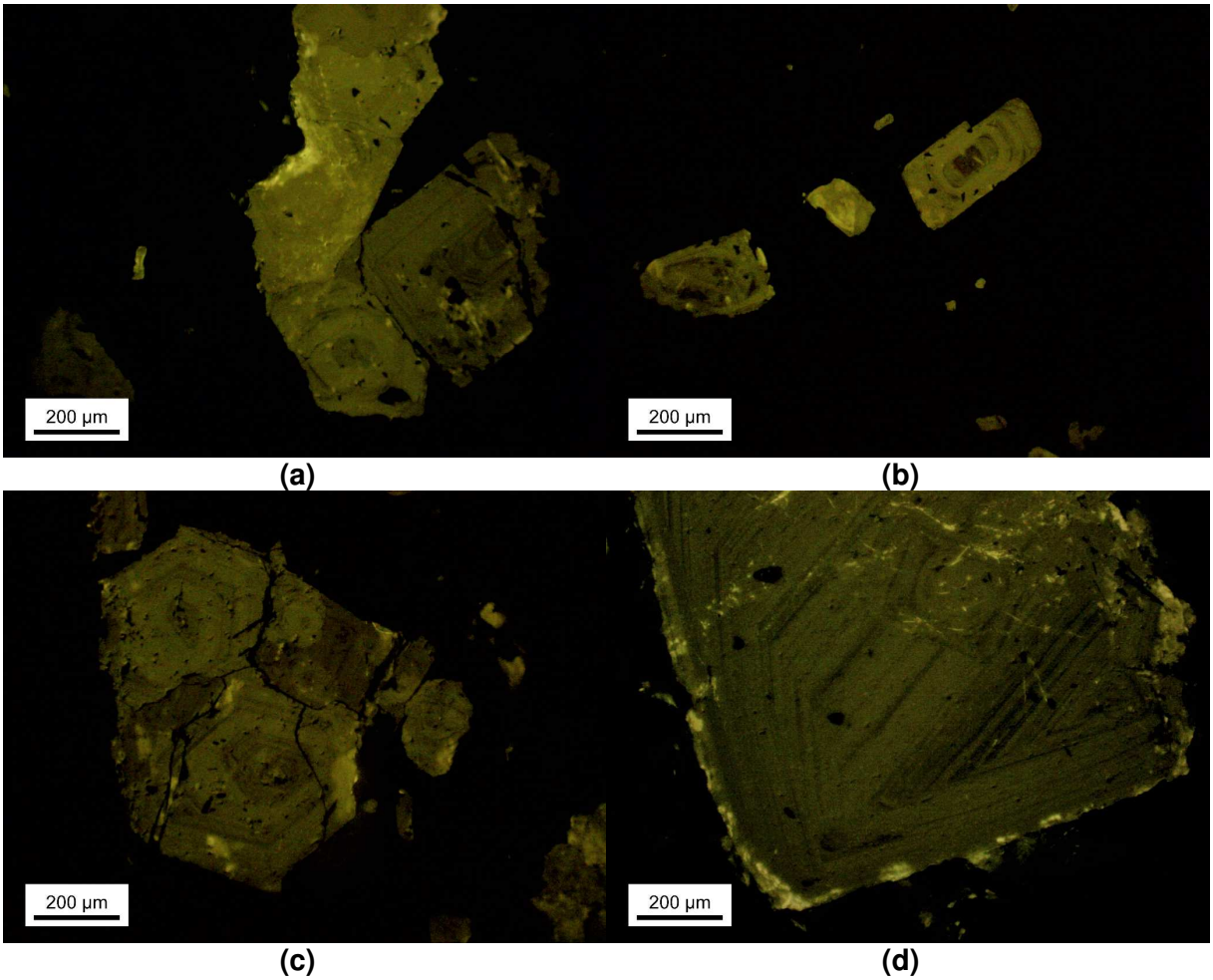

Figure III.13.

Petrographic aspects of the Bajoca aplite-pegmatite host-rocks..

(a, b) Large sphene (or titanite; Sph) crystal in a heavily tourmalinized (Turm) layer of a psammo-pelitic sample.

(c, d) Fracture sub-parallel to the main foliation (Sn) filled with epidote (probably pistacite; Ept).

(e, f) Epidote (Ept) widely disperse in the granolepidoblastic matrix.

Figure III.13.

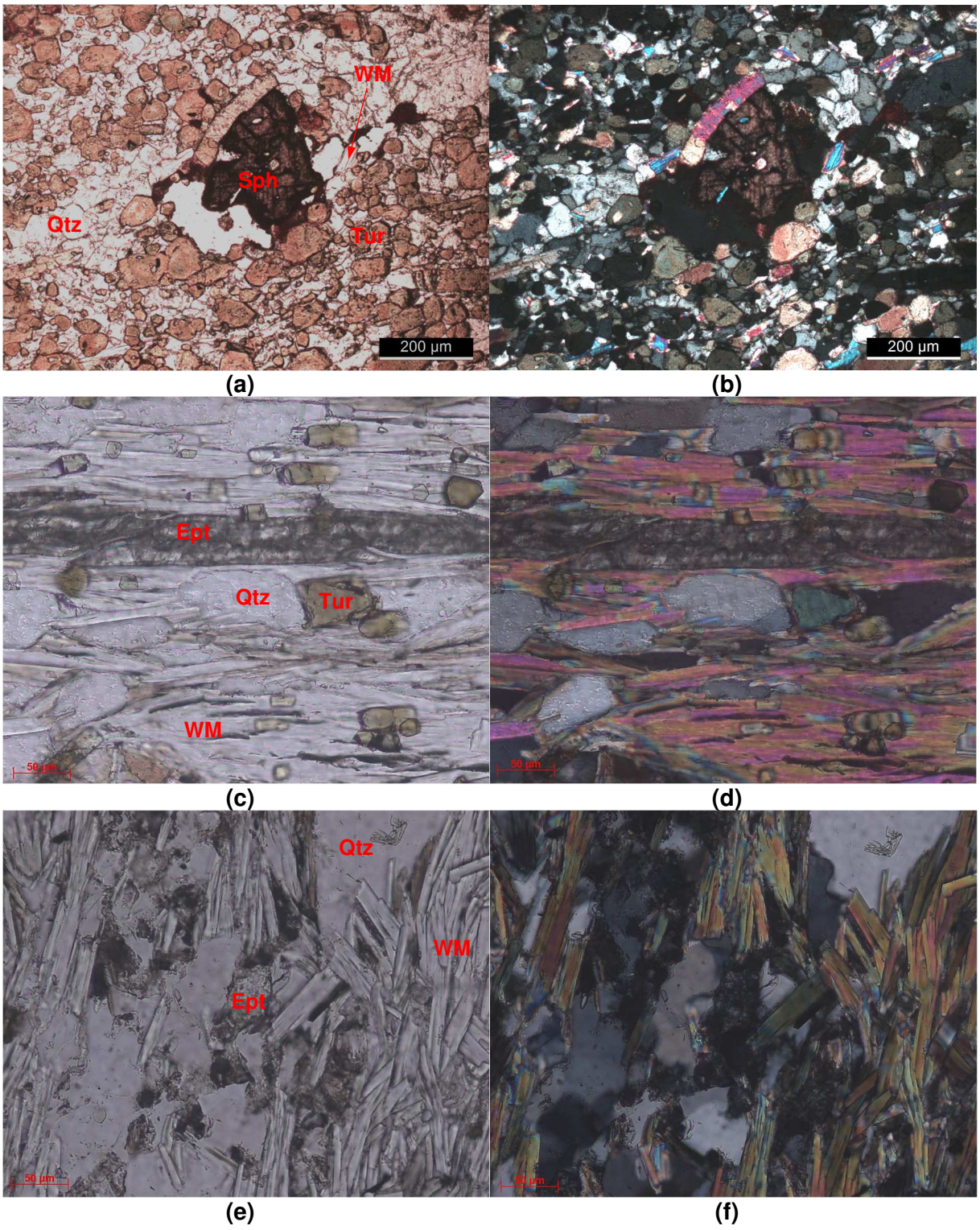

Figure III.14.

Petrographic aspects of deformation mechanisms.

(a, b) Boudinated quartz vein displaying slight undulose extinction in a semi-pelitic rock. The main deformation component is coaxial, although there is a small noncoaxial dextral component.

(c, d) Late to post-cinematic recuperation, with polygonal tendency, as a result of static recrystallization after syn-cinematic subgranulation through dynamic recrystallization in a semi-pelitic sample.

Figure III.14.

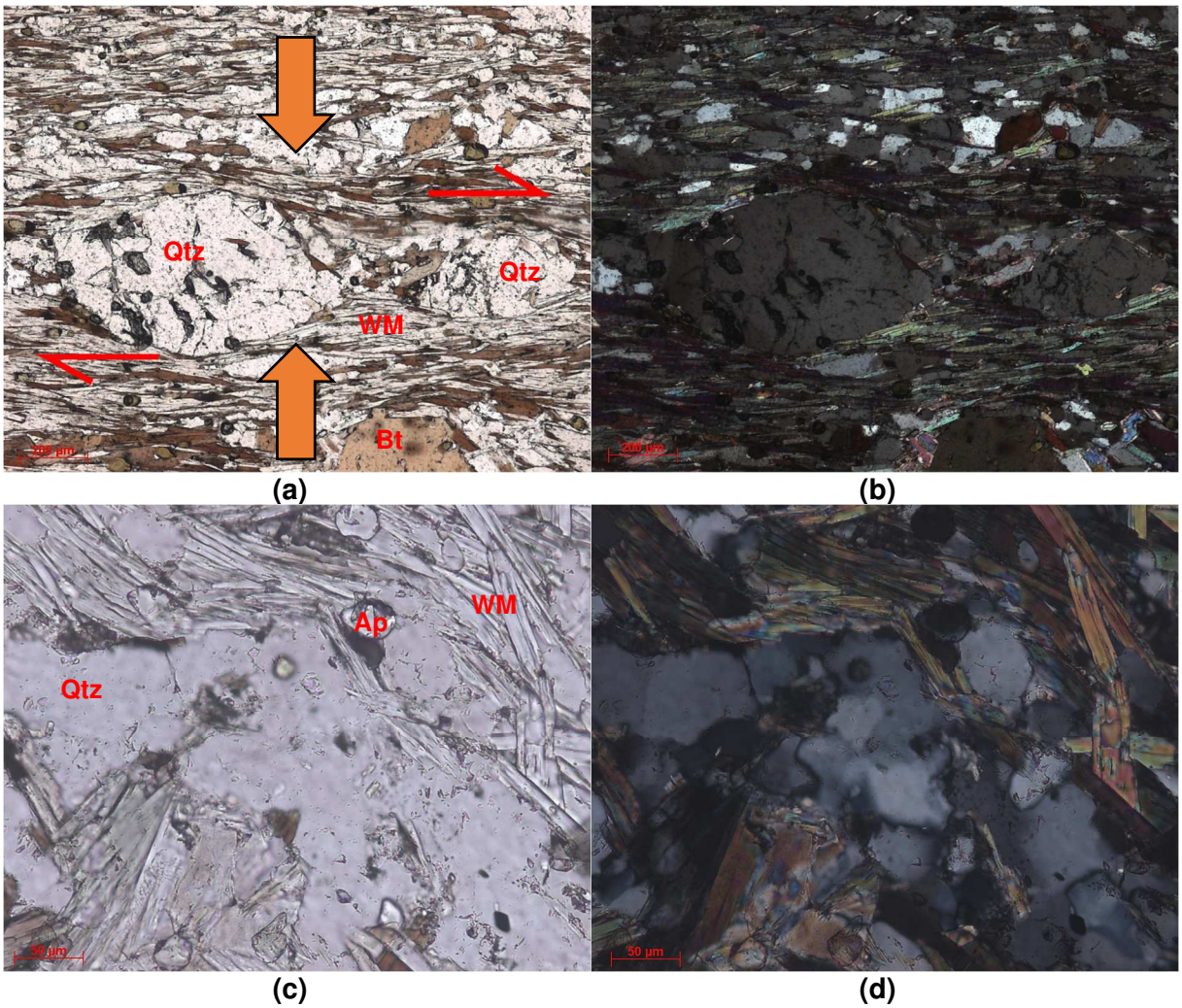

Figure III.15.

Petrographic aspects of late recrystallization phenomena.

(a, b) Late, secondary white mica (WM) with large, poikilitic crystals.

(c, d) Large randomly oriented late white mica (WM) crystals over a micaceous layer mostly composed of biotite (Bt), in a thick section (magnification of 5x).

(e, f) Late white mica (WM) intergrown with chlorite (Chl), transverse to the main foliation (Sn), often growing in fibro-radiated nuclei. The matrix is composed of quartz (Qtz), partially chloritized biotite (Bt), and epidote (Ept).

Figure III.15.

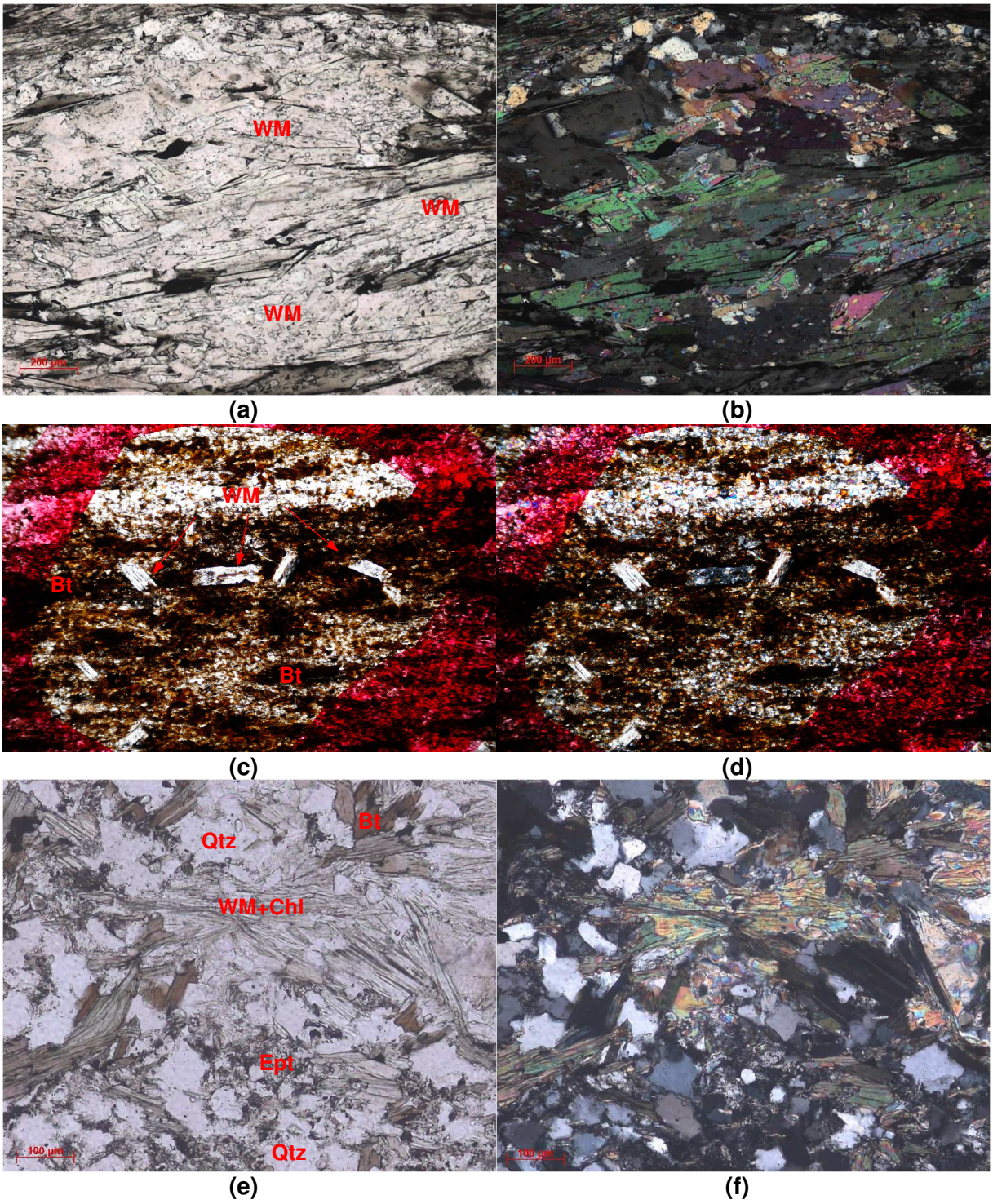

Figure III.16.

Petrographic aspects of late replacement phenomena.

(a, b) Complete sericitization (Ser) of previous anhedral crystals (probably andalusite or cordierite) elongated according to the main foliation (Sn) that were in equilibrium with biotite (Bt).

(c-f) Pseudomorph replacement of previous anhedral andalusite or cordierite crystals by an intergrowth of sericite (Ser) and chlorite (Chl), probably as a result of hydrothermal alteration.

Figure III.16.

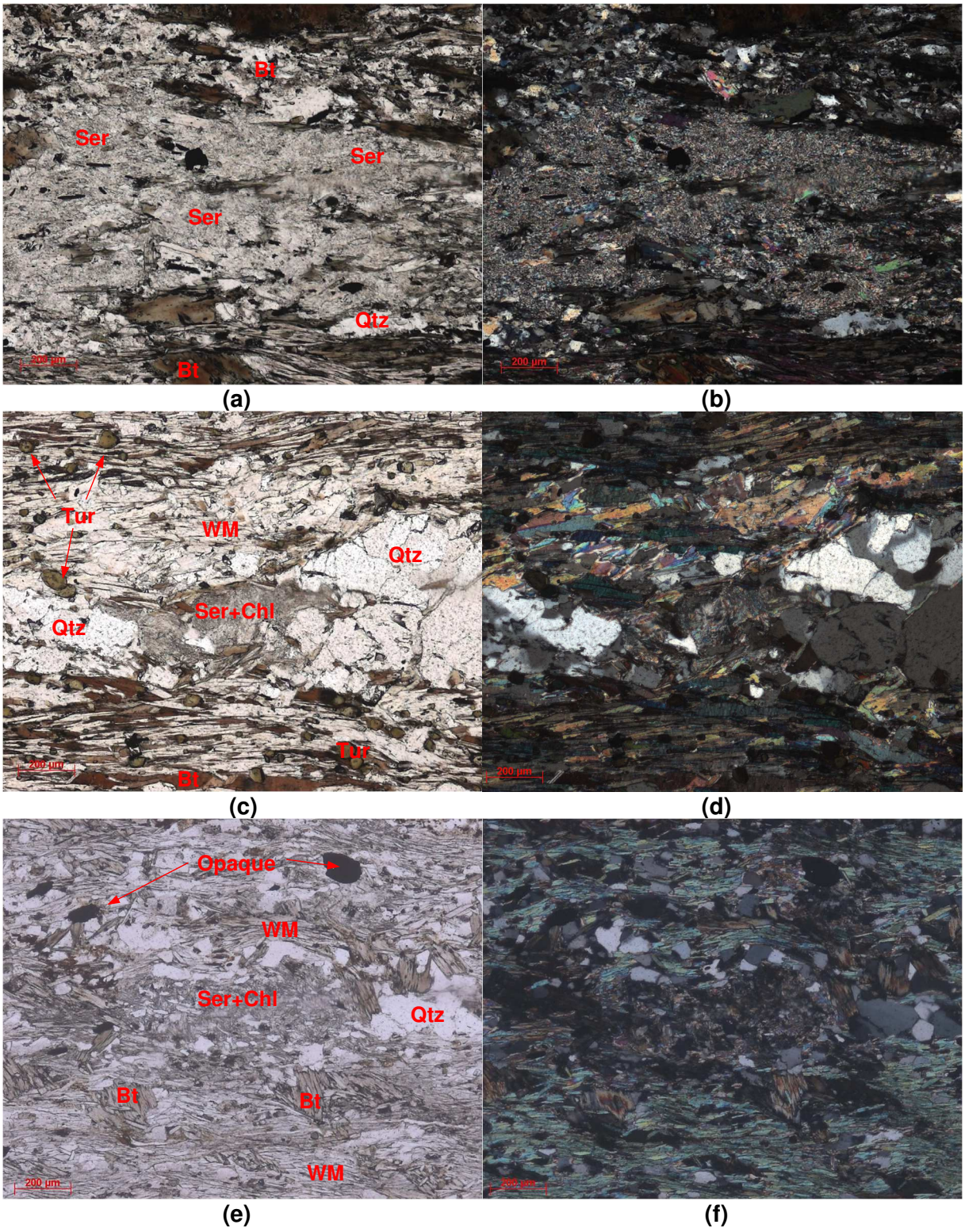

Figure III.17.

Petrographic aspects of the calcsilicated levels.

(a, b) Arborescent tremolite-actinolite (Tr-Act) in a granoblastic heterogranular matrix with polygonal tendency (triple points at quartz grain boundary).

(c, d) Epidote (Ept) widely disperse in the granoblastic matrix

Figure III.17.

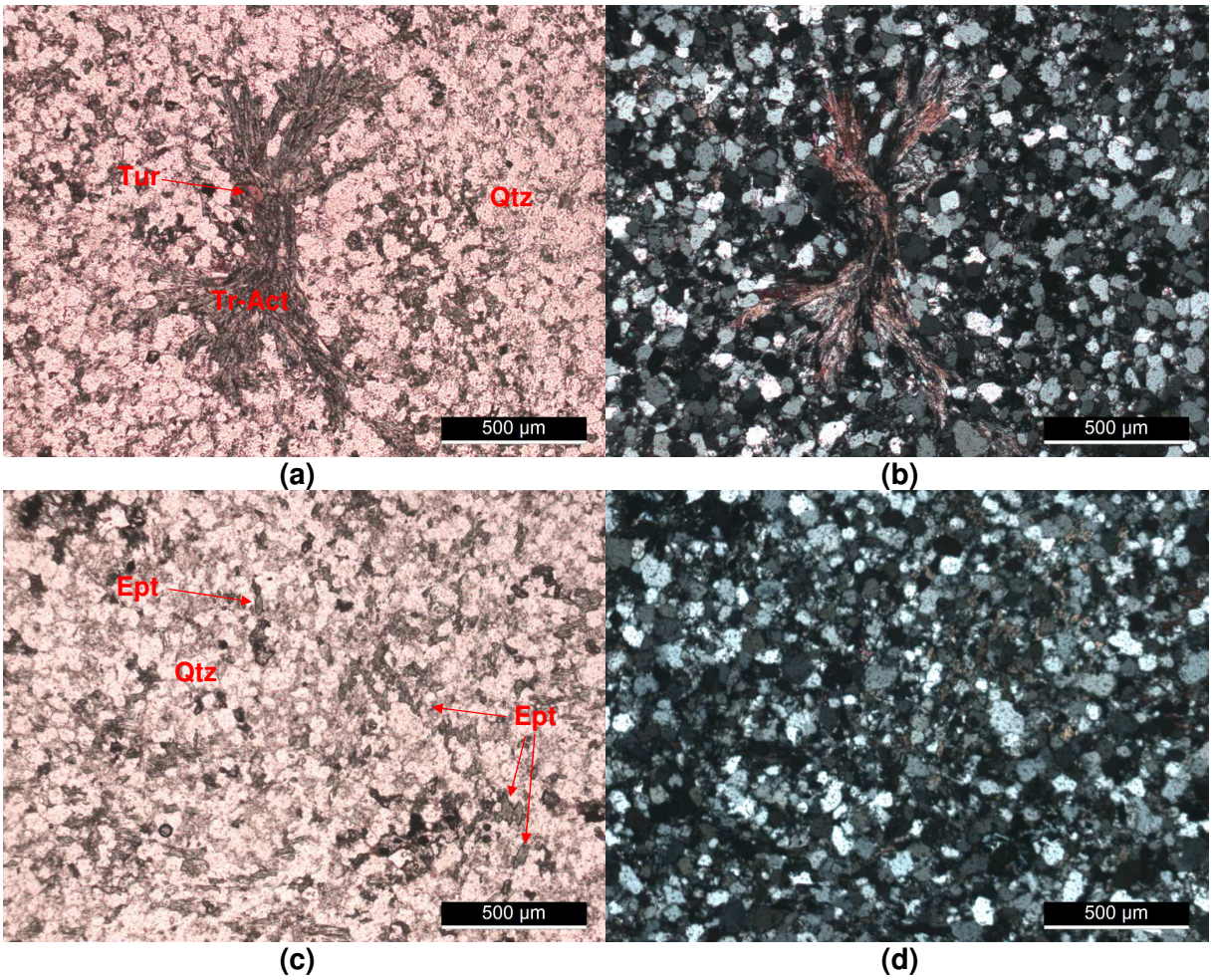

Figure III.18.

Petrographic aspects of some of the control samples near the Saucelle granite.

The semi-pelitic rocks, presenting a porphyroblastic texture over a granolepidoblastic matrix **(a)**, display evidence of thermal granitic influence, namely obliteration of previous structures through heating, generating a cust texture **(b)** where the micas do not present any preferred orientation. This type of cust texture is typical of hornfels, indicating that the samples were affected by contact metamorphism.

(c, d) Pseudomorph replacement of an andalusite or cordierite porphyroblast.

(e, f) High-temperature, inequigranular quartz vein (saccharoidal quartz with sutured edges, undulose extinction in cpl, and visible fluid inclusions).

Figure III.18.

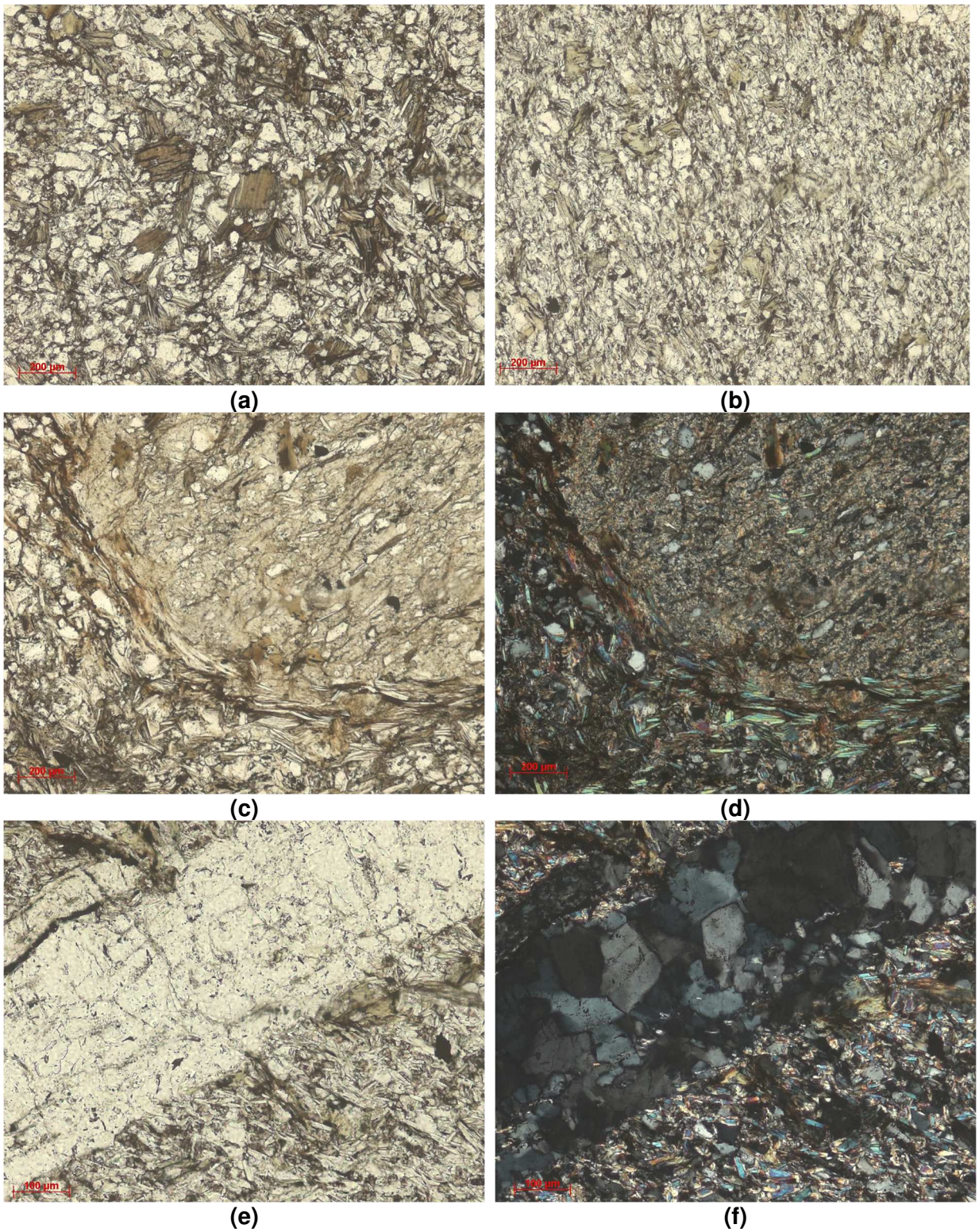

Appendix IV. Hyperspectral studies for halo detection

IV.1. Equipment and measurements

All reflectance spectroscopy studies were conducted at FCUP, using the available ASD FieldSpec 4 spectrometer (Figure IV.1). The equipment has a standard resolution of 3.0 nm @ 700 nm, 10.0 nm @ 1400 nm, and 10.0 nm @ 2100 nm. All measurements were made with a Contact Probe containing an internal light source (halogen bulb). For calibration, a Spectralon (Labsphere) plate with a maximum reflectance above 95% for the 250-2500 nm range and above 99% for the 400-1500 nm region was measured every 30 to 45 minutes. Each final spectra represented an average of 5 measurements of 40 scans per point.

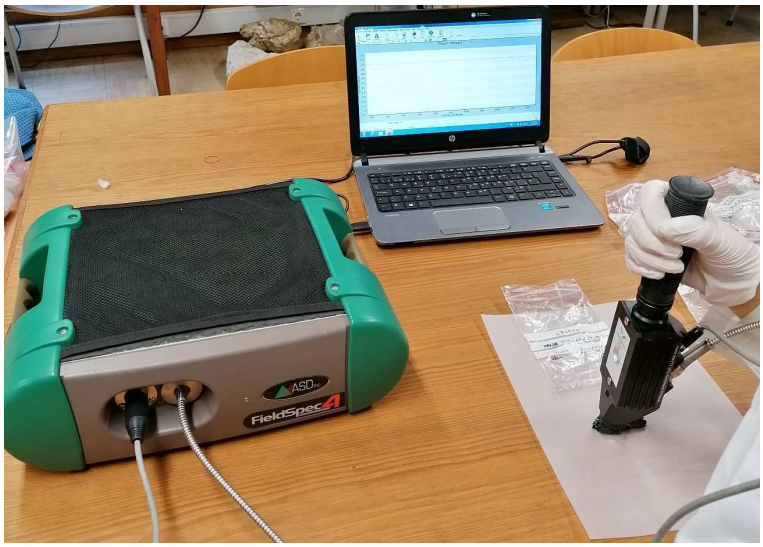

Figure IV.1. FieldSpec 4 spectroradiometer operating with the contact probe.

No sampling preparation is needed for this kind of study. It was only necessary to check that the samples were properly dry and clean. For each sample, several spectra were acquired considering the different types of faces (naturally exposed, fractured, sawn, etc.) and the existence of alteration minerals such as clays or iron oxides. All analyzed spots were photographed for reference.

IV.2. Sample list and selection of key spectra

At this stage, the hyperspectral studies were only conducted in the samples from the LIGHTS campaign. It is expected, in the future, to expand the analysis to the GREENPEG campaign as well. For each sample, a general description was made and the characteristics of each measured spot were summarized in the following tables. Where multiple samples per sampling spot were available, all were analyzed and named from A1 to An, where n equals the number of samples. In the end, the SpectraGryph software was employed to individually inspect each spectrum and select the most representative spectra in each sampling point for further analysis. This procedure allowed to discard equal or similar spectra, thus reducing the number of spectra for interpretation from 467 to 214 (last column of the following tables). Additional information on sample collection and provenance can be found on Appendix II.

Table IV.1. Sample list, description and observations of the spots analyzed through reflectance spectroscopy studies. CXG – control group.

Sample group	Spectrum name	Sample description	Observations	Color	Key spectra
CXG	CXG_436_A1_01	Siliceous rock with compositional layering	Sawn	—	No
	CXG_436_A1_02		Sawn	—	Yes
	CXG_436_A1_03		Exposed	—	No
	CXG_436_A1_04		Exposed, irregular	—	No
	CXG_436_A1_05		Covered with red soil	Redish	Yes
	CXG_436_A2_01	Siliceous rock with compositional layering	Sawn	—	Yes
	CXG_436_A2_02		Sawn	—	No
	CXG_436_A2_03		Covered with red soil	Redish	Yes
	CXG_437_01	Spotted mica schist with either andalusite or cordierite porphyroblasts	Sawn	—	Yes
	CXG_437_02		Exposed	—	No
	CXG_437_03		Exposed (visible white mica)	—	No
	CXG_437_04		Natural break	Redish	Yes
	CXG_438_01	Biotite mica schist with visible interbedded siliceous layers	Iron oxides	Redish	No
	CXG_438_02		Iron oxides	Redish	No
	CXG_438_03		Iron oxides	Redish	Yes
	CXG_438_04		Fresh	—	No
	CXG_438_05		Fresh	—	No
	CXG_438_06		Fresh	—	No

Table IV. 2. Sample list, description and observations of the spots analyzed through reflectance spectroscopy studies. T4 – host rocks of barren, concordant pegmatite dykes; B – base profile; T – top profile; .1/2 – number of the profile.

Sample group	Spectrum name	Sample description	Observations	Color	Key spectra
T4-1B	T4-19-01_01	Biotite mica schist with visible tourmaline and white mica	Fresh; parallel to foliation	—	No
	T4-19-01_02		Iron/manganese oxides	—	No
	T4-19-01_03		Iron oxides	—	Yes
	T4-19-01_04		Iron oxides	—	Yes
	T4-19-01_05		Abundance of white mica	—	No
	T4-19-02_01	Biotite mica schist with visible tourmaline white mica, and andalusite	Sawn	—	No
	T4-19-02_02		Sawn	—	Yes
	T4-19-02_03		Sawn	—	No
	T4-19-02_04		Exposed	—	No
	T4-19-02_05		Exposed	—	No
	T4-19-02_06		Altered; iron oxides	—	No
	T4-19-02_07		Altered	—	Yes
	T4-19-03_01	Pelitic rock with compositional layering and visible biotite, white mica, andalusite and tourmaline	Exposed	Light grey	Yes
	T4-19-03_02		Exposed	Light grey	No
	T4-19-03_03		Exposed	Light grey	No
	T4-19-03_04		Altered	—	No
	T4-19-03_05		Altered; iron oxides	Red	Yes
	T4-19-03_06		Normal to foliation	—	No
	T4-19-04_A1_01	Biotite mica schist with visible tourmaline and andalusite	Sawn	—	Yes
	T4-19-04_A1_02		Sawn	—	No
	T4-19-04_A1_03		Normal to foliation	—	Yes
	T4-19-04_A1_04		Normal to foliation	—	No
	T4-19-04_A2_01	Biotite mica schist with visible tourmaline and andalusite	Exposed	—	Yes
	T4-19-04_A2_02		Exposed	—	No
	T4-19-04_A2_03		Natural break	—	Yes
	T4-19-04_A2_04		Natural break	—	No
T4-1T	T4-19-05_01	Biotite mica schist with interbedded siliceous layers, and visible tourmaline and andalusite	Sawn	—	Yes
	T4-19-05_02		Sawn	—	No
	T4-19-05_03		Altered; parallel to foliation	—	Yes
	T4-19-05_04		Altered; parallel to foliation	—	No
	T4-19-05_05		Altered; parallel to foliation	—	No
	T4-19-05_06		Altered; parallel to foliation	—	No
	T4-19-05_07		Fracture; normal to foliation	—	No
	T4-19-05_08		Fracture; normal to foliation	—	No
	T4-19-06_A1_01		Sawn	—	No

Sample group	Spectrum name	Sample description	Observations	Color	Key spectra
	T4-19-06_A1_02	Rock with a compositional layering; sample A2 is more siliceous than A1; visible white mica and tourmaline	Sawn	—	No
	T4-19-06_A1_03		Iron oxides	—	No
	T4-19-06_A1_04		Altered; clays	—	Yes
	T4-19-06_A1_05		Altered; clays	—	No
	T4-19-06_A1_06		Normal to foliation	Dark	Yes
	T4-19-06_A1_07		Fracture	Dark	No
	T4-19-06_A2_01	Rock with a compositional layering; sample A2 is more siliceous than A1; visible white mica and tourmaline	Iron oxides; vegetation coverage	—	Yes
	T4-19-06_A2_02		Normal to foliation	Dark	No
	T4-19-06_A2_03		Fracture; altered	Dark	Yes
T4	T4-19-07_01	Siliceous rock with a compositional layering; visible biotite, white mica and tourmaline	Iron oxides.	—	Yes
	T4-19-07_02		Iron oxides.	—	No
	T4-19-07_03		Altered; iron oxides	—	No
	T4-19-07_04		Altered; iron oxides	—	No
	T4-19-07_05		Sawn	—	No
	T4-19-07_06		Normal to foliation	—	No

Table IV. 3. Sample list, description and observations of the spots analyzed through reflectance spectroscopy studies. T5 – host rocks of potassium feldspar-bearing aplite-pegmatite dykes; E – east profile; 1/2 – number of the profile.

Sample group	Spectrum name	Sample description	Observations	Color	Key spectra
T5	T5-19-04_01	Altered siliceous rock	Siliceous cover	—	Yes
	T5-19-04_02		Siliceous cover	Brown	No
	T5-19-04_03		Fracture	Brown	No
	T5-19-04_04		Altered	Reddish	Yes
T5-1E	T5-19-01a_01	Biotite mica schist	Natural break	—	No
	T5-19-01a_02		Exposed	—	Yes
	T5-19-01a_03		Fracture	—	No
	T5-19-02_01	Biotite mica schist; fractures normal to the foliation with quartz filling	Fresh	—	No
	T5-19-02_02		Fresh; fractures filled with quartz and iron oxides	—	No
	T5-19-02_03		Exposed	—	Yes
	T5-19-02_04		Alteration cover	Brown	No
	T5-19-02_05		Normal to foliation	—	No
	T5-19-02_06		Fracture; iron oxides	—	No
	T5-19-03_01	Biotite mica schist; fractures normal to the foliation	Fresh	—	Yes
	T5-19-03_02		Fresh	—	No
	T5-19-03_03		Alteration cover	—	No

Table IV. 4. Sample list, description and observations of the spots analyzed through reflectance spectroscopy studies. T6 – host rocks of simple, discordant aplite-pegmatite dykes; E – east profile; W – west profile; 1/2 – number of the profile.

Sample group	Spectrum name	Sample description	Observations	Color	Key spectra
T6-1E	T6-19-01_01	Dark siliceous rock; visible biotite and tourmaline	Dust on the surface	—	No
	T6-19-01_02		Dust on the surface	—	Yes
	T6-19-01_03		Fracture; iron oxides	—	Yes
	T6-19-01_04		Irregular surface	—	No
	T6-19-02_01	Slightly altered siliceous rock; visible White mica and tourmaline	Altered	—	No
	T6-19-02_02		Very altered	White	Yes
	T6-19-02_03		Irregular; dust on the surface	—	No
	T6-19-02_04		Fracture; iron oxides	—	Yes
	T6-19-03_A1_01	Pelitic rock; visible biotite, tourmaline and white mica	Sawn	—	No
	T6-19-03_A1_02		Sawn	—	Yes
	T6-19-03_A1_03		Irregular surface; slightly altered	—	No
	T6-19-03_A1_04		Iron oxides	—	Yes
	T6-19-03_A1_05		Altered	—	No
	T6-19-03_A2_01	Pelitic rock; visible biotite, tourmaline and white mica	Slightly altered	—	Yes
	T6-19-03_A2_02		Slightly altered	—	No
	T6-19-03_A2_03		Exposed; iron oxides	—	Yes
	T6-19-03_A2_04		Exposed; iron oxides	—	No
	T6-19-03_A2_05		Exposed; iron oxides	—	No
	T6-19-03_A2_06		Fresh	Dark	No
	T6-19-04_01	Biotite mica schist	Sawn	—	Yes
	T6-19-04_02		Exposed; iron oxides	—	No
	T6-19-04_03		Fracture filled with micas and iron oxides	—	Yes
T6-1W	T6-19-05_A1_01	Rock with a compositional layering; visible tourmaline	Sawn; dust on the surface	—	No
	T6-19-05_A1_02		Slightly altered	—	Yes
	T6-19-05_A1_03		Altered; iron oxides	—	Yes
	T6-19-05_A2_01	Rock with a compositional layering; visible tourmaline	Sawn; dust on the surface	—	No
	T6-19-05_A2_02		Slightly altered	—	Yes
	T6-19-05_A2_03		Altered	—	No
	T6-19-06_01	Biotite mica schist with interbedded siliceous layers	Sawn	—	Yes
	T6-19-06_02		Sawn	—	No
	T6-19-06_03		Iron oxides	—	Yes
	T6-19-06_04		Siliceous cover	—	Yes
	T6-19-07_01	Dark siliceous rock with visible tourmaline	Altered; iron oxides	—	No
	T6-19-07_02		Normal to foliation	—	No
	T6-19-07_03		Normal to foliation	—	No
	T6-19-07_04		Altered; iron oxides	—	Yes
	T6-19-07_05		Fracture; iron oxides	—	Yes

Table IV. 5. Sample list, description and observations of the spots analyzed through reflectance spectroscopy studies. TC – Tumbo de la Caldera, host rocks of simple, discordant aplite-pegmatite dykes; E – east profile; W – west profile; 1/2 – number of the profile.

Sample group	Spectrum name	Sample description	Observations	Color	Key spectra
TC-1W	TC-19-01.1	Dark phyllite with visible white mica and tourmaline	Natural break	—	No
	TC-19-01.2		Natural break	—	No
	TC-19-01.3		Exposed	—	Yes
	TC-19-01.4		Exposed	—	No
	TC-19-01.5		Iron oxides	—	No
	TC-19-02.1	Dark siliceous rock with visible white mica	Natural break	—	No
	TC-19-02.2		Exposed; dust on the surface	—	Yes
	TC-19-02.3		Exposed; dust on the surface	Brown	No
	TC-19-03.1	Dark phyllite with visible white mica	Fresh	—	No
	TC-19-03.2		Iron oxides	—	No
	TC-19-03.3		Iron oxides	—	Yes
	TC-19-03.4		Iron oxides	—	Yes
TC-1E	TC-19-04_A1.1	Dark siliceous rock with visible tourmaline	Fracture; iron oxides	—	No
	TC-19-04_A1.2		Fracture; iron oxides	—	No
	TC-19-04_A1.3		Exposed	—	Yes
	TC-19-04_A1.4		Altered	Light	No
	TC-19-04_A1.5		Altered	Light	Yes
	TC-19-04_A1.6		Slightly altered	—	Yes
	TC-19-04_A2.1	Dark siliceous rock with visible tourmaline	Exposed	Yellow; orange	No
	TC-19-04_A2.2		Iron oxides	Orange	Yes
	TC-19-04_A2.3		Fresh	—	No
	TC-19-04_A2.4		Fresh; exposed	—	Yes
	TC-19-04_A2.5		Altered	—	No
	TC-19-05.1	Biotite mica schist with interbedded calcsilicated level; visible tourmaline	Iron oxides	—	No
	TC-19-05.2		Iron oxides	—	Yes
	TC-19-05.3		Iron oxides	—	No
	TC-19-05.4		Normal to foliation	—	No
	TC-19-05.5		Calcsilicated level	—	No
	TC-19-05.6		Calcsilicated level	—	Yes
	TC-19-05.7		Calcsilicated level	—	Yes
TC-2	TC-19-06.1.	Biotite mica schist with interbedded siliceous layers	Siliceous layer	—	Yes
	TC-19-06.2		Iron oxides	—	Yes
	TC-19-06.3		Altered	—	Yes
	TC-19-06.4		Altered	—	No
	TC-19-06.5		Altered	—	No
	TC-19-07.1		Fresh	—	Yes
	TC-19-07.2		Fresh	—	No

Sample group	Spectrum name	Sample description	Observations	Color	Key spectra
	TC-19-07.3	Biotite mica schist with interbedded siliceous layers	Altered	—	Yes
	TC-19-07.4		Altered	—	No
	TC-19-07.5		Normal to foliation	—	Yes
	TC-19-08.1	Biotite mica schist with white mica and tourmaline	Fresh	—	No
	TC-19-08.2		Fresh	—	No
	TC-19-08.3		Altered; iron oxides; dust on the surface	—	Yes
	TC-19-08.4		Altered; iron oxides; dust on the surface	—	Yes
	TC-19-08.5		Normal to foliation	—	Yes
	TC-19-09.1	Rock with a fine compositional layering	Very altered; iron oxides	Brown	No
	TC-19-09.2		Very altered; iron oxides	Brown	Yes
	TC-19-09.3		Very altered; iron oxides	Brown	No
	TC-19-09.4		Dust on the surface	—	Yes
	TC-19-09.5		Dust on the surface	—	Yes
	TC-19-09.6		Normal to foliation	—	No
	TC-19-09.7		Normal to foliation	—	No
	TC-19-10.1	Biotite mica schist	Exposed	—	Yes
	TC-19-10.2		Exposed	—	No
	TC-19-10.3		Iron oxides	—	No
	TC-19-10_04		Iron oxides	—	Yes
	TC-19-10.5		Normal to foliation	—	Yes
	TC-19-11.1	Biotite mica schist with white mica and tourmaline	Exposed	Light grey	No
	TC-19-11.2		Altered	Brown	No
	TC-19-11.3		Altered	Dark	No
	TC-19-11.4		Altered	Brown	Yes
	TC-19-11.5		Manganese oxides	—	No
	TC-19-11.6		Exposed	Light grey	Yes
	TC-19-12.1	Biotite mica schist	Slightly altered	—	Yes
	TC-19-12.2		Iron oxides	—	No
	TC-19-12.3		Iron oxides	—	No
	TC-19-12.4		Normal to foliation	—	Yes
	TC-19-12.5		Iron oxides	—	No

Table IV. 6. Sample list, description and observations of the spots analyzed through reflectance spectroscopy studies. T7 – host rocks of petalite-bearing aplite-pegmatite dykes; 1/2 – number of the profile.

Sample group	Spectrum name	Sample description	Observations	Color	Key spectra
T7-1	T7-19-01_A1.1	Biotite mica schist with interbedded siliceous layers; visible tourmaline	Altered	—	Yes
	T7-19-01_A1.2		Sawn	—	No
	T7-19-01_A1.3		Swan	—	Yes
	T7-19-01_A1.4		Altered	Green	No
	T7-19-01_A2.1	Biotite mica schist with interbedded siliceous layers; visible tourmaline	Altered; iron oxides	—	No
	T7-19-01_A2.2		Altered	—	No
	T7-19-01_A2.3		Altered	—	Yes
	T7-19-01_A2.4		Altered	—	No
	T7-19-01_A2.5		Altered	—	No
	T7-19-01_A2.6		Fresh	—	No
	T7-19-01_A2.7		Natural break; iron oxides	—	Yes
	T7-19-01_A2.8		Altered; clays	—	Yes
	T7-19-01_A2.9		Altered; clays	—	No
	T7-19-02_A1.1	Biotite mica schist with visible white mica	Manganese oxides	—	No
	T7-19-02_A1.2		Manganese oxides	—	No
	T7-19-02_A1.3		Fresh	—	No
	T7-19-02_A1.4		Fresh	—	Yes
	T7-19-02_A1.5		Iron oxides	—	Yes
	T7-19-02_A2.1	Biotite mica schist with visible white mica	Fresh	—	No
	T7-19-02_A2.2		Fresh	—	No
	T7-19-02_A2.3		Altered; clays	—	No
	T7-19-02_A2.4		Altered; clays	—	Yes
	T7-19-03.1	Biotite mica schist with interbedded siliceous layers	Natural break	—	No
	T7-19-03.2		Natural break	—	Yes
	T7-19-03.3		Alteration cover	Yellow	Yes
	T7-19-04.1	Biotite mica schist with visible white mica	Sawn	—	No
	T7-19-04.2		Altered	—	Yes
	T7-19-04.3		Natural break	—	No
	T7-19-04.4		Iron oxides	—	Yes

Table IV. 7. Sample list, description and observations of the spots analyzed through reflectance spectroscopy studies. BJ – Bajoca, host rocks of petalite-bearing aplite-pegmatite dykes; E – east profile; W – west profile; 1/2 – number of the profile.

Sample group	Spectrum name	Sample description	Observations	Color	Key spectra
BJ-1E	BJ-02-LT1(1)_01	Biotite mica schist with interbedded siliceous layers	Altered; iron oxides	Red	Yes
	BJ-02-LT1(1)_02		Exposed; vegetation	—	Yes
	BJ-02-LT1(2)_01		Altered; iron oxides	Redish	Yes
	BJ-02-LT1(2)_02		Exposed; vegetation	—	Yes
	BJ-03-384_01	Light colored biotite mica schist	Exposed; iron oxides	Red	Yes
	BJ-03-384_02		Exposed; iron oxides	Red	No
	BJ-03-384_03		Sawn	—	No
	BJ-04-383_01	Light colored biotite mica schist; with white mica	Irregular surface	—	No
	BJ-04-383_02		Sawn	—	No
	BJ-04-383_03		Irregular surface; iron oxides	—	Yes
	BJ-05-382_01	Light colored biotite mica schist; with white mica; affected by a shearing zone	Exposed	Redish	No
	BJ-05-382_02		Sawn	—	Yes
	BJ-07-377_A1_01	Light colored phyllite; visible white mica	Exposed	—	Yes
	BJ-07-377_A1_02		Exposed; iron oxides	Redish	No
	BJ-07-377_A2_01	Light colored phyllite; visible white mica	Exposed; iron oxides	Redish	Yes
	BJ-09-379_01	Light colored siliceous rock with visible compositional layering	Iron and manganese oxides	—	Yes
	BJ-09-379_02		Fractures filled with iron oxides	—	No
	BJ-09-379_03		Fracture filled with quartz	—	Yes
	BJ-09-379_04		Sawn	—	No
	BJ-10-378b_02	Dark tourmalinite	Sawn	—	Yes
	BJ-10-378b_03		Iron oxides	—	No
	BJ-11-376_01	Light colored siliceous rock	Sawn	—	Yes
BJ	BJ-19-02_01	Biotite mica schist with visible white mica	Natural break	Dark grey	No
	BJ-19-02_02		Natural break	Dark grey	No
	BJ-19-02_03		Natural break; iron oxides	Dark grey	Yes
	BJ-19-02_04		Natural break; iron oxides	Dark grey	No
	BJ-19-02_05		Natural break	Dark grey	No
	BJ-19-02_06		Natural break; iron oxides	Dark grey	No
	BJ-19-02_07		Natural break; iron oxides	Dark grey	Yes
	BJ-19-02_08		Natural break; iron oxides	Dark grey	No

Sample group	Spectrum name	Sample description	Observations	Color	Key spectra
	BJ-19-03_01	Dark tourmalinite	Irregular surface	Dark grey	Yes
	BJ-19-03_02		Irregular surface	Dark grey	No
	BJ-19-03_03		Irregular surface; quartz vein	Greenish white	Yes
	BJ-19-03_04		Irregular surface	Dark grey	No
	BJ-19-04_01	Light colored biotite mica schist	Natural break	Yellow	No
	BJ-19-04_02		Natural break; iron oxides	Dark grey	Yes
	BJ-19-04_03		Natural break; iron oxides	Dark grey	No
	BJ-19-04_04		Normal to foliation; dirt on the surface	Yellow	No
	BJ-19-05(1)_01	Light colored biotite mica schist; with visible white mica	Natural break; iron oxides	White; red	No
	BJ-19-05(1)_02		Natural break; iron oxides	White; red	No
	BJ-19-05(1)_03		Natural break	Grey	Yes
	BJ-19-05(1)_04		Natural break; iron oxides	White; red	Yes
	BJ-19-05(1)_05		Normal to foliation	Dark grey	No
	BJ-19-05(2)_01	Light colored biotite mica schist; with visible white mica	Natural break; altered	Grey	Yes
	BJ-19-05(2)_02		Normal to foliation	Grey	No
	BJ-19-05(2)_03		Natural break; iron oxides	Grey; red	Yes
	BJ-19-07_05	Biotite mica schist	Exposed	Dark grey	No
	BJ-19-07_02		Expose	Dark grey	Yes
	BJ-19-07_03		Exposed	Dark grey	No
	BJ-19-07_04		Natural break; dirt on the surface	Brown	No
	BJ-19-07_05		Natural break; dirt on the surface	Brown	Yes
	BJ-19-09_01	Light colored biotite mica schist; with visible white mica	Exposed; iron oxides; vegetation	Grey	Yes
	BJ-19-09_02		Exposed; iron oxides	Reddish	Yes
	BJ-19-09_03		Natural break; iron oxides	Grey	Yes
	BJ-19-09_04		Natural break; iron oxides	Grey	No
	BJ-19-12(1)_01	Biotite mica schist with interbedded siliceous layers; white mica	Exposed; iron oxides	Reddish	Yes
	BJ-19-12(1)_02		Exposed; iron oxides	Dark	No
	BJ-19-12(1)_03		Natural break	Dark	Yes
	BJ-19-12(1)_04		Natural break	Dark	No
	BJ-19-12(2)_01	Biotite mica schist; white mica	Natural break	Grey	Yes
	BJ-19-12(2)_02		Exposed	Dark	No
	BJ-19-12(2)_03		Exposed; iron oxides	Brown	No
	BJ-19-12(2)_04		Exposed; iron oxides	Reddish	Yes
	BJ-19-12(2)_05		Exposed	Dark	No

Sample group	Spectrum name	Sample description	Observations	Color	Key spectra
	BJ-20-01_01	Light colored biotite mica schist; with visible white mica	Exposed; iron oxides	Reddish	Yes
	BJ-20-01_02		Exposed; iron oxides	Orange	No
	BJ-20-01_03		Natural break; iron oxides	Grey	No
	BJ-20-01_04		Natural break; iron oxides	Grey	Yes
	BJ-20-02_01	Light colored biotite mica schist; with visible white mica	Natural break	Yellowish grey	Yes
	BJ-20-02_02		Natural break	Grey	Yes
	BJ-20-02_03		Exposed; iron oxides	Reddish	No
	BJ-20-02_04		Exposed; iron oxides	Reddish	No
	BJ-20-02_05		Exposed; iron oxides	Reddish	No
	BJ-20-03_01	Light colored biotite mica schist; with visible white mica	Natural break	Grey	No
	BJ-20-03_02		Natural break; iron oxides	Grey	No
	BJ-20-03_03		Exposed; dirt on the surface	Brown	Yes
	BJ-20-03_04		Exposed; vegetation	Grey	Yes
	BJ-20-03_05		Natural break	Yellowish grey	No
	BJ-LT5(1)_01	Dark tourmalinite	Irregular surface; altered	—	Yes
	BJ-LT5(1)_02		Sawn	—	Yes
	BJ-LT5(1)_03		Sawn	—	No
	BJ-LT5(2)_01	Dark tourmalinite	Sawn	—	Yes
	BJ03-B-DD_01	Light colored biotite mica schist	Iron oxides	—	Yes
	BJ03-B-DD_02		Exposed; iron oxides	—	No
	BJ03-B-DD_03		Exposed; iron oxides	—	Yes
BJ-1W	LT6_01	Light colored biotite mica schist; with visible white mica	Exposed	—	No
	BJ-12-LT6 _01		Exposed	—	Yes
	BJ-12-LT6 _02		Exposed; iron oxides	—	Yes
	LT7_01	Light colored biotite mica schist; with visible white mica	Sawn	—	No
	LT7_02		Iron oxides	Red	No
BJ-2W	BJ-20-04_01	Light colored biotite mica schist; with visible white mica	Exposed	Grey	Yes
	BJ-20-04_02		Exposed; iron oxides	Reddish	Yes
	BJ-20-04_03		Natural break	Grey	No
	BJ-20-04_04		Natural break	Grey	No
	BJ-20-05(1)_01	Light colored biotite mica schist; with visible white mica	Exposed; iron oxides	Reddish	No
	BJ-20-05(1)_02		Natural break; iron oxides	Grey	Yes
	BJ-20-05(1)_03		Exposed; iron oxides	Reddish	Yes
	BJ-20-05(2)_01	Light colored biotite mica schist; with visible white mica	Natural break	Grey	Yes
	BJ-20-05(2)_02		Natural break	Grey	No
	BJ-20-06_01		Natural break; iron oxides	Grey	No

Sample group	Spectrum name	Sample description	Observations	Color	Key spectra
	BJ-20-06_02	Light colored biotite mica schist; with visible white mica	Natural break; iron oxides	Grey	Yes
	BJ-20-06_03		Exposed; iron oxides	Grey	Yes
	BJ-20-06_04		Exposed; iron oxides	Reddish	No
	BJ-20-07_01	Biotite mica schist; with visible white mica	Exposed; iron oxides	Yellow	Yes
	BJ-20-07_02		Exposed; iron oxides	Reddish	No
	BJ-20-07_03		Exposed; iron oxides	Reddish	Yes
	BJ-20-08_01	Biotite mica schist; with visible white mica	Natural break; iron oxides	Grey	No
	BJ-20-08_02		Natural break	Grey	No
	BJ-20-08_03		Natural break	Grey	Yes
	BJ-20-08_04		Exposed	Grey	No
	BJ-20-09(1)_01	Light colored biotite mica schist; with visible white mica	Natural break	Yellowish grey	Yes
	BJ-20-09(1)_02		Natural break	Yellowish grey	No
	BJ-20-09(2)_01	Light colored biotite mica schist; with visible white mica	Natural break	Yellowish grey	Yes
	BJ-20-09(2)_02		Natural break	Yellowish grey	No
	BJ-20-09(3)_01	Light colored biotite mica schist; with visible white mica	Natural break	Yellowish grey	No
	BJ-20-09(3)_02		Natural break	Yellowish grey	Yes
	BJ-20-10_01	Light colored biotite mica schist; with visible white mica	Natural break; iron oxides	Yellowish grey	Yes
	BJ-20-10_02		Exposed; iron oxides	Yellowish grey; red	Yes
	BJ-20-10_03		Natural break; iron oxides	Yellowish grey	No
	BJ-20-11_01	Light colored biotite mica schist; with visible white mica	Natural break; iron oxides	Yellowish grey	Yes
	BJ-20-11_02		Natural break; iron oxides	Yellowish grey	Yes
	BJ-20-11_03		Natural break; iron oxides	Yellowish grey	Yes
	BJ-20-11_04		Natural break; iron oxides	Yellowish grey	No

Table IV. 8. Sample list, description and observations of the spots analyzed through reflectance spectroscopy studies. BJ – Bajoca, host rocks of petalite-bearing aplite-pegmatite dykes; DD – diamond drilling (drill core samples).

Sample group	Spectrum name	Sample description	Observations	Color	Key spectra
BJ-DD-4	BJ04-A_01	Light biotite mica schist; visible white mica	Altered; iron oxides	Red	Yes
	BJ04-A_02		Altered; iron oxides	Red	Yes
	BJ04-B_01	Rock with visible compositional layering	Fracture; iron oxides	Red	Yes
	BJ04-B_02		Fracture; iron oxides	Red	Yes
	BJ04-B_03		Sawn; fresh	—	No
	BJ04-C_01	Light biotite mica schist with interbedded siliceous layers	Natural break	—	No
	BJ04-C_02		Exposed	Reddish	Yes
	BJ04-D_01	Biotite mica schist	Natural break	—	Yes
	BJ04-D_02		Exposed	Whitish	No
	BJ04-E_01	Biotite mica schist	Natural break	—	Yes
	BJ04-E_02		Natural break	—	No
	BJ04-F_01	Biotite mica schist	Sawn	—	No
	BJ04-F_02		Exposed	Yellow	No
	BJ04-F_03		Sawn	—	Yes

Table IV. 9. Sample list, description and observations of the spots analyzed through reflectance spectroscopy studies. ALB – Alberto, host rocks of spodumene-bearing aplite-pegmatite dykes; S – south profile; N – north profile; 1/2 – number of the profile.

Sample group	Spectrum name	Sample description	Observations	Color	Key spectra
ALB-1S	ALB-19-01.1	Biotite mica schist with visible tourmaline	Sawn	—	No
	ALB-19-01.4		Iron oxides	—	Yes
	ALB-19-01.5		Iron oxides	—	No
	ALB-19-01.6		Iron oxides	—	Yes
	ALB-19-02.1	Siliceous biotite mica schist	Iron oxides	—	No
	ALB-19-02.2		Fresh	—	Yes
	ALB-19-02.3		Altered; manganese oxides	Yellow	Yes
	ALB-19-02.4		Sawn	—	No
	ALB-19-03.1	Siliceous biotite mica schist with visible white mica	Sawn	—	Yes
	ALB-19-03.2		Irregular surface	—	No
	ALB-19-03.3		Iron oxides	—	Yes
	ALB-19-04_A1.1	Biotite mica schist with visible tourmaline	Iron oxides	—	No
	ALB-19-04_A1.2		Iron oxides	—	Yes
	ALB-19-04_A1.3		Natural break	—	No
	ALB-19-04_A1.4		Natural break	—	Yes
	ALB-19-04_A2.1	Biotite mica schist with visible tourmaline	Sawn	Dark	Yes
	ALB-19-04_A2.2		Sawn	—	No
	ALB-19-04_A2.3		Natural break; fresh	—	Yes
ALB-1N	ALB-19-05_A1.1	Siliceous biotite mica schist	Natural break	—	No
	ALB-19-05_A1.2		Natural break	—	Yes
	ALB-19-05_A2.1	Siliceous biotite mica schist	Natural break	—	No
	ALB-19-05_A2.2		Natural break	—	No
	ALB-19-05_A2.3		Altered; clays	—	Yes
	ALB-19-05_A2.4		Altered; clays	—	Yes
	ALB-19-05_A2.5		Natural break	—	No
	ALB-19-06.1	Biotite mica schist with interbedded siliceous layers	Sawn	—	No
	ALB-19-06.2		Sawn	—	Yes
	ALB-19-06.3		Exposed	—	Yes
	ALB-19-06.4		Exposed; clays	Yellow	No
	ALB-19-06.5		Exposed	—	No

Table IV. 10. Sample list, description and observations of the spots analyzed through reflectance spectroscopy studies. FE – Feli, host rocks of Li-mica and spodumene -bearing aplite-pegmatite dykes; E – east profile; W – west profile; 1/2 – number of the profile.

Sample group	Spectrum name	Sample description	Observations	Color	Key spectra
FE-1E	FE-19-01_A1.1	Dark siliceous rock with a compositional layering and visible tourmaline	Sawn; quartz veins	—	No
	FE-19-01_A1.2		Sawn	—	Yes
	FE-19-01_A1.3		Sawn	—	No
	FE-19-01_A1.4		Sawn	—	Yes
	FE-19-01_A1.5		Exposed	—	No
	FE-19-01_A1.6		Natural break	—	No
	FE-19-01_A2.1.	Dark siliceous rock with a compositional layering and visible tourmaline	Sawn	—	Yes
	FE-19-01_A2.2		Sawn	—	No
	FE-19-01_A2.3		Exposed	—	Yes
	FE-19-02.1	Light colored phyllite with visible tourmaline needles	Exposed	—	Yes
	FE-19-02.2		Exposed	—	No
	FE-19-02.3		Sawn	—	Yes
	FE-19-03.1	Dark siliceous rock with a compositional layering; visible quartz veins	Sawn	—	No
	FE-19-03.2		Sawn; quartz veins	—	No
	FE-19-03.3		Sawn	—	No
	FE-19-03.4		Sawn	—	Yes
	FE-19-04.1	Dark siliceous rock	Sawn	—	Yes
	FE-19-04.2		Altered	Yellow	No
	FE-19-04.3		Altered; iron oxides	Yellow; red	Yes
	FE-19-05.1	Dark siliceous rock	Sawn	—	Yes
	FE-19-05.2		Sawn	—	Yes
	FE-19-05.3		Exposed	—	Yes
	FE-19-06.1	Light siliceous rock	Clays on the surface	—	Yes
	FE-19-06.3		Clays on the surface	Yellow	Yes
	FE-19-06.4		Clays on the surface	Yellow	No
	FE-19-06.5		Natural break	—	No
	FE-19-07.1	Dark siliceous rock	Sawn	—	Yes
	FE-19-07.2		Sawn	—	No
	FE-19-07.3		Sawn	—	No
	FE-19-07.4		Exposed	—	Yes
	FE-19-07.5		Exposed	—	No
	FE-19-07.6		Exposed	—	No
	FE-19-08.1	Dark siliceous rock; fine compositional layering	Sawn	—	Yes
	FE-19-08.2		Sawn	—	No
	FE-19-08.3		Altered	Yellow	Yes
	FE-19-08.4		Altered	Brown	No
	FE-19-08.5		Exposed; iron oxides	—	No
	FE-19-09.1	Dark siliceous rock; visible tourmaline	Sawn	—	No
	FE-19-09.2		Sawn	—	Yes

Sample group	Spectrum name	Sample description	Observations	Color	Key spectra
	FE-19-09.3		Exposed	—	No
	FE-19-09.4		Altered	Yellow	Yes
FE-2E	FE-20-01(1)_01	Dark siliceous rock	Exposed; iron oxides	Greenish; red	Yes
	FE-20-01(1)_02		Natural break	Grey	No
	FE-20-01(1)_03		Exposed	Greenish	Yes
	FE-20-01(2)_01	Dark siliceous rock	Natural break	Greenish	Yes
	FE-20-01(2)_02		Natural break; iron oxides	Grey; red	No
	FE-20-01(2)_03		Natural break	Grey	No
	FE-20-02_01	Light siliceous rock	Exposed	Dark green	No
	FE-20-02_02		Exposed	Dark green	Yes
	FE-20-02_03		Exposed; iron oxides	Dark; red	No
	FE-20-02_04		Exposed; vegetation	Dark	Yes
	FE-20-02_05		Exposed	Dark	No
	FE-20-03(1)_01	Light siliceous rock	Exposed; iron oxides	—	Yes
	FE-20-03(1)_02		Natural break; iron oxides	—	No
	FE-20-03(2)_01	Dark siliceous rock	Exposed; iron oxides	Red	No
	FE-20-03(2)_02		Exposed; iron oxides	Red	No
	FE-20-03(2)_03		Exposed; iron oxides	Orange	Yes
	FE-20-03(2)_04		Natural break	Yellow	No
	FE-20-03(2)_05		Natural break	Yellow	Yes
	FE-20-04(1)_01	Light siliceous rock	Natural break	Grey; green	No
	FE-20-04(1)_02		Natural break	Grey	Yes
	FE-20-04(1)_03		Exposed	Dark	No
	FE-20-04(2)_01	Light siliceous rock	Natural break	Grey; green	Yes
	FE-20-04(2)_02		Natural break	Grey; green	No
	FE-20-04(2)_03		Exposed; iron oxides	Red	Yes
	FE-20-05_01	Siliceous rock	Natural break; iron oxides	Red	Yes
	FE-20-05_02		Natural break; iron oxides	Red	No
	FE-20-05_03		Natural break; iron oxides	Red	No
	FE-20-05_04		Exposed; dirt and vegetation on the surface	Brown	Yes
	FE-20-05_05		Exposed; lichen	Brown	Yes
	FE-20-05_06		Exposed; dirt and vegetation on the surface	Brown	No

IV.3. First results

All 214 representative spectra were analyzed through AusSpec International Ltd.'s Aisiris software. Table IV. 11 shows the number of identified minerals per spectrum. In most spectra, at least three minerals were identified through their diagnostic spectral features, while in nine samples only one mineral was identified.

Table IV. 11. The number of identified minerals per spectrum.

Minerlas per spectrum		
No. of minerals	**No. of spectrum**	**%**
1	9	4.21
2	59	27.57
3	113	52.80
4	27	12.62
5	6	2.80
Total	214	100

White mica is the most common mineral identified through its spectral properties, being present in more than half of the spectra, followed by chlorite (Table IV. 12).

Table IV. 12. Frequency in which a given mineral was identified in the analyzed spectra.

Mineral frequency	
Minerals	**No. of spectrum**
White mica	167
Chlorite	144
Carbonate	73
Kaolinite	62
Montmorillonite	31
Nontronite	25
Biotite	25
Water_silica (quartz)	24
Tourmaline	24
Jarosite	12
Gypsum	9
Nh4 white mica	1
Nh4 mineral	1

Equally, white mica features are dominant in more than half of the spectra. The second more dominant features are those of montmorillonite followed by chlorite (Table IV. 13).

Table IV. 13. Spectral contribution of minerals in each spectrum, reflecting the prevailing diagnostic features.

Predominance of diagnostic features		
Mineral	**No. of spectrum**	**%**
White mica	115	53.74
Montmorillonite	25	11.68
Chlorite	17	7.94
Tourmaline	14	6.54
Biotite	11	5.14
Kaolinite	9	4.21
Water_silica (quartz)	8	3.74
Jarosite	5	2.34
Gypsum	3	1.40
Nontronite	3	1.40
Nh4 mineral	1	0.47
Total	214	100

As shown in the following figures and tables, it was possible to detect changes in the mineral chemistry of white mica and chlorite. In the case of white mica, phengite has been reported to form as a consequence of either metamorphism or hydrothermal alteration processes[1]. Muscovitic tending to phengitic compositions are observed in the contact samples of the Feli and Alberto aplite-pegmatite dykes. Similarly, in the same locations, magnesium-bearing chlorites are observed near the contact with the mineralized dykes, while iron-richer chlorites in Bajoca are associated with lower Li contents. These correlations and their potential use for exploration need to be further investigated through mineral chemistry studies.

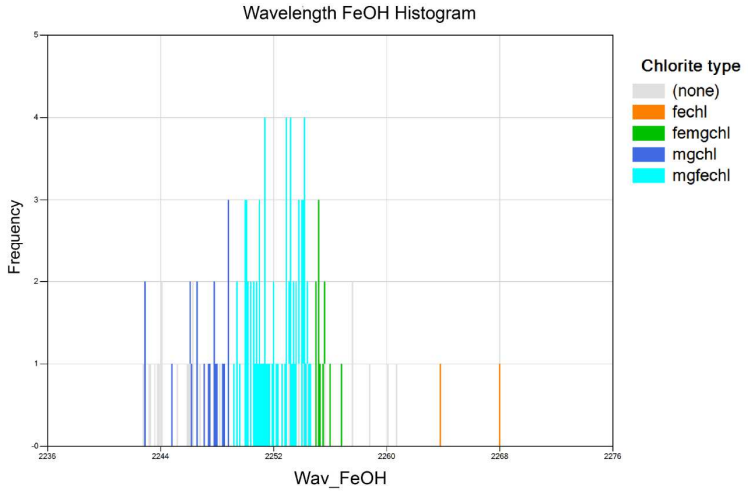

Figure IV 1. Distribution of the wavelength position of the FeOH absorption feature of chlorite and respective inferred composition. Wav – wavelength.

[1] Tappert, M. C., Rivard, B., Giles, D., Tappert, R., & Mauger, A. (2013). The mineral chemistry, near-infrared, and mid-infrared reflectance spectroscopy of phengite from the Olympic Dam IOCG deposit, South Australia. *Ore Geology Reviews, 53*, 26-38. doi: https://doi.org/10.1016/j.oregeorev.2012.12.006.

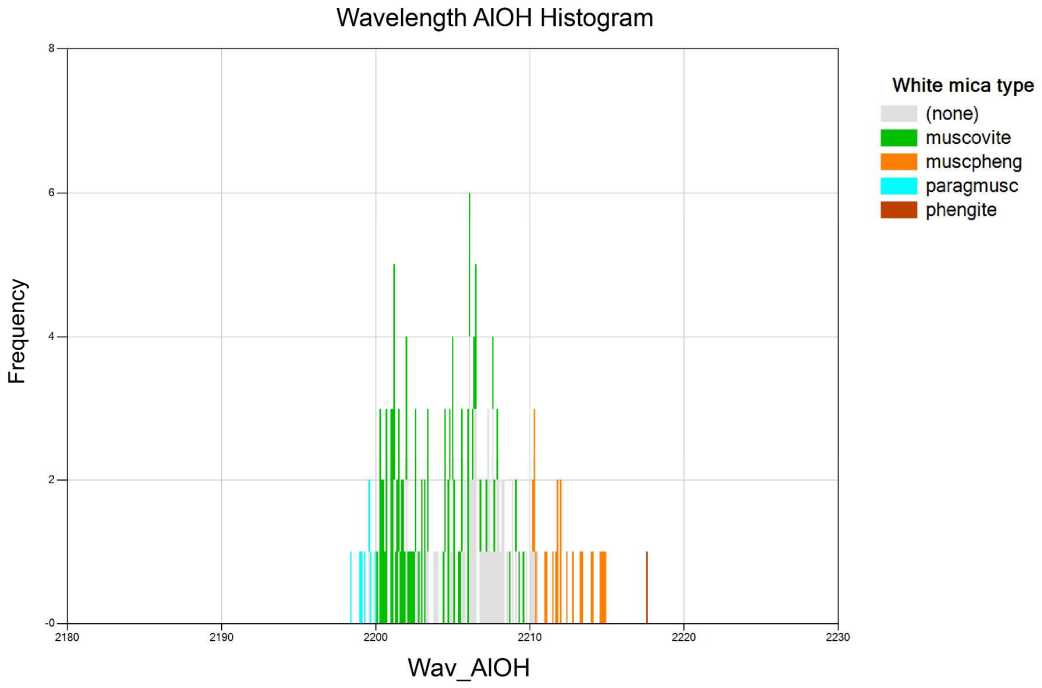

(a)

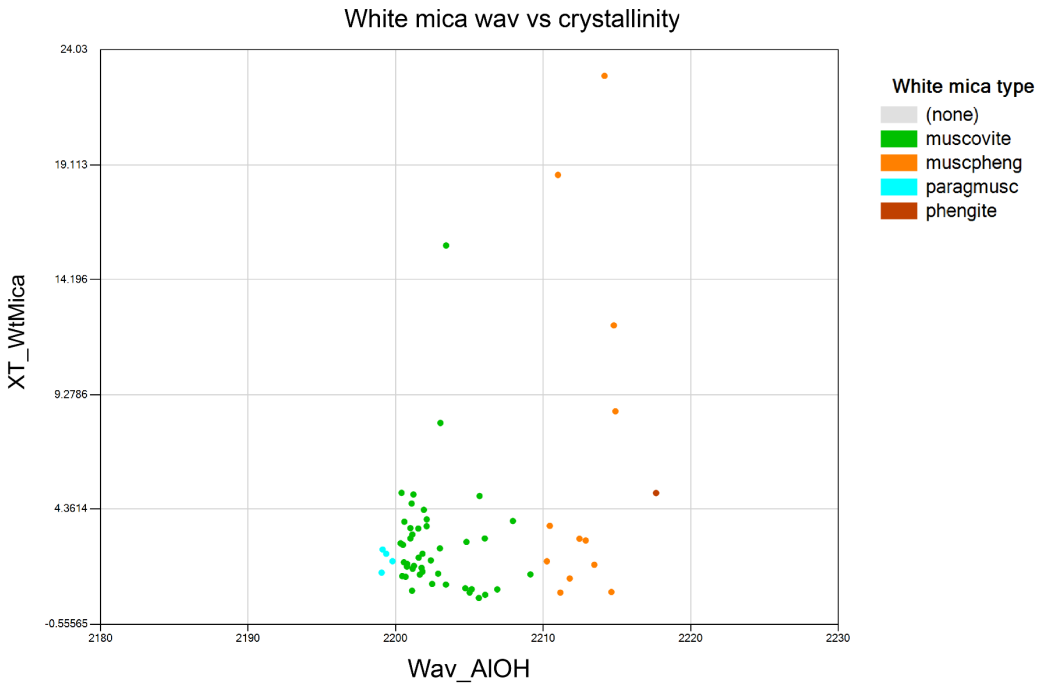

(b)

Figure IV 2. (a) Distribution of the wavelength position of the AlOH absorption feature of white mica and respective inferred composition. (b) Inferred white mica crystallinity and wavelength position of the AlOH absorption. Wav – wavelength; XT – crystallinity; WtMica – White mica.

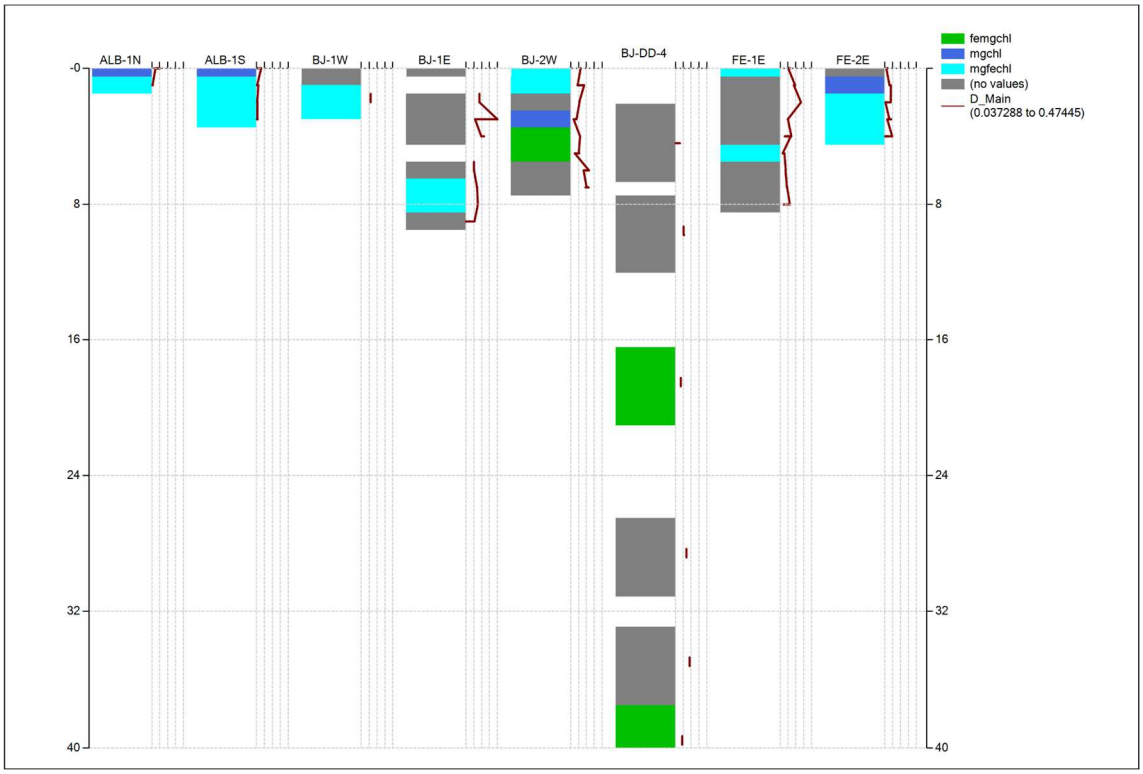

(a)

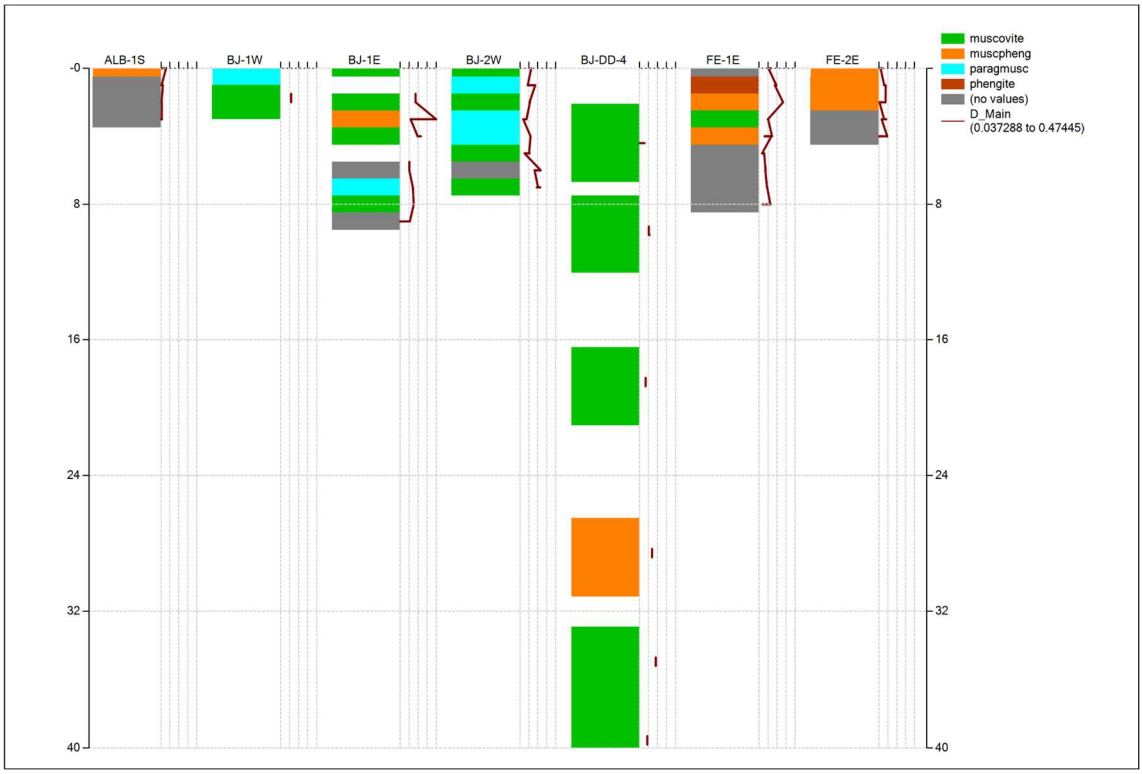

(b)

Figure IV 3. Inferred chlorite (a) and white mica (b) composition along with the sampling profiles. ALB – Alberto; BJ – Bajoca; FE – Feli; S – south; W -west; E – east; DD – diamond drilling; chl – chlorite; D_Main – the deepest feature between the AlOH-FeOH-MgOH absorption bands. Profiles not to scale, except for the drill core samples (BJ-DD-4).

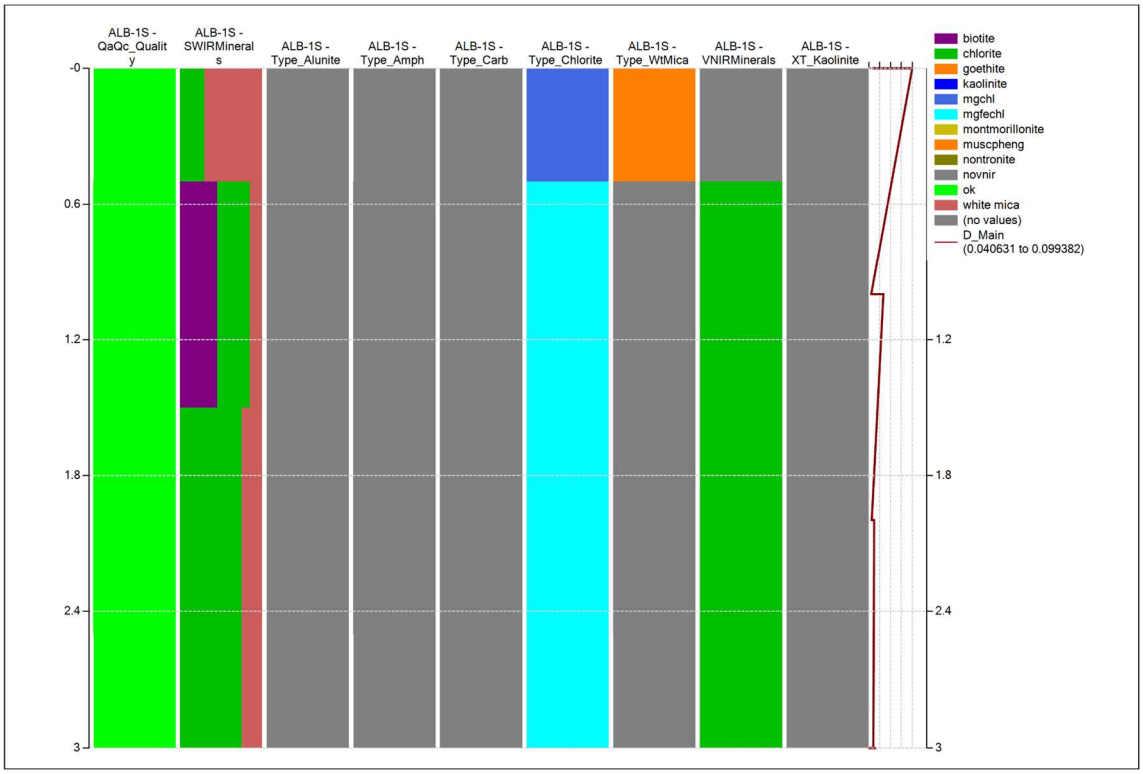

(a)

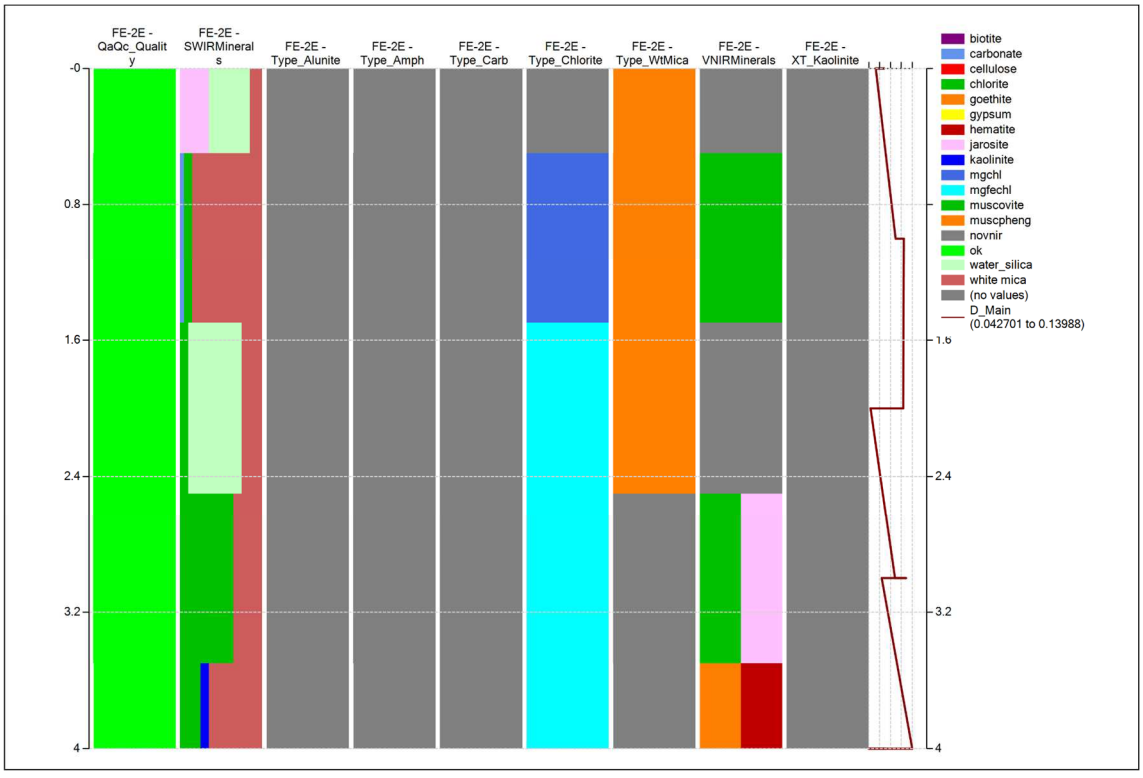

(b)

Figure IV 4. Detailed spectral summary of the two sampling profiles in the Alberto (a) and Feli (b) mines. ALB – Alberto; FE – Feli; S – south; E – east; QaQc – quality assurance and quality control; Amph – amphibolite; Carb – carbonates; WtMica – white mica; XT – crystallinity; D_Main – the deepest feature between the AlOH-FeOH-MgOH absorption bands. Profiles not to scale (fictitious distances).

Table IV. 14. presents (i) the mineral interpretation results with up to five minerals identified in the SWIR region and the list of minerals VNIR active minerals identified in each spectrum, (ii) the spectral quality assessment of each spectrum, (iii) the aiSIRIS estimated relative mineral percentages, i.e. relative Spectral Contribution (SC) of the minerals which were detected in the SWIR region and discrimination of the VNIR spectrally active minerals; and (iv) the spectral parameters extracted for each spectrum. This table is available at: https://docs.google.com/spreadsheets/d/1YA6Fm_aVKzm9jC9r2_nFKFq2Dsi0YO0s/edit?usp=sharing&ouid=109284842719792190654&rtpof=true&sd=true

Header information: The **HoleID** column corresponds to the sample group defined in Appendix IV.2.; **Reflectance** – measure of the average SWIR brightness of the sample; **QaQc_Reflec** – flags spectra with low and very low reflectance values; **SWIRNoise** – measure of the noisiness of the spectrum in the SWIR; **QaQc_Noise** – flags potentially noisy spectra; **QaQc_Quality** – assessment of the noise and reflectance to highlight spectrally flat spectra; **QaQc_Water** – flags spectra with water absorptions which may be associated with sample wetness or fluid inclusions; **Montmor** – montmorillonite; **Tourm** – tourmaline; **NH4WtMica** – ammonium-bearing white mica; **NH4Min** – ammonium-bearing minerals; **Hem** – hematite; **Goeth** – goethite; **Chl** – chlorite; **Wav_WtMica** – wavelength of the white mica AlOH absorption; **Type_WtMica** – probable white mica phase, based on Wav_WtMica data; **XT_WtMica** – crystallinity index for white mica; **Wav_Chlorite** – wavelength of the chlorite FeOH absorption; **Type_Chlorite** – probable chlorite phase, based on Wav_Chlorite; **XT_Kaolinite** – classification of kaolinite crystallinity, for samples that contain kaolinite (HXT – highly crystalline, MXT = moderately, PXT = poorly, DIS = disordered); **XT_Kaol2160, XT_Kaol2180** – parameters of kaolinite crystallinity using the slope around the 2160 and 2180 kandite features; **KaDiWtM** – index for differentiating between kaolinite, dickite and white mica; **Slope2160** – slope around the 2160 region for all spectra; **Wav_Main** – wavelength of the deepest absorption feature, spanning the AlOH, FeOH and MgOH regions; **D_Main** – depth of the deepest absorption feature, spanning the AlOH, FeOH and MgOH regions; **Wav_AlOH** – wavelength of the AlOH absorption; **D_AlOH** – depth of the AlOH absorption; **Wd_AlOH** – width of the AlOH absorption; **Wav_FeOH** – wavelength of the FeOH absorption; **D_FeOH** – depth of the FeOH absorption; **Wd_FeOH** – width of the FeOH absorption; **Wav_MgOHCb** – wavelength of the MgOH and/or carbonate absorption; **D_MgOHCb** – depth of the MgOH and/or carbonate absorption; **Wd_MgOHCb** – width of the MgOH absorption; **RelSmectite** – ratio of the depth of the water absorption (D_H2O) to the D_Main value; **Wav_OH1400** – wavelength of the deepest OH absorption; **D_OH1400** – depth of the deepest OH absorption; **Wd_OH1400** – width of the deepest OH absorption; **Wav_H2O** – wavelength of the water

absorption; **D_H2O** – depth of water absorption near 1900nm; **FeSlope** – slope of the spectrum into the ferrous iron absorption; **Int_FeOxide** – intensity of the charge transfer slope for iron oxide in the VNIR; **Wav_FeOxide** – wavelength of the iron oxide absorption; **D_FeOxide** – intensity of the iron oxide crystal field absorption of hematite and/or goethite; **FInt_FeOxide** – same as “Int_FeOxide” but filtered to show values ONLY where hematite or goethite are present.